From Membranes to Motor Oil: Exploring the Opportunities and Limitations of Phenoxazine and Phenothiazine Antioxidants by the Application of Fundamental Physical Organic Chemistry

Luke Farmer

A thesis submitted in partial fulfillment of the requirements for the degree of

Doctorate of Philosophy in Chemistry

Department of Chemistry and Biomolecular Sciences
Faculty of Science
University of Ottawa

© Luke Farmer, Ottawa, Canada, 2023

Abstract

Autoxidation is a radical mediated chain-process that involves initiation, propagation, branching and termination reactions and is responsible for the spontaneous peroxidation of hydrocarbons, formally appearing as RH + O_2 → ROOH. Autoxidation is a consequentially damaging process in many domains, ranging from materials to automotive transportation to biology and medicine. One of the key intermediates in the propagation of autoxidation is the peroxyl radical (ROO•) which can be targeted by radical-trapping antioxidants (RTAs) that promote chain-termination, mitigating the damage of autoxidation. Chapter 1 lays out the fundamental chemistry of both autoxidation and RTAs as well as a history of the rational design of phenol and diarylamine-type RTAs.

Lipid-peroxidation (i.e. autoxidation) is a key feature of ferroptosis which is a form of cell death that has been associated with many serious conditions such as ALS, Alzheimer's, Huntington's and Parkinson's disease, and lipid-soluble RTAs such as Vitamin E have been shown to acutely suppress ferroptosis. An aspect of RTA chemistry that has not been well studied/understood hitherto is their kinetic behaviour in phospholipid membranes, and we hypothesized that this would be a very relevant consideration for designing compounds that target lipid-peroxidation and ferroptosis. In Chapter 2 we systematically examine the kinetic behaviour for a series of hindered and unhindered phenolic RTAs in various mediums, particularly in phosphatidylcholine (PC) liposomes. The key chemical interaction in the PC membrane that fundamentally changed the observed kinetics of the phenolic RTAs is a very strong hydrogen-bonding interaction with the phosphate-diester headgroup that suppresses the phenols' ability to trap ROO•, an effect that was previously overlooked.

In Chapter 3 we further expanded/validated the model by studying over 40 phenoxazine (PNX) and phenothiazine-based (PTZ) RTAs, which showed the quantitative/predictive capabilities of the H-bonding effect. By introducing a water-soluble co-antioxidant, Vitamin C (ascorbate), we were able to study many features of the PNX/PTZ radical intermediates with respect to their reactivity and dynamics. The PNX/PTZ were far more persistent than the Vitamin E analogue 2,2,5,7,8-pentamethyl-6-chromanol (PMC), meaning that they catalytically trapped lipid-peroxyls far more efficiently (i.e., higher turnover number). Additionally, there is strong evidence suggesting that the PNX/ascorbate synergism is a diffusion-controlled process. The

study was further expanded to biological models. Ferroptosis *in vitro* was inhibited by every single one of these compounds, and there was a general positive correlation between RTA kinetics (k_{inh}) and ferroptosis rescue potency (EC_{50}) as well as a positive correlation between lipophilicity (logP) and ferroptosis rescue potency. A lead PNX compound, 3-trifluoromethyl-8-*tert*-butylphenoxazine, was identified in this study on the basis of superior potency and metabolic stability. When used to treat mice with GPx4 deletion in kidneys, an *in vivo* model of ferroptosis, it was found to extend the life of the mice in a statistically significant fashion compared to the vehicle control.

In Chapter 4 there is further elaboration on the dynamics of PNX/ascorbate synergy and a demonstration of the early works toward developing a drug-like-PNX ferroptosis inhibitor, based on the conclusions from the work in Chapter 3.

In Chapters 5 and 6 the research is focused on the development novel RTAs for the application of inhibiting autoxidation in lubricants in high temperature environments. Heavy machinery and most transportation technologies require lubrication to aid safe and efficient movement, and these lubricants/greases are highly susceptible to autoxidation. Large quantities of RTA additives are expended to extend the service life of these materials and there is a constant appetite for innovation to find new and improved RTAs for improved economics and competitiveness. In Chapter 5 the behaviour of PNX and PTZ in a simulated high temperature lubricant autoxidations are analyzed, revealing that PNX is highly susceptible to direct O_2-mediated oxidation due to its rapid electron-transfer kinetics, while PTZ is far more resilient despite both compounds having nearly identical oxidation potentials. In Chapter 6, in this same context, previously unreported substituent effects are analyzed which significantly enhance the period of inhibition (t_{inh}) for PTZ compounds. Particular alkyl substituents on the PTZ can increase the number of chains-trapped at high temperatures by fortuitous substituent oxidation that promotes termination, substantially improving their atom-economy. These findings prompt a broader critique of putative catalytic RTA mechanisms which have been taken for granted for nearly three decades.

Acknowledgements

During my tenure as a graduate student, I have had the immense pleasure of working with many kind, courteous and interesting colleagues, so numerous that I hope I do not overlook anyone. In no particular order, I would like to thank Dr. Jean-Phillipe Chauvin, Dr. Zosia Zielinski, Dr. Ron Shah, Omkar Zilka, Kareem Harrison, Emily Schaefer, Katie Shirley, Anthony Van Kessel, Dr. Evan Haidasz, Dr. Markus Griesser, Dr. Jia-Fei Poon, Dr. Demar Pitter, Melodie Mallais, Derek Meng, Neill Penner, Dr. Pierre Faudot dit Bel, Dr. Mark Raycroft, Dr. Manuel Petroselli, Dr. Zijun Wu, Dr. Alireza Dehdari, Dr. Nayal Onkar, Dr. Aditya Upadhyay, Dr. Julian Helberg, Dr. Carly Hanson, Matthew Dods, Eda Kilic, Lulu, Matthew Chebet, Michael Donohoe, Jacob Leong and Amr Al-Farhan. All of you in your unique way have enriched my graduate school experience. I would also like to thank my colleagues from the Gagosz Lab for making me feel especially welcome in their lab and patiently offering to show me how to use their TLC-MS, microwave reactor and glovebox.

Secondly, I would like to thank my supervisor and mentor Prof. Derek Pratt for all his support over the years. Not only did he provide an environment for me to explore the amazing world of organic chemistry, he has also been influential in the development of my scientific philosophy and writing craft, and I hope that some of that comes through in the work you are about to read. He has also been very accommodating over the years, not only in overlooking my foibles and eccentricates, but also by being supportive and understanding of my role as a new father.

Which brings me to the most important acknowledgements. Words cannot describe my love and gratitude to my wife Carly Farmer who has been ever supportive in all of my endeavours, to my son Tobi who has brought me joy and has made glad my heart, to my parents Pam and Brian who fostered my love of science in my formative years and to the rest of my family whose encouragement and prayers have been the music of my life.

Finally, I would like to dedicate the research contained in Ch. 2, 3 and 4 to my cousin Justin and my late cousin Sarah Diane and their family (Scott, Faith, Jenifer and Devin). While no one can change what has passed, your longsuffering continues to push me forward to a brighter tomorrow.

Statement of Originality

I hereby declare that the research in this document is the original work of the author, Luke Farmer, expect for contributions from fellow researchers (both published and unpublished) which are explicitly identified in the form of statements in a chapter's "Preface" or citations to published work found in the "References" section.

Luke Farmer

Published Works Resulting from My PhD Research

The research presented in Chapter 2 first appeared in:

1. Shah, R.; Farmer, L. A.; Zilka, O.; Van Kessel, A. T. M.; Pratt, D. A. Beyond DPPH: Use of Fluorescence-Enabled Inhibited Autoxidation to Predict Oxidative Cell Death Rescue. *Cell Chem. Biol.* **2019**, *26* (11), 1594-1607.e7. https://doi.org/10.1016/j.chembiol.2019.09.007.

But has been rewritten and expanded for this present work. The research in Chapter 3 and Chapter 5 have been reproduced/adapted from:

2. Farmer, L. A.; Wu, Z.; Poon, J.-F.; Zilka, O.; Lorenz, S. M.; Huehn, S.; Proneth, B.; Conrad, M.; Pratt, D. A. Intrinsic and Extrinsic Limitations to the Design and Optimization of Inhibitors of Lipid Peroxidation and Associated Cell Death. *J. Am. Chem. Soc.* **2022**, *144* (32), 14706–14721. https://doi.org/10.1021/jacs.2c05252.

3. Poon, J.-F.; Farmer, L. A.; Haidasz, E. A.; Pratt, D. A. Temperature-Dependence of Radical-Trapping Activity of Phenoxazine, Phenothiazine and Their Aza-Analogues Clarifies the Way Forward for New Antioxidant Design. *Chem. Sci.* **2021**, *12* (33), 11065–11079. https://doi.org/10.1039/D1SC02976B.

Respectively, in full or in part with permission. Finally, in collaboration with Cheng Yang under the supervision of Prof. Corey Stephenson and Prof. Stephen Maldonado, I (under the supervision/direction of Prof. Derek Pratt) rendered assistance in resolving a longstanding conundrum with respect to the mechanism of decomposition of phthalimide-*N*-oxyl (PINO) radicals, which are used in catalytic oxidations:

4. Yang, C.; Farmer, L. A.; Pratt, D. A.; Maldonado, S.; Stephenson, C. R. J. Mechanism of Electrochemical Generation and Decomposition of Phthalimide-N-Oxyl. *J. Am. Chem. Soc.* **2021**, *143* (27), 10324–10332. https://doi.org/10.1021/jacs.1c04181.

This, however, was not included in the present work as it was incongruent with the overall theme of the rest of the thesis.

Table of Contents

Chapter 1 – Introduction to Autoxidation and Radical-Trapping Antioxidants..... 1

1.1 Foreword 1

1.2 Autoxidation 3

1.2.1 Initiation and Chain Branching 3

1.2.2 Propagation 8

1.2.3 Termination 14

1.2.4 Methods of Measurement 16

1.3 Radical-Trapping Antioxidants 20

1.3.1 Reactivity of Radical-Trapping Phenols and Aromatic Amines: Electronic and Steric Substituent Effects 25

1.3.2 Reactivity of Radical-Trapping Phenols and Aromatic Amines: Medium Effects 40

1.4 Ferroptosis, Lipid Peroxidation, Vitamin E and Other RTAs in Biology and Medicine 45

1.5 Research Objectives 49

1.6 References 51

Chapter 2 – Quantification of Kinetic Medium Effects on Hindered Phenol Radical-Trapping Antioxidants in a Phospholipid Membrane 62

2.1 Foreword 62

2.2 Introduction 63

2.3 Results 65

2.4 Discussion 73

2.5 Conclusion 78

2.6 References 79

2.7 Materials and Synthesis 83

2.8 Methods and Supplementary Data 85

2.9 References (Experimental) 115

Chapter 3 – Intrinsic & Extrinsic Limitations to the Design and Optimization of Inhibitors of Lipid Peroxidation and Associated Cell Death 117

3.1 Foreword 117

3.2 Abstract 118

3.3 Introduction 118

3.4 Results 121

3.4.1 RTA Activity in a Phospholipid Membrane: Suppression due to H-Bonding can be Severe, but is Generally Predictable. 121

3.4.2 Synergy with Ascorbate Boosts Efficacy and Enables Kinetic Measurements for the Most Potent RTAs. 127

3.4.3 Ferroptosis Inhibition, First-Pass Metabolic Stability and Validation in Vivo. 133

3.5 Discussion 136

3.6 Conclusion 145

3.7 References 147

3.8 Methods and Protocols 154

3.9 Supplementary Data 165

3.9.1 Kinetic Data 166

3.9.2 Cell, Microsome and Animal Data 183

3.10 Materials and Synthesis 191

3.11 References (Experimental) 216

Chapter 4 – Toward a Phenoxazine RTA Drug Candidate 218

4.1 Foreword 218

4.2 Introduction 218

4.3 Results and Discussion 222
4.4 Prospectus and Conclusions 227
4.5 References 235
4.6 Synthesis 237
Chapter 5 – Temperature-Dependence of Radical-Trapping Activity of Phenoxazine, Phenothiazine and Their Aza-Analogues 249
5.1 Foreword 249
5.2 Abstract 250
5.3 Introduction 250
5.4 Results 252
5.5 Discussion 259
5.6 Conclusion 265
5.7 References 266
5.8 Materials/Synthesis 269
5.9 Methods 270
5.10 Supplementary Data 273
5.11 References (Experimental) 286
Chapter 6 – Enhancing High Temperature Efficiency of Phenoxazine/Phenothiazine-Type Radical-Trapping Antioxidants: Teeing-Up Alkyl-Sidechains to be Co-Reductants 287
6.1 Foreword 287
6.2 Introduction 287
6.3 Results 291
6.4 Discussion 305
6.5 Conclusion and Prospectus 311
6.6 References 313

6.7 Materials/Synthesis 317
6.8 Methods 334
6.9 Supplementary Data 336
6.10 References (Experimental) 361
Chapter 7 (Appendix) 362
7.1 Chapter 2 NMR Spectra 362
7.2 Chapter 3 NMR Spectra 367
7.3 Chapter 4 NMR Spectra 483
7.4 Chapter 6 NMR Spectra 520
7.5 Chapter 5 Cartesian Coordinates for CBS-QB3 587
7.6 Chapter 6 Cartesian Coordinates for DFT (M062X/cc-pVTZ) 600

Table of Figures, Schemes & Tables

Figure 1.1. (A) Representative BODIPY co-autoxidation traces with no inhibition (black), an RTA with a low k_{inh} (red) and an RTA with a high k_{inh} (blue). (B) A scheme representing the competition between substrate oxidation and RTA-driven peroxyl termination. 24

Figure 1.2. The Evans-Polanyi relationship between BDE_{O-H}/ BDE_{N-H} and the peroxyl inhibition rate constants for phenols and diarylamines. Thermodynamic data was taken from Lucarini and co-workers.[41,59,65] Kinetic data is from various sources.[45,58,65] 30

Figure 1.3. Systematic examples demonstrating the stereoelectronic lone pair donor effect. 33

Figure 1.4. (A) Pro-oxidant fate of 1,2,3,4-tetrahydro-6-hydroxy-5,7,8-trimethylquinoline by single electron-transfer to O_2. (B) Activated pyridinol and pyrimidinol-type RTAs by Pratt, Valgimigli and co-workers.[74,76,77] 35

Figure 1.5. (A) Planarity of phenoxazine and phenothiazine compared. (B) Peroxyl-PNX PCET transition-state. (C) Dissection of the resonance and inductive/field effects of the O-bridge on radical and radical-cation stability. 39

Figure 1.6. Comparison of the co-autoxidation of PBD-BODIPY (10 μM with 6 mM AIBN at 37 °C) with styrene, dioxane and dioxane w/ DMSO. For the 1:1 styrene/PhCl and 1:3 dioxane/PhCl systems, -d[BODIPY]/dt = 0 M s^{-1} when inhibited by PNX (2 μM). 43

Figure 1.7. An overview of the network of key systems involved with the promotion/suppression of ferroptosis laid out by Dixon and Pratt (2023).[120] Reproduction of this figure is in accordance with the license explicitly granted by the publisher (Elsevier). 48

Figure 2.1. (A) Competition between STY/PBD-BODIPY and RTA for propagation vs. inhibition. (B) Example of inhibited (and uninhibited) co-autoxidation of STY-BODIPY in PBS Buffer (pH 7.4, 10 mM) with 100nm unilamellar Egg-PC liposomes (1 mM) initiated by V70 at 37 °C (monitored by absorbance loss at 565nm). (C) Structures of initiators and phenolic RTAs. 67

Figure 2.2. (A) Demonstration of ^{1}H NMR method of determining $\alpha 2H$ values. (B) Demonstration of ^{19}F NMR method of measuring K_f between 4-fluorophenol and PC in CCl_4.. 69

Figure 2.3. (Left) The log$kinhS$ plotted against the $\beta 2H$ of each respective system. (Right) The $\alpha 2H$ determinations by the NMR and KSE methods compared *and* the EC_{50} for recusing pfa-1 cells from RSL3 induced ferroptosis. 72

Figure 2.4. (A) Proposed model of H-bonding of phenols in a phospholipid membrane. Shown are the proposed behaviours for "unhindered" phenols (top) and of very hindered phenols (bottom). (B) Scheme representing the proposed steric clash that is present for 2.6 but not 2.5. (C) Estimates of the rate constants that would be expected in an inhibited liposome autoxidation assuming a $\beta 2H$ of 0.79, using $kinhPhCl$ from the literature.[27] 74

Figure 2.5. Estimates of the rate constants that would be expected in an inhibited liposome autoxidation assuming a $\beta 2H$ of 0.79, using rate constants of inhibition in organic solutions obtained from the literature.[9,19,20,26] 78

Figure 2.6. Uv-Vis spectra for 2-12 μM PBD-BODIPY (Left) and extinction coefficient for PBD-BODIPY in *m*-xylene, λ_{max} = 590 nm, ε = 124877 M^{-1} cm^{-1}. Average of three measurements. 87

Figure 2.7. Rate of PBD-BODIPY consumption as a function of concentration in *m*-xylene initiated by AIBN (6 mM). Reaction progress was monitored by absorbance at 590nm (124877 M^{-1} cm^{-1}). The $kPBD-BODIPY$ was calculated to be 2426 M^{-1} s^{-1} assuming $2kt$ is equivalent to the peroxyl of *m*-xylene (3×10^8 M^{-1} s^{-1})[8] and Ri is 2.1×10^{-9} M s^{-1} (see Figure 2.7). 87

Figure 2.8. Co-autoxidation of PBD-BODIPY (10 μM) in *m*-xylene at 37ºC initiated with AIBN (6 mM). Reaction progress was monitored by absorbance at 590nm (124877 M^{-1} cm^{-1}). *Ri* ($2.1 \pm 0.1 \times 10^{-9}$ M s^{-1}) was determined from the t_{inh} of PMC (2 μM) assuming n = 2. 88

Figure 2.9. Uv-Vis spectra for 2-12 μM PBD-BODIPY (Left) and extinction coefficient for PBD-BODIPY in THF, λ_{max} = 583 nm, ε = 118510 M^{-1} cm^{-1}. Average of three measurements. 89

Figure 2.10. Rate of PBD-BODIPY consumption as a function of concentration in THF initiated by AIBN (6 mM). Reaction progress was monitored by absorbance at 583nm (118510 M^{-1} cm^{-1}). The $kPBD-BODIPY$ was calculated to be 3324 M^{-1} s^{-1} assuming $2kt$ is equivalent to the peroxyl of THF (3.1×10^7 M^{-1} s^{-1})[9] and Ri is 2.4×10^{-9} M s^{-1} (see Figure 2.11). 89

Figure 2.11. Co-autoxidation of PBD-BODIPY (10 μM) in THF at 37ºC initiated with AIBN (6 mM). Reaction progress was monitored by absorbance at 583nm (118510 M^{-1} cm^{-1}). *Ri* (2.4 ± 0.2 × 10^{-9} M s^{-1}) was determined from the t_{inh} of PMC (4 μM) assuming n = 2. 90

Figure 2.12. Co-autoxidation of PBD-BODIPY (10 μM) in 2.9 M hexadecene in chlorobenezene at 37ºC initiated with AIBN (8 mM). Reaction progress was monitored by absorbance at 588nm (139163 M^{-1} cm^{-1}). *Ri* (1.2 ± 0.1 × 10^{-9} M s^{-1}). (TOP) Uninhibited (black); 2 μM 2.2 (blue); 2 μM 2.4 (green); 2 μM 2.5 (navy); (BOTTOM) 10 μM 2.1 (orange). 91

Figure 2.13. Co-autoxidation of PBD-BODIPY (10 μM) in *m*-xylene at 37ºC initiated with AIBN (6 mM). Reaction progress was monitored by absorbance at 590nm (124877 M^{-1} cm^{-1}). *Ri* (2.1 ± 0.1 × 10^{-9} M s^{-1}). (TOP) Uninhibited (black); 4 μM 2.2 (blue); 2 μM 2.3 (magenta); 2 μM 2.4 (green); (BOTTOM) 2 μM 2.5 (navy); 10 μM 2.6 (purple); 12 μM 2.1 (orange)..... 92

Figure 2.14. Co-autoxidation of PBD-BODIPY (10 μM) in 2.9 M 1,4-dioxane in chlorobenzene at 37ºC initiated with AIBN (6 mM). Reaction progress was monitored by absorbance at 587nm (123023 M^{-1} cm^{-1}). *Ri* (3.1 ± 0.1 × 10^{-9} M s^{-1}). (TOP) Uninhibited (black); 4 μM PMC (red); 10 μM 2.2 (blue); 10 μM 2.3 (magenta); (BOTTOM) 10 μM 2.4 (green); 10 μM 2.5 (navy); 10 μM 2.6 (Purple); 100 μM 2.1 (orange). 93

Figure 2.15. Co-autoxidation of PBD-BODIPY (10 μM) in THF at 37ºC initiated with AIBN (6 mM). Reaction progress was monitored by absorbance at 583nm (118510 M^{-1} cm^{-1}). *Ri* (2.4 ± 0.2 × 10^{-9} M s^{-1}). (TOP) Uninhibited (black); 30 μM 2.2 (blue); 8 μM 2.3 (magenta); 8 μM 2.4 (green); (BOTTOM) 8 μM 2.5 (navy); 8 μM 2.6 (purple); 100 μM 2.1 (orange)..... 94

Figure 2.16. Co-autoxidation of PBD-BODIPY (10 μM) in 2.9 M 1,4-dioxane in a 1:1 mixture of DMSO and chlorobenzene at 37ºC initiated with AIBN (6 mM). Reaction progress was monitored by absorbance at 587nm (118217 M^{-1} cm^{-1}). *Ri* (3.1 ± 0.1 × 10^{-9} M s^{-1}). (TOP) Uninhibited (black); 20 μM PMC (red); 50 μM 2.2 (blue); 20 μM 2.3 (magenta); (BOTTOM) 20 μM 2.4 (green); 20 μM 2.5 (navy); 20 μM 2.6 (purple); 400 μM 2.1 (orange). 95

Figure 2.17. DTUN initiated co-autoxidations (0.2 mM) of STY-BODIPY (1 μM; k_{BODIPY} = 894 M^{-1} s^{-1}) in egg PC liposomes (1 mM) monitored by fluorescence ($\lambda_{ex}/\lambda_{em}$ = 488/518 nm). (TOP) Uninhibited (black); 4 μM 2.2 (red); 4 μM 2.3 (blue); 4 μM 2.4 (magenta); 4 μM 2.5 (dark green); 4 μM 2.6 (navy); (BOTTOM) 4 μM PMC (wine); 100 μM 2.1 (light green)..... 96

Figure 2.18. (TOP) Linear regression of Eq. 2.10 for 2.1: $y = 0.972x + 0.532$; R^2 = 1.000; ($\alpha 2H = 0.53$). (BOTTOM) For 2.2: $y = 0.987x + 0.460$; R^2 = 1.000; ($\alpha 2H = 0.46$). 99

Figure 2.19. (TOP) Linear regression of Eq. 2.10 for 2.3: $y = 0.993x + 0.400$; R^2 = 1.000; ($\alpha 2H = 0.40$). (BOTTOM) For 2.4: $y = 0.994x + 0.393$; R^2 = 1.000; ($\alpha 2H = 0.39$). 100

Figure 2.20. (TOP) Linear regression of Eq. 2.10 for 2.5: $y = 0.991x + 0.383$; R^2 = 1.000; ($\alpha 2H = 0.38$). (BOTTOM) For 2.6: $y = 1.020x + 0.207$; R^2 = 1.000; ($\alpha 2H = 0.21$). 101

Figure 2.21. ^{1}H NMR of 2.1 in benzene-d_6 (top) and DMSO-d_6 (bottom). The phenolic O-H is highlighted. 103

Figure 2.22. ^{1}H NMR of 2.2 in benzene-d_6 (top) and DMSO-d_6 (bottom). The phenolic O-H is highlighted. 104

Figure 2.23. ^{1}H NMR of 2.3 in benzene-d_6 (top) and DMSO-d_6 (bottom). The phenolic O-H is highlighted. 105

Figure 2.24. ^{1}H NMR of 2.4 in benzene-d_6 (top) and DMSO-d_6 (bottom). The phenolic O-H is highlighted. 106

Figure 2.25. ^{1}H NMR of 2.5 in benzene-d_6 (top) and DMSO-d_6 (bottom). The phenolic O-H is highlighted. 107

Figure 2.26. ^{1}H NMR of 2.6 in benzene-d_6 (top) and DMSO-d_6 (bottom). The phenolic O-H is highlighted. 108

Figure 2.27. ^{19}F NMR of 4-fluorophenol (0.01 M) and 4-fluoroanisole (0.01 M) in CCl_4 in the absence of PLPC (top) and at 0.005 M PLPC (bottom). 111

Figure 2.28. ^{19}F NMR of 4-fluorophenol (0.01 M) and 4-fluoroanisole (0.01 M) in CCl_4 with 0.010 M (top) and 0.015 M PLPC (bottom). 112

Figure 2.29. ^{19}F NMR of 4-fluorophenol (0.01 M) and 4-fluoroanisole (0.01 M) in CCl_4 with 0.020 M (top) and 0.030 M PLPC (bottom). 113

Figure 2.30. ^{19}F NMR of 4-fluorophenol (0.01 M) and 4-fluoroanisole (0.01 M) in CCl_4 with 0.200 M PLPC. 114

Figure 3.1. (A) The autoxidation of polyunsaturated phospholipids leads to a loss in membrane integrity and drives ferroptosis. **(B)** The inhibition of lipid autoxidation (peroxidation) by radical-trapping antioxidants (RTAs) illustrated with BHT. **(C)** The range of reactivity of representative RTAs (phenolic and aminic) expressed in terms of their inhibition rate constants (k_{inh}) as measured in solution (chlorobenzene) at 37°C. 121

Figure 3.2. (A) Co-autoxidation of STY-BODIPY and PBD-BODIPY can be monitored by either absorbance or fluorescence. Inhibition rate constants (k_{inh}) and radical-trapping stoichiometries (n) are determined from the initial rates and duration of the inhibited periods using Eq. 1 and 2, respectively. **(B)** Representative data for azine-inhibited co-autoxidation of PBD-BODIPY (10 μM) and 1,4-dioxane (2.9 M) in chlorobenzene initiated with AIBN (6 mM) at 37°C and monitored at 587 nm (123 000 M^{-1} cm^{-1}). **(C)** Kinetic scheme for the suppression in azine RTA activity due to H-bonding interactions between the RTA and solvent, where $kinhS$ is the inhibition rate constant in a given solvent S, K^S is the equilibrium constant for formation of a 1:1 H-bonded complex between the RTA and solvent, and $kinh0$ is the inhibition rate constant in the absence of any H-bonding interactions. **(D)** Representative data for azine-inhibited co-autoxidation of PBD-BODIPY (10 μM) and 1,4-dioxane (2.9 M) in 2:1 chlorobenzene:DMSO) initiated with AIBN (6 mM) at 37°C and monitored at 587 nm (118 200 M^{-1} cm^{-1}). **(E)** Representative data for azine-inhibited co-autoxidation of STY-BODIPY (1 μM) and liposomal egg phosphatidylcholine (1 mM) suspended in phosphate-buffered saline (PBS, pH 7.4) initiated with MeOAMVN (200 μM) at 37°C and monitored by fluorescence ($\lambda_{ex}/\lambda_{em}$ = 488/518 nm). **(F)** *Top*: Correlation of log$kinh0$ and log$kinhlip$ (N=29; R^2=0.417). *Bottom*: Correlation of log $(kinh0/8.3\alpha 2H)$ and log $(kinhlip/8.3\alpha 2H)$ (N=29; R^2=0.991).[44] **(G)** Predicted $kinhlip$ for RTAs which were too reactive for it to be determined directly. Values obtained using Eq 5 with experimental $kinh0$ and $\alpha 2H$ with $\beta 2H$ = 0.69. 125

Figure 3.3. (A) Proposed mechanism of catalytic trapping of phospholipid-derived peroxyl radicals by azine RTAs and ascorbate. **(B-F)** Representative data from co-autoxidations of STY-BODIPY (1 μM) and liposomal egg phosphatidylcholine (1 mM) suspended in PBS (pH 7.4) initiated with DTUN (200 μM) at 37°C and monitored by fluorescence ($\lambda_{ex}/\lambda_{em}$ = 488/518 nm). **(D-F)** Inhibited autoxidations were carried out with either 4 μM RTA (solid line) *or* 400 nM

RTA (dashed/dotted lines) with varying concentrations of ascorbate. **(G)** Summary of the radical-trapping stoichiometries and regeneration coefficients of the compound library. 129

Figure 3.4. (A) Correlation of *kinhlip* values determined from DTUN-initiated autoxidations of egg PC liposomes versus those determined (or predicted) from MeOAMVN-initiated autoxidations. MeOAMVN-initiated vs DTUN-initiated + 100 μM ascorbate (●); predicted from Eq. 4 vs DTUN-initiated + 100 μM ascorbate (●); MeOAMVN-initiated vs DTUN -initiated without ascorbate (□). **(B)** Representative data from co-autoxidations of STY-BODIPY (1 μM) and liposomal egg phosphatidylcholine (1 mM) suspended in PBS (pH 7.4) initiated with DTUN (200 μM) at 37°C and monitored by fluorescence ($\lambda_{ex}/\lambda_{em}$ = 488/518 nm). *(Top)* 3,7-Me-PNX (**3.35**), 3,7-Et-PNX (**3.41**), 3,7-iPr-PNX (**3.42**) and 3,7-tBu-PNX (**3.34**) at 4 μM in the absence of ascorbate; *(Bottom)* aforementioned at 400 nM in the presence of 100 μM of ascorbate..... 132

Figure 3.5. (A-C) Examples of RSL3 induced ferroptosis of Pfa-1 MEFS inhibited by lipid soluble RTAs. **(D)** Results from liver microsomal stability experiments (BALB/c mouse). [a] 10 μM of compound (separated by RP-UPLC and monitored by PDA). [b] Compound at 1 μM (monitored by MS-ESI+) [c] [Fer-1] = 30 μM [d] Standard conditions: 0.5 mg/mL liver microsomes; 1 mM NADPH; 100 mM phosphate buffer (pH 7.4); 37°C. [e] Liver microsomes increased (1.0 mg/mL). [f] At 0.5 mg/mL, Fer-1 was undetectable at 5 min, decreased to 0.1 mg/mL microsomes where $t_{1/2}$ = 5.3 ± 0.1 min was observed. **(F)** Compound **3.11** delays acute renal failure induced by *Gpx4* deletion and extends survival of mice at dose levels of 10 mg/kg (n=5) and 20 mg/kg (n=6), respectively, compared to vehicle control treatment (n=10); median survival was calculated to be 15.5 and 16 days for 10 and 20 mg/kg, respectively, and 11.5 days for the vehicle-treated group; Log-rank (Mantel-Cox) test: p = 0.0005. **(G)** Western Blot analysis at Day 9 after Tamoxifen treatment confirms GPx4 deletion in kidneys of *ROSA26-CreER^{T2}; Gpx4$^{fl/fl}$* animals, *Gpx4$^{fl/fl}$*mice were used as controls. *ROSA26-CreER^{T2};Gpx4$^{fl/fl}$* animals treated with vehicle only showed significantly elevated levels of the kidney injury biomarker Kidney Injury Molecule-1 (KIM-1), compared to compound **3.11** treated mice. **(H)** Serum analysis of Tamoxifen-treated *ROSA26-CreER^{T2};Gpx4$^{fl/fl}$* mice at Day 9 shows a significant reduction in creatinine levels of compound **3.11** (n=9) versus vehicle treated mice (n=10) (p = 0.0275) as well as a decrease in blood urea nitrogen (BUN). **(I)** Histological analysis of kidneys by periodic acid–Schiff (PAS) staining of Tamoxifen-treated *ROSA26-CreER^{T2};Gpx4$^{fl/fl}$* animals showed

widespread tubular necrosis in the vehicle group, compared to compound **3.11** treatment (Day 9 after Tamoxifen induction). *Gpx4*$^{fl/fl}$ animals were included as control (scale bar 50 μm). 135

Figure 3.6. (**A)** The expected polarization of the transition state for H-atom transfer from substituted PNX and PTZ derivatives to peroxyl radicals. (**B**) $\Sigma\sigma p +$ vs log$kinh0$ for the 3 and 3,7-susbtituted PNX (♦) (R^2 = 0.977; y = -0.590x + 8.093) and PTZ (●) (R^2 = 0.983; y = -0.461x + 7.124). **(C)** $\Sigma\sigma p +$ vs log$kinhlip$ (initiated by MeOAMVN). Only compounds that could be measured directly (see Table 3.1). PNX (R^2 = 0.745) and PTZ (R^2 = 0.916). **(D)** The polarization of the H-bonding interaction between the substituted PNX and PTZ derivatives and phospholipids is expected to be opposite to the TS in (A). (**E**) $\Sigma\sigma p -$ vs $\alpha 2H$ for PNX (R^2 = 0.940; y = 0.103x + 0.459) and PTZ (R^2 = 0.991; y = 0.095x + 0.383). **(F)** $[(m1\Sigma\sigma p+) - 5.73(m2\Sigma\sigma p+)]$ vs log$kinhlip$ where m_1 and m_2 are the slopes from A and C respectively and 5.73 = 8.3$\beta 2H$ (assuming $\beta 2H$ = 0.69). PNX (R^2 = 0.907; y = 0.789x + 5.226) and PTZ (R^2 = 0.956; y = 1.016x + 4.822)..... 138

Figure 3.7. Values of log$kinh$ determined at 37°C plotted as a function of medium. PNX (black), PTZ (red), PSZ (green), 1,9-Me-PTZ **3.31** (blue), and 3,7-NO_2-PNX **3.19** (orange). Empty squares (□) correspond to values previously reported by Lucarini *et al* in benzene.[42] ... 139

Figure 3.8. (A) Multi-regression correlation for logEC50 vs log$kinhlip$ and log$P$ ($Radj2 = 0.796$; $\log EC50 = 0.550\log kinhlip + 0.297\log P + 3.631$). Empty symbols correspond to predicted values of EC_{50} from the estimated values of log$kinhlip$ given in Figure 3.2G. **(B)** Structures of compounds **3.43** and **3.44** and the predicted EC_{50} using $kinhlip$ (MeOAMVN) and log$P$.[55] [a] Estimated using Eq. 4. 143

Figure 3.9. (A) Representative ABIN initiated (6 mM; R_i = 2.40 × 10^{-9} M s^{-1}) PBD-BODIPY (10 μM; k_{BODIPY} = 5310 M^{-1} s^{-1}) and 1,4-dioxane (1:3 dioxane/PhCl; 37 °C) co-autoxidation monitored by loss of absorbance (λ_{max} = 587 nm; ε = 123 000 M^{-1} cm^{-1}) inhibited by **3.21** (2 μM; n = 2.2 ± 0.1; k_{inh} = (1.8 ± 0.1) × 10^6 M^{-1} s^{-1}). **(B)** MeOAMVN initiated co-autoxidation (0.2 mM; R_i = 2.55 × 10^{-9} M s^{-1}) of STY-BODIPY (10 μM; k_{BODIPY} = 894 M^{-1} s^{-1}) in egg PC liposomes (1 mM) monitored by loss of absorbance (λ_{max} = 565 nm; ε = 123 676 M^{-1} cm^{-1}) inhibited by **3.21** (6 μM; n = 3.1 ± 0.1; k_{inh} = (4.7 ± 0.1) × 10^4 M^{-1} s^{-1}). 160

Figure 3.10. (A) Representative MeOAMVN initiated (0.2 mM; $R_i = 9.14 \times 10^{-10}$ M s^{-1}) **(B)** and DTUN initiated co-autoxidations (0.2 mM; $R_i = 7.47 \times 10^{-10}$ M s^{-1}) of STY-BODIPY (1 μM; $k_{BODIPY} = 894$ M^{-1} s^{-1}) in egg PC liposomes (1 mM) monitored by fluorescence ($\lambda_{ex}/\lambda_{em}$ = 488/518 nm). Both were inhibited by 4 μM of **3.21** ($n = 3.5 \pm 0.1$; $k_{inh} = (4.4 \pm 0.6) \times 10^4$ M^{-1} s^{-1} and $n = 4.8 \pm 0.2$; $k_{inh} = (5.3 \pm 0.3) \times 10^4$ M^{-1} s^{-1} respectively.) **(C)** DTUN initiated co-autoxidation (0.2 mM; $R_i = 7.57 \times 10^{-10}$ M s^{-1}) of STY-BODIPY (1 μM) in egg PC liposomes (1 mM) with 10 μM ascorbic acid ($k_{BODIPY} = 563$ M^{-1} s^{-1}) and **(D)** with 100 μM ascorbic acid ($k_{BODIPY} = 191$ M^{-1} s^{-1}). Both were inhibited by 0.4 μM of **3.21** ($n = 24.8 \pm 0.5$; $k_{inh} = (6.9 \pm 0.2) \times 10^4$ M^{-1} s^{-1} and $n = 78.9 \pm 1.0$; $k_{inh} = (3.1 \pm 0.1) \times 10^4$ M^{-1} s^{-1} respectively.) 161

Figure 3.11. Representative ^{1}H NMR of phenoselenazine (PSZ) in DMSO-d_6 with the N-H proton highlighted (8.59 ppm). 163

Figure 3.12. Representative ^{1}H NMR of phenoselenazine (PSZ) in benzene-d_6 with the N-H proton highlighted (5.13 ppm). 164

Figure 3.13. Comparison of correlation of $\log(kinh0/8.3\alpha 2H)$ and $\log(kinhlip/8.3\alpha 2H)$ with and without **3.30** and **3.31**. If $\log kinhlip = -8.3\alpha 2H\beta 2H + \log kinh0$ is true, slope should be 1. 168

Figure 3.14. ABIN initiated (6 mM) PBD-BODIPY (10 μM) and 1,4-dioxane (1:3 dioxane/PhCl; 37 ºC) co-autoxidation monitored by loss of absorbance (λ_{max} = 587 nm; ε = 123 000 M^{-1} cm^{-1}) inhibited by various RTAs (**3.3**, **3.5**, **3.12**, **3.13**, **3.14**, **3.16**, **3.18**, **3.22**, **3.24**, **3.25**, **3.26**, **3.27**, **3.28**, **3.29** and **3.31**.) 169

Figure 3.15. ABIN initiated (6 mM) PBD-BODIPY (10-20 μM; $k_{BODIPY} = 5900$ M^{-1} s^{-1}) and 1,4-dioxane (1:2:1 dioxane/PhCl/DMSO; 37 ºC) co-autoxidation monitored by loss of absorbance (λ_{max} = 587 nm; ε = 118 200 M^{-1} cm^{-1}) inhibited by various RTAs (**3.4**, **3.7**, **3.8**, **3.10**, **3.11**, **3.18**, **3.35**, **3.36**, **3.37**, **3.38** and **3.44**.) Compound **3.18** was corrected for its change in absorbance due to the consumption of **3.18** (see Figure S16). 170

Figure 3.16. MeOAMVN initiated (0.2 mM) co-autoxidation of STY-BODIPY (10-20 μM) in egg PC liposomes (1 mM) monitored by loss of absorbance (λ_{max} = 565 nm; ε = 123 676 M^{-1} cm^{-1}) inhibited by various RTAs (**3.1**, **3.3**, **3.4**, **3.6**, **3.7**, **3.8**, **3.9**, **3.10**, **3.15**, **3.16**, **3.17**, and **3.18**.)171

Figure 3.17. MeOAMVN initiated (0.2 mM) co-autoxidation of STY-BODIPY (10-18 μM) in egg PC liposomes (1 mM) monitored by loss of absorbance (λ_{max} = 565 nm; ε = 123 676 M^{-1} cm^{-1}) inhibited by various RTAs (**3.20**, **3.22**, **3.23**, **3.24**, **3.25**, **PMC**, **3.34**, **3.35** and **3.36**.)..... 172

Figure 3.18. MeOAMVN initiated (0.2 mM) co-autoxidation of STY-BODIPY (1 μM) in egg PC liposomes (1 mM) monitored by fluorescence ($\lambda_{ex}/\lambda_{em}$ = 488/518 nm) inhibited by various RTAs (**PMC**, **3.1**, **3.2**, **3.3**, **3.4**, **3.5**, **3.6**, **3.7**, **3.8**, **3.9**, **3.10** and **3.11**.) 173

Figure 3.19. MeOAMVN initiated (0.2 mM) co-autoxidation of STY-BODIPY (1 μM) in egg PC liposomes (1 mM) monitored by fluorescence ($\lambda_{ex}/\lambda_{em}$ = 488/518 nm) inhibited by various RTAs (**3.12**, **3.13**, **3.14**, **3.20**, **3.24**, **3.25**, **3.26**, **3.27**, **3.28**, **3.29**, **3.30** and **3.31**.)..... 174

Figure 3.20. MeOAMVN initiated (0.2 mM) co-autoxidation of STY-BODIPY (1 μM) in egg PC liposomes (1 mM) monitored by fluorescence ($\lambda_{ex}/\lambda_{em}$ = 488/518 nm) inhibited by various RTAs (**3.32**, **3.33**, **3.34**, **3.35**, **3.36**, **3.37**, **3.38**, **3.39**, **3.40**, **3.41**, **3.42**, **3.43** and **3.44**.)..... 175

Figure 3.21. DTUN initiated (0.2 mM) co-autoxidation of STY-BODIPY (1 μM) in egg PC liposomes (1 mM) monitored by fluorescence ($\lambda_{ex}/\lambda_{em}$ = 488/518 nm) inhibited by various RTAs (**3.2**, **3.3**, **3.4**, **3.5**, **3.6**, **3.7**, **3.8**, **3.9**, **3.10**, **3.11**, **3.12**, and **3.13**.) No ascorbate (solid line); 10 μM ascorbate (dashed line); 100 μM ascorbate (dotted line). 178

Figure 3.22. DTUN initiated (0.2 mM) co-autoxidation of STY-BODIPY (1 μM) in egg PC liposomes (1 mM) monitored by fluorescence ($\lambda_{ex}/\lambda_{em}$ = 488/518 nm) inhibited by various RTAs (**3.14**, **3.15**, **3.16**, **3.17**, **3.18**, **3.19**, **3.22**, **3.23**, **3.24**, **3.25**, **3.26**, and **3.27**.) No ascorbate (solid line); 10 μM ascorbate (dashed line); 100 μM ascorbate (dotted line). 179

Figure 3.23. DTUN initiated (0.2 mM) co-autoxidation of STY-BODIPY (1 μM) in egg PC liposomes (1 mM) monitored by fluorescence ($\lambda_{ex}/\lambda_{em}$ = 488/518 nm) inhibited by various RTAs (**3.28**, **3.29**, **3.30**, **3.31**, **3.32**, **3.37**, **3.38**, **3.40**, **3.41**, **3.42**, **3.43**, and **3.44**.) No ascorbate (solid line); 10 μM ascorbate (dashed line); 100 μM ascorbate (dotted line). 180

Figure 3.24. Conditions: 1 mM Egg-PC liposomes in 10 mM PBS buffer (pH 7.4). **(A)** On account of the relatively high extinction coefficient of **3.18** from 450-600 nm, it interferes with the excitation/emission of the STY-BODIPY fluorescence assay at 4 μM of **3.18** (does not interfere significantly at 0.4 μM). **(B)** Under the STY-BODIPY absorbance assay the relative contribution to absorbance at 565 nm is minor. **(C)** Absorbance from 450-600 nm for **3.18**

decreases as the RTA is consumed (0.2 mM MeOAMVN, 37 ºC). To correct for this contribution, in parallel with the STY/PBD-BODIPY co-autoxidations inhibited by **3.18**, an identical parallel experiment in the absence of STY/PBD-BODIPY is carried out and the change of absorbance is subtracted from the co-autoxidation data. **(D)** MeOAMVN initiated (0.2 mM; R_i = 1.7 × 10^{-9} M s^{-1}) co-autoxidation of STY-BODIPY (18 μM) in egg PC liposomes (1 mM) monitored by loss of absorbance (λ_{max} = 565 nm; ε = 123 676 M^{-1} cm^{-1}) inhibited by **3.18** (corrected). 181

Figure 3.25. DTUN initiated (0.2 mM; R_i = 9.0 × 10^{-10} M s^{-1}) co-autoxidation of STY-BODIPY (16 μM) in egg PC liposomes (1 mM) monitored by loss of absorbance (λ_{max} = 565 nm; ε = 123 676 M^{-1} cm^{-1}) inhibited by **3.18** (corrected) and **3.17**. 182

Figure 3.26. Single/multi-variable linear regressions developed for the observed EC_{50} values (Table 3.5) of compounds **3.1**-**3.28** and **3.30**-**3.31** using Microsoft Excel the Analysis ToolPak add-in (the 'Regression' function; set to 95% confidence level). **(A)** Developed from observed |logEC_{50}| and measured log$kinhlip$ (MeOAMVN) (Table 3.3): |logEC_{50}| = 0.8116 log$kinhlip$ + 3.8575. **(B)** Developed from observed |logEC_{50}| and predicted log$P$ (Table 3.4): |logEC_{50}| = 0.3991 log$P$ + 5.6312. 184

Figure 3.27. RSL3 induced ferroptosis inhibited by both electron-rich (**3.2** and **3.32**) and electron-poor (**3.28** and **3.29**) phenothiazine derivatives. Compound **3.29** showed a decrease in apparent cell viability above 1000 μM. "Dummy-data points" (*) were used to generate the observed sigmoidal curve for **3.29**. 185

Figure 3.28. RSL3 induced ferroptosis (pfa-1 MEFS) inhibited by various RTAs (**3.3**, **3.4**, **3.5**, **3.6**, **3.7**, **3.8**, **3.9**, **3.10** and **3.12**.) 186

Figure 3.29. RSL3 induced ferroptosis (pfa-1 MEFS) inhibited by various RTAs (**3.13**, **3.14**, **3.16**, **3.17**, **3.18**, **3.20**, **3.21**, **3.22** and **3.23**.) 187

Figure 3.30. RSL3 induced ferroptosis (pfa-1 MEFS) inhibited by various RTAs (**3.24**, **3.25**, **3.26**, **3.27**, **3.30**, **3.31**, **3.33**, **3.34**, **3.37**, **3.38**, **3.43** and **3.44**.) 188

Figure 3.31. Erastin (5 μM) induced ferroptosis in HT1080 (3000 cells per well) inhibited by PTZ, PNX, **3.43** and **3.44** over 26 hours. 189

Figure 3.32. (A) Representative UPLC traces for quantification by PDA (253 nm) of analyte (PTZ) remaining during the liver microsome stability assay relative to 0 min, normalized to the HPLC/internal standard (**3.25**). **(B-D)** Conditions: 0.5 mg/mL liver microsomes; 1 mM NADPH; 100 mM phosphate buffer (pH 7.4); 37ºC, 10 μM RTA. **(E)** Conditions: 1.0 mg/mL liver microsomes; 1 mM NADPH; 100 mM phosphate buffer (pH 7.4); 37ºC, 10 μM **3.11**. 190

Figure 3.33. *ROSA26-CreER^{T2};Gpx4$^{fl/fl}$ and Gpx4$^{fl/fl}$* mice were injected with Tamoxifen on day 0 and 2 to induce deletion of *Gpx4*. Surviving animals were sacrificed on day 25 after daily treatment with **3.11** at a dose of 20 mg/kg. Western blot analysis of kidneys confirms knockout of GPx4. Kidney Injury Molecule-1 (KIM-1) was used as a biomarker for kidney injury. 191

Figure 4.1. (A) Co-autoxidation of STY-BODIPY (1 μM) in 100 nm L-α-phosphatidylcholine liposomes (1 mM) suspended in pH 7.4 PBS initiated by DTUN (200 μM) (dashed lines with 10 μM ascorbic acid). Concentrations of PNX (blue) of 50, 100, 200, and 400 nM (t_{inh} of 1893 ± 56 s, 3487 ± 59 s, 7539 ± 103 s and 15290 ± 400 s, respectively) and PMC (red) at 400 nM (t_{inh} = 5015 ± 220 s). $R_i = 7.57 \times 10^{-10}$ M s^{-1}. (B) Free energy of hydroperoxyl addition to PMC and PNX derived radicals (according to CBS-QB3).[2] 219

Figure 4.2. (A) Proposed interfacial/inter-phase effects on PNX/ascorbate synergy. (B) Key examples of the proposed orientation effect, comparing lipophilic substituents at the 3,7 and 2,8-positions. 221

Figure 4.3. DTUN initiated (200 μM) co-autoxidation of STY-BODIPY (1 μM) in Egg-PC liposomes with ascorbate (100 μM). (A) Inhibited by 400 nM **4.1** (red, $R_i = 7.50 \times 10^{-10}$ M s^{-1}) compared to **4.4a-4.6a** ($R_i = 8.52 \times 10^{-10}$ M s^{-1}). (B) Inhibition of 400 nM PMC (red) compared to **4.7-4.11** ($R_i = 9.77 \times 10^{-10}$ M s^{-1})..... 225

Figure 4.4. Concentration of **4.5a** found in plasma, liver, kidney, brain and spinal cord post-oral administration (10 mg/kg) in C57BL/6 mice monitored for up to 96 h (n = 3 for each timepoint). Converted from ng/mL or ng/g to nM (from a MW of 427.44 ng/nmol and assuming density of tissue ~1 g/mL). 228

Figure 4.5. (A) Linear behaviour of the DTUN/V70 initiated liposome autoxidation compared to a hypothetical exponential/branched model of behaviour that might occur in GPx4-inhibited

cells. (B) Minimizing chain-propagation early prevents many future propagation/branching events. 231

Figure 4.6. Potency of Edaravone and **4.5a** in the RSL3-induced pfa-1 ferroptosis rescue assay. 234

Figure 5.1. (A) Selected diarylamine RTAs and their corresponding inhibition rate constants (k_{inh}) measured in PhCl at 37 °C and standard potentials ($E°$) measured in CH_3CN *versus* NHE. (B) The Korcek cycle is proposed to account for the catalytic inhibition of diarylamines at elevated temperature. (C) The cross-dismutation of alkylperoxyl and hydroperoxyl radicals is catalysed by diarylnitroxides derived from diarylamines. 253

Figure 5.2. (A) A phosphine–coumarin conjugate enables the quantification of hydroperoxides produced during *n*-hexadecane autoxidation at 160 °C. (B) Hydroperoxide formation from the autoxidation of *n*-hexadecane at 160 °C in the presence of diphenylamine (DPA, 150 μM), PNX (150 μM), PTZ (150 μM), phenoxazine-*N*-oxyl (PNX-NO, 150 μM) and phenothiazine-*S*-oxide (PTZ-SO, 150 μM). (C) Structures of primary oxidation products derived from PNX and PTZ observed in the autoxidations. (D and E) Consumption of PNX and PTZ over the course of the autoxidations in (B) and corresponding formation of the products shown in (C) as determined by UPLC analysis. (F and G) EPR spectra of autoxidation samples withdrawn at 5400 s (top) and authentic PNX- and PTZ-derived nitroxides (bottom) recorded at 20 °C in 1 : 1 hexadecane/benzene.[20–22] 254

Figure 5.3. (A) Representative co-autoxidations of 1-hexadecene (2.68 M) and PBD-BODIPY (10 μM) initiated by dicumyl peroxide (1 mM) at 100 °C and inhibited by 2 μM 1-azaPNX, 2-azaPNX, 3-azaPNX, 4-azaPNX and PNX. (B) Corresponding autoxidations inhibited by 2 μM 1-azaPTZ, 2-azaPTZ, 3-azaPTZ, 4-azaPTZ and PTZ. Reactions were monitored at 587 nm (λ = 119 166 M^{-1} cm^{-1}). (C) RTA profiles of azaPNX and azaPTZ. (D and E) Nitroxide concentration monitored in representative autoxidations ([dicumyl peroxide] = 2 mM, $R_i = 1.2 \times 10^{-8}$ M s^{-1}) by EPR. 258

Figure 5.4. (A) CBS-QB3-calculated reorganisation energies (λ_i) for oxidation of PNX and PTZ and the structures of the minimum energy structures of the starting materials and radical cations highlighting the deviation from planarity of the starting structures. (B) Calculated free energy change for the reaction of phenothiazine-N-oxyl (PTZ-NO) with each of the phenothiazine

aminyl radical (top) and PTZ (bottom). (C) The oxidation of PTZ by PNX-NO. (D) UV-Vis spectra of PTZ, PNX-NO, and PTZ-SO in *n*-hexadecane at 100 °C. (E) Representative spectra acquired upon mixing PTZ (600 μM) and PNX-NO (300 μM) in *n*-hexadecane at 100 °C and corresponding initial rate plot derived from the increase at 278 nm corresponding to PTZ-SO (ε = 8667 M^{-1} cm^{-1}). 261

Figure 5.5. (A) Hydroperoxide formation from the autoxidation of *n*-hexadecane at 160 °C in the presence of 1 mM Primene and inhibited by 200 μM 1-azaPNX, 2-azaPNX, 3-azaPNX, 4-azaPNX and PNX. (B) Corresponding experiments inhibited by 200 μM 1-azaPTZ, 2-azaPTZ, 3-azaPTZ, 4-azaPTZ and PTZ. 264

Figure 5.6. *(Left)* Representative chromatogram of PNX-ONE standard (50 μM) monitored at 352 nm; *(Right)* UV-Vis spectrum of PNX-ONE standard. 273

Figure 5.7. *(Left)* Table of integrals of PNX-ONE standard monitored at 352 nm; *(Right)* Calibration curve for PNX-ONE at 352 nm (R^2 = 0.9995, y = 0.00191x + 0.3768). 273

Figure 5.8. (A) *Top*: Representative UPLC-PDA trace of unoxidized PNX extracted from hexadecane (monitored at 350 nm); *Bottom*: Representative UPLC-PDA trace of PNX derived products extracted from hexadecane from an intermediate state of autoxidation (monitored at 350 nm). (B) ESI+ spectra of 'Unknown 1' (UPLC-MS). (C) The integral of 'Unknown 1' overlayed with the time-course concentrations of [PNX] and [PNX-NO]. 274

Figure 5.9. *(Left)* Representative chromatogram of PTZ-ONE standard (50 μM) monitored at 370.5 nm; *(Right)* UV-Vis spectrum of PTZ-ONE standard. 276

Figure 5.10. *(Left)* Table of integrals of PTZ-ONE standard monitored at 370.5 nm; *(Right)* Calibration curve for PTZ-ONE at 370.5 nm (R^2 = 0.9998, y = 0.00264x – 1.3676). 276

Figure 5.11. *(Left)* Representative chromatogram of PTZ-SO standard (50 μM) monitored at 269.5 nm; *(Right)* UV-Vis spectrum of PTZ-SO standard. 277

Figure 5.12. *(Left)* Table of integrals of PTZ-SO standard monitored at 269.5 nm; *(Right)* Calibration curve for PTZ-SO at 269.5 nm (R^2 = 0.9998, y = 0.00179x - 0.9414). 277

Figure 5.13. *(Top)* Representative UPLC-PDA trace of unoxidized PTZ extracted from hexadecane (monitored at 350nm); *(Bottom)* Representative UPLC-PDA trace of PTZ derived

products extracted from hexadecane from an intermediate state of autoxidation (monitored at 350nm). 278

Figure 5.14. *(Top)* ^{1}H-NMR (400 MHz; benzene-d_6) of 30 mM PNX-H stock solution; *(Bottom)* ^{1}H-NMR (400 MHz; benzene-d_6) of 30 mM PNX-D stock solution. 280

Figure 5.15. Time-course loss of PNX-H/PNX-D overlayed with [ROOH] from the autoxidation of n-hexadecane inhibited by 300 μM PNX-H/PNX-D at 160 °C..... 281

Figure 5.16. *(Left)* Kinetic UV-Vis scan (225 to 500 nm) of 300 μM PNX-NO in hexadecane at 80 °C; *(Right)* Kinetic UV-Vis scan (225 to 500 nm) of 300 μM PNX-NO with 600 μM PTZ in hexadecane at 80 °C. 282

Figure 5.17. Observing the increase of absorbance at 278 nm (ε_{278} = 9129 M^{-1} cm^{-1}) with 300 μM PNX-NO at various concentrations of PTZ in hexadecane at 80 °C. *(Right)* Molar-absorptivity plot of PTZ-SO at 278 nm in hexadecane at 80 °C (ε_{278} = 9129 M^{-1} cm^{-1}). 283

Figure 5.18. *(Left)* Observing the increase of absorbance at 278 nm (ε_{278} = 9004 M^{-1} cm^{-1}) with 300 μM PNX-NO at various concentrations of PTZ in hexadecane at 85 °C; *(Right)* Observing the increase of absorbance at 278 nm (ε_{278} = 8886 M^{-1} cm^{-1}) with 300 μM PNX-NO at various concentrations of PTZ in hexadecane at 90 °C. 283

Figure 5.19. *(Left)* Observing the increase of absorbance at 278 nm (ε_{278} = 8784 M^{-1} cm^{-1}) with 300 μM PNX-NO at various concentrations of PTZ in hexadecane at 95 °C; *(Right)* Observing the increase of absorbance at 278 nm (ε_{278} = 8867 M^{-1} cm^{-1}) with 300 μM PNX-NO at various concentrations of PTZ in hexadecane at 100 °C. 284

Figure 5.20. *(Left)* UV-Visible spectrum of PTZ-SO; *(Right)* Molar-absorptivity plot of PTZ-SO at 278 nm in hexadecane at 80 °C (ε_{278} = 9129 M^{-1} cm^{-1}). 285

Figure 5.21. *(Left)* Table of rate constants for PTZ-SO formation (k_{ox}) at 80-100 °C; *(Right)* Eyring plot (R^2 = 0.9836, $\Delta H^{\ddagger}$ = 22.9 kcal/mol, $\Delta S^{\ddagger}$ = -1.4 cal/mol K). 285

Figure 6.1. (Left) Basic k_{inh} and electrochemical data for diarylamine compounds. (Right) Korcek mechanism proposed for catalytic inhibition of diarylamines at elevated temperatures. 290

Figure 6.2. (A) Phosphine-coumarin based fluorescence probe for determining [ROOH] in autoxidation samples. (B) Autoxidation of *n*-hexadecane at 160 ºC with constant flow of O_2 (0.4 L/min) Filled circles are [ROOH] concentration (left-axis), empty circles are remaining concentration (starting from 150 μM) of BHT (right-axis). 292

Figure 6.3. Autoxidation of *n*-hexadecane at 160 ºC inhibited by (A) 3,7-di-akyl-PNX and (B) 3,7-di-akyl-PTZ (methyl, ethyl, isopropyl, *tert*-butyl). 294

Figure 6.4. (A) Autoxidation products of **6.4 and 6.12** (B) and **6.14**. (C-E) Time course loss of RTA and formation of oxidation products for (C) **6.4**, (D) **6.12** (E) and **6.14**. The oxidation products were quantified by UPLC calibrated using authentic standards. The "[RAD]" is the concentration of persistent radical detected in the samples by EPR. These are likely the nitroxides of **6.13** (red) and **6.15** (green). (An EPR of **6.15** oxidation is shown in 6.10) (F) Autoxidation of *n*-hexadecane inhibited by **6.13** and **6.15**. (G) Inhibition with other EWG containing PNX compounds. 297

Figure 6.5. Time course loss of **6.20** and the formation of major oxidation products in *n*-hexadecane at 160 ºC with O_2..... 298

Figure 6.6. (A) Reaction coordinate diagram of the autoxidation of **6.26** (M06-2X/cc-pVTZ). (B) Alternative tautomerization pathway for propide intermediate. (C) Truncated schematic of proposed sequential autoxidation of 3-*n*-hexyl-PTZ and 3-cyclohexyl-PTZ (see Fig. 6.32 and 6.33 for complete set of intermediates)..... 301

Figure 6.7. (A) Comparison of isopropyl and cyclohexyl substituted 3- and 3,7-di-alkyl-PTZ. (B) Time course loss of **6.27** and the formation of **6.29** and its oxidation products..... 303

Figure 6.8. Time course loss of 3-phenyl-PTZ (**6.29**) compared to 3-phenyl-PNX (**6.32**). 304

Figure 6.9. (A) Inhibition with DPA, BHT and PTZ compared. (B) Proposed behaviour of BHT and DPA in the 160 ºC autoxidation system..... 307

Figure 6.10. (A) Time course loss of **6.16** and the formation of major oxidation products in *n*-hexadecane at 160 ºC with O_2. **(B)** EPR of 0 min and 75 min hexadecane samples compared (diluted by 1/3 into benzene). 336

Figure 6.11. Time course loss of **6.29** and the formation of major oxidation products in *n*-hexadecane at 160 °C with O_2..... 337

Figure 6.12. (A) Autoxidation of *n*-hexadecane inhibited by **6.33** and **6.34** compared. **(B)** Appearance of hexadecane after 10 h at a low concentration of **6.33**/**6.34** (*left*) vs. hexadecane after 3 h at a high concentration (*right*). 338

Figure 6.13. *(Top)* Representative UPLC-PDA trace of **6.12** at 0 min extracted from hexadecane (shown at 238-272nm); *(Bottom)* Representative UPLC-PDA trace of **6.12** derived products extracted from hexadecane from an intermediate state of autoxidation (shown at 238-272nm).339

Figure 6.14. *(Top)* Representative UPLC-PDA trace of **6.14** at 0 min extracted from hexadecane (shown at 238-272nm); *(Bottom)* Representative UPLC-PDA trace of **6.14** derived products extracted from hexadecane from an intermediate state of autoxidation (shown at 238-272nm).340

Figure 6.15. *(Top)* Representative UPLC-PDA trace of **6.20** at 0 min extracted from hexadecane (shown at 190-390nm); *(Bottom)* Representative UPLC-PDA trace of **6.20** derived products extracted from hexadecane from an intermediate state of autoxidation (shown at 190-390nm).341

Figure 6.16. *(Top)* Representative UPLC-PDA trace of **6.27** at 0 min extracted from hexadecane (shown at 264nm); *(Middle)* Representative UPLC-PDA trace of **6.27** derived products extracted from hexadecane from an intermediate state of autoxidation (shown at 264nm); (*Bottom*) Shown at 285nm to emphasize **6.30**..... 342

Figure 6.17. *(Top)* Representative UPLC-PDA trace of **6.29** at 0 min extracted from hexadecane (shown at 190-390nm); *(Bottom)* Representative UPLC-PDA trace of **6.29** derived products extracted from hexadecane from an intermediate state of autoxidation (shown at 190-390nm).343

Figure 6.18. (A) Representative chromatogram of **6.12** standard (100 μM) monitored at 269 nm (*left*); UV-Vis spectrum of **6.12** standard (*right*). **(B)** Table of integrals and calibration curve of **6.12** standard monitored at 269 nm (y = 0.00162x)..... 344

Figure 6.19. (A) Representative chromatogram of **6.13** standard (100 μM) monitored at 275 nm (*left*); UV-Vis spectrum of **6.13** standard (*right*). **(B)** Table of integrals and calibration curve of **6.13** standard monitored at 275 nm (y = 0.000737x)..... 345

Figure 6.20. (A) Representative chromatogram of **6.15** standard (100 μM) monitored at 272 nm (*left*); UV-Vis spectrum of **6.15** standard (*right*). **(B)** Table of integrals and calibration curve of **6.15** standard monitored at 272 nm (y = 0.00166x)..... 346

Figure 6.21. (A) Representative chromatogram of **6.21** standard (100 μM) monitored at 290 nm (*left*); UV-Vis spectrum of **6.21** standard (*right*). **(B)** Table of integrals and calibration curve of **6.21** standard monitored at 290 nm (y = 0.00151x)..... 347

Figure 6.22. (A) Representative chromatogram of **6.22** standard (100 μM) monitored at 273 nm (*left*); UV-Vis spectrum of **6.22** standard (*right*). **(B)** Table of integrals and calibration curve of **6.22** standard monitored at 273 nm (y = 0.00166x)..... 348

Figure 6.23. (A) Representative chromatogram of **6.23** standard (100 μM) monitored at 342 nm (*left*); UV-Vis spectrum of **6.23** standard (*right*). **(B)** Table of integrals and calibration curve of **6.23** standard monitored at 342 nm (y = 0.00112x)..... 349

Figure 6.24. **(A)** Representative chromatogram of **6.29** standard (100 μM) monitored at 263 nm (*left*); UV-Vis spectrum of **6.29** standard (*right*). **(B)** Table of integrals and calibration curve of **6.29** standard monitored at 263 nm (y = 0.000846x)..... 350

Figure 6.25. (A) Representative chromatogram of **6.30** standard (100 μM) monitored at 285 nm (*left*); UV-Vis spectrum of **6.30** standard (*right*). **(B)** Table of integrals and calibration curve of **6.30** standard monitored at 285 nm (y = 0.0011x)..... 351

Figure 6.26. (A) Representative chromatogram of **6.31** standard (100 μM) monitored at 264 nm (*left*); UV-Vis spectrum of **6.31** standard (*right*). **(B)** Table of integrals and calibration curve of **6.31** standard monitored at 264 nm (y = 0.000972x)..... 352

Figure 6.27. Cyclic voltammograms of ferrocene, **6.4**, **6.5**, **6.6**, **6.14** and **6.15** vs. Ag/Ag^+..... 353

Figure 6.28. Cyclic voltammograms of **6.12**, **6.13**, **6.17**, **6.19**, **6.32** and **6.35** vs. Ag/Ag^+..... 354

Figure 6.29. Cyclic voltammograms of **6.8**, **6.9**, **6.10**, **6.20**, and **6.21** vs. Ag/Ag^+..... 355

Figure 6.30. Cyclic voltammograms of **6.24**, **6.25**, **6.26**, **6.27**, **6.29** and **6.28** vs. Ag/Ag^+..... 356

Figure 6.31. Cyclic voltammograms of **6.33** and **6.34** vs. Ag/Ag^+..... 357

Figure 6.32. Thermochemistry of the oxidation of 3-*n*-hexylphenothiazine to the triene derivative calculated using the M062X/cc-PVTZ DFT method..... 358

Figure 6.33. Thermochemistry of the oxidation of 3-cyclcohexylphenothiazine (**6.27**) to 3-phenylphenothiazine (**6.29**) calculated using the M062X/cc-PVTZ DFT method. 359

Figure 6.34. Thermochemistry of the oxidation of 3-cyclcohexylphenoxazine (**6.35**) to 3-phenylphenoxazine (**6.32**) calculated using the M062X/cc-PVTZ DFT method. 360

Scheme 1.1 – Oxidation and Dimerization of the Triphenylmethyl Radical 2

Scheme 1.2 – The Basic Autoxidation Scheme..... 3

Scheme 1.3 – Spontaneous Thermal Initiation of Styrene 4

Scheme 1.4 – Initiator Fragmentation and Substrate HAT/Addition 4

Scheme 1.5 – In Solvent Cage Reactions of AIBN..... 5

Scheme 1.6 – Thermal Fragmentation of DTUN 8

Scheme 1.7 – Propagation Reactions of Autoxidation..... 8

Scheme 1.8 – Rate Constants for Alkoxyl, Alkyl and Peroxyl Radical Intermediates Compared. 9

Scheme 1.9 – Hypothetical Termination Reactions 14

Scheme 1.10 – Preposed Tetroxide Decomposition Mechanisms..... 15

Scheme 1.11 – Fates of Peroxyl Self Termination Reactions 16

Scheme 1.12 – Methods of Hydroperoxide Quantification..... 19

Scheme 1.13 – Structures of BODIPY Reporters 20

Scheme 1.14 – Catalytic Reduction of Phospholipid-Hydroperoxides by GPx4..... 21

Scheme 1.15 – Radical-Trapping Antioxidant Activity of α-Tocopherol..... 22

Scheme 1.16 – The Naturally Occurring Forms of Vitamin E..... 31

Scheme 1.17 – Family Tree of Vitamin E Inspired Lipid Soluble RTAs 34

Scheme 1.18 – Snelgrove-Ingold H-Bond Pre-Equilibrium Model 41

Scheme 1.19 – Therapy Candidates Based on Synthetic Antioxidants..... 46

Scheme 2.1 – The Snelgrove/Ingold Pre-Equilibrium Model of Radical-Trapping KSE..... 65

Scheme 2.2 – The Synthesis of 2.2-2.5 From Their Corresponding p-Quinones 68

Scheme 4.1 – Proposed Enhancements to Compound 4.1. 222

Scheme 4.2 – Synthesis of 4.2a and 4.4-4.6. 223

Scheme 4.3 – Potential Pathways for Inhibiting Ferroptosis in Addition to Trapping LOO•. ... 233

Scheme 5.1 – The Oxidation of PTZ by PNX-NO. 282

Scheme 6.1 – Basic Autoxidation Scheme. 288

Scheme 6.2 – Proposed Methyl Substituent Effect of Compound 6.2. 291

Scheme 6.3 – Catalytic Inhibition by Nitroxide-Mediated Hydroperoxyl Dismutation. 309

Scheme 6.4 – Proposed Pathways for Carbaldehyde Formation from 3-Me-PNX Derivatives. 311

Table 1.1. Structures and Stability of Representative Azo and Peroxide Thermal Initiators 6

Table 1.2. Autoxidation Data Table for Various Hydrocarbons 11

Table 1.3. Autoxidation Data Table for Various Lipids 12

Table 1.4. Summary of Steric and Electronic Substituent Effects on the Thermodynamics and Kinetics of Simple Phenols 27

Table 1.5. Inhibition Rate Constants of Vitamin E and Related Phenols 32

Table 1.6. Data Table for Key Diarylamine RTAs (Circa 2015) 37

Table 1.7. Kinetic Data for Substituted Phenoxazines/Phenothiazines in Organic Solution 44

Table 2.1. Inhibition Rate Constants in PhCl Compared to Liposomes Analyzed Using Snelgrove/Ingold Pre-Equilibrium Model. 70

Table 2.2. Inhibition Rate Constant Data in Four Additional Organic Solutions/Substrates..... 71

Table 2.3. Key parameters for substrates used in PBD-BODIPY co-autoxidations. 86

Table 2.4. Summary of the inhibition rate constants. 97

Table 2.5. Summary of $\alpha 2H$ values determined by ^{1}H NMR and by kinetic solvent effect. 102

Table 2.6. Summary of K_f and $\beta 2H$ measurements of PLPC by ^{19}F NMR. 110

Table 3.1. Inhibition Rate Constants ($kinhlip$)[35] and Radical-Trapping Stoichiometries (n) of PNX and PTZ Derivatives Determined from Co-Autoxidations of STY-BODIPY and the Polyunsaturated Phospholipids of Egg PC Liposomes. 123

Table 3.2. Summary of the Hydrogen Bond Acidity Parameters ($\alpha 2H$) of Compounds 1-44. . 165

Table 3.3. Inhibition Rate Constants and Radical Trapping Stoichiometries in Organic Solution ($kinhS$) and in Egg PC Liposomes ($kinhlip$) 166

Table 3.4. Inhibition Rate Constants and Radical Trapping Stoichiometries in DTUN Initiated Egg PC Liposomes With/Without Ascorbate 176

Table 3.5. Summary of the Anti-Ferroptosis Activity in RSL3 Induced Mouse-Embryonic Fibroblasts 183

Table 4.1. Inhibition Rate Constants and Stoichiometries in Liposomes with and Without Ascorbate 224

Table 4.2. Microsome Stability and Ferroptosis Rescue Potency of 4.4-4.6 and Related Compounds. 226

Table 5.1. Summary of Data for PNX, PTZ and Their Aza-Derivatives 257

Table 6.1. Times of Inhibition for Substituted PNX and PTZ Derivatives in Hexadecane Autoxidations 296

List of Symbols and Abbreviations

α_2^H	Abraham's hydrogen bond acidity parameter
β_2^H	Abraham's hydrogen bond basicity parameter
υ	kinetic chain length
k_d	rate constant of decay/decomposition
k_{inh}	rate constant of inhibition
k_p	rate constant of propagation
k_t	rate constant of termination
n	stoichiometry
R_i	rate of initiation
R_p	rate of propagation
R_t	rate of termination
t_{inh}	time/period of inhibition

α-Toc/α-TOH	α-tocopherol
ADPA	alkylated diphenylamine
BDE	bond dissociation enthalpy
DPA	diphenylamine
DTUN	di-*tert*-undecylhyponitrite
Fer-1	ferrostatin-1
GPx	glutathione peroxidase
HAT	hydrogen atom transfer
HBA	hydrogen bond acceptor
HBD	hydrogen bond donor
KSE	kinetic solvent effect
Lip-1	liproxstatin-1
LOOH	lipid hydroperoxide
PC	phosphatidylcholine
PCET	proton-coupled electron transfer
PMC	2,2,5,7,8-pentamethyl-6-chromanol
PNX	phenoxazine
PUFA	polyunsaturated fatty acid
PTZ	phenothiazine
ROOH	hydroperoxide
RTA	radical trapping antioxidant

Chapter 1

Introduction to Autoxidation and Radical-Trapping Antioxidants

1.1 Foreword

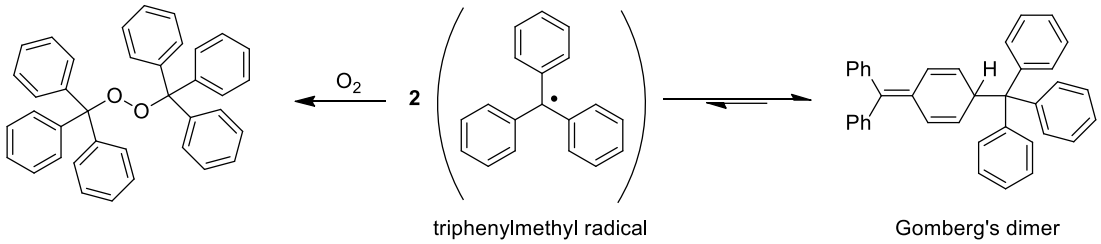
It would difficult to overstate the extent to which the invention of radical-polymerization has impacted society. From clothing, furniture, appliances, electronic devices, automobiles, buildings, and countless other examples it is not an exaggeration to state that the development and understanding of these chemical reactions has profoundly changed our culture even down to the most mundane interactions with our surroundings. During the decades of intensive research to quantitatively describe radical-polymerization (initially for its utility in producing synthetic rubber from olefins), a complete kinetic description of radical-mediated oxidation, or "autoxidation," inevitably ensued. While the bulk effects of autoxidation have been evident from time and memoriam, the first systematically detailed observations of radical-mediated oxidation can be traced to Moses Gomberg's famous preparation of the persistent triphenylmethyl radical at the turn of the 20th century.[1] Two key observations of the previously theoretical trivalent carbon species were: (i) the dynamic equilibrium between the triphenylmethyl radical and its dimer under inert atmosphere, and (ii) the irreversible formation of the peroxide in the presence of O_2.[2] Gomberg later reflecting on his account of the discovery wrote:[3]

> *"At first, the results were very erratic, but when the operations were carried out in an atmosphere of carbon dioxide, nitrogen, or hydrogen, they were reproducible. The resulting substance, however, possessed not one of the predicted characteristics. Instead of being colorless, the substance proved to be colored, at least in solution; instead of being stable and inert, it was the very opposite—it combined with the oxygen of the atmosphere with an avidity reminding one of the reaction between yellow phosphorus and oxygen."*

Of course, this elementary reaction between a carbon-centred radical and triplet oxygen (a diradical) only marked the beginning of a comprehensive understanding of the autoxidation process. Like with radical-polymerization, it was recognized at an early period of development that autoxidation operated under a chain mechanism. The seminal experimental work of

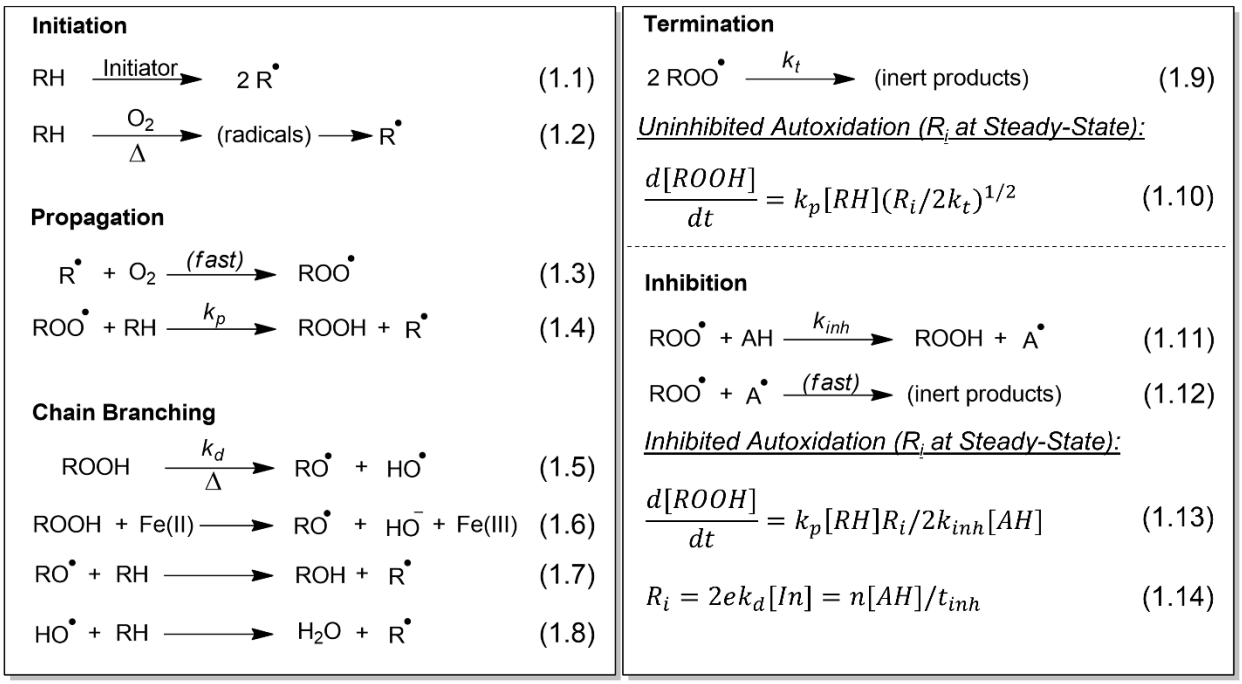
Bäckström demonstrated the photo-oxidation of benzaldehyde and heptaldehyde had quantum yields far in excess of unity (10000-15000).[4] Additionally later work demonstrated that small quantities of phenolic additives would suppress oxidation to an extent consistent with chain breaking.[5] The radical-chain mechanism was further supported by the work of Ziegler, demonstrating that dissociation of Gomberg's dimer (erroneously identified as hexaphenylethane at the time)[6] could initiate the reactions between oxygen and aldehydes/olefins greatly exceeding the stoichiometry of the dimer.[7,8]

Scheme 1.1 – Oxidation and Dimerization of the Triphenylmethyl Radical



As with nearly every area of scientific inquiry, the early authors of autoxidation research are many, but as far as the underlying kinetic theory is concerned, much of our present understanding is owed to J. L. Bolland and L. Bateman of the *British Rubber Producers' Research Association*.[9,10] Their formalizations of the kinetics, with some refinement, by in large remains in use to this day. Their systematic olefin oxidation experiments which varied initiation methods (benzoyl peroxide, UV photo-oxidation, oxidation of 1,4-dienes), as well as their experiments using phenolic inhibitors allowed them to dissect the elementary reactions involved in autoxidation and enabled the derivation of rate equations under both inhibited and uninhibited conditions. The essential elementary processes of autoxidation, initiation, propagation, chain-branching, termination and inhibition, what one might call a "basic autoxidation scheme" is laid out in Scheme 1.2. Each stage will be described in more detail in the proceeding sections.

Scheme 1.2 – The Basic Autoxidation Scheme



Naturally, the seminal work by these early investigators has been continually built upon and refined by subsequent generations of researchers even into the present era. While most of what will be discussed going forward in this introductory chapter will focus on later developments in this field of research, we should always be mindful of the foundation on which it was built. After describing the elementary processes of autoxidation, the main subject matter of the thesis will be introduced; the systematic design of high-performance inhibitors of autoxidation and an exploration of their applications in medicine and materials.

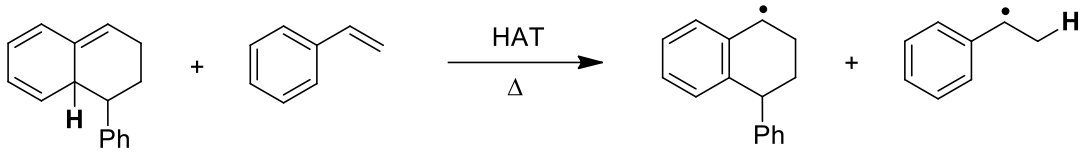
1.2 Autoxidation

1.2.1 Initiation and Chain Branching

Every chain-process, radical or otherwise, begins with *initiation*. For autoxidation, a new chain is initiated with the formation of a carbon-centred radical (Eq. 1.1, 1.2, 1.7, 1.8) followed by rapid combination with O_2 to form a peroxyl radical (Eq. 1.3). Several different initiators have been found to affect radical polymerization, and by extension autoxidation, whether they are activated thermally, photolytically, or by one electron reduction.[11] Exposure to ionizing radiation (γ-rays and X-rays) can also initiate radical chain reactions. Some substrates in the absence of any added

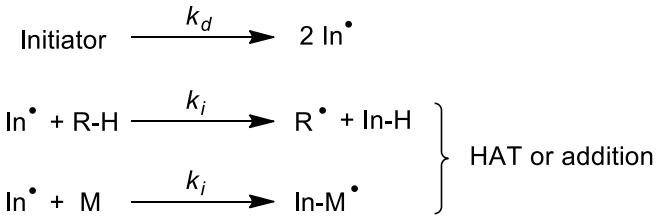
initiators, such as styrene, can undergo radical polymerization simply by heating (the Diels-Alder dimer of styrene acts as an *in-situ* initiator.)[12] The focus will be on thermolysis of peroxides and azo-initiators/hyponitrites, as they are the most pertinent to this body of work.[13,14]

Scheme 1.3 – Spontaneous Thermal Initiation of Styrene



Thermolysis of peroxides, hyponitrites and azo-initiators generate two initiating radicals. The product of alkyl peroxides (*e.g.*, di-*tert*-butylperoxide) and hyponitrites are alkoxyl radicals (RO$^{\bullet}$), while hydroperoxides (*e.g.*, *tert*-butyl-hydroperoxide) produce an alkoxyl radical and a hydroxyl radical (HO$^{\bullet}$). Not all peroxides produce alkoxyl/hydroxyl radicals however. Benzoyl peroxide, for example, produces benzoyloxyl radicals which subsequently fragment to give phenyl radicals and CO_2. Azo-initiators like α,α'-azobis(isobutyronitrile) (AIBN) produce carbon-centred radicals (alkyl radicals, R$^{\bullet}$) either by a concerted fragmentation or rapid sequential C-N homolysis.[15] In an aerobic environment these alkyl radicals will rapidly combine with O_2, near the rate of diffusion,[16] rendering the corresponding peroxyl radicals (ROO$^{\bullet}$). While the decomposition of some of the aforementioned examples may involve multiple steps, broadly speaking there are essentially two principal reactions in the initiation process: initiator fragmentation/decomposition (k_d) and initiation of the substrate (k_i) whether that be by hydrogen-atom transfer (HAT) or radical addition:

Scheme 1.4 – Initiator Fragmentation and Substrate HAT/Addition



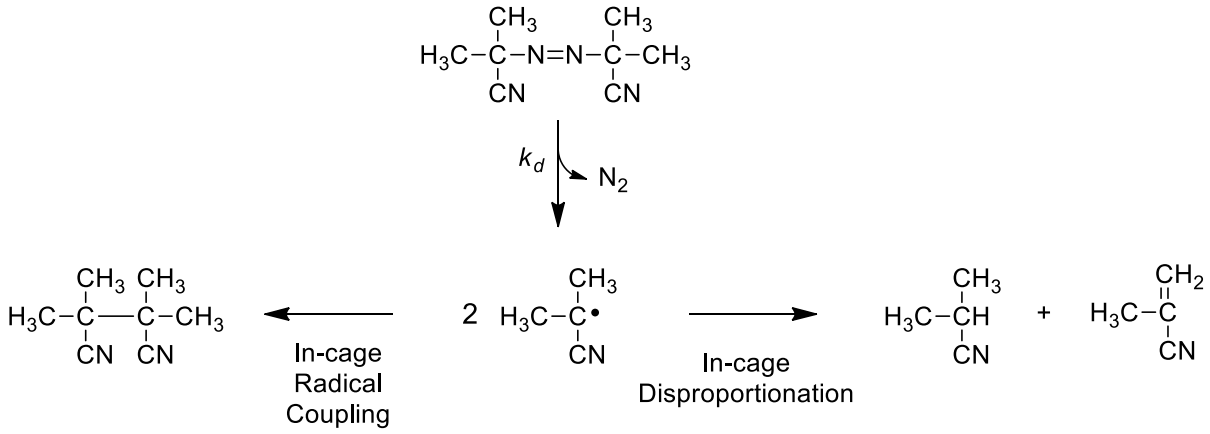
The decomposition is a unimolecular first-order reaction (k_d[In]). The substrate initiation is a bimolecular second-order reaction (k_i[In$^{\bullet}$][R-H]), however the steady state concentration of [In$^{\bullet}$] << [R-H], so this can be treated as a pseudo-first-order process (k_i' [In$^{\bullet}$]). Typically, (k_d[In]) <<

(k_i[In$^{\bullet}$][R-H]), so the observed rate of initiation (R_i) is (nearly) in unity with the rate of initiator decomposition:

$$R_i = 2ek_d[In] \qquad (1.14)$$

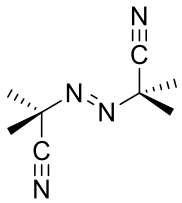
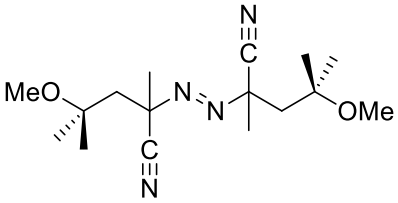
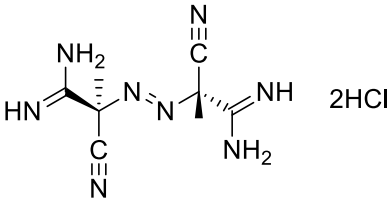
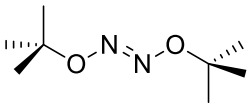
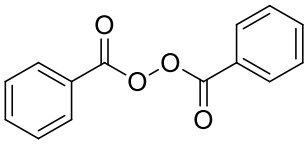
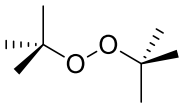
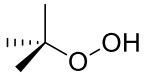
Not every initiator-derived radical generated will result in a radical chain. There is a discrepancy between loss of initiator (-*d*[In]/*dt*) and the observed R_i, a discrepancy which is attributable to initiator radical termination reactions in the solvent cage, such as non-reversible coupling and/or disproportionation of the generated alkyl/alkoxyl radicals. The ratio between radicals that actually initiate chains and radicals formed from the initiator is referred to as initiator efficiency (*e*). For instance the *e* of AIBN tends to range between 0.5-0.7, but this cage-effect is solvent dependent as viscosity has a significant impact on the rate of cage escape (higher viscosity favours in-cage reactions.)[17]

Scheme 1.5 – In Solvent Cage Reactions of AIBN



The thermal stability varies considerably between different initiators. The concerted fragmentation of AIBN is substantially faster than the thermolytic cleavage of di-*tert*-butylperoxide, for example. Expressed in terms of temperature required for a 10-hour half-life ($T_{10h}^{t_{1/2}}$) the difference is 65 °C and 123 °C respectively. 2,2'-Azobis(4-methoxy-2,4-dimethylvaleronitrile) (MeOAMVN) is even less stable than AIBN with a $T_{10h}^{t_{1/2}}$ of only 30 °C. Table 1.1 summarizes information for these and some additional thermal initiators.

Table 1.1. Structures and Stability of Representative Azo and Peroxide Thermal Initiators

Name	Structure	$T_{10h}^{t_{1/2}}$ (°C) [a]
2,2'-Azobis(isobutyronitrile) (**AIBN**)		65
2,2'-Azobis(4-methoxy-2,4-dimethylvaleronitrile) (**MeOAMVN**)		30
2,2'-Azobis(2-methylpropionamidine)dihydrochloride (**AAPH**)		56
Di-*tert*-butylhyponitrite (**DBHN**)		44 [b]
Benzoyl peroxide		72
Di-(*tert*-butyl)-peroxide		123
tert-Butyl hydroperoxide		169

(a) Temperature data for 10 hour half-life was obtained from either the Fujifilm Wako Chemical website or polymerdatabase.com.[18,19] (b) Estimated temperature from TS theory parameters for thermal fragmentation of DBHN ($\Delta H^{\ddagger}$ = 27.9 kcal mol^{-1}; $\Delta S^{\ddagger}$ = 8.2 cal K^{-1}) to obtain a k_d of 1.93 × 10^{-5} s^{-1} (which corresponds to a $t_{1/2}$ = 3.6 × 10^4 s).[20]

Hydroperoxides, the principal product of autoxidation when propagation is mediated by HAT, are relatively stable as far as thermal initiators are concerned (*tert*-butyl hydroperoxide has a $T_{10h}^{t_{1/2}}$ 169 °C). At more modest temperatures (<100 °C) the hydroperoxide produced from initiation/propagation will have a negligible impact on the on the *Ri*. At significantly elevated temperatures however, the very nature of the autoxidation can change as each initiation will produce multiple equivalents of ROOH which will themselves each "branch-off" into multiple chains, accelerating the rate of initiation with time (i.e. autoinitiation). *Chain branching* (Eq. 1.5-1.8) is distinguished as another reaction-type alongside initiation, propagation and termination. Though the elementary steps are initiation reactions, the relationship with hydroperoxide-producing propagation creates a positive feedback loop that accelerates *Ri*. At high temperatures where Eq. 1.5 is the predominant initiation reaction, the rate law for d[ROOH]/dt is described by Eq. 1.15:[21,22]

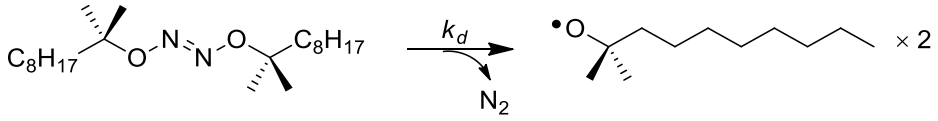
$$\frac{d[ROOH]}{dt} = k_p[RH](k_d/k_t)^{1/2}[ROOH]^{1/2} \qquad (1.15)$$

Certain reagents can promote fragmentation of peroxides, greatly enhancing their efficacy as initiators even at comparatively low temperatures. A well-known example is the Fenton reaction which is depicted in Eq. 1.6 in Scheme 1.2. While canonically between Fe^{2+} and hydrogen peroxide, it can be generalized to other redox-active metals and to peroxides of varying composition. For example, to chemically stimulate the oxidation of low-density lipoprotein (LDL), a major contributing factor to the formation of atherosclerotic plaque, Cu^{2+} salts are added to the LDL-containing media.[23] It is presumed that Cu^{+}, from some non-descript reduction of Cu^{2+},[24] facilitates initiation of background lipid-hydroperoxides (LOOH) leading to depletion of α-tocopherol followed by a rapid increase in lipid peroxidation derived products. Similarly, the LOOH fueled Fenton reaction is believed to play an important role in a more recently recognized form of non-apoptotic cell death referred to as "ferroptosis", which as the name would suggest, has a dependence on iron (and which can be suppressed by the addition of chelating agents).[25]

One further consideration that bears discussing is the solubility/partitioning of initiators. This is particularly relevant when studying bi-phasic systems, such as aqueous liposomal or micellar

suspensions. Initiation that occurs in the aqueous phase can be readily quenched by water soluble inhibitors like ascorbic acid and uric acid but radicals initiated in the lipid domain are inaccessible to such reductants[26,27] making lipid-soluble inhibitors such as α-tocopherol far better suited for this (and inhibiting lipid peroxidation in general). A good example of a water-soluble azo-initiator would be 2,2'-azobis(2-amidinopropane) dihydrochloride (AAPH). For the purposes of modelling/studying radical-mediated lipid peroxidation, our group has found great utility in the lipophilic hyponitrite initiator di-*tert*-undecyl hyponitrite (DTUN),[28] which is a more lipophilic analogue of DBHN shown in Table 1.1. DTUN, and presumably the radicals generated therefrom (Scheme 1.6), is retained within the lipid-domain of egg-phosphatidylcholine (egg-PC) small unilamellar vesicles (SUV) with negligible partitioning with the aqueous-phase making it an ideal source of lipid-like alkoxyl radicals under physiologically relevant conditions.

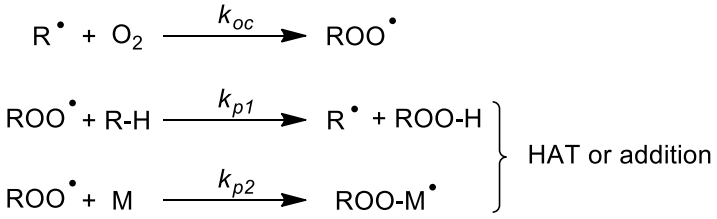
Scheme 1.6 – Thermal Fragmentation of DTUN



1.2.2 Propagation

Once the radical chain has been initiated the process of *propagation* begins. Fundamentally during the propagation of autoxidation there are two reaction types: (i) combination of substrate-derived radical (R•) with triplet O_2 to form a peroxyl radical (ROO•) and (ii) the chain transfer from the peroxyl to another equivalent of substrate (completing the cycle of propagation.)

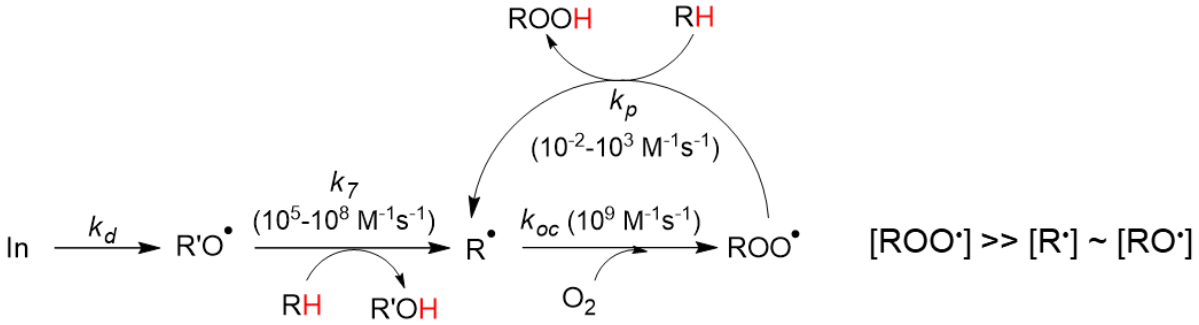
Scheme 1.7 – Propagation Reactions of Autoxidation



The combination of O_2 with a carbon-centred radical is very rapid and often irreversible. The rate constant in solution (k_{oc}) has been measured for several radicals using laser flash photolysis (LFP).[16] The reactivity is unaffected by the solvent polarity or hydrogen-bonding ability, but the structure of the carbon-centred radical matters to some degree. While a resonance stabilized

benzyl radical (k_{oc} = 2.4 × 10^9 M^{-1} s^{-1}) reacts more slowly than a less stable *tert*-butyl radical (k_{oc} = 4.9 × 10^9 M^{-1} s^{-1}), both reactions will easily exceed the chain transfer reactions (k_p) by several orders of magnitude unless the system is deprived of O_2. Similarly, the reactions between hydroxyl/alkoxyl radicals and hydrocarbon substrates (Eq. 1.7 and 1.8) are orders of magnitude faster (10^5-10^8 M^{-1} s^{-1})[29,30] than the propagation reactions with peroxyl radicals (10^{-2}-10^3 M^{-1} s^{-1}).[31–35] The steady-state abundance of ROO$^\bullet$ as a chain-carrying radical, relative to R$^\bullet$ and RO$^\bullet$, makes it the species of greatest interest with respect to mitigation by radical-trapping. Thus, the discussion of propagation in autoxidation will revolve around the reactivity of the peroxyl radical towards oxidizable substrate as this is the rate determining reaction of the overall process.

Scheme 1.8 – Rate Constants for Alkoxyl, Alkyl and Peroxyl Radical Intermediates Compared



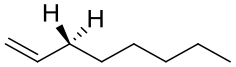
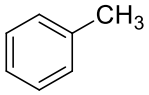
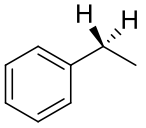
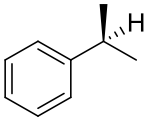
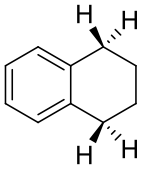
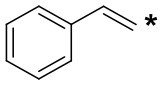
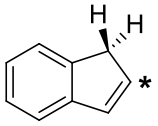
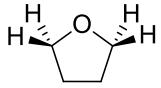
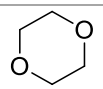
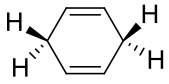
Broadly speaking, the reactivity trends for k_p are couched in terms of the reactivity of the oxidizable hydrocarbon rather than the reactivity of the specific peroxyl radical. Comparing the rates of HAT between different peroxyl radicals (cumyl and tetralyl) and a common substrate (cumene or tetralin) reveals that the reactivity of tertiary peroxyl radicals is less than secondary peroxyls (approx. 3 to 4-fold difference) on the basis of steric effects.[36] However, these cross-over experiments to isolate and study reactivity of particular peroxyl species have been quite limited compared to the volumes of substrate-specific k_p data available. The overall "oxidizability" of a substrate, in the absence of inhibitor, is defined by:

$$k_p/(2k_t)^{1/2} \qquad (1.16)$$

where k_t is the termination rate constant of the substrate-derived peroxyls (Eq. 1.9). In the early development of the field isolation of these rate constants was a challenge, but through the use of clever non-steady-state photoinitiation techniques, absolute determinations of k_t (and thus k_p)

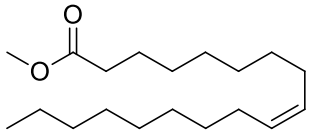
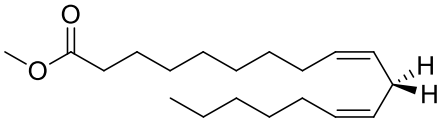
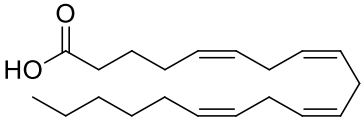
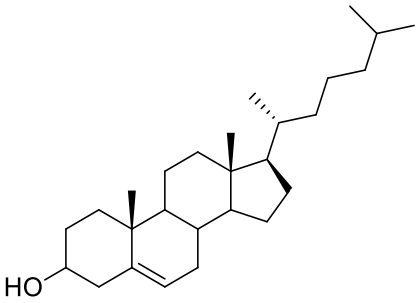
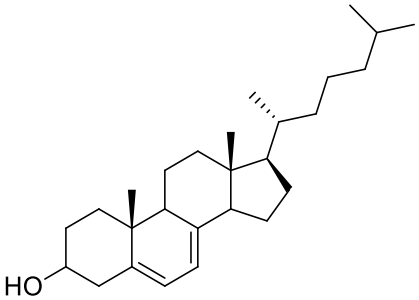
were made possible.[32,37] A range of substrate-specific rate constants for representative hydrocarbons and some representative lipids of biological interest are given in Table 1.2 and 1.3 respectively.

Table 1.2. Autoxidation Data Table for Various Hydrocarbons

Hydrocarbon Substrates					
Name	*Structure*	$BDE_{C\text{-}H}$ *(kcal mol^{-1})* [a]	k_p *(M^{-1} s^{-1})* [a]	k_t *(10^6 M^{-1} s^{-1})* [c]	$k^{BuO\bullet}$ *(10^6 M^{-1} s^{-1})* [d]
Cyclohexane		95	0.044	-	1.6
1-Octene		83	1.0	130	1.5
Toluene		85	0.24	150	0.23
Ethylbenzene		82	1.3	20	1.05
Cumene		79	0.18	0.0075	0.83
Tetralin		82	6.4	3.8	-
Styrene		-	(41)[b]	21	-
Indene		-	14 / (128)[b]	25	-
THF		92	4.3	15.5	8.3
1,4-Dioxane		91	0.50	25	1.5
1,4-Cylcohexyl-diene		71	1480	630	53

(a) A summary of the $BDE_{C\text{-}H}$ and k_p values from Howard, Ingold and co-workers (1972).[38] (b) Explicit rate constants for peroxyl addition (k_{p2}).[31] (c) Peroxyl termination rate constants (k_t).[31,34] (d) Rate constants for HAT by *tert*-butyl alkoxyl radical (tBuO•) for the corresponding substrates.[29,30]

Table 1.3. Autoxidation Data Table for Various Lipids

Lipid Substrates				
Name	*Structure*	*$BDE_{C\text{-}H}$ (kcal mol^{-1})*	*k_p (M^{-1} s^{-1})*	*k_t (10^6 M^{-1} s^{-1})*
Methyl Oleate [a]		-	0.88	0.53
Methyl Linoleate [a]		76 [b]	62	4.4
Arachidonic Acid [c]		76 [b]	197	-
Cholesterol [c]		-	11	-
7-Dehydro-cholesterol [c] (7-DHC)		-	2260	-

(a) k_p and k_t for methyl oleate and methyl linoleate determine by O_2-uptake method. (b) $BDE_{C\text{-}H}$ of bis-allylic estimated from experimental value for 1,4-pentadiene (76.4 kcal mol^{-1}).[39] (c) k_p values determined by the linoleate clocking method.[35]

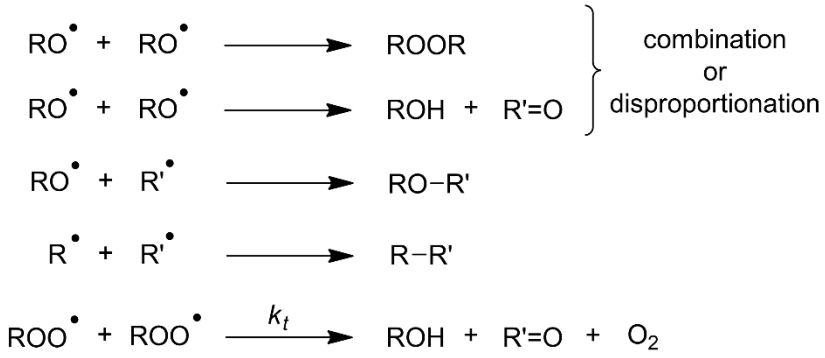
The reactions of peroxyl radicals with substrates that generate a carbon-centred radical are either HAT (k_{p1}) or addition reactions (k_{p2}). Rate constants for the former typically correlate with the BDE of the substrate's weakest C-H bond(s) which follows the elementary principles of radical-stabilization of carbon-centred radicals (dictated largely by conjugation and hyperconjugation). From a thermodynamic perspective, the O-H BDE of methyl hydroperoxide (86.2 kcal mol^{-1})[40] is comparable to the tertiary C-H BDE of a typical allylic/benzylic C-H bond (~84 kcal mol^{-1}). Bis-allylic C-H bonds, frequently found in nature in polyunsaturated fatty-acids (PUFA) such as linoleic or arachidonic acid, are even weaker (~76 kcal mol^{-1}) which makes the moiety particularly susceptible to HAT by peroxyls. While being rather exothermic, these C-H HAT reactions have rather modest kinetics. For instance, methyl linoleate has a k_p of only 62 $M^{-1}s^{-1}$ meanwhile a thermally equivalent HAT from the phenol α-tocopherol (O-H BDE ~ 77 kcal/mol)[41] to a peroxyl radical has a bimolecular rate constant of ~3 x 10^6 $M^{-1}s^{-1}$ (more information *vide infra*).

The other major mode of propagation, as already mentioned, is peroxyl radical addition to an alkene. Again, the efficacy of the chemistry is related to the stability of the resultant carbon-centred radical. In general, if the double bond is conjugated (aromatic, carbonyl, polyene etc.) addition will be the favoured mode for propagation over an available allylic site for HAT, whereas a simple alkene such as 1-octene will favour HAT. The autoxidation of indene sees both formation of di-alkyl-peroxide (the product of addition) and hydroperoxide products (the product of HAT) but in approximately a 9 to 1 ratio favouring addition.[31]

1.2.3 Termination

Termination occurs when two chain-carrying species react together to create non-propagating products. Technically, of the radical species involved in the autoxidation process, there are several potential terminating combinations which are possible (Scheme 1.9):

Scheme 1.9 – Hypothetical Termination Reactions



However, in the context of autoxidation, only peroxyl-peroxyl termination (Eq. 1.9) is considered as the steady-state concentrations of $RO^{\bullet}$ and $R^{\bullet}$ are negligible compared to $ROO^{\bullet}$ (see Scheme 1.8). The termination kinetics are an important factor when considering the 'oxidizability' of a substrate/system as it directly impacts the chain-length of propagation. The kinetic chain length (υ), defined as the ratio of the rate of propagation (R_p) to rate of initiation (R_i) (Eq. 1.17), can also be expressed as in Eq. 1.18.

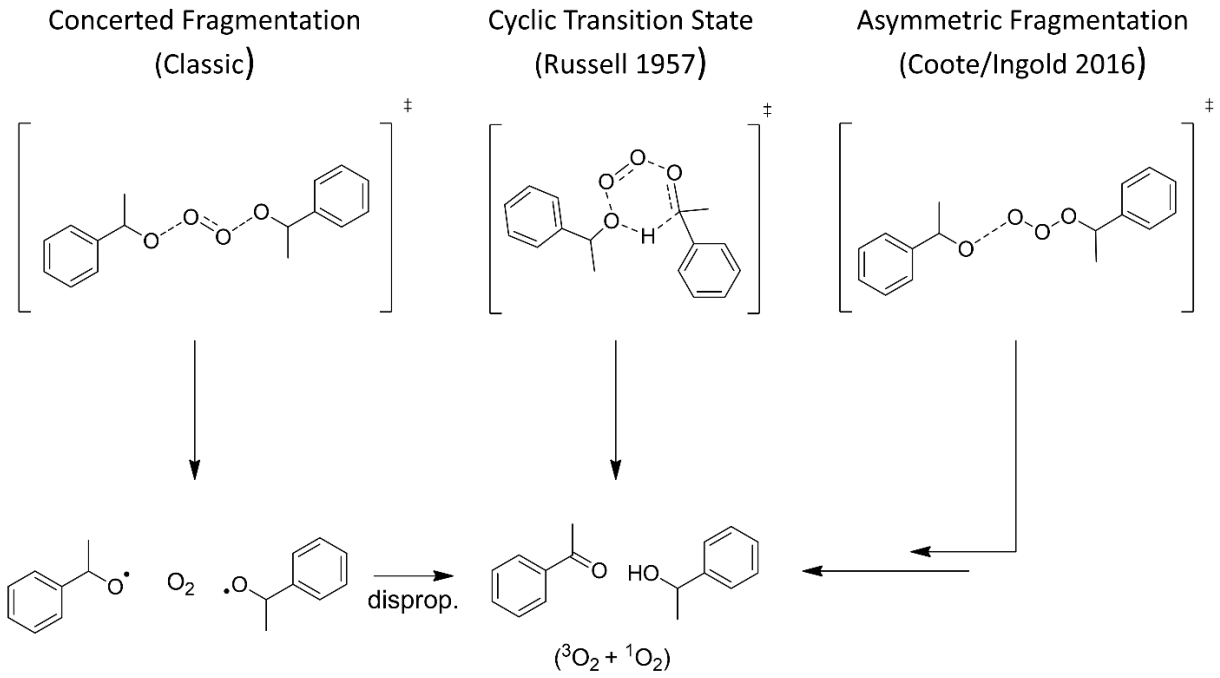
$$\upsilon = \frac{R_p}{R_i} \qquad (1.17)$$

$$\upsilon = \frac{k_p[RH]}{2k_t[ROO^{\bullet}]} \qquad (1.18)$$

Substrate derived peroxyls that have low k_t values relative to k_p will be able to oxidize many equivalents of substrate per initiation event (e.g., the υ for cumene would be orders of magnitude greater than toluene). Peroxyl-peroxyl termination reactions are substantially slower than many of the diffusion-controlled radical-radical termination reactions. The rate constant of peroxyl-peroxyl termination generally follows a trend where tertiary < secondary < primary. The tetroxide intermediate (ROOOOR) arising from the combination of *tert*-butyl peroxyl radicals has previously been studied by Bartlett and Guaraldi using quantitative EPR.[42] They found that

between -70 °C and -85 °C the concentration of *tert*-butyl peroxyl could be reversibly increased or decreased with increasing and decreasing the temperature. The results implicated a shift in the peroxyl-peroxyl/tetroxide equilibrium where the formation of tetroxide was exothermic (ΔH = -6 kcal/mol). The barrier to the (forward) decomposition of the tetroxides derived from combination of primary and secondary peroxyl radicals is much lower than di-tertiary tetroxides (hence the low k_t for cumene). Based on cumene and ethylbenzene autoxidations, G. A. Russell proposed a unique mechanism for tetroxide decomposition when secondary and primary structures are involved. He invoked a concerted cyclic transition-state rather than the traditional view of concerted fragmentation of tetroxide (giving alkoxyls that could dissociate, recombine or disproportionate).

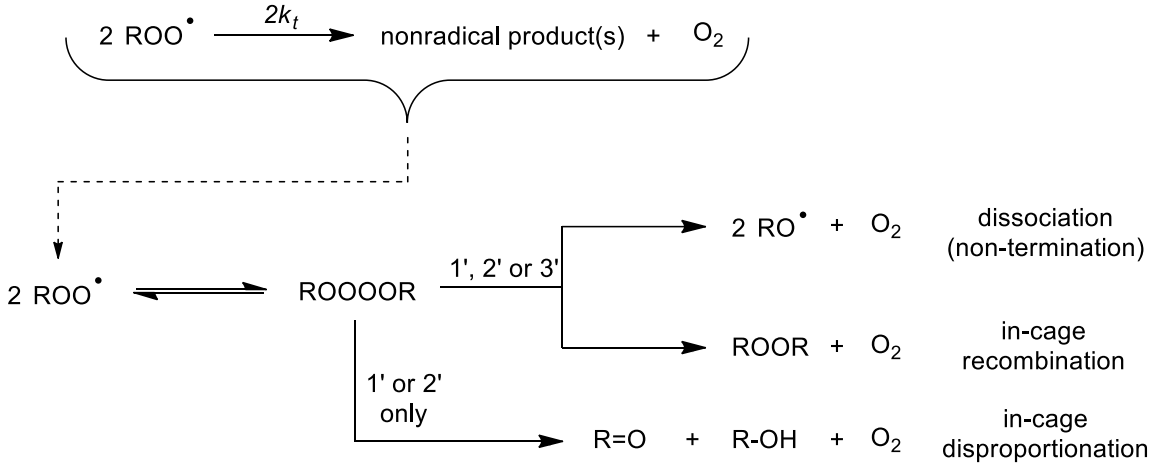
Scheme 1.10 – Preposed Tetroxide Decomposition Mechanisms



Russell's mechanistic proposal, for many years, was the widely accepted explanation. More recently however, the Russell termination mechanism came under scrutiny as some anomalous conflicting results were reported by other investigators. Among the most persuasive experimental arguments against the concerted mechanism was that the Arrhenius pre-exponential factor of various secondary peroxyl radicals (7.8, 9.0 and 10) was not substantially different than that of *tert*-butylperoxyl termination (9.2).[43] The highly ordered TS for Russell's proposed mechanism

is not reflected by the low entropy of activation for the termination processes observed by Howard and Bennet, which implies that the tetroxide of both secondary-secondary and tertiary-tertiary peroxyls likely decay in a similar manner. M.L. Coote and co-workers, in collaboration with Ingold, seem to have provided a satisfactory resolution to the large enthalpic differences between the putative activated complexes of these tetroxide intermediates.[44] Using DFT, they demonstrated that the C_α-H on the primary and secondary tetroxides H-bond to the interior O atoms which substantially weakens the O-O bonds ($\Delta\Delta G^{\ddagger} \leq$ -3.3 kcal/mol) that ultimately render the triplet O_2 and the 2 alkoxyl radicals by *sequential* homolysis (and subsequent in-cage disproportionation).

Scheme 1.11 – Fates of Peroxyl Self Termination Reactions



1.2.4 Methods of Measurement

Before continuing further, some elaboration on the derivation of Eq. 1.10 is in order. In a chain reaction, generally considered to be the case when the kinetic chain length is $\upsilon \geq 10$, the rate of ROOH production is dependent on the rate of propagation (R_p):

$$R_p = k_p[RH][ROO^{\bullet}] \qquad (1.19)$$

$$\frac{d[ROOH]}{dt} = k_p[RH][ROO^{\bullet}] \qquad (1.20)$$

Under conditions of continuous initiation, a steady-state concentration of ROO$^{\bullet}$ is established where the rate of initiation (R_i) and rate of termination (R_t) are equivalent:

$$R_i = 2ek_d[In] \qquad (1.14a)$$

$$R_t = 2k_t[ROO^{\bullet}]^2 \qquad (1.21)$$

$$R_i = R_t = 2k_t[ROO^{\bullet}]^2 \qquad (\textit{steady-state assumption})$$

$$[ROO^{\bullet}] = (R_i/2k_t)^{1/2} \qquad (1.22)$$

Substituting [ROO$^{\bullet}$] in Eq. 1.20 with Eq. 1.22 gives:

$$\frac{d[ROOH]}{dt} = k_p[RH](R_i/2k_t)^{1/2} \qquad (1.10)$$

The expression for υ shown in Eq. 1.18 also derives from the steady-state assumption where:

$$\upsilon = \frac{R_p}{R_i} = \frac{R_p}{R_t} \qquad (\textit{steady-state assumption})$$

$$\upsilon = \frac{k_p[RH][ROO^{\bullet}]}{2k_t[ROO^{\bullet}]^2} = \frac{k_p[RH]}{2k_t[ROO^{\bullet}]} \qquad (1.18)$$

And substituting [ROO$^{\bullet}$] for Eq. 1.22 (in its expanded form) gives:

$$\upsilon = \frac{k_p[RH]}{2(ek_tk_d[In])^{1/2}} \qquad (1.23)$$

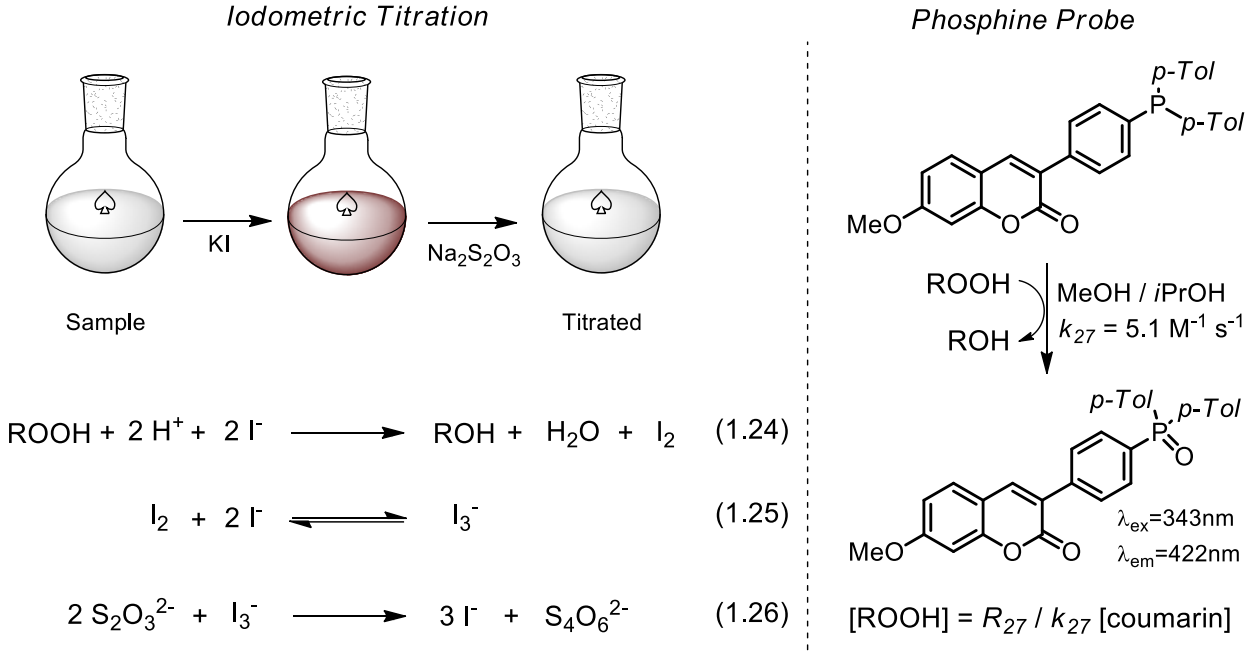
Many different methods have been employed over the years for the purpose of monitoring autoxidation, and I only intend to highlight some common methods, from which much of the referenced data is derived, as well as ones used in my research. As autoxidation is largely dependent on R_p, one can either monitor product formation (ROOH) or starting material consumption (RH or O_2):

$$\frac{d[ROOH]}{dt} = -\frac{d[RH]}{dt} = -\frac{d[O_2]}{dt}$$

One of the traditional kinetic assays is the O_2-consumption method.[45–47] The most popular variant measures $-d[O_2]/dt$ by monitoring differential changes in pressure over time using a

pressure transducer. Both a reference and a sample cell are loaded with substrate, solvent and identical initiator, and both start with the same partial pressure of O_2 (typically 760 torr). The sample cell in addition to these also contains the inhibitor or co-substrate that is under study. The differential pressure between sample and reference is given in d(mV/V)/dt (via barro-potential relationship), which is converted to $d[O_2]/dt$ using a known autoxidation standard (typically styrene).[47] While the setup is a bit involved, it is a direct continuous assay which has proven very reliable for a number of investigators. One advantage which should be appreciated is that the measuring method of differential pressure change is completely orthogonal to the optical properties of the substrate or the lighting conditions (i.e., photoinitiation) which circumvents many potential errors from visual artifacts one might encounter using a spectrophotometric method. Another standard method is the monitoring of d[ROOH]/dt, which involves the quantification of [ROOH] at intermittent time points. Two commonplace methods of quantification are HPLC analysis, which has particular utility in the quantification of diene hydroperoxides derived from the lipid-peroxidation of PUFA, and iodometric titration. Incubation of the ROOH containing sample with potassium iodide gives iodine (Eq. 1.24) and the dark red triiodide anion (Eq. 1.25), which is then titrated with a calibrated standard of sodium thiosulfate solution (Eq. 1.26). An alternative method for quantifying [ROOH] developed in our own lab, which we feel is more convenient, is a fluorescence method using a phosphine-based coumarin probe that is readily oxidized by hydroperoxides (Scheme 1.12).[48] The fluorescence of the coumarin probe increases 10-fold when the triaryl phosphine moiety is oxidized to the phosphine oxide ($(\Phi_{f,Ox}/\Phi_{f,Red}) = 10.6$), giving a strong signal for tracking oxidation of the probe in the presence of ROOH. A second order rate constant (k_{27}) can be established for a given system using known concentrations of tetralin hydroperoxides, after which the [ROOH] from an unknown sample can be calculated from the initial rate of the probe's oxidation (R_{27}).

Scheme 1.12 – Methods of Hydroperoxide Quantification

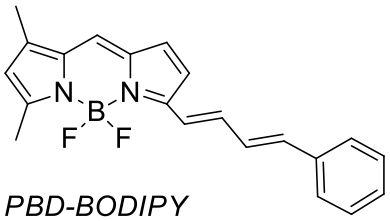


While, in principle, autoxidation can be monitored by loss of substrate (-*d*[RH]/*dt*), generally this has not been a practical option given the signal-to-noise of detecting relatively small decreases in [RH], usually making up the majority of the solution. That being said, we have successfully adopted a modified version of this approach over the last 7 years and have carried out many studies measuring kinetics for a wide range of radical-trapping antioxidants (RTAs) in a wide range of systems.[49–54] Taking inspiration from C11-BODIPY, a probe used in cell biology to visualize lipid-peroxidation, workers from our lab used this and other similar BODIPY reporters to monitor RTA kinetics in bulk substrates (a co-autoxidation if you will).[28,55] Phenyl-butadiene-BODIPY (PBD-BODIPY) and styrene-BODIPY (STY-BODIPY) contain those respective moieties conjugated to the BODIPY core (Scheme 1.13), which upon peroxyl radical addition leads to large changes with respect to their absorbance and fluorescence characteristics. The principal advantage of this methodology, of course, is that reaction progress can be continuously monitored using standard visible spectrophotometry or fluorometry, which are more scalable and accessible than previous techniques such as monitoring differential pressure of O_2. The rate law for the (uninhibited) BODIPY autoxidation method is given in Eq. 1.28:

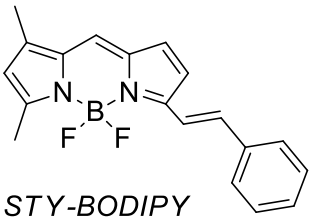
$$-\frac{[BODIPY]}{dt} = k_p[BODIPY](R_i/2k_t)^{1/2} \qquad (1.28)$$

Bear in mind that the small amount of BODIPY reporter (10^{-6}-10^{-5} M) is swimming in substrate that readily autoxidizes (10^{0}-10^{1} M), so the same steady-state assumptions apply. The only difference is that as part of chain propagation occasionally a substrate-derived peroxyl will react with a reporter molecule which can be visually monitored. The observed 'k_p' for BODIPY is calculated from replicate autoxidation experiments at varying initial [BODIPY] using the k_t reported for the bulk substrate, assuming that statistically most chain terminations are going to be between 2 bulk substrate-derived peroxyls.

Scheme 1.13 – Structures of BODIPY Reporters



PBD-BODIPY



STY-BODIPY

1.3 Radical-Trapping Antioxidants

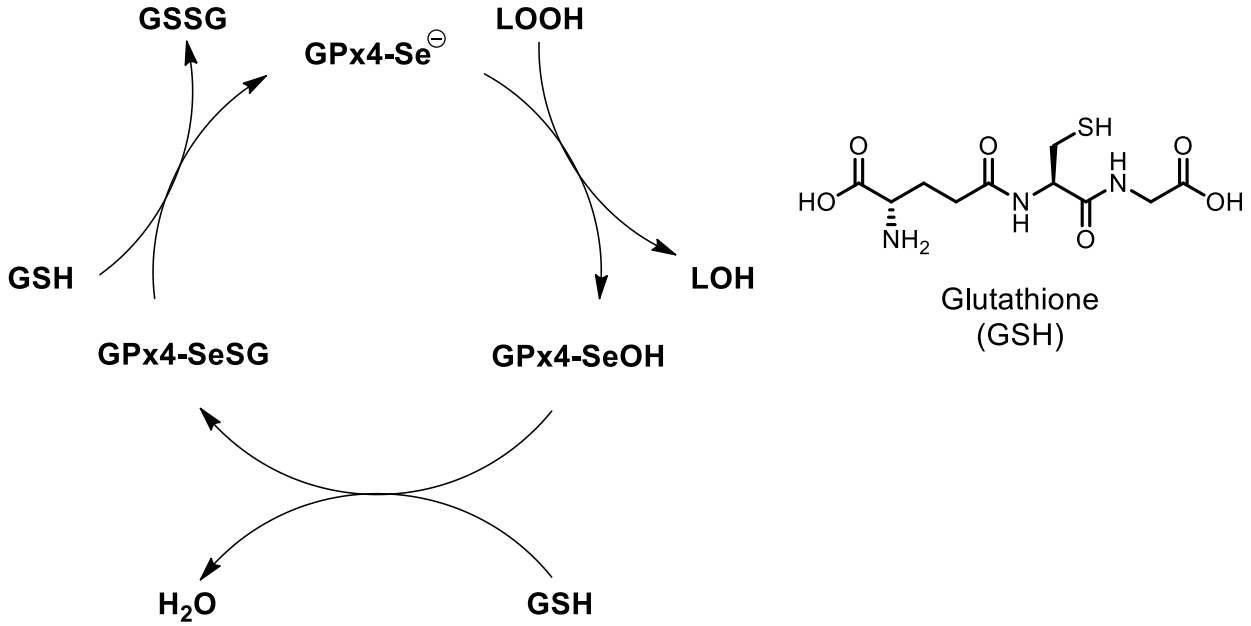
In many circumstances the process of autoxidation, as described above, results in undesirable outcomes leading to degradation of materials or even the deterioration of one's health. Compounds which act to suppress autoxidation are known as antioxidants. While antioxidants comprise a large scope of small molecules and enzymatic systems, by in large they fall under two categories:

a) Preventative Antioxidants
b) Radical-Trapping Antioxidants

Preventative antioxidants operate by reducing the peroxide products of autoxidation to corresponding alcohols. In systems where initiation is facilitated by hydroperoxides via homolysis (Eq. 1.5) or a Fenton-type process (Eq. 1.6), decreasing [ROOH] by reduction can profoundly improve resistance to autoxidation simply by preventing initiation to begin with (hence the name). One enzymatic preventative antioxidant system which mitigates lipid-peroxidation in mammalian cells is glutathione peroxidase 4 (GPx4). GPx4 contains a selenocysteine residue in the active site which facilitates the catalytic reduction of phospholipid-

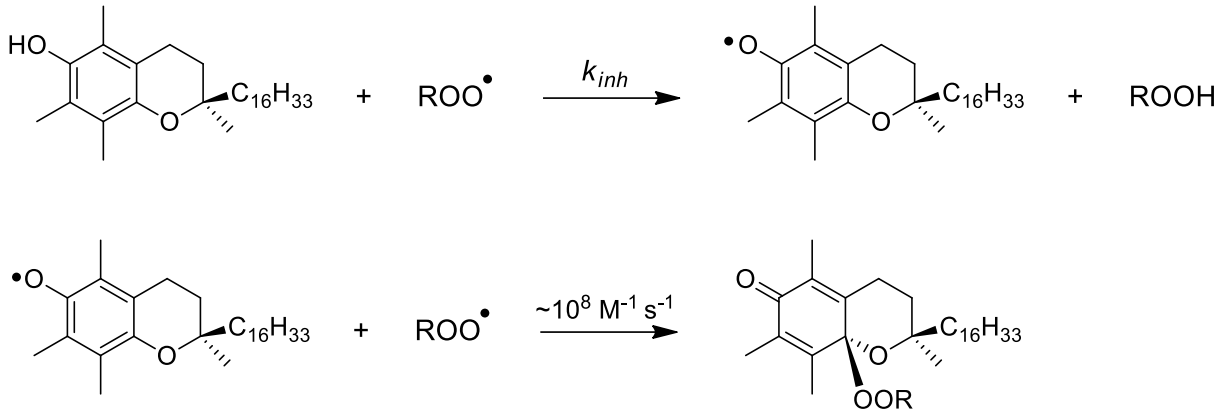
hydroperoxides (LOOH), using glutathione (GSH) as a stoichiometric co-factor/reductant (Scheme 1.14).

Scheme 1.14 – Catalytic Reduction of Phospholipid-Hydroperoxides by GPx4



Radical-trapping antioxidants (RTAs), which are the focus of my dissertation research, mitigate autoxidation by trapping peroxyl radicals which prematurely terminates the chain reaction. Keeping with the theme of biological antioxidant systems, two prominent dietary RTAs are vitamin C (ascorbic acid) and vitamin E (specifically α-tocopherol). As cells are heterogenous systems with respect to water-lipid partitions, we draw an important distinction between water-soluble (ascorbic acid) and lipid-soluble (α-Toc) RTAs. Generally, a water-soluble RTA does not affect termination of lipid-peroxidation, at least directly.[26] As our present interests lie in inhibiting lipid-peroxidation, the discussions in the foregoing will almost exclusively be about lipid-soluble RTAs. A brief overview of the mechanism of action of a phenolic RTA, using α-Toc as an example, is provided in Scheme 1.15.

Scheme 1.15 – Radical-Trapping Antioxidant Activity of α-Tocopherol



α-Toc first transfers its phenolic hydrogen atom to a peroxyl radical, resulting in a hydroperoxide and a persistent non-propagating phenoxyl radical. This is subsequently followed by peroxyl addition to the α-Toc-derived radical, creating a stable peroxide adduct. In total, this traps two radical chains, making the stoichiometry of α-Toc n = 2. The rate of the inhibited autoxidation (R_{inh}) is defined in Eq. 1.29:

$$R_{inh} = nk_{inh}[AH][ROO^{\bullet}] \qquad (1.29)$$

Where k_{inh} is the rate constant for the first reaction, and [AH] is the concentration of the RTA. The peroxyl-phenoxyl radical combination is usually a much faster reaction, so when $n \leq 2$, $k_{inh}[AH]$ is multiplied by this factor. The rate law for an inhibited autoxidation (Eq. 1.13) is derived in a similar manner to the uninhibited rate law (Eq. 1.10) except that peroxyl-peroxyl termination is replaced with the RTA inhibition reactions, as self-termination reactions have a negligible contribution to chain-termination.

$$R_i = R_{inh} = nk_{inh}[AH][ROO^{\bullet}] \qquad (\textit{steady-state assumption})$$

$$[ROO^{\bullet}] = (R_i/nk_{inh}[AH]) \qquad (1.30)$$

$$\frac{d[ROOH]}{dt} = k_p[RH]R_i/nk_{inh}[AH] \qquad (1.13)$$

The rate law assumptions also apply to inhibited BODIPY co-autoxidation:

$$-\frac{d[BODIPY]}{dt} = k_p[BODIPY]R_i/nk_{inh}[AH] \qquad (1.31)$$

The stoichiometry (n) of an RTA can be ascertained using the inhibition period (t_{inh}) if the R_i is known (Eq. 1.32). The t_{inh} is calculated by determining the intercept between the tangents of the inhibited and uninhibited periods (tangents are typically calculated from the first 20% of each respective period). Conversely, if the stoichiometry of an RTA is known, which for numerous phenols an n = 2 has been experimentally established, it can be used as a convenient means of determining the R_i of a system (Eq. 1.14b):

$$n = t_{inh}R_i/[AH] \quad (1.32)$$

$$R_i = n[AH]/t_{inh} \quad (1.14b)$$

Taken together, properties such as k_{inh} and n are important for assessing the efficacy of various RTA compounds and will form the basis of much of the discussion going forward. The k_{inh} informs on the intrinsic ability to suppress chain propagation, the ideal being chain length (υ) approaching 0 since k_p[RH]<< k_{inh}[AH], while the n informs on how long the system remains in an inhibited state, ideally n approaching ∞. Though most the k_{inh} in this dissertation are derived from the inhibition of BODIPY co-autoxidation (Figure 1.1), these are interchangeable with the values determined by other means (such as O_2-consumption) which we have demonstrated experimentally numerous times. But in addition to our published work using the method, the provided derivations demonstrate that the foundation is also solid on the basis of first principles.

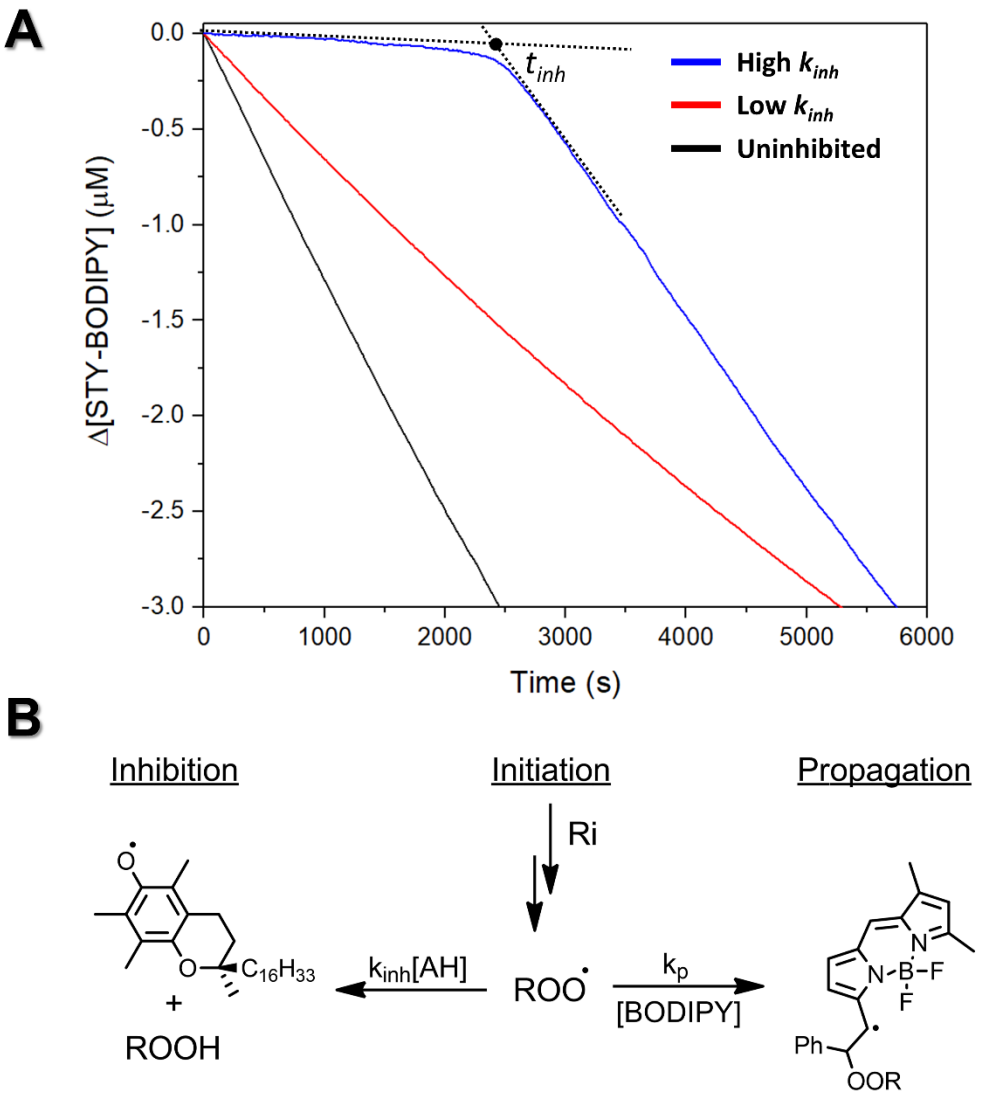


Figure 1.1. (A) Representative BODIPY co-autoxidation traces with no inhibition (black), an RTA with a low k_{inh} (red) and an RTA with a high k_{inh} (blue). **(B)** A scheme representing the competition between substrate oxidation and RTA-driven peroxyl termination.

While we have just described both the importance of RTA kinetics and how to measure them, we are left with the question of how to predict if an RTA will have a "high" or "low" k_{inh}. In any realistic context, the concentration of RTA will be orders of magnitude lower than the oxidizable substrate, so for an RTA to be reasonably competitive in a given system the k_{inh} should be at least 3-orders of magnitude greater than the k_p of the substrate. Many factors potentially influence the observed inhibition kinetics, and I will attempt to summarize them in two sections, first

addressing electronic and steric substituent effects followed by a section covering medium effects.

1.3.1 Reactivity of Radical-Trapping Phenols and Aromatic Amines: Electronic and Steric Substituent Effects

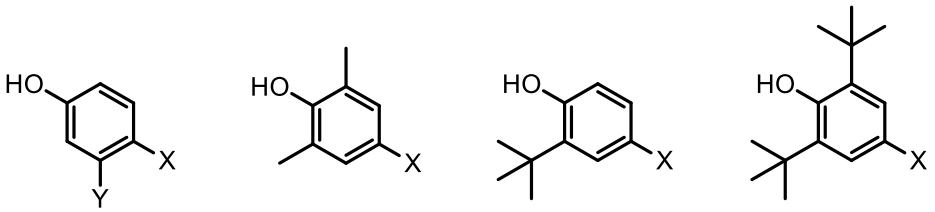
Until the early 1960's the actual mechanism by which phenols inhibited autoxidation was not entirely certain, despite the fact that they had been in use as lubricant and rubber additives for several decades. A large part of the confusion was due to a failure to detect a KIE for deuterated phenolic RTAs which would be commensurate with a HAT-type inhibition mechanism. In 1962, J. A. Howard and K. U. Ingold working at the National Research Council in Ottawa Canada reported the first proper primary KIE (k_H/k_D ~ 10.6) for BHT (2,6-di-*tert*-butylphenol) in a series of inhibited styrene autoxidation experiments (using the aforementioned O_2-uptake methodology).[56] Where many before them had failed, Howard and Ingold correctly identified the propensity of BHT's hydroxyl group to rapidly exchange H/D with hydroperoxide produced in the autoxidation and even the moisture in the air. Thus, special precautions in the experimental design had to be taken, such as the addition of D_2O to the autoxidation mixture, to counteract the effects of incidental H/D exchange. This provided the missing piece of data confirming the transfer of phenol's H-atom to peroxyl (Eq. 11) was indeed the rate determining mechanism of inhibition.

This would only be the first in an impressive series of papers not only on RTA kinetics, but also for most of the absolute propagation and termination rate constants which are foundational to this whole area of research. The follow up paper, published in 1963, looked at the electronic substituent effects on phenols bearing a wide range of electron-donating and electron-withdrawing substituents either in the 3-position (meta) or 4-position (para).[57] Depending on the substituent and the position, the k_{inh} ranged from ~10^2-10^5 $M^{-1}s^{-1}$. Using Brown and Okamoto's electrophilic substituent constants (σ^+), a recent innovation at the time, Howard and Ingold were able to establish a clear linear-free energy relationship:

$$\log\left(\frac{k}{k_0}\right) = -1.59\sigma^+ + 0.002 \qquad (1.33)$$

The strong negative slope indicated a polarized TS where a partial positive charge developed on the phenolic part of the phenol-peroxyl activated complex. The strong resonance stabilizing effect was very obvious particularly when comparing the kinetics of 4-methoxyphenol and 3-methoxyphenol, the former being 20-fold faster on account of the lone-pair donating effect. Using laser-flash photolysis (LFP), a similar kinetic trend was observed for the HAT to tBuO$^{\bullet}$ as reported by Scaiano and co-workers (albeit the absolute rate constants are ~5-orders of magnitude higher).[30] Howard and Ingold immediately followed up with another paper which expanded the scope to various ortho-alkylated phenols (a summary of results from both papers is given in Table 1.4).[58]

Table 1.4. Summary of Steric and Electronic Substituent Effects on the Thermodynamics and Kinetics of Simple Phenols



Substituents	$\Sigma\sigma^{+}$ [a]	$BDE_{O\text{-}H}$ *(kcal mol^{-1})* [b]	$k_{inh,X}/k_{inh,BHT}$	k_{inh} *(10^3 M^{-1} s^{-1})* [c]	$k^{BuO\bullet}$ *(10^7 M^{-1} s^{-1})* [d]
Unhindered Phenols					
Phenol	(0)	86.7 ± 0.7	0.37	2.91	33
4-MeO	-0.778	(82.3)	6.0	47.8	160
3-MeO	+0.047	(85.8)	0.32	2.57	-
4-Me	-0.311	(85.0)	1.15	9.17	55
3-Me	-0.066	(85.7)	0.39	3.07	-
4-Cl	+0.114	(86.4)	0.27	2.15	29
4-CN	+0.659	(88.1)	0.036	0.29	9.7
2,6-Dimethyl Phenols					
4-H	-0.622	83.4 ± 0.4	1.12	8.9	-
4-Me	-0.933	81.6 ± 0.2	3.5	28	-
4-Cl	-0.508	(82.8)	1.45	11.5	-
4-CN	+0.037	(84.6)	0.164	1.3	-
2-*tert*-Butyl Phenols					
4-H	-0.256	(85.0)	0.94	7.47	-
4-MeO	-1.034	(80.6)	13.5	107	-
4-Me	-0.567	(83.3)	3.0	24	-
4-CN	+0.403	(86.4)	0.11	0.87	-
2,6-Di-*tert*-Butyl Phenols					
4-H	-0.512	81.7 ± 0.2	0.28	2.25	-
4-MeO	-1.290	77.2 ± 0.1	3.9	31.2	-
4-Me (BHT)	-0.823	79.9 ± 0.1	(1)	7.95	-
4-CN	+0.147	83.2	0.10	0.77	-

(a) σ^{+} parameters as shown in the Howard/Ingold papers.[57,58] (b) $BDE_{O\text{-}H}$ values either from experimental determinations by Lucarini and co-workers[41,59] using the revised value for phenol (86.7 ± 0.7 kcal mol^{-1})[60] or calculated using their empirically derived substituent additivity rules (values in parenthesis).[59] (c) Inhibition rate constants are shown as presented in the Howard/Ingold papers, which were relative to their measured value for BHT from their seminal

1961 paper (7.95×10^3 M^{-1} s^{-1}).[56] The absolute rate constant later reported for BHT, using a more reliable setup, was about 1.8-fold higher (14×10^3 M^{-1} s^{-1})[45] so the other entries should be adjusted accordingly. (d) Rate constants for PCET with *tert*-butyl alkoxyl radical (tBuO•) for the corresponding phenols.

The general observations were that 2,6-dimethyl and 2-*tert*-butyl phenols had higher k_{inh} values than the unhindered counterparts (~3-fold increase), while the 2,6-di-*tert*-butyl phenols were similar to the unhindered phenols. Corresponding thermodynamic data for these reactions were not abundant until the mid-90's when Pedulli and co-workers developed a straightforward approach for measuring phenolic O-H BDEs.[41,59] Using 2,4,6-tri-*tert*-butyl phenol ($BDE_{O\text{-}H}$ = 81.2 kcal mol^{-1}, which was later revised to 80.1 kcal mol^{-1})[60] as a point of reference, persistent radical-equilibria experiments were carried out by EPR to determine the $BDE_{O\text{-}H}$ values for a wide range of phenols. Taking this together with corresponding kinetic data from the literature,[45] a nice Evans-Polanyi relationship can be established between $BDE_{O\text{-}H}$ and the log(k_{inh}) (Figure 1.2). While the 2,6-di-*tert*-butyl phenols have rather weak O-H bonds, the reaction site is also sterically encumbered, increasing $\Delta\Delta G^{\ddagger}$ for the trapping of peroxyl relative to the 2,6-dimethyl phenols.

Now would be as good a time as any to address why these hydrogen-atom transfer (HAT) reactions from phenol to peroxyl are so much faster than thermodynamically equivalent propagation reactions. For instance, the $BDE_{C\text{-}H}$ for toluene is roughly equivalent to the $BDE_{O\text{-}H}$ of 4-methylphenol, yet the k_{inh} of the latter is nearly 5-orders of magnitude higher than the k_p of toluene. It has been generally observed HAT reactions between two heteroatom species have lower $\Delta G^{\ddagger}$ than thermodynamically equivalent reactions where one or both of the partner sites are carbon. The general phenomenon led to a semi-empirical model, first proposed by Zavitsas in 1972, where the bond strength between the partner donor/acceptor (C-C, C-O, O-O, N-O, etc.) could be used to predict the activation energy (E_a) of a given HAT reaction.[61] The conceptual model depicts the HAT activated complex as the valence bond structure $[X\uparrow\text{---}H\downarrow\text{---}Y\uparrow]^{\ddagger\bullet}$ where antibonding triplet repulsion between X and Y is a major contributing term to the E_a.[62] All other factors being equal, O-O bonds are weaker than C-O bonds, and so the triplet repulsion term is lower. In modernity the semi-empirical explanation for phenol-peroxyl reactivity has been succeeded by the proton-coupled electron-transfer mechanism (PCET) which is a distinct alternative to HAT, exclusive to heteroatom-heteroatom H-atom exchange.[63,64] For a HAT, the

proton and the electron from the O-H bonding orbital of the phenol would pass “together” to the SOMO of the peroxyl. Instead, a pre-reaction H-bond complex forms between the phenol’s O-H and the lone-pair of the terminal oxygen of the peroxyl, after which the lone-pair orthogonal to the plane of phenolic ring transfers an electron to the aligned SOMO of the peroxyl. As this electron-transfer happens, negative charge builds up on the peroxyl adduct (and positive on the phenol), promoting a concerted transfer of a proton to the pseudo-anionic peroxyl-adduct. The advantage of the PCET mechanism is that the “new” SOMO that is developing on the phenolic-adduct benefits from aromatic resonance stabilization through the entire process, which contributes to the lower barrier of the reaction compared to a HAT between toluene and peroxyl. A rendering of 4-methylphenol-peroxyl PCET is shown in Fig. 1.2, where the peroxyl is shown in a *syn*-configuration with respect to the phenol. This is typically the most favorable geometry on account of a secondary orbital overlap between the aromatic ring and the interior O-atom of the peroxyl which provides additional stability for the TS.

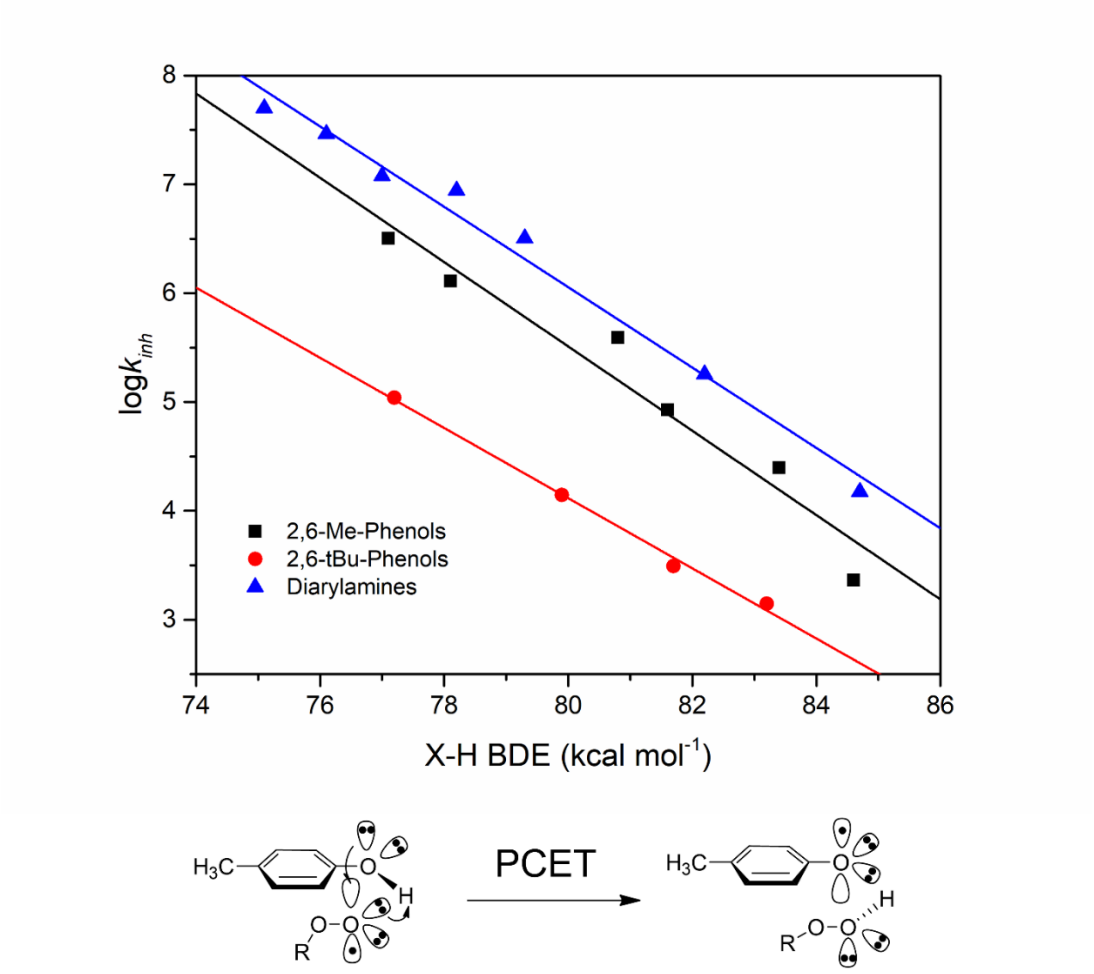
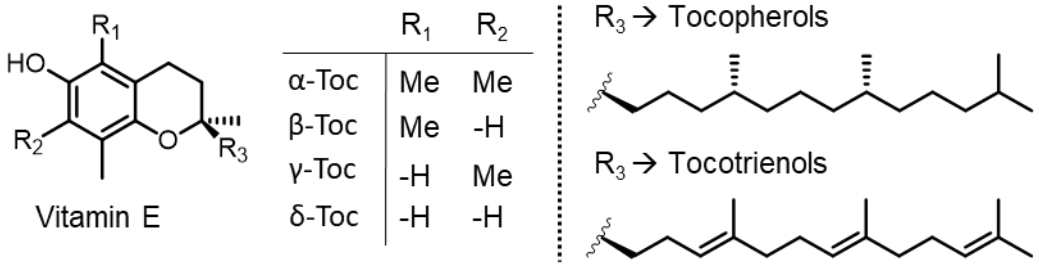


Figure 1.2. The Evans-Polanyi relationship between BDE_{O-H}/ BDE_{N-H} and the peroxyl inhibition rate constants for phenols and diarylamines. Thermodynamic data was taken from Lucarini and co-workers.[41,59,65] Kinetic data is from various sources.[45,58,65]

There is another whole family of RTAs which I have neglected to mention up until this point, which are aromatic amines. Early mechanistic work by Brownlie and Ingold in 1967 revealed that these compounds operated by an analogous mechanism to the phenols, where a primary deuterium KIE was observed and the electronic substituent effects fit well to the σ^+ Brown and Okamoto parameters.[66] Primary anilines and N-alkyl secondary anilines had fairly mediocre inhibition kinetics, while diphenylamines, especially those with electron donating substituents, were highly active by comparison. It is diarylamine-type compounds which are in fact the focus of the thesis, specifically phenoxazines and phenothiazines. While not wishing to bury the lead, pedagogically it was more straightforward to first focus on the development of the mechanistic

theories underpinning phenols as these have a history of more than 60-years of continuous study, while similarly intensive mechanistic interrogation of diarylamine-type compounds has been more intermittent, with many of the advances being within the last couple of decades. As peroxyl trapping by the aromatic amines occurs by the same PCET mechanism, all of the reactivity trends discussed thus far and in the foregoing are just as applicable to these as they are to the phenols (see the Evans-Polanyi in Figure 1.2). These will be discussed at length in due course, but for now let us continue where we left off with phenols.

Scheme 1.16 – The Naturally Occurring Forms of Vitamin E



After taking more than a decade long hiatus from studying the RTA kinetics of phenols, in 1981 Ingold, now working with G. W. Burton, would once again return to this research, tackling the subject of Vitamin E.[67] Vitamin E is a small family of naturally occurring lipid-soluble phenolic compounds which can be found in a variety of dietary sources. The chromanol headgroup comes in four variants (α, β, γ and δ) depending on the degree of methylation, and the phytyl tail is either saturated (tocopherols) or unsaturated (tocotrienols), though we will only be discussing tocopherols. In particular, α-tocopherol (α-Toc) has an essential role in mammalian biology (*vide infra*) being a highly efficacious and bioavailable lipid-soluble RTA. While the role of vitamin E as an inhibitor of lipid peroxidation was widely accepted by the early 80's, there was no reliable information with respect to absolute rate constants for the various forms or even consensus on their efficacy relative to one another. Earlier qualitative measurements led to a belief that γ-Toc was more effective than α-Toc,[68–70] and apparently even some commercial hindered phenols such as BHT were considered competitive with α-Toc in some *in vitro* testing.[71] As you may appreciate, these conclusions run contrary to the linear free-energy relationship established by Howard and Ingold in the 60's, which would have predicted precisely the opposite. Ingold and Burton, furnished with a more sophisticated and accurate variant of the inhibited styrene method used in the 60's, found indeed that the k_{inh} of the tocopherols (Table 1.5) were such that α-Toc >

β-Toc ~ γ-Toc > δ-Toc and all forms of vitamin E were orders of magnitude more reactive than BHT. Furthermore α-Toc became the most reactive RTA measured at that time with a k_{inh} of 2.4 × 10^6 M^{-1} s^{-1} (later being revised to 3.2 × 10^6 M^{-1} s^{-1}.)[45]

Table 1.5. Inhibition Rate Constants of Vitamin E and Related Phenols

Vitamin E			Related Phenols		
	k_{inh} (10^4 M^{-1} s^{-1}) [a]	$k_{inh,X}/k_{inh,BHT}$		k_{inh} (10^4 M^{-1} s^{-1}) [a]	$k_{inh,X}/k_{inh,BHT}$
α-Toc	320	229	BHT	1.4	(1)
β-Toc	130	93	TeMMP	39	28
γ-Toc	140	100	TrMMP	130	93
δ-Toc	44	31	PMC	380	271
			PMF	570	407

(a) Data taken from Burton *et al.* (1985).[45]

One curious finding was that 2,3,5,6-tetramethyl-4-methoxy phenol (TeMMP), which they had anticipated would be electronically analogous to the α-Toc chromanol head, was <10% as reactive as α-Toc. This anomaly led to another important discovery with respect to understanding the impressive RTA kinetics of α-Toc: the stereoelectronic effect. Examining the X-ray crystal structure of various *p*-methoxy phenols and the chromanol of 2,2,5,7,8-pentamethyl-6-hydroxychroman (PMC, an analogue of α-Toc with the phytyl replaced with methyl), a correlation between their relative k_{inh} values and the dihedral angle between the alkoxy group's alkyl and the plane of the aromatic ring (θ') was noted, with increasing k_{inh} as θ' approaches 0°. For TMMP, the θ' of the methoxy group was 89°, implying that the lone-pair was orthogonal to the π-system of the phenol (θ ~ 90°), while the cyclic chroman alkoxy of PMC had a θ' of 17°.[67] In a follow up paper, they underscored the importance of this effect with two additional examples. The first was to remove the methyl group at the 5-position of TeMMP (making TrMMP) which, despite having fewer donor substituents, had more than a 3-fold increase in k_{inh}.[45] The removal of this methyl ortho with respect to the methoxy group removed the steric hinderance that forces the methoxy of TeMMP into an orthogonal conformation.

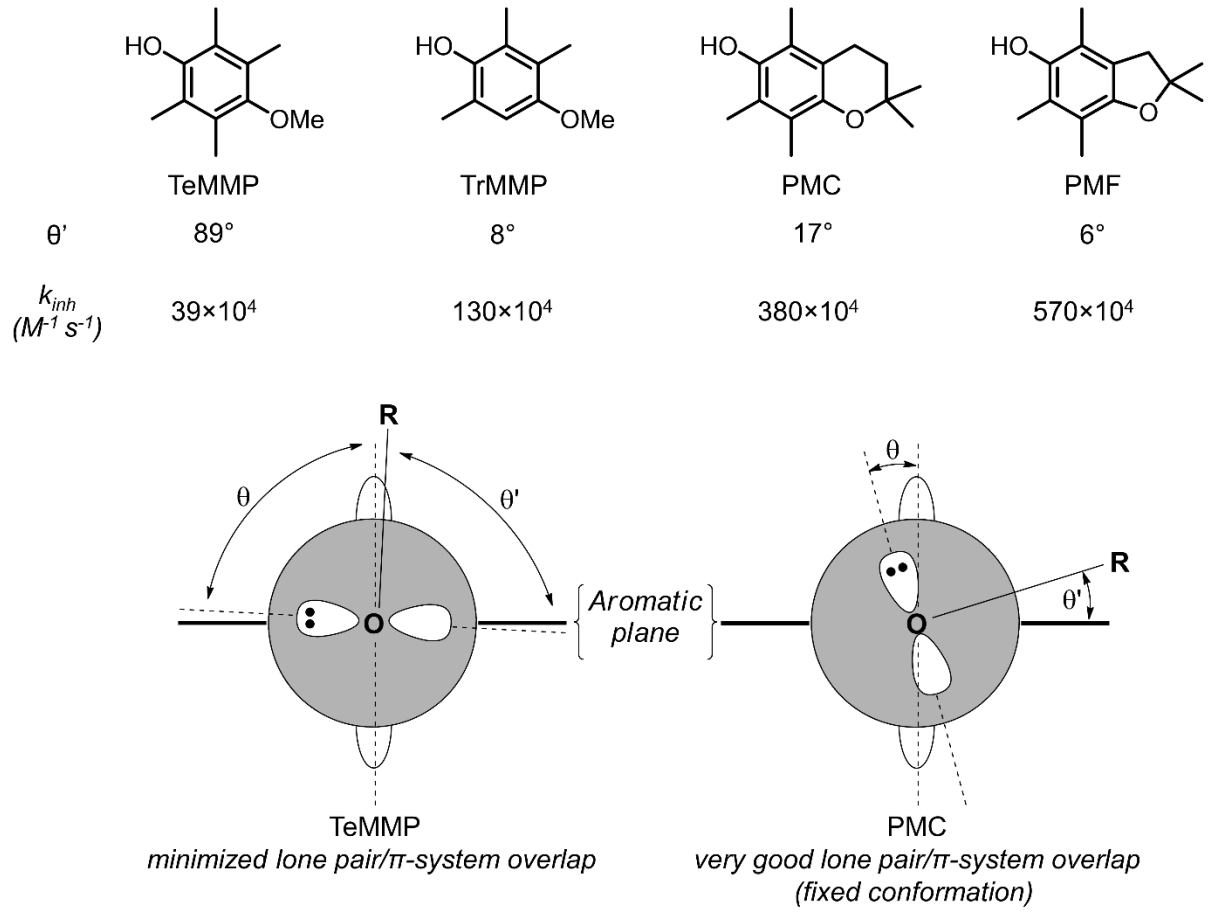
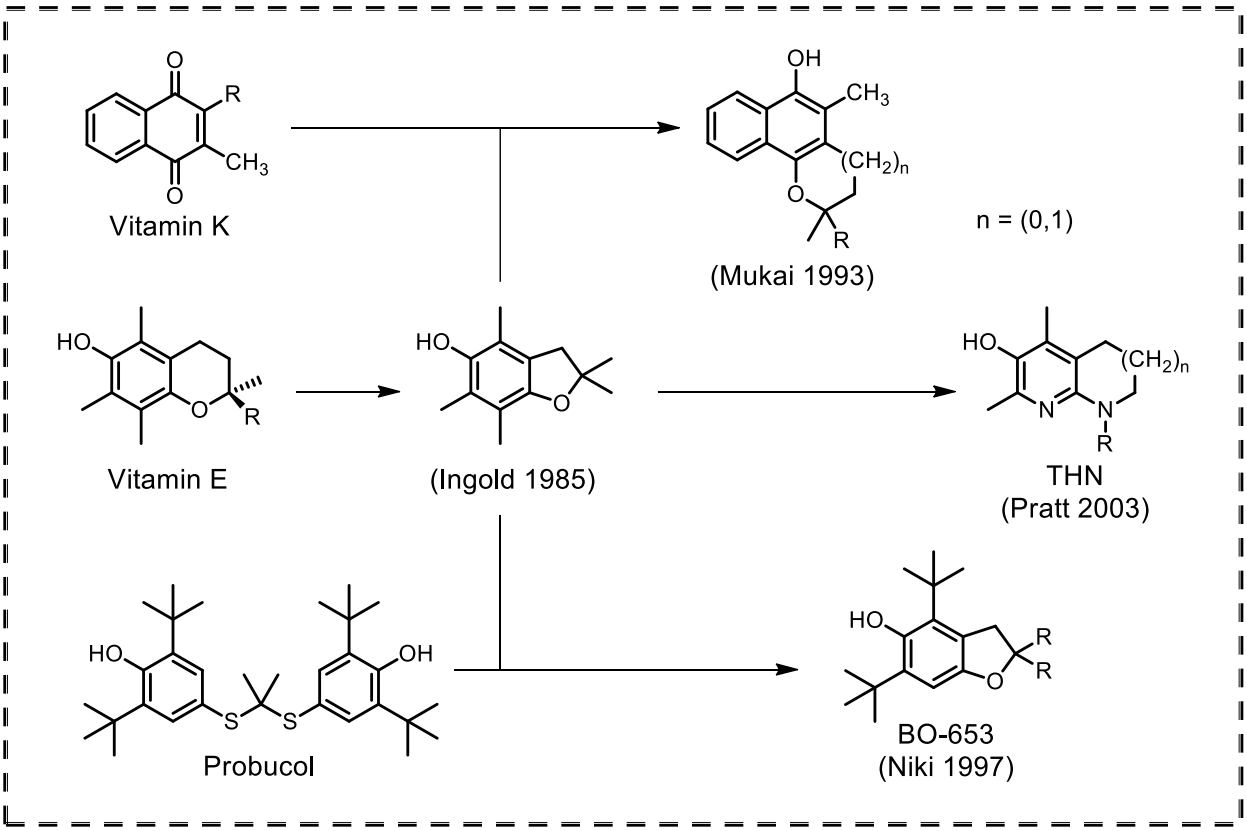


Figure 1.3. Systematic examples demonstrating the stereoelectronic lone pair donor effect.

The second example which further supported their model was replacing the chromanol of α-Toc/PMC with a benzofuran, as in 2,3-dihydro-5-hydroxy-2,2,4,6,7-pentamethylbenzofuran (PMF). Like PMC, the lone pair is held in a fixed confirmation but the θ for PMF is only 6°. The result is a decreased $\Delta G^{\ddagger}$ for the PCET, which is evident by the 50% increase in k_{inh} compared to PMC. These insights inspired a number of interesting Vitamin E inspired RTAs from other researchers (a few of which are highlighted in Scheme 1.17.)[72–74]

Scheme 1.17 – Family Tree of Vitamin E Inspired Lipid Soluble RTAs



From this point one might reason that the next logical iteration would be to replace the alkoxy donor group (σ_p^+ = -0.78) with a more aggressive donor such as an amino group (σ_p^+ = -1.81), which would further lower $BDE_{O\text{-}H}$ and further enhance the peroxyl trapping kinetics. Evidently following this line of reasoning, Burton and Ingold produced 1,2,3,4-tetrahydro-6-hydroxy-5,7,8-trimethylquinoline (TTMQ) but discovered, much to their chagrin, that it was not stable in air (even as a crystalline solid) making it useless as an RTA.[45] As it turns out, the same electronic factors that lower the barrier for the PCET with peroxyl, also enhance the electron-transfer reaction with O_2. The electron-transfer reaction is a pro-oxidant process which produces superoxide ($O_2^{-\bullet}$) followed by hydroperoxyl ($HOO^\bullet$) which can *initiate* autoxidation. If one intended to push RTAs to the theoretical limits with respect to the trapping of peroxyls, where the diffusion limit in the liquid-phase would be 10^9-10^{10} M^{-1} s^{-1}, they would first have to contend with the concomitant pro-oxidant tendencies. A workaround developed by my supervisor, D. A. Pratt, in collaboration with Valgimigli and co-workers was to modify the phenolic scaffold to discourage radical cation formation.[74–76] By using substituted 3-pyridinols and 5-pyrimidinols,

which have N-heteroatoms in the 3 and 3,5 positions relative to the hydroxy respectively, the inductive effect sharply increases the ionization potential (IP) relative to a modest increase of the $BDE_{O\text{-}H}$. This strategy was further adapted to make tetrahydronaphthyridinols (THNs), a structure analogous to TTMQ in order to take advantage of the stereoelectronic effect. Unlike TTMQ, however, THN was a potent RTA (k_{inh} = (8.8 ± 3.2) × 10^7 M^{-1} s^{-1}) which was approximately 25-fold faster than α-Toc. Substituted dihydropyrrolopyridinols (DHPyP) benefitted from a further enhanced stereoelectronic effect (k_{inh} = (2.8 ± 1.8) × 10^8 M^{-1} s^{-1}), however its stability in air was comparatively poor. To be clear, though THN is a very capable RTA, there is no "free lunch" with respect to oxidative stability. The standard oxidation potential (vs. NHE) was still much lower than would be ideal for a vitamin E mimic (E^o = 0.25 V vs. 0.98 V for THN and α-Toc respectively).[77]

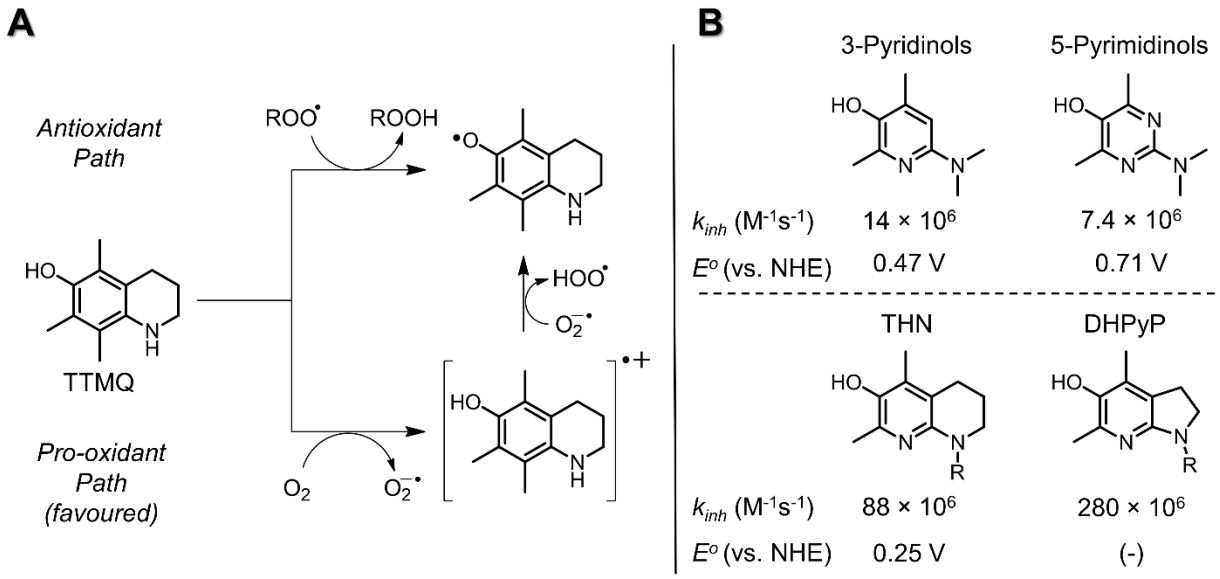
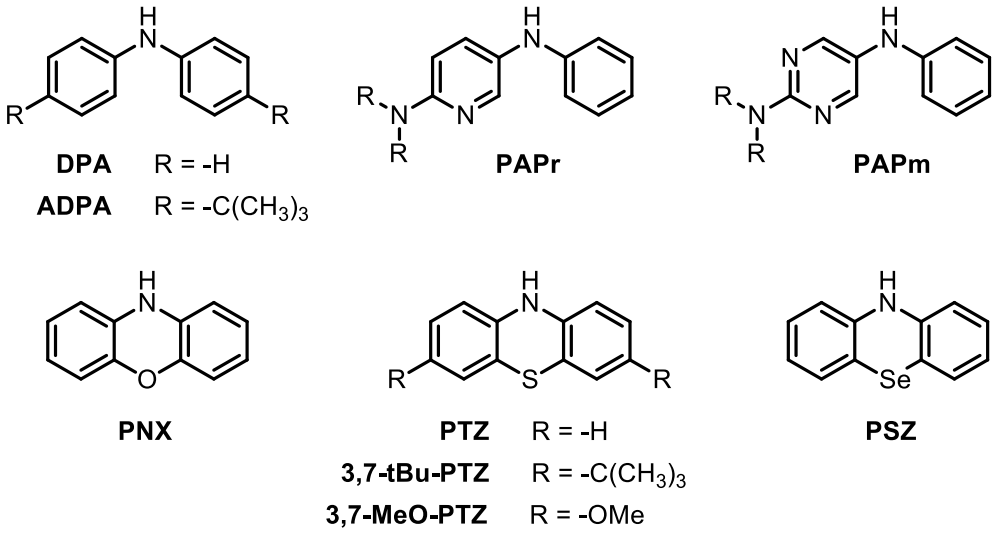


Figure 1.4. (A) Pro-oxidant fate of 1,2,3,4-tetrahydro-6-hydroxy-5,7,8-trimethylquinoline by single electron-transfer to O_2. **(B)** Activated pyridinol and pyrimidinol-type RTAs by Pratt, Valgimigli and co-workers.[74,76,77]

Thus, the search parameters for a hypothetically "perfect" RTA going into the 2000's and 2010's held both the peroxyl-trapping kinetics (k_{inh}) and stability to single-electron oxidation (E^o) in tension. How fast can the RTA trap chain-carrying peroxyls without severely compromising air-stability? Having thoroughly explored the heterocyclic "phenol-analogues" in the aught years, Pratt, Valgimigli and Hanthorn applied the same strategy to make heterocyclic "diphenylamine-

analogues" which were the subject of a series of papers published in 2012.[78–80] Similar to the amino activated 3-pyridinols and 5-pyrimidinols, the amino activated phenyl-pyridines (PAPr) and phenyl-pyrimidines (PAPm) had very impressive inhibition kinetics (~1×10^7 and ~3×10^6 M^{-1} s^{-1} resp.), but the former was particularly compromised with respect to oxidation potential (0.60 V vs. 0.81 V). This dichotomy of balancing these reactivity and stability parameters seemed further validated when many of these heterocyclic diarylamines were systematically compared in high temperature (160 °C) autoxidations of n-hexadecane published February of 2015.[81] On the one hand, the 4,4'-di-*tert*-butyldiphenylamine (or ADPA for alkylated-diphenylamine) was very stable (E_{pa} = 1.02 V) but had comparatively modest peroxyl trapping kinetics at ambient temperatures (i.e. k_{inh} = 1.8×10^5 M^{-1} s^{-1} at 37 °C). On the other hand, PAPr, and other similarly activated heterocyclic diarylamines, had impressive kinetics ($\geq10^7$ $M^{-1}s^{-1}$) but were not stable ($E^o \leq 0.6$V). Both ADPA and PAPr were greatly outperformed by PAPm which was a midpoint between these with respect to "reactivity and stability." The interpretation being that PAPm was more kinetically competitive than ADPA for quenching chain-propagation, while also being "stable-enough" to not be directly oxidized by O_2 (unlike PAPr). There was also much speculation on potential enhanced catalytic-antioxidant activity of PAPm compared ADPA,[81–83] which will be critically addressed in the latter chapters (particularly Ch. 6).

Table 1.6. Data Table for Key Diarylamine RTAs (Circa 2015)



Diarylamine-Type RTAs			
	BDE_{N-H} (kcal mol^{-1}) [a]	*k_{inh} (10^4 M^{-1} s^{-1})* [b]	*E^o vs. NHE (V)* [d]
DPA	84.7 ± 0.7	1.5	-
ADPA	82.2 ± 0.6	18 [c]	1.02 [e]
PAPr	-	1100 [c]	0.60
PAPm	-	300 [c]	0.81
PNX	76.1 ± 0.3	2900	0.87
PTZ	78.2 ± 0.3	880	0.85
3,7-tBu-PTZ	77.0 ± 0.4	1200	0.75
3,7-MeO-PTZ	75.2 ± 0.3	5000	0.61
PSZ	79.3 ± 0.4	320	0.87 [f]

(a) Measured by EPR equilibration technique in benzene.[65,80] (b) Reported by Lucarini *et al*. by EPR-based O_2 consumption method.[65] (c) Reported by Hanthorn *et al.* using perester clock method.[80] (d) Half-wave of oxidation potential measured by cyclic-voltametry.[50,80] (e) Oxidation is irreversible, anodic peak potential (E_{pa}) by differential pulse voltammetry is reported instead. (f) Unpublished result.

This was the "state-of-the-art" when I began my graduate work, as a Master's student, in September of 2015. The next step? Find an RTA which had $E^o \geq 0.8$ V *and* a $k_{inh} \geq 10^7$ $M^{-1}s^{-1}$. I was directed by my mentors, Prof. D. A. Pratt and E. A. Haidasz, to study phenoxazine (PNX) as an RTA scaffold. Seminal work by Lucarini *et al.* in 1999 indicated that phenoxazine and phenothiazine (PTZ) were highly active RTAs (2.9×10^7 and 8.8×10^6 M^{-1} s^{-1} resp.) relative to other diarylamines *and* relative to α-Toc.[65] While the results were promising, there did not

appear to be much in the way of follow up work, thus an opportunity. Apart from the impressive kinetics of PNX, what made it of even greater interest was that, according to our internal measurements, it was incredibly stable (E^o = 0.87 V).[50] Interestingly, PTZ which had a higher $BDE_{N\text{-}H}$ (76.1 vs. 78.2 kcal mol^{-1} respectively) and a concomitant ~3-fold decrease in k_{inh}, was no more stable toward single-electron oxidation (E^o = 0.85 V), suggesting there was a unique set of structural features in PNX that not only yielded a weak N-H bond but also an unusually high oxidation potential.

With respect to the weak N-H bond, one could draw some analogies between diphenylamine (DPA) compared to PNX and phenol compared to Vitamin E. The oxygen-bridge at the 5-position on PNX is a lone-pair donor, but unlike a simple alkoxy group on a DPA or phenol, there are multiple stereoelectronic implications. Based on the highly planar geometry between the neighbouring rings on PNX over the bridging heteroatoms (167°), a high degree of lone pair/π-system overlap can be inferred contributing to lower enthalpy for a PCET. Furthermore, unlike DPA-like compounds that have freely rotating aromatic rings, the two rings of PNX are *fixed* in-plane with respect to each other. This aligned configuration closely resembles the aminyl radical product (180°) and the PCET activated-complex, which should result in a lower entropy of activation as well.[84] Understanding the facile PCET with PNX in comparison to PTZ is straightforward as the planar angle from amine to aminyl radical (147°→180°) is larger due to sulfur's size. Additionally, sulfur is a less potent lone pair donor and its lone pair orbitals are more diffuse. Going down the table to selenium, as found in phenoselenazine (PSZ), reactivity is further attenuated,[65] presumably for the same reasons.

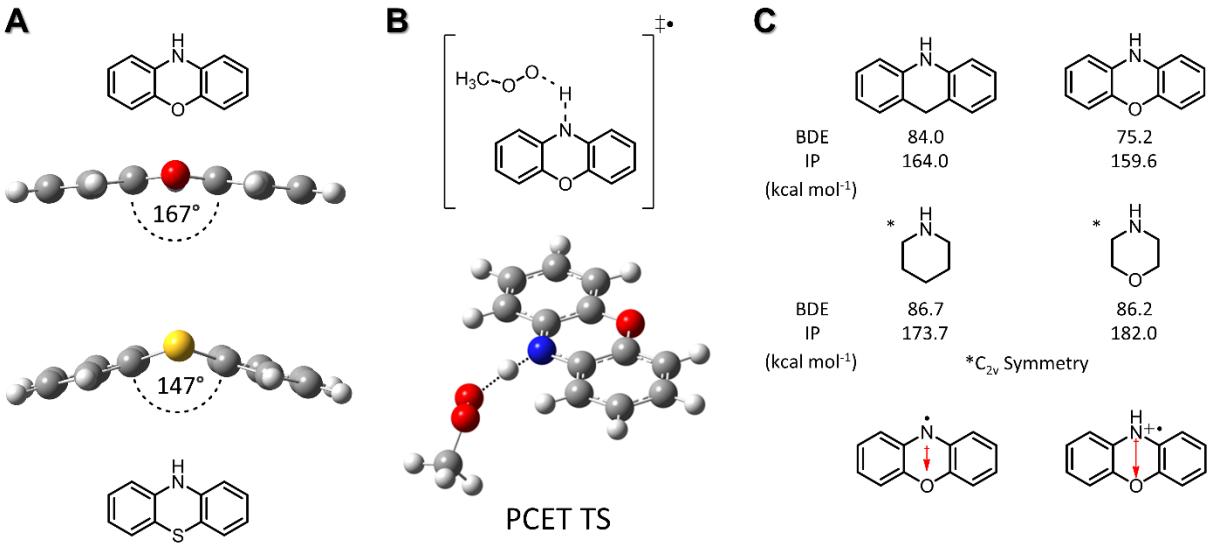


Figure 1.5. (A) Planarity of phenoxazine and phenothiazine compared. **(B)** Peroxyl-PNX PCET transition-state. **(C)** Dissection of the resonance and inductive/field effects of the O-bridge on radical and radical-cation stability.

What was not immediately obvious was how to reconcile the high oxidation potential relative to the very weak N-H bond. After much internal debate over how to separate the contributions of resonance and inductive/field-effects of the oxygen-bridge, E. A. Haidasz proposed that morpholine in a C_{2v} configuration could be used simulate just the inductive/field-effects. Using the highly accurate CBS-QB3 theoretical method, the BDE_{N-H} of PNX was found to be 8.8 kcal mol^{-1} lower than that of 9,10-dihydroacridine (75.2 vs. 84.0 kcal mol^{-1}) while the ionization potential (IP) difference is only 4.4 kcal mol^{-1} (159.6 vs. 164.0 kcal mol^{-1}). Looking at morpholine and piperidine with a C_{2v}-symetry, the difference in BDE_{N-H} was essentially flat (86.2 vs. 86.7 kcal mol^{-1}) while the IP sharply increased for morpholine (182.0 vs. 173.7 kcal mol^{-1}). In summary, while resonance donor effects would stabilize both formation of the neutral radical and radical-cation derived from PNX, the radical-cation is disproportionately *destabilized* by a strong inductive/field-effect induced by the oxygen directly across from the amine. The effect is also at play with PTZ, though to a lessened extent as sulfur is less electronegative.

With respect the reactivity/stability profile of PNX, whether activating or deactivating with EDGs or EWGs, PNX demonstrated a very favourable RTA-profile. The most activated compound tested, 3,7-dimethoxyphenoxazine (3,7-MeO-PNX) had an unprecedented inhibition

rate constant (k_{inh}^{PhCl} = 6.6 ± 1.1 × 10^8 M^{-1} s^{-1}) yet maintained a manageable level of stability (E^o = 0.59 V).[50] Meanwhile the most deactivated derivative tested at the time, 3-cyano-7-nitrophenoxazine (3-CN-7-NO_2-PNX) had a very high oxidation potential (E^o = 1.38 V) while still managing to be more reactive than *even* α-Toc in chlorobenzene (k_{inh}^{PhCl} = 4.5 ± 0.1 × 10^6 M^{-1} s^{-1}). In terms of a hypothetically "perfect" RTA, one would be hard pressed to find a more suitable candidate.

1.3.2 Reactivity of Radical-Trapping Phenols and Aromatic Amines: Medium Effects

Up until this point solvent effects have not been discussed, and essentially all of the kinetic data described thus far had been measured in similar and largely non-polar aromatic solvents/substrate mixtures (benzene, chlorobenzene, styrene, etc.) While this conformity is useful for the purposes of basic research, it certainly does not represent the range of possible applications for RTAs. In one of Howard and Ingold's early papers some basic trends of phenol reactivity in polar and non-polar solvents were established:[85]

i) The effect of solvents on the phenolic inhibition of styrene can be attributed to H-bonding of the phenolic hydroxyl to the solvent.
ii) The magnitude of the effect depends first on the acidity of the phenol (more acidic, slower inhibition).
iii) The magnitude of the effect also depends on steric hinderance of the phenol (more hindered, smaller solvent effect).

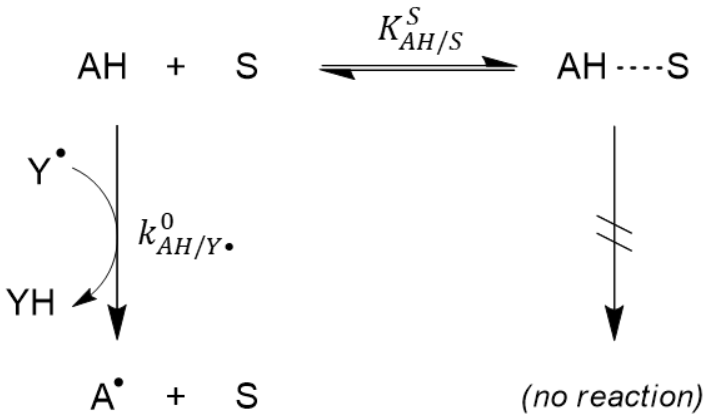
While the trends were identified very early on (1963), a quantitatively predictive model of the effect is a relatively recent innovation. After about a decade of data collection and theory crafting, a fully descriptive model emerged in 2001 from Snelgrove and Ingold and co-workers which addressed not only H-atom abstraction reactions of phenol, but a generalized model for all sorts of HAT/PCET reaction combinations.[86] An overview of their model is shown in Scheme 1.18, which encompasses three assumptions:

i) Each H-*atom* donor (e.g., phenol), can act as a H-*bond* donor (HBD) to a single H-bond acceptor (HBA) solvent molecule at any one time.

ii) The magnitude of the H-bond equilibrium constant is independent of the surrounding medium.

iii) Due to steric hinderance, the H-atom engaged in the 1:1 H-bond complex cannot be directly abstracted.

Scheme 1.18 – Snelgrove-Ingold H-Bond Pre-Equilibrium Model



$$k^S_{AH/Y•} = \frac{k^0_{AH/Y•}}{1 + K^S_{AH/S}[S]} \quad (34)$$

The effect applies to any H-atom donor (AH) that can form H-bond complexes, so H-atoms from abstractable C-H sites (hydrocarbon substrates) are essentially immune to this effect.[87,88] Importantly, the magnitude of the solvent effect is independent of the radical species (Y•) whether it be an alkoxyl,[89] alkyl,[90] peroxyl[91] or even a DPPH radical.[89] Indeed, through a systematic process of elimination, Eq. 1.34 more or less completely describes the situation: a simple H-bond pre-equilibrium where $k^S_{AH/Y•}$ is the observed rate constant and $k^0_{AH/Y•}$ is the intrinsic rate constant in the absence of H-bonding. While having robust explanatory scope, if this were the extent of the theory it would have somewhat limited practical utility as it would require measurement of K^S for *each* combination of HBD/HBA. Fortunately, it was found that H-bond acidity (α_2^H) and H-bond basicity (β_2^H) parameters mapped on very well on to the kinetic data of Snelgrove *et al*. using the various phenols in various solvents. First pioneered by Taft co-workers in the late 1960's,[92,93] and later expanded by M. H. Abraham in the late 80's / early 90's,[94,95] the β_2^H and α_2^H are complementary parameters that were designed to describe/predict the 1:1 H-bond complexation equilibrium constants (K_f) of a wide range HBA and HBD, respectively, without the need to individually measure each "new" combination:

$$logK_f = 7.354\alpha_2^H\beta_2^H - 1.094 \quad (1.35)$$

Simply by applying the assumptions presented in the Snelgrove-Ingold model to Abraham's equations, it was found there was reasonable conformity between the empirical linear-free energy relationship obtained by Snelgrove *et al.* (Eq. 1.36) and the equation derived from "first principles" (Eq. 1.37):[86]

$$logk^{S}_{AH/Y\bullet} = logk^{0}_{AH/Y\bullet} - 8.3\alpha_2^H\beta_2^H \qquad (1.36)$$

$$logk^{S}_{AH/Y\bullet} = logk^{0}_{AH/Y\bullet} - 7.8\alpha_2^H\beta_2^H \qquad (1.37)$$

The discrepancy between Eq. 1.36 and 1.37 may arise from the fact that the α_2^H/β_2^H parameters are derived from solute-solute complexation (dilute H-bonding interactions in non-H-bonding CCl_4 solution), but the system being described by Snelgrove *et al*. is a solute-solvent interaction. While there is often agreement between solute and bulk solvent scales of β, they are not equivalent and discrepancies in H-bond basicity exist between the respective approaches.[96] However, the empirical nature of Eq. 1.36 may simply "iron out" some auxiliary bulk solvent effects in a semi-systematic fashion.

The Snelgrove-Ingold model played a vital role in our seminal work on substituted PNX RTAs in 2017.[50] One of the difficulties we faced was simply that inhibition of PBD-BODIPY by the PNX-based compounds in the autoxidation of styrene was so efficient that -d[BODIPY]/dt ~ 0 M s^{-1} (Eq. 1.31), even at RTA loadings as low as 2×10^{-6} M. Lowering the [AH] even further was not feasible as the t_{inh} would simply be too short to establish an inhibited steady-state suitable for kinetic analysis. We first tried changing the styrene/PhCl mixture (1:1 v/v) to a 1,4-dioxane/PhCl mixture (1:3) to lower the steady-state concentration of "free" PNX to a level where propagation could compete with inhibition (Fig. 1.6). Using Abraham's ^{1}H NMR[97] method to determine the α_2^H of PNX (0.44) and Taft's ^{19}F NMR method[92] to determine the β_2^H of the dioxane/PhCl mixture at 310K (0.35),[98] the observed inhibition rate constant in the dioxane/PhCl mixture (k_{inh}^{Diox}) would be 9-fold lower than in the styrene/PhCl system (according to Eq. 1.36 assuming a β_2^H of 0.09 for the latter). Even this was not enough to make propagation competitive with inhibition, so DMSO was added (1:1:2, dioxane/DMSO/PhCl) which raised the β_2^H to 0.60, theoretically lowering the rate constant (k_{inh}^{DMSO}) by 73-fold relative the styrene/PhCl system. With this a rate constant was obtained (k_{inh}^{DMSO} = 5.3 × 10^5 M^{-1} s^{-1}), which corresponded to a

k_{inh}^{PhCl} of 3.9 × 10^7 M^{-1} s^{-1} when accounting for the H-bonding effect, in excellent agreement with the value reported by Lucarini *et al.* (2.9 × 10^7 M^{-1} s^{-1}).[65]

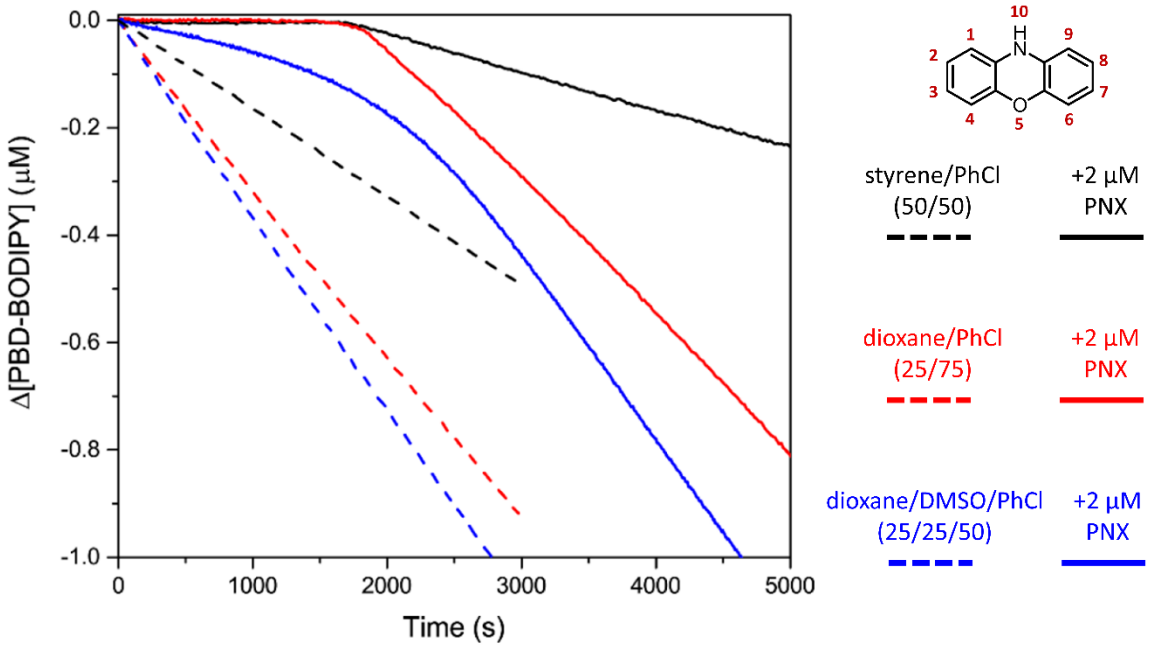


Figure 1.6. Comparison of the co-autoxidation of PBD-BODIPY (10 μM with 6 mM AIBN at 37 °C) with styrene, dioxane and dioxane w/ DMSO. For the 1:1 styrene/PhCl and 1:3 dioxane/PhCl systems, -d[BODIPY]/dt = 0 M s^{-1} when inhibited by PNX (2 μM).

Examining several other reference RTA compounds (phenols, aromatic amines, hydropersulfide), we similarly observed excellent agreement with the reported rate constants in non-polar aromatic solvents using k_{inh}^{DMSO} (or k_{inh}^{Diox} for the slower ones), their α_2^H, and Eq. 1.36 to correct for the difference in H-bond basicity (0.60 or 0.35 → 0.09). Here is an example of the calculation for PNX:

$$logk_{inh}^{0} = logk_{inh}^{DMSO} + 8.3\alpha_2^H\beta_2^H \quad logk_{inh}^{DMSO} = 5.72 \quad \alpha_2^H = 0.44 \quad \beta_2^H = 0.60$$

$$logk_{inh}^{0} = 7.91 \qquad k_{inh}^{0} = 8.2 \times 10^7 M^{-1}s^{-1}$$

$$logk_{inh}^{PhCl} = logk_{inh}^{0} - 8.3\alpha_2^H\beta_2^H \quad \alpha_2^H = 0.44 \quad \beta_2^H = 0.09$$

$$logk_{inh}^{PhCl} = 7.58 \quad k_{inh}^{PhCl} = 3.9 \times 10^7 M^{-1}s^{-1}$$

Using this approach, we measured several inhibition rate constants for substituted PNX and PTZ derivatives which could then be directly compared to existing data in non-polar solutions. Additionally, we measured their standard oxidation potentials (E^o vs. NHE) finding that the PNX-derived RTAs consistently exhibited impressive kinetics and stability whether the rings were substituted with EDG(s), EWG(s), or a combination of thereof.

Table 1.7. Kinetic Data for Substituted Phenoxazines/Phenothiazines in Organic Solution

Substituents	α_2^H	k_{inh}^{Diox} (10^4 M^{-1} s^{-1})	k_{inh}^{DMSO} (10^4 M^{-1} s^{-1})	Stoich. (n)	k_{inh}^{PhCl} (10^4 M^{-1} s^{-1}) [c]	BDE_{N-H} (kcal mol^{-1}) CBS-QB3	E^o vs NHE (V)
Phenoxazines							
PNX	0.44	-	53 ± 5	2.2 ± 0.1	3900 ± 400	75.2	0.87
3-CN-7-NO_2	0.69	15 ± 1	-	2.4 ± 0.1	450 ± 10	77.5	1.38
3-NO_2	0.62	73 ± 2	-	2.5 ± 0.1	1600 ± 100	76.5	1.15
3-CN	0.56	110 ± 10	-	2.2 ± 0.2	1800 ± 100	76.2	1.13
3-CF_3	0.53	150 ± 20	-	2.3 ± 0.1	2000 ± 300	76.1	1.06
3-SO_2NEt_2	0.53	150 ± 10	-	2.2 ± 0.1	2100 ± 200	76.3	1.06
2-CF_3	0.51	200 ± 10	-	2.3 ± 0.1	2500 ± 200	76.2	1.05
3-MeO-7-NO_2	0.60	280 ± 20	-	1.5 ± 0.1	5600 ± 500	74.0	0.97
2-tBu	0.43	-	90 ± 3	2.0 ± 0.1	6000 ± 200	74.6	0.83
3-tBu	0.43	-	110 ± 10	2.1 ± 0.1	7400 ± 600	74.5	0.81
2,8-tBu	0.43	-	150 ± 10	1.8 ± 0.1	10000 ± 1000	74.0	0.78
3,7-tBu	0.41	-	260 ± 20	1.9 ± 0.1	14000 ± 1000	73.9	0.75
3-MeO	0.42	-	310 ± 20	1.8 ± 0.1	18000 ± 1000	72.8	0.72
2,4,6,8-tBu	0.39	-	470 ± 80	1.7 ± 0.1	21000 ± 4000	-	0.67
3,7-MeO	0.40	-	1300 ± 200	1.4 ± 0.1	66000 ± 11000	70.7	0.59
Phenothiazines							
PTZ	0.38	120 ± 10	-	2.1 ± 0.1	760 ± 30	-	0.85
3-NO_2 [b]	0.52	19 ± 1	-	2.0 ± 0.1	250 ± 10	-	1.09[f]
3,7-tBu	0.35	300 ± 80	36 ± 2	1.6 ± 0.1	1700 ± 500 [d] 1100 ± 100 [e]	-	0.75
3,7-MeO	0.34	-	150 ± 10	1.6 ± 0.1	4100 ± 400	-	0.61

(a) Data from Farmer *et al.* (2017) unless otherwise indicated.[50] (b) For 3-NO_2-PTZ data, see ref. 52.[54] (c) Calculated value using Snelgrove-Ingold equation, assuming β_2^H = 0.09. (d) Calculated from k_{inh}^{Diox}. (e) Calculated from k_{inh}^{DMSO}. (f) Unpublished data.

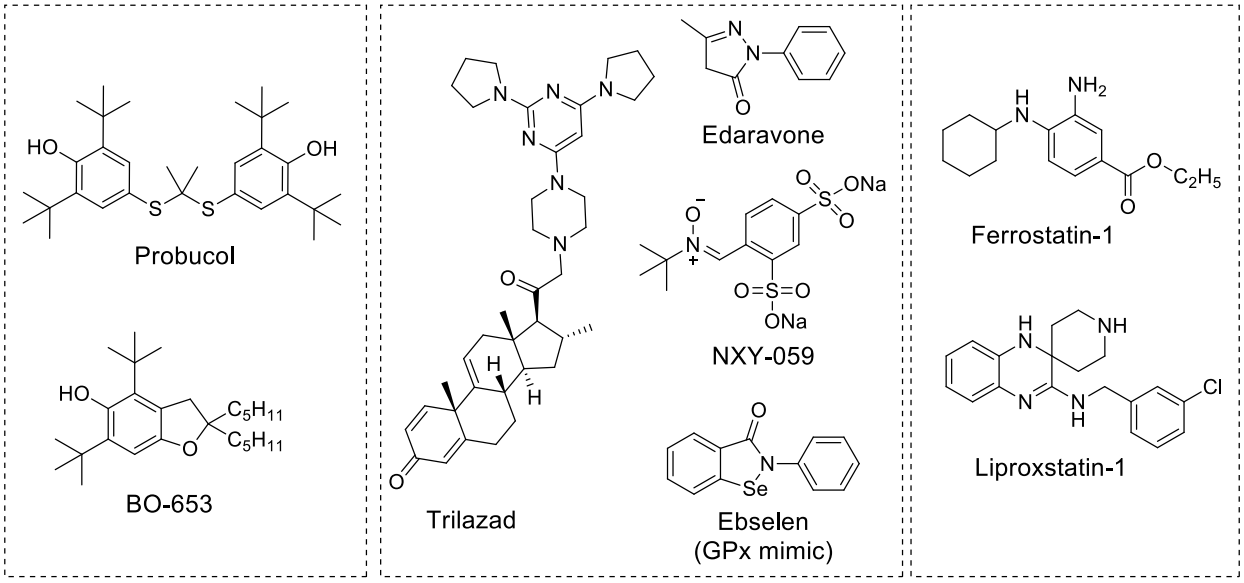
1.4 Ferroptosis, Lipid Peroxidation, Vitamin E and Other RTAs in Biology and Medicine

The subjects of biology and medicine are outside of my expertise and scope of practice, but lipid peroxidation manifests itself in *such* a wide range of ailments from neurodegeneration[99] to cardiovascular disease[100] to viral infections,[101,102] that this is an obvious (and pressing) application of the research into novel (lipid-soluble) RTAs. Given the immensity of the subject, which would easily fill several volumes, the aim is merely to highlight some of the biological aspects of Vitamin E, present the therapeutic precedence of RTAs in disease and introduce the topic of ferroptosis.

The research area has been reinvigorated in the past decade with a widespread recognition of a non-apoptotic mode of cell death linked to excess/uncontrolled lipid peroxidation known as "ferroptosis." While much of the current research uses the ferroptosis framing, lipid peroxidation with respect to disease has been researched for many decades. The first isolation of Vitamin E (1935)[103] and subsequent structural elucidation and total synthesis (1938)[104] was prompted by the discovery of an unaccounted dietary factor (i.e. Vitamin E) observed in 1922 which led to near complete infertility in female rats who were deprived.[105] While many health problems would arise from its exclusion in the diets of domestic animals,[106] particularly during early development, such dietary deficiencies in humans were essentially unheard of. By the late 1960's, though the general chemical mechanism of action was known (antioxidant), many questions surrounded the therapeutic benefit (or lack thereof) in any known human disease(s).[107] However, through the 1980's theories invoking free radical oxidation in the progression of atherosclerosis[23] and in cerebral ischemia[108] (stroke) became quite popular, bringing antioxidant research to the forefront. Not only did this stimulate some renewed interest in α-tocopherol, the most bioavailable form of Vitamin E,[109] but also prompted the study and development of synthetic RTA/radical scavenger-based pharmaceuticals. Probucol contains 2 hindered-phenol moieties and was historically used as an antihyperlipidemic drug that also manifested potent RTA activity in LDL,[110] though its clinical usage declined when statins were introduced to the market.[111] Inspired by Probucol and α-Toc, BO-653 was developed which showed antiatherogenic effects in animal models,[112] but never proceeded past phase II clinical trials. Three radical scavenging drugs developed for the treatment of stroke in the late 90's, Trilazad, Edaravone and NXY-059 as well as one GPx mimic (Ebselen) proceeded through phase III trials

though none of them were particularly successful in this regard.[113] Notably these structures are rather distinct from the phenol/Vitamin E "template".

Scheme 1.19 – Therapy Candidates Based on Synthetic Antioxidants



Focusing on the current paradigm, ferroptosis research finds its origins in a series of papers published by M. Conrad and co-workers beginning in 2008.[114–116] In addition to small molecule antioxidants, several antioxidant enzymes participate in the defense against free radical oxidation in cells such as catalase, superoxide dismutase (SOD) and glutathione peroxidase (GPx). The existence of many of these has been known for decades, but identifying which ones are individually essential to make an organism viable (and furthermore relevant in human diseases) has been somewhat of an exercise in trial and error. GPx4, the only isoform that reduces phospholipid hydroperoxides,[117] became of particular interest as it seemed to be the only isoform of GPx that was universally expressed and essential to the viability of embryonic development.[118] In Conrad and co-workers' seminal 2008 paper, inducing neuron-specific inactivation of GPx4 caused an acute neurodegenerative effect in their knockout mice, which they characterized as being a novel mode of cell death distinct from apoptosis or necroptosis.[114] A few years later Dixon, Stockwell and co-workers would give it the moniker "ferroptosis", noting the protective effect of iron chelation on the GPx4 inhibited cells, and this was the name that would "stick".[119] Different triggering mechanisms of ferroptosis exist, such as inhibition of

GPx4 or the depletion of the GSH co-factor, and many different sensitizers, desensitizers, modulators and inhibitors of ferroptosis have subsequently been identified. Indeed, like any complex biological system (which is most of them), a sophisticated network of interdependencies exists and more details are unraveled all the time. That being said, at least as we currently understand it, the process of radical-mediated lipid peroxidation lies at the foundation of it all (Fig. 1.7).[120]

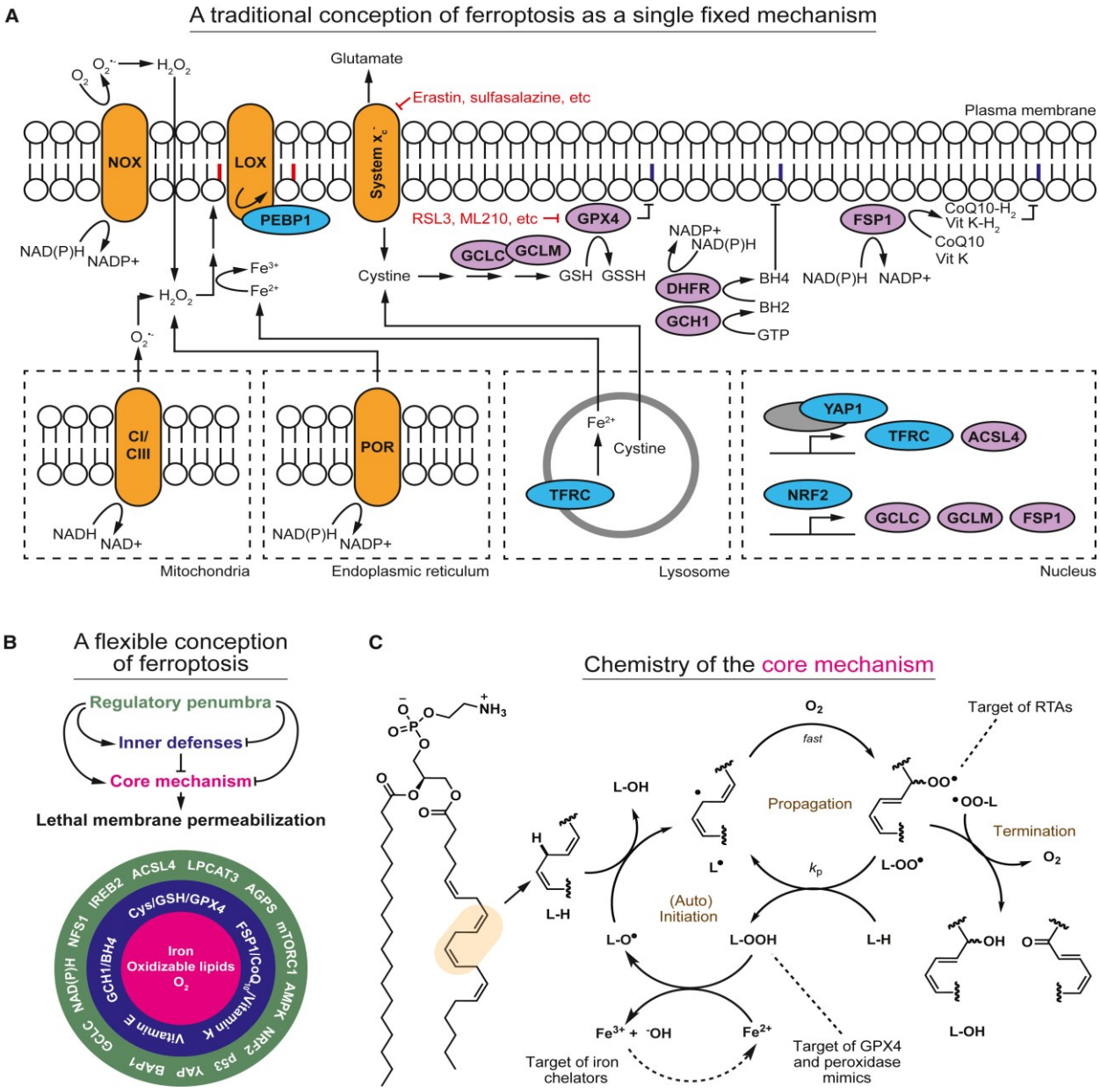


Figure 1.7. An overview of the network of key systems involved with the promotion/suppression of ferroptosis laid out by Dixon and Pratt (2023).[120] Reproduction of this figure is in accordance with the license explicitly granted by the publisher (Elsevier).

How do RTAs fit into the picture? The protective effect of α-Toc in the absence of GPx4 functionality was recognized in Conrad's seminal work,[114] but furthermore a number of other endogenous RTA-based systems have been subsequently identified through the course of researching ferroptosis. Some notable examples include the NADPH-dependent ferroptosis-

suppressor protein (FSP1) which reduces lipophilic *para*-quinones (such as co-enzyme Q10 and Vitamin K) their corresponding hydroquinones (potent RTAs)[53,121,122] and the enzymatic co-factor tetrahydrobiopterin (BH_4), the production of which depends on GCH1 and DHFR, can also inhibit lipid-peroxidation.[123] Very recent work has also indicated a role for exogenous and endogenous hydropersulfides (RSSH) in the suppression of ferroptosis via an RTA mechanism.[124] Interestingly the first small molecule inhibitors of ferroptosis (ferrostatin-1 and liproxstatin-1)[119,125] identified through two separate library screening efforts (9517 and 40000 compounds respectively) were later characterized by our group to be relatively potent lipid soluble RTAs.[51] The sheer statistics of 2 of the most potent compounds out of 49517 also being RTAs painted a pretty clear picture with respect to the key molecular targets for ferroptosis. Using a curated selection of aromatic amines, possessing anywhere from excellent to non-existent RTA activity, workers in our group were able to correlate RTA kinetics with rescue potency in Pfa-1 mouse embryonic fibroblasts using multiple GPx4 inhibition methods.[126] Of the tested compounds, PNX was the most potent ferroptosis inhibitor, beating both Fer-1 and Lip-1. These results not only highlighted the therapeutic potential of RTAs in these models, but also underscored the importance of spontaneous radical mediated lipid peroxidation in the progression of ferroptosis as opposed an enzymatic process driven primarily by lipoxygenase.[127]

1.5 Research Objectives

Having previously explored the fundamental peroxyl-trapping chemistry of substituted PNX and PTZ based RTAs in organic solution during my MSc studies, and concluding that these are uniquely privileged RTAs, the primary intention for my PhD studies was to explore their broader potential. Firstly in the suppression of lipid peroxidation in a biological context (i.e., ferroptosis) and secondly to inhibit autoxidations at high temperatures, such as those to which combustion engine lubricants and thermoplastics are subjected. The former will be the subject matter of Chapters 2, 3 and 4, while the latter will be covered in Chapters 5 and 6.

For studying the inhibition of lipid peroxidation the primary objectives were to:

i) Develop a kinetic model that quantitatively describes the behaviour of phenolic and diarylamine-type RTAs in a phospholipid membrane.

ii) Explore the bi-phasic synergy between novel lipid-soluble PNX/PTZ compounds and water-soluble co-reductant (ascorbic acid).

iii) Determine the intrinsic and extrinsic limitations to the reactivity of RTAs in phospholipid bilayers.

iv) Attempt to correlate the kinetic data of the PNX/PTZ RTAs to *in vitro* ferroptosis inhibition potency.

v) Transpose the novel RTA(s) into effective ferroptosis inhibitor(s) *in vivo*.

For the inhibition of high temperature autoxidations the objectives primarily were to:

i) Develop a systematic understanding of PNX and PTZ RTA behaviour in our model lubricant system (*n*-hexadecane with continuous flow of O_2 at ca. 160 °C).

ii) To understand the underlying reasons for the enhanced RTA activity of PTZ over PNX in this context, which has been historically observed[128] but the reasons for this are not immediately obvious.

iii) To optimize PNX and PTZ derivatives for this application/context through an iterative process of substituent optimization and product analysis.

iv) To further our understanding of the high temperature catalytic inhibition phenomenon often reported for diarylamine-type RTAs, and in particular the mechanistic proposal described by Korcek and co-workers[83] (shown and described in Ch. 5 and 6.)

1.6 References

(1) Gomberg, M. AN INSTANCE OF TRIVALENT CARBON: TRIPHENYLMETHYL. *J. Am. Chem. Soc.* **1900**, *22* (11), 757–771.

(2) Gomberg, M. ON TRIVALENT CARBON. *J. Am. Chem. Soc.* **1902**, *24* (7), 597–628.

(3) Gomberg, M. A Survey of the Chemistry of Free Radicals. *J. Chem. Educ.* **1932**, *9* (3), 439.

(4) Bäckström, H. L. J. THE CHAIN-REACTION THEORY OF NEGATIVE CATALYSIS. *J. Am. Chem. Soc.* **1927**, *49* (6), 1460–1472.

(5) Jeu, K.-K.; Alyea, H. N. A Comparison of Organic Inhibitors in Chain Reactions. *J. Am. Chem. Soc.* **1933**, *55* (2), 575–588.

(6) Lankamp, H.; Nauta, W. T.; MacLean, C. A New Interpretation of the Monomer-Dimer Equilibrium of Triphenylmethyl- and Alkylsubstituted-Diphenyl Methyl-Radicals in Solution. *Tetrahedron Lett.* **1968**, *9* (2), 249–254.

(7) Ziegler, K.; Ewald, L. Zur Kenntnis Des ”dreiwertigen„ Kohlenstoffs. XIII. Kettenreaktionen Bei Der Autoxydation von Radikalen. *Justus Liebigs Ann. Chem.* **1933**, *504* (1), 162–181.

(8) Ziegler, K.; Gänicke, K. Zur Kenntnis Des „dreiwertigen” Kohlenstoffs. XX. Radikale Als Katalysatoren Der Autoxydation. *Justus Liebigs Ann. Chem.* **1942**, *551* (1), 213–221.

(9) Bolland, J. L. Kinetics of Olefin Oxidation. *Q. Rev. Chem. Soc.* **1948**, *3*, 1–21.

(10) Bateman, L. Olefin Oxidation. *Q. Rev. Chem. Soc.* **1954**, *8*, 147–167.

(11) Stevens, M. P. *Polymer Chemistry: An Introduction*, 3rd ed.; Oxford Universty Press: New York, 1999.

(12) Graham, W. D.; Green, J. G.; Pryor, W. A. Radical Production from the Interaction of Closed-Shell Molecules. 10. Chemistry of Methylenecyclohexadiene and the Thermal Polymerization of Styrene. *J. Org. Chem.* **1979**, *44* (6), 907–914.

(13) For a comprehensive resource on radical initiators I would recommend the *Handbook of Free Radical Initiators* by E. T. Denisov published in 2003. See ref. 14.

(14) Denisov, E. T.; Denisova, T. G.; Pokidova, T. S. *Handbook of Free Radical Initiators*, 1st ed.; John Wiley & Sons Inc.: Hoboken, 2003.

(15) The precise mechanism of AIBN thermal decomposition is still a matter of debate, but Denisov favours concerted fragmentation, citing the low ΔV of the TS (ca. 3.8 cm^3/mol) as evidence of a compact TS, characteristic of a concerted mechanism. See Ch 1. of ref 14.

(16) Maillard, B.; Ingold, K. U.; Scaiano, J. C. Rate Constants for the Reactions of Free Radicals with Oxygen in Solution. *J. Am. Chem. Soc.* **1983**, *105*, 5095–5099.

(17) Denisov, E. T.; Denisova, T. G.; Pokidova, T. S. Azo Compounds. In *Handbook of Free Radical Initiators*; 2003; pp 303–358.

(18) Azo Polymerization Initiators Comprehensive Catalog. Fujifilm Wako Pure Chemical Corporation pp 1–34.

(19) Half-Life of Initiators http://polymerdatabase.com/polymer chemistry/t-half.html (accessed Mar 25, 2023).

(20) Kiefer, H.; Traylor, T. G. Di-t-Butyl Hyponitrite. A Convenient Source of t-Butoxy Radicals. *Tetrahedron Lett.* **1966**, *7* (49), 6163–6168.

(21) Bennett, J. E.; Eyre, J. A.; Summers, R. Electron Spin Resonance Measurements of Propagation and Termination Rate Constants during the Liquid-Phase Oxidation of Hydrocarbons. *J. Chem. Soc. Perkin Trans. 2* **1974**, No. 7, 797–800.

(22) Zinbo, M.; Jensen, R. K.; Johnson, M. D.; Korcek, S. Relative Inhibiting Efficiency of Base Oils. *Ind. Eng. Chem. Res.* **1987**, *26* (5), 902–906.

(23) Esterbauer, H.; Gebicki, J.; Puhl, H.; Jürgens, G. The Role of Lipid Peroxidation and Antioxidants in Oxidative Modification of LDL. *Free Radic. Biol. Med.* **1992**, *13* (4), 341–390.

(24) The review by Esterbauer *et al.* suggests initial reduction of Cu^{2+} could be facilitated by native α-tocopherol or LOOH in the LDL ($LOOH + Cu^{2+} \rightarrow LOO^{\bullet} + H^{+} + Cu^{1+}$), though the authors acknowledge that the latter would be very thermodynamically unfavourable.

(25) Conrad, M.; Pratt, D. A. The Chemical Basis of Ferroptosis. *Nat. Chem. Biol.* **2019**, *15* (12), 1137–1147.

(26) Niki, E.; Kawakami, A.; Yamamoto, Y.; Kamiya, Y. Oxidation of Lipids. VIII. Synergistic Inhibition of Oxidation of Phosphatidylcholine Liposome in Aqueous Dispersion by Vitamin E and Vitamin C. *Bull. Chem. Soc. Jpn.* **1985**, *58* (7), 1971–1975.

(27) Niki, E.; Saito, M.; Yoshikawa, Y.; Yamamoto, Y.; Kamiya, Y. Oxidation of Lipids, XII. Inhibition of Oxidation of Soybean Phosphatidylcholine and Methyl Linoleate in Aqueous Dispersions by Uric Acid. *Bull. Chem. Soc. Jpn.* **1986**, *59* (2), 471–477.

(28) Shah, R.; Farmer, L. A.; Zilka, O.; Van Kessel, A. T. M.; Pratt, D. A. Beyond DPPH: Use of Fluorescence-Enabled Inhibited Autoxidation to Predict Oxidative Cell Death Rescue. *Cell Chem. Biol.* **2019**, *26* (11), 1594-1607.

(29) Paul, H.; Small, R. D. J.; Scaiano, J. C. Hydrogen Abstraction by Tert-Butoxy Radicals. A Laser Photolysis and Electron Spin Resonance Study. *J. Am. Chem. Soc.* **1978**, *100* (14), 4520–4527.

(30) Scaiano, J. C. Kinetic Studies of Alkoxyl Radicals BT - Oxygen Radicals in Biology and Medicine; Simic, M. G., Taylor, K. A., Ward, J. F., von Sonntag, C., Eds.; Springer US: Boston, MA, 1988; pp 59–66.

(31) Howard, J. A.; Ingold, K. U. Absolute Rate Constants for Hydrocarbon Autoxidation. VI. Alkyl Aromatic and Olefinic Hydrocarbons. *Can. J. Chem.* **1967**, *45* (8), 793–802.

(32) Howard, J. A.; Ingold, K. U. Absolute Rate Constants For Hydrocarbon Autoxidation: I. Styrene. *Can. J. Chem.* **1965**, *43*, 2729–2736.

(33) Howard, J. A.; Furimsky, E. Arrhenius Parameters for Reaction of Tert-Butylperoxy Radicals with Some Hindered Phenols and Aromatic Aminesl. *Can. J. Chem.* **1973**, *51*, 3738–3745.

(34) Howard, J. A.; Ingold, K. U. Absolute Rate Constants for Hydrocarbon Autoxidation. XVII. The Oxidation of Some Cyclic Ethers. *Can. J. Chem.* **1969**, *47* (20), 3809–3815.

(35) Xu, L.; Davis, T. A.; Porter, N. A. Rate Constants for Peroxidation of Polyunsaturated Fatty Acids and Sterols in Solution and in Liposomes. *J. Am. Chem. Soc.* **2009**, *131* (36), 13037–13044.

(36) Ingold, K. U. Peroxy Radicals. *Acc. Chem. Res.* **1969**, *2* (1), 1–9.

(37) The rotating sector technique is where an opaque rotating disc with a slit is placed between a sample containing the oxidizable substrate and is photoinitiated and the incident beam of light is intermittently disrupted. Unlike a typical autoxidation experiment, intermittent photoinitiation leads to a non-steady-state radical-mediated chain reaction. The oxidation rates are measured at different rotation speeds which can enable the derivation of the radical chain length, from which the k_p and k_t can be calculated. Generally, if the chain length is greater than 5 these rate constants can be accurately resolved. See ref. 32.

(38) Korcek, S.; Chenier, J. H. B.; Howard, J. A.; Ingold, K. U. Absolute Rate Constants for Hydrocarbon Autoxidation. XXI. Activation Energies for Propagation and the Correlation of Propagation Rate Constants with Carbon-Hydrogen Bond Strengths. *Can. J. Chem.* **1972**, *50*, 2285–2297.

(39) Trenwith, A. B. Dissociation of 3-Methylpenta-1, 4-Diene and the Resonance Energy of the Pentadienyl Radical. *J. Chem. Soc. Faraday Trans. 1 Phys. Chem. Condens. Phases* **1982**, *78* (10), 3131–3136.

(40) $BDE_{O\text{-}H}$ of methyl hydroperoxide (CH3OO-H) determined by a high accuracy theoretical computational method (CBS-QB3).

(41) Lucarini, M.; Pedrielli, P.; Pedulli, G. F.; Cabiddu, S.; Fattuoni, C. Bond Dissociation Energies of O-H Bonds in Substituted Phenols from Equilibration Studies. *J. Org. Chem.* **1996**, *61* (26), 9259–9263.

(42) Bartlett, P. D.; Guaraldi, G. Di-Tert-Butyl Trioxide and Di-Tert-Butyl Tertoxide. *J. Am. Chem. Soc.* **1967**, *89* (18), 4799–4801.

(43) Howard, J. A.; Bennett, J. E. The Self-Reaction of Sec-Alkylperoxy Radicals: A Kinetic Electron Spin Resonance Study. *Can. J. Chem.* **1972**, *50*, 2374–2377.

(44) Lee, R.; Gryn'ova, G.; Ingold, K. U.; Coote, M. L. Why Are Sec-Alkylperoxyl Bimolecular Self-Reactions Orders of Magnitude Faster than the Analogous Reactions of Tert-Alkylperoxyls? The Unanticipated Role of CH Hydrogen Bond Donation. *Phys. Chem. Chem. Phys.* **2016**, *18*, 23673–23679.

(45) Burton, G. W.; Doba, T.; Gabe, E. J.; Hughes, L.; Lee, F. L.; Prasad, L.; Ingoldo, K. U. Autoxidation of Biological Molecules. 4. Maximizing the Antioxidant Activity of Phenols. *J. Am. Chem. Soc.* **1985**, *107* (24), 7053–7065.

(46) Barclay, L. R. C.; Baskin, K. A.; Locke, S. J.; Schaefer, T. D. Benzophenone-Photosensitized Autoxidation of Linoleate in Solution and Sodium Dodecyl Sulfate Micelles. *Can. J. Chem.* **1987**, *65* (11), 2529–2540.

(47) Amorati, R.; Baschieri, A.; Valgimigli, L. Measuring Antioxidant Activity in Bioorganic Samples by the Differential Oxygen Uptake Apparatus: Recent Advances. *J. Chem.* **2017**, *2017*, 6369358.

(48) Hanthorn, J. J.; Haidasz, E. A.; Gebhardt, P.; Pratt, D. A. A Versatile Fluorescence Approach to Kinetic Studies of Hydrocarbon Autoxidations and Their Inhibition by Radical-Trapping Antioxidants. *Chem. Commun.* **2012**, *48*, 10141–10143.

(49) Chauvin, J.-P. R.; Griesser, M.; Pratt, D. A. Hydropersulfides: H-Atom Transfer Agents Par Excellence. *J. Am. Chem. Soc.* **2017**, *139* (18), 6484–6493.

(50) Farmer, L. A.; Haidasz, E. A.; Griesser, M.; Pratt, D. A. Phenoxazine: A Privileged Scaffold for Radical-Trapping Antioxidants. *J. Org. Chem.* **2017**, *82* (19), 10523–10536.

(51) Zilka, O.; Shah, R.; Li, B.; Friedmann Angeli, J. P.; Griesser, M.; Conrad, M.; Pratt, D. A. On the Mechanism of Cytoprotection by Ferrostatin-1 and Liproxstatin-1 and the Role of Lipid Peroxidation in Ferroptotic Cell Death. *ACS Cent. Sci.* **2017**, *3* (3), 232–243.

(52) Harrison, K. A.; Haidasz, E. A.; Griesser, M.; Pratt, D. A. Inhibition of Hydrocarbon Autoxidation by Nitroxide-Catalyzed Cross-Dismutation of Hydroperoxyl and Alkylperoxyl Radicals. *Chem. Sci.* **2018**, *9* (28), 6068–6079.

(53) Mishima, E.; Ito, J.; Wu, Z.; Nakamura, T.; Wahida, A.; Doll, S.; Tonnus, W.; Nepachalovich, P.; Eggenhofer, E.; Aldrovandi, M.; Henkelmann, B.; Yamada, K.; Wanninger, J.; Zilka, O.; Sato, E.; Feederle, R.; Hass, D.; Maida, A.; Mourão, A. S. D.; Linkermann, A.; Geissler, E. K.; Nakagawa, K.; Abe, T.; Fedorova, M.; Proneth, B.; Pratt, D. A.; Conrad, M. A Non-Canonical Vitamin K Cycle Is a Potent Ferroptosis Suppressor. *Nature* **2022**, *608* (7924), 778–783.

(54) Farmer, L. A.; Wu, Z.; Poon, J.-F.; Zilka, O.; Lorenz, S. M.; Huehn, S.; Proneth, B.; Conrad, M.; Pratt, D. A. Intrinsic and Extrinsic Limitations to the Design and Optimization of Inhibitors of Lipid Peroxidation and Associated Cell Death. *J. Am. Chem. Soc.* **2022**, *144* (32), 14706–14721.

(55) Haidasz, E. A.; Van Kessel, A. T. M.; Pratt, D. A. A Continuous Visible Light Spectrophotometric Approach to Accurately Determine the Reactivity of Radical-Trapping Antioxidants. *J. Org. Chem.* **2016**, *81* (3), 737–744.

(56) Howard, J. A.; Ingold, K. U. THE INHIBITED AUTOXIDATION OF STYRENE: PART I.THE DEUTERIUM ISOTOPE EFFECT FOR INHIBITION BY 2,6-DI- Tert -BUTYL-4-METHYLPHENOL. *Can. J. Chem.* **1962**, *40*, 1851–1864.

(57) Howard, J. A.; Ingold, K. U. The Inhibited Autoxidation of Styrene: Part II. The Relative Inhibiting Efficiencies of Meta- and Para-Substituted Phenols. *Can. J. Chem.* **1963**, *41*, 1744–1751.

(58) Howard, J. A.; Ingold, K. U. THE INHIBITED AUTOXIDATION OF STYRENE: PART III. THE RELATIVE INHIBITING EFFICIENCIES OF ORTHO-ALKYL PHENOLS. *Can. J. Chem.* **1963**, *41* (11), 2800–2806.

(59) Brigati, G.; Lucarini, M.; Mugnaini, V.; Pedulli, G. F. Determination of the Substituent Effect on the O−H Bond Dissociation Enthalpies of Phenolic Antioxidants by the EPR Radical Equilibration Technique. *J. Org. Chem.* **2002**, *67* (14), 4828–4832.

(60) Mulder, P.; Korth, H.-G.; Pratt, D. A.; Dilabio, G. A.; Valgimigli, L.; Pedulli, G. F.; Ingold, K. U. Critical Re-Evaluation of the O-H Bond Dissociation Enthalpy in Phenol. *J. Phys. Chem. A* **2005**, *109*, 2647–2655.

(61) Zavitsas, A. A. Activation Energy Requirements in Hydrogen Abstractions. Quantitative Description of the Causes in Terms of Bond Energies and Infrared Frequencies. *J. Am. Chem. Soc.* **1972**, *94* (8), 2779–2789.

(62) Zavitsas, A. A.; Chatgilialoglu, C. Energies of Activation. The Paradigm of Hydrogen Abstractions by Radicals. *J. Am. Chem. Soc.* **1995**, *117* (43), 10645–10654.

(63) Mayer, J. M.; Hrovat, D. A.; Thomas, J. L.; Borden, W. T. Proton-Coupled Electron Transfer versus Hydrogen Atom Transfer in Benzyl/Toluene, Methoxyl/Methanol, and Phenoxyl/Phenol Self-Exchange Reactions. *J. Am. Chem. Soc.* **2002**, *124* (37), 11142–11147.

(64) DiLabio, G. A.; Johnson, E. R. Lone Pair−π and Π−π Interactions Play an Important Role in Proton-Coupled Electron Transfer Reactions. *J. Am. Chem. Soc.* **2007**, *129*, 6199–6203.

(65) Lucarini, M.; Pedrielli, P.; Pedulli, G. F.; Valgimigli, L.; Gigmes, D.; Tordo, P. Bond Dissociation Energies of the N-H Bond and Rate Constants for the Reaction with Alkyl, Alkoxyl, and Peroxyl Radicals of Phenothiazines and Related Compounds. *J. Am. Chem.*

Soc. **1999**, *121*, 11546–11553.

(66) Brownlie, I. T.; Ingold, K. U. The Inhibited Autoxidation of Styrene. Part VI. The Relative Efficiences and the Kinetics for Inhibition by N-Aryl Anilines and N-Alkyl Anilines. *Can. J. Chem* **1967**, *45*, 2419–2425.

(67) Burton, G. W.; Ingold, K. U. Autoxidation of Biological Molecules. 1. The Antioxidant Activity of Vitamin E and Related Chain-Breaking Phenolic Antioxidants in Vitro. *J. Am. Chem. Soc.* **1981**, *103* (21), 6472–6477.

(68) Olcott, H. S.; Emerson, O. H. Antioxidants and the Autoxidation of Fats. IX. The Antioxidant Properties of the Tocopherols. *J. Am. Chem. Soc.* **1937**, *59* (6), 1008–1009.

(69) Golumbic, C. Antioxidants and the Autoxidation of Fats. XII. The Antioxidant Properties of Tocopherols, Hydroxychromans, Hydroxycoumarans and Related Compounds. *J. Am. Chem. Soc.* **1941**, *63* (4), 1142.

(70) KANNO, C.; YAMAUCHI, K.; TSUGO, T. Antioxidant Effect of Tocopherols on Autoxidation of Milk Fat. *Agric. Biol. Chem.* **1970**, *34* (6), 886–890.

(71) Chipault, J. R. . In *Autoxidation and Antioxidants*; Lundberg, W. O., Ed.; Interscience: New York, 1962; pp 477–542.

(72) Barclay, L. R. C.; Vinqvist, M. R.; Mukai, K.; Itoh, S.; Morimoto, H. Chain-Breaking Phenolic Antioxidants: Steric and Electronic Effects in Polyalkylchromanols, Tocopherol Analogs, Hydroquinones, and Superior Antioxidants of the Polyalkylbenzochromanol and Naphthofuran Class. *J. Org. Chem.* **1993**, *58* (26), 7416–7420.

(73) Noguchi, N.; Iwaki, Y.; Takahashi, M.; Komuro, E.; Kato, Y.; Tamura, K.; Cynshi, O.; Kodama, T.; Niki, E. 2,3-Dihydro-5-Hydroxy-2,2-Dipentyl-4,6-Di-Tert-Butylbenzofuran: Design and Evaluation as a Novel Radical-Scavenging Antioxidant against Lipid Peroxidation. *Arch. Biochem. Biophys.* **1997**, *342* (2), 236–243.

(74) Wijtmans, M.; Pratt, D. A.; Valgimigli, L.; DiLabio, G. A.; Pedulli, G. F.; Porter, N. A. 6-Amino-3-Pyridinols: Towards Diffusion-Controlled Chain-Breaking Antioxidants. *Angew. Chemie Int. Ed.* **2003**, *42*, 4370–4373.

(75) Pratt, D. A.; DiLabio, G. A.; Brigati, G.; Pedulli, G. F.; Valgimigli, L. 5-Pyrimidinols: Novel Chain-Breaking Antioxidants More Effective than Phenols. *J. Am. Chem. Soc.* **2001**, *123*, 4625–4626.

(76) Valgimigli, L.; Bartolomei, D.; Amorati, R.; Haidasz, E.; Hanthorn, J. J.; Nara, S. J.; Brinkhorst, J.; Pratt, D. A. 3-Pyridinols and 5-Pyrimidinols: Tailor-Made for Use in Synergistic Radical-Trapping Co-Antioxidant Systems. *Beilstein J. Org. Chem.* **2013**, *9* (1), 2781–2792.

(77) Li, B.; Harjani, J. R.; Cormier, N. S.; Madarati, H.; Atkinson, J.; Cosa, G.; Pratt, D. A. Besting Vitamin E: Sidechain Substitution Is Key to the Reactivity of Naphthyridinol

Antioxidants in Lipid Bilayers. *J. Am. Chem. Soc.* **2013**, *135* (4), 1394–1405.

(78) Hanthorn, J. J.; Valgimigli, L.; Pratt, D. A. Incorporation of Ring Nitrogens into Diphenylamine Antioxidants: Striking a Balance between Reactivity and Stability. *J. Am. Chem. Soc.* **2012**, *134*, 8306–8309.

(79) Hanthorn, J. J.; Valgimigli, L.; Pratt, D. A. Preparation of Highly Reactive Pyridine- and Pyrimidine-Containing Diarylamine Antioxidants. *J. Org. Chem.* **2012**, *77*, 6908–6916.

(80) Hanthorn, J. J.; Amorati, R.; Valgimigli, L.; Pratt, D. A. The Reactivity of Air-Stable Pyridine- and Pyrimidine-Containing Diarylamine Antioxidants. *J. Org. Chem.* **2012**, *77* (16), 6895–6907.

(81) Shah, R.; Haidasz, E. A.; Valgimigli, L.; Pratt, D. A. Unprecedented Inhibition of Hydrocarbon Autoxidation by Diarylamine Radical-Trapping Antioxidants. *J. Am. Chem. Soc.* **2015**, *137*, 2440–2443.

(82) Haidasz, E. A.; Shah, R.; Pratt, D. A. The Catalytic Mechanism of Diarylamine Radical-Trapping Antioxidants. *J. Am. Chem. Soc.* **2014**, *136* (47), 16643–16650.

(83) Jensen, R. K.; Korcek, S.; Zinbo, M.; Gerlock, J. L. Regeneration of Amine in Catalytic Inhibition of Oxidation. *J. Org. Chem.* **1995**, *60*, 5396–5400.

(84) On the basis of first-principles, eliminating 2 free-rotors should increase the Arrhenius pre-exponential factor of PNX by an order of magnitude relative to DPA (i.e. log (A+1).

(85) Howard, J. A.; Ingold, K. U. THE INHIBITED AUTOXIDATION OF STYREN: PART IV. SOLVENT EFFECTS. *Can. J. Chem.* **1964**, *42* (5), 1044–1056.

(86) Snelgrove, D. W.; Lusztyk, J.; Banks, J. T.; Mulder, P.; Ingold, K. U. Kinetic Solvent Effects on Hydrogen-Atom Abstractions: Reliable, Quantitative Predictions via a Single Empirical Equation. *J. Am. Chem. Soc.* **2001**, *123* (3), 469–477.

(87) Avila, D. V.; Brown, C. E.; Ingold, K. U.; Lusztyk, J. Solvent Effects on the Competitive .Beta.-Scission and Hydrogen Atom Abstraction Reactions of the Cumyloxyl Radical. Resolution of a Long-Standing Problem. *J. Am. Chem. Soc.* **1993**, *115*, 466–470.

(88) Wayner, D. D. M.; Lusztyk, E.; Page, D.; Ingold, K. U.; Mulder, P.; Laarhoven, L. J. J.; Aldrich, H. S. Effects of Solvation on the Enthalpies of Reaction of Tert-Butoxyl Radicals and on the Calculated O-H Bond Strength in Phenol. *J. Am. Chem. Soc.* **1995**, *117*, 8737–8744.

(89) Valgimigli, L.; Banks, J. T.; Ingold, K. U.; Lusztyk, J. Kinetic Solvent Effects on Hydroxylic Hydrogen Atom Abstractions Are Independent of the Nature of the Abstracting Radical. Two Extreme Tests Using Vitamin E and Phenol. *J. Am. Chem. Soc.* **1995**, *117* (40), 9966–9971.

(90) Franchi, P.; Lucarini, M.; Pedulli, G. F.; Valgimigli, L.; Lunelli, B. Reactivity of

Substituted Phenols Toward Alkyl Radicals. *J. Am. Chem. Soc.* **1999**, *121* (3), 507–514.

(91) Valgimigli, L.; Banks, J. T.; Lusztyk, J.; Ingold, K. U. Solvent Effects on the Antioxidant Activity of Vitamin E. *J. Org. Chem.* **1999**, *64*, 3381–3383.

(92) Taft, R. W.; Gurka, D.; Joris, L.; von Schleyer, R.; Rakshys, J. W. Studies of Hydrogen-Bonded Complex Formation with p-Fluorophenol. IV. The Fluorine Nuclear Magnetic Resonance Method. *J. Am. Chem. Soc.* **1969**, *91*, 4794–4801.

(93) Taft, R. W.; Gurka, D.; Rakshys, J. W. Studies of Hydrogen-Bonded Complex Formation with p-Fluorophenol. V. Linear Free Energy Relationships with OH Reference Acids. *J. Am. Chem. Soc.* **1969**, *91* (17), 4801–4808.

(94) Abraham, M. H.; Grellier, P. L.; Prior, D. V.; Duce, P. P.; Morris, J. J.; Taylor, P. J. Hydrogen Bonding. Part 7. A Scale of Solute Hydrogen-Bond Acidity Based on Log K Values for Complexation in Tetrachloromethane. *J. Chem. Soc. Perkin Trans. 2* **1989**, 699–711.

(95) Abraham, M. H.; Grellier, P. L.; Prior, D. V.; Morris, J. J.; Taylor, P. J. Hydrogen Bonding. Part 10. A Scale of Solute Hydrogen-Bond Basicity Using Log K Values for Complexation in Tetrachloromethane. *J. Chem. Soc. Perkin Trans. 2* **1990**, 521–529.

(96) Abraham, M. H.; Buist, G. J.; Grellier, P. L.; McGill, R. A.; Prior, D. V.; Oliver, S.; Turner, E.; Morris, J. J.; Taylor, P. J.; Nicolet, P.; Maria, P.-C.; Gal, J.-F.; Abboud, J.-L. M.; Doherty, R. M.; Kamlet, M. J.; Shuely, W. J.; Taft, R. W. Hydrogen-Bonding 8. Possible Equivalence of Solute and Solvent Scales of Hydrogen-Bond Basicity of Non-Associated Compounds. *J. Phys. Org. Chem.* **1989**, *2* (7), 540–552.

(97) Abraham, M. H.; Abraham, R. J.; Byrne, J.; Griffiths, L. NMR Method for the Determination of Solute Hydrogen Bond Acidity. *J. Org. Chem.* **2006**, *71*, 3389–3394.

(98) Both NMR methods for determining α_2^{H} and β_2^{H} are discussed and demonstrated in detail in Chapter 2.

(99) Wang, T.; Tomas, D.; Perera, N. D.; Cuic, B.; Luikinga, S.; Viden, A.; Barton, S. K.; McLean, C. A.; Samson, A. L.; Southon, A.; Bush, A. I.; Murphy, J. M.; Turner, B. J. Ferroptosis Mediates Selective Motor Neuron Death in Amyotrophic Lateral Sclerosis. *Cell Death Differ.* **2022**, *29* (6), 1187–1198.

(100) Steinberg, D.; Parthasarathy, S.; Carew, T. E.; Khoo, J. C.; Witztum, J. L. Beyond Cholesterol. *N. Engl. J. Med.* **1989**, *320* (14), 915–924.

(101) Mileva, M.; Bakalova, R.; Tancheva, L.; Galabov, A.; Ribarov, S. Effect of Vitamin E Supplementation on Lipid Peroxidation in Blood and Lung of Influenza Virus Infected Mice. *Comp. Immunol. Microbiol. Infect. Dis.* **2002**, *25* (1), 1–11.

(102) Yasui, F.; Sudoh, M.; Arai, M.; Kohara, M. Synthetic Lipophilic Antioxidant BO-653

Suppresses HCV Replication. *J. Med. Virol.* **2013**, *85* (2), 241–249.

(103) Evans, H. M.; Emerson, O. H.; Emerson, G. A. THE ISOLATION FROM WHEAT GERM OIL OF AN ALCOHOL, α-TOCOPHEROL, HAVING THE PROPERTIES OF VITAMIN E. *J. Biol. Chem.* **1936**, *113* (1), 319–332.

(104) KARRER, P.; FRITZSCHE, H.; RINGIER, B. H.; SALOMON, H. Synthesis of α-Tocopherol (Vitamin E). *Nature* **1938**, *141* (3580), 1057.

(105) Evans, H. M.; Bishop, K. S. On the Existence of a Hitherto Unrecognized Dietary Factor Essential for Reproduction. *Science (80-.).* **1922**, *56* (1458), 650–651.

(106) Mead, J. F. CHAPTER 2 - Free Radical Mechanisms of Lipid Damage and Consequences for Cellular Membranes; Pryor, W. A. B. T.-F. R. in B., Ed.; Academic Press, 1976; pp 51–68.

(107) VITAMIN IN SEARCH OF A DISEASE. *JAMA* **1967**, *201* (3), 195–196.

(108) Flamm, E. S.; Demopoulos, H. B.; Seligman, M. L.; Poser, R. G.; Ransohoff, J. Free Radicals in Cerebral Ischemia. *Stroke* **1978**, *9* (5), 445–447.

(109) Burton, G. W.; Traber, M. G.; Acuff, R. V; Walters, D. N.; Kayden, H.; Hughes, L.; Ingold, K. U. Human Plasma and Tissue Alpha-Tocopherol Concentrations in Response to Supplementation with Deuterated Natural and Synthetic Vitamin E. *Am. J. Clin. Nutr.* **1998**, *67* (4), 669–684.

(110) Buckley, M. M.-T.; Goa, K. L.; Price, A. H.; Brogden, R. N. Probucol. *Drugs* **1989**, *37* (6), 761–800.

(111) Yamamoto, A. A Uniqe Antilipidemic Drug - Probucol. *J. Atheroscler. Thromb.* **2008**, *15* (6), 304–305.

(112) Cynshi, O.; Kawabe, Y.; Suzuki, T.; Takashima, Y.; Kaise, H.; Nakamura, M.; Ohba, Y.; Kato, Y.; Tamura, K.; Hayasaka, A.; Higashida, A.; Sakaguchi, H.; Takeya, M.; Takahashi, K.; Inoue, K.; Noguchi, N.; Niki, E.; Kodama, T. Antiatherogenic Effects of the Antioxidant BO-653 in Three Different Animal Models. *Proc. Natl. Acad. Sci.* **1998**, *95* (17), 10123–10128.

(113) Margaill, I.; Plotkine, M.; Lerouet, D. Antioxidant Strategies in the Treatment of Stroke. *Free Radic. Biol. Med.* **2005**, *39* (4), 429–443.

(114) Seiler, A.; Schneider, M.; Förster, H.; Roth, S.; Wirth, E. K.; Culmsee, C.; Plesnila, N.; Kremmer, E.; Rådmark, O.; Wurst, W.; Bornkamm, G. W.; Schweizer, U.; Conrad, M. Glutathione Peroxidase 4 Senses and Translates Oxidative Stress into 12/15-Lipoxygenase Dependent- and AIF-Mediated Cell Death. *Cell Metab.* **2008**, *8* (3), 237–248.

(115) Schneider, M.; Forster, H.; Boersma, A.; Seiler, A.; Wehnes, H.; Sinowatz, F.; Neumüller, C.; Deutsch, M. J.; Walch, A.; de Angelis, M. H.; Wurst, W.; Ursini, F.; Roveri, A.;

Maleszewski, M.; Maiorino, M.; Conrad, M. Mitochondrial Glutathione Peroxidase 4 Disruption Causes Male Infertility. *FASEB J.* **2009**, *23* (9), 3233–3242.

(116) Conrad, M. Transgenic Mouse Models for the Vital Selenoenzymes Cytosolic Thioredoxin Reductase, Mitochondrial Thioredoxin Reductase and Glutathione Peroxidase 4. *Biochim. Biophys. Acta - Gen. Subj.* **2009**, *1790* (11), 1575–1585.

(117) Roveri, A.; Maiorino, M.; Nisii, C.; Ursini, F. Purification and Characterization of Phospholipid Hydroperoxide Glutathione Peroxidase from Rat Testis Mitochondrial Membranes. *Biochim. Biophys. Acta - Protein Struct. Mol. Enzymol.* **1994**, *1208* (2), 211–221.

(118) Yant, L. J.; Ran, Q.; Rao, L.; Van Remmen, H.; Shibatani, T.; Belter, J. G.; Motta, L.; Richardson, A.; Prolla, T. A. The Selenoprotein GPx4 Is Essential for Mouse Development and Protects from Radiation and Oxidative Damage Insults. *Free Radic. Biol. Med.* **2003**, *34* (4), 496–502.

(119) Dixon, S. J.; Lemberg, K. M.; Lamprecht, M. R.; Skouta, R.; Zaitsev, E. M.; Gleason, C. E.; Patel, D. N.; Bauer, A. J.; Cantley, A. M.; Yang, W. S.; Morrison, B.; Stockwell, B. R. Ferroptosis: An Iron-Dependent Form of Nonapoptotic Cell Death. *Cell* **2012**, *149* (5), 1060–1072.

(120) Dixon, S. J.; Pratt, D. A. Ferroptosis: A Flexible Constellation of Related Biochemical Mechanisms. *Mol. Cell* **2023**, *83* (7), 1030–1042.

(121) Doll, S.; Freitas, F. P.; Shah, R.; Aldrovandi, M.; da Silva, M. C.; Ingold, I.; Goya Grocin, A.; Xavier da Silva, T. N.; Panzilius, E.; Scheel, C. H.; Mourão, A.; Buday, K.; Sato, M.; Wanninger, J.; Vignane, T.; Mohana, V.; Rehberg, M.; Flatley, A.; Schepers, A.; Kurz, A.; White, D.; Sauer, M.; Sattler, M.; Tate, E. W.; Schmitz, W.; Schulze, A.; O'Donnell, V.; Proneth, B.; Popowicz, G. M.; Pratt, D. A.; Angeli, J. P. F.; Conrad, M. FSP1 Is a Glutathione-Independent Ferroptosis Suppressor. *Nature* **2019**, *575* (7784), 693–698.

(122) Bersuker, K.; Hendricks, J. M.; Li, Z.; Magtanong, L.; Ford, B.; Tang, P. H.; Roberts, M. A.; Tong, B.; Maimone, T. J.; Zoncu, R.; Bassik, M. C.; Nomura, D. K.; Dixon, S. J.; Olzmann, J. A. The CoQ Oxidoreductase FSP1 Acts Parallel to GPx4 to Inhibit Ferroptosis. *Nature* **2019**, *575* (7784), 688–692.

(123) Soula, M.; Weber, R. A.; Zilka, O.; Alwaseem, H.; La, K.; Yen, F.; Molina, H.; Garcia-Bermudez, J.; Pratt, D. A.; Birsoy, K. Metabolic Determinants of Cancer Cell Sensitivity to Canonical Ferroptosis Inducers. *Nat. Chem. Biol.* **2020**, *16* (12), 1351–1360.

(124) Wu, Z.; Khodade, V. S.; Chauvin, J.-P. R.; Rodriguez, D.; Toscano, J. P.; Pratt, D. A. Hydropersulfides Inhibit Lipid Peroxidation and Protect Cells from Ferroptosis. *J. Am. Chem. Soc.* **2022**, *144* (34), 15825–15837.

(125) Friedmann Angeli, J. P.; Schneider, M.; Proneth, B.; Tyurina, Y. Y.; Tyurin, V. A.; Hammond, V. J.; Herbach, N.; Aichler, M.; Walch, A.; Eggenhofer, E.; Basavarajappa,

D.; Radmark, O.; Kobayashi, S.; Seibt, T.; Beck, H.; Neff, F.; Esposito, I.; Wanke, R.; Forster, H.; Yefremova, O.; Heinrichmeyer, M.; Bornkamm, G. W.; Geissler, E. K.; Thomas, S. B.; Stockwell, B. R.; O'Donnell, V. B.; Kagan, V. E.; Schick, J. A.; Conrad, M. Inactivation of the Ferroptosis Regulator GPx4 Triggers Acute Renal Failure in Mice. *Nat. Cell Biol.* **2014**, *16* (12), 1180–1191.

(126) Shah, R.; Margison, K.; Pratt, D. A. The Potency of Diarylamine Radical-Trapping Antioxidants as Inhibitors of Ferroptosis Underscores the Role of Autoxidation in the Mechanism of Cell Death. *ACS Chem. Biol.* **2017**, *12* (10), 2538–2545.

(127) Shah, R.; Shchepinov, M. S.; Pratt, D. A. Resolving the Role of Lipoxygenases in the Initiation and Execution of Ferroptosis. *ACS Cent. Sci.* **2018**, *4* (3), 387–396.

(128) Murphy, C. M.; Ravner, H.; Smith, N. L. Mode of Action of Phenothiazine-Type Antioxidants. *Ind. Eng. Chem.* **1950**, *42* (12), 2479–2489.

Chapter 2

Quantification of Kinetic Medium Effects on Hindered Phenol Radical-Trapping Antioxidants in a Phospholipid Membrane

2.1 Foreword

The following research was featured in *Beyond DPPH: Use of Fluorescence-Enabled Inhibited Autoxidation to Predict Oxidative Cell Death Rescue* which was published in Cell Chemical Biology in November of 2019.[1] The larger context of the paper was to highlight the necessity of relevant *in vitro* chemical models for the evaluation of RTAs in a biologically relevant context. First and foremost, it was a repudiation of the rather prolific use of 2,2-di-phenyl-1-picrylhydrazyl (DPPH) equilibration/titration assays as an appropriate means to ascertain RTA efficacy as it relates to autoxidation. Second, and arguably of equal importance, is that kinetic evaluation of inhibited autoxidations should be carried out within aqueous-phospholipid suspensions (i.e. unilamellar liposomes) as cellular membranes are putatively the structure of interest with respect to ferroptosis. The first author, Ron Shah, was principally responsible for the development of the liposome microplate "fluorescence-enabled inhibited autoxidation" (FENIX) assay and the corroborating ferroptosis rescue cell data. The third author, Omkar Zilka, developed and validated the lipophilic hyponitrite-based initiator, di-*tert*-undecyl hyponitrite (DTUN), which allows for exclusive initiation in the lipid-domain preventing "false-positive" inhibition from water-soluble RTAs. The fourth author, Antonius Van Kessel, developed an early prototype of the FENIX assay.

As for my part, it really was independent of the development of FENIX, but it turned out to be an ideal "proof of concept" for the utility of the assay. My aim was, at the outset, to systematically determine the role of H-bonding in the phospholipid membrane with respect to the kinetic solvent effect (KSE) that have been observed for radical-trapping reactions in various organic solvents. Primarily the approach involved taking multiple kinetic measurements with phenols of increasing steric hinderance around the hydroxyl, in multiple solvent systems and comparing the

results to those obtained in liposomes (i.e. FENIX). Apart from the cell assay determinations, and the aforementioned development of FENIX, the work presented below is my own.

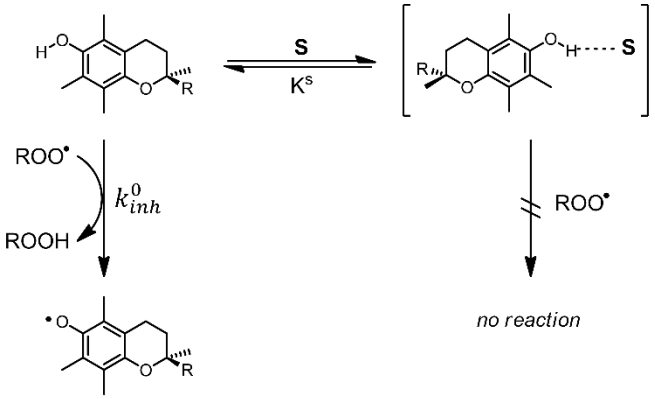
2.2 Introduction

For several decades there has been established associations between elevated levels of lipid peroxidation products with many serious medical conditions ranging from atherosclerosis[2] to ischemic/reperfusion injury[3,4] to neurodegenerative disorders.[5,6] The natural extension of these observations has been widespread speculation on the potential benefit of antioxidants in a range of therapeutic contexts. Phenols, in their various iterations, are by far the most recognizable antioxidants and have certainly received the most scrutiny. While much of the data from a chemical perspective is of a rather poor quality, being based on DPPH titration measurements or other equally misleading "antioxidant assays",[7] there is a rather sizable body of research which systematically looks at structure and function in kinetic-based autoxidation assays. In the "pre-ferroptosis era" much of the research and development was focused on Vitamin E (α-Tocopherol in particular) as this is viewed as the most biologically relevant and efficacious of the naturally occurring lipid-soluble RTAs.[8] Rather extensive kinetic measurements of α-Toc and related phenols have been carried out in organic solutions (styrene/chlorobenzene) which revealed important structure-function relationships for the differing rates of inhibition on the basis of substituent and stereoelectronic effects.[9–11] While these provided a logical framework for rational RTA design, when comparing it to the experimental work in biphasic systems it was clear to us that the model for RTA reactivity, established in solution, was incomplete and unable to quantitatively account for the inhibited lipid-peroxidation trends observed within membranes. Of the handful of quantitative works in this area, independent investigators reported absolute inhibition rate constants within linoleic acid filled sodium dodecyl sulfate (SDS) micelles which were generally at least an order of magnitude (often 2) less than those reported in chlorobenzene.[12–14] Furthermore, the absolute inhibition rate constants in dilinoleoylphosphatidylcholine (DLPC) liposomes reported by L. R. C. Barclay and coworkers were *even lower* than those in SDS by at least a few factors.[15] To make matters more confusing, it was generally observed that the inhibition with sterically hindered phenols such as 2,6-di-*tert*-butyl-4-methoxyphenol (DBHA) and 2,6-di-*tert*-butyl-4-methylphenol (BHT) were far less diminished in micelles and liposomes to the extent that their comparative reactivity with respect

to less hindered phenols could actually be *greater* in liposomes (a reversal of the trends observed in chlorobenzene). It was surmised by Pryor, and reinforced later by Barclay, that the effect was a consequence of H-bond accepting *as well as* donating effects from water, though these theories were not consistently applied across the range of RTAs they measured.[13,15]

These investigations carried out through the 1980's and into the 90's really represent the most robust attempts to characterize/model RTA reactivity in membrane-like systems. The dearth of follow up was likely a product of the wanning interest in antioxidants as a therapeutic target combined with the challenges of the research using the methodology available in that era (as alluded to by Pryor).[13] Since then, a far more quantitative understanding of the relationship between H-bonding and RTA activity has been established in the context of polar vs non-polar isotropic solutions. In 2001, D. W. Snelgrove with K. U. Ingold and coworkers produced an elegant and reliable semi-empirical expression that, with a remarkable degree of accuracy, predictively describes the magnitude of the KSE on RTAs.[16] Their model invokes a simple pre-equilibrium (Eq. 2.1) to the trapping of radicals where the phenolic RTA would form a 1:1 H-bond complex with a solvent molecule, with the phenol being an H-bond donor (HBD) and the solvent being an H-bond acceptor (HBA). According to their theory, the phenolic RTA cannot transfer its hydrogen atom while engaged in the 1:1 complex, thus only "free" phenol is available to trap radicals. As the steady-state concentration of free RTA decreases in stronger HBA solvents, the observed bimolecular inhibition rate constant decreases. The magnitude of the pre-equilibrium can be accurately estimated using "H-bond acidity" and "H-bond basicity" parameters of the HBD/HBA combination (Eq. 2.2) which were previously developed by Michael Abraham (designated as α_2^H and β_2^H respectively).[17,18]

Scheme 2.1 – The Snelgrove/Ingold Pre-Equilibrium Model of Radical-Trapping KSE



$$k_{inh}^{s} = \frac{k_{inh}^{0}}{1 + K^{s}[\boldsymbol{S}]} \qquad (2.1)$$

$$\log k_{inh}^{s} = -8.3\alpha_2^H\beta_2^H + \log k_{inh}^{0} \qquad (2.2)$$

We previously made extensive use of this relationship for the measurement of inhibition rate constants of phenoxazine (PNX) and phenothiazine (PTZ)-based RTAs in mixtures of chlorobenzene, 1,4-dioxane and DMSO and found systematic agreement with uncorrected measurements taken in benzene by Lucarini et al.[19,20] Given the proven reliability of Snelgrove/Ingold's equation for many phenolic and aminic RTAs in several solvent systems, we wondered whether this theory could be applied to autoxidations carried out in liposomal suspension. Given the renewed interest in lipid peroxidation research within the ferroptosis paradigm, it would seem rather timely to provide a quantitative explanation for the seemingly counter-intuitive trends noted for membrane targeted RTAs (which seemed to be the most potent type of ferroptosis inhibitor).[21] Furnished with the benefits of three decades of additional theory and a far less cumbersome suite of spectrophotometric/fluorescence-based autoxidation assays,[1,22] we sought to carry out a systematic study on a series of structurally-related phenolic RTAs to interrogate the role of H-bonding in the suppression of inhibition kinetics within phospholipid membranes.

2.3 Results

Our radical-initiated autoxidation experiments in organic solutions and liposomes are compositionally similar to prior work but not identical. In Barclay's work, the most relevant point of comparison, they use dilinoleoylphosphatidylcholine-based (DLPC) multilamellar buffer-phospholipid suspension, while we employed unilamellar liposomes (diameter ≤ 100nm) comprised of a mixture of phosphatidylcholine-lipids (ca. 20% PUFA) derived from chicken egg-yolk (Egg-PC). Additionally rather than using the O_2-consumption methodology used by

Barclay and coworkers, our kinetic protocols employ BODIPY-based autoxidation probes that contain either conjugated styrene (STY-BODIPY) or phenyl butadiene moieties (PBD-BODIPY).[22] The kinetics of the uninhibited and the inhibited co-autoxidation of STY/PBD-BODIPY conform to Eq. 2.3 and 2.4 respectively:

$$-\frac{d[BODIPY]}{dt} = k_p[BODIPY](R_i/2k_t)^{1/2} \qquad (2.3)$$

$$-\frac{d[BODIPY]}{dt} = k_p[BODIPY]R_i/nk_{inh}[RTA] \qquad (2.4)$$

Where k_p is the rate constant of peroxyl radical addition to the probe (propagation) and k_t is the termination rate constant.[23] The methods of determining k_{BODIPY} in particular substrate mixtures have been described previously,[19,22,24] though substrates new to this work (*m*-xylene and THF) are detailed in the supplemental for this chapter. The advantage of the BODIPY approach is that progress of the autoxidation can be reliably monitored by changes in absorbance or fluorescence, enabling a far higher level of throughput than was possible using a pressure transducer to monitor consumption of O_2. The rate of initiation (R_i) is calculated using Eq. 2.5 by taking a parallel measurement of the inhibition period (t_{inh}) for the RTA 2,2,5,7,8-pentamethyl-6-chromanol (PMC) where the stoichiometry (n) is assumed to be 2:[25]

$$R_i = n[RTA]/t_{inh} \qquad (2.5)$$

For our preliminary experiments we compared PMC, 2,6-dimethyl-4-methoxyphenol (DMHA) and DBHA in an STY-BODIPY/Egg-PC liposome co-autoxidation thermally initiated with V70. PMC is structurally equivalent to α-Toc apart from replacement of α-tocopherol's phytyl tail (-$C_{16}H_{33}$) with a methyl group. PMC is therefore used as an isoelectronic "stand-in" for α-Toc that will have a diffusion coefficient comparable to other low MW RTAs (<300amu). The inhibition rate constants in the liposomal suspension (k_{inh}^{lip}) were (3.3±0.2)×10^4, (2.8±0.1)×10^3 and (1.09±0.03)×10^4 $M^{-1}s^{-1}$ for PMC, DMHA and DBHA, respectively. Compared to previously reported values in chlorobenzene (k_{inh}^{PhCl}= 3.2×10^6, 9.4×10^5 and 1.1×10^5 $M^{-1}s^{-1}$) the rate constants decreased by 97-fold, 336-fold and 10-fold respectively.[26–28] The trend was fairly consistent with the observations in azobis-2,4-dimethylvaleronitrile (DMVN) initiated DLPC suspension previously reported by Barclay and coworkers for PMC and DBHA (1.78×10^4 and 2.75×10^4 M^{-}

$^{1}s^{-1}$ respectively).[15] Through the process of testing different RTAs under the aforementioned conditions (Egg-PC w/ V70) it was discovered that there was little discrimination between water-soluble and lipid-soluble radical-trapping inhibitors. We suspected this was due to initiation occurring in both the aqueous and lipid compartments on account of low incorporation of the V70 in the lipid-domain, an inference which was subsequently verified through various control experiments. In contrast, when using di-*tert*-undecyl hyponitrite (DTUN) instead, a new initiator synthesized in-house, it was gratifyingly found to only allow inhibition by lipid-soluble RTAs.[1] Using DTUN, the measured k_{inh}^{lip} for PMC, DMHA and DBHA were $(2.9\pm0.3)\times10^{4}$, $(3.3\pm0.3)\times10^{3}$ and $(4.3\pm0.3)\times10^{4}$ $M^{-1}s^{-1}$. While PMC and DMHA were similar to the results from the V70 initiated experiments, interestingly the k_{inh}^{lip} of DBHA increased by a factor of 4 when using the more lipophilic initiator. Given the discernible difference initiator choice makes for DBHA, we elected in the remainder to continue using DTUN for the liposome experiments as we anticipated that this was a more representative model of lipid peroxidation.

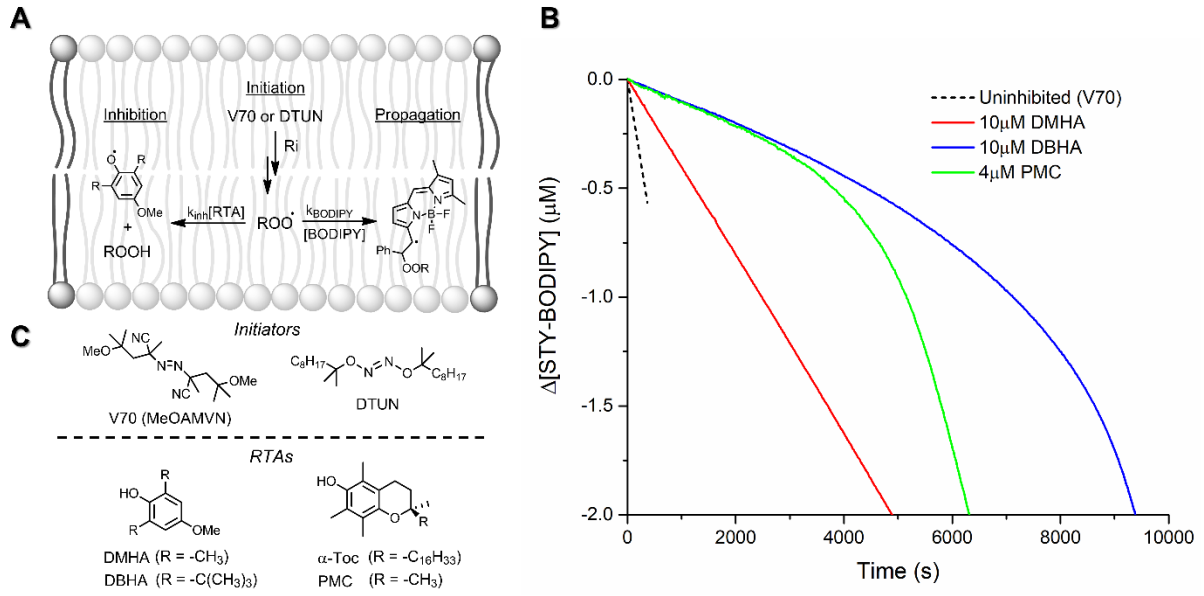
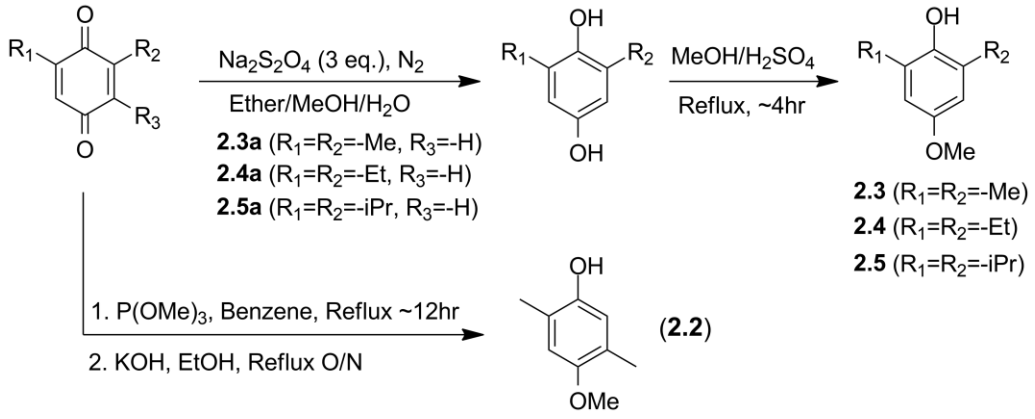


Figure 2.1. (A) Competition between STY/PBD-BODIPY and RTA for propagation vs. inhibition. **(B)** Example of inhibited (and uninhibited) co-autoxidation of STY-BODIPY in PBS Buffer (pH 7.4, 10 mM) with 100nm unilamellar Egg-PC liposomes (1 mM) initiated by V70 at 37 °C (monitored by absorbance loss at 565nm). **(C)** Structures of initiators and phenolic RTAs.

Having initially corroborated the observations reported by Barclay and coworkers, we set to work expanding the dataset in an effort to elucidate a model for phenolic inhibition within the liposome. Having ascertained the importance of steric hinderance with respect to the phenol's activity, we first synthesized 2,6-diethyl-4-methoxyphenol (**2.4**) and 2,6-di-*iso*-propyl-4-methoxyphenol (**2.5**) to observe the effect of incremental increases in steric hinderance between DMHA (**2.3**) and DBHA (**2.6**). We also acquired 4-methoxyphenol (**2.1**) and prepared 2,5-dimethyl-4-methoxyphenol (**2.2**) to serve as examples of decreasing steric demand compared to DMHA. Compounds **2.2**, **2.3**, **2.4**, and **2.5** were synthesized from their corresponding para-quinones as shown in Scheme 2.2.

Scheme 2.2 – The Synthesis of 2.2-2.5 From Their Corresponding p-Quinones



With this modest series of phenols in hand, we attempted to estimate their H-bond acidity parameters (α_2^H) by the empirical ^{1}H NMR method established by Abraham and coworkers.[29] By taking an NMR in both a poor HBA ($CDCl_3$) and a strong HBA solvent (DMSO-^{d6}), a reasonable estimate of α_2^H can be produced by taking the $\Delta\delta$ of the O-H proton in each solvent (via an empirical equation of known α_2^H vs. $\Delta\delta$). We elected to use C_6D_6 rather than $CDCl_3$ as the poor HBA solvent to maintain consistency with our existing dataset of PNX/PTZ α_2^H determinations.[30] In a complimentary fashion, we measured the H-bond basicity (β_2^H) of Egg-PC dissolved in CCl_4 using a ^{19}F NMR-based method originally pioneered by Taft.[31,32] By monitoring the chemical shift of 4-fluorophenol vs. 4-fluoroanisole in CCl_4 with increasing concentrations of HBA solute (PC), the 1:1 H-bond formation equilibrium constant (K_f) between 4-fluorophenol and the HBA could be ascertained (Eq. 2.6). From the K_f, the β_2^H of the HBA was be calculated using Eq. 2.7 as the H-bond acidity of 4-fluorophenol has been well established.[18]

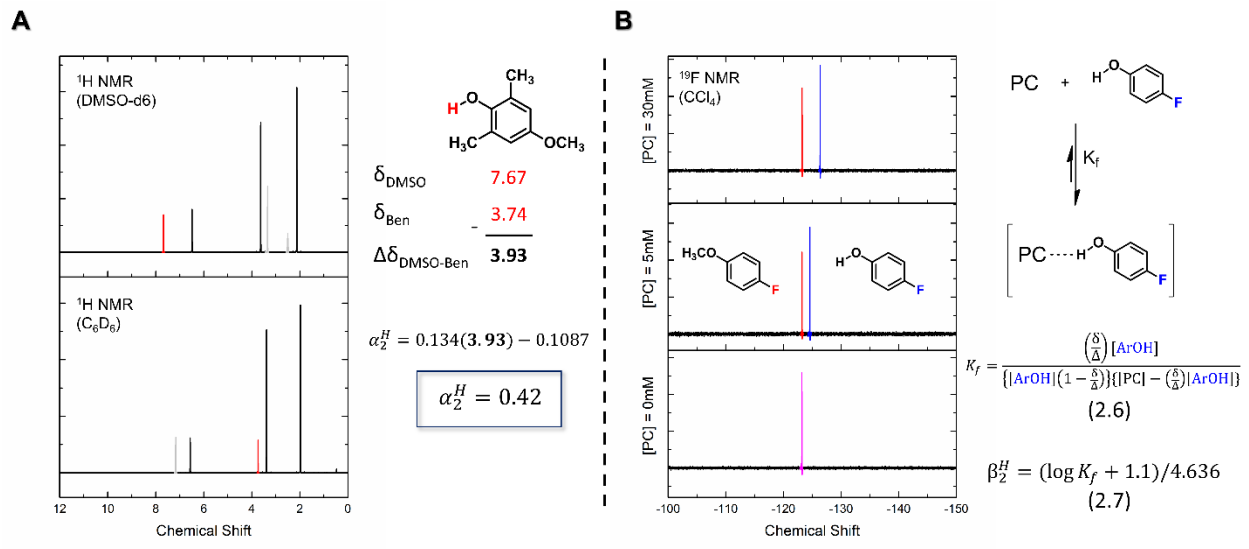
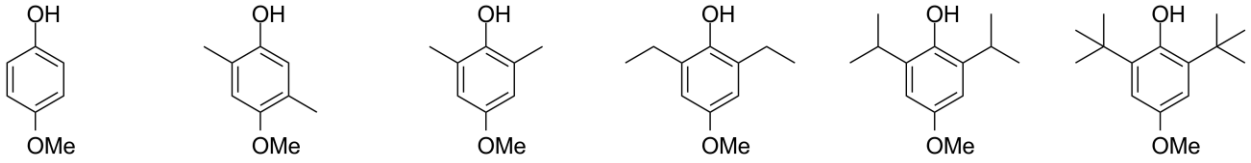


Figure 2.2. (A) Demonstration of ^{1}H NMR method of determining $\boldsymbol{\alpha_2^H}$ values. **(B)** Demonstration of ^{19}F NMR method of measuring K_f between 4-fluorophenol and PC in CCl_4.

By the method described, we obtained K_f = (390±80) from which a β_2^H = (0.79±0.02) was calculated for Egg-PC (in CCl_4). Notably this is far greater than the H-bond basicity of H_2O (β_2^H=0.38) which was previously implicated as the principle HBA species responsible for the suppressed RTA activity in micelles and liposomes.[13,15] To obtain a complimentary set of data for **2.1**, **2.2**, **2.4** and **2.5** in both chlorobenzene (β_2^H=0.09) and Egg-PC liposomes, we carried out inhibited co-autoxidations of PBD-BODIPY/1-hexadecene in PhCl to obtain the former and DTUN initiated liposome autoxidations for the latter. Using Eq. 2.2, we calculated the k_{inh}^0 (the "intrinsic" inhibition rate constant in the absence of H-bonding) from the k_{inh}^{PhCl} and the α_2^H values of the phenols. Using this we estimated the expected k_{inh} in H_2O (k_{inh}^{H2O}) and Egg-PC (k_{inh}^{PC}) using their respective β_2^H values and compared it to the actual rate constants observed in liposomes (k_{inh}^{lip}).

Table 2.1. Inhibition Rate Constants in PhCl Compared to Liposomes Analyzed Using Snelgrove/Ingold Pre-Equilibrium Model.



Chlorobenzene vs. Liposomes						
	k_{inh}^{PhCl} $(10^3\ M^{-1}s^{-1})^a$	α_2^H (NMR)	k_{inh}^0 $(10^3\ M^{-1}s^{-1})$	k_{inh}^{H2O} $(10^3\ M^{-1}s^{-1})^d$	k_{inh}^{PC} $(10^3\ M^{-1}s^{-1})^e$	k_{inh}^{lip} $(10^3\ M^{-1}s^{-1})^f$
2.1	260±20	0.59	717	9.9	0.097	0.11
2.2	790±70	0.55	2035	38	0.50	1.6
2.3	(940)[b]	0.42	1936	92	3.4	3.3
2.4	910±70	0.40	1811	99	4.3	8.9
2.5	930±80	0.37	1757	120	6.6	16
2.6	(110)[b,c]	0.16	145	45	13	43
PMC	(3200)[c]	0.38	6152	390	20	29

(a) k_{inh}^{PhCl} measured by PBD-BODIPY co-autoxidation in 4:1 1-hexadecene/PhCl initiated by AIBN. ($\beta_2^H = 0.09$) (b) Value from Burton et al. measured by O_2 uptake. (c) Value from Valgimigli et al. measured by O_2 uptake. (d) Calculated from k_{inh}^0 and α_2^H with Eq. 2.2 using the β_2^H of H_2O given by Abraham et al. (0.38). (e) Calculated from k_{inh}^0 and α_2^H with Eq. 2.2 using the β_2^H we determined for Egg-PC in CCl_4 (0.79). (f) k_{inh}^{lip} measured by STY-BODIPY co-autoxidation in PBS Buffer (pH 7.4, 10 mM) with 100nm unilamellar Egg-PC liposomes (1 mM) initiated by DTUN.

When comparing the k_{inh}^{lip} to the estimated values in H_2O (k_{inh}^{H2O}) projected by Snelgrove/Ingold's KSE model, it is clear that the absolute rate constants for **2.1**-**2.5** and PMC in liposomes are an order of magnitude (or more) lower than what could be reasonably expected in H_2O. On the other hand, using our measured β_2^H for Egg-PC in CCl_4, we see that there is far better agreement with the measured values, at worst falling within a few fold of k_{inh}^{lip}. This is, of course, with the exception of **2.6** which, being the least affected by the H-bonding pre-equilibrium in general, was anticipated to be the most error prone extrapolation.

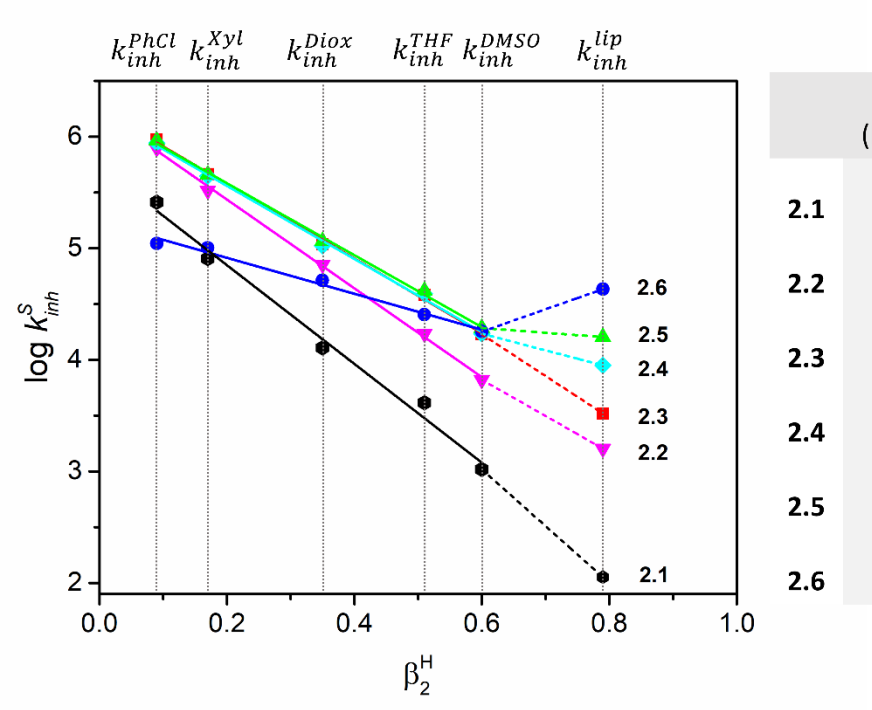
While the convergence with k_{inh}^{PC} rather than k_{inh}^{H2O} provided a compelling case for a model predicated on H-bonding to the phosphodiester headgroup rather than invoking solvation with H_2O, we felt that comparing k_{inh}^{lip} to multiple different isotropic systems would be far more

persuasive for establishing the continuity between the Snelgrove/Ingold pre-equilibrium model and what is happening to the phenols in the phospholipid bilayer. To this end, we measured k_{inh} for each of the phenols in 4 additional organic systems (*m*-xylene, dioxane/PhCl, THF and dioxane/DMSO) with β_2^H values that ranged from 0.17 to 0.60 (Table 2.2).[18,19] Doing this also afforded us the opportunity to independently verify the α_2^H estimated by the NMR method by analyzing the observed KSE over 5 organic systems with known β_2^H values. The results of these additional experiments are summarized in Table 2.2 and Figure 2.3.

Table 2.2. Inhibition Rate Constant Data in Four Additional Organic Solutions/Substrates.

Xylene, Dioxane, THF and DMSO				
	k_{inh}^{Xyl} $(10^3\ M^{-1}s^{-1})^a$	k_{inh}^{Diox} $(10^3\ M^{-1}s^{-1})^b$	k_{inh}^{THF} $(10^3\ M^{-1}s^{-1})^c$	k_{inh}^{DMSO} $(10^3\ M^{-1}s^{-1})^d$
2.1	81±1	13±1	4.1±0.3	1.1±0.2
2.2	330±30	71±1	17±1	6.6±0.3
2.3	460±30	110±10	38±3	17±1
2.4	440±10	110±10	39±2	17±1
2.5	460±20	120±20	42±4	19±1
2.6	100±10	52±3	25±1	18±1
PMC	1300±200	390±40	140±20	61±8

(a) k_{inh}^{Xyl} measured by PBD-BODIPY co-autoxidation in *m*-xylene initiated by AIBN. ($\beta_2^H = 0.17$). (b) k_{inh}^{Diox} measured by PBD-BODIPY co-autoxidation in 3:1 PhCl/1,4-dioxane initiated by AIBN. ($\beta_2^H = 0.35$). (c) k_{inh}^{THF} measured by PBD-BODIPY co-autoxidation in THF initiated by AIBN. ($\beta_2^H = 0.51$). (d) k_{inh}^{DMSO} measured by PBD-BODIPY co-autoxidation in 2:1:1 PhCl/DMSO/1,4-dioxane initiated by AIBN. ($\beta_2^H = 0.60$).



	α_2^H (NMR)	α_2^H (KSE)	EC_{50} (μM)
2.1	0.59	0.53	n/a
2.2	0.55	0.46	n/a
2.3	0.42	0.40	6.1
2.4	0.40	0.39	0.7
2.5	0.37	0.38	0.2
2.6	0.16	0.21	0.1

Figure 2.3. (Left) The $\log k_{inh}^{S}$ plotted against the β_2^H of each respective system. (Right) The α_2^H determinations by the NMR and KSE methods compared *and* the EC_{50} for recusing pfa-1 cells from RSL3 induced ferroptosis.

The agreement in α_2^H values, whether obtained by the ^{1}H NMR or KSE method, ranged from fair to excellent. The notable exception was **2.2** which received a sizeable downward correction (0.55 vs 0.46) by applying the KSE method (which should be considered a more direct measure of H-bond acidity within the Snelgrove/Ingold model). Using this revised value for calculating k_{inh}^{PC} from k_{inh}^{PhCl}, it goes from 0.5 × 10^3 to 1.7 × 10^3 $M^{-1}s^{-1}$, which is in perfect agreement with the k_{inh}^{lip} of **2.2** (1.6 × 10^3 $M^{-1}s^{-1}$). For compounds **2.1**-**2.3**, the linear continuity from the isotropic solutions (solid line) to the Egg-PC liposomes (dash line) is quite seamless. Interestingly, while **2.4** and **2.5** behave identically to **2.3** in all 5 solution oxidation experiments, there appears to be a trend of increasing k_{inh} as the size of the 2,6-alkyl groups increases, but only in the context of liposomes. This phenomenon appears even more pronounced with **2.6**. We also evaluated the compounds' abilities to rescue pfa-1 cells from RSL3 induced ferroptosis (RSL3 is a GPx4 inhibitor). While the 2 compounds with the lowest k_{inh}^{lip}, **2.1** and **2.2**, were unable to rescue the cells to any significant extent at the tested range of concentration (max [RTA] = 20 μM), a sharp

increase in the potency from **2.3** to **2.6** was observed. The trend appears to be in line with the substantial increases in k_{inh}^{lip} over the series of phenols.

2.4 Discussion

Within this panel of examples, the decrease in the observed inhibition rate constant simply by moving from chlorobenzene to Egg-PC liposomes can range anywhere from 2.5-fold to 2360-fold depending on the structure of the phenol. When looking at the k_{inh} of **2.1**-**2.5** (and PMC) in a range of HBA solvent systems in comparison to their respective k_{inh}^{lip} values, it is apparent that the H-bond basicity of PC (β_2^H=0.79±0.02) is primarily responsible for the dramatic differences. Analyzing the individual HBA moieties available in an aqueous dispersion of phosphatidylcholine, the available options are water, ester and the phosphate diester. Looking through Abraham's H-bond basicity parameters it is clear that neither ester (β_2^H=0.45) nor H_2O (β_2^H=0.39) are nearly H-bond basic enough to account for the effect, however the reported β_2^H for $O{=}P(OR)_3$ was 0.77 which agrees nearly perfectly with our K_f measurements of PC.[18] One can readily infer from this that lipophilic phenols in the bilayer spend the vast majority of their time complexed to the phosphate group, unable to trap lipid-peroxyl radicals. The exceptions to this state of affairs are instances where the steric hinderance about the -OH is substantial, such as the case of **2.6**. While our initial inclination was to ascribe the lessened effect on **2.6** to the low H-bond acidity (α_2^H) of the hindered HBD, the rather obvious break in linear extrapolation from solvents to liposomes prompted us to consider the role of the hydrophobic effect in "pushing" **2.6** away from the phosphodiester headgroup, further into the lipid-domain (as shown in Figure 2.4A). This interpretation is consistent with the incremental increases in k_{inh} when moving from -Me to -Et to -iPr at the 2,6-positions (**2.3** < **2.4** < **2.5**), a trend only observed in the liposome experiments but not the isotropic solutions. When originally designing the study, we had anticipated the H-bond acidity of **2.4** and **2.5** would be incrementally lower than that of **2.3**, but according to both the NMR and KSE method all three are nearly the same. Presumably the intermediate size alkyl groups (-Et/-iPr) orient their -H group(s) toward the phenolic -OH to minimize steric interactions making the hydroxyl nearly as accessible as that of **2.3** (Fig. 2.4B). The uniform behaviour of **2.3**-**2.5** in solution turned out to be an asset as it underscores that while organic solution and membranes share a common feature (the prominence of the H-bond

pre-equilibrium), the anisotropic nature of liposomes still needs to be considered. Rather than universally ascribing a "fixed" β_2^H of 0.79 to PC liposomes, it is probably more accurate to view this as the "upper limit" of H-bond basicity in the membrane. For RTAs that reside much deeper within the lipid-domain, as presumed for **2.6**, we would anticipate the "lower limit" of H-bond basicity to be that of the ester (~0.45). It would follow that the hydrophobic effect has a more modest influence on **2.4** and **2.5** and that the "effective" β_2^H in those instances are intermediate values within that range, though evidently their kinetic behavior is still mostly dominated by complexation to the phosphate moiety.[33]

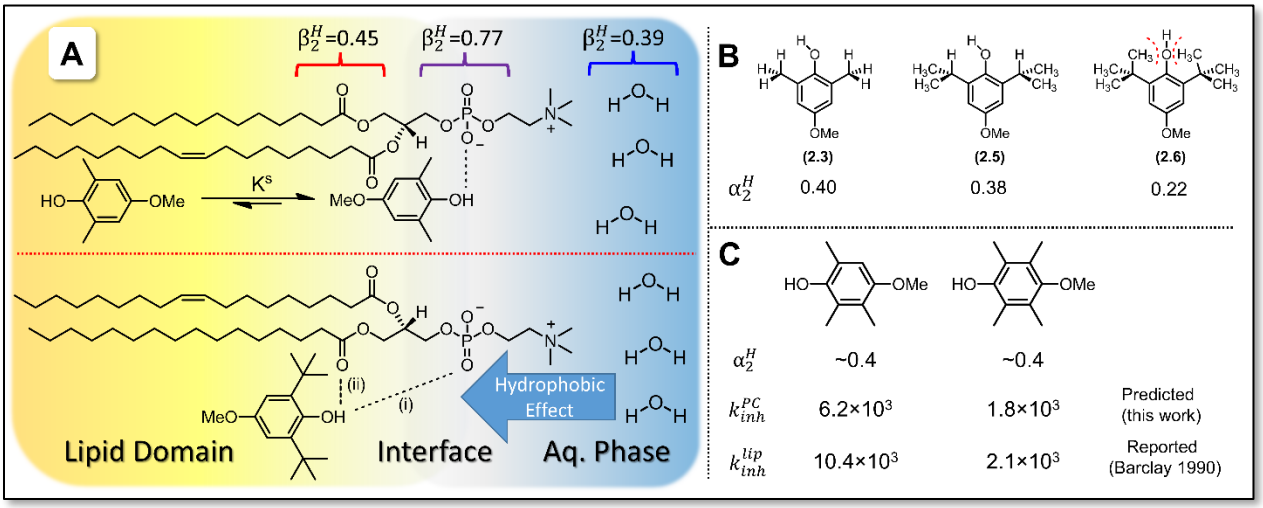


Figure 2.4. (A) Proposed model of H-bonding of phenols in a phospholipid membrane. Shown are the proposed behaviours for "unhindered" phenols (top) and of very hindered phenols (bottom). **(B)** Scheme representing the proposed steric clash that is present for **2.6** but not **2.5.** **(C)** Estimates of the rate constants that would be expected in an inhibited liposome autoxidation assuming a $\boldsymbol{\beta_2^H}$ of 0.79, using $\boldsymbol{k_{inh}^{PhCl}}$ from the literature.[27]

We took an opportunity to reinterpret results from the seminal work of Barclay and coworkers using this new model. Using the k_{inh}^{PhCl} values reported by Burton/Ingold and coworkers for 2,3,6-trimethyl-4-methoxyphenol (1.3×10^6 $M^{-1}s^{-1}$) and 2,3,5,6-tetramethyl-4-methoxyphenol (3.9×10^5 $M^{-1}s^{-1}$),[27] and operating under the assumption that they have a similar α_2^H to **2.3** (~0.4), we would anticipate rate constants in the phospholipid bilayer of 6.2×10^3 and 1.8×10^3 $M^{-1}s^{-1}$, respectively, which is in very good agreement with the experimental values (Fig. 2.4C).[15] The model proposed above, rather than the original suggestion of water complexation put forward by Pyror and Barclay, is almost certainly the cause of the suppression of RTA activity in

phospholipid membranes. Indeed, I would further hazard that an analogous complexation occurs in micellar SDS experiments, though this would need to be experimentally verified as the β_2^H of sodium sulfonate has not been reported, at least to the best of my knowledge.

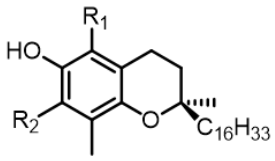
The point about the insufficient H-bond basicity of water is not a novel critique. Valgimigli *et al.* first in 1996 and again in 1998 accurately demonstrated the quantitative inability of H_2O to imbue that large of an effect on α-Toc inhibition kinetics in micelles/liposomes.[34,35] So emphatic were they with their findings that they, in hindsight quite ironically, concluded:

> *"It seems highly unlikely that the SDS micelles and the phospholipid bilayer could contain HBA molecules that were so very much better HBA's than water or tert-butyl alcohol (which is a slightly stronger HBA than esters)."*

They instead attributed the suppression to poor inter-lipid particle diffusion of α-Toc making it "inaccessible" for trapping radicals in neighbouring micelles/liposomes. While it is true that α-Toc is slow to diffuse passively between vesicles,[36] this overlooks the fact that many low MW RTAs (including PMC) which do not suffer from this impediment also have their rate constants decreased to a similar degree. L.R.C. Barclay and M. R. Vinqvist, writing about it in a thoroughly researched book chapter on *Phenols as Antioxidants* in 2009, reiterated the slow diffusion hypothesis in addition to a handful of other proposed contributions unrelated to H-bonding.[37] Thus, after a careful review of the authoritative literature, we believe that our proposed model is a novel interpretation of the facts and successfully resolves a more than three decade-old scientific riddle.

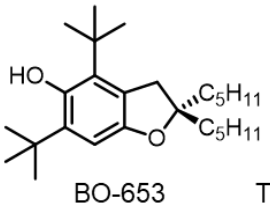
With this new understanding of phenol inhibition kinetics in phospholipid membranes, there are some interesting implications with respect to the various forms of Vitamin E. Indeed, while previously the superiority of α-Tocopherol compared to β, γ and δ were appreciated within the context of an electron-donor lowering effect on the O-H BDE, and the concomitant increased k_{inh}^{PhCl},[27] if the H-bond acidity differences between **2.2** and **2.3** are any indication of trends to expect, β-Toc and γ-Toc would have an additional ~2-fold penalty in a membrane compared to α-Toc. If δ-Toc and **2.1**, being bereft of ortho methyl substituents, are to be considered structurally analogous one would anticipate similarly catastrophic levels of suppressed activity on account of prodigious H-bond interactions with the phosphate.

Scheme 2.3 – Structures of Vitamin E and α-Tocopherol Inspired Phenols

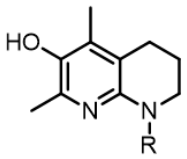


Vitamin E

	R_1	R_2
α-Toc	Me	Me
β-Toc	Me	-H
γ-Toc	-H	Me
δ-Toc	-H	-H



BO-653
(Niki 1997)



Tetrahydro-1,8-naphthyridinol
(Pratt 2003)

Given the apparent benefits of increasing steric-bulk about the phenol's hydroxyl group in this application, exchanging α-Toc methyl groups with larger alkyl substituents would seem to be a logical optimization for potent mimics of α-Toc. If we take this premise for granted, the "ideal" phenolic design already exists in the form of antioxidant BO-653, developed as an RTA-based anti-atherogenic drug.[38] BO-653 embodies the best electronic attributes of the 5-hydroxybenozfuran scaffold[27] along with the steric hinderance of 2 ortho *tert*-butyl groups, as found in the phenolic anti-atherogenic drug probucol, though the inclusion of the latter was predicated on a different set of rationale.[39] One of the attributes many of the vitamin E inspired RTAs lack with respect to α-Toc, however, is an ability to utilize tocopherol transfer protein (TTP) which both protects α-Toc from metabolic clearance and, as the name would suggest, facilitates active transport between low density lipoproteins and peripheral tissues *in vivo*.[40] While it is possible to create novel RTAs that mimic α-Toc in this respect, as our group has previously demonstrated *in vitro* in collaboration with Atkinson and coworkers using a naphthyridinol-based design,[41] designing novel and potent lipid-soluble RTAs while *simultaneously* tailoring them to the highly specific TTP binding pocket is a rather restrictive mandate to operate a medicinal chemistry campaign within.

If, by in large, novel phenolic RTA-based drug designs do not operate under the auspices of TTP binding, it does beg the question: are phenols even the ideal scaffold for inhibiting membrane oxidation? In the "pre-ferroptosis era" aromatic amines received far less consideration than phenols, though there were some indications of their merits as inhibitors of lipid-peroxidation. For example, the activity of N,N'-diphenyl-p-phenylenediamine (DPPD) and ethoxyquin (two amine-based RTAs) were found by Pryor and coworkers to be equivalent or slightly superior to that of PMC in their SDS micelle autoxidation experiments.[13] Another point of interest is that two of the most widely studied ferroptosis inhibitors, ferrostatin-1 (Fer-1) and liproxstatin-1

(Lip-1), are also relatively potent aminic-RTAs.[42,43] When we assess the intrinsic activity (k_{inh}^{0}) and the H-bond acidity (α_2^H) of phenol and diphenylamine (DPA), it becomes rather apparent that the amine possesses a natural advantage in both respects (Fig. 2.5). In the absence of H-bonding, DPA holds a modest 4-fold advantage over phenol,[44] but that difference would be anticipated to grow to a staggering 380-fold difference in the strong H-bond accepting environment of the phospholipid membrane. Though the strong H-bond acidity of phenol is mitigated by relatively modest steric interventions, as is in place with α-Toc/PMC, it still remains that a simple aminic RTA like DPA appears to be a fundamentally better starting point for a membrane targeted application. This analysis appears to be reflected in our prior observations with generic diarylamines, such as 4,4'-di-*tert*-butyldiphenylamine, where the inhibition of ferroptosis in cell-based assays generally fell in the mid-to-high double digit nanomolar range (EC_{50} = 30-100nM).[43] The excellent kinetics of PNX and PTZ derived antioxidants in solution,[19] as well their exceptional potency as ferroptosis inhibitors (EC_{50} of 9 and 22nM respectively),[43] prompted us to run a similar analysis to see how electronically "optimized" analogues of DPA would stack up against PMC. The H-bond acidity of PNX (0.44) and PTZ (0.38) increases by a considerable margin compared to DPA (0.30), possibly a consequence of an inductive effect from the chalcogen bridge, however the respective 2400 and 440-fold increase in k_{inh}^{0} more than compensates this loss. Assuming an effective β_2^H of 0.79 is in operation, PNX and PTZ would have a projected 5.4 and 2.4-fold advantage over PMC in liposomes. The experimental k_{inh}^{lip} values (see Chapter 3) were found to be 8 and 3.8-fold greater than PMC, slightly better than expected though still in excellent agreement with the theory.[45,46] Crucially, PNX and PTZ the significantly faster inhibition kinetics is achieved while maintaining stability toward O_2, in contrast to many of the enhanced phenolic Vitamin E mimics which tended to be quite oxidatively labile.[19]

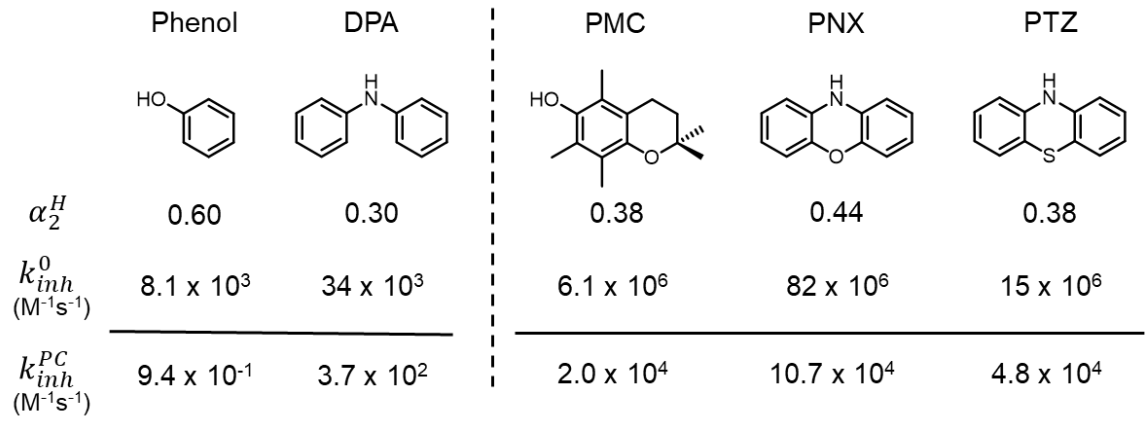


Figure 2.5. Estimates of the rate constants that would be expected in an inhibited liposome autoxidation assuming a $\boldsymbol{\beta_2^H}$ of 0.79, using rate constants of inhibition in organic solutions obtained from the literature.[9,19,20,26]

2.5 Conclusion

In summary, using the Snelgrove/Ingold pre-equilibrium model, we have been able to establish that the principal cause of the dramatic decrease in k_{inh} observed when moving from chlorobenzene solution to PC liposomes is the strong H-bond basicity of the liposomal environment. We first established this by determining the β_2^H of Egg-PC dissolved in CCl_4 (0.79 ± 0.02), combined with the α_2^H values for **2.1**-**2.6** determined using Abraham's ^{1}H NMR method to estimate the magnitude of the decreases that should be expected. We subsequently followed this with measurements of the KSE for **2.1**-**2.6** in a series of organic solutions (5 total) with H-bond basicity ranging from 0.09 to 0.60. From this we were able to corroborate the α_2^H and β_2^H determinations made using the NMR methods. We propose that the phosphate diester is the major constituent with which the phenols engage in H-bond complexes. Furthermore, we propose that the decreased 'effective β_2^H' values observed for **2.4**-**2.6** is due to the hydrophobic effect on the larger ortho-alkyl substituents, which appears to be supported by the trends. The more sterically hindered phenols have higher k_{inh}^{lip} and seem to be correspondingly more potent inhibitors of ferroptosis as a result, which would support the predictive capabilities of this kinetic approach. On the basis of the above theory and observations, aromatic amine-derived RTAs, rather than phenols, appear to be a more attractive target for future development of RTAs that target lipid-peroxidation/ferroptosis.

2.6 References

(1) Shah, R.; Farmer, L. A.; Zilka, O.; Van Kessel, A. T. M.; Pratt, D. A. Beyond DPPH: Use of Fluorescence-Enabled Inhibited Autoxidation to Predict Oxidative Cell Death Rescue. *Cell Chem. Biol.* **2019**, *26* (11), 1594-1607.e7.

(2) Gianazza, E.; Brioschi, M.; Martinez Fernandez, A.; Casalnuovo, F.; Altomare, A.; Aldini, G.; Banfi, C. Lipid Peroxidation in Atherosclerotic Cardiovascular Diseases. *Antioxid. Redox Signal.* **2020**, *34* (1), 49–98.

(3) Lucas, D. T.; Szweda, L. I. Cardiac Reperfusion Injury: Aging, Lipid Peroxidation, and Mitochondrial Dysfunction. *Proc. Natl. Acad. Sci. U.S.A.* **1998**, *95* (2), 510–514.

(4) Zhou, L.; Han, S.; Guo, J.; Qiu, T.; Zhou, J.; Shen, L. Ferroptosis - A New Dawn in the Treatment of Organ Ischemia-Reperfusion Injury. *Cells* **2022**, *11* (22), 3653.

(5) Farooqui, A. A.; Horrocks, L. A. Lipid Peroxides in the Free Radical Pathophysiology of Brain Diseases. *Cell. Mol. Neurobiol.* **1998**, *18* (6), 599–608.

(6) Ren, J.-X.; Sun, X.; Yan, X.-L.; Guo, Z.-N.; Yang, Y. Ferroptosis in Neurological Diseases. *Front. Cell. Neurosci.* **2020**, *14*, 218.

(7) Foti, M. C. Use and Abuse of the DPPH• Radical. *J. Agric. Food Chem.* **2015**, *63* (40), 8765–8776. https://doi.org/10.1021/acs.jafc.5b03839.

(8) Burton, G. W.; Joyce, A.; Ingold, K. U. Is Vitamin E the Only Lipid-Soluble, Chain-Breaking Antioxidant in Human Blood Plasma and Erythrocyte Membranes? *Arch. Biochem. Biophys.* **1983**, *221* (1), 281–290.

(9) Howard, J. A.; Ingold, K. U. The Inhibited Autoxidation of Styrene: Part II. The Relative Inhibiting Efficiencies of Meta- and Para-Substituted Phenols. *Can. J. Chem.* **1963**, *41*, 1744–1751.

(10) Howard, J. A.; Ingold, K. U. THE INHIBITED AUTOXIDATION OF STYRENE: PART III. THE RELATIVE INHIBITING EFFICIENCIES OF ORTHO-ALKYL PHENOLS. *Can. J. Chem.* **1963**, *41* (11), 2800–2806.

(11) Burton, G. W.; Ingold, K. U. Vitamin E: Application of the Principles of Physical Organic Chemistry to the Exploration of Its Structure and Function. *Acc. Chem. Res.* **1986**, *19*, 194–201.

(12) Castle, L.; Perkins, M. J. Inhibition Kinetics of Chain-Breaking Phenolic Antioxidants in SDS Micelles. Evidence That Intermicellar Diffusion Rates May Be Rate-Limiting for Hydrophobic Inhibitors Such as .Alpha.-Tocopherol. *J. Am. Chem. Soc.* **1986**, *108* (20), 6381–6382.

(13) Pryor, W. A.; Strickland, T.; Church, D. F. Comparison of the Efficiencies of Several Natural and Synthetic Antioxidants in Aqueous SDS [Sodium Dodecyl Sulfate] Micelle Solutions. *J. Am. Chem. Soc.* **1988**, *110* (7), 2224–2229.

(14) Barclay, L. R. C.; Baskin, K. A.; Locke, S. J.; Schaefer, T. D. Benzophenone-Photosensitized Autoxidation of Linoleate in Solution and Sodium Dodecyl Sulfate Micelles. *Can. J. Chem.* **1987**, *65* (11), 2529–2540.

(15) Barclay, L. R. C.; Baskin, K. A.; Dakin, K. A.; Locke, S. J.; Vinqvist, M. R. The Antioxidant Activities of Phenolic Antioxidants in Free Radical Peroxidation of Phospholipid Membranes. *Can. J. Chem.* **1990**, *68* (12), 2258–2269.

(16) Snelgrove, D. W.; Lusztyk, J.; Banks, J. T.; Mulder, P.; Ingold, K. U. Kinetic Solvent Effects on Hydrogen-Atom Abstractions: Reliable, Quantitative Predictions via a Single Empirical Equation. *J. Am. Chem. Soc.* **2001**, *123* (3), 469–477.

(17) Abraham, M. H.; Grellier, P. L.; Prior, D. V.; Duce, P. P.; Morris, J. J.; Taylor, P. J. Hydrogen Bonding. Part 7. A Scale of Solute Hydrogen-Bond Acidity Based on Log K Values for Complexation in Tetrachloromethane. *J. Chem. Soc. Perkin Trans. 2* **1989**, 699–711.

(18) Abraham, M. H.; Grellier, P. L.; Prior, D. V.; Morris, J. J.; Taylor, P. J. Hydrogen Bonding. Part 10. A Scale of Solute Hydrogen-Bond Basicity Using Log K Values for Complexation in Tetrachloromethane. *J. Chem. Soc. Perkin Trans. 2* **1990**, 521–529.

(19) Farmer, L. A.; Haidasz, E. A.; Griesser, M.; Pratt, D. A. Phenoxazine: A Privileged Scaffold for Radical-Trapping Antioxidants. *J. Org. Chem.* **2017**, *82* (19), 10523–10536.

(20) Lucarini, M.; Pedrielli, P.; Pedulli, G. F.; Valgimigli, L.; Gigmes, D.; Tordo, P. Bond Dissociation Energies of the N-H Bond and Rate Constants for the Reaction with Alkyl, Alkoxyl, and Peroxyl Radicals of Phenothiazines and Related Compounds. *J. Am. Chem. Soc.* **1999**, *121*, 11546–11553.

(21) Conrad, M.; Pratt, D. A. The Chemical Basis of Ferroptosis. *Nat. Chem. Biol.* **2019**, *15* (12), 1137–1147.

(22) Haidasz, E. A.; Van Kessel, A. T. M.; Pratt, D. A. A Continuous Visible Light Spectrophotometric Approach to Accurately Determine the Reactivity of Radical-Trapping Antioxidants. *J. Org. Chem.* **2016**, *81* (3), 737–744.

(23) The rate constant of termination is assumed to be in unity with the reported $2k_t$ for the bulk substrate.

(24) Chauvin, J.-P. R.; Griesser, M.; Pratt, D. A. Hydropersulfides: H-Atom Transfer Agents Par Excellence. *J. Am. Chem. Soc.* **2017**, *139* (18), 6484–6493.

(25) Burton, G. W.; Ingold, K. U. Autoxidation of Biological Molecules. 1. The Antioxidant Activity of Vitamin E and Related Chain-Breaking Phenolic Antioxidants in Vitro. *J. Am. Chem. Soc.* **1981**, *103* (21), 6472–6477.

(26) Valgimigli, L.; Bartolomei, D.; Amorati, R.; Haidasz, E.; Hanthorn, J. J.; Nara, S. J.; Brinkhorst, J.; Pratt, D. A. 3-Pyridinols and 5-Pyrimidinols: Tailor-Made for Use in Synergistic Radical-Trapping Co-Antioxidant Systems. *Beilstein J. Org. Chem.* **2013**, *9* (1), 2781–2792.

(27) Burton, G. W.; Doba, T.; Gabe, E. J.; Hughes, L.; Lee, F. L.; Prasad, L.; Ingoldo, K. U. Autoxidation of Biological Molecules. 4. Maximizing the Antioxidant Activity of Phenols. *J. Am. Chem. Soc.* **1985**, *107* (24), 7053–7065.

(28) For PMC we elected to use the rate constant reported by Valgimigli and co-workers (3.2×10^6 $M^{-1}s^{-1}$) rather than the frequently cited Burton value (3.8×10^6 $M^{-1}s^{-1}$), both of which

were determined by the oxygen-uptake method. Our regular internal measurements tend to range 2.7-3.4 × 10^6, and Burton's value for α-Toc is reported 3.2 × 10^6 $M^{-1}s^{-1}$, so we feel that the value reported by Valgimigli et al. is more representative of the median result.

(29) Abraham, M. H.; Abraham, R. J.; Byrne, J.; Griffiths, L. NMR Method for the Determination of Solute Hydrogen Bond Acidity. *J. Org. Chem.* **2006**, *71*, 3389–3394.

(30) Phenoxazine and phenothiazines tend to have poorly resolved ^{1}H NMR in $CDCl_3$ (formation of radical cation). We found when correlating α_2^H using C_6D_6 as the poor HBA solvent that we observed the same slope (0.134) as Abraham did with $CDCl_3$ and that similar results were obtained outside the train set.

(31) Taft, R. W.; Gurka, D.; Joris, L.; von Schleyer, R.; Rakshys, J. W. Studies of Hydrogen-Bonded Complex Formation with p-Fluorophenol. IV. The Fluorine Nuclear Magnetic Resonance Method. *J. Am. Chem. Soc.* **1969**, *91*, 4794–4801.

(32) Taft, R. W.; Gurka, D.; Rakshys, J. W. Studies of Hydrogen-Bonded Complex Formation with p-Fluorophenol. V. Linear Free Energy Relationships with OH Reference Acids. *J. Am. Chem. Soc.* **1969**, *91* (17), 4801–4808.

(33) Comparing the KSE in the organic solutions to the observed k_{inh}^{lip} values, we calculated effective β_2^H values of the liposomes were 0.71 and 0.65 for **2.4** and **2.5** respectively.

(34) Valgimigli, L.; Ingold, K. U.; Lusztyk, J. Antioxidant Activities of Vitamin E Analogues in Water and a Kamlet - Taft β-Value for Water. *J. Am. Chem. Soc.* **1996**, *118* (15), 3545–3549.

(35) Lucarini, M.; Pedulli, G. F.; Valgimigli, L. Do Peroxyl Radicals Obey the Principle That Kinetic Solvent Effects on H-Atom Abstraction Are Independent of the Nature of the Abstracting Radical? *J. Org. Chem.* **1998**, *63* (13), 4497–4499.

(36) Niki, E.; Kawakami, A.; Saito, M.; Yamamoto, Y.; Tsuchiya, J.; Kamiya, Y. Effect of Phytyl Side Chain of Vitamin E on Its Antioxidant Activity. *J. Biol. Chem.* **1985**, *260* (4), 2191–2196.

(37) Ross, L.; Barclay, C.; Vinqvist, M. R. Phenols as Antioxidants. In *PATAI'S Chemistry of Functional Groups*; 2009.

(38) Noguchi, N.; Iwaki, Y.; Takahashi, M.; Komuro, E.; Kato, Y.; Tamura, K.; Cynshi, O.; Kodama, T.; Niki, E. 2,3-Dihydro-5-Hydroxy-2,2-Dipentyl-4,6-Di-Tert-Butylbenzofuran: Design and Evaluation as a Novel Radical-Scavenging Antioxidant against Lipid Peroxidation. *Arch. Biochem. Biophys.* **1997**, *342* (2), 236–243.

(39) The primary rationale given for using ortho *tert*-butyl substituents by Noguchi et al. was to increase the persistence of the phenoxyl radical to mitigate chain-transfer which has been observed for α-Tocopherol in LDL (a phenomenon sometimes referred to as Tocopherol-mediated peroxidation).

(40) Qian, J.; Morley, S.; Wilson, K.; Nava, P.; Atkinson, J.; Manor, D. Intracellular Trafficking of Vitamin E in Hepatocytes: The Role of Tocopherol Transfer Protein. *J. Lipid Res.* **2005**, *46* (10), 2072–2082.

(41) Li, B.; Harjani, J. R.; Cormier, N. S.; Madarati, H.; Atkinson, J.; Cosa, G.; Pratt, D. A.

Besting Vitamin E: Sidechain Substitution Is Key to the Reactivity of Naphthyridinol Antioxidants in Lipid Bilayers. *J. Am. Chem. Soc.* **2013**, *135* (4), 1394–1405.

(42) Zilka, O.; Shah, R.; Li, B.; Friedmann Angeli, J. P.; Griesser, M.; Conrad, M.; Pratt, D. A. On the Mechanism of Cytoprotection by Ferrostatin-1 and Liproxstatin-1 and the Role of Lipid Peroxidation in Ferroptotic Cell Death. *ACS Cent. Sci.* **2017**, *3* (3), 232–243.

(43) Shah, R.; Margison, K.; Pratt, D. A. The Potency of Diarylamine Radical-Trapping Antioxidants as Inhibitors of Ferroptosis Underscores the Role of Autoxidation in the Mechanism of Cell Death. *ACS Chem. Biol.* **2017**, *12* (10), 2538–2545.

(44) The intrinsic rate constants were calculated from the rate constants reported by Lucarini et al. and Howard/Ingold for DPA (1.5×10^4 $M^{-1}s^{-1}$) and phenol (2.9×10^3 $M^{-1}s^{-1}$) respectively. See ref. 20 & 9.

(45) The calculated rate constants were systematically underestimated because the effective β_2^H in Egg-PC liposomes for PNX/PTZ-type compounds is 0.69 rather than 0.79. See ref. 46.

(46) Farmer, L. A.; Wu, Z.; Poon, J.-F.; Zilka, O.; Lorenz, S. M.; Huehn, S.; Proneth, B.; Conrad, M.; Pratt, D. A. Intrinsic and Extrinsic Limitations to the Design and Optimization of Inhibitors of Lipid Peroxidation and Associated Cell Death. *J. Am. Chem. Soc.* **2022**, *144* (32), 14706–14721.

2.7 Materials and Synthesis

General. Reagents and solvents were procured from commercial sources and were used without further purification unless otherwise indicated. 2,2,5,7,8-pentamethyl-6-chromanol (PMC), 2,6-di-*tert*-butyl-4-methoxyphenol (**2.6**) and 4-hydroxyanisole (**2.1**) were purchased from Sigma-Aldrich. **2.1** was recrystallized out of hexanes to afford colourless needles. 2.6-Dimethyl-4-methoxyphenol was prepared from 2,6-dimethylhydroquionone using a previously described procedure.[1] 2,6-Di-isopropylphenol was purchased from Oakwood Chemicals. 2,6-Diethylphenol was prepared from 2,6-diethylaniline using previously described method.[2] Solvents/substrates such as chlorobenzene, DMSO, THF, 1,4-dioxane, *m*-xylene and 1-hexadecene contained no stabilizers (e.g., BHT etc.) and were of the highest quality commercially available (ACS or HPLC grade). 1-Hexadecene was pass through silica and alumina-B before use in spectrophotometric experiments. L-α-phosphatidylcholine (Egg) was purchased from Avanti® as a powder, and the liposomes were prepared by means previously described.[3]

2,6-Diethylhydroquinone (2.4b). A 100-mL double neck round bottom flask was charged with glacial acetic acid (35 mL), concentrated sulfuric acid (0.4 mL) and 2,6-diethylphenol (3.89 g; 25.9 mmol). With mixing, 30% H_2O_2 (13 mL) was added by dropping funnel. While monitoring the temperature of the solution with an alcohol thermometer (affixed through side neck) the mixture was gradually heated to 50ºC (heat gun) after which the reaction was sufficiently exothermic to maintain its temperature. The reaction was kept between 55-65ºC for ~30 minutes after which the heat of the reaction subsided until cooling to room temperature. The reaction was poured into water and extracted with ethyl acetate three times. The combined organic extracts were rinsed three times with 1 M NaOH solution, and subsequently dried with $MgSO_4$, filtered, and concentrated under reduced pressure. The residue was dissolved into ether (40 mL) and transferred to a 250 mL round bottom flask charged with methanol (25 mL), water (90 mL), and sodium dithionite (13 g). The flask was sealed, evacuated, and backfilled with N_2 and left to stir overnight. The ether was then separated, and the aqueous phases was extracted with ether. The combined organic solutions were subsequently dried with $MgSO_4$, filtered, and concentrated under reduced pressure. The product was isolated by column chromatography (30% EtOAc in hexanes) and recrystallized out of hexanes affording 2,6-diethylhydroquinone as white needles (1.00 g, 23.2%); mp 90-92 ºC; ^{1}H NMR (400 MHz; DMSO-d_6): δ 8.49 (s, 1H), 7.32 (s, 1H), 6.32

(s, 2H), 2.48 (q, J = 7.5 Hz, 4H), 1.08 (t, J = 7.5 Hz, 6H); ^{13}H NMR (101 MHZ; DMSO-d_6): δ 150.2, 144.2, 131.93, 112.7, 23.0, 14.38; HRMS (EI, magnetic sector): calcd for $C_{10}H_{14}O_2$ 166.0994, found 166.1007.

2,6-Di-isopropylhydroquinone (2.5b). The same general procedure for the preparation of 2,6-diethylhydroquinone was used in the preparation of 2,6-di-isopropylhydroquinone from 2,6-di-isopropylphenol (6.04 g; 33.9 mmol). The product was isolated by column chromatography (30% EtOAc in hexanes) and recrystallized out of hexanes affording 2,6-di-isopropylhydroquinone as white leaflets (1.34 g, 20.4%); mp 94-96 ºC; ^{1}H NMR (400 MHz; DMSO-d_6): δ 8.49 (s, 1H), 7.26 (s, 1H), 6.37 (s, 2H), 3.23 (sept., J = 6.9 Hz, 2H), 1.10 (d, J = 6.9 Hz, 12H); ^{13}C NMR (101 MHz; DMSO-d_6): δ 150.7, 142.75, 136.9, 109.4, 26.2, 23.0; HRMS (EI, magnetic sector): calcd for $C_{12}H_{18}O_2$ 194.1307, found 194.1297.

2,6-Diethyl-4-methoxyphenol (2.4). Methanol (15 mL) and 2,6-diethylhydroquionone (0.95 g; 5.7 mmol) were placed in a 100-mL round bottom flask equipped with a stir bar and reflux condenser. Carefully, 4.5 mL of concentrated sulfuric acid was added and the reaction mixture was heated to reflux for ~4 hours. Once cooled the reaction mixture was poured into water followed by extraction with ether (three times). The combined organic extracts were dried with $MgSO_4$, filtered, and concentrated under reduced pressure. The product was isolated by column chromatography (10% EtOAc in hexanes). Two recrystallizations out of hexanes (minimum of hexanes at room temperature, followed by chilling on dry ice resulted in rapid crystallization) afforded the 2,6-diethyl-4-methoxyphenol as white needles (0.39 g, 38%); mp 34-36 ºC; ^{1}H NMR (400 MHz; DMSO-d_6): δ 7.58 (s, 1H), 6.49 (s, 2H), 3.65 (s, 3H), 2.54 (q, J = 7.5 Hz, 4H), 1.10 (t, J = 7.5 Hz, 6H). ^{13}C NMR (101 MHz; DMSO-d_6): δ 152.5, 145.6, 132.0, 111.6, 55.1, 23.2, 14.4; HRMS (EI, magnetic sector): calcd for $C_{11}H_{16}O_2$ 180.1150, found 180.1141.

2,6-Di-isopropyl-4-methoxyphenol (2.5). Methanol (20 mL) and 2,6-di-isopropylhydroquionone (1.25 g; 6.4 mmol) were placed in a 100-mL round bottom flask equipped with a stir bar and reflux condenser. Carefully, 6 mL of concentrated sulfuric acid was added and the reaction mixture was heated to reflux for ~4 hours. Once cooled the reaction mixture was poured into water followed by extraction with ether (three times). The combined organic extracts were dried with $MgSO_4$, filtered, and concentrated under reduced pressure. The

product was isolated by column chromatography (10% EtOAc in hexanes). After drying under vacuum, the residue was chilled (-20 ºC) affording 2,6-di-isopropyl-4-methoxyphenol as a beige crystalline solid (1.06 g, 79.5%); mp 48-50 ºC; ^{1}H NMR (400 MHz; DMSO-d_6): δ 7.53 (s, 1H), 6.51 (s, 2H), 3.66 (s, 3H), 3.28 (sept, *J* = 6.9 Hz, 2H), 1.13 (d, *J* = 6.9 Hz, 12H); ^{13}C NMR (101 MHz; DMSO-d_6): δ 153.0, 144.2, 136.9, 108.3, 55.0, 26.4, 22.9. HRMS (EI, magnetic sector): calcd for $C_{13}H_{20}O_2$ 208.1463, found 208.1487.

2.8 Methods and Supplementary Data

Inhibited Co-autoxidation of PBD-BODIPY and 1,4-Dioxane. Into a 3 mL quartz cuvette were added 620 µL 1,4-dioxane (ACS grade) to either 1.80 mL of PhCl or 1.18 mL of PhCl with 620 µL of DMSO (ACS grade). The cuvette was placed in the sample holder of a UV−visible spectrophotometer and equilibrated to 37 °C. PBD-BODIPY (12.5 µL of a 2.0 mM solution in 1,2,4-trichlorobenzene), 50 µL AIBN solution (0.3 M in PhCl) followed by 10 µL of RTA solution (0.5 mM or desired concentration.) The contents were thoroughly mixed and the loss of PBD-BODIPY absorbance was monitored at 587 nm (without DMSO ε = 123 000 M^{-1} cm^{-1}, with DMSO ε = 118 200 M^{-1} cm^{-1}.) In parallel with the compounds of interest, an uninhibited experiment (no RTA) and one with a known concentration of PMC (2-6 µM) were recorded (the latter being used to calculate the rate of initiation assuming the n = 2 for PMC.) The rate constants of inhibition ($k_{inh}^{dioxane}$ or k_{inh}^{DMSO}), radical trapping stoichiometries (n) and associated standard deviations were ascertained from a minimum of three experimental replicates.

The same standard procedure is used for the other organic substrate systems (1-hexadecene/PhCl, *m*-xylene and THF). The differences are summarized in Table 2.3.

Table 2.3. Key parameters for substrates used in PBD-BODIPY co-autoxidations.

Substrate	β_2^H	$k_{PBD\text{-}BODIPY}$ ($M^{-1}s^{-1}$)	λ_{max} (nm)	ε (cm^{-1})
Hexadecene/PhCl (4:1)[4]	0.09	3790	588	148700
m-Xylene	(0.17)[5]	2426	590	124877
1,4-Dioxane/PhCl (1:3)[6]	0.35	5310	587	123000
THF	(0.51)[5]	3324	583	118510
Dioxane/PhCl/DMSO (1:2:1)[6]	0.60	5900	587	118200

Inhibited Co-autoxidation of STY-BODIPY in Egg-PC Liposomes (Absorbance). Into a 3 mL quartz cuvette were combined 2.34 mL of 10 mM PBS (pH 7.4) and 125 μL of a suspension of egg-PC unilamellar liposomes (100 nm; 20 mM in the same PBS.) The cuvette was placed in the sample holder of a UV−visible spectrophotometer and equilibrated to 37 °C. STY-BODIPY (12.5 μL of a 2.0 mM solution in DMSO), 10 μL MeOAMVN solution (0.05 M in MeCN) followed by 10 μL of RTA solution (0.5 mM or desired concentration.) The contents were thoroughly mixed and the loss of STY-BODIPY absorbance was monitored at 565 nm (ε = 123 676 M^{-1} cm^{-1}.) In parallel with the compounds of interest, an uninhibited experiment (no RTA) and one with a known concentration of PMC (2-6 μM) were recorded (the latter being used to calculate the rate of initiation assuming the n = 2 for PMC.) The rate constants of inhibition (k_{inh}^{lip}), radical trapping stoichiometries (n) and associated standard deviations were ascertained from a minimum of three experimental replicates.

(See Chapter 3 supplemental for 96-well fluorescence protocol i.e. FENIX).

Standardization of *m*-Xylene/PBD-BODIPY Co-Autoxidation Assay

For a more detailed breakdown of the standardization methodology, see our first paper on the subject.[7]

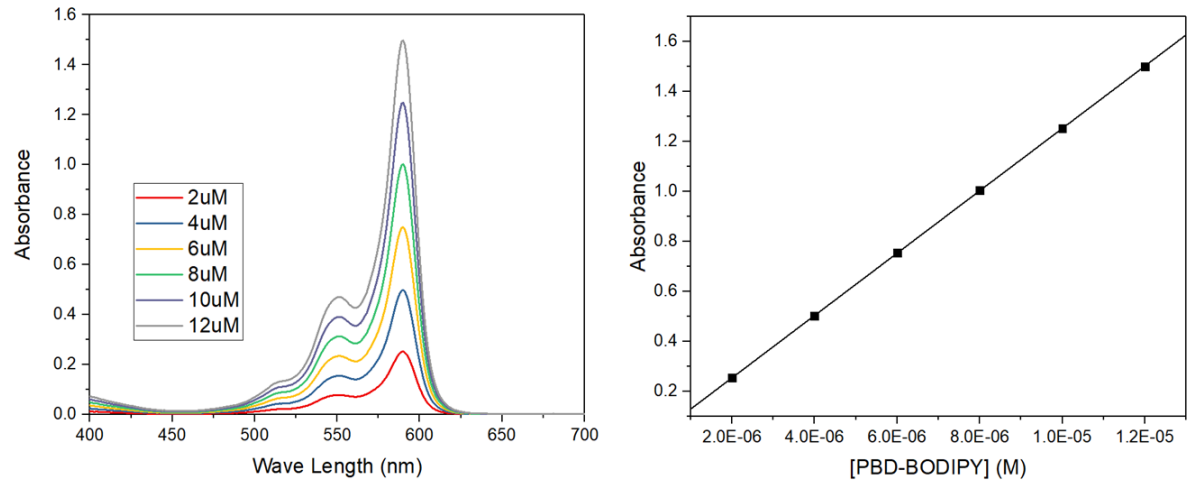


Figure 2.6. Uv-Vis spectra for 2-12 µM PBD-BODIPY (Left) and extinction coefficient for PBD-BODIPY in *m*-xylene, λ_{max} = 590 nm, ε = 124877 M^{-1} cm^{-1}. Average of three measurements.

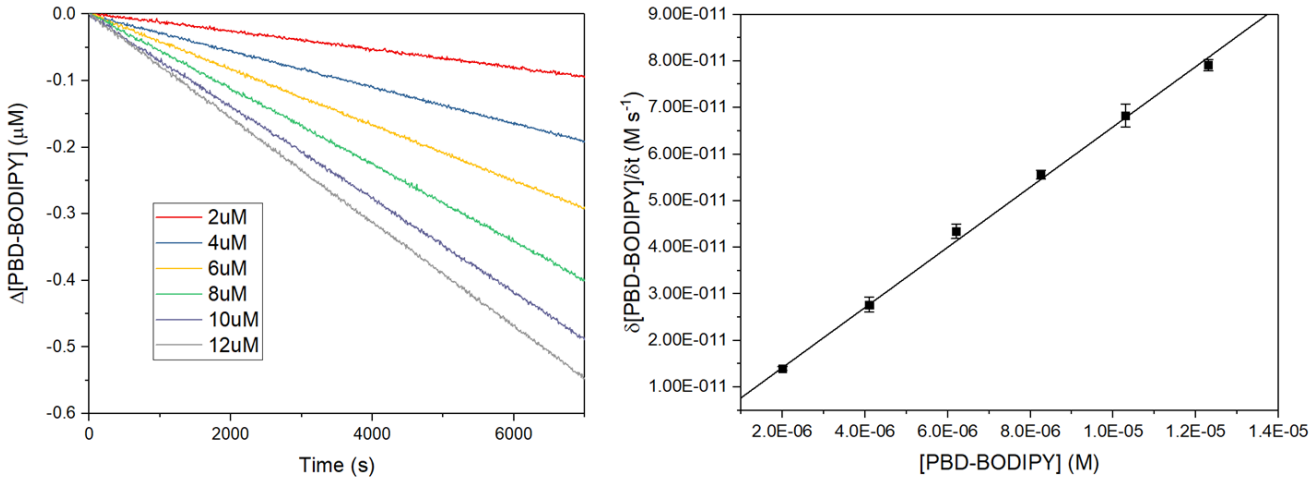


Figure 2.7. Rate of PBD-BODIPY consumption as a function of concentration in *m*-xylene initiated by AIBN (6 mM). Reaction progress was monitored by absorbance at 590 nm (124877 M^{-1} cm^{-1}). The $\boldsymbol{k_{PBD-BODIPY}}$ was calculated to be 2426 M^{-1} s^{-1} assuming $2\boldsymbol{k_t}$ is equivalent to the peroxyl of *m*-xylene (3×10^8 M^{-1} s^{-1})[8] and Ri is 2.1×10^{-9} M s^{-1} (see Figure 2.7).

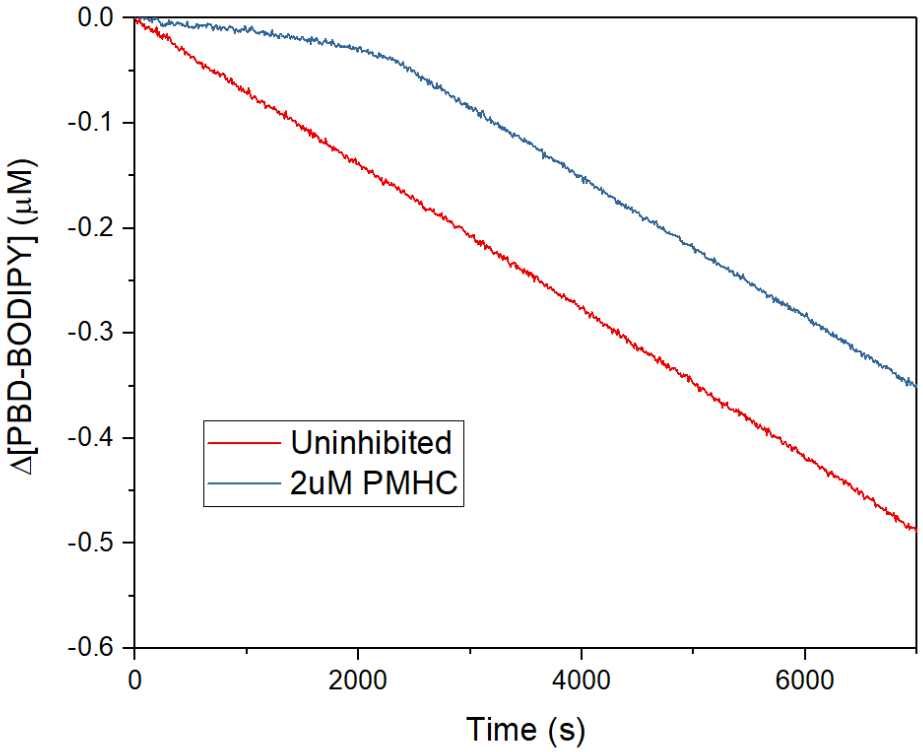


Figure 2.8. Co-autoxidation of PBD-BODIPY (10 μM) in *m*-xylene at 37ºC initiated with AIBN (6 mM). Reaction progress was monitored by absorbance at 590 nm (124877 M^{-1} cm^{-1}). *Ri* (2.1 ± 0.1 × 10^{-9} M s^{-1}) was determined from the t_{inh} of PMC (2 μM) assuming n = 2.

Standardization of THF/PBD-BODIPY Co-Autoxidation Assay.

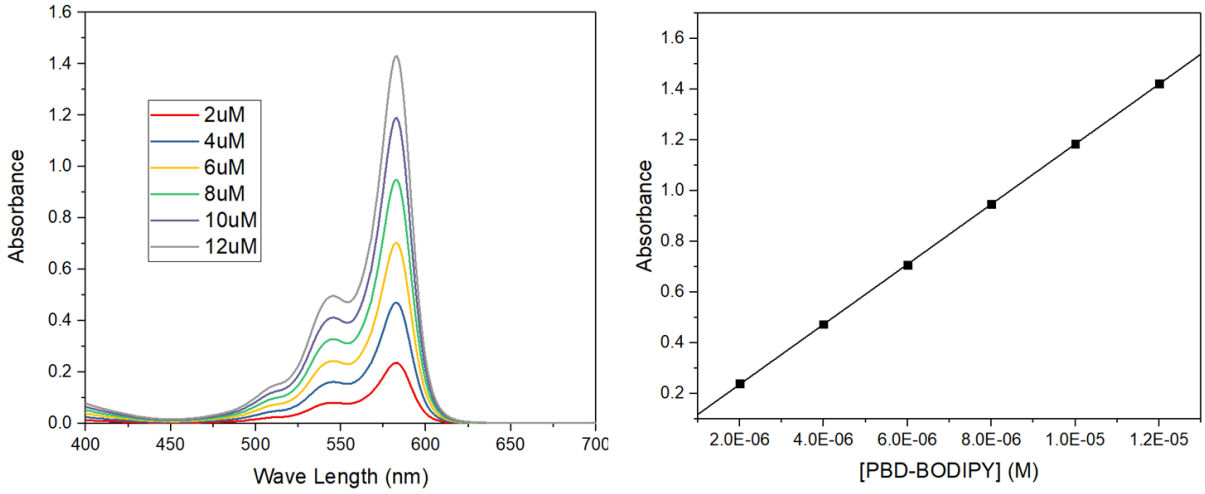


Figure 2.9. Uv-Vis spectra for 2-12 µM PBD-BODIPY (Left) and extinction coefficient for PBD-BODIPY in THF, λ_{max} = 583 nm, ε = 118510 M^{-1} cm^{-1}. Average of three measurements.

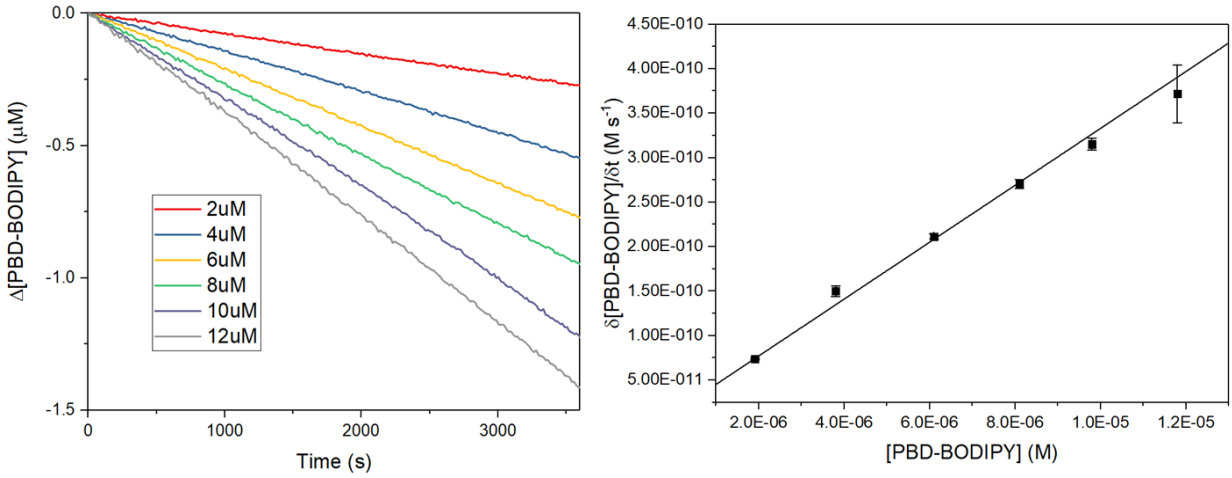


Figure 2.10. Rate of PBD-BODIPY consumption as a function of concentration in THF initiated by AIBN (6 mM). Reaction progress was monitored by absorbance at 583 nm (118510 M^{-1} cm^{-1}). The $\boldsymbol{k_{PBD-BODIPY}}$ was calculated to be 3324 M^{-1} s^{-1} assuming $2\boldsymbol{k_t}$ is equivalent to the peroxyl of THF (3.1×10^7 M^{-1} s^{-1})[9] and R_i is 2.4×10^{-9} M s^{-1} (see Figure 2.11).

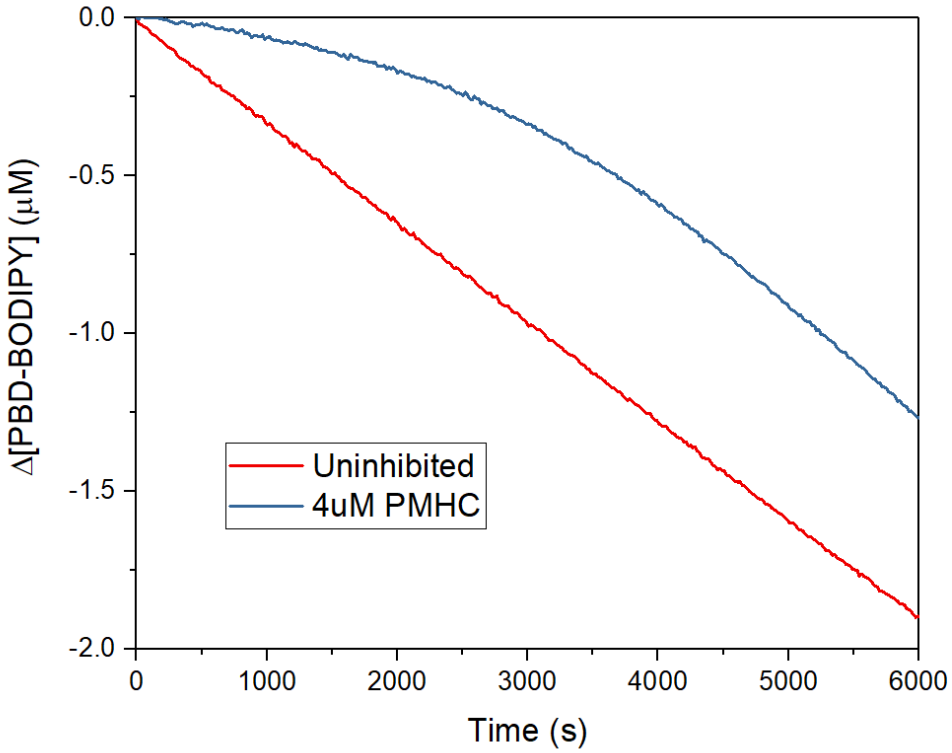


Figure 2.11. Co-autoxidation of PBD-BODIPY (10 μM) in THF at 37°C initiated with AIBN (6 mM). Reaction progress was monitored by absorbance at 583 nm (118510 M^{-1} cm^{-1}). *Ri* (2.4 ± 0.2 × 10^{-9} M s^{-1}) was determined from the t_{inh} of PMC (4 μM) assuming n = 2.

Inhibited Co-autoxidation Data

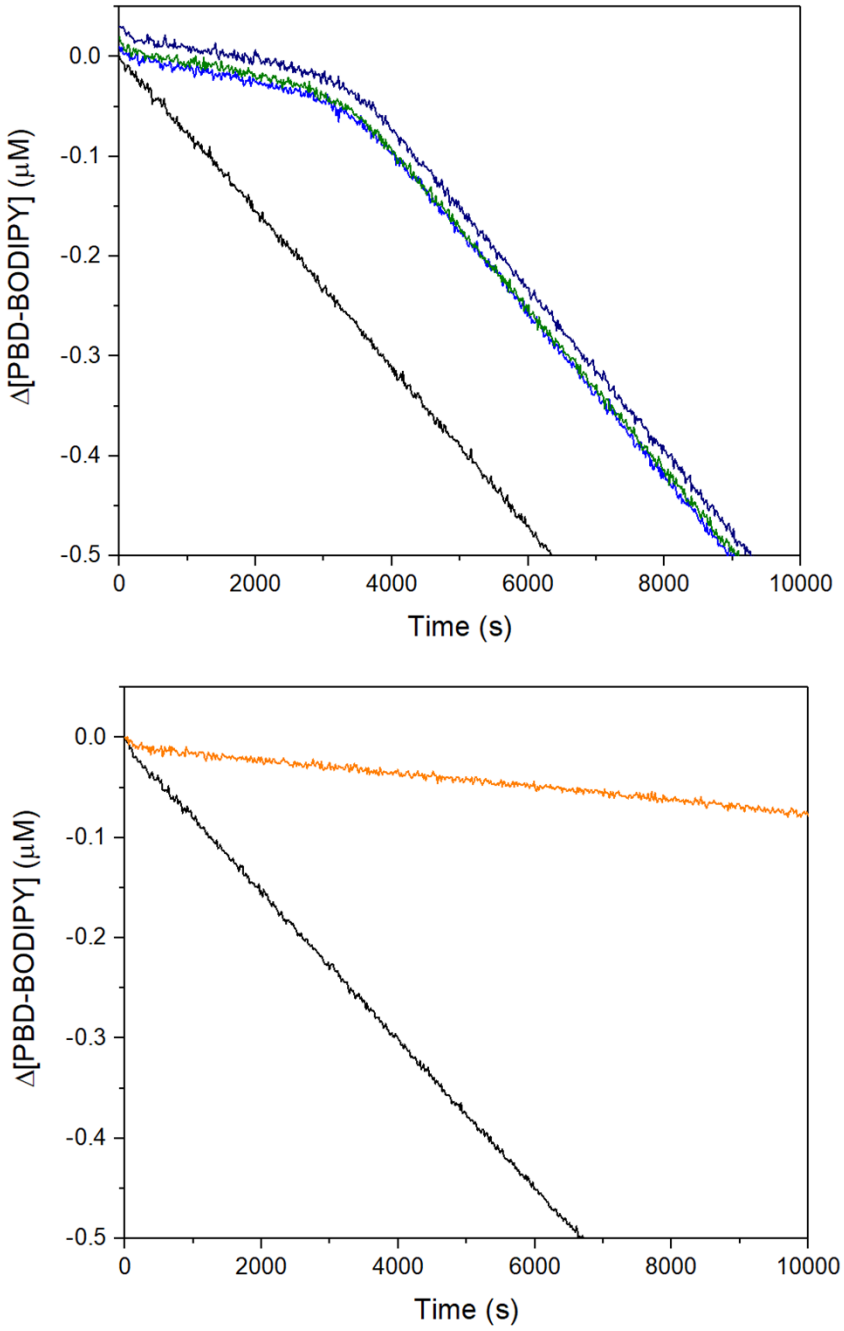


Figure 2.12. Co-autoxidation of PBD-BODIPY (10 μM) in 2.9 M hexadecene in chlorobenezene at 37ºC initiated with AIBN (8 mM). Reaction progress was monitored by absorbance at 588 nm (139163 M^{-1} cm^{-1}). *Ri* (1.2 ± 0.1 × 10^{-9} M s^{-1}). **(TOP)** Uninhibited (black); 2 μM **2.2** (blue); 2 μM **2.4** (green); 2 μM **2.5** (navy); **(BOTTOM)** 10 μM **2.1** (orange).

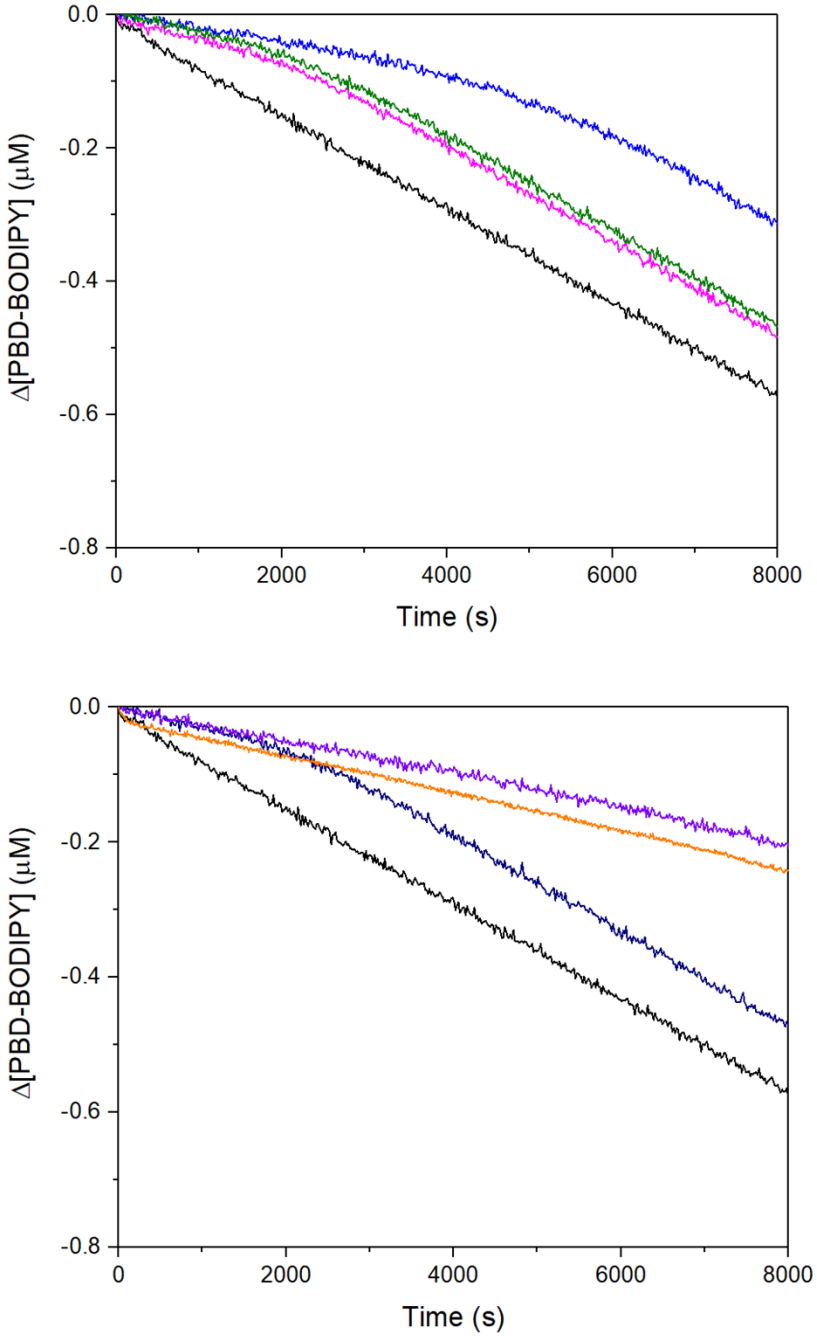


Figure 2.13. Co-autoxidation of PBD-BODIPY (10 μM) in *m*-xylene at 37°C initiated with AIBN (6 mM). Reaction progress was monitored by absorbance at 590 nm (124877 M^{-1} cm^{-1}). *Ri* (2.1 ± 0.1 × 10^{-9} M s^{-1}). **(TOP)** Uninhibited (black); 4 μM **2.2** (blue); 2 μM **2.3** (magenta); 2 μM **2.4** (green); **(BOTTOM)** 2 μM **2.5** (navy); 10 μM **2.6** (purple); 12 μM **2.1** (orange).

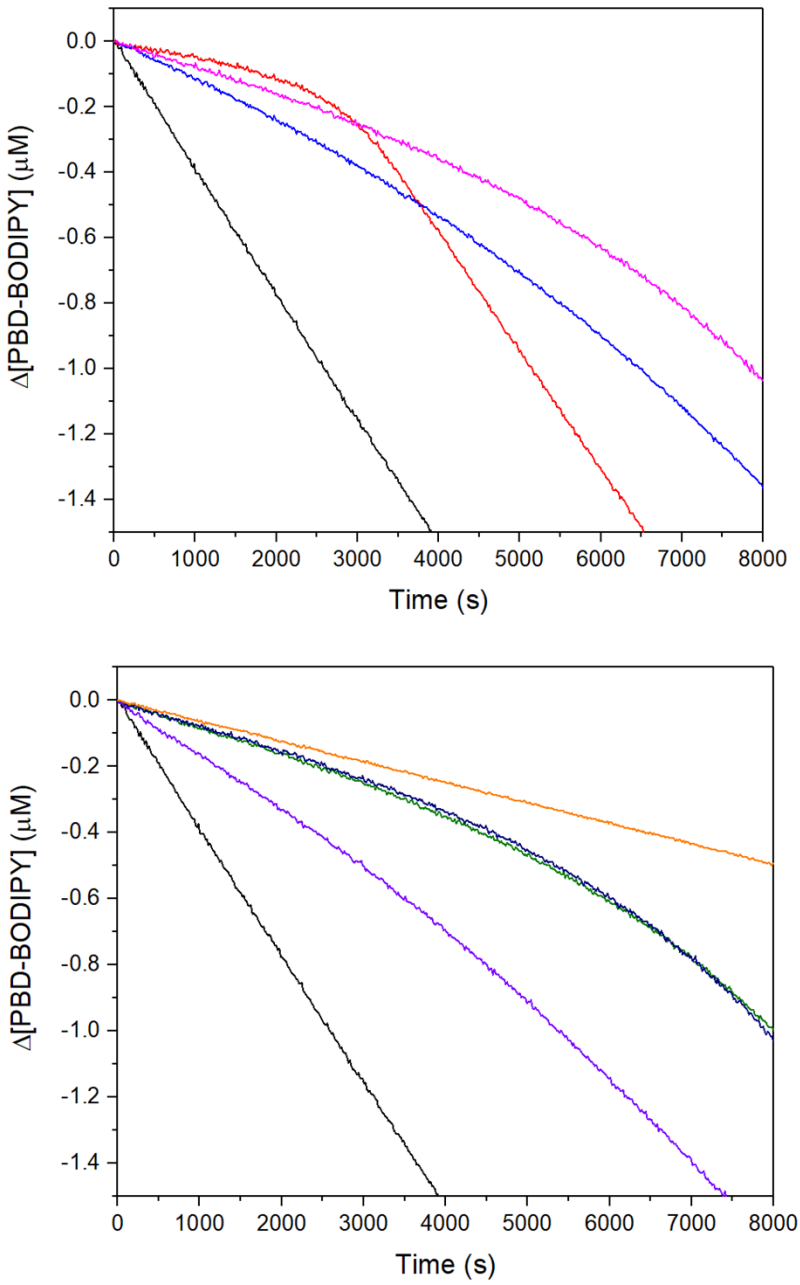


Figure 2.14. Co-autoxidation of PBD-BODIPY (10 μM) in 2.9 M 1,4-dioxane in chlorobenzene at 37ºC initiated with AIBN (6 mM). Reaction progress was monitored by absorbance at 587 nm (123023 M^{-1} cm^{-1}). *Ri* (3.1 ± 0.1 × 10^{-9} M s^{-1}). **(TOP)** Uninhibited (black); 4 μM PMC (red); 10 μM **2.2** (blue); 10 μM **2.3** (magenta); **(BOTTOM)** 10 μM **2.4** (green); 10 μM **2.5** (navy); 10 μM **2.6** (Purple); 100 μM **2.1** (orange).

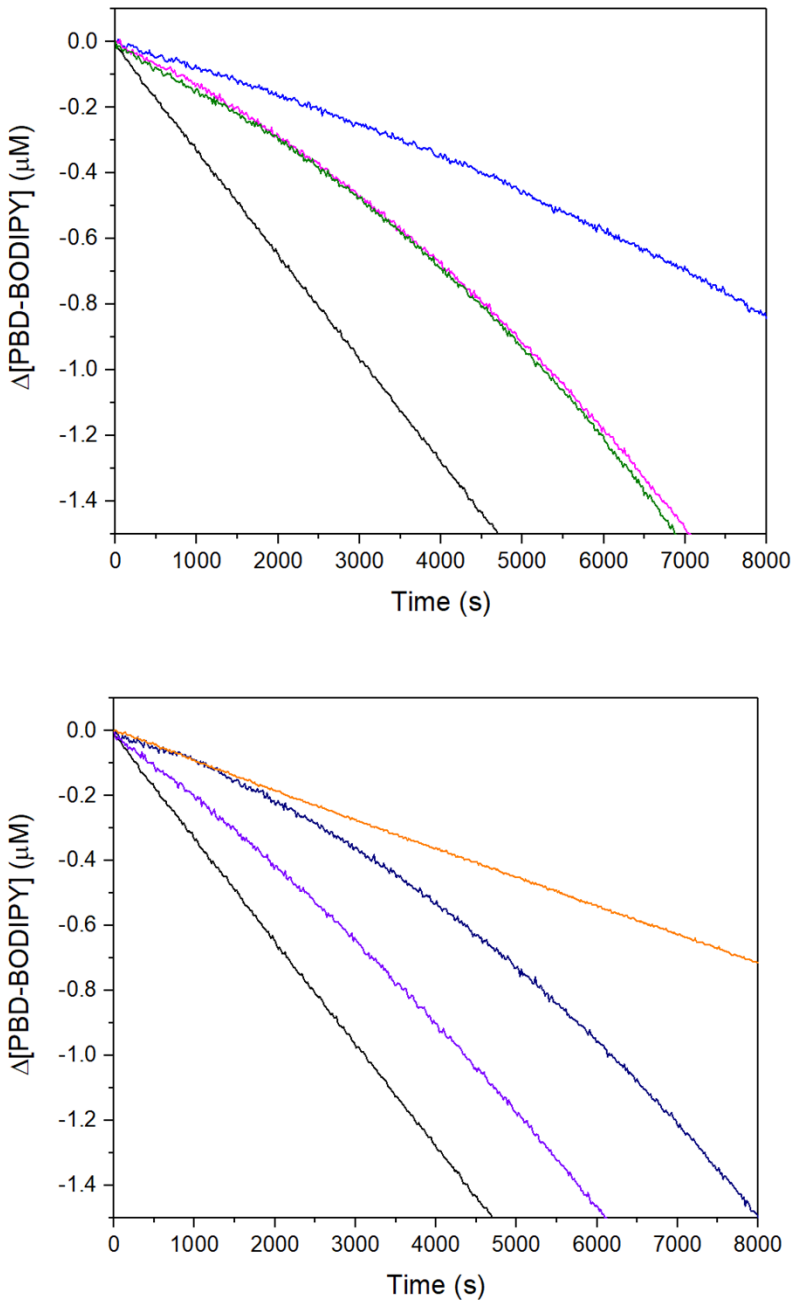


Figure 2.15. Co-autoxidation of PBD-BODIPY (10 μM) in THF at 37°C initiated with AIBN (6 mM). Reaction progress was monitored by absorbance at 583 nm (118510 M^{-1} cm^{-1}). *Ri* (2.4 ± 0.2 × 10^{-9} M s^{-1}). **(TOP)** Uninhibited (black); 30 μM **2.2** (blue); 8 μM **2.3** (magenta); 8 μM **2.4** (green); **(BOTTOM)** 8 μM **2.5** (navy); 8 μM **2.6** (purple); 100 μM **2.1** (orange).

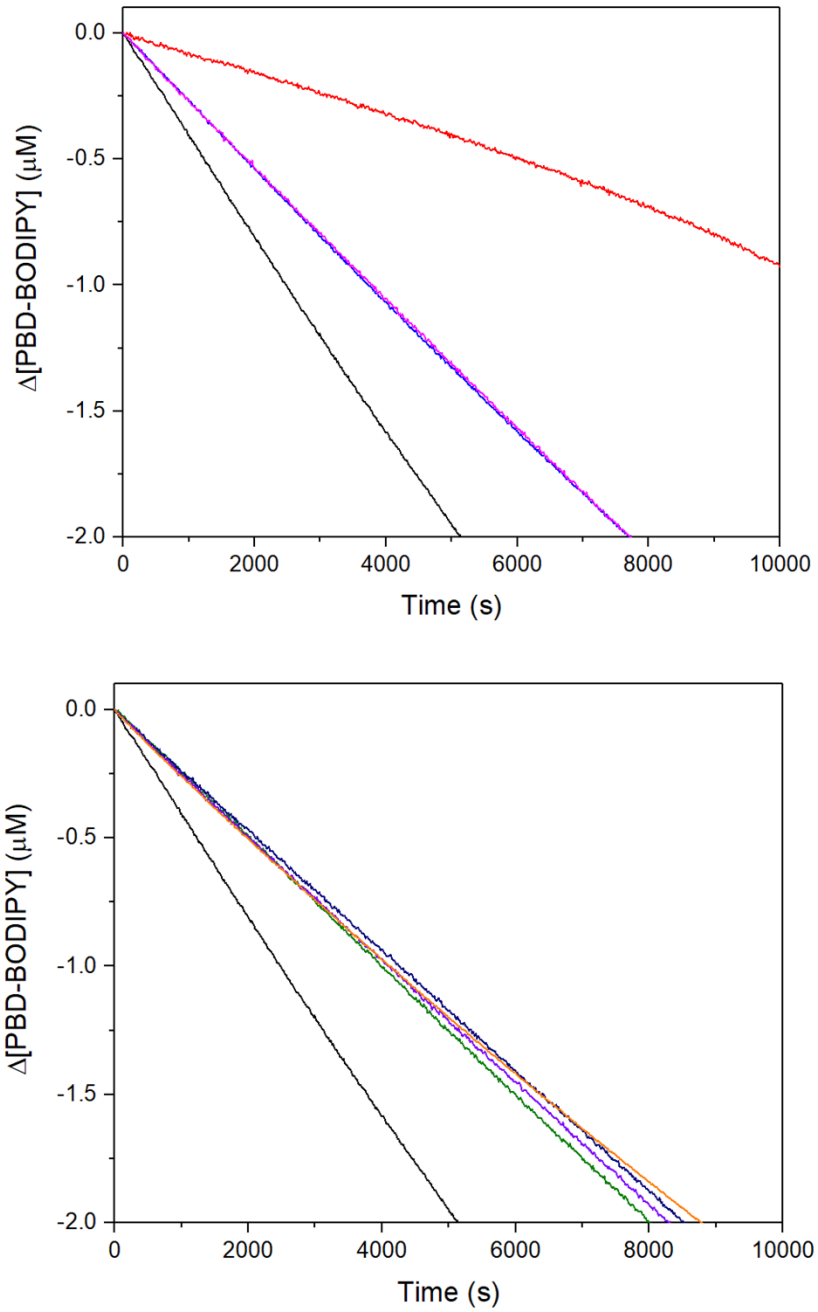
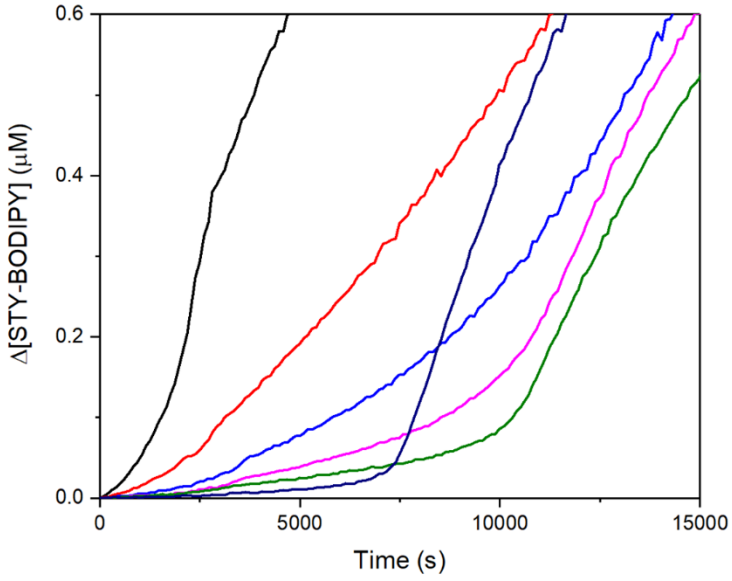


Figure 2.16. Co-autoxidation of PBD-BODIPY (10 μM) in 2.9 M 1,4-dioxane in a 1:1 mixture of DMSO and chlorobenzene at 37°C initiated with AIBN (6 mM). Reaction progress was monitored by absorbance at 587 nm (118217 M^{-1} cm^{-1}). *Ri* (3.1 ± 0.1 × 10^{-9} M s^{-1}). **(TOP)** Uninhibited (black); 20 μM PMC (red); 50 μM **2.2** (blue); 20 μM **2.3** (magenta); **(BOTTOM)** 20 μM **2.4** (green); 20 μM **2.5** (navy); 20 μM **2.6** (purple); 400 μM **2.1** (orange).



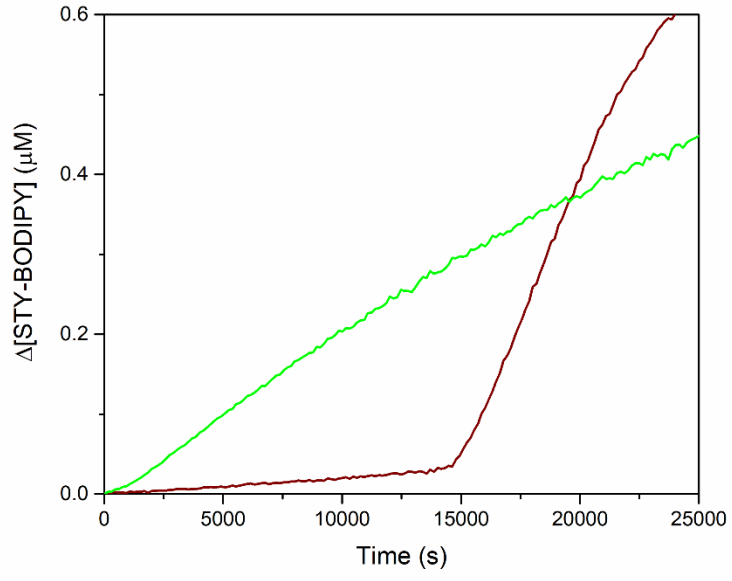


Figure 2.17. DTUN initiated co-autoxidations (0.2 mM) of STY-BODIPY (1 μM; k_{BODIPY} = 894 M^{-1} s^{-1}) in egg PC liposomes (1 mM) monitored by fluorescence ($\lambda_{ex}/\lambda_{em}$ = 488/518 nm). **(TOP)** Uninhibited (black); 4 μM **2.2** (red); 4 μM **2.3** (blue); 4 μM **2.4** (magenta); 4 μM **2.5** (dark green); 4 μM **2.6** (navy); **(BOTTOM)** 4 μM PMC (wine); 100 μM **2.1** (light green).

For a tutorial for calculating k_{inh}, see supplemental of Chapter 3.

Table 2.4. Summary of the inhibition rate constants.

	PhCl (β_2^H = 0.09) [$M^{-1}s^{-1}$]	*m*-Xylene (β_2^H = 0.17) [$M^{-1}s^{-1}$]	Dioxane/PhCl (β_2^H = 0.35) [$M^{-1}s^{-1}$]	THF (β_2^H = 0.51) [$M^{-1}s^{-1}$]	Dioxane/DMSO (β_2^H = 0.60) [$M^{-1}s^{-1}$]	Liposomes (DTUN) [$M^{-1}s^{-1}$]
2.1	$2.6 \pm 0.2 \times 10^5$	$8.1 \pm 0.1 \times 10^4$	$1.3 \pm 0.1 \times 10^4$	$4.1 \pm 0.3 \times 10^3$	$1.1 \pm 0.2 \times 10^3$	$1.1 \pm 0.1 \times 10^2$
2.2	$7.9 \pm 0.7 \times 10^5$	$3.3 \pm 0.3 \times 10^5$	$7.1 \pm 0.1 \times 10^4$	$1.7 \pm 0.1 \times 10^4$	$6.6 \pm 0.3 \times 10^3$	$1.6 \pm 0.2 \times 10^3$
2.3	(9.4×10^5)[a]	$4.6 \pm 0.3 \times 10^5$	$1.1 \pm 0.1 \times 10^5$	$3.8 \pm 0.3 \times 10^4$	$1.7 \pm 0.1 \times 10^4$	$3.3 \pm 0.3 \times 10^3$
2.4	$9.1 \pm 0.7 \times 10^5$	$4.4 \pm 0.1 \times 10^5$	$1.1 \pm 0.1 \times 10^5$	$3.9 \pm 0.2 \times 10^4$	$1.7 \pm 0.1 \times 10^4$	$8.9 \pm 1.2 \times 10^3$
2.5	$9.3 \pm 0.8 \pm 10^5$	$4.6 \pm 0.2 \times 10^5$	$1.2 \pm 0.2 \times 10^5$	$4.2 \pm 0.4 \times 10^4$	$1.9 \pm 0.1 \times 10^4$	$1.6 \pm 0.1 \times 10^4$
2.6	(1.1×10^5)[a]	$1.0 \pm 0.1 \times 10^5$	$5.2 \pm 0.3 \times 10^4$	$2.5 \pm 0.1 \times 10^4$	$1.8 \pm 0.1 \times 10^4$	$4.3 \pm 0.3 \times 10^4$
PMC	(3.2×10^6)[b]	$1.3 \pm 0.2 \times 10^6$	$3.9 \pm 0.4 \times 10^5$	$1.4 \pm 0.2 \times 10^5$	$6.1 \pm 0.8 \times 10^4$	$2.9 \pm 0.2 \times 10^4$

[a] From Burton et al.[10] [b] From Valgimigli et al.[11]

Determination of α_2^H by Kinetic Solvent Effect

Utilizing the Ingold-Abraham relationship (Eq. 2.8) in the form of Eq. 2.9, α_2^H is determined as the intercept of Eq. 2.10:

$$log k_{inh}^{0} = log k_{inh}^{S} + 8.3\alpha_2^H\beta_2^H \quad (2.8)$$

$$log k_{inh}^{PhCl} + 8.3\alpha_2^H\beta_2^{H(PhCl)} = log k_{inh}^{S} + 8.3\alpha_2^H\beta_2^{H(S)} \quad (2.9)$$

$$\frac{log k_{inh}^{PhCl}}{8.3(\beta_2^{H(S)} - \beta_2^{H(PhCl)})} = \frac{log k_{inh}^{S}}{8.3(\beta_2^{H(S)} - \beta_2^{H(PhCl)})} + \alpha_2^H \quad (2.10)$$

The rate constant measured in PhCl (k_{inh}^{PhCl}; β_2^H = 0.09) is compared to k_{inh}^{S} of at least 3 solvent systems in order to determine the apparent α_2^H based on the magnitude of the KSE: *m*-xylene (k_{inh}^{Xyl}; β_2^H = 0.17); 1:3 1,4-dioxane/PhCl (k_{inh}^{Diox}; β_2^H = 0.35); THF (k_{inh}^{THF}; β_2^H = 0.51); 1:1:2 1,4-dioxane/DMSO/PhCl (k_{inh}^{DMSO}; β_2^H = 0.60).

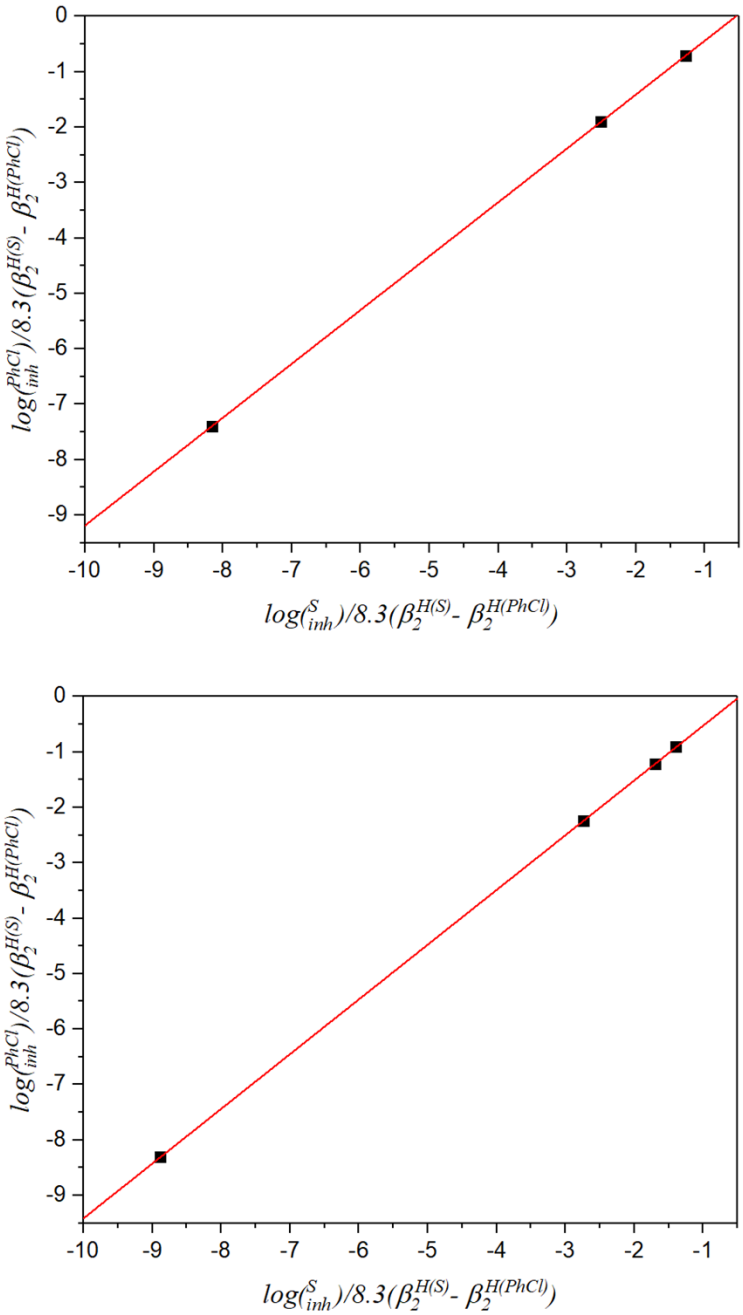


Figure 2.18. **(TOP)** Linear regression of Eq. 2.10 for **2.1:** $\boldsymbol{y = 0.972x + 0.532}$; R^2 = 1.000; $\boldsymbol{(\alpha_2^H = 0.53)}$. **(BOTTOM)** For **2.2:** $\boldsymbol{y = 0.987x + 0.460}$; R^2 = 1.000; $\boldsymbol{(\alpha_2^H = 0.46)}$.

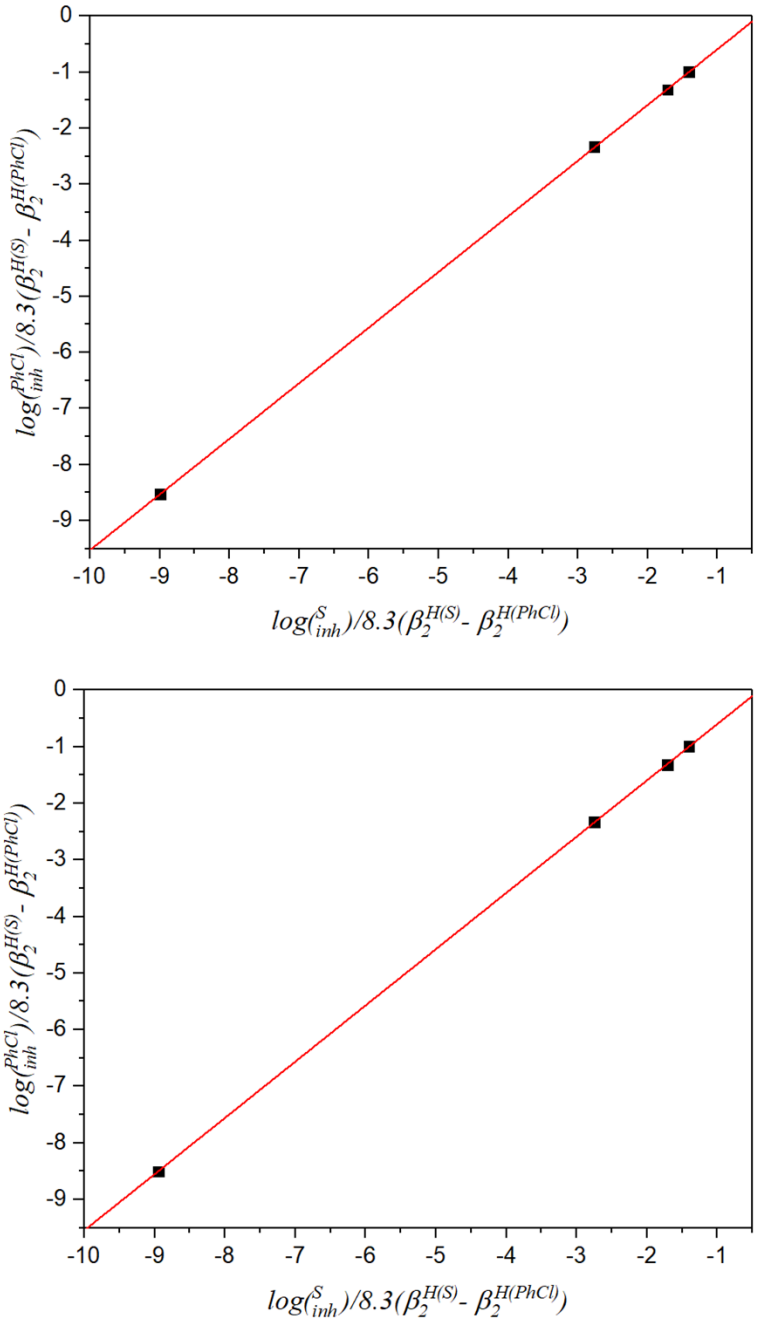


Figure 2.19. (TOP) Linear regression of Eq. 2.10 for **2.3**: $\boldsymbol{y = 0.993x + 0.400}$; R^2 = 1.000; $(\boldsymbol{\alpha_2^H = 0.40})$. **(BOTTOM)** For **2.4**: $\boldsymbol{y = 0.994x + 0.393}$; R^2 = 1.000; $(\boldsymbol{\alpha_2^H = 0.39})$.

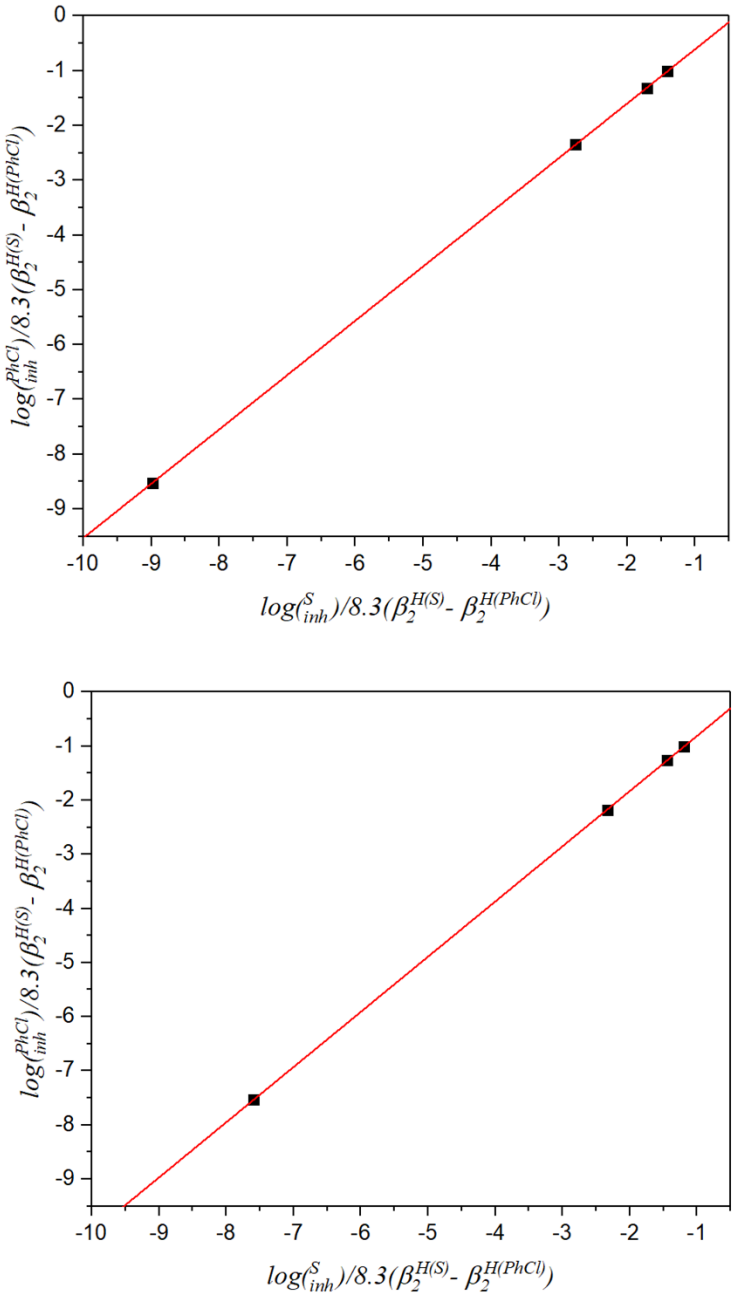


Figure 2.20. (TOP) Linear regression of Eq. 2.10 for **2.5**: $\boldsymbol{y = 0.991x + 0.383}$; R^2 = 1.000; $(\boldsymbol{\alpha_2^H = 0.38})$. **(BOTTOM)** For **2.6**: $\boldsymbol{y = 1.020x + 0.207}$; R^2 = 1.000; $(\boldsymbol{\alpha_2^H = 0.21})$.

Determination of α_2^H by ^{1}H NMR

Functional groups which engage significantly as hydrogen bond donors (having measurable α_2^H values) demonstrate substantially lower-field chemical shifts in a strongly hydrogen bonding solvent (DMSO-d6) compared to a weakly hydrogen bonding solvent ($CDCl_3$ or benzene-d6). The correlation between α_2^H values and the $\Delta\delta$ of DMSO-d_6 and $CDCl_3$ was described by Abraham et al. to afford the empirical relationship Eq. 2.11.[12] In a previous work we utilized benzene-d_6 instead of $CDCl_3$ (due to an incompatibility between $CDCl_3$ and several of our phenoxazines/phenothiazines)[6] which afforded a similar correlation rendering Eq. 2.12.

$$\alpha_2^H = 0.133\Delta\delta_{DMSO-CDCl3} + 0.0066 \qquad (2.11)$$

$$\alpha_2^H = 0.134\Delta\delta_{DMSO-Ben} - 0.1087 \qquad (2.12)$$

Table 2.5. Summary of α_2^H values determined by ^{1}H NMR and by kinetic solvent effect.

	δBenzene-d_6 (ppm)	**δDMSO-d_6 (ppm)**	**$\Delta\delta_{DMSO-Ben}$ (ppm)**	**Calculated α_2^H (^{1}H NMR)**	**Calculated α_2^H (KSE)**
2.1	3.64	8.87	5.23	0.59	0.53
2.2	3.65	8.57	4.92	0.55	0.46
2.3	3.74	7.67	3.93	0.42	0.40
2.4	3.81	7.58	3.77	0.40	0.39
2.5	3.96	7.53	3.57	0.37	0.38
2.6	4.53	6.53	2.00	0.16	0.21

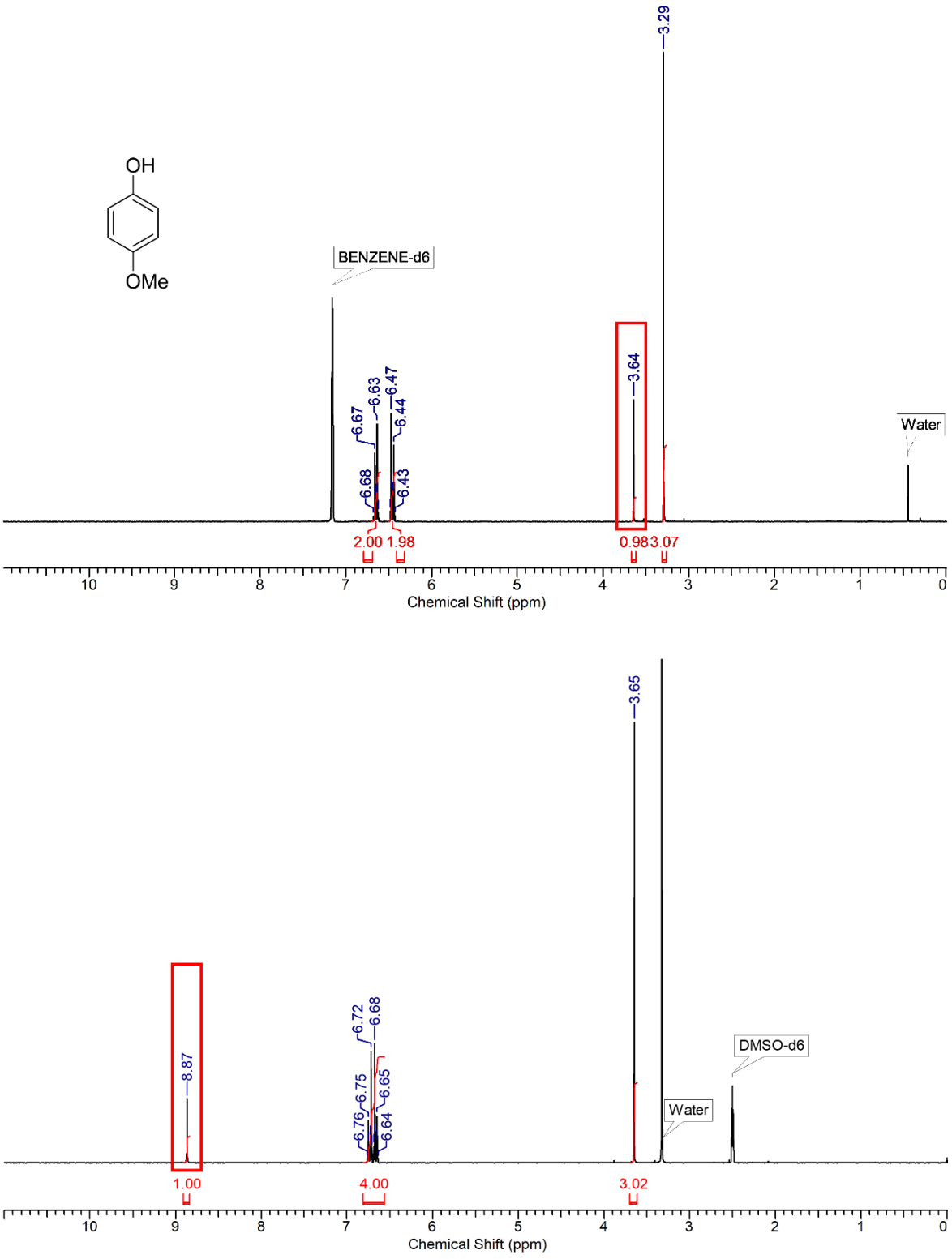


Figure 2.21. ^{1}H NMR of **2.1** in benzene-d_6 (top) and DMSO-d_6 (bottom). The phenolic O-H is highlighted.

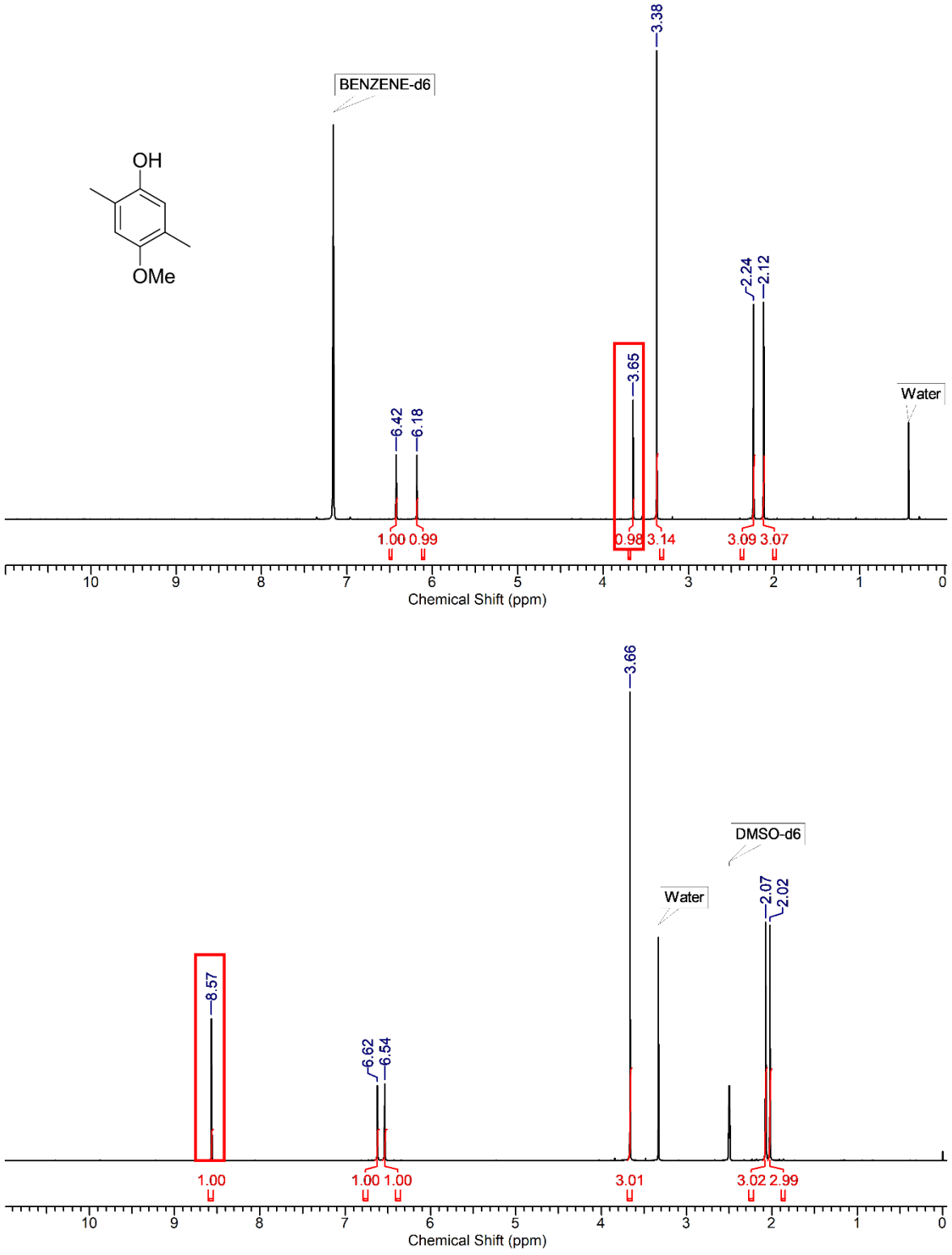


Figure 2.22. ^{1}H NMR of **2.2** in benzene-d_6 (top) and DMSO-d_6 (bottom). The phenolic O-H is highlighted.

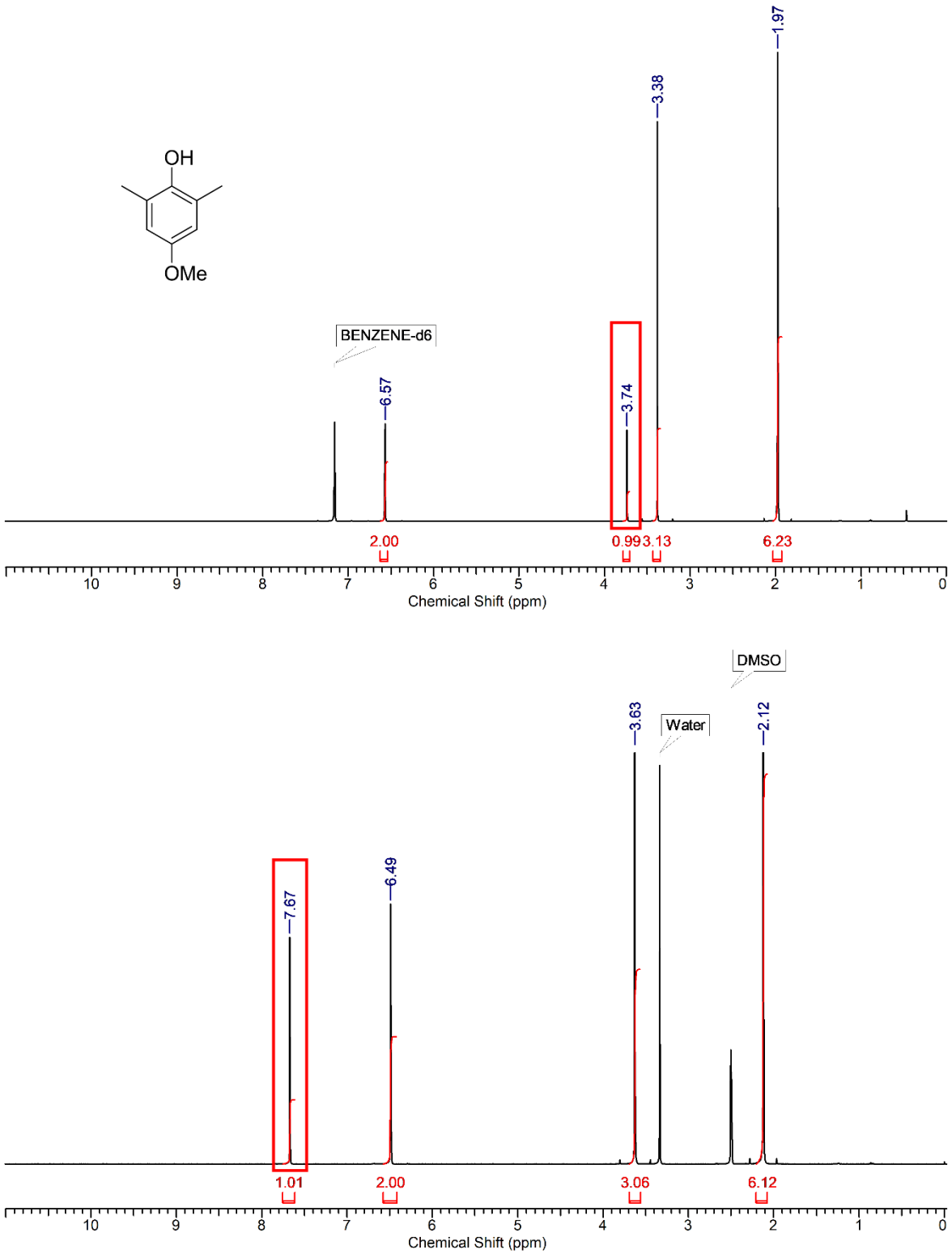


Figure 2.23. ^{1}H NMR of **2.3** in benzene-d_6 (top) and DMSO-d_6 (bottom). The phenolic O-H is highlighted.

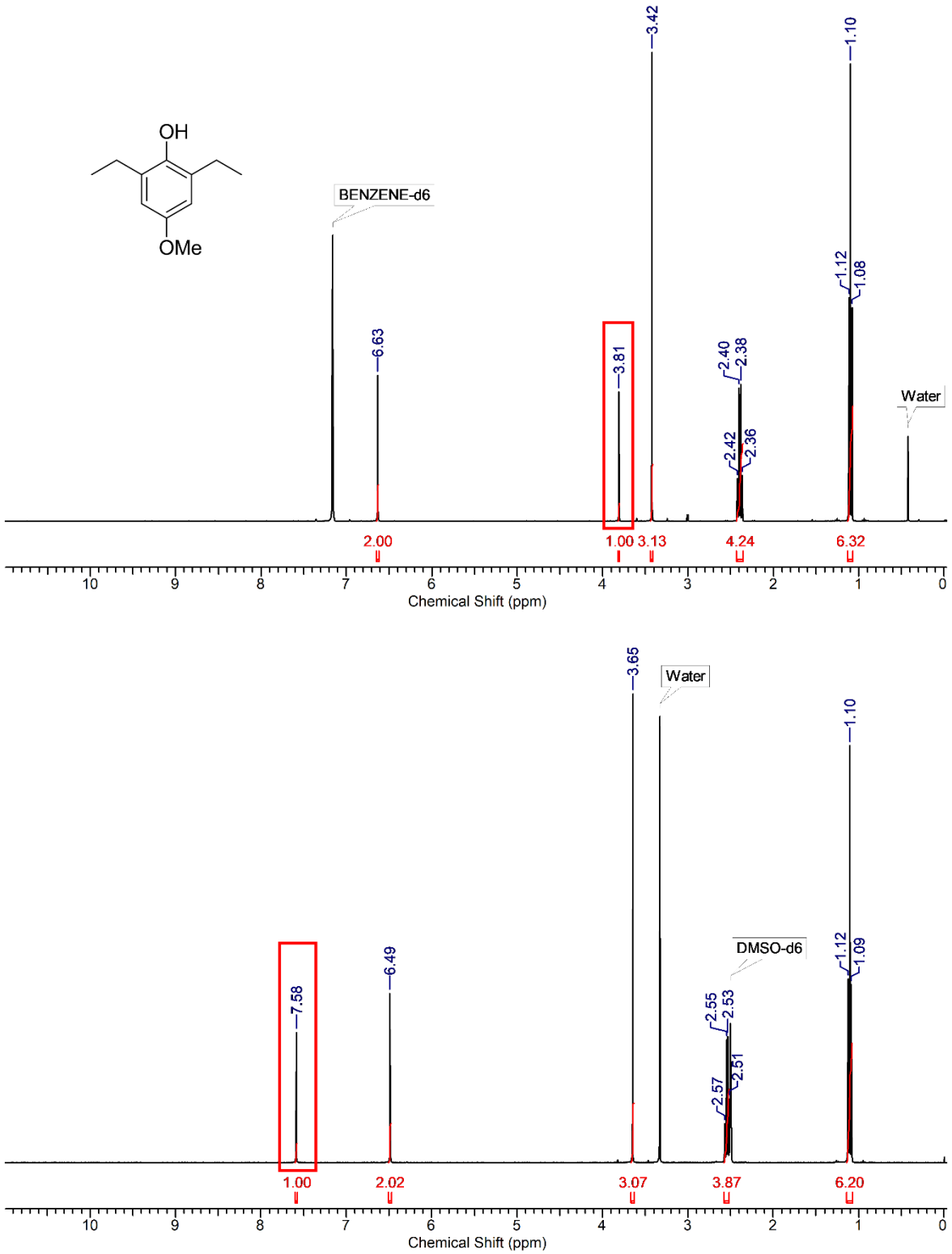


Figure 2.24. ^{1}H NMR of **2.4** in benzene-d_6 (top) and DMSO-d_6 (bottom). The phenolic O-H is highlighted.

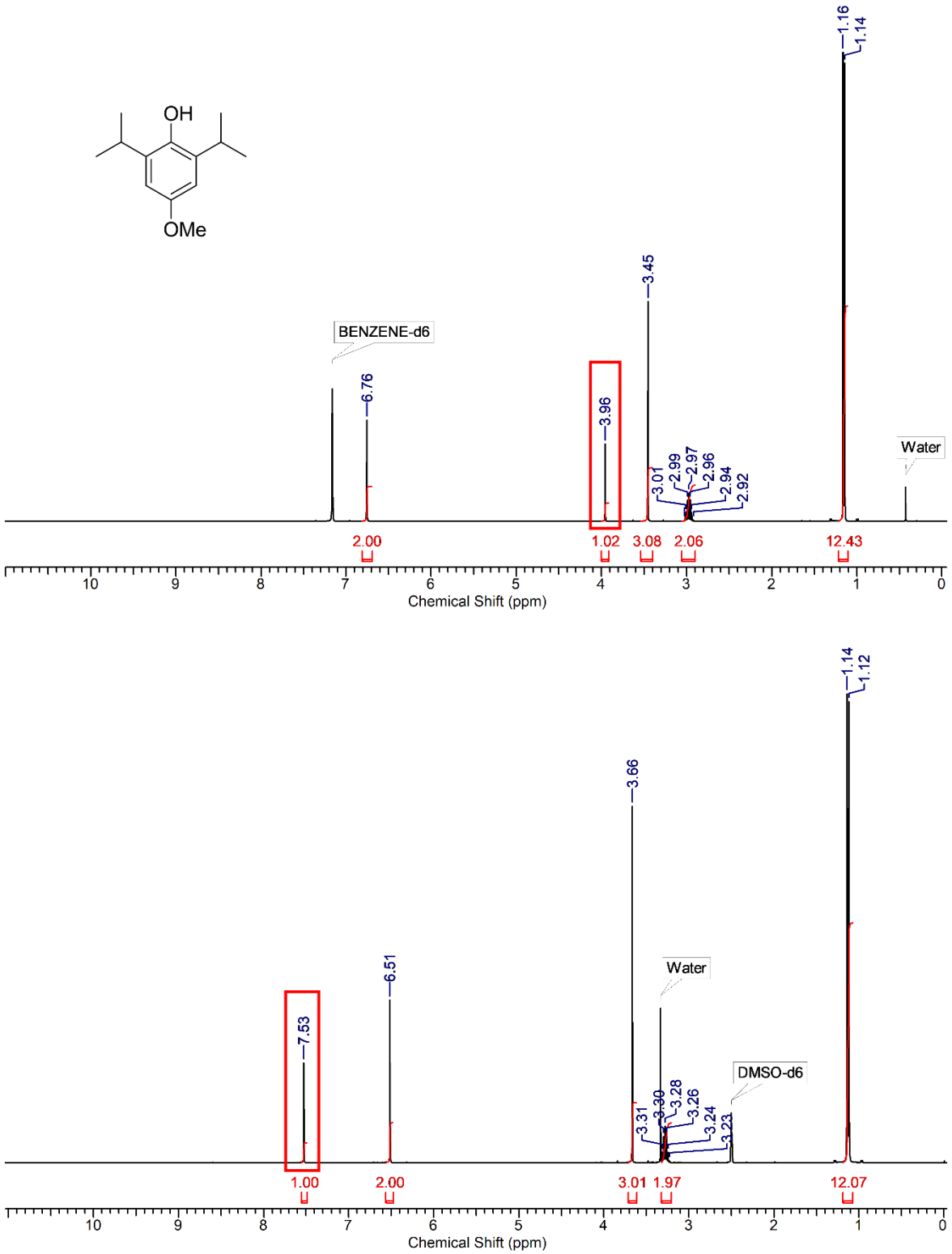


Figure 2.25. ^{1}H NMR of **2.5** in benzene-d_6 (top) and DMSO-d_6 (bottom). The phenolic O-H is highlighted.

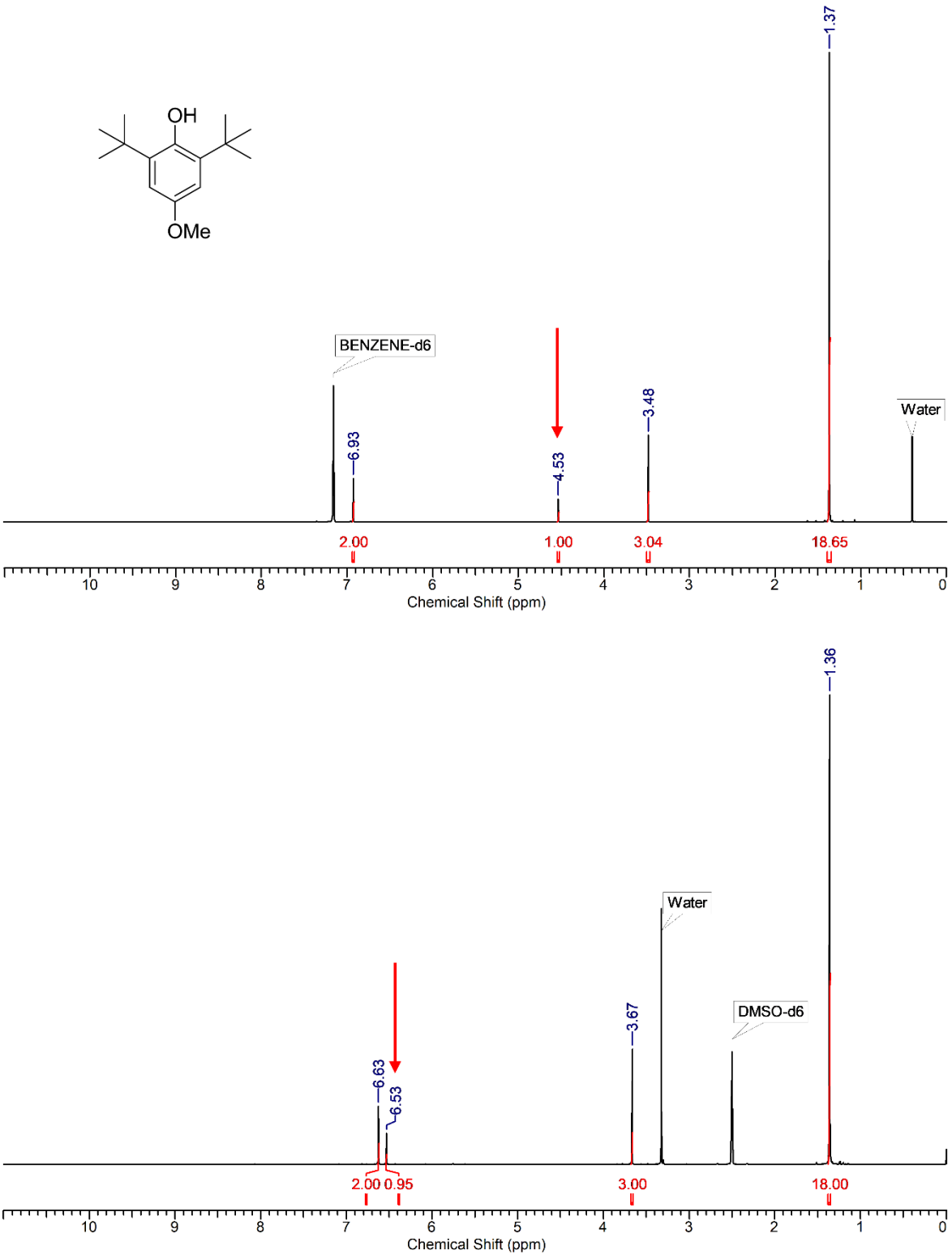


Figure 2.26. ^{1}H NMR of **2.6** in benzene-d_6 (top) and DMSO-d_6 (bottom). The phenolic O-H is highlighted.

Determination of β_2^H for PLPC by ^{19}F NMR

The H-bond accepting solute (PLPC) was diluted in CCl_4 to render five dilute solutions of differing concentrations and one 0.20 M solution. To these were added 4-fluorophenol and 4-fluoroanisole for a final concentration of 0.01 M of each. The solutions were transferred into NMR tubes containing seal capillaries of benzene-d_6 with α,α,α-trifluorotoluene, after which their ^{19}F spectra were recorded with a Bruker Avance II 300 equipped with a thermostat (sample kept at 37°C). The 1:1 H-bond formation constant (K_f) of 4-fluorophenol and the H-bond acceptor(s) can be determined with by Eq. 2.13 as described by Taft and co-workers:[13]

$$K_f = \frac{\left(\frac{\delta}{\Delta}\right)A_0}{\left\{A_0\left[1-\left(\frac{\delta}{\Delta}\right)\right]\right\}\left[B_0-\left(\frac{\delta}{\Delta}\right)A_0\right]} \qquad (2.13)$$

Where A_0 is the concentration of 4-fluorophenol, B_0 is the concentration of the H-bond acceptor (PLPC), Δ is the difference in chemical shift between 4-fluorophenol and 4-fluoroanisole sufficient to saturate H-bonding with 4-fluorophenol (maximum δ, [PLPC] = 0.20 M), and δ is the observed difference in chemical shift between 4-fluorophenol and 4-fluoroanisole at the corresponding B_0 and A_0. The β_2^H can be calculated from the measured K_f using Eq. 2.14.[5]

$$\beta_2^H = (logK_f + 1.1)/4.636 \qquad (2.14)$$

Table 2.6. Summary of K_f and β_2^H measurements of PLPC by ^{19}F NMR.

B_0 [PLPC] (M)	Chemical Shift α,α,α-trifluorotoluene (ppm)	Chemical Shift 4-Fluoroanisole (ppm)	Chemical Shift 4-Fluorophenol (ppm)	Normalized δ (ppm)	K_f	β_2^H
0	-62.60	-123.23	-123.20	-	-	-
0.005	-62.60	-123.24	-124.60	1.36	524	0.79 ± 0.02
0.010	-62.60	-123.24	-125.39	2.15	385	
0.015	-62.60	-123.24	-125.83	2.59	346	
0.020	-62.60	-123.24	-126.10	2.86	341	
0.030	-62.60	-123.25	-126.25	3.14	353	
0.200	-62.60	-123.33	-126.89	3.56	-	-

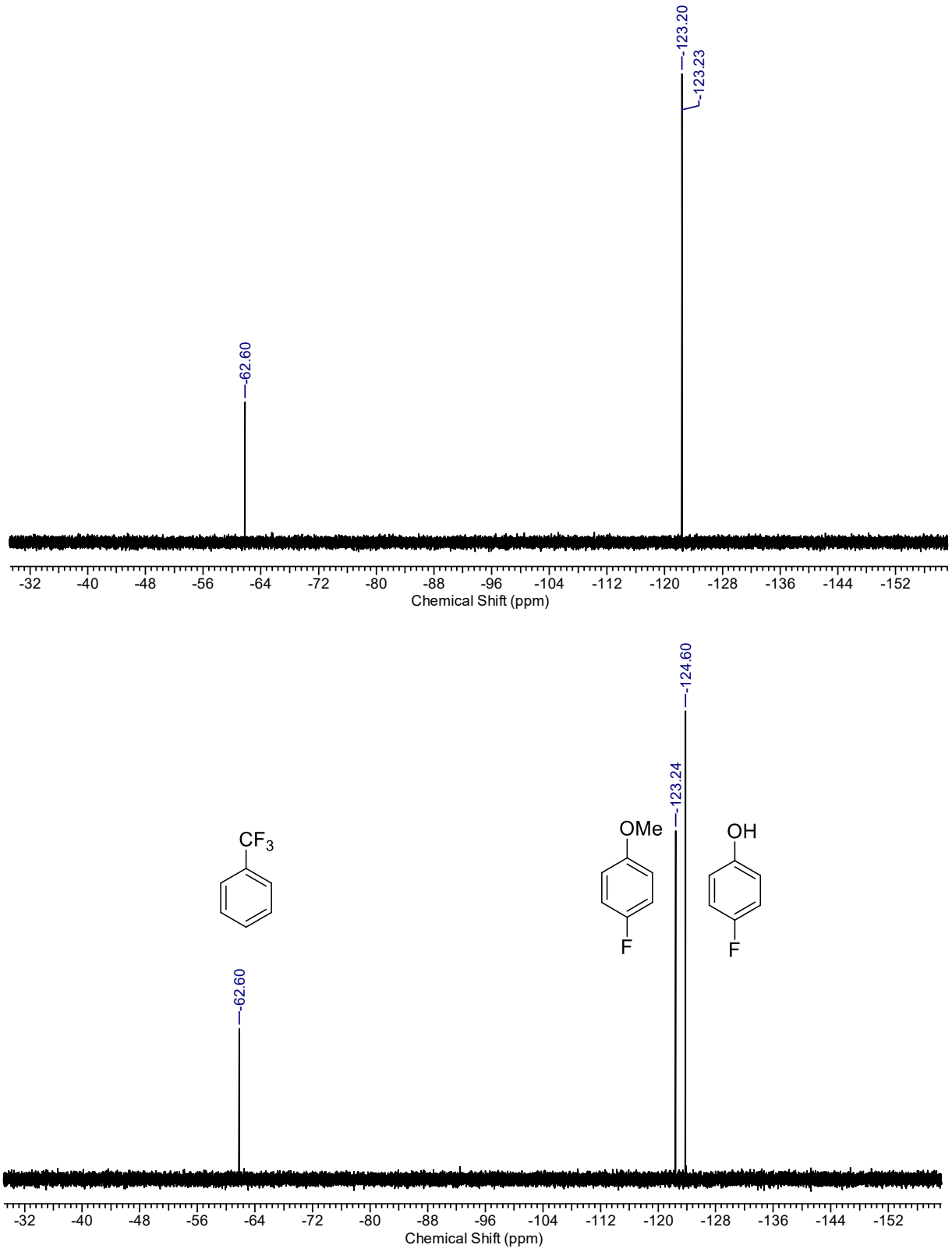


Figure 2.27. ^{19}F NMR of 4-fluorophenol (0.01 M) and 4-fluoroanisole (0.01 M) in CCl_4 in the absence of PLPC (top) and at 0.005 M PLPC (bottom).

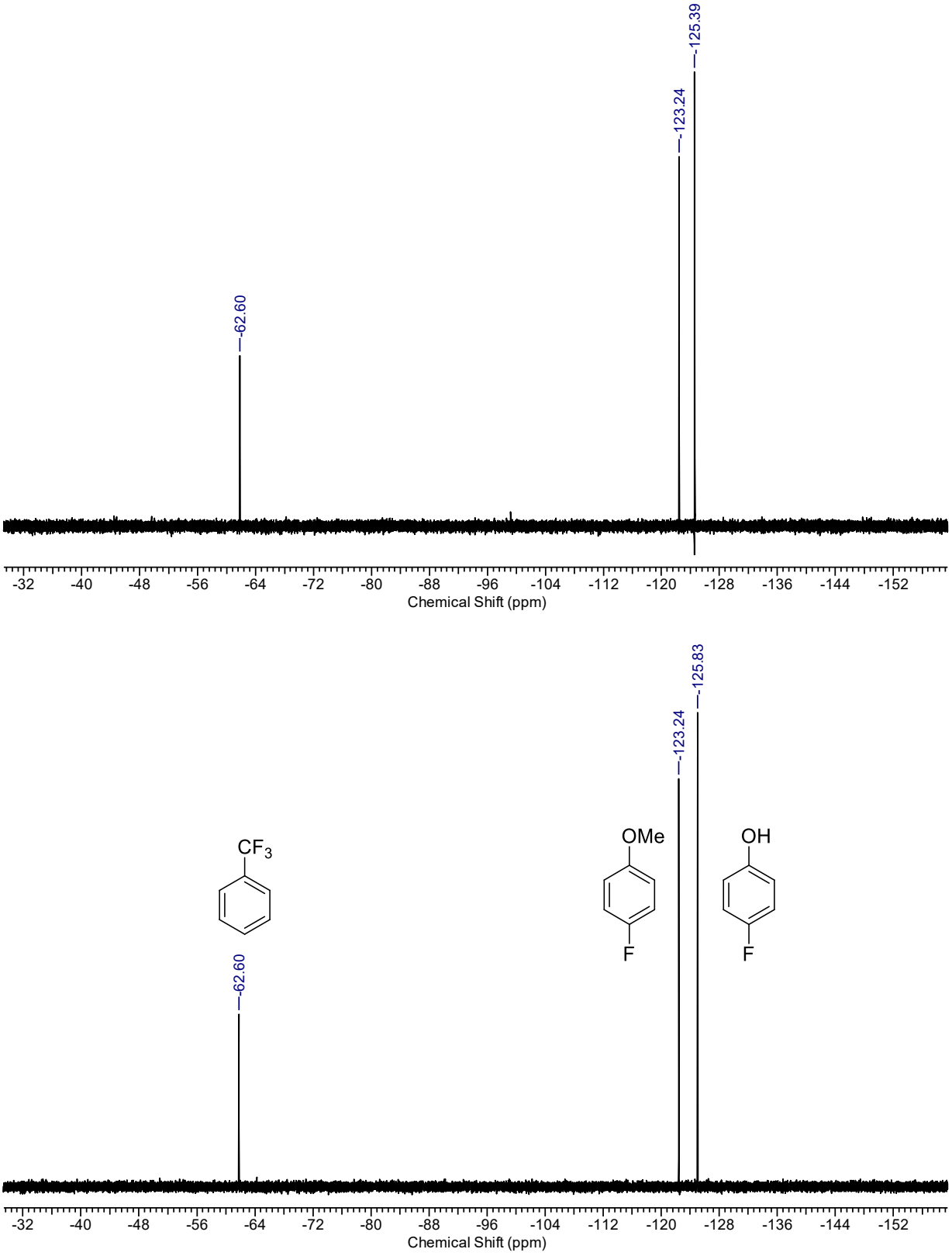


Figure 2.28. ^{19}F NMR of 4-fluorophenol (0.01 M) and 4-fluoroanisole (0.01 M) in CCl_4 with 0.010 M (top) and 0.015 M PLPC (bottom).

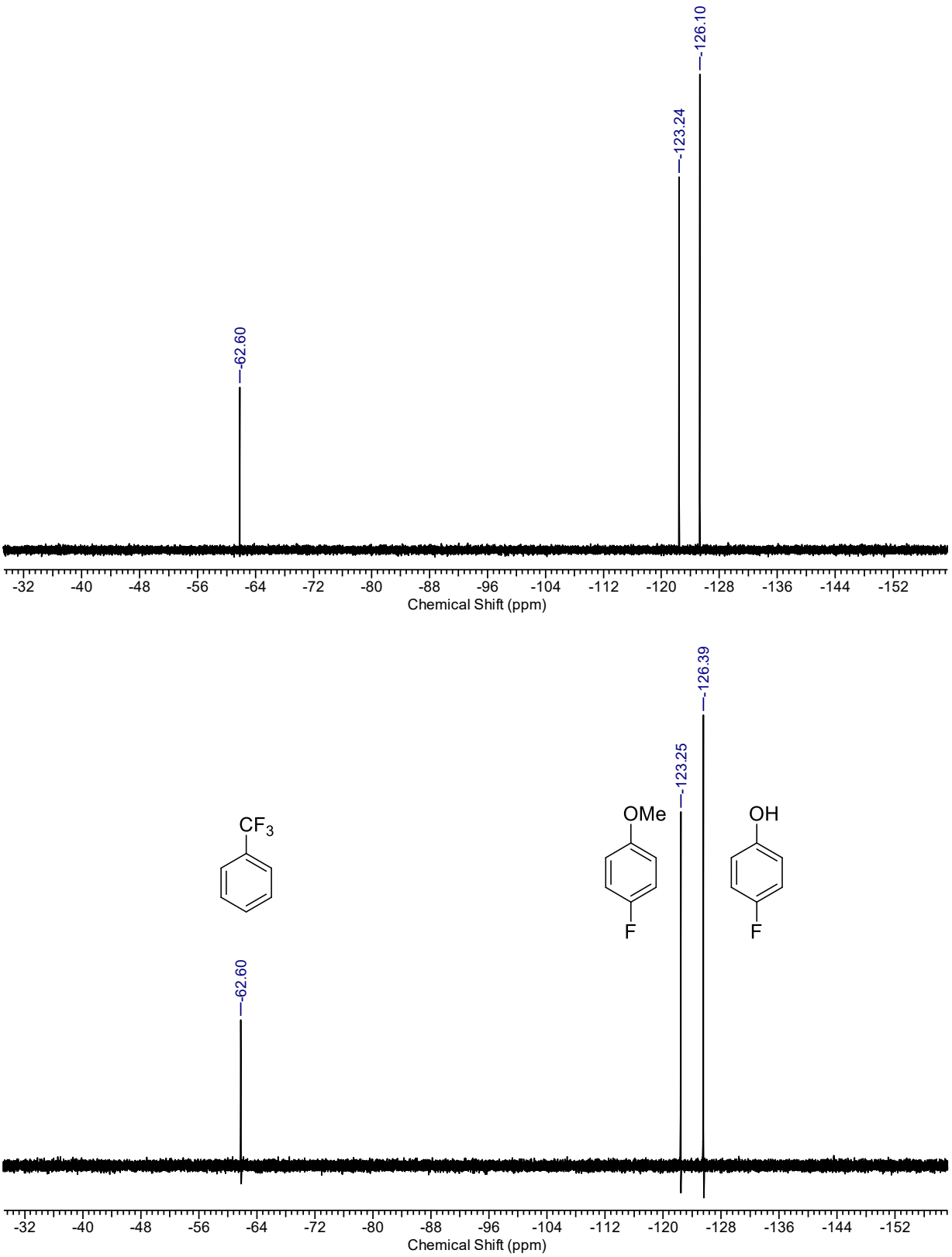


Figure 2.29. ^{19}F NMR of 4-fluorophenol (0.01 M) and 4-fluoroanisole (0.01 M) in CCl_4 with 0.020 M (top) and 0.030 M PLPC (bottom).

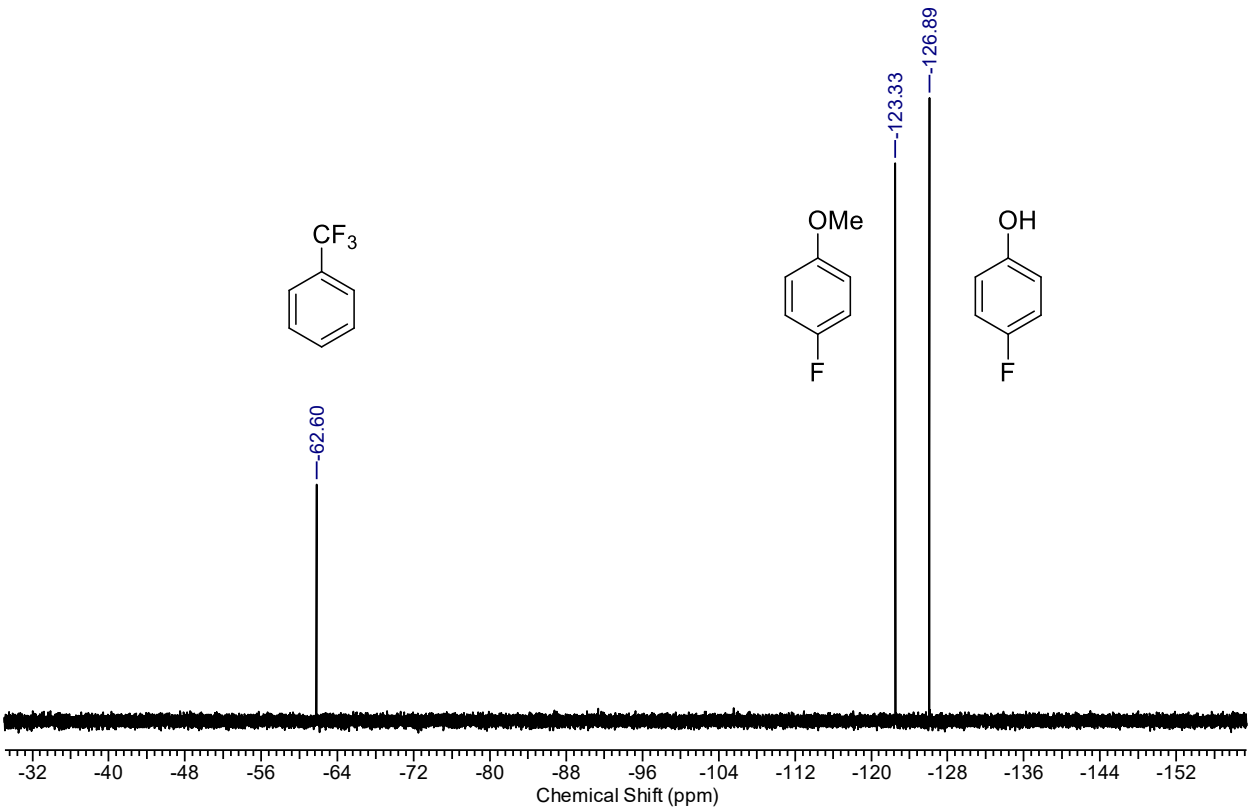


Figure 2.30. ^{19}F NMR of 4-fluorophenol (0.01 M) and 4-fluoroanisole (0.01 M) in CCl_4 with 0.200 M PLPC.

2.9 References (Experimental)

(1) Zhao, W.; Huang, L.; Guan, Y.; Wulff, W. D. Three-Component Asymmetric Catalytic Ugi Reaction—Concinnity from Diversity by Substrate-Mediated Catalyst Assembly. *Angew. Chemie Int. Ed.* **2014**, *53* (13), 3436–3441. https://doi.org/https://doi.org/10.1002/anie.201310491.

(2) Breslow, R.; Groves, K.; Mayer, M. U. Antihydrophobic Cosolvent Effects for Alkylation Reactions in Water Solution, Particularly Oxygen versus Carbon Alkylations of Phenoxide Ions. *J. Am. Chem. Soc.* **2002**, *124* (14), 3622–3635. https://doi.org/10.1021/ja012293h.

(3) Li, B.; Harjani, J. R.; Cormier, N. S.; Madarati, H.; Atkinson, J.; Cosa, G.; Pratt, D. A. Besting Vitamin E: Sidechain Substitution Is Key to the Reactivity of Naphthyridinol Antioxidants in Lipid Bilayers. *J. Am. Chem. Soc.* **2013**, *135* (4), 1394–1405. https://doi.org/10.1021/ja309153x.

(4) Chauvin, J.-P. R.; Griesser, M.; Pratt, D. A. Hydropersulfides: H-Atom Transfer Agents Par Excellence. *J. Am. Chem. Soc.* **2017**, *139* (18), 6484–6493. https://doi.org/10.1021/jacs.7b02571.

(5) Abraham, M. H.; Grellier, P. L.; Prior, D. V.; Morris, J. J.; Taylor, P. J. Hydrogen Bonding. Part 10. A Scale of Solute Hydrogen-Bond Basicity Using Log K Values for Complexation in Tetrachloromethane. *J. Chem. Soc. Perkin Trans. 2* **1990**, 521–529. https://doi.org/10.1039/p29900000521.

(6) Farmer, L. A.; Haidasz, E. A.; Griesser, M.; Pratt, D. A. Phenoxazine: A Privileged Scaffold for Radical-Trapping Antioxidants. *J. Org. Chem.* **2017**, *82* (19), 10523–10536. https://doi.org/10.1021/acs.joc.7b02025.

(7) Haidasz, E. A.; Van Kessel, A. T. M.; Pratt, D. A. A Continuous Visible Light Spectrophotometric Approach to Accurately Determine the Reactivity of Radical-Trapping Antioxidants. *J. Org. Chem.* **2016**, *81* (3), 737–744. https://doi.org/10.1021/acs.joc.5b02183.

(8) Howard, J. A.; Ingold, K. U. Absolute Rate Constants for Hydrocarbon Autoxidation. VI. Alkyl Aromatic and Olefinic Hydrocarbons. *Can. J. Chem.* **1967**, *45* (8), 793–802. https://doi.org/10.1139/v67-132.

(9) Howard, J. A.; Ingold, K. U. Absolute Rate Constants for Hydrocarbon Autoxidation. XVII. The Oxidation of Some Cyclic Ethers. *Can. J. Chem.* **1969**, *47* (20), 3809–3815. https://doi.org/10.1139/v69-635.

(10) Burton, G. W.; Doba, T.; Gabe, E. J.; Hughes, L.; Lee, F. L.; Prasad, L.; Ingoldo, K. U. Autoxidation of Biological Molecules. 4. Maximizing the Antioxidant Activity of Phenols. *J. Am. Chem. Soc.* **1985**, *107* (24), 7053–7065. https://doi.org/10.1021/ja00310a049.

(11) Valgimigli, L.; Bartolomei, D.; Amorati, R.; Haidasz, E.; Hanthorn, J. J.; Nara, S. J.; Brinkhorst, J.; Pratt, D. A. 3-Pyridinols and 5-Pyrimidinols: Tailor-Made for Use in Synergistic Radical-Trapping Co-Antioxidant Systems. *Beilstein J. Org. Chem.* **2013**, *9* (1), 2781–2792. https://doi.org/10.3762/bjoc.9.313.

(12) Abraham, M. H.; Abraham, R. J.; Byrne, J.; Griffiths, L. NMR Method for the Determination of Solute Hydrogen Bond Acidity. *J. Org. Chem.* **2006**, *71*, 3389–3394. https://doi.org/10.1021/JO052631N.

(13) Taft, R. W.; Gurka, D.; Joris, L.; von Schleyer, R.; Rakshys, J. W. Studies of Hydrogen-Bonded Complex Formation with p-Fluorophenol. IV. The Fluorine Nuclear Magnetic Resonance Method. *J. Am. Chem. Soc.* **1969**, *91*, 4794–4801.

Chapter 3

Intrinsic & Extrinsic Limitations to the Design and Optimization of Inhibitors of Lipid Peroxidation and Associated Cell Death

3.1 Foreword

The following research was published in The Journal of the American Chemical Society in August of 2022, under the same title.[1] Reprinted/adapted with permission from *J. Am. Chem. Soc.* 2022, 144, 32, 14706–14721. Copyright © 2022 American Chemical Society.

As a follow up to Chapter 2, the motivations of this research were many-fold. Apart from expanding our membrane H-bonding kinetic model to encompass a much larger number of examples, we wanted to explore the limits of RTA molecular design with respect to kinetics in biological models. Given the prodigious RTA activities of PNX and PTZ derived compounds, a comprehensive study in the context of ferroptosis was an essential next step for my research into novel (lipid-soluble) RTAs. This type of research, of course, is not feasible to carry out without robust collaboration of a multi-disciplinary nature. While I am the proprietor of the synthesis, kinetics, microsome assays, analysis and theory crafting (under the supervision of D. A. Pratt of course), much of the impact would not have been achieved without the efforts of Dr. Jia-Fei Poon, Dr. Zijun Wu and Omkar Zilka who provided all of the cell data used in the final analysis. Moreover, the *in vivo* data and related analysis (Western blots, serum analysis, histology, etc.) were generously provided by Marcus Conrad and his group (Svenja Lorenz, Stephanie Huehn and Bettina Proneth) which further elevated the work. Preparation of **3.43** and **3.44** were carried out by Dr. Wu.

N.B.: All Figures, Tables and Schemes appear as they do in the original publication, with the exception of Figure 3.8 where '$|\log EC_{50}|$' has been substituted with the more conventional 'pEC_{50}'. As such, compound and equations in the Figures, Tables and Schemes will not appear with the chapter number prefix (e.g. 3.#), but the prefix is applied throughout the main text of the chapter.

3.2 Abstract

The archetype inhibitors of ferroptosis, ferrostatin-1 and liproxstatin-1, were identified via high-throughput screening of compound libraries for cytoprotective activity. These compounds have been shown to inhibit ferroptosis by suppressing propagation of lipid peroxidation, the radical chain reaction that drives cell death. Herein we present the first rational design and optimization of ferroptosis inhibitors targeting this mechanism of action. Engaging the most potent RTA scaffold known (phenoxazine, PNX), and its less reactive chalcogen cousin (phenothiazine, PTZ), we explored the structure-reactivity-potency relationships to elucidate the intrinsic and extrinsic limitations of this approach. The results delineate the roles of inherent RTA activity, H-bonding interactions with phospholipid headgroups and lipid-solubility in determining activity/potency. We show that modifications which increase inherent RTA activity beyond that of the parent compounds do not substantially improve RTA kinetics in phospholipids or potency in cells, while modifications that decrease intrinsic RTA activity lead to corresponding erosions to both. The apparent 'plateau' of RTA activity in phospholipid bilayers ($k_{inh} \sim 2\times10^5$ $M^{-1}s^{-1}$) and cell potency ($EC_{50} \sim 4$ nM) may be a result of diffusion-controlled reactivity between the RTA and lipid-peroxyl radicals and/or the potential limitations on RTA turnover/regeneration by endogenous reductants. The metabolic stability of selected derivatives was assessed to identify a candidate for *in vivo* experimentation as a proof-of-concept. The resulting PNX-derivative (**3.11**) demonstrated stability in mouse liver microsomes comparable to liproxstatin-1, and was successfully used to suppress acute renal failure in mice brought on by tissue-specific inactivation of the ferroptosis regulator GPx4.

3.3 Introduction

Ferroptosis is an iron-dependent form of cell death resulting from a lethal accumulation of lipid hydroperoxides.[2–4] Excessive accumulation of these products of lipid peroxidation, if unabated, is believed to result in the formation of pores in the cellular plasma membrane, followed by cell swelling and, finally, osmolysis.[5] Ferroptosis has been associated with a variety of pathologies, with particularly strong links to neurodegeneration and ischemic reperfusion injury.[6,7] It is triggered when the cell's ability to suppress (phospho)lipid hydroperoxide formation is overcome.[8,9] Phospholipid peroxidation can be enzyme-catalyzed (by lipoxygenases)[10] or can

occur spontaneously via autoxidation, a radical chain reaction (Figure 3.1A).[11–13] The latter process is auto-initiated since product hydroperoxides can be converted to initiating radicals in the presence of low-valent iron (or other competent one-electron reductants). The activity of glutathione peroxidase-4 (GPx4), a selenoprotein that catalyzes the reduction of (phospho)lipid hydroperoxides to their corresponding alcohols by glutathione (GSH),[14] prevents auto-initiation. Small molecules which chelate free iron or possess GPx4-like peroxidase activity can also be effective.[8]

In the initial characterization of ferroptosis, phenolic radical-trapping antioxidants (RTAs), such as BHT and Trolox, a water-soluble analog of α-tocopherol (α-TOH, the most biologically active form of Vitamin E), were found to suppress cell death.[8] RTAs trap lipid-derived peroxyl radicals,[15] impeding the propagation of the chain reaction that leads to the accumulation of lipid hydroperoxides (Figures 3.1B and C). This key observation linked lipid autoxidation to ferroptosis; a result which has since been underscored by the fact that lipoxygenase activity is not required for ferroptosis[16] and that the most potent ferroptosis inhibitors identified to date are highly competent RTAs. For example, ferrostatin-1 (Fer-1)[8] and liproxstatin-1 (Lip-1),[9] identified by high-throughput screening to be potent ferroptosis inhibitors, were subsequently found to be very good RTAs (Figure 3.1C).[17] Moreover, the recent discoveries of biochemical pathways which regenerate and/or synthesize RTAs *de novo* to suppress ferroptosis (e.g. FSP1/reduced coenzyme Q_{10}[18,19] and GCH1/tetrahydro-biopterin,[20,21] respectively) further highlight the central role of lipid peroxidation in ferroptosis and the function of RTAs to keep it in check.

In the decades preceding the characterization of ferroptosis, the RTA activity of α-TOH (and other forms of Vitamin E) was meticulously studied in organic solutions, micelles, phospholipid bilayers and lipoproteins.[22–29] On the basis of that work, it was evident that α-TOH acts by trapping (phospho)lipidperoxyl radicals that are inaccessible to ubiquitous water-soluble RTAs such as uric acid and ascorbic acid.[30,31] The principal reasons it functions well in this capacity are: (1) it is highly lipophilic and partitions into biological membranes, (2) its trapping of peroxyl radicals is significantly faster than the propagation reaction with (phospho)lipids, and (3) it is highly bioavailable, with its own transport protein to provide protection from primary metabolism and ensure systemic distribution.[32,33] Although the concentration of autoxidizable (phospho)lipids can be 2 to 3 orders of magnitude greater than α-TOH in lipid bilayers,[34] it

remains effective at suppressing chain propagation because its inhibition rate constant (k_{inh})[34] is greater than the propagation rate constants (k_p) of most (phospho)lipids (*cf.* k_{inh}^{lip} ~ 6×10^3 $M^{-1}s^{-1}$ and k_p ~ 60 $M^{-1}s^{-1}$), [26,36] enabling it to compete – *albeit just barely*. Although α-TOH can be much more reactive to peroxyl radicals in organic solution (e.g. k_{inh}^{PhCl} = 3×10^6 $M^{-1}s^{-1}$),[35] its reactivity is significantly suppressed in phospholipids. We recently attributed this observation to strong H-bond formation between the phenolic O-H and phosphodiester moieties of the phospholipids.[38] The fact that arylamines (such as Fer-1 and Lip-1) form weaker H-bonds than phenols (such as α-TOH) underlies the milder suppression in reactivity of Fer-1 and Lip-1 as RTAs on moving from organic solution to lipid bilayers – and suggests that aminic RTAs are better lead structures for optimization.

Cell-based high-throughput screens, such as those which led to Lip-1 and Fer-1, can provide promising leads for optimization efforts.[39,40] However, given that the target of the vast majority of inhibitors identified to date is not an enzyme or protein, but a membrane-embedded transient radical, optimization requires a non-traditional approach. We recently developed a high-throughput assay of RTA activity in phospholipid bilayers dubbed FENIX (Fluorescence ENabled Inhibited autoXidation)[38] and demonstrated that it is predictive of potency to inhibit ferroptosis for a wide variety of compounds. Herein we make use of the FENIX approach to carry out a structure-reactivity-potency study of an inhibitor scaffold to illustrate the rational optimization of a ferroptosis inhibitor from a reactivity standpoint. We chose phenoxazine (PNX, Figure 3.1C) as the scaffold for optimization since it is one of the most inherently reactive RTAs known[41,42] (compare k_{inh}^{PhCl} ~ 4×10^7 $M^{-1}s^{-1}$ *vs.* 2×10^5 and 3×10^5 $M^{-1}s^{-1}$ for Lip-1 and Fer-1, respectively, at 37°C in PhCl). Moreover, PNX has been demonstrated to be one of the most potent inhibitors of ferroptosis described to date (EC_{50} = 9 nM *vs.* 35 and 45 nM, respectively, for inhibition of RSL3-induced ferroptosis in mouse embryonic fibroblasts).[43] We also explored a limited set of analogous phenothiazine (PTZ, Figure 3.1C) derivatives. We surmised that its structural similarity, but lower inherent RTA activity (k_{inh}^{PhCl} ~ 8×10^6 $M^{-1}s^{-1}$ at 37°C in PhCl),[41] would enable us to corroborate trends observed with the PNX derivatives while increasing the range of reactivity from which structure-reactivity-potency relationships could be established. The results and their implications for the rational design and/or optimization of RTA-based ferroptosis inhibitors are described below.

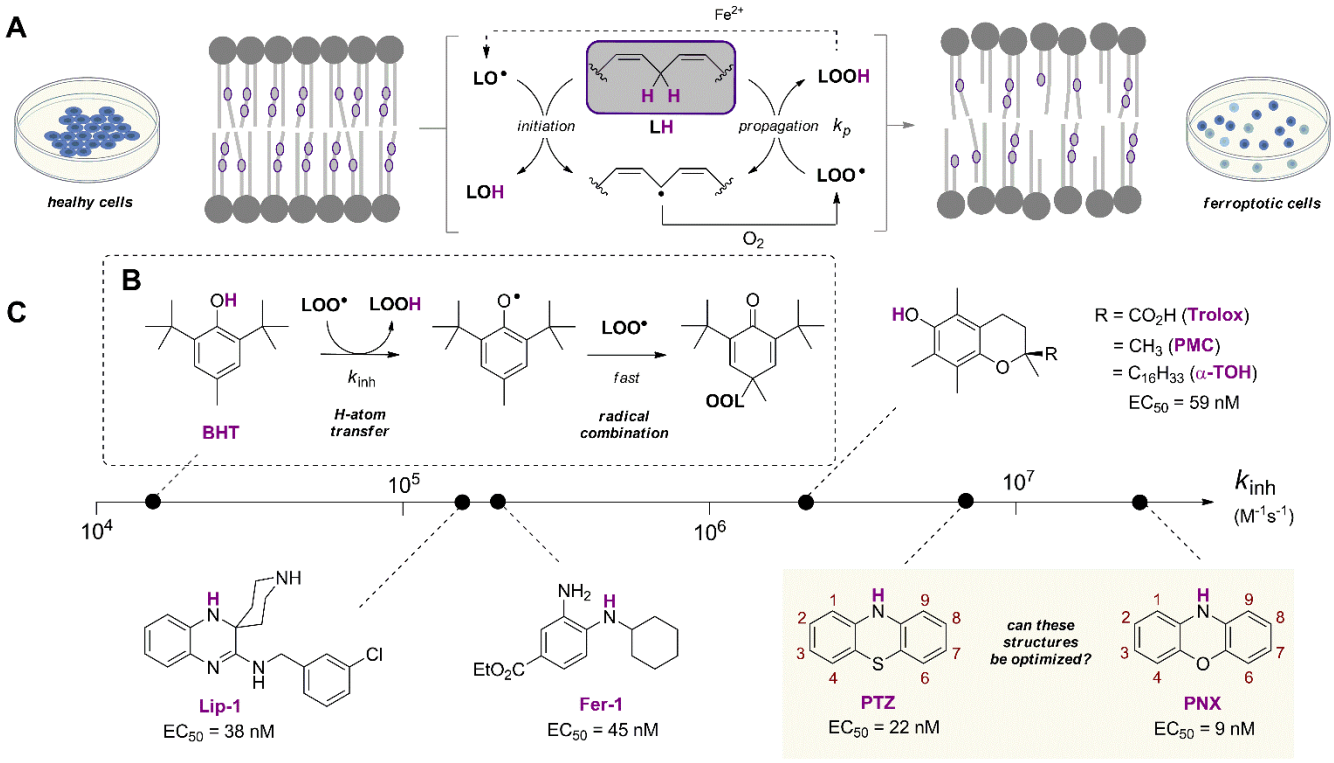


Figure 3.1. (A) The autoxidation of polyunsaturated phospholipids leads to a loss in membrane integrity and drives ferroptosis. **(B)** The inhibition of lipid autoxidation (peroxidation) by radical-trapping antioxidants (RTAs) illustrated with BHT. **(C)** The range of reactivity of representative RTAs (phenolic and aminic) expressed in terms of their inhibition rate constants (k_{inh}) as measured in solution (chlorobenzene) at 37°C.

3.4 Results

3.4.1 RTA Activity in a Phospholipid Membrane: Suppression due to H-Bonding can be Severe, but is Generally Predictable.

In earlier work, we had examined substituent effects on the intrinsic RTA activity of PNX.[41] With these 15 PNX derivatives still in hand, we added to the library to cover a broader range of electronics, i.e. electron-donating (ED) or electron-withdrawing (EW) groups or combinations thereof, as well as their positions on the two aromatic rings, in order to systematically probe how intrinsic RTA activity translates to phospholipid bilayers. We also investigated a less extensive set of PTZ derivatives, but which nonetheless covered the same range in electronics. Structures are numbered **3.1-3.40** (Table 3.1 & Figure 3.2G) and abbreviated according to the substituent(s)

and its (their) position(s) according to the convention in Figure 3.1. Details of the preparation of all derivatives and their characterization are provided as Supporting Information.

The intrinsic RTA activities of the PNX and PTZ derivatives were determined in azobis(isobutyronitrile) (AIBN)-initiated co-autoxidations of PBD-BODIPY and dioxane (Figure 3.2A).[41] PBD-BODIPY enables reaction progress to be monitored by conventional spectrophotometry, and since its rate of reaction with dioxane-derived peroxyl radicals is known (i.e. $k_{\text{PBD-BODIPY}}$ = 5310 $M^{-1}s^{-1}$),[41] $k_{inh}^{dioxane}$ of the RTA can be calculated simply from the initial rate of PBD-BODIPY oxidation, with which it competes (Eq 3.1).[17,38,41,43,44] Moreover, the length of the inhibited period (t_{inh}) is related to the radical-trapping stoichiometry of the RTA as in Eq 3.2. Using this approach, multiple kinetic experiments can be carried out in parallel, enabling convenient systematic comparisons of several RTAs. Representative inhibited co-autoxidation data are shown for three derivatives of each of PNX (left) and PTZ (right) in Figure 3.2B. In the limited number of cases where the amine completely suppressed PBD-BODIPY oxidation, (such as 3,7-tBu-PNX (**3.34**) in Figure 3.2B), which precludes determination of $k_{inh}^{dioxane}$ from the initial rate, a strong H-bond accepting co-solvent (DMSO) was added to lower the concentration of free RTA in solution (Figure 3.2C). This increased the rate of PBD-BODIPY oxidation (Figure 3.2D) and enabled accurate determination of k_{inh}^{DMSO}.

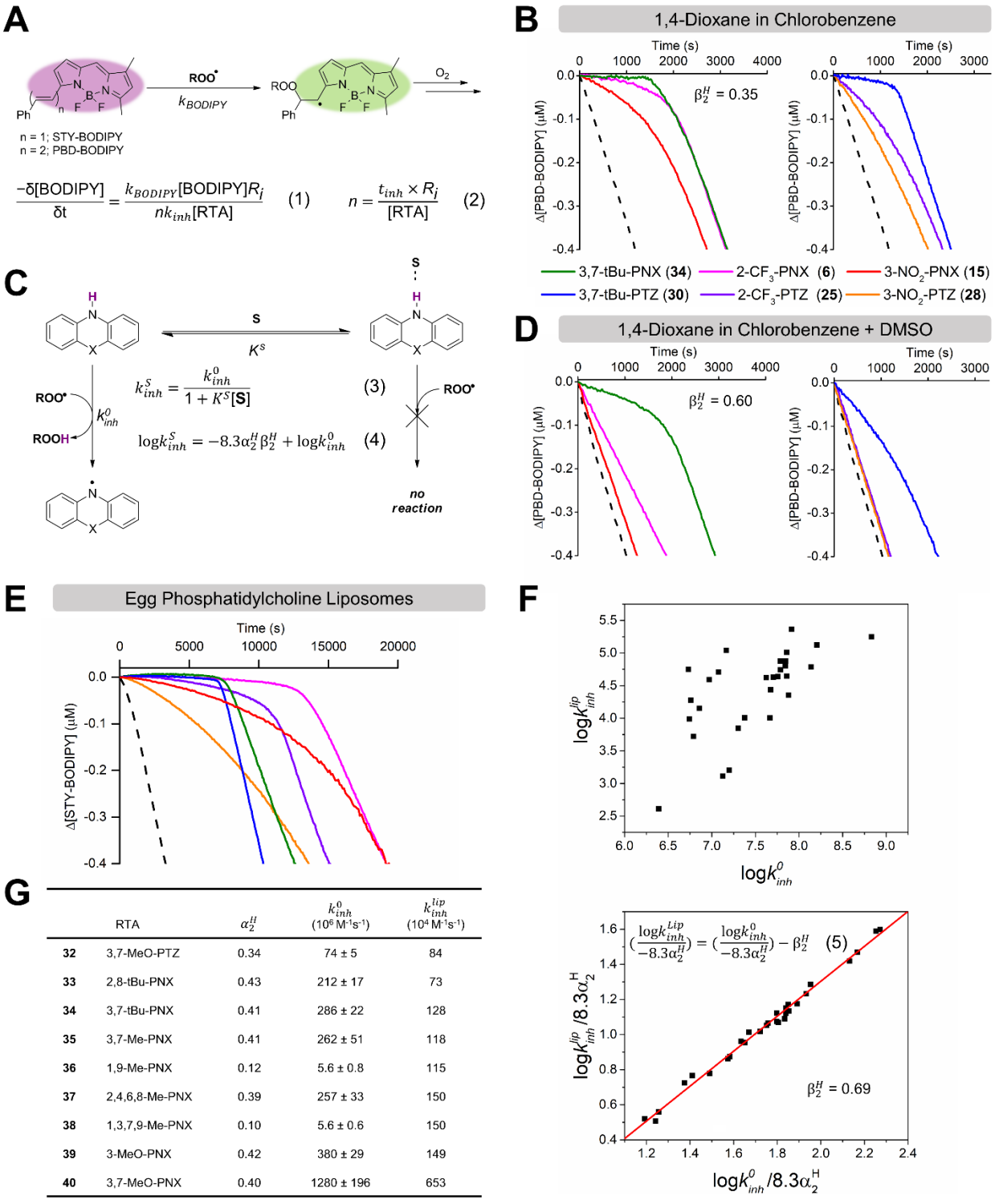
Table 3.1. Inhibition Rate Constants (k_{inh}^{lip})[35] and Radical-Trapping Stoichiometries (n) of PNX and PTZ Derivatives Determined from Co-Autoxidations of STY-BODIPY and the Polyunsaturated Phospholipids of Egg PC Liposomes.

		α_2^H [a]	k_{inh}^0 (10^5 $M^{-1}s^{-1}$) [b]	k_{inh}^{lip} (10^3 $M^{-1}s^{-1}$)[d]	n
1	PNX	0.44	(820 ± 77)[c]	(232 ± 23)[e]	2.0 ± 0.1
2	PTZ	0.38	(147 ± 6)	(110 ± 20)[e]	1.9 ± 0.1
3	PSZ	0.36	(54 ± 2)	(56 ± 3)[e]	2.3 ± 0.1
4	Benzo(b)-PNX	0.49	(723 ± 42)[c]	(101 ± 12)	2.4 ± 0.1
5	Benzo(b)-PTZ	0.40	(120 ± 3)	(51 ± 3)	1.9 ± 0.1
6	2-CF_3-PNX	0.51	(610 ± 30)	(75 ± 11)	3.0 ± 0.1
7	2-CF_3-7-tBu-PNX	0.50	(703 ± 8)[c]	(75 ± 13)	2.8 ± 0.1
8	2-CF_3-8-tBu-PNX	0.51	(699 ± 15)[c]	(64 ± 9)	2.3 ± 0.1
9	3-CF_3-PNX	0.53	(508 ± 56)	(42 ± 2)	3.0 ± 0.1
10	3-CF_3-7-tBu-PNX	0.51	(613 ± 14)[c]	(55 ± 10)	2.8 ± 0.1
11	3-CF_3-8-tBu-PNX	0.52	(574 ± 4)[c]	(44 ± 3)	2.6 ± 0.1
12	3-CHO-PNX	0.55	(421 ± 57)	(42 ± 2)	2.9 ± 0.1
13	3,7-CHO-PNX	0.63	(238 ± 37)	(10 ± 1)	3.2 ± 0.1
14	3-CHO-7-CN-PNX	0.64	(200 ± 12)	(7.1 ± 0.1)	*nd*[f]
15	3-NO_2-PNX	0.62	(463 ± 14)	(10 ± 1)[e]	2.2 ± 0.1
16	3-NO_2-7-Me-PNX	0.60	(757 ± 92)	(23 ± 2)[e]	3.8 ± 0.3
17	3-NO_2-7-MeO-PNX	0.60	(1370 ± 186)	(61 ± 4)[e]	2.9 ± 0.2
18	3-NO_2-7-NEt_2-PNX	0.58	(6784 ± 342)[c]	(177 ± 37)[e]	2.4 ± 0.4
19	3,7-NO_2-PNX	0.72	(134 ± 8)	(1.3 ± 0.1)[e]	*nd*[f]
20	3-CN-PNX	0.56	(472 ± 33)	(27 ± 2)	3.6 ± 0.1
21	3-CN-7-Me-PNX	0.55	(726 ± 43)	(44 ± 6)	3.5 ± 0.1
22	3-CN-7-MeO-PNX	0.55	(1605 ± 154)	(133 ± 15)[e]	3.1 ± 0.3
23	3-CN-7-NO_2-PNX	0.69	(158 ± 2)	(1.6 ± 0.1)[e]	*nd*[f]
24	2-Cl-PTZ	0.43	(94 ± 8)	(39 ± 4)	2.1 ± 0.1
25	2-CF_3-PTZ	0.44	(57 ± 3)	(19 ± 1)	2.5 ± 0.1
26	3-CF_3-PTZ	0.45	(55 ± 3)	(9.8 ± 0.5)	2.6 ± 0.1
27	3-CHO-PTZ	0.47	(72 ± 4)	(14 ± 1)	2.2 ± 0.1
28	3-NO_2-PTZ	0.52	(62 ± 2)	(5.3 ± 0.3)	2.0 ± 0.1
29	3,7-NO_2-PTZ	0.62	(25 ± 2)	(0.41 ± 0.04)	*nd*[f]
30	3,7-tBu-PTZ	0.35	(199 ± 11)[c]	(106 ± 14)	1.6 ± 0.1
31	1,9-Me-PTZ	0.06	(3.7 ± 0.2)	(98 ± 5)	1.7 ± 0.1
	PMC	0.38	(52 ± 3)	(29 ± 2)	(2)

(a) Estimated from the ^{1}H NMR chemical shift difference of the amine proton in DMSO-d_6 and benzene-d_6 (see Supporting Information). (b) Determined from inhibition rate constants measured in 1:3 dioxane:PhCl ($k_{inh}^{dioxane}$, see Table 3.3), which has β_2^H = 0.35 and α_2^H from the preceding column using Eq 4. (c) Determined from inhibition rate constants measured in 1:2:1 dioxane:PhCl:DMSO (k_{inh}^{DMSO}, Table 3.3), which has β_2^H = 0.60 and α_2^H from the preceding column using Eq 4. (d) Apparent inhibition rate constants from MeOAMVN-initiated autoxidations of egg PC liposomes determined by fluorescence. (e) Apparent inhibition rate constants from MeOAMVN-initiated autoxidations of egg PC liposomes determined by absorbance (STY-BODIPY, 10-20 μM, λ_{max} = 565 nm, ε = 123 676 M^{-1} cm^{-1}. (f) Not determined (*nd*) due to the lack of a well-defined inhibited period. An n = 2 was used in the calculation of k_{inh}^{lip} (see SI for further elaboration).

For direct comparison of the intrinsic RTA activity of all derivatives, the rate constants were normalized for the contribution of the H-bonding pre-equilibrium of the RTA and solvent(s) (Figure 3.2C).[45] Doing so involved determination of the H-bond acidity (α_2^H) of the RTA by ^{1}H NMR (values are included in Table 3.1, see Supporting Information for corresponding spectra)[41,46] and using it along with the H-bond basicity (β_2^H) of the solvent system to determine the intrinsic inhibition rate constant k_{inh}^0 using the Abraham-Ingold equation (Eq 4).[45] The data, which are given in Table 3.1 and Figure 3.2G, span three orders of magnitude, from 2.5×10^6 to 1.3×10^9 $M^{-1}s^{-1}$ for 3,7-NO_2-PTZ (**3.29**) and 3,7-MeO-PNX (**3.40**), respectively. Two trends are immediately evident when scrutinizing the data: the intrinsic reactivity of PNX derivatives is systematically higher than equivalently-substituted PTZ derivatives, and reactivity increases with increasing electron-richness of either the PNX and PTZ derivatives, consistent with previous observations.[41]

The k_{inh}^0 data were used to provide a baseline for comparison to the reactivity of the same set of compounds determined in egg phosphatidylcholine (PC) liposomes using the FENIX approach.[38] Therein, reaction progress was monitored for MeOAMVN-initiated autoxidations via the formation of oxidized STY-BODIPY as determined by fluorescence, and k_{inh}^{lip} of the RTA determined using $k_{\text{STY-BODIPY}}$ = 894 $M^{-1}s^{-1}$.[47] Representative traces for the same three derivatives of each of PNX and PTZ are shown in Figure 3.2E and the data for these and the other compounds tabulated alongside the k_{inh}^0 data in Table 3.1. While the absolute values of the rate constants were significantly suppressed in phospholipids, they spanned a similarly large range, from 4×10^2 to 2.3×10^5 $M^{-1}s^{-1}$ for 3,7-NO_2-PTZ (**29**) and PNX, respectively. Electron-rich PNX derivatives were more reactive, but the complete suppression of STY-BODIPY oxidation precluded the determination of their k_{inh}^{lip} values (such as compound **3.34** in Figure 3.2E). Nevertheless, with data available for 29 compounds,[48] we could evaluate how well the intrinsic reactivities of the RTAs correlate to their kinetics in phospholipid bilayers. The plot in Figure 3.2F (top) clearly indicates that they do not correlate particularly well.



G

	RTA	α_2^H	k_{inh}^0 (10^6 $M^{-1}s^{-1}$)	k_{inh}^{lip} (10^4 $M^{-1}s^{-1}$)
32	3,7-MeO-PTZ	0.34	74 ± 5	84
33	2,8-tBu-PNX	0.43	212 ± 17	73
34	3,7-tBu-PNX	0.41	286 ± 22	128
35	3,7-Me-PNX	0.41	262 ± 51	118
36	1,9-Me-PNX	0.12	5.6 ± 0.8	115
37	2,4,6,8-Me-PNX	0.39	257 ± 33	150
38	1,3,7,9-Me-PNX	0.10	5.6 ± 0.6	150
39	3-MeO-PNX	0.42	380 ± 29	149
40	3,7-MeO-PNX	0.40	1280 ± 196	653

Figure 3.2. (A) Co-autoxidation of STY-BODIPY and PBD-BODIPY can be monitored by either absorbance or fluorescence. Inhibition rate constants (k_{inh}) and radical-trapping stoichiometries (n) are determined from the initial rates and duration of the inhibited periods using Eq. 1 and 2, respectively. **(B)** Representative data for azine-inhibited co-autoxidation of

PBD-BODIPY (10 μM) and 1,4-dioxane (2.9 M) in chlorobenzene initiated with AIBN (6 mM) at 37°C and monitored at 587 nm (123 000 M^{-1} cm^{-1}). **(C)** Kinetic scheme for the suppression in azine RTA activity due to H-bonding interactions between the RTA and solvent, where k_{inh}^{S} is the inhibition rate constant in a given solvent S, K^S is the equilibrium constant for formation of a 1:1 H-bonded complex between the RTA and solvent, and k_{inh}^{0} is the inhibition rate constant in the absence of any H-bonding interactions. **(D)** Representative data for azine-inhibited co-autoxidation of PBD-BODIPY (10 μM) and 1,4-dioxane (2.9 M) in 2:1 chlorobenzene:DMSO) initiated with AIBN (6 mM) at 37°C and monitored at 587 nm (118 200 M^{-1} cm^{-1}). **(E)** Representative data for azine-inhibited co-autoxidation of STY-BODIPY (1 μM) and liposomal egg phosphatidylcholine (1 mM) suspended in phosphate-buffered saline (PBS, pH 7.4) initiated with MeOAMVN (200 μM) at 37°C and monitored by fluorescence ($\lambda_{ex}/\lambda_{em}$ = 488/518 nm). **(F)** *Top*: Correlation of $\log k_{inh}^{0}$ and $\log k_{inh}^{lip}$ (N=29; R^2=0.417). *Bottom*: Correlation of $\log (k_{inh}^{0}/8.3\alpha_2^H)$ and $\log (k_{inh}^{lip}/8.3\alpha_2^H)$ (N=29; R^2=0.991).[44] **(G)** Predicted k_{inh}^{lip} for RTAs which were too reactive for it to be determined directly. Values obtained using Eq 5 with experimental k_{inh}^{0} and α_2^H with β_2^H = 0.69.

Since our previous work had suggested that the phosphodiester moiety of egg phosphatidylcholine is a strong H-bond acceptor,[38] we replotted the kinetic data as in Figure 3.2F (bottom), normalizing for the differences in H-bond acidity (α_2^H) of the individual RTAs. The excellent correlation which results from this treatment clearly demonstrates that H-bonding is uniquely responsible for the attenuation in RTA activity in lipid bilayers (at least for this group of compounds under the specific conditions of the experiment). Moreover, the Y-intercept of the correlation provides the effective H-bond basicity (β_2^H) of liposomal egg phosphoatidylcholine (0.69). This value is in good agreement with the value we derived from ^{19}F NMR studies of H-bond formation between egg PC and 4-fluorophenol in dilute solutions of CCl_4 (0.79).[38,49] Clearly, the intrinsic reactivities of the PNX and PTZ derivatives translate very well from organic solution to egg PC liposomes when the strong H-bonding interaction to the phosphatidylcholine headgroup is taken into account.

On the basis of the excellent correlation in Figure 3.2F, we estimated k_{inh}^{lip} for the 9 compounds that fully suppressed STY-BODIPY oxidation using the k_{inh}^{0} values obtained from the experiments in organic solution and the effective β_2^H value for the egg PC liposomes. The k_{inh}^{lip} values for these 9 amines (Figure 3.2G) are up to 26-fold larger than that of PNX (i.e k_{inh}^{lip} = 6×10^6 $M^{-1}s^{-1}$ for 3,7-MeO-PNX (**3.40**)), suggesting that electron-rich PNX derivatives have the

potential to be ferroptosis inhibitors of unprecedented potency. Confidence in these estimates can be derived not only from the excellent correlation from which they were derived, but also the fact that k_{inh}^{lip} could be predicted for PMC (a phenol) from its k_{inh}^{0} and α_2^H within a margin of the precision of the measured value (3.5×10^4 and 2.9×10^4 $M^{-1}s^{-1}$, respectively).

3.4.2 Synergy with Ascorbate Boosts Efficacy and Enables Kinetic Measurements for the Most Potent RTAs.

Although ascorbate is not itself an efficient inhibitor of the propagation of lipid peroxidation, it can act as an inhibitor indirectly via regeneration of a lipophilic RTA at the lipid-water interface. The synergism between α-TOH and ascorbate has been well documented,[50–52] but other lipid-soluble RTAs have seldom been studied in such detail. In principle, persistent aminyl radicals derived from azines such as PNX and PTZ should be substrates for reduction analogous to the phenoxyl radical derived from α-TOH (Figure 3.3A). To systematically examine if this is indeed the case, azine-inhibited STY-BODIPY/egg PC co-autoxidations were carried out in the presence of ascorbate (at 10 and 100 μM). These experiments employed the more lipophilic initiator (di-*tert*-undecylhyponitrite, DTUN) to minimize trapping of initiator-derived radicals by ascorbate (which is acutely observed when the more amphiphilic MeOAMVN initiator is used).[38] Representative inhibited autoxidation traces are shown for a panel of compounds in Figures 3B-F. Synergism is easily identified by an increase in the duration of the inhibited period, without corresponding change to the rate of the inhibited oxidation. For example, addition of ascorbate (10 μM) increases the inhibition period due to the RTA activity of PMC (400 nM) from ~1400 s to >5000s (Figure 3.3B).

The data in Figure 3.3 reveal that, in general, the PNX derivatives are readily regenerated when ascorbate is added to the system (as are PTZ derivatives, see Supporting Information). Interestingly, PNX (Figure 3.3C) was more efficiently regenerated than PMC with inhibition times that were >3-fold longer under otherwise identical conditions. The inhibited periods for PNX derivatives with EW or ED groups were similarly extended, as shown for 3-CN-PNX (**3.20**) and 3-MeO-PNX (**3.39**) in Figure 3.3D. Interestingly, the positioning of substituents can have a pronounced effect on propensity to undergo regeneration. For instance, the t_{inh} of 2,8-tBu-PNX (**3.33**) and 3,7-tBu-PNX (**3.34**), while equivalent in the absence of ascorbate, are >4-fold

larger for 3,7-tBu-PNX in the presence of 100 μM of ascorbate (Figure 3.3E). Moreover, while 3,7-Me-PNX (**3.35**) exhibited the expected synergy with ascorbate, the inhibited period of 1,9-Me-PNX (**3.36**) was only marginally affected by added ascorbate (Figure 3.3F). A similar deficit was observed for other PNX/PTZ compounds with methyl groups in the 1- and 9-positions (compounds **3.31** and **3.38**). The whole library of compounds was surveyed, and efficiency of regeneration was expressed both in terms of radical-trapping stoichiometry (relative to the concentration of the RTA using Eq 2) and in terms of a regeneration efficiency (α) (Figure 3.3G).

$$\alpha = \frac{(observed\ stoichiometry)}{(theoretical\ stoichiometry)} \times 100\% \qquad (3.6)$$

Assuming each equivalent of ascorbate can provide two reducing equivalents, the maximum stoichiometry expected from 400 nM RTA combined with 10 and 100 μM ascorbate would be ~ 52 and ~ 502, respectively (assuming n ~ 2 for the RTA itself). With 10 μM of ascorbate, regeneration of PNX leads to a >10-fold increase in radical-trapping stoichiometry (n = 28.9), corresponding to a regeneration efficiency of α = 55%. The stoichiometry of PNX increases further with additional ascorbate (n = 41.9), but with a decrease in regeneration efficiency (α = 8.3%) – presumably due to the greater opportunity for alternative fates of the PNX-derived radical as the duration of the experiment increases. With 100 μM ascorbate, the largest determined α was observed for 3-CHO-PNX (**3.12**) at 17%, however, inhibition with PSZ exceeded the duration of the experiment (54,000 s) indicating $n \geq 100$ (or an $\alpha \geq 20\%$).

On the basis of the foregoing, we wondered if DTUN-initiated autoxidations carried out at a lower concentration of RTA (i.e. 400 nM in lieu of 4 μM) in the presence of excess ascorbate would provide initial rates of sufficient slope and duration to enable determination of k_{inh}^{lip} values of compounds that were too reactive for quantification in the MeOAMVN-initiated autoxidations (i.e. **3.32-3.40**, for which they were estimated using Eq 5). Indeed, after correcting for the retardation in STY-BODIPY oxidation owing to the presence of ascorbate (factors of 1.6 and 4.7 for 10 and 100 μM ascorbate, respectively), values of k_{inh}^{lip} could be derived which were generally in very good agreement with those determined at higher RTA concentrations in the absence of ascorbate (see Table 3.4 of the Supporting Information).

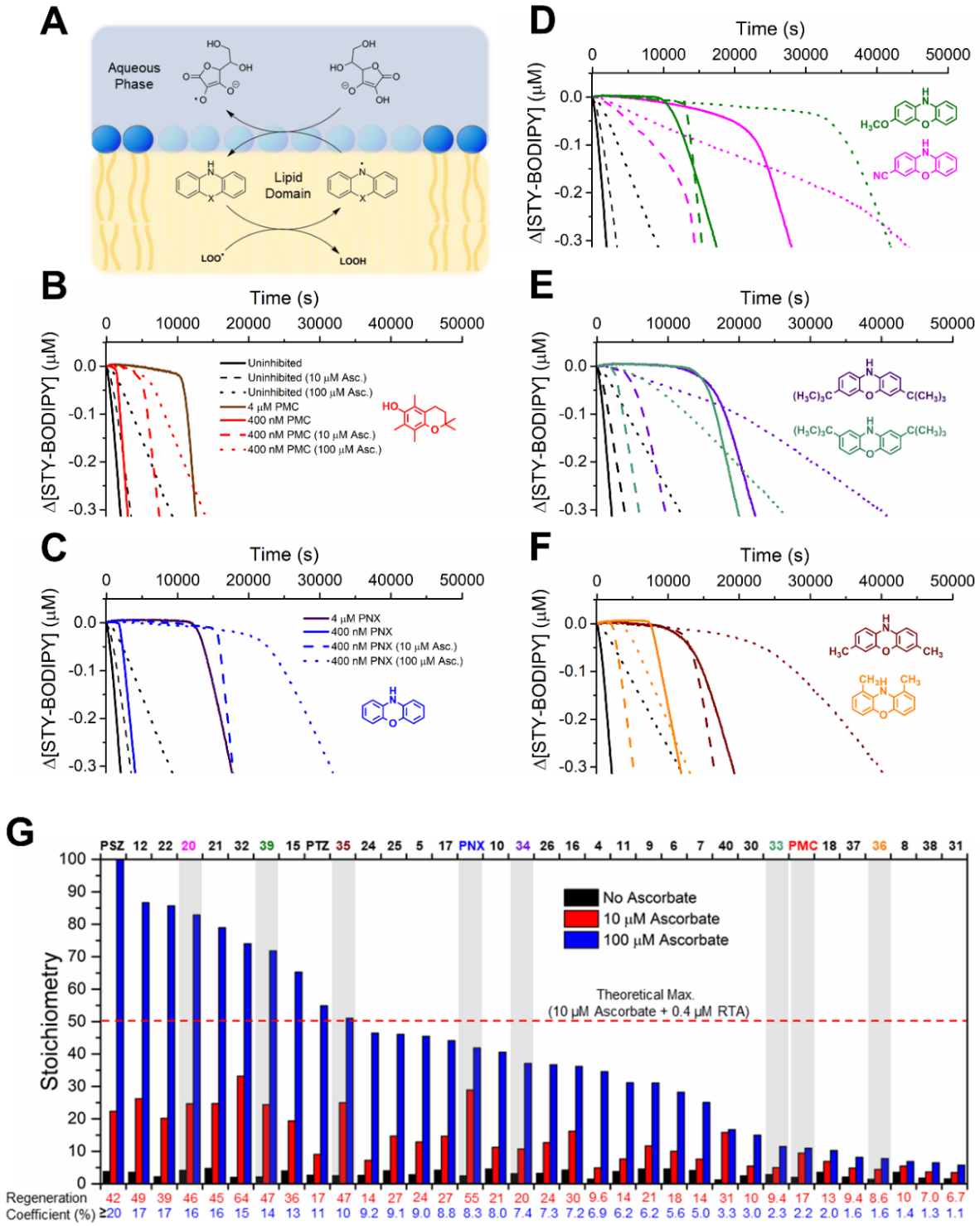


Figure 3.3. (A) Proposed mechanism of catalytic trapping of phospholipid-derived peroxyl radicals by azine RTAs and ascorbate. **(B-F)** Representative data from co-autoxidations of STY-BODIPY (1 μM) and liposomal egg phosphatidylcholine (1 mM) suspended in PBS (pH 7.4) initiated with DTUN (200 μM) at 37°C and monitored by fluorescence ($\lambda_{ex}/\lambda_{em}$ = 488/518 nm).

(D-F) Inhibited autoxidations were carried out with either 4 μM RTA (solid line) *or* 400 nM RTA (dashed/dotted lines) with varying concentrations of ascorbate. **(G)** Summary of the radical-trapping stoichiometries and regeneration coefficients of the compound library.

With k_{inh}^{lip} values available for the more reactive PNX and PTZ derivatives, an interesting and unexpected trend emerges: the increased inherent reactivity of the electron-rich compounds does not translate from organic solution to liposomes. For example, the most inherently reactive derivative, 3,7-MeO-PNX (**3.40**), was characterized by k_{inh}^{lip} of only 1.6×10^5 $M^{-1}s^{-1}$ – 30-fold lower than the prediction made based on its reactivity in solution and indistinguishable from that determined for unsubstituted PNX (k_{inh}^{lip} = 1.6×10^5 $M^{-1}s^{-1}$). Likewise, 3,7-MeO-PTZ (**32**), 3,7-Me-PNX (**3.35**) and 3-MeO-PNX (**3.39**) were found to also have essentially equivalent rate constants (1.3-1.9×10^5 $M^{-1}s^{-1}$), again in contrast to their predicted increase in k_{inh}^{lip} relative to PNX (of 3.8-fold, 5.1-fold and 6.7-fold, respectively). It is important to note that the rate of STY-BODIPY consumption ($-d[BODIPY]/dt$) in the presence of these compounds did not drop below a slow (but consistently measurable) ~1 pM s^{-1}, seemingly agnostic to differences in intrinsic reactivity of the added RTAs. Thus, while the reactivity of electron-poor PNX and PTZ derivatives in phospholipid bilayers can be predicted from their solution phase kinetics, the reactivity of electron-rich PNX and PTZ derivatives cannot. Instead, these compounds never appear to exceed the reactivity exhibited by 'electron-neutral' PNX. This is most obvious when k_{inh}^{lip} values determined from the DTUN-initiated autoxidations are plotted against the values determined (or predicted) from the MeOAMVN-initiated autoxidations (Figure 3.4A). The saturation-like behavior suggests an inherent limit to k_{inh}^{lip}.

Curiously, certain electron-rich compounds such as 3,7-tBu-PNX (**3.34**) and 2,8-tBu-PNX (**3.33**) appeared to be substantially slower inhibitors than expected based upon their complete suppression of the MeOAMVN-initiated autoxidations. Their k_{inh}^{lip} values (4.8×10^4 and 3.9×10^4 $M^{-1}s^{-1}$, respectively) did not correspond to the plateau of ~1-2 $\times10^5$ $M^{-1}s^{-1}$ observed for unsubstituted PNX and the other activated PNX derivatives – including the electronically analogous 3,7-Me-PNX (**3.35**) (log*P* = 4.76). We wondered if the increased lipid-solubility and smaller diffusion-coefficient of **3.34** (log*P* = 7.22), and ostensibly **3.33**, could render its regeneration by ascorbate at least partially rate-limiting. To examine this further, 3,7-Et-PNX

(**3.41**) and 3,7-*i*-Pr-PNX (**3.42**) (log*P* = 5.83 and 6.52 respectively) were prepared and tested to see if k_{inh}^{lip} systematically changes along the simple alkyl series. Indeed, while in the absence of ascorbate regeneration all four compounds (at 4 μM) fully suppress the autoxidation of STY-BODIPY (Figure 3.4B, *top*), but under synergistic conditions (Figure 3.4B, *bottom*) the k_{inh}^{lip} of 3,7-Et-PNX (**3.41**) (7.7×10^4 $M^{-1}s^{-1}$) and 3,7-iPr-PNX (**3.42**) (6.1×10^4 $M^{-1}s^{-1}$) were found to be incrementally – and reproducibly – larger than that of 3,7-tBu-PNX (**3.34**) (4.8×10^4 $M^{-1}s^{-1}$), and smaller than that of 3,7-Me-PNX (**3.35**) (1.4×10^5 $M^{-1}s^{-1}$).

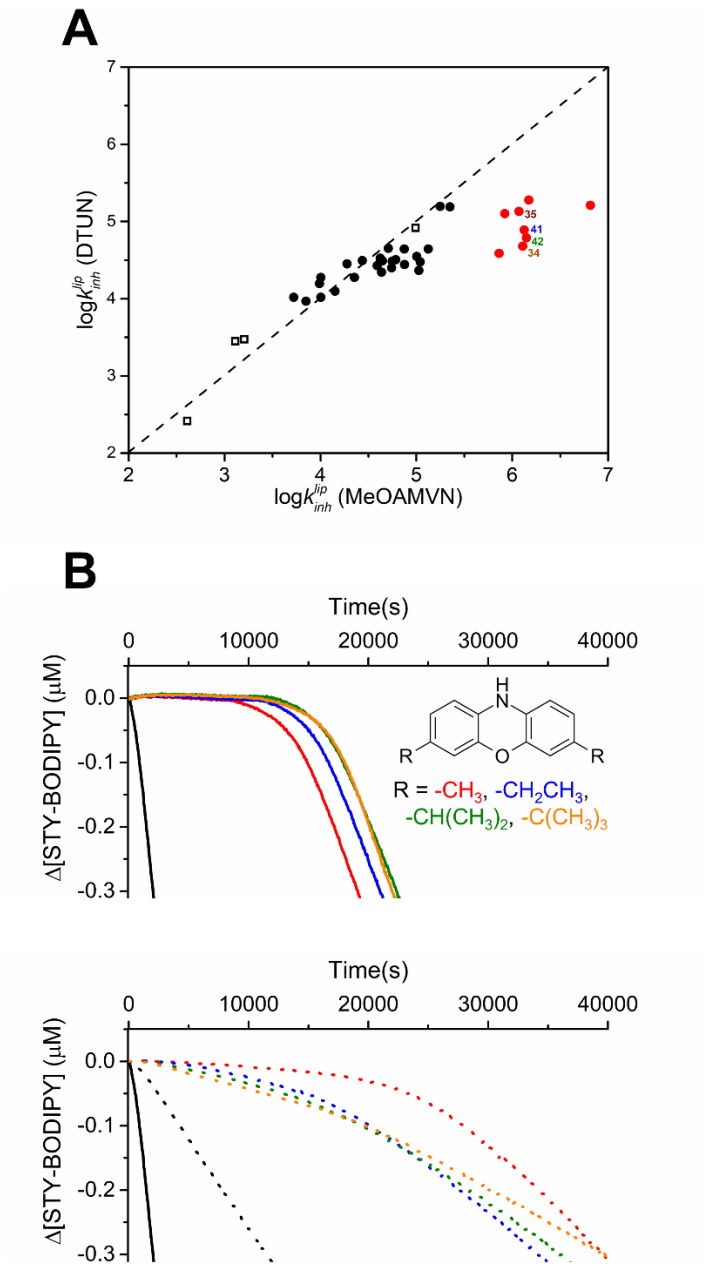


Figure 3.4. (A) Correlation of k_{inh}^{lip} values determined from DTUN-initiated autoxidations of egg PC liposomes versus those determined (or predicted) from MeOAMVN-initiated autoxidations. MeOAMVN-initiated vs DTUN-initiated + 100 μM ascorbate (●); predicted from Eq. 4 vs DTUN-initiated + 100 μM ascorbate (●); MeOAMVN-initiated vs DTUN -initiated without ascorbate (□). **(B)** Representative data from co-autoxidations of STY-BODIPY (1 μM) and liposomal egg phosphatidylcholine (1 mM) suspended in PBS (pH 7.4) initiated with DTUN (200 μM) at 37°C and monitored by fluorescence ($\lambda_{ex}/\lambda_{em}$ = 488/518 nm). *(Top)* 3,7-Me-PNX (**3.35**), 3,7-Et-PNX (**3.41**), 3,7-iPr-PNX (**3.42**) and 3,7-tBu-PNX (**3.34**) at 4 μM in the absence of ascorbate; *(Bottom)* aforementioned at 400 nM in the presence of 100 μM of ascorbate.

3.4.3 Ferroptosis Inhibition, First-Pass Metabolic Stability and Validation in Vivo.

The potencies of the PNX and PTZ derivatives as ferroptosis inhibitors were evaluated in Pfa-1 mouse embryonic fibroblasts (MEFs).[9] Protection from RSL3-induced cell death (150 nM for 5 hours) was assessed by AquaBluer assay and EC_{50} values were derived from the corresponding survival curves. Representative examples are shown in Figures 5A-C with all data given in the Supporting Information (see Table 3.5). EC_{50} values ranged over three orders of magnitude, from 4 nM to upwards of >1 μM, but importantly, all of the PNX and PTZ derivatives inhibited cell death. Furthermore, many of the compounds were more potent than the 'benchmark' ferroptosis inhibitors Fer-1 and Lip-1, for which EC_{50} values of 27 and 18 nM, respectively, were determined under the assay conditions.

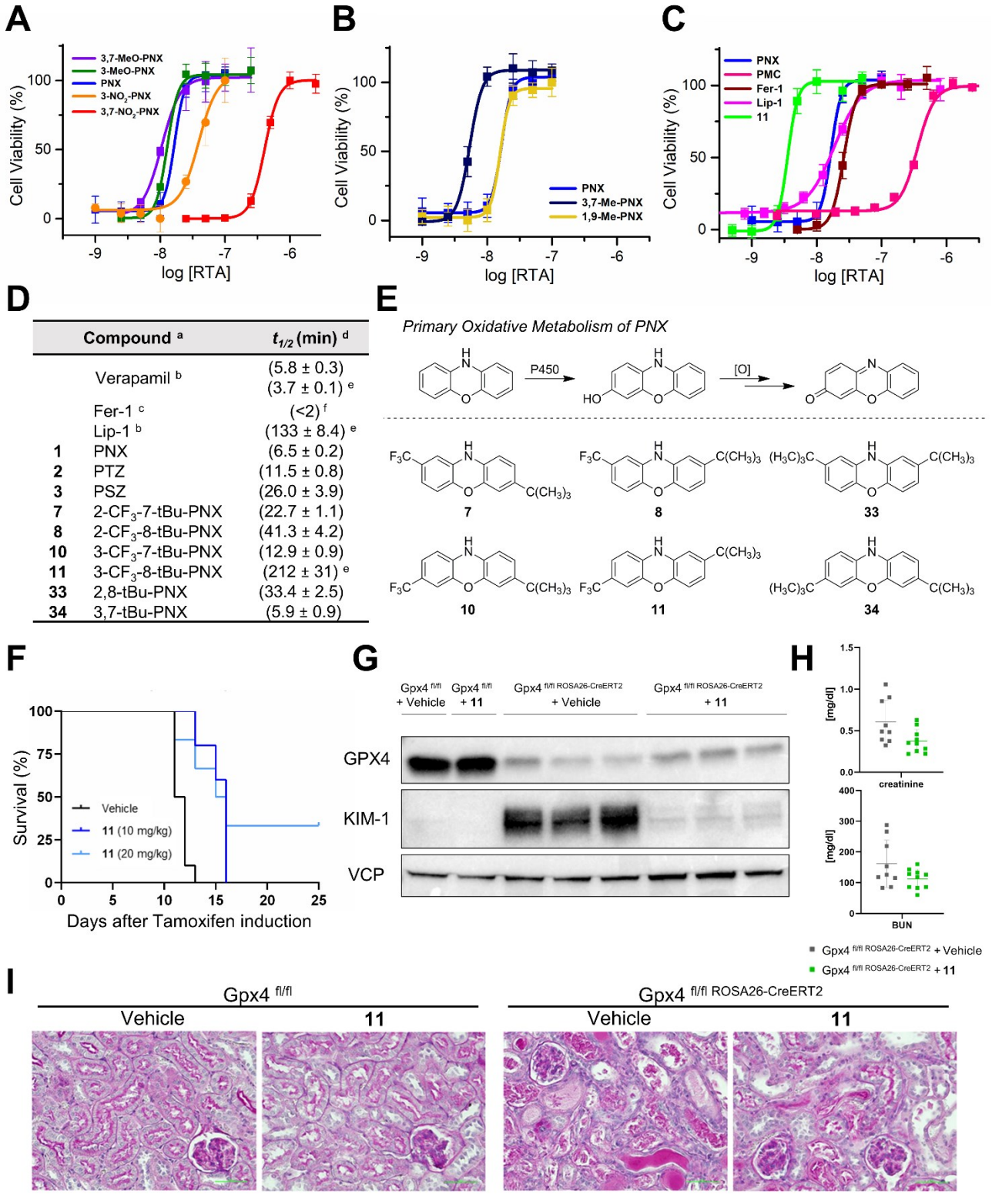
Introduction of EW groups on PNX (Figure 3.5A) led to an obvious decrease in potency (e.g. EC_{50}s of 16, 43 and 405 nM were determined for PNX, 3-NO_2-PNX **3.15** and 3,7-NO_2-PNX **3.19**, respectively), consistent with the decrease in inherent RTA activity (*vide supra*). However the introduction of ED groups did not lead to a corresponding increase in potency (e.g. EC_{50}s of 16, 12 and 11 nM were determined for PNX, 3-MeO-PNX **3.39** and 3,7-MeO-PNX **3.40**, respectively). A similar trend was observed with the PTZ derivatives (Figure 3.27); EC_{50}s for 3,7-NO_2-PTZ **3.29**, 3-NO_2-PTZ **3.28**, PTZ and 3,7-MeO-PTZ **3.32** are ≥1000, 140, 24 and 9 nM, respectively. Second, when comparing compounds with similar electronics, derivatives of greater lipophilicity possess greater potency. This is most obvious from compounds which feature CF_3 substitution; despite being an EW group, its introduction leads to greater potency, e.g. 2-CF_3-PNX **3.6** and 3-CF-PNX **3.9** have lower EC_{50}s (9 and 12 nM, respectively) than PNX (16 nM). Third, steric hinderance around the reactive N-H has only a marginal impact on potency; 3,7-di-Me-PNX **3.35** and 1,9-di-Me-PNX **3.36** (Figure 3.5B) have EC_{50}s of 6 and 14 nM, respectively, such that the modest electronic effect of methyl substitution is effectively negated by the steric effect.

PNX is known to be metabolically labile, undergoing P450 mediated hydroxylation at the 3- and/or 7-positions to yield phenoxazone and resorufin derivatives (Figure 3.5D).[53,54] Since all but the very electron-poor PNX (and PTZ) derivatives were potent ferroptosis inhibitors, we expected that appropriately-substituted derivatives may exhibit good metabolic stability and

remain sufficiently potent to display activity *in vivo*. Thus, a subset of PNX derivatives with non-oxidizable substituents (i.e. *t*Bu and CF_3) were subjected to liver microsome (BALB/c mouse) stability assays (Figure 3.5E). To maintain a common basis for comparison, verapamil hydrochloride was used as a high clearance standard. Fer-1 and Lip-1 were also included in the test set.

As expected, PNX was rapidly metabolized, with a half-life similar to that of verapamil. Fer-1 was even more rapidly metabolized, and had to be evaluated at a lower microsome concentration (0.1 mg/mL) to determine a reliable half-life. The lack of first-pass metabolic stability of Fer-1, particularly in mouse liver microsomes, has been documented and has motivated a medicinal chemistry campaign aimed to ameliorate this shortcoming.[40] In contrast, and fully consistent with earlier data,[9] Lip-1 was quite stable, with a half-life >2 hours. While PNX derivatives featuring substitution at the 3- and 7-positions (**3.10** and **3.34**) were no more stable than PNX itself, other isomers that may protect from hydroxylation at both ortho and para positions relative to the key N-H (i.e. **3.7**, **3.8**, **3.11** and **3.33**), demonstrated greater stability. The most stable PNX derivative we examined was **3.11** ($t_{1/2}$ = 212 ± 31 min) which compared favourably with Lip-1 ($t_{1/2}$ = 133 ± 8 min) under the same conditions (1 mg/mL microsomes).

Given its apparent tolerance to first-pass metabolism and high potency in preventing ferroptosis in MEFs (EC_{50} = 3.6 nM; Figure 3.5C), we assessed the potential of **3.11** to protect mice from kidney failure due to tissue-specific tamoxifen (TAM)-inducible GPx4 disruption. Following TAM treatment, *ROSA26-CreERT2*;*Gpx4fl/fl* mice – which were initially used to validate the in vivo efficacy of Lip-1[9] – were treated daily with **3.11** at either 10 or 20 mg/kg or vehicle. Gratifyingly, treatment with **3.11** was associated with substantially extended survival (median = 15.5 and 16 days, respectively) relative to the vehicle-treated group (median = 11.5 days), see Figure 3.5F. Survival coincided with reduced markers of kidney damage, such as kidney injury molecule-1 formation (Figure 3.5G), serum creatinine and blood urea nitrogen levels (Figure 3.5H), as well as fewer signs of tubular necrosis as determined by periodic acid Schiff (PAS)-staining in kidney tissue sections (Figure 3.5I). These results imply that **3.11** delays ferroptosis in kidney tubule cells, slowing kidney failure and prolonging the survival of these animals.



	Compound [a]	$t_{1/2}$ (min) [d]
	Verapamil [b]	(5.8 ± 0.3) (3.7 ± 0.1) [e]
	Fer-1 [c]	(<2) [f]
	Lip-1 [b]	(133 ± 8.4) [e]
1	PNX	(6.5 ± 0.2)
2	PTZ	(11.5 ± 0.8)
3	PSZ	(26.0 ± 3.9)
7	2-CF_3-7-tBu-PNX	(22.7 ± 1.1)
8	2-CF_3-8-tBu-PNX	(41.3 ± 4.2)
10	3-CF_3-7-tBu-PNX	(12.9 ± 0.9)
11	3-CF_3-8-tBu-PNX	(212 ± 31) [e]
33	2,8-tBu-PNX	(33.4 ± 2.5)
34	3,7-tBu-PNX	(5.9 ± 0.9)

Figure 3.5. (A-C) Examples of RSL3 induced ferroptosis of Pfa-1 MEFS inhibited by lipid soluble RTAs. **(D)** Results from liver microsomal stability experiments (BALB/c mouse). [a] 10

μM of compound (separated by RP-UPLC and monitored by PDA). [b] Compound at 1 μM (monitored by MS-ESI+) [c] [Fer-1] = 30 μM [d] Standard conditions: 0.5 mg/mL liver microsomes; 1 mM NADPH; 100 mM phosphate buffer (pH 7.4); 37ºC. [e] Liver microsomes increased (1.0 mg/mL). [f] At 0.5 mg/mL, Fer-1 was undetectable at 5 min, decreased to 0.1 mg/mL microsomes where $t_{1/2}$ = 5.3 ± 0.1 min was observed. **(F)** Compound **3.11** delays acute renal failure induced by *Gpx4* deletion and extends survival of mice at dose levels of 10 mg/kg (n=5) and 20 mg/kg (n=6), respectively, compared to vehicle control treatment (n=10); median survival was calculated to be 15.5 and 16 days for 10 and 20 mg/kg, respectively, and 11.5 days for the vehicle-treated group; Log-rank (Mantel-Cox) test: p = 0.0005. **(G)** Western Blot analysis at Day 9 after Tamoxifen treatment confirms GPx4 deletion in kidneys of *ROSA26-CreER^{T2}; Gpx4$^{fl/fl}$* animals, *Gpx4$^{fl/fl}$*mice were used as controls. *ROSA26-CreER^{T2};Gpx4$^{fl/fl}$* animals treated with vehicle only showed significantly elevated levels of the kidney injury biomarker Kidney Injury Molecule-1 (KIM-1), compared to compound **3.11** treated mice. **(H)** Serum analysis of Tamoxifen-treated *ROSA26-CreER^{T2};Gpx4$^{fl/fl}$* mice at Day 9 shows a significant reduction in creatinine levels of compound **3.11** (n=9) versus vehicle treated mice (n=10) (p = 0.0275) as well as a decrease in blood urea nitrogen (BUN). **(I)** Histological analysis of kidneys by periodic acid–Schiff (PAS) staining of Tamoxifen-treated *ROSA26-CreER^{T2};Gpx4$^{fl/fl}$* animals showed widespread tubular necrosis in the vehicle group, compared to compound **3.11** treatment (Day 9 after Tamoxifen induction). *Gpx4$^{fl/fl}$* animals were included as control (scale bar 50 μm).

3.5 Discussion

The well-established structure-activity relationships in phenolic and aminic RTAs are based on linear free energy relationships (LFERs) of inhibition rate constants (k_{inh}) with substituent constants, particularly Brown and Okamoto's electrophilic substituent constants, σ_p^+.[45,55,56] These excellent (negative) correlations arise because ED substituents stabilize the H-atom transfer transition state leading to the electron-poor phenoxyl/aminyl radical (Figure 3.6A), while EW substituents destabilize it. Plotting the k_{inh}^0 values for the PNX and PTZ derivatives versus the sum of the values of σ_p^+ of the substituents affords similarly excellent negative correlations, as shown in Figure 3.6B. The two correlations are roughly parallel, but vertically offset by roughly one order of magnitude due to the greater inherent reactivity of PNX compared to PTZ – a fact underpinned by their N-H BDEs (76.1 kcal/mol for the former *vs* 78.2 kcal/mol for the latter).[41,42,57] Plotting the corresponding k_{inh}^{lip} values versus $\sum\sigma_p^+$ leads to poorer correlations with much larger slopes and a convergence in the reactivity of the PNX and PTZ derivatives (Figure 3.6C). Indeed, due to the very strong H-bond basicity of the phosphodiester moiety, a LFER for RTA activity in phospholipids must account not only for how electronics change the intrinsic

reactivity, but also the engagement of the RTA in H-bonds (Figure 3.6D). To that end, the α_2^H H-bond acidity values of the PNX and PTZ derivatives correlate very well with nucleophilic substituent constants, σ_p^- (Figure 3.6E), given that H-bond donation increases the polarization of the N-H bond. Again, the correlations are vertically offset since the PNX derivatives are systematically more H-bond acidic than their PTZ counterparts. However, since ED substituents destabilize the N-H bond dipole, while EW substituents stabilize it, the α_2^H *vs* σ_p^- correlations have opposite slopes to those of the k_{inh}^{Lip} *vs* σ_p^+ correlations. Thus, the reason behind the poor correlations in Figure 3.6C is clear: the two key factors affecting reactivity in phospholipid bilayers are modulated by electronic changes in opposing ways. Both factors can be taken into account in the two-parameter correlation in Figure 3.6F, where the k_{inh}^{lip} values are plotted as a function of σ_p^+ and σ_p^-. Since this effectively accounts for the suppression in k_{inh} due to H-bonding via σ_p^- (as opposed to measured α_2^H values), k_{inh}^{lip} values (and ferroptosis inhibitor potency, vide infra) for PNX and PTZ derivatives can be predicted direct from σ_{p}^+ and σ_{p}^- substituent constants, of which hundreds are available.[58]

Significantly augmented substituent effects on k_{inh}^{lip} relative to k_{inh}^0 are evident on comparing the correlations in Figures 3.6B and 3.6C. Indeed, in such a prodigious H-bond accepting environment as phospholipid bilayers (β_2^H ~0.69), substituent effects on H-bond acidity can be at least as important as substituent effects on inherent H-atom transfer reactivity. This is underscored by the fact that the coefficients for $\sum\sigma_p^+$ and $\sum\sigma_p^-$ in the two-parameter correlation in Figure 3.6F are so similar. Thus, H-bonding is not only key to understanding the difference in reactivity of classes of RTAs in phospholipids and rationalizing their anti-ferroptotic potency (*vide infra*), but also to substituent effects within classes of RTA. Consider, as highlighted in Figure 3.7, that although the sterically-hindered PTZ derivative **3.31** has relatively poor inherent RTA activity (k_{inh}^0 = 3.7×10^5 M^{-1}s^{-1}), it almost fully translates to liposomes (k_{inh}^{lip} = 9.8×10^4 M^{-1}s^{-1}) because it is such a poor H-bond donor (α_2^H = 0.06). At the other extreme is PNX derivative **3.19**; while it is 36-fold *more* inherently reactive than **3.31**, it is 75-fold *less* reactive in phospholipids due to its high H-bond acidity (α_2^H = 0.72). These results highlight that minimizing H-bonding interactions should be a key consideration in the design and/or optimization of ferroptosis inhibitors.

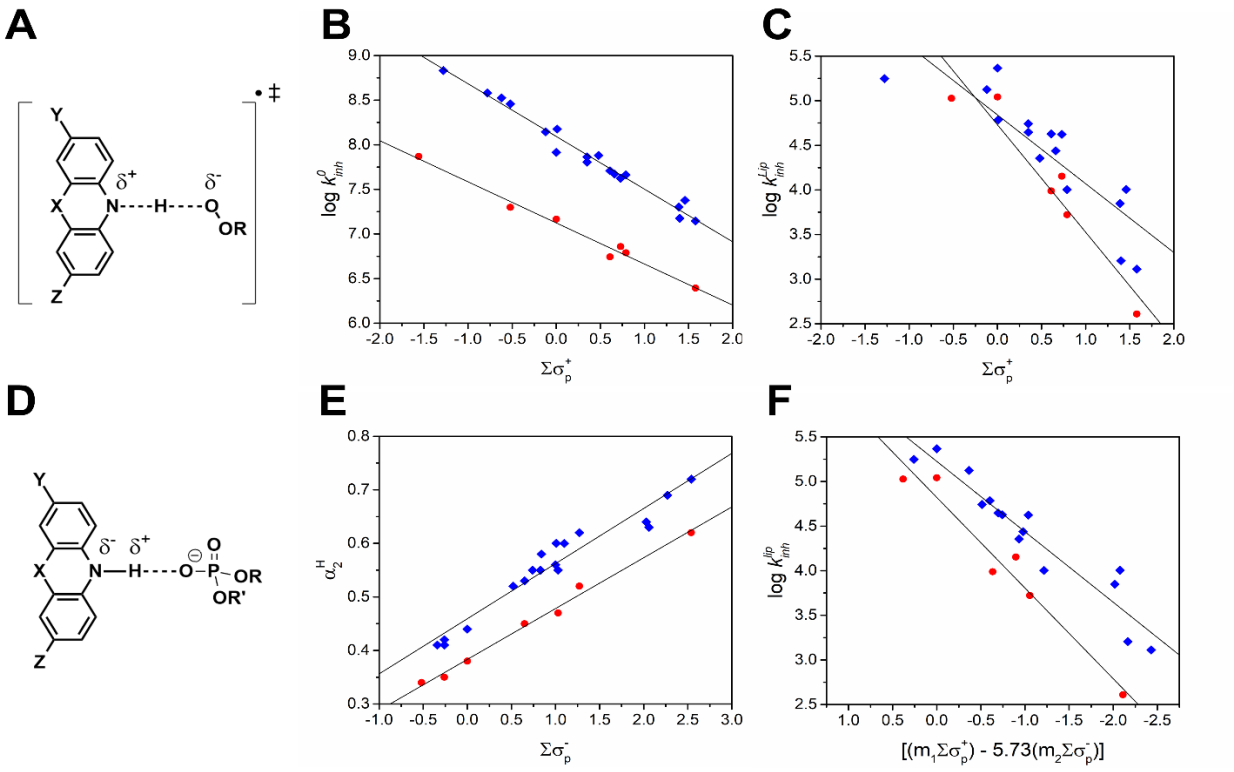


Figure 3.6. (**A**) The expected polarization of the transition state for H-atom transfer from substituted PNX and PTZ derivatives to peroxyl radicals. (**B**) $\Sigma\sigma_p^+$ vs $\log(k^0_{inh})$ for the 3 and 3,7-susbtituted PNX (♦) (R^2 = 0.977; y = -0.590x + 8.093) and PTZ (●) (R^2 = 0.983; y = -0.461x + 7.124). **(C)** $\Sigma\sigma_p^+$ vs $\log(k^{lip}_{inh})$ (initiated by MeOAMVN). Only compounds that could be measured directly (see Table 3.1). PNX (R^2 = 0.745) and PTZ (R^2 = 0.916). **(D)** The polarization of the H-bonding interaction between the substituted PNX and PTZ derivatives and phospholipids is expected to be opposite to the TS in (A). (**E**) $\Sigma\sigma_p^-$ vs α_2^H for PNX (R^2 = 0.940; y = 0.103x + 0.459) and PTZ (R^2 = 0.991; y = 0.095x + 0.383). **(F)** $[(m_1\Sigma\sigma_p^+) - 5.73(m_2\Sigma\sigma_p^+)]$ vs $\log(k^{lip}_{inh})$ where m_1 and m_2 are the slopes from A and C respectively and $5.73 = 8.3\beta_2^H$ (assuming $\beta_2^H = 0.69$). PNX (R^2 = 0.907; y = 0.789x + 5.226) and PTZ (R^2 = 0.956; y = 1.016x + 4.822).

Deconvolution of observed k^{lip}_{inh} in terms of k^0_{inh} and α_2^H is useful for understanding substituent effects on RTA kinetics beyond the series of PNX and PTZ derivatives above. For example, changing the chalcogen bridge of PNX from oxygen to selenium (PSZ) results in 15-fold decrease in k^0_{inh}, but the difference in k^{lip}_{inh} is a mere factor of 4. While the selenium atom is a comparatively poor electron-donor to the amine/aminyl than the oxygen in PNX (or sulfur in PTZ), raising the N-H BDE in PSZ relative to PNX (and PTZ),[42] its lower electronegativity is associated with a lower H-bond acidity (α_2^H= 0.36 *vs* 0.44). Although this appears to be a modest

difference, in such a potent H-bond accepting medium as phospholipids, this makes up for more than half the intrinsic reactivity difference.

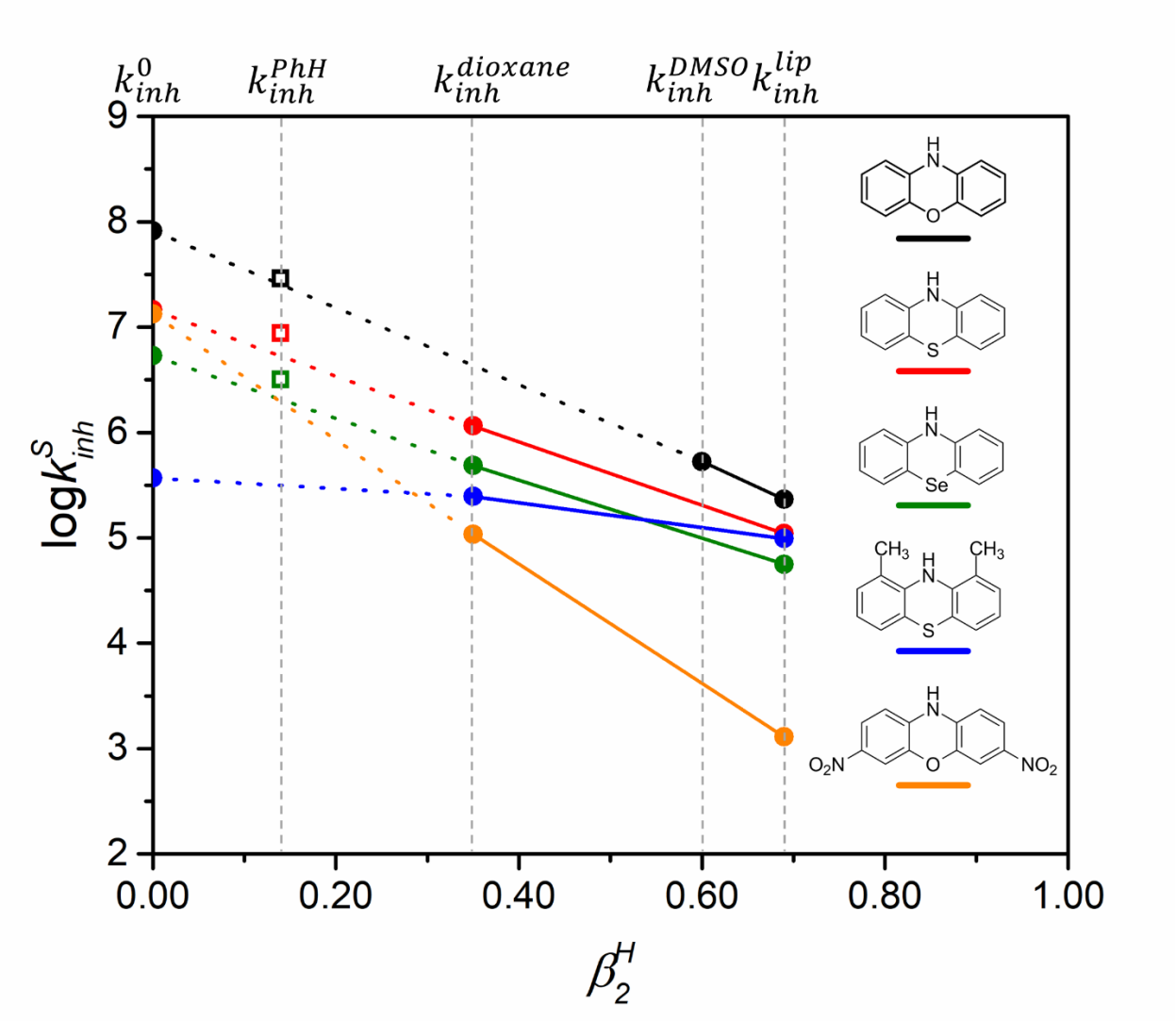
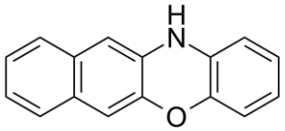


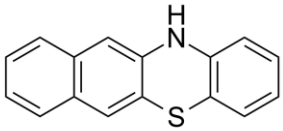
Figure 3.7. Values of $\log k_{inh}$ determined at 37°C plotted as a function of medium. PNX (black), PTZ (red), PSZ (green), 1,9-Me-PTZ **3.31** (blue), and 3,7-NO_2-PNX **3.19** (orange). Empty squares (□) correspond to values previously reported by Lucarini *et al* in benzene.[42]

Application of these structure-reactivity concepts to rationalize trends in cytoprotective potency is further nuanced. For example, it has been previously observed that benzo(*b*)-PTZ (**3.5**) better protects HT-22 cells from glutamate-induced death than PTZ (EC_{50} = 8 nM *vs.* 30 nM, respectively). At the time, the result was rationalized by increased stabilization of the radical derived from **3.5** relative to that derived from PTZ.[59] However, we have found that benzo(*b*)-

PTZ (**3.5**) and benzo(*b*)-PNX (**3.4**) have similar inherent reactivity (k_{inh}^{0}) to PTZ and PNX, respectively (Table 3.1). Moreover, in liposomes, the k_{inh}^{lip} values of the benzannulated derivatives are actually lower than those of the parent PTZ and PNX structures – an observation which we can attribute to their higher H-bond acidities (i.e. α_2^H = 0.49 for benzo(*b*)-PNX *vs.* 0.44 for PNX, Table 3.1). Nevertheless, consistent with the previous results in HT-22 cells, we found that each of benzo(*b*)-PTZ and benzo(*b*)-PNX were more potent inhibitors of cell death in RSL3-treated Pfa1 MEFs (EC_{50} = 8 nM and 5 nM) than PTZ and PNX (EC_{50} = 24 nM and 16 nM), respectively (coincidently by about a factor of 3). Given how otherwise similar the structures are, it would seem that the increased potency is associated with the increased lipophilicity of the benzannulated structures (*cf.* benzo(*b*)-PNX (log*P* = 5.07) over PNX (log*P* = 3.84)).[60]



4



5

Ferroptosis inhibitor potency has hitherto been rationalized either by changes in lipophilicity[59,61] and/or intrinsic reactivity.[38,43] We assessed the contribution of these factors to the potency of the PNX and PTZ derivatives to inhibit ferroptosis in Pfa1 MEFs in terms of log*P* and $\log k_{inh}^{lip}$, respectively. Using only the compounds which had directly measurable k_{inh}^{lip} values (for autoxidations initiated with MeOAMVN), we found positive, but poor, correlations between potency (|logEC_{50}|) and calculated log*P* (R_{adj}^2 = 0.587) or $\log k_{inh}^{lip}$ (R_{adj}^2 = 0.506), (Figure 3.26). Performing a multiple linear regression with both variables rendered a much better correlation, with an adjusted R^2 of 0.796 (Figure 3.8A),[62] which seems sufficient to be of practical use.

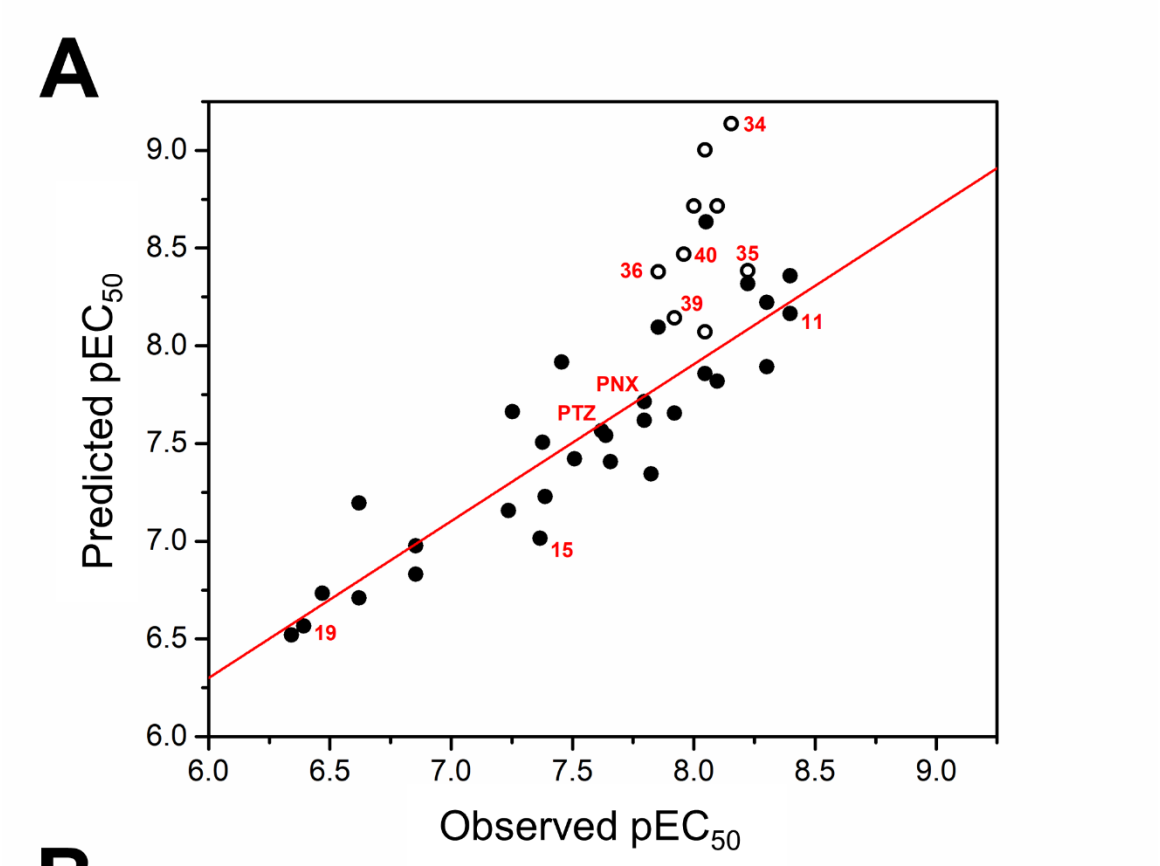
The observation that potency correlates with both k_{inh}^{lip} and lipophilicity prompts the obvious question: will potency continually improve upon maximizing these parameters? Assuming the increases in log*P* would manifest as a higher concentration of RTA in a bilayer, at a certain level of lipophilicity the added RTA will be entirely in the lipid with no partitioning into the cytosol/extracellular space. Moosmann and coworkers, working with alkylated phenothiazines,[59] as well as Hecht and coworkers, working with alkylated methylene blue derivatives,[61]

independently observed that systematic increases in the chain length of the alkyl moiety improved cytoprotection relative to their respective parent structures. However, they also observed that there was a point where further increases in lipophilicity did *not* further enhance potency, and in fact, caused some diminution in activity.[59,61] We made similar observations with aza-analogues of α-TOH.[17] Some of the current results are consistent with these observations, albeit not in terms of absolute chain length, but overall lipophilicity. For instance, **3.35** (log*P* = 4.76) and **3.34** (log*P* = 7.22) have essentially equivalent potency (6 nM *vs* 7 nM). The regression observed by Moosmann and Hecht for very lipophilic compounds may be due to attenuated recycling of the compounds analogous to the differences in k_{inh}^{lip} and *n* we observed comparing **3.35** and **3.34** in the presence of ascorbic acid. Beyond these examples, more lipophilic compounds tended to have lower k_{inh}^{lip} under the ascorbate conditions compared to less lipophilic compounds with similar k_{inh}^{0} and α_2^H values (e.g. **3.6** vs **3.7**/**3.8** and **3.9** vs **3.10**/**3.11**). Comparative studies of α-TOH and PMC have revealed that large alkyl substituents can adversely affect diffusion/mobility in a membrane,[30,63] so similar trends can be expected for scaffolds such as PNX and PTZ.

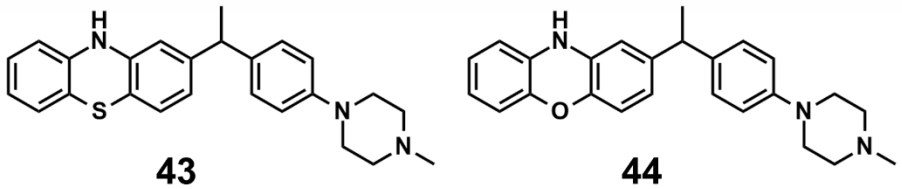
The relationship between k_{inh}^{lip} and potency is most obvious with heavily deactivated derivatives of PNX and PTZ. For instance, comparing PNX, **3.15**, and **3.19** which possess similar predicted log*P* values, there is a wide spread in terms measured k_{inh}^{lip} values (2-orders of magnitude), and this is seemingly reflected in the observed EC_{50} values (16 nM, 43 nM, and 405 nM, respectively). Similarly, the decrease in k_{inh}^{lip} between PTZ and **3.28** also appears to correspond to a lower EC_{50} (24 nM vs 140 nM). The matter, however, becomes somewhat more nuanced when the RTAs are only moderately deactivated. The 4-fold decrease in k_{inh}^{lip} between **3.9** and **3.26** (4.2×10^4 $M^{-1}s^{-1}$ and 9.8×10^3 $M^{-1}s^{-1}$) translates to about a 3.4-fold difference in EC_{50} (12 nM and 41 nM), but the similar 4-fold decrease between **3.6** and **3.25** (7.5×10^4 $M^{-1}s^{-1}$ and 1.9×10^4 $M^{-1}s^{-1}$) renders a more subtle change in potency (9 nM and 16 nM). As is the case with increasing lipophilicity, there seems to be a threshold of diminished returns where further increases in k_{inh} is of little benefit. In fact, the most potent compound is **3.11** (3.6 nM) which does not have the largest k_{inh}^{lip} (4.4×10^4 $M^{-1}s^{-1}$). Although there are several compounds characterized by k_{inh}^{lip}

values that are 4 to 5-fold greater, including the related positional isomers, they do not exceed its potency.

It seems reasonable to consider that the plateau in potency arises because the rate at which an RTA reacts with a propagating (phospho)lipid peroxyl radical in the membrane has reached its maximum, which appears to be in the vicinity of k_{inh}^{lip} ~2.0×10^5 M^{-1}s^{-1}. The largest k_{inh}^{0} we have derived is 1.3×10^9 M^{-1}s^{-1} (for 3,7-MeO-PNX **3.40**). In principle, a bimolecular reaction could be up to an order of magnitude faster in a non-viscous solvent (e.g. PhCl, η ~ 0.75 cP at 25 °C),[64] where a diffusion-limited reaction would correspond to ~1×10^{10} M^{-1}s^{-1}. Starting from this point, and taking into account the microviscosity of the lipid bilayers of egg PC liposomes (70-110 cP at 37 °C),[65] application of the Einstein-Stokes equation suggests a maximum k_{inh}^{lip} in the range of 6 to 10×10^7 M^{-1}s^{-1}. If the H-bonding interactions between the RTA and the phosphate diester headgroup are then taken into account, the maximum observable k_{inh} (for PNX, as an example, for which α_2^H = 0.44) would drop another 2.5 orders of magnitude, to 2 to 3×10^5 M^{-1}s^{-1}, strikingly coincident with the largest values of k_{inh}^{lip} that we can measure (either directly with MeOAMVN as an initiator or indirectly with DTUN as initiator and ascorbate to regenerate small quantities of RTA). Of course, RTAs which experience less H-bonding will have higher maximum k_{inh} values (and hence, possibly greater potency), but this generally requires steric hinderance which also decreases the inherent reactivity. For example, 1,9-Me-PNX **3.36** has a low α_2^H of 0.12, but since its k_{inh}^{0} is only 5.6×10^6 M^{-1}s^{-1}, k_{inh}^{lip} is predicted to be 1.1×10^6 M^{-1}s^{-1}. This may indeed be the case, but because its regeneration by ascorbate is inefficient, we cannot accurately measure it. Still, using this predicted k_{inh}^{lip} and predicted log$P$ = 4.76, an EC_{50} of 4 nM can be expected (Figure 3.8) in good agreement with the observed value of 14±2 nM, and well within the vicinity of the apparent plateau.[66]



B



	43	**44**
k_{inh}^{lip}	8.9 × 10^4 $M^{-1}s^{-1}$	31 × 10^4 $M^{-1}s^{-1}$ [a]
log*P*	6.07	5.76
EC_{50}	6.5 ± 0.5 nM	7.4 ± 0.5 nM
(Predicted)	(7.0 nM)	(4.4 nM)

Figure 3.8. (A) Multi-regression correlation for pEC_{50} vs $\log k_{inh}^{lip}$ and log*P* ($R_{adj}^2 = 0.796$; $pEC_{50} = 0.550(\log k_{inh}^{lip}) + 0.297(\log P) + 3.631$). Empty symbols correspond to predicted values of pEC_{50} from the estimated values of $\log k_{inh}^{lip}$ given in Figure 3.2G. **(B)** Structures of compounds **3.43** and **3.44** and the predicted EC_{50} using k_{inh}^{lip} (MeOAMVN) and log*P*.[55] [a] Estimated using Eq. 4.

In light of the plateau in reactivity/potency observed for PNX and PTZ derivatives substituted with activating (i.e. electron-donating) groups, we were intrigued by a recent report that a substituted PTZ (**3.43**) was 2 orders of magnitude more potent than PTZ in an erastin-induced ferroptosis rescue assay in HT-1080 cells (i.e. EC_{50} of 0.5 nM and 49 nM, respectively).[67] We wondered if the particular substitution of the PTZ scaffold in **3.43** conferred some exceptional RTA dynamics in the lipid bilayer, or if instead, the compound could act by some other non-RTA mechanism. Thus, we synthesized **3.43** as well as its PNX counterpart (**3.44**), which we anticipated would be slightly more potent than **3.43**. In inhibited autoxidations of liposomal phospholipids, **3.43** and **3.44** exhibited essentially indistinguishable activity to their parent structures, fully consistent with our other observations. Although **3.43** and **3.44** were indeed more potent than their parent structures in ferroptosis rescue in MEFs, the difference was relatively modest (EC_{50} = 6.5 and 7.4 nM *vs* 24 and 16 nM, respectively), and can be attributed simply to their increased predicted log*P* (6.07 and 5.76 *vs* 4.15 and 3.84, respectively). Indeed, using the multi-parameter fit of the data in Figure 3.8, EC_{50} values of 7.0 and 4.4 nM were predicted for **3.43** and **3.44** on the basis of their log*P* and k_{inh}^{lip} values, scarcely different from our measured values.[68]

Ferroptosis inhibitors with sub-nanomolar potency have yet to be reported in cell rescue experiments (with the aforementioned exception). The existence of a threshold to inhibitor potency is not particularly surprising in view of the autoxidative process that leads to cell death and how RTAs function as inhibitors. Since the RTA mechanism relies on its competition with oxidizable lipids for propagating peroxyl radicals, at some point, the margin by which it wins no longer matters; the chain reactions will be fully suppressed to the extent physically possible. At that point, a key determinant could be the extent to which the RTA can be regenerated. The relevance of RTA regeneration in ferroptosis suppression is unclear. It is noteworthy that although we chose to use ascorbate in the above investigations, it could simply be considered a 'model' reductant, since there are several other reductants that may regenerate ferroptosis-suppressing RTAs in situ. For example, we recently showed that PNX and PTZ can even be efficiently recycled from their corresponding aminyl radicals by hydroperoxyl, the conjugate acid of superoxide.[73] These observations, and the linkage of the ferroptosis-resistant phenotype associated with FSP1 expression to its ability to maintain reduced coenzyme Q_{10} to act either

directly as an RTA or indirectly via its capacity to regenerate the more reactive α-TOH, suggests RTA regeneration can be important. The availability of potent structurally-related inhibitors that vary dramatically in the efficiency with which they can be regenerated may enable clarification of the role of inhibitor regeneration in ferroptosis suppression.

Although this investigation was motivated by our interest in probing the limitations to optimization of RTA activity in the development of ferroptosis inhibitors, we sought to demonstrate proof-of-principle by evaluating one of the more promising compounds in an animal model of ferroptosis-related disease. In the event, phenoxazine **3.11** successfully suppressed kidney failure due to tissue-specific disruption of GPx4, similarly to the archetype ferroptosis inhibitor Lip-1. We consider this finding to be tremendously exciting; Lip-1 was identified from screening a 40,000-compound library of drug-like molecules, whereas **3.11** was selected for *in vivo* study simply on the basis of its good RTA activity and acceptable microsomal stability. As such, we believe it to be a very attractive lead compound for a medicinal chemistry campaign aimed at optimizing its non-RTA characteristics. This is underscored by the structure-reactivity-potency data provided above, which clearly show that the PNX scaffold can tolerate varied substitution with little impact on its excellent anti-ferroptotic potency. It should also be pointed out that related phenothiazine compounds are well-established as blood-brain barrier permeable therapeutics,[69,70] (and indeed have been shown to mitigate post-ischemia and post-TBI brain damage in animal models)[67,71–73] a feature which, if held in common, will greatly enable their development as therapeutics for neurodegeneration.

3.6 Conclusion

Our investigations of the RTA kinetics and anti-ferroptotic activity of over 40 different PNX, PTZ and related azine structures have revealed structure-reactivity-potency relationships that provide key insights on the design and/or optimization of ferroptosis inhibitors. The suppression of RTA activity in phospholipids due to strong H-bond interactions between the inhibitor and the phospholipid headgroup was validated in phosphatidylcholine liposomes. Although this diminution in activity ranged from mild (4-fold) to severe (10,000-fold), it could nevertheless be reliably predicted from the H-bond acidity (α_2^H) of the inhibitor. The introduction of EWGs at the 2-, 3-, 7- and/or 8-positions of the PNX/PTZ derivatives expectedly decreased the intrinsic

reactivity of the azine derivative, which was compounded by a corresponding increase in α_2^H. In contrast, EDGs increased intrinsic reactivity, but had little effect on α_2^H and did not translate to significant gains in phospholipids or cells. We expect that the compounded suppression of RTA activity in phospholipid bilayers by EWGs will universally apply to other phenolic and aromatic amine scaffolds and could be even more significant for less inherently reactive ferroptosis inhibitor scaffolds. We demonstrate that an additional advantage of azine RTAs are their efficient regeneration by ascorbate (and presumably other appropriate one-electron donors), which is demonstrably superior to the canonical couple of vitamins E and C, and may contribute to their superiority as ferroptosis inhibitors. This synergy was utilized for the kinetic characterization of RTAs which were too reactive in liposomes to do so otherwise, and enabled quantification and rationalization of the apparent ceiling in RTA reactivity in phospholipids due to diffusion-limited encounter of propagating radicals. Having revealed this intrinsic limitation, we identified a PNX derivative that was resistant to mouse primary metabolism and demonstrated in vivo anti-ferroptotic activity in a model of acute kidney failure. It remains to be seen which pathologies/tissues may be most suitable for targeting using an RTA-based approach. Nevertheless, this proof-of-principle highlights key considerations for the future rational design and/or optimization of ferroptosis inhibitors for therapeutic purposes.

3.7 References

(1) Farmer, L. A.; Wu, Z.; Poon, J.-F.; Zilka, O.; Lorenz, S. M.; Huehn, S.; Proneth, B.; Conrad, M.; Pratt, D. A. Intrinsic and Extrinsic Limitations to the Design and Optimization of Inhibitors of Lipid Peroxidation and Associated Cell Death. *J. Am. Chem. Soc.* **2022**, *144* (32), 14706–14721. https://doi.org/10.1021/jacs.2c05252.

(2) Jiang, X.; Stockwell, B. R.; Conrad, M. Ferroptosis: Mechanisms, Biology and Role in Disease. *Nat. Rev. Mol. Cell Biol.* **2021**, *22* (4), 266–282. https://doi.org/10.1038/s41580-020-00324-8.

(3) Stockwell, B. R.; Jiang, X. The Chemistry and Biology of Ferroptosis. *Cell Chem. Biol.* **2020**, *27* (4), 365–375. https://doi.org/https://doi.org/10.1016/j.chembiol.2020.03.013.

(4) Conrad, M.; Pratt, D. A. The Chemical Basis of Ferroptosis. *Nat. Chem. Biol.* **2019**, *15* (12), 1137–1147. https://doi.org/10.1038/s41589-019-0408-1.

(5) Riegman, M.; Sagie, L.; Galed, C.; Levin, T.; Steinberg, N.; Dixon, S. J.; Wiesner, U.; Bradbury, M. S.; Niethammer, P.; Zaritsky, A.; Overholtzer, M. Ferroptosis Occurs through an Osmotic Mechanism and Propagates Independently of Cell Rupture. *Nat. Cell Biol.* **2020**, *22* (9), 1042–1048. https://doi.org/10.1038/s41556-020-0565-1.

(6) Stockwell, B. R.; Friedmann Angeli, J. P.; Bayir, H.; Bush, A. I.; Conrad, M.; Dixon, S. J.; Fulda, S.; Gascón, S.; Hatzios, S. K.; Kagan, V. E.; Noel, K.; Jiang, X.; Linkermann, A.; Murphy, M. E.; Overholtzer, M.; Oyagi, A.; Pagnussat, G. C.; Park, J.; Ran, Q.; Rosenfeld, C. S.; Salnikow, K.; Tang, D.; Torti, F. M.; Torti, S. V; Toyokuni, S.; Woerpel, K. A.; Zhang, D. D. Ferroptosis: A Regulated Cell Death Nexus Linking Metabolism, Redox Biology, and Disease. *Cell* **2017**, *171* (2), 273–285. https://doi.org/https://doi.org/10.1016/j.cell.2017.09.021.

(7) Masaldan, S.; Bush, A. I.; Devos, D.; Rolland, A. S.; Moreau, C. Striking While the Iron Is Hot: Iron Metabolism and Ferroptosis in Neurodegeneration. *Free Radic. Biol. Med.* **2019**, *133*, 221–233. https://doi.org/https://doi.org/10.1016/j.freeradbiomed.2018.09.033.

(8) Dixon, S. J.; Lemberg, K. M.; Lamprecht, M. R.; Skouta, R.; Zaitsev, E. M.; Gleason, C. E.; Patel, D. N.; Bauer, A. J.; Cantley, A. M.; Yang, W. S.; Morrison, B.; Stockwell, B. R. Ferroptosis: An Iron-Dependent Form of Nonapoptotic Cell Death. *Cell* **2012**, *149* (5), 1060–1072. https://doi.org/10.1016/j.cell.2012.03.042.

(9) Friedmann Angeli, J. P.; Schneider, M.; Proneth, B.; Tyurina, Y. Y.; Tyurin, V. A.; Hammond, V. J.; Herbach, N.; Aichler, M.; Walch, A.; Eggenhofer, E.; Basavarajappa, D.; Radmark, O.; Kobayashi, S.; Seibt, T.; Beck, H.; Neff, F.; Esposito, I.; Wanke, R.; Forster, H.; Yefremova, O.; Heinrichmeyer, M.; Bornkamm, G. W.; Geissler, E. K.; Thomas, S. B.; Stockwell, B. R.; O'Donnell, V. B.; Kagan, V. E.; Schick, J. A.; Conrad, M. Inactivation of the Ferroptosis Regulator GPx4 Triggers Acute Renal Failure in Mice. *Nat. Cell Biol.* **2014**, *16* (12), 1180–1191.

(10) Haeggström, J. Z.; Funk, C. D. Lipoxygenase and Leukotriene Pathways: Biochemistry, Biology, and Roles in Disease. *Chem. Rev.* **2011**, *111* (10), 5866–5898. https://doi.org/10.1021/cr200246d.

(11) Yin, H.; Xu, L.; Porter, N. A. Free Radical Lipid Peroxidation: Mechanisms and Analysis.

Chem. Rev. **2011**, *111* (10), 5944–5972. https://doi.org/10.1021/cr200084z.

(12) Zielinski, Z. A. M.; Pratt, D. A. Lipid Peroxidation: Kinetics, Mechanisms, and Products. *J. Org. Chem.* **2017**, *82* (6), 2817–2825. https://doi.org/10.1021/acs.joc.7b00152.

(13) Helberg, J.; Pratt, D. A. Autoxidation vs. Antioxidants – the Fight for Forever. *Chem. Soc. Rev.* **2021**, *50* (13), 7343–7358. https://doi.org/10.1039/D1CS00265A.

(14) Ursini, F.; Maiorino, M.; Valente, M.; Ferri, L.; Gregolin, C. Purification from Pig Liver of a Protein Which Protects Liposomes and Biomembranes from Peroxidative Degradation and Exhibits Glutathione Peroxidase Activity on Phosphatidylcholine Hydroperoxides. *Biochim. Biophys. Acta - Lipids Lipid Metab.* **1982**, *710* (2), 197–211. https://doi.org/https://doi.org/10.1016/0005-2760(82)90150-3.

(15) Ingold, K. U.; Pratt, D. A. Advances in Radical-Trapping Antioxidant Chemistry in the 21st Century: A Kinetics and Mechanisms Perspective. *Chem. Rev.* **2014**, *114* (18), 9022–9046. https://doi.org/10.1021/cr500226n.

(16) Shah, R.; Shchepinov, M. S.; Pratt, D. A. Resolving the Role of Lipoxygenases in the Initiation and Execution of Ferroptosis. *ACS Cent. Sci.* **2018**, *4* (3), 387–396. https://doi.org/10.1021/acscentsci.7b00589.

(17) Zilka, O.; Shah, R.; Li, B.; Friedmann Angeli, J. P.; Griesser, M.; Conrad, M.; Pratt, D. A. On the Mechanism of Cytoprotection by Ferrostatin-1 and Liproxstatin-1 and the Role of Lipid Peroxidation in Ferroptotic Cell Death. *ACS Cent. Sci.* **2017**, *3* (3), 232–243. https://doi.org/10.1021/acscentsci.7b00028.

(18) Doll, S.; Freitas, F. P.; Shah, R.; Aldrovandi, M.; da Silva, M. C.; Ingold, I.; Goya Grocin, A.; Xavier da Silva, T. N.; Panzilius, E.; Scheel, C. H.; Mourão, A.; Buday, K.; Sato, M.; Wanninger, J.; Vignane, T.; Mohana, V.; Rehberg, M.; Flatley, A.; Schepers, A.; Kurz, A.; White, D.; Sauer, M.; Sattler, M.; Tate, E. W.; Schmitz, W.; Schulze, A.; O'Donnell, V.; Proneth, B.; Popowicz, G. M.; Pratt, D. A.; Angeli, J. P. F.; Conrad, M. FSP1 Is a Glutathione-Independent Ferroptosis Suppressor. *Nature* **2019**, *575* (7784), 693–698. https://doi.org/10.1038/s41586-019-1707-0.

(19) Bersuker, K.; Hendricks, J. M.; Li, Z.; Magtanong, L.; Ford, B.; Tang, P. H.; Roberts, M. A.; Tong, B.; Maimone, T. J.; Zoncu, R.; Bassik, M. C.; Nomura, D. K.; Dixon, S. J.; Olzmann, J. A. The CoQ Oxidoreductase FSP1 Acts Parallel to GPx4 to Inhibit Ferroptosis. *Nature* **2019**, *575* (7784), 688–692. https://doi.org/10.1038/s41586-019-1705-2.

(20) Soula, M.; Weber, R. A.; Zilka, O.; Alwaseem, H.; La, K.; Yen, F.; Molina, H.; Garcia-Bermudez, J.; Pratt, D. A.; Birsoy, K. Metabolic Determinants of Cancer Cell Sensitivity to Canonical Ferroptosis Inducers. *Nat. Chem. Biol.* **2020**, *16* (12), 1351–1360. https://doi.org/10.1038/s41589-020-0613-y.

(21) Kraft, V. A. N.; Bezjian, C. T.; Pfeiffer, S.; Ringelstetter, L.; Müller, C.; Zandkarimi, F.; Merl-Pham, J.; Bao, X.; Anastasov, N.; Kössl, J.; Brandner, S.; Daniels, J. D.; Schmitt-Kopplin, P.; Hauck, S. M.; Stockwell, B. R.; Hadian, K.; Schick, J. A. GTP Cyclohydrolase 1/Tetrahydrobiopterin Counteract Ferroptosis through Lipid Remodeling. *ACS Cent. Sci.* **2020**, *6* (1), 41–53. https://doi.org/10.1021/acscentsci.9b01063.

(22) Burton, G. W.; Ingold, K. U. Autoxidation of Biological Molecules. 1. The Antioxidant Activity of Vitamin E and Related Chain-Breaking Phenolic Antioxidants in Vitro. *J. Am. Chem. Soc.* **1981**, *103* (21), 6472–6477. https://doi.org/10.1021/ja00411a035.

(23) Barclay, L. R. C.; Ingold, K. U. Autoxidation of Biological Molecules. 2. The Autoxidation of a Model Membrane. A Comparison of the Autoxidation of Egg Lecithin Phosphatidylcholine in Water and in Chlorobenzene. *J. Am. Chem. Soc.* **1981**, *103* (21), 6478–6485. https://doi.org/10.1021/ja00411a036.

(24) Barclay, L. R. C.; Locke, S. J.; MacNeil, J. M.; VanKessel, J.; Burton, G. W.; Ingold, K. U. Autoxidation of Micelles and Model Membranes. Quantitative Kinetic Measurements Can Be Made by Using Either Water-Soluble or Lipid-Soluble Initiators with Water-Soluble or Lipid-Soluble Chain-Breaking Antioxidants. *J. Am. Chem. Soc.* **1984**, *106* (8), 2479–2481. https://doi.org/10.1021/ja00320a066.

(25) Barclay, L. R. C.; Locke, S. J.; MacNeil, J. M.; Vankessel, J. Quantitative Studies of the Autoxidation of Linoleate Monomers Sequestered in Phosphatidylcholine Bilayers. Absolute Rate Constants in Bilayers. *Can. J. Chem.* **1985**, *63* (10), 2633–2638. https://doi.org/10.1139/v85-437.

(26) Barclay, L. R. C.; Baskin, K. A.; Dakin, K. A.; Locke, S. J.; Vinqvist, M. R. The Antioxidant Activities of Phenolic Antioxidants in Free Radical Peroxidation of Phospholipid Membranes. *Can. J. Chem.* **1990**, *68* (12), 2258–2269. https://doi.org/10.1139/v90-348.

(27) Niki, E. Antioxidants in Relation to Lipid Peroxidation. *Chem. Phys. Lipids* **1987**, *44* (2–4), 227–253. https://doi.org/10.1016/0009-3084(87)90052-1.

(28) Takahashi, M.; Tsuchiya, J.; Niki, E. Scavenging of Radicals by Vitamin E in the Membranes As Studied by Spin Labeling. *J. Am. Chem. Soc.* **1989**, *111*, 6350–6353. https://doi.org/10.1021/ja00198a054.

(29) Gotoh, N.; Noguchi, N.; Tsuchiya, J.; Morita, K.; Sakai, H.; Shimasaki, H.; Niki, E. Inhibition of Oxidation of Low Density Lipoprotein by Vitamin E and Related Compounds. *Free Radic. Res.* **1996**, *24* (2), 123–134. https://doi.org/10.3109/10715769609088008.

(30) Niki, E.; Noguchi, N. Dynamics of Antioxidant Action of Vitamin E. *Acc. Chem. Res.* **2004**, *37* (1), 45–51. https://doi.org/10.1021/ar030069m.

(31) Niki, E. Role of Vitamin E as a Lipid-Soluble Peroxyl Radical Scavenger: In Vitro and in Vivo Evidence. *Free Radic. Biol. Med.* **2014**, *66*, 3–12. https://doi.org/10.1016/j.freeradbiomed.2013.03.022.

(32) Burton, G. W.; Traber, M. G.; Acuff, R. V; Walters, D. N.; Kayden, H.; Hughes, L.; Ingold, K. U. Human Plasma and Tissue Alpha-Tocopherol Concentrations in Response to Supplementation with Deuterated Natural and Synthetic Vitamin E. *Am. J. Clin. Nutr.* **1998**, *67* (4), 669–684. https://doi.org/10.1093/ajcn/67.4.669.

(33) Meier, R.; Tomizaki, T.; Schulze-Briese, C.; Baumann, U.; Stocker, A. The Molecular Basis of Vitamin E Retention: Structure of Human α-Tocopherol Transfer Protein. *J. Mol. Biol.* **2003**, *331* (3), 725–734. https://doi.org/https://doi.org/10.1016/S0022-

2836(03)00724-1.

(34) Kornbrust, D. J.; Mavis, R. D. Relative Susceptibility of Microsomes from Lung, Heart, Liver, Kidney, Brain and Testes to Lipid Peroxidation: Correlation with Vitamin E Content. *Lipids* **1980**, *15* (5), 315–322.

(35) In order to disambiguate between inhibition rate constants measured in different solvents/mediums, these values will be presented in the form k_{inh}^{S}, where the superscript '*S*' will indicate the solvent/medium used (i.e. chlorobenzene = PhCl, Egg PC liposomes = lip, intrinsic inhibition rate constant = 0).

(36) Burton, G. W.; Doba, T.; Gabe, E. J.; Hughes, L.; Lee, F. L.; Prasad, L.; Ingoldo, K. U. Autoxidation of Biological Molecules. 4. Maximizing the Antioxidant Activity of Phenols. *J. Am. Chem. Soc.* **1985**, *107* (24), 7053–7065. https://doi.org/10.1021/ja00310a049.

(37) Xu, L.; Davis, T. A.; Porter, N. A. Rate Constants for Peroxidation of Polyunsaturated Fatty Acids and Sterols in Solution and in Liposomes. *J. Am. Chem. Soc.* **2009**, *131* (36), 13037–13044. https://doi.org/10.1021/ja9029076.

(38) Shah, R.; Farmer, L. A.; Zilka, O.; Van Kessel, A. T. M.; Pratt, D. A. Beyond DPPH: Use of Fluorescence-Enabled Inhibited Autoxidation to Predict Oxidative Cell Death Rescue. *Cell Chem. Biol.* **2019**, *26* (11), 1594-1607.e7. https://doi.org/10.1016/j.chembiol.2019.09.007.

(39) Hofmans, S.; Berghe, T. Vanden; Devisscher, L.; Hassannia, B.; Lyssens, S.; Joossens, J.; Van Der Veken, P.; Vandenabeele, P.; Augustyns, K. Novel Ferroptosis Inhibitors with Improved Potency and ADME Properties. *J. Med. Chem.* **2016**, *59* (5), 2041–2053. https://doi.org/10.1021/acs.jmedchem.5b01641.

(40) Devisscher, L.; Van Coillie, S.; Hofmans, S.; Van Rompaey, D.; Goossens, K.; Meul, E.; Maes, L.; De Winter, H.; Van Der Veken, P.; Vandenabeele, P.; Berghe, T. Vanden; Augustyns, K. Discovery of Novel, Drug-Like Ferroptosis Inhibitors with in Vivo Efficacy. *J. Med. Chem.* **2018**, *61* (22), 10126–10140. https://doi.org/10.1021/acs.jmedchem.8b01299.

(41) Farmer, L. A.; Haidasz, E. A.; Griesser, M.; Pratt, D. A. Phenoxazine: A Privileged Scaffold for Radical-Trapping Antioxidants. *J. Org. Chem.* **2017**, *82* (19), 10523–10536. https://doi.org/10.1021/acs.joc.7b02025.

(42) Lucarini, M.; Pedrielli, P.; Pedulli, G. F.; Valgimigli, L.; Gigmes, D.; Tordo, P. Bond Dissociation Energies of the N-H Bond and Rate Constants for the Reaction with Alkyl, Alkoxyl, and Peroxyl Radicals of Phenothiazines and Related Compounds. *J. Am. Chem. Soc.* **1999**, *121*, 11546–11553. https://doi.org/10.1021/ja992904u.

(43) Shah, R.; Margison, K.; Pratt, D. A. The Potency of Diarylamine Radical-Trapping Antioxidants as Inhibitors of Ferroptosis Underscores the Role of Autoxidation in the Mechanism of Cell Death. *ACS Chem. Biol.* **2017**, *12* (10), 2538–2545. https://doi.org/10.1021/acschembio.7b00730.

(44) Haidasz, E. A.; Van Kessel, A. T. M.; Pratt, D. A. A Continuous Visible Light Spectrophotometric Approach to Accurately Determine the Reactivity of Radical-

Trapping Antioxidants. *J. Org. Chem.* **2016**, *81* (3), 737–744. https://doi.org/10.1021/acs.joc.5b02183.

(45) Snelgrove, D. W.; Lusztyk, J.; Banks, J. T.; Mulder, P.; Ingold, K. U. Kinetic Solvent Effects on Hydrogen-Atom Abstractions: Reliable, Quantitative Predictions via a Single Empirical Equation. *J. Am. Chem. Soc.* **2001**, *123* (3), 469–477. https://doi.org/10.1021/ja002301e.

(46) Abraham, M. H.; Abraham, R. J.; Byrne, J.; Griffiths, L. NMR Method for the Determination of Solute Hydrogen Bond Acidity. *J. Org. Chem.* **2006**, *71*, 3389–3394. https://doi.org/10.1021/JO052631N.

(47) Monitoring STY-BODIPY either by fluorescence or by absorbance can generally be done interchangeably (see the Supporting Information for some examples where both are used). Strongly absorbing RTAs, e.g. **3.17** and **3.18**, were incompatible with fluorescence assay due to fluorescence quenching.

(48) Compounds **3.30** and **3.31** were excluded from the analysis. Their low α_2^H values resulted in a substantial increase in the range of the plot with too few data points to populate the expanded range (strongly skewing the slope and intercept). See the Supporting Information for further details (Figure 3.13).

(49) The lower β_2^H value derived from the kinetic data in liposome suspension compared to that obtained directly from spectroscopic measurements in dilute solution may be related to the anisotropic nature of a phospholipid bilyaer. While a prospective H-bond donor species can access the phosphate ester of PC from any trajectory in an isotropic solution, in a liposome suspension the hydrophic effect may prevent some of the 'ideal' angles of hydrogen bonding from being accessed. Additionally, the water molecules at the interface will competively H-bond to the phosphate ester, lowering the effective β_2^H of PC in this context.

(50) Doba, T.; Burton, G. W.; Ingold, K. U. Antioxidant and Co-Antioxidant Activity of Vitamin C. The Effect of Vitamin C, Either Alone or in the Presence of Vitamin E or a Water-Soluble Vitamin E Analogue, upon the Peroxidation of Aqueous Multilamellar Phospholipid Liposomes. *Biochim. Biophys. Acta - Lipids Lipid Metab.* **1985**, *835* (2), 298–303. https://doi.org/https://doi.org/10.1016/0005-2760(85)90285-1.

(51) Niki, E.; Kawakami, A.; Yamamoto, Y.; Kamiya, Y. Oxidation of Lipids. VIII. Synergistic Inhibition of Oxidation of Phosphatidylcholine Liposome in Aqueous Dispersion by Vitamin E and Vitamin C. *Bull. Chem. Soc. Jpn.* **1985**, *58* (7), 1971–1975. https://doi.org/10.1246/bcsj.58.1971.

(52) Sato, K.; Niki, E.; Shimasaki, H. Free Radical-Mediated Chain Oxidation of Low Density Lipoprotein and Its Synergistic Inhibition by Vitamin E and Vitamin C. *Arch. Biochem. Biophys.* **1990**, *279* (2), 402–405. https://doi.org/10.1016/0003-9861(90)90508-V.

(53) Sutherland, J. B.; Freeman, J. P.; Heinze, T. M.; Moody, J. D.; Parshikov, I. A.; Williams, A. J.; Zhang, D. Oxidation of Phenothiazine and Phenoxazine by Cunninghamella Elegans. *Xenobiotica* **2001**, *31* (11), 799–809. https://doi.org/10.1080/00498250110069140.

(54) Danny Burke, M.; Mayer, R. T. Differential Effects of Phenobarbitone and 3-

Methylcholanthrene Induction on the Hepatic Microsomal Metabolism and Cytochrome P-450-Binding of Phenoxazone and a Homologous Series of Its n-Alkyl Ethers (Alkoxyresorufins). *Chem. Biol. Interact.* **1983**, *45* (2), 243–258. https://doi.org/https://doi.org/10.1016/0009-2797(83)90072-8.

(55) Howard, J. A.; Ingold, K. U. The Inhibited Autoxidation of Styrene: Part II. The Relative Inhibiting Efficiencies of Meta- and Para-Substituted Phenols. *Can. J. Chem.* **1963**, *41*, 1744–1751.

(56) Howard, J. A.; Ingold, K. U. THE INHIBITED AUTOXIDATION OF STYRENE: PART III. THE RELATIVE INHIBITING EFFICIENCIES OF ORTHO-ALKYL PHENOLS. *Can. J. Chem.* **1963**, *41* (11), 2800–2806. https://doi.org/10.1139/v63-411.

(57) Poon, J.-F.; Farmer, L. A.; Haidasz, E. A.; Pratt, D. A. Temperature-Dependence of Radical-Trapping Activity of Phenoxazine, Phenothiazine and Their Aza-Analogues Clarifies the Way Forward for New Antioxidant Design. *Chem. Sci.* **2021**, *12* (33), 11065–11079. https://doi.org/10.1039/D1SC02976B.

(58) Hansch, C.; Leo, A.; Taft, R. W. A Survey of Hammett Substituent Constants and Resonance and Field Parameters. *Chem. Rev.* **1991**, *91* (2), 165–195. https://doi.org/10.1021/cr00002a004.

(59) Ohlow, M. J.; Sohre, S.; Granold, M.; Schreckenberger, M.; Moosmann, B. Why Have Clinical Trials of Antioxidants to Prevent Neurodegeneration Failed? - A Cellular Investigation of Novel Phenothiazine-Type Antioxidants Reveals Competing Objectives for Pharmaceutical Neuroprotection. *Pharm. Res.* **2017**, *34* (2), 378–393. https://doi.org/10.1007/s11095-016-2068-0.

(60) Log*P* values were calculated in ACD/ChemSketch 2020 (v. 14.50), ACD/Labs.

(61) Liu, J.; Bandyopadhyay, I.; Zheng, L.; Khdour, O. M.; Hecht, S. M. Antiferroptotic Activity of Phenothiazine Analogues: A Novel Therapeutic Strategy for Oxidative Stress Related Disease. *ACS Med. Chem. Lett.* **2020**, *11* (11), 2165–2173. https://doi.org/10.1021/acsmedchemlett.0c00293.

(62) Radical-trapping stoichiometry could be an important third parameter. However, it remains unclear how/which data is most appropriate to include in the correlation, since the stoichiometry varies with experimental conditions. For example, *n* measured in the absence of ascorbaterange from 1.2 to 4.8, while in the presence of ascorbate, they could be greater than 100, and trend quite differently.

(63) Takahashi, M.; Tsuchiya, J.; Niki, E. Scavenging of Radicals by Vitamin E in the Membranes As Studied by Spin Labeling. *J. Am. Chem. Soc.* **1989**, *111* (16), 6350–6353. https://doi.org/10.1021/ja00198a054.

(64) Lide, D. R. *CRC Handbook of Chemistry and Physics 89th Edition*; CRC press, 2009.

(65) Zachariasse, K. A.; Vaz, W. L. C.; Sotomayor, C.; Kühnle, W. Investigation of Human Erythrocyte Ghost Membranes with Intramolecular Excimer Probes. *Biochim. Biophys. Acta - Biomembr.* **1982**, *688* (2), 323–332. https://doi.org/https://doi.org/10.1016/0005-2736(82)90343-1.

(66) The predicted EC_{50} of **3.36** was somewhat lower than what was observed. This could be a

consequence of its inefficient regeneration, but further experimentation will be required to properly test this hypothesis, which is outside the scope of the present work. The phenothiazine analogue **3.31**, which regenerates even less efficiently, has a similar disparity between predicted (12 nM) and observed (35 ± 2 nM) potency.

(67) Yang, W.; Liu, X.; Song, C.; Ji, S.; Yang, J.; Liu, Y.; You, J.; Zhang, J.; Huang, S.; Cheng, W.; Shao, Z.; Li, L.; Yang, S. Structure-Activity Relationship Studies of Phenothiazine Derivatives as a New Class of Ferroptosis Inhibitors Together with the Therapeutic Effect in an Ischemic Stroke Model. *Eur. J. Med. Chem.* **2021**, *209*, 112842. https://doi.org/https://doi.org/10.1016/j.ejmech.2020.112842.

(68) Since structure-activity relationships in anti-ferroptotic potency could, in principle, be cell-type specific, we also tested these four compounds in an erastin-induced HT1080 rescue assay (see Supporting Information for the details). Consistent with the data in MEFs, we found that **3.43** and **3.44** were more potent than PTZ and PNX (compare EC_{50} = 2.3 ± 0.2 and 1.2 ± 0.2 nM to 15 ± 3 and 9.0 ± 0.7 nM, respectively), but the difference was substantially less than the drastic enhancement reported by Yang et al.[67]

(69) Tadros, F. W.; Wahab, F. A. THE SITE OF ACTION OF PHENOTHIAZINE S35 IN THE CENTRAL NERVOUS SYSTEM. *J. Ment. Sci.* **1961**, *108*, 816–821.

(70) Zhang, X.; Jin, H.; Padakanti, P. K.; Li, J.; Yang, H.; Fan, J.; Mach, R. H.; Kotzbauer, P.; Tu, Z. Radiosynthesis and in Vivo Evaluation of Two PET Radioligands for Imaging α-Synuclein. *Applied Sciences*. 2014. https://doi.org/10.3390/app4010066.

(71) Yu, M. J.; McCowan, J. R.; Thrasher, K. J.; Keith, P. T.; Luttman, C. A.; Ho, P. P. K.; Towner, R. D.; Bertsch, B.; Horng, J. S.; Um, S. L.; Phebus, L. A.; Saunders, R. D. Phenothiazines as Lipid Peroxidation Inhibitors and Cytoprotective Agents. *J. Med. Chem.* **1992**, *35* (4), 716–724. https://doi.org/10.1021/jm00082a012.

(72) Yu, M. J.; McCowan, J. R.; Smalstig, E. B.; Bennett, D. R.; Roush, M. E.; Clemens, J. A. A Phenothiazine Derivative Reduces Rat Brain Damage after Global or Focal Ischemia. *Stroke* **1992**, *23* (9), 1287–1291. https://doi.org/10.1161/01.STR.23.9.1287.

(73) Songarj, P.; Luh, C.; Staib-Lasarzik, I.; Engelhard, K.; Moosmann, B.; Thal, S. C. The Antioxidative, Non-Psychoactive Tricyclic Phenothiazine Reduces Brain Damage after Experimental Traumatic Brain Injury in Mice. *Neurosci. Lett.* **2015**, *584*, 253–258. https://doi.org/10.1016/j.neulet.2014.10.037.

3.8 Methods and Protocols

Inhibited Co-autoxidation of PBD-BODIPY and 1,4-Dioxane. Into a 3 mL quartz cuvette were added 620 μL 1,4-dioxane (ACS grade) to either 1.80 mL of PhCl or 1.18 mL of PhCl with 620 μL of DMSO (ACS grade). The cuvette was placed in the sample holder of a UV−visible spectrophotometer and equilibrated to 37 °C. PBD-BODIPY (12.5 μL of a 2.0 mM solution in 1,2,4-trichlorobenzene), 50 μL AIBN solution (0.3 M in PhCl) followed by 10 μL of RTA solution (0.5 mM or desired concentration.) The contents were thoroughly mixed and the loss of PBD-BODIPY absorbance was monitored at 587 nm (without DMSO ε = 123 000 M^{-1} cm^{-1}, with DMSO ε = 118 200 M^{-1} cm^{-1}.) In parallel with the compounds of interest, an uninhibited experiment (no RTA) and one with a known concentration of PMC (2-6 μM) were recorded (the latter being used to calculate the rate of initiation assuming the n = 2 for PMC.) The rate constants of inhibition ($k_{inh}^{dioxane}$ or k_{inh}^{DMSO}), radical trapping stoichiometries (n) and associated standard deviations were ascertained from a minimum of three experimental replicates.

Inhibited Co-autoxidation of STY-BODIPY in Egg-PC Liposomes (Absorbance). Into a 3 mL quartz cuvette were combined 2.34 mL of 10 mM PBS (pH 7.4) and 125 μL of a suspension of egg-PC unilamellar liposomes (100 nm; 20 mM in the same PBS.) The cuvette was placed in the sample holder of a UV−visible spectrophotometer and equilibrated to 37 °C. STY-BODIPY (12.5 μL of a 2.0 mM solution in DMSO), 10 μL MeOAMVN solution (0.05 M in MeCN) followed by 10 μL of RTA solution (0.5 mM or desired concentration.) The contents were thoroughly mixed and the loss of STY-BODIPY absorbance was monitored at 565 nm (ε = 123 676 M^{-1} cm^{-1}.) In parallel with the compounds of interest, an uninhibited experiment (no RTA) and one with a known concentration of PMC (2-6 μM) were recorded (the latter being used to calculate the rate of initiation assuming the n = 2 for PMC.) The rate constants of inhibition (k_{inh}^{lip}), radical trapping stoichiometries (n) and associated standard deviations were ascertained from a minimum of three experimental replicates.

Inhibited Co-autoxidation of STY-BODIPY in Egg-PC Liposomes (Fluorescence). Into a conical centrifuge tube of appropriate volume (15-50 mL) were charged with 10 mM PBS (pH 7.4), 1.04 mM egg-PC unilamellar liposomes (100 nm; 20 mM initial concentration) and 0.2 mM initiator (30 mM MeOAMVN in MeCN or 30 mM DTUN in EtOH) after which the tube was

vortexed. When the RTA stock solutions were prepared and ready for addition by multi-channel pipette (240 μM or desired concentration in MeCN), the 1.04 μM STY-BODIPY (2 mM in DMSO initial concentration) was added to the liposome/initiator mixture and was subsequently vortexed (from this point the experiment should be set up as quickly as possible as the STY-BODIPY will progressively decompose). The liposome/initiator/dye mixture was then transferred to a reservoir and using a 300 μL multi-channel pipette a 96-well plate (black, Nunc) was charged with the mixture (295 μL per well). Using a 10 μL, the RTA solutions were added (5 μL) bringing the final volume with 300 μL. The contents were mixed manually by taking up/dispensing the well contents 3-4 times with the 300 μL multi-channel pipette. The plate was mixed in the microplate reader for 1 min at 37 °C, after which monitoring loss of STY-BODIPY by fluorescence ($\lambda_{ex}/\lambda_{em}$ = 488/518 nm) commenced for 15 h. In parallel with the compounds of interest, uninhibited experiments (no RTA) at multiple concentrations of STY-BODIPY (0.25, 0.5, 0.75, and 1 μM) and experiments with a known concentration of PMC (4 μM) were recorded. The former was used to determine the response factor of the oxidized STY-BODIPY at their maximum, while the latter was used to calculate the rate of initiation (R_i) assuming the n = 2 for PMC. The rate constants of inhibition (k_{inh}^{lip}), radical trapping stoichiometries (n) and associated standard deviations were ascertained from a minimum of three experimental replicates. **Ascorbate Variant/Modification.** Immediately before adding the STY-BODIPY, 10.4 or 104 μM of ascorbate solution (10 or 100 mM initial concentration in PBS) is added to the conical tube. The RTA stocks are diluted further (from 240 μM to 24 μM) before addition to 96-well plate. The response factor and R_i are determined by the DTUN initiated autoxidation *in the absence* of ascorbate using the aforementioned uninhibited/PMC experiments.

Cell Culture. Cells were cultured at 37 °C under an atmosphere of 5% CO_2. Pfa-1 mouse embryonic fibroblasts (MEFs) were cultured in high glucose DMEM (no phenol red) with 10% FBS, 10 mM glutamine, 100 μg/mL streptomycin and 100 IU/mL penicillin. The cells were passaged every other day by dissociation with 0.05% trypsin and 0.2% EDTA.

Inhibition of Ferroptosis in Cells Induced by (1*S*,3*R*)-RSL3. Into 96-well culture plates were seeded Pfa-1 MEFs (3000 in 100 μL of media) which were subsequently incubated overnight. The following day aliquots (1 μL) of test compound (i.e. RTA) serial diluted from a 10-50 mM DMSO stock were added and the plates were subsequently incubated for 1 h. This incubation

was followed by the addition of (1*S*,3*R*)-RSL3 (10 μL at 1.65 μM in DPBS). The plate was incubated for 5 h after which cell viability was determined using the AquaBluer assay (MultiTarget Pharmaceuticals, LLC). Each experiment was carried out with a minimum of three technical replicates repeated three times.

Liver Microsome Stability Assay. A suspension of mouse (Balb-c) liver microsomes (Gibco^{TM}; BCMCPL; 20 mg/mL) are initially brought out of -78 °C storage and allowed to thaw in a container of crushed ice. Meanwhile, stock solutions of the test compounds are prepared and diluted to 0.1-1 mM in acetonitrile. A solution of 3:1 (v/v) MeCN/MeOH containing an HPLC standard (compound **3.25**) at 15 μM was prepared and subsequently aliquoted (100 μL) into labelled microcentrifuge tubes. The tubes were placed in a freezer for later use. At this point, to 1155 μL of phosphate buffer (100 mM) was added 11.3 μL of $MgCl_2$ solution (0.36 M) and 33.6 μL (or 67.2 μL) of the thawed liver microsomes. A 10 mM solution of beta-nicotinamide adenine dinucleotide phosphate reduced tetrasodium salt (NADPH) in phosphate buffer was prepared. The microsome solution was aliquoted into 4 wells in a 96-well culture plate (267 μL each) and the NADPH solution into a fifth well and the plate was heated in a microplate reader for ~5min (with a lid.) The NADPH solution (30 μL), three test compounds, and Verapamil (positive control) were loaded (3 μL) into the wells containing the microsomes for a final concentration of 10 μM (or 1 μM) of test compound (or Verapamil), 1 mM NADPH, 3 mM $MgCl_2$ and 0.5 mg/mL (or 1.0) microsomes. The suspensions were well-mixed, incubated for ~1 min in the reader (37 °C with double-orbital shaking) and the first aliquots (50 μL) were quenched into the previously prepared cold MeCN/MeOH microcentrifuge tubes. The process was repeated four times at the desired time intervals after which the quenched samples were centrifuged (14 000 G, 10 min) and the supernatant was transferred to HPLC vials with low volume inserts. **UPLC Analysis (Microsome Assay)**. The percent remaining concentration present in the samples was determined by the change of test compounds' integral (normalized to the HPLC standard) relative to the initial '0 min' sample. Apart from Verapamil and Lip-1, which were monitored by ESI+ mass scan, the compounds were monitored by PDA (190-390 nm). The chromatography conditions were as follows: Column: Hypersil GOLD C-18 reverse phase column (250 mm × 4.6 mm, 5 mm). UPLC method: injection volume of 10 mL; mobile phase A (pH 5.5 10 mM ammonium acetate buffer) and mobile phase B (methanol); flow rate: 0.5 mL/min; run time: 30

min; the gradient elution method: 80% to 100% B from 0 to 10 min, hold at 100% B from 10 to 25 min, 100% to 80% B from 25 to 30 min.

Animal Studies. The generation and use of tamoxifen-inducible *ROSA26-CreERT2;Gpx4fl/fl* mice was described previously (PMID 2540268). To induce *Gpx4* deletion in mice, Tamoxifen (TAM) was dissolved in Miglyol at a concentration of 20 mg/mL (TAM: Sigma, T5648-1G; Miglyol: Caelo, 3274-250 mL). Subsequently, 100 µL of TAM solution was used for i.p injections on Day 0 and 2. For the treatment study, compound **3.11** (10 mg/kg and 20 mg/kg, respectively) and vehicle (PEG400/5 % Solutol HS15/PBS; PEG E 400 obtained from Sigma-Aldrich, Cat# 06855-1KG and Solutol HS 15 obtained from Sigma-Aldrich, Cat# 42966-1KG) were administered once daily by i.p. injection. Once mice showed signs of acute kidney failure (reaching the humane endpoint), they were euthanized by cervical dislocation. Kaplan-Meier survival analysis was conducted using the GraphPad Prism 9 software. For the endpoint study, mice were treated daily with compound **3.11** (20 mg/kg) and vehicle control, respectively, until Day 9, whereupon animals were euthanized for blood and tissue collection. Animals were kept under SPF-IVC standard conditions with food and water ab libitum and all studies have been approved by the government of Upper Bavaria.

Immunohistochemistry. Formalin-fixed paraffin embedded (FFPE) tissue sections (7 µm) were stained with Periodic acid (Sigma-Aldrich, Cat. Nr. 3951) and Schiff's reagent (Sigma-Aldrich, Cat. Nr. 3952) according to a standardized protocol. First, sections were incubated for 15 min at 60 °C and then deparaffinized by three 5 min incubation steps in Xylene (Carl Roth GmbH + Co. KG). Subsequently, sections were rehydrated using decreasing ethanol concentrations (100 %, 95 % and 70 %) and washed twice for 2 min with ddH_2O. Residual water was discarded, whereupon periodic acid was applied. After a 5 min incubation, slides were washed for 5 min under running tap water. Excess water was discarded and Schiff's reagent applied to each section for 20 min, followed by a 3 min washing step under running tap water. Nuclei were counterstained with Mayer's Hematoxylin (Carl Roth GmbH + Co. KG) for 90 s. Two 3 min washing steps in ddH_2O were followed by 6 min bluing under running tap water. After a final 3 min washing step in ddH_2O, sections were dehydrated using increasing ethanol concentrations (70 %, 95 % and 100 %), followed by xylene treatment and mounting with Roti Histokitt (Carl Roth GmbH + Co. KG). Pictures were taken using an Nikon Eclipse microscope with a DS-Fi3 camera.

Western Blot Analysis. A Eurostar RW16 tissue homogenizer was used for lysis of freshly dissected tissue in 500 µL buffer (0.5% Triton X-100, 0.5% sodium deoxycholate salt, 150 mM NaCl, 20 mM Tris/HCl, 10 mM EDTA, 30 mM sodium pyrophosphate, 1% protease and 1% phosphatase inhibitor cocktail (both Roche)). Protein quantification was done using a BCA Protein Assay Kit (Thermo Fisher Scientific) according to manufacturers' recommendations. Subsequently, Western blot analysis was performed using the following antibodies and dilutions; anti-GPx4 (1:1000, Abcam Cat#ab125066), anti-KIM1 (1:1000, R&D System Cat#AF1817), anti-VCP (1:10000, Abcam Cat#ab11433), β-Actin-HRP (1:50000, Sigma-Aldrich, Cat#A3854) and HRP conjugated secondary antibodies, such as anti-rabbit (1:3000, Cell Signaling Cat#7074S) anti-mouse (1:3000, Cell Signaling Cat#7076S).

Serum Analysis. Blood was collected under anaesthesia by retrobulbar bleeding at Day 9 after TAM injection, into serum collection tubes. Subsequently, serum was obtained by centrifugation and creatinine and blood urea concentrations were determined using the Serum Analyzer AU480.

Stoichiometry and Rate Constant Determination

Rate of STY/PBD-BODIPY consumption during inhibition by the RTA:

$$\frac{-d[BODIPY]}{dt} = \frac{k_{BODIPY}[BODIPY]R_i}{nk_{inh}[RTA]} \qquad (3.8)$$

Rearranged to isolate the rate constant of inhibition (k_{inh}):

$$k_{inh} = \frac{k_{BODIPY}[BODIPY]R_i}{n\frac{-d[BODIPY]}{dt}[RTA]} \qquad (3.9)$$

Where:

'k_{BODIPY}' is the rate constant of radical addition to STY or PBD-BODIPY (M^{-1} s^{-1}); '[BODIPY]' is the initial concentration (M) of STY or PBD-BODIPY; 'R_i' is the rate of initiation (determined from the t_{inh} of 2,2,5,7,8-Pentamethyl-6-chromanol (PMC) using Eq. 3.11 assuming n = 2); 'n' is the stoichiometry[a] of the radical trapping antioxidant (RTA) calculated using Eq. 3.10; '[RTA]' is the initial concentration of the radical trapping antioxidant (M).

RTA stoichiometry (n):

$$n = \frac{t_{inh} \times R_i}{[RTA]} \qquad (3.10)$$

Rearranged to isolate the rate of initiation (R_i):

$$R_i = \frac{n[RTA]}{t_{inh}} \qquad (3.11)$$

Where 't_{inh}' is the time of inhibition (which is the intercept between the tangent of the slope inhibition and slope of post-inhibition).

[a] Stoichiometry for the determination of k_{inh} was assumed to be 2 when the observed $n \geq 2$. When $n < 2$, the observed n was used in the calculation of k_{inh}.

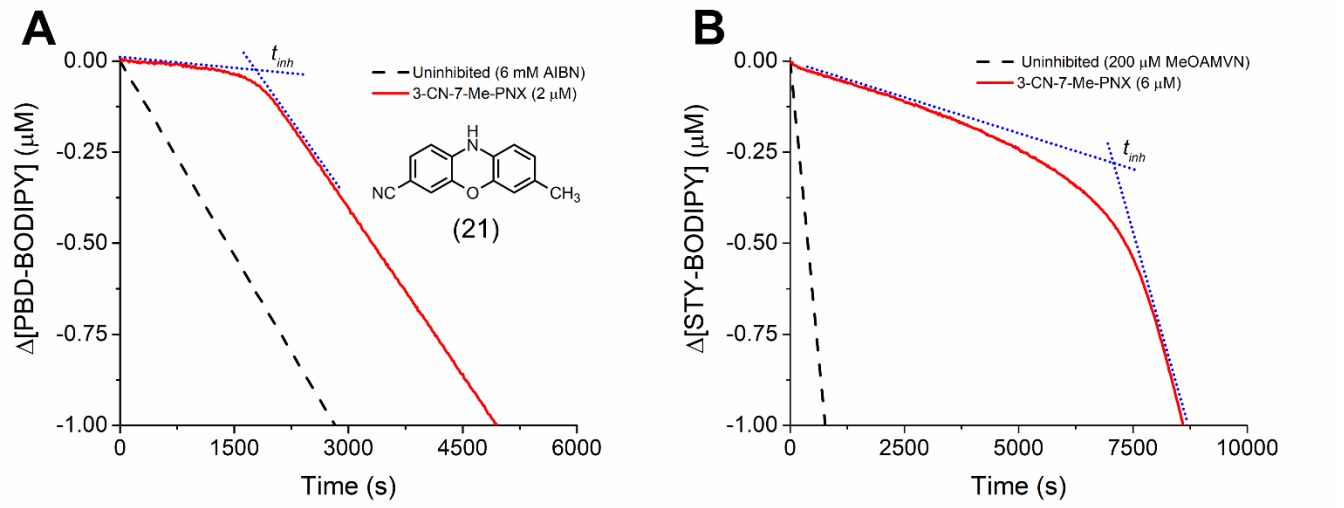


Figure 3.9. (A) Representative ABIN initiated (6 mM; $R_i = 2.40 \times 10^{-9}$ M s^{-1}) PBD-BODIPY (10 μM; k_{BODIPY} = 5310 M^{-1} s^{-1}) and 1,4-dioxane (1:3 dioxane/PhCl; 37 °C) co-autoxidation monitored by loss of absorbance (λ_{max} = 587 nm; ε = 123 000 M^{-1} cm^{-1}) inhibited by **3.21** (2 μM; n = 2.2 ± 0.1; k_{inh} = (1.8 ± 0.1) × 10^6 M^{-1} s^{-1}). **(B)** MeOAMVN initiated co-autoxidation (0.2 mM; $R_i = 2.55 \times 10^{-9}$ M s^{-1}) of STY-BODIPY (10 μM; k_{BODIPY} = 894 M^{-1} s^{-1}) in egg PC liposomes (1 mM) monitored by loss of absorbance (λ_{max} = 565 nm; ε = 123 676 M^{-1} cm^{-1}) inhibited by **3.21** (6 μM; n = 3.1 ± 0.1; k_{inh} = (4.7 ± 0.1) × 10^4 M^{-1} s^{-1}).

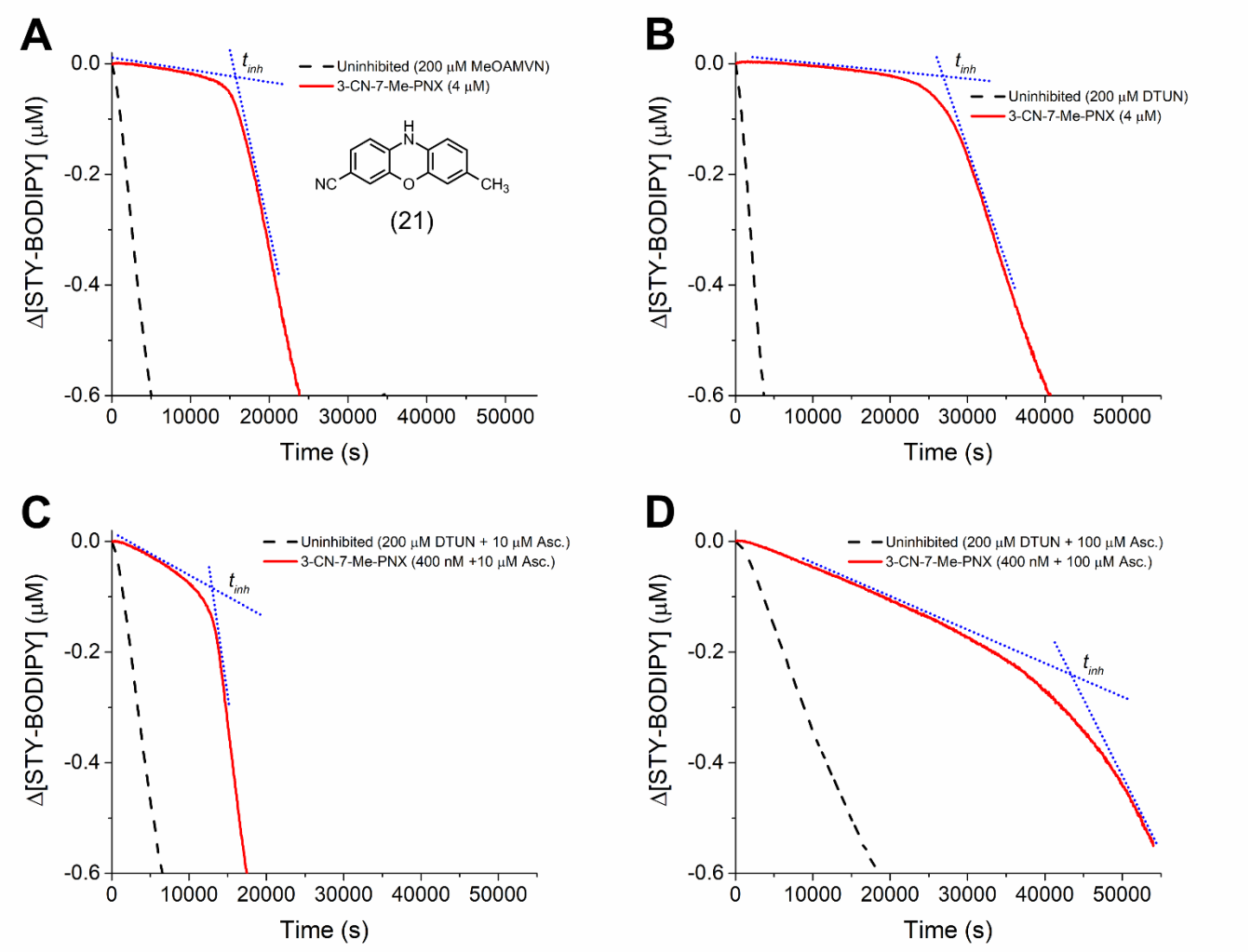


Figure 3.10. (A) Representative MeOAMVN initiated (0.2 mM; $R_i = 9.14 \times 10^{-10}$ M s^{-1}) **(B)** and DTUN initiated co-autoxidations (0.2 mM; $R_i = 7.47 \times 10^{-10}$ M s^{-1}) of STY-BODIPY (1 μM; $k_{BODIPY} = 894$ M^{-1} s^{-1}) in egg PC liposomes (1 mM) monitored by fluorescence ($\lambda_{ex}/\lambda_{em}$ = 488/518 nm). Both were inhibited by 4 μM of **3.21** ($n = 3.5 \pm 0.1$; $k_{inh} = (4.4 \pm 0.6) \times 10^4$ M^{-1} s^{-1} and $n = 4.8 \pm 0.2$; $k_{inh} = (5.3 \pm 0.3) \times 10^4$ M^{-1} s^{-1} respectively.) **(C)** DTUN initiated co-autoxidation (0.2 mM; $R_i = 7.57 \times 10^{-10}$ M s^{-1}) of STY-BODIPY (1 μM) in egg PC liposomes (1 mM) with 10 μM ascorbic acid ($k_{BODIPY} = 563$ M^{-1} s^{-1}) and **(D)** with 100 μM ascorbic acid ($k_{BODIPY} = 191$ M^{-1} s^{-1}). Both were inhibited by 0.4 μM of **3.21** ($n = 24.8 \pm 0.5$; $k_{inh} = (6.9 \pm 0.2) \times 10^4$ M^{-1} s^{-1} and $n = 78.9 \pm 1.0$; $k_{inh} = (3.1 \pm 0.1) \times 10^4$ M^{-1} s^{-1} respectively.)

Determination of α_2^H

Abraham and co-workers previously demonstrated a convenient and robust method of determining α_2^H of H-bond donor functional groups by correlating the delta chemical shift (Δδ) between X-H observed in DMSO-d_6 (δ_{DMSO}) and $CDCl_3$ (δ_{CDCl3}):

$$\Delta\delta_{DMSO-CDCl3} = \delta_{DMSO} - \delta_{CDCl3}$$

$$\alpha_2^H = 0.133\Delta\delta_{DMSO-CDCl3} + 0.0066$$

We have consistently observed that phenoxazine and phenothiazine RTAs do not generally give resolved ^{1}H NMR spectra in $CDCl_3$. Substituting $CDCl_3$ with benzene-d_6 has the advantage of being compatible with aforementioned compounds while rendering a similar linear correlation:

$$\Delta\delta_{DMSO-Ben} = \delta_{DMSO} - \delta_{Ben}$$

$$\alpha_2^H = 0.134\Delta\delta_{DMSO-Ben} - 0.1087$$

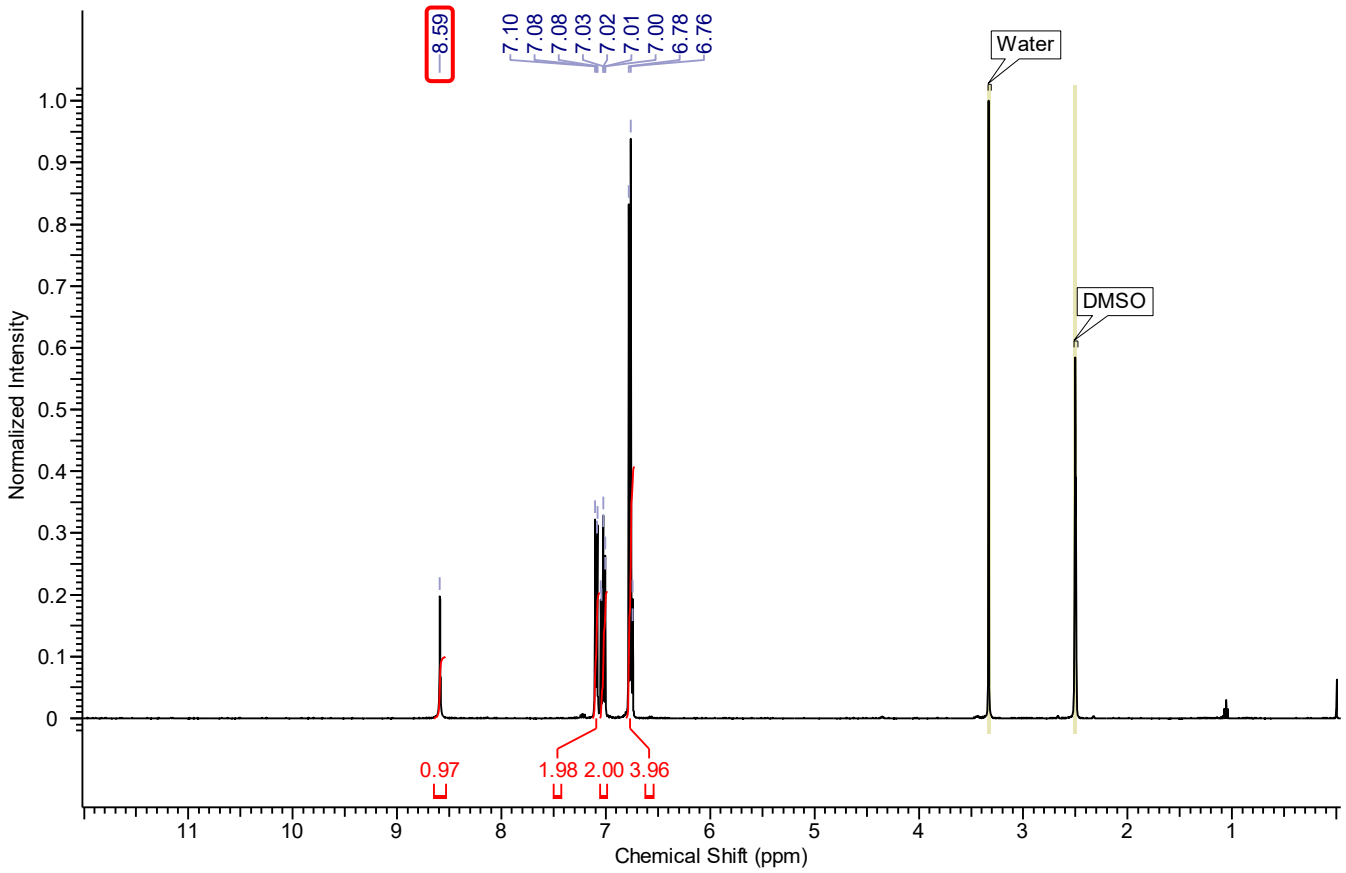


Figure 3.11. Representative ^{1}H NMR of phenoselenazine (PSZ) in DMSO-d_6 with the N-H proton highlighted (8.59 ppm).

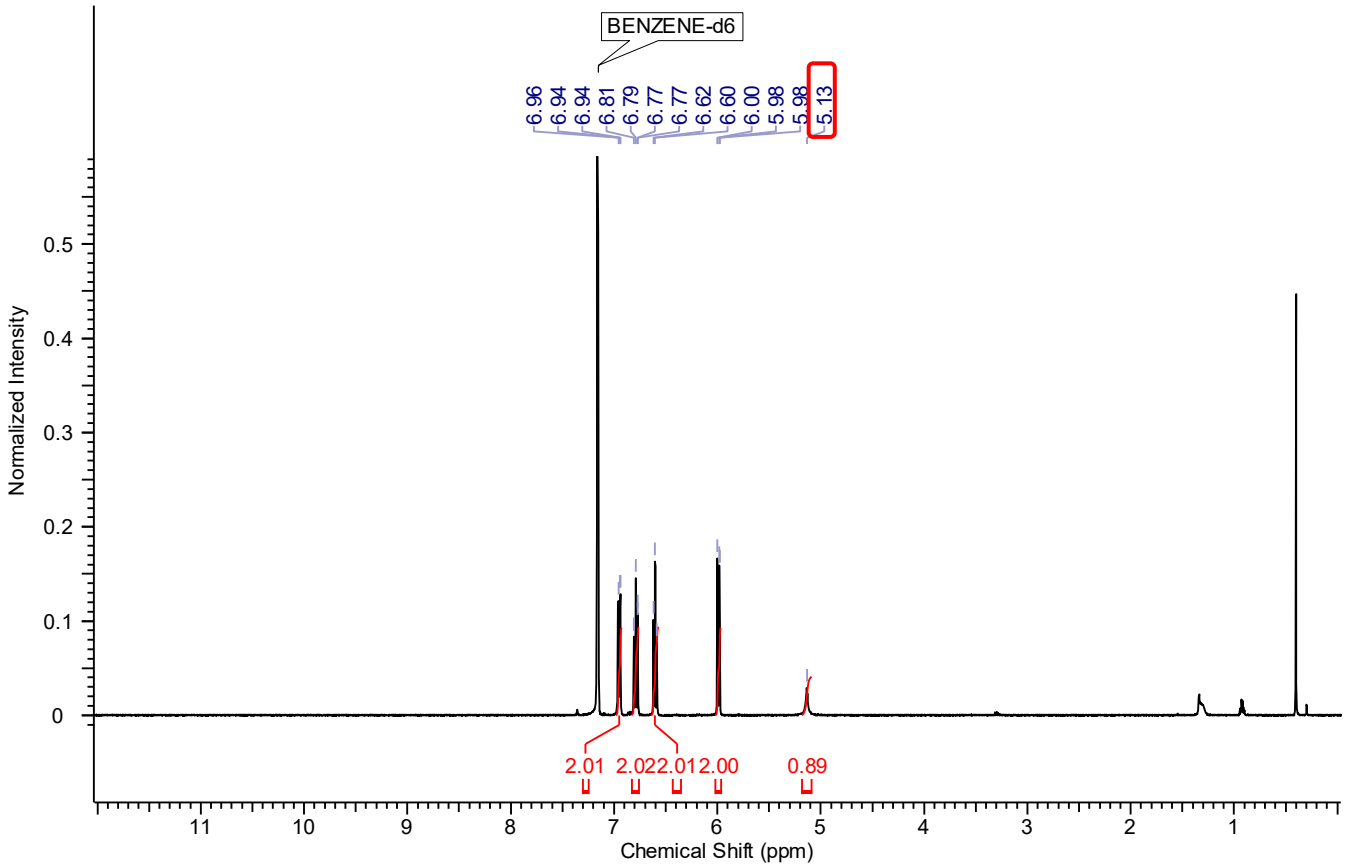


Figure 3.12. Representative ^{1}H NMR of phenoselenazine (PSZ) in benzene-d_6 with the N-H proton highlighted (5.13 ppm).

3.9 Supplementary Data

Table 3.2. Summary of the Hydrogen Bond Acidity Parameters (α_2^H) of Compounds 1-44.

	RTA	δ_{DMSO} [b] (ppm)	δ_{Ben} [b] (ppm)	$\Delta\delta_{DMSO-Ben}$ (ppm)	α_2^H
	PMC [a]	7.36	3.72	3.64	0.38
1	PNX [a]	8.16	4.05	4.11	0.44
2	PTZ [a]	8.57	4.92	3.65	0.38
3	PSZ	8.59	5.13	3.46	0.36
4	Benzo(b)-PNX	8.84	4.45	4.39	0.49
5	Benzo(b)-PTZ	8.97	5.17	3.80	0.40
6	2-CF_3-PNX [a]	8.51	3.89	4.62	0.51
7	2-CF_3-7-tBu-PNX	8.43	3.93	4.50	0.50
8	2-CF_3-8-tBu-PNX	8.45	3.89	4.56	0.51
9	3-CF_3-PNX [a]	8.70	3.98	4.72	0.53
10	3-CF_3-7-tBu-PNX	8.63	4.04	4.59	0.51
11	3-CF_3-8-tBu-PNX	8.65	3.99	4.66	0.52
12	3-Form-PNX	9.04	4.14	4.90	0.55
13	3,7-Form-PNX	9.67	4.20	5.47	0.63
14	3-Form-7-CN-PNX	9.59	3.99	5.60	0.64
15	3-NO_2-PNX [a]	9.34	3.97	5.37	0.62
16	3-NO_2-7-Me-PNX	9.28	4.04	5.24	0.60
17	3-NO_2-7-MeO-PNX [a]	9.27	3.99	5.28	0.60
18	3-NO_2-7-NEt_2-PNX	9.18	4.07	5.11	0.58
19	3,7-NO_2-PNX	10.11	3.91	6.20	0.72
20	3-CN-PNX [a]	8.91	3.92	4.99	0.56
21	3-CN-7-Me-PNX	8.81	3.92	4.89	0.55
22	3-CN-7-MeO-PNX	8.75	3.85	4.90	0.55
23	3-CN-7-NO_2-PNX [a]	9.83	3.85	5.98	0.69
24	2-Cl-PTZ	8.75	4.77	3.98	0.43
25	2-CF_3-PTZ	8.86	4.75	4.11	0.44
26	3-CF_3-PTZ	9.03	4.85	4.18	0.45
27	3-Form-PTZ	9.25	4.91	4.34	0.47
28	3-NO_2-PTZ	9.49	4.79	4.70	0.52
29	3,7-NO_2-PTZ	10.13	4.66	5.47	0.62
30	3,7-tBu-PTZ [a]	8.38	5.01	3.37	0.35
31	1,9-Me-PTZ	6.64	5.38	1.26	0.06
32	3,7-MeO-PTZ [a]	8.12	4.82	3.30	0.34
33	2,8-tBu-PNX [a]	8.03	4.07	3.96	0.43
34	3,7-tBu-PNX [a]	7.96	4.14	3.82	0.41
35	3,7-Me-PNX	7.89	4.07	3.82	0.41
36	1,9-Me-PNX	5.96	4.27	1.69	0.12
37	2,4,6,8-Me-PNX	7.86	4.22	3.64	0.39
38	1,3,7,9-Me-PNX	5.78	4.23	1.55	0.10
39	3-MeO-PNX [a]	7.93	3.99	3.94	0.42
40	3,7-MeO-PNX [a]	7.68	3.92	3.76	0.40
41	3,7-Et-PNX	7.93	4.10	3.83	0.41
42	3,7-iPr-PNX	7.93	4.12	3.81	0.40
43		8.50	4.86	3.64	0.38
44		8.09	3.97	4.12	0.44

(a) ^{1}H NMR and α_2^H previously reported (see ref. 4). (b) Annotated ^{1}H NMR spectra for these compounds in DMSO-d_6 and benzene-d_6 is included in 'NMR Spectra' section of the Appendix.

3.9.1 Kinetic Data

Table 3.3. Inhibition Rate Constants and Radical Trapping Stoichiometries in Organic Solution (k_{inh}^{S}) and in Egg PC Liposomes (k_{inh}^{lip})

	RTA	k_{inh}^{S} (10^5 $M^{-1}s^{-1}$) [a] / *n*	k_{inh}^{lip} (10^3 $M^{-1}s^{-1}$) / *n*		k_{inh}^{lip} (10^3 $M^{-1}s^{-1}$) (Predicted) [h]
			Fluorescence [e]	Absorbance [f]	
	PMC	(4.1 ± 0.2) [c] / (2)	(29 ± 2) / (2)	(33 ± 2) / (2)	(35)
1	PNX	(5.3 ± 0.5) [b,c] / 2.2 ± 0.1	(224 ± 42) / 1.9 ± 0.1	(232 ± 23) / 2.0 ± 0.1	(248)
2	PTZ	(11.5 ± 0.4) [c] / 2.1 ± 0.1	(86 ± 3) / 1.9 ± 0.1	(110 ± 15) [g] / 1.9 ± 0.1	(98)
3	PSZ	(4.9 ± 0.1) / 3.2 ± 0.1	(47 ± 4) / 1.8 ± 0.1	(56 ± 3) / 2.3 ± 0.1	(47)
4	Benzo(b)-PNX	(2.9 ± 0.2) [b] / 2.4 ± 0.1	(101 ± 12) / 2.4 ± 0.1	(103 ± 12) / 2.4 ± 0.1	(113)
5	Benzo(b)-PTZ	(8.2 ± 0.2) / 2.4 ± 0.1	(51 ± 3) / 1.9 ± 0.1	-	(61)
6	2-CF_3-PNX	(20 ± 1) [c] / 2.3 ± 0.1	(75 ± 11) / 3.0 ± 0.1	(58 ± 2) / 2.8 ± 0.1	(73)
7	2-CF_3-7-tBu-PNX	(2.4 ± 0.1) [b] / 2.0 ± 0.1	(75 ± 13) /2.8 ± 0.1	(64 ± 2) / 2.4 ± 0.1	(96)
8	2-CF_3-8-tBu-PNX	(2.0 ± 0.1) [b] / 2.3 ± 0.1	(64 ± 9) / 2.3 ± 0.1	(60 ± 3) / 2.2 ± 0.2	(84)
9	3-CF_3-PNX	(14.7 ± 1.6) [c] / 2.3 ± 0.1	(42 ± 2) / 3.0 ± 0.1	(32 ± 1) / 2.8 ± 0.1	(47)
10	3-CF_3-7-tBu-PNX	(1.8 ± 0.1) [b] / 2.7 ± 0.1	(55 ± 10) / 2.8 ± 0.1	(64 ± 4) / 2.9 ± 0.1	(74)
11	3-CF_3-8-tBu-PNX	(1.5 ± 0.1) [b] / 2.5 ± 0.1	(44 ± 3) / 2.6 ± 0.1	-	(60)
12	3-CHO-PNX	(10.6 ± 1.4) / 2.1 ± 0.1	(42 ± 2) / 2.9 ± 0.1	-	(30)
13	3,7-CHO-PNX	(3.5 ± 0.5) / 2.2 ± 0.1	(10 ± 1) / 3.2 ± 0.1	-	(5.9)
14	3-CHO-7-CN-PNX	(2.8 ± 0.2) / 2.4 ± 0.1	(7.1 ± 0.1) / *nd*	-	(4.3)
15	3-NO_2-PNX	(7.3 ± 0.2) [c] / 2.5 ± 0.1	-	(10 ± 1) / 2.2 ± 0.1	(13)
16	3-NO_2-7-Me-PNX	(14.6 ± 1.8) / 2.1 ± 0.1	-	(23 ± 2) / 3.8 ± 0.3	(28)
17	3-NO_2-7-MeO-PNX	(27.6 ± 3.4) [c] / 1.5 ± 0.1	-	(61 ± 4) / 2.9 ± 0.2	(50)
18	3-NO_2-7-NEt_2-PNX	(8.8 ± 0.4) [b] / 2.1 ± 0.1	-	(177 ± 37) / 2.4 ± 0.4	(323)
19	3,7-NO_2-PNX	(1.1 ± 0.1) / 2.2 ± 0.2	-	(1.3 ± 0.1) / *nd*	(1.0)
20	3-CN-PNX	(11.1 ± 0.8) [c] / 2.2 ± 0.2	(27 ± 2) / 3.6 ± 0.1	(31 ± 3) / 3.0 ± 0.1	(29)
21	3-CN-7-Me-PNX	(18.3 ± 1.1) / 2.2 ± 0.2	(44 ± 6) / 3.5 ± 0.1	(47 ± 1) / 3.1 ± 0.1	(51)
22	3-CN-7-MeO-PNX	(40.5 ± 3.9) / 2.1 ± 0.1	-	(133 ± 15) / 3.1 ± 0.3	(114)
23	3-CN-7-NO_2-PNX	(1.5 ± 0.1) [c] / 2.4 ± 0.1	-	(1.6 ± 0.1) / *nd*	(1.8)
24	2-Cl-PTZ	(5.3 ± 0.4) / 2.0 ± 0.1	(39 ± 4) / 2.1 ± 0.1	(41 ± 1) / 1.9 ± 0.1	(32)
25	2-CF_3-PTZ	(3.0 ± 0.2) / 2.1 ± 0.1	(19 ± 1) / 2.5 ± 0.1	(22 ± 1) / 2.3 ± 0.1	(17)
26	3-CF_3-PTZ	(2.7 ± 0.1) / 2.1 ± 0.1	(9.8 ± 0.5) / 2.6 ± 0.1	-	(15)
27	3-CHO-PTZ	(3.1 ± 0.2) / 2.1 ± 0.1	(14 ± 1) / 2.2 ± 0.1	-	(15)
28	3-NO_2-PTZ	(1.9 ± 0.1) / 2.0 ± 0.1	(5.3 ± 0.3) / 2.0 ± 0.1	-	(6.5)
29	3,7-NO_2-PTZ	(1.08 ± 0.07) / 2.2 ± 0.2	(0.41 ± 0.04) / *nd*	-	(0.70)
30	3,7-tBu-PTZ	(3.6 ± 0.2) [b,c] / 1.6 ± 0.1	(106 ± 14) / 1.6 ± 0.1	-	(197)
31	1,9-Me-PTZ	(2.5 ± 0.1) / 2.2 ± 0.1	(98 ± 5) / 1.7 ± 0.1	-	(167)
32	3,7-MeO-PTZ	(15 ± 1) [b,c] / (1.6 ± 0.1)	(too fast) / 2.3 ± 0.1	-	(840)
33	2,8-tBu-PNX	(15 ± 1) [b,c] / (1.8 ± 0.1)	(too fast) / 1.8 ± 0.1	-	(730)
34	3,7-tBu-PNX	(26 ± 2) [b,c] / (1.9 ± 0.1)	(too fast) / 1.7 ± 0.1	(too fast) / 1.8 ± 0.1	(1280)
35	3,7-Me-PNX	(23.8 ± 4.6) [b] / (2.2 ± 0.2)	(too fast) / 1.8 ± 0.1	(too fast) / 2.4 ± 0.1	(1150)
36	1,9-Me-PNX	(14.2 ± 1.9) [b] / (2.2 ± 0.1)	(too fast) / 1.4 ± 0.1	(too fast) / 1.6 ± 0.1	(1150)
37	2,4,6,8-Me-PNX	(29.4 ± 3.8) [b] / 2.0 ± 0.2	(too fast) / 1.7 ± 0.1	-	(1500)
38	1,3,7,9-Me-PNX	(17.8 ± 1.9) [b] / (1.9 ± 0.1)	(too fast) / 1.6 ± 0.1	-	(1500)
39	3-MeO-PNX	(31 ± 2) [b,c] / (1.8 ± 0.1)	(too fast) / 2.1 ± 0.1	-	(1490)
40	3,7-MeO-PNX	(130 ± 20) [b,c] / (1.4 ± 0.1)	(too fast) / 1.0 ± 0.1	-	(6530)
41	3,7-Et-PNX	(27 ± 4) [b,d] / 2.0 ± 0.1	(too fast) / 2.3 ± 0.1	-	(1340)
42	3,7-iPr-PNX	(28 ± 1) [b,d] / 2.0 ± 0.1	(too fast) / 2.3 ± 0.1	-	(1410)
43		(13.4 ± 1.7) / 1.6 ± 0.1	(89 ± 4) / 1.9 ± 0.1	-	(114)
44		(6.5 ± 0.2) [b] / 2.2 ± 0.1	(too fast) / 2.0 ± 0.1	-	(305)

(a) Inhibition rate constants measured in 1:3 1,4-dioxane/PhCl ($k_{inh}^{dioxane}$; $\beta_2^H = 0.35$.) (b) Inhibition rate constants measured in 1:2:1 1,4-dioxane/PhCl/DMSO (k_{inh}^{DMSO}; $\beta_2^H = 0.60$.) (c) Rate constants and *n* reported previously, see ref 4. (d) Inferred from relative rate with concurrent measurement of **3.34** standard. (e) Apparent inhibition rate constants from MeOAMVN-initiated autoxidations of egg PC liposomes determined by fluorescence (STY-BODIPY; $\lambda_{ex}/\lambda_{em}$ = 488/518 nm.) (f) Apparent inhibition rate constants from MeOAMVN-initiated autoxidations of egg PC liposomes determined by absorbance (STY-BODIPY; λ_{max} = 565 nm; ε = 123 676 M^{-1} cm^{-1}.) (g) Taken from Shah *et al.*[1] (h) Inhibition rate constants predicted from $\log k_{inh}^0$, α_2^H and β_2^H = 0.69 via $\log k_{inh}^{lip} = -8.3\alpha_2^H\beta_2^H + \log k_{inh}^0$ (see main text.)

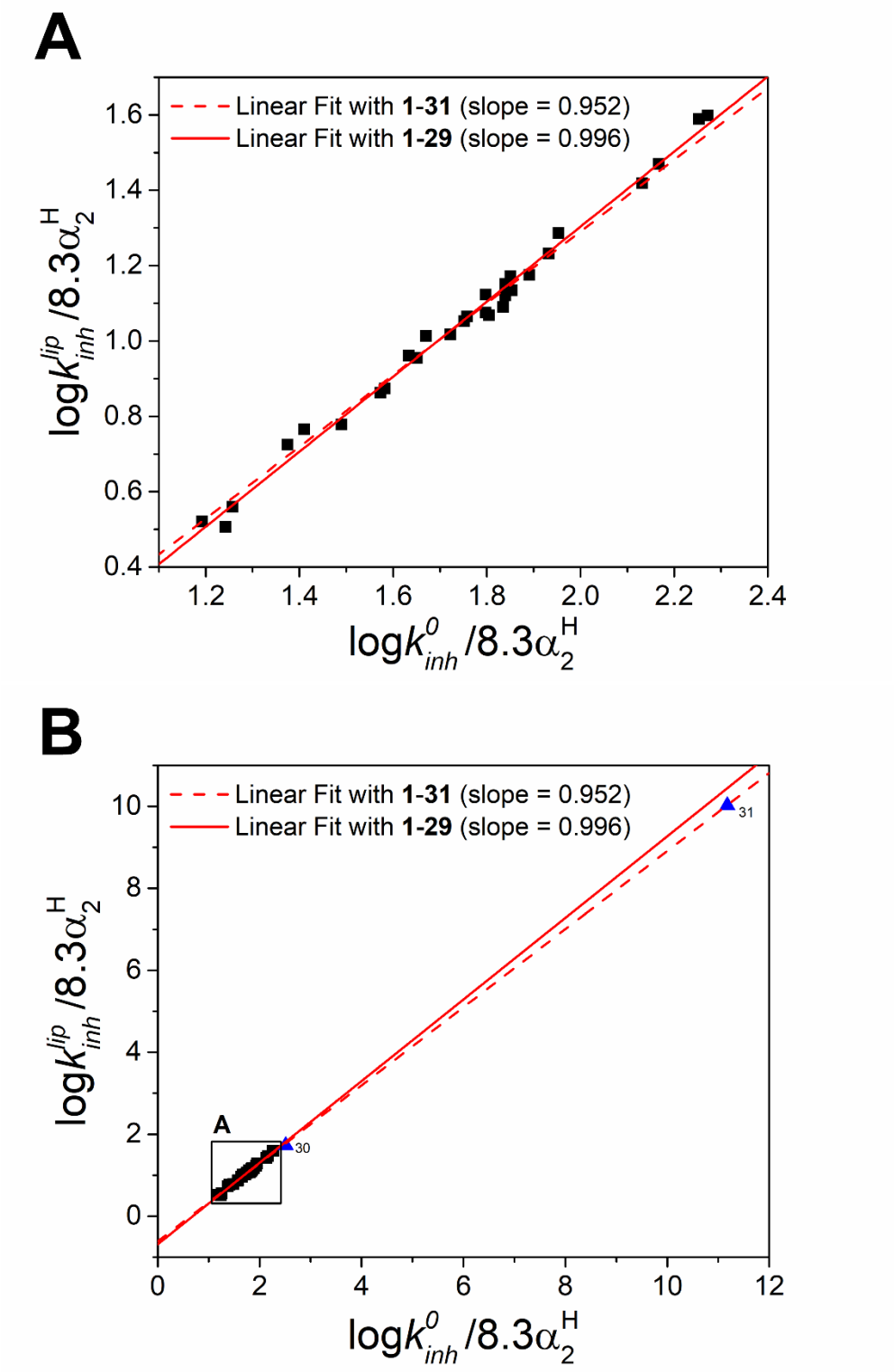


Figure 3.13. Comparison of correlation of $\log(k_{inh}^{0}/8.3\alpha_2^H)$ and $\log(k_{inh}^{lip}/8.3\alpha_2^H)$ with and without **3.30** and **3.31**. If $\log k_{inh}^{lip} = -8.3\alpha_2^H\beta_2^H + \log k_{inh}^{0}$ is true, slope should be 1.

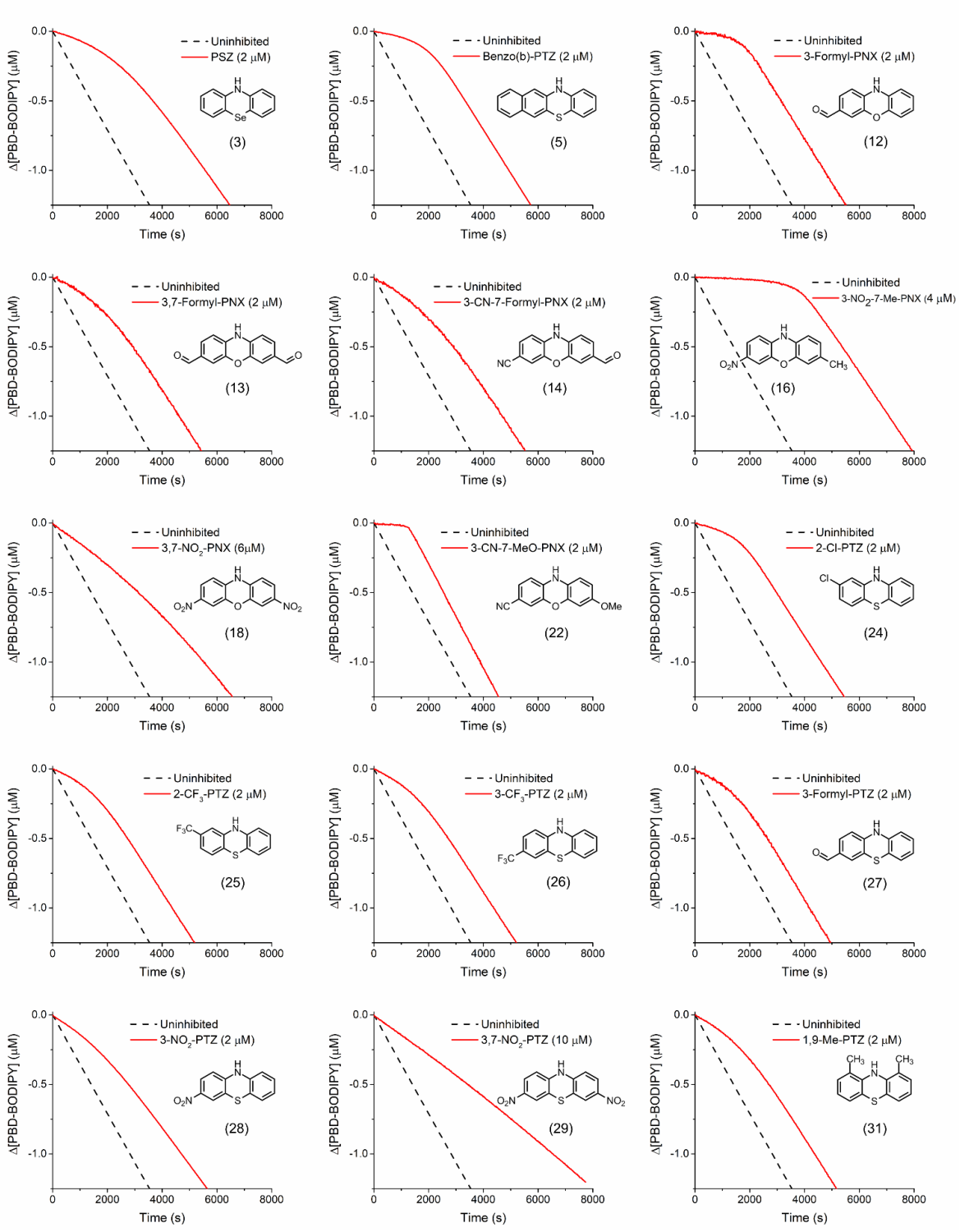


Figure 3.14. ABIN initiated (6 mM) PBD-BODIPY (10 μM) and 1,4-dioxane (1:3 dioxane/PhCl; 37 ºC) co-autoxidation monitored by loss of absorbance (λ_{max} = 587 nm; ε = 123 000 M^{-1} cm^{-1}) inhibited by various RTAs (**3.3**, **3.5**, **3.12**, **3.13**, **3.14**, **3.16**, **3.18**, **3.22**, **3.24**, **3.25**, **3.26**, **3.27**, **3.28**, **3.29** and **3.31**.)

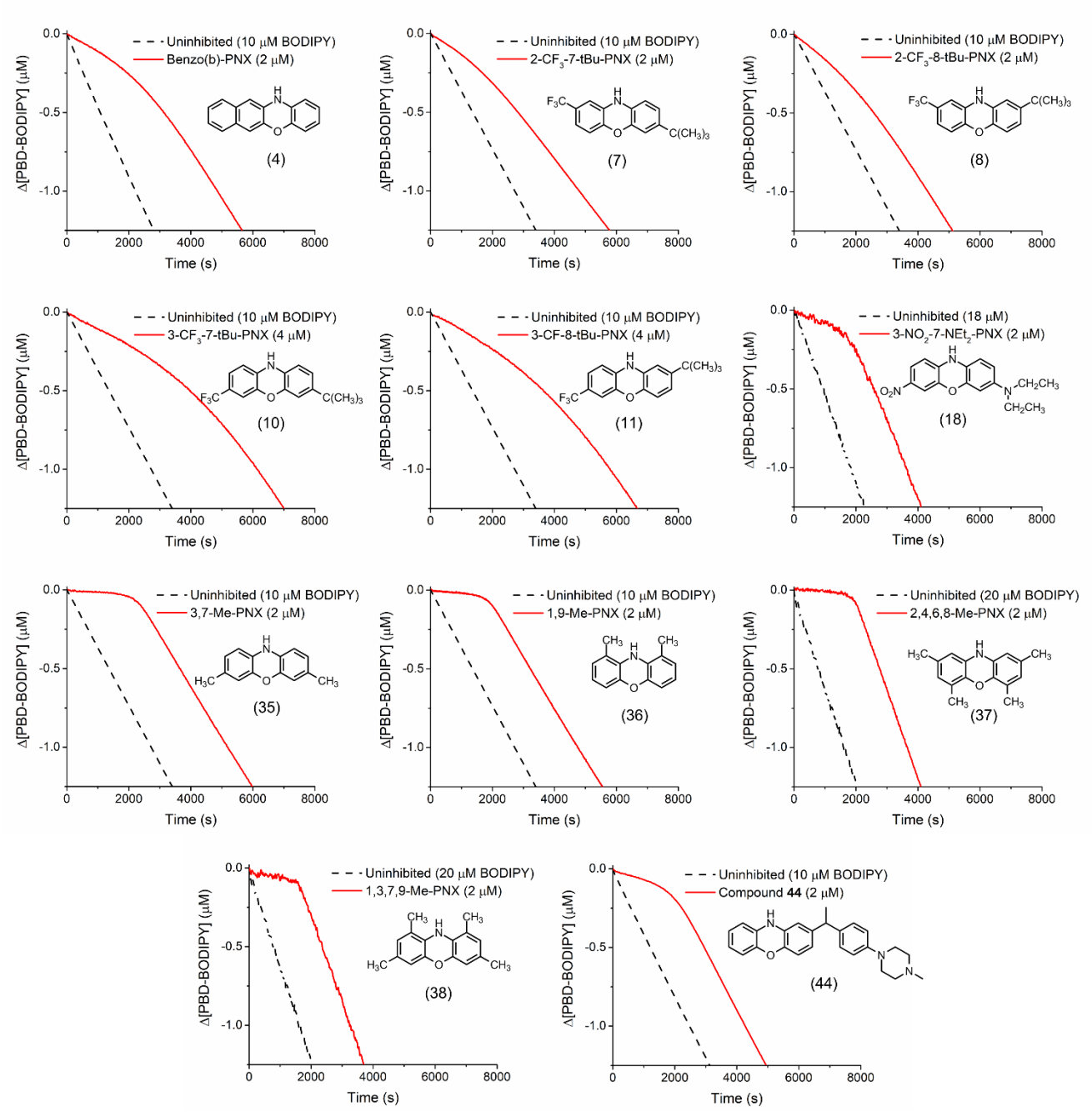


Figure 3.15. ABIN initiated (6 mM) PBD-BODIPY (10-20 μM; k_{BODIPY} = 5900 M^{-1} s^{-1}) and 1,4-dioxane (1:2:1 dioxane/PhCl/DMSO; 37 ºC) co-autoxidation monitored by loss of absorbance (λ_{max} = 587 nm; ε = 118 200 M^{-1} cm^{-1}) inhibited by various RTAs (**3.4**, **3.7**, **3.8**, **3.10**, **3.11**, **3.18**, **3.35**, **3.36**, **3.37**, **3.38** and **3.44**.) Compound **3.18** was corrected for its change in absorbance due to the consumption of **3.18** (see Figure S16).

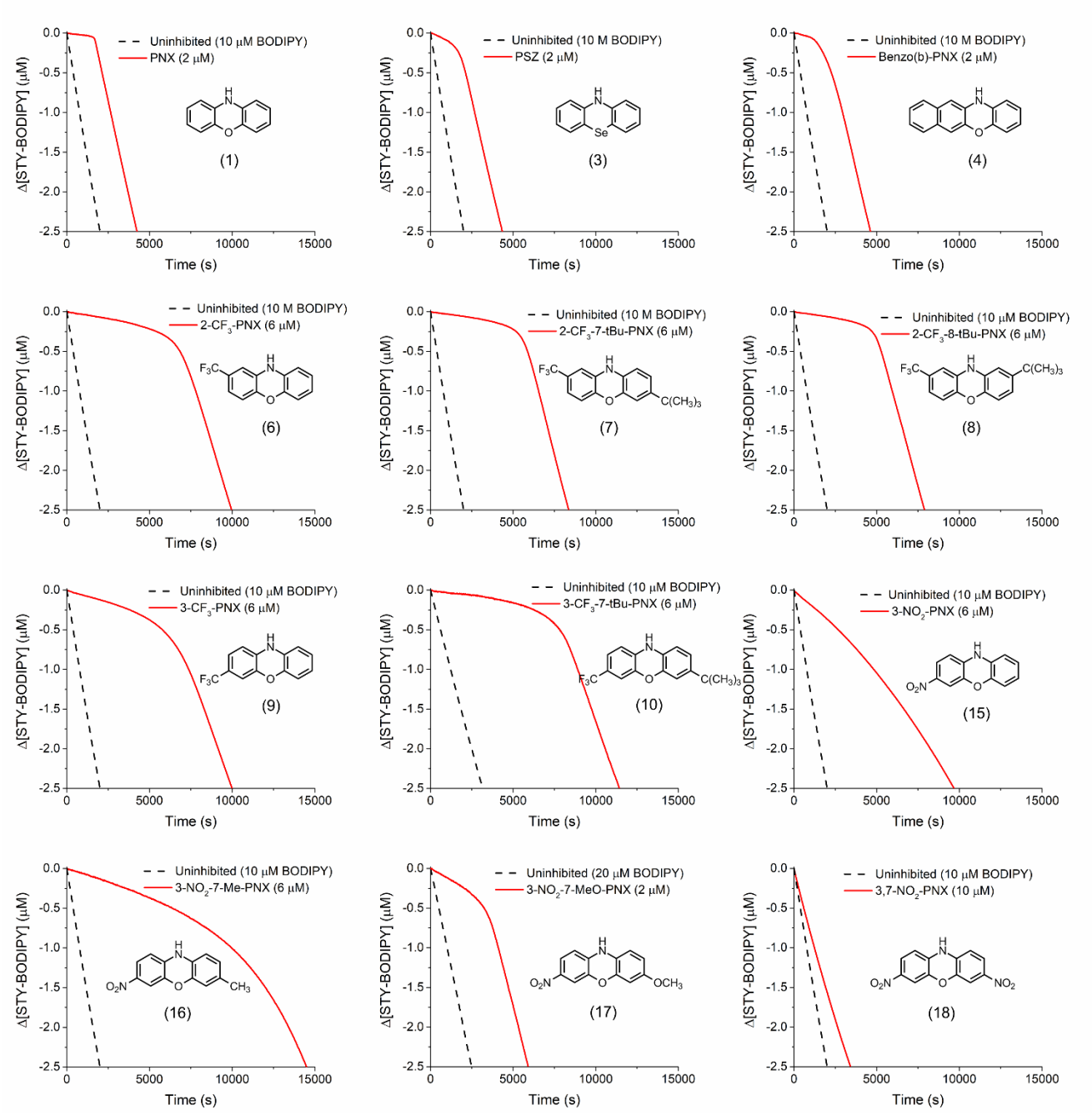


Figure 3.16. MeOAMVN initiated (0.2 mM) co-autoxidation of STY-BODIPY (10-20 μM) in egg PC liposomes (1 mM) monitored by loss of absorbance (λ_{max} = 565 nm; ε = 123 676 M^{-1} cm^{-1}) inhibited by various RTAs (**3.1**, **3.3**, **3.4**, **3.6**, **3.7**, **3.8**, **3.9**, **3.10**, **3.15**, **3.16**, **3.17**, and **3.18**.)

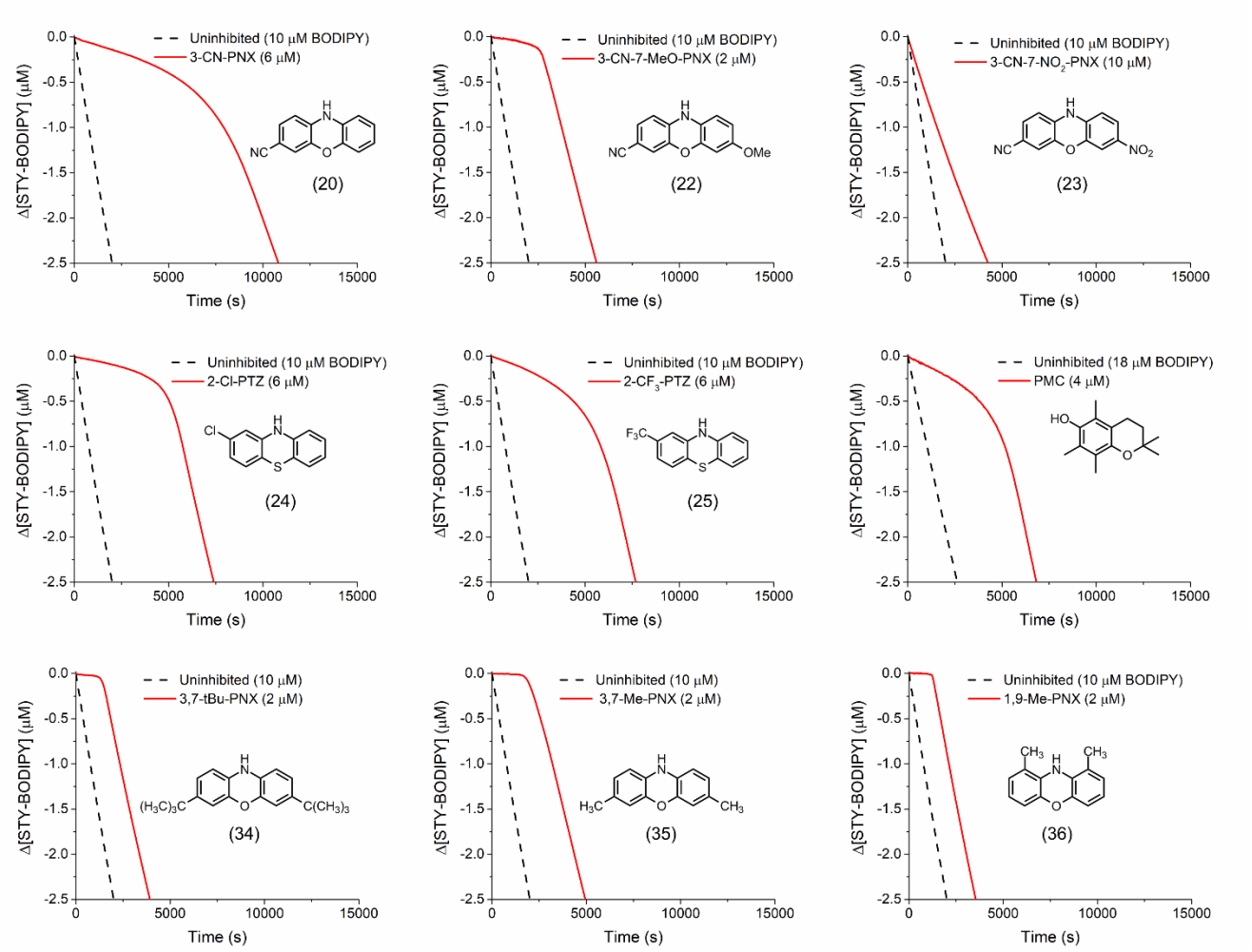


Figure 3.17. MeOAMVN initiated (0.2 mM) co-autoxidation of STY-BODIPY (10-18 μM) in egg PC liposomes (1 mM) monitored by loss of absorbance (λ_{max} = 565 nm; ε = 123 676 M^{-1} cm^{-1}) inhibited by various RTAs (**3.20**, **3.22**, **3.23**, **3.24**, **3.25**, **PMC**, **3.34**, **3.35** and **3.36**.)

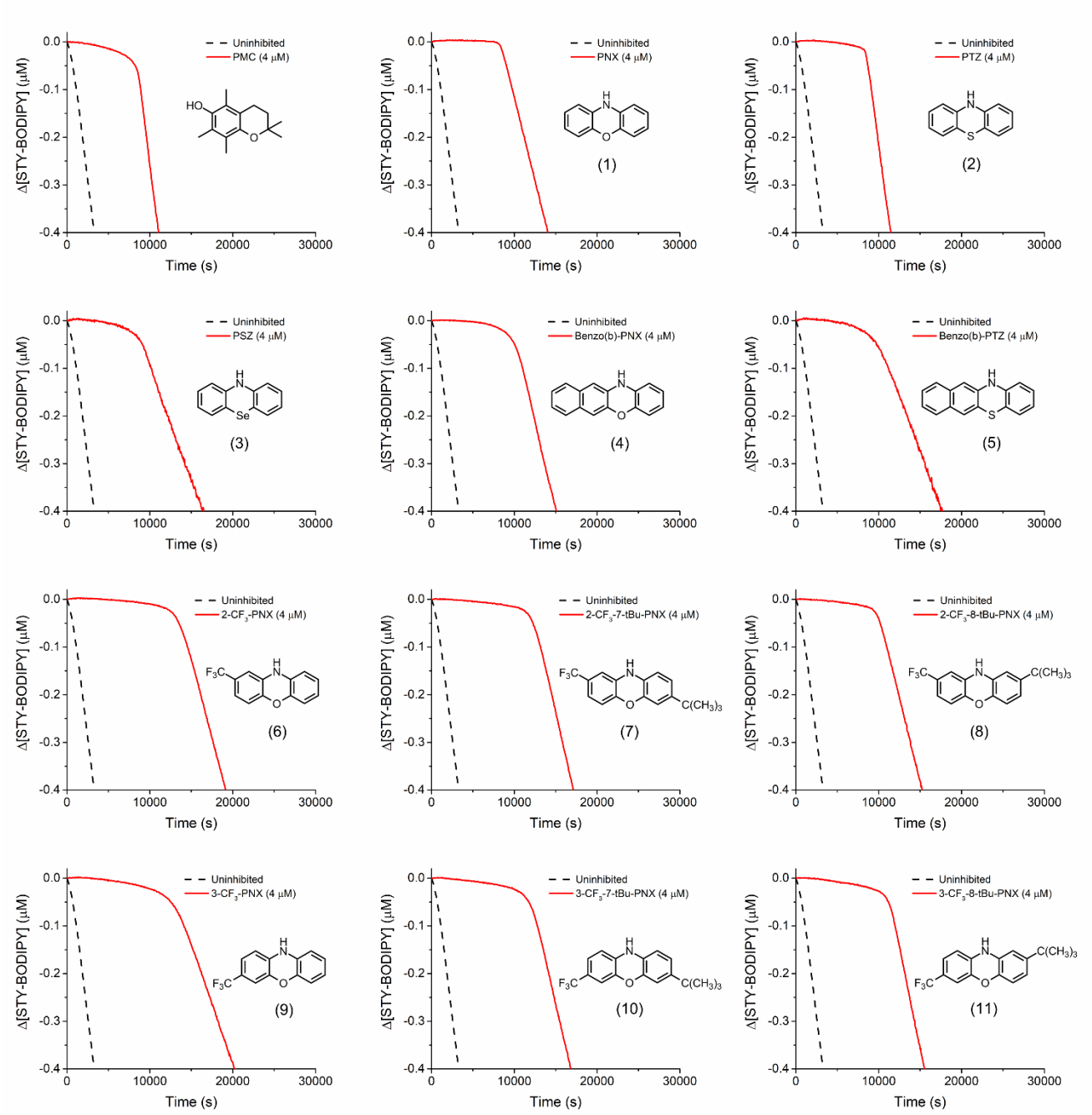


Figure 3.18. MeOAMVN initiated (0.2 mM) co-autoxidation of STY-BODIPY (1 μM) in egg PC liposomes (1 mM) monitored by fluorescence ($\lambda_{ex}/\lambda_{em}$ = 488/518 nm) inhibited by various RTAs (**PMC**, **3.1**, **3.2**, **3.3**, **3.4**, **3.5**, **3.6**, **3.7**, **3.8**, **3.9**, **3.10** and **3.11**.)

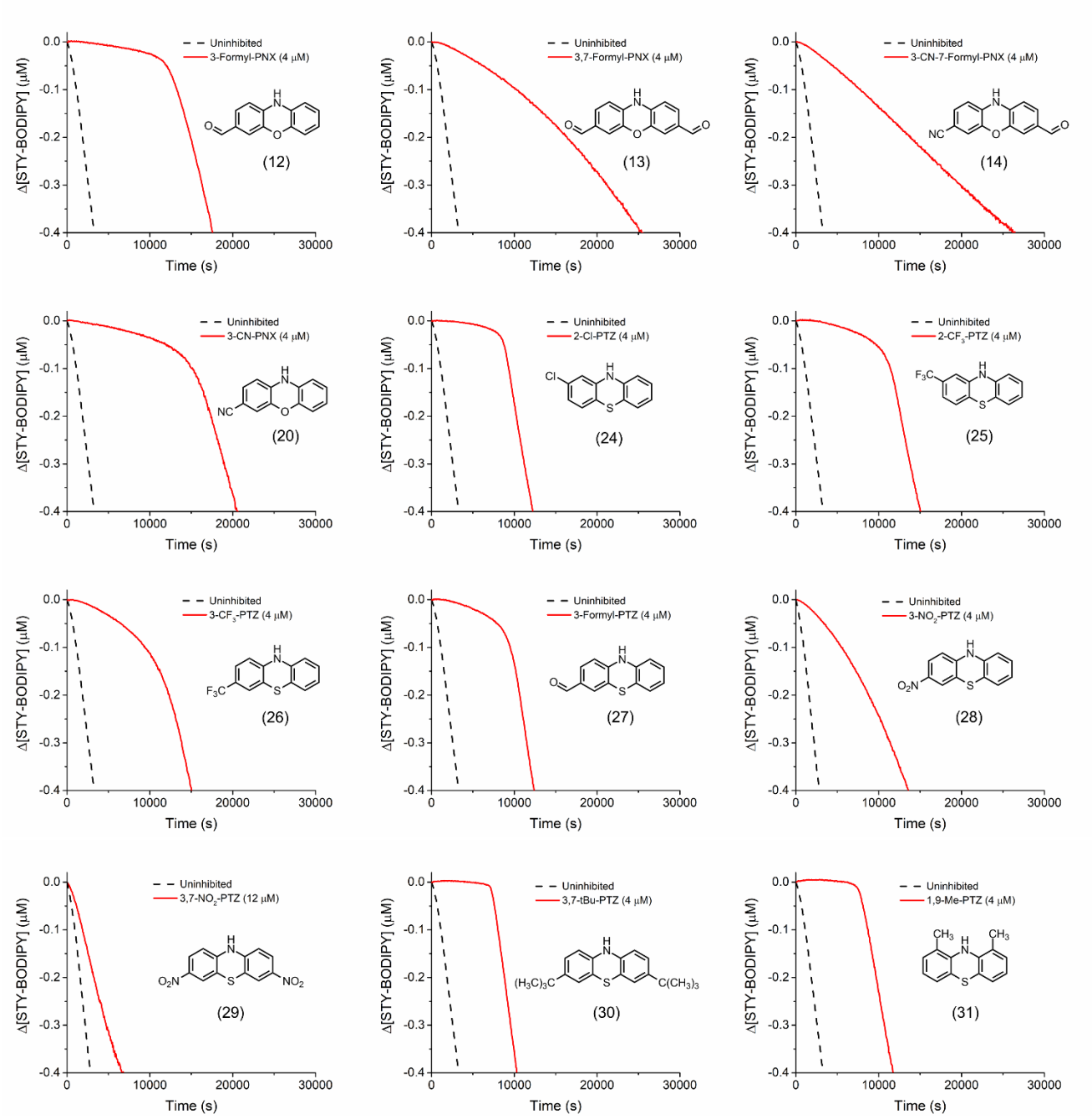


Figure 3.19. MeOAMVN initiated (0.2 mM) co-autoxidation of STY-BODIPY (1 μM) in egg PC liposomes (1 mM) monitored by fluorescence ($\lambda_{ex}/\lambda_{em}$ = 488/518 nm) inhibited by various RTAs (**3.12**, **3.13**, **3.14**, **3.20**, **3.24**, **3.25**, **3.26**, **3.27**, **3.28**, **3.29**, **3.30** and **3.31**.)

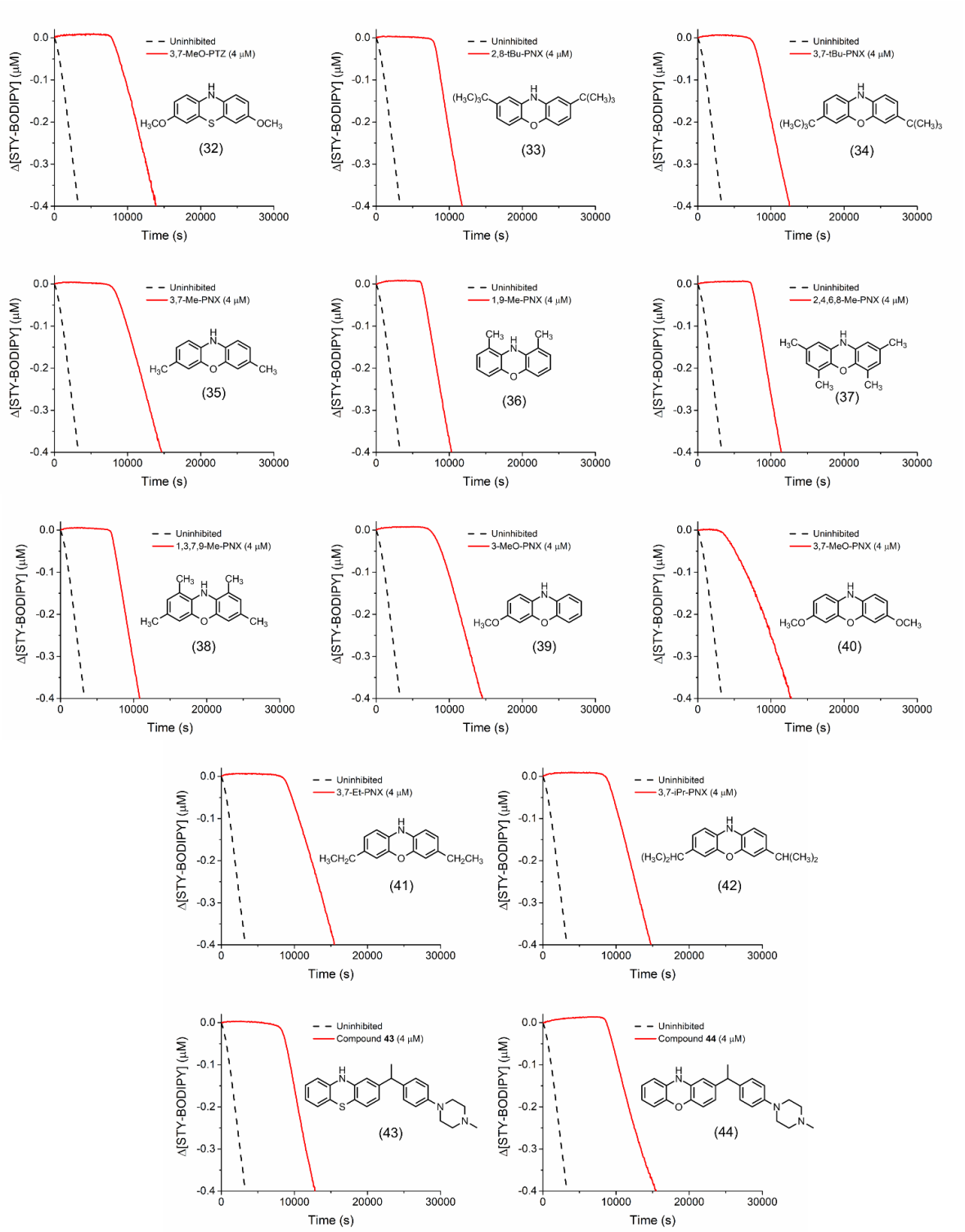


Figure 3.20. MeOAMVN initiated (0.2 mM) co-autoxidation of STY-BODIPY (1 μM) in egg PC liposomes (1 mM) monitored by fluorescence ($\lambda_{ex}/\lambda_{em}$ = 488/518 nm) inhibited by various RTAs (**3.32**, **3.33**, **3.34**, **3.35**, **3.36**, **3.37**, **3.38**, **3.39**, **3.40**, **3.41**, **3.42**, **3.43** and **3.44**.)

Table 3.4. Inhibition Rate Constants and Radical Trapping Stoichiometries in DTUN Initiated Egg PC Liposomes With/Without Ascorbate

		k_{inh}^{lip} (10^3 $M^{-1}s^{-1}$) / n			Log$P$ [e]
		No Ascorbate	10 μM Ascorbate	100 μM Ascorbate	
	PMC	(35 ± 1.3) / (2)	(83 ± 9.7) / 8.6 ± 0.2	(37 ± 3.1) / 11.0 ± 0.3	4.48 ± 0.26
1	PNX	(183 ± 19) / 2.5 ± 0.1	(396 ± 68) / 28.9 ± 0.8	(155 ± 26) / 41.9 ± 0.4	3.84 ± 0.44
2	PTZ	(58 ± 6.4) / 2.7 ± 0.1	(66 ± 3.7) / 9.1 ± 0.2	(30 ± 0.4) / 54.9 ± 1.0	4.15 ± 0.26
3	PSZ	(37 ± 4.7) / 3.8 ± 0.1	(36 ± 0.7) / 22.4 ± 0.5	(31 ± 0.7) / ≥100	4.37 ± 0.70
4	Benzo(b)-PNX	(too fast) / 1.5 ± 0.1 ((10.6 ± 0.6) / 0.9 ± 0.1)	(too short) / 4.9 ± 0.1	(35 ± 1.7) / 34.6 ± 0.8	5.07 ± 0.44
5	Benzo(b)-PTZ	(too fast) / 2.8 ± 0.1	(55 ± 4.6) / 12.9 ± 0.3	(45 ± 2.6) / 45.5 ± 1.7	5.38 ± 0.26
6	2-CF_3-PNX	(57 ± 0.8) / 4.6 ± 0.1	(131 ± 25) / 10.1 ± 0.2	(44 ± 3.7) / 28.2 ± 0.2	5.20 ± 0.51
7	2-CF_3-7-tBu-PNX	(72 ± 13) / 4.1 ± 0.3	(82 ± 1.0) / 7.6 ± 0.1	(28 ± 0.4) / 25.1 ± 0.6	6.88 ± 0.52
8	2-CF_3-8-tBu-PNX	(76 ± 7.4) / 3.6 ± 0.2	(too short) / 5.5 ± 0.1	(too short) / 6.9 ± 0.3 ((11.2 ± 0.4) / - [b])	6.88 ± 0.52
9	3-CF_3-PNX	(34 ± 1.4) / 4.6 ± 0.1	(72 ± 5.0) / 11.7 ± 0.5	(31 ± 2.7) / 31.1 ± 0.6	4.98 ± 0.50
10	3-CF_3-7-tBu-PNX	(48 ± 2.5) / 4.6 ± 0.3	(68 ± 2.3) / 11.3 ± 0.1	(25 ± 0.2) / 40.6 ± 0.6	6.67 ± 0.51
11	3-CF_3-8-tBu-PNX	(56 ± 11) / 3.8 ± 0.1	(71 ± 2.4) / 7.7 ± 0.1	(22 ± 0.6) / 31.2 ± 0.3	6.67 ± 0.51
12	3-CHO-PNX	(39 ± 5.5) / 3.6 ± 0.1	(45 ± 0.6) / 26.2 ± 0.6	(33 ± 0.8) / 86.7 ± 2.3	3.44 ± 0.48
13	3,7-CHO-PNX	(8.8 ± 0.8) / 4.5 ± 0.1	(11.2 ± 0.1) / - [b]	(10.4 ± 0.2) / - [b]	3.03 ± 0.52
14	3-CHO-7-CN-PNX	(8.6 ± 0.9) / >5	(9.1 ± 0.1) / - [b]	(9.3 ± 0.3) / - [b]	3.24 ± 0.53
15	3-NO_2-PNX	(15.7 ± 1.1) / 4.0 ± 0.1	(25 ± 0.7) / 19.4 ± 0.8	(19 ± 0.5) / 65.3 ± 1.2	3.98 ± 0.46
16	3-NO_2-7-Me-PNX	(22 ± 2.7) / 4.2 ± 0.4	(37 ± 1.0) / 16.2 ± 0.2	(19 ± 0.1) / 36.2 ± 0.9	4.44 ± 0.46
17	3-NO_2-7-MeO-PNX	(49 ± 11) [a] / 4.2 ± 0.8	(66 ± 2.0) / 14.7 ± 0.2	(32 ± 0.4) / 44.1 ± 0.2	3.90 ± 0.48
18	3-NO_2-7-NEt_2-PNX	(47 ± 9.4) [a] / 3.6 ± 0.2	(185 ± 10) / 6.9 ± 0.1	(157 ± 34) / 10.3 ± 0.1	5.31 ± 0.48
19	3,7-NO_2-PNX	(2.8 ± 0.1) / - [b]	((6.3 ± 0.1) / -) [b,c]	((6.2 ± 0.1) / -) [b,c]	4.12 ± 0.48
20	3-CN-PNX	(25 ± 3.0) / 4.2 ± 0.1	(41 ± 0.9) / 24.7 ± 0.1	(31 ± 1.4) / 82.9 ± 0.7	3.65 ± 0.49
21	3-CN-7-Me-PNX	(53 ± 2.5) / 4.8 ± 0.2	(69 ± 2.3) / 24.8 ± 0.5	(31 ± 0.4) / 78.9 ± 1.0	4.11 ± 0.49
22	3-CN-7-MeO-PNX	(79 ± 4.8) / 2.2 ± 0.1	(107 ± 4.7) / 20.2 ± 0.4	(44 ± 2.1) / 85.7 ± 1.0	3.56 ± 0.50
23	3-CN-7-NO_2-PNX	(3.0 ± 0.1) / - [b]	((6.6 ± 0.1) / -) [b,c]	((6.2 ± 0.2) / -) [b,c]	3.79 ± 0.51
24	2-Cl-PTZ	(36 ± 2.7) / 2.6 ± 0.1	(64 ± 5.2) / 7.3 ± 0.1	(27 ± 0.3) / 46.5 ± 0.2	5.07 ± 0.27
25	2-CF_3-PTZ	(19 ± 0.7) / 4.0 ± 0.2	(42 ± 3.6) / 14.7 ± 0.5	(28 ± 0.5) / 46.1 ± 0.4	5.50 ± 0.35
26	3-CF_3-PTZ	(11.1 ± 0.7) / 3.2 ± 0.1	(23 ± 0.6) / 12.7 ± 0.1	(15.7 ± 0.5) / 36.7 ± 0.4	4.72 ± 0.77
27	3-CHO-PTZ	(11.7 ± 1.1) / 2.4 ± 0.1	(16.6 ± 0.1) / - [b]	(12.5 ± 0.3) / - [b]	3.57 ± 0.77
28	3-NO_2-PTZ	(5.0 ± 0.3) / 1.8 ± 0.1	(10.4 ± 0.1) / - [b,c]	(10.4 ± 0.1) / - [b,c]	3.88 ± 0.75
29	3,7-NO_2-PTZ	(0.26 ± 0.01) / -	(-) [d]	(-) [d]	3.61 ± 1.03
30	3,7-tBu-PTZ	(46 ± 5.5) / 2.5 ± 0.1	(too short) / 5.4 ± 0.1	(23 ± 0.3) / 15.0 ± 0.3	7.53 ± 0.29
31	1,9-Me-PTZ	(83 ± 8.6) / 1.5 ± 0.1	(too short) / 3.5 ± 0.1	(too short) / 5.7 ± 0.1	5.18 ± 0.28
32	3,7-MeO-PTZ	(too fast) / 2.0 ± 0.1	(404 ± 68) / 33.2 ± 0.8	(127 ± 14) / 74.0 ± 0.9	3.98 ± 1.03
33	2,8-tBu-PNX	(too fast) / 2.8 ± 0.1	(too short) / 5.0 ± 0.2	(39 ± 2.5) / 11.5 ± 0.1	7.22 ± 0.46
34	3,7-tBu-PNX	(too fast) / 3.1 ± 0.1	(98 ± 4.9) / 10.8 ± 0.1	(48 ± 4.3) / 37.1 ± 0.8	7.22 ± 0.46
35	3,7-Me-PNX	(too fast) / 2.5 ± 0.1	(435 ± 27) / 25.0 ± 0.3	(135 ± 8.6) / 51.1 ± 1.4	4.76 ± 0.44
36	1,9-Me-PNX	(too fast) / 1.4 ± 0.1	(too short) / 4.4 ± 0.1	(too short) / 7.8 ± 0.1	4.76 ± 0.44
37	2,4,6,8-Me-PNX	(too fast) / 2.1 ± 0.1	(too short) / 4.9 ± 0.1	(too short) / 8.2 ± 0.2	5.68 ± 0.45
38	1,3,7,9-Me-PNX	(too fast) / 1.8 ± 0.1	(too short) / 3.7 ± 0.7	(too short) / 6.5 ± 0.3	5.68 ± 0.45
39	3-MeO-PNX	(too fast) / 2.1 ± 0.1	(480 ± 179) / 24.4 ± 0.5	(189 ± 37) / 71.8 ± 4.0	3.76 ± 0.45
40	3,7-MeO-PNX	(too fast) / 1.2 ± 0.1	(491 ± 69) / 15.9 ± 0.2	(162 ± 6.7) / 16.7 ± 0.1	3.67 ± 0.47
41	3,7-Et-PNX	(too fast) / 2.9 ± 0.1	(149 ± 6.4) / 15.9 ± 0.3	(77 ± 5.0) / 35.5 ± 0.7	5.83 ± 0.44
42	3,7-iPr-PNX	(too fast) / 3.0 ± 0.1	(108 ± 3.7) / 13.2 ± 0.1	(61 ± 2.8) / 30.8 ± 0.1	6.52 ± 0.45
43		(78 ± 7.4) / 2.6 ± 0.1	(61 ± 3.8) / 6.9 ± 0.1	(35 ± 2.1) / 10.8 ± 0.1	6.07 ± 0.46
44		(too fast) / 2.5 ± 0.1	(264 ± 27) / 8.6 ± 0.1	(114 ± 27) / 12.5 ± 0.1	5.76 ± 0.57

Typical conditions: Egg-PC liposomes (1 mM); [STY-BOIDPY] = 1 μM ($\lambda_{ex}/\lambda_{em}$ = 488/518 nm); 0.2 mM DTUN; [RTA] = 4 μM *or* [RTA] = 0.4 μM + 10/100 μM ascorbate. [a] Measured by monitoring loss of absorbance of STY-BOIDPY (λ_{max} = 565 nm) at [RTA] = 2 μM. [b] Definitive end/inflection to inhibition/retardation not observed for calculation of t_{inh}/n. [c] At low rates of inhibition, the assumption that k_{inh}[RTA] >> $2k_t$[ROO.] may breakdown leading to an overestimated k_{inh}. [d] No change in $-[BODIPY]/dt$ was observed compared to an uninhibited experiment. [e] Log*P* values were calculated in ACD/ChemSketch 2020 (v. 14.50), ACD/Labs.

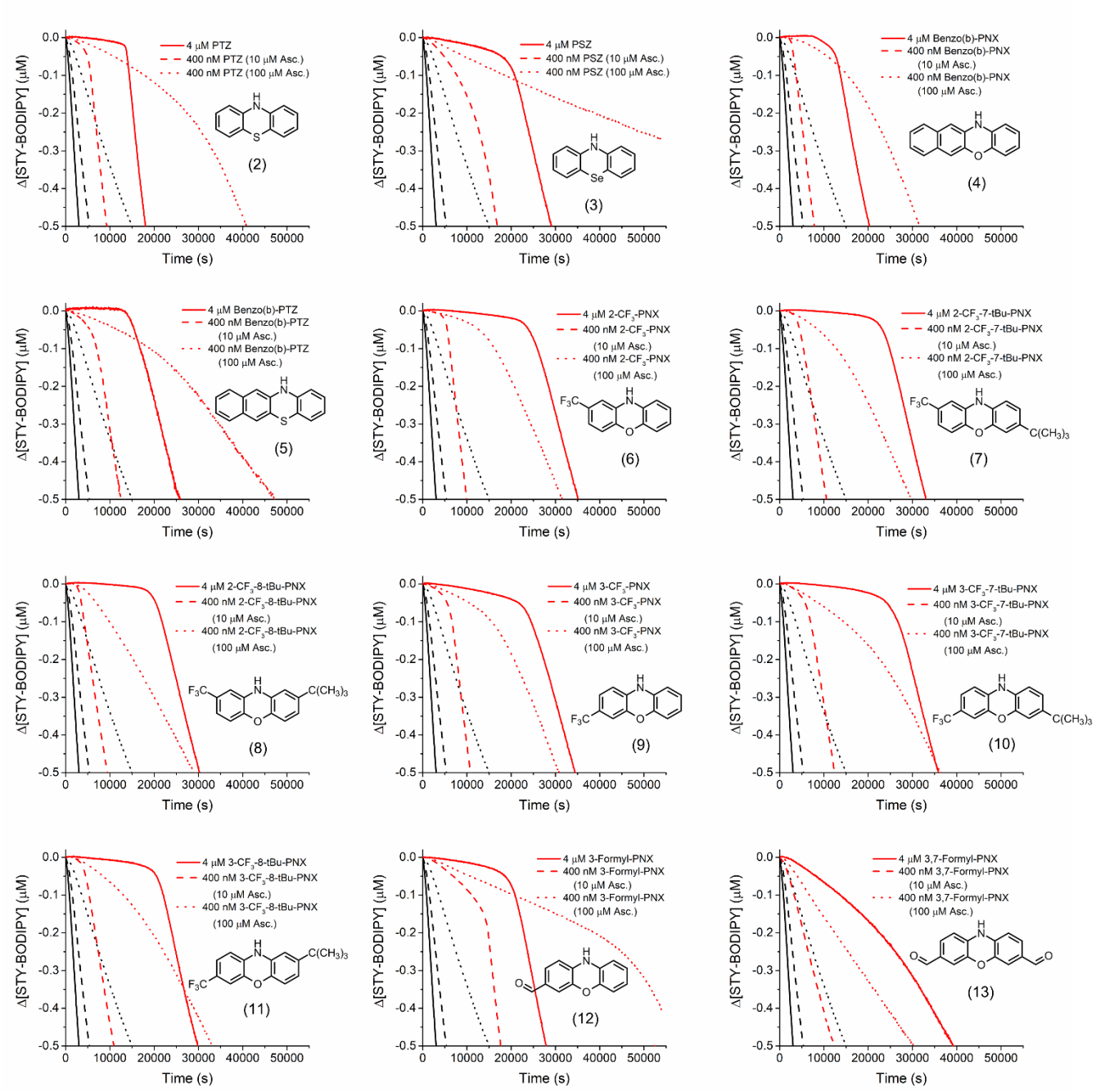


Figure 3.21. DTUN initiated (0.2 mM) co-autoxidation of STY-BODIPY (1 μM) in egg PC liposomes (1 mM) monitored by fluorescence ($\lambda_{ex}/\lambda_{em}$ = 488/518 nm) inhibited by various RTAs (**3.2**, **3.3**, **3.4**, **3.5**, **3.6**, **3.7**, **3.8**, **3.9**, **3.10**, **3.11**, **3.12**, and **3.13**.) No ascorbate (solid line); 10 μM ascorbate (dashed line); 100 μM ascorbate (dotted line).

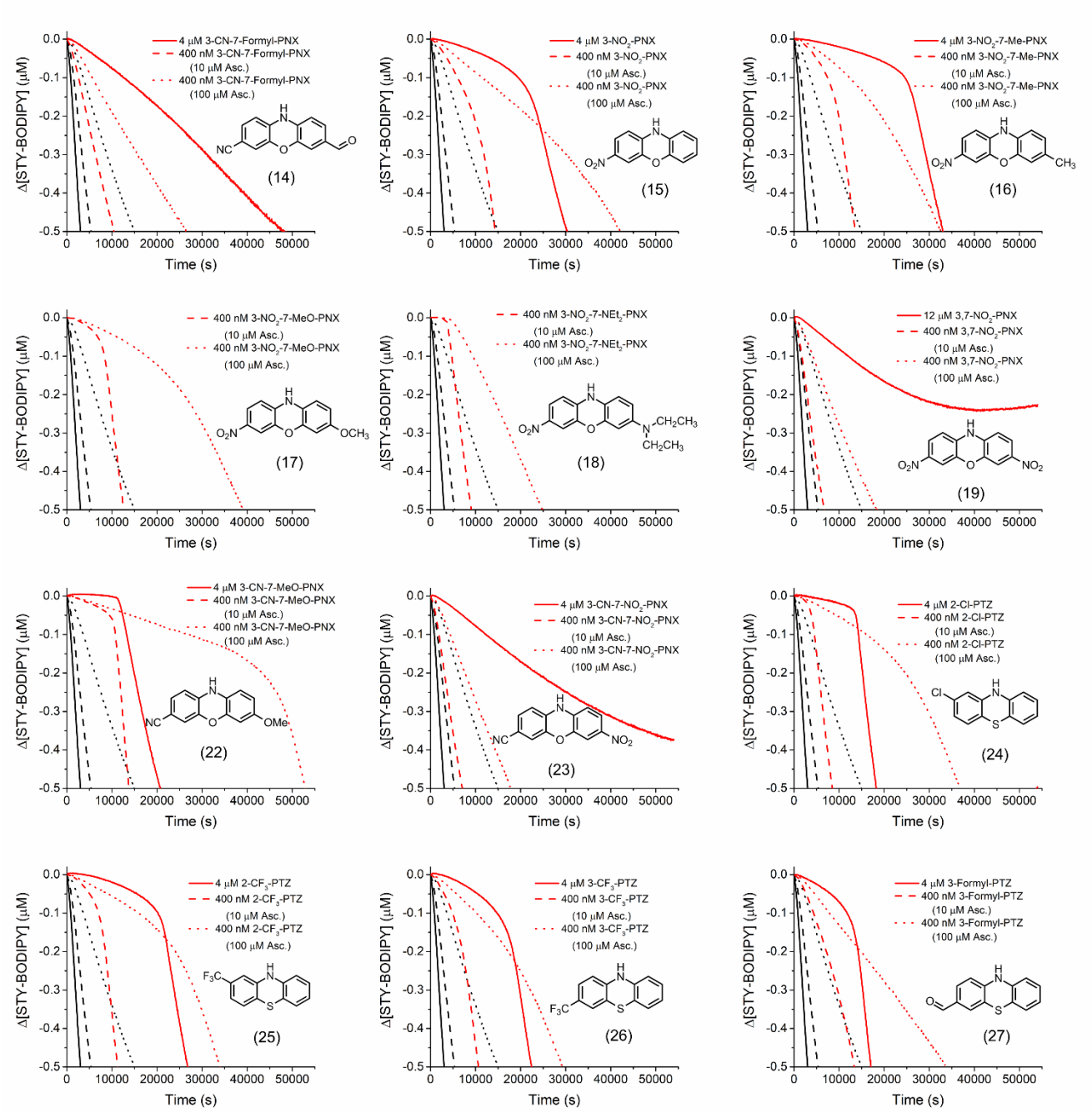


Figure 3.22. DTUN initiated (0.2 mM) co-autoxidation of STY-BODIPY (1 μM) in egg PC liposomes (1 mM) monitored by fluorescence ($\lambda_{ex}/\lambda_{em}$ = 488/518 nm) inhibited by various RTAs (**3.14**, **3.15**, **3.16**, **3.17**, **3.18**, **3.19**, **3.22**, **3.23**, **3.24**, **3.25**, **3.26**, and **3.27**.) No ascorbate (solid line); 10 μM ascorbate (dashed line); 100 μM ascorbate (dotted line).

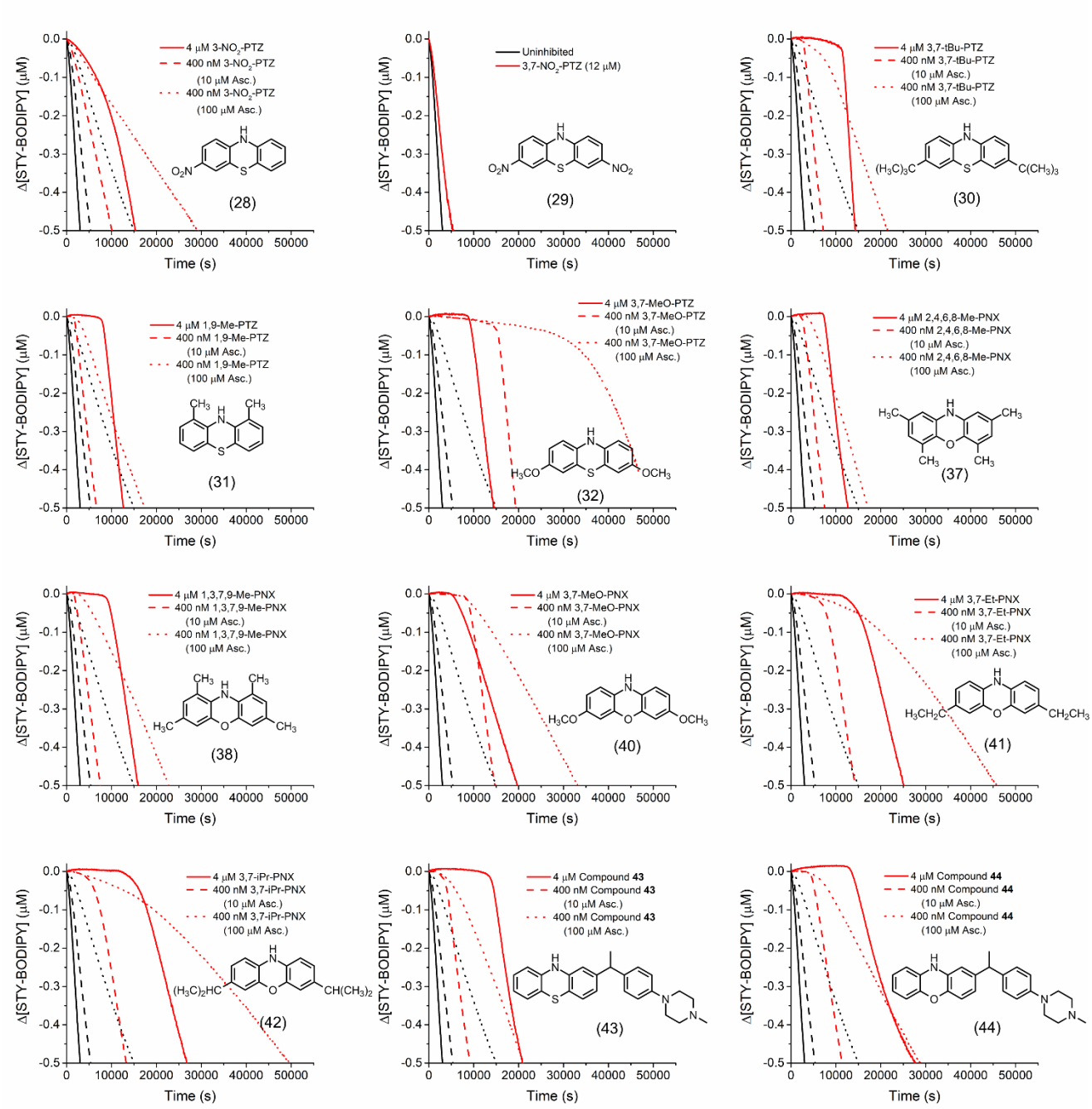


Figure 3.23. DTUN initiated (0.2 mM) co-autoxidation of STY-BODIPY (1 μM) in egg PC liposomes (1 mM) monitored by fluorescence ($\lambda_{ex}/\lambda_{em}$ = 488/518 nm) inhibited by various RTAs (**3.28**, **3.29**, **3.30**, **3.31**, **3.32**, **3.37**, **3.38**, **3.40**, **3.41**, **3.42**, **3.43**, and **3.44**.) No ascorbate (solid line); 10 μM ascorbate (dashed line); 100 μM ascorbate (dotted line).

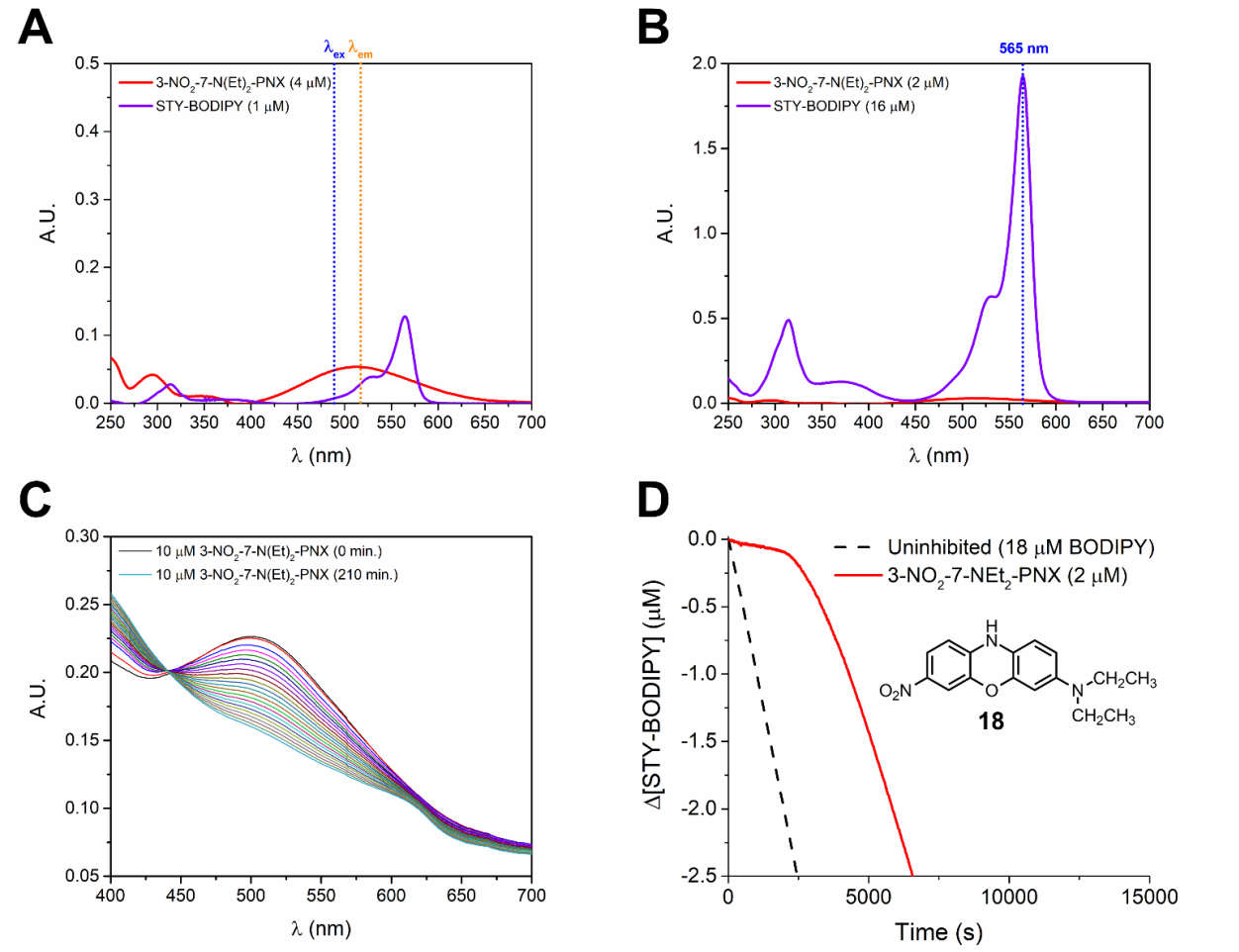


Figure 3.24. Conditions: 1 mM Egg-PC liposomes in 10 mM PBS buffer (pH 7.4). **(A)** On account of the relatively high extinction coefficient of **3.18** from 450-600 nm, it interferes with the excitation/emission of the STY-BODIPY fluorescence assay at 4 μM of **3.18** (does not interfere significantly at 0.4 μM). **(B)** Under the STY-BODIPY absorbance assay the relative contribution to absorbance at 565 nm is minor. **(C)** Absorbance from 450-600 nm for **3.18** decreases as the RTA is consumed (0.2 mM MeOAMVN, 37 ºC). To correct for this contribution, in parallel with the STY/PBD-BODIPY co-autoxidations inhibited by **3.18**, an identical parallel experiment in the absence of STY/PBD-BODIPY is carried out and the change of absorbance is subtracted from the co-autoxidation data. **(D)** MeOAMVN initiated (0.2 mM; R_i = 1.7 × 10^{-9} M s^{-1}) co-autoxidation of STY-BODIPY (18 μM) in egg PC liposomes (1 mM) monitored by loss of absorbance (λ_{max} = 565 nm; ε = 123 676 M^{-1} cm^{-1}) inhibited by **3.18** (corrected).

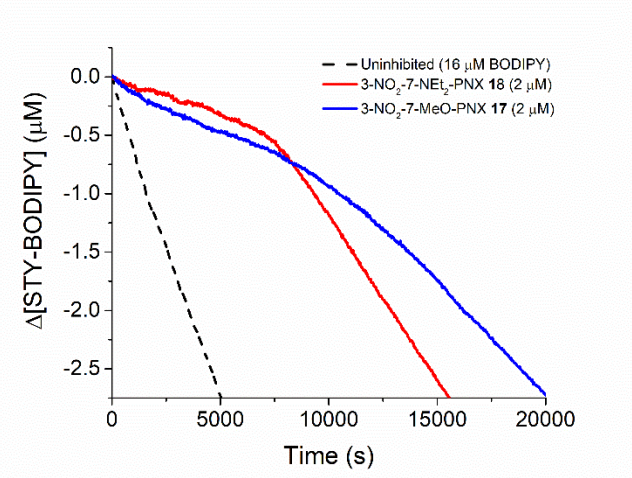


Figure 3.25. DTUN initiated (0.2 mM; $R_i = 9.0 \times 10^{-10}$ M s^{-1}) co-autoxidation of STY-BODIPY (16 μM) in egg PC liposomes (1 mM) monitored by loss of absorbance (λ_{max} = 565 nm; ε = 123 676 M^{-1} cm^{-1}) inhibited by **3.18** (corrected) and **3.17**.

3.9.2 Cell, Microsome and Animal Data

Table 3.5. Summary of the Anti-Ferroptosis Activity in RSL3 Induced Mouse-Embryonic Fibroblasts

	RTA	Pfa-1 MEF Ferroptosis EC_{50} (nM)
	Fer-1	27 ± 2
	Lip-1	18 ± 1
	PMC	360 ± 30
1	PNX	16 ± 1
2	PTZ	24 ± 1
3	PSZ	23 ± 2
4	Benzo(b)-PNX	5.2 ± 0.9
5	Benzo(b)-PTZ	7.8 ± 0.2
6	2-CF_3-PNX	8.8 ± 0.5
7	2-CF_3-7-tBu-PNX	4.1 ± 0.1
8	2-CF_3-8-tBu-PNX	5.6 ± 0.3
9	3-CF_3-PNX	12 ± 1
10	3-CF_3-7-tBu-PNX	5.2 ± 0.2
11	3-CF_3-8-tBu-PNX	3.6 ± 0.2
12	3-CHO-PNX	240 ± 23
13	3,7-CHO-PNX	340 ± 49
14	3-CHO-7-CN-PNX	240 ± 16
15	3-NO_2-PNX	43 ± 5
16	3-NO_2-7-Me-PNX	15 ± 1
17	3-NO_2-7-MeO-PNX	31 ± 1
18	3-NO_2-7-NEt_2-PNX	14 ± 2
19	3,7-NO_2-PNX	405 ± 16
20	3-CN-PNX	58 ± 1
21	3-CN-7-Me-PNX	22 ± 5
22	3-CN-7-MeO-PNX	42 ± 6
23	3-CN-7-NO_2-PNX	455 ± 19
24	2-Cl-PTZ	56 ± 10
25	2-CF_3-PTZ	16 ± 1
26	3-CF_3-PTZ	41 ± 5
27	3-CHO-PTZ	140 ± 10
28	3-NO_2-PTZ	140 ± 18
29	3,7-NO_2-PTZ [a]	≥1000
30	3,7-tBu-PTZ	8.9 ± 0.2
31	1,9-Me-PTZ	35 ± 2
32	3,7-MeO-PTZ	9.0 ± 0.5
33	2,8-tBu-PNX	7.2 ± 0.4
34	3,7-tBu-PNX	7.4 ± 0.1
35	3,7-Me-PNX	5.4 ± 0.2
36	1,9-Me-PNX	14 ± 2
37	2,4,6,8-Me-PNX	9.6 ± 0.2
38	1,3,7,9-Me-PNX	7.6 ± 0.2
39	3-MeO-PNX	12 ± 1
40	3,7-MeO-PNX	11 ± 1
43		6.5 ± 0.5
44		7.4 ± 0.5

(a) Compound **29** showed ~50% viability at 1000 μM but a decrease in apparent cell viability above 1000 μM.

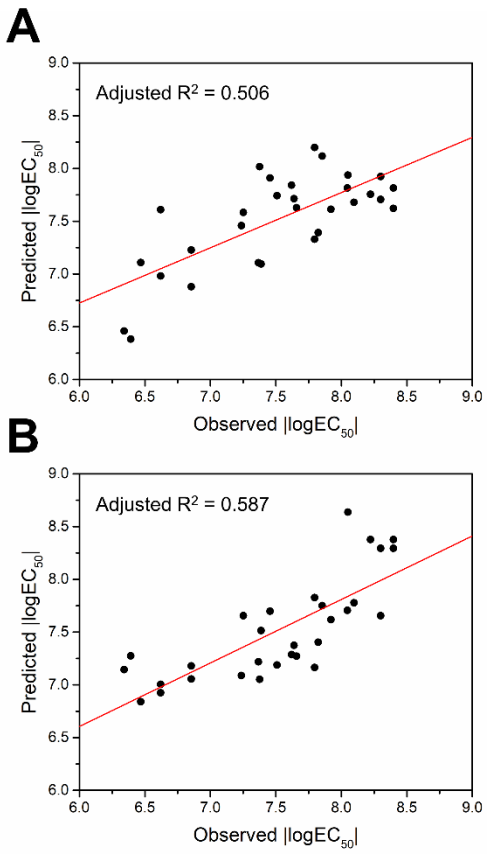


Figure 3.26. Single/multi-variable linear regressions developed for the observed EC_{50} values (Table 3.5) of compounds **3.1-3.28** and **3.30-3.31** using Microsoft Excel the Analysis ToolPak add-in (the 'Regression' function; set to 95% confidence level). **(A)** Developed from observed $|\log EC_{50}|$ and measured $\log k_{inh}^{lip}$ (MeOAMVN) (Table 3.3): $|\log EC_{50}| = 0.8116 \log k_{inh}^{lip} + 3.8575$. **(B)** Developed from observed $|\log EC_{50}|$ and predicted $\log P$ (Table 3.4): $|\log EC_{50}| = 0.3991 \log P + 5.6312$.

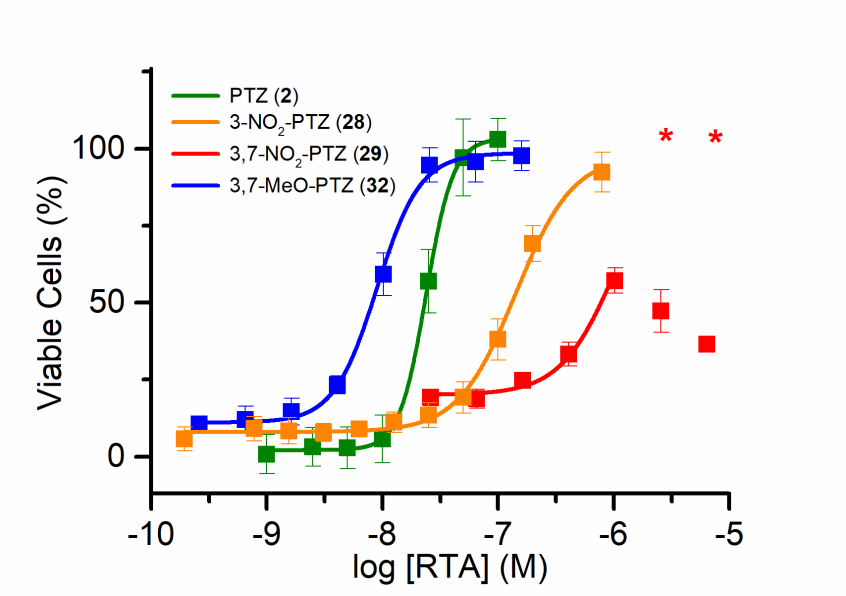


Figure 3.27. RSL3 induced ferroptosis inhibited by both electron-rich (**3.2** and **3.32**) and electron-poor (**3.28** and **3.29**) phenothiazine derivatives. Compound **3.29** showed a decrease in apparent cell viability above 1000 μM. "Dummy-data points" (*) were used to generate the observed sigmoidal curve for **3.29**.

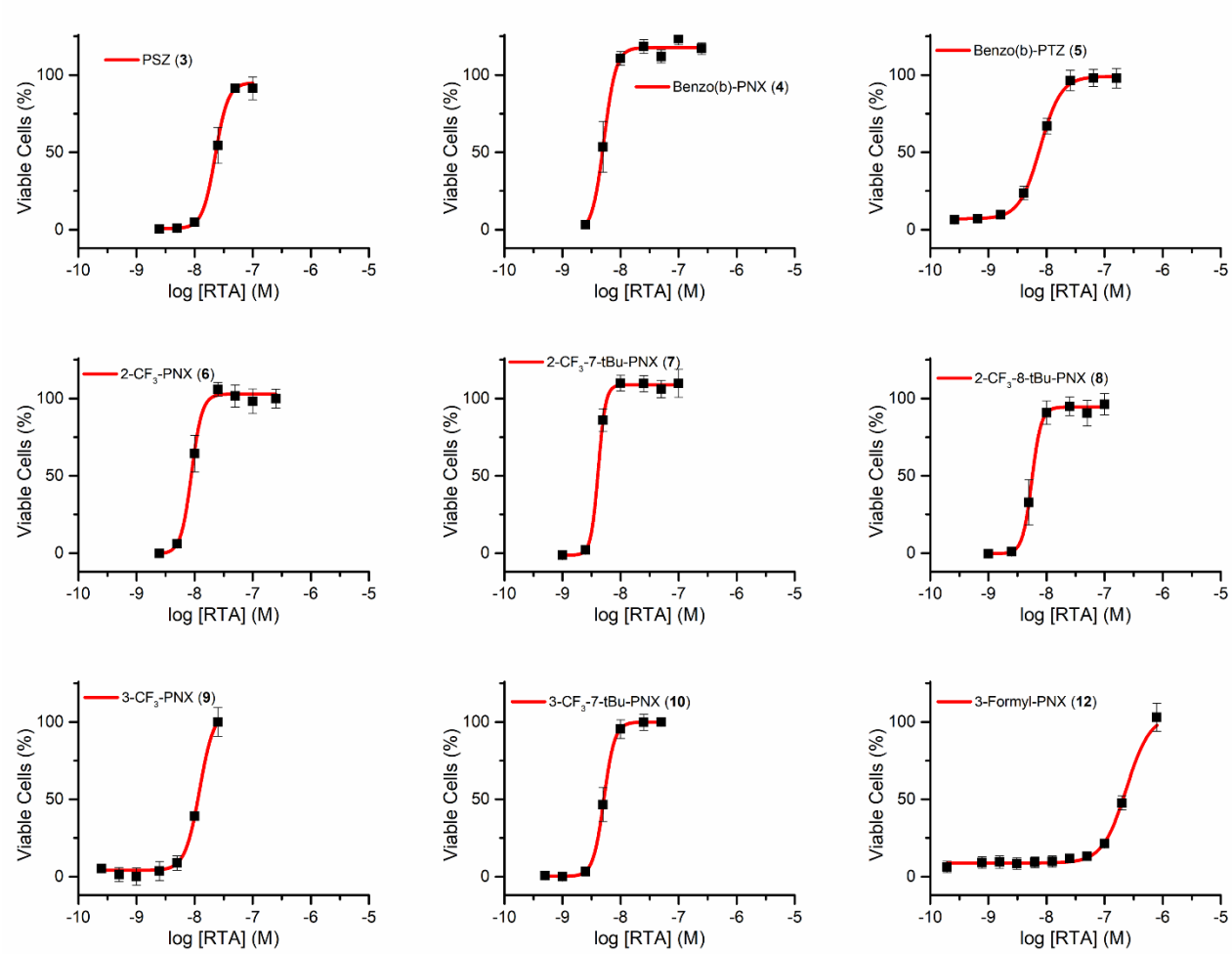


Figure 3.28. RSL3 induced ferroptosis (pfa-1 MEFS) inhibited by various RTAs (**3.3**, **3.4**, **3.5**, **3.6**, **3.7**, **3.8**, **3.9**, **3.10** and **3.12**.)

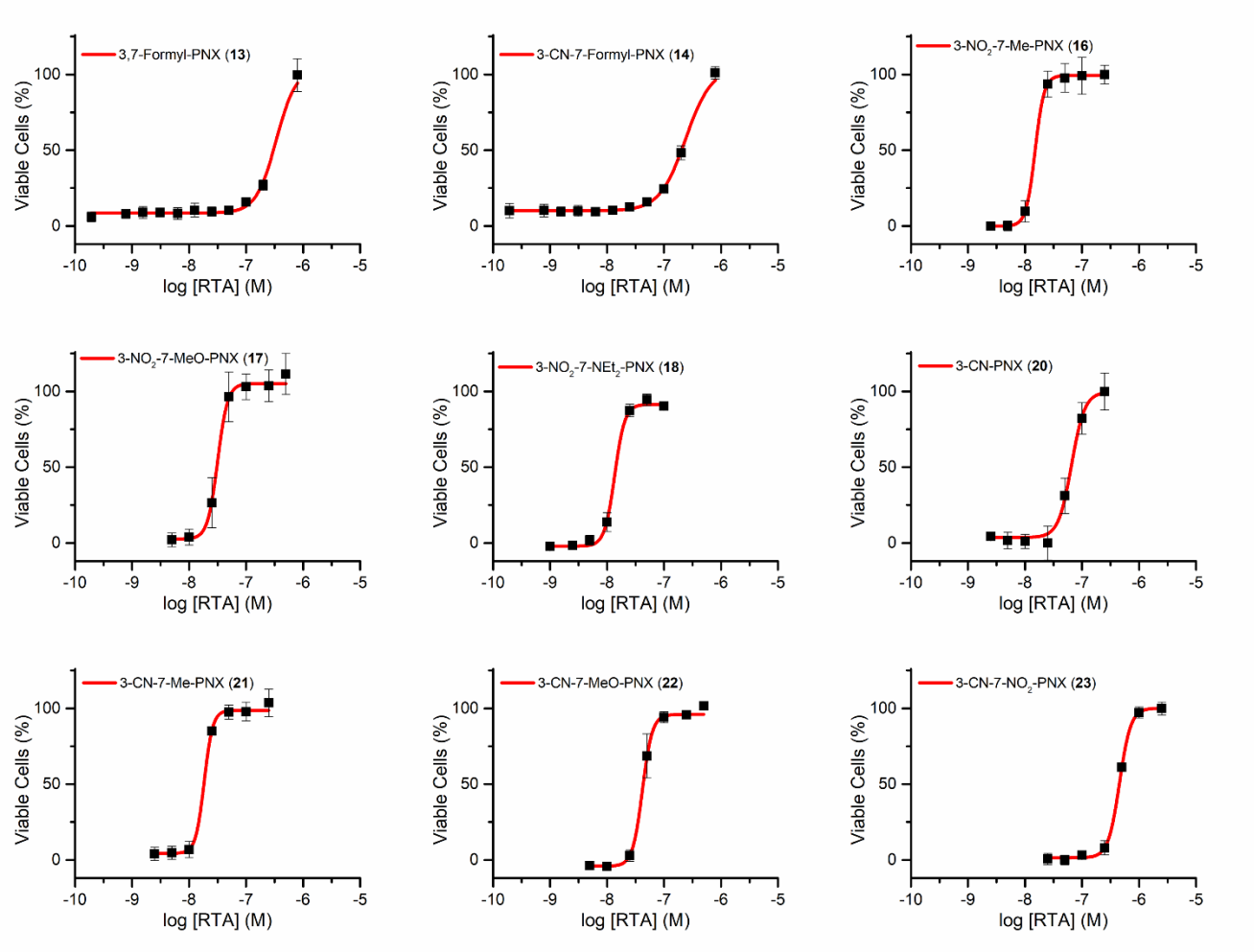


Figure 3.29. RSL3 induced ferroptosis (pfa-1 MEFS) inhibited by various RTAs (**3.13**, **3.14**, **3.16**, **3.17**, **3.18**, **3.20**, **3.21**, **3.22** and **3.23**.)

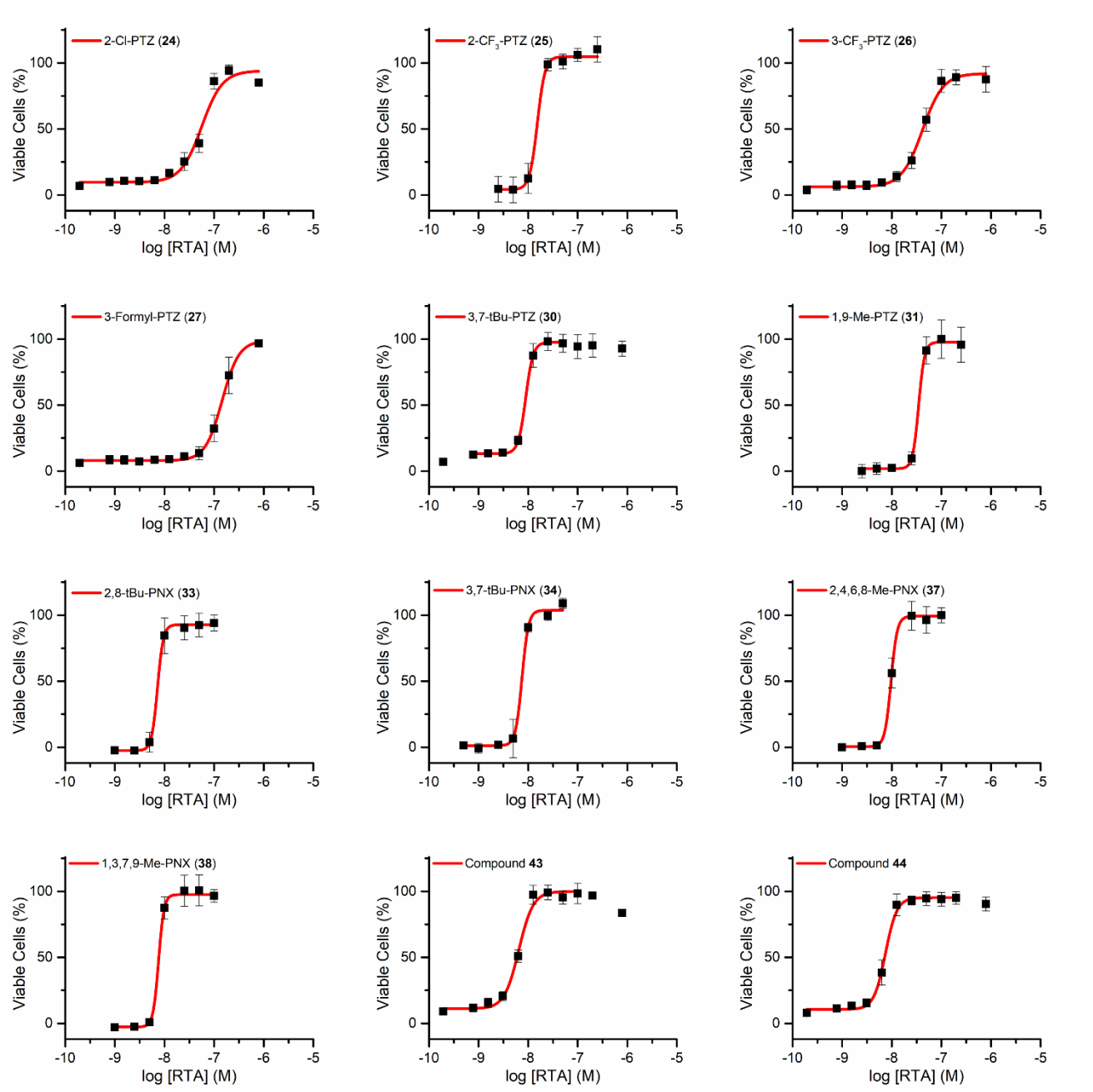


Figure 3.30. RSL3 induced ferroptosis (pfa-1 MEFS) inhibited by various RTAs (**3.24**, **3.25**, **3.26**, **3.27**, **3.30**, **3.31**, **3.33**, **3.34**, **3.37**, **3.38**, **3.43** and **3.44**.)

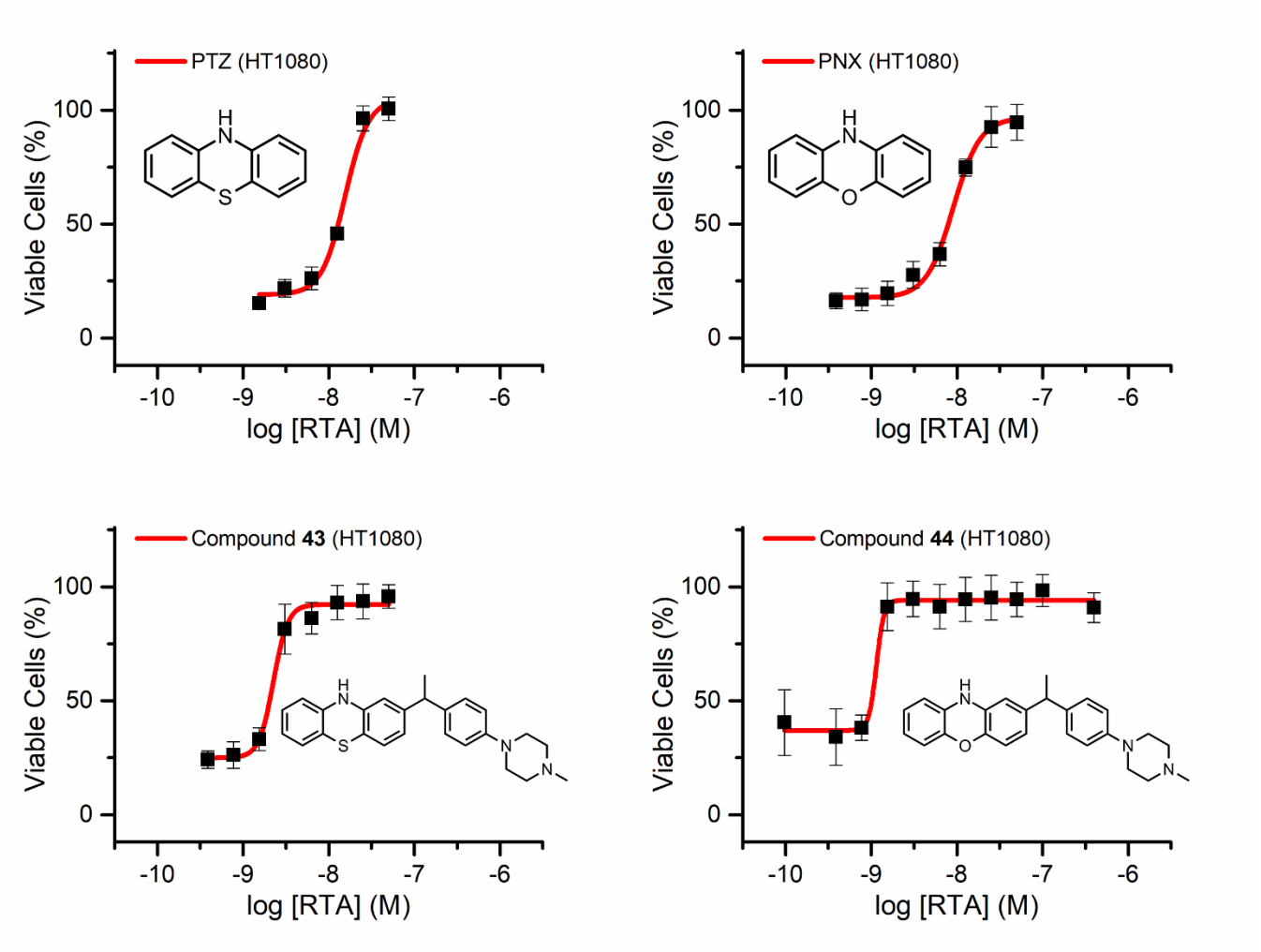


Figure 3.31. Erastin (5 μM) induced ferroptosis in HT1080 (3000 cells per well) inhibited by PTZ, PNX, **3.43** and **3.44** over 26 hours.

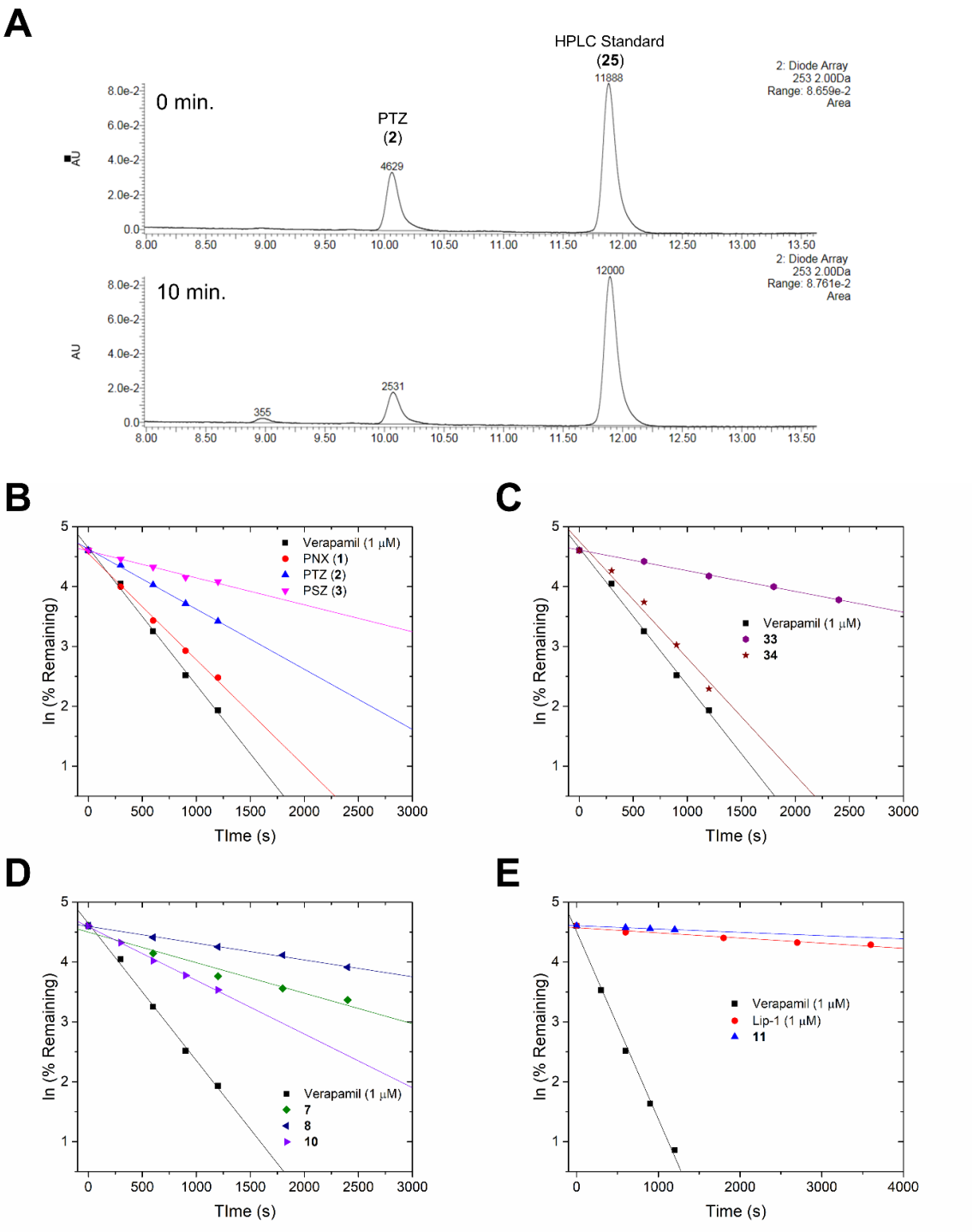


Figure 3.32. (A) Representative UPLC traces for quantification by PDA (253 nm) of analyte (PTZ) remaining during the liver microsome stability assay relative to 0 min, normalized to the HPLC/internal standard (**3.25**). **(B-D)** Conditions: 0.5 mg/mL liver microsomes; 1 mM NADPH; 100 mM phosphate buffer (pH 7.4); 37ºC, 10 μM RTA. **(E)** Conditions: 1.0 mg/mL liver microsomes; 1 mM NADPH; 100 mM phosphate buffer (pH 7.4); 37ºC, 10 μM **3.11**.

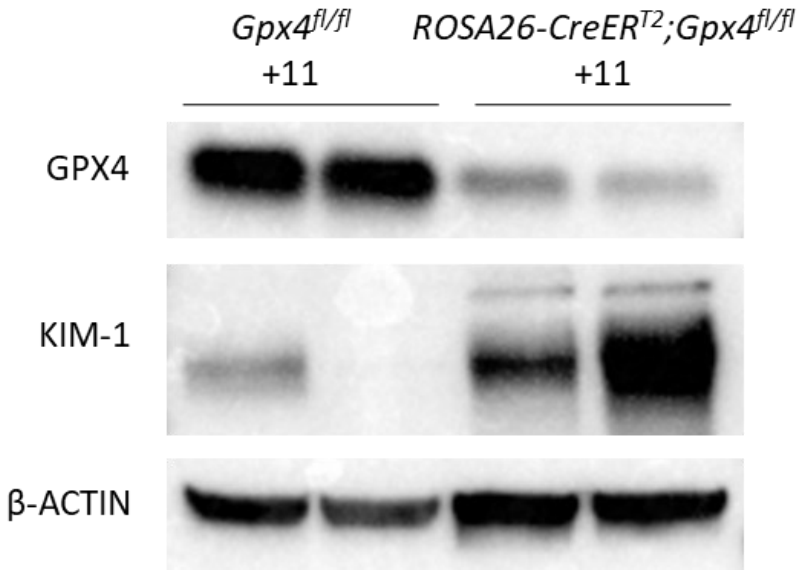
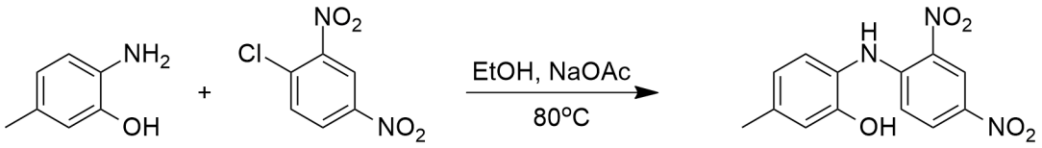


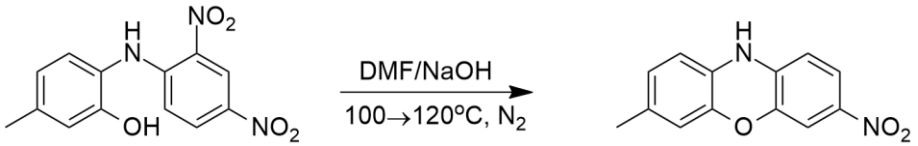
Figure 3.33. *ROSA26-CreER^{T2};Gpx4$^{fl/fl}$ and Gpx4$^{fl/fl}$* mice were injected with Tamoxifen on day 0 and 2 to induce deletion of *Gpx4*. Surviving animals were sacrificed on day 25 after daily treatment with **3.11** at a dose of 20 mg/kg. Western blot analysis of kidneys confirms knockout of GPx4. Kidney Injury Molecule-1 (KIM-1) was used as a biomarker for kidney injury.

3.10 Materials and Synthesis

General. Reagents and solvents were procured from commercial sources and were used without further purification unless otherwise indicated. The preparation and characterization of phenoselenazine,[2] 12H-Benzo[b]phenoxazine,[3] 12H-Benzo[b]phenothiazine,[3] 2-trifluoromethylphenoxazine,[4] 3-trifluoromethylphenoxazine,[4] 3-trifluoromethylphenothiazine,[5,6] 3-cyanophenoxazine,[4] 3-cyano-7-nitrophenoxazine,[4] 3-nitrophenoxazine,[4] 3-nitrophenothiazine,[6,7] 3-nitro-7-methoxyphenoxazine,[4] 3-formylphenothiazine,[8] 1,9-dimethylphenothiazine,[9] 3,7-di-*tert*-butylphenoxazine,[4] 3-methoxyphenoxazine,[4] 2,8-di-*tert*-butylphenoxazine,[4] 3,7-dimethoxyphenoxazine,[4] 3,7-dimethoxyphenothiazine,[9] 2-amino-3,5-dimethylphenol,[10] 2-amino-4,6-dimethylphenol,[11] 2-acetylphenoxazine[12] and 2-(1-(4-(4-methylpiperazin-1-yl)phenyl)ethyl)-10H-phenothiazine[13] have been previously described.

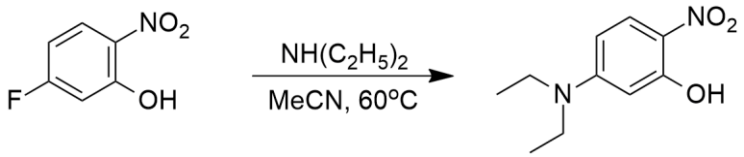


2-((2,4-Dinitrophenyl)amino)-5-methylphenol (3.16a). In a round bottom flask affixed with a reflux condenser were combined ethanol (60 mL), 2-amino-5-methylphenol (1.85 g, 15 mmol), 1-chloro-2,4-dinitrobenzene (3.04 g, 15 mmol) and sodium acetate (1.23 g, 15 mmol). With stirring the mixture was refluxed (80 °C) for 4 hours after which the solution was allowed to cool to room temperature. The solution was poured into water and the red solid was filtered and rinsed with excess water. The filtered solid was recrystallized out of ethanol to afford the title product as red/orange needles (3.33 g, 77%). ^{1}H NMR (400 MHz; DMSO-d6): 9.87 (br, 2H), 8.89 (d, J = 2.7 Hz, 1H), 8.21 (dd, J = 2.7, 9.6 Hz, 1H), (d, J = 7.9 Hz, 1H), 6.85-6.83 (m, 2H), 6.74 (dd, J = 1.0, 8.0 Hz, 1H), 2.28 (s, 3H). ^{13}C NMR (101 MHz; DMSO-d6): δ 152.0, 147.2, 138.3, 135.9, 130.6, 129.7, 127.1, 123.3, 121.6, 120.4, 117.2, 117.1, 20.9. (EI, magnetic sector): calcd for $C_{13}H_{11}N_3O_5$ 289.06987, found 289.06685. mp = 166-168 °C (lit. 166-167 °C).[14]

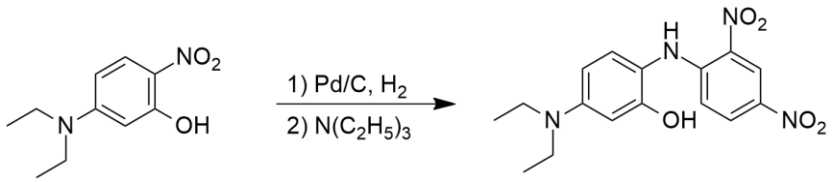


3-Methyl-7-nitrophenoxazine (3.16). 2-((2,4-Dinitrophenyl)amino)-5-methylphenol (**3.16a**) (3.30 g, 11.4 mmol) was dissolved in dry DMF sparged with N_2 (57 mL) and heated to 100 °C with stirring under a N_2 atmosphere. At 100 °C, crushed NaOH was added (1.14 g, 28.5 mmol) and the mixture was heated to 120 °C for 4 h. The reaction mixture was subsequently poured into ~250 mL of water and extracted with ethyl acetate three times. The organic phase was washed several times with 1 M NaOH solution (to remove unreacted phenolic starting material which is inseparable by chromatography otherwise). The organic layer was dried with $MgSO_4$, filtered, and the solvent removed under reduced pressure. The title compound was isolated by column chromatography (40% EtOAc in hexanes) appearing as a black solid which makes a deep red solution when dissolved (1.72 g, 62%). ^{1}H NMR (400 MHz; DMSO-d6): 9.28 (br, 1H), 7.68 (dd, J = 2.5, 8.7 Hz, 1H), 7.30 (d, J = 2.6 Hz, 1H), 6.60 (dd, J = 1.6, 7.9 Hz, 1H), 6.51 (d, J = 1.3 Hz, 1H), 6.48 (d, J = 8.8 Hz, 1H), 6.42 (d, J = 7.8 Hz, 1H), 2.11 (s, 3H). ^{13}C NMR (101 MHz;

DMSO-d6): δ 142.0(3), 141.9(7), 139.8, 139.1, 132.0, 126.7, 124.6, 121.9, 115.9, 114.0, 111.7, 110.0, 20.2. (EI, magnetic sector): calcd for $C_{13}H_{10}N_2O_3$ 242.06914, found 242.07162.

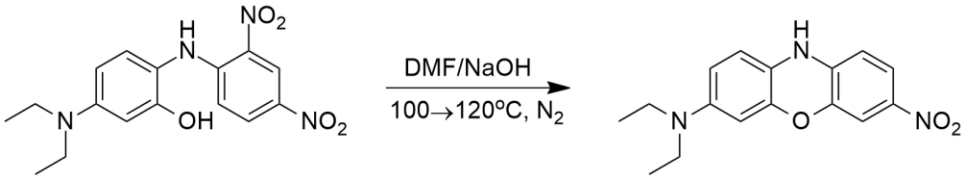


5-(Diethylamino)-2-nitrophenol (3.18a). 5-Fluoro-2-nitrophenol (6.28 g, 40 mmol), acetonitrile (80 mL) and diethylamine were combined in a round bottom flask and stirred for 12 h at 60 °C. The solvent was removed under reduced pressure and the yellow residue was purified by column chromatography (15% EtOAc in hexanes) and the product was subsequently further purified by recrystallization out of hexanes to afford yellow needles (2.93 g, 35%). ^{1}H NMR (400 MHz; DMSO-d6): δ 11.11 (br, 1H), 7.85 (d, J = 9.7 Hz, 1H), 6.45 (dd, J = 2.7, 9.7 Hz, 1H), 6.16 (d, J = 2.7 Hz, 1H), 3.45 (q, J = 7.1 Hz, 4H), 1.12 (t, J = 7.1 Hz, 6H). ^{13}C NMR (101 MHz; DMSO-d6): δ 157.2, 154.3, 127.4, 122.9, 106.1, 96.6, 44.5, 12.4. HRMS (EI, magnetic sector): calcd for $C_{10}H_{14}N_2O_3$ 210.10044, found 210.09749. mp = 110-113 °C.

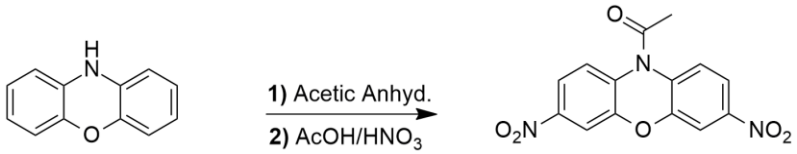


5-(Diethylamino)-2-((2,4-dinitrophenyl)amino)phenol (3.18b). In a Schlenk flask flushed with N_2 were combined 5-(Diethylamino)-2-nitrophenol (**3.18a**) (2.91 g, 13.8 mmol) and degassed absolute ethanol (55 mL) with a magnetic stir bar. Under a stream of N_2 10 wt.% Pd/C (0.29 g) was added and the flask was sealed. The N_2 was evacuated and replaced with H_2 with a balloon of excess H_2 appended through the rubber septum. The reaction was heated to 50 °C and was vigorously stirred until the starting material had been consumed (monitored by TLC). In a separate flask equipped with a stir bar was measured 1-chloro-2,4-dinitrobenzene (2.62 g, 13 mmol). After completion of the hydrogenation, the first solution was rapidly filtered through celite (to remove the Pd/C) directly into the flask containing 1-chloro-2,4-dinitrobenzene. This was followed by 40 mL of clean ethanol through the celite (the transfer step should be performed quickly as the colourless aminophenol solution from the hydrogenation rapidly oxidizes when

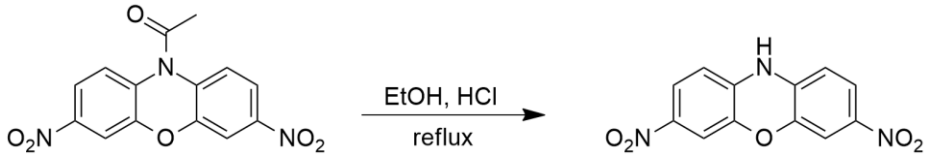
exposed to oxygen giving the solution a deep blue colour.) The while sparging the solution with N_2, triethylamine (2.1 mL) was added and the flask was evacuated then backfilled with N_2. The reaction was stirred overnight at 40 °C after which the solvent was removed under reduced pressure. The title product was isolated by column chromatography (30-50% EtOAc gradient in hexanes) appearing as a black solid which makes a deep red solution when dissolved (2.75 g, 61%). ^{1}H NMR (400 MHz; DMSO-d6): δ 9.76 (br, 1H), 9.50 (br, 1H), 8.88 (d, *J* = 2.7 Hz, 1H), 8.20 (dd, *J* = 2.7, 9.6 Hz, 1H), 7.01 (d, *J* = 8.7 Hz, 1H), 6.86 (d, *J* = 9.7 Hz, 1H), 6.28 (d, *J* = 2.6 Hz, 1H), 6.23 (dd, *J* = 2.7, 8.7 Hz, 1H), 3.31 (q, *J* = 7.0 Hz, 4H), 1.11 (t, *J* = 7.0 Hz, 6H). ^{13}C NMR (101 MHz; DMSO-d6): δ 153.2, 148.0(6), 148.0(3), 135.4, 130.1, 129.6, 128.2, 123.4, 117.2, 111.9, 103.2, 98.9, 43.9, 12.5. HRMS (EI, magnetic sector): calcd for $C_{16}H_{18}N_4O_5$ 346.12772, found 346.12509. mp = 193-197 °C (decomp.).



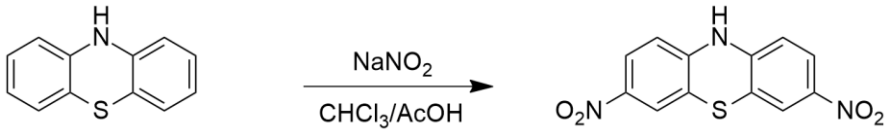
***N,N*-diethyl-3-amine-7-nitrophenoxazine (3.18).** 5-(Diethylamino)-2-((2,4-dinitrophenyl)amino)phenol (**3.18b**) (2.75 g, 8 mmol) was dissolved in dry DMF sparged with N_2 (40 mL) and heated to 100 °C with stirring under a N_2 atmosphere. At 100 °C, crushed NaOH was added (0.80 g, 20 mmol) and the mixture was heated to 120 °C for 4 h. The reaction mixture was subsequently poured into ~250 mL of water and extracted with ethyl acetate three times. The organic phase was washed several times with 1 M NaOH solution (to remove unreacted phenolic starting material which is inseparable by chromatography otherwise). The organic layer was dried with $MgSO_4$, filtered, and the solvent removed under reduced pressure. The title compound was isolated by column chromatography (40% EtOAc in hexanes) appearing as a dark purple solid (0.64 g, 27%). ^{1}H NMR (400 MHz; DMSO-d6): δ 9.18 (br, 1H), 7.65 (dd, *J* = 2.4, 8.8 Hz, 1H), 7.27 (d, *J* = 2.2 Hz, 1H), 6.42-6.40 (m, 2H), 6.13-6.06 (m, 2H), 3.21 (q, *J* = 7.0 Hz, 4H), 1.02 (t, *J* = 7.0 Hz, 6H). ^{13}C NMR (101 MHz; DMSO-d6): δ 144.3, 143.1, 141.4, 140.2, 138.0, 122.2, 117.6, 117.6, 115.2, 111.1, 109.9, 107.0, 100.0, 43.8, 12.4. HRMS (EI, magnetic sector): calcd for $C_{16}H_{17}N_3O_3$ 299.12699, found 299.12670. mp = 185-188 °C (decomp.).



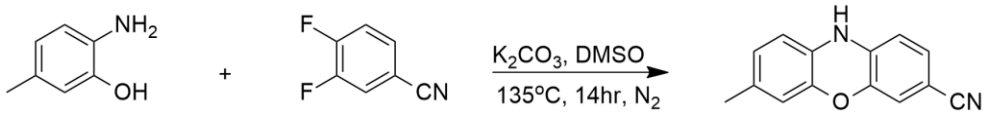
3,7-Dinitro-10-acetylphenoxazine (3.19a). Phenoxazine (2.74 g, 15.0 mmol) and acetic anhydride (10 mL) were placed into a round bottom flask with a reflux condenser affixed to it. The mixture was refluxed for 3 hours after which the flask was cooled to room temperature then further cooled in a freezer. The 10-acetylphenoxazine intermediate crystallized and the acetic anhydride was decanted. The crystalline solid was suspended in glacial acetic acid (24 mL) and 1:1 mixture of 70% nitric acid (4 mL) in acetic acid (4 mL) was added. The fuming red solution was swirled for about 5 minutes, and the flask was placed in an ice bath and stood overnight. The next morning scratching promoted spontaneous crystallization. The solid recrystallized out of ethanol to afford the product (2.34 g, 49%) as orange needles. ^{1}H NMR (300 MHz; DMSO-d6): δ 8.12 (dd, *J* = 2.5, 8.8 Hz, 2H), 8.03 (d, *J* = 2.5 Hz, 2H), 7.91 (d, *J* = 8.8 Hz, 2H), 2.37 (s, 3H). ^{13}C NMR (75 MHz; DMSO-d6): δ 149.3, 145.6, 134.3, 125.9, 119.7, 112.1, 23.2. HRMS (EI, magnetic sector): calcd for $C_{14}H_9N_3O_6$ 315.04914, found 315.05416. mp 187-190 °C.



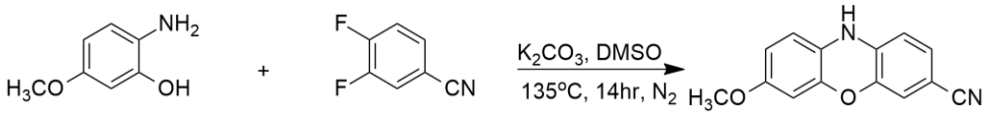
3,7-Dinitrophenoxazine (3.19). In a round bottom flask equipped with a reflux condenser and magnetic stir bar were added 3,7-dinitro-10-acetylphenoxazine (**3.19a**) (2.15 g, 6.8 mmol), ethanol (50 mL) and 33% aqueous HCl (15 mL). The mixture was refluxed for several hours until the starting material had been completely converted to the title product. The product was recrystallized out of glacial acetic acid to afford red needles (1.55 g, 81%). ^{1}H NMR (400 MHz; DMSO-d6): δ 10.11 (s, 1H), 7.73 (dd, J = 2.5, 8.7 Hz, 2H), 7.39 (d, J = 2.5 Hz, 2H), 6.62 (d, J = 8.7 Hz, 2H). ^{13}C NMR (101 MHz; DMSO-d6): δ 142.0, 141.2, 137.1, 121.9, 113.4, 110.4. HRMS (EI, magnetic sector): calcd for $C_{12}H_7N_3O_5$ 273.03857, found 273.04144. mp = 220 °C (decomp.).



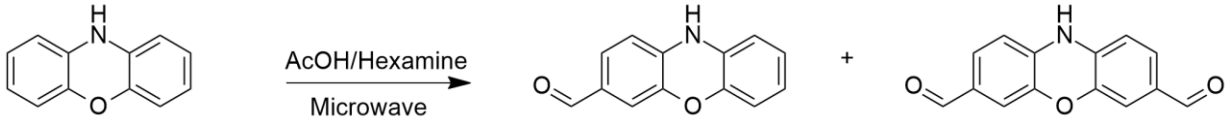
3,7-Dinitrophenothiazine (3.29). Preparation of 3,7-dinitrophenothiazine was conducted in accordance to a previously described method.[15] Into a round bottom flask equipped with a magnetic stir bar was dissolved phenothiazine (5 g, 25 mmol) in a chloroform (50 mL) acetic acid (20 mL) mixture. With stirring, $NaNO_2$ was added (5 g, 73 mmol) and the reaction was allowed to stir for several hours. The brown precipitate was filtered off and rinsed with acetic acid, H_2O then ethanol. The crude product was recrystallized twice out of DMF and rinsed with acetone to afford the title product as dark red needles (2.53 g, 35%). ^{1}H NMR (400 MHz; DMSO-d6): δ 10.13 (s, 1H), 7.88 (dd, *J* = 2.4, 8.8 Hz, 2H), 7.79 (dd, *J* = 2.3 Hz, 2H), 6.74 (dd, *J* = 8.9 Hz, 2H). ^{13}C NMR (101 MHz; DMSO-d6): δ 145.2, 142.6, 124.8, 121.8, 116.8, 114.8. HRMS (EI, magnetic sector): calcd for $C_{12}H_7N_3O_4S$ 289.01573, found 289.01762.



3-Methyl-7-cyanophenoxazine (3.21). 3,4-Difluorobenzonitrile (0.84 g, 6.0 mmol), 2-amino-5-methylphenol (0.74 g, 6.0 mmol), K_2CO_3 (1.71 g, 12.4 mmol) and DMSO (30 mL) were placed in a round bottom flask. Under N_2 the reaction mixture was heated to 135 °C for 14 hours with vigorous stirring after which the reaction was cooled, quenched with water and the aqueous mixture extracted three times with EtOAc. The organic phase was washed twice with water, dried over $MgSO_4$, filtered and the solvent removed under reduced pressure. The crude solid was purified by column chromatography (50% EtOAc in hexanes) to render the product as a yellow solid (0.67 g, 50%). ^{1}H NMR (400 MHz; DMSO-d6): δ 8.81 (s, 1H), 7.14 (dd, *J* = 1.9, 8.2 Hz, 1H), 6.95 (d, *J* = 1.7 Hz, 1H), 6.58-6.56 (m, 1H), 6.46-6.44 (m, 2H), 6.37 (d, *J* = 7.8 Hz, 1H), 2.09 (s, 3H). ^{13}C NMR (101 MHz; DMSO-d6): δ 142.6, 142.2, 137.6, 131.1, 129.6, 127.6, 124.4, 119.2, 117.6, 115.8, 113.7, 113.1, 100.6, 20.11. HRMS (EI, magnetic sector): calcd for $C_{14}H_{10}N_2O$ 222.07931, found 222.08020. mp = 215-217 °C (decomp.).

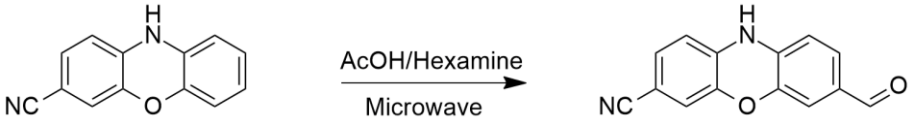


3-Methoxy-7-cyanophenoxazine (3.22). With 3,4-Difluorobenzonitrile (1.39 g, 10.0 mmol) and 2-amino-5-methoxyphenol (1.39 g, 10.0 mmol), the synthesis was carried out in a fashion analogous to (**3.21**). The crude solid was purified by column chromatography (40% EtOAc in hexanes) to render the product as a light-yellow solid (1.55 g, 65%). ^{1}H NMR (400 MHz; DMSO-d6): δ 8.75 (s, 1H), 7.15 (dd, *J* = 1.8, 8.1 Hz, 1H), 6.95 (d, *J* = 1.9 Hz, 1H), 6.46-6.41 (m, 2H), 6.37 (dd, *J* = 2.7, 8.5 Hz, 1H), 6.32 (d, *J* = 2.6 Hz, 1H), 3.64 (s, 3H). ^{13}C NMR (101 MHz; DMSO-d6): δ 154.6, 143.0, 141.9, 137.7, 129.8, 123.4, 119.3, 117.6, 114.1, 113.0, 108.5, 102.5, 100.2, 55.3. HRMS (EI, magnetic sector): calcd for $C_{14}H_{10}N_2O_2$ 238.07423, found 238.07274. mp = 194-200 (decomp).

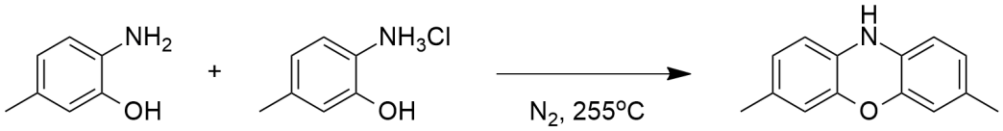


3-Formylphenoxazine (3.12). Phenoxazine (0.92 g, 5 mmol), hexamine (1.40 g, 10 mmol), glacial acetic acid (20 mL) and magnetic stir bar were placed in an Anton Parr G30 borosilicate microwave vessel. The solution was sparged with N_2 for 10 min after which the vessel was sealed and the reaction vessel was placed in the microwave reactor (Monowave 400). With stirring (600 RPM) the tube was heated to 120 °C (held for 30 min), then 150 °C (held for 80 min), back to 120 °C (held for 30 min) then cooled to room temperature. The reaction mixture was poured into water and Na_2CO_3 was added to neutralize the solution. The slurry was extracted several times with dichloromethane, after which the organic solution was dried with $MgSO_4$, filtered and solvent removed under reduced pressure. 3-Formylphenoxazine (**12**) (1:1 EtOAc:hexanes Rf = 0.61) was isolated by column chromatography (40% EtOAc gradient in hexanes) to afford a brownish orange solid that makes a fluorescent solution when dissolved (0.14 g, 13%). ^{1}H NMR (400 MHz; DMSO-d6): δ 9.59 (s, 1H), 9.04 (br, 1H), 7.32 (dd, *J* = 1.8, 8.1 Hz, 1H), 6.98 (d, *J* = 1.5 Hz, 1H), 6.79-6.74 (m, 1H), 6.66-6.63 (m, 2H), 6.54 (d, *J* = 8.0 Hz, 1H), 6.51 (d, *J* = 7.4 Hz, 1H). ^{13}C NMR (101 MHz; DMSO-d6): δ 189.8, 143.0, 142.6, 138.7, 130.2, 129.3, 128.9, 124.2, 121.9, 115.3, 113.9, 112.6. (EI, magnetic sector): calcd for $C_{13}H_9NO_2$

211.06333, found 211.06383. mp = 169-172 °C. **3,7-Diformylphenoxazine (3.13).** 3,7-Diformylphenoxazine (**3.13**) (1:1 EtOAc:hexanes Rf = 0.29) eluted after (**3.12**). The fractions containing the product were combined in a single flask and the solvent was removed under reduced pressure. The residue was rinsed with a minimum of acetone to remove coeluted impurities rendering an orange solid that makes a strongly fluorescent solution when dissolved (90 mg, 7.5%). ^{1}H NMR (400 MHz; DMSO-d6): δ 9.67 (br, 1H), 9.64 (s, 2H), 7.36 (dd, *J* = 1.7, 8.0 Hz, 2H), 7.04 (d, *J* = 1.8 Hz, 2H), 6.63 (d, *J* = 8.0 Hz, 2H). ^{13}C NMR (101 MHz; DMSO-d6): δ 190.1, 142.9, 136.6, 130.6, 128.6, 114.2, 113.6. (EI, magnetic sector): calcd for $C_{14}H_9NO_3$ 239.13101, found 239.129113. mp = 250 °C (decomp.).

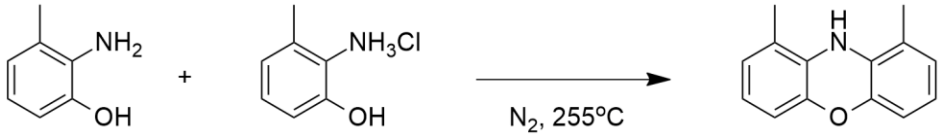


3-Cyano-7-formylphenoxazine (3.14). The reaction was carried out in an analogous fashion to the preparation of 3-formylphenoxazine (**3.12**) using 3-cyanophenoxazine (**3.20**) as a starting material (1.04 g, 5 mmol). The title product was isolated by column chromatography (40% EtOAc in hexanes) which appeared as a bright yellow solid (0.10 g, 8.5%). ^{1}H NMR (400 MHz; DMSO-d6): δ 9.63 (s, 1H), 9.59 (br, 1H), 7.36 (dd, *J* = 1.7, 8.0 Hz, 1H), 7.22 (dd, *J* = 1.8, 8.1 Hz, 1H), 7.07 (d, *J* = 1.8 Hz, 1H), 7.01 (d, *J* = 1.7 Hz, 1H), 6.60 (d, *J* = 8.0 Hz, 1H), 6.56 (d, *J* = 8.1 Hz, 1H). ^{13}C NMR (101 MHz; DMSO-d6): δ 190.1, 142.8, 142.7, 136.7, 135.5, 130.5, 129.9, 128.8, 118.8, 118.0, 114.1(6), 114.1(3), 113.6, 102.8. (EI, magnetic sector): calcd for $C_{14}H_8N_2O_2$ 236.05858, found 236.05727. mp = 270 °C (decomp.).

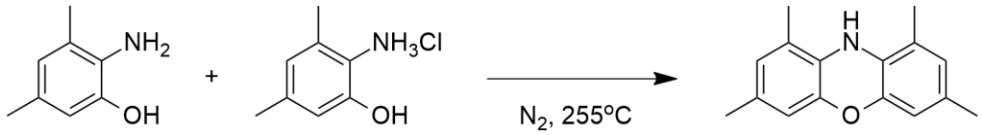


3,7-Dimethylphenoxazine (3.35). In a sealable tube was charged 5-methyl-2-aminophenol (7.02 g, 57 mmol) and 1 equivalent of 5-methyl-2-aminophenol hydrochloride (9.12 g, 57 mmol). The tube was purged under a stream of N_2 and sealed with the Teflon screwcap. The tube was placed in a sand bath and was heated to ~255 ºC for 2.5 hours then allowed to cool to room temperature. The black residue was broken up and treated with hot acetone (Soxhlet extraction for several

hours). The residue from the extraction was purified by column chromatography (20% EtOAc in hexanes). The title product were colourless crystals which precipitated out of the eluent. The eluent which contained the product were collected (~400 mL) and the volume was reduced to ~100 mL under reduced pressure and the flask was placed in a freezer overnight. The solvent was decanted and the solid was recrystallized out of ethanol to afford white/beige platelets (0.96 g, 7.9%). ^{1}H NMR (400 MHz; DMSO-d6): δ 7.89 (br, 1H), 6.52 (dd, *J* = 1.7, 7.8 Hz, 2H), 6.43 (d, *J* = 1.4 Hz, 2H), 6.32 (d, *J* = 7.8 Hz, 2H), 2.08 (s, 6H). ^{13}C NMR (151 MHz; C_6D_6): δ 144.3, 131.2, 130.0, 124.2, 117.3, 113.9, 20.9. (EI, magnetic sector): calcd for $C_{14}H_{13}NO$ 211.09971, found 211.09715. mp = 203-205 °C.

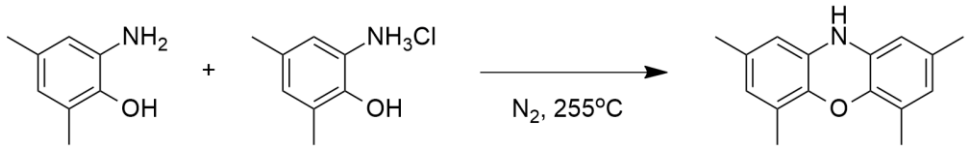


1,9-Dimethylphenoxazine (3.36). The synthesis was carried out in an analogous fashion to (**3.35**) using 3-methyl-2-aminophenol (6.16 g, 50 mmol) and 3-methyl-2-aminophenol hydrochloride (7.98 g, 50 mmol) as the starting materials. The product was isolated by column chromatography (10% EtOAc in hexanes) and was subsequently recrystallized out of a minimum of cold hexanes (product very soluble in hexanes at room temperature) to afford beige needles (0.73 g, 6.9%). ^{1}H NMR (400 MHz; DMSO-d6): δ 6.64 (d, *J* = 7.3 Hz, 2H), 6.56 (dd, *J* = 7.5, 7.8 Hz, 2H), 6.49 (d, *J* = 7.6 Hz, 2H), 5.96 (br, 1H), 2.13 (s, 6H). ^{13}C NMR (101 MHz; DMSO-d6): δ 143.2, 129.6, 125.2, 123.5, 120.7, 112.8, 16.2. (EI, magnetic sector): calcd for $C_{14}H_{13}NO$ 211.09971, found 211.09768. mp = 97-100 °C.

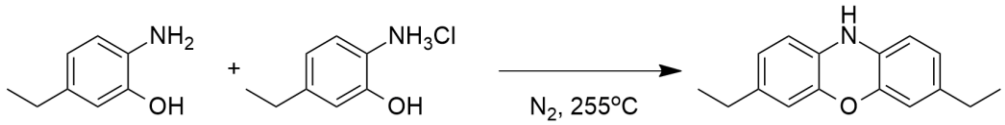


1,3,7,9-Tetramethylphenoxazine (3.38). The synthesis was carried out in an analogous fashion to (**3.35**) using 3,5-dimethyl-2-aminophenol (2.74 g, 20 mmol) and 3,5-dimethyl-2-aminophenol hydrochloride (3.47 g, 20 mmol) as the starting materials. The product was isolated by column chromatography (10% EtOAc in hexanes) and was subsequently recrystallized out of a minimum of cold hexanes (product very soluble in hexanes at room temperature) to afford beige needles

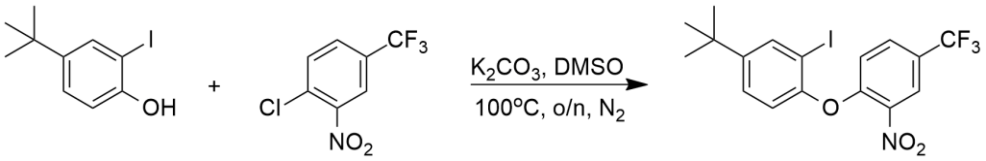
(0.34 g, 7.2%). ^{1}H NMR (400 MHz; DMSO-d6): δ 6.45 (d, *J* = 1.1 Hz, 2H), 6.32 (d, *J* = 1.2 Hz, 2H), 5.78 (br, 1H), 2.08 (s, 12H). ^{13}C NMR (101 MHz; DMSO-d6): δ 142.9, 129.4, 127.1, 125.4, 123.3, 113.4, 20.1, 16.2. (EI, magnetic sector): calcd for $C_{16}H_{17}NO$ 239.13101, found 239.13357. mp = 91-93 °C.



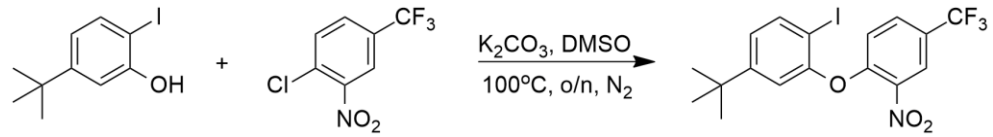
2,4,6,8-Tetramethylphenoxazine (3.37). The synthesis was carried out in an analogous fashion to (**3.35**) using 4,6-dimethyl-2-aminophenol (2.33 g, 17 mmol) and 4,6-dimethyl-2-aminophenol hydrochloride (2.95 g, 17 mmol) as the starting materials. The product was isolated by column chromatography (15% EtOAc in hexanes) and was subsequently recrystallized out of hexanes to afford white needles (0.31 g, 7.6%). ^{1}H NMR (400 MHz; DMSO-d6): δ 7.86 (br, 1H), 6.25 (d, *J* = 1.2 Hz, 2H), 6.09 (d, *J* = 1.6 Hz, 2H), 2.05 (s, 6H), 2.03 (s, 6H). ^{13}C NMR (101 MHz; DMSO-d6): δ 138.8, 132.0, 131.6, 123.5, 122.3, 111.5, 20.4, 14.7. (EI, magnetic sector): calcd for $C_{16}H_{17}NO$ 239.13101, found 239.12913. mp = 199-201 °C.



3,7-Diethylphenoxazine (3.41). The synthesis was carried out in an analogous fashion to (**3.35**) using 5-ethyl-2-aminophenol (2.20 g, 16 mmol) and 5-ethyl-2-aminophenol hydrochloride (2.95 g, 16 mmol) as the starting materials. The product was isolated by column chromatography (15% EtOAc in hexanes) and was subsequently recrystallized out of hexanes to afford beige needles (0.29 g, 7.6%). ^{1}H NMR (400 MHz; DMSO-d6): δ 7.93 (br, 1H), 6.55 (dd, *J* = 1.9, 7.8 Hz, 2H), 6.34 (d, *J* = 7.8 Hz, 2H), 2.38 (q, *J* = 7.6 Hz, 4H), 1.08 (t, *J* = 7.5 Hz, 6H). ^{13}C NMR (101 MHz; DMSO-d6): δ 142.5, 135.8, 130.2, 122.7, 114.5, 113.0, 27.3, 15.6. (EI, magnetic sector): calcd for $C_{16}H_{17}NO$ 239.13101, found 239.12834. mp = 100-102 °C.

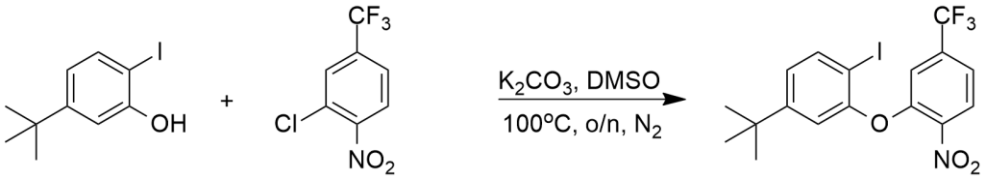


4-(*tert*-Butyl)-2-iodo-1-(2-nitro-4-(trifluoromethyl)phenoxy)benzene (3.8a). 2-Iodo-4-*tert*-butylphenol (2.8 g, 10 mmol) and 1 equivalent of 4-chloro-3-nitrobenzotrifluoride (2.3 g, 10 mmol) were dissolved in DMSO (15 mL, 0.67 M) to which 2 equivalents of K_2CO_3 was added (2.8 g, 20 mmol) and the reaction mixture was placed under a N_2 atmosphere. With vigorous stirring, the reaction was heated to 100 °C overnight. The reaction mixture was poured into water and extracted three times with EtOAc. The organic phase was washed twice with water, dried over MgSO4, filtered and the solvent removed under reduced pressure. The product was purified by silica gel chromatography (10% EtOAc in hexanes) and subsequently recrystallized out of hexanes to afford white needles (2.93 g, 63%). ^{1}H NMR (400 MHz; $CDCl_3$): δ 8.28 (d, *J* = 2.1 Hz, 1H), 7.90 (d, *J* = 2.4 Hz, 1H), 7.69 (dd, *J* = 2.3, 8.8 Hz, 1H), 7.45 (dd, *J* = 2.1, 8.4 Hz, 1H), 7.05 (d, J = 8.5 Hz, 1H), 6.88 (d, J = 8.8 Hz, 1H), 1.35 (s, 9H); 13C NMR (101 MHz; CDCl3): δ 153.3, 151.5, 151.3, 139.6, 137.5, 130.8 (q, JC-F = 3.3 Hz), 127.5, 124.9 (q, JC-F = 34.5 Hz), 123.7 (q, JC-F = 3.7 Hz), 122.9 (q, JC-F = 272.2 Hz), 121.1, 118.3, 89.3, 34.6, 31.3. 19F NMR (376 MHz; CDCl3) δ -63.3. HRMS (EI, magnetic sector): calcd for $C_{17}H_{15}F_3INO_3$ 465.00487, found 465.00109. mp = 88-89 °C.

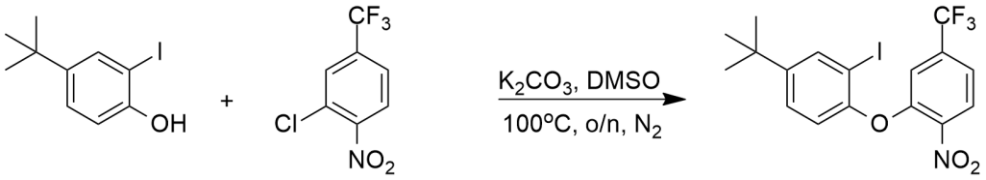


4-(*tert*-butyl)-1-iodo-2-(2-nitro-4-(trifluoromethyl)phenoxy)benzene (3.7a). Synthesis was carried out in an analogous fashion to (**3.8a**) using 2-iodo-5-*tert*-butylphenol. The product was purified to the extent that was possible by column chromatography (10% EtOAc in hexanes) affording a light-coloured oil (3.3 g, 72%) which was used without further treatment in the preparation of **(3.7b)**. ^{1}H NMR (400 MHz; $CDCl_3$): δ 8.30 (d, *J* = 2.0 Hz, 1H), 7.82 (d, *J* = 8.3 Hz, 1H), 7.70 (dd, *J* = 2.0, 8.8 Hz, 1H), 7.18 (d, *J* = 2.3 Hz, 1H), 7.11 (dd, *J* = 2.3, 8.3 Hz, 1H), 6.82 (d, *J* = 8.7 Hz, 1H), 1.32 (s, 9H). ^{13}C NMR (101 MHz; $CDCl_3$): δ 155.0, 153.3, 153.2,

140.0, 130.9 (q, J_{C-F} = 3.7 Hz), 125.5, 124.7 (q, J_{C-F} = 34.5 Hz), 123.8 (q, J_{C-F} = 3.7 Hz), 122.9 (q, J_{C-F} = 272.2 Hz), 119.4, 117.8, 85.5, 34.9, 31.1. ^{19}F NMR (376 MHz; $CDCl_3$) δ -63.3. HRMS (EI, magnetic sector): calcd for $C_{17}H_{15}F_3INO_3$ 465.00487, found 465.00223.

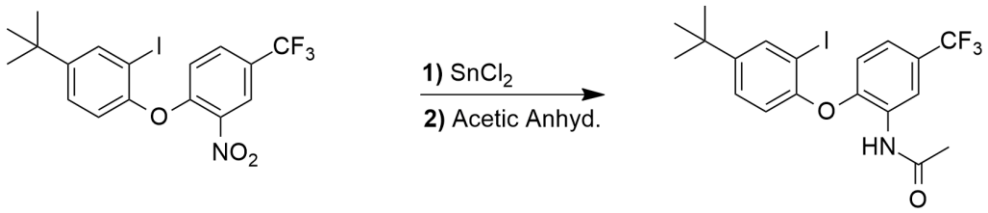


4-(*tert*-butyl)-1-iodo-2-(2-nitro-5-(trifluoromethyl)phenoxy)benzene (3.10a). Synthesis was carried out in an analogous fashion to (**3.8a**) using 2-iodo-5-*tert*-butylphenol and 3-chloro-4-nitrobenzotrifluoride at a slightly reduced scale (7 mmol). The product was purified to the extent that was possible by column chromatography (10% EtOAc in hexanes) affording a light-coloured oil (2.3 g, 70%) which was used without further treatment in the preparation of **(3.10b)**. ^{1}H NMR (400 MHz; $CDCl_3$): δ 8.07 (d, *J* = 8.4 Hz, 1H), 7.82 (d, *J* = 8.3 Hz, 1H), 7.45 (d, *J* = 1.8, 8.4 Hz, 1H), 7.13 (d, *J* = 2.3 Hz, 1H), 7.10 (dd, *J* = 2.3, 8.2 Hz, 1H), 7.00 (d, *J* = 1.6 Hz, 1H), 1.30 (s, 9H). ^{13}C NMR (101 MHz; $CDCl_3$): δ 154.8, 153.3, 150.7, 142.2, 140.0, 135.5 (q, J_{C-F} = 33.7 Hz), 126.4, 125.2, 122.5 (q, J_{C-F} = 273.3 Hz), 119.3 (q, J_{C-F} = 3.7 Hz), 118.7, 115.0 (q, J_{C-F} = 3.7 Hz), 85.1, 34.9, 31.0. ^{19}F NMR (376 MHz, $CDCl_3$): δ -64.5. HRMS (EI, magnetic sector): calcd for $C_{17}H_{15}F_3INO_3$ 465.00487, found 465.00231.

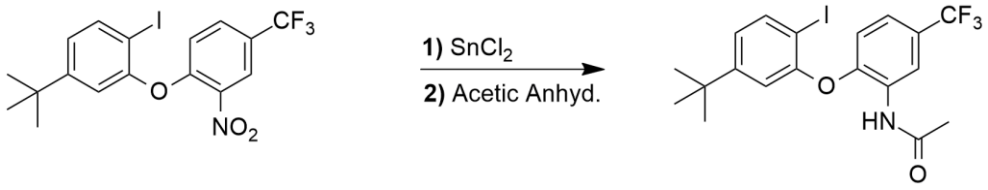


4-(*tert*-butyl)-2-iodo-1-(2-nitro-5-(trifluoromethyl)phenoxy)benzene (3.11a). Synthesis was carried out in an analogous fashion to (**3.8a**) using 3-chloro-4-nitrobenzotrifluoride at a slightly reduced scale (7 mmol). The product was recrystallized out of hexanes to afford white needles (64% 2.1 g). ^{1}H NMR (400 MHz; $CDCl_3$): δ 8.06 (d, *J* = 8.4 Hz, 1H), 7.90 (d, *J* = 2.3 Hz, 1H), 7.47-7.41 (m, 2H), 7.06 (d, *J* = 1.4 Hz, 1H). 6.99 (d, *J* = 8.5 Hz, 1H), 1.35 (s, 9H). ^{13}C NMR (101 MHz); $CDCl_3$): δ 151.5, 151.1, 150.6, 142.5, 137.6, 135.5 (q, J_{C-F} = 33.7 Hz), 127.5, 126.4, 122.5 (q, J_{C-F} = 273.6 Hz), 120.2, 119.6 (q, J_{C-F} = 3.7 Hz), 115.6 (q, J_{C-F} = 3.7 Hz) 88.8, 34.6,

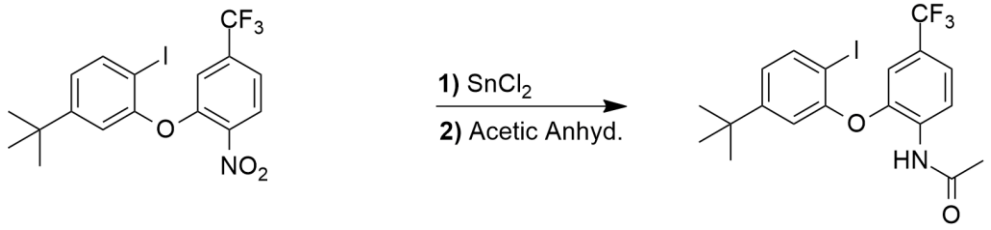
31.3. ^{19}F NMR (376 MHz; $CDCl_3$): δ -64.3. HRMS (EI, magnetic sector): calcd for $C_{17}H_{15}F_3INO_3$ 465.00487, found 465.00748. mp = 92-95 °C.



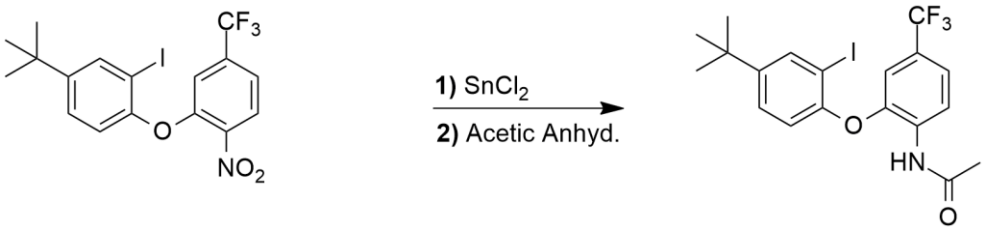
N-(2-(4-(*tert*-butyl)-2-iodophenoxy)-5-(trifluoromethyl)phenyl)acetamide (3.8b). 4-(*tert*-butyl)-2-iodo-1-(2-nitro-4-(trifluoromethyl)phenoxy)benzene (**3.8a**) (2.9 g, 6.2 mmol) and 5 equivalents of $SnCl_2$ (5.9 g, 31 mmol) were dissolved in EtOAc. The reaction stirred at room temperature overnight, then was poured into water and extracted three times with EtOAc. The organic phase was washed twice with water, dried over $MgSO_4$, filtered and the solvent removed under reduced pressure. The residue was dissolved in neat acetic anhydride (4.4 mL) and allowed to stir overnight. The reaction was quenched with saturated Na_2CO_3 solution and extracted three times with EtOAc. The organic phase was washed once with water, dried over $MgSO_4$, filtered and the solvent removed under reduced pressure. The product was isolated by silica gel chromatography (15% EtOAc in hexanes) and subsequently recrystallized out of hexanes to afford white platelets (2.22 g, 75%). ^1H NMR (400 MHz; $CDCl_3$): δ 8.82 (d, *J* = 1.4 Hz, 1H), 7.93 (br, 1H), 7.89 (d, *J* = 2.3 Hz, 1H), 7.41 (dd, *J* = 2.4, 8.5 Hz, 1H), 7.22 (dd, *J* = 1.6, 8.5 Hz, 1H), 6.97 (d, *J* = 8.5 Hz, 1H), 6.70 (d, *J* = 8.4 Hz, 1H), 2.27 (s, 3H), 1.35 (s, 9H). ^{13}C NMR (101 MHz; $CDCl_3$): δ 168.4, 151.7, 150.8, 147.8, 137.2, 129.0, 127.3, 125.6 (q, J_{C-F} = 32.6 Hz), 123.9 (q, J_{C-F} = 272.2 Hz), 120.6 (q, J_{C-F} = 3.7 Hz), 120.4, 117.8 (q, J_{C-F} = 3.7 Hz), 114.9, 89.3, 34.5, 31.3, 25.0. ^{19}F NMR (376 MHz; $CDCl_3$): δ -63.1. HRMS (EI, magnetic sector): calcd for $C_{19}H_{19}F_3INO_2$ 477.04126, found 477.03980. mp = 107-108 °C.



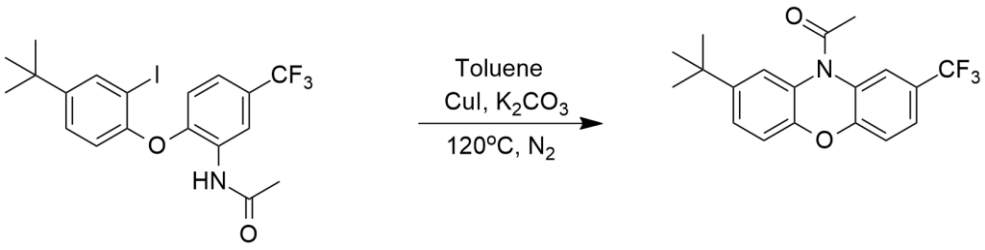
N-(2-(5-(*tert*-butyl)-2-iodophenoxy)-5-(trifluoromethyl)phenyl)acetamide (3.7b). Synthesis was carried out in an analogous fashion to (**3.8b**) using 4-(*tert*-butyl)-1-iodo-2-(2-nitro-4-(trifluoromethyl)phenoxy)benzene (**3.7a**). The product was purified by column chromatography (15% EtOAc in hexanes) to afford an amorphous solid (66% 2.23 g). ^{1}H NMR (400 MHz; $CDCl_3$): δ 8.83 (d, *J* = 1.4 Hz, 1H), 7.96 (br, 1H), 7.81 (d, *J* = 8.3 Hz, 1H), 7.22 (dd, *J* = 1.6, 8.5 Hz, 1H), 7.11 (d, *J* = 2.3 Hz, 1H), 7.08 (dd, *J* = 2.3, 8.3 Hz, 1H), 2.28 (s, 3H), 1.30 (s, 9H). ^{13}C NMR (101 MHz; $CDCl_3$): δ 168.5, 154.7, 153.6, 147.8, 139.6, 128.7, 125.3 (q, J_{C-F} = 32.6 Hz), 124.8, 123.0 (q, J_{C-F} = 272.2), 120.7 (q, J_{C-F} = 3.7 Hz), 118.9, 117.8 (q, J_{C-F} = 3.7 Hz), 114.2, 85.7, 34.9, 31.1, 25.0. ^{19}F NMR (376 MHz; $CDCl_3$): δ -63.0. HRMS (EI, magnetic sector): calcd for $C_{19}H_{19}F_3INO_2$ 477.04126, found 477.04069.



N-(2-(5-(*tert*-butyl)-2-iodophenoxy)-4-(trifluoromethyl)phenyl)acetamide (3.10b). Synthesis was carried out in an analogous fashion to (**3.8b**) using 4-(*tert*-butyl)-1-iodo-2-(2-nitro-5-(trifluoromethyl)phenoxy)benzene (**3.10a**). The product was purified by column chromatography (15% EtOAc in hexanes) then subsequently recrystallized out of hexanes (74% 1.65 g). ^{1}H NMR (400 MHz; $CDCl_3$): δ 8.63 (d, *J* = 8.6 Hz, 1H), 8.00 (br, 1H), 7.81 (d, *J* = 8.6 Hz, 1H), 7.37 (dd, *J* = 1.3, 8.6 Hz, 1H), 7.07-7.05 (m, 2H), 6.86 (d, *J* = 1.7 Hz, 1H), 2.28 (s, 3H), 1.29 (s, 9H). ^{13}C NMR (101 MHz; $CDCl_3$): δ 168.6, 154.6, 153.7, 145.1, 139.7, 131.8, 125.4 (q, J_{C-F} = 33.0 Hz), 124.5, 123.7 (q, J_{C-F} = 271.8 Hz), 120.6 (q, J_{C-F} = 3.8 Hz), 120.4, 118.0, 112.0 (q, J_{C-F} = 3.7 Hz), 85.1, 34.9, 31.0, 25.0. ^{19}F NMR (376 MHz; $CDCl_3$): δ -63.4. HRMS (EI, magnetic sector): calcd for $C_{19}H_{19}F_3INO_2$ 477.04126, found 477.04121. mp = 128-131 °C.

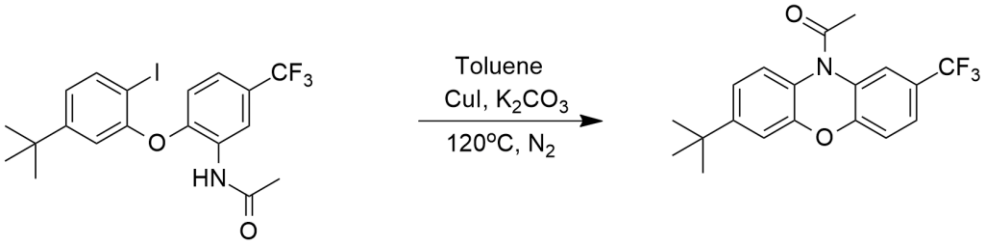


N-(2-(4-(*tert*-butyl)-2-iodophenoxy)-4-(trifluoromethyl)phenyl)acetamide (3.11b). Synthesis was carried out in an analogous fashion to (**3.8b**) using 4-(*tert*-butyl)-2-iodo-1-(2-nitro-5-(trifluoromethyl)phenoxy)benzene (**3.11a**). The product was purified by column chromatography (15% EtOAc in hexanes) then subsequently recrystallized out of hexanes (70% 1.46 g). ^{1}H NMR (400 MHz; $CDCl_3$): δ 8.62 (d, *J* = 8.6 Hz, 1H), 7.97 (br, 1H), 7.89 (d, *J* = 2.3 Hz, 1H), 7.41-7.36 (m, 2H), 6.93-6.91 (m, 2H), 2.27 (s, 3H), 1.35 (s, 9H). ^{13}C NMR (101 MHz; $CDCl_3$): δ 168.6, 151.9, 150.4, 145.0, 137.23, 132.1, 127.3, 125.5 (q, J_{C-F} = 33.4 Hz), 123.7 (q, J_{C-F} = 271.8 Hz), 120.9 (q, J_{C-F} = 4.0 Hz), 120.5, 119.4, 112.8 (q, J_{C-F} = 3.7 Hz), 88.7, 34.5, 31.3, 25.0. ^{19}F NMR (376 MHz; $CDCl_3$): δ -63.2. HRMS (EI, magnetic sector): calcd for $C_{19}H_{19}F_3INO_2$ 477.04126, found 477.03974. mp = 139-141 °C.

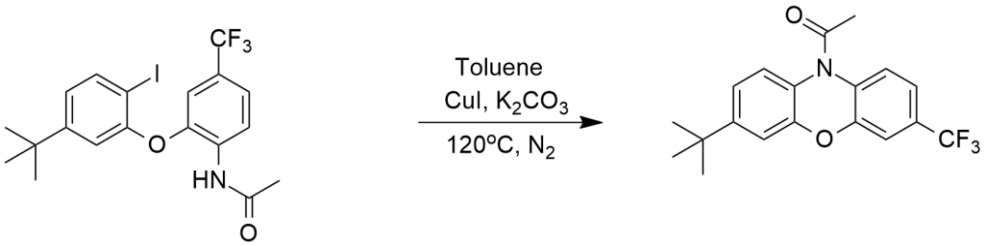


10-Acetyl-2-*tert*-butyl-8-trifluoromethylphenoxazine (3.8c). Into a sealable tube were charged *N*-(2-(4-(*tert*-butyl)-2-iodophenoxy)-5-(trifluoromethyl)phenyl)acetamide (**3.8b**) (2.20 g, 4.6 mmol), K_2CO_3 (1.27 g, 9.2 mmol), copper(I) iodide (44 mg, 0.05 equiv), *N*,*N*′-dimethylethylenediamine (45 μL, 0.10 equiv), and toluene (25 mL). The reaction mixture was sparged with a steady stream of N_2 after which the Teflon screwcap was affixed. The reaction mixture was heated to 120 °C for 10 h with rapid stirring. After completion, the reaction mixture was diluted with dichloromethane and passed through a plug of silica, after which the solvents were removed under reduced pressure. The crude product was purified by column chromatography (20% EtOAc in hexanes) to render 10-acetyl-2-*tert*-butyl-8-trifluoromethylphenoxazine as an off-white solid (1.42 g, 88%). ^{1}H NMR (300 MHz; $CDCl_3$): δ

7.91 (d, *J* = 1.9 Hz, 1H), 7.45 (dd, *J* = 1.9, 8.5 Hz, 1H), 7.39 (d, *J* = 2.2 Hz, 1H), 7.26 (dd, *J* = 2.2, 8.5 Hz, 1H), 7.19 (d, *J* = 8.5 Hz, 1H), 7.08 (d, *J* = 8.5, 1H), 2.35 (s, 3H), 1.34 (s, 9H). ^{13}C NMR (75 MHz; $CDCl_3$): δ 169.1, 148.1, 147.4, 129.6, 128.4, 125.5 (q, J_{C-F} = 33.0 Hz), 124.1, 123.9 (q, J_{C-F} = 4.4 Hz) 123.8 (q, J_{C-F} = 271.8 Hz), 123.0 (q, J_{C-F} = 4.4 Hz), 122.1, 117.1, 116.3, 34.6, 31.3, 22.9. ^{19}F NMR (376 MHz; $CDCl_3$): δ -63.0. HRMS (EI, magnetic sector): calcd for $C_{19}H_{18}F_3NO_2$ 349.12896, found 349.12775. mp = 102-105 °C.

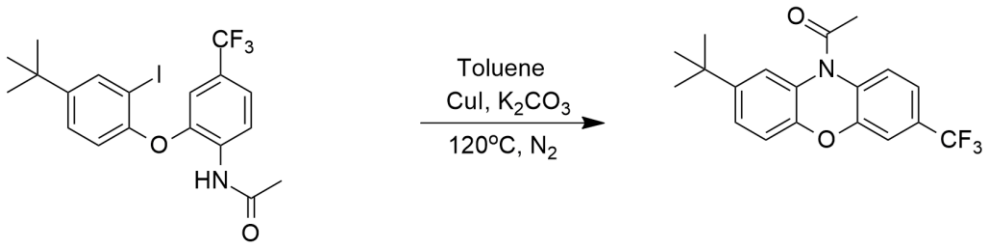


10-Acetyl-3-*tert*-butyl-8-trifluoromethylphenoxazine (3.7c). Synthesis was carried out in an analogous fashion to (**3.8c**) using *N*-(2-(5-(*tert*-butyl)-2-iodophenoxy)-5-(trifluoromethyl)phenyl)acetamide (**3.7b**). The product was purified by column chromatography (20% EtOAc in hexanes) then subsequently recrystallized out of hexanes to afford white needles (1.48 g, 92%). ^{1}H NMR (400 MHz, $CDCl_3$): δ 7.87 (d, *J* = 1.7 Hz, 1H), 7.46 (dd, *J* = 2.2, 8.5 Hz, 1H), 7.32 (d, *J* = 8.2 Hz, 1H), 7.21-7.17 (m, 3H), 2.36 (s, 3H), 1.33 (s, 9H). ^{13}C NMR (101 MHz; $CDCl_3$): δ 169.1, 153.4, 151.3, 150.0, 129.6, 126.2, 125.6 (q, J_{C-F} = 33.0 Hz), 124.1, 123.9 (q, J_{C-F} = 3.7 Hz), 123.8 (q, J_{C-F} = 271.8 Hz), 122.9 (q, J_{C-F} = 3.7 Hz), 121.0, 117.1, 114.2, 34.7, 31.2, 22.9. ^{19}F NMR (376 MHz; $CDCl_3$): δ -63.0. HRMS (EI, magnetic sector): calcd for $C_{19}H_{18}F_3NO_2$ 349.12896, found 349.12727. mp = 69-71 °C.

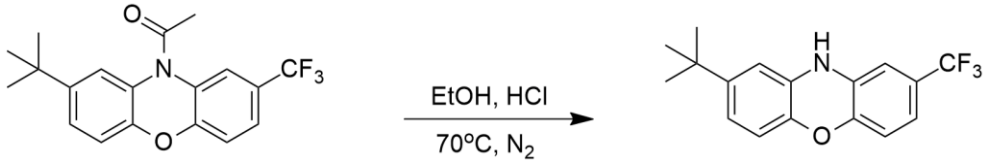


10-Acetyl-3-*tert*-butyl-7-trifluoromethylphenoxazine (3.10c). Synthesis was carried out in an analogous fashion to (**3.8c**) using *N*-(2-(5-(*tert*-butyl)-2-iodophenoxy)-4-(trifluoromethyl)phenyl)acetamide (**3.10b**). The product was purified by column chromatography

(20% EtOAc in hexanes) then subsequently recrystallized out of hexanes to afford white needles (0.90 g, 81%). ^{1}H NMR (400 MHz, $CDCl_3$): δ 7.69 (d, *J* = 8.0 Hz, 1H), 7.41-7.38 (m, 2H), 7.32 (dd, *J* = 1.1, 7.7 Hz, 1H), 7.20-7.17 (m, 2H), 2.36 (s, 3H), 1.33 (s, 9H). ^{13}C NMR (101 MHz; $CDCl_3$): δ 169.1, 151.3, 151.0, 150.2, 132.6, 128.9 (q, J_{C-F} = 33.4 Hz), 126.2, 125.7, 124.1, 123.5 (q, J_{C-F} = 272.2 Hz), 120.9, 120.2 (q, J_{C-F} = 3.7 Hz), 114.2, 114.2 (q, J_{C-F} = 3.7 Hz), 34.7, 31.2, 23.0. ^{19}F NMR (376 MHz; $CDCl_3$): δ -63.7. HRMS (EI, magnetic sector): calcd for $C_{19}H_{18}F_3NO_2$ 349.12896, found 349.13058. mp = 102-104 °C.

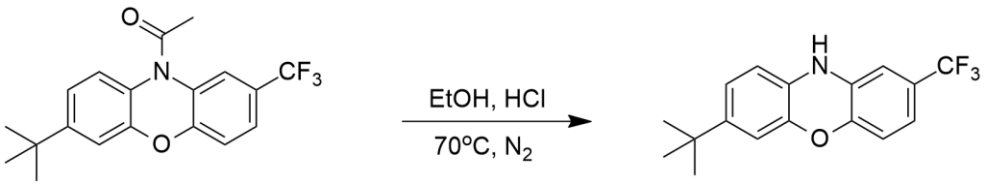


10-Acetyl-2-*tert*-butyl-7-trifluoromethylphenoxazine (3.11c). Synthesis was carried out in an analogous fashion to (**3.8c**) using *N*-(2-(4-(*tert*-butyl)-2-iodophenoxy)-4-(trifluoromethyl)phenyl)acetamide (**3.11b**). The product was purified by column chromatography (20% EtOAc in hexanes) then subsequently recrystallized out of hexanes to afford white needles (0.63 g, 64%). ^{1}H NMR (400 MHz, $CDCl_3$): δ 7.73 (d, *J* = 8.3 Hz, 1H), 7.42-7.37 (m, 3H), 7.26 (dd, *J* = 2.2, 8.5 Hz, 1H), 7.08 (d, *J* = 8.5 Hz, 1H), 2.36 (s, 3H), 1.34 (s, 9H). ^{13}C NMR (101 MHz; $CDCl_3$): δ 169.2, 160.0, 148.3, 147.3, 132.5, 128.9 (q, J_{C-F} = 33.4 Hz), 128.4, 125.9, 124.1, 123.5 (q, J_{C-F} = 271.8 Hz), 122.0, 120.1 (q, J_{C-F} = 3.7 Hz), 116.3, 114.1 (q, J_{C-F} = 3.7 Hz), 34.6, 31.3, 23.0. ^{19}F NMR (376 MHz; $CDCl_3$): δ -63.7. HRMS (EI, magnetic sector): calcd for $C_{19}H_{18}F_3NO_2$ 349.12896, found 349.13046. mp = 146-148 °C.

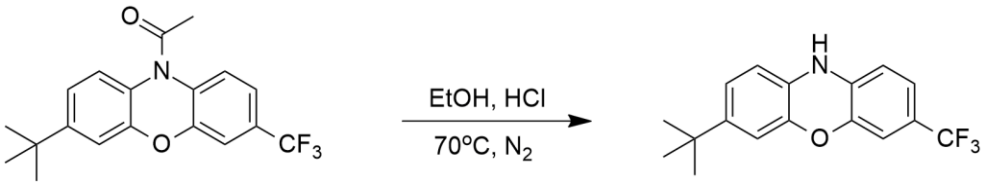


2-*tert*-Butyl-8-trifluoromethylphenoxazine (3.8). Into a double-neck flask were charged 10-acetyl-2-*tert*-butyl-8-trifluoromethylphenoxazine (**3.8c**) (1.40 g, 4.0 mmol) and ethanol (25 mL). The ethanol was degassed under a continuous stream of N_2 and degassed 33% aqueous HCl (4

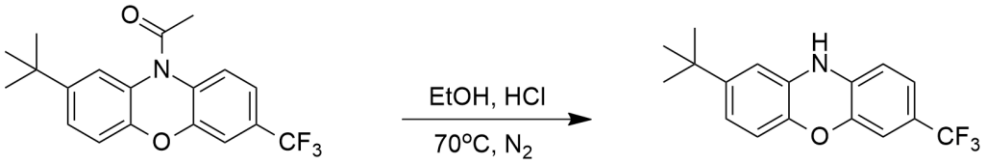
mL) was added. (If the solutions contain significant amounts of O_2 the HCl will promote the product (**3.8**) to oxidize giving the solution a strong magenta colour as the reaction proceeds). While under N_2 the solution was heated to 70 °C with stirring and the reaction was monitored by TLC. When the starting material had been completely consumed (≥2 h), the reaction was quenched with Na_2CO_3 solution. The aqueous mixture was extracted 3 times with EtOAc and the organic phase was washed twice with water. The organic solution was dried over $MgSO_4$, and filtered, and the solvent was removed under reduced pressure. The product was recrystallized from hexanes to afford white needles (1.13 g, 92%). ^{1}H NMR (400 MHz; DMSO-d6): δ 8.45 (br, 1H), 6.87 (dd, *J* = 2.0, 8.2 Hz, 1H), 6.73 (d, *J* = 8.2 Hz, 1H), 6.64-6.61 (m, 2H), 6.56 (d, *J* = 8.3 Hz, 1H), 6.46 (d, *J* = 2.2 Hz, 1H), 1.19 (s, 9H). ^{13}C NMR (101 MHz; DMSO-d6): δ 147.0, 145.9, 133.4, 130.5, 124.4 (q, J_{C-F} = 31.9 Hz), 124.0 (q, J_{C-F} = 271.4 Hz), 117.5, 117.3 (q, J_{C-F} = 4.0 Hz), 115.3, 114.7, 110.7, 109.2 (q, J_{C-F} = 3.7 Hz), 33.9, 31.0. ^{19}F NMR (376 MHz; DMSO-d6): δ -61.5. HRMS (EI, magnetic sector): calcd for $C_{17}H_{16}F_3NO$ 307.11840, found 307.11644. mp = 74-76 °C.



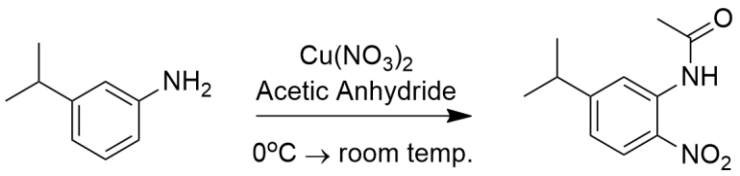
3-*tert*-Butyl-8-trifluoromethylphenoxazine (3.7). Synthesis was carried out in an analogous fashion to (**8**) using 10-acetyl-3-*tert*-butyl-8-trifluoromethylphenoxazine (**3.7c**). The product was recrystallized from hexanes to afford white needles (1.09 g, 89%). ^{1}H NMR (400 MHz; DMSO-d6): δ 8.43 (br, 1H), 6.87 (dd, *J* = 2.2, 8.2 Hz, 1H), 6.77 (dd, *J* = 2.1, 8.2 Hz, 1H), 6.72 (d, *J* = 8.2 Hz, 1H), 6.66 (d, *J* = 2.1 Hz, 1H), 6.65 (d, *J* = 2.1 Hz, 1H), 6.39 (d, *J* = 8.0 Hz, 1H), 1.18 (s, 9H). ^{13}C NMR (101 MHz; DMSO-d6): δ 145.8, 144.0, 141.8, 133.5, 128.5, 124.4 (q, J_{C-F} = 31.9 Hz), 124.0 (q, J_{C-F} = 271.4 Hz), 120.7, 117.2 (q, J_{C-F} = 4.0 Hz), 115.3, 113.0, 112.6, 109.1 (q, J_{C-F} = 3.7 Hz), 33.8, 31.0. ^{19}F NMR (376 MHz; DMSO-d6): δ -61.5. HRMS (EI, magnetic sector): calcd for $C_{17}H_{16}F_3NO$ 307.11840, found 307.11403. mp = 167-169 °C.



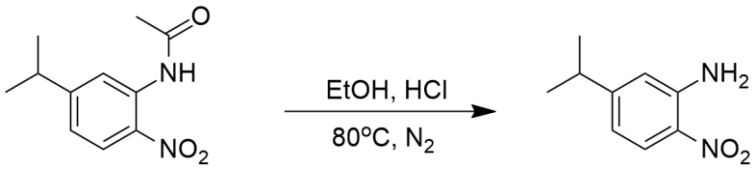
3-*tert*-Butyl-7-trifluoromethylphenoxazine (3.10). Synthesis was carried out in an analogous fashion to (**3.8**) using 10-acetyl-3-*tert*-butyl-7-trifluoromethylphenoxazine (**3.10c**). The product was recrystallized from hexanes to afford white needles (0.70 g, 94%). ^{1}H NMR (400 MHz; DMSO-d6): δ 8.63 (br, 1H), 7.05 (dd, *J* = 1.9, 8.2 Hz, 1H), 6.82 (d, *J* = 1.9 Hz, 1H), 6.77 (dd, *J* = 2.2, 8.2 Hz, 1H), 6.64 (d, *J* = 2.1 Hz, 1H), 6.52 (d, *J* = 8.2 Hz, 1H), 6.41 (d, *J* = 8.1 Hz, 1H), 1.18 (s, 9H). ^{13}C NMR (101 MHz; DMSO-d6): δ 144.3, 142.8, 142.0, 136.5, 128.3, 124.2 (q, J_{C-F} = 270.7 Hz), 121.4 (q, J_{C-F} = 4.0 Hz), 120.5, 119.9 (q, J_{C-F} = 32.6 Hz), 113.1, 112.8, 112.4, 111.6 (q, J_{C-F} = 3.7 Hz), 33.8, 30.9. ^{19}F NMR (376 MHz; DMSO-d6): δ -60.6. HRMS (EI, magnetic sector): calcd for $C_{17}H_{16}F_3NO$ 307.11840, found 307.11665. mp = 95-97 °C.



2-*tert*-Butyl-7-trifluoromethylphenoxazine (3.11). Synthesis was carried out in an analogous fashion to (**8**) using 10-acetyl-2-*tert*-butyl-7-trifluoromethylphenoxazine (**3.11c**). The product was recrystallized from hexanes to afford white needles (0.47 g, 96%). ^{1}H NMR (400 MHz; DMSO-d6): δ 8.65 (br, 1H), 7.05 (dd, *J* = 1.9, 8.2 Hz, 1H), 6.84 (d, *J* = 1.9 Hz, 1H), 6.64 (dd, *J* = 2.3, 8.3 Hz, 1H), 6.56-6.51 (m, 2H), 6.49 (d, *J* = 2.3 Hz, 1H), 1.19 (s, 9H). ^{13}C NMR (101 MHz; DMSO-d6): δ 146.8, 142.9, 140.2, 136.3, 130.3, 124.2 (q, *J* = 270.7 Hz), 121.4 (q, *J* = 4.0 Hz), 120.2 (q, *J* = 32.3 Hz), 117.8, 114.6, 112.9, 111.6 (q, *J* = 3.7 Hz), 110.8, 33.8, 31.0. ^{19}F NMR (376 MHz; DMSO-d6): δ -60.7. HRMS (EI, magnetic sector): calcd for $C_{17}H_{16}F_3NO$ 307.11840, found 307.11864. mp = 162-165 °C.

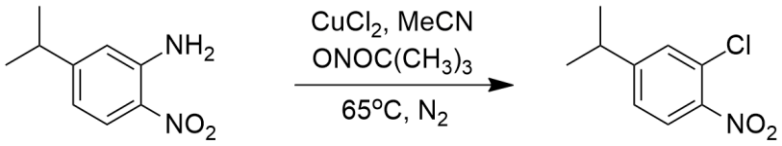


***N*-(5-isopropyl-2-nitrophenyl)acetamide (3.42a)**. Into a 50 mL round bottom flask equipped with a magnetic stir bar was charged acetic anhydride (15 mL). The flask was chilled on an ice bath, and with stirring 3-isopropylaniline (4.05 g, 30 mmol) was gradually added. After ~30 minutes copper (II) nitrate trihydrate (3.38 g) was added and the reaction mixture was allowed to heat to room temperature overnight. After 16 hours the reaction was quenched in a large flask of saturated $NaHCO_3$ solution. The aqueous mixture was extracted 3 times with EtOAc and the organic phase was washed twice with water. The organic solution was dried over $MgSO_4$, and filtered, and the solvent was removed under reduced pressure. The title product was isolated by column chromatography (20% EtOAc in hexanes) appearing as yellow needle like crystals (3.20 g, 48%). ^{1}H NMR (400 MHz; DMSO-d6): δ 10.23 (br, 1H), 7.87 (d, J = 8.4 Hz, 1H), 7.51 (d, J = 1.9 Hz, 1H), 7.23 (dd, J = 2.0, 8.5 Hz, 1H), 2.97 (sept, J = 7.0 Hz, 1H), 2.06 (s, 3H), 1.21 (d, J = 7.0 Hz, 6H). ^{13}C NMR (101 MHz; DMSO-d6): δ 168.5, 155.1, 140.3, 131.5, 125.0, 123.1, 122.7, 33.33, 23.4, 23.2. HRMS (EI, magnetic sector): calcd for $C_{11}H_{14}N_2O_3$ 222.10044, found 222.10045. mp = 69-71°C.

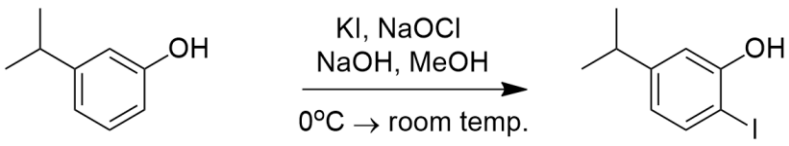


5-Isopropyl-2-nitroaniline (3.42b). Into a double-neck flask were charged *N*-(5-isopropyl-2-nitrophenyl)acetamide (**3.42a**) (3.11 g, 14.0 mmol) and ethanol (100 mL). The ethanol was degassed under a continuous stream of N_2 and concentrated HCl was added (5 mL), after which the flask was sealed with a rubber septa and balloon with N_2 affixed to a needle was poked into the septa. With stirring the mixture was heated to 80 °C for 16 hours. Under reduced pressure, the solvent was reduced to ~20 mL and was poured into 1 M NaOH solution. The aqueous suspension was extracted with Et_2O 3 times, then the organic extracts were dried over $MgSO_4$, and filtered, and the solvent was removed under reduced pressure. The product appeared as a

yellow oil and was used without further purification (2.50 g, 99%). ^{1}H NMR (400 MHz; DMSO-d6): δ 7.88 (d, *J* = 8.9 Hz, 1H), 7.36 (br, 2H), 6.85 (d, *J* = 1.7 Hz, 1H), 6.53 (dd, *J* = 1.9, 9.0 Hz, 1H), 2.79 (sept, *J* = 6.9 Hz, 1H), 1.16 (d, *J* = 7.0 Hz, 6H). ^{13}C NMR (101 MHz; DMSO-d6): δ 156.7, 146.4, 128.6, 125.5, 115.7, 114.8, 33.4, 22.9. HRMS (EI, magnetic sector): calcd for $C_9H_{12}N_2O_2$ 180.08988, found 180.08705.

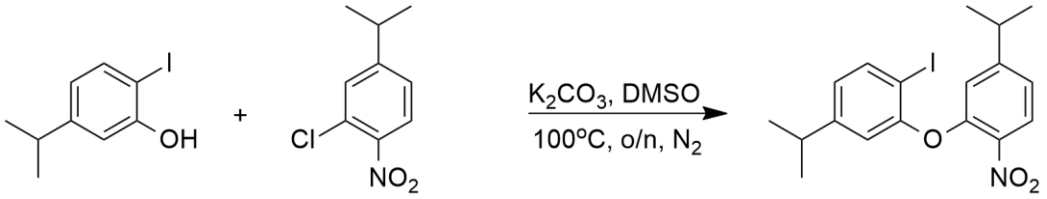


2-Chloro-4-isopropyl-1-nitrobenzene (3.42c). The procedure is based on the method described by Doyle et al.[16] In a double-necked round-bottom flask equipped with a magnetic stir bar and reflux condenser was added anhydrous MeCN (47 mL), anhydrous copper (II) chloride (2.10 g, 15.6 mmol) and 90% *tert*-butyl nitrite (2.23 g, 19.5 mmol). The mixture was stirred and heated to 65 °C for ~5 minutes after which 5-isopropyl-2-nitroaniline (**3.42b**) (2.34 g, 13.0 mmol) dissolved in MeCN (5 mL) was added by dropping funnel over a period of 5-10 min. When evolution of N_2 had ceased (approx. 10 min) the reaction was cooled to room temperature and the mixture was poured into 20% aqueous HCl. The aqueous suspension was extracted with Et_2O, and the organic phase was washed once with 20% aqueous HCl. The organic extracts were dried over $MgSO_4$, and filtered, and the solvent was removed under reduced pressure. The product was isolated by column chromatography (10% EtOAc in hexanes) to afford the title product which appeared as a light-yellow oil (2.21 g, 85%). ^{1}H NMR (400 MHz; $CDCl_3$): δ 7.86 (d, *J* = 8.3 Hz, 1H), 7.40 (d, *J* = 1.9 Hz, 1H), 7.26 (dd, *J* = 1.9, 8.4 Hz, 1H), 2.98 (sept, *J* = 7.0 Hz, 1H), 1.29 (d, *J* = 7.0 Hz, 6H). ^{13}C NMR (101 MHz; $CDCl_3$): δ 155.5, 129.9, 127.2, 125.9, 125.7, 34.0, 23.4. HRMS (EI, magnetic sector): calcd for $C_9H_{10}ClNO_2$ 199.04001, found 199.03838.

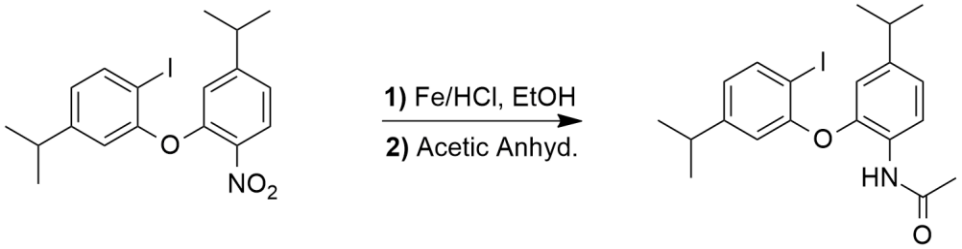


2-Iodo-5-isopropylphenol (3.42d). 3-Isopropylphenol (4.09 g, 30 mmol), sodium iodide (4.50 g, 30 mmol), and NaOH (1.20 g, 30 mmol) were dissolved in MeOH (85 mL) with stirring, cooled

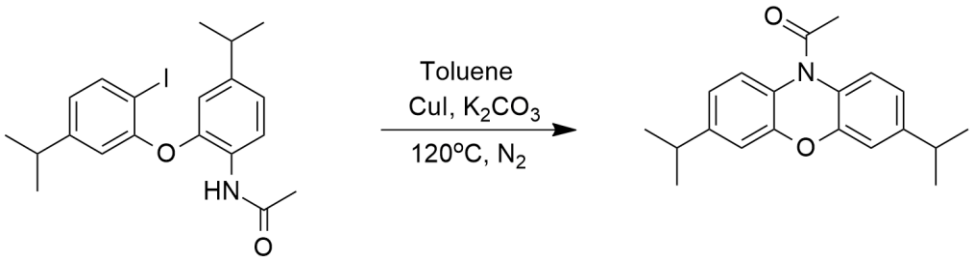
with an ice bath. Approximately 40 mL of 6% sodium hypochlorite solution (bleach) were added dropwise over 1 h until the sodium iodide was consumed. On completion, the reaction mixture was poured into water, and the aqueous mixture was extracted 3 times with EtOAc, and the organic phase was washed twice with water. The organic extracts were dried over MgSO4, filtered, and the solvent was removed under reduced pressure. The title product was isolated by column chromatography (5% EtOAc in hexanes) appearing as a colourless oil (2.93 g, 37%). ^{1}H NMR (400 MHz; $CDCl_3$): δ 7.55 (d, *J* = 8.3 Hz, 1H), 6.90 (d, *J* = 2.0 Hz, 1H), 6.59 (dd, *J* = 2.2, 8.3 Hz, 1H), 5.23 (br, 1H), 2.85 (sept, *J* = 6.9 Hz, 1H), 1.24 (d, *J* = 6.9 Hz, 6H). The spectra were consistent with those previously reported.[17]



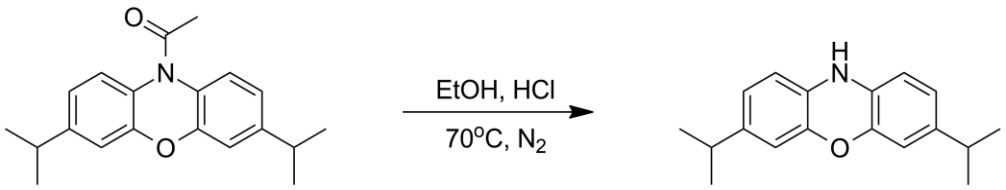
1-Iodo-4-isopropyl-2-(5-isopropyl-2-nitrophenoxy)benzene (3.42e). Synthesis was carried out in an analogous fashion to **(3.8a)** using 2-iodo-5-isopropylphenol (2.62 g, 10 mmol) and 2-chloro-4-isopropyl-1-nitrobenzene (2.00 g, 10 mmol). The title product was purified by column chromatography to the extent that was possible (5% EtOAc in hexanes) appearing as a light-yellow oil (2.71 g, 64%) and carried forward without further purification. ^{1}H NMR (400 MHz; $CDCl_3$): δ 7.98 (d, *J* = 8.4 Hz, 1H), 7.78 (d, *J* = 8.0 Hz, 1H), 7.07 (dd, *J* = 1.8, 8.5 Hz, 1H), 6.86-6.82 (m, 2H), 6.70 (d, *J* = 1.8 Hz, 1H), 2.87 (sept, *J* = 6.9 Hz, 2H), 1.20 (d, *J* = 6.9 Hz, 6H), 1.19 (d, *J* = 6.9 Hz, 6H). ^{13}C NMR (101 MHz; $CDCl_3$): δ 156.7, 155.0, 151.7, 150.3, 139.8, 126.2, 124.8, 121.2, 118.0, 117.5, 84.8, 34.2, 33.7, 23.7, 23.4. HRMS (EI, magnetic sector): calcd for $C_{18}H_{20}INO_3$ 425.04879, found 425.04885.



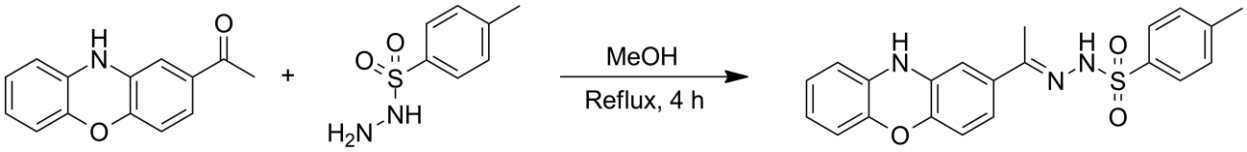
***N*-(2-(2-iodo-5-isopropylphenoxy)-4-isopropylphenyl)acetamide (3.42f).** To a round-bottom flask equipped with a magnetic stir bar were combined 1-iodo-4-isopropyl-2-(5-isopropyl-2-nitrophenoxy)benzene (**3.42e**) (2.67 g, 6.3 mmol), absolute ethanol (30 mL) iron powder (1.40 g, 25 mmol). With stirring the flask was heated to 60 °C and concentrated HCl (6 mL) were added by dropping funnel. The reaction was allowed to proceed until the starting material was consumed (as monitored by TLC) after which the mixture was cooled and was poured into 1 M NaOH. The aqueous suspension was extracted several times with EtOAc and the organic extracts were dried over $MgSO_4$, filtered and the solvent removed under reduced pressure. The residue was dissolved in neat acetic anhydride (3 mL) and allowed to stir overnight. The reaction was quenched with saturated Na_2CO_3 solution and extracted three times with EtOAc. The organic phase was washed once with water, dried over $MgSO_4$, filtered and the solvent removed under reduced pressure. The product was isolated by silica gel chromatography (20% EtOAc in hexanes) appearing as a light-coloured oil (1.93 g, 70%). ^{1}H NMR (400 MHz; $CDCl_3$): δ 8.30 (d, *J* = 8.4 Hz, 1H), 7.77 (d, *J* = 8.0 Hz, 1H), 7.67 (br, 1H), 7.01 (dd, *J* = 2.0, 8.3 Hz, 1H), 6.82-6.79 (m, 2H), 6.68 (d, *J* = 1.9 Hz, 1H), 2.87-2.77 (m, 2H), 2.18 (s, 3H), 1.18 (d, *J* = 6.9 Hz, 6H), 1.17 (d, *J* = 7.0 Hz, 6H). ^{13}C NMR (151 MHz; DMSO-d6): δ 168.6, 155.7, 150.9, 147.5, 145.4, 139.2, 127.0, 124.3, 124.0, 121.0, 117.4, 115.1, 85.7, 33.0, 32.8, 23.7, 23.6, 23.5. HRMS (EI, magnetic sector): calcd for $C_{20}H_{24}INO_2$ 437.08517, found 437.08308.



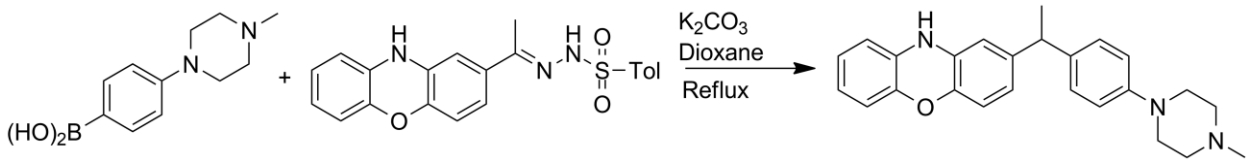
10-Acetyl-3,7-diisopropylphenoxazine (3.42g). Synthesis was carried out in an analogous fashion to (**3.8c**) using *N*-(2-(2-iodo-5-isopropylphenoxy)-4-isopropylphenyl)acetamide (**3.42f**). The product was purified by column chromatography (15% EtOAc in hexanes) appearing as a colourless resin (1.11 g, 88%). ^{1}H NMR (400 MHz; DMSO-d6): δ 7.49 (d, *J* = 8.1 Hz, 2H), 7.06-7.03 (m, 4H), 2.89 (sept, *J* = 6.9 Hz, 2H), 2.25 (s, 3H), 1.19 (d, *J* = 6.9 Hz, 12H). ^{13}C NMR (101 MHz; DMSO-d6): δ 168.7, 150.3, 147.7, 127.0, 125.0, 121.4, 114.2, 33.0, 23.7, 22.7. calcd for $C_{20}H_{23}NO_2$ 309.17288, found 309.17279.



3,7-diisopropylphenoxazine (3.42). Synthesis was carried out in an analogous fashion to (**3.42**) using 10-acetyl-3,7-diisopropylphenoxazine (**3.42g**). The product was purified by column chromatography (10% EtOAc in hexanes) to afford the product as an off-white solid (0.67 g, 72%). ^{1}H NMR (400 MHz; DMSO-d6): δ 7.93 (br, 1H), 6.58 (dd, *J* = 1.2, 7.8 Hz, 2H), 6.48 (d, *J* = 1.2 Hz, 2H), 6.35 (d, *J* = 7.9 Hz, 2H), 2.66 (sept, *J* = 6.9 Hz, 2H), 1.11 (d, *J* = 6.9 Hz, 12H). ^{13}C NMR (101 MHz; DMSO-d6): δ 142.5, 140.6, 130.3, 121.2, 113.0, 112.9, 32.5, 23.8. calcd for $C_{18}H_{21}NO$ 267.16231, found 267.16251.



(*E*)-N'-(1-(10H-phenoxazin-2-yl)ethylidene)-4-methylbenzenesulfonohydrazide (3.44a). In a round bottom flask were added 2-acetylphenoxazine (1.00 g, 4.44 mmol), 4-methylbenzenesulfonohydrazide (0.83 g, 4.44 mmol) and MeOH (40 mL). The suspension was refluxed with stirring for 4 h affording the product as a grey precipitate which was filtered and rinsed (1.59 g, 91%). ^{1}H NMR (400 MHz; DMSO-d6): δ 10.39 (s, 1H), 8.36 (br, 1H), 7.81 (d, *J* = 8.2 Hz, 2H), 7.41 (d, *J* = 8.1 Hz, 2H), 6.85-6.72 (m, 3H), 6.61-6.54 (m, 3H), 6.45 (dd, *J* = 7.6, 1.0 Hz, 1H), 2.37 (s, 3H), 2.05 (s, 3H). ^{13}C NMR (101 MHz; DMSO-d6): δ 152.2, 144.1, 143.3, 142.4, 136.3, 133.1, 132.2, 131.9, 129.5, 127.5, 124.2, 120.4, 119.0, 115.2, 114.6, 113.3, 110.0, 21.0, 13.9. calcd for $C_{21}H_{19}N_3O_3S$ 393.11471, found 393.11389.



2-(1-(4-(4-methylpiperazin-1-yl)phenyl)ethyl)-10*H*-phenoxazine (3.44). To a mixture of (*E*)-*N*'-(1-(10*H*-phenoxazin-2-yl)ethylidene)-4-methylbenzenesulfonohydrazide (**3.44a**) (596 mg, 1.52 mmol), (4-(1-methylpiperidin-4-yl)phenyl)boronic acid (500 mg, 2.27 mmol) in dioxane (40 mL) was added potassium carbonate (314 mg, 2.27 mmol). The reaction mixture was heated to 110 °C with stirring and the reaction was monitored by TLC. When the starting material was consumed, the reaction was cooled to room temperature and was subsequently quenched in saturated $NaHCO_3$ solution, and was extracted three time with DCM. The organic phase was washed with brine and subsequently dried with $MgSO_4$ and filtered. The product was isolated using flash chromatography (1% MeOH in DCM) affording a beige solid (475 mg, 81%). ^{1}H NMR (600 MHz; DMSO-d6): δ 8.09 (br, 1H), 7.05 (d, *J* = 8.6 Hz, 2H), 6.85 (d, *J* = 8.6, 2H), 6.69 (ddd, *J* = 7.7, 7.5, 1.6 Hz, 1H), 6.57-6.50 (m, 3H), 6.44 (dd, *J* = 8.3, 1.8 Hz, 1H), 6.40 (dd, *J* = 7.7, 1.3 Hz, 1H) 6.23 (d, *J* = 2.0 Hz, 1H), 3.83 (q, *J* = 7.2 Hz, 1H), 3.06 (br, 4H), 2.45 (br, 4H), 2.22 (s, 3H), 1.43 (d, *J* = 7.2 Hz, 3H). ^{13}C NMR (151 MHz; DMSO-d6): δ 149.2, 142.8, 142.6, 140.8, 136.6, 132.3, 132.0, 127.7, 123.8, 120.2, 118.7, 115.5, 115.0, 114.6, 113.2, 112.3, 54.6, 48.3, 45.7, 42.4, 21.6. HRMS (EI, magnetic sector): calcd for $C_{25}H_{27}N_3O$ 385.21541, found 385.21422.

3.11 References (Experimental)

(1) Shah, R.; Margison, K.; Pratt, D. A. The Potency of Diarylamine Radical-Trapping Antioxidants as Inhibitors of Ferroptosis Underscores the Role of Autoxidation in the Mechanism of Cell Death. *ACS Chem. Biol.* **2017**, *12* (10), 2538–2545. https://doi.org/10.1021/acschembio.7b00730.

(2) Tin, G.; Mohamed, T.; Gondora, N.; Beazely, M. A.; Rao, P. P. N. Tricyclic Phenothiazine and Phenoselenazine Derivatives as Potential Multi-Targeting Agents to Treat Alzheimer's Disease. *Med. Chem. Commun.,* **2015**, *6* (11), 1930–1941. https://doi.org/10.1039/c5md00274e.

(3) Crivello, J. V. Benzophenothiazine and Benzophenoxazine Photosensitizers for Triarylsulfonium Salt Cationic Photoinitiators. *J. Polym. Sci. Part A Polym. Chem.* **2008**, *46* (11), 3820–3829.

(4) Farmer, L. A.; Haidasz, E. A.; Griesser, M.; Pratt, D. A. Phenoxazine: A Privileged Scaffold for Radical-Trapping Antioxidants. *J. Org. Chem.* **2017**, *82* (19), 10523–10536. https://doi.org/10.1021/acs.joc.7b02025.

(5) Roe, A.; Little, W. F. The Preparation of Some Fluoro- and Trifluoromethyl-Phenothiazines, and Some Observations Regarding Determination of Their Structure by Infrared Spectroscopy. *J. Org. Chem.* **1955**, *20* (11), 1577–1590. https://doi.org/10.1021/jo01128a018.

(6) Ma, D.; Geng, Q.; Zhang, H.; Jiang, Y. Assembly of Substituted Phenothiazines by a Sequentially Controlled CuI/ L-Proline-Catalyzed Cascade C-S and C-N Bond Formation. *Angew. Chemie Int. Ed.* **2010**, *49* (7), 1291–1294. https://doi.org/https://doi.org/10.1002/anie.200905646.

(7) Mital, R. L.; Jain, S. K. Synthesis of Some 5-Substituted 2-Aminobenzenethiols and Their Conversion into Phenothiazines via Smiles Rearrangement. *J. Chem. Soc. C Org.* **1969**, No. 16, 2148–2150. https://doi.org/10.1039/J39690002148.

(8) Gaina, L.; Porumb, D.; Silaghi-Dumitrescu, I.; Cristea, C.; Silaghi-Dumitrescu, L. On the Microwave-Assisted Synthesis of Acylphenothiazine Derivatives — Experiment versus Theory Synergism. *Can. J. Chem.* **2009**, *88* (1), 42–49. https://doi.org/10.1139/V09-163.

(9) Lucarini, M.; Pedrielli, P.; Pedulli, G. F.; Valgimigli, L.; Gigmes, D.; Tordo, P. Bond Dissociation Energies of the N-H Bond and Rate Constants for the Reaction with Alkyl, Alkoxyl, and Peroxyl Radicals of Phenothiazines and Related Compounds. *J. Am. Chem. Soc.* **1999**, *121*, 11546–11553. https://doi.org/10.1021/ja992904u.

(10) Chepuri, V. R.; Beeran, S. One Pot Process for the Conversion of Aroyl Chlorides to Acyl Thioureas. WO2014087431A1, 2014.

(11) Gao, M.; Wang, M.; Hutchins, G. D.; Zheng, Q.-H. Synthesis of New Carbon-11 Labeled Benzoxazole Derivatives for PET Imaging of 5-HT3 Receptor. *Eur. J. Med. Chem.* **2008**, *43* (7), 1570–1574.

(12) VANDERHAEGHE, H. Phenoxazines. I. Ring-Substituted Derivatives. *J. Org. Chem.* **1960**, *25* (5), 747–753. https://doi.org/10.1021/jo01075a019.

(13) Liu, J.; Bandyopadhyay, I.; Zheng, L.; Khdour, O. M.; Hecht, S. M. Antiferroptotic Activity of Phenothiazine Analogues: A Novel Therapeutic Strategy for Oxidative Stress Related Disease. *ACS Med. Chem. Lett.* **2020**, *11* (11), 2165–2173. https://doi.org/10.1021/acsmedchemlett.0c00293.

(14) Roberts, K. C.; Rhys, J. A. 8. A Rearrangement of o-Aminodiphenyl Ethers. Part V. *J. Chem. Soc.* **1937**, 39–41. https://doi.org/10.1039/JR9370000039.

(15) Bodea, C.; Raileanu, M. Nitration of Phenothiazine. *Stud. si Cercet. Chim.* **1957**, *8*, 303–313.

(16) Doyle, M. P.; Siegfried, B.; Dellaria, J. F. Alkyl Nitrite-Metal Halide Deamination Reactions. 2. Substitutive Deamination of Arylamines by Alkyl Nitrites and Copper(II) Halides. A Direct and Remarkably Efficient Conversion of Arylamines to Aryl Halides. *J. Org. Chem.* **1977**, *42* (14), 2426–2431. https://doi.org/10.1021/jo00434a017.

(17) Hermann, G. J.; Annis, M. C.; Edwards, P. D.; Corrales, M.; Díaz, L.; Goodnow, R. A. An Efficient Synthetic Route to Novel 3-Alkyl- and 3-Aryl-4-Iodophenols. *Synthesis (Stuttg).* **2008**, 221–224.

Chapter 4

Toward a Phenoxazine RTA Drug Candidate

4.1 Foreword

Chapter 4 is the final section in this thesis addressing the topic of RTAs in the context of phospholipid membrane peroxidation. The initial motivation for what is described below was to iterate on the lessons learned from Chapter 3,[1] with an orientation toward more "drug-like" phenoxazine-RTAs. That is not to say that fundamental questions of reactivity and dynamics are neglected here. Indeed, more attention is given to structure and function with respect to enhancing the synergy with water soluble reductants (e.g., ascorbic acid) by means of exploring how structure affects interfacial-interactions of the phenoxazine-radical intermediates. Having given a thorough treatise of structure-function relationships using relatively simple substituents in the previous chapter, we also felt it was incumbent on us to explore what a drug based on this scaffold/concept could look like. Admittedly this is a work-in-progress, but I hope that it can serve as part of the foundation for a future medicinal chemistry campaign *and* as a prospectus for the long term aims of the research. Here I would like to acknowledge the contributions from Dr. Zijun Wu for the ferroptosis rescue cell data and Matthew Chebet who carried some kinetic experiments as part of his summer internship (Fig. 4.3B). I would also like to thank Prothegen Inc. for arranging and financing a pilot pharmacokinetic study which is discussed in the prospectus.

4.2 Introduction

In the previous chapter, we demonstrated with many examples that PNX-based RTAs (and to a slightly lesser extent PTZ) are quite amenable for suppressing lipid-peroxidation in phospholipid membranes both with and without the aid of a water-soluble co-reductant (ascorbate). The intrinsic potency of the scaffold(s) is such that even derivatives that were intentionally "deactivated" with EWGs are generally competent as inhibitors of ferroptosis. Provided that the fidelity of the scaffold's "active site" is maintained (i.e., leaving the aminic 10-position unsubstituted), making potent inhibitors of ferroptosis based on PNX/PTZ becomes a trivial endeavour with respect to *in vitro* assays. Nevertheless, a significant challenge remains when

making the leap from cell models to animal models, as is often the case. While our preliminary results with 3-CF_3-8-tBu-PNX in the murine GPx4 knockout model showed some promising results with respect to kidney injury,[1] there were some signs of liver toxicity under the practiced dosing regimen (10-20 mg/kg per day).

It also remains unclear to us how stoichiometry/regeneration factors into the observed potency with respect to cell assays. In principle, more chains trapped should equate to a lower [RTA] required to quench lipid peroxidation in the cell's membrane, though obviously as [RTA] decreases the inhibited autoxidation rate goes up. While we seem to have reached somewhat of an impasse between k_{inh}^{lip} and the diffusion-limit, deliberate attempts to enhance stoichiometry/regeneration-efficiency would be a logical optimization for inhibitors of even greater potency.

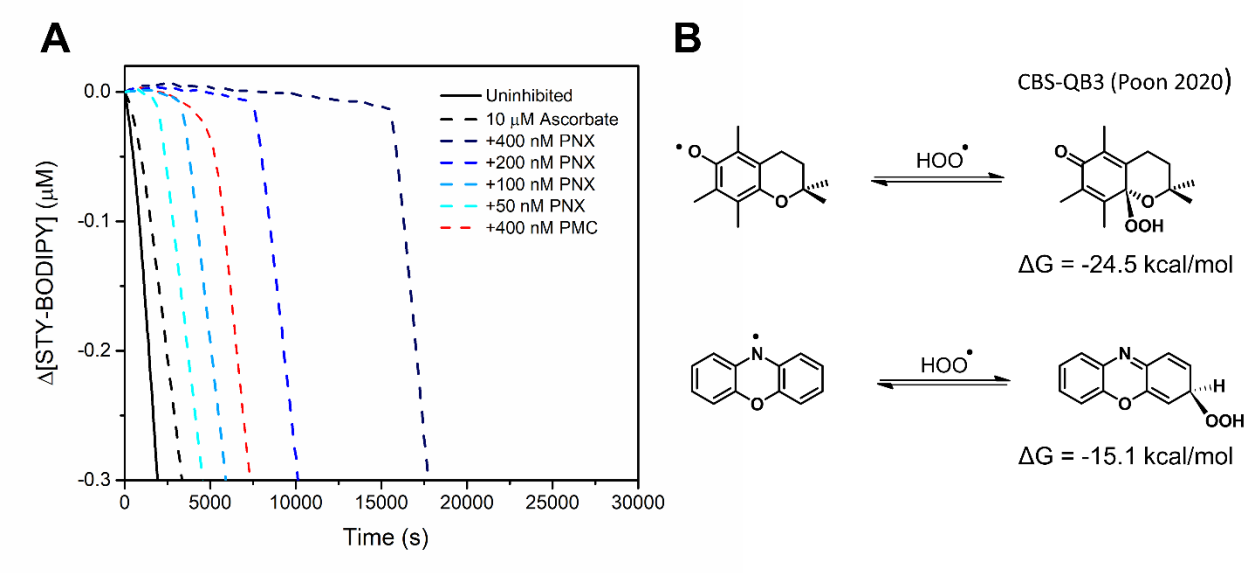


Figure 4.1. (A) Co-autoxidation of STY-BODIPY (1 μM) in 100 nm L-α-phosphatidylcholine liposomes (1 mM) suspended in pH 7.4 PBS initiated by DTUN (200 μM) (dashed lines with 10 μM ascorbic acid). Concentrations of PNX (blue) of 50, 100, 200, and 400 nM (t_{inh} of 1893 ± 56 s, 3487 ± 59 s, 7539 ± 103 s and 15290 ± 400 s, respectively) and PMC (red) at 400 nM (t_{inh} = 5015 ± 220 s). R_i = 7.57 × 10^{-10} M s^{-1}. (B) Free energy of hydroperoxyl addition to PMC and PNX derived radicals (according to CBS-QB3).[2]

From the data accrued thus far, there are at least two determinants of regeneration efficiency that can be readily inferred. The first pertains to the persistence of the RTA-derived radical. A clear example of this is the regeneration of PMC compared to PNX. When provided with an

abundance of ascorbic acid (10 μM) relative to the RTA (400 nM), PNX is able to trap ~29 radical chains per equivalent (n = 28.9 ± 0.8) while PMC traps less than 10 (n = 9.5 ± 0.4). Increasing the concentration of ascorbate 10-fold (100 μM) sees the PNX break an additional 13 chains (n = 41.9 ± 0.4), but for PMC the increase is marginal (n = 11.0 ± 0.3). Unlike PNX, as well as numerous other PNX/PTZ-derived structures, the turnover of PMC is practically unaffected by the increase in co-reductant suggesting that its regeneration is entirely limited by the off-cycle reactions. The increase in stoichiometry for PNX falls well short of a ~10-fold increase at 100 μM of ascorbate, while decreasing the concentration of PNX relative to ascorbate (Fig. 4.1A) sees a linear decrease in t_{inh} and a consistent stoichiometry of ~28, again indicating at least a partial limitation with respect to the persistence of the aminyl radical. The competing likely fate for RTA-derived radicals is generally the addition of lipid-peroxyl radicals, trapping the adduct within the lipid domain. We previously calculated a 9.4 kcal/mol free energy difference between peroxyl addition to a PMC-derived phenoxyl radical compared to the PNX-derived aminyl radical (Fig. 4.1B).[2] The PMC addition adduct is stabilized by the strength of the carbonyl double-bond which may provide insight into the general trends in persistency when comparing PMC to the azine-derived radical intermediates, to say nothing of how bulkier ring substituents on PNX could be used to further enhance persistence. In fact, the latter point may explain why 2,8 and 3,7-di-*tert*-butyl do not return to an uninhibited state after their 'primary' inhibited period is over (see Fig. 4.2B).

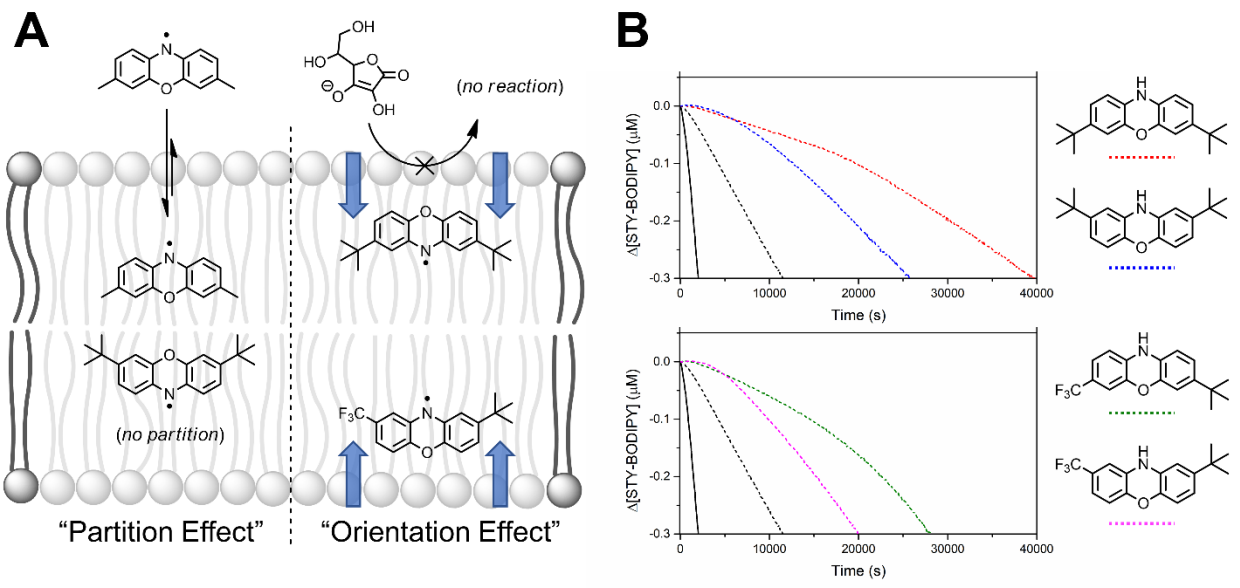


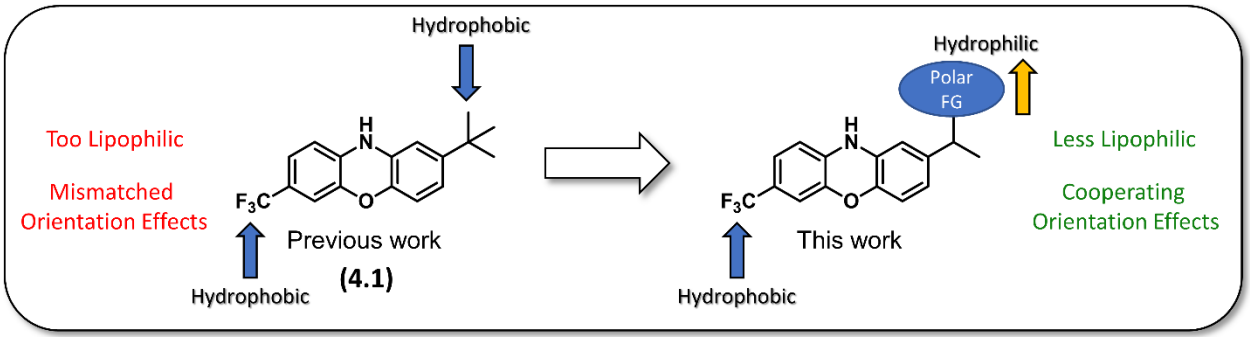
Figure 4.2. (A) Proposed interfacial/inter-phase effects on PNX/ascorbate synergy. (B) Key examples of the proposed orientation effect, comparing lipophilic substituents at the 3,7 and 2,8-positions.

The second determinant of regeneration appears to be predicated on the interfacial interactions between ascorbate in the aqueous phase and the aminyl radical intermediate. Looking over the ascorbate-PNX synergy data we noted that compounds with higher partition coefficients (log*P*) tended to have shorter primary inhibited periods. For instance, 3,7-Me-PNX (log*P* = 4.76) had stoichiometries of 25 and 51 with 10 μM and 100 μM of ascorbate, respectively, while 3,7-tBu-PNX (log*P* = 7.22) only broke 11 and 37 chains under the same set of conditions. A straightforward interpretation is that the more lipophilic compound is buried in the lipid domain, while the former more amphiphilic compounds is able to better sample the interface, thereby having more opportunity to be reduced. Perhaps even more insightful is how much substituent positioning effects regeneration. Indeed, by orienting *tert*-butyl groups towards the same face as the N-H, as is the case with 2,8-tBu-PNX (log*P* = 7.22), we observe a dramatic drop in stoichiometry under both sets of test conditions ($n = 5.0 \pm 0.2$ and $n = 11.5 \pm 0.1$, respectively). The same trend is seen when comparing 3-CF_3-7-tBu-PNX ($n = 11.3 \pm 0.1$ and $n = 40.6 \pm 0.6$) to 2-CF_3-8-tBu-PNX ($n = 5.5 \pm 0.1$ and $n = 6.9 \pm 0.3$). We propose, as shown in Figure 4.2, that the hydrophobic effect causes the nitrogen centred radical intermediates of 2,8-tBu-PNX and 2-CF_3-

8-tBu-PNX to orient away from the aqueous interface, greatly decreasing the efficiency of reduction by ascorbate.

Taking the template established with 3-CF_3-8-tBu-PNX (**4.1**), as it is metabolically stable and has proven effective in a pilot animal model for ferroptosis, we wondered if we could mitigate the drug-induced liver toxicity previously observed. High lipophilicity in combination with frequent dosing and an anticipated low clearance presents several red flags with respect to the likelihood of drug-induced liver injury,[3] so we set out to moderate lipophilicity while maintaining the efficacy of the inhibitor. This aim coincided with our interests in enhancing synergy with ascorbate, as we hypothesized that replacing the *tert*-butyl functional group in the '8-position' with something more hydrophilic would orient the nitrogen of the radical intermediate toward the interface resulting in higher stoichiometries.

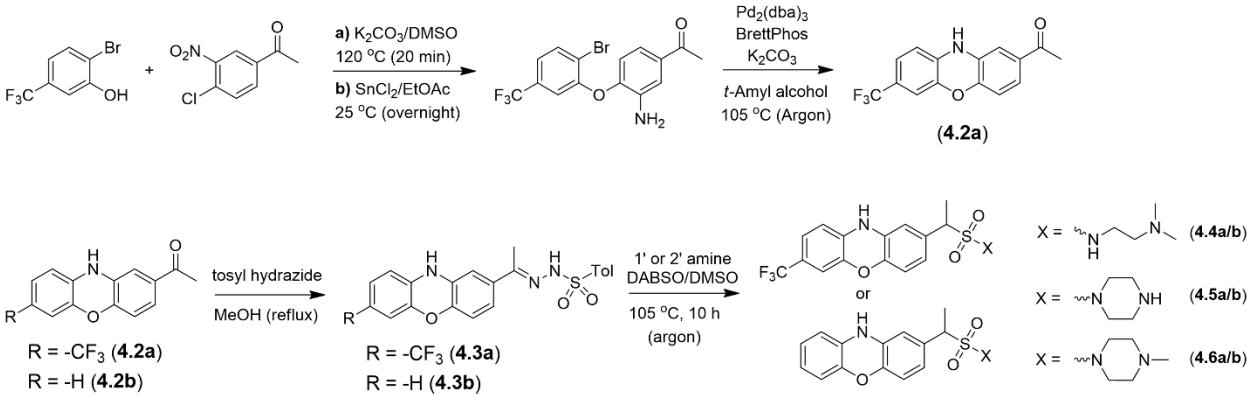
Scheme 4.1 – Proposed Enhancements to Compound 4.1.



4.3 Results and Discussion

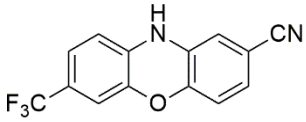
Taking inspiration from Yang and co-workers and their medicinal chemistry efforts on PTZ-based ferroptosis inhibitors,[4] we sought to use the tosyl-hydrazone (**4.3a**) derived from 2-acetyl-7-CF_3-PNX (**4.2a**) to make a series of alkyl sulfonamide derivatives using the method described by Tsai et al.[5] After dealing with some initial troubles related to undesired enolization of the acetyl moiety, we developed a relatively efficient 3-step synthesis of **4.2a**. From **4.3a** we prepared 3 alkyl sulfonamide derivatives (**4.4a**-**4.6a**), and also proceeded to make an analogous series without the -CF_3 group on the PNX core (**4.4b**-**4.6b**).

Scheme 4.2 – Synthesis of 4.2a and 4.4-4.6.

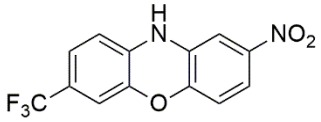


Having prepared a small series of derivatives with hydrophilic moieties on the 'front face' of the PNX scaffold, containing sulfonamide and alkyl amine(s), we proceeded to compare **4.4**-**4.6** to **4.1** in the STY-BODIPY/liposome co-autoxidation assay (the results are summarized in Table 4.1). In addition to these examples, we prepared an additional set of compounds with both polar (-C≡N, -NO_2, -NH_2) and hydrophobic substituents (-Br, -I) at the "8-position" to further test our proposed "orientation-effect", since up to this point the only substituents tested had been *tert*-butyl and trifluoromethyl.

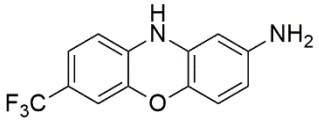
Table 4.1. Inhibition Rate Constants and Stoichiometries in Liposomes with and Without Ascorbate



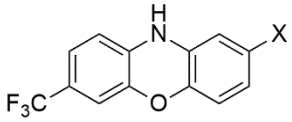
(**4.7**)



(**4.8**)



(**4.9**)



X = -Br (**4.10**)

X = -I (**4.11**)

	No Ascorbate [a]		w/ Ascorbate (100 μM)		
	k_{inh}^{lip} (10^3 $M^{-1}s^{-1}$)	*n*	k_{inh}^{lip} (10^3 $M^{-1}s^{-1}$)	*n*	*LogP* [e]
PMC	35 ± 1.3	(2)	37 ± 3.1	11.0 ± 0.3	4.48 ± 0.26
PNX	183 ± 16	2.5 ± 0.1	155 ± 26	41.9 ± 0.4	3.84 ± 0.44
3-CF_3-PNX	34 ± 1.4	4.6 ± 0.1	31 ± 2.7	31.1 ± 0.6	4.98 ± 0.50
4.1	56 ± 11	3.8 ± 0.1	22 ± 0.6	31.2 ± 0.3	6.67 ± 0.51
4.4a	25 ± 0.3	7.3 ± 0.1	23 ± 1.4	≥100	(4.09 ± 0.72) [f]
4.5a	24 ± 3	4.2 ± 0.3	23 ± 0.5	≥100	(4.21 ± 0.62) [f]
4.6a	25 ± 3.9	4.2 ± 0.4	23 ± 0.3	≥100	(4.61 ± 0.62) [f]
4.4b	65 ± 6.6	5.0 ± 0.1	35 ± 2.1	≥100	(2.95 ± 0.69) [f]
4.5b	93 ± 7.3	2.5 ± 0.2	45 ± 2.6	45.5 ± 1.8	(3.07 ± 0.60) [f]
4.6b	78 ± 6.6	2.4 ± 0.2	49 ± 1	58.8 ± 1.5[d]	(3.47 ± 0.60) [f]
4.7	24 ± 1.4	5.5 ± 0.1	30 ± 2.7	58.1 ± 3.9	5.09 ± 0.55
4.8	14 ± 0.6	3.4 ± 0.1	30 ± 2.6	63.6 ± 3.3	5.37 ± 0.53
4.9	- [b]	3.8 ± 0.1	- [c]	~12	3.84 ± 0.51
4.10	49 ± 2.3	4.0 ± 0.1	29 ± 2.9	40.3 ± 3.4	6.19 ± 0.57
4.11	54 ± 0.9	3.5 ± 0.1	26 ± 4	41.3 ± 2.0	6.45 ± 0.57

(a) Inhibited egg-PC/STY-BODIPY co-autoxidation initiated with DTUN. (b) Primary inhibition period (first ~5000s) is negative/flat (complete inhibition of autoxidation and/or visual artifact of oxidation). (c) Inhibition period too short or $-d[BODIPY]/dt \leq 0$, precluding a report of a steady/reliable rate of inhibition. (d) Still appears to be inhibiting toward the end of the experiment but at a lower k_{inh}^{lip} (~1 × 10^4 M^{-1} s^{-1}). (e) Log*P* values were calculated in ACD/ChemSketch 2020 (v. 14.50), ACD/Labs. (f) The calculated log*P* is of the neutral amine.[6]

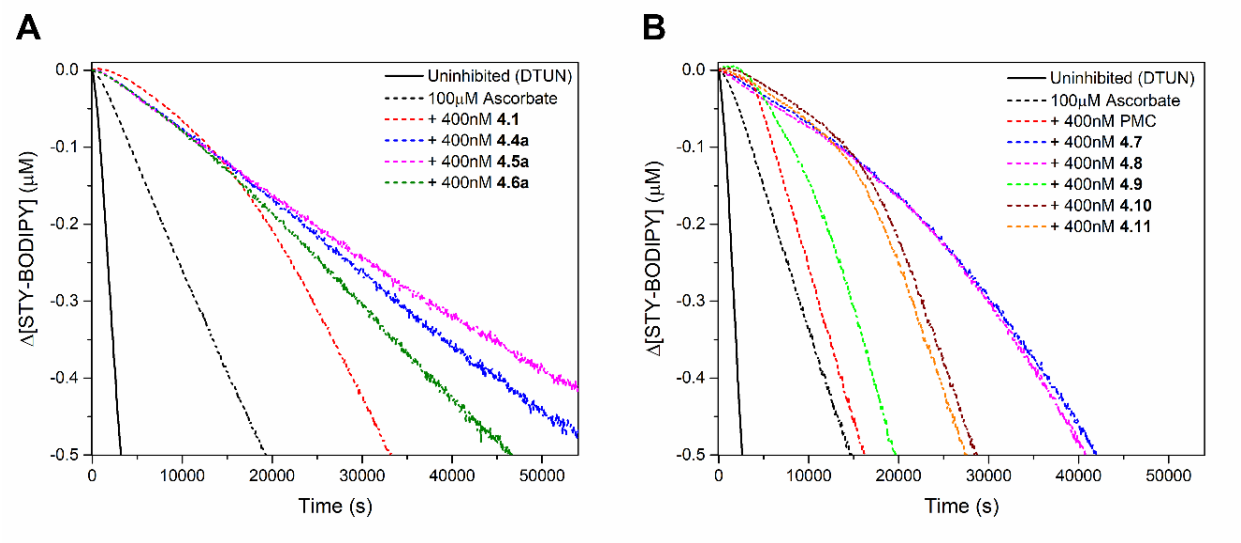


Figure 4.3. DTUN initiated (200 μM) co-autoxidation of STY-BODIPY (1 μM) in Egg-PC liposomes with ascorbate (100 μM). (A) Inhibited by 400 nM **4.1** (red, $R_i = 7.50 \times 10^{-10}$ M s^{-1}) compared to **4.4a-4.6a** ($R_i = 8.52 \times 10^{-10}$ M s^{-1}). (B) Inhibition of 400 nM PMC (red) compared to **4.7-4.11** ($R_i = 9.77 \times 10^{-10}$ M s^{-1}).

Surveying the results, there are several interesting features with respect to stoichiometry worth highlighting. First, looking at the results without ascorbate, it is remarkable that many of the compounds trap far more radicals than PMC for reasons that are not immediately obvious. While PNX (2.5 ± 0.1) seems within the margin of error of "expectations" (~2), many of the other examples range anywhere from 3.4 all the way up to 7.3. With the exception of **4.4b**, all of the compounds that feature these higher stoichiometries contain the $-CF_3$ functional group. Compound **4.4b** (5.0 ± 0.1) seems to be an exceptional case, related to the particular alkyl sulfonamide as **4.4a** (7.3 ± 0.1), which also has a large delta ($\Delta n \sim 3$) compared to the other $-CF_3$ containing counterparts. When we look over the data from the previous chapter, we see that this behaviour is also observed with PNX compounds that contain at least one cyano, nitro or formyl group in the 3-position. The trend is also observed with PTZ whether $-CF_3$ is at the 2 or 3 position. While there is a clear correlation between strong EWGs and these unexpectedly high *n* values, at present we do not have a mechanistic explanation for it. Likely there is a system/substrate dependency, as this trend was not observed in our 1,4-dioxane co-autoxidations in our seminal work on PNX RTAs.[7]

Looking at the results from the ascorbate buffered experiments, the trends appear consistent with our proposed model shown in Figure 4.2A. Indeed, both **4.7** and **4.8** with their polar groups on the 'front face' regenerate more efficiently compared to the examples with more hydrophobic groups (**4.1**, **4.10** and **4.11**). Compound **4.9** does not regenerate efficiently at all, though this is most likely predicated on lack of intermediate persistence rather than interfacial phenomena.[8] Gratifyingly, **4.4a**-**4.6a** and **4.4b** inhibit for the entire duration of the experiment, though given that these contain highly ionizable amines, the effect may be on account of efficient partitioning rather than just optimized orientation. While arguments for either effect are not fundamentally contradicted with these additional data points, the examples given in Figure 4.2B remain the most unambiguous with respect to the orientation effect as essentially all other differences are normalized apart from substituent positioning.

Table 4.2. Microsome Stability and Ferroptosis Rescue Potency of 4.4-4.6 and Related Compounds.

Compound [a]	**$t_{1/2}$ (min)** [c]	**Relative $t_{1/2}$** [f]	**EC_{50} (nM)** [g]
Verapamil [b]	(5.8 ± 0.3) (3.7 ± 0.1) [d]	1.1 1.0	N/A
PNX	(6.5 ± 0.2) (3.7) [d]	(1) (1)	16 ± 1
3-CF_3-PNX	- [e]	1.4 [e]	12 ± 1
4.1	(212 ± 31) [d]	57	3.6 ± 0.2
4.4a	(209) [d]	56	2.2 ± 0.1
4.4b	(15.1) [d]	4.1	15 ± 1
4.5a	(276) [d]	75	3.0 ± 0.1
4.5b	(18.8) [d]	5.1	13 ± 1
4.6a	(56.8) [d]	15	16 ± 2
4.6b	(3.8) [d]	1.0	45 ± 6

(a) Results from liver microsomal stability experiments (BALB/c mouse). 10 μM of compound (separated by RP-UPLC and monitored by PDA.) (b) Verapamil high-clearance standard at 1 μM (monitored by MS-ESI+) (c) Standard conditions: 0.5 mg/mL liver microsomes; 1 mM NADPH; 100 mM phosphate buffer (pH 7.4); 37°C. (d) Liver microsomes increased (1.0 mg/mL). (e) Reported as relative half-life with respect to PNX positive control from the experiment (this batch liver microsomes were substantially less active giving $t_{1/2}$ of 12.8 min for PNX and 17.4 min for 3-CF_3-PNX, respectively, at 0.5 mg/mL microsomes). (f) Half-life relative to PNX under equivalent experimental conditions. (g) EC50 derived from survival curve of RSL3 induced ferroptosis of pfa-1 MEFS inhibited by ferroptosis inhibitors.

Eager to see how our second-generation iterations of **4.1** would fare in the context of ferroptosis, we proceeded to evaluate the potency of **4.4**-**4.6** in the RSL3 induced pfa-1 rescue assay. Additionally, we also carried out preliminary evaluations of liver microsome stability (Table 4.2). With respect to metabolic stability, we were pleased to find that swapping the *tert*-butyl group of **4.1** with the benzylic sulfonamide group(s) rendered a similar level of ferroptosis suppression for **4.4a** and **4.5a**. Comparing the relative change in half-life, with respect to PNX, neither 3-CF_3-PNX nor **4.4b**-**4.6b** are particularly stable in the way **4.1** and **4.4a**-**4.6a** are. The removal of either the -CF_3 from the '3-position' or the blocking alkyl/alkyl-sulfonamide at the '8-position' systematically demonstrates that both substituents are necessary to stabilize these PNX-compounds toward oxidation by NADPH-dependent CYP450 in the liver microsomes. It should also be noted that there is a peculiar decrease systematic to the N-methyl piperazine group found in the **4.6** compounds. In terms of *in vitro* ferroptosis inhibition, the -CF_3 containing **4.4a**-**4.6a** are systematically superior to their unsubstituted counterparts (**4.4b**-**4.6b**). Once again, this underscores that higher k_{inh}^{lip} is *not* the universal absolute predictor of potency in the cell-based ferroptosis rescue assay. All of the data collected thus far indicates that a when the -CF_3 is present, a substituent that both reduces k_{inh}^{0} and increases α_2^H, the PNX-compound is imbued with an enhanced level of potency, contravening purely kinetic explanations.

4.4 Prospectus and Conclusions

The primary objective of this follow-up work, which was to make **4.1** more "drug-like", has so far been successful. Indeed, both **4.4a** and **4.5a** match the potency and stability of **4.1** while also significantly decreasing the calculated log*P*.[6] We believe that this should meaningfully decrease the risk of drug-induced liver toxicity and issues generally associated with excessive lipophilicity and low-clearance. In anticipation of imminent *in vivo* studies in relevant ferroptosis-related animal models, we partnered with Prothegen Inc. who commissioned a pharmacokinetic (PK) study of **4.5a** in mice both by IP injection and oral administration. To our delight, **4.5a** demonstrated excellent oral bioavailability in the pilot study and demonstrated an ability to cross the blood-brain-barrier (BBB), as it was detected in both the brain and spinal cord in meaningful quantities at each assayed time point. The clearance was somewhat sluggish in the liver, kidney and plasma ($t_{1/2}$ ~18-20 h), but to our surprise the concentration in the brain and spinal cord went *up* relative to the levels in plasma through the course of the experiment. Even after 96h,

concentrations in the brain (104 ± 11 nM) and spinal cord (85 ± 22 nM) were *well over* an order of magnitude greater than the single nM concentrations required to achieve EC_{50} in the cell-based assay, to say nothing of the maximal concentrations at 24 h (625 ± 35 nM and 473 ± 70 nM, respectively). Moreover, no signs of acute toxicity were evident in any of the animals at any time points. While one should not get too carried away with extrapolating between cell-models and *in vivo* experiments, the initial impressions from these pilot studies are highly encouraging nevertheless.

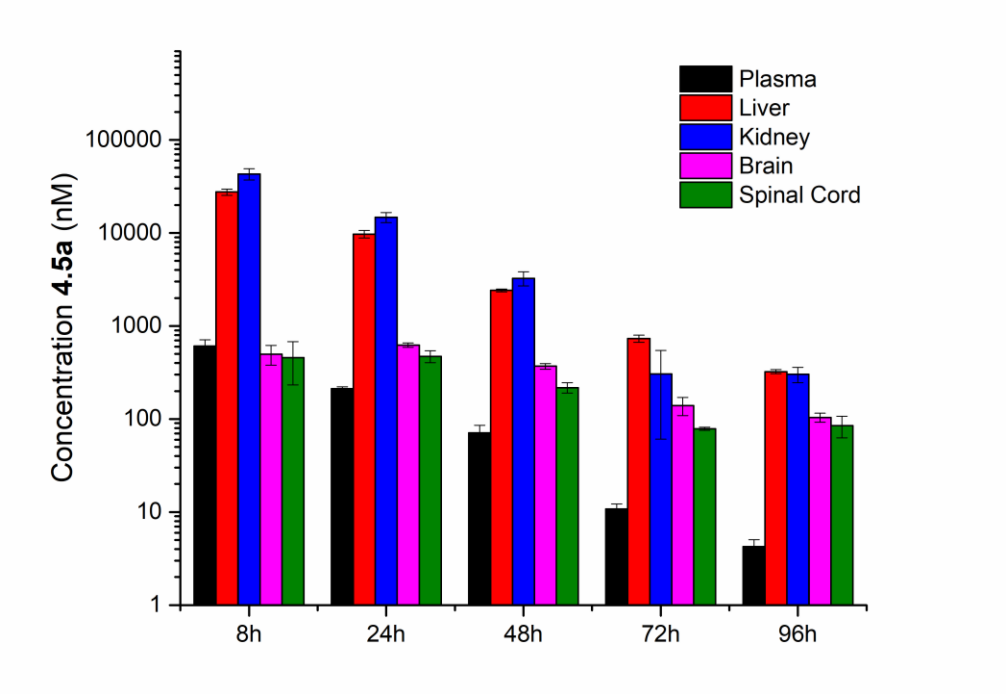


Figure 4.4. Concentration of **4.5a** found in plasma, liver, kidney, brain and spinal cord post-oral administration (10 mg/kg) in C57BL/6 mice monitored for up to 96 h (n = 3 for each timepoint). Converted from ng/mL or ng/g to nM (from a MW of 427.44 ng/nmol and assuming density of tissue ~1 g/mL).

It will be interesting to see how a more measured dosing regimen of **4.5a** (≤10 mg/kg every 3-4 days) will impact the outcome of a future kidney IRI study, particularly in comparison to our initial results with **4.1**, given the high concentrations of **4.5a** found in the kidneys in this preliminary pharmacokinetic trial. Of course, of even greater interest will be testing the efficacy of **4.5a** in neurodegeneration models where ferroptosis is seen to be particularly relevant.

Speaking of the work exhibited in these past 3 chapters more generally, I believe it is fair to say that a significant amount of progress and understanding has been achieved through primarily physical-chemical means and methods. Now with a well-defined chemical model of RTA kinetic-behaviour in a membrane environment, sensible and reliable predictions with respect to ferroptosis inhibition can be made for two of the most prominent classes of RTAs – phenols and aromatic amines. The search parameters for a potent 'anti-ferroptosis' drug is significantly narrowed on the basis of this understanding alone. A relentless systematic study of PNX and PTZ-based RTAs has uncovered the cutting-edge limit of RTA-based ferroptosis inhibitors. The reasons behind their excellent activity are now well defined, and a sensible set of guidelines for retaining their potency has been established.

All of that being said, we seem to have also reached the limits of the absolute predictive power purely on the basis of first principals for RTA-design. If ambitions of parlaying this theoretical potential into a clinical candidate are to be realized, I fail to see any alternative but to employ the more conventional medicinal chemistry approach with wild abandon. Indeed, it would seem that chemical intuition and *in vitro* kinetic models can only take one so far until the law of diminished returns takes hold, necessitating a greater emphasis on the biochemical considerations.

A small exhibition of this point can be seen in our identification of **3.11** (A.K.A. **4.1**) as a proto-drug-candidate of promise. Theory on the basis of radical-trapping kinetics would have identified it as a competent but middling ferroptosis inhibitor (relative to PNX), yet it was the most potent in a library of over 40 competitive examples. My chemical intuition with respect to optimizing metabolic stability predicted that the 3,7-substituted compounds (**3.10** and **3.34**) would be the most likely to resist CYP450-mediated oxidation, yet they were the *worst* in this respect compared to all the regioisomers tested. In contrast, **3.11** was only supposed to be a collected "stamp", almost an afterthought, yet that innocuous combination of substituents completely subverted expectations by being practically impervious to primary metabolism (a non-trivial feat when one considers how electron-rich the PNX-scaffold is). These more biochemically oriented tools changed the course of the project in a fundamental way, underscoring that while the physical-chemical model has played an invaluable role in narrowing the search to a particular

"neighbourhood", finding the "exact address" (a working drug) will require a greater emphasis on the conventional tools of drug discovery/development.

That is not to say that there are not still *many* fundamental questions of chemistry regarding the true nature of lipid peroxidation with respect to ferroptosis. While we have uncovered some basic physical-chemical foundations of RTA-ascorbate synergy in model membranes, particularly using examples that go well outside the traditional α-tocopherol/ascorbate dichotomy, the actual role such factors play in a cell (or a tissue) in transit to a ferroptotic state remains rather opaque. I suspect the confusion stems from an incongruency between the nature of chain initiation between our thermally initiated liposome assay and GPx4-inhibited approach used in the cell experiments. While analogies can be drawn between these two scenarios, hence the predictive capabilities of the inhibited liposome experiments, their differences could be quite substantial depending on the extent to which chain-branching occurs in a ferroptosis sensitive cell (a proposed concept is visualized in Figure 4.5A). In the DTUN initiated liposomal oxidations, a constant rate of initiation (R_i) regime is at play as initiation is predicated on the temperature and concentration of DTUN, rather than iron-mediated reduction of LOOH. Most likely the R_i in the liposome experiment is arbitrarily high with respect to the 'R_i' of the cell, at least compared to the initial stages of ferroptosis when GPx4 is not yet fully overwhelmed and/or compromised. These are deliberate features of the experimental design as the priorities in the liposome co-autoxidations are well defined k_{inh}^{lip} / n values, which can only be feasibly obtained if R_i is: (i) constant and (ii) appropriately high (to consume the RTA in a reasonable timeframe). Most likely, ferroptosis triggered by GPx4-inhibition operates in an auto-initiating fashion, where the R_i starts very low but grows exponentially through chain-branching when propagation is not properly managed forthwith.

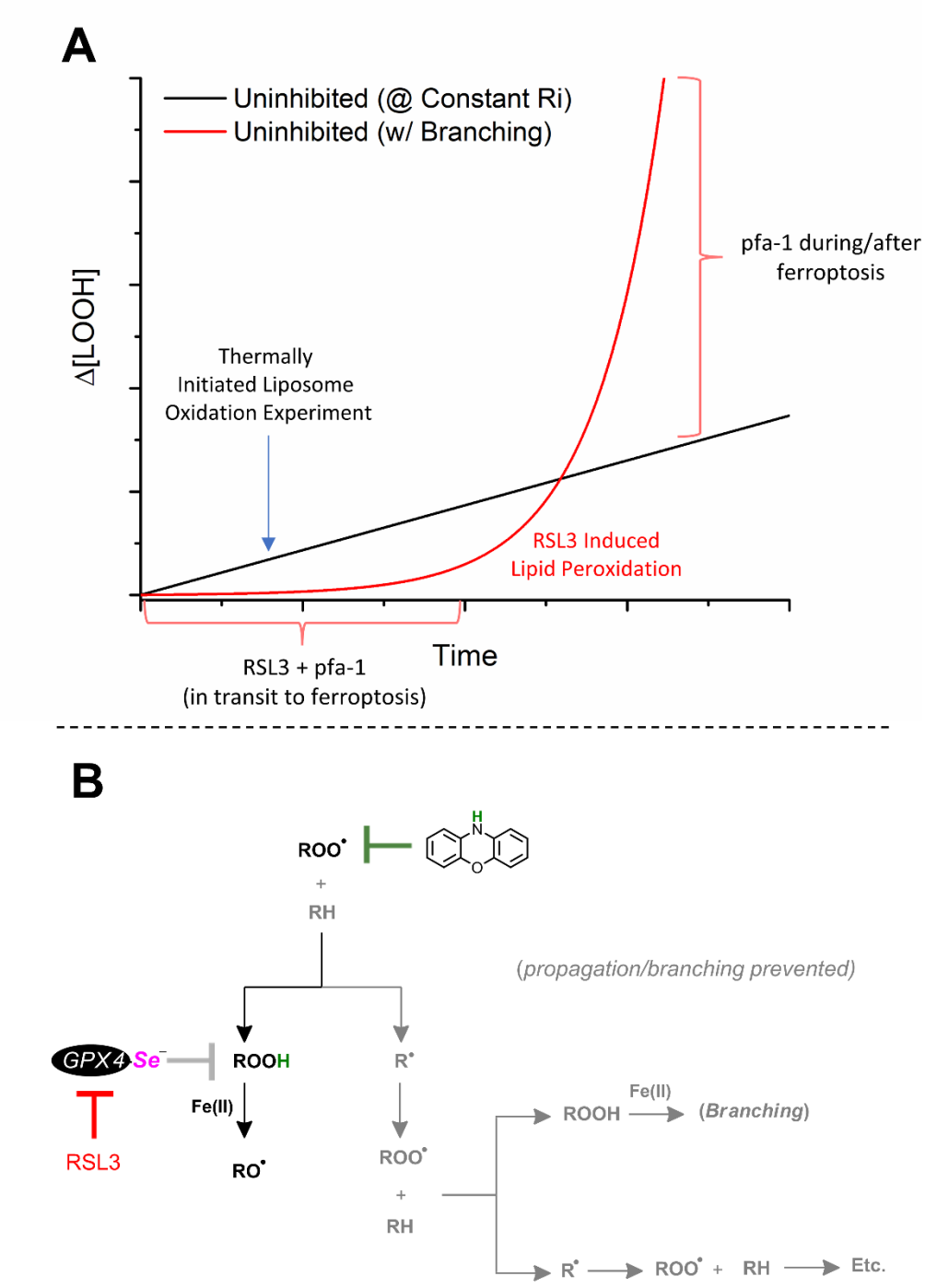


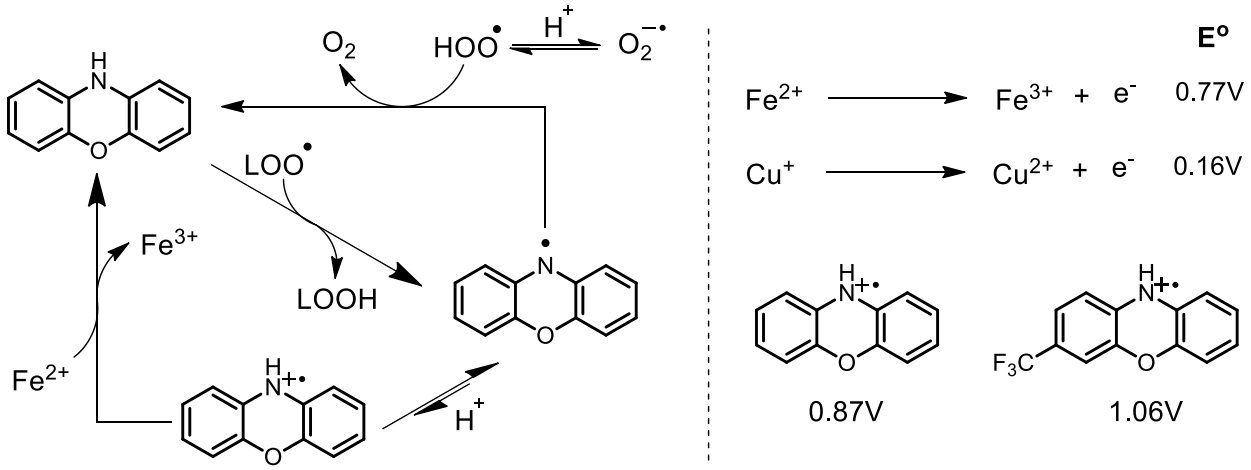
Figure 4.5. (A) Linear behaviour of the DTUN/V70 initiated liposome autoxidation compared to a hypothetical exponential/branched model of behaviour that might occur in GPx4-inhibited cells. (B) Minimizing chain-propagation early prevents many future propagation/branching events.

Many of the differences between the RTAs may be obscured simply because the pfa-1 cells are pre-treated with the RTA *before* the GPx4 inhibitor is added, quashing propagation so thoroughly that the R_i is more or less constant and never increases past a very low basal level. One must keep in mind that within a chain-branching regime, how quickly a chain is quenched (ideally at initiation) is as important as how many total chains are trapped, because a radical trapped at initiation prevents all the downstream branching, and thus fewer 'total chains' need to be trapped (Figure 4.5B). If this speculative reasoning is taken for granted, an even deeper set of questions emerges: at what point along this auto-initiated reaction progress curve is it 'too late' to stop ferroptosis (even with a hypothetically 'perfect' RTA)? And what point along this curve would resemble a *bone fide* tissue-wide ferroptosis event seen in an animal model of neurodegeneration? Such lofty questions lie at the interface of chemistry and various disciplines of bioscience, but answering them could provide a rational basis for identifying the therapeutic window these hypothetical drugs could operate effectively within. A proper understanding of this could be critical to the design of both animal and clinical studies implementing an RTA-based intervention approach.

To date, there are very few, if any, true success stories with respect to antioxidant-based drug therapies, not from a lack of trying mind you. Attempts to make competitive RTA-based antiatherogenic drugs (inspired from the initial success of probucol in the 80's)[9] have apparently come up dry (at least as a matter of public record)[10] while the push for antioxidant-drugs to treat post-stroke injury in the 90's and the 2000's ultimately proved to be similarly unfruitful from a clinical perspective.[11,12] Given the track record, a critical question must be asked: How will this attempt be different? I hope I have been able to convey the importance of our systematic approach to designing RTAs and its basis in sound physical organic chemistry rationale. Taking the same principles which elevates phenol to α-Toc, we have applied them to aromatic amines to essentially find a perfect RTA scaffold with PNX. But these are not merely slightly faster mimics of vitamin E. Indeed, an exciting feature unique to the aromatic amines (particularly PNX) is their ability to use superoxide/hydroperoxyl, which are normally purveyors of oxidation, as *reductants* for synergistic trapping of lipidperoxyls.[2] It has also been suggested for Fer-1, another aminic RTA/ferroptosis inhibitor, that it can be regenerated by metal ions in their reduced state, deactivating an initiation catalyst while promoting further inhibition.[13] Perhaps it is an ability to

catalytically hit multiple parts of the radical-mediated oxidation in a stressed cell which underlies the excellent potency of these compounds over some phenolic based RTAs.

Scheme 4.3 – Potential Pathways for Inhibiting Ferroptosis in Addition to Trapping LOO•.



The fruits of our systematic approach are quite evident when we draw direct comparisons to past attempts by the pharmaceutical industry. One of the only novel antioxidant-based drugs currently used in clinical practice is Edaravone which was initially approved for post-ischemic stroke recovery (in Japan)[14] but was subsequently approved for ALS as it showed a marginal positive effect in early-stages of the disease (though failing phase III trials with patients off all stages).[15] Both of these conditions have since been associated with ferroptosis.[16,17] By our own measurements, Edaravone performs rather abysmally in both kinetic assays and ferroptosis rescue (Fig. 4.6), but it is technically both an RTA and ferroptosis inhibitor.[18] Assuming that the principal mechanism of action is its RTA-activity, think of how much could be accomplished with a pharmacologically optimized derivative of PNX! Indeed, with the rapid growth of ferroptosis research in the one hand and a more robust understanding of RTA activity in the other, I would hazard (to borrow from an earlier analogy) that we are now in the right neighbourhood, perhaps even on the right street, all that remains is canvasing door-to-door until we find the right address.

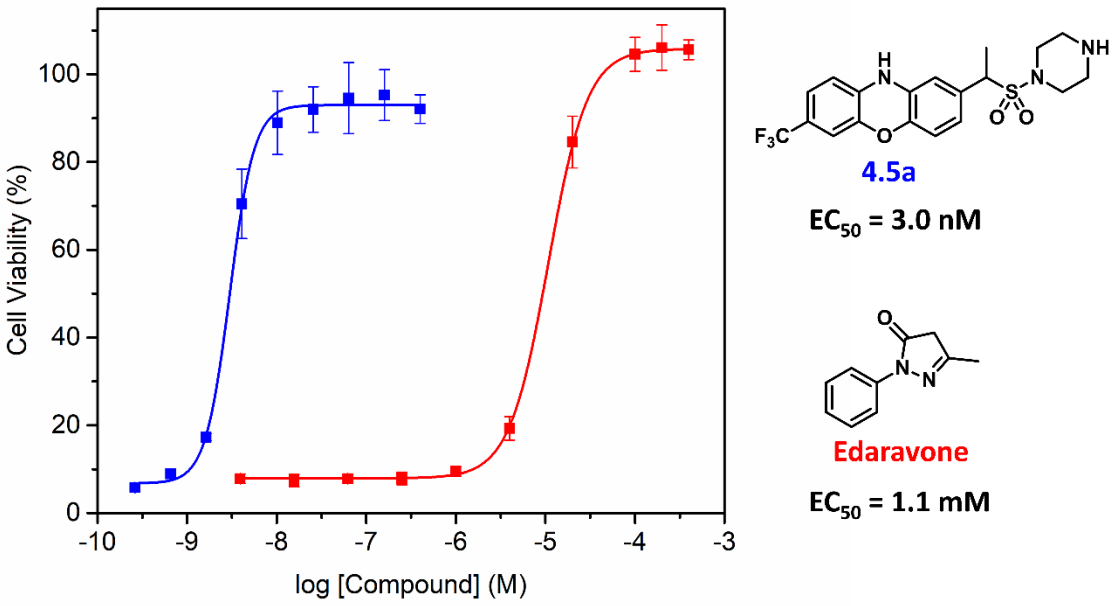


Figure 4.6. Potency of Edaravone and **4.5a** in the RSL3-induced pfa-1 ferroptosis rescue assay.

4.5 References

(1) Farmer, L. A.; Wu, Z.; Poon, J.-F.; Zilka, O.; Lorenz, S. M.; Huehn, S.; Proneth, B.; Conrad, M.; Pratt, D. A. Intrinsic and Extrinsic Limitations to the Design and Optimization of Inhibitors of Lipid Peroxidation and Associated Cell Death. *J. Am. Chem. Soc.* **2022**, *144* (32), 14706–14721. https://doi.org/10.1021/jacs.2c05252.

(2) Poon, J.-F.; Zilka, O.; Pratt, D. A. Potent Ferroptosis Inhibitors Can Catalyze the Cross-Dismutation of Phospholipid-Derived Peroxyl Radicals and Hydroperoxyl Radicals. *J. Am. Chem. Soc.* **2020**, *142* (33), 14331–14342. https://doi.org/10.1021/jacs.0c06379.

(3) Chen, M.; Borlak, J.; Tong, W. High Lipophilicity and High Daily Dose of Oral Medications Are Associated with Significant Risk for Drug-Induced Liver Injury. *Hepatology* **2013**, *58* (1), 388–396.

(4) Yang, W.; Liu, X.; Song, C.; Ji, S.; Yang, J.; Liu, Y.; You, J.; Zhang, J.; Huang, S.; Cheng, W.; Shao, Z.; Li, L.; Yang, S. Structure-Activity Relationship Studies of Phenothiazine Derivatives as a New Class of Ferroptosis Inhibitors Together with the Therapeutic Effect in an Ischemic Stroke Model. *Eur. J. Med. Chem.* **2021**, *209*, 112842.

(5) Tsai, A. S.; Curto, J. M.; Rocke, B. N.; Dechert-Schmitt, A.-M. R.; Ingle, G. K.; Mascitti, V. One-Step Synthesis of Sulfonamides from N-Tosylhydrazones. *Org. Lett.* **2016**, *18* (3), 508–511. https://doi.org/10.1021/acs.orglett.5b03545.

(6) The log*P* from ACD/ChemSketch 2020 (v. 14.50) only accounts for the partitioning of the neutral amine. The distribution coefficient (log*D*), which accounts for the partitioning of the ammonium and the acid-base equilibrium of amine vs. ammonium, would certainly be lower.

(7) Farmer, L. A.; Haidasz, E. A.; Griesser, M.; Pratt, D. A. Phenoxazine: A Privileged Scaffold for Radical-Trapping Antioxidants. *J. Org. Chem.* **2017**, *82* (19), 10523–10536. https://doi.org/10.1021/acs.joc.7b02025.

(8) The amino group in the 2-position is highly activated and would readily react with peroxyl radicals, fundamentally changing the nature of the RTA intermediate(s).

(9) Cynshi, O.; Tamura, K.; Niki, E. Design, Synthesis, and Action of Antiatherogenic Antioxidants BT - Free Radicals and Antioxidant Protocols; Uppu, R. M., Murthy, S. N., Pryor, W. A., Parinandi, N. L., Eds.; Humana Press: Totowa, NJ, 2010; pp 91–107. https://doi.org/10.1007/978-1-60327-029-8_6.

(10) Steinberg, D.; Witztum, J. L. Is the Oxidative Modification Hypothesis Relevant to Human Atherosclerosis? *Circulation* **2002**, *105* (17), 2107–2111. https://doi.org/10.1161/01.CIR.0000014762.06201.06.

(11) Shirley, R.; Ord, E. N. J.; Work, L. M. Oxidative Stress and the Use of Antioxidants in Stroke. *Antioxidants*. 2014, pp 472–501. https://doi.org/10.3390/antiox3030472.

(12) Margaill, I.; Plotkine, M.; Lerouet, D. Antioxidant Strategies in the Treatment of Stroke. *Free Radic. Biol. Med.* **2005**, *39* (4), 429–443.

(13) Miotto, G.; Rossetto, M.; Di Paolo, M. L.; Orian, L.; Venerando, R.; Roveri, A.; Vučković, A.-M.; Bosello Travain, V.; Zaccarin, M.; Zennaro, L.; Maiorino, M.; Toppo,

S.; Ursini, F.; Cozza, G. Insight into the Mechanism of Ferroptosis Inhibition by Ferrostatin-1. *Redox Biol.* **2020**, *28*, 101328.

(14) Miyaji, Y.; Yoshimura, S.; Sakai, N.; Yamagami, H.; Egashira, Y.; Shirakawa, M.; Uchida, K.; Kageyama, H.; Tomogane, Y. Effect of Edaravone on Favorable Outcome in Patients with Acute Cerebral Large Vessel Occlusion: Subanalysis of RESCUE-Japan Registry. *Neurol. Med. Chir. (Tokyo).* **2015**, *55* (3), 241–247. https://doi.org/10.2176/nmc.ra.2014-0219.

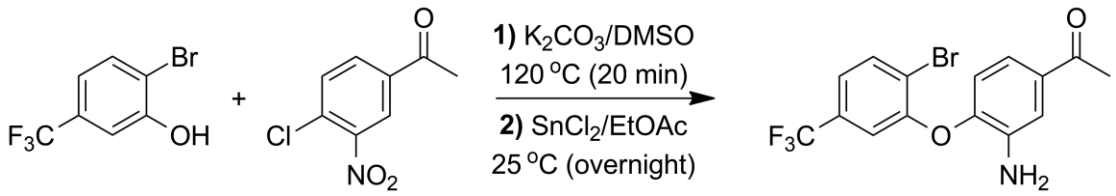
(15) Petrov, D.; Mansfield, C.; Moussy, A.; Hermine, O. ALS Clinical Trials Review: 20 Years of Failure. Are We Any Closer to Registering a New Treatment? *Frontiers in Aging Neuroscience*. **2017**, *9*. https://doi.org/10.3389/fnagi.2017.00068.

(16) Zhang, Y.; Lu, X.; Tai, B.; Li, W.; Li, T. Ferroptosis and Its Multifaceted Roles in Cerebral Stroke. *Frontiers in Cellular Neuroscience*. **2021**, *15*, https://doi.org/10.3389/fncel.2021.615372.

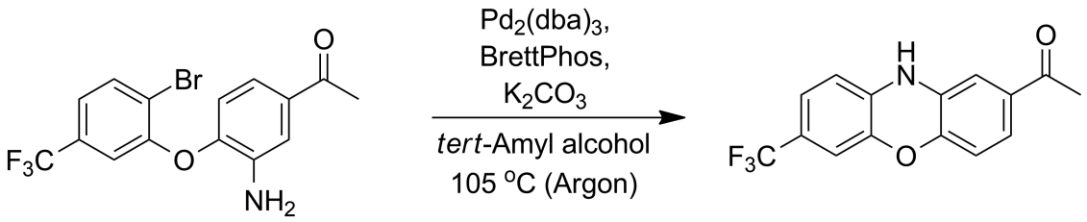
(17) Wang, T.; Tomas, D.; Perera, N. D.; Cuic, B.; Luikinga, S.; Viden, A.; Barton, S. K.; McLean, C. A.; Samson, A. L.; Southon, A.; Bush, A. I.; Murphy, J. M.; Turner, B. J. Ferroptosis Mediates Selective Motor Neuron Death in Amyotrophic Lateral Sclerosis. *Cell Death Differ.* **2022**, *29* (6), 1187–1198. https://doi.org/10.1038/s41418-021-00910-z.

(18) The Edaravone data is from unpublished work (courtesy of Dr. Zijun Wu).

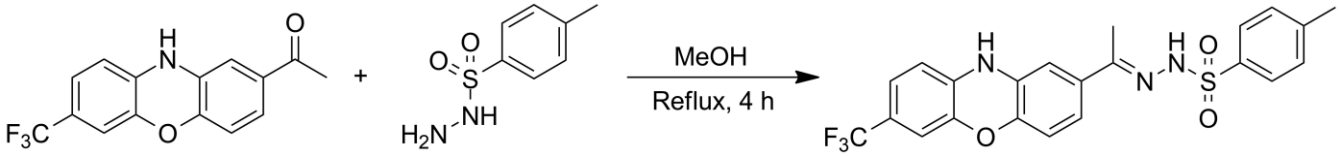
4.6 Synthesis



1-(3-amino-4-(2-bromo-5-(trifluoromethyl)phenoxy)phenyl)ethanone. In a round bottom flask with a magnetic stir bar were combined 2-bromo-5-trifluoromethylphenol (6.02 g, 25 mmol), 4-chloro-3-nitroacetophenone (5.00 g, 25 mmol), DMSO (25 mL) and potassium carbonate (6.90 g, 50 mmol). With rapid stirring the reaction was heated to 120 °C for 20 minutes (or sooner if CO_2 evolution ceases. Even leaving it for ~1 h under these conditions will reduce the yield by more than half as this intermediate product is unstable under these conditions.) The reaction was cooled to room temperature and poured into 150 mL 1 M HCl and extracted with ~120 mL of ethyl acetate. The organic layer was subsequently washed with 100 mL 1 M HCl, and the water saturated organic layer was transferred to a 250 mL round bottom flask containing tin chloride (23.7 g, 125 mmol). The reaction was stirred at room temperature overnight (or until the intermediate product was consumed), after which the reaction was poured into a 1 L Erlenmeyer with 300 mL of saturated $NaHCO_3$ solution with stirring. The organic layer was washed several times with distilled water and the initial aqueous phase was extracted several times with ethyl acetate (gently to minimize emulsion.) The organic portions were combined, dried with $MgSO_4$, filtered then the solvent removed under reduced pressure. The resulting residue was purified by flash chromatography (25% ethyl acetate in hexanes). The fractions containing the product were combined and reduced to ~10% of the total volume, and addition of hexanes at ~3 times that volume promoted crystallization of the title product on standing. The decanted and dried product appeared as vanilla-coloured needles (6.56 g, 70.1 %); mp = 125-128 °C. ^{1}H NMR (400 MHz; DMSO-d6): 7.99 (d, J = 8.3 Hz, 1H), 7.48-7.44 (m, 2H), 7.18 (dd, J = 8.3, 2.2 Hz, 1H), 7.11 (d, J = 2.0 Hz, 1H), 6.76 (d, J = 8.3 Hz, 1H), 5.39 (br, 2H), 2.49 (s, 3H). ^{13}C NMR (101 MHz; DMSO-d6): δ 197.1, 153.5, 145.0, 139.9, 135.0, 134.1, 129.7 (q, J = 32.6 Hz), 123.4 (q, J = 272.5 Hz), 121.6 (q, J = 3.7 Hz), 118.2, 117.3, 115.2, 115.1 (q, J = 3.3 Hz), 26.6. ^{19}F NMR (376 MHz; DMSO-d6): δ -61.6. HRMS (EI, magnetic sector): calcd for $C_{15}H_{11}BrF_3NO_2$ 372.99253, found 372.99394.

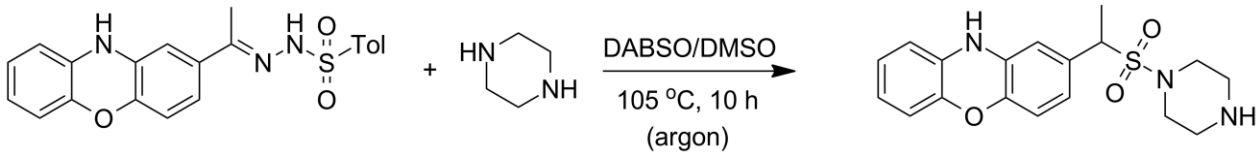


2-acetyl-7-trifluoromethylphenoxazine (4.2a). In a Schlenk tube backfilled with argon were added *tert*-amyl alcohol (28 mL), $Pd_2(dba)_3$ (33 mg, 36 μmol) and BrettPhos (40 mg, 74 μmol). Stirring under a continuous flow of argon, the mixture was sparged with argon for ~10 min To the tube were then added K_2CO_3 (4.26 g, 30.8 mmol) and 1-(3-amino-4-(2-bromo-5-(trifluoromethyl)phenoxy)phenyl)ethanone (5.23 g, 14 mmol). The sealed Schlenk tube was heated to 105 °C for 2 h, the product precipitating as yellow needles. After cooling, the mixture was poured over a silica plug and the product was washed through using hot acetone. The filtrate was reduced to ~15 mL under reduced pressure and ~100 mL diethyl ether was added and the flask was allowed to stand for ~1 h covered. The product was filtered and rinsed with diethyl ether then hexanes. The product, 2-acetyl-7-trifluoromethylphenoxazine (**4.2a**), appeared as bright yellow needles (3.27 g, 79.7%); mp = 275 °C (decomp.) ^{1}H NMR (400 MHz; DMSO-d6): 8.94 (br, 1H), 7.30 (dd, *J* = 8.2, 2.1 Hz, 1H), 7.10 (dd, *J* = 8.2, 1.2 Hz, 1H), 6.98 (d, *J* = 2.1 Hz, 1H), 6.90 (d, *J* = 1.8 Hz, 1H), 6.71 (d, *J* = 8.2 Hz, 1H), 6.54 (d, *J* = 8.1 Hz, 1H), 2.44 (s, 3H). ^{13}C NMR (101 MHz; DMSO-d6): δ 196.0, 146.6, 142.2, 135.6, 133.3, 131.3, 124.0 (q, *J* = 270.7 Hz), 123.3, 122.2 (q, *J* = 4.4 Hz), 120.5 (q, *J* = 33.0 Hz), 115.0, 113.2, 112.4, 112.0 (q, *J* = 3.7 Hz), 26.3. ^{19}F NMR (376 MHz; DMSO-d6): δ -60.8. HRMS (EI, magnetic sector): calcd for $C_{15}H_{10}F_3NO_2$ 293.06636, found 293.06348.

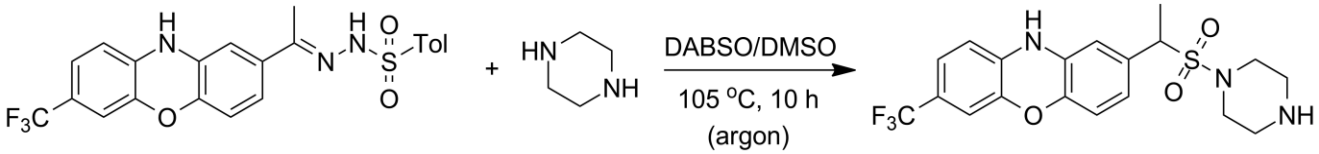


(*E*)-4-methyl-*N*'-(1-(7-(trifluoromethyl)-10*H*-phenoxazin-2-yl)ethylidene)benzenesulfonohydrazide (4.3a). In a round bottom flask were added 2-acetyl-7-trifluoromethylphenoxazine (1.17 g, 4.0 mmol), 4-methylbenzenesulfonohydrazide (0.90 g, 4.8 mmol) and MeOH (40 mL). The suspension was refluxed with stirring for 4 h affording the

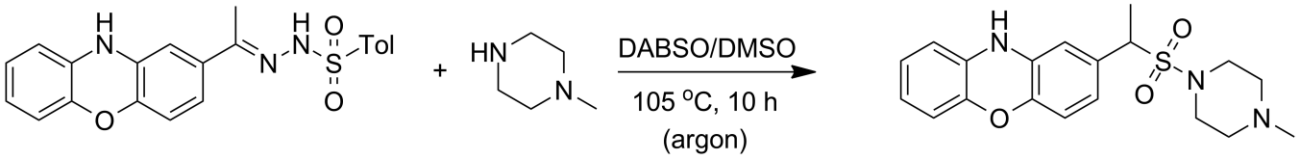
product as a white precipitate which was filtered and rinsed with methanol, diethyl ether and hexanes (1.51 g, 81.8%). mp = 235 °C (decomp.) ^{1}H NMR (400 MHz; DMSO-d6): δ 10.43 (br, 1H), 8.89 (br, 1H), 7.80 (d, *J* = 8.2 Hz, 2H), 7.41 (d, *J* = 8.0 Hz, 2H), 7.08 (d, *J* = 8.2 Hz, 1H), 6.89-6.87 (m, 3H), 6.62-6.60 (m, 1H), 6.55 (d, *J* = 8.2 Hz, 1H), 2.38 (s, 3H), 2.05 (s, 3H). ^{13}C NMR (101 MHz; DMSO-d6): δ 151.9, 143.7, 143.3, 142.5, 136.3, 135.8, 133.5, 130.8, 129.5, 127.5, 124.1 (q, *J* = 270.3 Hz), 121.8 (q, *J* = 4.4 Hz), 120.3 (q, *J* = 32.6 Hz), 119.9, 114.8, 113.0, 111.8 (q, *J* = 3.7 Hz), 110.4, 21.0, 13.8. ^{19}F NMR (376 MHz; DMSO-d6): δ -60.7. HRMS (EI, magnetic sector): calcd for $C_{22}H_{18}F_3N_3O_3S$ 461.10210, found 461.10473.



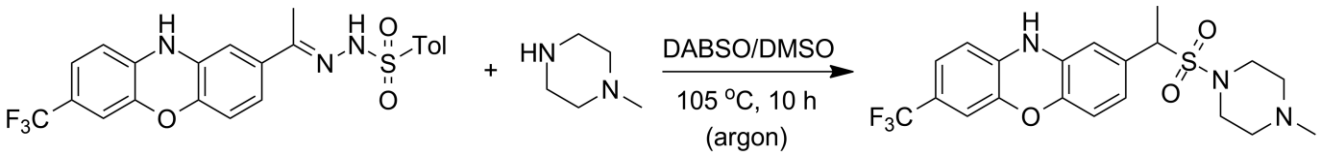
2-(1-(piperazin-1-ylsulfonyl)ethyl)-10H-phenoxazine (4.5b). Into a 10 mL sealable tube equipped with a stir bar were added (*E*)-*N*'-(1-(10*H*-phenoxazin-2-yl)ethylidene)-4-methylbenzenesulfonohydrazide (**4.3b**) (263 mg, 0.67 mmol), piperazine (346 mg, 4.02 mmol) and 6 mL of DMSO. While stirring, the mixture was continuously sparged with a steady stream of argon for 10 min after which DABSO (90 mg, 0.37 mmol) was added and the vessel was sealed. The tube was heated to 105 °C and was allowed to stir for 10 h. After cooling, the reaction mixture was poured into saturated $NaHCO_3$ solution which was subsequently extracted with ethyl acetate. The organic layer was dried with $MgSO_4$, filtered, then the solvent removed under reduced pressure. The product was isolated by flash chromatography (gradient of 100:0 to 98:2 DCM/MeOH) rendering 2-(1-(piperazin-1-ylsulfonyl)ethyl)-10H-phenoxazine (**4.5b**) as a white solid (185 mg, 73%). ^{1}H NMR (400 MHz; DMSO-d6): δ 8.33 (br, 1H), 6.74-6.70 (m, 1H), 6.65-6.54 (m, 5H), 6.45-6.42 (m, 1H), 4.34 (q, *J* = 7.1 Hz, 1H), 3.33 (br, 1H), 3.02-2.96 (m, 2H), 2.86-2.82 (m, 2H), 2.63-2.54 (m, 4H), 1.49 (d, *J* = 7.1 Hz, 3H). ^{13}C NMR (101 MHz; DMSO-d6): δ 142.9, 142.6, 132.3, 132.0, 130.9, 124.1, 121.3, 120.5, 115.1, 114.7, 113.5, 113.3, 60.0, 46.7, 45.5, 16.1. HRMS (EI, magnetic sector): calcd for $C_{18}H_{21}N_3O_3S$ 359.13036, found 359.13301.



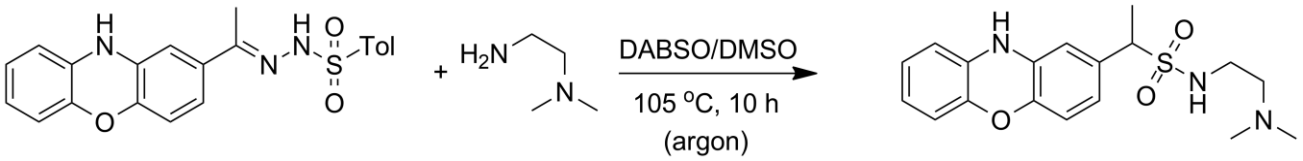
2-(1-(piperazin-1-ylsulfonyl)ethyl)-7-(trifluoromethyl)-10H-phenoxazine (4.5a). Synthesis was carried out in an analogous fashion to **(4.5b)** using (*E*)-4-methyl-*N*'-(1-(7-(trifluoromethyl)-10*H*-phenoxazin-2-yl)ethylidene)benzenesulfonohydrazide (**4.3a**). The product was purified by column chromatography (gradient of 100:0 to 98:2 DCM/MeOH) to afford the product as a white solid (204 mg, 73%). ^{1}H NMR (400 MHz; DMSO-d6): δ 8.87 (br, 1H), 7.07 (dd, *J* = 8.2, 0.9 Hz, 1H), 6.87 (d, *J* = 1.6 Hz, 1H), 6.71 (dd, *J* = 8.2, 2.0 Hz, 1H), 6.63 (d, *J* = 8.1 Hz, 1H), 6.58 (d, *J* = 1.9 Hz, 1H), 6.54 (d, *J* = 8.1 Hz, 1H), 4.37 (q, *J* = 7.1 Hz, 1H), 3.29 (br, 1H), 3.02-2.97 (m, 2H), 2.87-2.83 (m, 2H), 2.64-2.54 (m, 4H), 1.50 (d, *J* = 7.1 Hz, 3H). ^{13}C NMR (101 MHz; DMSO-d6): δ 142.6, 142.5, 136.0, 131.5, 130.9, 124.1 (q, *J* = 270.7 Hz), 122.3, 121.7 (q, *J* = 4.0 Hz), 120.4 (q, *J* = 32.3 Hz), 114.9, 113.9, 113.1, 111.8 (q, *J* = 3.7 Hz), 59.9, 46.6, 45.5, 16.0. ^{19}F NMR (376 MHz; DMSO-d6): δ -60.7. HRMS (EI, magnetic sector): calcd for $C_{19}H_{20}F_3N_3O_3S$ 427.11775, found 427.11607.



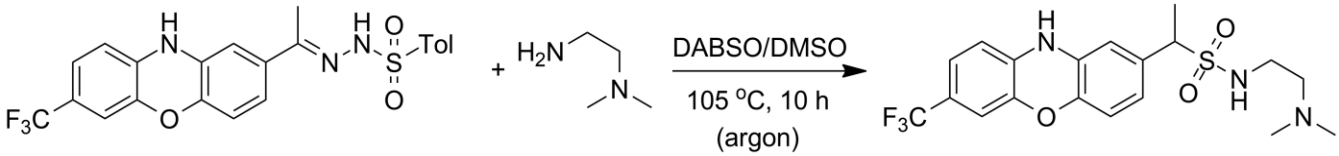
2-(1-((4-methylpiperazin-1-yl)sulfonyl)ethyl)-10H-phenoxazine (4.6b). Synthesis was carried out in an analogous fashion to **(4.5b)** using 1-methylpiperazine as the aminic nucleophile. The product was purified by column chromatography (gradient of 100:0 to 98:2 DCM/MeOH) to afford the product as a white solid (400 mg, 70%). ^{1}H NMR (400 MHz; DMSO-d6): δ 8.33 (br, 1H), 6.75-6.70 (m, 1H), 6.65-6.54 (m, 5H), 6.44 (dd, *J* = 7.7, 1.3 Hz, 1H), 4.36 (q, *J* = 7.1 Hz, 1H), 3.09-3.04 (m, 2H), 2.93-2.87 (m, 2H), 2.25-2.17 (m, 4H), 2.12 (s, 1H), 1.50 (d, *J* = 7.1 Hz, 3H). ^{13}C NMR (101 MHz; DMSO-d6): δ 142.9, 142.6, 132.3, 132.0, 130.8, 124.1, 121.3, 120.5, 115.1, 114.8, 113.5, 113.4, 60.2, 54.4, 45.5(3), 45.4(6), 16.0. (EI, magnetic sector): calcd for $C_{19}H_{23}N_3O_3S$ 373.14601, found 373.15108.



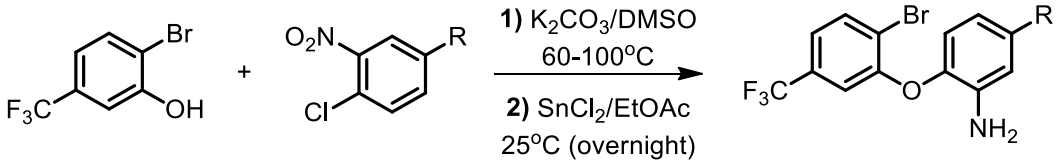
2-(1-((4-methylpiperazin-1-yl)sulfonyl)ethyl)-7-(trifluoromethyl)-10H-phenoxazine (4.6a). Synthesis was carried out in an analogous fashion to **(4.5a)** using 1-methylpiperazine as the aminic nucleophile. The product was purified by column chromatography (gradient of 100:0 to 98:2 DCM/MeOH) to afford the product as a white solid (210 mg, 63%). ^{1}H NMR (400 MHz; DMSO-d6): δ 8.86 (br, 1H), 7.08-7.06 (m, 1H), 6.87 (d, *J* = 1.9 Hz, 1H), 6.71 (dd, *J* = 8.2, 2.0 Hz, 1H), 6.63 (d, *J* = 8.2 Hz, 1H), 6.58 (d, *J* = 2.0 Hz, 1H), 6.54 (d, *J* = 8.1 Hz, 1H), 4.40 (q, *J* = 7.1 Hz, 1H), 3.10-3.04 (m, 2H), 2.92-2.89 (m, 2H), 2.25-2.17 (m, 4H), 2.12 (s, 3H), 1.50 (d, *J* = 7.1 Hz, 3H). ^{13}C NMR (101 MHz; DMSO-d6): δ 142.6(4), 142.5(5), 135.9, 131.4, 130.9, 124.1 (q, *J* = 270.7), 122.3, 121.7 (q, *J* = 4.0 Hz), 120.4 (q, *J* = 32.6 Hz), 115.0, 114.0, 113.1, 111.8 (q, *J* = 4.0 Hz), 60.1, 54.4, 45.5(4), 45.4(6), 15.9. ^{19}F NMR (376 MHz; DMSO-d6): δ -60.7. (EI, magnetic sector): calcd for $C_{20}H_{22}F_3N_3O_3S$ 441.13340, found 441.13243.



N-(2-(dimethylamino)ethyl)-1-(10H-phenoxazin-2-yl)ethanesulfonamide (4.4b). Synthesis was carried out in an analogous fashion to **(4.5b)** using *N*,*N*-dimethylethylenediamine as the aminic nucleophile. The product was purified by column chromatography (gradient of 100:0 to 98:2 DCM/MeOH) to afford the product as an off-white solid (120 mg, 49%). ^{1}H NMR (400 MHz; DMSO-d6): δ 8.29 (br, 1H), 6.91 (t, *J* = 5.3 Hz, 1H) 6.74-6.70 (m, 1H), 6.61-6.52 (m, 5H), 6.44 (dd, *J* = 7.7, 1.4 Hz, 1H), 4.24 (q, *J* = 7.1 Hz, 1H), 2.91-2.82 (m, 2H), 2.26 (t, *J* = 6.9 Hz, 2H), 2.13 (s, 6H), 1.50 (d, *J* = 7.1 Hz, 3H). ^{13}C NMR (101 MHz; DMSO-d6): δ 142.6(9), 142.6(3), 132.1(8), 132.1(7), 131.3, 124.0, 121.3, 120.4, 115.1, 114.6, 113.7, 113.3, 60.6, 59.0, 45.0, 40.8, 15.8. (EI, magnetic sector): calcd for $C_{18}H_{23}N_3O_3S$ 361.14601, found 361.14858.

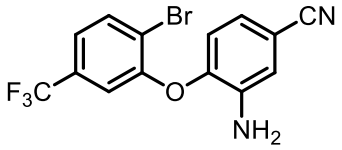


N-(2-(dimethylamino)ethyl)-1-(7-(trifluoromethyl)-10H-phenoxazin-2-yl)ethanesulfonamide (4.4a). Synthesis was carried out in an analogous fashion to **(4.5a)** using *N*,*N*-dimethylethylenediamine as the aminic nucleophile. The product was purified by column chromatography (gradient of 100:0 to 98:2 DCM/MeOH) to afford the product as a white solid (148 mg, 45%). ^{1}H NMR (400 MHz; DMSO-d6): δ 8.83 (br, 1H), 7.07 (d, *J* = 8.1 Hz, 1H), 6.94 (br, 1H), 6.87 (br, 1H), 6.67 (dd, *J* = 8.3, 2.0 Hz, 1H), 6.61 (d, *J* = 8.1 Hz, 1H), 6.55-6.53 (m, 2H), 4.27 (q, *J* = 7.1 Hz, 1H), 2.88 (br, 2H), 2.25 (t, *J* = 6.9 Hz, 2H), 2.12 (s, 6H), 1.50 (d, *J* = 7.1 Hz, 3H). ^{13}C NMR (101 MHz; DMSO-d6): δ 142.7, 142.3, 136.1, 131.9, 130.8, 124.1 (q, *J* = 270.7 Hz), 122.4, 121.6 (q, *J* = 3.7 Hz), 120.3 (q, *J* = 32.7 Hz), 114.8, 114.1, 113.0, 111.8 (q, *J* = 4.0 Hz), 60.5, 59.0, 45.1, 40.9, 15.8. ^{19}F NMR (376 MHz; DMSO-d6): δ -60.7. (EI, magnetic sector): calcd for $C_{19}H_{22}F_3N_3O_3S$ 429.13340, found 429.13419.

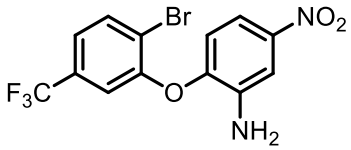


Preparation of 2-(2-Bromophenoxy)aniline Intermediates. A general 2-step procedure for the preparation of 2-(2-bromophenoxy)aniline derivatives, intermediates to the preparation of **4.7-4.11**, is given. In a round bottom flask equipped with a stir bar were combined 2-bromo-5-trifluoromethylphenol (1 eq.), K_2CO_3 (2 eq.) and DMSO (0.5 M with respect to the phenol). This mixture was heated with stirring to reach the target temperature for the reaction (60-100 °C, depending on the substitution partner), after which the 2-chloronitrobenzene derivative was added (1 eq.). The temperature was maintained until complete conversion was observed, after which the reaction was cooled to room temperature and poured into approx. 6 times the volume of water. This was extracted with ethyl acetate, and the organic layer was washed with water, then 1 M HCl. The organic layer was drawn-off into a round bottom flask with a stir bar and 5 eq. of anhydrous $SnCl_2$ (with respect to the phenol) was added and stirred at room temperature overnight. After confirming that the reduction was successful, the reaction mixture was poured

into a 1 L Erlenmeyer flask containing saturated $NaHCO_3$ solution. The flask was swirled (not shaken, in order to minimize emulsions of Sn(OH)Cl in the organic phase), and the organic phase was carefully decanted into a separatory funnel. More ethyl acetate was added to the Erlenmeyer flask and the process was repeated until the product appeared only faintly on TLC. The combined organics are rinsed, then dried with $MgSO_4$, then filtered. This residue was either purified via silica gel chromatography to isolate the aniline product, or when applicable it was dissolved in acetic anhydride overnight and the acetamide was isolated instead.

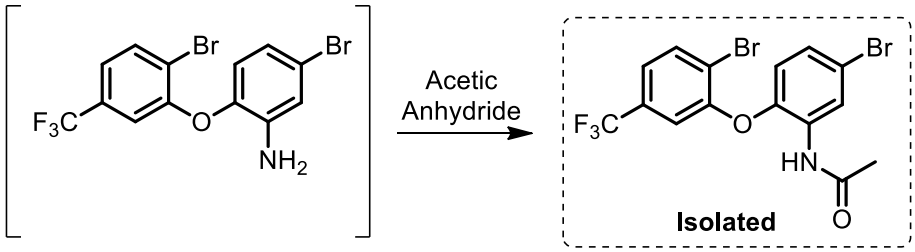


3-Amino-4-(2-bromo-5-(trifluoromethyl)phenoxy)benzonitrile. This synthesis was carried out at a 14 mmol scale, using 4-chloro-3-nitrobenzonitrile as the electrophile. The substitution step was run at 100 °C for approximately 50 min The isolated yield of title product was 66% appearing as a white solid; mp = 145-147 °C. ^{1}H NMR (400 MHz; DMSO-d6): δ 8.01 (d, *J* = 8.3 Hz, 1H), 7.52 (dd, *J* = 2.2, 8.3 Hz, 1H), 7.26 (d, *J* = 2.0 Hz, 1H), 7.14 (d, *J* = 2.1 Hz, 1H), 6.93 (dd, *J* = 2.1, 8.2 Hz, 1H), 6.74 (d, *J* = 8.2 Hz, 1H), 5.66 (br, 2H). ^{13}C NMR (101 MHz; DMSO-d6): δ 152.8, 145.2, 140.6, 135.1, 129.9 (q, *J* = 32.6 Hz), 123.3 (q, *J* = 272.5 Hz), 122.3 (q, *J* = 4.0 Hz), 120.2, 119.3, 118.8, 118.3, 117.9, 116.4 (q, *J* = 4.0 Hz), 107.3. ^{19}F NMR (376 MHz; DMSO-d6): δ -61.6. (EI, magnetic sector): calcd for $C_{14}H_8BrF_3N_2O$ 335.97721, found 335.97707.

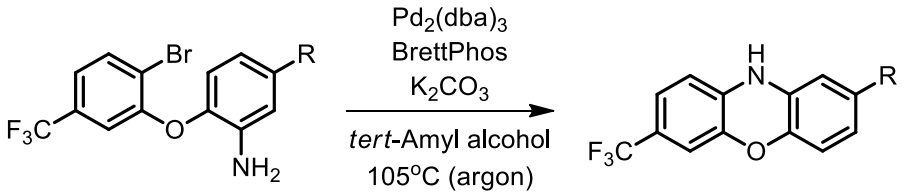


2-(2-Bromo-5-(trifluoromethyl)phenoxy)-5-nitroaniline. This synthesis was carried out at a 10 mmol scale, using 1-chloro-2,4-dinitrobenzene as the electrophile. The substitution step was run at 60 °C for approximately 30 min The isolated yield of title product was 44% appearing as a yellow crystalline solid; mp = 89-91 °C. ^{1}H NMR (400 MHz; DMSO-d6): δ 8.04 (d, *J* = 8.3 Hz, 1H), 7.68 (d, *J* = 2.7 Hz, 1H), 7.56 (dd, *J* = 1.1, 8.3 Hz, 1H), 7.41 (d, *J* = 1.6 Hz, 1H), 7.37 (dd, *J* = 2.8, 8.8 Hz, 1H), 6.72 (d, *J* = 8.8 Hz, 1H), 5.86 (br, 2H). ^{13}C NMR (101 MHz; DMSO-d6): δ

152.6, 146.9, 144.2, 140.3, 135.2, 130.0 (q, *J* = 32.7 Hz), 123.3 (q, *J* = 272.5 Hz), 122.8 (q, *J* = 3.7 Hz), 119.2, 117.3 (q, *J* = 3.7 Hz), 116.8, 111.4, 109.2. ^{19}F NMR (376 MHz; DMSO-d6): δ -61.6.

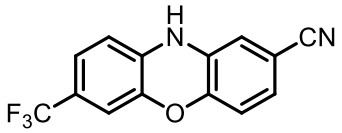


***N*-(5-Bromo-2-(2-bromo-5-(trifluoromethyl)phenoxy)phenyl)acetamide.** This synthesis was carried out at a 14 mmol scale, using 2-chloro-5-bromonitrobenzene as the electrophile. The substitution step was run at 100 °C for approximately 10 h. The aniline product was not isolated, instead the crude residue was dissolved in neat acetic anhydride to make the corresponding acetamide. The title product was isolated by chromatography and was subsequently recrystallized from ethanol appearing as white crystals with a final yield of 76%; mp = 123-125 °C. ^{1}H NMR (400 MHz; DMSO-d6): δ 9.75 (s, 1H), 8.30 (d, *J* = 2.1 Hz, 1H), 7.68 (d, *J* = 8.2 Hz, 1H), 7.54 (dd, *J* = 1.6, 8.3 Hz, 1H), 7.37 (d, 1.7 Hz, 1H), 7.25 (dd, 2,5, 8.7 Hz, 1H), 6.74 (d, 8.7 Hz, 1H), 2.09 (s, 3H).). ^{13}C NMR (101 MHz; DMSO-d6): δ 169.2, 153.2, 145.8, 135.1, 131.0, 129.9 (q, *J* = 32.7 Hz), 127.2, 125.6, 123.3 (q, *J* = 272.5 Hz), 122.5 (q, *J* = 3.7 Hz), 119.2(5), 119.1(5), 117.5 (q, *J* = 3.3 Hz), 115.6, 23.7. ^{19}F NMR (376 MHz; DMSO-d6): δ -61.2. (EI, magnetic sector): calcd for $C_{15}H_{10}Br_2F_3NO_2$ 450.90304, found 450.90456.

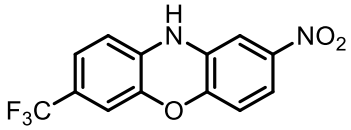


Preparation of Phenoxazines by Buchwald-Hartwig Amination. A general procedure for the preparation of phenoxazines by intramolecular coupling of 2-(2-bromophenoxy)anilines is given. In a Schlenk tube backfilled with argon were added *tert*-amyl alcohol or toluene (0.5 M with respect to the aniline), $Pd_2(dba)_3$ (0.005 eq.) and BrettPhos (0.01 eq.). Stirring under a continuous flow of argon, the mixture was sparged with argon for ~10 min To the tube were then added

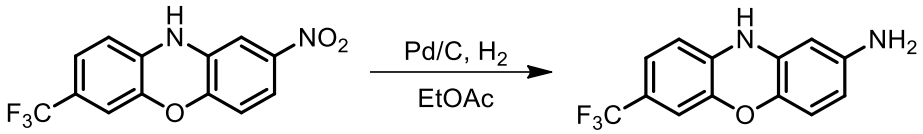
K_2CO_3 (2.2 eq.) and the aniline (1 eq.). The sealed Schlenk tube was heated to 105 ºC and the reaction was closely monitored by TLC (usually done within 2 h). After cooling to room temperature, the reaction mixture was diluted in DCM and evaporated over silica. The products are then purified/isolated by column chromatography.



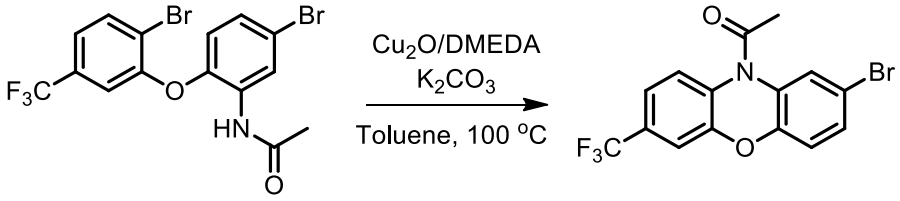
2-Cyano-7-trifluoromethylphenoxazine (4.7). The reaction was only run for ~1 h with 3-amino-4-(2-bromo-5-(trifluoromethyl)phenoxy)benzonitrile (1.834 g, 5.1 mmol) using toluene as the solvent. In a previous attempt it was observed that leaving the reaction for too long led to formation of a deep red by-product that would coelute when attempting chromatography. Isolation of the title product (0.64 g, 2.3 mmol) afforded white crystals. Accounting for the recovered starting material (1.54 mmol) we calculated a converted yield of 64%; mp = 224-227 °C. ^{1}H NMR (400 MHz; DMSO-d6): δ 9.05 (br, 1H), 7.11-7.07 (m, 2H), 6.90 (d, *J* = 1.7 Hz, 1H), 6.74-6.72 (m, 2H), 6.57 (d, *J* = 8.2 Hz, 1H). ^{13}C NMR (101 MHz; DMSO-d6): δ 146.4, 142.2, 135.0, 132.4, 126.5, 123.9 (q, *J* = 270.7 Hz), 122.3 (q, *J* = 4.4 Hz), 121.0 (q, *J* = 32.6 Hz), 118.5, 116.1, 115.8, 113.5, 112.1 (q, *J* = 3.7 Hz), 106.7. ^{19}F NMR (376 MHz; DMSO-d6): δ -61.6. (EI, magnetic sector): calcd for $C_{14}H_7F_3N_2O$ 276.05105, found 276.05180.



2-Nitro-7-trifluoromethylphenoxazine (4.8). The reaction run for ~3 h with 2-(2-bromo-5-(trifluoromethyl)phenoxy)-5-nitroaniline (3.55 g, 9.4 mmol) using *tert*-amyl alcohol as the solvent. Isolation of the title product (2.21 g, 7.5 mmol) afforded a dark red solid at a yield of 79%; mp = 265 °C (decomp.). ^{1}H NMR (400 MHz; DMSO-d6): δ 9.16 (br, 1H) 7.47 (d, *J* = 8.6 Hz, 1H), 7.17 (br, 1H), 7.09 (d, *J* = 8.0 Hz, 1H), 6.91 (br, 1H), 6.75 (d, *J* = 8.7 Hz, 1H), 6.53 (d, *J* = 8.0 Hz, 1H). ^{13}C NMR (101 MHz; DMSO-d6): δ 148.1, 143.8, 142.0, 134.6, 132.2, 123.9 (q, *J* = 270.7 Hz), 122.6 (br), 121.2 (q, *J* = 32.6 Hz), 117.7, 115.4, 113.5, 112.3 (br), 107.7. ^{19}F NMR (376 MHz; DMSO-d6): δ -61.0. (EI, magnetic sector): calcd for $C_{13}H_7F_3N_2O_3$ 296.04088, found 296.03920.

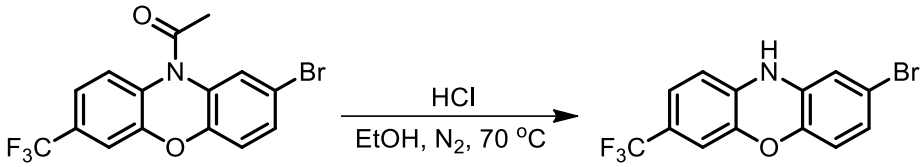


2-Amino-7-trifluoromethylphenoxazine (4.9). First, a flame dried Schlenk tube with a stir bar was evacuated and backfilled with argon. Under a continuous flow of argon, the tube was charged with ethyl acetate which was sparged with argon for 10 minutes. 2-Nitro-7-trifluoromethylphenoxazine (0.43 g, 1.44 mmol) and Pd/C (10 wt. %, 43 mg) were added and the tube sealed with a rubber septum. After evacuating the argon under vacuum, a H_2 filled balloon with a needle was placed through the septum and the reaction was stirred vigorously. On completion of the reduction, the Pd/C was filtered and the product was isolated/purified by column chromatography (60% ethyl acetate in hexanes). The fractions with the title product were concentrated to approximately 5-10 mL under reduced pressure, and addition of hexanes to this induced crystallization of the title product as white platelets (0.20 g, 52%); mp = 204-208 °C (decomp.). ^{1}H NMR (400 MHz; DMSO-d6): δ 8.51 (br, 1H), 7.01 (dd, *J* = 1.0, 8.3 Hz, 1H), 6.78 (d, *J* = 1.4 Hz, 1H), 6.51 (d, *J* = 8.1 Hz, 1H), 6.34 (d, *J* = 8.1 Hz, 1H), 5.84-5.80 (m, 2H), 4.78 (br, 2H). ^{13}C NMR (101 MHz; DMSO-d6): δ 145.4, 143.4, 136.3, 133.1, 130.8, 124.3 (q, *J* = 270.3 Hz), 120.7 (q, *J* = 4.0 Hz), 119.9 (q, *J* = 32.3 Hz), 115.4, 112.7, 111.3 (q, *J* = 4.0 Hz), 105.7, 99.9. (EI, magnetic sector): calcd for $C_{13}H_9F_3N_2O$ 266.06670, found 266.06648.



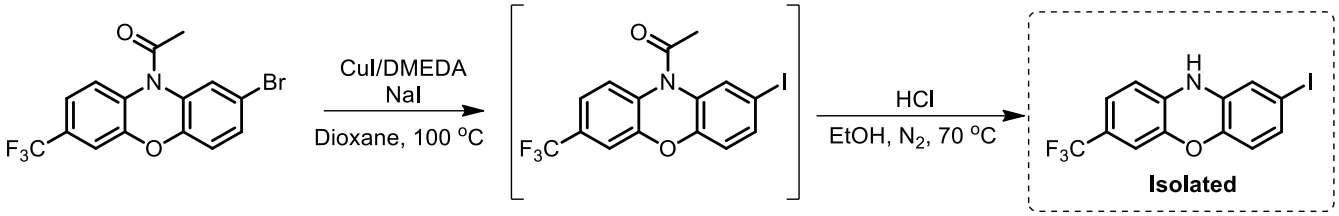
10-Acetyl-2-bromo-7-trifluoromethylphenoxazine. Into a 150-mL Teflon screw-cap sealable tube were combined copper(I) oxide (32 mg, 0.22 mmol), toluene (60 mL) and 1,2-dimethylethylenediamine (92 μL, 0.85 mmol) which were sparged with argon continuously while stirring rapidly on magnetic stir plate (approx. 10 min). The *N*-(5-Bromo-2-(2-bromo-5-(trifluoromethyl)phenoxy)phenyl)acetamide starting material (3.85 g, 8.5 mmol) and 2 equivalents of K_2CO_3 (2.4 g, 17 mmol) were added after which the vessel was sealed. The vessel was heated on an oil bath to ~110 °C which was maintained for 16 h. After cooling, the reaction mixture was filtered and these vessel and filter paper were successively rinsed with ethyl acetate

until quantitative transfer was achieved (visualized by TLC). After removing the solvent under reduced pressure, the title product was isolated by column chromatography (20% ethyl acetate in hexanes) which appeared as a white solid (2.60 g, 82.2%); mp = 132-134 °C. ^{1}H NMR (400 MHz; DMSO-d6): δ 7.87 (d, *J* = 2.3 Hz, 1H), 7.81 (d, *J* = 8.3 Hz, 1H), 7.61-7.57 (m 2H), 7.48 (dd, *J* = 2.3, 8.6 Hz, 1H), 7.20 (d, *J* = 8.7 Hz, 1H), 2.32 (s, 1H). ^{13}C NMR (101 MHz; DMSO-d6): δ 168.9, 150.1, 149.1, 132.3, 130.0(0), 129.9(3), 127.8, 127.5 (q, *J* = 32.6 Hz), 126.3, 123.5 (q, *J* = 272.2 Hz), 120.9 (q, *J* = 4.0 Hz), 118.5, 115.3, 113.9 (q, *J* = 3.7 Hz), 22.8. ^{19}F NMR (376 MHz; DMSO-d6): δ -61.2. (EI, magnetic sector): calcd for $C_{15}H_9BrF_3NO_2$ 370.97688, found 370.97719.



2-Bromo-7-trifluoromethylphenoxazine (4.10). First, a Schlenk tube was evacuated then backfilled with argon. The flask was then opened with a steady flow of argon passing through the side arm and out the top, throughout addition of reagents. The flask was charged with ethanol (13 mL), concentrated HCl (1 mL) and a magnetic stir bar, and an argon filled balloon affixed with a long needle was placed through the top to sparge the solvent while stirring (for at least 10 min). 10-Acetyl-2-bromo-7-trifluoromethylphenoxazine was added (0.50 g, 1.34 mmol) and the suspension was stirred while heating to 70 °C (while maintaining a continuous flow of argon). Once up to temperature, flask was sealed with a septum, the gas side arm was closed, and a balloon of argon was placed in the septa and the reaction progress was closely monitored by TLC. When all of the starting material had been consumed, the reaction was cooled to room temperature after which reaction mixture was carefully quenched in a saturated $NaHCO_3$ solution. After extracting with ethyl acetate, the organic layer was subsequently rinsed, dried ($MgSO_4$), filtered and the solvent was removed under reduced pressure. The title product appeared as a white solid (0.35 g, 79%); mp = 132-134 °C. ^{1}H NMR (400 MHz; DMSO-d6): δ 8.89 (br, 1H), 7.08 (dd, *J* = 0.9, 8.1 Hz, 1H), 6.76 (dd, *J* = 2.3, 8.4 Hz, 1H), 6.59-6.54 (m, 3H). ^{13}C NMR (101 MHz; DMSO-d6): δ 142.6, 141.9, 135.3, 132.9, 124.0 (q, *J* = 270.7 Hz), 123.5, 121.7 (q, *J* = 4.0 Hz), 120.9 (q, *J* = 32.7 Hz), 116.9, 115.8, 115.5, 113.3, 111.9 (q, *J* = 4.0 Hz).

^{19}F NMR (376 MHz; DMSO-d6): δ -60.9. (EI, magnetic sector): calcd for $C_{13}H_7BrF_3NO$ 328.96631, found 328.96610.



2-Iodo-7-trifluoromethylphenoxazine (4.11). In a 10 mL sealed test tube with a stir bar were combined 10-acetyl-2-bromo-7-trifluoromethylphenoxazine (744 mg, 2 mmol), sodium iodide (600 mg, 4 mmol), copper(I) iodide (19.2 mg), 1,2-dimethylethylenediamine (32 μL) and 1,4-dioxane (2 mL). After sparging with argon for 5 minutes, the vessel was sealed and the mixture was heated on a test tube block with rapid stirring. The reaction was maintained at 100 °C for ≥12 h, after which the reaction was cooled to room temperature (successful halogen exchange was confirmed by TLC-MS/APCI). The mixture was filtered and rinsed through a plug of silica using ethyl acetate. After the solvent was removed under reduced pressure, the intermediate product (10-acetyl-2-iodo-7-trifluoromethylphenoxazine) was subjected to amide hydrolysis (analogous to the procedure for **4.10**). After work-up and column, the title product was obtained in a 69% yield (1.04 g) appearing as a white solid; mp = 149-151 °C. ^{1}H NMR (400 MHz; DMSO-d6): δ 8.79 (br, 1H), 7.03 (d, *J* = 8.1 Hz, 1H), 6.89 (dd, *J* = 2.0, 8.2 Hz, 1H), 6.83 (br, 1H), 6.70 (d, *J* = 2.0 Hz, 1H), 6.50 (d, *J* = 8.2 Hz, 1H), 6.39 (d, *J* = 8.2 Hz, 1H). ^{13}C NMR (101 MHz; DMSO-d6): δ 142.5(9), 142.5(5), 135.4, 133.0, 129.7, 124.0 (q, *J* = 270.7 Hz), 121.7 (q, *J* = 4.0 Hz), 121.5, 120.8 (q, *J* = 32.3 Hz), 117.3, 113.3, 111.9 (q, *J* = 3.7 Hz), 87.2. δ -60.9. (EI, magnetic sector): calcd for $C_{13}H_7IF_3NO$ 376.95244, found 376.95245.

Chapter 5

Temperature-Dependence of Radical-Trapping Activity of Phenoxazine, Phenothiazine and Their Aza-Analogues

5.1 Foreword

The following research was featured in *Temperature-dependence of radical-trapping activity of phenoxazine, phenothiazine and their aza-analogues clarifies the way forward for new antioxidant design* which was published in Chemical Science in July of 2021.[1] While being one paper, there are really two works joined together to try to provide clarity to an enigmatic puzzle. Through the process of studying a greater diversity of amine-based RTAs in both ambient and high temperature contexts it became clear to us, in spite of our group's initial successes with heterocyclic diarylamines, that the well-defined trends in reactivity at ambient temperatures often did not lead to accurate predictions with respect to the high temperature autoxidation experimental outcomes. One half of the work is an SAR study of various aza-PNX/PTZ compounds carried out under a in a range of substrates and temperatures. The synthesis of 1-azaPNX, 2-azaPNX, 3-azaPNX, 4-azaPNX, 1-azaPTZ, 2-azaPTZ, 3-azaPTZ and 4-azaPTZ were carried out by the first and third authors Jia-Fei Poon (JFP) and Evan Haidasz, respectively, while all experiments using aforementioned compounds them were carried out by the first author. The experiments in 1-hexadecene were also carried out by JFP.

My contribution involved a detailed look at the fate of PNX and PTZ over the course of a high-temperature inhibited hydrocarbon autoxidation (specifically *n*-hexadecane at 160 °C). In addition to probing mechanisms *in silico*, I also designed and carried out a series of mechanistic experiments with respect to the nitroxide mediated formation of phenothiazine-*S*-oxide. In this chapter I will be focusing on these latter aspects, which in many parts will be verbatim from the aforementioned publication, however data regarding the aza-PNX/PTZ counterparts will be included as it suits the broader discussion. Figures and schemes are reproduced with the permission of the Royal Society for Chemistry under their *Using copyrighted material* policy as described under the *Author rights* subheading.

5.2 Abstract

The prediction and/or rationalization of diarylamine radical-trapping antioxidant (RTA) activity at the elevated temperatures where they are most useful presents a significant challenge, precluding the development of new technology. Whilst structure–activity relationships at ambient temperatures are well established, their predictive capacity at elevated temperatures is poor due to competing reactions. A striking example involves phenoxazine, which is a superior RTA relative to its sulfur analog phenothiazine at ambient temperature (*e.g.* $k = 3.9 \times 10^7$ *vs.* 7.6×10^6 M^{-1} s^{-1} at 37 °C, respectively), but is demonstrably inferior at elevated temperatures. Despite being inherently less oxidizable in electrochemical experiments and high-accuracy computations, phenoxazine is more rapidly consumed than phenothiazine in autoxidations at 160 °C – a result which we attribute to a lower reorganization energy barrier to oxidation. Given these observations, we surmised that incorporation of an electronegative N-atom into the phenoxazine ring system would decrease the driving force for oxidation and 'rescue' its activity. Indeed, this was found to be the case for nitrogen incorporation at any position, regardless of the impact on the inherent RTA activity. Analogous experiments were carried out on phenothiazines into which nitrogen atoms were incorporated, revealing little benefit at 160 °C. These results suggest that for highly reactive diarylamines (*i.e.* those with $k > 10^6$ M^{-1} s^{-1}), further enhancements in reactivity do not materially improve their ability to inhibit hydrocarbon autoxidation at elevated temperatures. Instead, their stability to one-electron oxidation determines their efficacy.

5.3 Introduction

Alkylated diphenylamines (ADPAs, *e.g.* ***5.1***, Fig. 5.1A) are used as additives to preserve hydrocarbon-based products such as motor oils, rubber and polymers.[2,3] They are radical-trapping antioxidants (RTAs) – compounds that inhibit the autoxidation chain reaction by reacting with chain-carrying peroxyl radicals ($ROO^{\cdot}$).[4,5] ADPAs are particularly useful at elevated temperatures where autoxidation is auto-initiated (*i.e.* product peroxides decompose to yield initiating radicals) where they have been reported to trap many equivalents of peroxyl radicals. For example, a stoichiometry of 52 was reported for an ADPA in a paraffin oil oxidation at 130 °C.[6,7] A general mechanism accounting for this apparent catalytic activity was put forward by Korcek and co-workers in the mid 1990s (Fig. 5.1B).[8] Following H-atom transfer

from the ADPA to ROO˙, the canonical RTA reaction, the resultant diarylaminyl radical can be oxygenated to yield a diarylnitroxide, which subsequently combines with an alkyl radical to yield an alkoxyamine. The alkoxyamine may undergo N–O cleavage followed by disproportionation or a retro-carbonyl-ene reaction followed by tautomerization[9] to reform the ADPA. Alternatively, the diarylnitroxide may catalyse the cross-dismutation of alkylperoxyl and hydroperoxyl radicals (Fig. 5.1C); the latter arising from addition reactions in autoxidations of unsaturated substrates, as we have recently discovered.[10]

The sulfur- and oxygen-bridged diarylamines phenothiazine (PTZ) and phenoxazine (PNX) are among the most reactive RTAs known, with rate constants for reactions with peroxyl radicals of 7.6×10^6 and 3.9×10^7 M^{-1} s^{-1}, respectively, at 37 °C – roughly 40- and 200-fold greater than ADPAs, respectively ($\sim 2 \times 10^5$ M^{-1} s^{-1} under the same conditions).[11] However, PTZ, PNX and their derivatives are not commonly used to protect hydrocarbon products from autoxidation. Some time ago, PTZ derivatives were used as RTA additives to lubricants, but have since been supplanted by other RTAs due to their propensity for forming insoluble residues. Unlike ADPA and PTZ, widespread use of PNX-derived RTA additives, to the best of our knowledge, has not been documented. Early work by Murphy *et al.*,[12] showed that PNX was significantly less effective than PTZ as an inhibitor of di-(2-ethylhexyl) sebacate autoxidation at 150 °C. Such findings, presumably, left little incentive to consider PNX much further as a practical alternative. We wondered why PNX was so much less effective than PTZ in Murphy's experiments. In addition to being less reactive to peroxyl radicals, PTZ has a slightly lower oxidation potential than PNX ($E°$ = 0.85 compared to 0.87 V *vs.* NHE)[11] and can be oxidized to the corresponding sulfoxide, which is less reactive than the starting PTZ and may contribute to the formation of insoluble materials. Herein we report the results of PNX- and PTZ-inhibited autoxidations of *n*-hexadecane at 160 °C accompanied by product analyses which indicate that, under these conditions, PNX oxidizes more rapidly than PTZ.

Some time ago, we demonstrated that incorporation of ring nitrogens into very electron-rich diphenylamines could stabilize them to one-electron oxidation, leading to the design of potent RTAs, such as **5.2**.[13–15] We surmised that nitrogen incorporation into PNX may attenuate its oxidizability, leading to enhanced performance more commensurate with its inherent RTA activity, and that this strategy may enable the design of more potent RTAs for use at elevated

temperatures. At the least, we hoped this would better inform on the structure–activity relationships that govern translation of ambient temperature reactivity of aminic RTAs to elevated temperatures. The results of our interrogations of this hypothesis and their implications are also presented.

5.4 Results

n-Hexadecane autoxidations were carried out to compare the RTA activity of PNX and PTZ under well-precedented conditions that have been the subject of extensive study.[8,9,16,17] The autoxidations were performed at 160 °C in a stirred-flow reactor under a constant flow of O_2 (2 L min^{-1}) to prevent rate-limiting mass-transfer and reaction progress was followed by determination of product hydroperoxides using a fluorogenic phosphine–coumarin conjugate (Fig. 5.2A).[18,19]

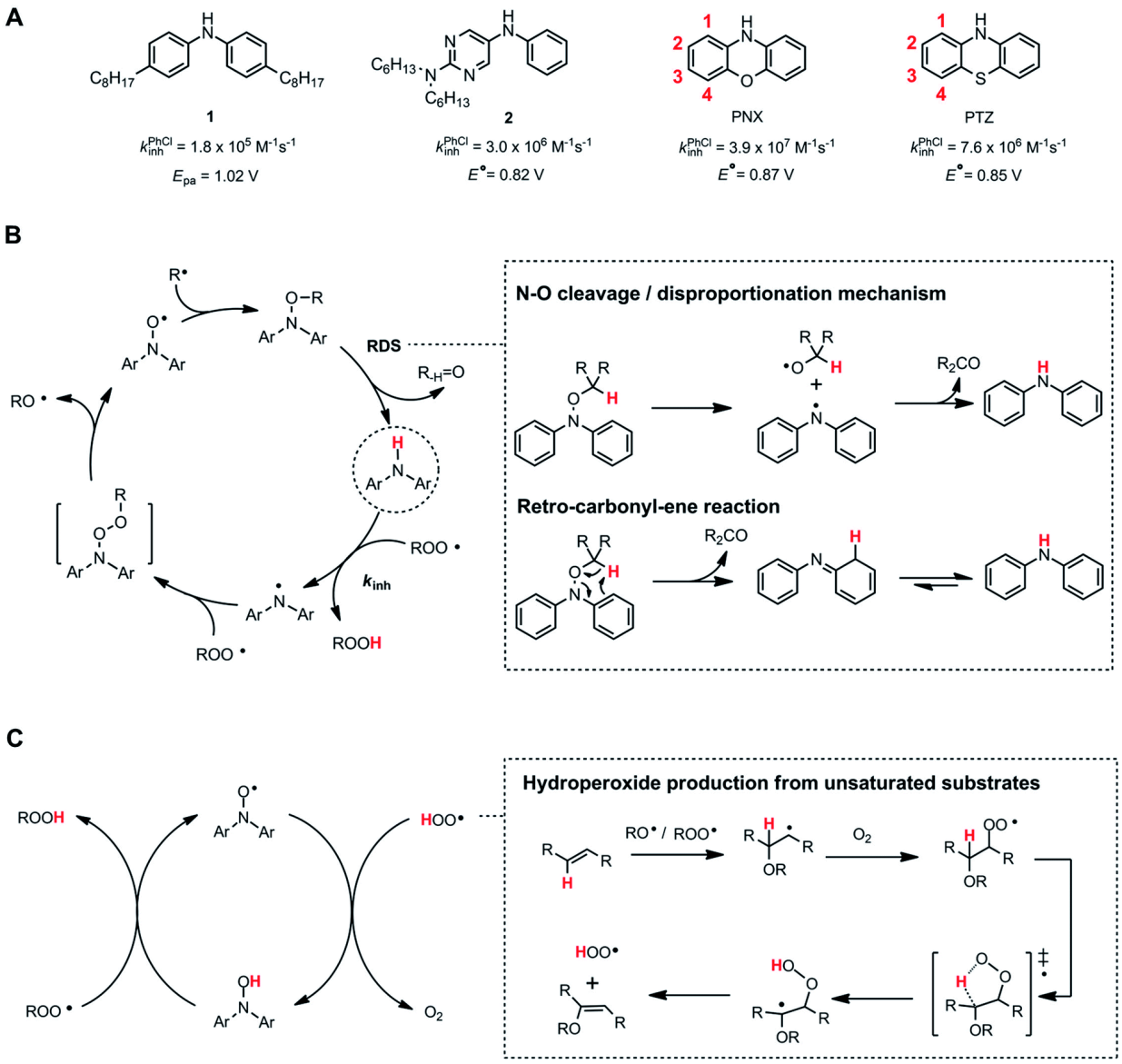


Figure 5.1. (A) Selected diarylamine RTAs and their corresponding inhibition rate constants (k_{inh}) measured in PhCl at 37 °C and standard potentials (E°) measured in CH_3CN *versus* NHE. (B) The Korcek cycle is proposed to account for the catalytic inhibition of diarylamines at elevated temperature. (C) The cross-dismutation of alkylperoxyl and hydroperoxyl radicals is catalysed by diarylnitroxides derived from diarylamines.

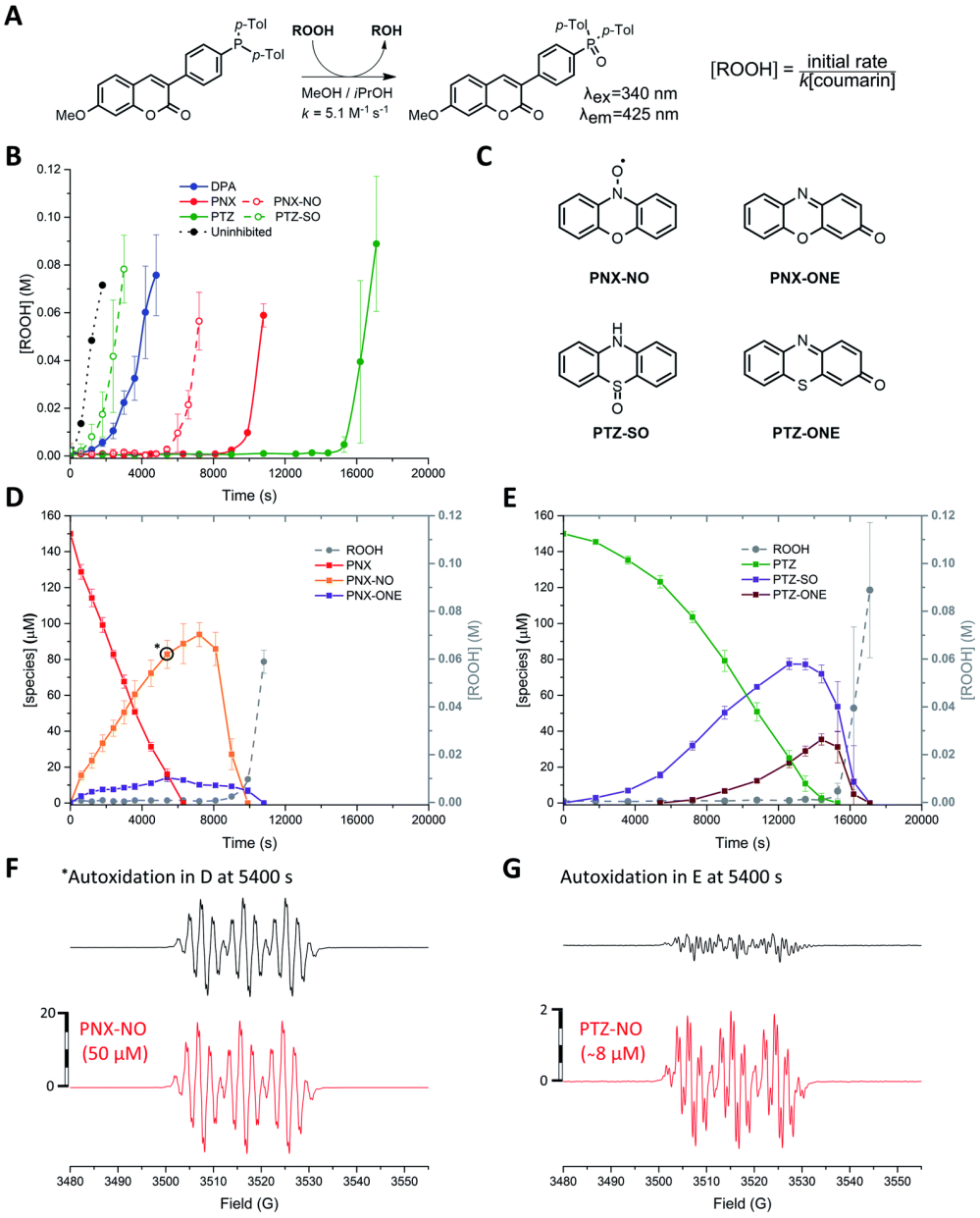


Figure 5.2. (A) A phosphine–coumarin conjugate enables the quantification of hydroperoxides produced during *n*-hexadecane autoxidation at 160 °C. (B) Hydroperoxide formation from the autoxidation of *n*-hexadecane at 160 °C in the presence of diphenylamine (DPA, 150 μM), PNX (150 μM), PTZ (150 μM), phenoxazine-*N*-oxyl (PNX-NO, 150 μM) and phenothiazine-*S*-oxide (PTZ-SO, 150 μM). (C) Structures of primary oxidation products derived from PNX and PTZ observed in the autoxidations. (D and E) Consumption of PNX and PTZ over the course of the autoxidations in (B) and corresponding formation of the products shown in (C) as determined by UPLC analysis. (F and G) EPR spectra of autoxidation samples withdrawn at 5400 s (top) and authentic PNX- and PTZ-derived nitroxides (bottom) recorded at 20 °C in 1 : 1 hexadecane/benzene.[20–22]

As expected, based on their significantly higher inherent reactivity, PTZ and PNX were much better inhibitors of *n*-hexadecane autoxidation than diphenylamine (Fig. 5.2B). Moreover, consistent with the original work by Murphy *et al.*,[12] the inhibited period observed for PTZ was significantly longer (>50%) than for PNX. To provide some insight to the basis for this difference, the concentrations of the RTAs were monitored during the autoxidations by UPLC/UV analyses of samples withdrawn at regular intervals. These experiments revealed that PNX was consumed much more rapidly than PTZ; after 1 hour, nearly ~66% of PNX had been consumed (~100 μM) while PTZ had only decreased by ~10% (Fig. 5.2D and E, respectively).

EPR analyses of the same samples revealed that PNX was converted largely to the corresponding nitroxide (PNX-NO, max. ~63%), with a small amount of phenoxazine-3-one also observed by UPLC/UV (PNX-ONE, max. ~9%, Fig. 5.2D). PTZ consumption was associated with the formation of the corresponding S-oxide (PTZ-SO, max. ~52%) and phenothiazine-3-one (PTZ-ONE, max. ~24%) (Fig. 5.2E). Interestingly, the PTZ-derived nitroxide (PTZ-NO) was not clearly observed in any of the sampled aliquots (Fig. 5.2G is a representative example). The end of the inhibited period quickly followed the consumption of PTZ, implying that the S-oxide is a poor RTA. Autoxidations carried out with authentic PTZ S-oxide confirm this to be the case (Fig. 5.2B). In contrast, the rate of the PNX-inhibited autoxidation remained suppressed after the rapid consumption of PNX, with the end of the inhibited period coinciding with the loss of PNX-NO. Interestingly, nitroxide continued to accumulate for a short period following complete consumption of PNX (from 7200 to 8100 s) before being quickly consumed. Autoxidations carried out with the authentic PNX-NO (150 μM) demonstrate that it is an effective inhibitor, albeit substantially less effective compared to PNX.

To corroborate the possibility that rapid oxidation of PNX underlies its inferiority as an RTA relative to PTZ, we investigated the RTA activity of aza-analogues of PNX. It was expected that incorporation of nitrogen, being more electronegative than carbon, would decrease the oxidizability of PNX. Electrochemical measurements confirmed that the aza-analogues of PNX and PTZ are less oxidizable than the parent compounds (data are summarized in Table 5.1). In addition, ionization potential (IP) calculations were carried out using the CBS-QB3 method which corroborated our electrochemical measurements, and were particularly useful for compounds that did not have well-defined cathodic/anodic peaks (e.g. 2-azaPNX, 3-azaPNX and

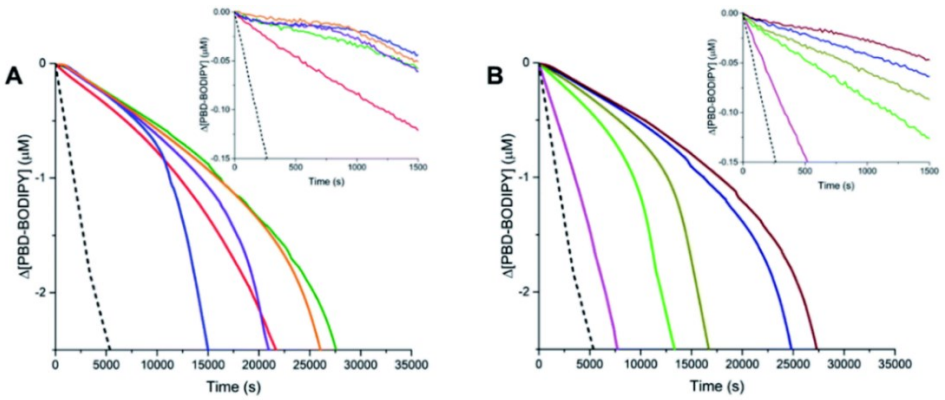
2-azaPTZ). Using either the PBD-BODIPY/dioxane co-autoxidation method, and transposing the $k_{inh}^{Dioxane}$ to k_{inh}^{PhCl} according the Snelgrove/Ingold pre-equilibrium model, or the co-autoxidation in styrene (k_{inh}^{PhCl}) we found that 2- and 4-azaPNXs (k_{inh}^{PhCl} = 2.5 × 10^7 and 4.2 × 10^7 M^{-1} s^{-1}, respectively) were essentially equally reactive to PNX (k_{inh}^{PhCl} = 3.9 × 10^7 M^{-1} s^{-1}) whereas 1- and 3-azaPNXs were 1 to 2 orders less reactive (k_{inh}^{PhCl} = 3 × 10^5 and 6.8 × 10^6 M^{-1} s^{-1}, respectively), fully consistent with their higher computed N–H BDEs. A similar trend was observed for the azaPTZ derivatives, whose k_{inh} values were generally 10-fold lower than those of the corresponding azaPNX derivatives. Of these compounds, 1-azaPTZ was too slow to efficiently inhibit the autoxidation. The stoichiometric factors varied from 2.0 to 2.5, as expected for initial H-atom transfer from the amine to the peroxyl radical followed by combination of the resultant aminyl radical with a second peroxyl radical. Overall, the fact that the oxidative stability of PNX and PTZ can be improved by incorporation of a nitrogen atom at either the 2 or 4 positions while maintaining their very high RTA reactivity makes them attractive scaffolds for further development.

Table 5.1. Summary of Data for PNX, PTZ and Their Aza-Derivatives

	E^o (V vs NHE)	IP (kcal/mol)	*BDE (kcal/mol)*	$k_{inh}^{Dioxane}$ *(10^5 M^{-1} s^{-1})*	α_2^H	k_{inh}^{PhCl} *(10^5 M^{-1} s^{-1})*	n
PNX	0.87	159.6	75.2	- [c]	0.44	390 ± 40	2.3 ± 0.1
1-azaPNX	0.92	164.0	81.7	- [d]	- [e]	3 ± 0.1 [f]	2.2 ± 0.1
2-azaPNX	- [a]	167.1	75.7	21 ± 2	0.50	250 ± 30	2.5 ± 0.1
3-azaPNX	- [a]	168.6	77.4	4.4 ± 0.2	0.55	68 ± 3	2.5 ± 0.1
4-azaPNX	0.92	164.2	75.0	31 ± 3	0.52	420 ± 30	2.0 ± 0.1
PTZ	0.85	154.0	78.7	12 ± 1	0.38	76 ± 3	2.1 ± 0.1
1-azaPTZ	0.97	161.3	85.3	- [d]	- [e]	- [d]	- [d]
2-azaPTZ	- [a]	165.2	79.0	3.5 ± 0.2	0.41	27 ± 2	2.3 ± 0.1
3-azaPTZ	0.95 [b]	165.1	80.3	- [d]	0.48	5 ± 0.1 [f]	2.2 ± 0.1
4-azaPTZ	0.93	160.8	77.7	9.9 ± 0.1	0.46	95 ± 1	2.2 ± 0.1

[a] Flat broad peak observed by differential-pulse voltammetry (DPV). [b] Anodic peak potential (E_{pa}) from DPV rather than half-wave from CV (E^o) due to irreversible electrochemical oxidation. [c] Too fast for 1,4-dioxane/PhCl co-autoxidation, k_{inh}^{PhCl} calculated from k_{inh}^{DMSO} (see ref. 11). [d] Too slow for k_{inh}^{S} and/or n to be measured. [e] Formation of H-bonded dimers in organic solution precludes accurate determination of α_2^H. [f] k_{inh}^{PhCl} was measured in AIBN-initiated styrene co-autoxidation at 37°C.

With the inherent RTA activity of the azaPNX and azaPTZ derivatives established, the compounds were investigated as RTAs at elevated temperatures, where their oxidative stability was expected to be more important. Initial experiments were carried out at 100 °C, since this is the maximum temperature at which we can acquire reliable, highly-reproducible quantitative data (*i.e.* k_{inh} and n) using the PBD-BODIPY co-autoxidation approach. 1-Hexadecene, a low volatility oxidizable substrate in which $k_{PBD\text{-}BODIPY}$ has been determined (8283 M^{-1} s^{-1}),[10,23] was used in the co-autoxidations (Fig. 5.3A and B). From the initial rates, the RTA activity of the PNX and PTZ derivatives follow the same trends at 100 °C as those observed at ambient temperature: 2- and 4-azaPNX (k_{inh}^{PhCl} = 2.5 × 10^7 and 2.0 × 10^7 M^{-1} s^{-1}, respectively) inhibit the autoxidation similarly to PNX (k_{inh}^{PhCl} = 2.5 × 10^7 M^{-1} s^{-1}) whereas the 1- and 3-isomers were slower (k_{inh}^{PhCl} = 3.4 × 10^6 and 7.9 × 10^6 M^{-1} s^{-1}, respectively) (Fig. 5.3C).



C

	PNX	1-azaPNX	2-azaPNX	3-azaPNX	4-azaPNX
k_{inh}^{First} (10^6 $M^{-1}s^{-1}$)	25 ± 3	—[a]	25 ± 1	7.9 ± 1.2	20 ± 1
n_1	3.5 ± 0.2	—[a]	4.3 ± 0.3	4.4 ± 0.2	3.2 ± 0.3
k_{inh}^{Second} (10^6 $M^{-1}s^{-1}$)	4.5 ± 0.4	3.4 ± 0.1	4.0 ± 0.1	4.8 ± 0.2	4.1 ± 0.2
n_2	67 ± 2	59 ± 3	29 ± 2	68 ± 2	49 ± 2

	PTZ	1-azaPTZ	2-azaPTZ	3-azaPTZ	4-azaPTZ
k_{inh}^{First} (10^6 $M^{-1}s^{-1}$)	—[a]	—[a]	—[a]	—[a]	13 ± 1
n_1	—[a]	—[a]	—[a]	—[a]	4.4 ± 0.1
k_{inh}^{Second} (10^6 $M^{-1}s^{-1}$)	3.9 ± 0.3	—	4.9 ± 0.1	2.7 ± 0.1	5.6 ± 0.6
n_2	42 ± 1	—	64 ± 1	26 ± 1	67 ± 1

[a] A clear distinction between the first and second inhibition phase was not observed.

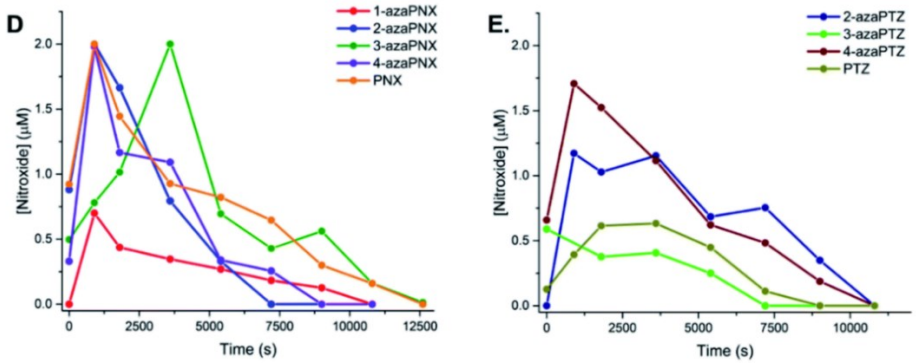


Figure 5.3. (A) Representative co-autoxidations of 1-hexadecene (2.68 M) and PBD-BODIPY (10 μM) initiated by dicumyl peroxide (1 mM) at 100 °C and inhibited by 2 μM 1-azaPNX, 2-azaPNX, 3-azaPNX, 4-azaPNX and PNX. (B) Corresponding autoxidations inhibited by 2 μM 1-azaPTZ, 2-azaPTZ, 3-azaPTZ, 4-azaPTZ and PTZ. Reactions were monitored at 587 nm (λ = 119 166 M^{-1} cm^{-1}). (C) RTA profiles of azaPNX and azaPTZ. (D and E) Nitroxide concentration monitored in representative autoxidations ([dicumyl peroxide] = 2 mM, $R_i = 1.2 \times 10^{-8}$ M s^{-1}) by EPR.

The more reactive derivatives (PNX, 2-azaPNX, 3-azaPNX, 4-azaPNX) were characterized by biphasic inhibited periods; a short initial phase with a very low oxidation rate and a much longer phase with a higher oxidation rate which was largely independent of the structure of the RTA. The overall lengths of the inhibited periods are consistent with very large stoichiometric factors, ranging from n = 52 for 4-azaPNX to 72 for 3-azaPNX. These profiles are reminiscent of those observed for nitroxide-inhibited autoxidations of unsaturated substrates (including 1-hexadecene),[10] suggesting that significant amounts of nitroxide are formed *in situ* from these derivatives. Similarly, the PTZ derivatives in general exhibited high stoichiometric trapping of radicals (n ranging from 26 to 67), with the exception of 1-azaPTZ which to this point had shown little evidence of RTA activity in general and appears to only slightly retard autoxidation under the present conditions. It does appear that the protracted inhibition in all of these cases is accompanied by persistent radicals detected by EPR, confirmed to be PNX-NO in the case of PNX and presumed to be the corresponding nitroxide in the other examples. These findings are consistent with the hydroperoxyl cross-dismutation mechanism depicted in Fig. 5.1C. The flipped trends between the 160 ºC experiments in n-hexadecane (PNX<PTZ) compared to the 1-hexadecene experiments at 100 ºC (PNX>PTZ), taken together with the disparate speciation of the oxidized products of PNX/PTZ, it is clear that a different set of mechanistic considerations are in operation in the hexadecane autoxidation.

5.5 Discussion

PNX is among the most potent RTAs known. In fact, to the best of our knowledge, the fastest RTA characterized to date is a substituted phenoxazine (3,7-dimethoxyphenoxazine, k_{inh} = 6.6 × 10^8 M^{-1} s^{-1} at 37 °C in PhCl).[11] PNX systematically outperforms its sulfur analog PTZ in various contexts – from typical autoxidizable hydrocarbons (*e.g.* dioxane and 1-hexadecene above) to liposomal phospholipids and mammalian cells, where the autoxidation of membrane lipids drives a cell death process known as ferroptosis.[24,25] However, PNX has been reported to be inferior to PTZ at the elevated temperatures where aminic antioxidants are particularly useful.[12] Indeed, we have found this to be the case in *n*-hexadecane at 160 °C.

Analyses of the samples withdrawn from *n*-hexadecane autoxidations reveal that PNX is consumed more rapidly than PTZ. At first glance, this seems reasonable, given that PNX is more reactive to chain-carrying peroxyl radicals than PTZ. However, since the autoxidation is at least

equally well-inhibited by PTZ, this cannot be the explanation. Instead, it implies that either PNX is depleted by a reaction with a non-initiating/propagating species or that PTZ is converted to something which is far more reactive than PTZ itself, effectively sparing unreacted PTZ while suppressing the autoxidation. The latter option seems rather unlikely. Although PTZ is less inherently reactive than PNX, it is still a very good RTA. Furthermore, the major PTZ-derived product observed during the autoxidation is PTZ S-oxide, which is a far worse RTA than PTZ. Thus, it seems more likely that PNX reacts in a non-productive way, and we suggest that this is initiated by means of electron-transfer to O_2. While both $E°$ values and gas phase ionization potentials indicate that PNX is less easily oxidized than PTZ, these are thermodynamic measures. The free energy barrier for electron transfer as defined by Marcus theory (Eq. 5.1) is not only dependent on the thermodynamic driving force, but also the energy required to reorganize the bonds in the reactants (λ_i) and to reorganize the solvent sphere (λ_o), referred to collectively as the reorganization energy ($\lambda = \lambda_i + \lambda_o$).

$$\Delta G^{\ddagger} = \frac{(\lambda + \Delta G^{o})^2}{4\lambda} \qquad (5.1)$$

Calculations of λ_i for oxidation of PNX and PTZ (7.6 and 13.5 kcal mol^{-1}, respectively) suggest the latter will have a significantly higher barrier to electron transfer.[26–29] The reorganization energy is largely associated with co-planarization of the aryl rings to achieve maximal delocalization in the radical cation – and the structure of PTZ is significantly more non-planar than the structure of PNX, with the bridging heteroatoms binding angles between the two aryl rings of 147° and 167°, respectively, see Fig. 5.4A.[28] Going forward, λ_i may be a useful parameter to consider in the evaluation/design of highly reactive high temperature RTAs.

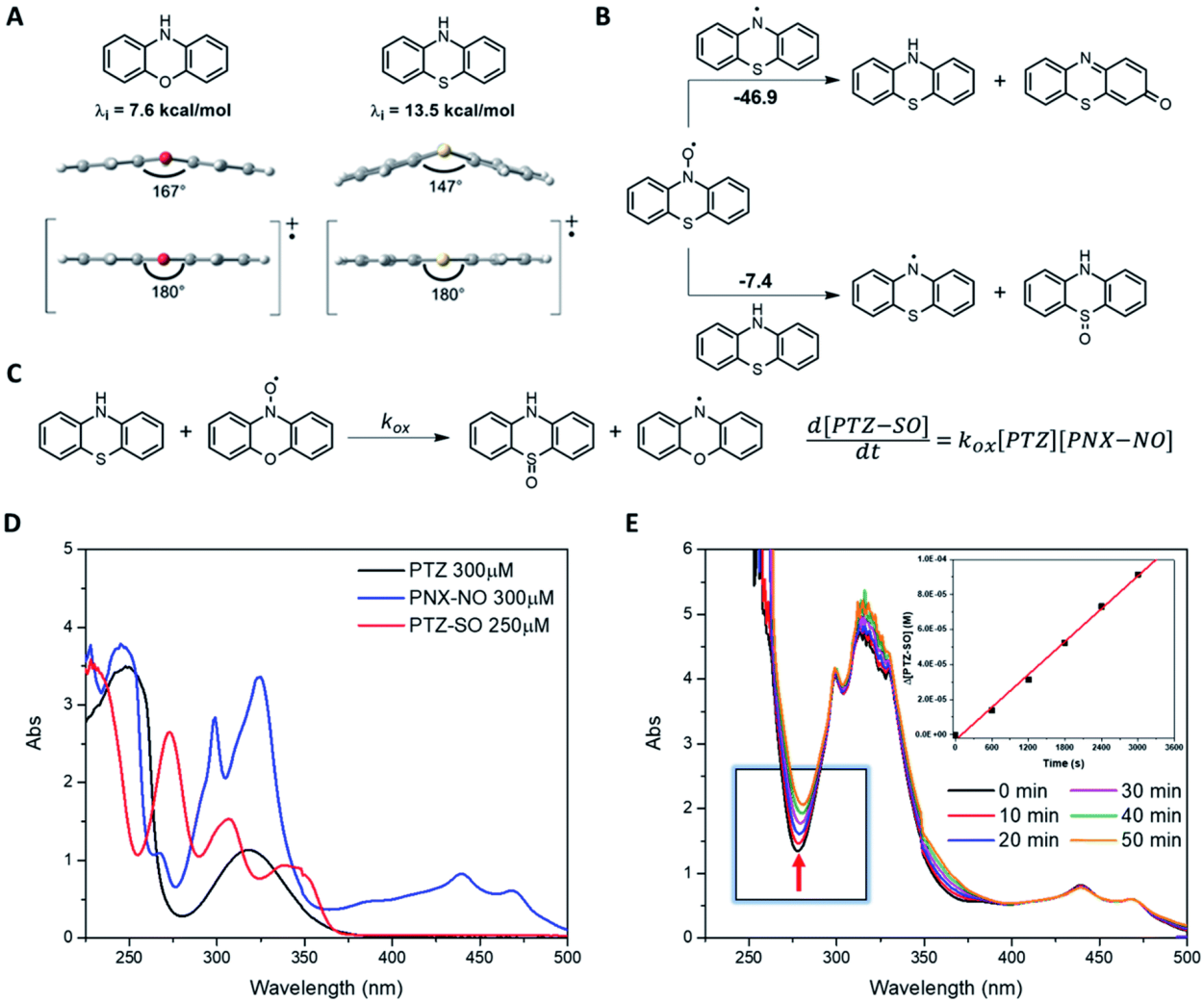


Figure 5.4. (A) CBS-QB3-calculated reorganisation energies (λ_i) for oxidation of PNX and PTZ and the structures of the minimum energy structures of the starting materials and radical cations highlighting the deviation from planarity of the starting structures. (B) Calculated free energy change for the reaction of phenothiazine-N-oxyl (PTZ-NO) with each of the phenothiazine aminyl radical (top) and PTZ (bottom). (C) The oxidation of PTZ by PNX-NO. (D) UV-Vis spectra of PTZ, PNX-NO, and PTZ-SO in *n*-hexadecane at 100 °C. (E) Representative spectra acquired upon mixing PTZ (600 μM) and PNX-NO (300 μM) in *n*-hexadecane at 100 °C and corresponding initial rate plot derived from the increase at 278 nm corresponding to PTZ-SO (ε = 8667 M^{-1} cm^{-1}).

Electron transfer from PNX to O_2 yields an ion pair that is expected to rapidly exchange a proton to yield the aminyl radical and HOO˙. Of course, there is also the possibility of direct H-atom

transfer from PNX to O_2 to yield the same intermediates, which would be expected to be more efficient from PNX than from PTZ based on the weaker N–H bond in the former compared to the latter. However, this formally 'spin-forbidden' reaction (the reactants have ground state singlet and triplet electronic configurations while the products have doublet electronic configurations), may have a prohibitively high barrier.[30] Regardless of the precise mechanism, the reaction sequence is predicted to be highly endergonic, as the stronger N–H bond in PNX is exchanged for the weaker bond in hydroperoxyl. However, since the thermodynamics are more favourable than for homolysis of the O–O bond in a hydroperoxide (which is responsible for radical initiation under these conditions), it should be competitive. Oxygen atom transfer could then occur *via* a combination/fragmentation sequence – with the newly formed hydroperoxyl radical (or a substrate-derived peroxyl radical) to yield the nitroxide.

Importantly, little nitroxide was observed in the PTZ-inhibited autoxidations. Given the structural similarity of PNX and PTZ, it may be expected that the products derived therefrom would be similar. Of course, PTZ has a bridging sulfur atom, and the S-oxide is a well-known oxidation product of PTZ. However, it has been generally assumed that S-oxidation arises primarily due to reactions with a hydroperoxide,[31] of which very little is present during the inhibited period. Alternatively, reaction with a peroxyl radical can be envisioned, since fragmentation of unactivated O–O bonds occur at these temperatures. However, addition of the peroxyl radical to the sulfur atom would have to be competitive with H-atom transfer from PTZ to the peroxyl radical, which is unlikely given how fast the latter process occurs. A third possibility involves the nitroxide derived from PTZ as the source of the O-atom of the S-oxide (Fig. 5.4B); addition of the nitroxide to the sulfur atom of PTZ followed by fragmentation of the O–N bond to release the highly-stabilized aminyl radical along with the S-oxide may occur. CBS-QB3 calculations suggest that this is a favourable transformation ($\Delta G = -7.4$ kcal mol^{-1}), and that the formation of the S-oxide easily makes up for the 8 kcal mol^{-1} loss in radical stabilization energy on going from PTZ-derived nitroxide to PTZ-derived aminyl (the CBS-QB3-calculated O–H and N–H bond dissociation enthalpies of the PTZ-derived hydroxylamine and PTZ are 70.7 and 78.7 kcal mol^{-1}, respectively). To the best of our knowledge, this reaction has never been suggested, but it offers a compelling explanation for the lack of PTZ-NO

accumulation observed during the PTZ-inhibited autoxidation (in contrast to that inhibited by PNX).

While we were unable to probe the reaction of PTZ-NO and PTZ directly given difficulties associated with preparing PTZ-NO, we found that the PNX-derived nitroxide reacted smoothly with PTZ to yield the S-oxide (Fig. 5.4C). Progress of the reaction could be conveniently monitored by UV-Vis spectrophotometry (Fig. 5.4D and E), which enabled characterization of its temperature-dependent kinetics and subsequent derivation of $\Delta H^{\ddagger} = 22.9$ kcal mol^{-1} and $\Delta S^{\ddagger} = -1.4$ cal mol^{-1} K^{-1}.[32] The negative entropy of activation is consistent with association of the nitroxide and PTZ in the rate-determining step of the reaction. Although the formation of *S*-oxide depletes PTZ, converting it from a good RTA to a poor one, PTZ remains a more efficient inhibitor than PNX at 160 °C since it is more resistant to direct oxidation.

In the 1-hexadecene autoxidations carried out at 100 °C, the PNX-inhibited reaction progress profiles are dominated by changes in stoichiometry rather than changes in k_{inh}. This can be rationalized in part by the fact that the activation energies for H-atom transfer from these highly reactive diarylamines are so small (<2 kcal mol^{-1})[15] that the reactions are largely entropy-controlled; this levelling effect is clear from the initial portions of the inhibited autoxidations for the PNX derivatives, which are largely invariant with structure. Most importantly, for all derivatives, the inhibited periods extend well beyond what is expected for the nominal trapping of ~2 radicals as observed in the autoxidations at 37 °C. This is due to the intervention of the nitroxide-catalyzed cross-dismutation of hydroperoxyl and alkyl peroxyl radicals that can take place in unsaturated substrates, such as hexadecene (Fig. 5.1C).[10]

The fact that PNX was significantly more efficient than PTZ in these autoxidations ($n = 67$ *vs.* $n = 42$), implies that deleterious oxidation of PNX is not a problem under these conditions, although it must also be acknowledged that the RTA concentration here is much lower (2 μM compared to 300 μM at 160 °C). The basis of the difference in observed inhibition times between PNX and PTZ was apparent from EPR studies, which revealed that nitroxide doesn't accumulate to nearly the same extent in the PTZ-inhibited autoxidations (~25%) compared to those inhibited by PNX (effectively quantitative). Insertion of nitrogen atoms at either the 2 or 4 positions of PTZ lead to much larger stoichiometries of $n = 64$ and 67, respectively, presumably because

electron withdrawal from the bridging sulfur atom deactivates it to S-oxidation making nitroxide formation the more favoured path. In contrast, the low inherent reactivity of the 1-aza and 3-aza isomers of PTZ and lesser stability of the aminyl radicals derived therefrom, preclude efficient formation of nitroxide and account for the poor activity of 1-azaPTZ and 3-azaPTZ.

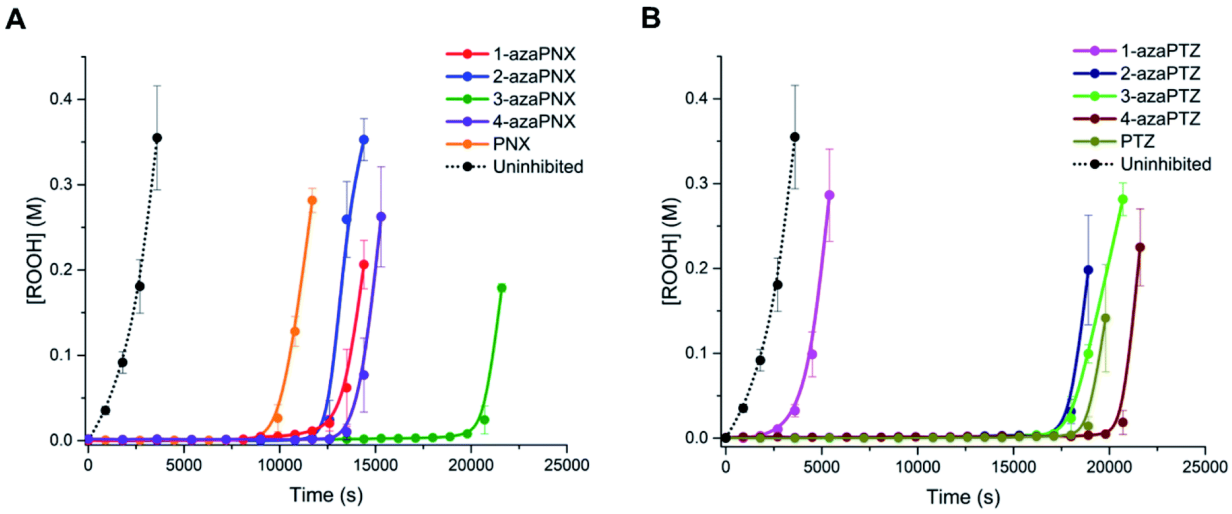


Figure 5.5. (A) Hydroperoxide formation from the autoxidation of *n*-hexadecane at 160 °C in the presence of 1 mM Primene and inhibited by 200 μM 1-azaPNX, 2-azaPNX, 3-azaPNX, 4-azaPNX and PNX. (B) Corresponding experiments inhibited by 200 μM 1-azaPTZ, 2-azaPTZ, 3-azaPTZ, 4-azaPTZ and PTZ.

Thus far there is an abundance of corroborating evidence for the catalytic trapping capability of these PNX/PTZ-type RTAs through a nitroxide-facilitated cross-dismutation in hexadecene. The number of chains trapped is 10 to 30-fold greater than a phenolic standard, an unambiguously stoichiometric RTA (PMC, n=2). In the case of the saturated n-hexadecane however, the matter remains rather ambiguous as to whether the proposed "Korcek cycle" (Fig. 5.1B) is playing any kind of role in the observed behaviour of these compounds. To the contrary, the nitroxide which supposedly should trap an alkyl radical to form the necessary alkoxyamine intermediate is measurably absent for PTZ, while for PNX nitroxide is in abundance, yet PNX has a much lower inhibition time. Nothing observed in these experiments to this point compels us to adopt a catalytic regime over a simple stoichiometric one. The differences in oxidative stability, evaluated on the basis of the thermodynamics *and* kinetics of electron-transfer, provides a more straightforward rationale for the trends seen and going forward should be a key consideration with respect to RTA design for this application. A "high" rate constant of inhibition ($k_{inh}^{PhCl} \geq 10^6$

M^{-1} s^{-1}), which we previously regarded one of the primary factors for the improved performance of **5.2** in n-hexadecane compared to **5.1**,[33] seems to hit a point of diminished returns above a certain threshold as most of the PNX derivatives are clearly out performed by their slower PTZ counterparts (Fig. 5.5). The exceptions to this state affairs is the abysmal performance of 1-azaPTZ, proving that possessing RTA activity is a prerequisite, and the better than expected performance of 3-azaPNX which is very competitive with the PTZ RTAs.[34]

5.6 Conclusion

Despite our best efforts, we have not been able to establish a quantitative structure–reactivity relationship that links high-temperature efficacy (*e.g.* inhibition times in *n*-hexadecane autoxidations at 160 °C) with inherent reactivity as defined by N–H BDE and/or k_{inh} at ambient temperatures and oxidative stability as defined by IP and/or $E°$. The results obtained with PNX and PTZ illustrate that IP or $E°$ are insufficient as they do not directly correspond to the oxidation kinetics. Moreover, the N–H BDE and k_{inh} values inform only on the initial H-atom reaction of the diarylamine, and do not clearly transpose into a systematic theory of RTA efficacy under the conditions of the *n*-hexadecane experiments. Evidence for an operational catalytic cycle, like the one proposed by Korcek and co-workers,[8] remains elusive at this time.

5.7 References

(1) Poon, J.-F.; Farmer, L. A.; Haidasz, E. A.; Pratt, D. A. Temperature-Dependence of Radical-Trapping Activity of Phenoxazine, Phenothiazine and Their Aza-Analogues Clarifies the Way Forward for New Antioxidant Design. *Chem. Sci.* **2021**, *12* (33), 11065–11079. https://doi.org/10.1039/D1SC02976B.

(2) Kröhnke, C.; Schacker, O.; Zäh, M. Antioxidants. In *Ullmann's Encyclopedia of Industrial Chemistry*; 2015; pp 1–36.

(3) Helberg, J.; Pratt, D. A. Autoxidation vs. Antioxidants – the Fight for Forever. *Chem. Soc. Rev.* **2021**, *50* (13), 7343–7358. https://doi.org/10.1039/D1CS00265A.

(4) Ingold, K. U. Inhibition of the Autoxidation of Organic Substances in the Liquid Phase. *Chem. Rev.* **1961**, *61* (6), 563–589. https://doi.org/10.1021/cr60214a002.

(5) Ingold, K. U.; Pratt, D. A. Advances in Radical-Trapping Antioxidant Chemistry in the 21st Century: A Kinetics and Mechanisms Perspective. *Chem. Rev.* **2014**, *114* (18), 9022–9046. https://doi.org/10.1021/cr500226n.

(6) Bolsman, T. A. B. M.; Blok, A. P.; Frijns, J. H. G. Catalytic Inhibition of Hydrocarbon Autoxidation by Secondary Amines and Nitroxides. *Recl. des Trav. Chim. des Pays-Bas* **1978**, *97* (12), 310–312.

(7) Bolsman, T. A. B. M.; Blok, A. P.; Frijns, J. H. G. Mechanism of the Catalytic Inhibition of Hydrocarbon Autoxidation by Secondary Amines and Nitroxides. *Recl. des Trav. Chim. des Pays-Bas* **1978**, *97* (12), 313–319. https://doi.org/10.1002/recl.19780971205.

(8) Jensen, R. K.; Korcek, S.; Zinbo, M.; Gerlock, J. L. Regeneration of Amine in Catalytic Inhibition of Oxidation. *J. Org. Chem.* **1995**, *60*, 5396–5400. https://doi.org/10.1021/jo00122a014.

(9) Haidasz, E. A.; Shah, R.; Pratt, D. A. The Catalytic Mechanism of Diarylamine Radical-Trapping Antioxidants. *J. Am. Chem. Soc.* **2014**, *136* (47), 16643–16650. https://doi.org/10.1021/ja509391u.

(10) Harrison, K. A.; Haidasz, E. A.; Griesser, M.; Pratt, D. A. Inhibition of Hydrocarbon Autoxidation by Nitroxide-Catalyzed Cross-Dismutation of Hydroperoxyl and Alkylperoxyl Radicals. *Chem. Sci.* **2018**, *9* (28), 6068–6079. https://doi.org/10.1039/C8SC01575A.

(11) Farmer, L. A.; Haidasz, E. A.; Griesser, M.; Pratt, D. A. Phenoxazine: A Privileged Scaffold for Radical-Trapping Antioxidants. *J. Org. Chem.* **2017**, *82* (19), 10523–10536. https://doi.org/10.1021/acs.joc.7b02025.

(12) Murphy, C. M.; Ravner, H.; Smith, N. L. Mode of Action of Phenothiazine-Type Antioxidants. *Ind. Eng. Chem.* **1950**, *42* (12), 2479–2489. https://doi.org/10.1021/ie50492a027.

(13) Hanthorn, J. J.; Valgimigli, L.; Pratt, D. A. Incorporation of Ring Nitrogens into Diphenylamine Antioxidants: Striking a Balance between Reactivity and Stability. *J. Am. Chem. Soc.* **2012**, *134*, 8306–8309. https://doi.org/10.1021/ja300086z.

(14) Hanthorn, J. J.; Valgimigli, L.; Pratt, D. A. Preparation of Highly Reactive Pyridine- and Pyrimidine-Containing Diarylamine Antioxidants. *J. Org. Chem.* **2012**, *77*, 6908–6916. https://doi.org/10.1021/jo301013c.

(15) Hanthorn, J. J.; Amorati, R.; Valgimigli, L.; Pratt, D. A. The Reactivity of Air-Stable Pyridine- and Pyrimidine-Containing Diarylamine Antioxidants. *J. Org. Chem.* **2012**, *77* (16), 6895–6907. https://doi.org/10.1021/jo301012x.

(16) Jensen, R. K.; Korcek, S.; Mahoney, L. R.; Zinbo, M. Liquid-Phase Autoxidation of Organic Compounds at Elevated Temperatures. The Stirred Flow Reactor Technique and Analysis of Primary Products from n-Hexadecane Autoxidation at 120-180 C. *J. Am. Chem. Soc.* **1979**, *101*, 7574–7584.

(17) Jensen, R. K.; Korcek, S.; Mahoney, L. R.; Zinbo, M. Liquid-Phase Autoxidation of Organic Compounds at Elevated Temperatures. 2. Kinetics and Mechanisms of the Formation of Cleavage Products in n-Hexadecane Autoxidation. *J. Am. Chem. Soc.* **1981**, *103* (7), 1742–1749. https://doi.org/10.1021/ja00397a026.

(18) Shah, R.; Pratt, D. A. Determination of Key Hydrocarbon Autoxidation Products by Fluorescence. *J. Org. Chem.* **2016**, *81*, 6649–6656.

(19) Hanthorn, J. J.; Haidasz, E. A.; Gebhardt, P.; Pratt, D. A. A Versatile Fluorescence Approach to Kinetic Studies of Hydrocarbon Autoxidations and Their Inhibition by Radical-Trapping Antioxidants. *Chem. Commun.* **2012**, *48*, 10141–10143.

(20) The nitroxide of phenothiazine (PTZ-NO) was generated in situ by oxidation of PTZ in benzene with 2.5% v/v *tert*-butyl hydroperoxide as described by Jackson and Patel and Gilbert and co-workers (see ref. 21 & 22). Its concentration was determined by quantitative EPR.

(21) Jackson, C.; Patel, N. K. D. Free Radicals Derived from Phenothiazine. *Tetrahedron Lett.* **1967**, *8* (24), 2255–2263. https://doi.org/10.1016/S0040-4039(00)90808-6.

(22) Chiu, M. F.; Gilbert, B. C.; Hanson, P. A Study by Electron Spin Resonance of Some Heterocyclic Radicals Containing Elements of Group VI. *J. Chem. Soc. B Phys. Org.* **1970**, No. 0, 1700–1708. https://doi.org/10.1039/j29700001700.

(23) Chauvin, J.-P. R.; Griesser, M.; Pratt, D. A. The Antioxidant Activity of Polysulfides: It's Radical! *Chem. Sci.* **2019**, *10* (19), 4999–5010. https://doi.org/10.1039/C9SC00276F.

(24) Shah, R.; Margison, K.; Pratt, D. A. The Potency of Diarylamine Radical-Trapping Antioxidants as Inhibitors of Ferroptosis Underscores the Role of Autoxidation in the Mechanism of Cell Death. *ACS Chem. Biol.* **2017**, *12* (10), 2538–2545. https://doi.org/10.1021/acschembio.7b00730.

(25) Poon, J.-F.; Zilka, O.; Pratt, D. A. Potent Ferroptosis Inhibitors Can Catalyze the Cross-Dismutation of Phospholipid-Derived Peroxyl Radicals and Hydroperoxyl Radicals. *J. Am. Chem. Soc.* **2020**, *142* (33), 14331–14342. https://doi.org/10.1021/jacs.0c06379.

(26) The internal reorganizational energy ($\lambda_i = \lambda_i^1 + \lambda_i^2$) was calculated as the sum of ($\lambda_i^1 = E_{PNX}^{Geom}$-$E_{PNX}^{Geom^{+\cdot}}$) and ($\lambda_i^2 = E_{PNX^{+\cdot}}^{Geom}$-$E_{PNX^{+\cdot}}^{Geom^{+\cdot}}$), where E_{PNX}^{Geom} is the CBS-QB3 electronic energy of PNX and $E_{PNX}^{Geom^{+\cdot}}$ is the electronic energy of the PNX singlet using the PNX

radical cation geometry. λ_i^2 is calculated in a likewise fashion but with the radical cation spin state. (See ref. 27).

(27) Metri, N.; Sallenave, X.; Plesse, C.; Beouch, L.; Aubert, P.-H.; Goubard, F.; Chevrot, C.; Sini, G. Processable Star-Shaped Molecules with Triphenylamine Core as Hole-Transporting Materials: Experimental and Theoretical Approach. *J. Phys. Chem. C* **2012**, *116* (5), 3765–3772. https://doi.org/10.1021/jp2098872.

(28) Our observations and interpretations parallel those made by Lee et al. in recent work on organic p-type cathodes, where they noted that PNX-based donor materials demonstrated significantly faster rates of charge transfer compared to their PTZ counterparts. (See ref. 29).

(29) Lee, K.; Serdiuk, I. E.; Kwon, G.; Min, D. J.; Kang, K.; Park, S. Y.; Kwon, J. E. Phenoxazine as a High-Voltage p-Type Redox Center for Organic Battery Cathode Materials: Small Structural Reorganization for Faster Charging and Narrow Operating Voltage. *Energy Environ. Sci.* **2020**, *13* (11), 4142–4156.

(30) It is difficult to rule out a direct H-atom transfer mechanism by experiment; *n*-hexadecane autoxidations inhibited by PNX-d (and containing excess D in the form of D_2O) were indistinguishable from those inhibited by PNX, but it must be acknowledged that kinetic isotope effects could be quite small at these temperatures.

(31) Kennerly, G. W.; Patterson, W. L. Kinetic Studies of Petroleum Antioxidants. *Ind. Eng. Chem.* **1956**, *48* (10), 1917–1924. https://doi.org/10.1021/ie50562a042.

(32) It should be noted that the temperature range of the determination spanned only 20 °C due to practical limitations; the reaction was too slow to monitor at a temperature significantly lower than 80 °C (at concentrations that would be practical for monitoring spectroscopic changes). Meanwhile our thermostatted UV-Vis spectrophotometer cannot operate above 100 °C.

(33) Shah, R.; Haidasz, E. A.; Valgimigli, L.; Pratt, D. A. Unprecedented Inhibition of Hydrocarbon Autoxidation by Diarylamine Radical-Trapping Antioxidants. *J. Am. Chem. Soc.* **2015**, No. 137, 2440–2443.

(34) Incidentally, 3-azaPTZ has a k_{inh}^{PhCl} comparable to PTZ (6.8×10^6 vs. 7.6×10^6 M^{-1} s^{-1}).

(35) Gaussian 16, Revision C.01, Frisch, M. J.; Trucks, G. W.; Schlegel, H. B.; Scuseria, G. E.; Robb, M. A.; Cheeseman, J. R.; Scalmani, G.; Barone, V.; Petersson, G. A.; Nakatsuji, H.; Li, X.; Caricato, M.; Marenich, A. V.; Bloino, J.; Janesko, B. G.; Gomperts, R.; Mennucci, B.; Hratchian, H. P.; Ortiz, J. V.; Izmaylov, A. F.; Sonnenberg, J. L.; Williams-Young, D.; Ding, F.; Lipparini, F.; Egidi, F.; Goings, J.; Peng, B.; Petrone, A.; Henderson, T.; Ranasinghe, D.; Zakrzewski, V. G.; Gao, J.; Rega, N.; Zheng, G.; Liang, W.; Hada, M.; Ehara, M.; Toyota, K.; Fukuda, R.; Hasegawa, J.; Ishida, M.; Nakajima, T.; Honda, Y.; Kitao, O.; Nakai, H.; Vreven, T.; Throssell, K.; Montgomery, J. A., Jr.; Peralta, J. E.; Ogliaro, F.; Bearpark, M. J.; Heyd, J. J.; Brothers, E. N.; Kudin, K. N.; Staroverov, V. N.; Keith, T. A.; Kobayashi, R.; Normand, J.; Raghavachari, K.; Rendell, A. P.; Burant, J. C.; Iyengar, S. S.; Tomasi, J.; Cossi, M.; Millam, J. M.; Klene, M.; Adamo, C.; Cammi, R.; Ochterski, J. W.; Martin, R. L.; Morokuma, K.; Farkas, O.; Foresman, J. B.; Fox, D. J. Gaussian, Inc., Wallingford CT, 2016.

Materials/Synthesis

General. Reagents were purchased from commercial suppliers and used without further purification. For the preparation of 2-azaphenoxazine, 3-azaphenoxazine, 1-azaphenothiazine, 2-azaphenothiazine, 3-azaphenothiazine and 4-azaphenothiazine, see the original paper.[1] 1-Azaphenoxazine, 4-azaphenoxazine,[2] and phenothiazone[3] were prepared as previously described. Column chromatography was carried out using flash silica gel (40−63 μm, 230−400 mesh). ^{1}H and ^{13}C NMR were recorded on a Bruker AVANCE spectrometer at 600 and 125 MHz, respectively, unless specified otherwise. High-resolution mass spectra were obtained on a Kratos Concept Tandem mass spectrometer. The melting points are not corrected.

3*H*-phenoxazin-3-one. The synthesis of 3*H*-phenoxazin-3-one was based on the method described by Barret and Daudon.[4] A flame dried 100 mL round bottom flask was charged with 60 mL of benzene, 1.10 g of phenoxazine (6 mmol), 2.83 g of iodoxybenzene (12 mmol) and 320 mg vanadyl acetylacetonate (1.2 mmol). With stirring, the reaction mixture was brought to a reflux for 3 hours. The benzene was removed under reduced pressure, and the residue was purified using column chromatography (8:2 hexane/EtOAc). The fractions containing the product were consolidated into a single round bottom flask and the solvent was removed under reduced pressure. The partially purified product was dissolved in a minimum of ethyl acetate, after which hexanes were added to precipitate 3*H*-phenoxazin-3-one as an orange solid. The product was filtered and rinsed with hexanes (0.23 g, 1.1 mmol, 18.3% yield). ^{1}H-NMR (400 MHz; DMSO-d_6): δ 7.85 (dd, *J* = 7.9, 1.5 Hz, 1H), 7.66 (ddd, *J* = 7.4, 7.3, 1.6 Hz, 1H), 7.57 (d, *J* = 9.8 Hz, 1H), 7.50 (dd, *J* = 8.3, 1.1 Hz, 1H), 7.45 (ddd, *J* = 7.9, 7.4, 1.3 Hz, 1H), 6.84 (dd, *J* = 9.8, 2.1 Hz, 1H), 6.30 (d, *J* = 2.1 Hz, 1H). ^{13}C NMR (101 MHz; DMSO-d_6): δ 185.7, 149.7, 148.6, 143.5, 135.0, 134.8, 133.1, 133.0, 130.0, 125.6, 116.2, 105.8. Mp = 216 – 218 °C (lit. 214 °C).[4]

Phenothiazine-5-oxide. In 10 mL round bottom flask was dissolved 0.40 g of phenothiazine (2 mmol) into 4 mL of ethyl acetate with stirring. 2 equivalents of m-CPBA (4 mmol) were dissolved in 2 mL of diethyl ether. The ether layer (commercial m-CPBA contains a large amount of H_2O) was dropped into the flask containing the phenothiazine solution while stirring which resulted in immediate and quantitative precipitation of phenothiazine-5-oxide. The light-

yellow product was filtered, and rinsed with ethyl acetate, diethyl ether, then hexanes (0.42 g). This product was recrystallized out of absolute ethanol. The ^{1}H-NMR was consistent with the previously reported characterization of phenothiazine-5-oxide.[5] ^{1}H-NMR (400 MHz; DMSO-d_6): δ 10.98 (br, N-H, 1H), 7.89 (d, J = 7.0 Hz, 2H), 7.61 (ddd, J = 8.3, 8.3, 1.3 Hz, 2H), 7.38 (d, J = 8.1 Hz, 2H), 7.18 (dd, J = 7.4, 7.4 Hz, 2H).

Phenoxazine-*N*-oxyl. Phenoxazine 1.83 g (10 mmol) was dissolved in 30 mL of diethyl ether. Separately, 3.50 g of 77% mCPBA was dissolved in 14 mL of diethyl ether and then slowly added to the phenoxazine solution with swirling. After 2 min, the solution turned from colorless to yellow/black. Scratching the walls of the flask with a pipet induced crystallization, which proceeded for ∼1 h. The solvent was decanted, and the crystals were rinsed three times with cold diethyl ether and then three times with petroleum ether, which afforded 635 mg (32%) of the phenoxazine-*N*-oxyl; mp 127–129 °C; EPR (benzene, g = 2.0051, a (G)): 9.03 (N), 2.40 ($H_{1,3,7,9}$), 0.55 ($H_{2,4,6,8}$).[6] HRMS (EI, magnetic sector): calcd for $C_{12}H_8NO_2$ 198.0555, found 198.0571.

5.8 Methods

Inhibited co-autoxidation of PBD-BODIPY and 1-hexadecene at 100 °C. To a 3 mL cuvette were added purified 1-hexadecene (2.0 mL) and PhCl (440 μL). After equilibration for 10 min at 100 °C, the cuvette was blanked, and to the cuvette were added PBD-BODIPY (12.5 μL of 2.0 mM solution in 1,2,4-trichlorobenzene) and dicumyl peroxide (50 μL of 50 mM, 100 mM or 150 mM solution in PhCl) followed by thorough mixing. The absorbance at 587 nm (ε = 119 166 M^{-1} cm^{-1}) was monitored for 5 min to ensure linear reaction progress, after which the reading was halted and antioxidant (10 μL of 0.5 mM solution in PhCl) was added. The solution was thoroughly mixed and the reading were resumed. The propagation rate constant for the dye ($k_{PBD\text{-}BODIPY}$ = 8283 M^{-1} s^{-1}) and rate of initiation (R_i = 6 × 10^{-9} M s^{-1}, 1.2 × 10^{-8} M s^{-1} or 1.8 × 10^{-8} M s^{-1}), necessary to derive the kinetic data, were determined using PMC as a standard, which has an established stoichiometry of 2.0. The inhibition rate constant (k_{inh}) and stoichiometry (n) were determined, and are reported in ±SD from three independent experiments. An analogous procedure was followed when determining nitroxide formation during the autoxidation. Reactions were performed under identical conditions without addition of PBD-BODIPY in a heat-block at 100 °C wherein aliquots were removed at regular intervals and transferred to EPR tubes. EPR spectra were recorded on a Bruker EMXplus (X-band)

spectrometer equipped with an ER 4119HS cavity and the radical concentration was determined using the quantitative EPR package of the Bruker Xenon software.

Inhibited autoxidation of *n*-hexadecane at 160 °C. 10 mL of *n*-hexadecane (Alfa Aesar 95%), treated by percolation through basic alumina and silica (2 : 1 alumina/silica, with the silica packed on top of the alumina), was loaded into test tubes placed within an aluminium heat-block and each tube was purged with nitrogen *via* a capillary tube for 20 min at room temperature. While under the atmosphere of nitrogen, the block was heated to 168 °C (hexadecane had an average temperature of 160 ± 2 °C.) When the temperature had stabilized, 50 μL of the RTA stock solution (EtOAc), and when applicable, Primene solution (21 μL of 0.95 M in EtOAc) were injected. The flow of nitrogen was replaced by oxygen and aliquots (*ca.* 0.5 mL) were removed at regular intervals and cooled to room temperature. For the quantification of [ROOH], 5 μL of the sample were loaded on a well of a 96-well microplate for analysis wherein 215 μL of a mixture of 1 : 4 iPrOH/MeOH and 30 μL of a solution containing the fluorogenic coumarin phosphine dye (100 μM) were added using the automated reagent dispenser at 37 °C. After stirring for 30 seconds followed by a 5 second delay, the well was excited and the gain of fluorescence was measured every second for 60 seconds (coumarin phosphine dye: λ_{ex} = 340 nm, λ_{em} = 425 nm). The concentration of hydroperoxide in each well was determined from the rate of phosphine oxidation using the rate constant for the reaction of the dye with secondary peroxyl radicals (k = 5.1 $M^{-1}\,s^{-1}$) assuming pseudo-first-order kinetics. For EPR analysis (quantitative spin-counting), samples were diluted into benzene (either 1 : 1 or 2 : 1 benzene/hexadecane) for convenient handling. For UPLC product analysis, samples were extracted with HPLC-grade methanol prior to analysis.

UPLC analysis of *n*-hexadecane samples. A portion of an aliquot from the hexadecane oxidation (150 μL) and HPLC-grade methanol (150 μL). After separation of the layers, the methanol was transferred to a HPLC vial with a 200 μL glass insert. Column: Hypersil GOLD C-18 reverse phase column (250 mm × 4.6 mm, 5 μm). UPLC method: injection volume of 10 μL; mobile phase A (pH 5.5 10 mM ammonium acetate buffer) and mobile phase B (methanol); flow rate: 0.5 mL min^{-1}; run time: 30 min; the gradient elution method: 80% to 100% B from 0 to 10 min, hold at 100% B from 10 to 25 min, 100% to 80% B from 25 to 30 min. Elution was monitored by PDA from 190 to 390 nm and ESI+ scan from 150 to 750 *m*/*z*. The concentration

of PNX (236 nm) and PTZ (252.5 nm) were calculated from the amount remaining relative to the aliquot at 0 min. The concentration of PNX-ONE (352 nm), PTZ-ONE (370.5 nm), and PTZ-SO (269.5 nm) were calculated by calibrated curves using authentic standards.

Spectrophotometric studies of phenothiazine oxidation. To 3 mL quartz cuvettes were added 2.5 mL of *n*-hexadecane (Sigma-Aldrich ReagentPlus® 99%). After equilibration for 10 min at the desired temperature (80–100 °C), baseline correction was performed. The PTZ stock solution (50 mM in inhibitor-free HPLC-grade THF) were added to the cuvettes (final concentration of 0 μM to 900 μM). In short order, PNX-NO was added (50 mM THF) to each cuvette (300 μM) followed by mixing. The kinetic UV-VIS scan experiment was immediately started (500 nm to 200 nm) with full scans occurring at 10 minute intervals. The concentration change of PTZ-SO was determined by monitoring the increase in absorbance at 278 nm and calculating the Δ[PTZ-SO] from the $\varepsilon_{278\ nm}$ for PTZ-SO.

5.9 Supplementary Data

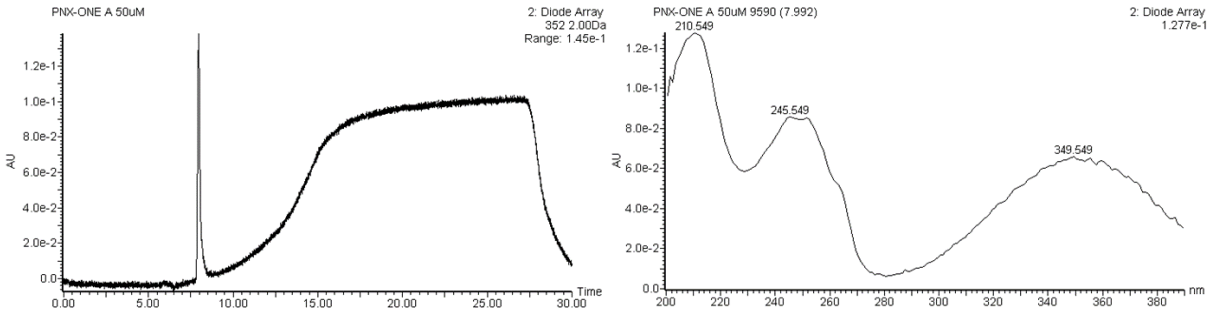


Figure 5.6. *(Left)* Representative chromatogram of PNX-ONE standard (50 µM) monitored at 352 nm; *(Right)* UV-Vis spectrum of PNX-ONE standard.

Concentration (µM)	Integral (at 352nm)	Error (±)
5	2746	194
10	5330	709
25	12578	1256
50	25392	1233
100	52536	678

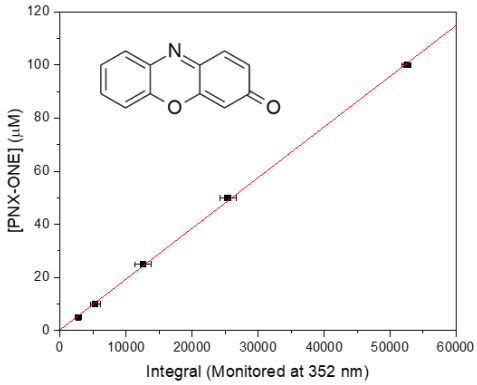


Figure 5.7. *(Left)* Table of integrals of PNX-ONE standard monitored at 352 nm; *(Right)* Calibration curve for PNX-ONE at 352 nm ($R^2 = 0.9995$, $y = 0.00191x + 0.3768$).

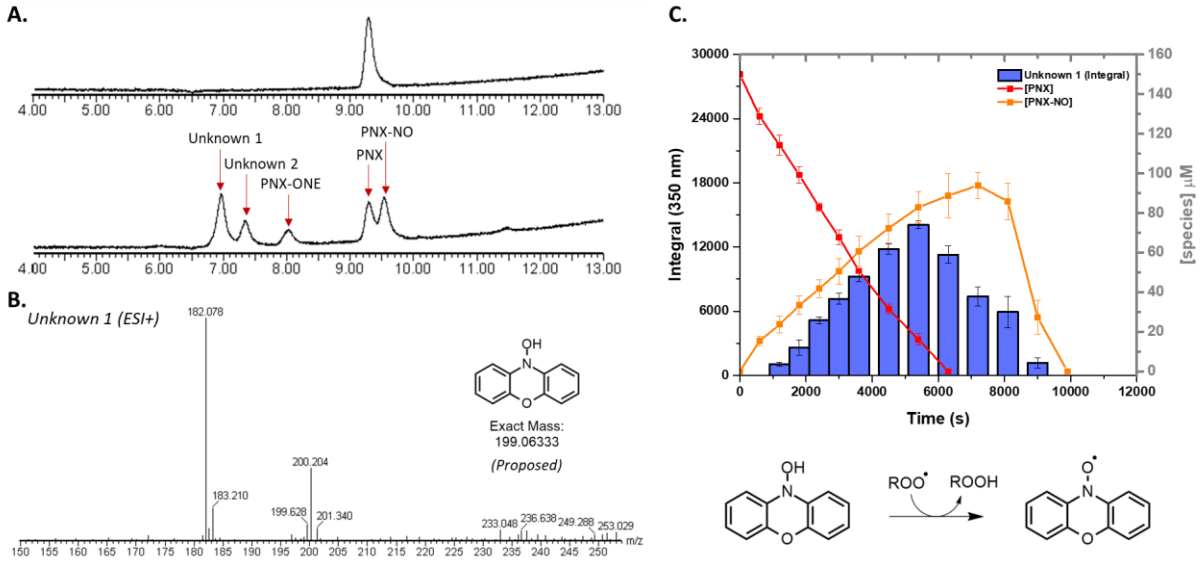


Figure 5.8. (A) *Top*: Representative UPLC-PDA trace of unoxidized PNX extracted from hexadecane (monitored at 350 nm); *Bottom*: Representative UPLC-PDA trace of PNX derived products extracted from hexadecane from an intermediate state of autoxidation (monitored at 350 nm). (B) ESI+ spectra of 'Unknown 1' (UPLC-MS). (C) The integral of 'Unknown 1' overlayed with the time-course concentrations of [PNX] and [PNX-NO].

Interestingly, in the PNX inhibited autoxidation PNX-NO is the most abundant oxidation product, accumulating to well over half of the original [PNX]. While formation of PNX-NO is not unexpected, the rapid oxidation/consumption of PNX compared to PTZ implies significant pro-oxidant activity on the part of PNX. What is not entirely clear is why PNX-NO actually increases between during the 15 minutes spanning 7200 s and 8100 s (observed by both EPR spin counting and UPLC) despite that fact that no trace of PNX can be detected by 7200 s. One would expect if the only source of PNX-NO originates from the oxidation of PNX that PNX-NO should only decrease once PNX is depleted. Of the species that can be observed by UPLC upon sample extraction, there are two products in addition to PNX-NO and PNX-ONE for which we do not have authentic standards (Fig. 5.8A). Of particular interest is 'Unknown 1' which has m/z values consistent with [M + H]+ and [M – HO]+ of a hydroxylated PNX product (Fig. 5.8B). Given the oxidative lability of PNX, it is unlikely that 1-hydroxyphenoxazine or 3-hydroxyphenoxazine would accumulate to a significant extent (as these are strong EDG which would further decrease E°). The hydroxylamine of PNX (PNX-NOH) was also considered, as it would provide a convenient source of PNX-NO in the absence of PNX. Interestingly, 'Unknown 1' increased as long as PNX is present, then sharply declined when PNX was depleted suggesting that it was being rapidly oxidized in the absence of the parent RTA and possibly caused the protracted increase of PNX-NO (Fig. 5.8C). Though we were unable to prepare/isolate PNX-NOH to further corroborate our theory,[7] the circumstantial evidence merits putting forward such a proposal.

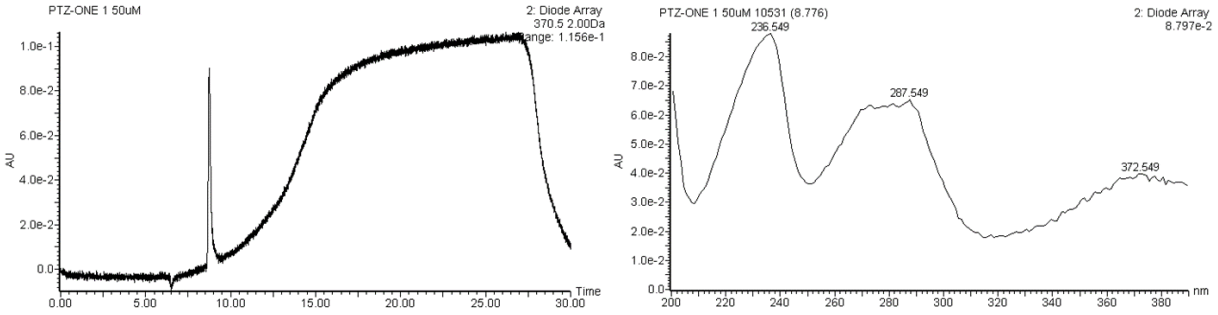


Figure 5.9. *(Left)* Representative chromatogram of PTZ-ONE standard (50 µM) monitored at 370.5 nm; *(Right)* UV-Vis spectrum of PTZ-ONE standard.

Concentration (µM)	Integral (at 370.5nm)	Error (±)
5	1587	154
25	10271	157
50	20166	575
100	38469	892
250	95120	1617

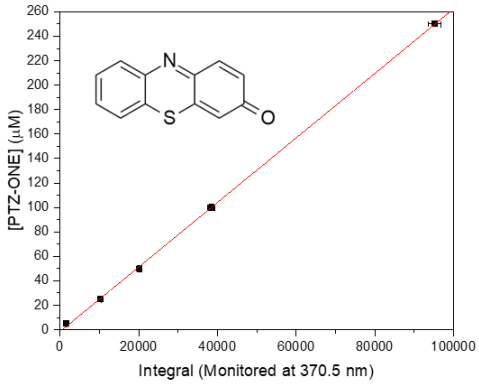


Figure 5.10. *(Left)* Table of integrals of PTZ-ONE standard monitored at 370.5 nm; *(Right)* Calibration curve for PTZ-ONE at 370.5 nm ($R^2 = 0.9998$, $y = 0.00264x - 1.3676$).

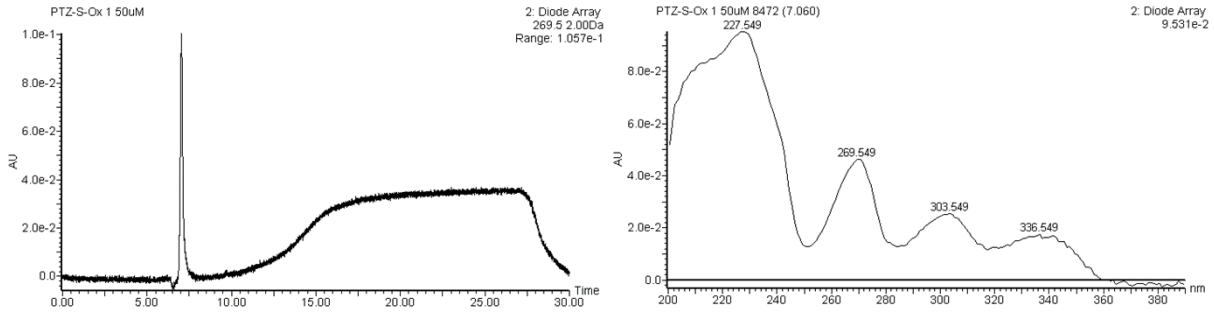


Figure 5.11. *(Left)* Representative chromatogram of PTZ-SO standard (50 µM) monitored at 269.5 nm; *(Right)* UV-Vis spectrum of PTZ-SO standard.

Concentration (µM)	Integral (at 269.5nm)	Error (±)
5	2282	127
25	15732	1778
50	28549	1161
100	56115	1153
250	140131	4974

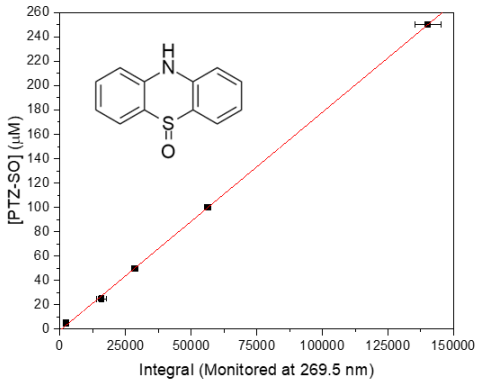


Figure 5.12. *(Left)* Table of integrals of PTZ-SO standard monitored at 269.5 nm; *(Right)* Calibration curve for PTZ-SO at 269.5 nm ($R^2 = 0.9998$, $y = 0.00179x - 0.9414$).

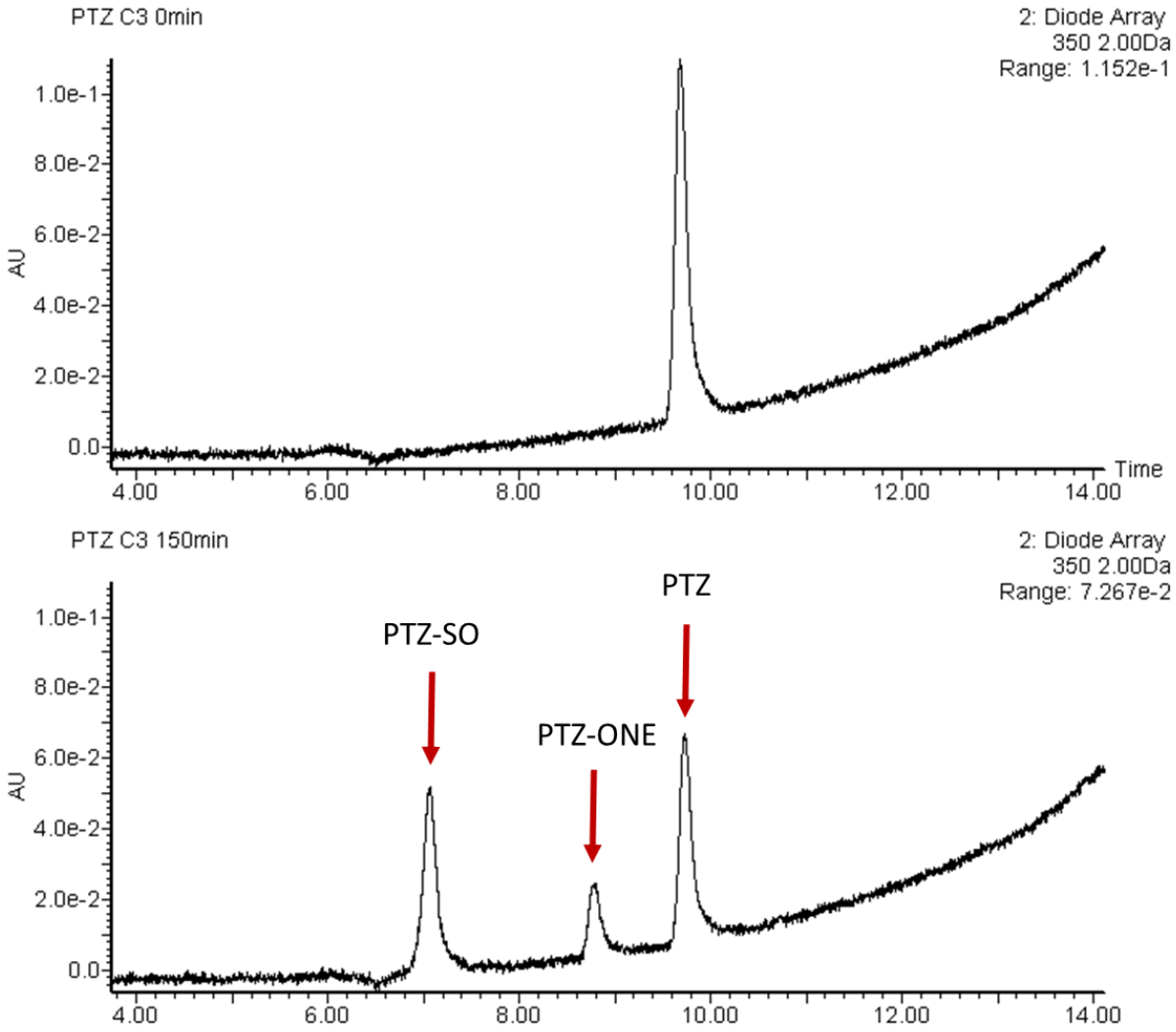


Figure 5.13. *(Top)* Representative UPLC-PDA trace of unoxidized PTZ extracted from hexadecane (monitored at 350 nm); *(Bottom)* Representative UPLC-PDA trace of PTZ derived products extracted from hexadecane from an intermediate state of autoxidation (monitored at 350 nm).

Inhibited Autoxidation with Deuterated Phenoxazine (PNX-D) in Hexadecane.

Sample Preparation. For the preparation of 10*D*-phenoxazine (PNX-D), 1 mmol (183 mg) of commercial PNX was dissolved in a minimum of MeOD and allowed to stir at room temperature for 1 hour. The MeOD was removed under reduced pressure rendering PNX-D with ≥70% deuterium incorporation. This ~70% PNX-D was dissolved in benzene-d_6 to make a 30 mM stock solution. The stock solution was vortexed with D_2O and the benzene-d_6 layer was transferred to an NMR tube for ^1H NMR to ascertain deuterium incorporation (≥95%). As a control, commercial PNX was dissolved in benzene-d_6 (30 mM) and vortexed with HPLC grade H_2O and the benzene-d_6 layer was transferred to an NMR tube for ^1H NMR.

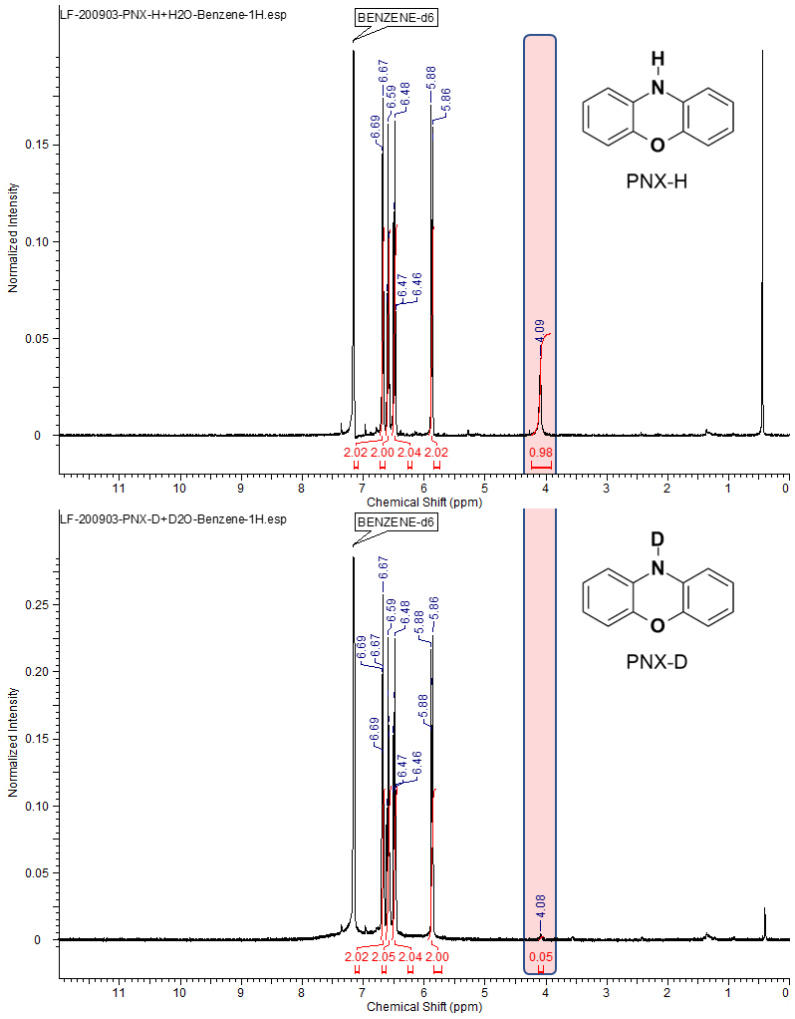


Figure 5.14. *(Top)* ^{1}H-NMR (400 MHz; benzene-d_6) of 30 mM PNX-H stock solution; *(Bottom)* ^{1}H-NMR (400 MHz; benzene-d_6) of 30 mM PNX-D stock solution.

Autoxidation of Hexadecane. The test tubes of hexadecane were continuously sparged with N_2 passed through a tube of anhydrous indicating Drierite® ($CaSO_4$, 8 mesh). The tubes were gradually heated to 160 ± 2 °C (block temperature 168 °C) and the 100 µL of either 30 mM PNX-H or PNX-D were added for a final concentration of 300 µM PNX. After the 0 s sample was taken, the N_2 was switched to O_2 (dried with $CaSO_4$) and the experiment proceeded as described in the experimental of the main text. The concentration of PNX-H/PNX-D for the first 3000 s was determined by loss of PNX using UPLC-PDA, and [ROOH] was determined in the same manner as described in the main text.

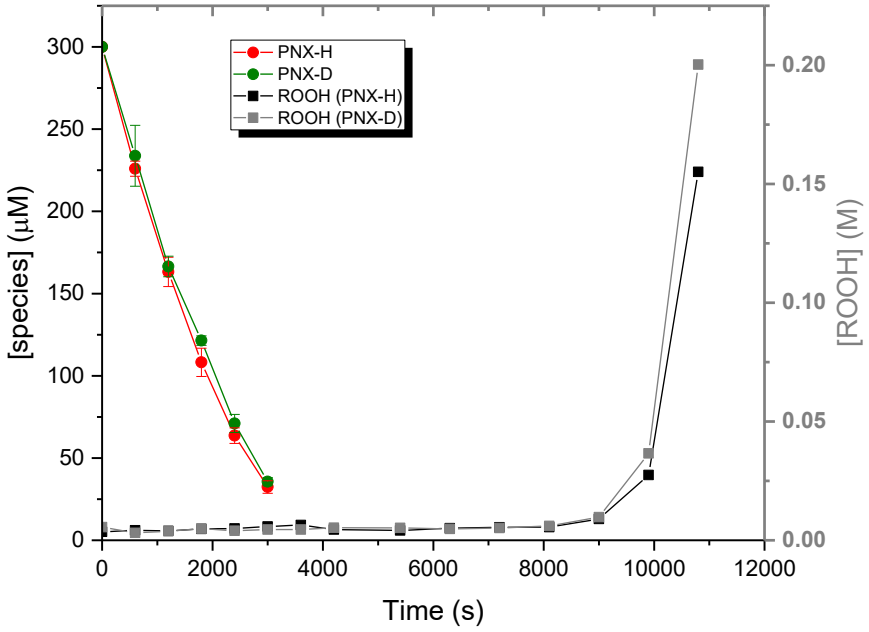
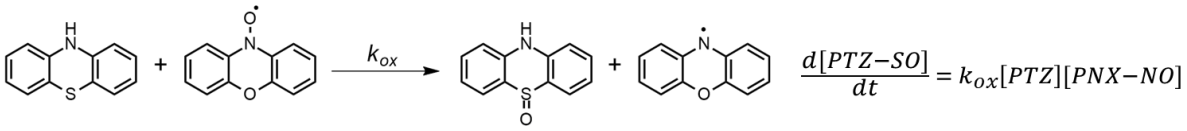


Figure 5.15. Time-course loss of PNX-H/PNX-D overlayed with [ROOH] from the autoxidation of n-hexadecane inhibited by 300 µM PNX-H/PNX-D at 160 °C.

Kinetics of the Oxidation of Phenothiazine with Phenoxazine-N-Oxyl.

Scheme 5.1 – The Oxidation of PTZ by PNX-NO.



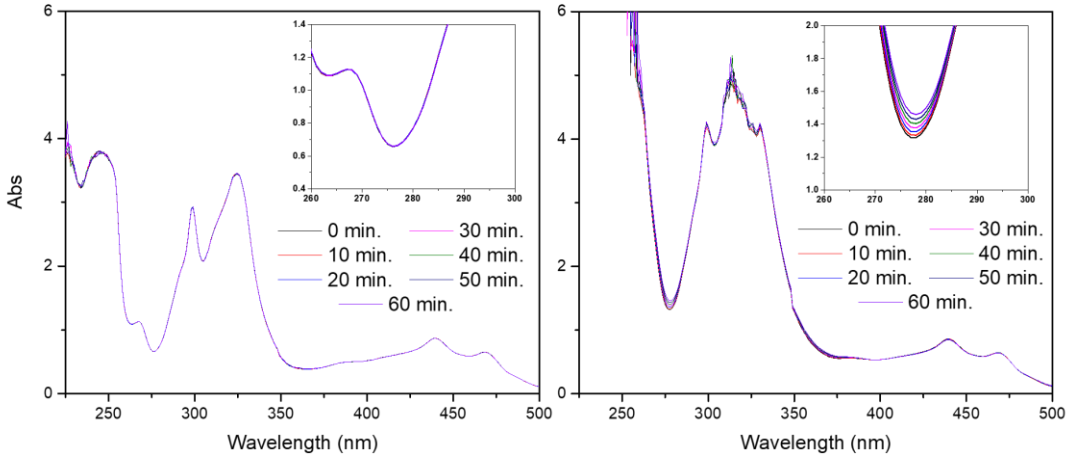


Figure 5.16. *(Left)* Kinetic UV-Vis scan (225 to 500 nm) of 300 µM PNX-NO in hexadecane at 80 °C; *(Right)* Kinetic UV-Vis scan (225 to 500 nm) of 300 µM PNX-NO with 600 µM PTZ in hexadecane at 80 °C.

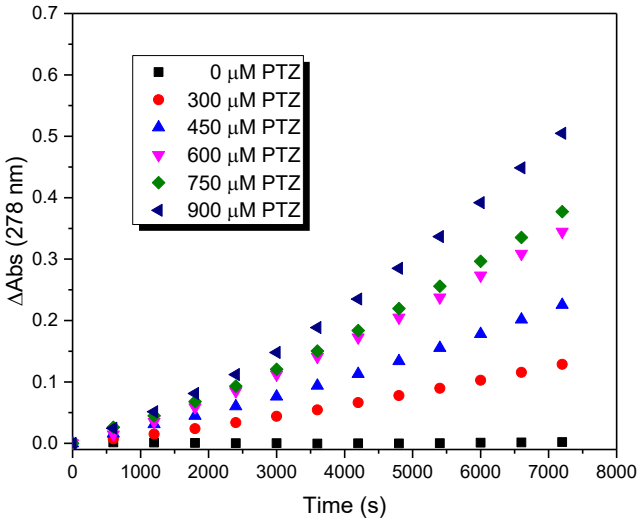


Figure 5.17. Observing the increase of absorbance at 278 nm (ε_{278} = 9129 M^{-1} cm^{-1}) with 300 μM PNX-NO at various concentrations of PTZ in hexadecane at 80 °C. *(Right)* Molar-absorptivity plot of PTZ-SO at 278 nm in hexadecane at 80 °C (ε_{278} = 9129 M^{-1} cm^{-1}).

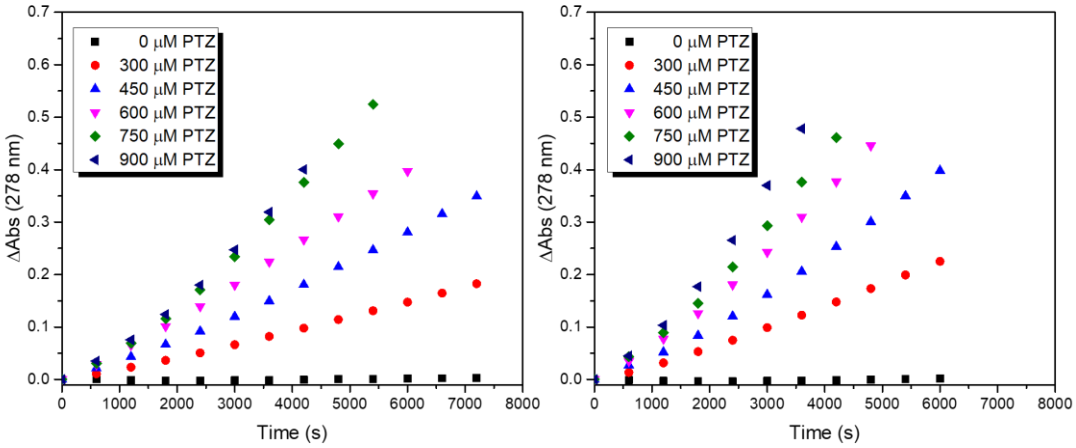


Figure 5.18. *(Left)* Observing the increase of absorbance at 278 nm (ε_{278} = 9004 M^{-1} cm^{-1}) with 300 μM PNX-NO at various concentrations of PTZ in hexadecane at 85 °C; *(Right)* Observing the increase of absorbance at 278 nm (ε_{278} = 8886 M^{-1} cm^{-1}) with 300 μM PNX-NO at various concentrations of PTZ in hexadecane at 90 °C.

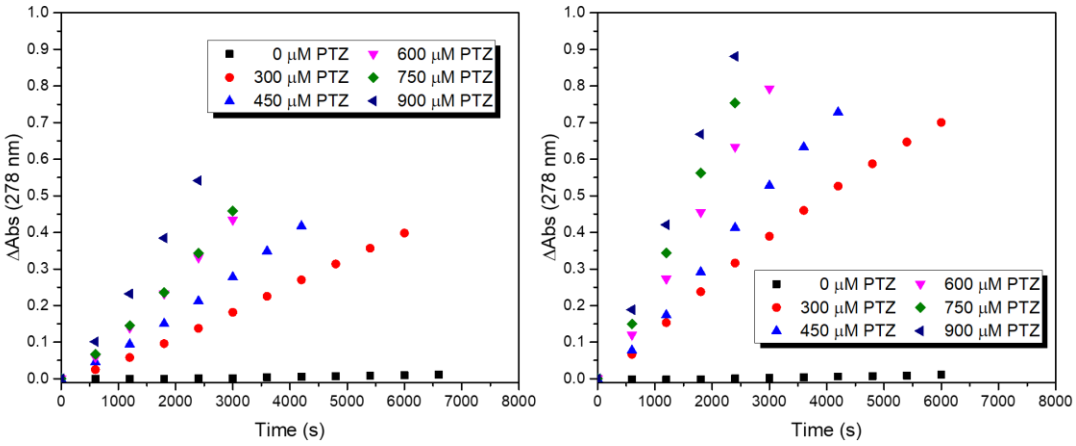


Figure 5.19. *(Left)* Observing the increase of absorbance at 278 nm (ε_{278} = 8784 M^{-1} cm^{-1}) with 300 μM PNX-NO at various concentrations of PTZ in hexadecane at 95 °C; *(Right)* Observing the increase of absorbance at 278 nm (ε_{278} = 8867 M^{-1} cm^{-1}) with 300 μM PNX-NO at various concentrations of PTZ in hexadecane at 100 °C.

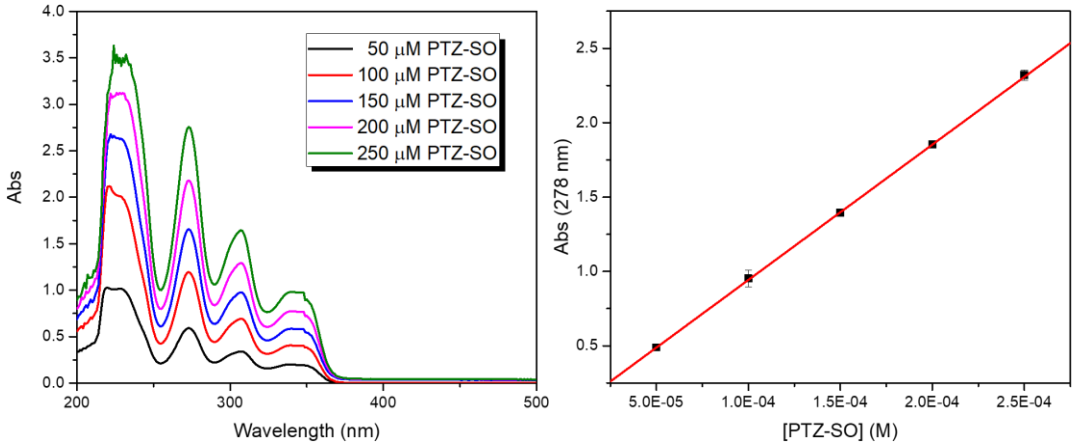


Figure 5.20. *(Left)* UV-Visible spectrum of PTZ-SO; *(Right)* Molar-absorptivity plot of PTZ-SO at 278 nm in hexadecane at 80 °C (ε_{278} = 9129 M^{-1} cm^{-1}).

Temperature (°C)	Rate Constant (M^{-1} s^{-1})	Ext Coefficient (278 nm)
80	$2.41 \pm 0.26 \times 10^{-2}$	9129
85	$3.94 \pm 0.48 \times 10^{-2}$	9004
90	$5.70 \pm 0.54 \times 10^{-2}$	8886
95	$8.21 \pm 0.51 \times 10^{-2}$	8784
100	$1.60 \pm 0.04 \times 10^{-1}$	8667

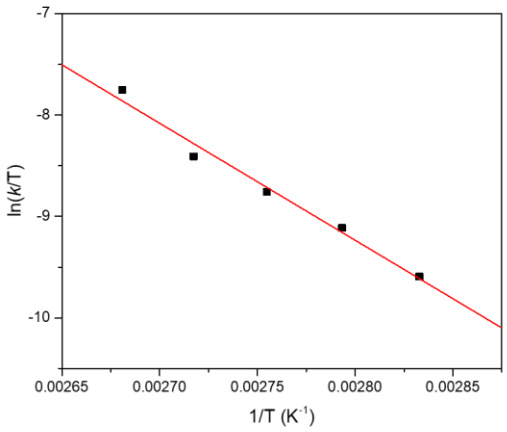


Figure 5.21. *(Left)* Table of rate constants for PTZ-SO formation (k_{ox}) at 80-100 °C; *(Right)* Eyring plot (R^2 = 0.9836, $\Delta H^{\ddagger}$ = 22.9 kcal/mol, $\Delta S^{\ddagger}$ = -1.4 cal/mol K).

5.10 References (Experimental)

(1) Poon, J.-F.; Farmer, L. A.; Haidasz, E. A.; Pratt, D. A. Temperature-Dependence of Radical-Trapping Activity of Phenoxazine, Phenothiazine and Their Aza-Analogues Clarifies the Way Forward for New Antioxidant Design. *Chem. Sci.* **2021**, *12* (33), 11065–11079. https://doi.org/10.1039/D1SC02976B.

(2) Haidasz, E. A.; Pratt, D. A. Diazaphenoxazines and Diazaphenothiazines: Synthesis of the "Correct" Isomers Reveals They Are Highly Reactive Radical-Trapping Antioxidants. *Org. Lett.* **2017**, *19* (7), 1854–1857. https://doi.org/10.1021/acs.orglett.7b00615.

(3) Houston, D. F.; Kester, E. B.; DeEds, F. Phenothiazine Derivatives: Di-Oxygenated Compounds. *J. Am. Chem. Soc.* **1949**, *71* (11), 3819–3822. https://doi.org/10.1021/ja01179a068.

(4) Barret, R.; Daudon, M. Synthesis of Quinone-Imines with Iodoxybenzene. *Synth. Commun.* **1990**, *20* (10), 1543–1549. https://doi.org/10.1080/00397919008052871.

(5) Shindo, K.; Ishikawa, S.; Nozoe, T. Cyclohepta[b][1,4]Benzothiazines and Their Diazine Analogues. 1. Formation and Reactions of Cyclohepta[b][1,4]Benzothiazines. *Bull. Chem. Soc. Jpn.* **1985**, *58* (1), 165–171. https://doi.org/10.1246/bcsj.58.165.

(6) Griesser, M.; Shah, R.; Van Kessel, A. T.; Zilka, O.; Haidasz, E. A.; Pratt, D. A. The Catalytic Reaction of Nitroxides with Peroxyl Radicals and Its Relevance to Their Cytoprotective Properties. *J. Am. Chem. Soc.* **2018**, *140* (10), 3798–3808. https://doi.org/10.1021/jacs.8b00998.

(7) Attempts to reduce PNX-NO to the corresponding hydroxylamine using conventional reductants (such as hydrazine) resulted to in near quantitative formation of PNX.

Chapter 6

Enhancing High Temperature Efficiency of Phenoxazine/Phenothiazine-Type Radical-Trapping Antioxidants: Teeing-Up Alkyl-Sidechains to be Co-Reductants

6.1 Foreword

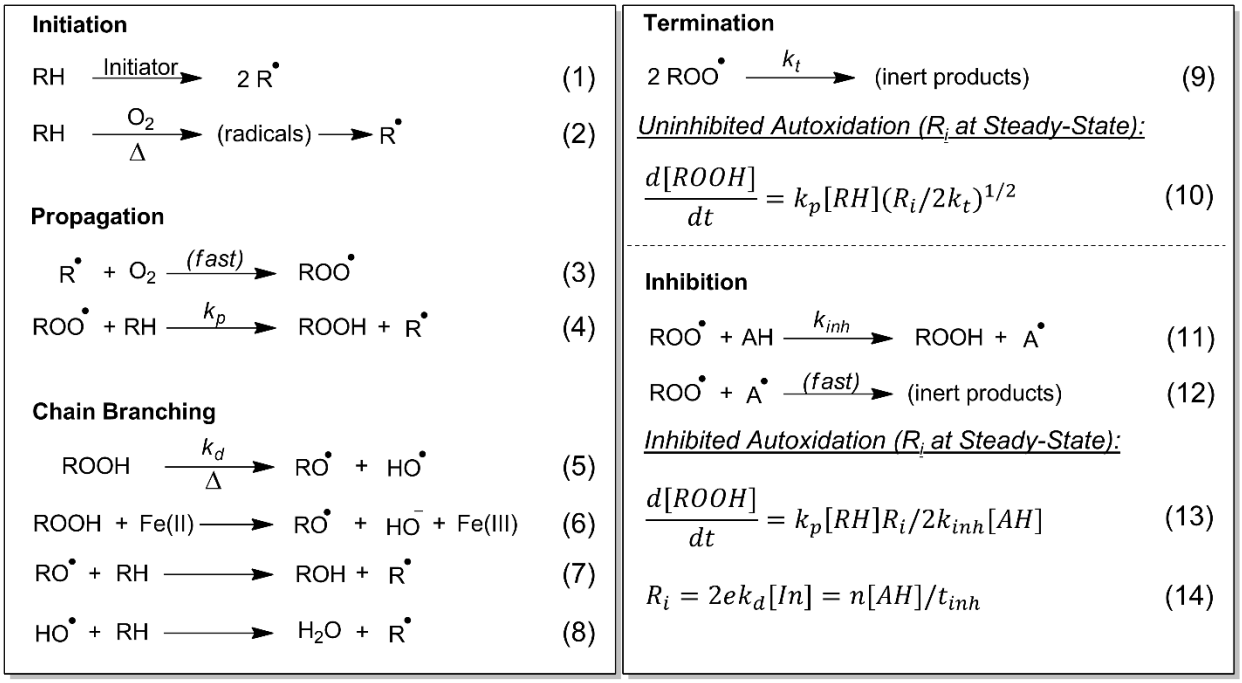
The contents of Chapter 6 are unpublished work which represent a concerted attempt to understand the effect(s) of 1', 2' and 3' alkyl substituents on the inhibitory activity of PNX and PTZ compounds in high-temperature autoxidations of a saturated substrate (ca. 160 °C in *n*-hexadecane), intended to be a model of inhibition of lubricant oxidation. Direct comparisons to hindered phenolic RTAs, an industry standard, showed these PNX/PTZ-based compounds protract autoinitiated oxidation with the most potent examples increasing the inhibited period 8-fold compared to an equivalent concentration of BHT, the archetype antioxidant. However, what became plainly evident is that these compounds operate in a stoichiometric paradigm rather than the putative catalytic one. Thus, an important critique of previous proposals of catalytic inhibition is provided, as well as a reflection on the future direction(s) for this area of research.

6.2 Introduction

As far as additives go, antioxidants are rather ubiquitous in wide variety of applications, and are routinely added to a plethora of petroleum-derived materials (plastics, rubbers, fuels etc.).[1] The widespread use of antioxidants is born out of a necessity to stifle the relentlessly spontaneous peroxidation of hydrocarbons in a chemical process often referred to as *autoxidation*. Autoxidation is a radical mediated chain-process which involves initiation, propagation, termination and (under certain circumstances) branching reactions. The net-effect is a highly efficient, but generally highly undesirable, oxidation process. Hindered phenols, such as BHT, are radical-trapping antioxidants (RTAs), and efficiently trap a maximum of 2 propagating peroxyl radicals ($ROO^{\bullet}$) per molar equivalent, and are often the only intervention required. Lubricants used in the combustion engines of automobiles, aircraft and other heavy-machinery represent a more extreme chemical environment where higher operating temperatures foster a rather prodigious amount of radical initiation, requiring a more substantial quantity of RTA (≥1

wt. %) then would be added to most materials. Moreover, these conditions erode the efficacy of BHT and related hindered phenolic RTAs, such that they generally trap only a single chain-propagating radical.

Scheme 6.1 – Basic Autoxidation Scheme.



In the absence of any formal initiator, liquid-phase autoxidation at high temperatures (>100ºC) can initialize by O_2 acting directly on the substrate (Eq. 6.2), until enough hydroperoxide (ROOH) has been "seeded" and thermolysis of ROOH becomes the dominant initiating pathway (Eq. 6.5).[2] Under these conditions peroxidation is said to be autoinitiated since the product of the radical chain process is the ROOH initiator. The autoinitiation process has been studied in some detail and is reliably described by Eq. 6.15 (assuming that chains are of sufficient length and initiation is only caused by unimolecular homolysis of ROOH).[3,4] During this period there is a concomitant increase in the rate of initiation (R_i) until non-initiating acid-catalyzed decomposition of ROOH becomes a competitive process and a steady-state is reached (Eq. 6.16).

$$\frac{d[ROOH]}{dt} = k_p[RH](k_d/k_t)^{1/2}[ROOH]^{1/2} \qquad (6.15)$$

$$(d[ROOH]/dt)_{ss-f} = (d[ROOH]/dt)_{ss-d} \qquad (6.16)$$

Naturally the economics of inhibiting these types of oxidations would be substantially improved if far less RTA were required for an equivalent effect. In the 1970s, several reports of RTAs that exhibited catalytic activity in a range of substrates emerged,[5] typically at elevated temperatures. Bolsman and co-workers, performing a systematic SAR in di-*tert*-butyl peroxide-initiated paraffin oil autoxidations (130°C) estimated radical trapping stoichiometries of 41 and 510 for diphenylamine (DPA) and 2,2,6,6-tertamethylpiperidinyloxyl (TEMPO), respectively, using their method.[6] The former result was of particular interest in the high temperature lubricant niche as alkylated diphenylamines (ADPA) were already in widespread use as RTA additives. Under Bolsman's conditions, the persistence/stability of the nitroxide intermediate was the key feature that correlated with catalytic turnover, and their results with 4,4'-di-*tert*-butyldiphenylamine (n = 52) seemed to corroborate this. Korcek and co-workers of the Ford Motor Company in 1995, finding that the nitroxide of ADPA could be converted back to the amine in their peroxide-initiated *n*-hexadecane system (160°C), proposed that regeneration of ADPA occurred via a thermal decomposition of an alkoxyamine intermediate, which was presumed to form by the opportunistic trapping of transient alkyl radicals by the nitroxide (Fig. 6.1).[7] This explanation was evidently rather persuasive, as the mechanistic proposal has proliferated within the relevant body of literature during the ensuing years.[8–11] We have also been proponents of this reaction framework, having studied the alkoxyamine decomposition mechanism in detail.[12] Furthermore part of our design rationale for heterocyclic diarylamine RTAs (**6.1**) and the enhanced activity we observed relative to ADPA at elevated temperatures, was similarly informed by this interpretation.[13,14]

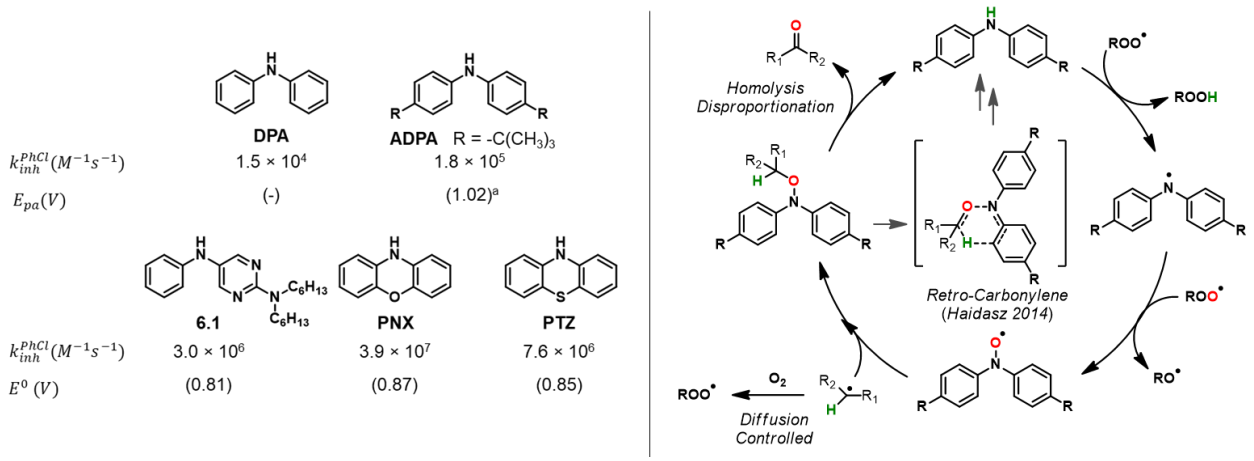
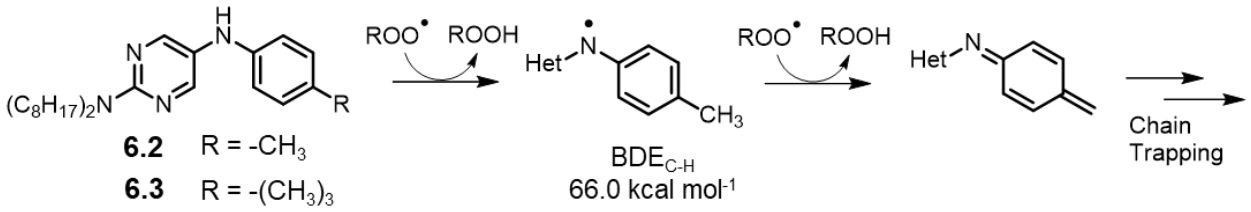


Figure 6.1. (Left) Basic k_{inh} and electrochemical data for diarylamine compounds. (Right) Korcek mechanism proposed for catalytic inhibition of diarylamines at elevated temperatures.

The results of our most current work in this area, however, have been difficult to reconcile with this mechanistic hypothesis. For instance, in a recent paper where we attempted to map out the structure and function of phenoxazine (PNX), phenothiazine (PTZ) and several N-heterocyclic variants (aza-PNX/PTZ),[15] their behaviour (at 160ºC in *n*-hexadecane) seemed inconsistent with the anticipated trends. Under continuous O_2 flow, a maximum of 66% of the PNX mass balance was nitroxide, the key intermediate for hypothetical alkoxyamine formation. PTZ meanwhile produced an undetectable amount of nitroxide, instead forming large quantities of the inactive sulfoxide. Yet, PTZ outperformed PNX by a sizable margin under these conditions (242 vs. 152 min). Another example of the incongruency with the catalytic hypothesis can be found in our recent paper describing an unanticipated large enhancement effect of *p*-tolyl on our premier heterocyclic diarylamine design (**6.2**).[16] We had forecasted that installing a large quaternary alkyl group in the 4-position on the phenyl of **6.1**, such as *tert*-butyl (**6.3**), would give rise to an even more potent high-temperature RTA by yielding a more persistent nitroxide intermediate. However, *n*-hexadecane autoxidations at 160°C were only modestly better inhibited by **6.3** compared to **6.1** (~1.4-fold), and this result was overshadowed by the dramatic increase observed for less-hindered **6.2** (2.8-fold). Computations suggested that the benzylic hydrogens of the aminyl radical intermediate of **6.2** would be quite labile (C-H BDE = 66.0 kcal/mol) and may provide additional opportunities for trapping chain-propagating peroxyl radicals (Scheme 6.3). Attributing this relatively large increase in t_{inh} to the additional chains broken by oxidizing a *p*-

methyl substituent, an *n* which would be on the order of single digits, appeals to stoichiometric arguments rather than the putative catalytic model.

Scheme 6.2 – Proposed Methyl Substituent Effect of Compound 6.2.



The aim of this study is to expand on both of these aforementioned works by studying the effect of 1', 2' and 3' benzylic alkyl substituents on the PNX and PTZ scaffolds. As our work with **6.1-6.3** only demonstrated the effect of *p*-methyl on a single RTA scaffold, the present study evaluates the generality of the phenomenon among other activated aromatic amines, and addresses various other benzylic alkyl substituents which were not covered in the previous papers (ethyl, isopropyl, etc.). In addition to fleshing out the SAR, with respect to inhibition at elevated temperatures, we identify several key oxidation products which may help elucidate possible inhibition mechanisms as well as provide insight into the overall nature of RTA behaviour in the system (stoichiometric vs. catalytic).

6.3 Results

The *n*-hexadecane autoxidations were carried out in similar fashion to those described in our previous publications.[15,16] Upon receiving the hexadecane it was percolated through silica (F60) and alumina-B to remove peroxides that may have accumulated in storage. Under a continuous flow of N_2 (0.4L/min/tube), the test tube block was heated (168°C) until the temperature stabilized and the RTAs were added (typically a final [AH] of 150 μM). After taking an initial sample, the N_2 flow was switched for O_2 and samples were taken at regular intervals. The samples were analyzed for [ROOH] using a kinetic-based fluorescence assay (Fig. 6.2A) which we have previously described. When applicable, hexadecane samples were extracted with methanol and analyzed by UPLC to quantify loss of RTA and/or formation of new oxidation products.

In previous work we used either DPA or ADPA as reference compound given the widespread recognition of alkylated DPAs as 'the standard' catalytic RTA. However, since the occurrence of catalytic RTA activity is a point of scrutiny in this work, we elected to use explicitly stoichiometric RTAs as the basis of comparison going forward. Hindered phenols 4-methyl-2,6-di-*tert*-butylphenol (BHT) and 4,4'-methylenebis(2,6-di-*tert*-butylphenol) (Bis-BHT) are suitable for this purpose as they are quite stable and have previously been studied under similar conditions.[17] Under our conditions the inhibited period (t_{inh}), which we define as the induction time before autoinitiation of autoxidation, for BHT at 150 μM was 78±10 min (Fig. 6.2B).[18] Using the same concentration of Bis-BHT (150 μM) or BHT at twice the starting concentration (300 μM), the inhibited period was about twice as long (149±10 and 147±10 min respectively). While the t_{inh} scaled in a linear fashion with molar equivalents of phenol, it should be noted that -d[BHT]/dt increases substantially in the latter half of inhibition which underscores that n cannot be calculated with Eq. 6.14 as R_i is not a constant.

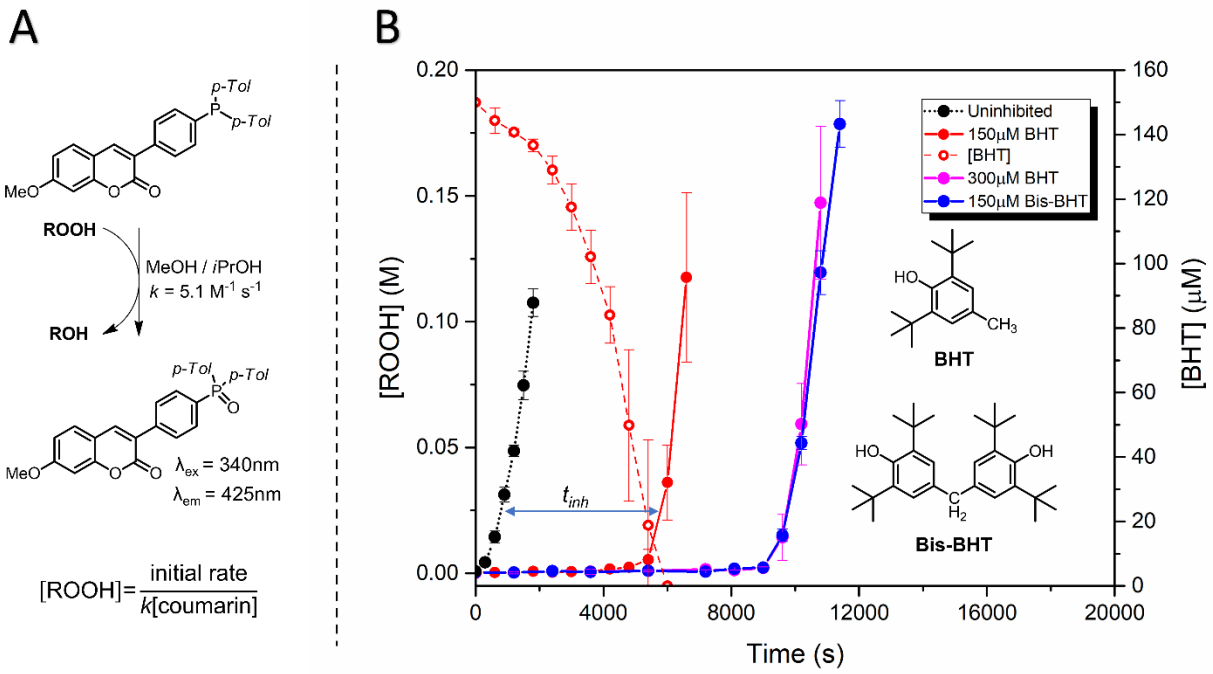


Figure 6.2. (A) Phosphine-coumarin based fluorescence probe for determining [ROOH] in autoxidation samples. (B) Autoxidation of *n*-hexadecane at 160 °C with constant flow of O_2 (0.4 L/min). Filled circles are [ROOH] concentration (left-axis), empty circles are remaining concentration (starting from 150 μM) of BHT (right-axis).

After benchmarking the hindered phenols, the first panel of compounds we prepared and subsequently tested (all at 150 μM) were **6.4**-**6.11** (Fig. 6.3), 3,7-di-alkyl PNXs and PTZs with each of methyl, ethyl, *iso*-propyl and *tert*-butyl substitution. Similar to our observations with **6.1**-**6.3**, the methyl containing structures (**6.4** and **6.8**) were substantially more effective than their respective unsubstituted and *tert*-butyl substituted (**6.7** and **6.11**) variants. The PTZ compounds were systematically superior to the PNX compounds, consistent with the poor oxidative stability of PNX we previously reported; however we found it interesting that the trends of the ethyl and *iso*-propyl containing structures varied significantly between the 2 scaffolds (**6.4** > **6.5** > PNX > **6.6** ~ **6.7**; **6.10** > **6.9** > **6.8** > **6.11** ~ PTZ), with **6.9** and **6.10** being particularly effective (473±10 and 553±10 min respectively).

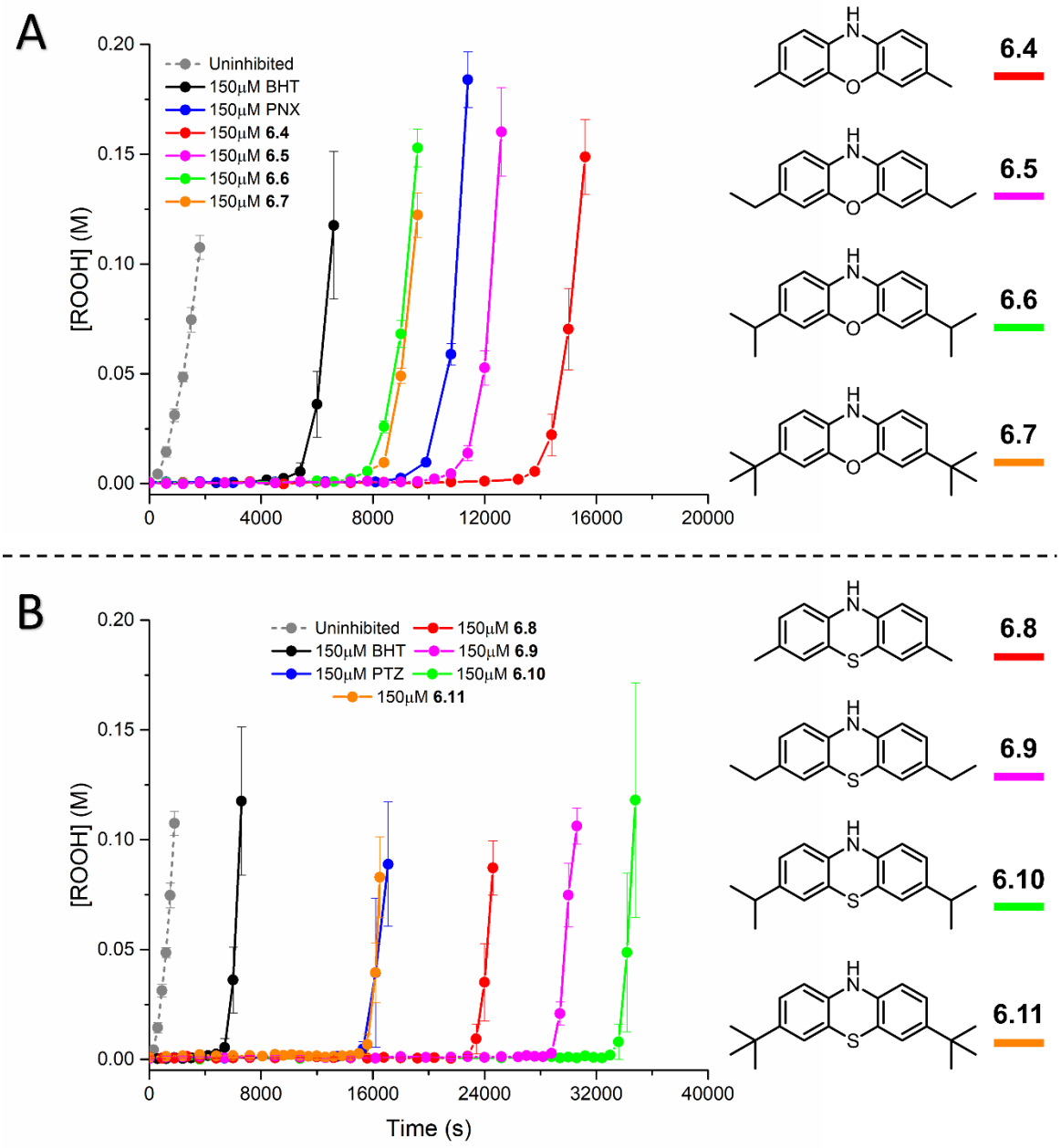


Figure 6.3. Autoxidation of *n*-hexadecane at 160 °C inhibited by (A) 3,7-di-akyl-PNX and (B) 3,7-di-akyl-PTZ (methyl, ethyl, isopropyl, *tert*-butyl).

Having established the relationship between alkyl group structure with respect to t_{inh}, we attempted to identify some of the key oxidation products involved in the inhibition. Noting a rather conspicuous increase in fluorescence when the autoxidation was inhibited with **6.4**,

extraction of the samples (MeOH) followed by TLC helped us identify the initial rapid formation of 3-formyl-7-methylphenoxazine (**6.12**) followed by a more gradual formation of 3,7-diformylphenoxazine (**6.13**). Preparing an authentic standard of **6.12** facilitated the preparation of 3-methylphenoxazine (**6.14**), both of which were tested and compared against **6.4**. While **6.14** inhibited longer than PNX (192±10 vs. 152±10 min), it was less than **6.4** (224±10 min) Curiously, **6.12** consistently performed better (266±10 min) than **6.4** and all of the alkylated PNX derivatives, indicating that the oxidation product of **6.4** was actually a superior RTA under these conditions. The primary oxidation product of **6.14**, 3-formylphenoxazine (**6.15**), while somewhat competent as an inhibitor was outclassed by **6.12** (104±10 vs. 266±10 min) which underscores that the methyl substituent is key to the longer inhibition. Apart from chain trapping that may occur during the oxidation of the methyl group of **6.12**, a significant amount of **6.13** is formed *in situ* which is also a very active RTA (204±10 min). Monitoring the loss of **6.4**, **6.12** and **6.14** and subsequent formation of oxidation products (Fig. 6.4C-E) showed that their rates of oxidation were quite distinct from each other. Within the first 10 minutes, where one would expect peroxide concentrations to be uniformly low, only 30% of **6.4** remained while 67% and 87% remained for **6.14** and **6.12**, respectively. These may correspond to their differences in redox potential (0.74 V, 0.81 V and 0.99 V) which would be consistent with a direct electron-transfer to O_2 being responsible for their consumption. As this process would be pro-oxidant in nature, the oxidation of the first methyl group on **6.4** may not be a *net* radical trapping process, resulting in an overall lower t_{inh} compared to **6.12**. It should be noted though that while the conversion of **6.12** and **6.14** to their corresponding aldehydes is relatively efficient (58% and 70%, respectively), the mass balance of **6.4** was comparatively meagre (~18%) indicating that other oxidation products (ones that apparently are not extracted with MeOH) are produced but not accounted for. To further exemplify the influence of the methyl (increased *n*) and formyl groups (increased stability) we also carried out autoxidations inhibited by **6.16**-**6.19** which have other electron-withdrawing groups (-CN and -NO_2) with and without methyl substituents. We found that these followed the same trend as **6.12** vs. **6.15** and both 3-Me-7-CN-PNX (**6.17**) and 3-Me-7-NO_2-PNX (**6.19**) inhibited longer than **6.14**. A summary of the t_{inh} data is in Table 6.1.

Table 6.1. Times of Inhibition for Substituted PNX and PTZ Derivatives in Hexadecane Autoxidations

ID	*Substituent(s)*	t_{inh} *(min)*	*Relative to BHT* ($t_{inh,BHT}/t_{inh}$)	E^o *vs. NHE (V)*
PNX	-	152 ± 10	1.95	0.87
6.4	3,7-Me	224 ± 10	2.87	0.74
6.5	3,7-Et	182 ± 10	2.33	0.75
6.6	3,7-iPr	124 ± 10	1.59	0.75
6.7	3,7-tBu	127 ± 10	1.63	0.75
6.14	3-Me	192 ± 10	2.46	0.81
6.15	3-Form	104 ± 10	1.33	1.06
6.12	3-Form-7-Me	266 ± 10	3.41	0.99
6.13	3,7-Form	204 ± 10	2.62	1.24
6.16	3-CN	154 ± 10	1.97	1.13
6.17	3-CN-7-Me	241 ± 10	3.09	1.03
6.18	3-NO_2	169 ± 10	2.17	1.15
6.19	3-NO_2-7-Me	210 ± 10	2.69	1.08
6.35	3-CycHex	160 ± 10	2.05	0.80
6.32	3-Phen	106 ± 10	1.36	0.85
PTZ	-	242 ± 10	3.10	0.85
6.8	3,7-Me	380 ± 10	4.87	0.74
6.9	3,7-Et	473 ± 10	6.06	0.74
6.10	3,7-iPr	553 ± 10	7.09	0.74
6.11	3,7-tBu	247 ± 10	3.17	0.75
6.20	3-Me	401 ± 10	5.14	0.80
6.21	3-Form	221 ± 10	2.83	1.01
6.24	3-Form-7-Me	267 ± 15	3.42	0.95
6.25	3-Et	489 ± 10	6.27	0.80
6.26	3-iPr	429 ± 10	5.50	0.80
6.27	3-CycHex	510 ± 10	6.54	0.79
6.29	3-Phen	216 ± 10	2.77	0.84
6.28	3,7-CycHex	592 ± 10	7.59	0.74
6.33	3-tBu	217 ± 10	2.78	0.80
6.34	3-*n*Bu	524 ± 10	6.72	0.79
BHT (150 μM)	-	78 ± 10	(1)	-
BHT (300 μM)	-	147 ± 10	1.88	-
Bis-BHT	-	149 ± 10	1.91	-

(a) Times of inhibition for autoxidation of *n*-hexadecane at 160 ºC with constant flow of O_2 (0.4 L/min). Initial RTA concentration [AH] was 1.5×10^{-4} M unless otherwise indicated. Estimated error reflects sampling interval at during autocatalytic period (ca. 10 min) *or* the calculated standard deviation of 3 replicate experiments (whichever was larger, nearly always the former).

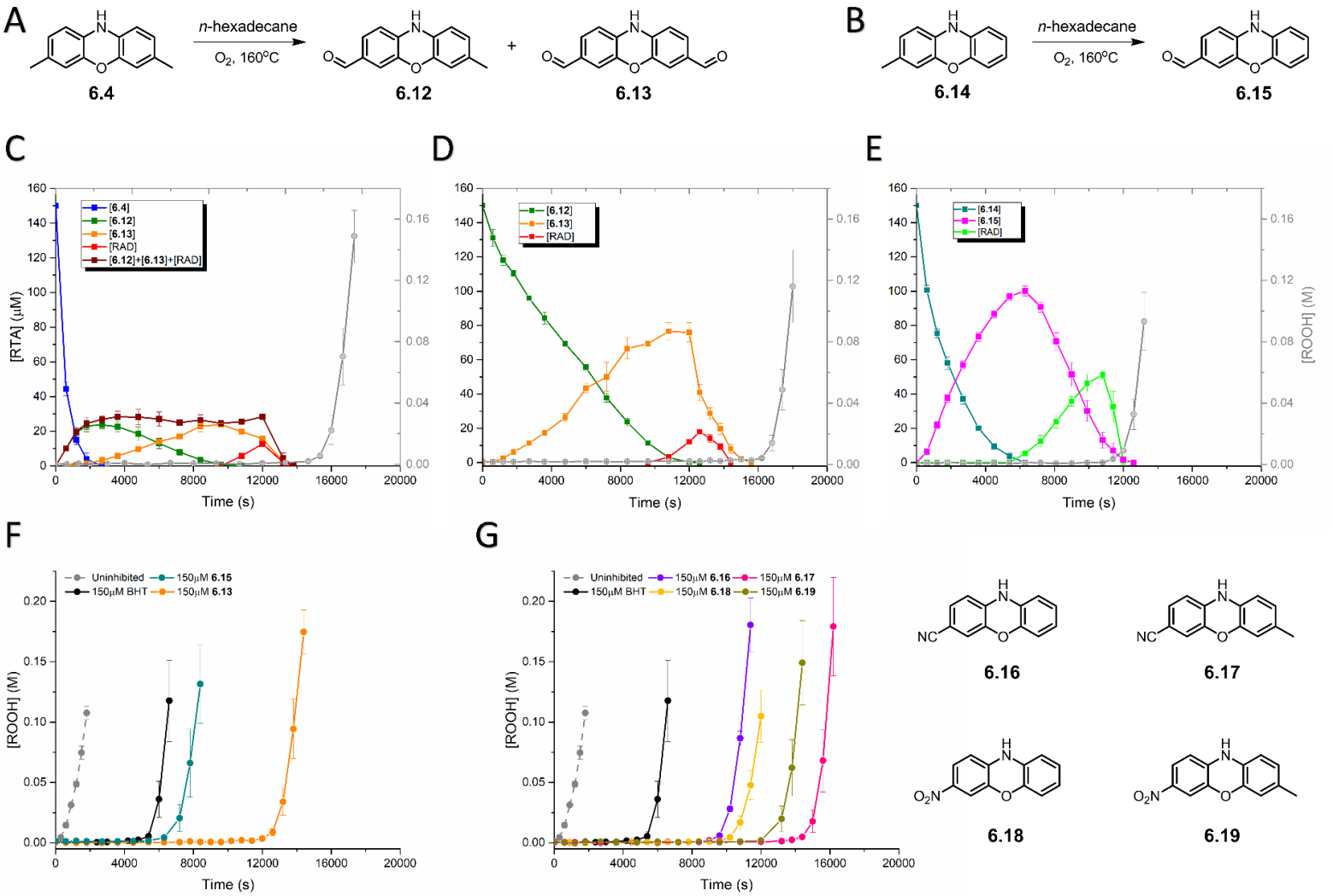


Figure 6.4. (A) Autoxidation products of **6.4 and 6.12** (B) and **6.14**. (C-E) Time course loss of RTA and formation of oxidation products for (C) **6.4**, (D) **6.12** (E) and **6.14**. The oxidation products were quantified by UPLC calibrated using authentic standards. The "[RAD]" is the concentration of persistent radical detected in the samples by EPR. These are likely the nitroxides of **6.13** (red) and **6.15** (green). (An EPR of **6.15** oxidation is shown in 6.10) (F) Autoxidation of *n*-hexadecane inhibited by **6.13** and **6.15**. (G) Inhibition with other EWG containing PNX compounds.

Anticipating analogous chemistry for *p*-methyl phenothiazines, we prepared 3-methylphenothiazine (**6.20**) along with its anticipated oxidation products: 3-formylphenothiazine (**6.21**), the sulfoxide of **6.20** (**6.22**) and the sulfoxide of **6.21** (**6.23**). Analyzing product formation during the autoxidation with **6.20**, we found that oxidation was initially bifurcated between **6.21** and **6.22**, while **6.23** began to accumulate ~3 h into the experiment. Assuming that **6.23** derives only from subsequent oxidation of **6.21**, the peak conversion of **6.21** and **6.22** was 17% and 15%, respectively. Unlike PTZ sulfoxide(s), which we have shown previously do not inhibit autoxidation,[15] **6.21** performs nearly at parity with PTZ (221±10 vs. 242±10 min) and its *in situ* formation should contribute to the protracted inhibition of **6.20** (401±10 min). Interestingly, unlike **6.12**, the 3-formyl-7-methylphenothiazine (**6.24**) was not an improvement (267±15 min) over **6.20** indicating that the EWG is not a benefit to the PTZ scaffold. The disappearance of **6.20** is much lower than the analogous PNX (**6.14**) which is consistent with the slower electron-transfer kinetics of the PTZ scaffold.[15,19]

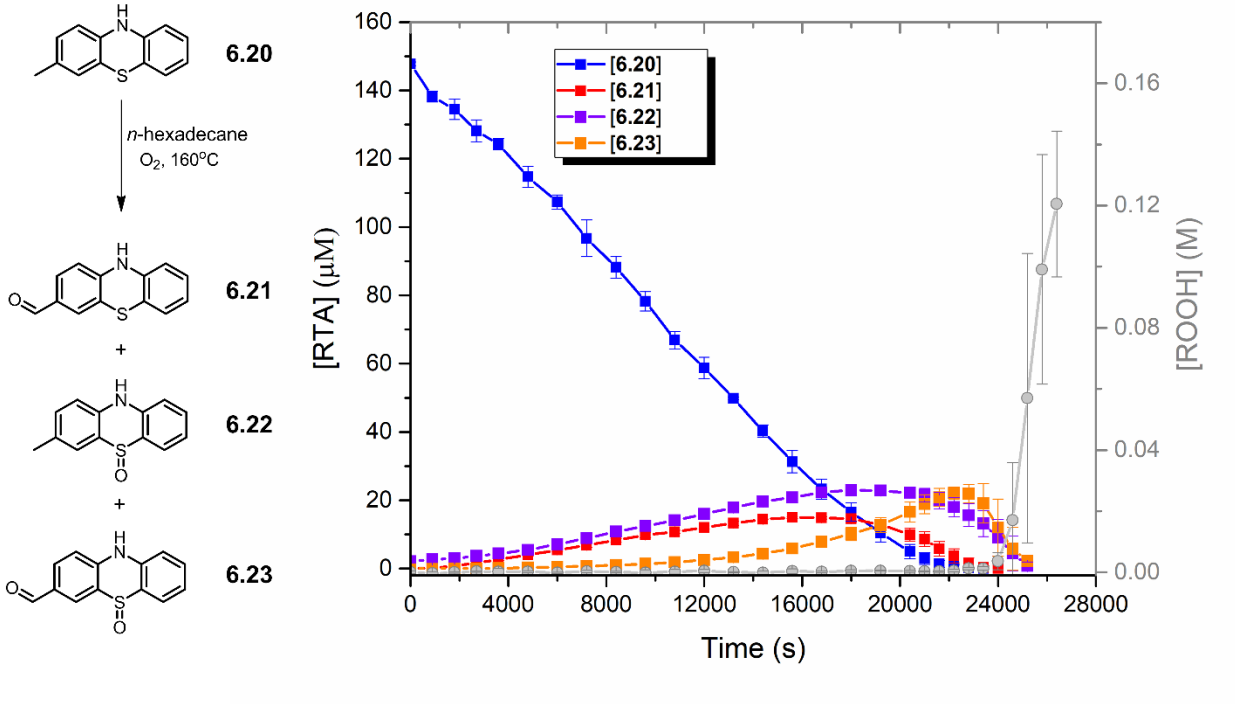


Figure 6.5. Time course loss of **6.20** and the formation of major oxidation products in *n*-hexadecane at 160 °C with O_2.

The phenomena with the 3-methyl PNX and PTZ compounds seems to be the same observed with **6.2**, and their mechanism of action would be, to a first approximation, the same. We were surprised, however, that 3,7-dimethylphenothiazine **6.8** (380±10 min) was surpassed by the ethyl and *iso*-propyl containing analogues **6.9** (473±10 min) and **6.10** (553±10). We prepared 3-ethyl (**6.25**) and 3-*iso*-propylphenothiazine (**6.26**) and found that they too had protracted inhibition times (489±10 and 429±10 min respectively) compared to **6.20**. We wondered about the fate of **6.10**/**6.26** in particular as they would not be able to oxidize to form products analogous to **6.21** (i.e., aldehyde or ketone). Using DFT (M06-2X/cc-pVTZ)[20] we looked at the analogous iminoquinone methide intermediate of **6.26** (iminoquinone *iso*-propide) and found that the C-H bond on the β-carbon of the propyl moiety (C-H BDE = 62.5 kcal/mol) was even weaker than that of the benzylic C-H of the aminyl radical (C-H BDE = 67.9 kcal/mol). The barrier for a HAT to methylperoxyl was 20.7 kcal/mol (Fig. 6.6A) which would result in a 3-α-methyl styryl phenothiazine radical. Transposed into a rate constant, using transition state theory and assuming T = 433K, the calculation would suggest 322 $M^{-1}s^{-1}$, though this seems overly pessimistic even if you statistically correct for the number of H-atoms available (6 × 322 $M^{-1}s^{-1}$ = 1932 $M^{-1}s^{-1}$) particularly when you consider the weak C-H bond on 1,4-cyclohexyldiene has a BDE of ~71 kcal/mol yet the HAT reaction with peroxyl has rate constant of 1480 $M^{-1}s^{-1}$ at only 30 ºC. Nevertheless, the weakness of this C-H bond can be attributed to the high stability of the PTZ radical relative to MeOO•, as well as rearomatization going from propide to the PTZ radical. An alternative to the HAT pathway would be the tautomerization of the propide to form the α-methylstyryl derivative of PTZ (Figure 6.6B), also thermodynamically driven by rearomatization, which would go on to trap a peroxyl through the PCET mechanism. Unlike the carbaldehydes formed with **6.14**, **6.20**, etc., we found it rather unlikely that the proposed α-methyl styryl would be a stable endpoint product that could be tracked. The number of different oxidation products one could anticipate from that point forward, chain-trapping or otherwise, made the prospect of experimental verification by quantification against authentic standards rather daunting. This dilemma prompted us to further consider if, in principle, the two proposed HAT-type processes could be repeated down a longer alkyl chain, oscillating between allylic C-H atoms of the PTZ radical form and the exo-alkene form. First using 3-*n*-hexylphenothiazine as a model in our DFT calculations (Fig. 6.6C), we found indeed that removing each C-H (6 H-atoms not counting the initial PCET with N-H) sequentially to get the triene that these were

similarly labile to the aforementioned example (BDE values ranged from 60.4 to 67.2 kcal/mol).[21] We wondered if a cyclohexyl group were used instead, if we would: a) observed longer inhibitions relative to the *iso*-propyl phenothiazines and b) observe formation of a stable phenyl phenothiazine end product in the hexadecane autoxidation experiment (formed from the exchange of H-atom from unreacted starting PTZ to the proposed 3-phenylphenothiazine radical "endpoint.")

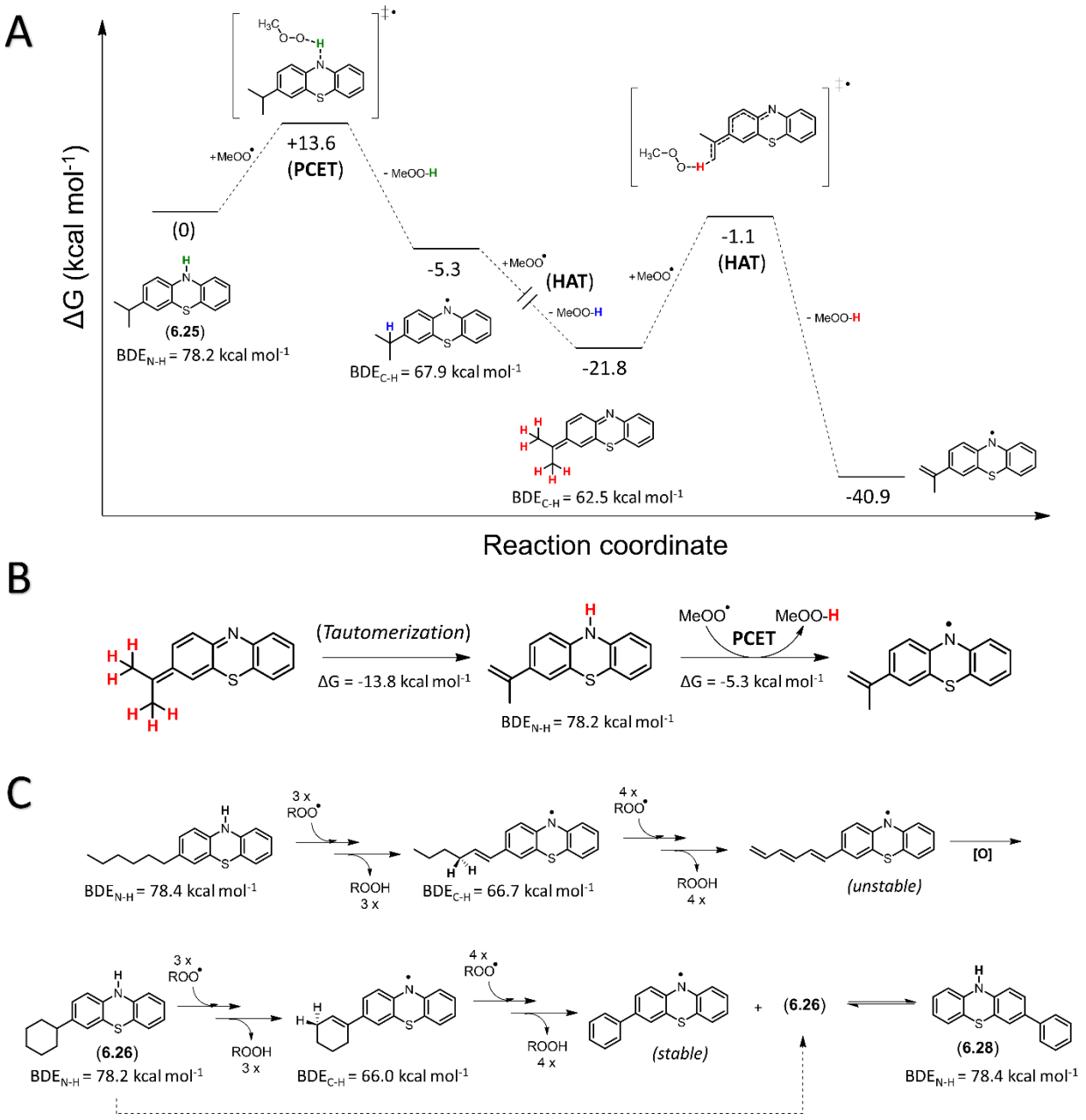


Figure 6.6. (A) Reaction coordinate diagram of the autoxidation of **6.26** (M06-2X/cc-pVTZ). (B) Alternative tautomerization pathway for propide intermediate. (C) Truncated schematic of proposed sequential autoxidation of 3-*n*-hexyl-PTZ and 3-cyclohexyl-PTZ (see Fig. 6.32 and 6.33 for complete set of intermediates).

Following the synthesis of 3-cyclohexylphenothiazine (**6.27**) and 3,7-dicyclohexylphenothiazine (**6.28**), we were gratified to find that both of these inhibited longer than their respective *iso*-propyl counterparts **6.25** (510±10 vs. 429±10 min) and **6.10** (592±10 vs. 553±10 min). We

subsequently prepared 3-phenylphenothiazine (**6.29**) as well as the 2 major oxidation products that would be derived from it: 3-phenylphenothiazine-S-oxide (**6.30**) and 7-phenylphenothiazin-3-one (**6.31**). Analyzing extracted samples from our inhibited autoxidations with **6.27**, we were pleased to find that all three of these oxidation products were observed, with **6.29** beginning to accumulate ~2 h into the experiment (Fig. 6.7B.) Although the peak concentration of **6.29** was only ~6.8 μM, if we again assume that all **6.30** and **6.31** is derived from **6.29**, a peak conversion of at least 14.6 μM is observed (almost 10%), to say nothing of the potential oxidation products further downstream which were not quantified. When one considers the long and particular sequence of oxidations needed to form **6.29** from **6.27** and the intermediate Michael acceptor that would be involved, it is a rather impressive level of conversion. Nevertheless, the low conversion may provide insight into why **6.28** exceeds PTZ by "only" ~2.5-fold (592±10 vs. 242±10 min) even if by this mechanism **6.28** would trap *up to* 13 peroxyls per molar equivalent. Interestingly, while similar thermochemistry was predicted for the oxidation of 3-cyclohexylphenoxazine (**6.35**) (Fig. 6.34), its inhibition period was rather unremarkable (being very similar to unsubstituted PNX) and the anticipated 3-phenylphenoxazine (**6.32**) product was not observed at any time.

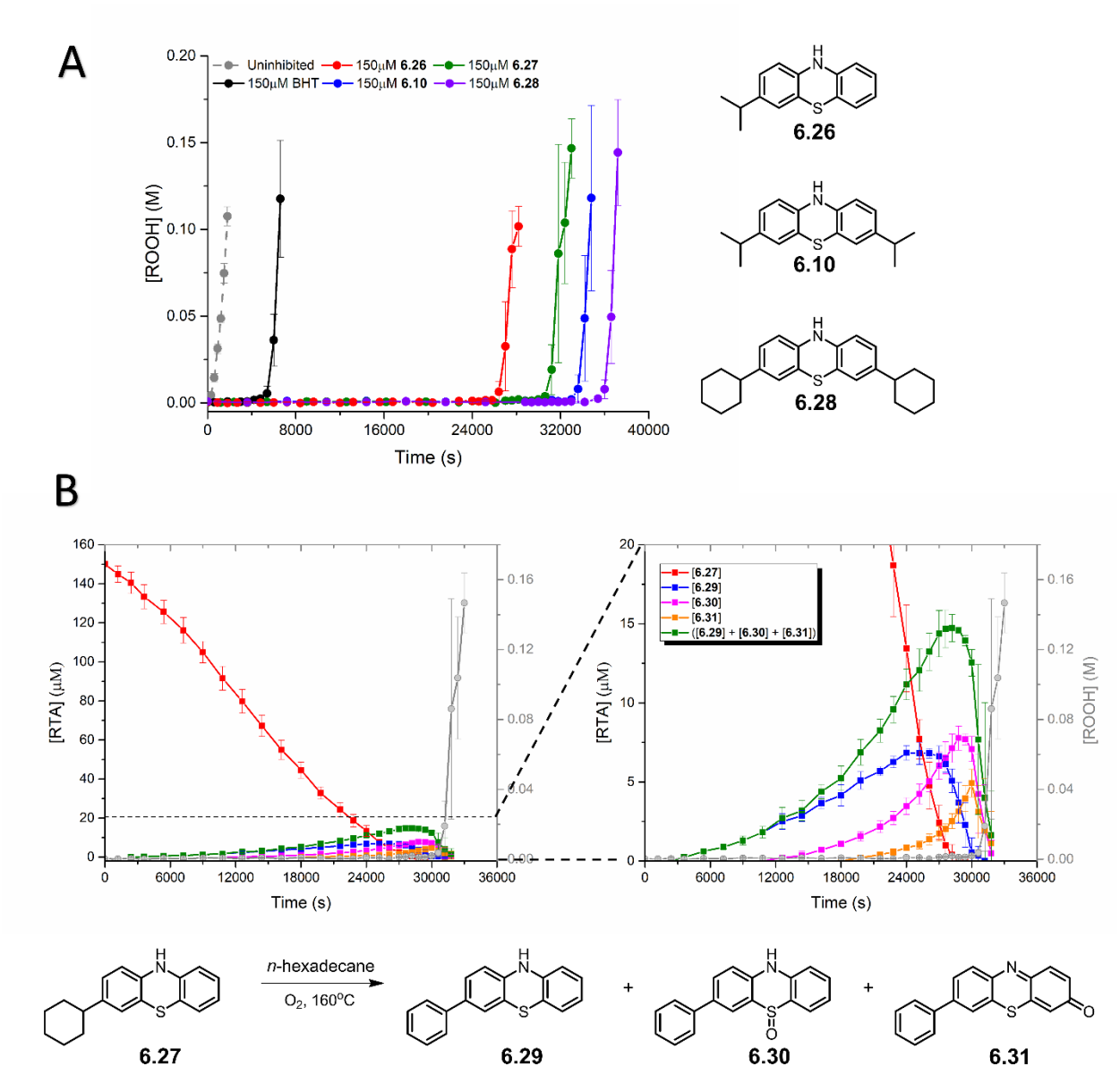


Figure 6.7. (A) Comparison of isopropyl and cyclohexyl substituted 3- and 3,7-di-alkyl-PTZ. (B) Time course loss of **6.27** and the formation of **6.29** and its oxidation products.

Which brings us to the lingering question of why, in contrast to PTZ, the ethyl and *iso*-propyl analogues of 3,7-dimethylphenoxazine (**6.5** and **6.6** respectively) perform as poorly as they do. Assuming that analogous unsaturation forms on these side groups, they would have a similar propensity to the pro-oxidation chemistry as their parent 3,7-alkyl-PNX. A side-by-side comparison of the consumption of 3-phenylphenoxazine (**6.32**) and **6.29** (Fig. 6.8) once again highlights that despite these having similar standard redox potentials (0.85 V and 0.84 V) the

PNX derivative is rapidly consumed in a fashion analogous to an alkyl-PNX (e.g., **6.14**), while the PTZ is more resilient in this respect. The 3-Me-PNX derivatives shown in Figure 6.4 happen to form an EWG (formyl) which helps ameliorate this deficiency in the PNX, while a hypothetical styryl or α-methyl styryl group would not.

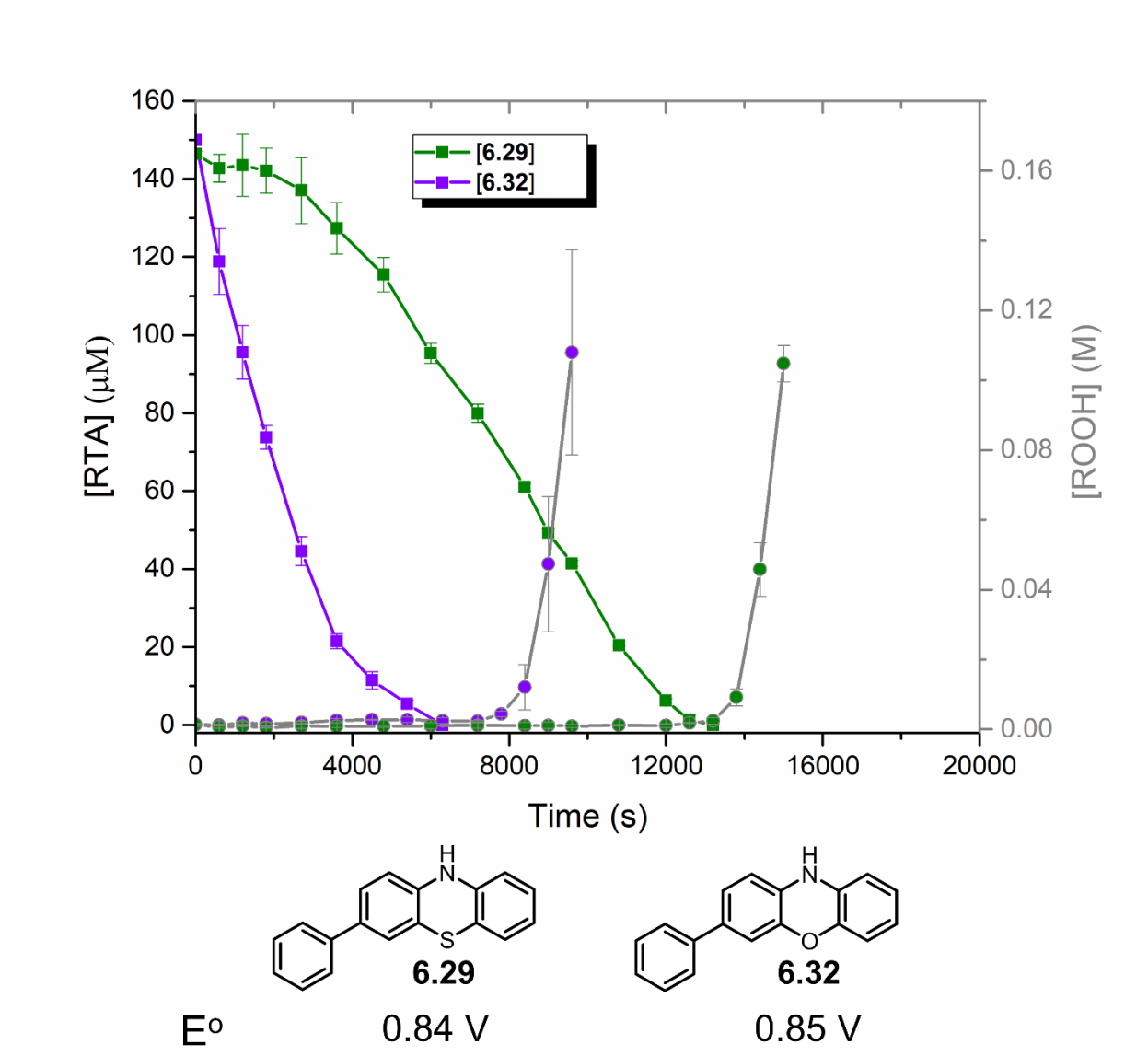


Figure 6.8. Time course loss of 3-phenyl-PTZ (**6.29**) compared to 3-phenyl-PNX (**6.32**).

6.4 Discussion

Through this systematic investigation of alkylated PNX/PTZ derivatives we have been able to corroborate our initial findings with **6.1**-**6.3** where seemingly innocuous changes to the alkyl substituent has rather profound impacts on the inhibition in high temperature system of present interest (160ºC with O_2 in *n*-hexadecane).[16] In particular this was manifested with the PTZ derivatives as these are more oxidatively robust molecules with respect to the direct autoxidation with O_2, whereas the PNX derivatives (based on this analysis and our previous work) have strong pro-oxidant tendencies acting against their antioxidant activity.[15] The most impressive of the compounds tested was **6.27** which inhibited for nearly 10 h at 150 μM whereas PTZ and BHT only inhibited for ~4 h and ~1:20 h at the same concentration, respectively. Before further discussing probable explanations for the PTZ results, we first must understand the significance of the results with BHT.

As part of their efforts to determine k_d of *n*-hexadecane peroxides in the 160-180ºC range, Korcek and co-workers reported n = 1.2 and 2.2 for BHT and Bis-BHT, respectively.[17] Based on this, under our conditions we expected linear scaling of t_{inh} at molar equivalents of phenol, expectations which were met when comparing BHT (at 150 μM and 300 μM) and Bis-BHT (150 μM) (Fig. 6.2). The previous work by Korcek was performed with pre-oxidized hexadecane where [ROOH] was more or less at a steady state during inhibition, such that n could be solved with a reasonable degree of certainty using k_d and the starting concentration of [ROOH]. Our inhibited autoxidations, on the other hand, uses fresh *n*-hexadecane and are only initiated by application of O_2 at 160 ºC (eq. 6.5). Thus, the concentration of [ROOH] and R_i meaningfully increase throughout the inhibition period making determinations of unknown n values impossible using Eq. 14. The rapid increase in BHT consumption during the latter half of our control experiments (Fig. 6.2B) attests to this. This experimental design is deliberate, however, as lubricants that are formulated with RTA additives can be considered 'fresh' given the presence of peroxide decomposers in addition to RTAs. As such, the rate law in Eq. 6.15 should be more relevant in practice than a steady-state regime. While t_{inh} is in a practical sense an irreducible parameter in our experiments, comparing the various novel RTAs under the same conditions at the same concentration (150 μM) was a workable compromise and discerning stoichiometric

behaviour (t_{inh} within a few factors of BHT) versus catalytic behaviour (t_{inh} >> 10-fold with respect to BHT) should be reasonably accommodated.

Looking back at the seminal Bolsman experiments, where DPA was reported to have an n of 41,[6] one might forecast a proportional advantage for DPA over BHT with respect to t_{inh} when moving from their conditions (130°C in paraffin oil) to the present experiments. Not so. In fact, DPA performs markedly *worse* than even BHT (Fig. 6.9). One would expect that, even if catalysis is not operating in this system, that at least it would match BHT as a stoichiometric RTA as both under more ambient conditions have nearly identical stoichiometry (n~2)[22,23] and inhibition rate constants (k_{inh} ~ 1.5 × 10^4 $M^{-1}s^{-1}$).[24,25] We were initially puzzled by this; however upon further reflection, it would seem that that HAT from DPA to peroxyl radical is highly reversible under these conditions, resulting in a modest retardation of ROOH formation via chain-transfer rather than full on inhibition. A comparison of the X-H BDE of DPA (84.7 kcal/mol)[25] and ROOH (86.2 kcal/mol) reveals that the desired trapping reaction is only slightly exothermic (-1.5 kcal/mol), certainly in comparison to the more persistent radical derived from BHT (O-H BDE = 79.9 kcal/mol, ΔH = -6.3 kcal/mol).[26] The reverse reaction ($DPA^{\bullet}$ + ROOH → DPA + $ROO^{\bullet}$) would become even more prevalent as [ROOH] increases throughout the oxidation. Reversible behaviour predicated on tepid thermodynamic favourability could also explain the poor performance of ADPA under these conditions despite its higher k_{inh} at ambient temperatures (~2 × 10^5 M^{-1} s^{-1}),[27,28] and why essentially no "methyl effect" enhancement was observed when we previously compared 4,4'-di-*tert*-butyldiphenylamine and 4,4'-dimethyldiphenylamine.[16] These results should not be a cause for alarm, however. Apart from substrate specific advantages simple diarylamines like DPA may enjoy, it is rare DPA or ADPA would be added to a lubricant in isolation from other co-antioxidants. DPA/ADPA can work in a heterosynergistic manner with additives such as ZDDP[29] as well as in a homosynergistic manner with hindered phenols like BHT,[9] which are almost always present. Hindered phenols act as a thermodynamic sink for the aminyl radicals by forming the more stable phenoxyl radical and regenerating the amine.

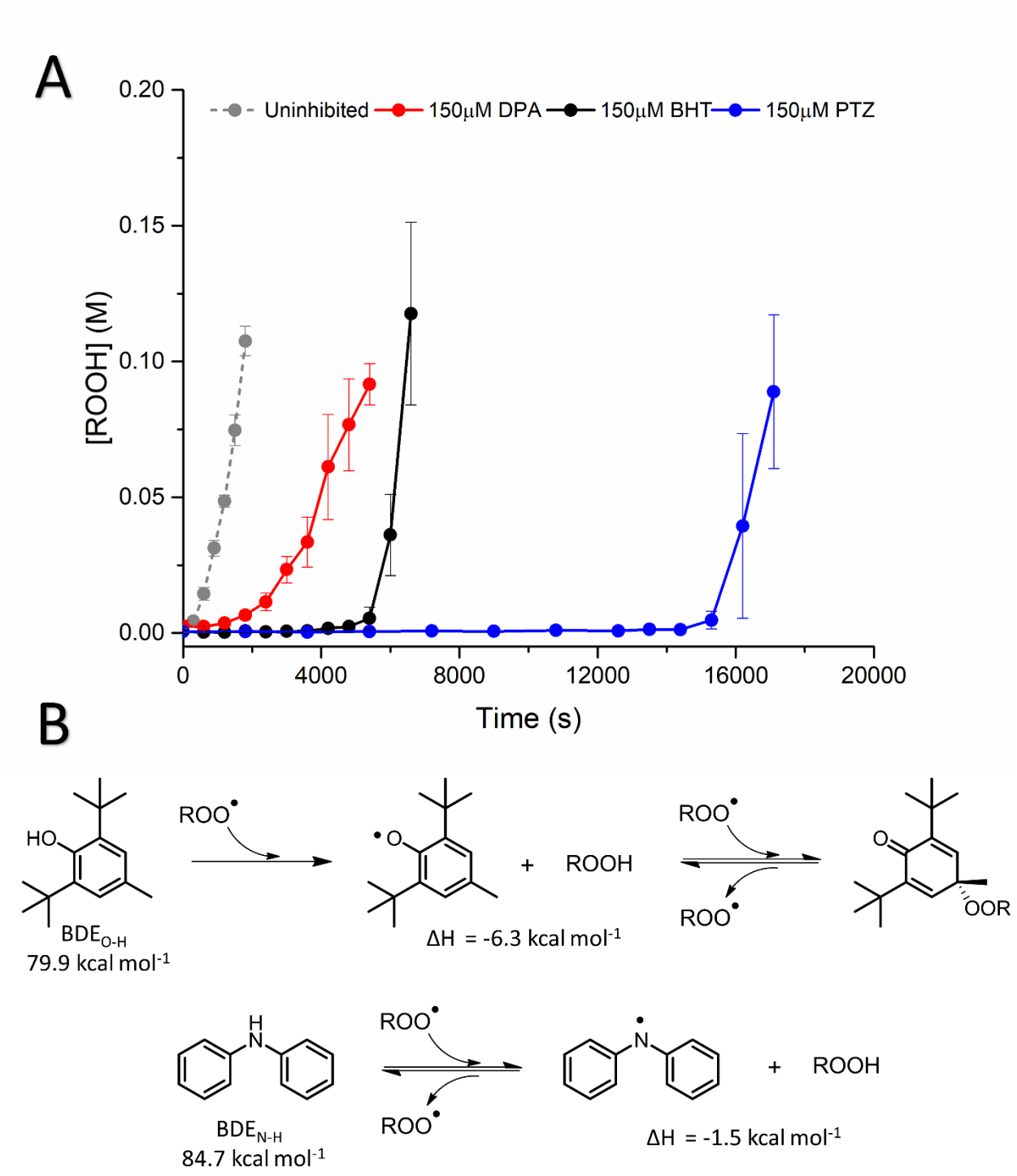


Figure 6.9. (A) Inhibition with DPA, BHT and PTZ compared. (B) Proposed behaviour of BHT and DPA in the 160 °C autoxidation system.

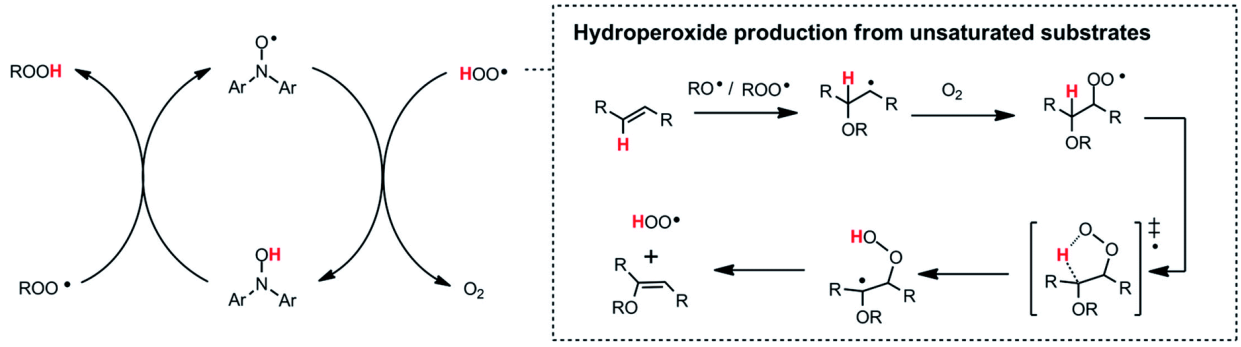
What of PTZ though? Can we assume that because it has much longer inhibition time than BHT that it also has a significantly higher n? As alluded earlier, this reduction would only apply if R_i (of the form $2ek_d$[ROOH]) were constant. Making similar assumptions to the ones made in Eq. 6.15, with the proviso of negligible contributions of Eq. 6.9 to chain termination, an inhibited rate law under the conditions of the hexadecane autoxidation could look like Eq. 6.17:

$$\frac{d[ROOH]}{dt} = \frac{2k_p[RH]k_d[ROOH]}{k_{inh}[AH]} \qquad (6.17)$$

As the R_i is dependent on d[ROOH]/dt (i.e., chain branching), the k_{inh} of PTZ being orders of magnitude higher than BHT would likely have a strong bearing on the *rate* of R_i increase, but this is not the same as having a higher n (a higher number of *actual* radicals trapped). Furthermore, it is possible that PTZ compounds could have a "autosynergistic" effect where the sulfur potentially reacts with residual ROOH in an ionic fashion[30] early in the experiment thereby suppressing R_i. With these additional factors to consider, and given the scale of the difference in t_{inh} between BHT and PTZ (3-fold), the inescapable conclusion that must be drawn is that there is no catalytic cycle of any consequence in operation here. Yet, there is no contest with Bolsman, Denisov and others who clearly observed catalytic behaviour with nitroxides derived from aromatic amines,[5,6,31] simply because the substrates are different and therefore not directly comparable. We know that in unsaturated substrates many different diarylamines (ADPA, **6.1**-**6.3**, PNX, PTZ, etc.) and hindered nitroxides (TEMPO) unambiguously break chains catalytically via the cross-dismutation of hydroperoxyl (HOO•) formed in these autoxidations (Scheme 6.3). A similar substrate-dependent steady-state formation of HOO• is a probable explanation for many of these earlier observations of catalytic function. As for the mechanism of Korcek *et al.* in Figure 6.1, which in principle could be essentially substrate independent, the matter of alkoxyamine formation under relevant conditions, or rather lack thereof, is a point which we have critiqued in publication[32] and has also been an ongoing debate within our research group since I started. Alkoxyamine has never actually been observed as a product of a DPA/ADPA autoxidation in any report that we are aware of, only that alkoxyamines formed *ex situ can* decompose to form their respective diarylamines and that somehow nitroxide can convert to ADPA, though this conversion is not necessarily a conserved process.[33] The complete absence of direct observational evidence with respect to the autoxidation of the amine

or nitroxide is quite conspicuous since decomposition experiments with alkoxyamine derivatives suggested that its decomposition would be a rate determining step.[12] Then there is the matter of trapping alkyl radicals to form alkoxyamine. Under the stirred-flow conditions, adapted from Korcek and co-workers, where continuous O_2 flow keeps the hexadecane more or less saturated, the dissolved [O_2] would be maintained somewhere on the order of 1×10^{-2} M.[34,35] It seems unlikely that at the low concentrations of diarylamine used in any of our work (4×10^{-5} to 3×10^{-4} M) or in the seminal study by Korcek (4×10^{-4} M) that the concentration of nitroxide formed *in situ* would be sufficient to compete with O_2, especially considering that the reaction between nitroxide and an alkyl radical (~6×10^8 M^{-1} s^{-1})[36] is typically several factors slower than that of oxygen and alkyl radical (~3 x 10^9 M^{-1} s^{-1}).[37] While we do not dispute that each step in Fig. 6.1B is a "good" reaction in insolation, we would now suggest however that as an operational catalytic cycle it is unlikely to be of much consequence under conditions relevant to the inhibition of autoxidation.

Scheme 6.3 – Catalytic Inhibition by Nitroxide-Mediated Hydroperoxyl Dismutation.

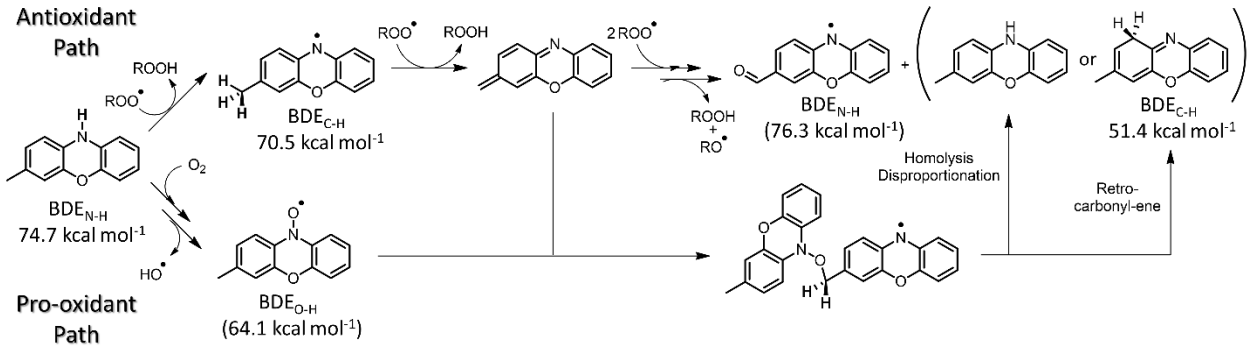


Debates over stoichiometric vs. catalytic behaviour aside, we have uncovered a new innovation here with respect to RTA atom economy. If stoichiometric trapping is the only means available, consider that while going from BHT to Bis-BHT there is a doubling of t_{inh} when [BHT] = [Bis-BHT], but the same effect is achieved by adding 2 molar equivalents of BHT (424.7 vs 2(220.4) g/mol) so from an atom economy standpoint it is equivalent (~39 h/(g/L)). On the other hand, for a very small increase in molecular weight (the cost of an ethyl group ~28 g/mol) the t_{inh} of PTZ was nearly doubled going from PTZ to **6.24** resulting in a large efficacy gain with respect to mass of the RTA (135 vs. 239 h/(g/L) respectively). Conceivably, 3' alkyl groups like *iso*-propyl (**6.10**/**6.26**) and cyclohexyl (**6.27**/**6.28**) could be appended to PTZ by a Friedel-Crafts approach

either directly or to a DPA precursor (similar to what is already done for the production of ADPA), making use of mature industrial chemical processes/methods.

One final addendum before closing. On the matter of the oxidation of **6.14** and other similar 3-Me-PNX compounds, until this point, we have not directly addressed how the major carbaldehyde product(s) form (i.e. **6.15** etc.). While there are many conceivable pathways for their formation, there are two key observations that incline us to favour particular mechanisms. One, of course, is the enhanced t_{inh} relative to PNX indicating that there a net trapping effect (in spite of PNX pro-oxidant tendencies). The other is the peculiar absence of detectable nitroxide as long as a 3-Me-PNX type species is still present in the system. Unlike PNX[15] and 3-Form-PNX (**6.15**), from which nitroxides immediately accumulate (Fig 6.10), the nitroxides derived from **6.4**, **6.12** and **6.14** only accumulate once carbaldehyde-containing PNX species have been formed (**6.13**/**6.15**). One interpretation is that the aminyl radical intermediate favours HAT from the methyl hydrogen to such a degree that nitroxide does not form. Under this scenario, one would expect the nitroxide of **6.13** or **6.15** would start accumulating before consumption of **6.12** or **6.14** was complete. Another possibility, which we favour, is that nitroxide is formed but rapidly decomposed when the iminoquinone methide is present. After addition of nitroxide to the methide, homolysis-disproportionation could give the amine of the former nitroxide and the aminyl radical of the carbaldehyde PNX, or a retro-carbonyl-ene (RCE) reaction would give 1-dihydro PNX derivative. The 3-formyl-PNX would finally form by exchanging an H-atom from unreacted 3-Me-PNX, as the former has a stronger N-H bond (76.3 kcal mol^{-1} vs. 74.7 kcal mol^{-1}.) Alternatively, if abstraction of the methyl H-atom were facilitated by the nitroxide forming a hydroxylamine and methide, nucleophilic addition followed by homolysis-disproportionation would result in a 3-formyl-PNX. However, the initial HAT is predicted to be quite endothermic. A summary of these proposals is given in Scheme 6.4.

Scheme 6.4 – Proposed Pathways for Carbaldehyde Formation from 3-Me-PNX Derivatives.



6.5 Conclusion and Prospectus

The original aim of the work was not a critique of purported catalytic mechanisms, it was merely to investigate the unexpected differing substituent effects of simple alkyl groups on diarylamine antioxidant activity, which to the best of our knowledge has never been previously reported. Through systematic testing of the alkyl substituents, the analysis of 3-Me-PNX/PTZ and 3-cyclohexyl-PTZ oxidation products and theoretical corroboration, the findings were most consistent with a stoichiometric radical-trapping mechanism. I believe this is an important turning point for this area of research. For unsaturated substrates the catalytic mechanism that remains and has substantial experimental support, nitroxide-mediated cross-dismutation of hydroperoxyl, does not really require anything more particular than a hindered alkyl nitroxide (e.g., TEMPO) leaving very little to do with respect to designing new RTAs for that system. While perhaps new insights into substrate dependence on catalytic vs. stoichiometric regimes could provide guidance to practitioners in this area (pairing the "right RTA(s)" with the "right substrate(s)") the only way to be certain is by exercising trial and error in the system of interest. Writing about *Lubricating Oil Oxidation and Stabilization*,[38] the author T. Colclough makes some fitting remarks with respect to extrapolating results from single additive models (ADPA vs. BHT vs. hindered alkyl nitroxides) to fully formulated systems:

"The activities of these three classes of antioxidant were compared in a fully formulated oil using a bench oxidation test at 165°C with soluble iron as a catalyst. An alkylated diphenylamine was found to be marginally better than a hindered phenol, but a hindered cyclic secondary amine showed negligible activity…. Thus the activity of an antioxidant depends very much on the conditions under which it is tested, and extrapolation from one set of conditions to another must be done with caution."

From a stoichiometric perspective, initial results with the non-quaternary alkylated phenothiazines appear promising. It would be negligent to omit that when we increased the concentration of these new compounds by ~2 orders of magnitude (10 mM), in line with the amount of ADPA that is typically added to a fully formulated lubricant, a fairly copious amount of precipitate was observed. Comparing between 3-*tert*-butyl-PTZ (**6.33**) and 3-*n*-butyl-PTZ (**6.34**) (Figure 6.12) clearly shows that the former, while performing worse at lower concentrations, remains clear after several hours of oxidation at the higher concentration. By adding 5% v/v dodecanol at the beginning, the turbidity of the 3-*n*-butyl-PTZ is markedly curbed. We believe the turbidity originates from oligomerization of the PTZ via addition to the Michael acceptor oxidation intermediates, and at the time of writing we are analyzing samples to find evidence of this. We intend to include this data in the inevitable publication of the above work. Assuming this is the case, we believe it can be ameliorated by applying a protection strategy to the PTZ, allowing it to release slowly throughout the autoxidation, which should hopefully eliminate this problem.

6.6 References

(1) Kröhnke, C.; Schacker, O.; Zäh, M. Antioxidants. In *Ullmann's Encyclopedia of Industrial Chemistry*; 2015; pp 1–36. https://doi.org/10.1002/14356007.a03_091.pub2.

(2) Ingold, K. U. Inhibition of the Autoxidation of Organic Substances in the Liquid Phase. *Chem. Rev.* **1961**, *61* (6), 563–589. https://doi.org/10.1021/cr60214a002.

(3) Bennett, J. E.; Eyre, J. A.; Summers, R. Electron Spin Resonance Measurements of Propagation and Termination Rate Constants during the Liquid-Phase Oxidation of Hydrocarbons. *J. Chem. Soc. Perkin Trans. 2* **1974**, No. 7, 797–800. https://doi.org/10.1039/P29740000797.

(4) Zinbo, M.; Jensen, R. K.; Johnson, M. D.; Korcek, S. Relative Inhibiting Efficiency of Base Oils. *Ind. Eng. Chem. Res.* **1987**, *26* (5), 902–906. https://doi.org/10.1021/ie00065a009.

(5) Evgenii T Denisov. Elementary Reactions of Oxidation Inhibitors. *Russ. Chem. Rev.* **1973**, *42* (3), 157. https://doi.org/10.1070/RC1973v042n03ABEH002572.

(6) Bolsman, T. A. B. M.; Blok, A. P.; Frijns, J. H. G. Catalytic Inhibition of Hydrocarbon Autoxidation by Secondary Amines and Nitroxides. *Recl. des Trav. Chim. des Pays-Bas* **1978**, *97* (12), 310–312.

(7) Jensen, R. K.; Korcek, S.; Zinbo, M.; Gerlock, J. L. Regeneration of Amine in Catalytic Inhibition of Oxidation. *J. Org. Chem.* **1995**, *60*, 5396–5400. https://doi.org/10.1021/jo00122a014.

(8) Yao, J. The Role of Sodium Perfluorobutyrate in Promoting the Antioxidancy of DODPA in Synthetic Esters. *Tribol. Trans.* **1999**, *42* (1), 84–89. https://doi.org/10.1080/10402009908982194.

(9) Gatto, V. J.; Moehle, W. E.; Cobb, T. W.; Schneller, E. R. Oxidation Fundamentals and Its Application to Turbine Oil Testing. *J. ASTM Int.* **2006**, *3* (4), 1–20. https://doi.org/10.1520/stp45720s.

(10) Gracia, N.; Thomas, S.; Thibault-Starzyk, F.; Lerasle, O.; Duponchel, L. Combination of Mid-Infrared Spectroscopy and Curve Resolution Method to Follow the Antioxidant Action of Alkylated Diphenylamines. *Chemom. Intell. Lab. Syst.* **2011**, *106* (2), 210–215.

(11) Andrews, N. L. P.; Fan, J. Z.; Omrani, H.; Dudelzak, A.; Loock, H.-P. Comparison of Lubricant Oil Antioxidant Analysis by Fluorescence Spectroscopy and Linear Sweep Voltammetry. *Tribol. Int.* **2016**, *94*, 279–287.

(12) Haidasz, E. A.; Shah, R.; Pratt, D. A. The Catalytic Mechanism of Diarylamine Radical-Trapping Antioxidants. *J. Am. Chem. Soc.* **2014**, *136* (47), 16643–16650. https://doi.org/10.1021/ja509391u.

(13) Hanthorn, J. J.; Valgimigli, L.; Pratt, D. A. Incorporation of Ring Nitrogens into Diphenylamine Antioxidants: Striking a Balance between Reactivity and Stability. *J. Am. Chem. Soc.* **2012**, *134*, 8306–8309. https://doi.org/10.1021/ja300086z.

(14) Shah, R.; Haidasz, E. A.; Valgimigli, L.; Pratt, D. A. Unprecedented Inhibition of

Hydrocarbon Autoxidation by Diarylamine Radical-Trapping Antioxidants. *J. Am. Chem. Soc.* **2015**, *137*, 2440–2443.

(15) Poon, J.-F.; Farmer, L. A.; Haidasz, E. A.; Pratt, D. A. Temperature-Dependence of Radical-Trapping Activity of Phenoxazine, Phenothiazine and Their Aza-Analogues Clarifies the Way Forward for New Antioxidant Design. *Chem. Sci.* **2021**, *12* (33), 11065–11079. https://doi.org/10.1039/D1SC02976B.

(16) Shah, R.; Poon, J.-F.; Haidasz, E. A.; Pratt, D. A. Temperature-Dependent Effects of Alkyl Substitution on Diarylamine Antioxidant Reactivity. *J. Org. Chem.* **2021**, *86* (9), 6538–6550. https://doi.org/10.1021/acs.joc.1c00365.

(17) Jensen, R. K.; Korcek, S.; Zinbo, M.; Johnson, M. D. Initiation in Hydrocarbon Autoxidation at Elevated Temperatures. *Int. J. Chem. Kinet.* **1990**, *22*, 1095–1107.

(18) The estimated error (±10 min) is based on the length of the sampling interval during the autocatalytic period. In cases where the standard deviation between three experimental replicates was greater than this, it was used instead though in nearly every case the standard deviation was much less than ±10 min.

(19) Lee, K.; Serdiuk, I. E.; Kwon, G.; Min, D. J.; Kang, K.; Park, S. Y.; Kwon, J. E. Phenoxazine as a High-Voltage p-Type Redox Center for Organic Battery Cathode Materials: Small Structural Reorganization for Faster Charging and Narrow Operating Voltage. *Energy Environ. Sci.* **2020**, *13* (11), 4142–4156. https://doi.org/10.1039/D0EE01003K.

(20) Zhao, Y.; Truhlar, D. G. The M06 Suite of Density Functionals for Main Group Thermochemistry, Thermochemical Kinetics, Noncovalent Interactions, Excited States, and Transition Elements: Two New Functionals and Systematic Testing of Four M06-Class Functionals and 12 Other Function. *Theor. Chem. Acc.* **2008**, *120* (1), 215–241. https://doi.org/10.1007/s00214-007-0310-x.

(21) DFT (M062X/cc-PVTZ) $BDE_{C\text{-}H}$ calculations for each oxidation intermediate of the 3-n-hexyl and 3-cylcohexyl phenothiazines is given in Fig. 6.32 and 6.33.

(22) Howard, J. A.; Ingold, K. U. THE INHIBITED AUTOXIDATION OF STYRENE: PART I.THE DEUTERIUM ISOTOPE EFFECT FOR INHIBITION BY 2,6-DI- Tert -BUTYL-4-METHYLPHENOL. *Can. J. Chem.* **1962**, *40*, 1851–1864. https://doi.org/10.1139/v62-281.

(23) Brownlie, I. T.; Ingold, K. U. The Inhibited Auotxidation of Styrene. Part VI. The Relative Efficiencies and the Kinetics for Inhibition by N-Aryl-Anilines and N-Alkyl Anilines. *Can. J. Chem.* **1967**, *45*, 2419–2425.

(24) Burton, G. W.; Doba, T.; Gabe, E. J.; Hughes, L.; Lee, F. L.; Prasad, L.; Ingoldo, K. U. Autoxidation of Biological Molecules. 4. Maximizing the Antioxidant Activity of Phenols. *J. Am. Chem. Soc.* **1985**, *107* (24), 7053–7065. https://doi.org/10.1021/ja00310a049.

(25) Lucarini, M.; Pedrielli, P.; Pedulli, G. F.; Valgimigli, L.; Gigmes, D.; Tordo, P. Bond Dissociation Energies of the N-H Bond and Rate Constants for the Reaction with Alkyl, Alkoxyl, and Peroxyl Radicals of Phenothiazines and Related Compounds. *J. Am. Chem.*

Soc. **1999**, *121*, 11546–11553. https://doi.org/10.1021/ja992904u.

(26) Lucarini, M.; Pedrielli, P.; Pedulli, G. F.; Cabiddu, S.; Fattuoni, C. Bond Dissociation Energies of O-H Bonds in Substituted Phenols from Equilibration Studies. *J. Org. Chem.* **1996**, *61* (26), 9259–9263. https://doi.org/10.1021/jo961039i.

(27) Comparing the computed BDE_{N-H} (CBS-QB3) values of DPA and ADPA are similar (86.4 and 85.2 kcal mol^{-1} respectively, see ref. 12) to the computed BDE_{O-H} of CH_3OOH (86.2 kcal mol^{-1}), it is very unlikely that the small improvement in exothermicity (ca. 1.2 kcal mol^{-1}) would make ADPA + $ROO^{\bullet}$ → an irreversible process under the present high temperature conditions.

(28) Interestingly, one can find independent verification of the poor inhibition activity of ADPA relative to BHT in the data of Korcek and co-workers, where under the same conditions BHT (see ref. 17) completely suppresses accumulation of ROOH (d[ROOH]/dt ~ 0 M s^{-1}) while 4,4'-diocyldiphenylamine (see ref. 7) only retards formation of ROOH, similar to our DPA data.

(29) SCOTT, G. Chapter 9 - SYNERGISM AND ANTAGONISM; Scott, G. B. T.-A. O. and A., Ed.; Elsevier: Amsterdam, 1993; pp 431–459. https://doi.org/https://doi.org/10.1016/B978-0-444-89616-2.50013-6.

(30) Kennerly, G. W.; Patterson, W. L. Kinetic Studies of Petroleum Antioxidants. *Ind. Eng. Chem.* **1956**, *48* (10), 1917–1924. https://doi.org/10.1021/ie50562a042.

(31) Bolsman, T. A. B. M.; Blok, A. P.; Frijns, J. H. G. Mechanism of the Catalytic Inhibition of Hydrocarbon Autoxidation by Secondary Amines and Nitroxides. *Recl. des Trav. Chim. des Pays-Bas* **1978**, *97* (12), 310–312. https://doi.org/10.1002/recl.19780971205.

(32) Harrison, K. A.; Haidasz, E. A.; Griesser, M.; Pratt, D. A. Inhibition of Hydrocarbon Autoxidation by Nitroxide-Catalyzed Cross-Dismutation of Hydroperoxyl and Alkylperoxyl Radicals. *Chem. Sci.* **2018**, *9* (28), 6068–6079. https://doi.org/10.1039/C8SC01575A.

(33) Jensen and co-workers when starting with 0.41 mM of (4,4'-dioctyldiphenylamino)-*N*-oxyl (i.e., ADPA nitroxide) observed a peak conversion to ADPA of ~45% under continuous O_2 flow in *n*-hexadecane at 160ºC. See ref. 7.

(34) Estimate was calculated from the mole fraction of O_2 dissolved n-octane at 313K ($x = 2.1 \times 10^{-3}$) at a partial pressure of 760 torr (giving $[O_2] = 0.013$ M). See ref. 35.

(35) Battino, R.; Rettich, T. R.; Tominaga, T. The Solubility of Oxygen and Ozone in Liquids. *J. Phys. Chem. Ref. Data* **1983**, *12* (2), 163–178. https://doi.org/10.1063/1.555680.

(36) Beckwith, A. L. J.; Bowry, V. W.; Ingold, K. U. Kinetics of Nitroxide Radical Trapping. 1. Solvent Effects. *J. Am. Chem. Soc.* **1992**, *114* (13), 4983–4992. https://doi.org/10.1021/ja00039a005.

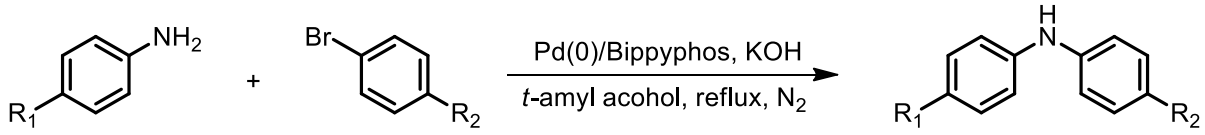
(37) Maillard, B.; Ingold, K. U.; Scaiano, J. C. Rate Constants for the Reactions of Free Radicals with Oxygen in Solution. *J. Am. Chem. Soc.* **1983**, *105*, 5095–5099.

(38) COLCLOUGH, T. Chapter 1 - LUBRICATING OIL OXIDATION AND STABILISATION; Scott, G. B. T.-A. O. and A., Ed.; Elsevier: Amsterdam, 1993; pp 1–69.

(39) Gaussian 16, Revision C.01, Frisch, M. J.; Trucks, G. W.; Schlegel, H. B.; Scuseria, G. E.; Robb, M. A.; Cheeseman, J. R.; Scalmani, G.; Barone, V.; Petersson, G. A.; Nakatsuji, H.; Li, X.; Caricato, M.; Marenich, A. V.; Bloino, J.; Janesko, B. G.; Gomperts, R.; Mennucci, B.; Hratchian, H. P.; Ortiz, J. V.; Izmaylov, A. F.; Sonnenberg, J. L.; Williams-Young, D.; Ding, F.; Lipparini, F.; Egidi, F.; Goings, J.; Peng, B.; Petrone, A.; Henderson, T.; Ranasinghe, D.; Zakrzewski, V. G.; Gao, J.; Rega, N.; Zheng, G.; Liang, W.; Hada, M.; Ehara, M.; Toyota, K.; Fukuda, R.; Hasegawa, J.; Ishida, M.; Nakajima, T.; Honda, Y.; Kitao, O.; Nakai, H.; Vreven, T.; Throssell, K.; Montgomery, J. A., Jr.; Peralta, J. E.; Ogliaro, F.; Bearpark, M. J.; Heyd, J. J.; Brothers, E. N.; Kudin, K. N.; Staroverov, V. N.; Keith, T. A.; Kobayashi, R.; Normand, J.; Raghavachari, K.; Rendell, A. P.; Burant, J. C.; Iyengar, S. S.; Tomasi, J.; Cossi, M.; Millam, J. M.; Klene, M.; Adamo, C.; Cammi, R.; Ochterski, J. W.; Martin, R. L.; Morokuma, K.; Farkas, O.; Foresman, J. B.; Fox, D. J. Gaussian, Inc., Wallingford CT, 2016.

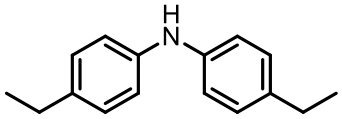
6.7 Materials/Synthesis

General. Reagents were purchased from commercial suppliers and used without further purification unless otherwise specified. Phenothiazine, 2,6-di-*tert*-butyl-4-methylphenol (BHT), and 4,4'-methylenebis(2,6-di-*tert*-butylphenol) were purchased from Sigma-Aldrich. BHT was recrystallized out of hexanes prior to use. Phenoxazine, 4-methyldiphenylamine and 4,4'-dimethyldiphenylamine were purchased from A2B chemicals. 3-Phenylphenol was purchased from Combi-Blocks. *n*-Hexadecane (95%) was purchased from Thermo Fisher, and was percolated through silica (F60) and alumina-B prior to use. Preparation of 3-cyanophenoxazine, 3-cyano-7-methylphenoxazine, 3-formylphenoxazine, 3,7-di-formylphenoxazine, 3-nitrophenoxazine, 3-nitro-7-methylphenoxazine, 3,7-dimethylphenoxazine, 3,7-diethylphenoxazine, 3,7-di-*iso*-propylphenoxazine, 3,7-di-*tert*-butylphenoxazine, 3,7-di-*tert*-butylphenothiazine and 3-formylphenothiazine have been previously described.[1,2] Column chromatography was carried out using flash silica gel (40−63 μm, 230−400 mesh). ^{1}H and ^{13}C NMR were recorded on a Bruker AVANCE spectrometer at 400 and 101 MHz, respectively, unless specified otherwise. High-resolution mass spectra were obtained on a Kratos Concept Tandem mass spectrometer.

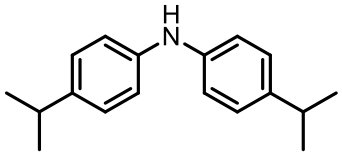


Synthesis of Alkylated Diphenylamines. Alkylated phenothiazines were prepared from their corresponding alkylated diphenylamines. These diarylamines were prepared in a single step using Buchwald-Hartwig amination (typical procedure given): An oven or flame-dried Schlenk flask/tube was evacuated then backfilled with N_2 or argon. The flask was then opened with a steady flow of N_2 or argon passing through the side arm and out the top, throughout addition of reagents. The flask was charged with 2-methyl-2-butanol (25-40 mL) and magnetic stir bar, and a nitrogen or argon filled balloon affixed with a long needle was placed through the top to sparge the solvent (approx. 10 min before adding next reagent). To the flask was then added $Pd_2(dba)_3$ (0.0025 eq.) and Bippyphos (0.01 eq.), closing the inert gas flow momentarily so the reagents wouldn't blow away. After ~10 min of stirring, crushed KOH pellets (1.5 eq.), aniline derivative (1.3 eq.) then bromobenzene derivative (1 eq., 1 M with respect to solvent, e.g., 25-40 mmol)

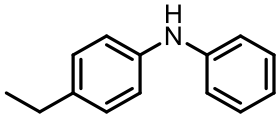
were added. After another 5 min of stirring and sparging, the balloon was removed, the top was sealed with a rubber stopper, and the gas inlet was closed. The rubber stopper was taped to prevent leaks, and the flask was heated on an oil bath heated to 110 ºC, and allowed to stir for ~10 h. After cooling, the contents of the flask were filtered and rinsed with DCM, and the filtrate was evaporated under reduced pressure on silica for preparative chromatography. The diarylamine product was isolated by column chromatography (typical eluent being 10% ethyl acetate in hexanes), and a portion of the product was recrystallized from hexanes (when applicable) before characterization. The isolated yield was consistently between 70-80%.



4-4'-Diethyldiphenylamine. Product appeared as a white solid; mp = 37-39 °C. ^{1}H NMR (400 MHz; DMSO-d6): δ 7.87 (br, 1H), 7.05 (d, *J* = 8.4 Hz, 4H), 6.95 (d, *J* = 8.5 Hz, 4H), 2.51 (q, *J* = 7.5 Hz, 4H), 1.15 (t, *J* = 7.5 Hz, 6H). ^{13}C NMR (101 MHz; DMSO-d6): δ 141.5, 134.6, 128.3, 166.7, 27.4, 15.9. HRMS (EI, magnetic sector): calcd for $C_{16}H_{19}N$ 225.15175, found 225.15126.

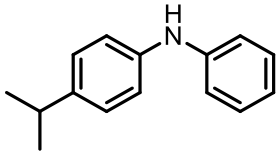


4-4'-Di-*iso*-propyldiphenylamine. Product appeared as a white needle-like crystals; mp = 51-53 °C. ^{1}H NMR (400 MHz; DMSO-d6): δ 7.87 (br, 1H), 7.07 (d, *J* = 8.4 Hz, 4H), 6.96 (d, *J* = 8.5 Hz, 4H), 2.79 (sept, *J* = 6.9 Hz, 2H), 1.15 (d, *J* = 6.9 Hz, 12H). ^{13}C NMR (101 MHz; DMSO-d6): δ 141.6, 139.3, 126.8, 116.6, 32.7, 24.1. HRMS (EI, magnetic sector): calcd for $C_{18}H_{23}N$ 253.18305, found 253.18554.

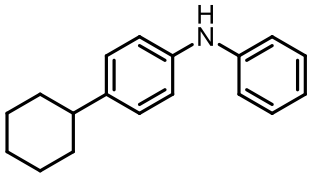


4-Ethyldiphenylamine. Product appeared as long colourless needles; mp = 82-84 °C. ^{1}H NMR (400 MHz; DMSO-d6): δ 7.99 (br, 1H), 7.19 (dd, *J* = 8.5 Hz, 2H), 7.07 (d, *J* = 8.5 Hz, 2H), 7.02-6.99 (m, 4H), 6.76 (dddd, *J* = 1.0, 7.3 Hz, 1H), 2.52 (q, *J* = 7.5 Hz, 2H), 1.15 (t, *J* = 7.5 Hz, 3H).

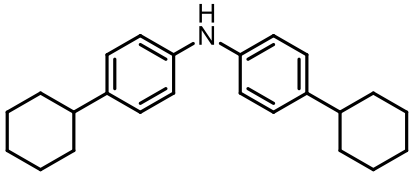
^{13}C NMR (101 MHz; DMSO-d6): δ 144.0, 140.9, 135.3, 129.1, 128.3, 119.0, 117.5, 115.9, 27.4, 15.8. HRMS (EI, magnetic sector): calcd for $C_{14}H_{15}N$ 197.12045, found 197.11975.



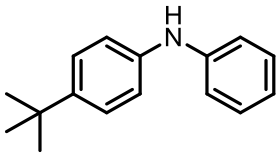
4-*iso*-Propyldiphenylamine. Product appeared as long colourless needles; mp = 66-68 °C. ^{1}H NMR (400 MHz; DMSO-d6): δ 8.00 (br, 1H), 7.19 (dd, *J* = 8.4 Hz, 2H), 7.10 (d, *J* = 8.5 Hz, 2H), 7.02-7.00 (m, 4H), 6.76 (dd, *J* = 7.3 Hz, 1H), 2.80 (sept, *J* = 6.9 Hz, 1H), 1.18 (d, *J* = 6.9 Hz, 6H). ^{13}C NMR (101 MHz; DMSO-d6): δ 144.0, 141.0, 139.9, 129.1, 126.8, 119.0, 117.4, 115.9, 32.7, 24.1. HRMS (EI, magnetic sector): calcd for $C_{15}H_{17}N$ 211.13610, found 211.13519.



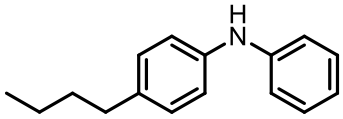
4-Cyclohexyldiphenylamine. Product appeared as light pink crystals; mp = 49-51 °C. ^{1}H NMR (400 MHz; DMSO-d6): δ 8.01 (br, 1H), 7.19 (dd, *J* = 8.4 Hz, 2H), 7.07 (d, *J* = 8.5 Hz, 2H), 7.02-6.98 (m, 4H), 6.76 (dddd, *J* = 1.0, 7.3 Hz, 1H), 2.42-2.37 (m, 1H), 1.78-1.67 (m, 5H) 1.40-1.19 (m, 5H). ^{13}C NMR (101 MHz; DMSO-d6): δ 144.0, 141.0, 139.3, 129.1, 127.2, 119.0, 117.3, 116.0, 43.1, 34.2, 26.4, 25.7. HRMS (EI, magnetic sector): calcd for $C_{18}H_{21}N$ 251.16740, found 251.16702.



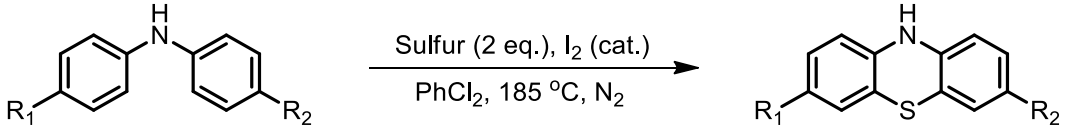
4,4'-Dicyclohexyldiphenylamine. Product appeared as white crystals; mp = 88-90 °C. ^{1}H NMR (400 MHz; DMSO-d6): δ 7.87 (br, 1H), 7.04 (d, *J* = 8.5 Hz, 4H), 6.93 (d, *J* = 8.5 Hz, 4H), 2.42-2.35 (m, 2H), 1.77-1.67 (m, 10H) 1.40-1.15 (m, 10H). ^{13}C NMR (101 MHz; DMSO-d6): δ 141.6, 138.6, 127.2, 116.6, 43.0, 34.2, 26.5, 25.7. HRMS (EI, magnetic sector): calcd for $C_{24}H_{31}N$ 333.24565, found 333.24355.



4-*tert*-Butyldiphenylamine. Product appeared as white needles; mp = 64-66 °C. ^{1}H NMR (400 MHz; DMSO-d6): δ 8.01 (br, 1H), 7.25 (d, *J* = 8.7 Hz, 2H), 7.19 (dd, *J* = 8.5 Hz, 2H), 7.03-7.00 (m, 4H), 6.76 (dddd, *J* = 1.0, 7.3 Hz, 1H), 1.26 (s, 9H). ^{13}C NMR (101 MHz; DMSO-d6): δ 144.0, 142.2, 140.6, 129.1, 125.7, 119.0, 117.0, 116.0, 33.7, 31.3. HRMS (EI, magnetic sector): calcd for $C_{16}H_{19}N$ 225.15175, found 225.15041.

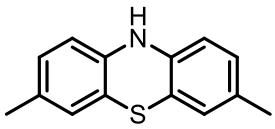


4-*n*-Butyldiphenylamine. Product appeared as light brown oil. ^{1}H NMR (400 MHz; DMSO-d6): δ 7.99 (br, 1H), 7.19 (dd, *J* = 8.5 Hz, 2H), 7.06-6.98 (m, 6H), 6.76 (ddd, *J* = 1.0, 7.3 Hz, 1H), 2.49 (t, *J* = 7.6 Hz, 2H), 1.52 (quin, *J* = 7.5 Hz, 2H), 1.30 (sext, *J* = 7.5 Hz, 2H), 0.89 (t, *J* = 7.3 Hz, 3H). ^{13}C NMR (101 MHz; DMSO-d6): δ 144.0, 140.9, 133.78, 129.0, 128.8, 119.0, 117.4, 115.9, 34.1, 33.3, 21.7, 13.8. HRMS (EI, magnetic sector): calcd for $C_{16}H_{19}N$ 225.15175, found 225.15029.

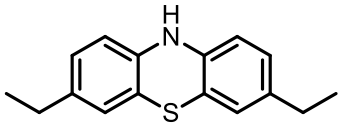


Synthesis of Alkylated Phenothiazines. A typical procedure for the thionation of alkylated diphenylamine is given: To an open 16 x 150 mm borosilicate test tube in a 4x6 test tube heating block was added the corresponding diphenylamine (1 eq., 15-25 mmol), sulfur (2 eq., 32.07 g/mol) and 1,2-dichlorobenzene (9 mL) and a magnetic stir bar. While stirring, the mixture was sparged with N_2 or argon via a balloon affixed with a long needle for approx. 10 min After removing the balloon, a needle was fixed above the surface of the mixture and a steady stream of N_2 or argon was blown over the reaction for the remainder of the experiment. A catalytic amount of I_2 was added (0.03 eq., 253.81 g/mol) and glass wool stuffed in the opening of the test tube. The mixture was heated to 183-187 °C and maintained for 1-3 h. As the reaction proceeded, evolution of H_2S could be detected (visually and olfactorily), and the formation of PTZ product

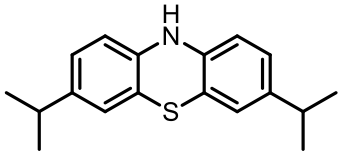
was monitored closely by TLC. After the majority of the starting material was consumed, the test tube was allowed to cool (by this time most of the $PhCl_2$ had blown off). The dark solid mass was removed by breaking the bottom of the test tube and crushing the contents in a large Erlenmeyer flask. The residue was stirred in hot ethanol (and for best results, activated charcoal and zinc dust were added), then filtered into a round bottom flask. The solvent was evaporated under reduced pressure on silica for preparative chromatography. The phenothiazine product was isolated by column chromatography (typical eluent being 10% ethyl acetate in hexanes), after which it was recrystallized from hexanes or ethanol. The isolated yield was typically 20-35%, with the notable exception of 3-phenylphenothiazine which was 58%.



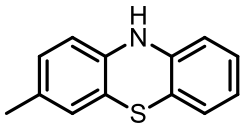
3,7-Dimethylphenothiazine. Product appeared as a light-yellow solid; mp = 226 °C (decomp). ^{1}H NMR (400 MHz; DMSO-d6): δ 8.32 (br, 1H), 6.77 (dd, *J* = 1.4, 8.0 Hz, 2H), 6.72 (d, *J* = 1.4 Hz, 2H), 6.55 (d, *J* = 8.0 Hz, 2H), 2.11 (s, 6H). ^{13}C NMR (101 MHz; DMSO-d6): δ 139.8, 130.3, 127.9, 126.5, 116.1, 114.1, 19.9. HRMS (EI, magnetic sector): calcd for $C_{14}H_{13}NS$ 227.07687, found 227.07848.



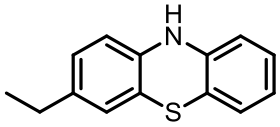
3,7-Diethylphenothiazine. Product appeared as a crystalline solid (white with a light-greenish hue); mp = 140-142 °C. ^{1}H NMR (400 MHz; C_6D_6): δ 6.80 (d, *J* = 1.6 Hz, 2H), 6.65 (dd, *J* = 1.9, 8.0 Hz, 2H), 5.97 (d, *J* = 8.0 Hz, 2H), 4.97 (br, 1H), 2.28 (q, *J* = 7.5 Hz, 4H), 1.01 (t, *J* = 7.5 Hz, 6H). ^{13}C NMR (101 MHz; C_6D_6): δ 140.5, 138.8, 127.0, 126.9, 119.2, 114.9, 28.6, 16.3. HRMS (EI, magnetic sector): calcd for $C_{16}H_{17}NS$ 255.10817, found 255.10741.



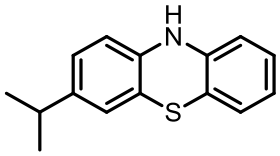
3,7-Di-*iso*-propylphenothiazine. Product appeared as white fluffy crystals; mp = 134-136 °C. ^{1}H NMR (400 MHz; C_6D_6): δ 6.90 (d, *J* = 1.9 Hz, 2H), 6.70 (dd, *J* = 2.0, 8.0 Hz, 2H), 5.99 (d, *J* = 8.0 Hz, 2H), 4.99 (br, 1H), 2.55 (sept, *J* = 6.9 Hz, 2H), 1.07 (d, *J* = 6.9 Hz, 12H). ^{13}C NMR (101 MHz; C_6D_6): δ 143.5, 140.7, 125.5(3), 125.5(1), 119.2, 114.9, 34.0, 24.5. HRMS (EI, magnetic sector): calcd for $C_{18}H_{21}NS$ 283.13947, found 283.13738.



3-Methylphenothiazine. Product appeared as light-yellow crystals; mp = 176-178 °C. ^{1}H NMR (400 MHz; DMSO-d6): δ 8.45 (br, 1H), 6.97 (ddd, *J* = 1.4, 7.6, 7.6 Hz, 1H), 6.89 (dd, *J* = 1.3, 7.6 Hz, 1H), 6.78 (dd, *J* = 1.2, 8.0 Hz, 1H), 6.79-6.70 (m, 2H), 6.66 (dd, *J* = 1.0, 7.8 Hz, 1H), 6.58 (d, *J* = 7.9 Hz, 2.12 (s, 3H). ^{13}C NMR (101 MHz; DMSO-d6): δ 142.4, 139.5, 130.7, 127.9, 127.5, 126.5, 126.2, 121.4, 116.2(4), 116.1(8), 114.3, 19.9. HRMS (EI, magnetic sector): calcd for $C_{13}H_{11}NS$ 213.06122, found 213.05947.

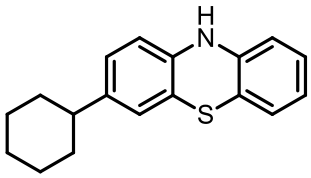


3-Ethylphenothiazine. Product appeared as a white crystalline solid; mp = 126-128 °C. ^{1}H NMR (400 MHz; DMSO-d6): δ 8.44 (br, 1H), 6.94 (ddd, *J* = 1.4, 7.6, 7.6 Hz, 1H), 6.87 (dd, *J* = 1.4, 7.6 Hz, 1H), 6.79 (dd, *J* = 2.0, 8.0 Hz, 1H), 6.73 (d, *J* = 1.9 Hz, 1H), 6.69 (ddd, *J* = 1.3, 7.5, 7.5 Hz, 1H), 6.63 (dd, *J* = 1.1, 7.9 Hz, 1H), 6.57 (d, *J* = 8.0 Hz, 1H), 2.39 (q, *J* = 7.5 Hz, 2H), 1.06 (t, *J* = 7.6 Hz, 3H). ^{13}C NMR (101 MHz; DMSO-d6): δ 142.4, 139.8, 137.3, 127.5, 126.8, 126.2, 125.4, 121.5, 116.2(5), 116.1(7), 114.3(2), 114.2(7), 27.2, 15.7. HRMS (EI, magnetic sector): calcd for $C_{14}H_{13}NS$ 227.07687, found 227.07739.

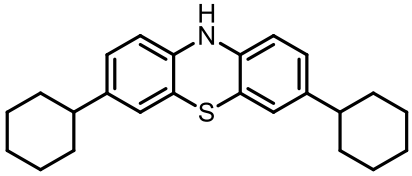


3-*iso*-Propylphenothiazine. Product appeared as white platelet crystals; mp = 158-160 °C. ^{1}H NMR (400 MHz; DMSO-d6): δ 8.46 (br, 1H), 6.97 (ddd, *J* = 1.3, 7.7, 7.7 Hz, 1H), 6.90 (dd, *J* =

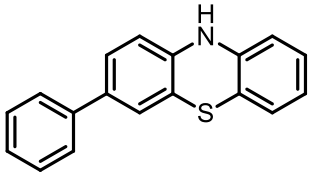
1.4, 7.6 Hz, 1H), 6.86 (dd, *J* = 2.0, 8.2 Hz, 1H), 6.78 (d, *J* = 2.0 Hz, 1H), 6.72 (ddd, *J* = 1.3, 7.5, 7.5 Hz, 1H), 6.67 (dd, *J* = 1.2, 7.9 Hz, 1H), 6.61 (d, *J* = 8.1 Hz, 1H), 2.71 (sept, *J* = 6.9 Hz, 1H), 1.12 (d, *J* = 6.9 Hz, 6H). ^{13}C NMR (101 MHz; DMSO-d6): δ 142.4, 142.0, 139.9, 127.4, 126.2, 125.3, 123.9, 121.4, 116.2(8), 116.1(3), 114.3(0), 114.2(5), 32.5, 23.8. HRMS (EI, magnetic sector): calcd for $C_{15}H_{15}NS$ 241.09252, found 241.09341.



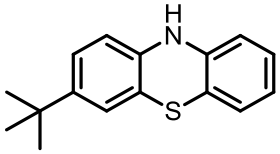
3-Cyclohexylphenothiazine. Product appeared as light-yellow flakes; mp = 154-156 °C. ^{1}H NMR (400 MHz; DMSO-d6): δ 8.47 (br, 1H), 6.97 (ddd, *J* = 1.5, 7.8, 7.8 Hz, 1H), 6.90 (dd, *J* = 1.3, 7.6 Hz, 1H), 6.83 (dd, *J* = 1.9, 8.1 Hz, 1H), 6.75-6.70 (m, 2H), 6.66 (dd, *J* = 1.2, 7.9 Hz, 1H), 6.60 (d, *J* = 8.0 Hz, 1H), 2.33-2.28 (m, 1H), 1.75-1.64 (m, 5H), 1.36-1.15 (m, 5H). ^{13}C NMR (101 MHz; DMSO-d6): δ 142.4, 141.3, 139.9, 127.4, 126.2, 125.7, 124.3, 121.5, 116.3, 116.1, 114.3(2), 114.2(7), 42.8, 34.0, 26.3, 25.5. HRMS (EI, magnetic sector): calcd for $C_{18}H_{19}NS$ 281.12382, found 281.12509.



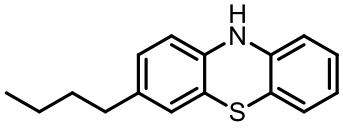
3,7-Dicyclohexylphenothiazine. Product appeared as light-yellow flakes; mp = 234-237 °C. ^{1}H NMR (400 MHz; DMSO-d6): δ 8.35 (br, 1H), 6.81 (dd, *J* = 1.9, 8.1 Hz, 2H), 6.74 (d, *J* = 1.8 Hz, 2H), 6.58 (d, *J* = 8.0 Hz, 2H), 2.33-2.27 (m, 2H), 1.74-1.64 (m, 10H), 1.36-1.11 (m, 10H). ^{13}C NMR (101 MHz; DMSO-d6): δ 141.0, 140.2, 125.6, 124.3, 116.1, 114.2, 42.8, 34.0, 26.3, 25.5. HRMS (EI, magnetic sector): calcd for $C_{18}H_{19}NS$ 363.20207, found 363.20350.



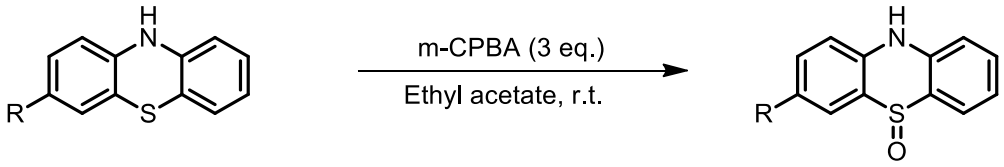
3-Phenylphenothiazine. Product appeared as a light-yellow flakes; mp = 222-224 °C. ^{1}H NMR (400 MHz; DMSO-d6): δ 8.71 (br, 1H), 7.57-7.55 (m, 2H), 7.41-7.37 (m, 2H), 7.32-7.26 (m, 2H), 7.22 (d, *J* = 2.2 Hz, 1H), 7.00 (ddd, *J* = 1.5, 7.5, 7.5 Hz, 1H), 6.93 (dd, *J* = 1.4, 7.6 Hz, 1H), 6.78-6.74 (m, 2H), 6.70 (dd, *J* = 1.2, 7.9 Hz, 1H). ^{13}C NMR (101 MHz; DMSO-d6): δ 141.7, 141.4, 139.1, 133.7, 128.8, 127.6, 126.8, 126.3, 125.8(7), 125.7(3), 124.1, 121.9, 117.0, 116.1, 114.7, 114.5. HRMS (EI, magnetic sector): calcd for $C_{18}H_{13}NS$ 275.07687, found 275.07673.



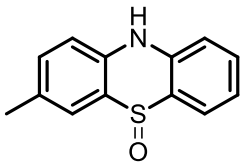
3-*tert*-Butylphenothiazine. Product appeared as yellow platelet crystals; mp = 155-158 °C. ^{1}H NMR (300 MHz; DMSO-d6): δ 8.49 (br, 1H), 7.57-6.89 (m, 4H), 6.75-6.62 (m, 4H), 1.19 (s, 9H). ^{13}C NMR (75 MHz; DMSO-d6): δ 144.2, 142.3, 139.5, 127.3, 126.1, 124.2, 122.9, 121.4, 116.3, 115.8, 114.1(7), 113.9(7), 33.7, 31.0. HRMS (EI, magnetic sector): calcd for $C_{16}H_{17}NS$ 255.10817, found 255.10634.



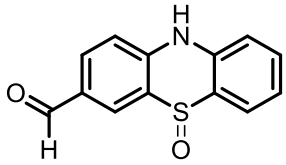
3-*n*-Butylphenothiazine. Product appeared as light-yellow flakes; mp = 124-126 °C. ^{1}H NMR (400 MHz; DMSO-d6): δ 8.47 (br, 1H), 6.97 (ddd, *J* = 1.5, 7.6 Hz, 1H), 6.90 (dd, *J* = 1.3, 7.6 Hz, 1H), 6.80 (dd, *J* = 2.0, 8.0 Hz, 1H), 6.74-6.70 (m, 2H), 6.67 (dd, *J* = 1.2, 7.9 Hz, 1H), 6.60 (d, *J* = 8.0 Hz, 1H), 2.39 (t, *J* = 7.5 Hz, 2H), 1.45 (quin, *J* = 7.6 Hz, 2H), 1.24 (sext, *J* = 7.6 Hz), 0.86 (t, 7.4 Hz, 3H). ^{13}C NMR (101 MHz; DMSO-d6): δ 142.4, 139.8, 135.8, 127.5, 127.3, 126.2, 125.9, 121.5, 116.3, 116.1, 114.3, 33.8, 33.1, 21.6, 13.8. HRMS (EI, magnetic sector): calcd for $C_{16}H_{17}NS$ 255.10817, found 255.10802.



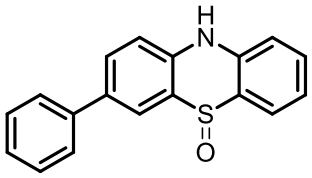
Synthesis of Phenothiazine-S-Oxides. In a 20 mL scintillation vial, the corresponding phenothiazine weighed out (0.5-1.1 mmol) along with a small stir bar. A minimum of ethyl acetate (approx. 4-8 mL) was used to dissolve the phenothiazine, using gentil heating when necessary. Once at room temperature, 3 eq. of m-CPBA was dissolved in a minimum of ether (approx. 2 mL), then added to the vial while stirring. The phenothiazine-S-oxide product precipitated nearly immediately and the suspension was left to stir for about 15 min (with the cap on). The solvent was decanted and the precipitate was rinsed several times with ethyl acetate, by diethyl ether, then finally by hexanes. After removing the residual solvent under vacuum, the product was characterized. Product recovery on this scale was typically between 55-65%.



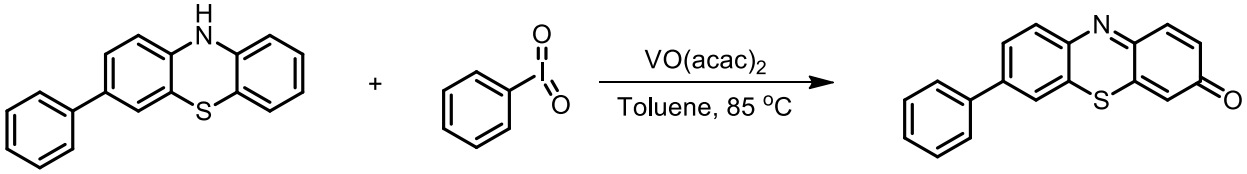
3-Methylphenothiazine-S-oxide. Product appeared as a white solid. ^{1}H NMR (400 MHz; DMSO-d6): δ 10.85 (br, 1H), 7.88 (dd, *J* = 1.3, 7.8 Hz, 1H), 7.69 (br, 1H), 7.59 (m, 1H), 7.44, (dd, *J* = 1.9, 8.5 Hz, 1H), 7.35 (d, *J* = 8.2 Hz, 1H), 7.29 (d, *J* = 8.4 Hz, 1H), 7.16 (ddd, *J* = 1.0, 7.9, 7.9 Hz, 1H). ^{13}C NMR (101 MHz; DMSO-d6): δ 137.0, 134.7, 133.7, 132.6, 131.2, 130.5(0), 130.3(6), 120.8(3), 120.6(4), 116.7(1), 116.6(5). HRMS (EI, magnetic sector): calcd for $C_{13}H_{11}NOS$ 229.05613, found 229.05667.



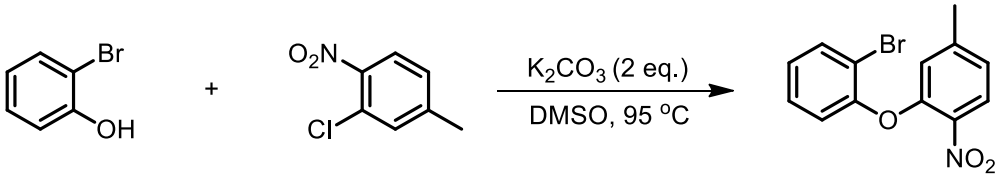
3-Formylphenothiazine-S-oxide. Product appeared as a pale-yellow solid. ^{1}H NMR (400 MHz; DMSO-d6): δ 11.55 (br, 1H), 9.95 (s, 1H), 8.54 (d, *J* = 1.5 Hz, 1H), 8.06 (dd, *J* = 1.4, 8.6 Hz, 1H), 7.99 (d, *J* = 7.7 Hz, 1H), 7.69 (dd, *J* = 7.4 Hz, 1H), 7.52-7.46 (m, 2H), 7.32 (dd, *J* = 7.4 Hz, 1H). ^{13}C NMR (101 MHz; DMSO-d6): δ 190.4, 140.9, 136.3, 135.6, 133.2, 131.4(6), 131.2(9), 129.7, 122.8, 121.7, 120.8, 117.6(5), 117.5(3). HRMS (EI, magnetic sector): calcd for $C_{13}H_{9}NO_{2}S$ 243.03540, found 243.03607.



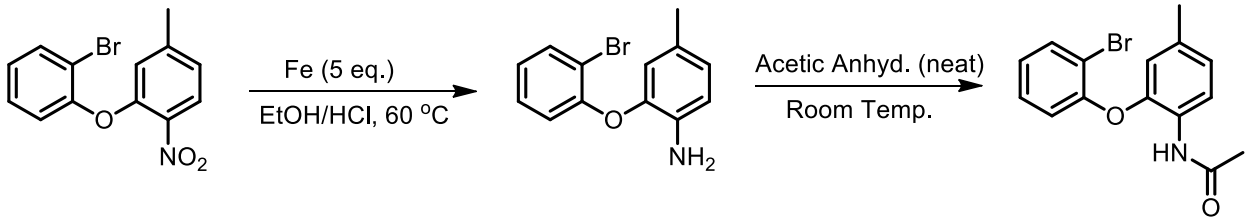
3-Phenylphenothiazine-S-oxide. Product appeared as an off-white solid. ^{1}H NMR (400 MHz; DMSO-d6): δ 11.09 (br, 1H), 8.22 (d, *J* = 2.0 Hz, 1H), 7.98-7.93 (m, 2H), 7.75 (d, *J* = 7.5 Hz, 2H), 7.64 (ddd, *J* = 1.3, 8.4, 8.4 Hz, 1H), 7.50-7.46 (m, 3H), 7.41 (d, *J* = 8.2 Hz, 1H), 7.36 (dd, *J* = 7.4 Hz, 1H), 7.22 (dd, *J* = 7.4 Hz, 1H). ^{13}C NMR (101 MHz; DMSO-d6): δ 138.7, 136.7, 136.1, 133.1, 132.8, 131.2, 131.0, 129.1, 128.8, 127.2, 126.2, 121.4(5), 121.3(6), 121.0, 117.5, 116.9. HRMS (EI, magnetic sector): calcd for $C_{18}H_{13}NOS$ 291.07178, found 291.06936.



7-Phenylphenothiazin-3-one. The preparation of this was based on Barret and Daudon's procedure for making phenothiazin-3-one.[3] One equivalent of 3-phenylphenothiazine (148 mg) and iodoxybenzene (127 mg) and 0.2 equivalents of vanadyl acetylacetonate (29 mg) were combined in a small round bottom flask and stirred in toluene (4 mL) at 85 °C overnight. After cooling, the mixture was diluted into some DCM and silica was added, and the solvents were removed under reduced pressure. The product was isolated by column chromatography (30% ethyl acetate in hexanes), a sparingly soluble deep red solid (34 mg, 22%). ^{1}H NMR (400 MHz; DMSO-d6): δ 8.15 (d, *J* = 2.0 Hz, 1H), 7.98 (d, *J* = 8.4 Hz, 1H), 7.92 (dd, *J* = 2.0, 8.4 Hz, 1H), 7.86 (d, *J* = 7.4 Hz, 2H), 7.71 (d, *J* = 9.8 Hz, 2H), 7.55-7.45 (m, 3H), 6.95 (d, *J* = 2.2 Hz, 1H), 6.92 (dd, *J* = 2.2, 9.8 Hz, 1H). ^{13}C NMR (101 MHz; DMSO-d6): δ 181.7, 145.8, 142.7, 139.7, 137.9(2), 137.6(8), 135.0(1), 134.7(6), 133.9, 129.2, 127.2, 126.6, 124.3, 123.3, 119.8. HRMS (EI, magnetic sector): calcd for $C_{18}H_{11}NOS$ 289.05613, found 289.05684.

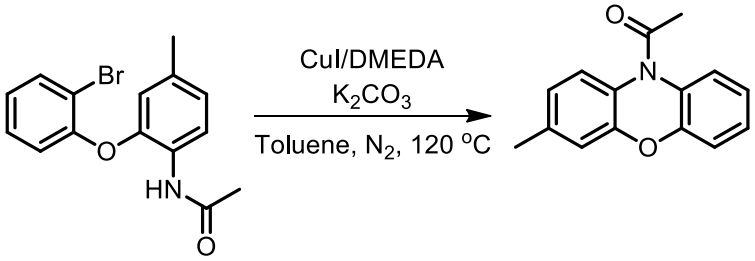


2-(2-Bromophenoxy)-4-methyl-1-nitrobenzene. The following was used in the preparation of 3-methylphenoxazine. In a 250-mL round bottom flask were combined 2-bromophenol (4.33 g, 25 mmol), 2-chloro-4-methyl-1-nitrobenzene (4.29 g, 25 mmol), 50 mL of DMSO, and potassium carbonate (6.9 g, 50 mmol). With stirring, this was heated on oil bath to 95 °C, which was maintained for approximately 9 h. After cooling to room temperature, the mixture was poured into 350 mL of water and was extracted three times with ethyl acetate, and the organic phase was subsequently washed with water then brine. The organic portion was dried with anhydrous $MgSO_4$, filtered, and the solvent was removed under reduced pressure. The title product was isolated by column chromatography (10% ethyl acetate in hexanes) as a yellow oil which on standing gave light yellow crystals (4.34 g, 56%); mp = 52-55 °C. ^{1}H NMR (400 MHz; $CDCl_3$): δ 7.94 (d, *J* = 8.4 Hz, 1H), 7.67 (dd, *J* = 1.6, 7.9 Hz, 1H), 7.33 (ddd, *J* = 1.6, 8.0, 8.0 Hz, 1H), 7.11 (ddd, *J* = 1.6, 7.9, 7.9 Hz, 1H), 7.03-7.00 (m, 2H), 6.65 (d, *J* = 0.9 Hz, 1H), 2.35 (s, 3H). ^{13}C NMR (101 MHz; $CDCl_3$): δ 152.3, 150.2, 146.2, 138.3, 134.1, 128.9, 126.1(4), 126.0(3), 124.1, 120.9, 119.7, 115.0, 21.7. HRMS (EI, magnetic sector): calcd for $C_{13}H_{10}BrNO_3$ 306.98441, found 306.98498.

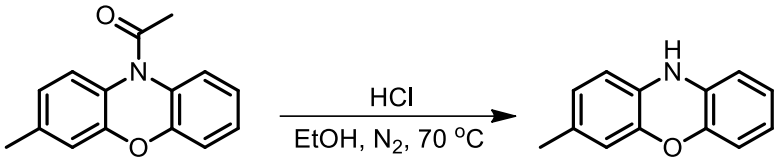


***N*-(2-(2-Bromophenoxy)-4-methylphenyl)acetamide.** In a 500-mL round bottom flask were combined 2-(2-bromophenoxy)-4-methyl-1-nitrobenzene (7.52 g, 24.4 mmol), ethanol (125 mL) and iron powder (6.8 g, 122 mmol). With rapid stirring, a mixture of ethanol (25 mL) and concentrated HCl (25 mL) were added gradually by dropping funnel, and then maintained at 60 °C until the starting material was consumed (approx. 2 h). After cooling, some of the ethanol (~2/3) was removed under reduced pressure and then suspension was gradually quenched in saturated $NaHCO_3$ solution. The aqueous suspension was extracted repeatedly with DCM, and the organic was subsequently rinsed, dried with $MgSO_4$, filtered, and then the solvent removed under reduced pressure. The residue was dissolved directly into acetic anhydride (~20 mL), which was allowed to stir until all of the intermediate product (2-(2-bromophenoxy)-4-methylaniline) had been consumed. The acetic anhydride solution was quenched by stirring it

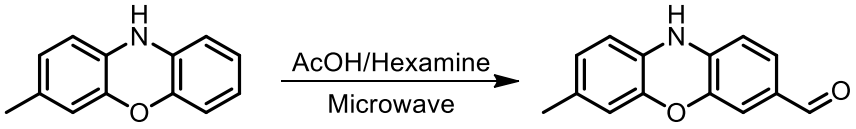
into saturated $NaHCO_3$ solution until bubbling stop, after which a typical extraction work-up into the ethyl acetate was carried out (extract, rinse, dry, filter etc.) The title product was isolated by column chromatography (20% ethyl acetate in hexanes) a white crystalline solid (6.63 g, 85%); mp = 114-116 °C. ^{1}H NMR (400 MHz; $CDCl_3$): δ 8.27 (d, *J* = 8.3 Hz, 1H), 7.68 (br, 1H), 7.66 (dd, *J* = 1.6, 7.9 Hz, 1H), 7.30 (ddd, *J* = 1.6, 8.1, 8.1 Hz, 1H), 7.07 (ddd, *J* = 1.5, 7.9, 7.9 Hz, 1H), 6.98 (dd, *J* = 1.4, 8.2 Hz, 1H), 6.94 (dd, *J* = 0.8, 8.3 Hz, 1H), 6.58 (d, 1.1 Hz, 1H), 2.25 (s, 3H), 2.18 (s, 3H). ^{13}C NMR (101 MHz; $CDCl_3$): δ 168.2, 152.9, 145.1, 134.0(3), 133.8(6), 128.9, 126.8, 125.5, 124.8, 121.1, 120.2, 117.7, 114.4, 24.8, 21.0. HRMS (EI, magnetic sector): calcd for $C_{15}H_{14}BrNO_2$ 319.02079, found 319.01822.



10-Acetyl-3-methylphenoxazine. Into a 150-mL Teflon screw-cap sealable tube were combined copper(I) iodide (400 mg, 2.1 mmol), toluene (42 mL) and 1,2-dimethylethylenediamine (0.46 mL, 4.2 mmol) which were sparged with N_2 continuously while stirring rapidly on magnetic stir plate (approx. 10 min). The *N*-(2-(2-bromophenoxy)-4-methylphenyl)acetamide starting material (6.63 g, 20.7 mmol) and 2 equivalents of K_2CO_3 (5.8 g, 42 mmol) were added after which the vessel was sealed. The vessel was heated on an oil bath to ~120 °C which was maintained for 16 h. After cooling, the reaction mixture was filtered and these vessel and filter paper were successively rinsed with ethyl acetate until quantitative transfer was achieved (visualized by TLC). After removing the solvent under reduced pressure, the title product was isolated by column chromatography (20% ethyl acetate in hexanes) which appeared as a white solid (4.28 g, 86.5%); mp = 113-116 °C. ^{1}H NMR (400 MHz; DMSO-d6): δ 7.60 (dd, *J* = 1.6, 7.8 Hz, 1H) 7.47 (d, *J* = 8.1 Hz, 1H), 7.27-7.16 (m, 3H), 7.04 (d, *J* = 1.6 Hz, 1H), 7.00 (dd, *J* = 1.9, 8.1 Hz, 1H), 2.30 (s, 3H), 2.25 (s, 3H). ^{13}C NMR (101 MHz; DMSO-d6): δ 168.8, 150.2(8), 150.1(2), 136.9, 129.3, 126.9, 126.6, 125.4, 124.9, 124.1, 123.5, 116.8(9), 116.5(5), 22.7, 20.5. HRMS (EI, magnetic sector): calcd for $C_{15}H_{13}NO_2$ 239.09463, found 239.09301.

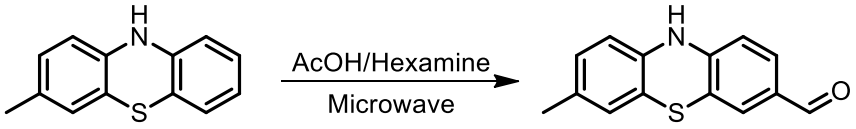


3-Methylphenoxazine. To begin, a Schlenk tube (>150 mL) was evacuated then backfilled with N_2. The flask was then opened with a steady flow of N_2 passing through the side arm and out the top, throughout addition of reagents. The flask was charged with ethanol (100 mL), concentrated HCl (6 mL) and a magnetic stir bar, and a N_2 filled balloon affixed with a long needle was placed through the top to sparge the solvent while stirring (for at least 10 min). 10-Acetyl-3-methylphenoxazine was added (4.26 g, 17.8 mmol) and the suspension was stirred while heating to 70 °C (while maintaining a continuous flow of N_2). Once up to temperature, flask was sealed with a septum, the gas side arm was closed, and a balloon of N_2 was placed in the septa and the reaction progress was closely monitored by TLC (if degassing was successful, the solution should be fairly colourless with only a hint of violet, if degassing failed it will turn a deep purple). After all of the starting material was consumed (approx. 2 h), the reaction was cooled to room temperature after which reaction mixture was carefully quenched in a saturated $NaHCO_3$ solution. After extracting with ethyl acetate, the organic layer was subsequently rinsed, dried ($MgSO_4$), filtered and the solvent was removed under reduced pressure. The product was further purified by column chromatography, rendering the 3-methylphenoxazine, a white solid (3.09 g, 88%); mp = 140-142 °C. ^{1}H NMR (400 MHz; DMSO-d6): δ 8.04 (br, 1H), 6.71 (ddd, J = 1.6, 7.5, 7.5 Hz, 1H) 6.59-6.51 (m, 3H), 6.44-6.41 (m, 2H), 6.34 (d, 1H), 2.09 (s, 3H). ^{13}C NMR (101 MHz; DMSO-d6): δ 142.6(5), 142.5(3), 132.6, 129.7, 129.3(7), 123.9(3), 123.8(2), 120.0, 115.7, 115.0, 113.1(5), 113.0(3), 20.1. HRMS (EI, magnetic sector): calcd for $C_{13}H_{11}NO$ 197.08406, found 197.08589.

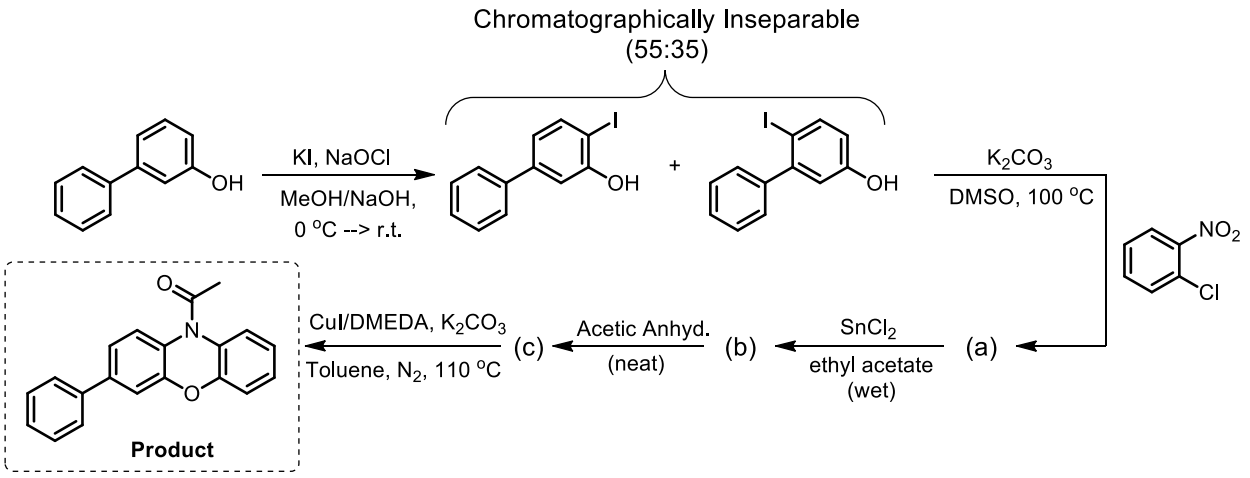


3-Formyl-7-methylphenoxazine. 3-Methylphenoxazine (0.986 g, 5 mmol), hexamine (1.05 g, 7.5 mmol), glacial acetic acid (18 mL) and magnetic stir bar were placed in an Anton Parr G30 borosilicate microwave vessel. The solution was sparged with N_2 for 10 min after which the vessel was sealed and the reaction vessel was placed in the microwave reactor (Monowave 400).

With stirring (600 RPM) the tube was heated to 120 °C (held for 30 min), then 150 °C (held for 80 min), back to 120 °C (held for 30 min) then cooled to room temperature. The reaction mixture was poured into water and Na_2CO_3 was added to neutralize the solution. The slurry was extracted several times with dichloromethane, after which the organic solution was dried with $MgSO_4$, filtered and solvent removed under reduced pressure. 3-Formyl-7-methylphenoxazine was isolated by column chromatography (40% EtOAc gradient in hexanes) to afford a brownish orange solid that makes a fluorescent solution when dissolved (73 mg, 6.5%); mp = 219-222 °C. ^{1}H NMR (400 MHz; DMSO-d6): δ 9.57 (s, 1H), 8.96 (br, 1H), 7.30 (d, *J* = 7.9 Hz, 1H), 6.97 (s, 1H), 6.58-6.49 (m, 3H), 6.40 (d, *J* = 7.7 Hz, 1H), 2.10 (s, 3H). ^{13}C NMR (101 MHz; DMSO-d6): δ 189.7, 142.8, 142.3, 138.9, 131.2, 128.9(8), 128.8(8), 127.5, 124.3, 115.9, 113.8(2), 113.7(0), 112.5, 20.2. HRMS (EI, magnetic sector): calcd for $C_{14}H_{11}NO_2$ 225.07898, found 225.07633.

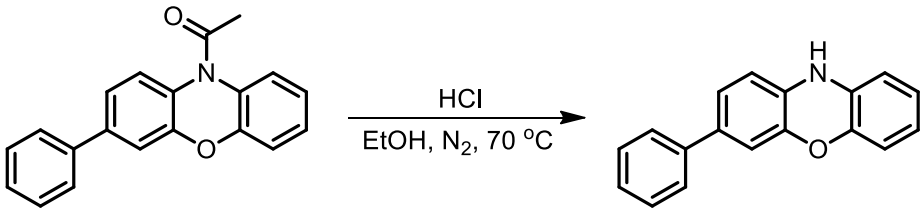


3-Formyl-7-methylphenothiazine. The reaction was carried out in an analogous fashion to the preparation of 3-formyl-7-methylphenoxazine using 3-methylphenothiazine as a starting material (0.853 g, 4 mmol). The title product was isolated by column chromatography (40% EtOAc in hexanes) which appeared as an orange solid (0.18 g, 18.6%); mp = 240-245 °C (decomp.). ^{1}H NMR (400 MHz; DMSO-d6): δ 9.62 (s, 1H), 9.15 (br, 1H), 7.47 (d, *J* = 8.2 Hz, 1H), 7.34 (s, 1H), 6.80 (d, *J* = 8.1 Hz, 1H) 6.73-6.68 (m, 2H), 6.58 (d, *J* = 8.0 Hz, 1H), 2.12 (s, 3H). ^{13}C NMR (101 MHz; DMSO-d6): δ 189.8, 147.3, 136.9, 132.2, 130.4, 130.1, 128.2, 127.4, 126.5, 116.5, 115.5, 115.0, 113.7, 19.9. HRMS (EI, magnetic sector): calcd for $C_{14}H_{11}NOS$ 241.05613, found 241.05636.



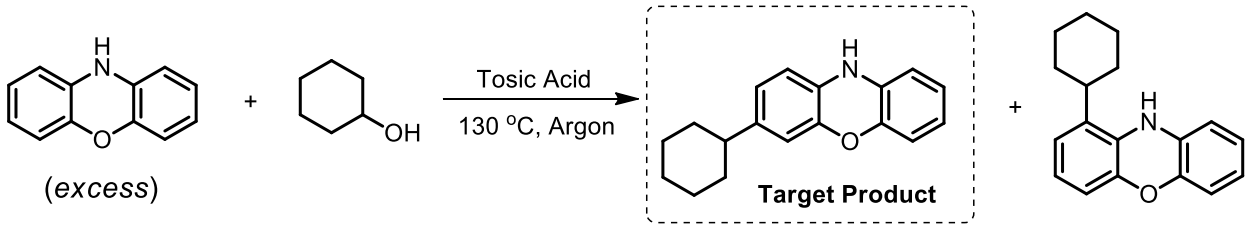
10-Acetyl-3-phenylphenoxazine. In the first step, 3-phenylphenol (2.55 g, 15 mmol) was dissolved in approximately 50 mL of methanol along with crushed NaOH (0.6 g, 15 mmol) and potassium iodide (2.99 g, 18 mmol). While stirring on an ice bath, a caustic solution of sodium hypochlorite (6% bleach solution) was added dropwise until all KI was consumed (~20 mL). Perceiving by TLC that all 3-phenylphenol had been consumed, the reaction was brought to a neutral pH and extracted multiple times with ethyl acetate (following a typical workup protocol). A ^{1}H NMR of the crude residue indicated that the major products were two different mono-iodo phenols, slightly favouring our desired 2-iodo-5-phenylphenol (approx. 55:35), however they did not appear to be readily separable. The synthesis was carried forward for multiple steps (described below) as a crude mixture until the formation of 10-acetyl-3-phenylphenoxazine which could be easily isolated. The crude mixture of iodophenols was dissolved in DMSO (30 mL) along with 2-nitrochlorobenzene (2.67 g, 17 mmol). With stirring, K_2CO_3 was added (4.15 g, 30 mmol) and the temperature was increased to 100 °C and maintained until the majority of the iodophenol(s) had been consumed. After cooling, the reaction mixture was poured into water and was extracted with 50 mL of ethyl acetate 3 times (150 mL total). The combined organic layer was rinsed once with 1 M HCl and the organic phase was drawn off into a 250-mL round bottom flask. (Note: Do *not* dry with $MgSO_4$). Anhydrous $SnCl_2$ (15.2 g, 80 mmol) was added to the flask and it was allowed to stir overnight. After confirming that the reduction was successful, the reaction mixture was poured into a 1-L Erlenmeyer flask containing 300 mL of saturated $NaHCO_3$ solution. The flask was swirled (not shaken, in order to minimize emulsions of Sn(OH)Cl in the organic phase), and the organic phase was carefully decanted into a separatory funnel. More ethyl acetate is added to the Erlenmeyer flask and the process is repeated until a

point of diminished returns. The combined organics are rinsed, then dried with $MgSO_4$, then filtered. The residue obtained by removing the solvent was dissolved in acetic anhydride (~10 mL) and was left to stir overnight. Finally, after quenching the acetic anhydride and working up the resulting intermediate acetamide product, it was dissolved in toluene (30 mL) and Cu(I) (0.57 g), 1,2-dimethylethylenediamine (0.65 mL), K_2CO_3 (5.2 g) and a stir bar were all combined in a Teflon screw-cap sealable tube. After sparging with argon for 10 minutes with stirring, the vessel was sealed and was heated to 110 °C (which was maintained for >12 h). After cooling, the reaction mixture was filtered and these vessel and filter paper were successively rinsed with ethyl acetate until quantitative transfer was achieved (visualized by TLC). After removing the solvent under reduced pressure, the title product was isolated by column chromatography (20% ethyl acetate in hexanes) which was a resin like substance. Calculated from the 3-phenylphenol (15 mmol), the yield of the entire synthesis of 10-acetyl-3-phenylphenoxazine was 16.7%, giving 755 mg of product. ^{1}H NMR (400 MHz; DMSO-d6): δ 7.72-7.68 (m, 3H), 7.64 (d, *J* = 7.8 Hz, 1H), 7.52-7.45 (m, 4H), 7.40-7.37 (m, 1H), 7.29-7.19 (m, 3H), 2.31 (s, 3H). ^{13}C NMR (101 MHz; DMSO-d6): δ 168.9, 150.6(9), 150.1(6), 139.0(1), 138.5(8), 129.1(3), 129.0, 128.5, 127.9, 127.1, 126.7, 125.4, 123.7, 121.8, 116.7, 114.5, 22.8. HRMS (EI, magnetic sector): calcd for $C_{20}H_{15}NO_2$ 301.11028, found 301.10719.



3-Phenylphenoxazine. The formation of the title product was carried out using the same procedure used to convert 10-acetyl-3-methylphenoxazine to 3-methylphenoxazine: 10-acetyl-3-phenylphenoxazine (685 mg, 2.27 mmol); ethanol (25 mL); concentrated HCl (1 mL). Once the reaction was worked up, the title product was further purified by recrystallization out of ethanol giving light-grey plate-like crystals. The isolated yield was 68% (400 mg); mp = 175-177 °C. ^{1}H NMR (400 MHz; DMSO-d6): δ 8.36 (br, 1H), 7.55 (d, *J* = 7.7 Hz, 2H), 7.38 (dd, *J* = 7.5 Hz, 2H), 7.26 (dd, *J* = 7.5 Hz, 1H), 7.07 (dd, *J* = 1.9, 8.0 Hz, 1H), 6.93 (d, *J* = 1.8 Hz, 1H), 6.74 (ddd, *J* = 1.3, 7.4, 7.4 Hz, 1H), 6.64-6.56 (m, 2H), 6.52 (d, *J* = 8.0 Hz, 1H), 6.47 (d, *J* = 7.8 Hz, 1H). ^{13}C NMR (101 MHz; DMSO-d6): δ 143.2, 142.6, 139.3, 132.3, 132.0, 131.8, 128.8, 126.6,

125.6, 124.0, 122.0, 120.5, 115.1, 113.5(4), 113.3(8), 113.(1). HRMS (EI, magnetic sector): calcd for $C_{18}H_{13}NO$ 259.09971, found 259.10149.



Friedel-Crafts Cyclohexanation of Phenoxazine. To obtain 3-cyclohexylphenoxazine, an excess of phenoxazine (4 eq.) was reacted with cyclohexanol (1 eq.) in the presence of tosic acid monohydrate (1.2 eq.), in order to mitigate over-alkylation. In a 1 dram scintillation vial with a stir bar was combined 733 mg of phenoxazine and 100 mg of cyclohexanol. After aerating the vial with a stream of argon, 228 mg of tosic acid monohydrate was added and the vial was sealed. Six more vials were identically configured (total of 7), and they were heated in a metal block to 130 °C, and the temperature was maintained for approximately 4 h. After cooling, the solid mass in each vial was rinsed into a large flask using DCM and the solvent was removed under reduced pressure in the presence of silica. The products were isolated by column chromatography (15% ethyl acetate in hexanes). The first isomer to elute was **1-Cyclohexylphenoxazine**, which solidified on standing as brownish crystals once the fractions were concentrated. Based on cyclohexanol being a limiting reagent (7 mmol total), yield of 15.9% was obtained (296 mg); mp = 82-84 °C. ^{1}H NMR (400 MHz; DMSO-d6): δ 7.42 (br, 1H), 6.77-6.70 (m, 2H), 6.68 (dd, *J* = 1.3, 7.8 Hz, 1H), 6.59-6.53 (m, 3H), 6.44 (dd, *J* = 1.0, 7.7 Hz, 1H), 2.67-2.60 (m, 1H), 1.78-1.67 (m, 5H), 1.51-1.41 (m, 2H), 1.33-1.16 (m, 3H). ^{13}C NMR (400 MHz; DMSO-d6): δ 142.8, 132.5, 131.4, 128.9, 123.6, 121.0(5), 120.4(4), 120.2(1), 114.6(8), 114.1(5), 112.8, 35.4, 32.7, 26.2(1), 25.6(9). HRMS (EI, magnetic sector): calcd for $C_{18}H_{19}NO$ 265.14666, found 265.14849. The target product, **3-Cyclohexylphenoxazine**, eluted next, coming out only slightly before the unreacted phenoxazine starting material (limiting the isolation of 3-cyclohexylphenoxazine). Fractions which contained only 3-cyclohexylphenoxazine were combined and concentrated giving a solid. The solid was triturated with a minimum of hexanes to remove discoloration and in the end 74 mg of pure product was obtained as a light-grey solid; mp = 147-150 °C. ^{1}H NMR (400 MHz; DMSO-d6): δ 8.05 (br, 1H), 6.70 (dd, *J* = 7.7, 7.7 Hz, 1H), 6.58-6.41 (m, 5H), 6.35 (d, *J* = 7.9 Hz, 1H), 2.31-2.22 (m, 1H), 1.73-1.64 (m, 5H),

1.35-1.12 (m, 5H). ^{13}C NMR (400 MHz; DMSO-d6): δ 142.7, 142.5, 140.2, 132.7, 130.0, 123.8, 121.6, 120.0, 115.0, 113.4(2), 113.1(6), 112.9(9), 42.8, 33.9, 26.3, 25.6. HRMS (EI, magnetic sector): calcd for $C_{18}H_{19}NO$ 265.14666, found 265.14693.

6.8 Methods

Inhibited autoxidation of *n*-hexadecane at 160 °C. 10-15 mL of *n*-hexadecane (Alfa Aesar 95%), treated by percolation through basic alumina and silica (2 : 1 alumina/silica, with the silica packed on top of the alumina), was loaded into test tubes placed within an aluminium heat-block and each tube was purged with nitrogen *via* a capillary tube for 20 min at room temperature. While under the atmosphere of nitrogen, the block was heated to 168 °C (hexadecane had an average temperature of 160 ± 2 °C.) When the temperature had stabilized, 50-150 μL of the RTA stock solution (EtOAc), were injected to for a final [RTA] of 150 μM. After removing the first sample (0 min), the flow of nitrogen was replaced by oxygen and aliquots (*ca.* 0.5 mL) were collected at regular intervals. For the quantification of [ROOH], 5 μL of the sample were loaded on a well of a 96-well microplate for analysis wherein 215 μL of a mixture of 1 : 4 iPrOH/MeOH and 30 μL of a solution containing the fluorogenic coumarin phosphine dye (100 μM) were added using the automated reagent dispenser at 37 °C. After stirring for 30 seconds followed by a 5 second delay, the well was excited and the gain of fluorescence was measured every second for 60 seconds (coumarin phosphine dye: λ_{ex} = 340 nm, λ_{em} = 425 nm). The concentration of hydroperoxide in each well was determined from the rate of phosphine oxidation using the rate constant for the reaction of the dye with secondary peroxyl radicals (k = 5.1 M^{-1} s^{-1}) assuming pseudo-first-order kinetics. For EPR analysis (quantitative spin-counting), samples were diluted into benzene (either 1 : 1 or 2 : 1 benzene/hexadecane) for convenient handling. EPR spectra were recorded on a Bruker EMXplus (X-band) spectrometer equipped with an ER 4119HS cavity and the radical concentration was determined using the quantitative EPR package of the Bruker Xenon software. For UPLC product analysis, samples were extracted with HPLC-grade methanol prior to analysis.

UPLC analysis of *n*-hexadecane samples. A portion of an aliquot from the hexadecane oxidation (150 μL) and HPLC-grade methanol (150 μL). After separation of the layers, the methanol was transferred to a HPLC vial with a 200 μL glass insert. Column: Hypersil GOLD C-18 reverse phase column (250 mm × 4.6 mm, 5 μm). UPLC method: injection volume of 10 μL;

mobile phase A (pH 5.5 10 mM ammonium acetate buffer) and mobile phase B (methanol); flow rate: 0.5 mL min^{-1}; run time: 30 min; the gradient elution method: 80% to 100% B from 0 to 10 min, hold at 100% B from 10 to 25 min, 100% to 80% B from 25 to 30 min. Elution was monitored by PDA from 190 to 390 nm and ESI+ scan from 150 to 750 *m*/*z*. Consumption of RTA starting material was estimated based on decreased integral of the peak relative to the 0 minute time point. The concentration of oxidation products derived from the RTA starting material were calculated by calibrated curves using authentic standards.

Electrochemistry. Standard potentials were measured by cyclic voltammetry at 25 °C in dry acetonitrile containing Bu4N·PF6 (0.1 M) as supporting electrolyte. Experiments were carried out with a potentiostat equipped with a glassy-carbon working electrode, a platinum auxiliary electrode, and a $Ag/AgNO_3$ (0.005 M) reference electrode. The given E° were determined relative to the ferrocene/ ferrocenium couple under the same conditions (Fc/Fc+ vs NHE + 0.64 V).[4]

Computations. Quantum chemical calculations were carried out using the M06-2X DFT method as it is implemented in the Gaussian 16 suite of programs.

6.9 Supplementary Data

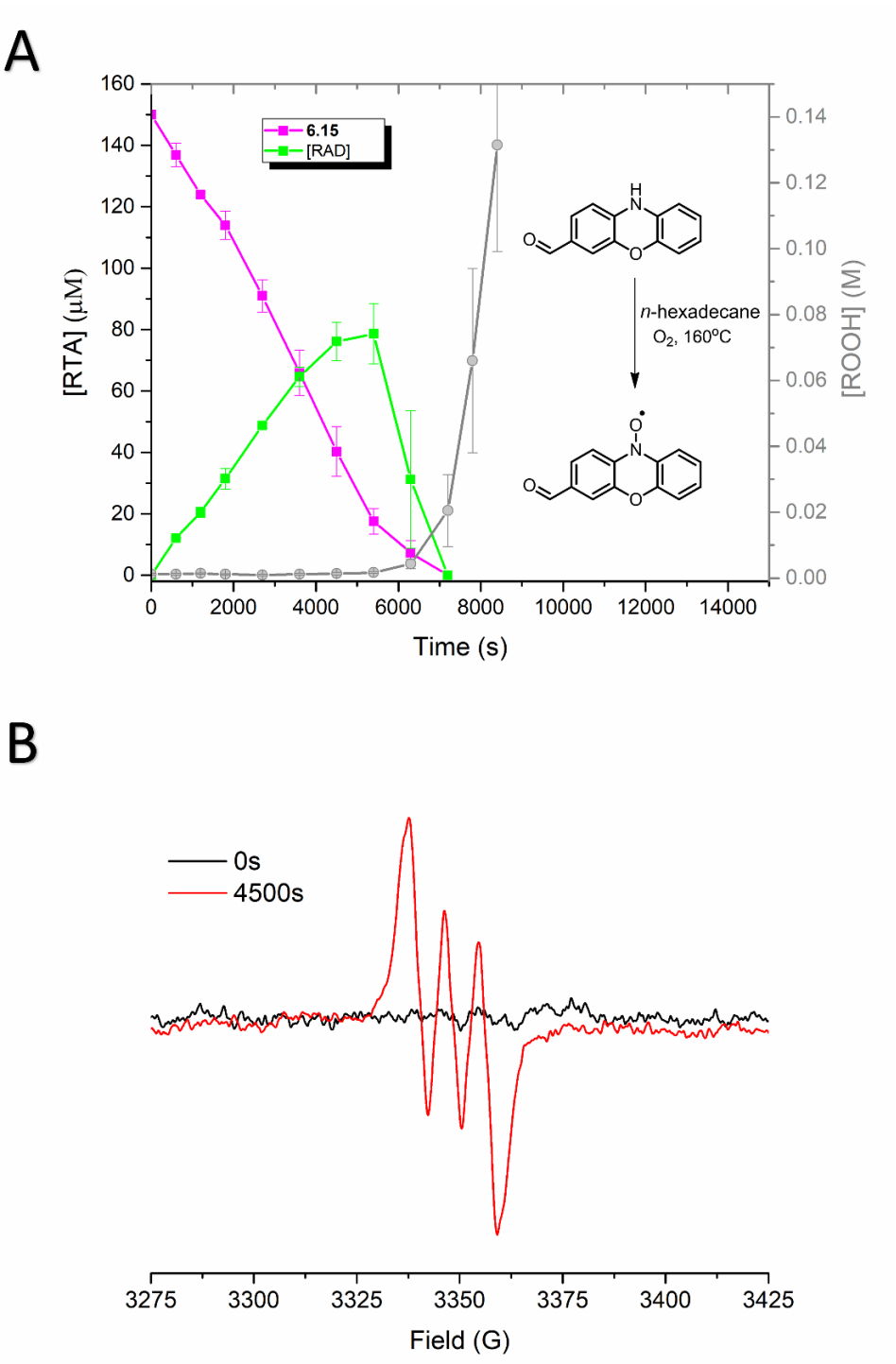


Figure 6.10. (A) Time course loss of **6.16** and the formation of major oxidation products in *n*-hexadecane at 160 °C with O_2. **(B)** EPR of 0 min and 75 min hexadecane samples compared (diluted by 1/3 into benzene).

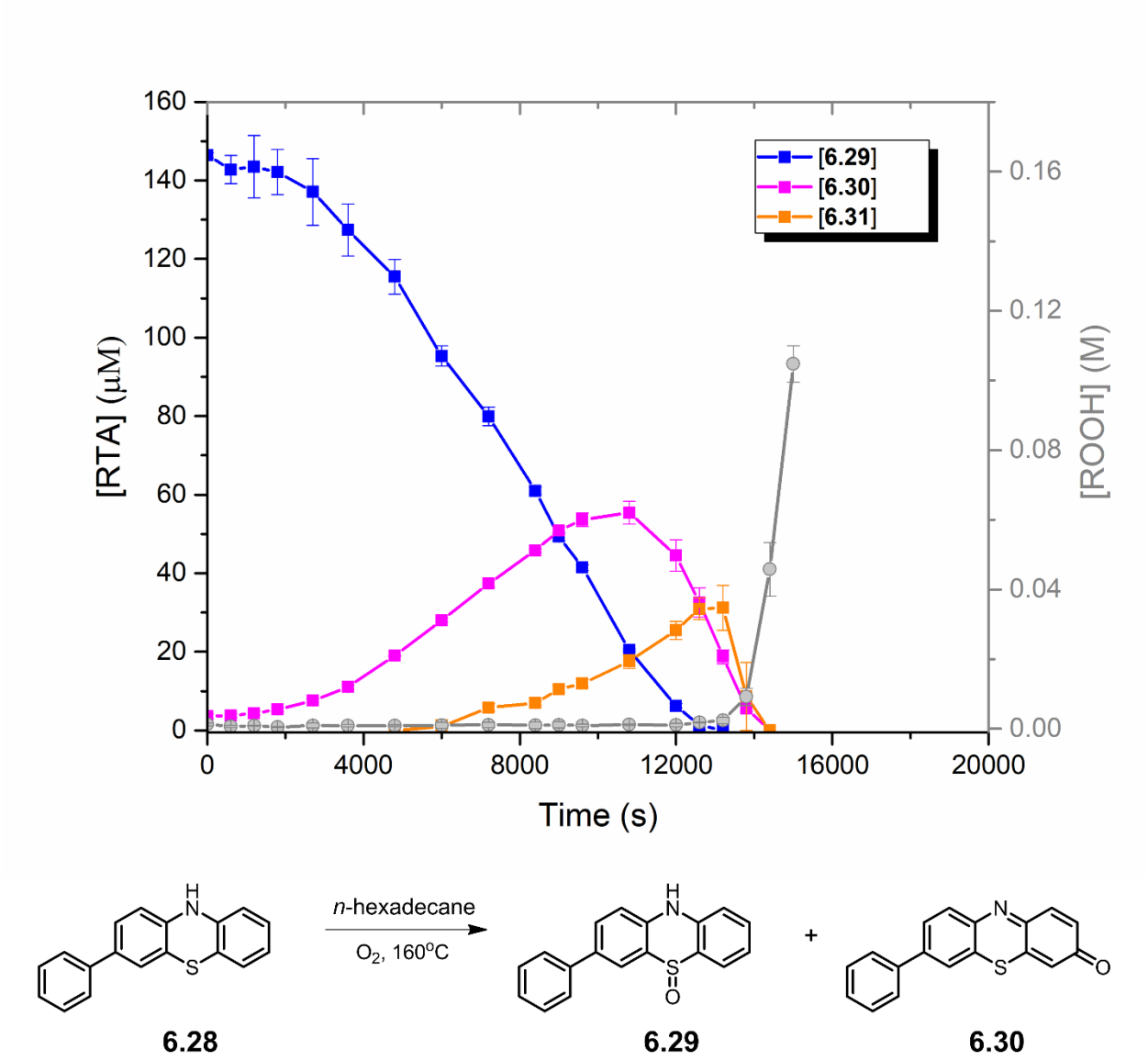


Figure 6.11. Time course loss of **6.29** and the formation of major oxidation products in *n*-hexadecane at 160 °C with O_2.

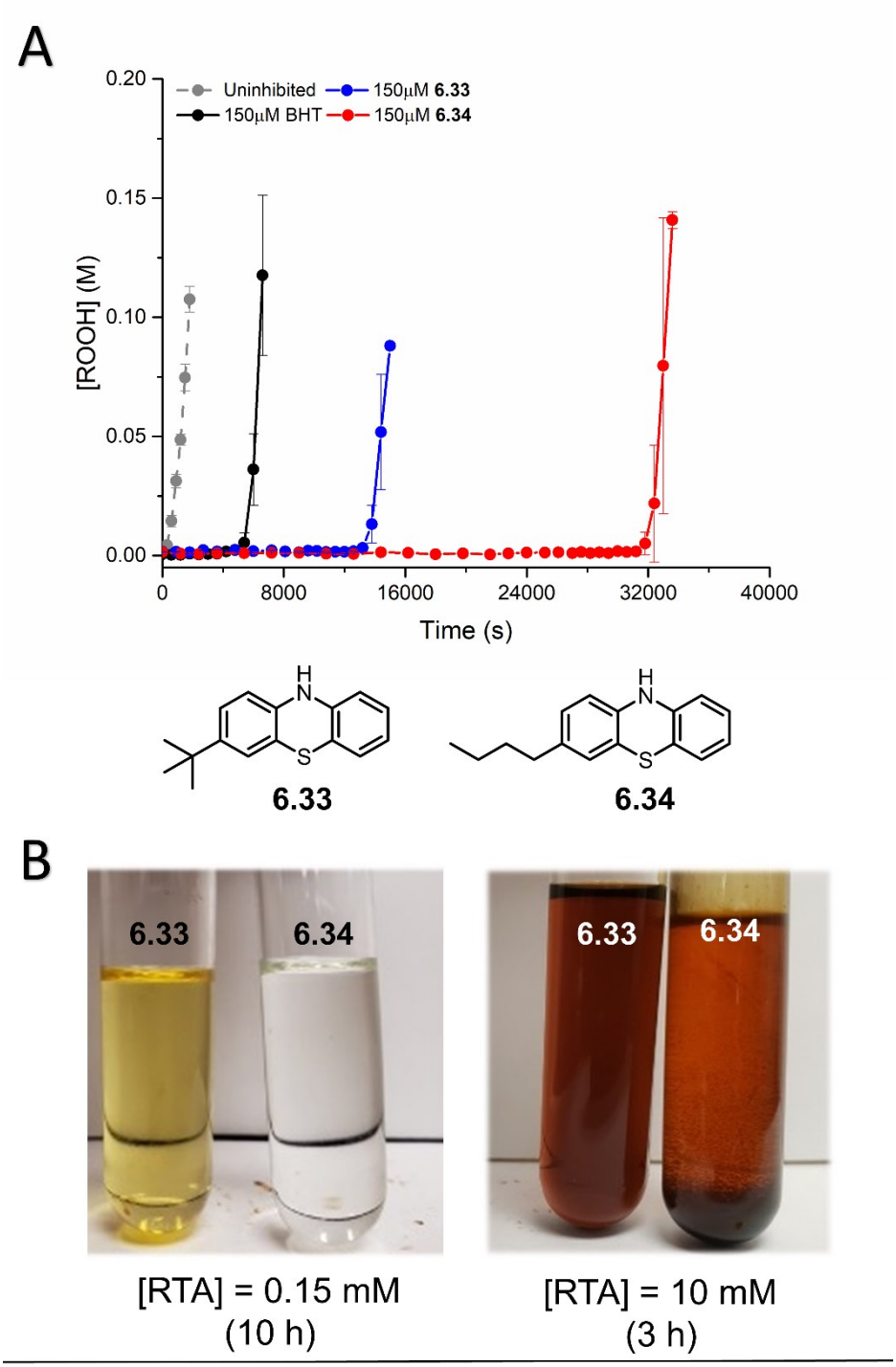


Figure 6.12. (A) Autoxidation of *n*-hexadecane inhibited by **6.33** and **6.34** compared. **(B)** Appearance of hexadecane after 10 h at a low concentration of **6.33**/**6.34** (*left*) vs. hexadecane after 3 h at a high concentration (*right*).

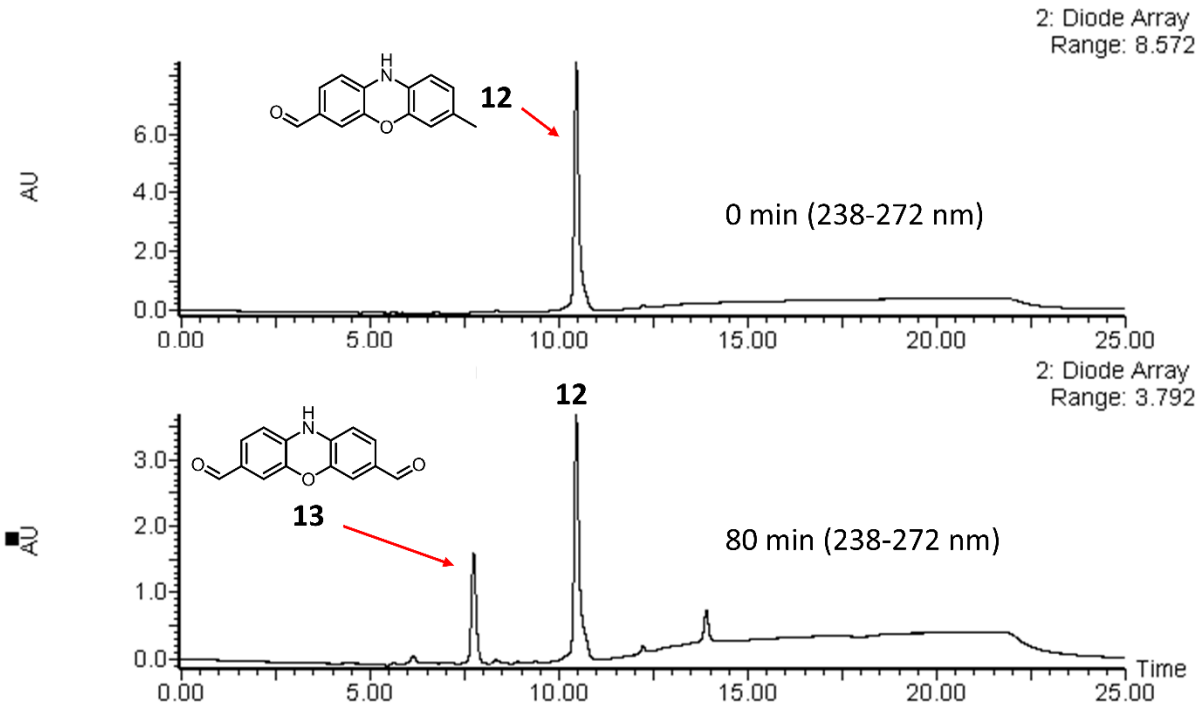


Figure 6.13. *(Top)* Representative UPLC-PDA trace of **6.12** at 0 min extracted from hexadecane (shown at 238-272 nm); *(Bottom)* Representative UPLC-PDA trace of **6.12** derived products extracted from hexadecane from an intermediate state of autoxidation (shown at 238-272 nm).

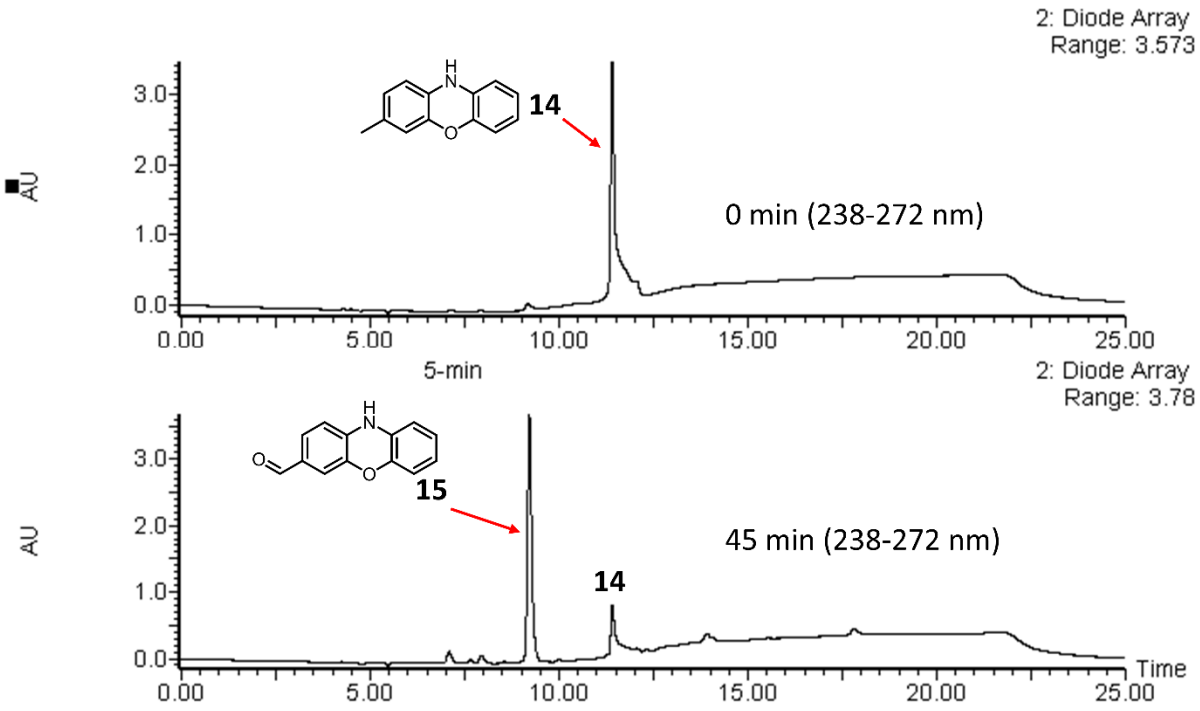


Figure 6.14. *(Top)* Representative UPLC-PDA trace of **6.14** at 0 min extracted from hexadecane (shown at 238-272 nm); *(Bottom)* Representative UPLC-PDA trace of **6.14** derived products extracted from hexadecane from an intermediate state of autoxidation (shown at 238-272 nm).

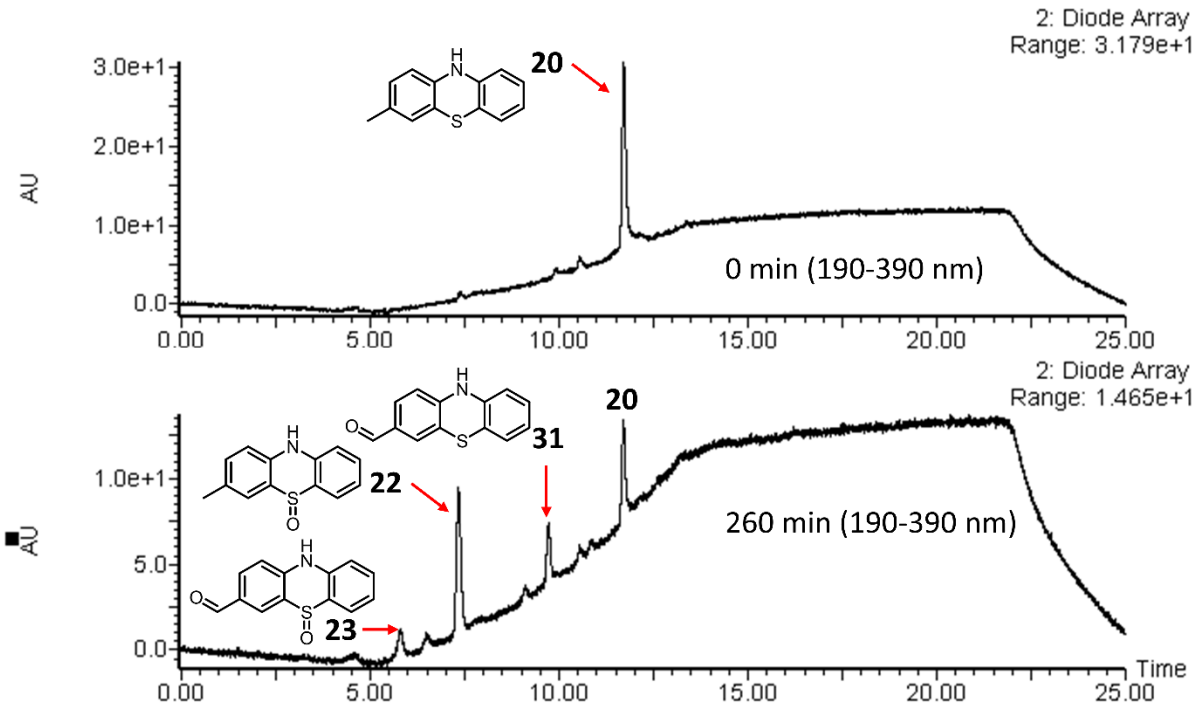


Figure 6.15. *(Top)* Representative UPLC-PDA trace of **6.20** at 0 min extracted from hexadecane (shown at 190-390 nm); *(Bottom)* Representative UPLC-PDA trace of **6.20** derived products extracted from hexadecane from an intermediate state of autoxidation (shown at 190-390 nm).

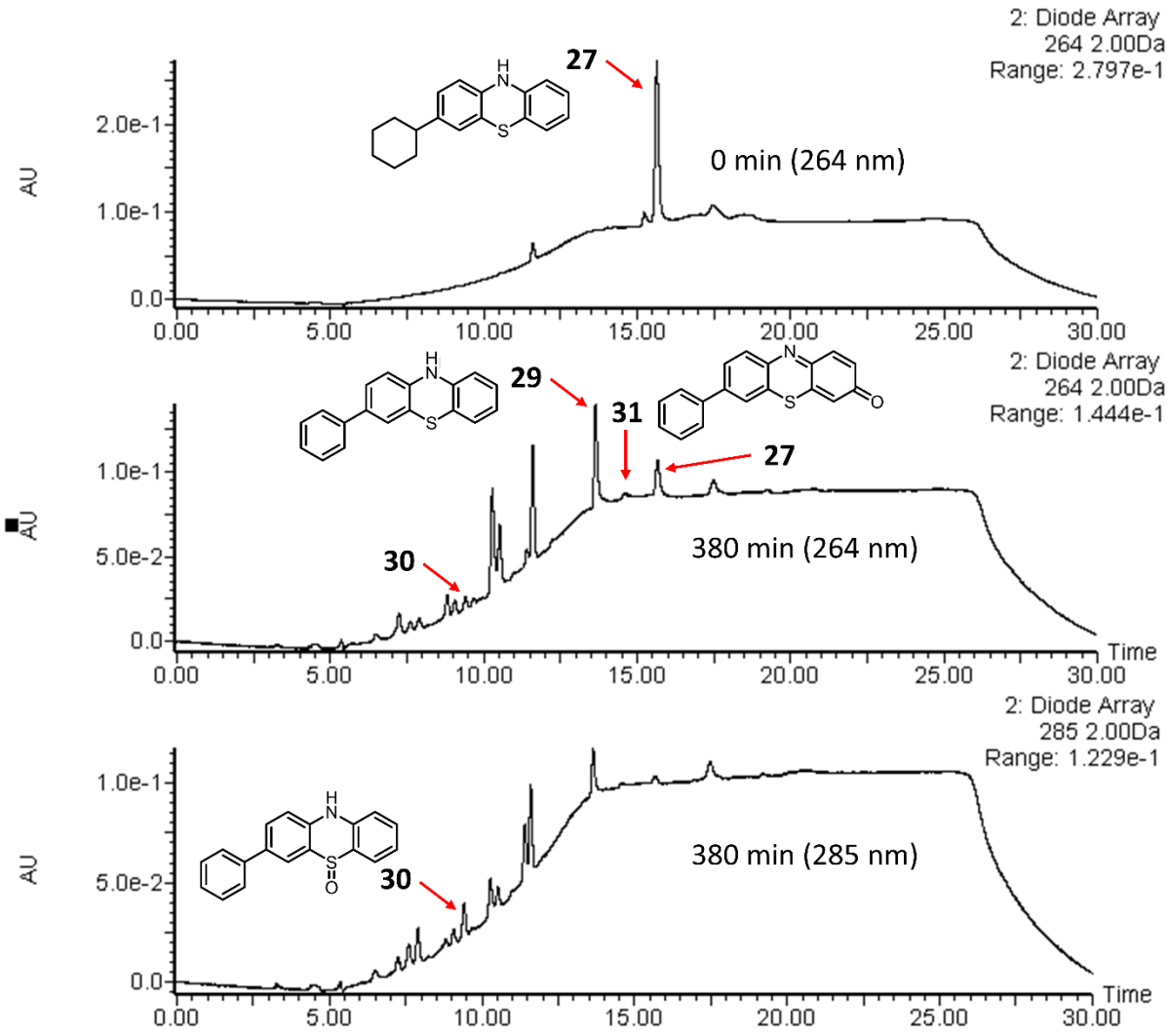


Figure 6.16. *(Top)* Representative UPLC-PDA trace of **6.27** at 0 min extracted from hexadecane (shown at 264 nm); *(Middle)* Representative UPLC-PDA trace of **6.27** derived products extracted from hexadecane from an intermediate state of autoxidation (shown at 264 nm); (*Bottom*) Shown at 285 nm to emphasize **6.30**.

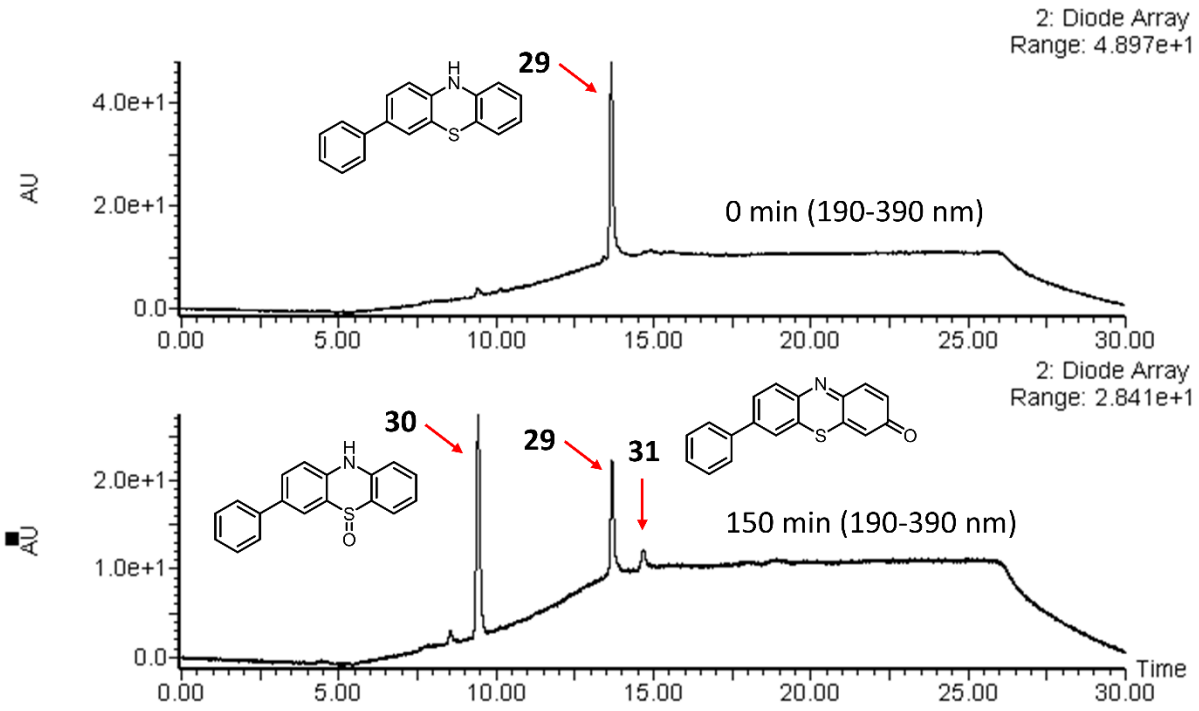
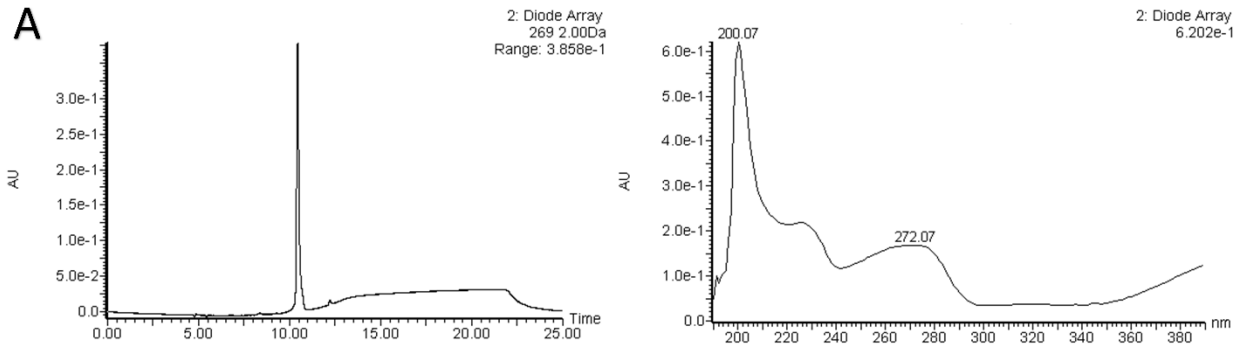


Figure 6.17. *(Top)* Representative UPLC-PDA trace of **6.29** at 0 min extracted from hexadecane (shown at 190-390 nm); *(Bottom)* Representative UPLC-PDA trace of **6.29** derived products extracted from hexadecane from an intermediate state of autoxidation (shown at 190-390 nm).

A



B

Concentration (μM)	Integral (at 269 nm)	Error (±)
10	4039	312
20	9502	439
40	19870	792
100	58751	974
200	119373	2591
400	245287	3910

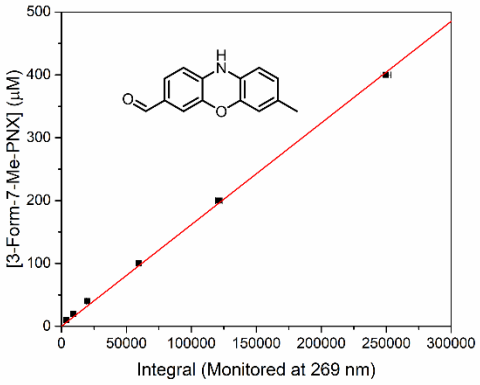
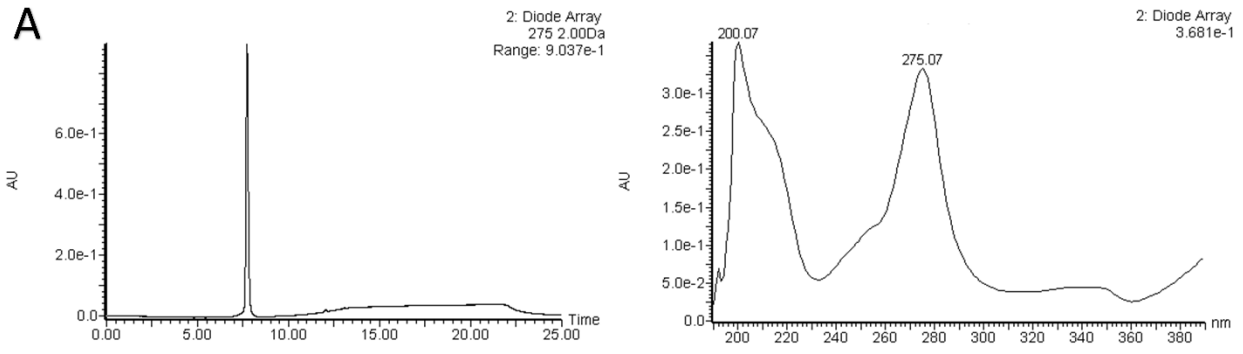


Figure 6.18. (A) Representative chromatogram of **6.12** standard (100 μM) monitored at 269 nm (*left*); UV-Vis spectrum of **6.12** standard (*right*). **(B)** Table of integrals and calibration curve of **6.12** standard monitored at 269 nm (y = 0.00162x).

A



B

Concentration (μM)	Integral (at 275 nm)	Error (±)
10	12761	696
20	26222	794
50	68683	1186
100	137537	3613
150	203731	3387
200	275521	5019

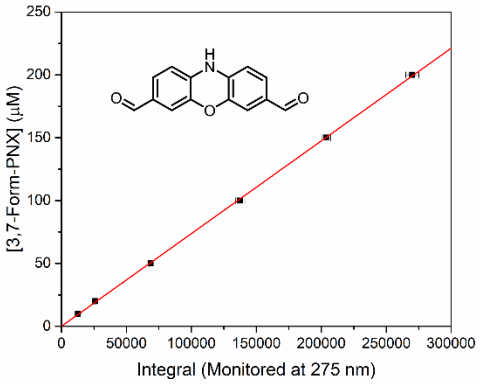
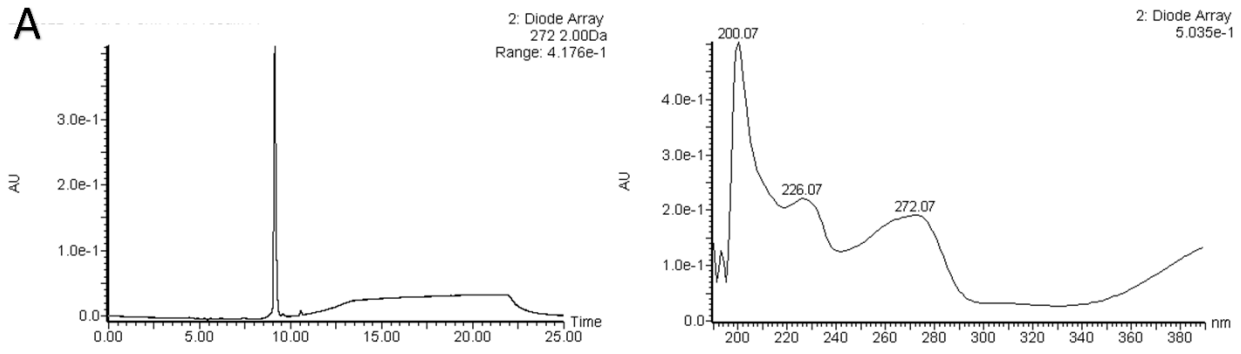


Figure 6.19. (A) Representative chromatogram of **6.13** standard (100 μM) monitored at 275 nm (*left*); UV-Vis spectrum of **6.13** standard (*right*). **(B)** Table of integrals and calibration curve of **6.13** standard monitored at 275 nm (y = 0.000737x).

A



B

Concentration (μM)	Integral (at 272 nm)	Error (±)
10	3721	345
20	8994	414
40	20443	364
100	51846	1968
200	114094	1657
400	246286	5154

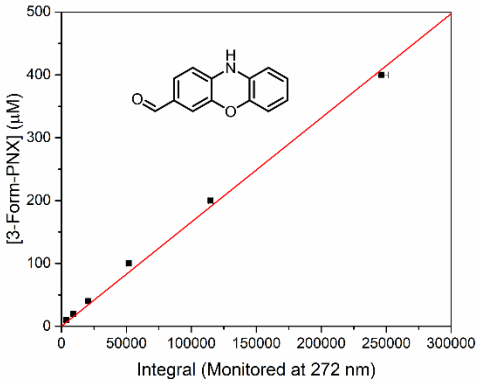
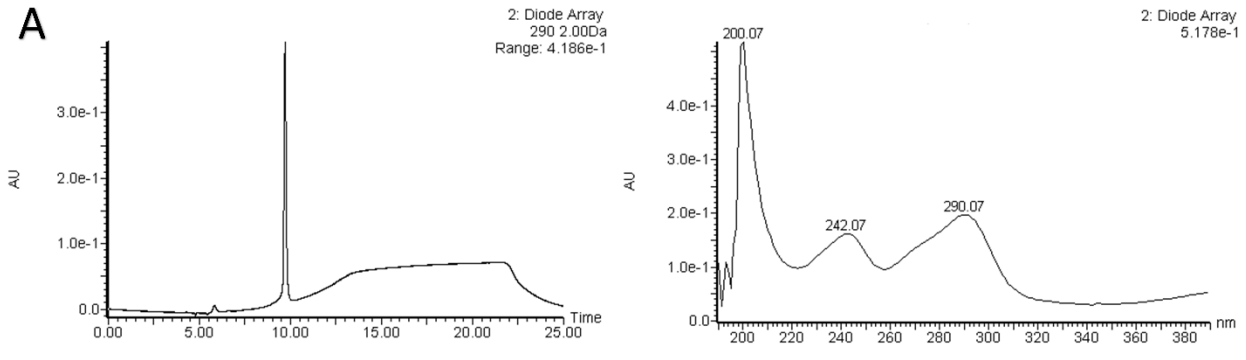


Figure 6.20. (A) Representative chromatogram of **6.15** standard (100 μM) monitored at 272 nm (*left*); UV-Vis spectrum of **6.15** standard (*right*). **(B)** Table of integrals and calibration curve of **6.15** standard monitored at 272 nm (y = 0.00166x).

A



B

Concentration (μM)	Integral (at 290 nm)	Error (±)
10	2943	160
20	6931	398
50	24030	673
100	60883	3605
150	98921	3705
200	136861	7302

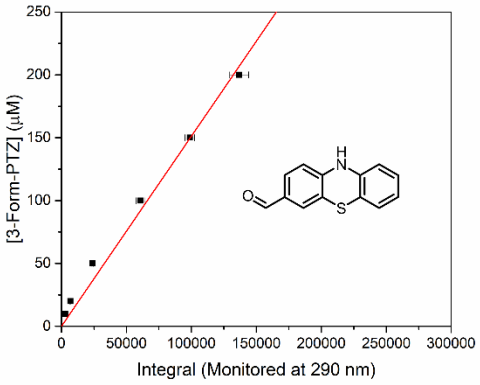
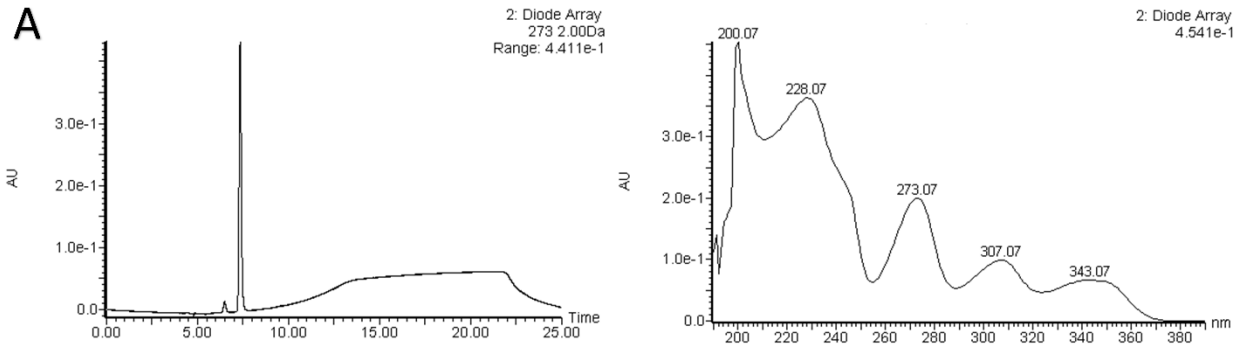


Figure 6.21. (A) Representative chromatogram of **6.21** standard (100 μM) monitored at 290 nm (*left*); UV-Vis spectrum of **6.21** standard (*right*). **(B)** Table of integrals and calibration curve of **6.21** standard monitored at 290 nm (y = 0.00151x).

A



B

Concentration (μM)	Integral (at 273 nm)	Error (±)
10	6009	164
20	12500	402
50	30536	230
100	60940	446
150	90342	566
200	119301	1024

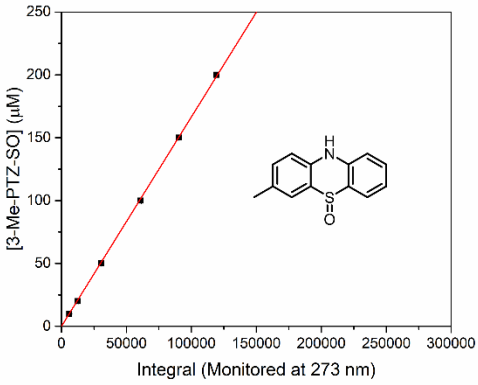
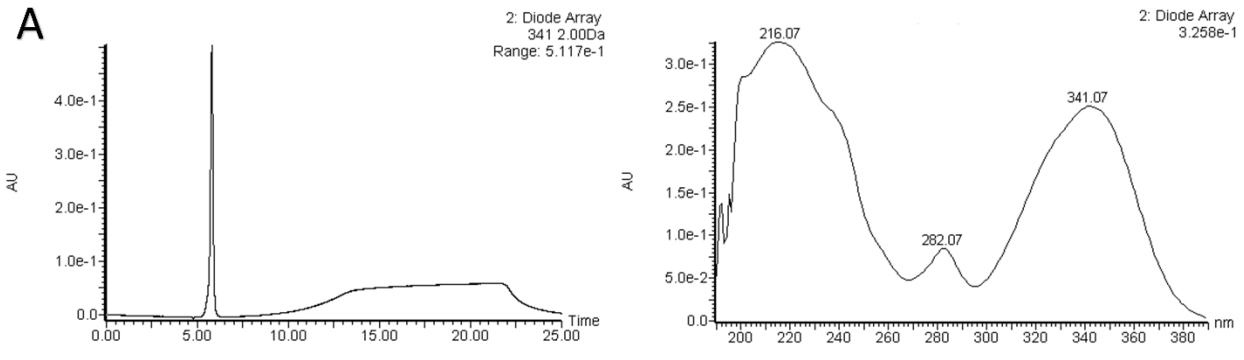


Figure 6.22. (A) Representative chromatogram of **6.22** standard (100 μM) monitored at 273 nm (*left*); UV-Vis spectrum of **6.22** standard (*right*). **(B)** Table of integrals and calibration curve of **6.22** standard monitored at 273 nm (y = 0.00166x).

A



B

Concentration (μM)	Integral (at 342 nm)	Error (±)
10	8875	125
20	17120	429
30	25902	371
50	46177	2216
100	90136	3244
150	133743	3526

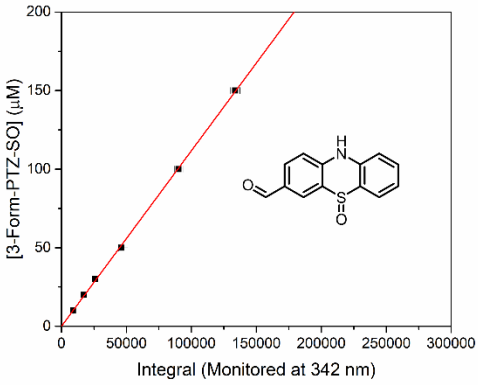
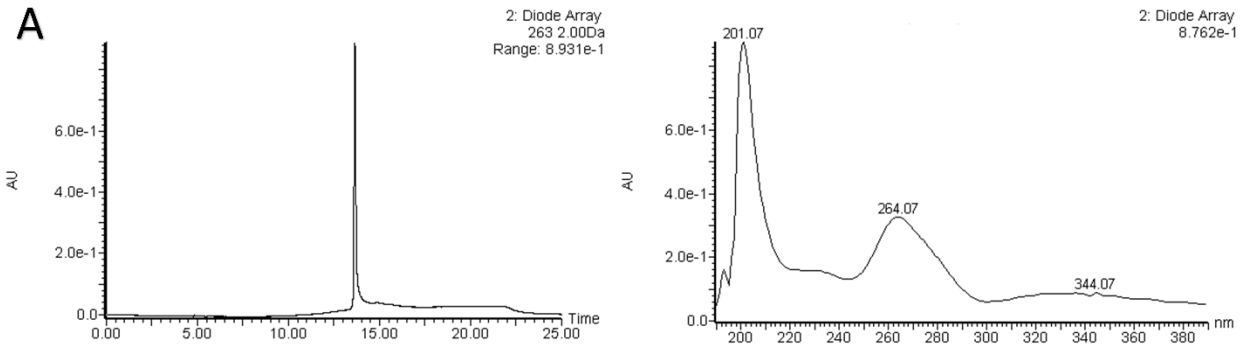


Figure 6.23. (A) Representative chromatogram of **6.23** standard (100 μM) monitored at 342 nm (*left*); UV-Vis spectrum of **6.23** standard (*right*). **(B)** Table of integrals and calibration curve of **6.23** standard monitored at 342 nm (y = 0.00112x).

A



B

Concentration (μM)	Integral (at 263 nm)	Error (±)
10	8544	837
20	17941	1804
40	37508	2069
100	110391	4672
200	241962	6550

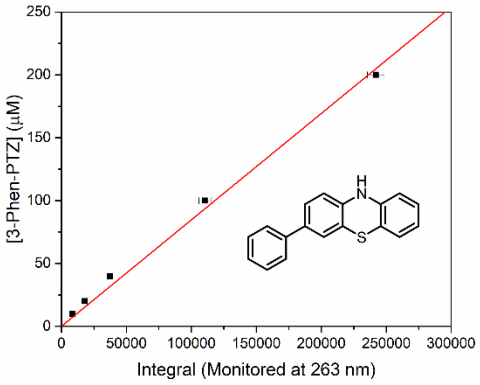
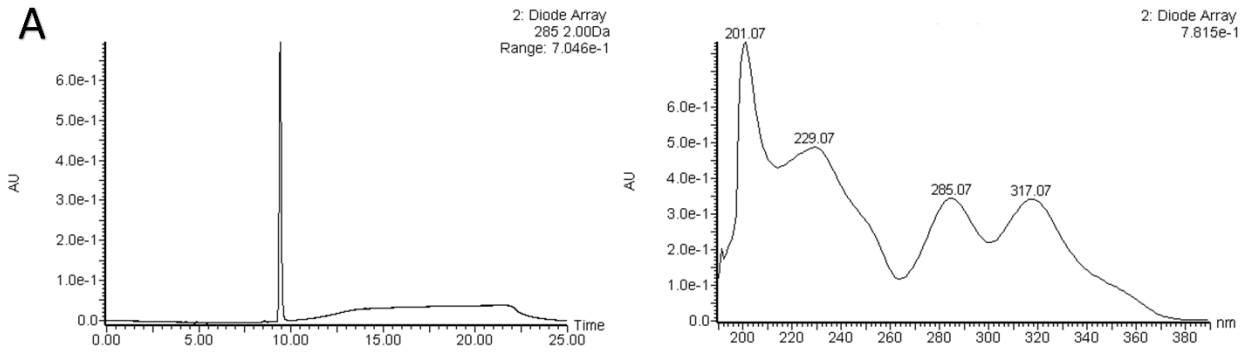


Figure 6.24. **(A)** Representative chromatogram of **6.29** standard (100 μM) monitored at 263 nm (*left*); UV-Vis spectrum of **6.29** standard (*right*). **(B)** Table of integrals and calibration curve of **6.29** standard monitored at 263 nm (y = 0.000846x).

A



B

Concentration (μM)	Integral (at 285 nm)	Error (±)
10	9288	130
20	18049	250
50	47412	810
100	92148	1103
150	135701	1773
200	180537	2171

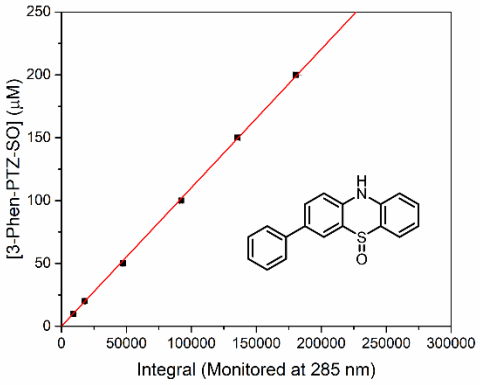
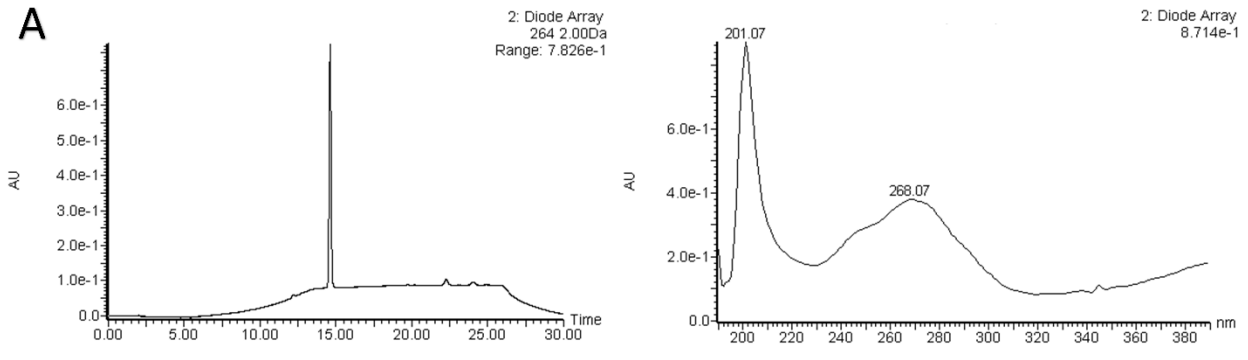


Figure 6.25. (A) Representative chromatogram of **6.30** standard (100 μM) monitored at 285 nm (*left*); UV-Vis spectrum of **6.30** standard (*right*). **(B)** Table of integrals and calibration curve of **6.30** standard monitored at 285 nm (y = 0.0011x).

A



B

Concentration (μM)	Integral (at 264 nm)	Error (±)
10	10010	142
20	19626	192
40	39270	112
60	63271	836
80	82188	630
100	102927	639

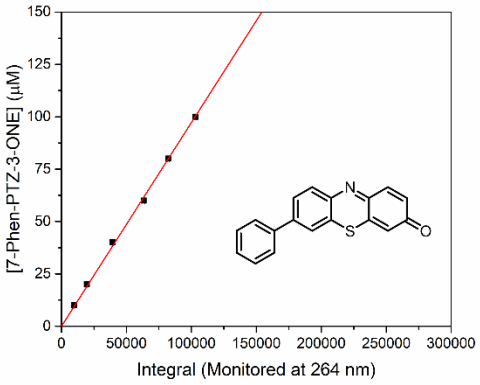


Figure 6.26. (A) Representative chromatogram of **6.31** standard (100 μM) monitored at 264 nm (*left*); UV-Vis spectrum of **6.31** standard (*right*). **(B)** Table of integrals and calibration curve of **6.31** standard monitored at 264 nm (y = 0.000972x).

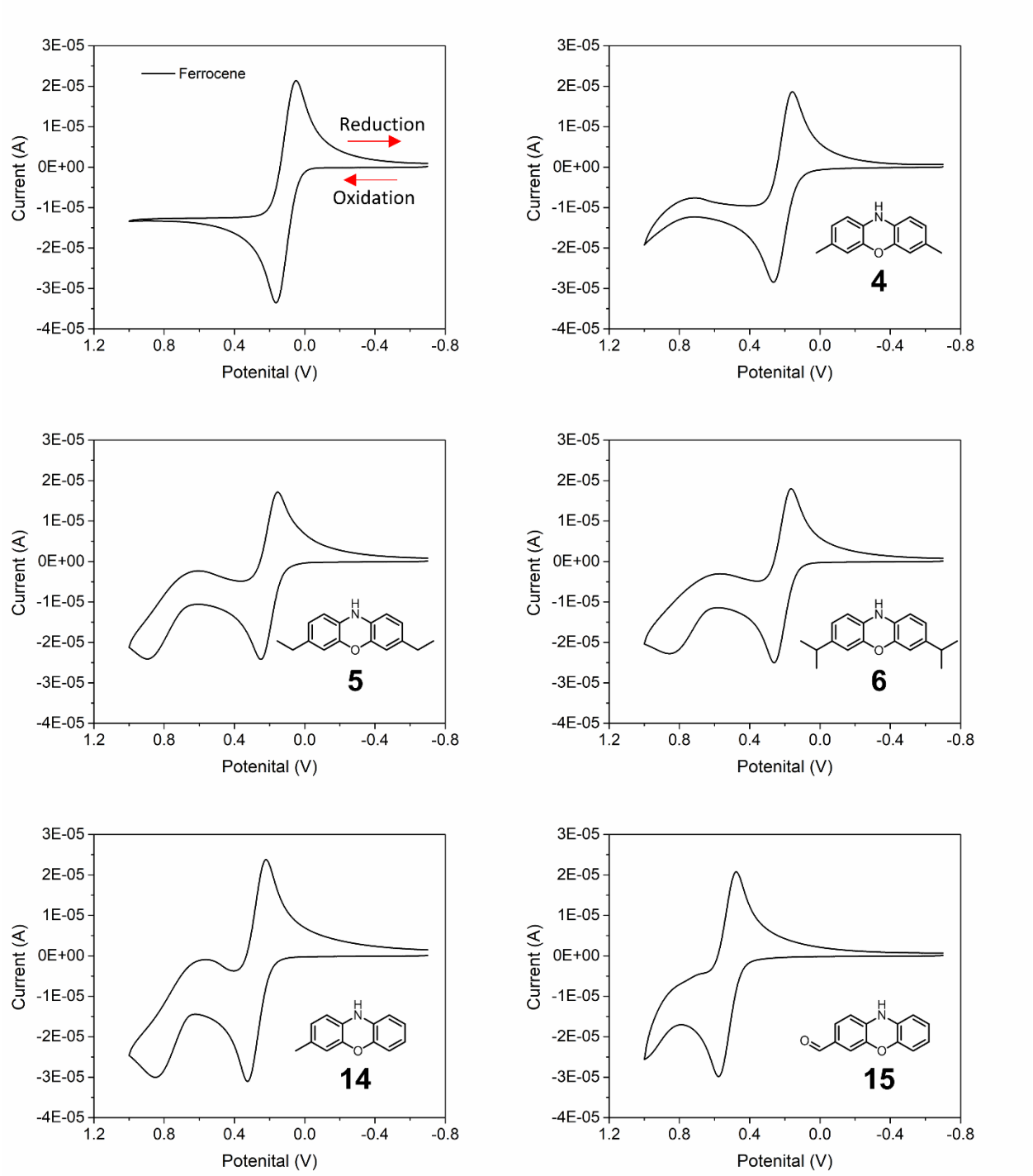


Figure 6.27. Cyclic voltammograms of ferrocene, **6.4**, **6.5**, **6.6**, **6.14** and **6.15** vs. Ag/Ag^{+}.

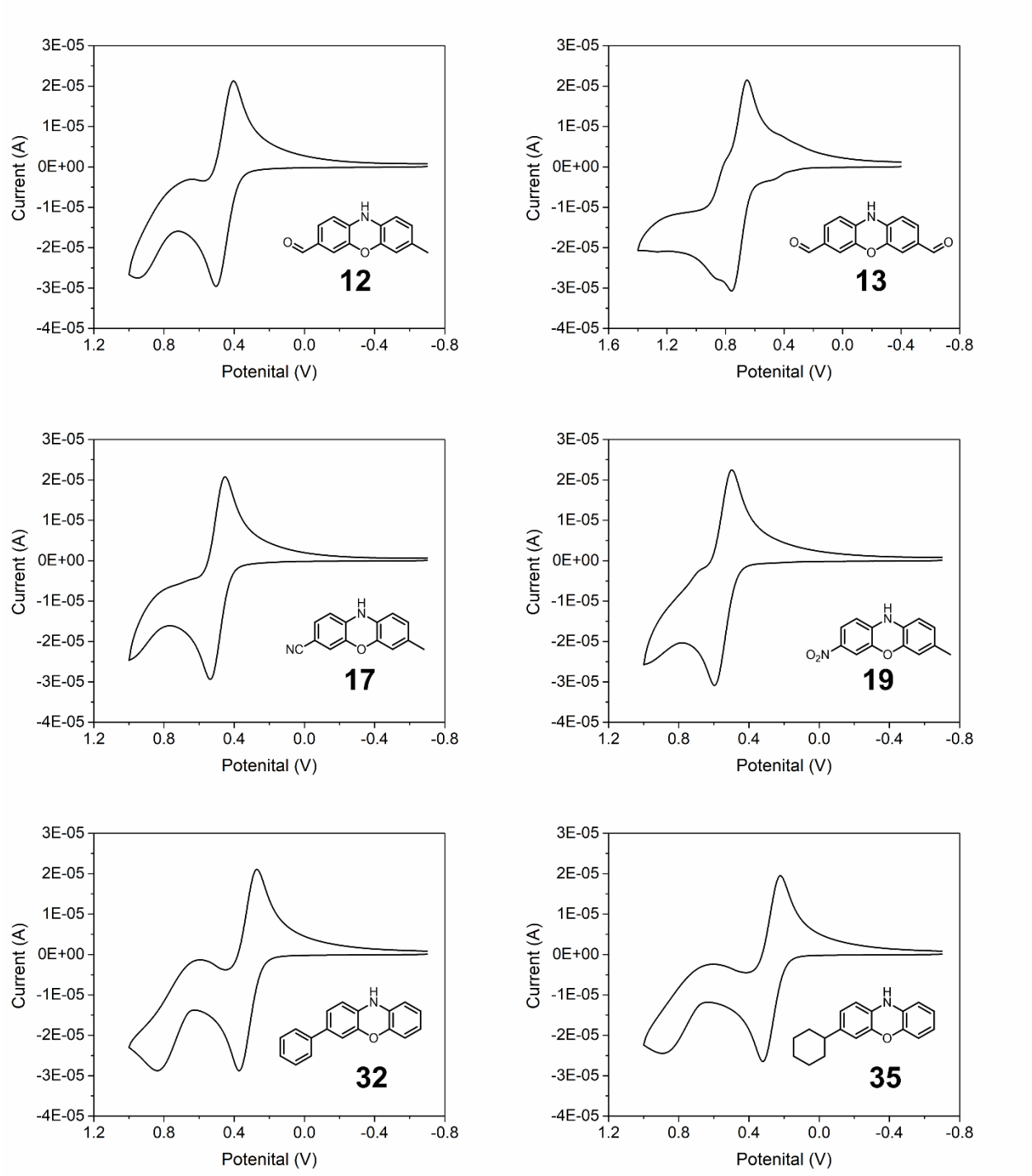


Figure 6.28. Cyclic voltammograms of **6.12**, **6.13**, **6.17**, **6.19**, **6.32** and **6.35** vs. Ag/Ag^{+}.

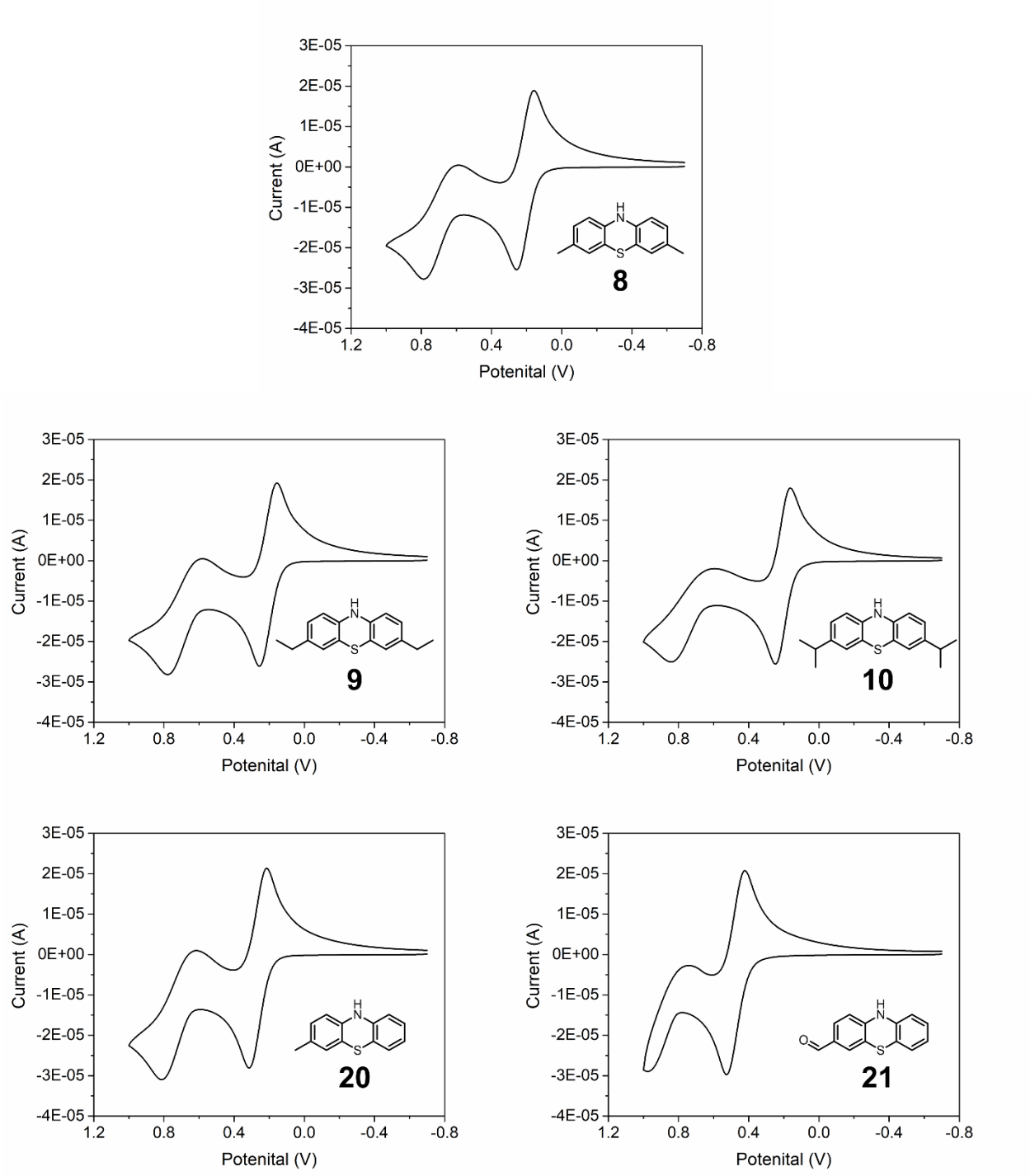


Figure 6.29. Cyclic voltammograms of **6.8**, **6.9**, **6.10**, **6.20**, and **6.21** vs. Ag/Ag^{+}.

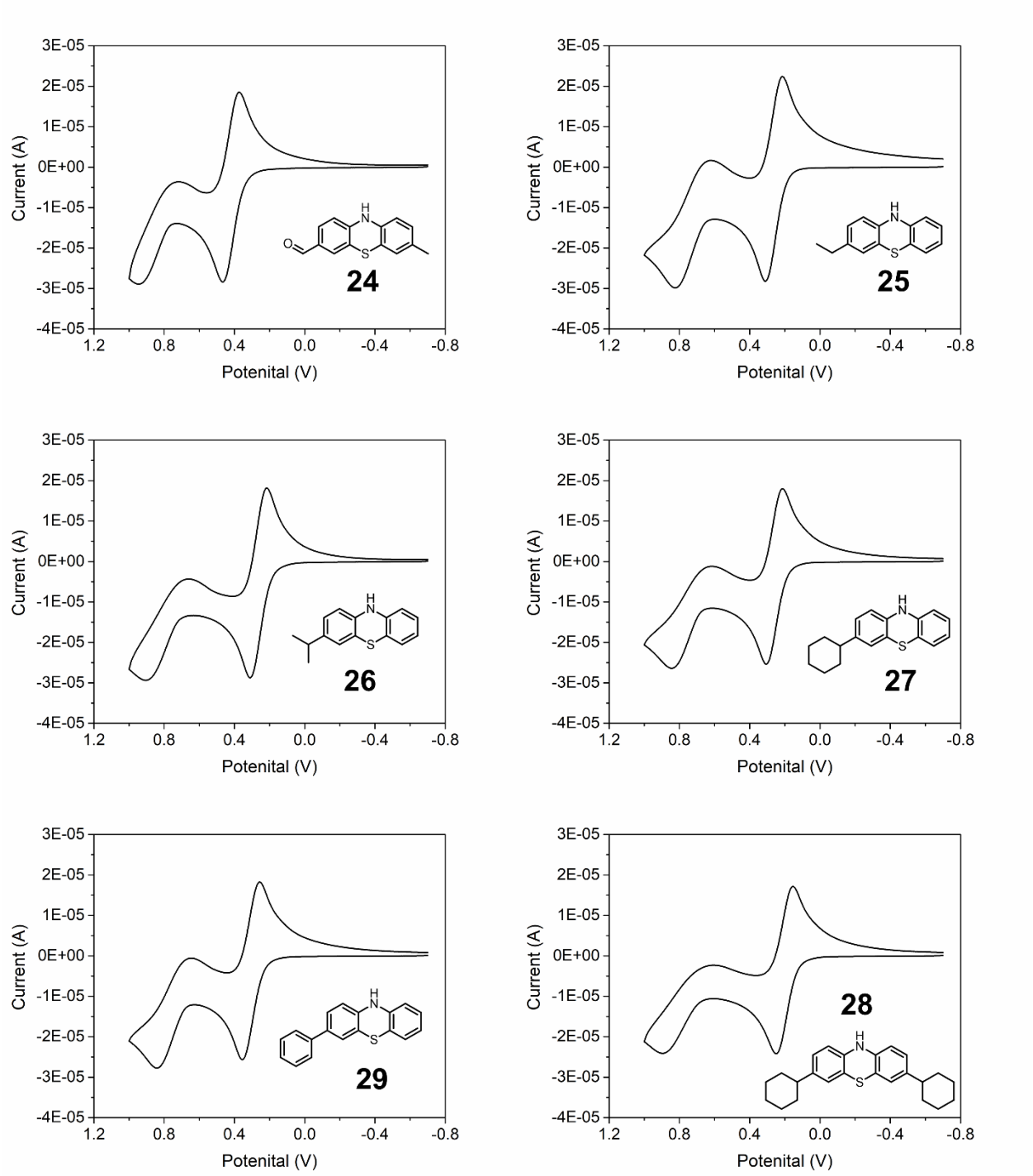


Figure 6.30. Cyclic voltammograms of **6.24**, **6.25**, **6.26**, **6.27**, **6.29** and **6.28** vs. Ag/Ag^{+}.

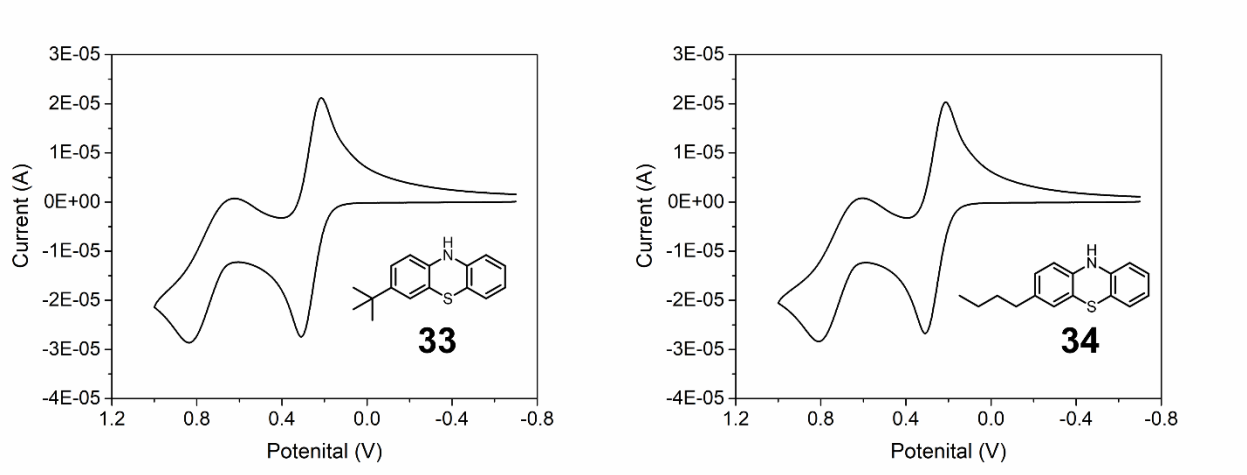


Figure 6.31. Cyclic voltammograms of **6.33** and **6.34** vs. Ag/Ag^{+}.

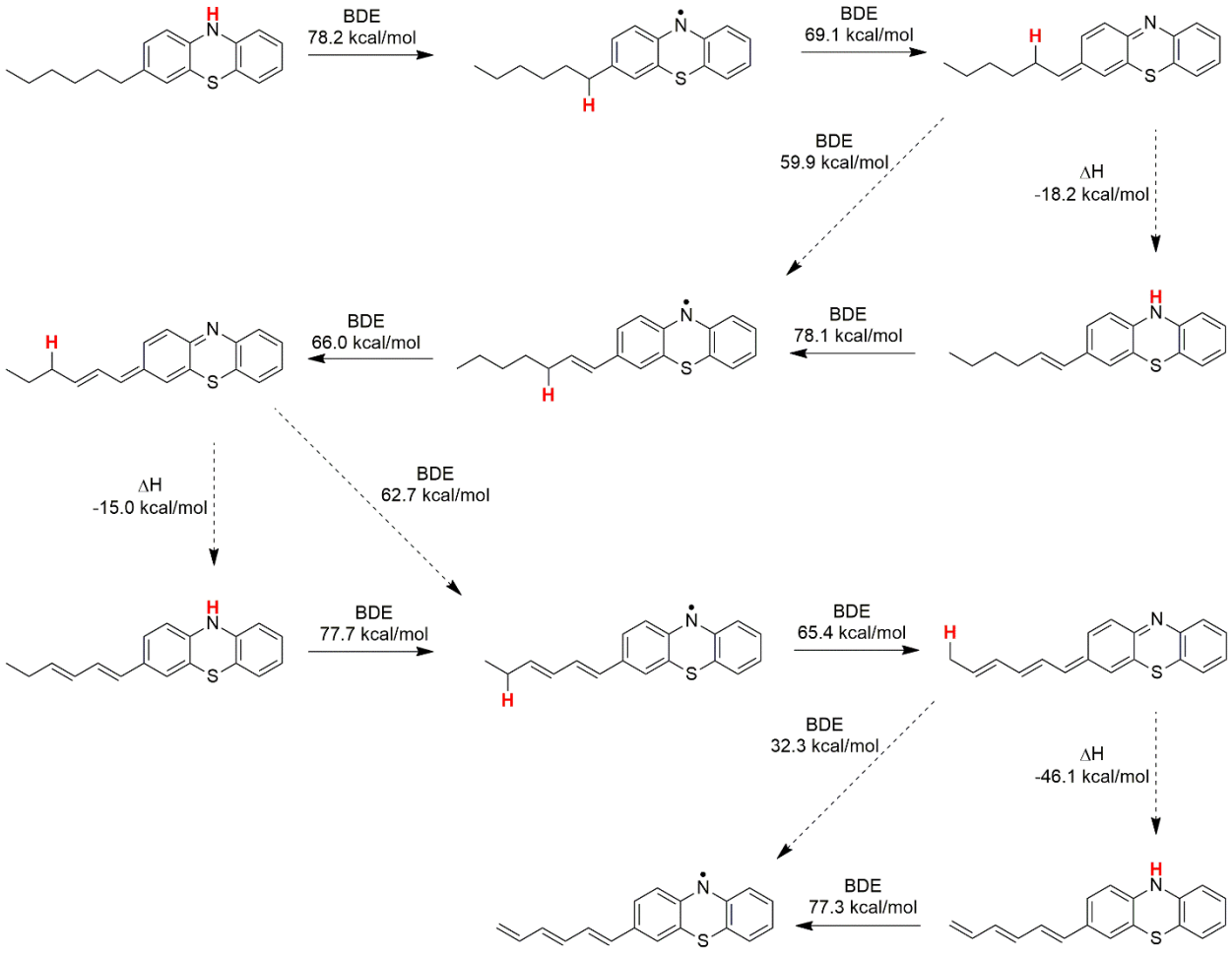


Figure 6.32. Thermochemistry of the oxidation of 3-*n*-hexylphenothiazine to the triene derivative calculated using the M062X/cc-PVTZ DFT method.

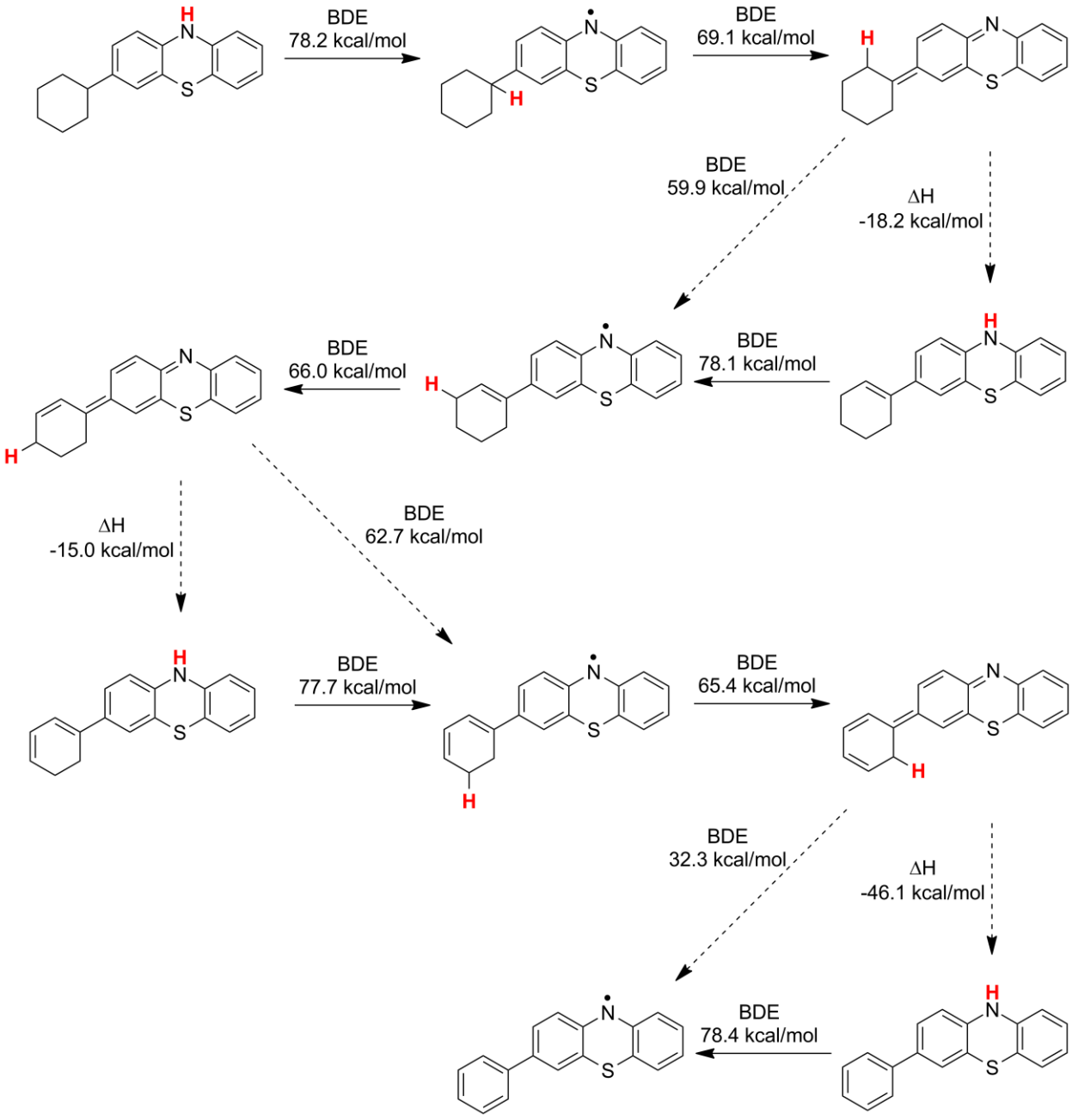


Figure 6.33. Thermochemistry of the oxidation of 3-cyclcohexylphenothiazine (**6.27**) to 3-phenylphenothiazine (**6.29**) calculated using the M062X/cc-PVTZ DFT method.

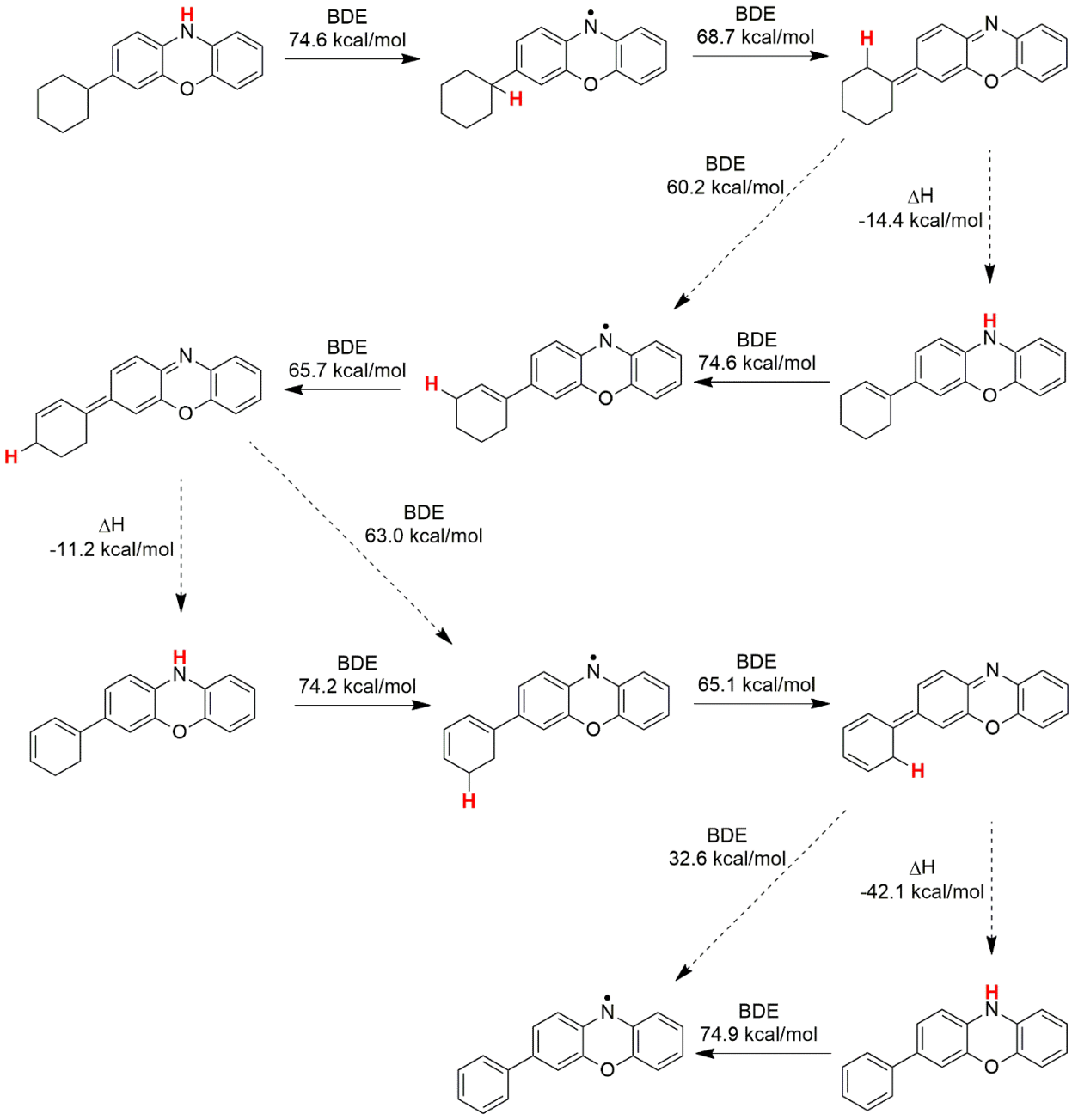


Figure 6.34. Thermochemistry of the oxidation of 3-cyclcohexylphenoxazine (**6.35**) to 3-phenylphenoxazine (**6.32**) calculated using the M062X/cc-PVTZ DFT method.

6.10 References (Experimental)

(1) Farmer, L. A.; Haidasz, E. A.; Griesser, M.; Pratt, D. A. Phenoxazine: A Privileged Scaffold for Radical-Trapping Antioxidants. *J. Org. Chem.* **2017**, *82* (19), 10523–10536. https://doi.org/10.1021/acs.joc.7b02025.

(2) Farmer, L. A.; Wu, Z.; Poon, J.-F.; Zilka, O.; Lorenz, S. M.; Huehn, S.; Proneth, B.; Conrad, M.; Pratt, D. A. Intrinsic and Extrinsic Limitations to the Design and Optimization of Inhibitors of Lipid Peroxidation and Associated Cell Death. *J. Am. Chem. Soc.* **2022**, *144* (32), 14706–14721. https://doi.org/10.1021/jacs.2c05252.

(3) Barret, R.; Daudon, M. Synthesis of Quinone-Imines with Iodoxybenzene. *Synth. Commun.* **1990**, *20* (10), 1543–1549. https://doi.org/10.1080/00397919008052871.

(4) Pegis, M. L.; Roberts, J. A. S.; Wasylenko, D. J.; Mader, E. A.; Appel, A. M.; Mayer, J. M. Standard Reduction Potentials for Oxygen and Carbon Dioxide Couples in Acetonitrile and *N* , *N* -Dimethylformamide. *Inorg. Chem.* **2015**, *54* (24), 11883–11888. https://doi.org/10.1021/acs.inorgchem.5b02136.

(5) Gaussian 16, Revision C.01, Frisch, M. J.; Trucks, G. W.; Schlegel, H. B.; Scuseria, G. E.; Robb, M. A.; Cheeseman, J. R.; Scalmani, G.; Barone, V.; Petersson, G. A.; Nakatsuji, H.; Li, X.; Caricato, M.; Marenich, A. V.; Bloino, J.; Janesko, B. G.; Gomperts, R.; Mennucci, B.; Hratchian, H. P.; Ortiz, J. V.; Izmaylov, A. F.; Sonnenberg, J. L.; Williams-Young, D.; Ding, F.; Lipparini, F.; Egidi, F.; Goings, J.; Peng, B.; Petrone, A.; Henderson, T.; Ranasinghe, D.; Zakrzewski, V. G.; Gao, J.; Rega, N.; Zheng, G.; Liang, W.; Hada, M.; Ehara, M.; Toyota, K.; Fukuda, R.; Hasegawa, J.; Ishida, M.; Nakajima, T.; Honda, Y.; Kitao, O.; Nakai, H.; Vreven, T.; Throssell, K.; Montgomery, J. A., Jr.; Peralta, J. E.; Ogliaro, F.; Bearpark, M. J.; Heyd, J. J.; Brothers, E. N.; Kudin, K. N.; Staroverov, V. N.; Keith, T. A.; Kobayashi, R.; Normand, J.; Raghavachari, K.; Rendell, A. P.; Burant, J. C.; Iyengar, S. S.; Tomasi, J.; Cossi, M.; Millam, J. M.; Klene, M.; Adamo, C.; Cammi, R.; Ochterski, J. W.; Martin, R. L.; Morokuma, K.; Farkas, O.; Foresman, J. B.; Fox, D. J. Gaussian, Inc., Wallingford CT, 2016.

Chapter 7 (Appendix)

7.1 Chapter 2 NMR Spectra

(Begins on next page)

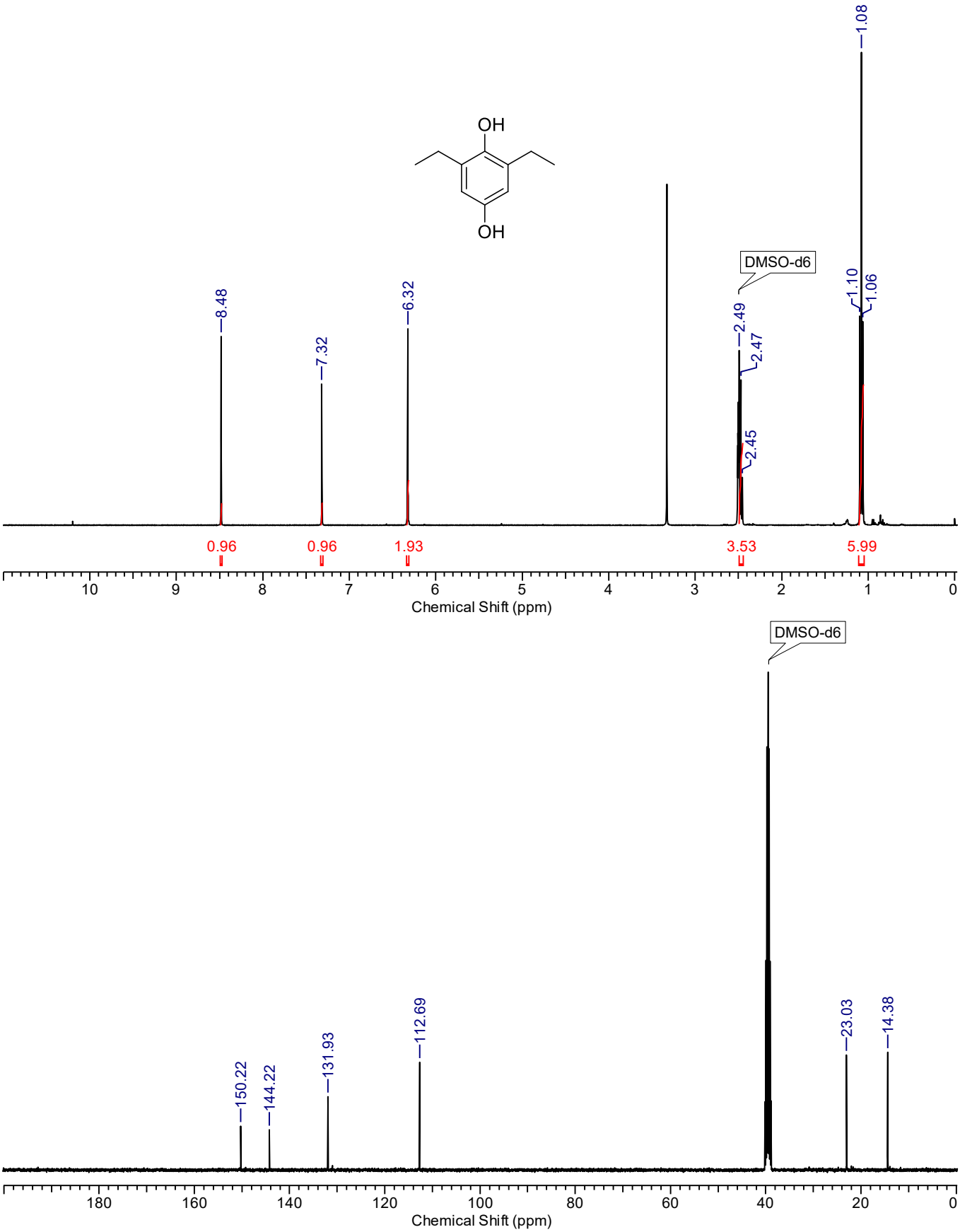


Figure S7.1. ^{1}H NMR spectra of 2,6-diethylhydroquionone (**2.4b**) in DMSO-d6 (*top*) and ^{13}C NMR (*bottom*).

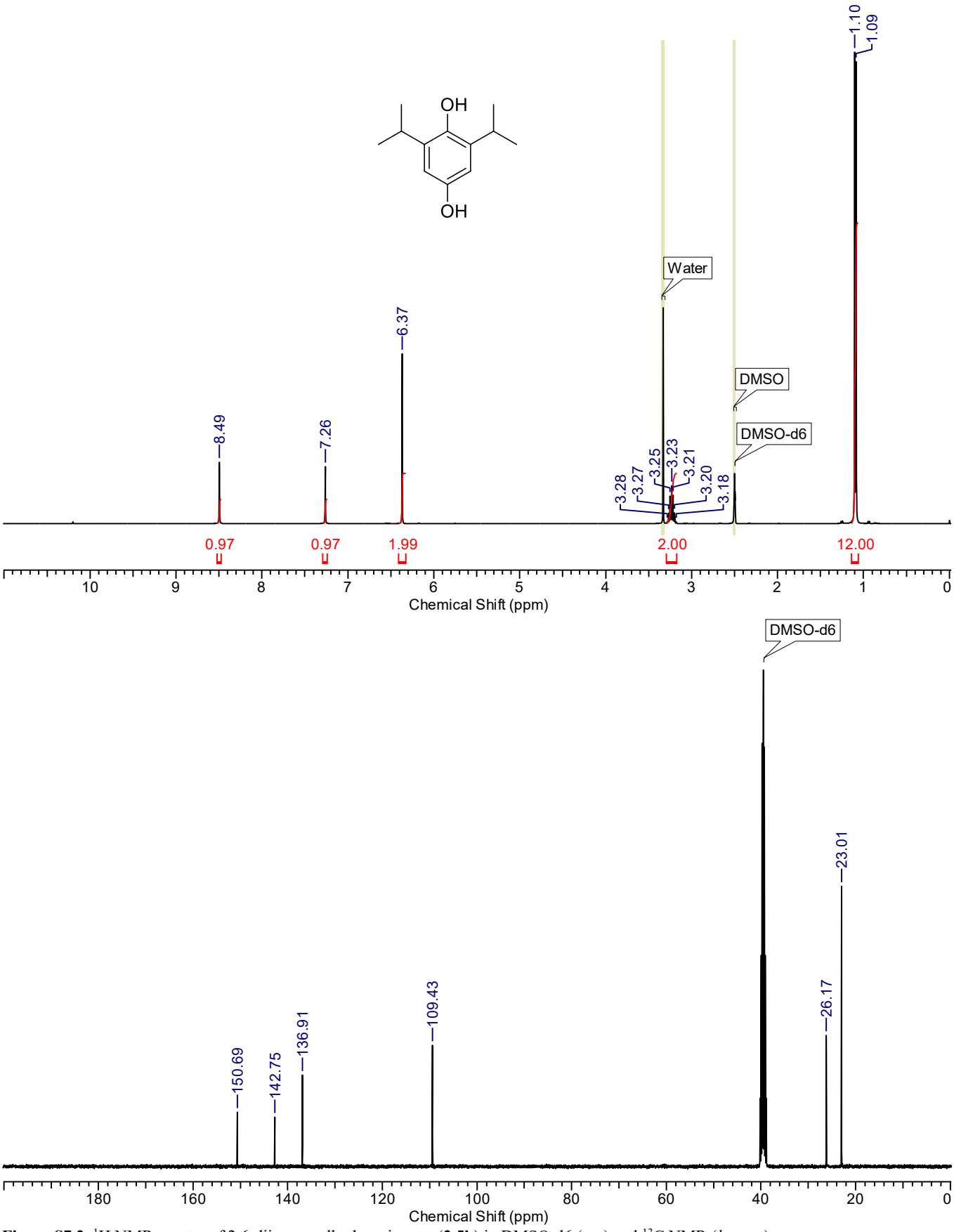


Figure S7.2. ^{1}H NMR spectra of 2,6-diisopropylhydroquionone (**2.5b**) in DMSO-d6 (*top*) and ^{13}C NMR (*bottom*).

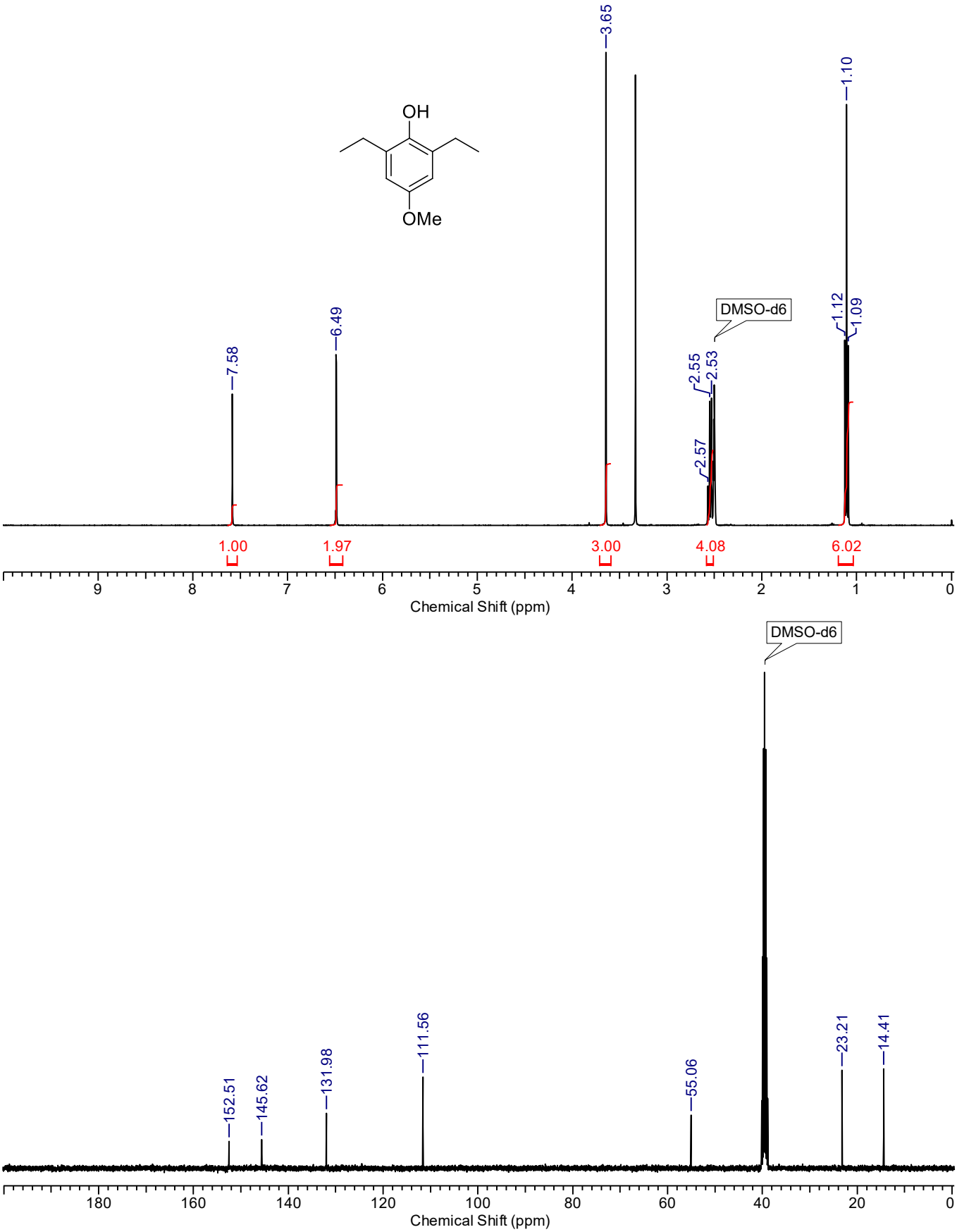


Figure S7.3. ^{1}H NMR spectra of 2,6-diethyl-4-methoxyphenol (**2.4**) in DMSO-d6 (*top*) and ^{13}C NMR (*bottom*).

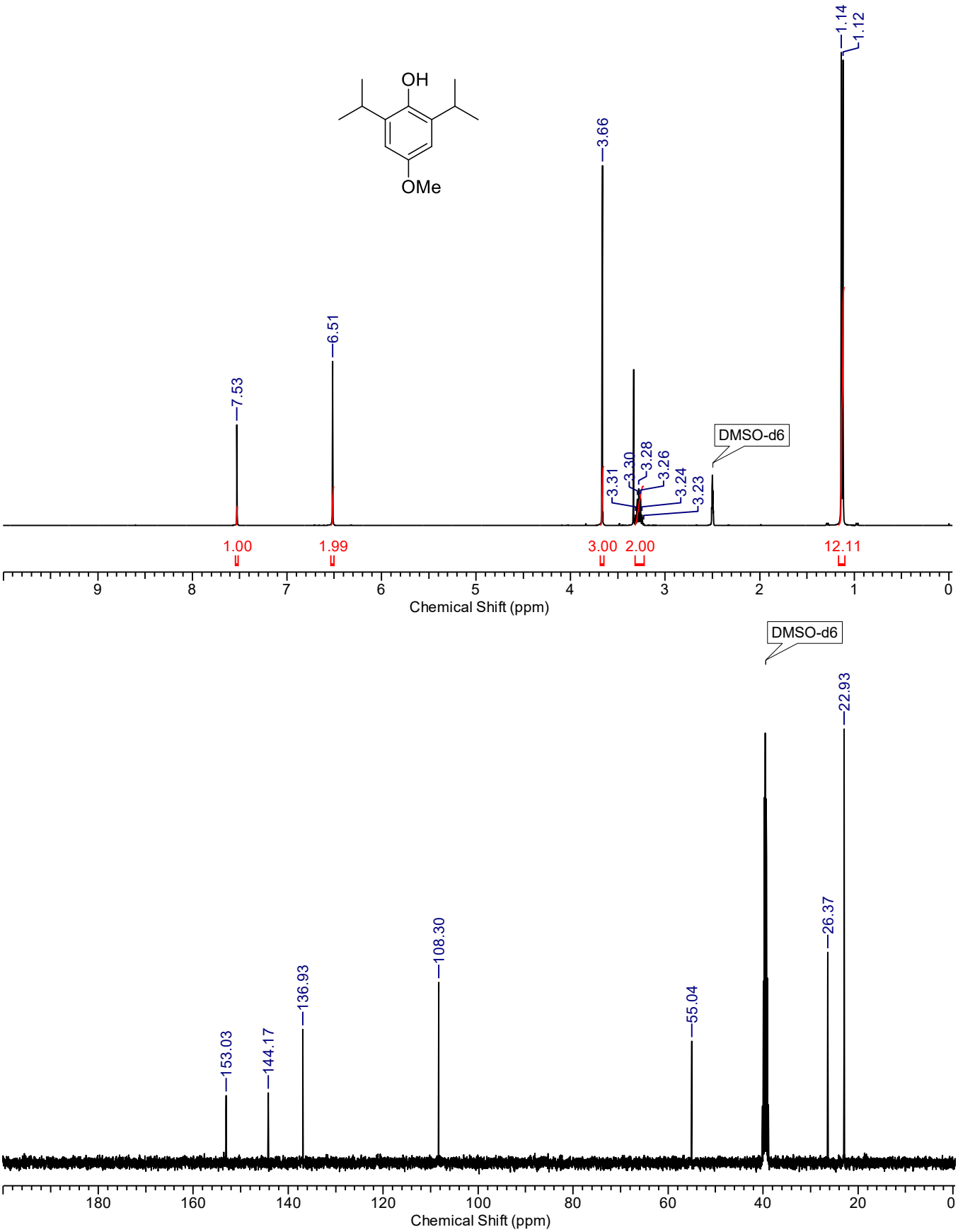


Figure S7.4. ^{1}H NMR spectra of 2,6-diisopropyl-4-methoxyphenol (**2.5**) in DMSO-d6 (*top*) and ^{13}C NMR (*bottom*).

7.2 Chapter 3 NMR Spectra

(Begins on next page)

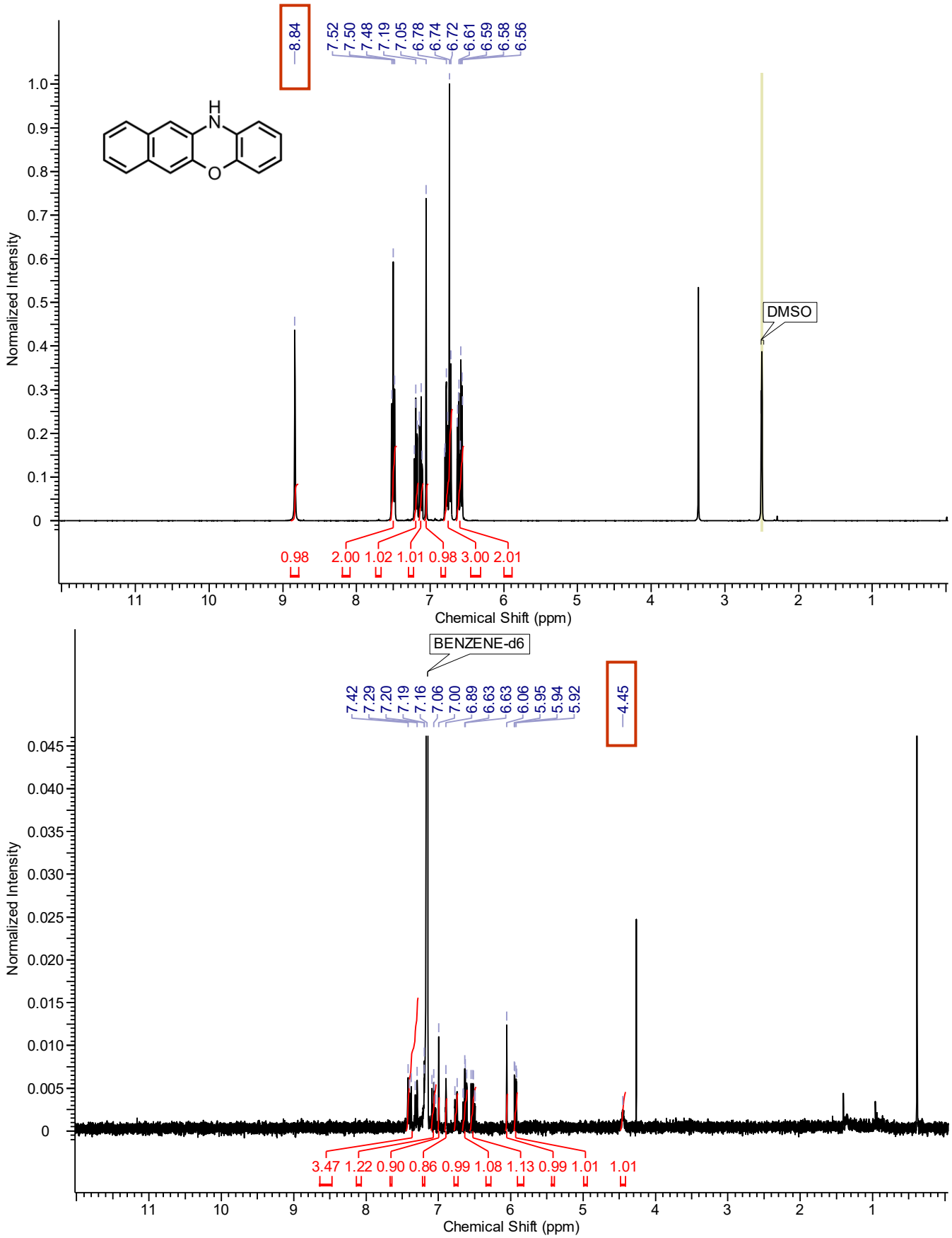


Figure S7.5. ^{1}H NMR spectra of Benzo(b)-PNX (**3.4**) in DMSO-d6 (*top*) and C_6D_6 (*bottom*) (N-H highlighted). Poorly soluble in C_6D_6.

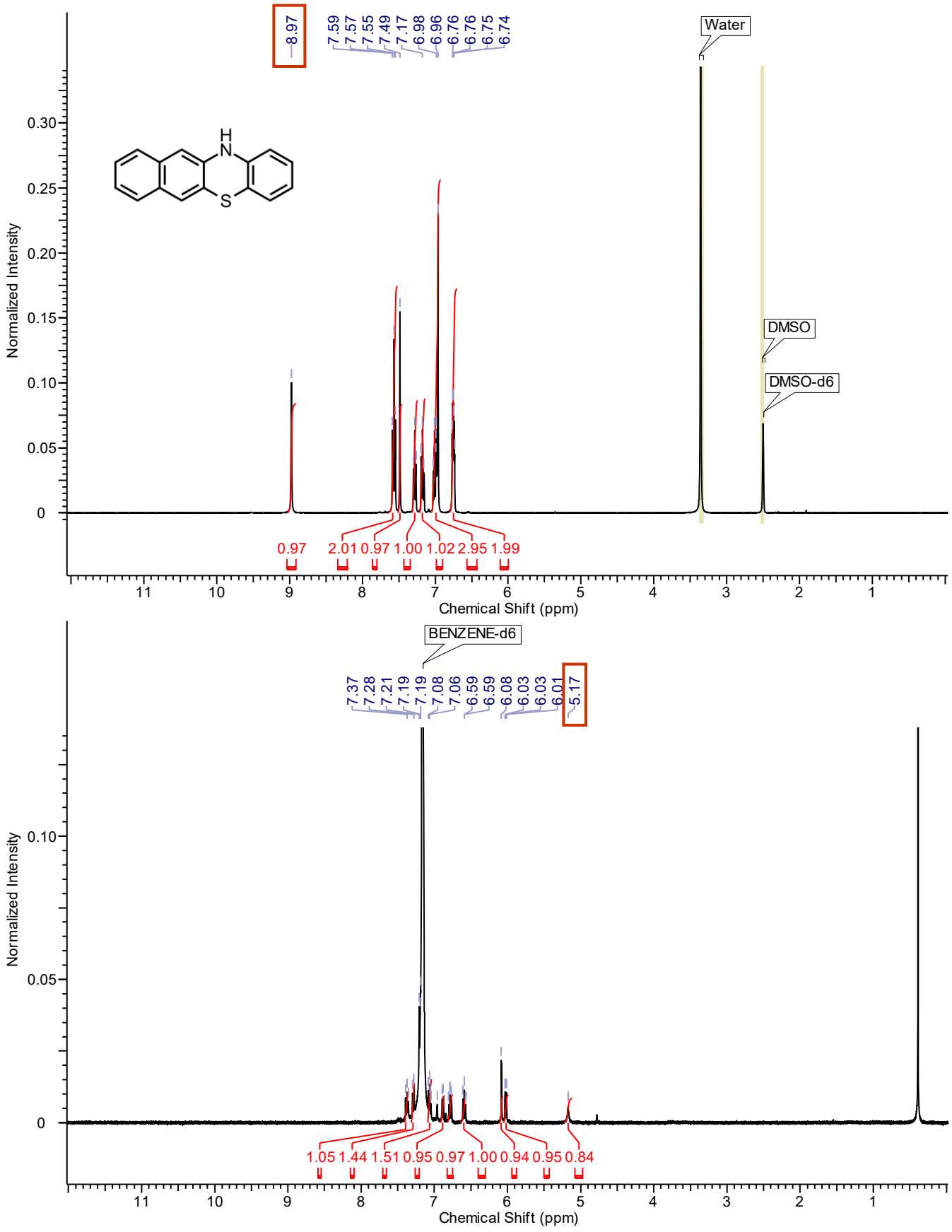


Figure S7.6. ^{1}H NMR spectra of Benzo(b)-PTZ (**3.5**) in DMSO-d6 (*top*) and C_6D_6 (*bottom*) (N-H highlighted). Poorly soluble in C_6D_6.

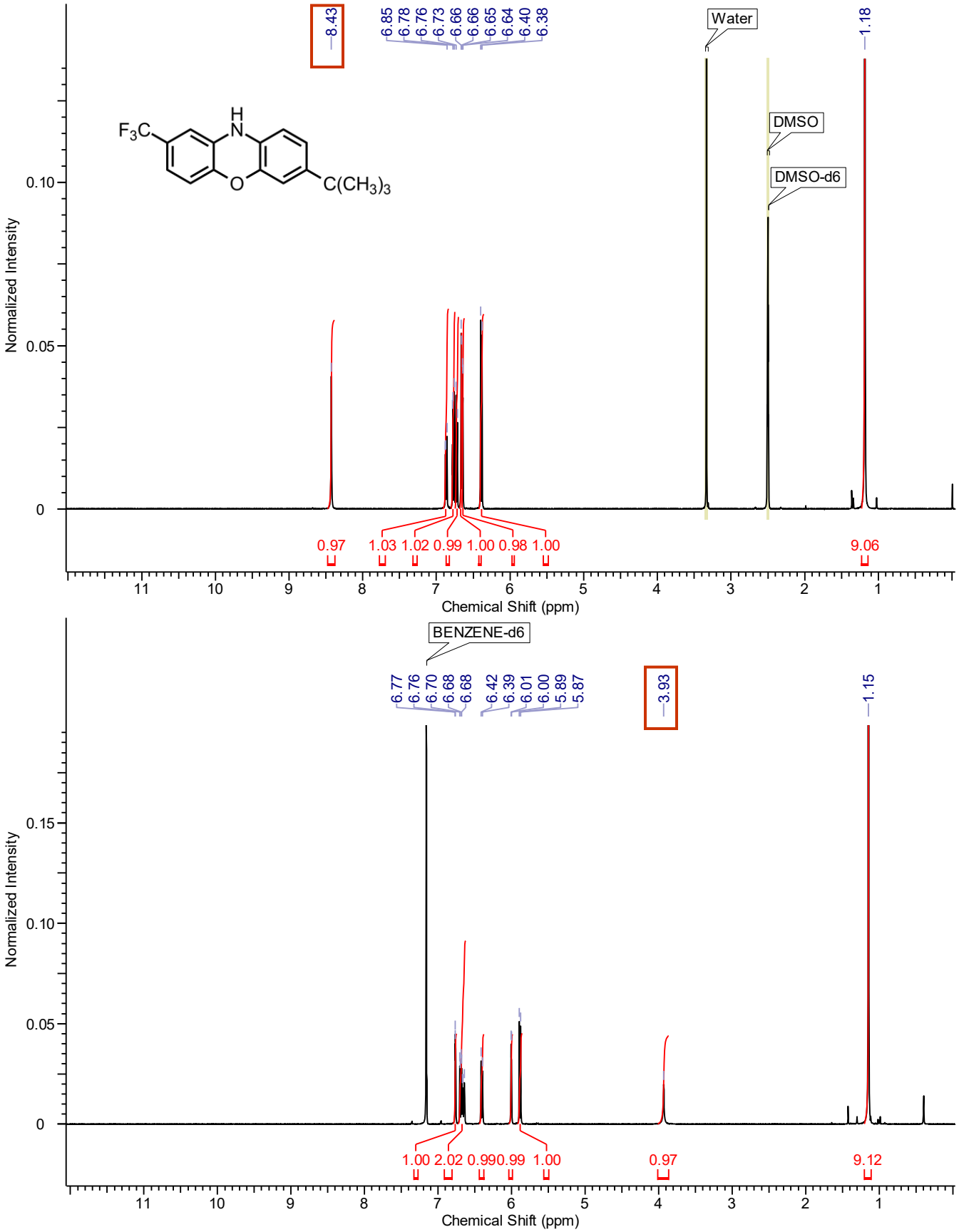


Figure S7.8. ^{1}H NMR spectra of 2-CF_3-7-tBu-PNX (**3.7**) in DMSO-d6 (*top*) and C_6D_6 (*bottom*) (N-H highlighted).

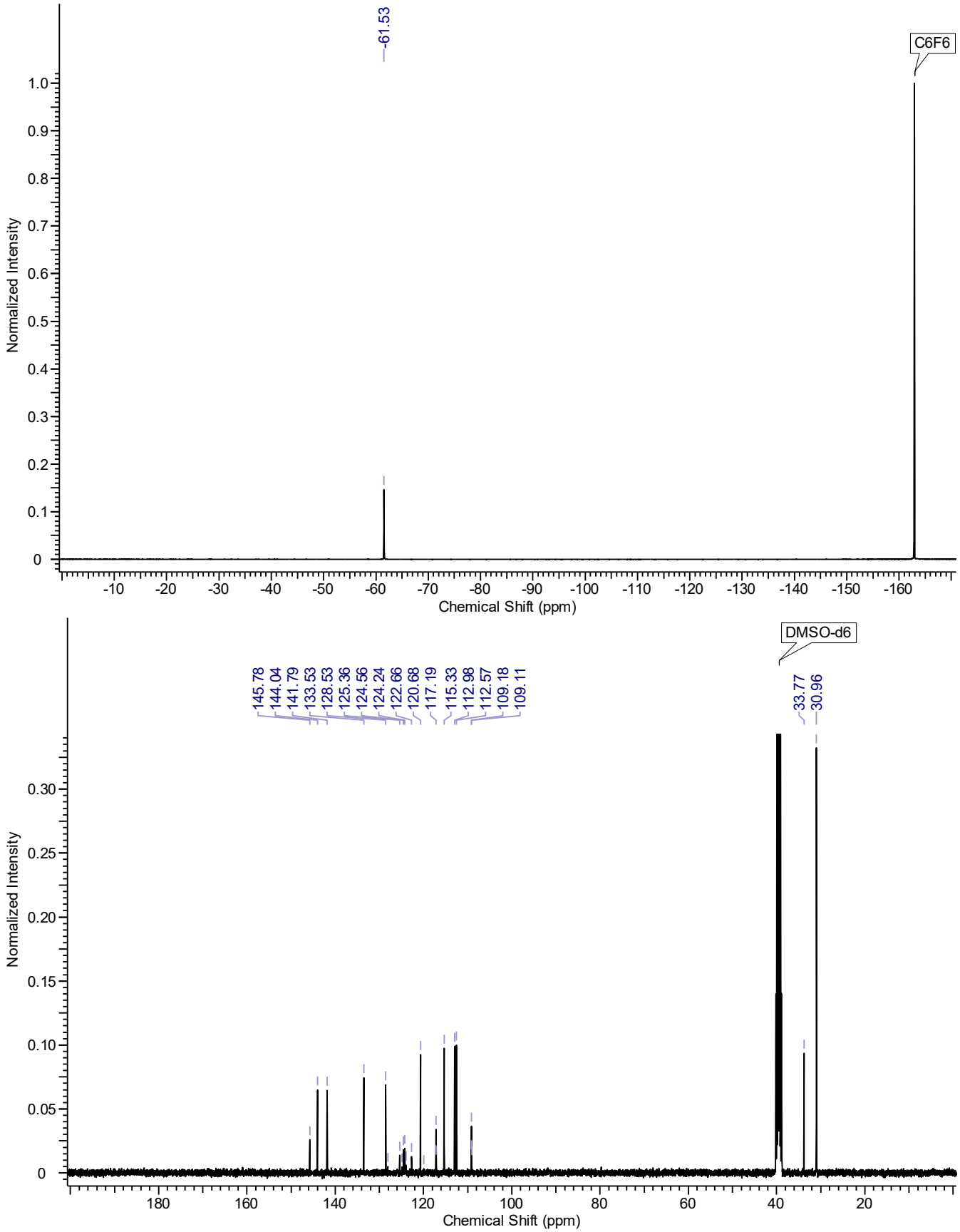


Figure S7.9. ^{19}F NMR (*top*) and ^{13}C NMR (*bottom*) spectra of 2-CF_3-7-tBu-PNX (**3.7**) in DMSO-d6.

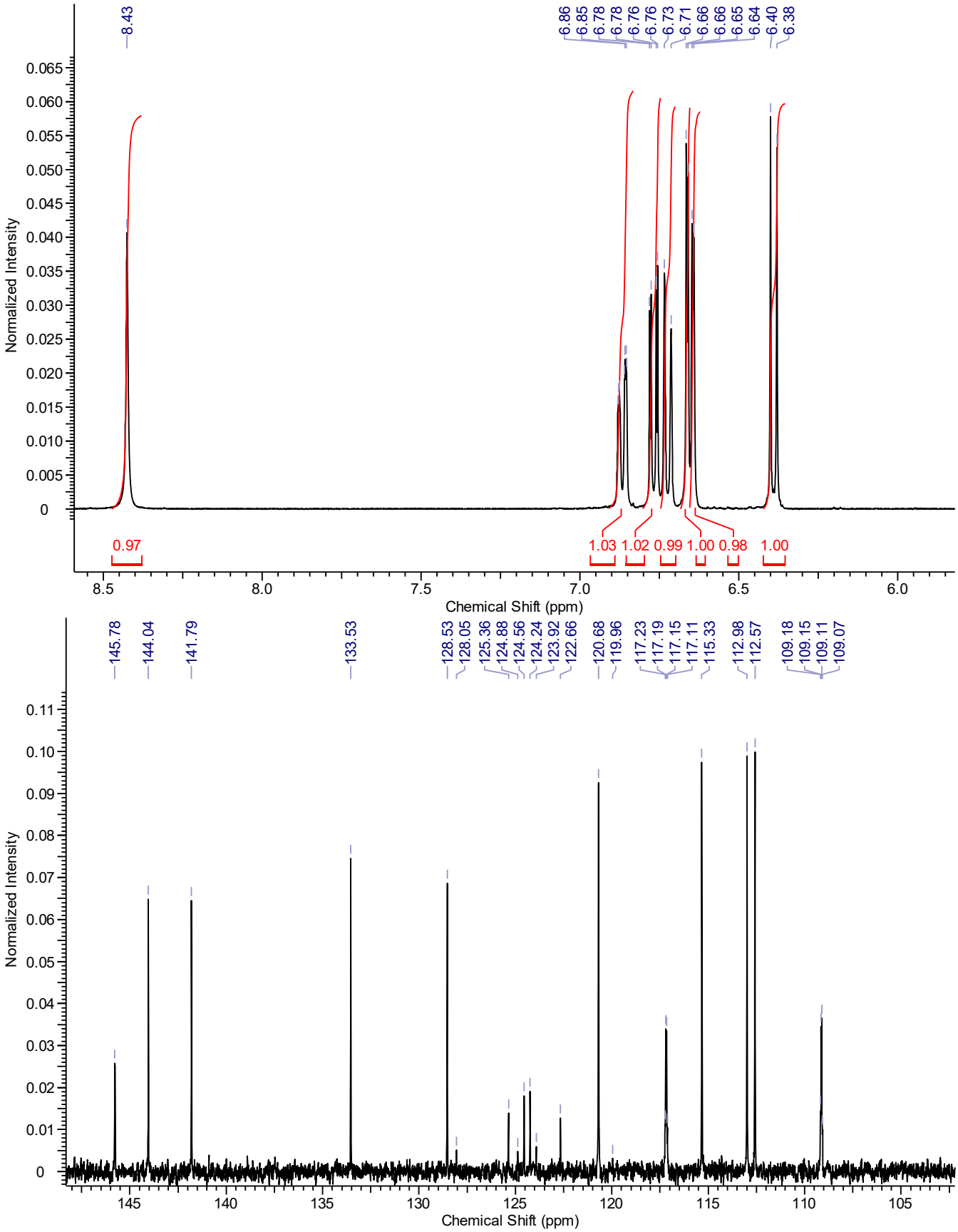


Figure S7.10. Aromatic regions of ^{1}H NMR (*top*) and ^{13}C NMR (*bottom*) spectra of 2-CF_3-7-tBu-PNX (**3.7**) in DMSO-d6.

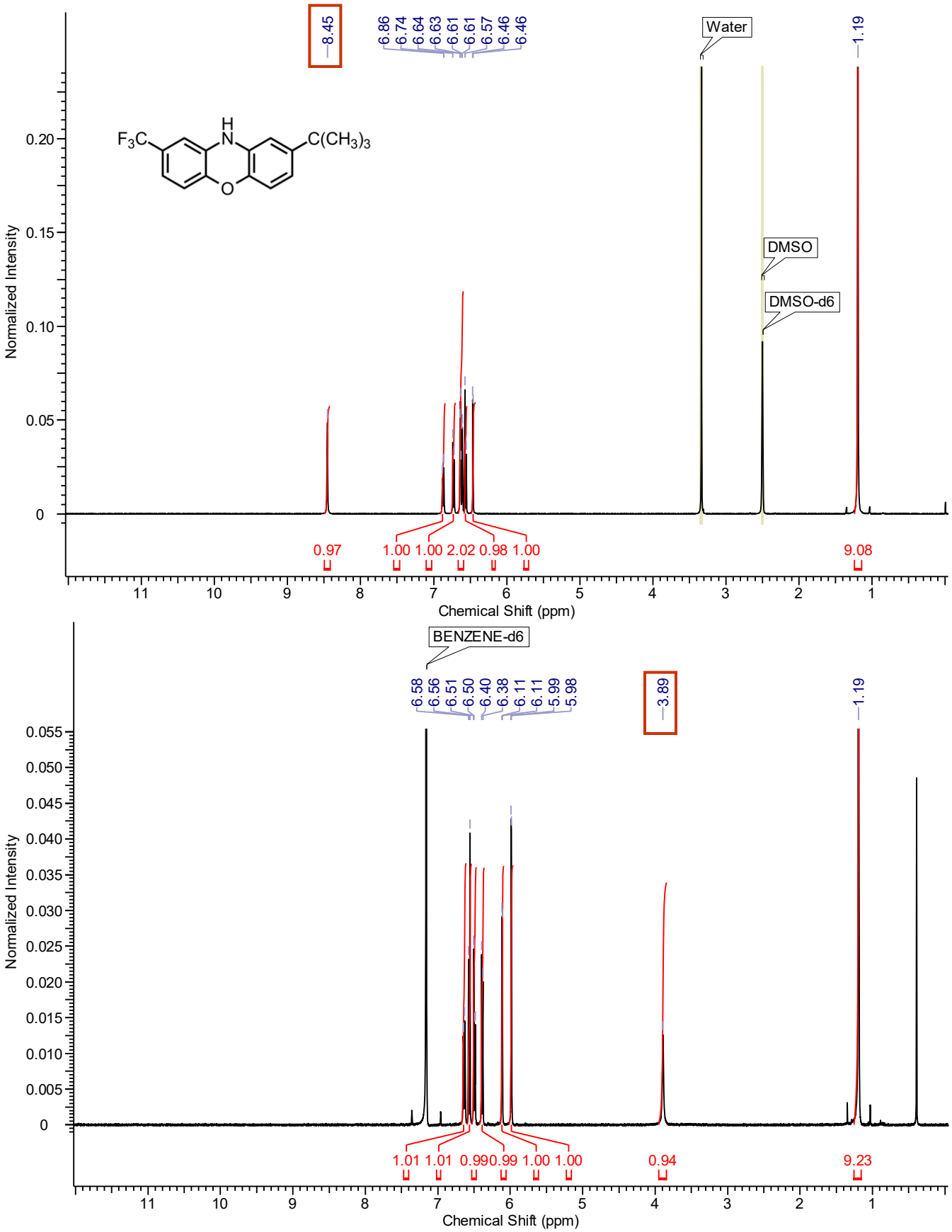


Figure S7.11. ^{1}H NMR spectra of 2-CF_3-8-tBu-PNX (**3.8**) in DMSO-d6 (*top*) and C_6D_6 (*bottom*) (N-H highlighted).

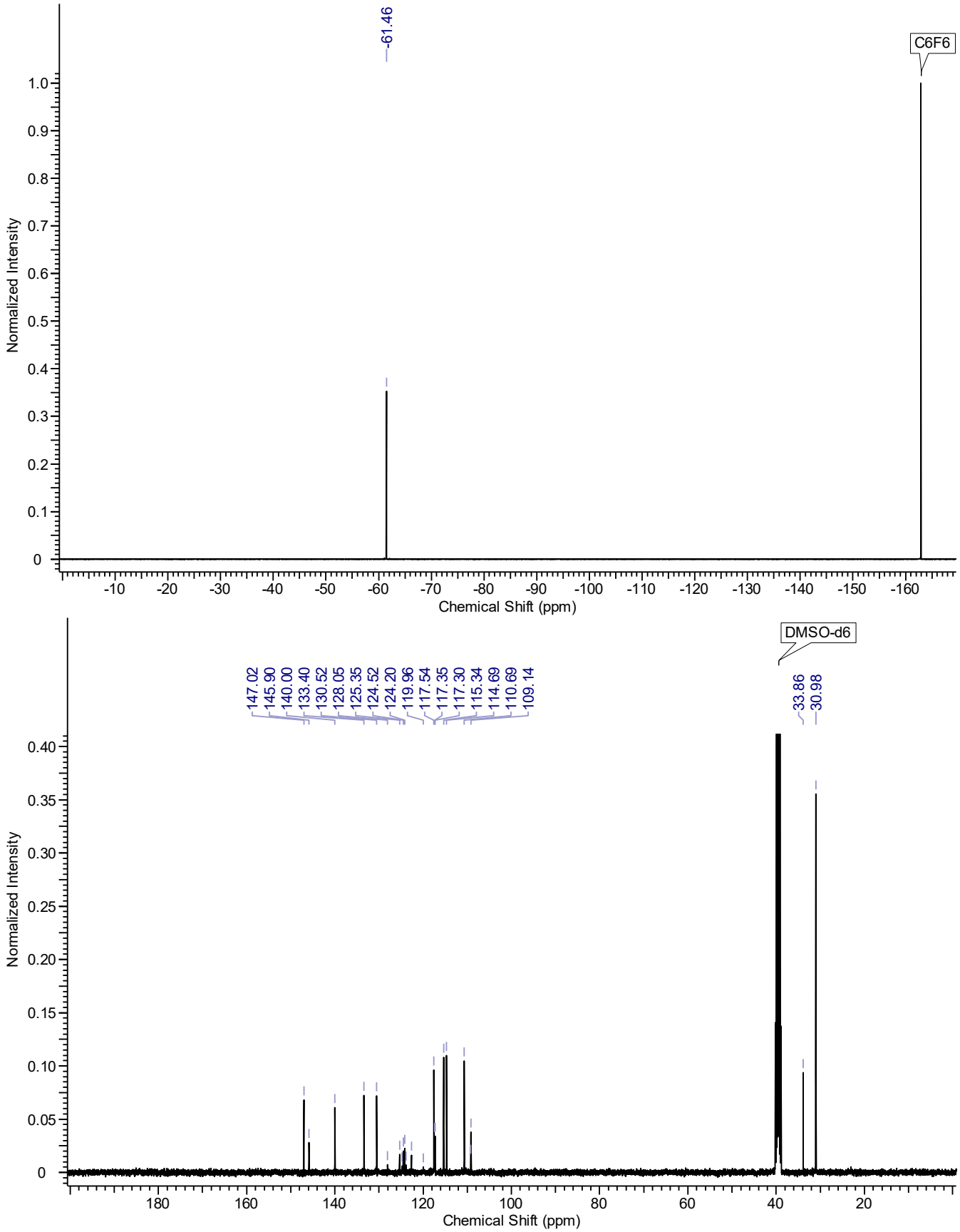


Figure S7.12. ^{19}F NMR (*top*) and ^{13}C NMR (*bottom*) spectra of 2-CF_3-8-tBu-PNX (**3.8**) in DMSO-d6.

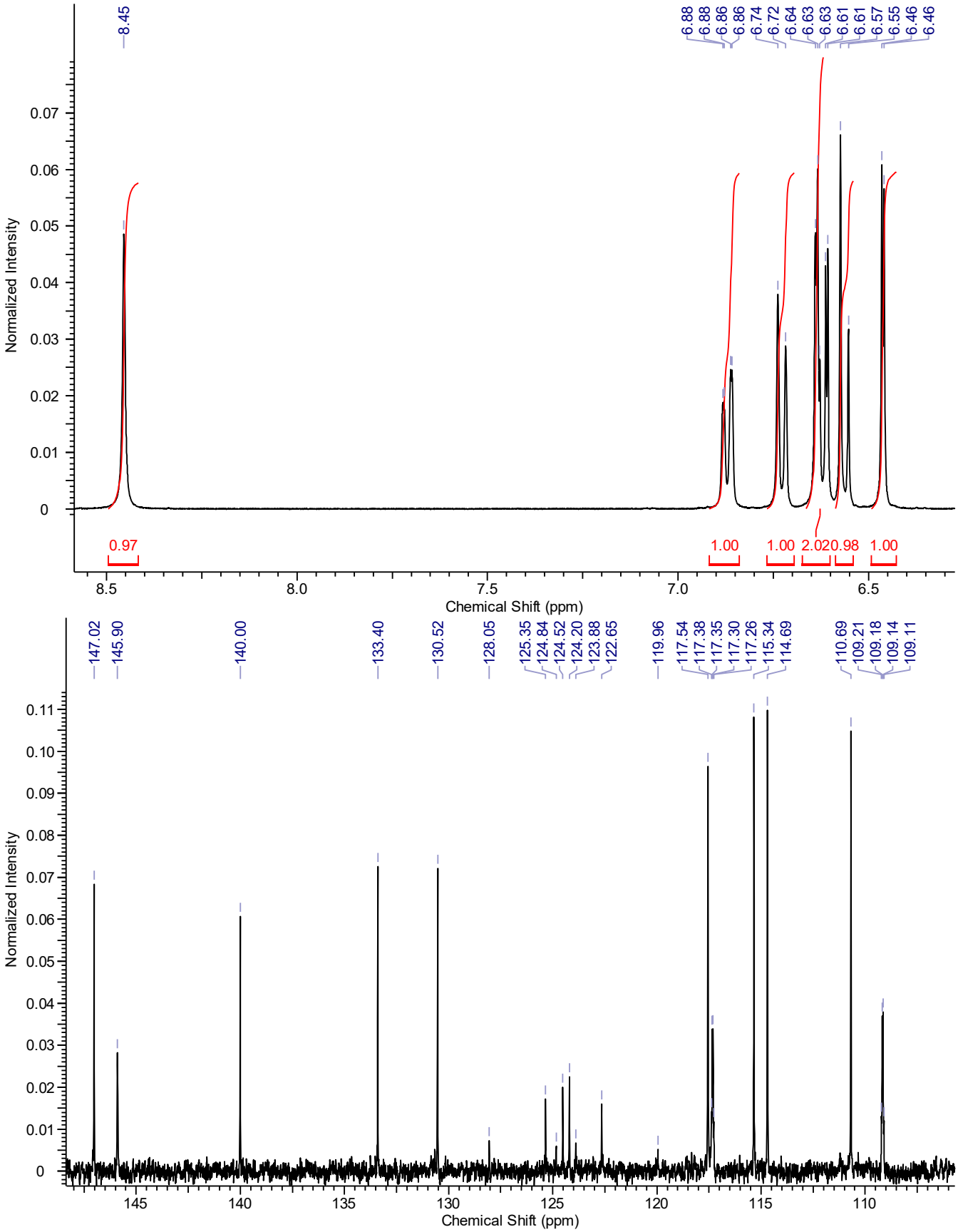


Figure S7.13. Aromatic regions of ^{1}H NMR (*top*) and ^{13}C NMR (*bottom*) spectra of 2-CF_3-8-tBu-PNX (**3.8**) in DMSO-d6.

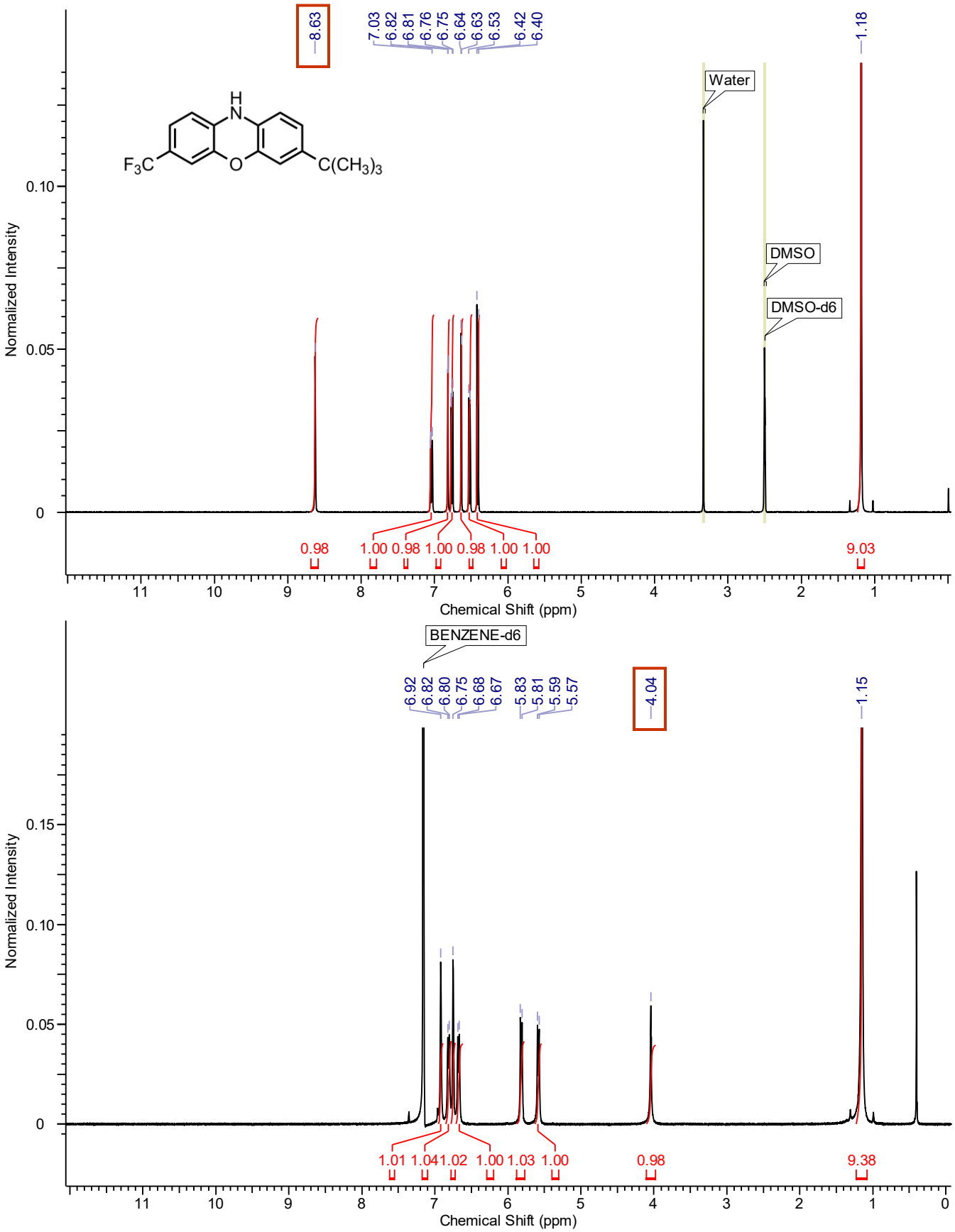


Figure S7.14. ^{1}H NMR spectra of 3-CF_3-7-tBu-PNX (**3.10**) in DMSO-d6 (*top*) and C_6D_6 (*bottom*) (N-H highlighted).

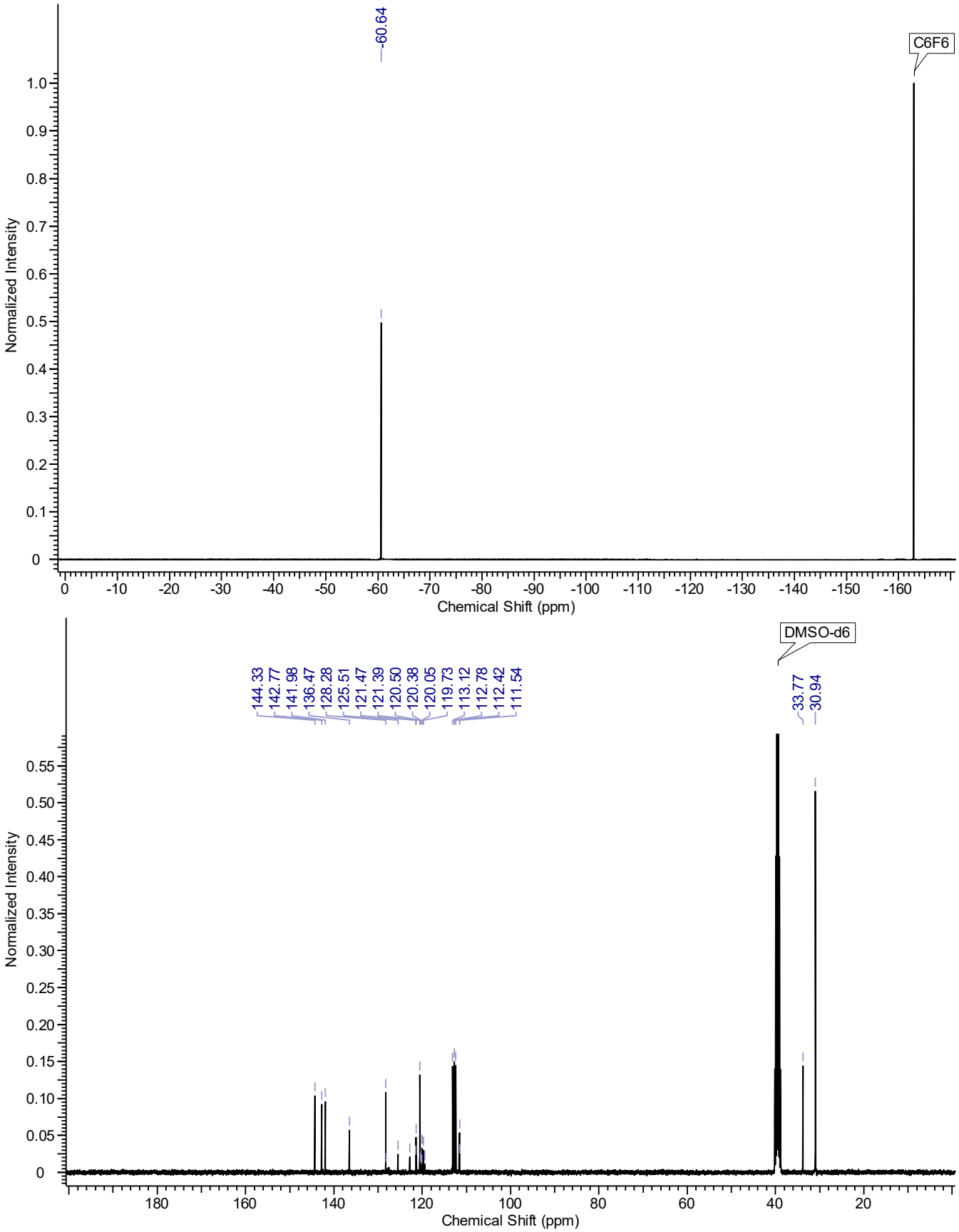


Figure S7.15. ^{19}F NMR (*top*) and ^{13}C NMR (*bottom*) spectra of 3-CF_3-7-tBu-PNX (**3.10**) in DMSO-d6.

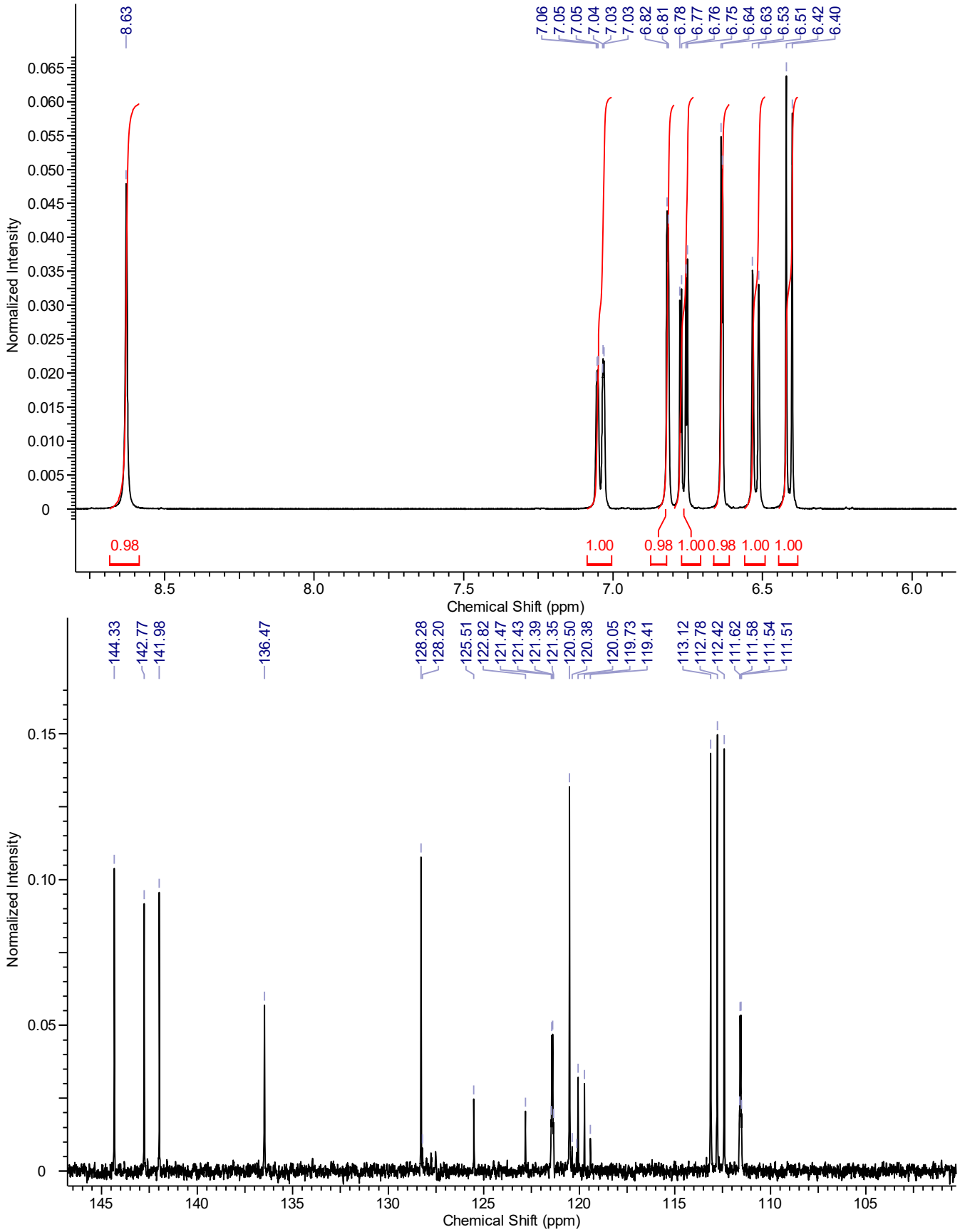


Figure S7.16. Aromatic regions of ^{1}H NMR (*top*) and ^{13}C NMR (*bottom*) spectra of 3-CF_3-7-tBu-PNX (**3.10**) in DMSO-d6.

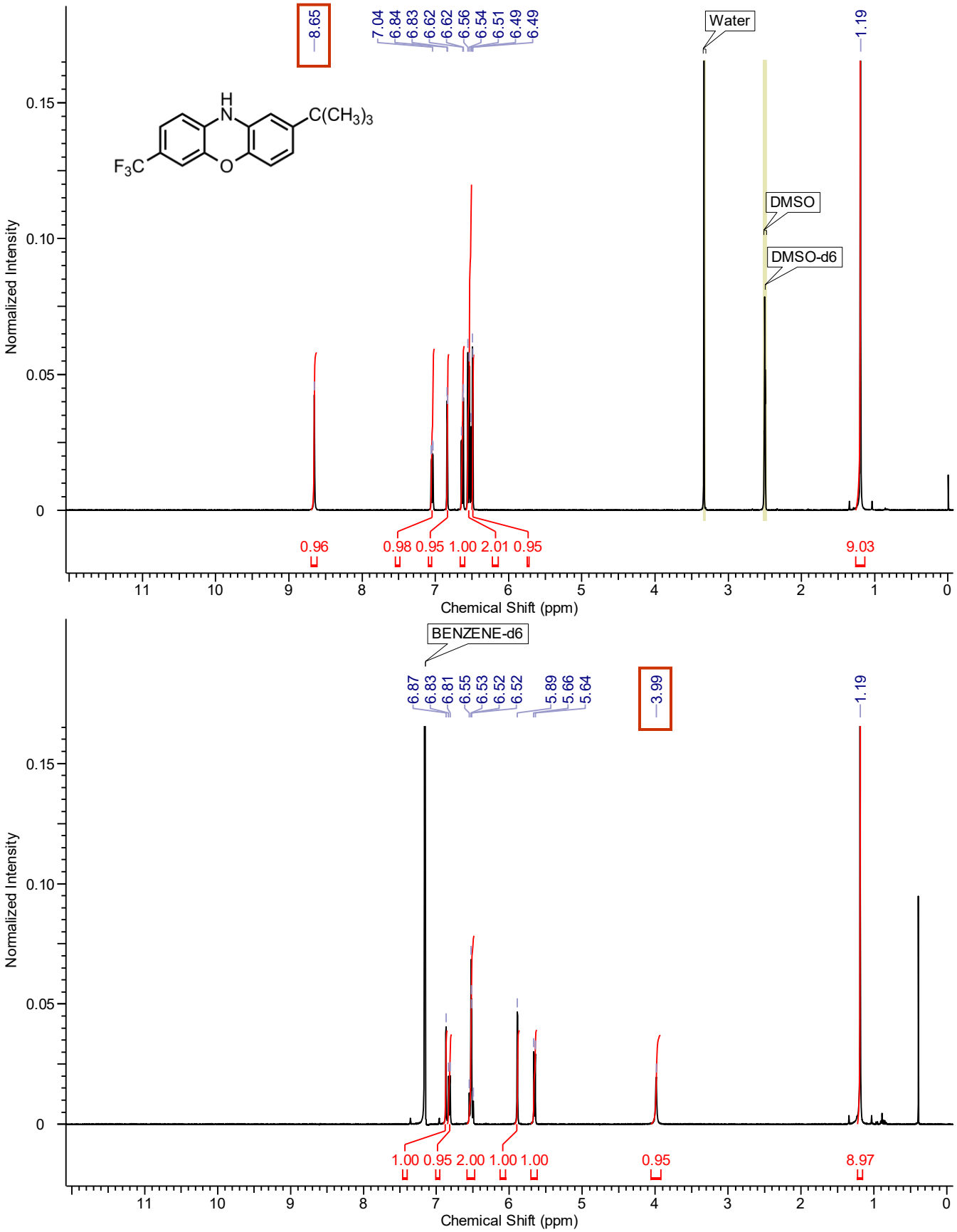


Figure S7.17. ^{1}H NMR spectra of 3-CF_3-8-tBu-PNX (**3.11**) in DMSO-d6 (*top*) and C_6D_6 (*bottom*) (N-H highlighted).

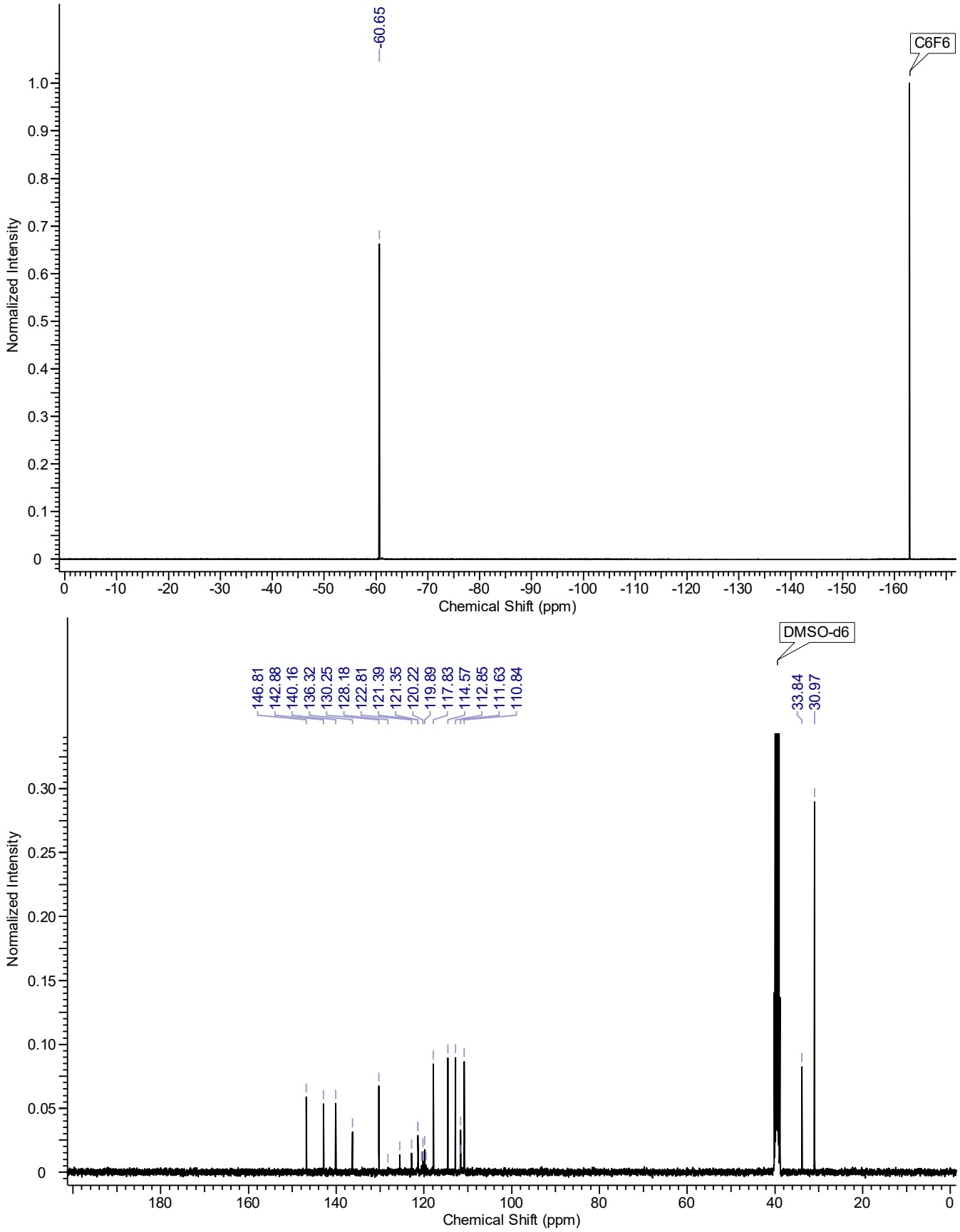


Figure S7.18. ^{19}F NMR (*top*) and ^{13}C NMR (*bottom*) spectra of 3-CF_3-8-tBu-PNX (**3.11**) in DMSO-d6.

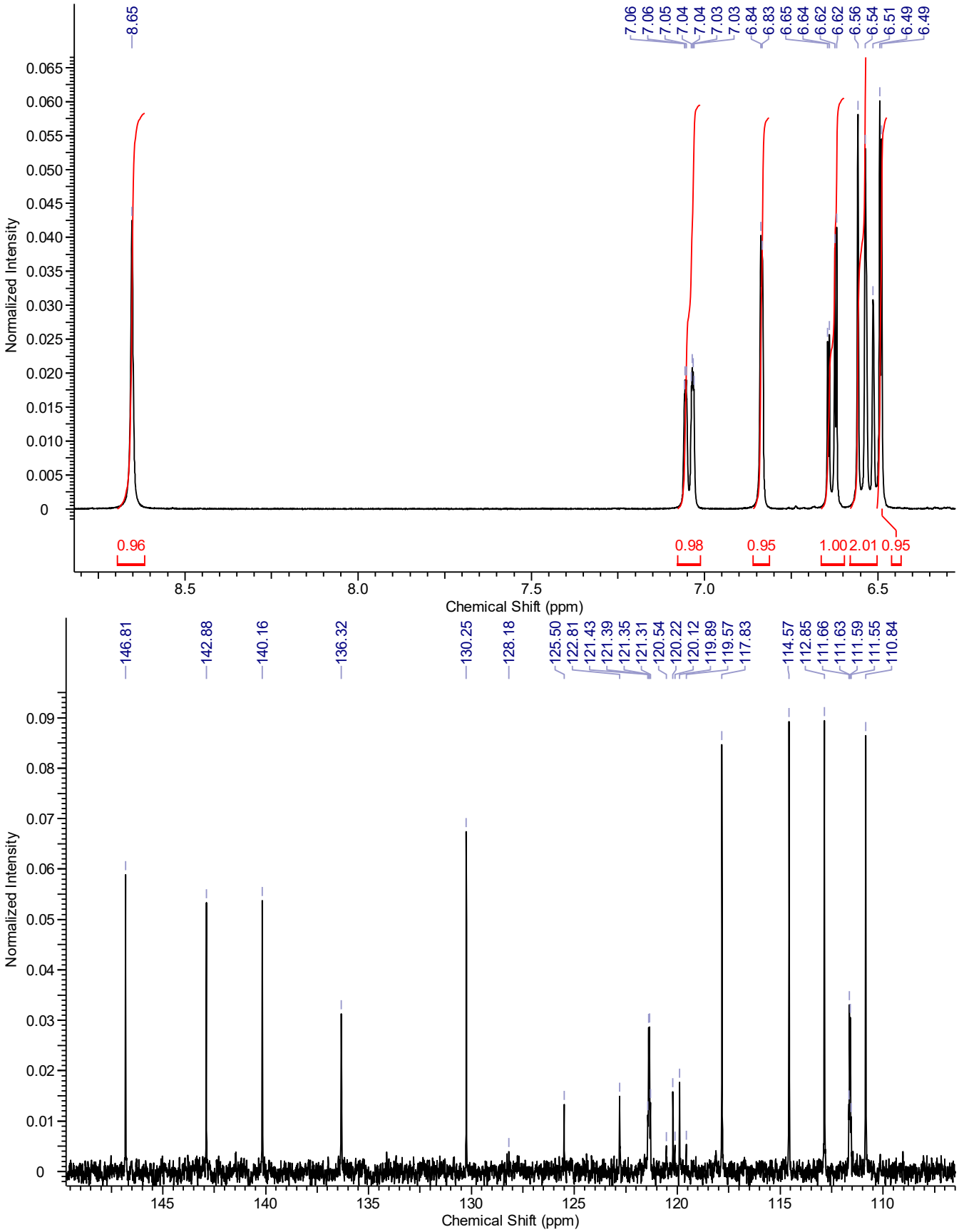


Figure S7.19. Aromatic regions of ^{1}H NMR (*top*) and ^{13}C NMR (*bottom*) spectra of 3-CF_3-8-tBu-PNX (**3.11**) in DMSO-d6.

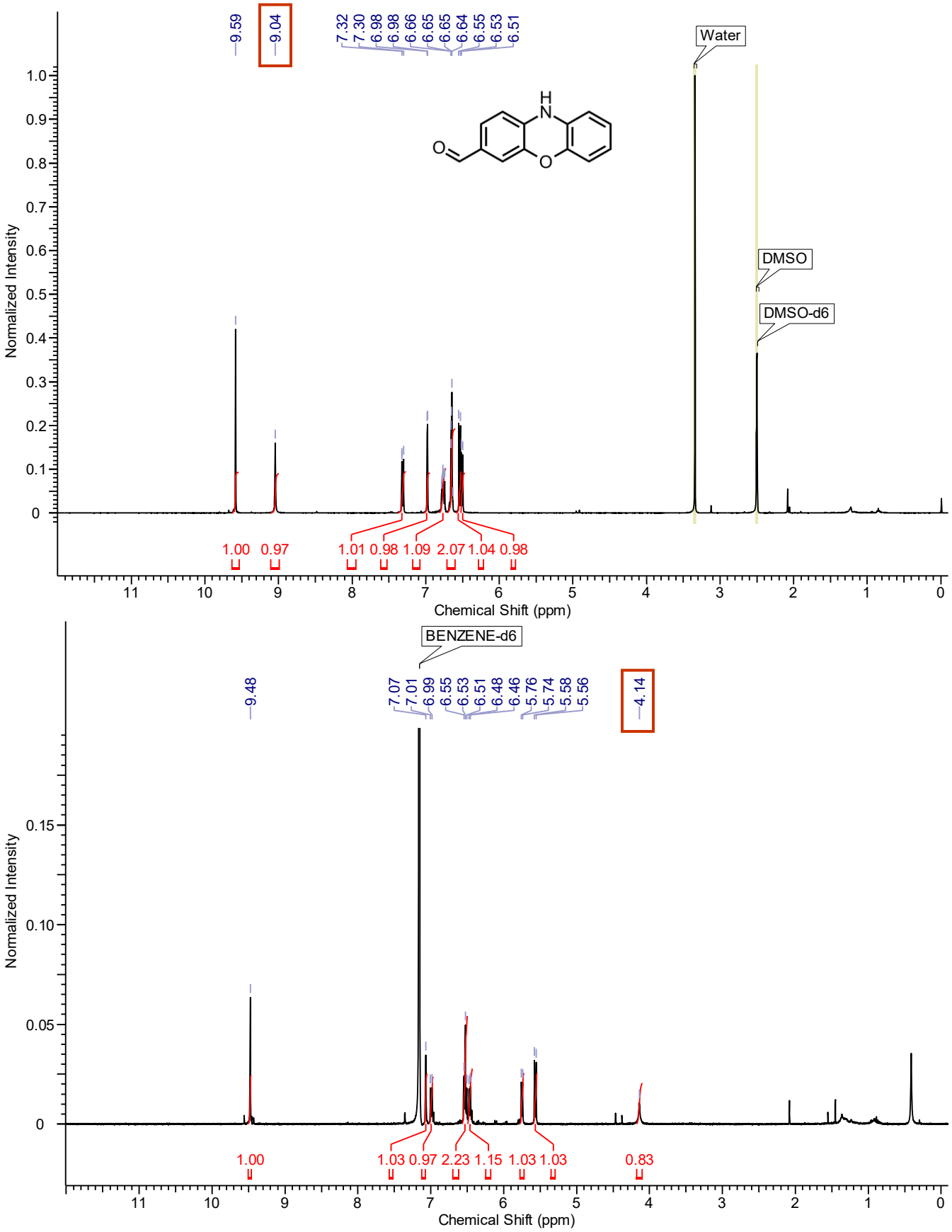


Figure S7.20. ^{1}H NMR spectra of 3-Formyl-PNX (**3.12**) in DMSO-d6 (*top*) and C_6D_6 (*bottom*) (N-H highlighted). Poorly soluble in C_6D_6.

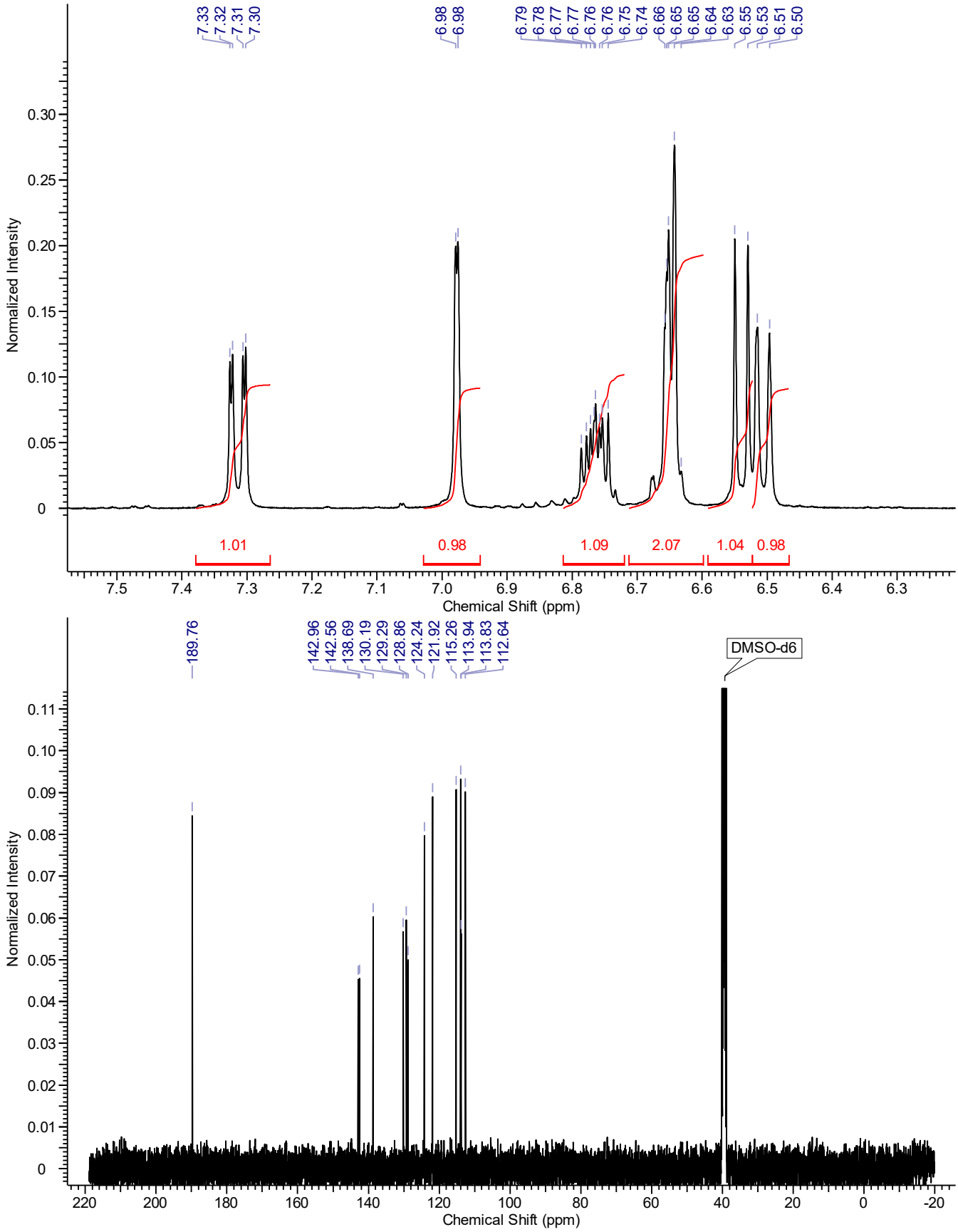


Figure S7.21. Aromatic region of ^{1}H NMR (*top*) and full ^{13}C NMR spectra (*bottom*) of 3-Formyl-PNX (**3.12**) in DMSO-d6.

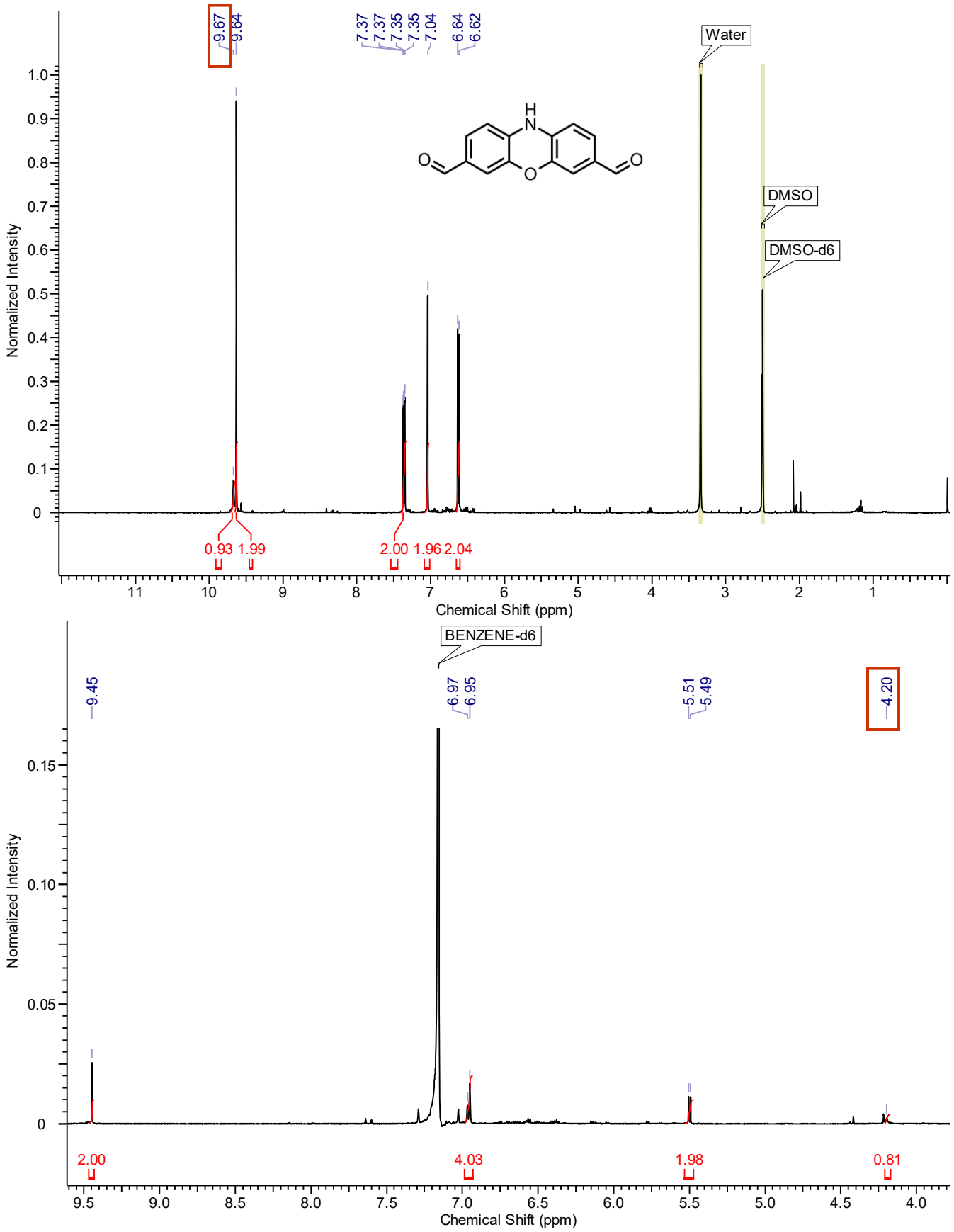


Figure S7.22. ^{1}H NMR spectra of 3,7-Formyl-PNX (**3.13**) in DMSO-d6 (*top*) and C_6D_6 (*bottom*) (N-H highlighted). *Very* poorly soluble in C_6D_6.

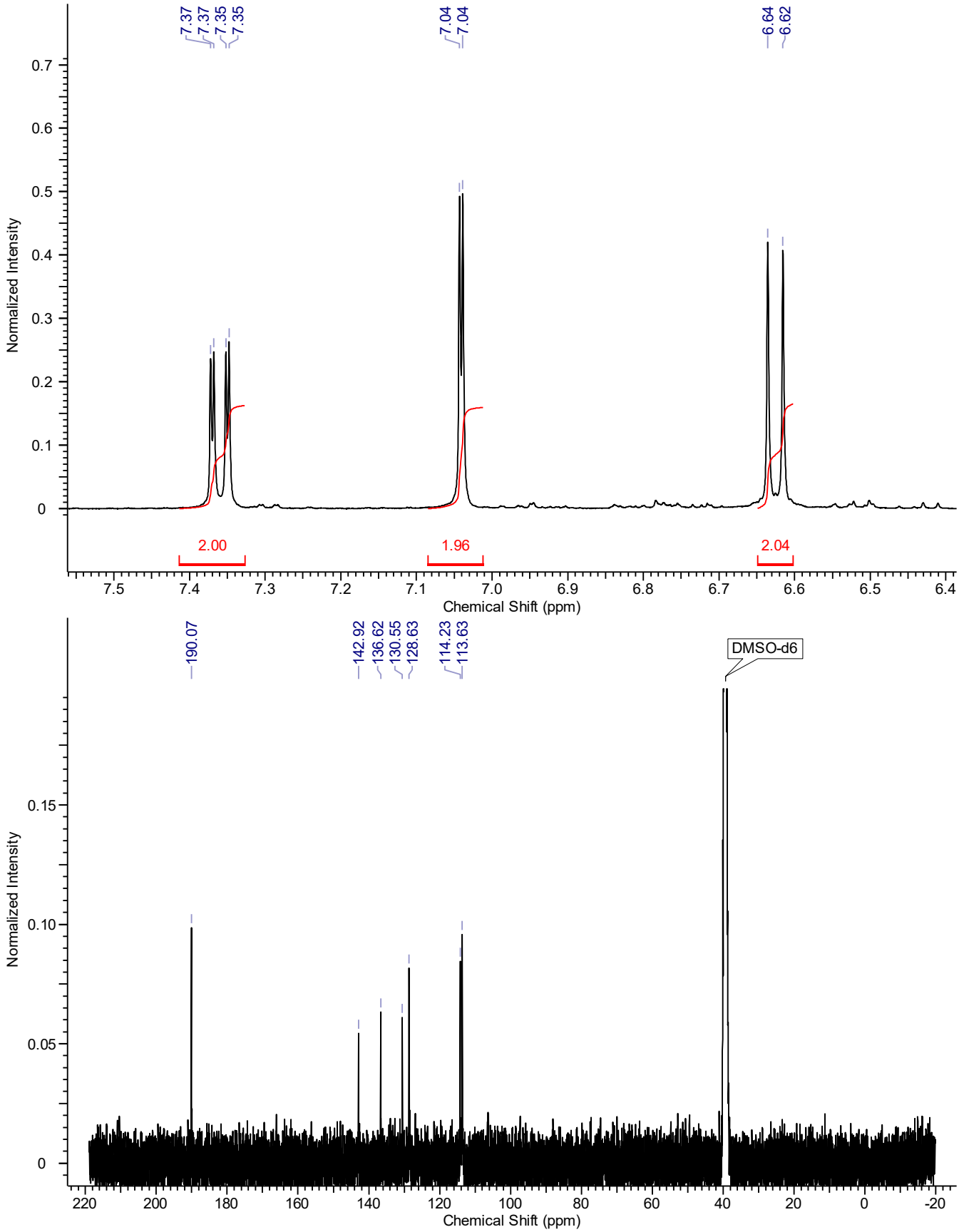


Figure S7.23. Aromatic region of ^{1}H NMR (*top*) and full ^{13}C NMR spectra (*bottom*) of 3,7-Formyl-PNX (**3.13**) in DMSO-d6.

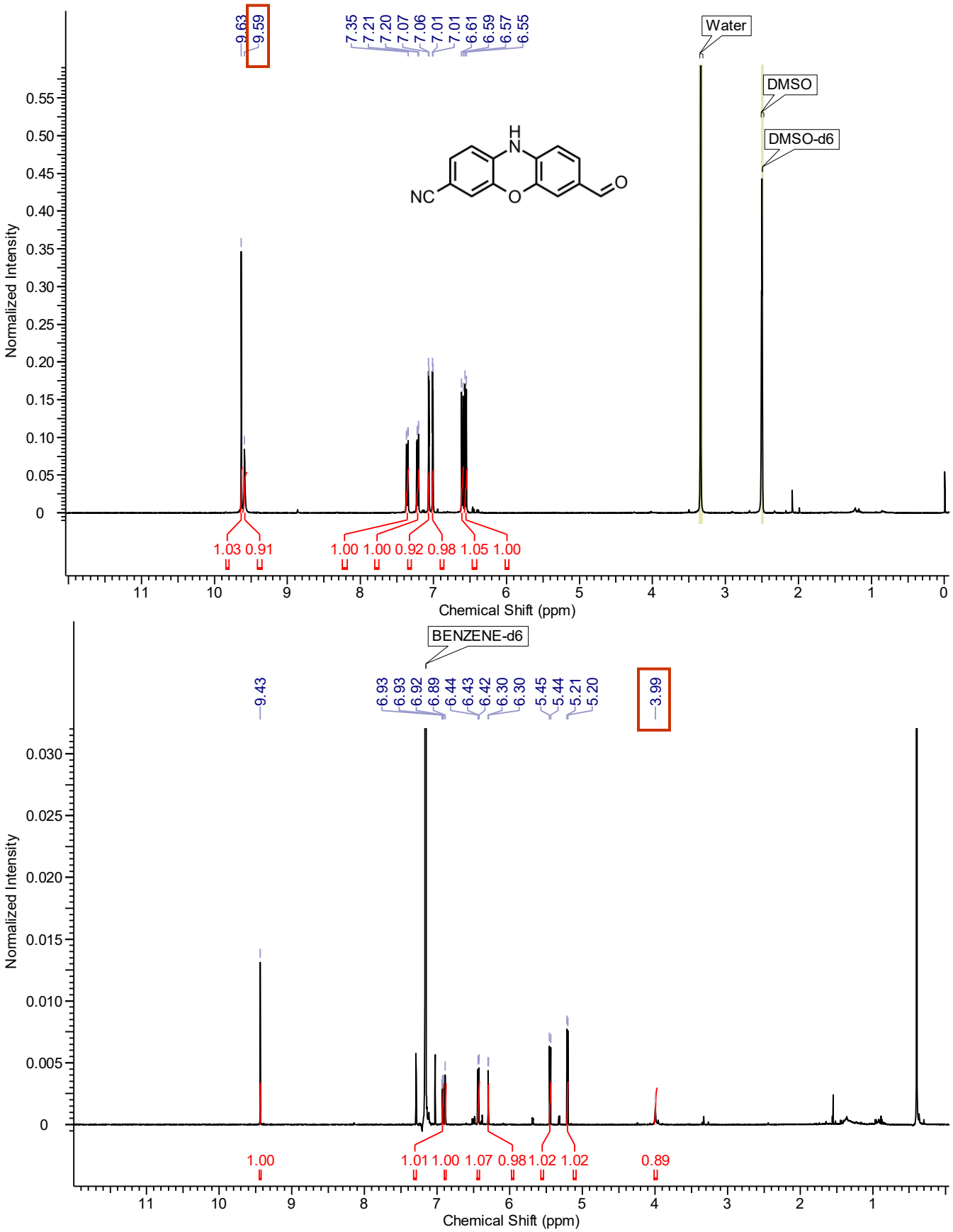


Figure S7.24. ^{1}H NMR spectra of 3-CN-7-Formyl-PNX (**3.14**) in DMSO-d6 (*top*) and C_6D_6 (*bottom*) (N-H highlighted). Poorly soluble in C_6D_6.

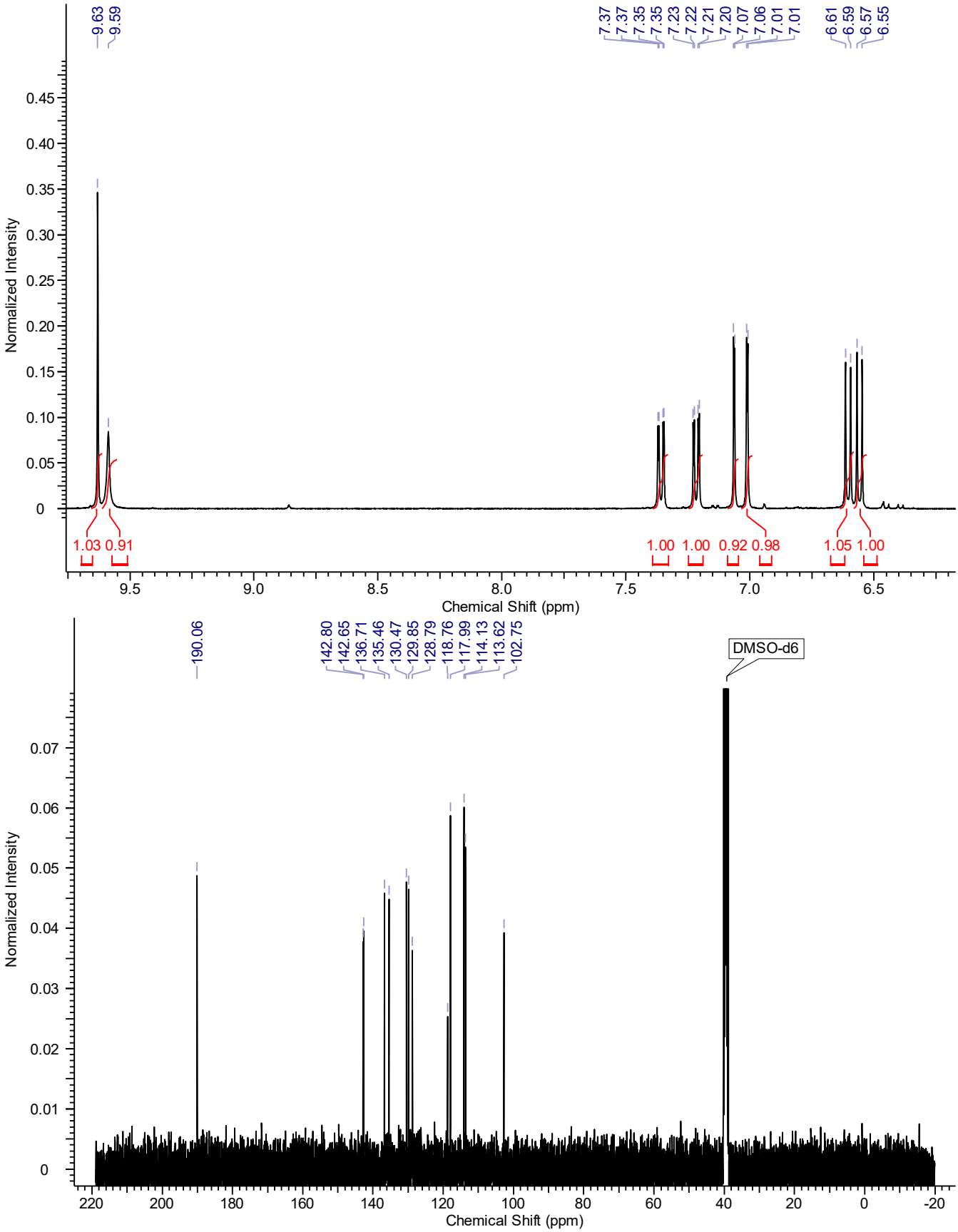


Figure S7.25. Aromatic region of ^{1}H NMR (*top*) and full ^{13}C NMR spectra (*bottom*) of 3-CN-7-Formyl-PNX (**3.14**) in DMSO-d6.

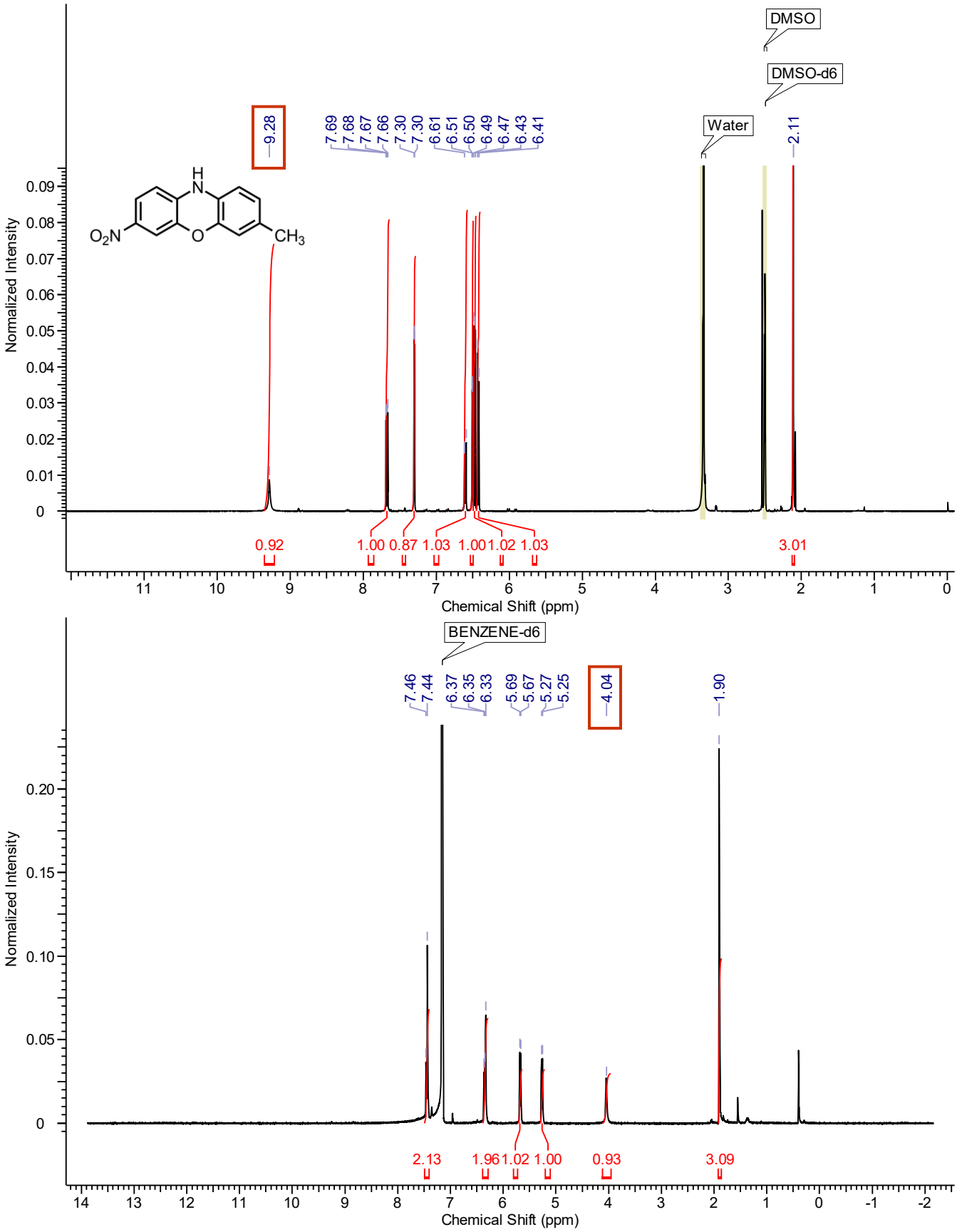


Figure S7.26. ^{1}H NMR spectra of 3-NO_2-7-Me-PNX (**3.16**) in DMSO-d6 (*top*) and C_6D_6 (*bottom*) (N-H highlighted).

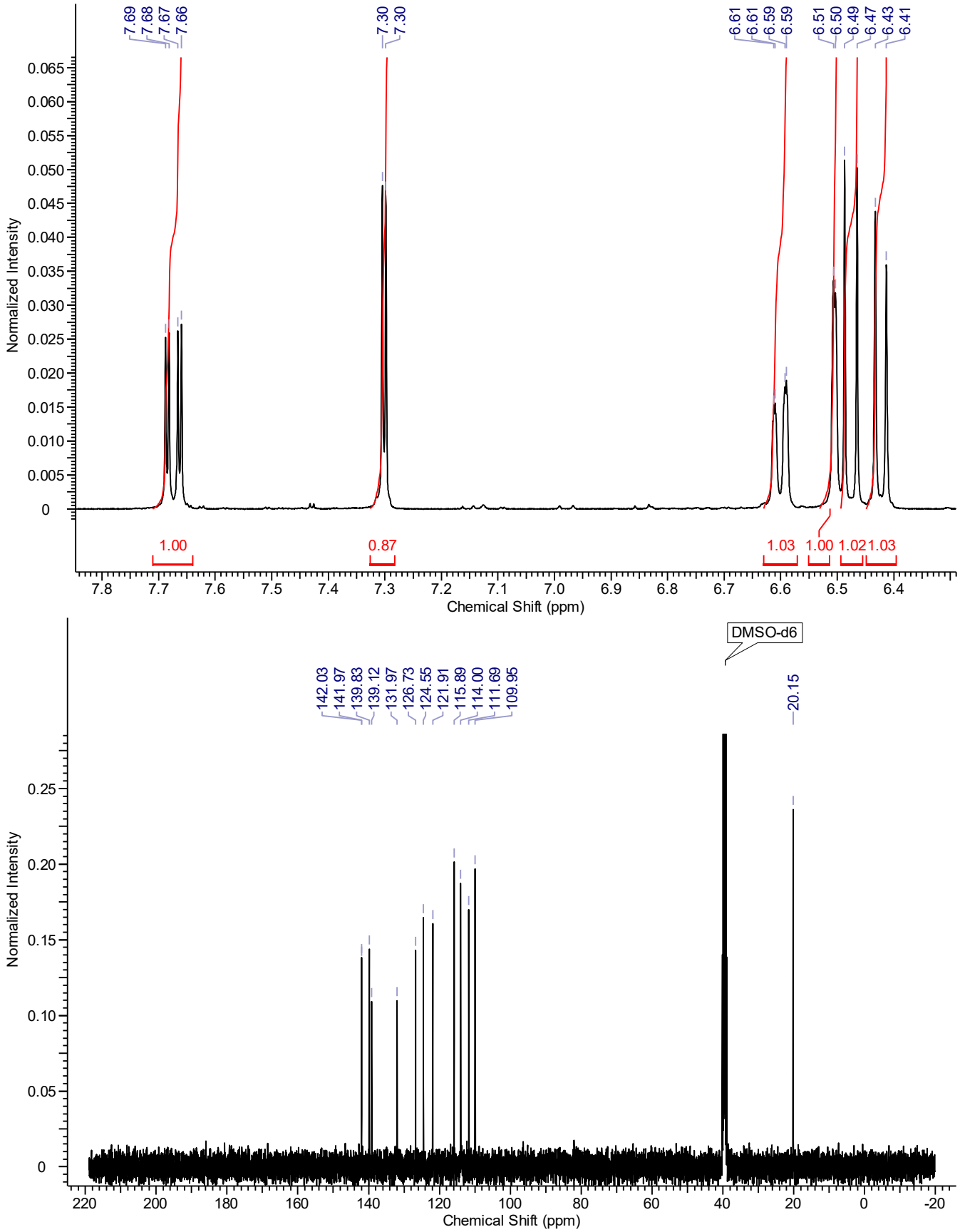


Figure S7.27. Aromatic region of ^{1}H NMR (*top*) and full ^{13}C NMR spectra (*bottom*) of 3-NO_2-7-Me-PNX (**3.16**) in DMSO-d6.

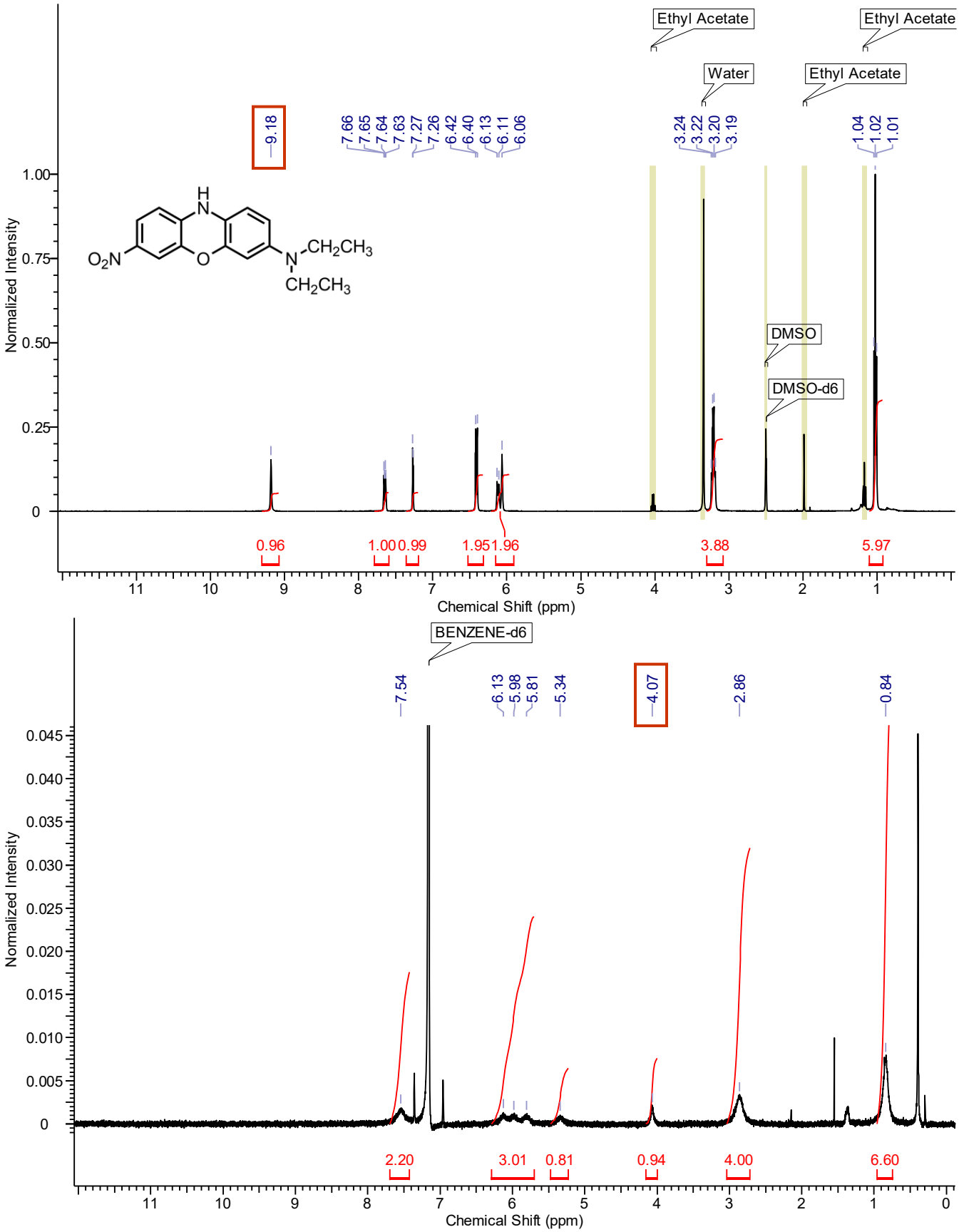


Figure S7.28. ^{1}H NMR spectra of 3-NO_2-7-NEt_2-PNX (**3.18**) in DMSO-d6 (*top*) and C_6D_6 (*bottom*) (N-H highlighted). Poorly soluble in C_6D_6.

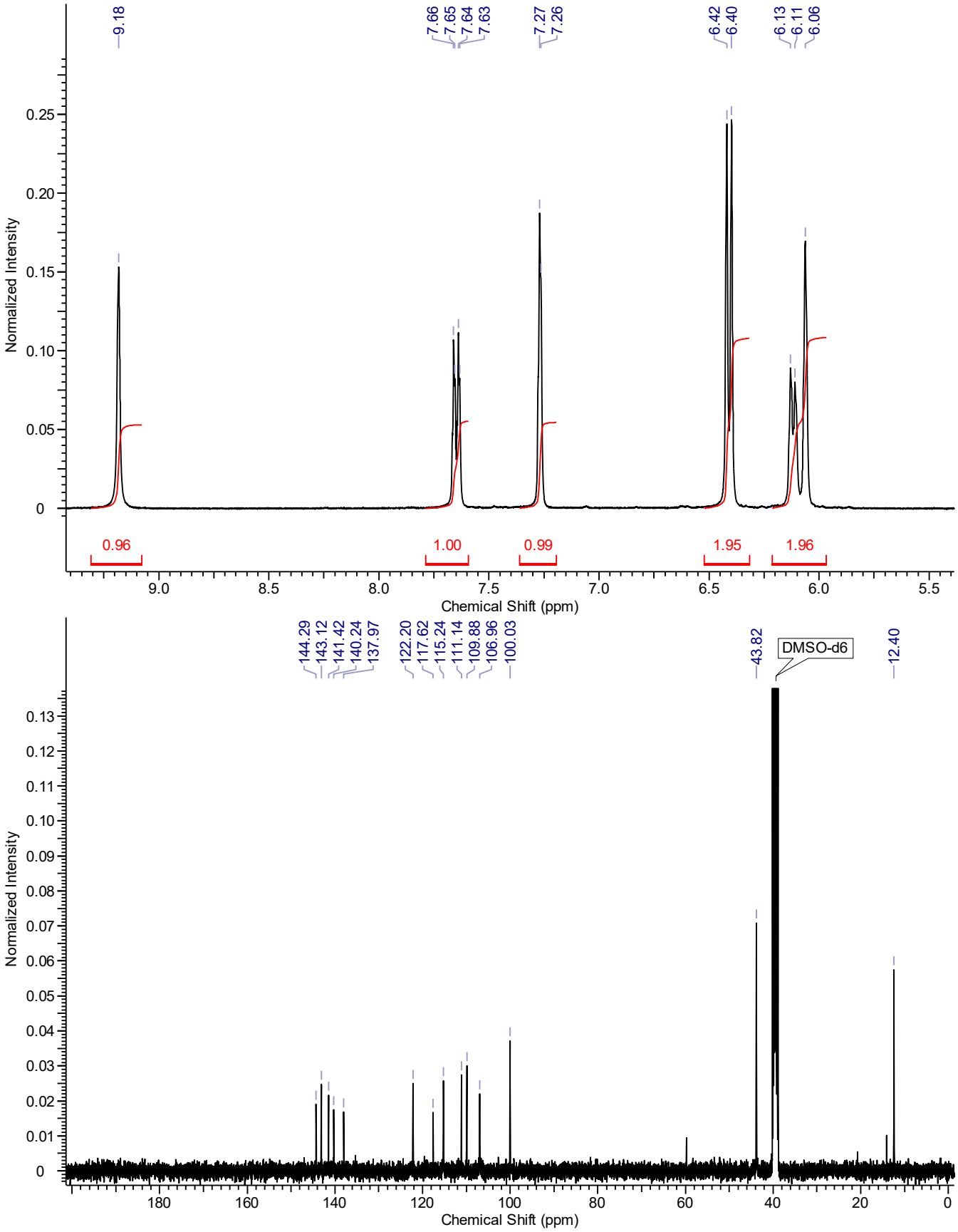


Figure S7.29. Aromatic region of ^{1}H NMR (*top*) and full ^{13}C NMR spectra (*bottom*) of 3-NO_2-7-NEt_2-PNX (**3.18**) in DMSO-d6.

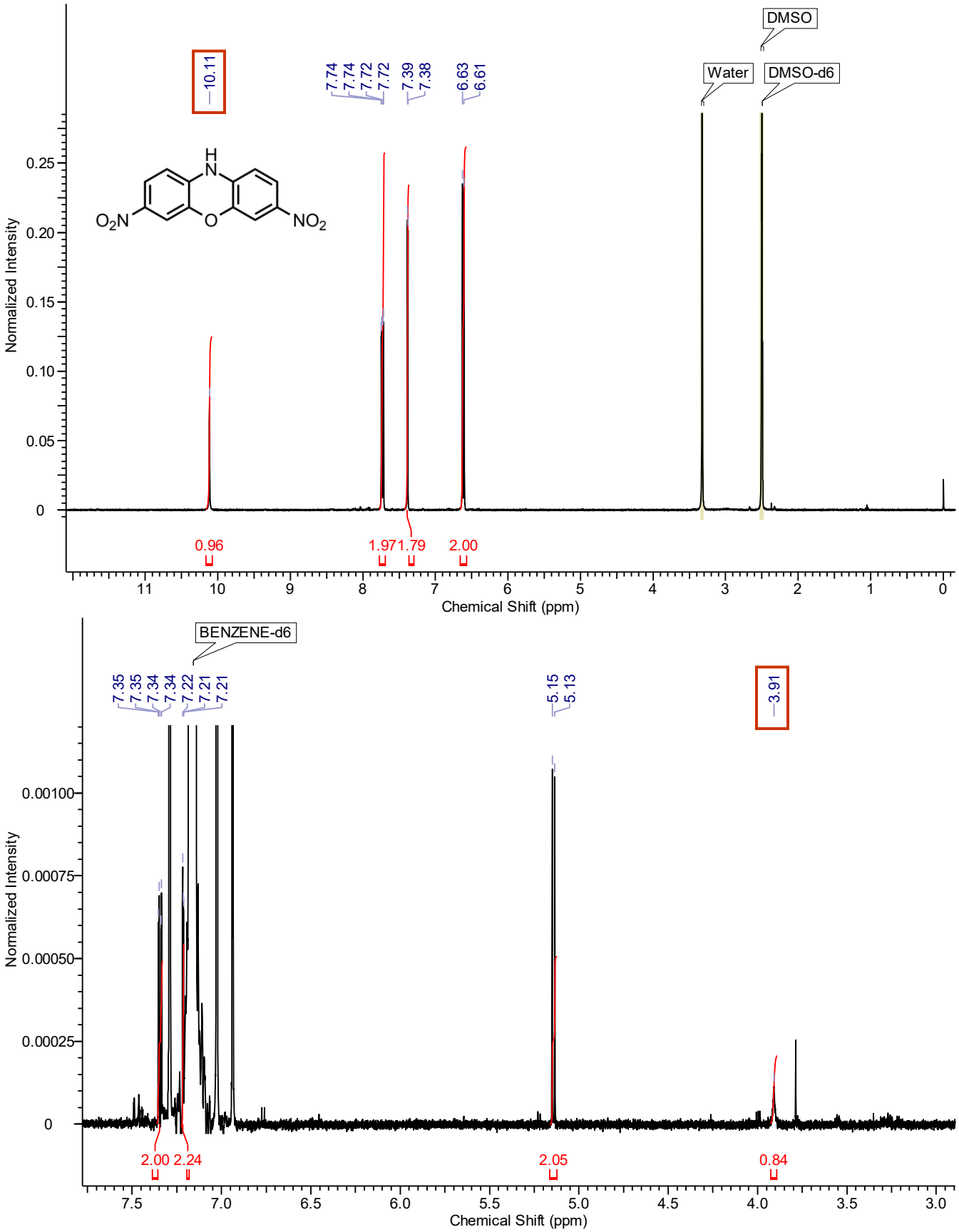


Figure S7.30. ^{1}H NMR spectra of 3,7-NO_2-PNX (**3.19**) in DMSO-d6 (*top*) and C_6D_6 (*bottom*) (N-H highlighted). Poorly soluble in C_6D_6.

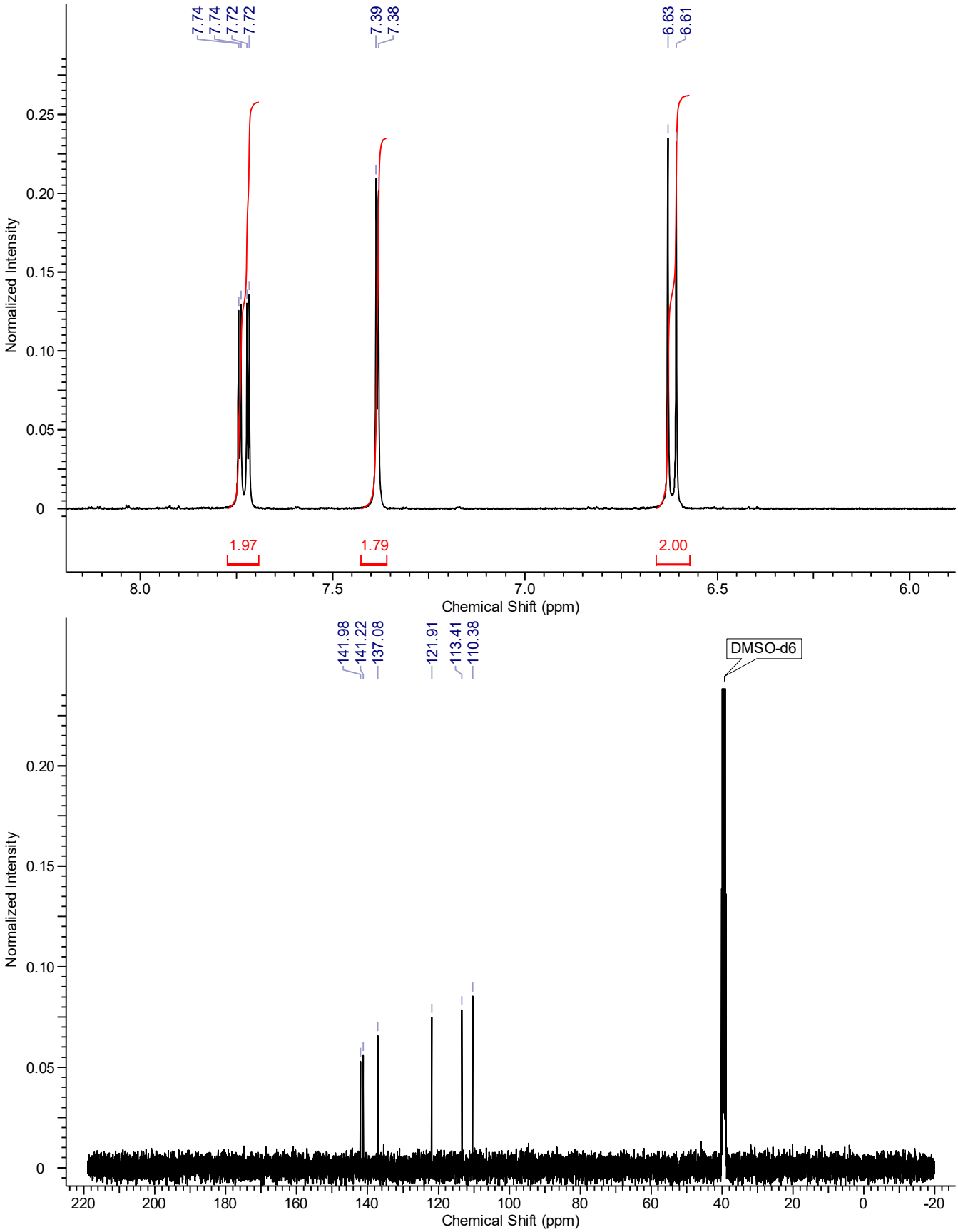


Figure S7.31. Aromatic region of ^{1}H NMR (*top*) and full ^{13}C NMR spectra (*bottom*) of 3,7-NO_2-PNX (**3.19**) in DMSO-d6.

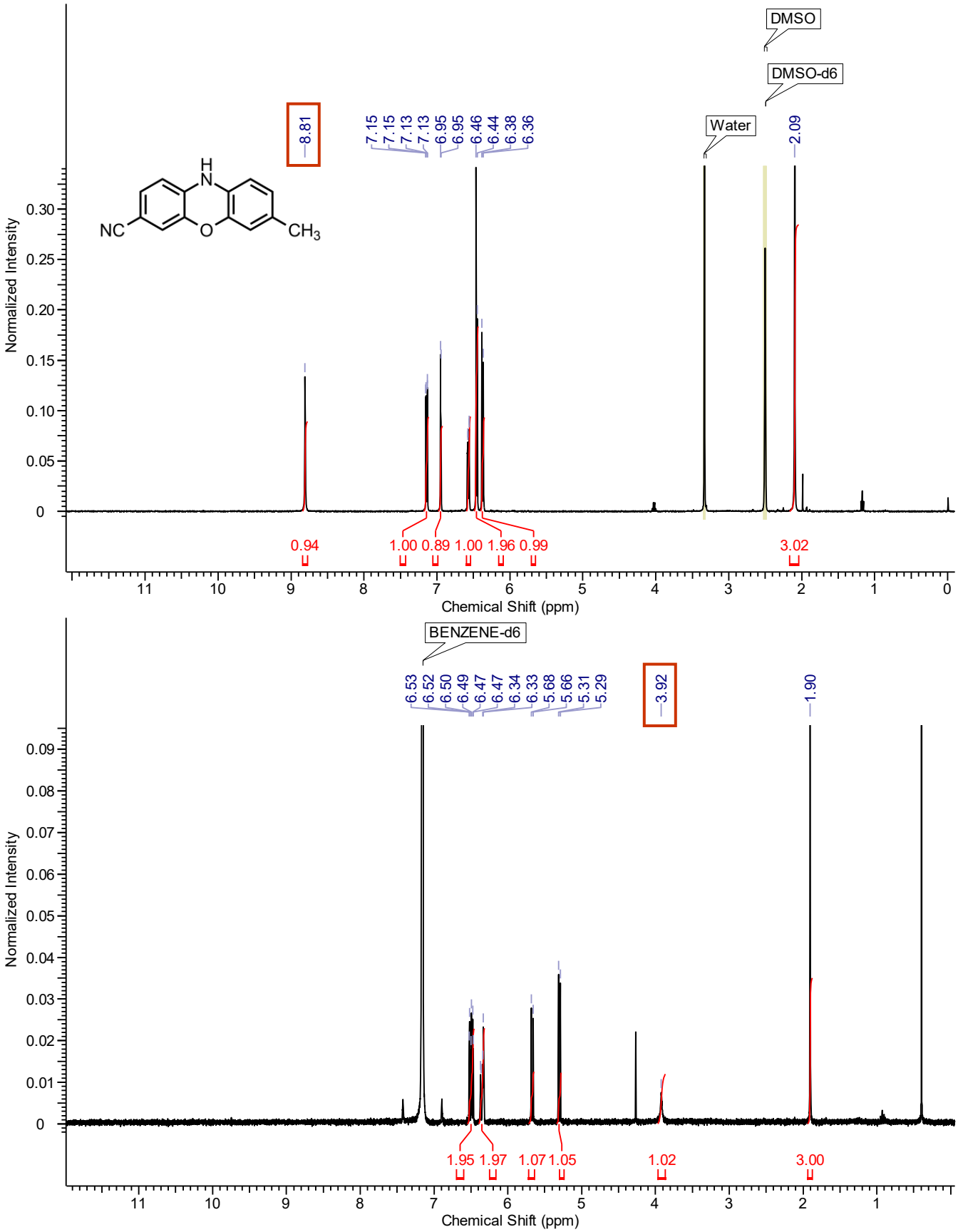


Figure S7.32. ^{1}H NMR spectra of 3-CN-7-Me-PNX (**3.21**) in DMSO-d6 (*top*) and C_6D_6 (*bottom*) (N-H highlighted). Poor soluble in C_6D_6.

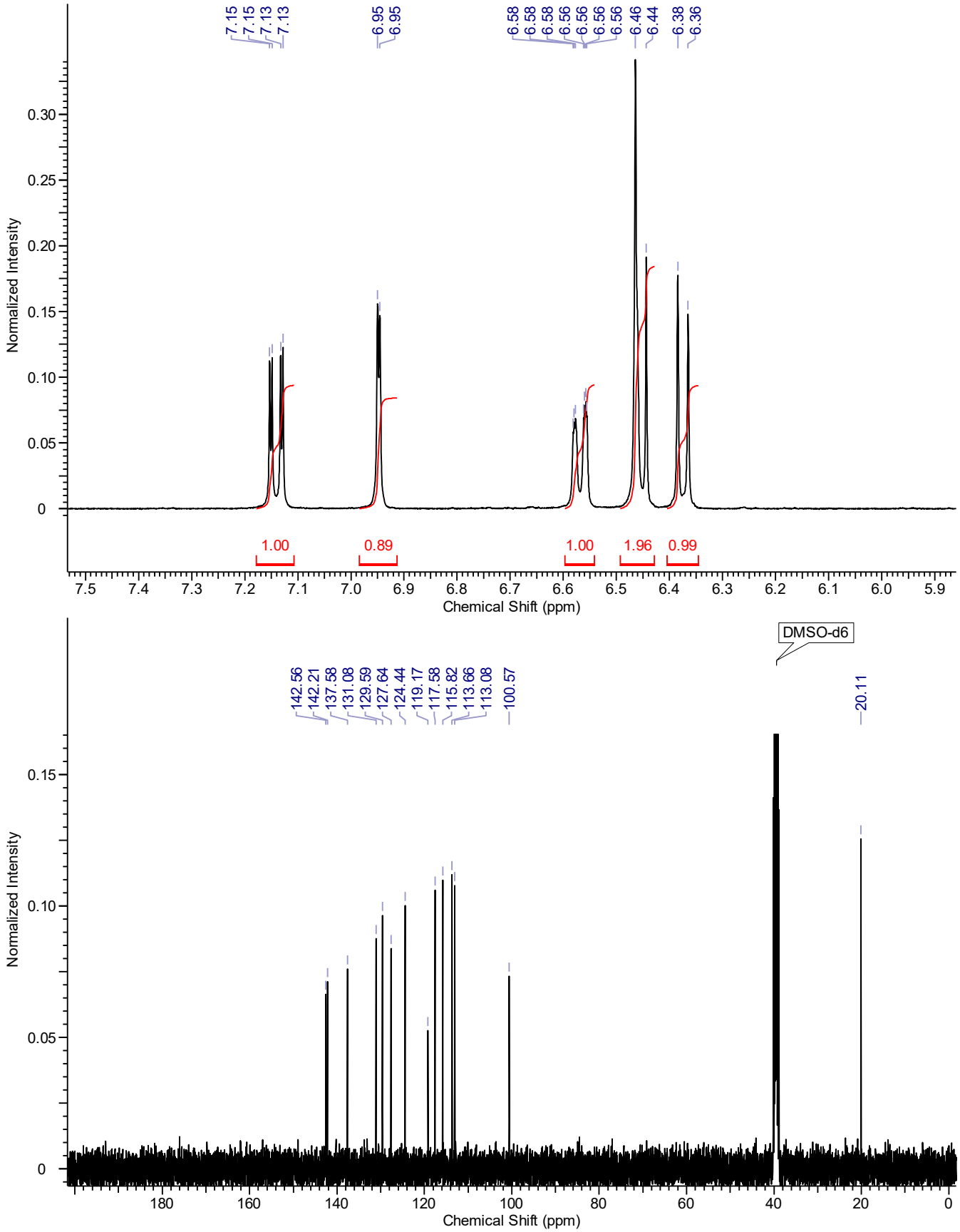


Figure S7.33. Aromatic region of ^{1}H NMR (*top*) and full ^{13}C NMR spectra (*bottom*) of 3-CN-7-Me-PNX (**3.21**) in DMSO-d6.

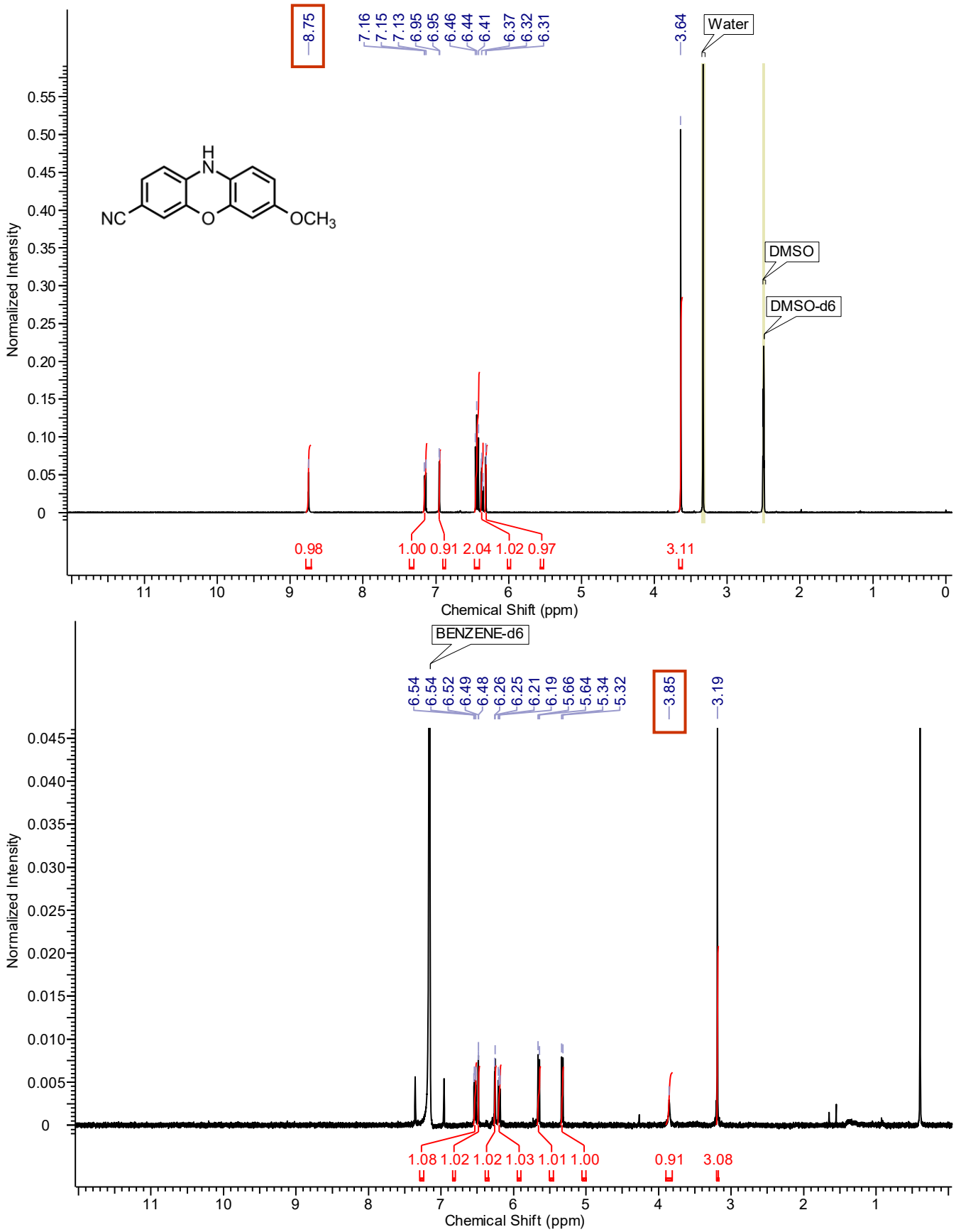


Figure S7.34. ^{1}H NMR spectra of 3-CN-7-MeO-PNX (**3.22**) in DMSO-d6 (*top*) and C_6D_6 (*bottom*) (N-H highlighted).

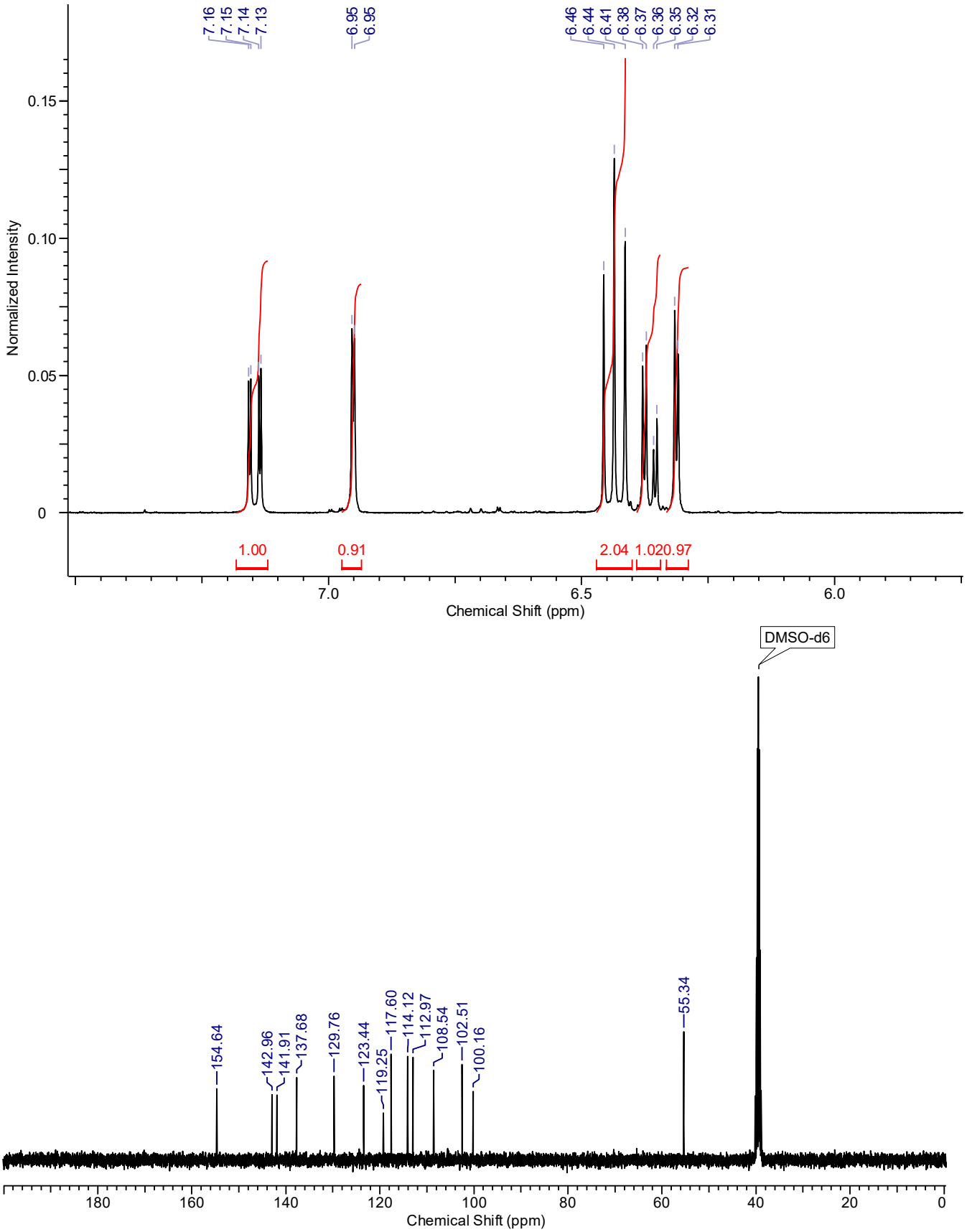


Figure S7.35. Aromatic region of ^{1}H NMR (*top*) and full ^{13}C NMR spectra (*bottom*) of 3-CN-7-MeO-PNX (**3.22**) in DMSO-d6.

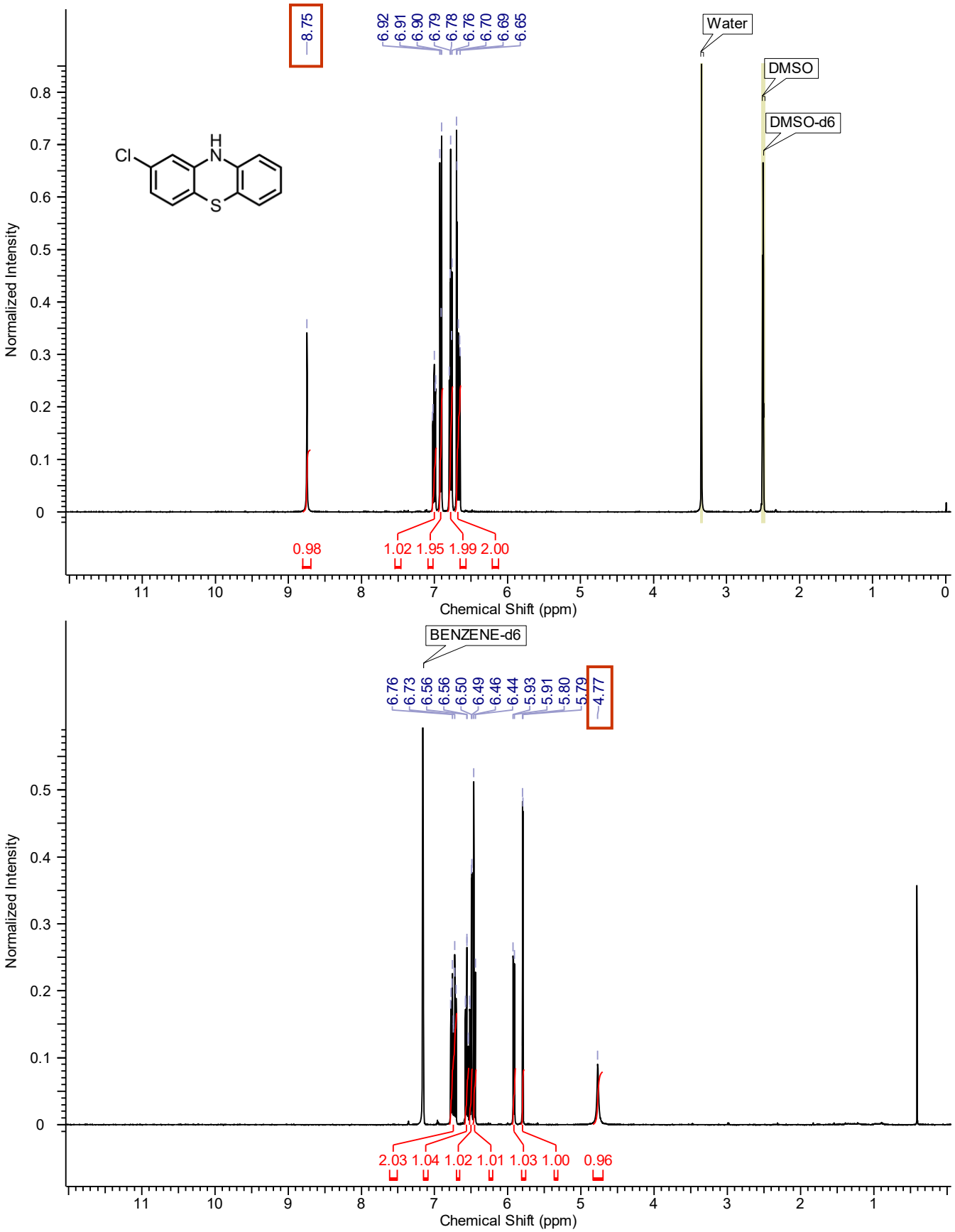


Figure S7.36. ^{1}H NMR spectra of 2-Cl-PTZ (**3.24**) in DMSO-d6 (*top*) and C_6D_6 (*bottom*) (N-H highlighted).

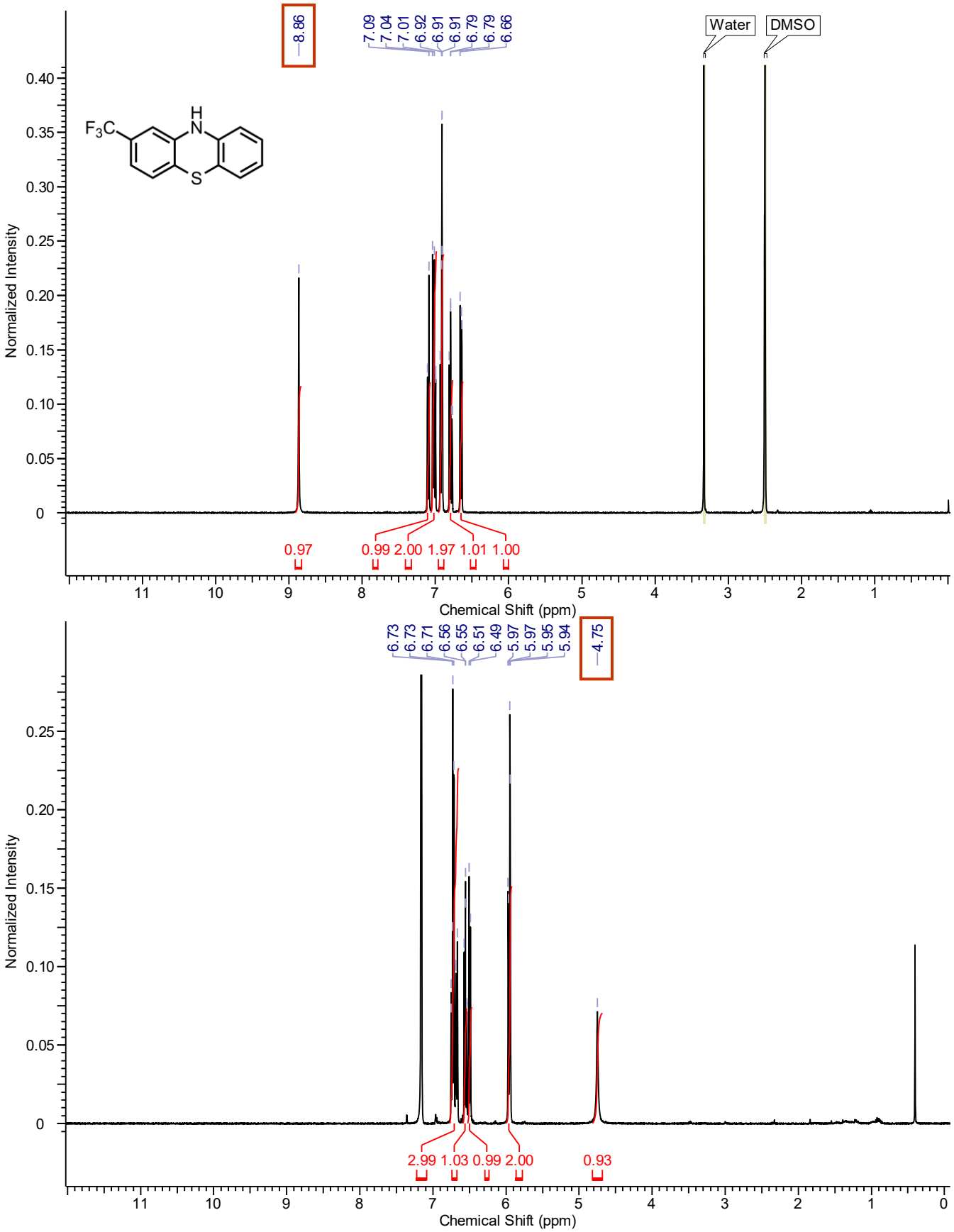


Figure S7.37. ^{1}H NMR spectra of 2-CF_3-PTZ (**3.25**) in DMSO-d6 (*top*) and C_6D_6 (*bottom*) (N-H highlighted).

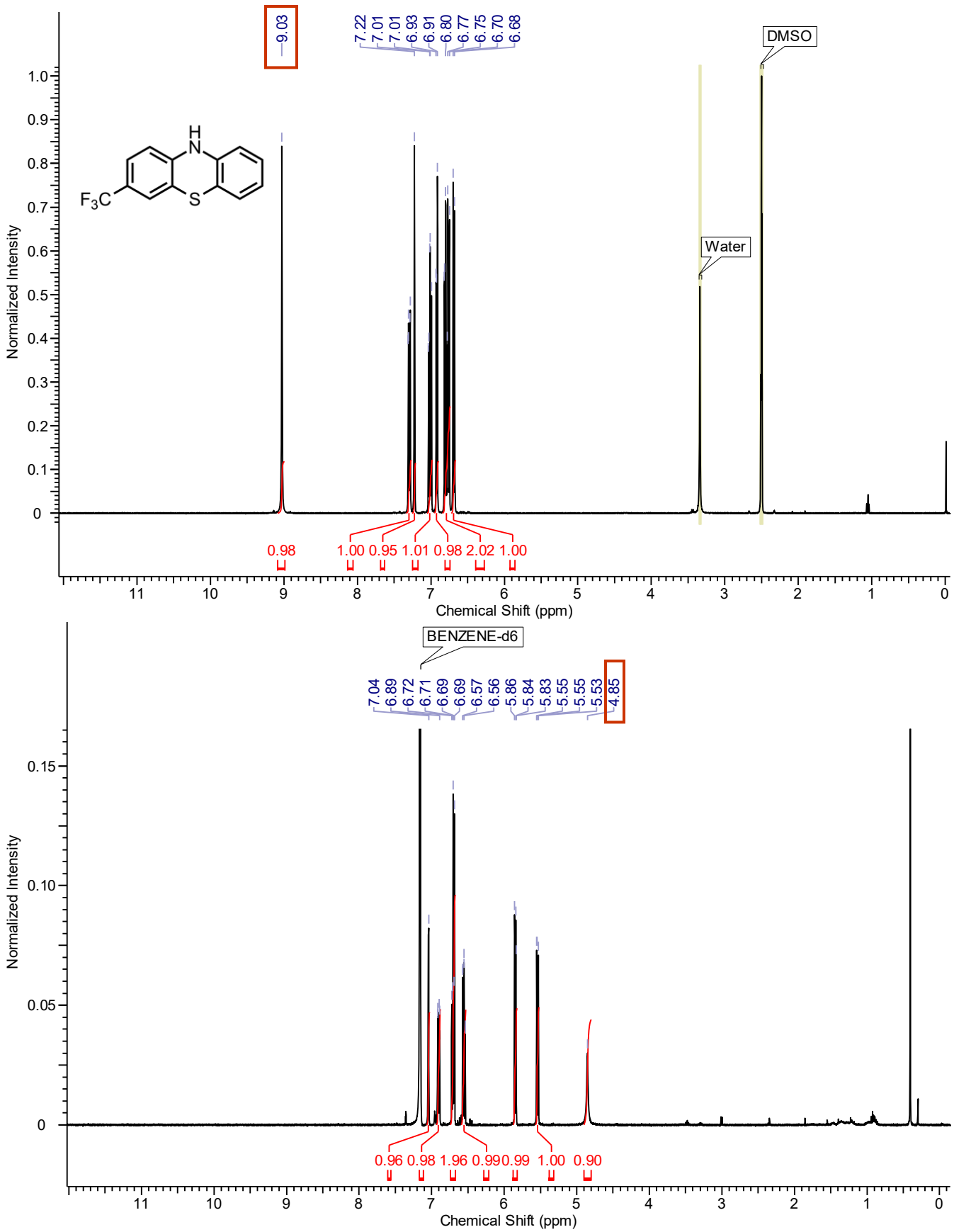


Figure S7.38. ^{1}H NMR spectra of 3-CF_3-PTZ (**3.26**) in DMSO-d6 (*top*) and C_6D_6 (*bottom*) (N-H highlighted).

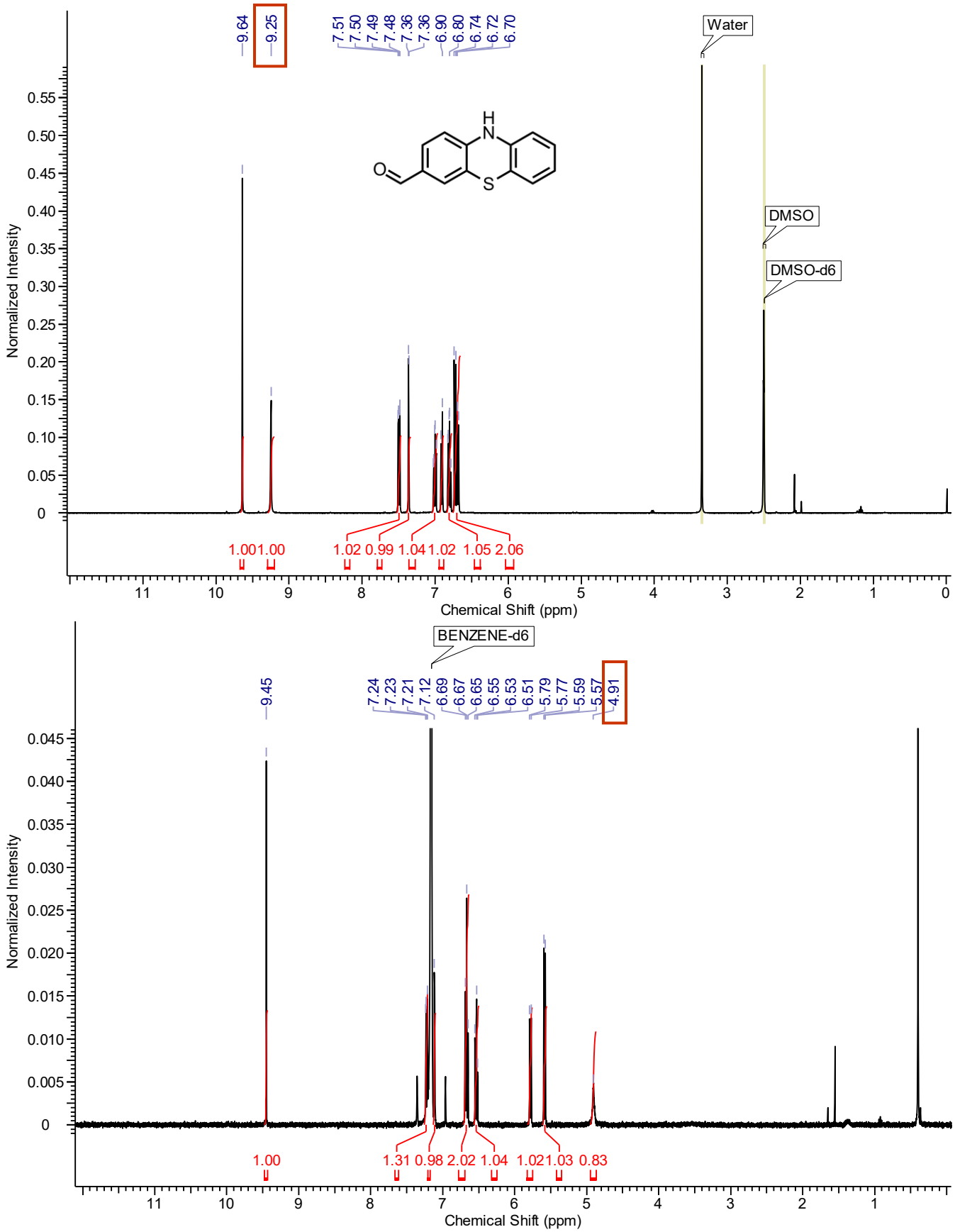


Figure S7.39. ^{1}H NMR spectra of 3-Formyl-PTZ (**3.27**) in DMSO-d6 (*top*) and C_6D_6 (*bottom*) (N-H highlighted).

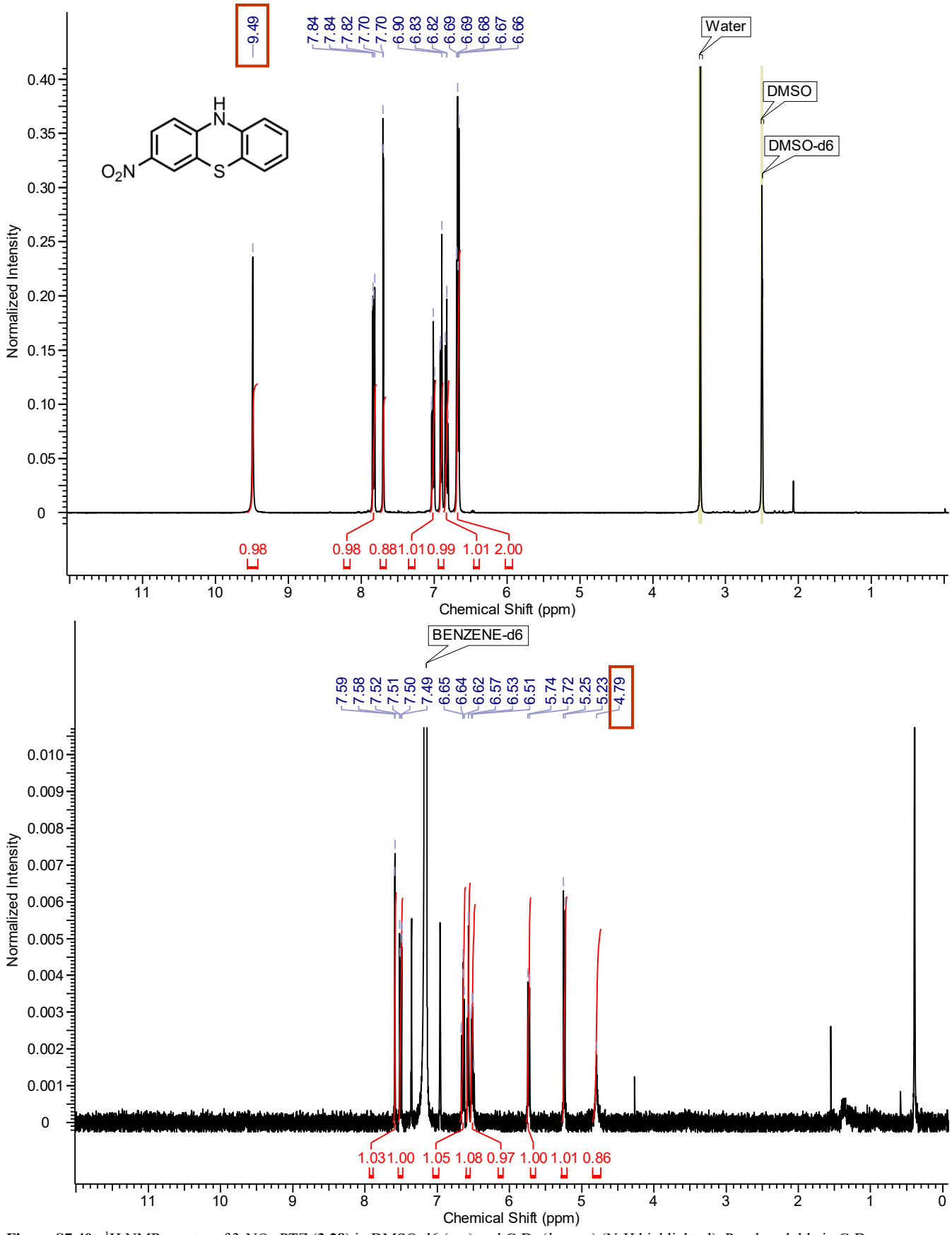


Figure S7.40. ^{1}H NMR spectra of 3-NO_2-PTZ (**3.28**) in DMSO-d6 (*top*) and C_6D_6 (*bottom*) (N-H highlighted). Poorly soluble in C_6D_6.

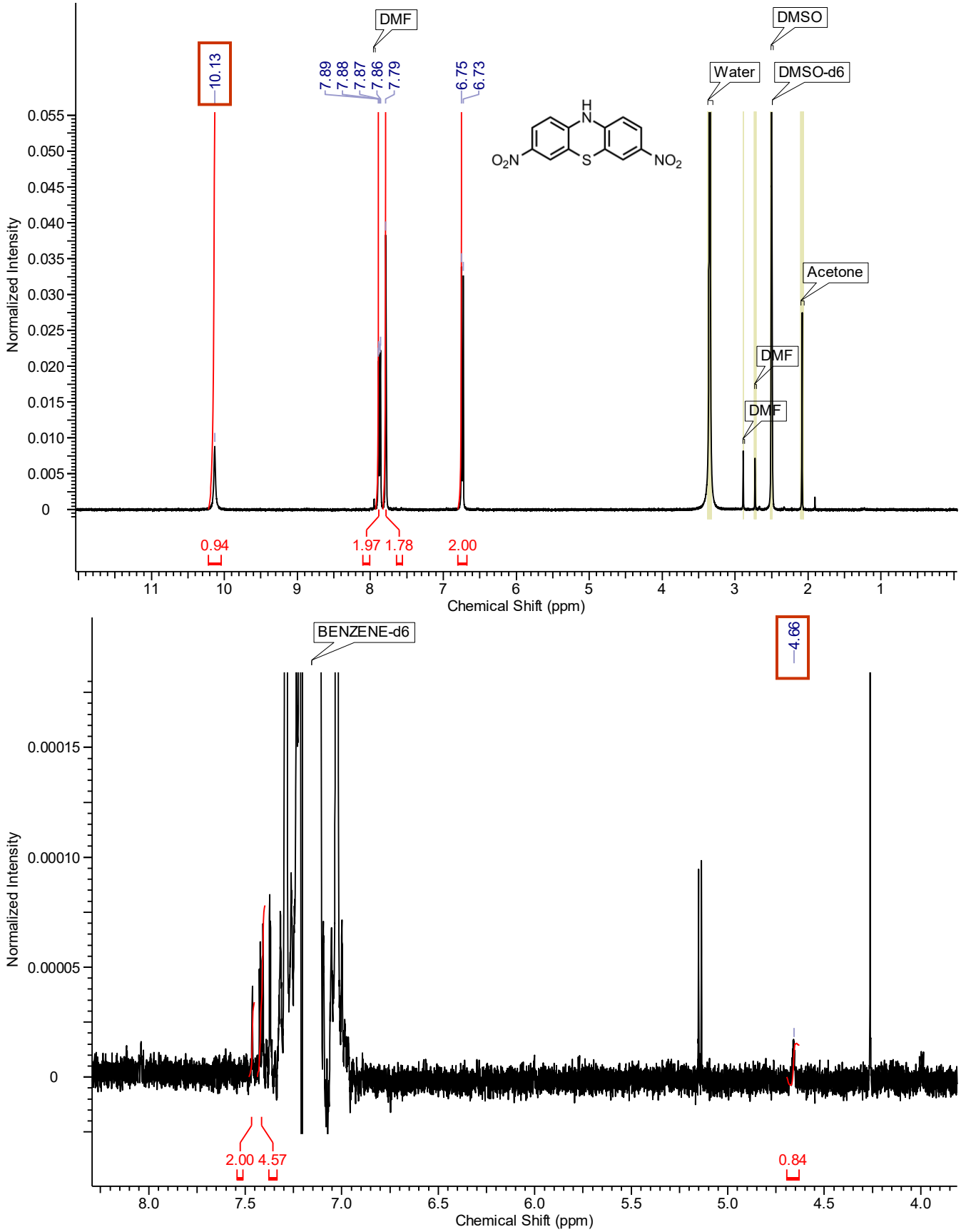


Figure S7.41. ^{1}H NMR spectra of 3,7-NO_2-PTZ (**3.29**) in DMSO-d6 (*top*) and C_6D_6 (*bottom*) (N-H highlighted). *Very* poorly soluble in C_6D_6.

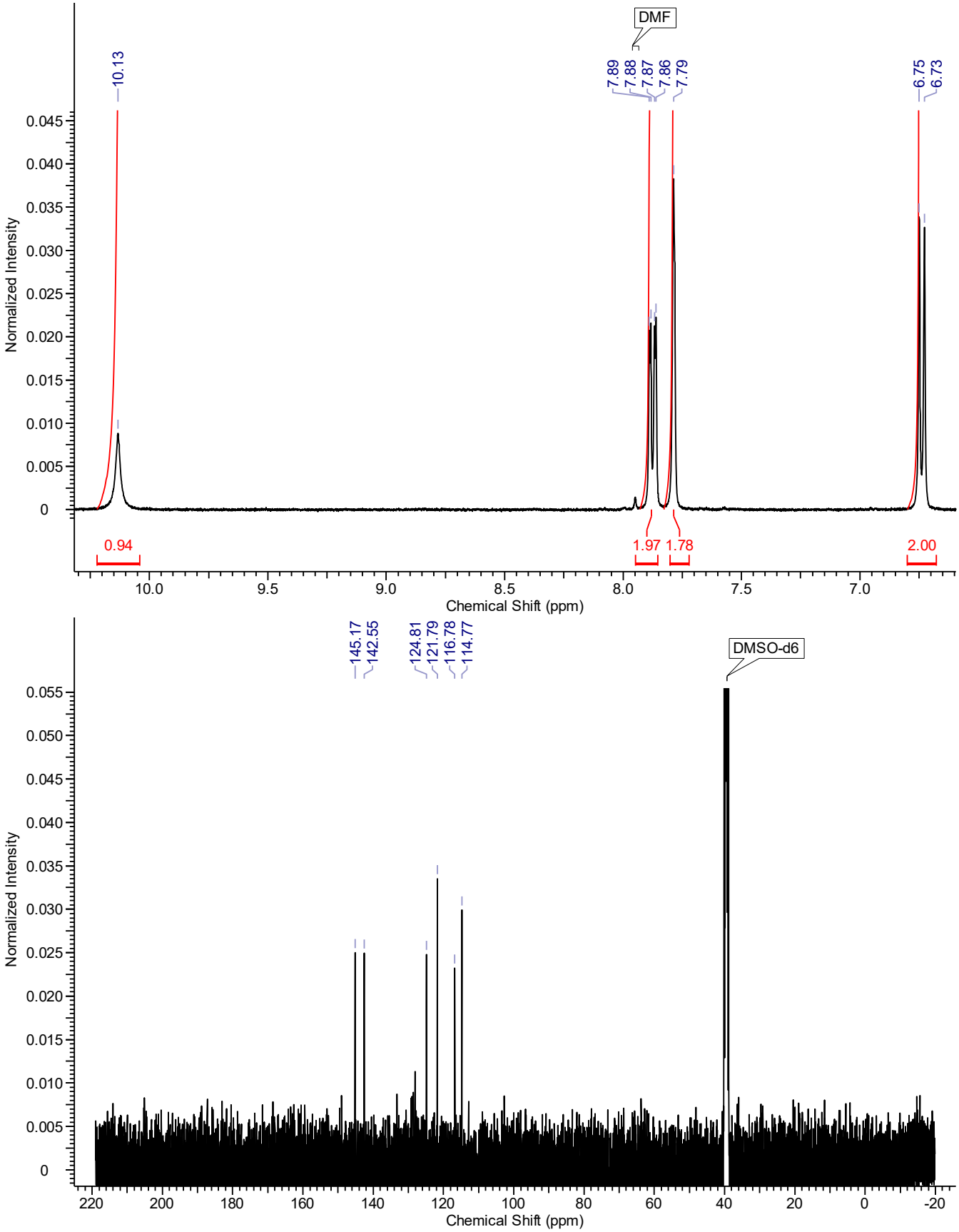


Figure S7.42. Aromatic region of ^{1}H NMR (*top*) and full ^{13}C NMR spectra (*bottom*) of 3,7-NO_2-PTZ (**3.29**) in DMSO-d6.

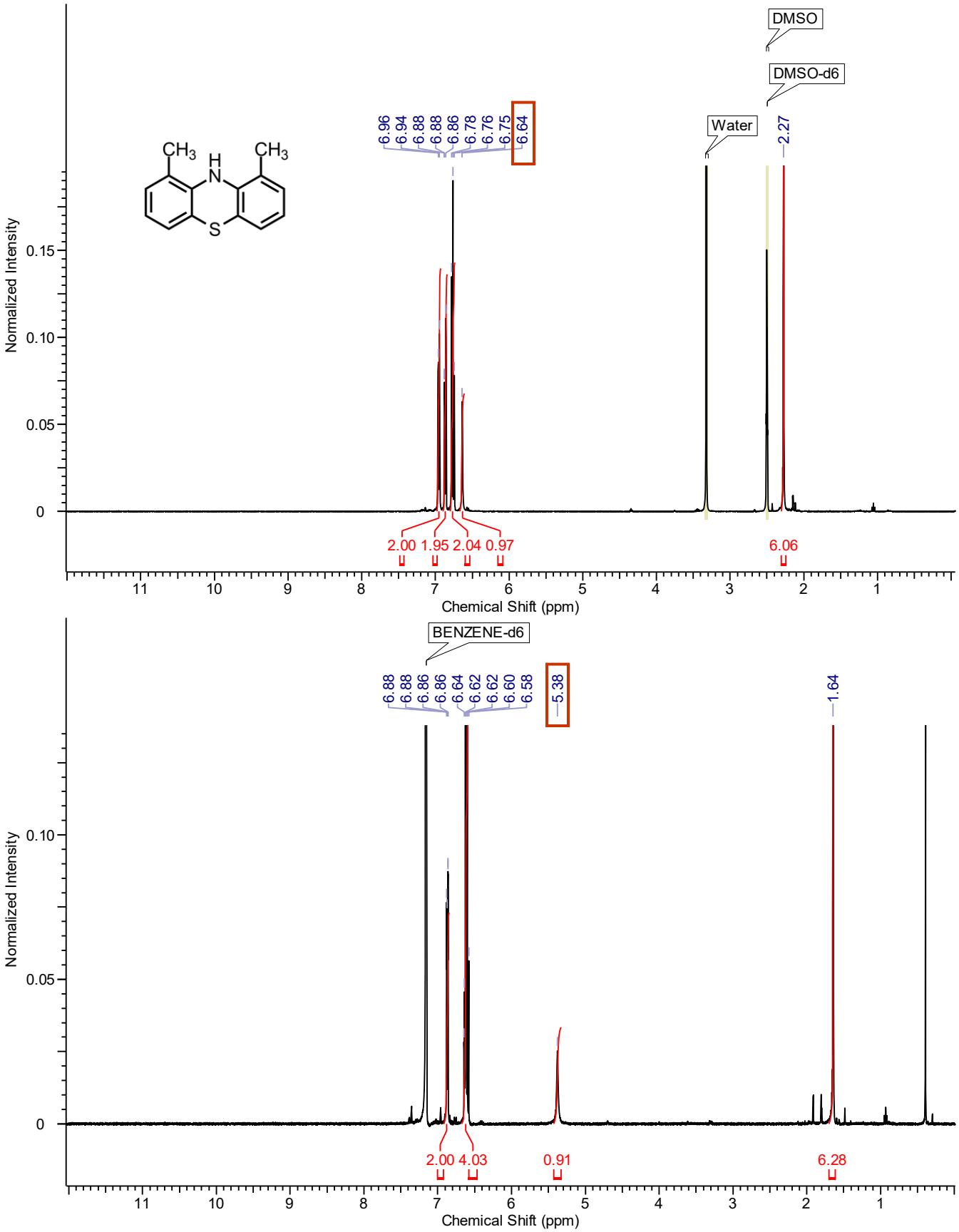


Figure S7.43. ^{1}H NMR spectra of 1,9-Me-PTZ (**3.31**) in DMSO-d6 (*top*) and C_6D_6 (*bottom*) (N-H highlighted).

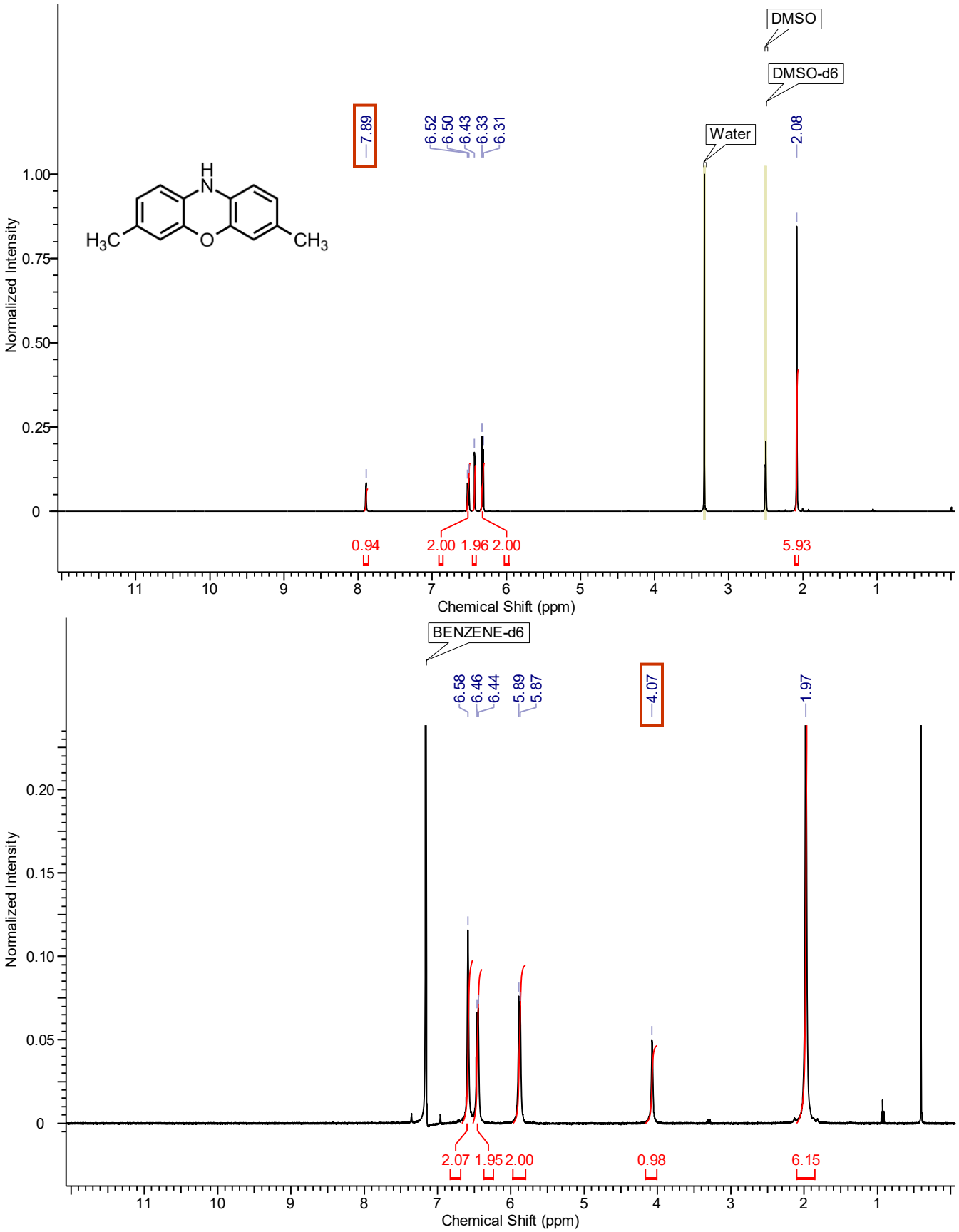


Figure S7.44. ^{1}H NMR spectra of 3,7-Me-PNX (**3.35**) in DMSO-d6 (*top*) and C_6D_6 (*bottom*) (N-H highlighted).

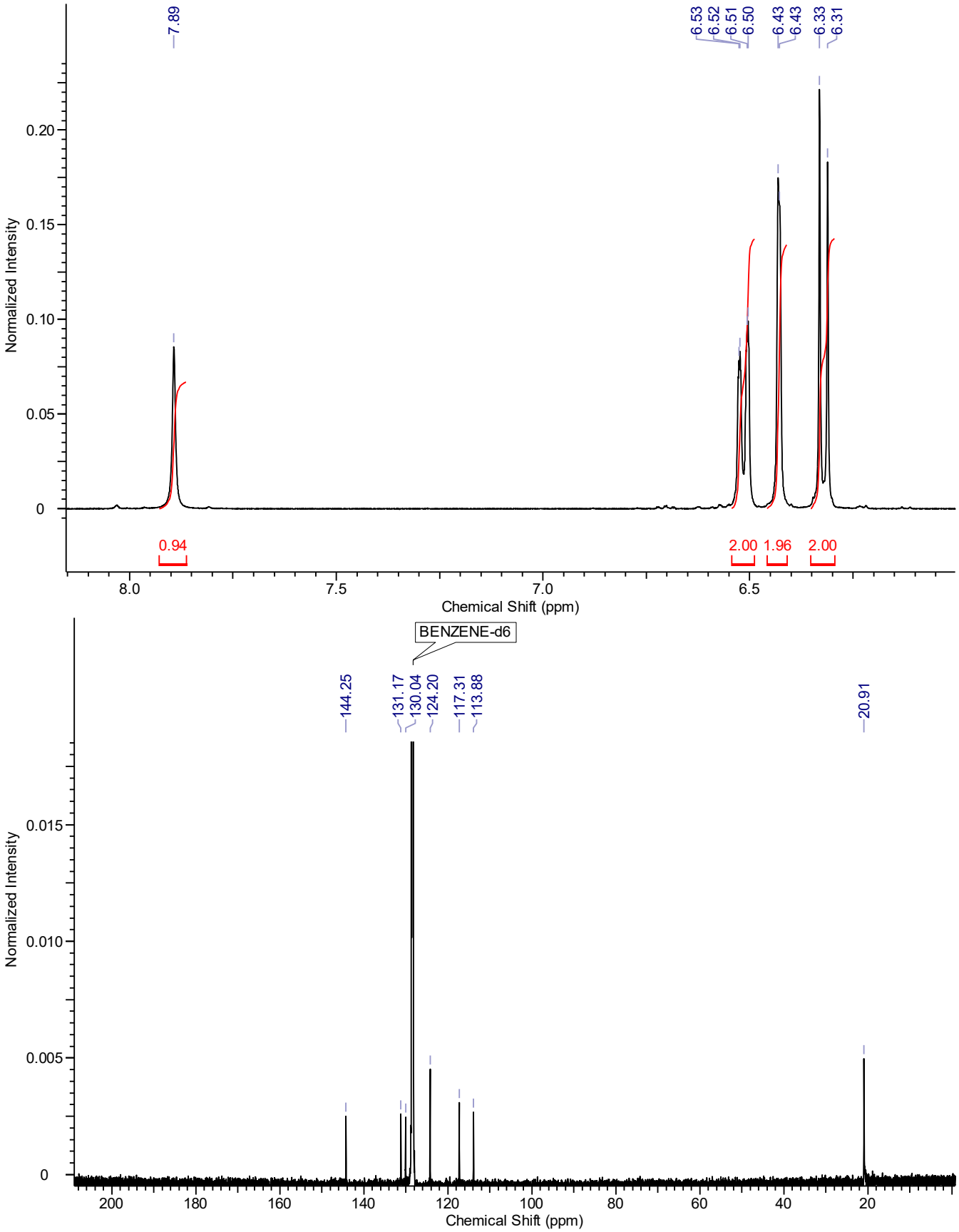


Figure S7.45. Aromatic region of ^{1}H NMR in DMSO-d6 (*top*) and full ^{13}C NMR spectra in C_6D_6 (*bottom*) of 3,7-Me-PNX (**3.35**).

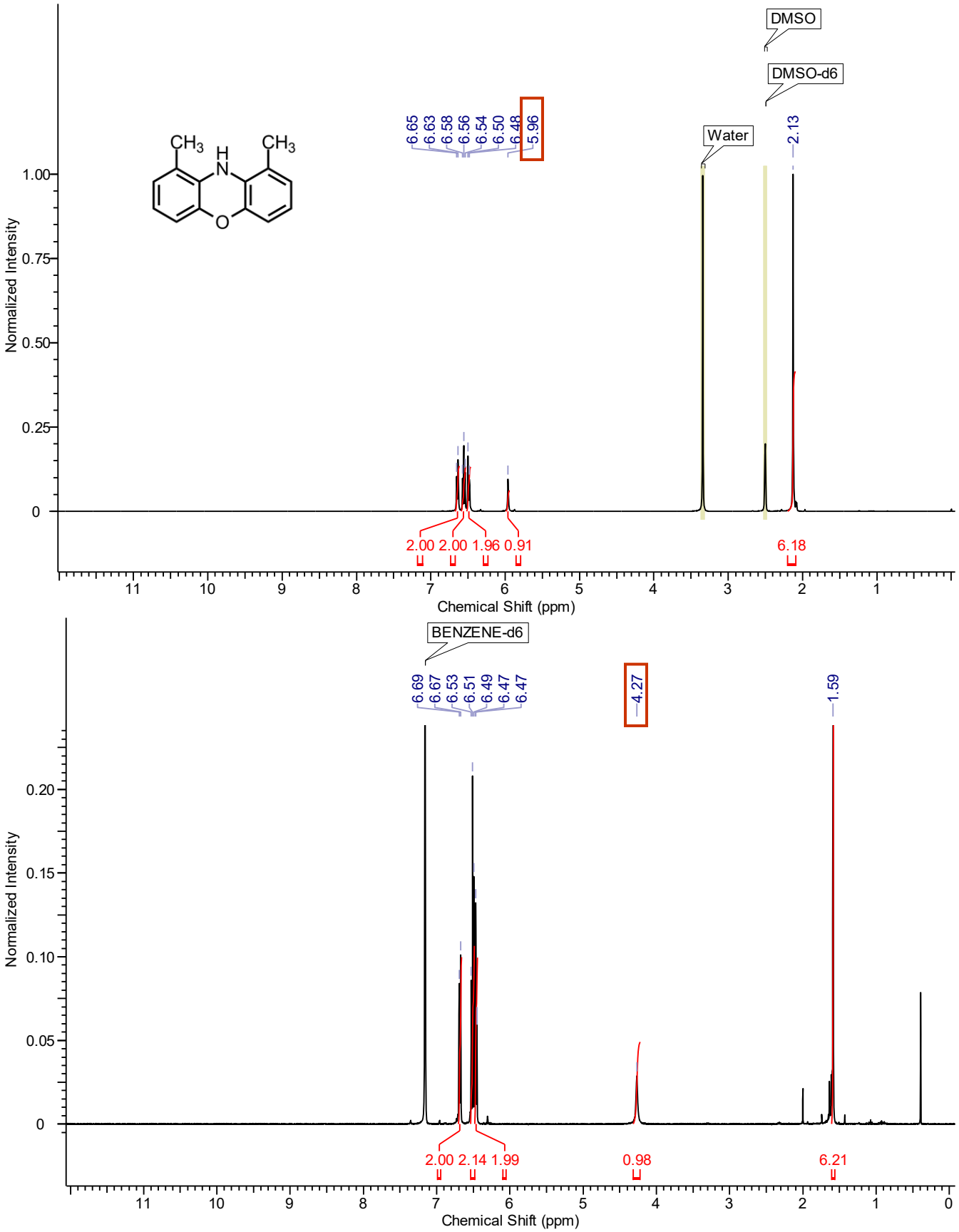


Figure S7.46. ^{1}H NMR spectra of 1,9-Me-PNX (**3.36**) in DMSO-d6 (*top*) and C_6D_6 (*bottom*) (N-H highlighted).

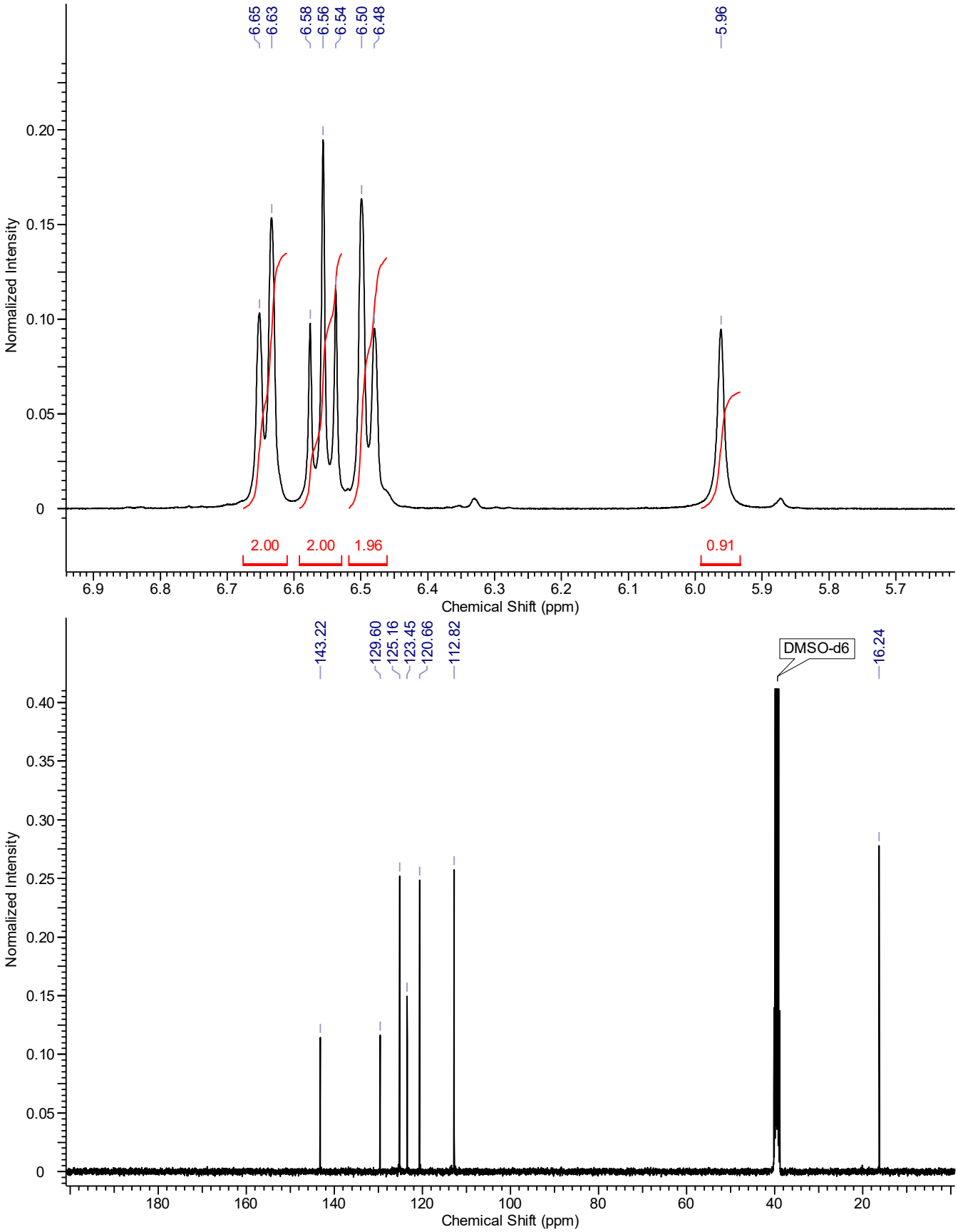


Figure S7.47. Aromatic region of ^{1}H NMR (*top*) and full ^{13}C NMR spectra (*bottom*) of 1,9-Me-PNX (**3.36**) in DMSO-d6.

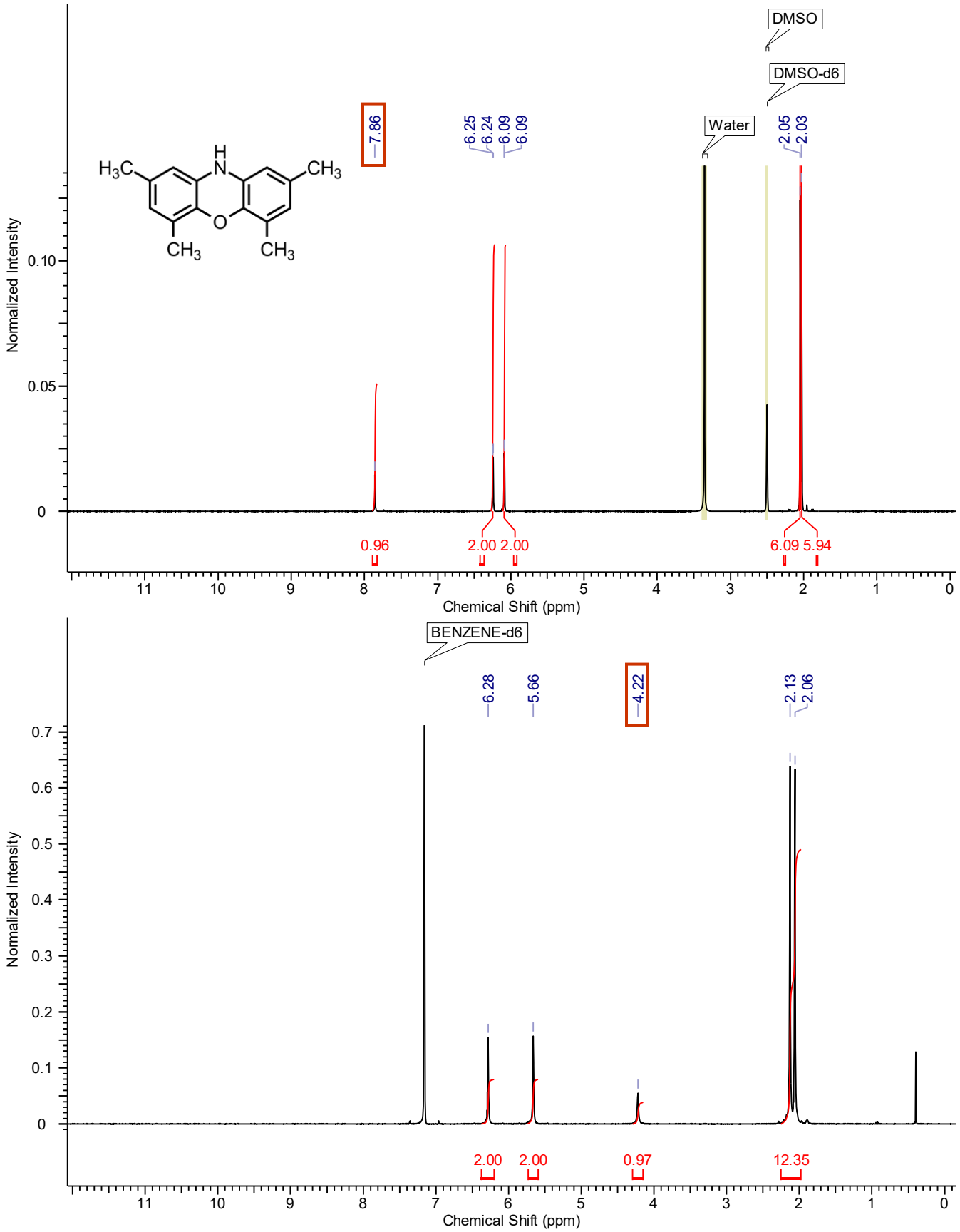


Figure S7.48. ^{1}H NMR spectra of 2,4,6,8-Me-PNX (**3.37**) in DMSO-d6 (*top*) and C_6D_6 (*bottom*) (N-H highlighted).

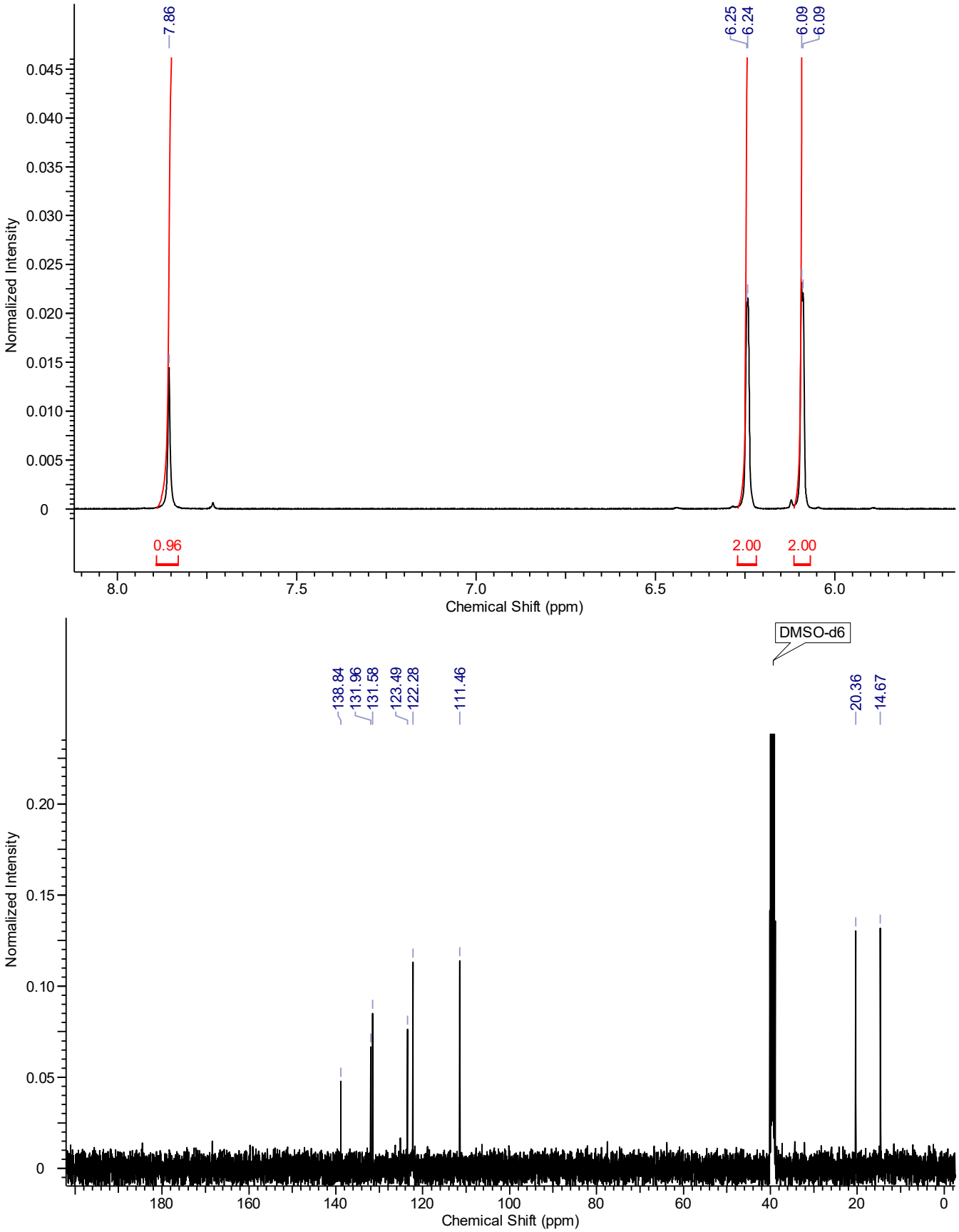


Figure S7.49. Aromatic region of ^{1}H NMR (*top*) and full ^{13}C NMR spectra (*bottom*) of 2,4,6,8-Me-PNX (**3.37**) in DMSO-d6.

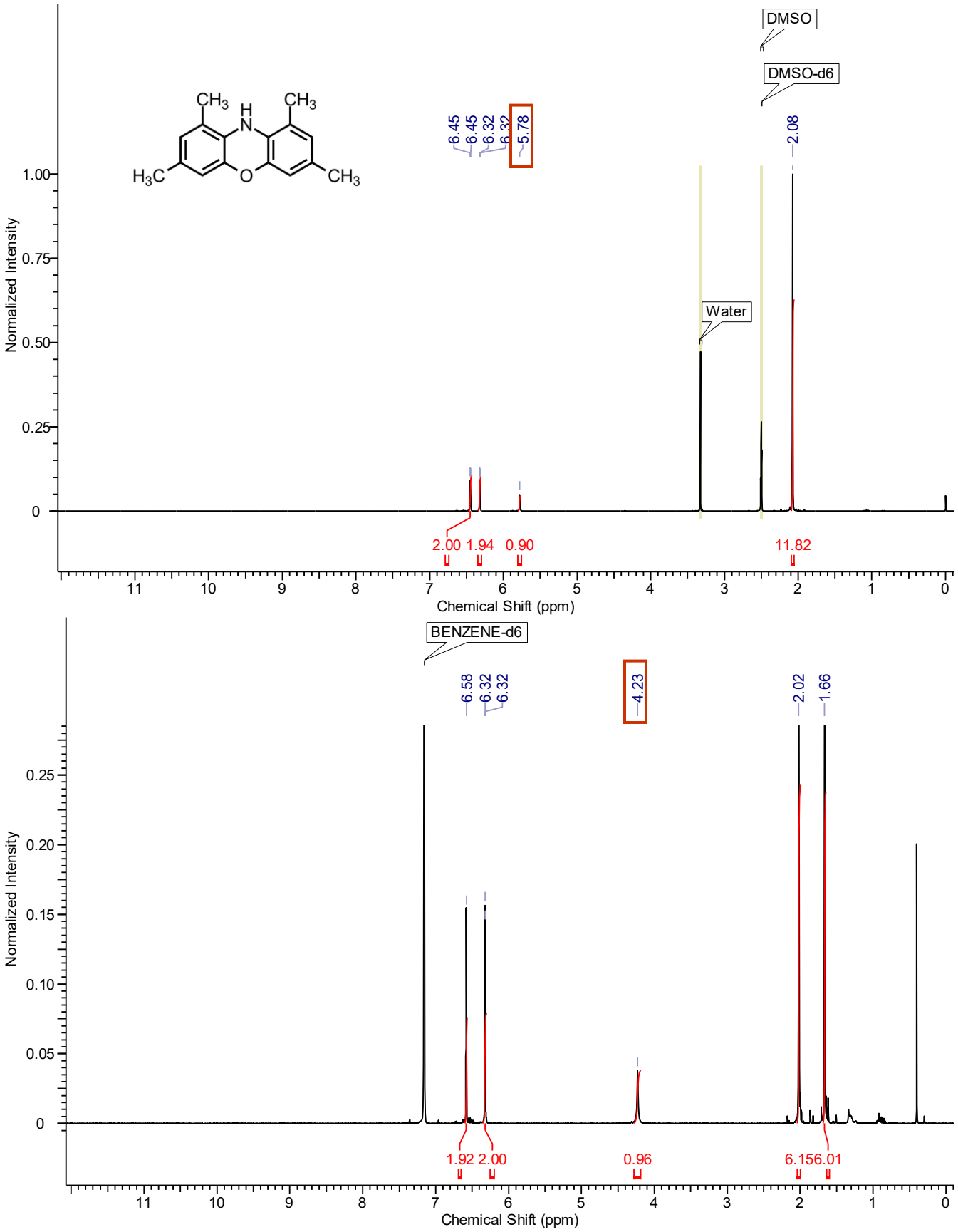


Figure S7.50. ^{1}H NMR spectra of 1,3,7,9-Me-PNX (**3.38**) in DMSO-d6 (*top*) and C_6D_6 (*bottom*) (N-H highlighted).

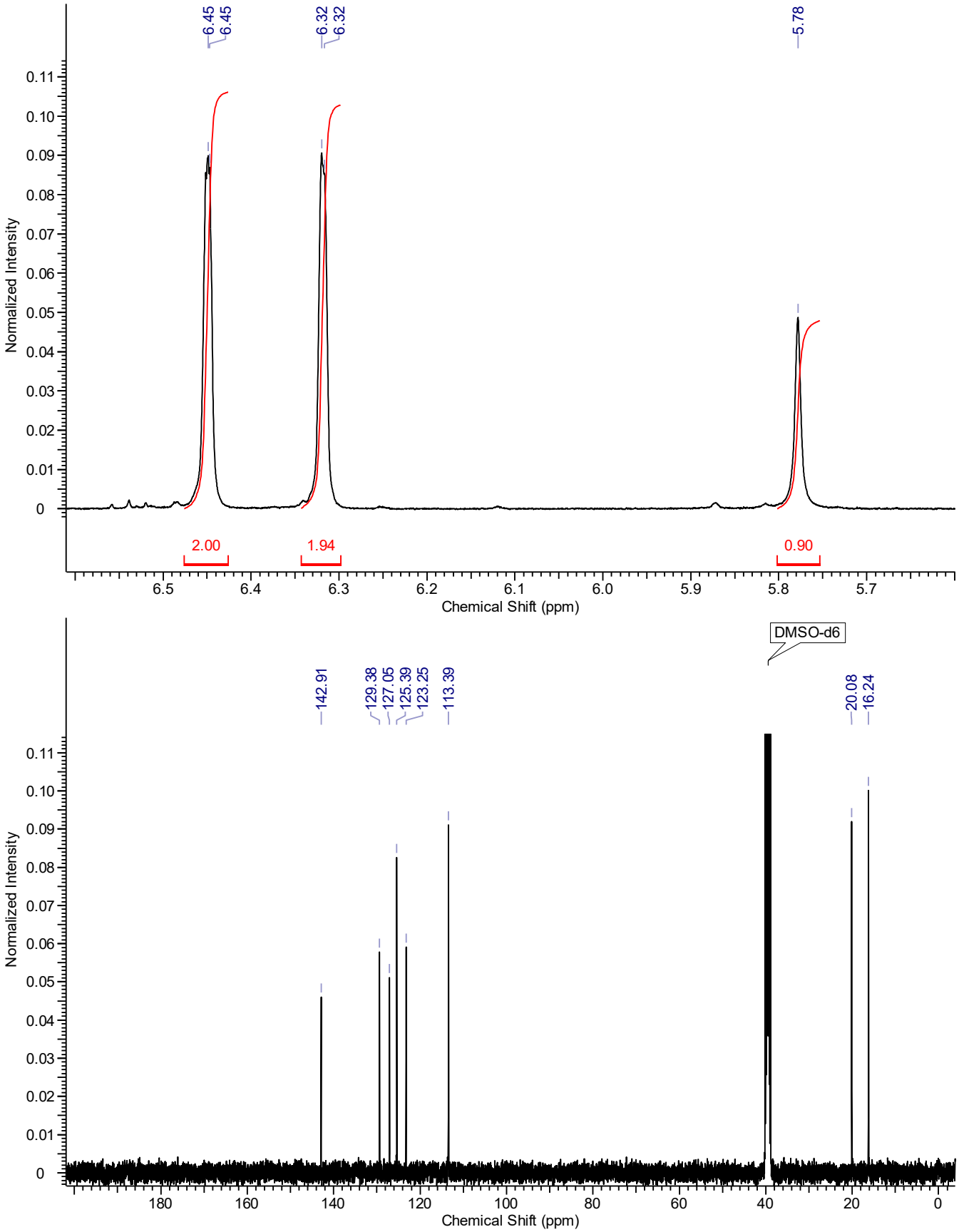


Figure S7.51. Aromatic region of ^{1}H NMR (*top*) and full ^{13}C NMR spectra (*bottom*) of 1,3,7,9-Me-PNX (**3.38**) in DMSO-d6.

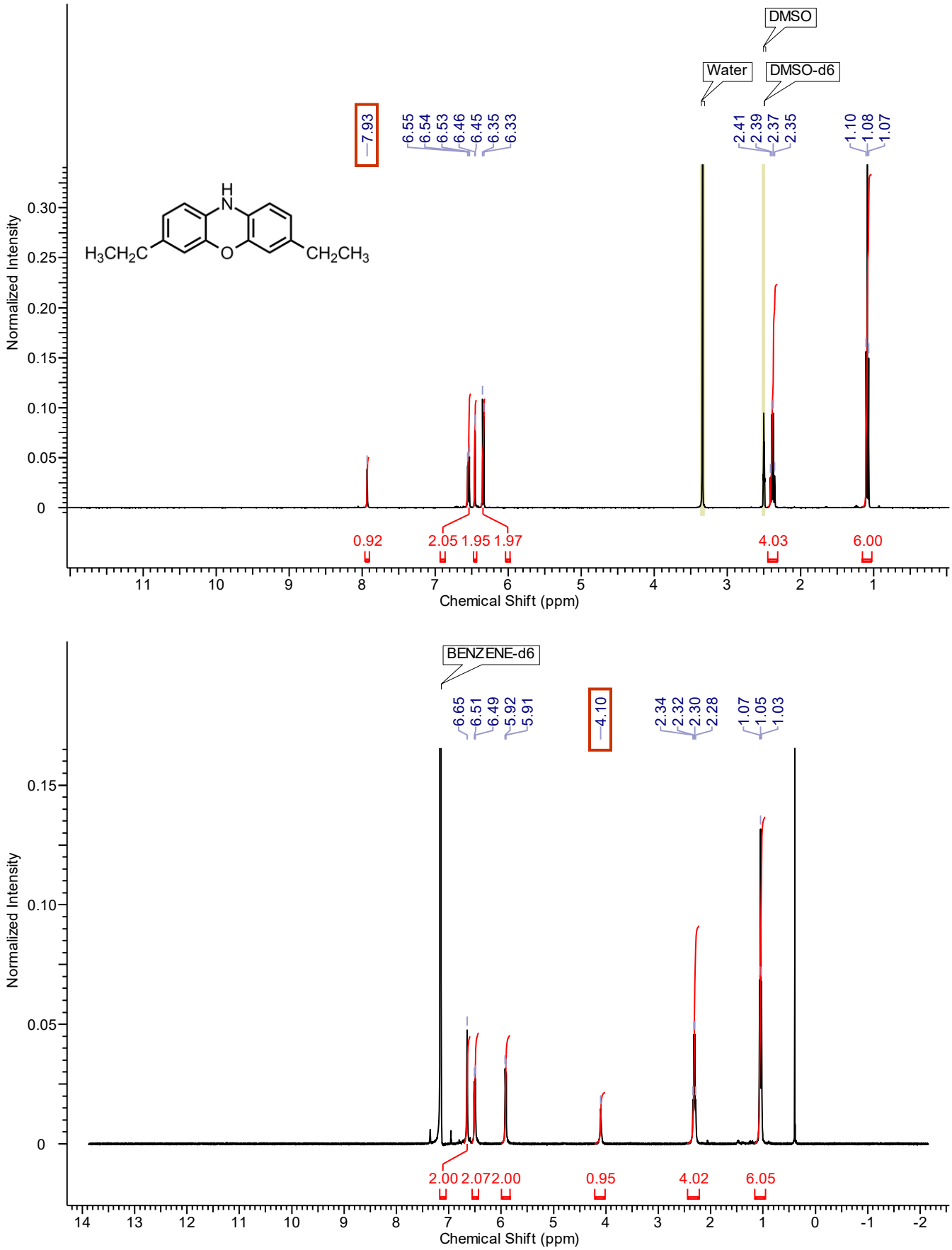


Figure S7.52. ^{1}H NMR spectra of 3,7-Et-PNX (**3.41**) in DMSO-d6 (*top*) and C_6D_6 (*bottom*) (N-H highlighted).

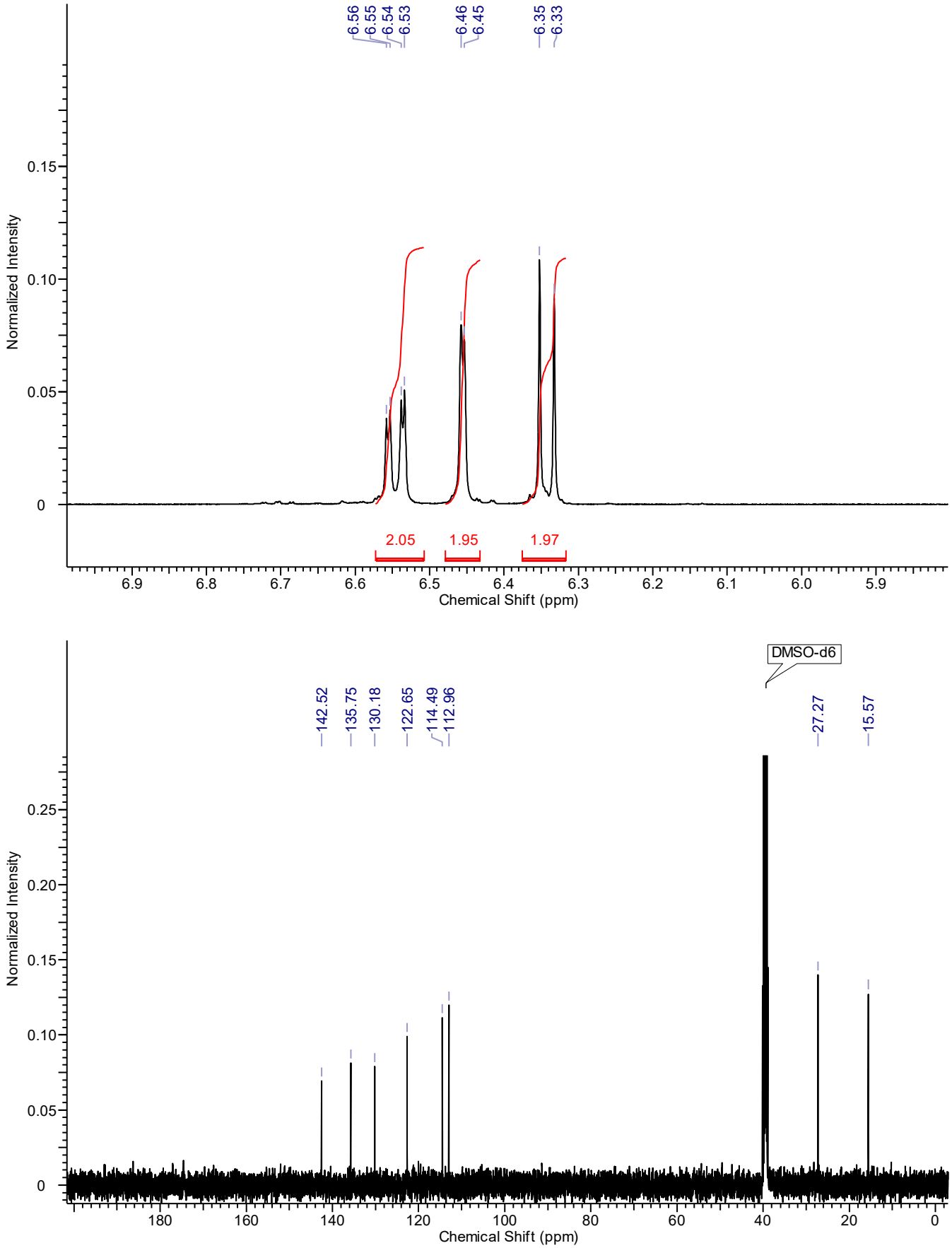


Figure S7.53. Aromatic region of ^{1}H NMR (*top*) and full ^{13}C NMR spectra (*bottom*) of 3,7-Et-PNX (**3.41**) in DMSO-d6.

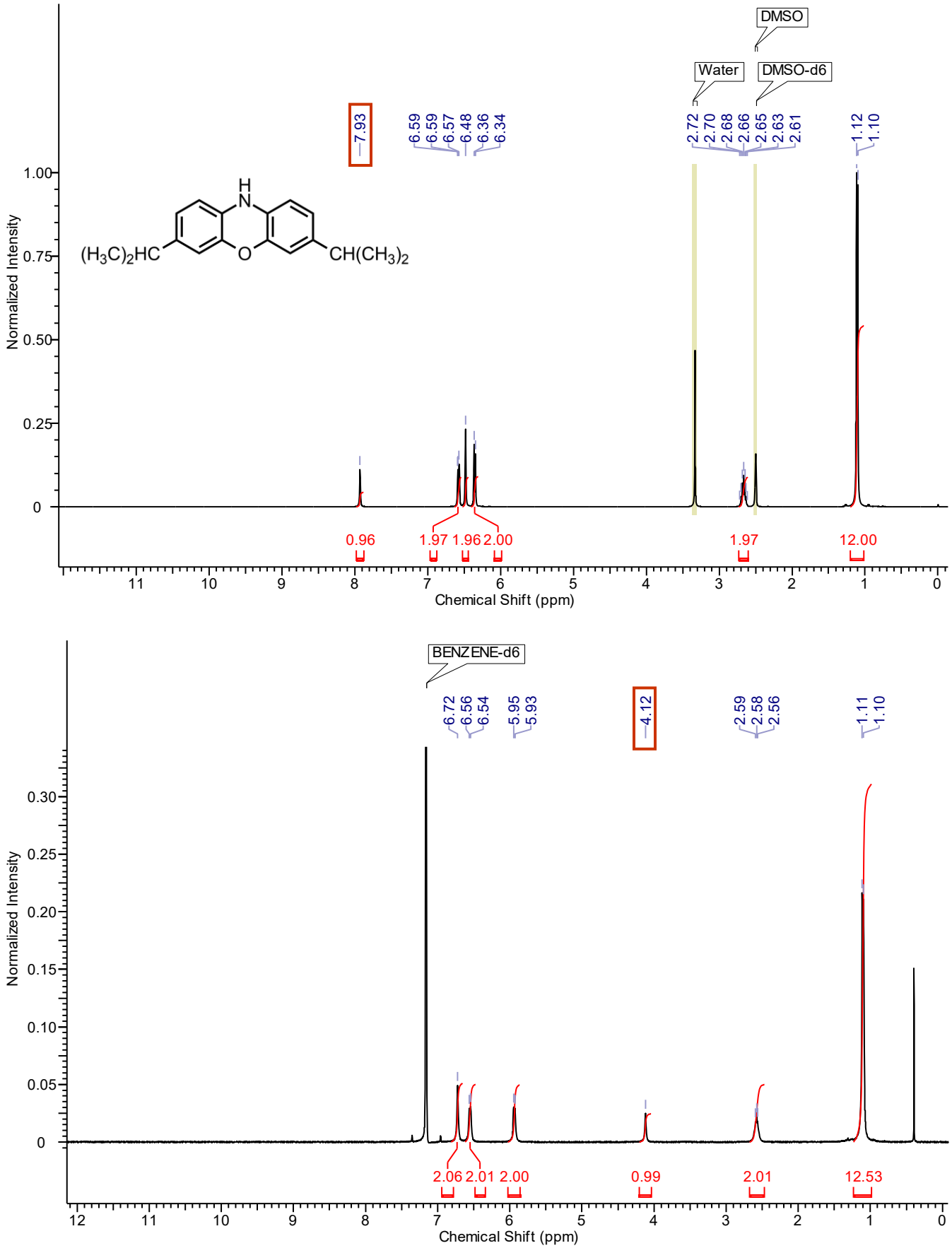


Figure S7.54. ^{1}H NMR spectra of 3,7-iPr-PNX (**3.42**) in DMSO-d6 (*top*) and C_6D_6 (*bottom*) (N-H highlighted).

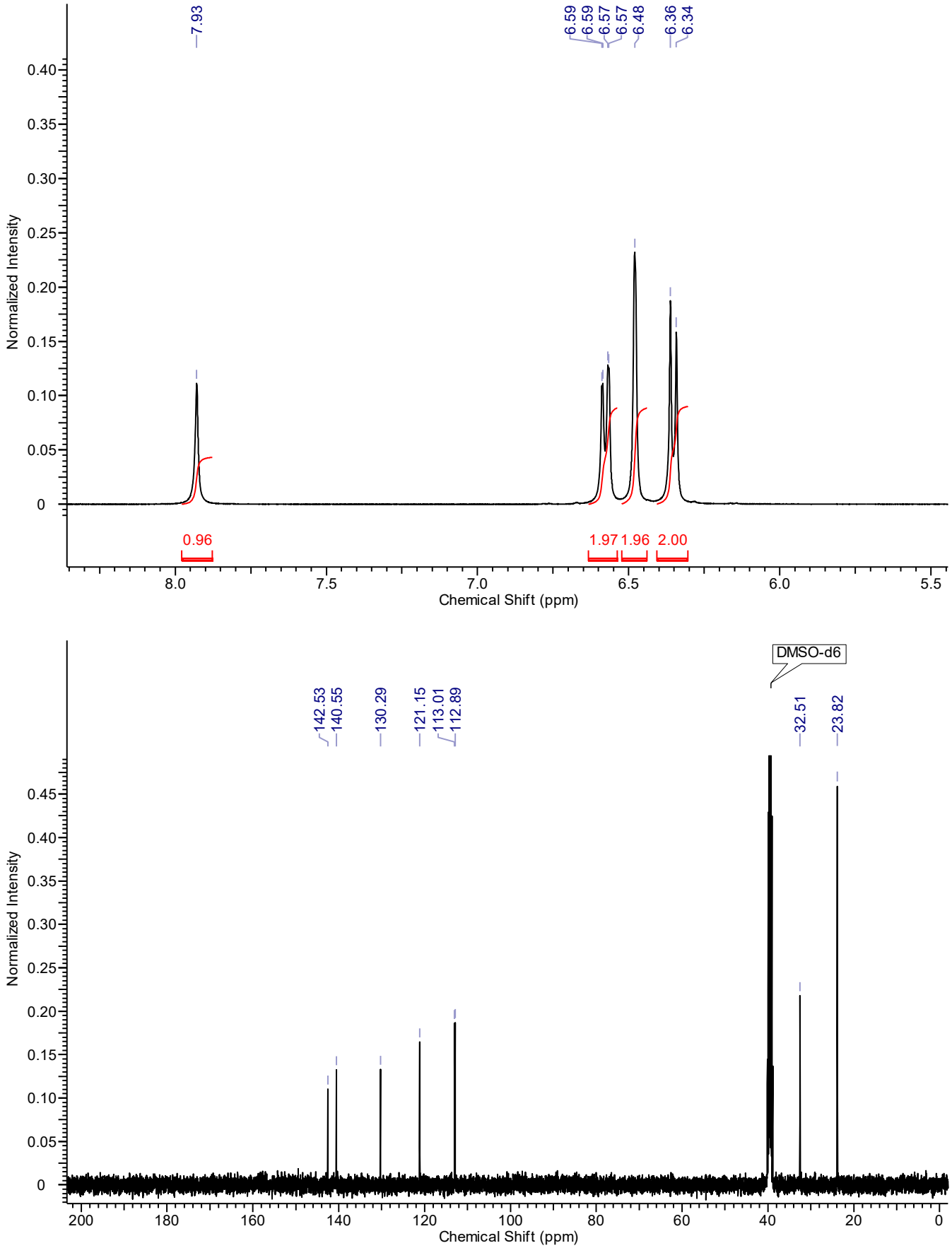


Figure S7.55. Aromatic region of ^{1}H NMR (*top*) and full ^{13}C NMR spectra (*bottom*) of 3,7-iPr-PNX (**3.42**) in DMSO-d6.

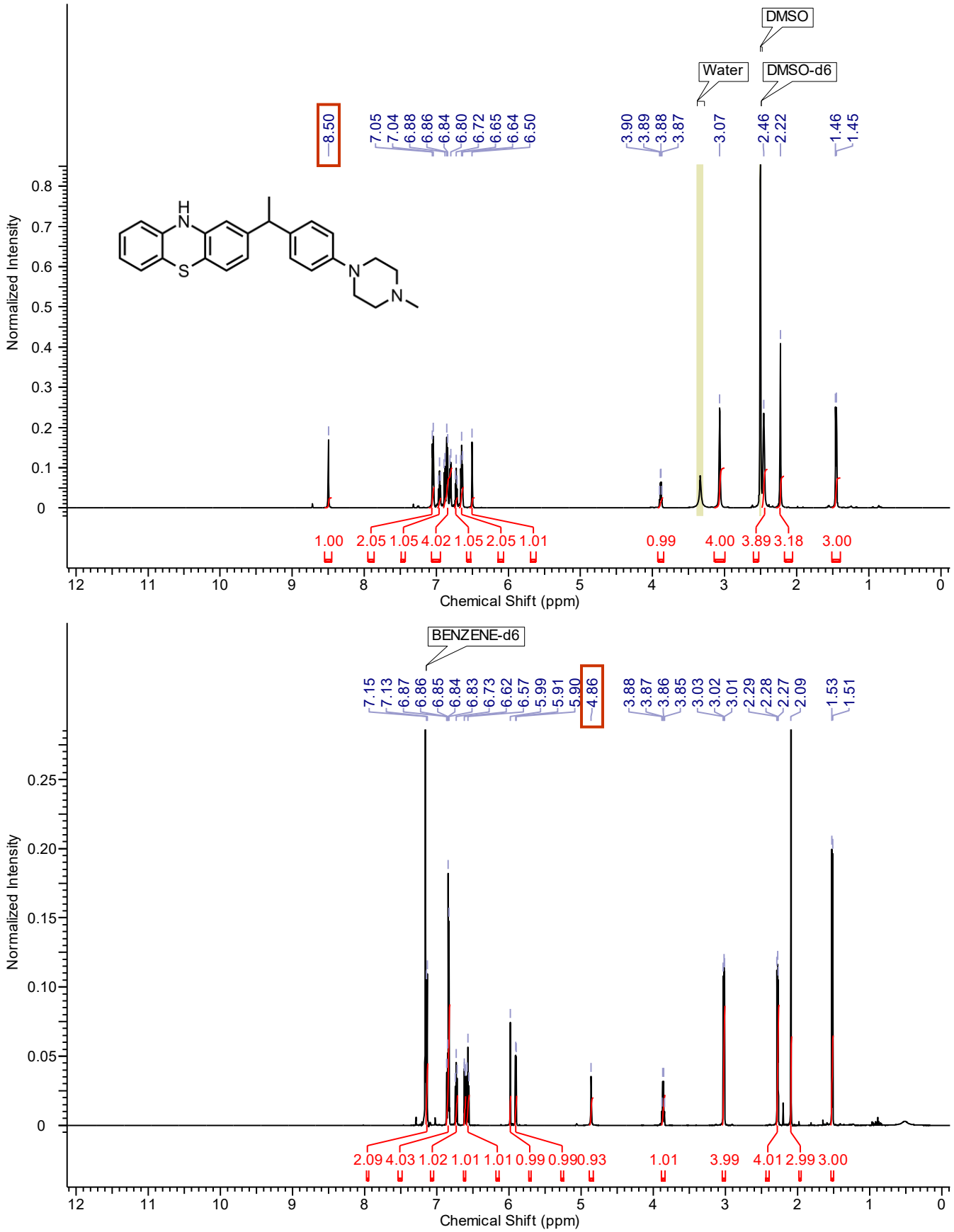


Figure S7.56. ^{1}H NMR spectra of 2-(1-(4-(4-methylpiperazin-1-yl)phenyl)ethyl)-10H-phenothiazine (**3.43**) in DMSO-d6 (*top*) and C_6D_6 (*bottom*) (N-H highlighted).

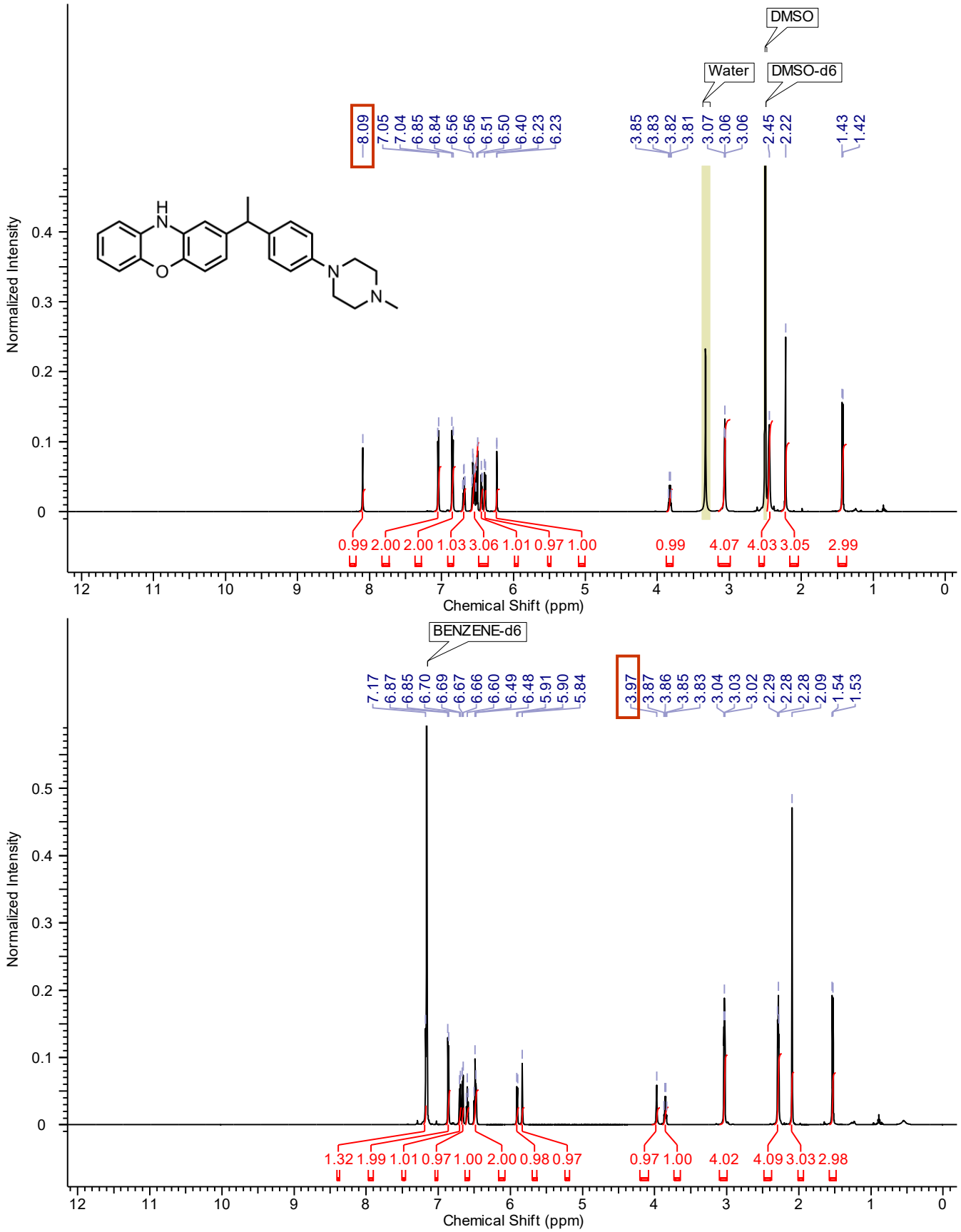


Figure S7.57. ^{1}H NMR spectra of 2-(1-(4-(4-methylpiperazin-1-yl)phenyl)ethyl)-10H-phenoxazine (**3.44**) in DMSO-d6 (*top*) and C_6D_6 (*bottom*) (N-H highlighted).

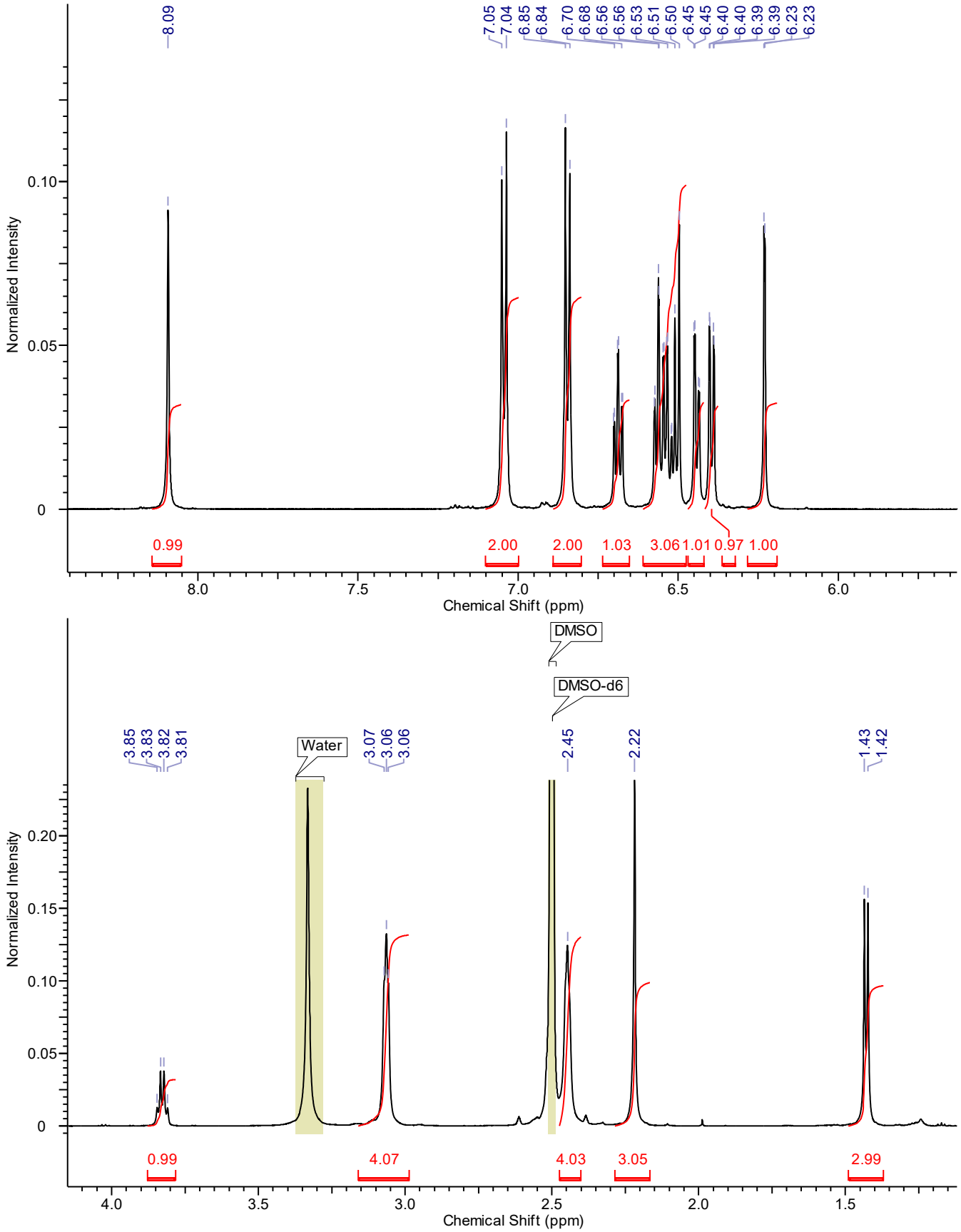


Figure S7.58. Aromatic region (*top*) and alkyl region (*bottom*) ^{1}H NMR of 2-(1-(4-(4-methylpiperazin-1-yl)phenyl)ethyl)-10H-phenoxazine (**3.44**) in DMSO-d6.

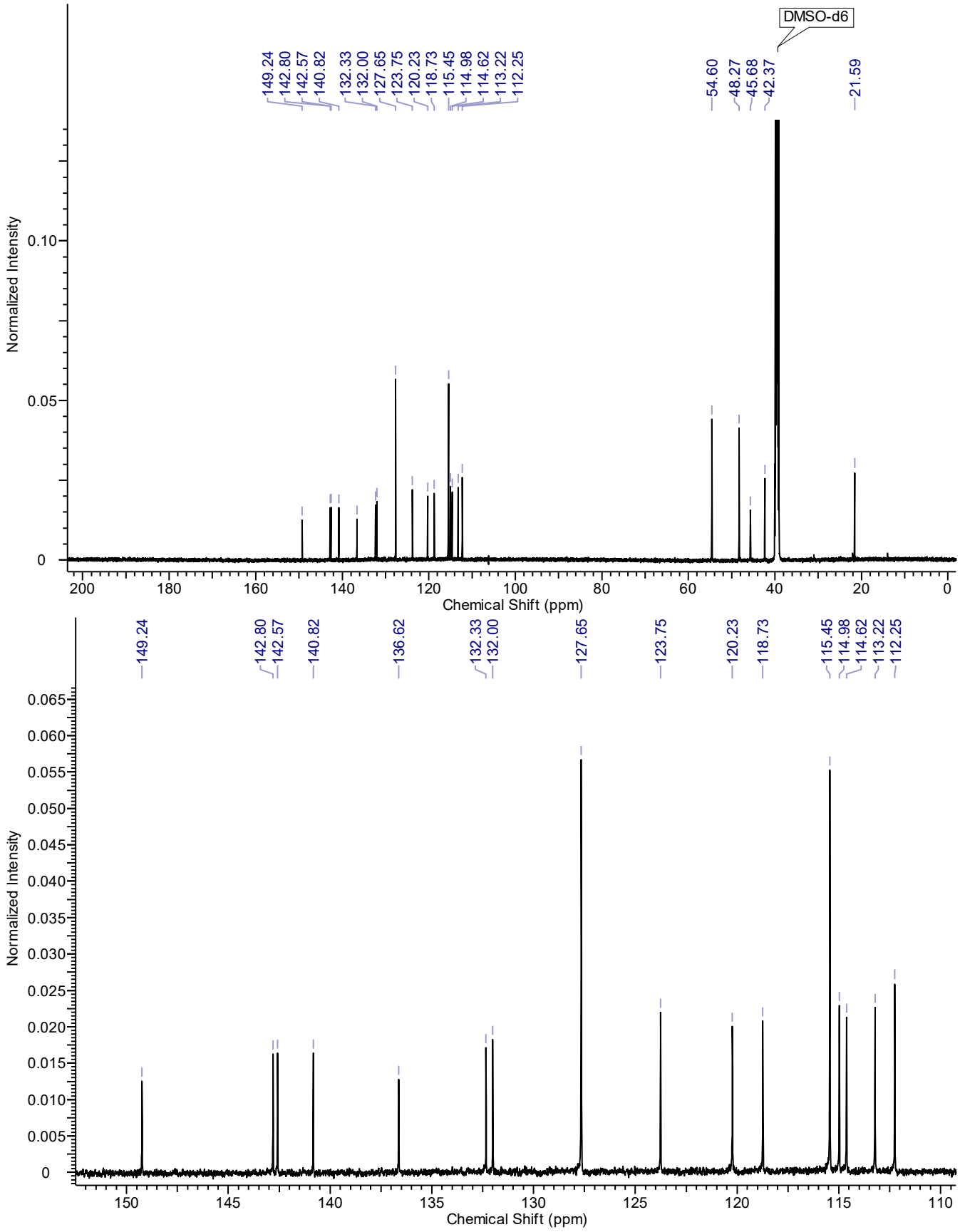


Figure S7.59. Full scale *(top)* and aromatic region (*bottom*) ^{13}C NMR of 2-(1-(4-(4-methylpiperazin-1-yl)phenyl)ethyl)-10H-phenoxazine (**3.44**) in DMSO-d6.

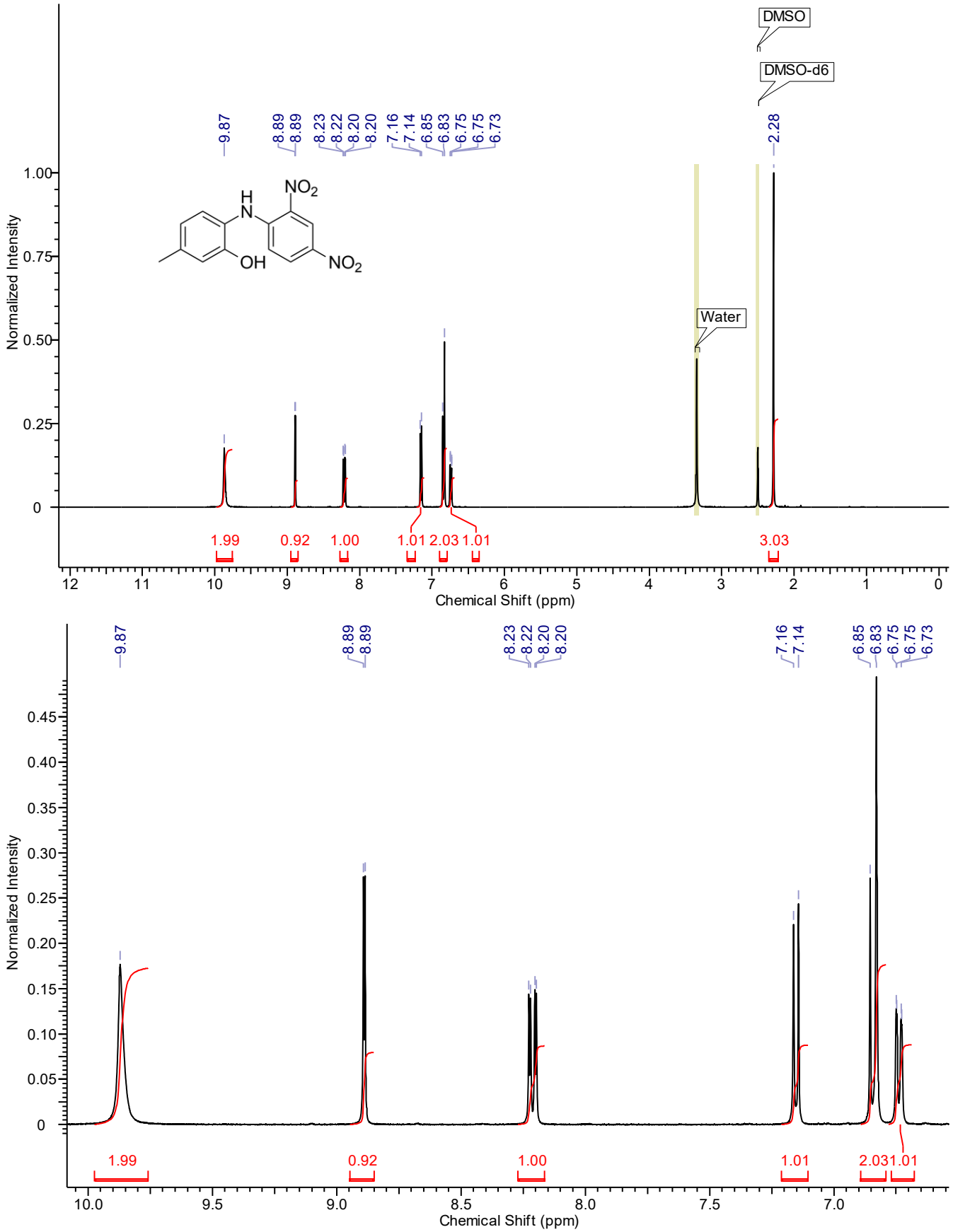


Figure S7.60. Full spectra (*top*) and aromatic region (*bottom*) ^{1}H NMR of 2-((2,4-dinitrophenyl)amino)-5-methylphenol (**3.16a**) in DMSO-d6.

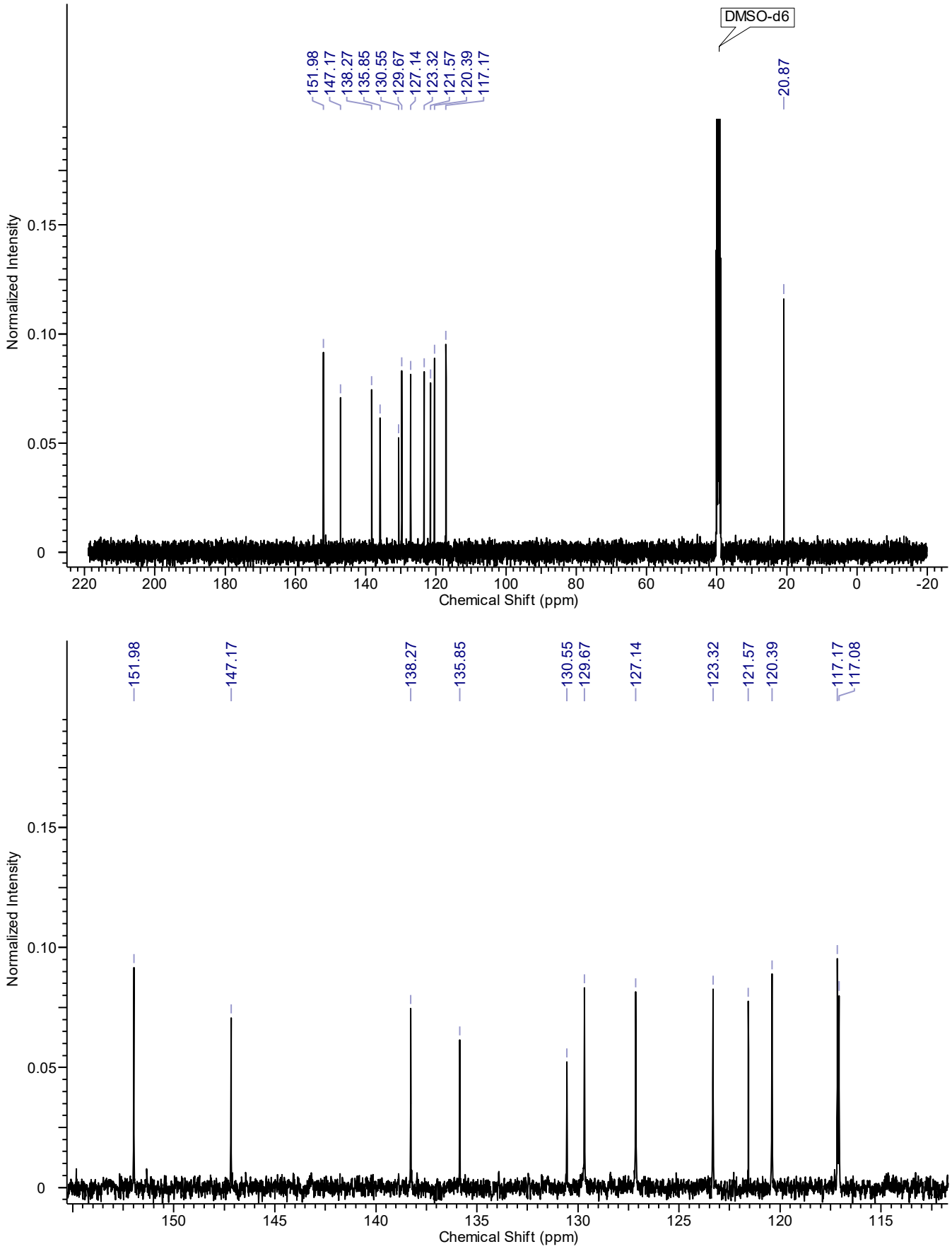


Figure S7.61. Full spectra (*top*) and aromatic region (*bottom*) ^{13}C NMR of 2-((2,4-dinitrophenyl)amino)-5-methylphenol (**3.16a**) in DMSO-d6.

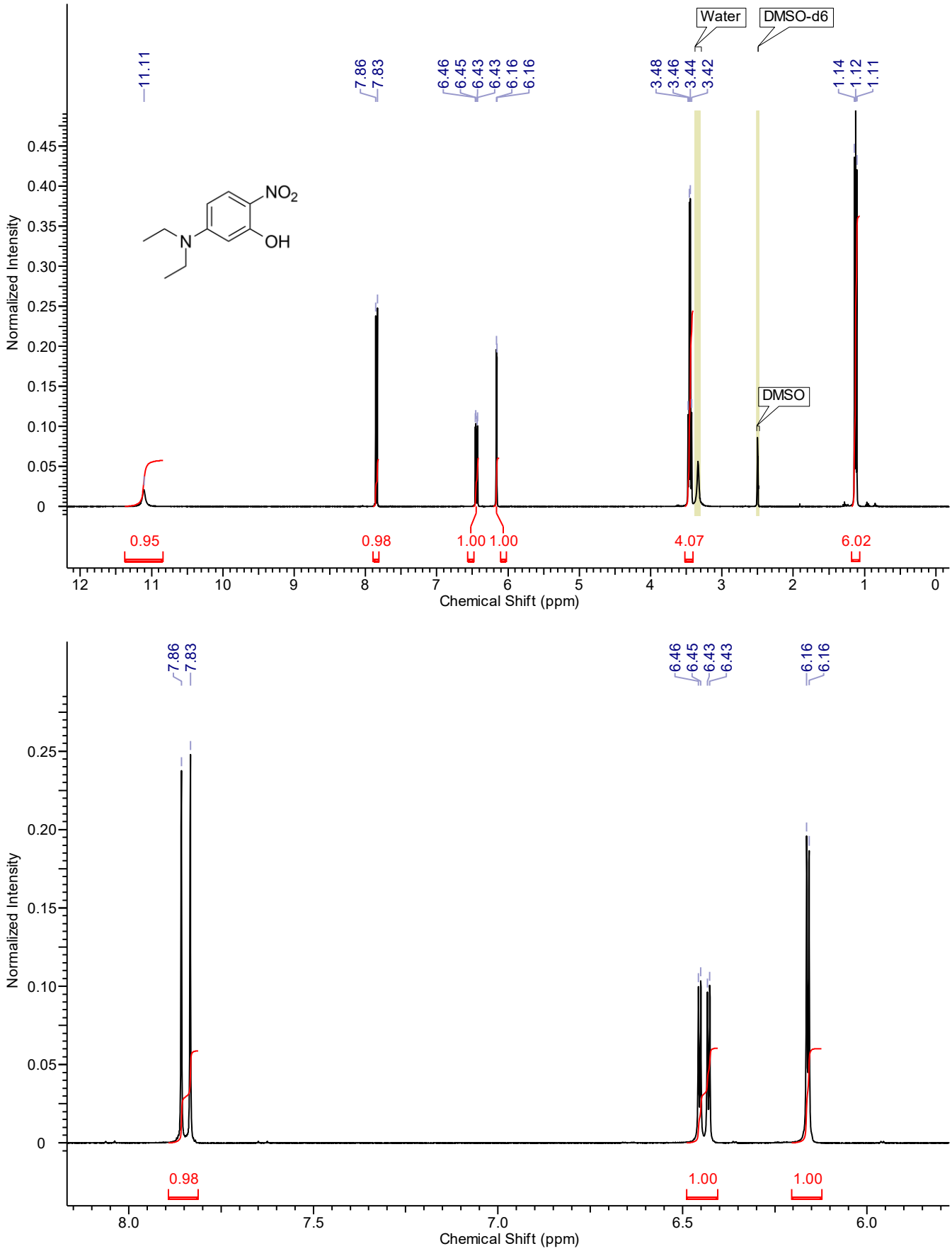


Figure S7.62. Full spectra (*top*) and aromatic region (*bottom*) ^{1}H NMR of 5-(diethylamino)-2-nitrophenol (**3.18a**) in DMSO-d6.

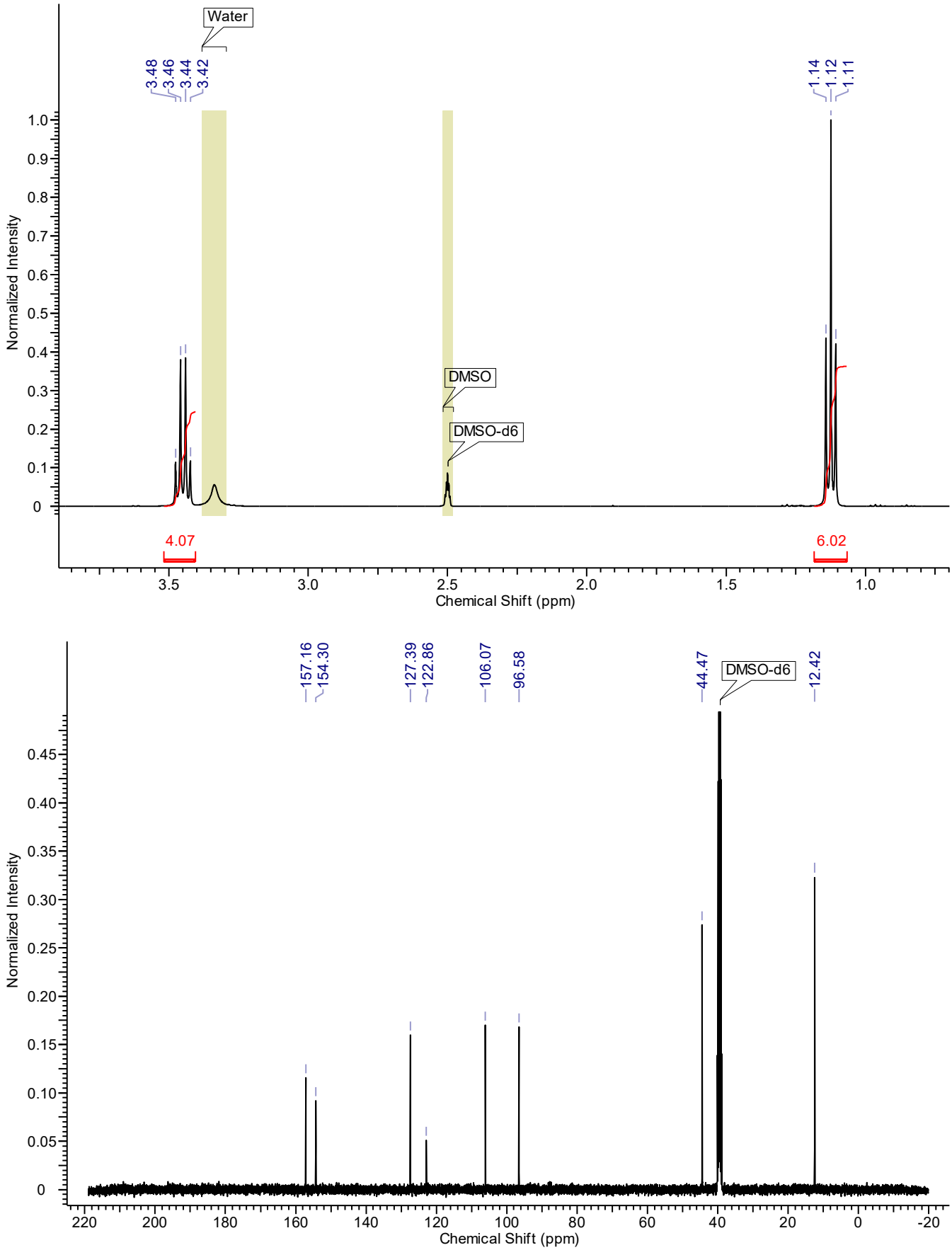


Figure S7.63. Alkyl region of ^{1}H NMR (*top*) and full ^{13}C NMR (*bottom*) of 5-(diethylamino)-2-nitrophenol (**3.18a**) in DMSO-d6.

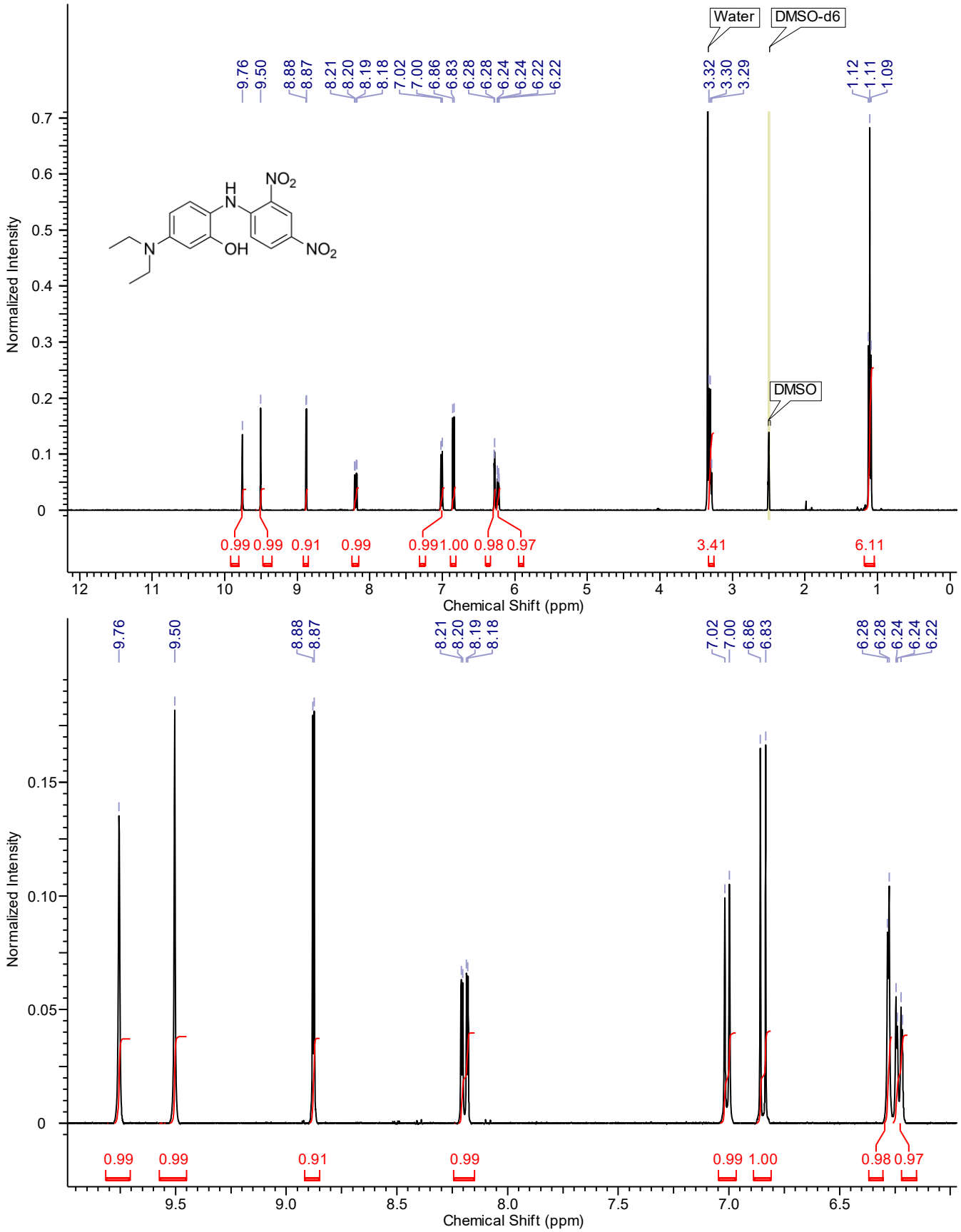


Figure S7.64. Full spectra (*top*) and aromatic region (*bottom*) ^{1}H NMR of 5-(diethylamino)-2-((2,4-dinitrophenyl)amino)phenol (**3.18b**) in DMSO-d6.

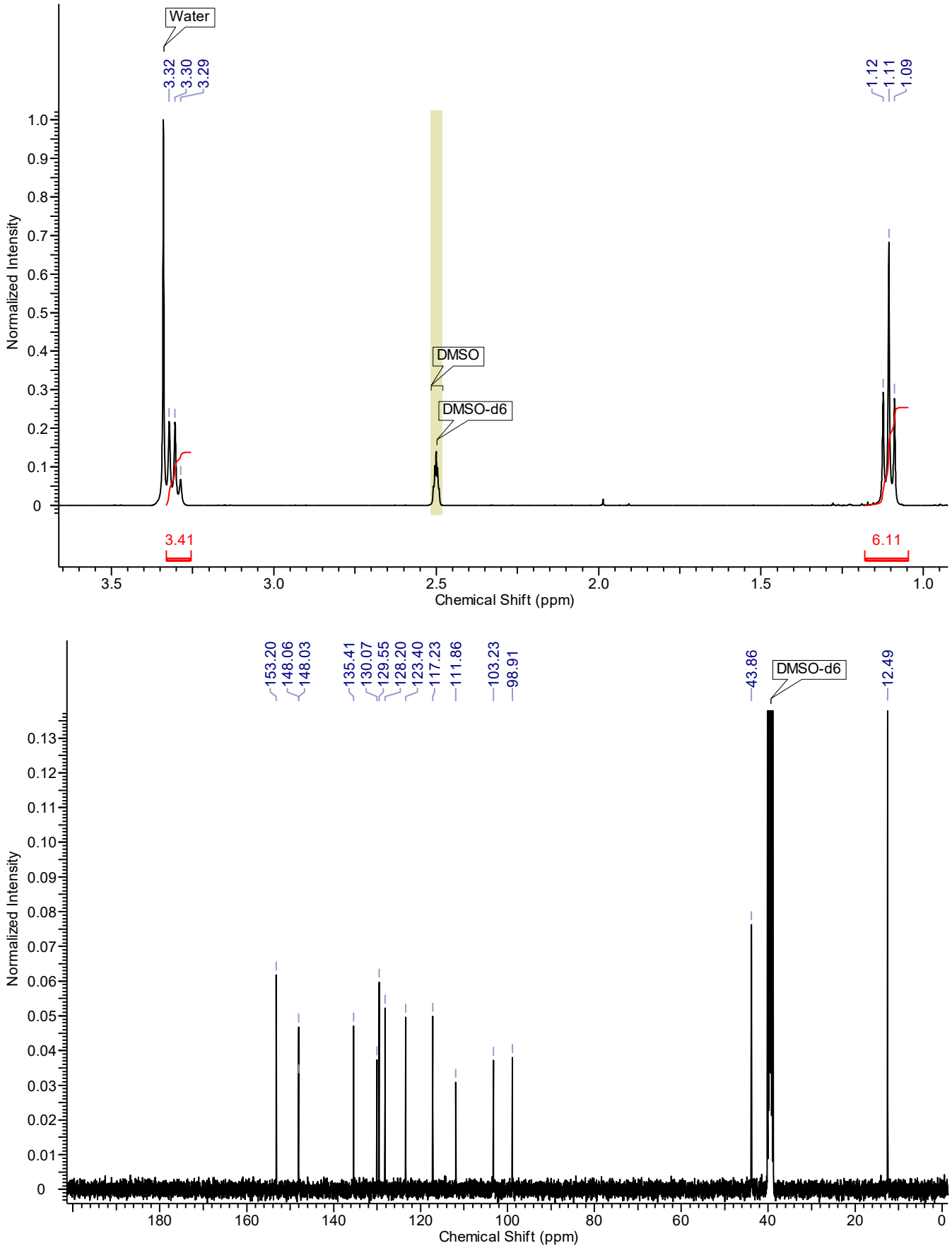


Figure S7.65. Alkyl region of ^{1}H (*top*) and full ^{13}C NMR (*bottom*) of 5-(diethylamino)-2-((2,4-dinitrophenyl)amino)phenol (**3.18b**) in DMSO-d6.

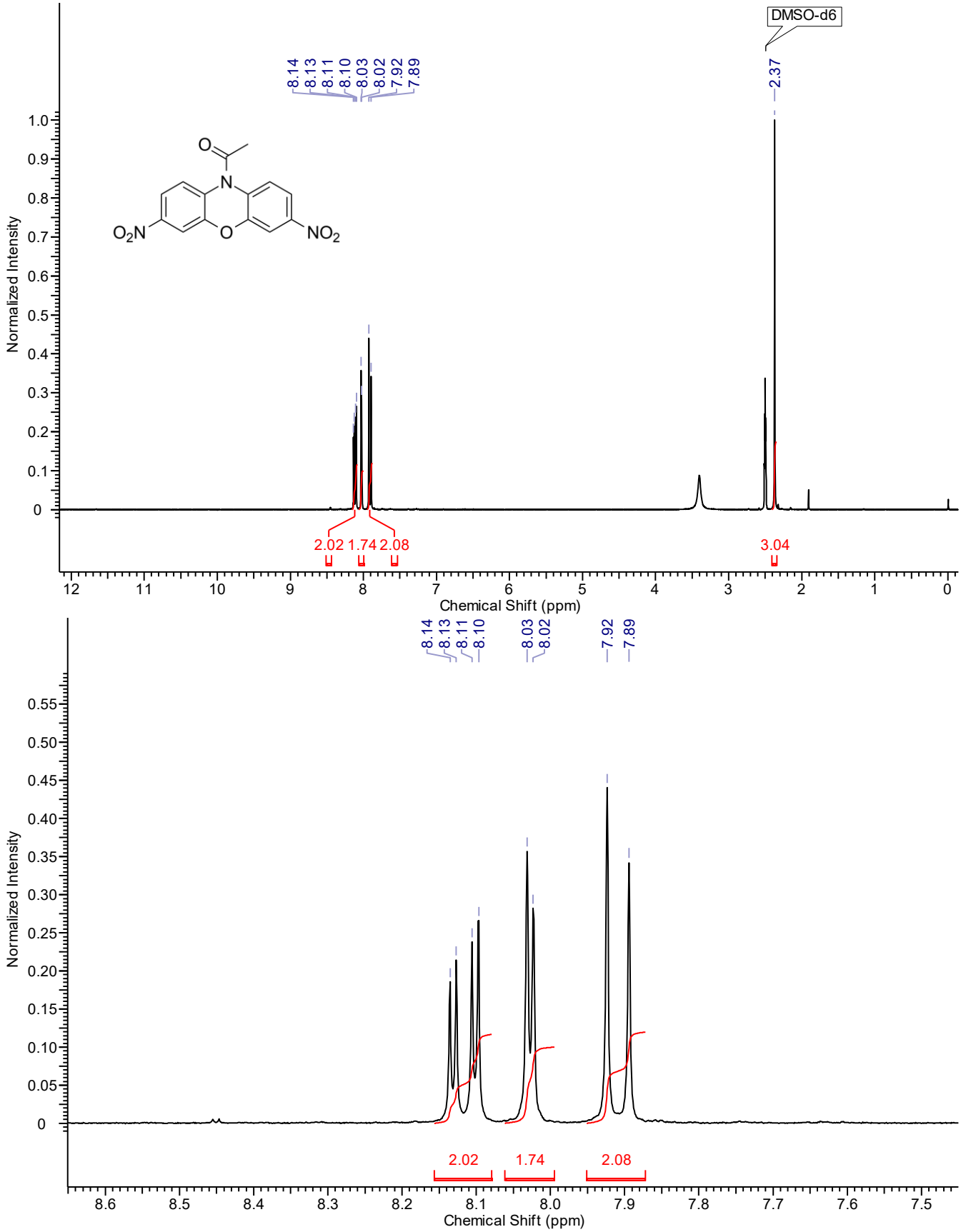


Figure S7.66. Full spectra (*top*) and aromatic region (*bottom*) ^{1}H NMR of 10-acetyl-3,7-dinitrophenoxazine (**3.19a**) in DMSO-d6.

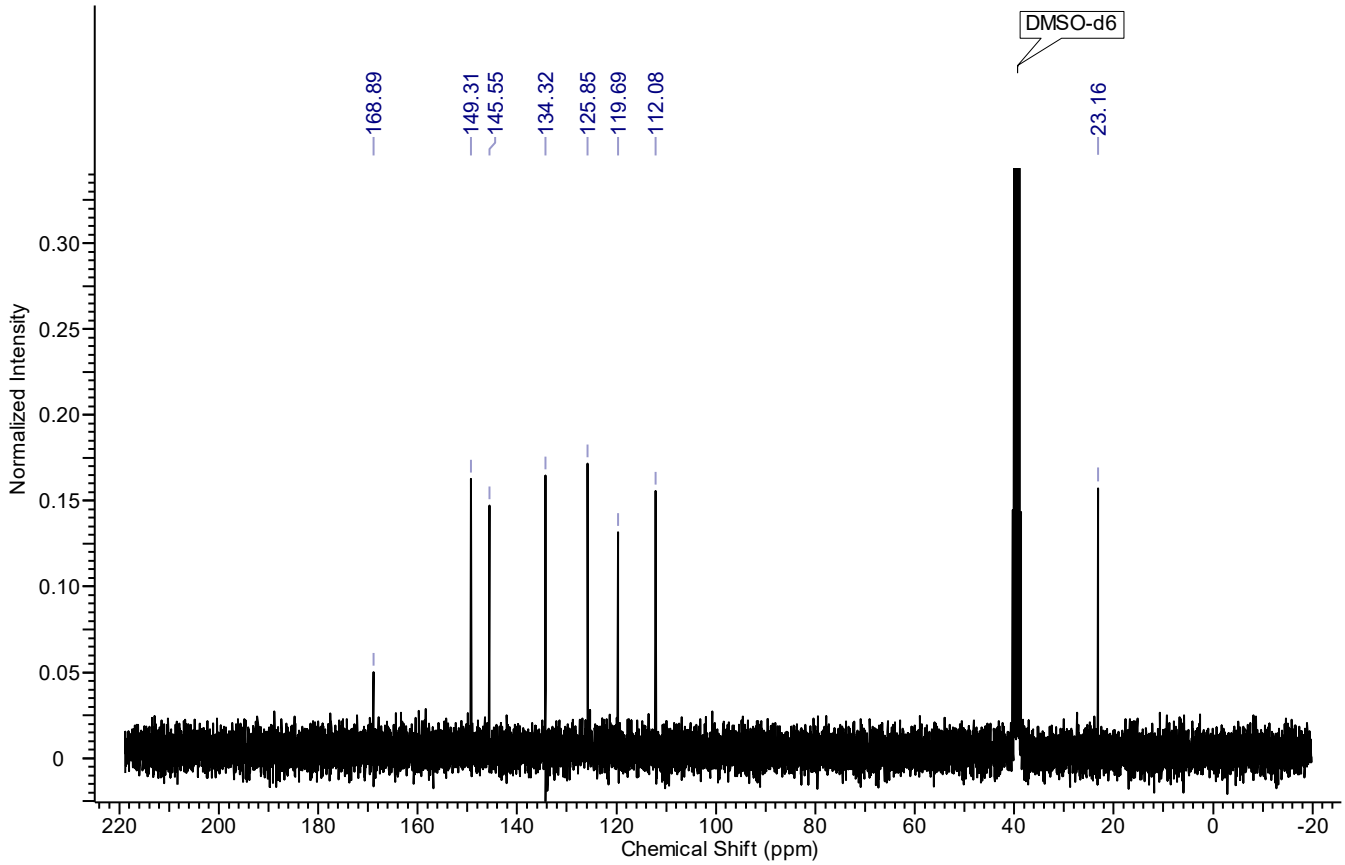


Figure S7.67. ^{13}C NMR of 10-acetyl-3,7-dinitrophenoxazine (**3.19a**) in DMSO-d6.

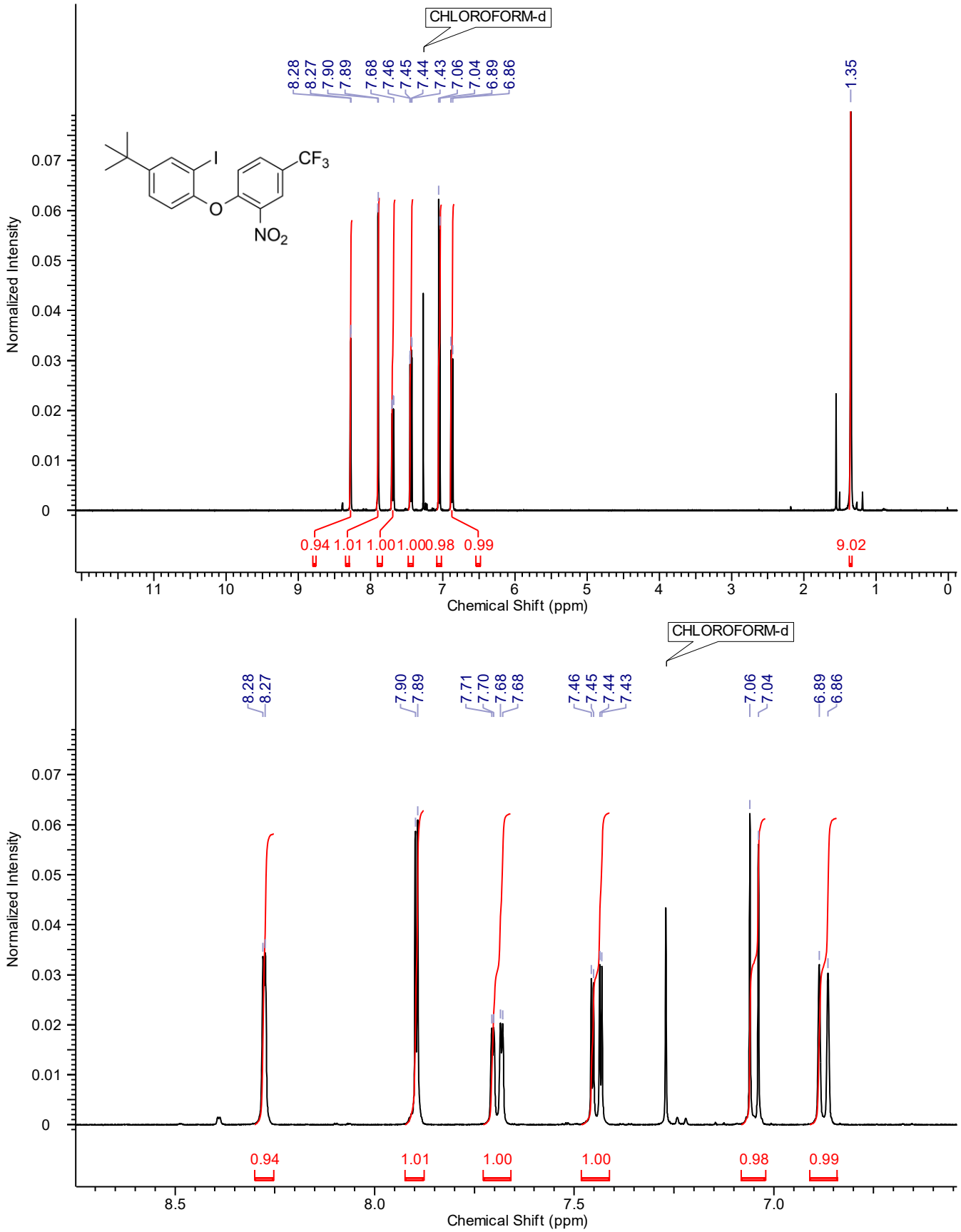


Figure S7.68. Full spectra (*top*) and aromatic region (*bottom*) ^{1}H NMR of 4-(*tert*-butyl)-2-iodo-1-(2-nitro-4-(trifluoromethyl)phenoxy)benzene (**3.8a**) in $CDCl_3$.

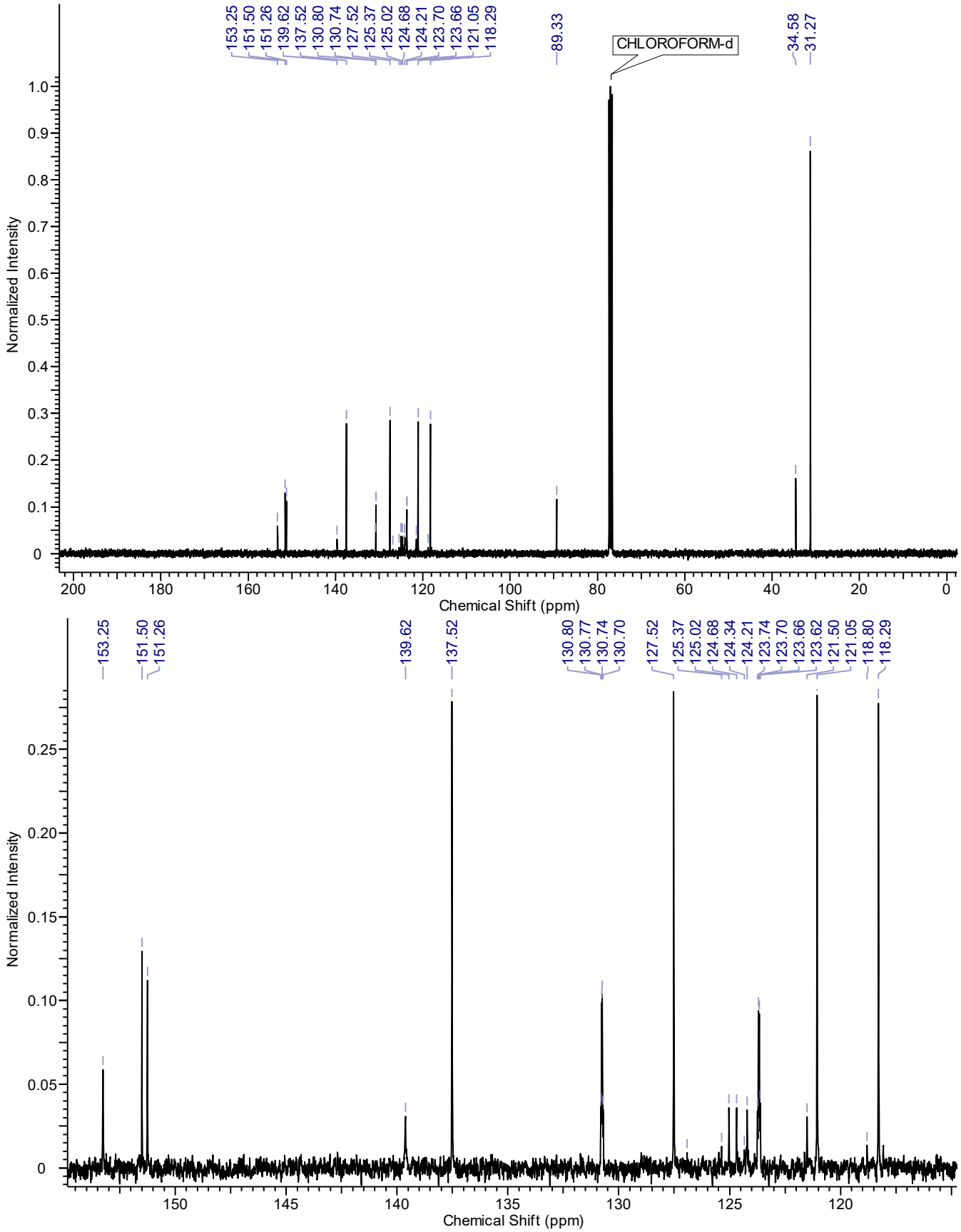


Figure S7.69. Full spectra (*top*) and aromatic region (*bottom*) ^{13}C NMR of 4-(*tert*-butyl)-2-iodo-1-(2-nitro-4-(trifluoromethyl)phenoxy)benzene (**3.8a**) in $CDCl_3$.

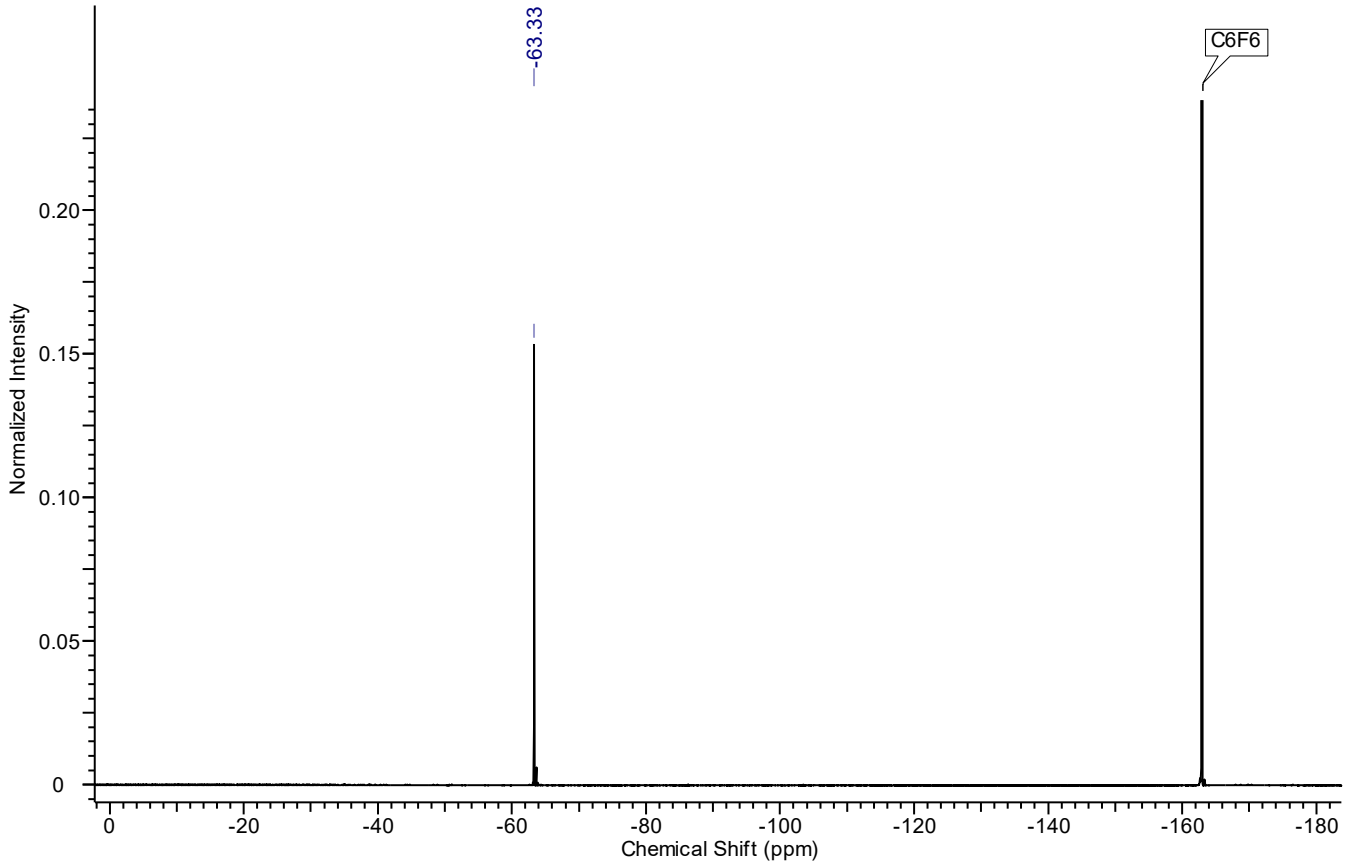


Figure S7.70. ^{19}F NMR spectra of 4-(*tert*-butyl)-2-iodo-1-(2-nitro-4-(trifluoromethyl)phenoxy)benzene (**3.8a**) in $CDCl_3$.

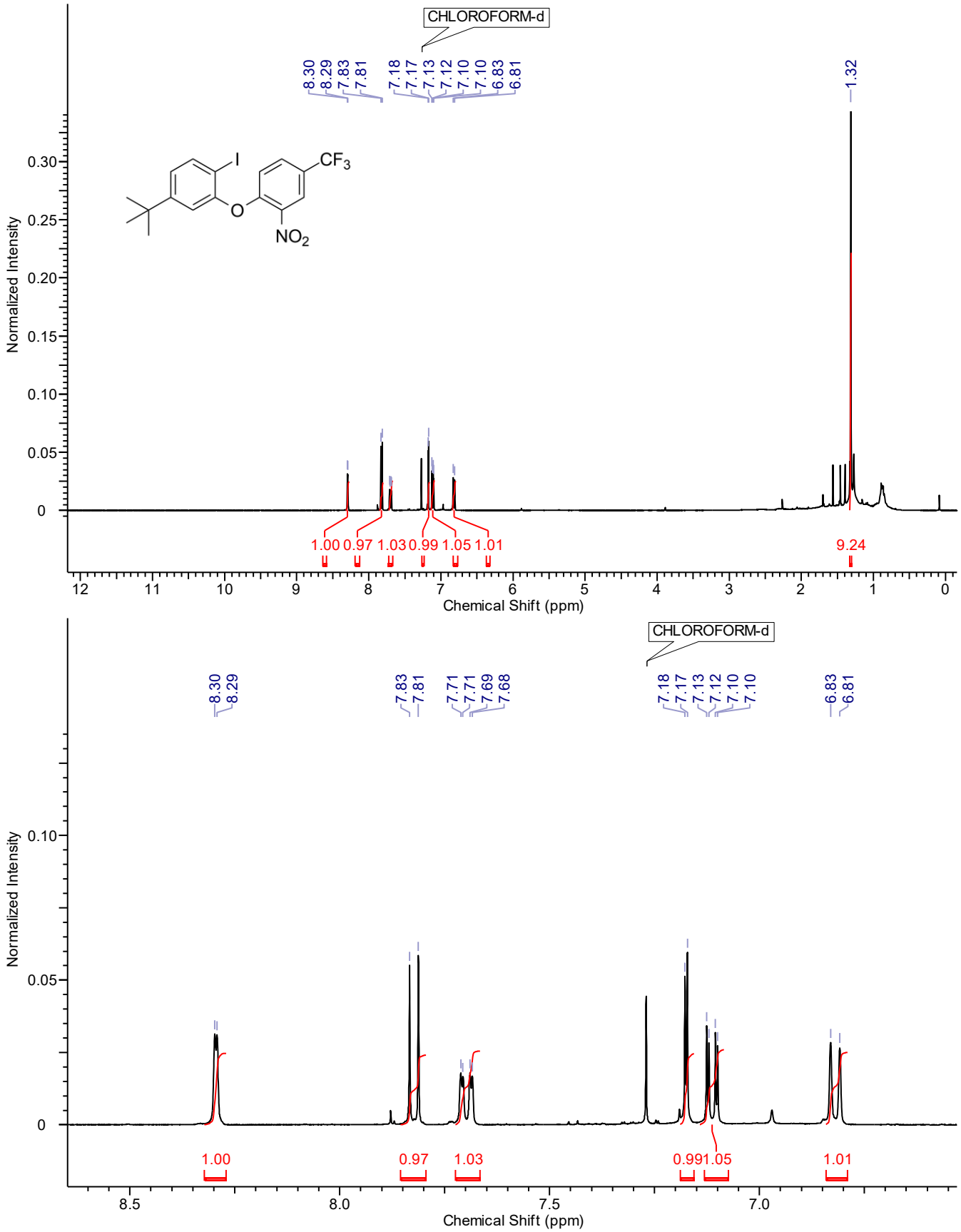


Figure S7.71. Full spectra (*top*) and aromatic region (*bottom*) ^{1}H NMR of 4-(*tert*-butyl)-1-iodo-2-(2-nitro-4-(trifluoromethyl)phenoxy)benzene (**3.7a**) in $CDCl_3$.

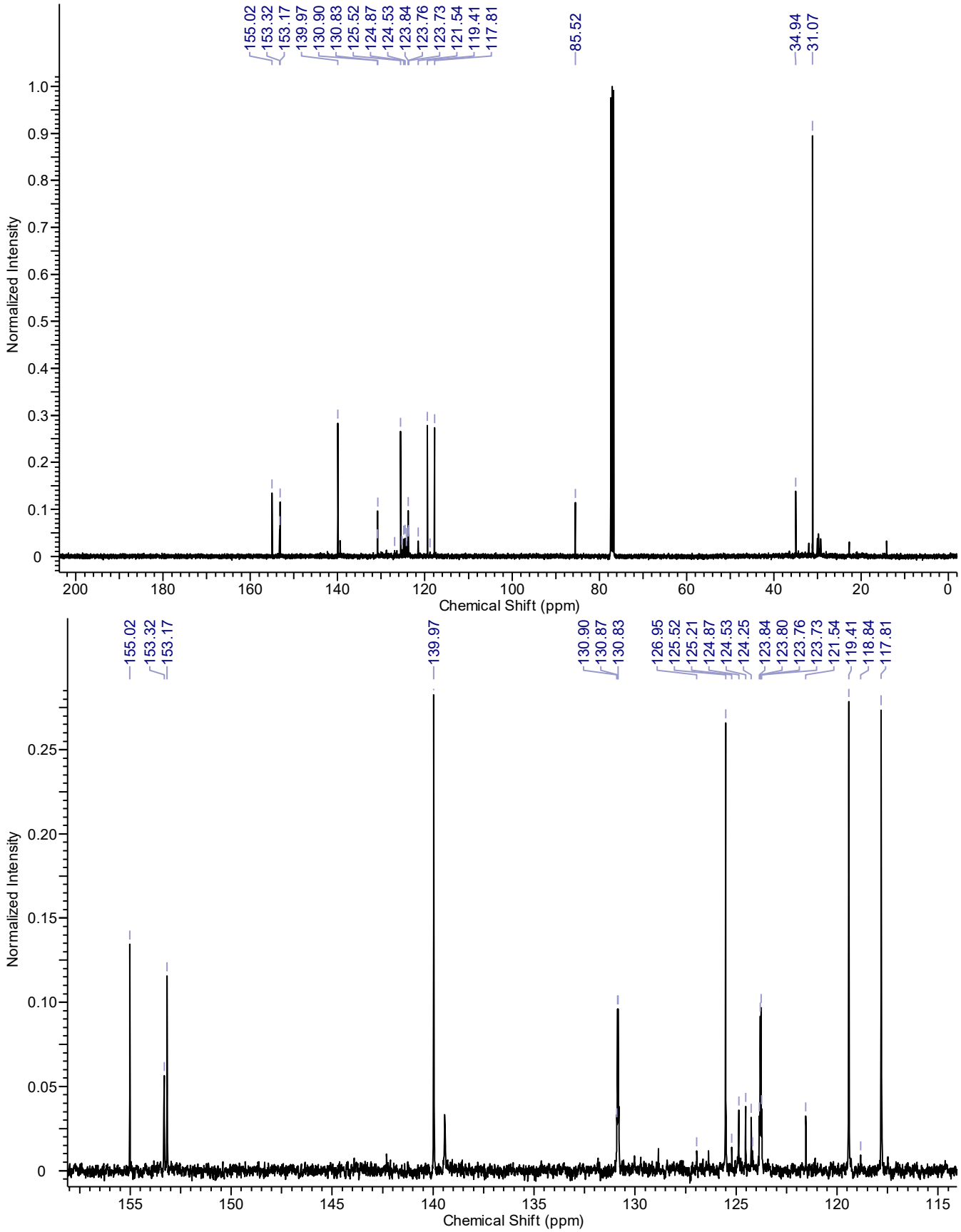


Figure S7.72. Full spectra (*top*) and aromatic region (*bottom*) ^{13}C NMR of 4-(*tert*-butyl)-1-iodo-2-(2-nitro-4-(trifluoromethyl)phenoxy)benzene (**3.7a**) in $CDCl_3$.

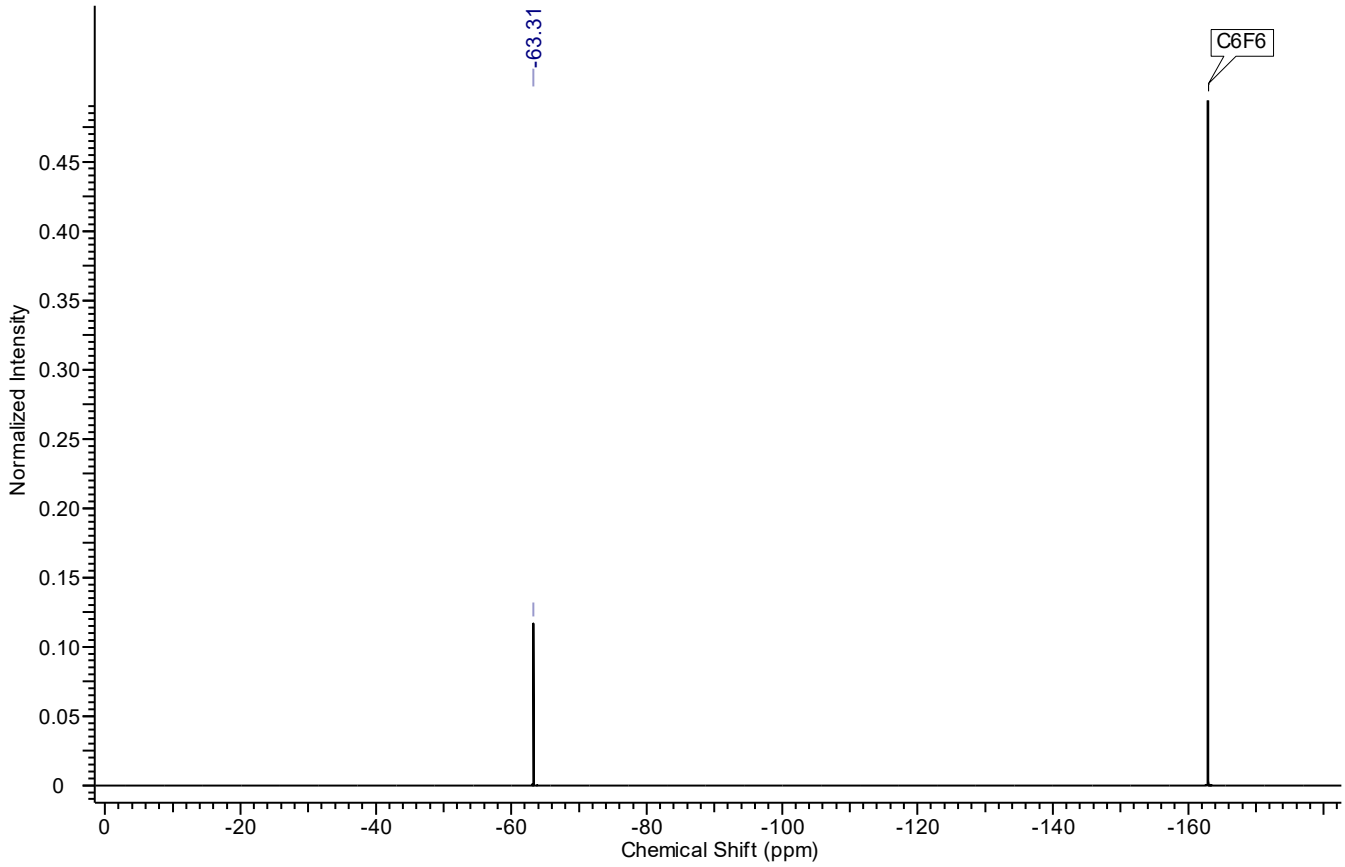


Figure S7.73. ^{19}F NMR spectra of 4-(*tert*-butyl)-1-iodo-2-(2-nitro-4-(trifluoromethyl)phenoxy)benzene (**3.7a**) in $CDCl_3$.

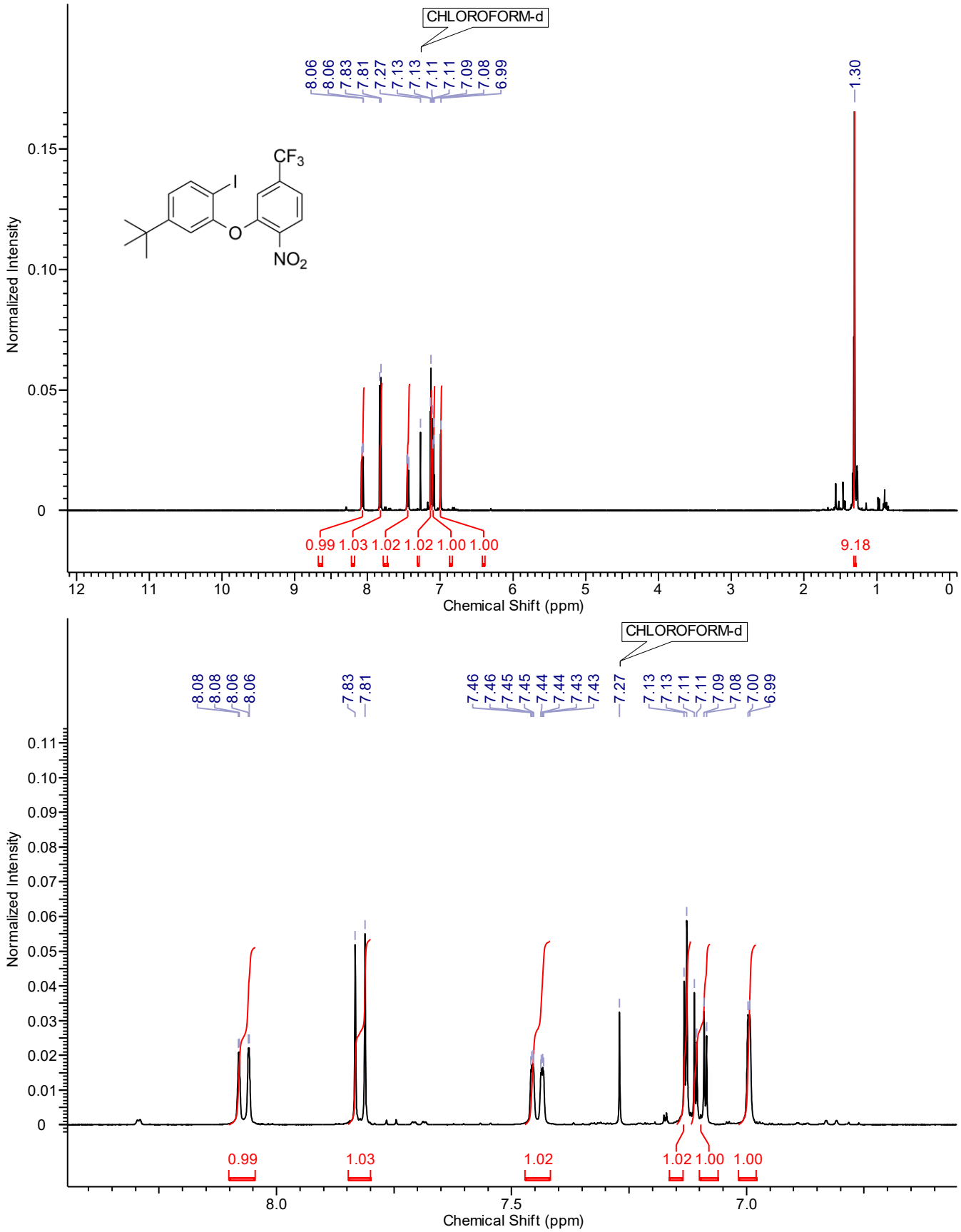


Figure S7.74. Full spectra (*top*) and aromatic region (*bottom*) ^{1}H NMR of 4-(*tert*-butyl)-1-iodo-2-(2-nitro-5-(trifluoromethyl)phenoxy)benzene (**3.10a**) in $CDCl_3$.

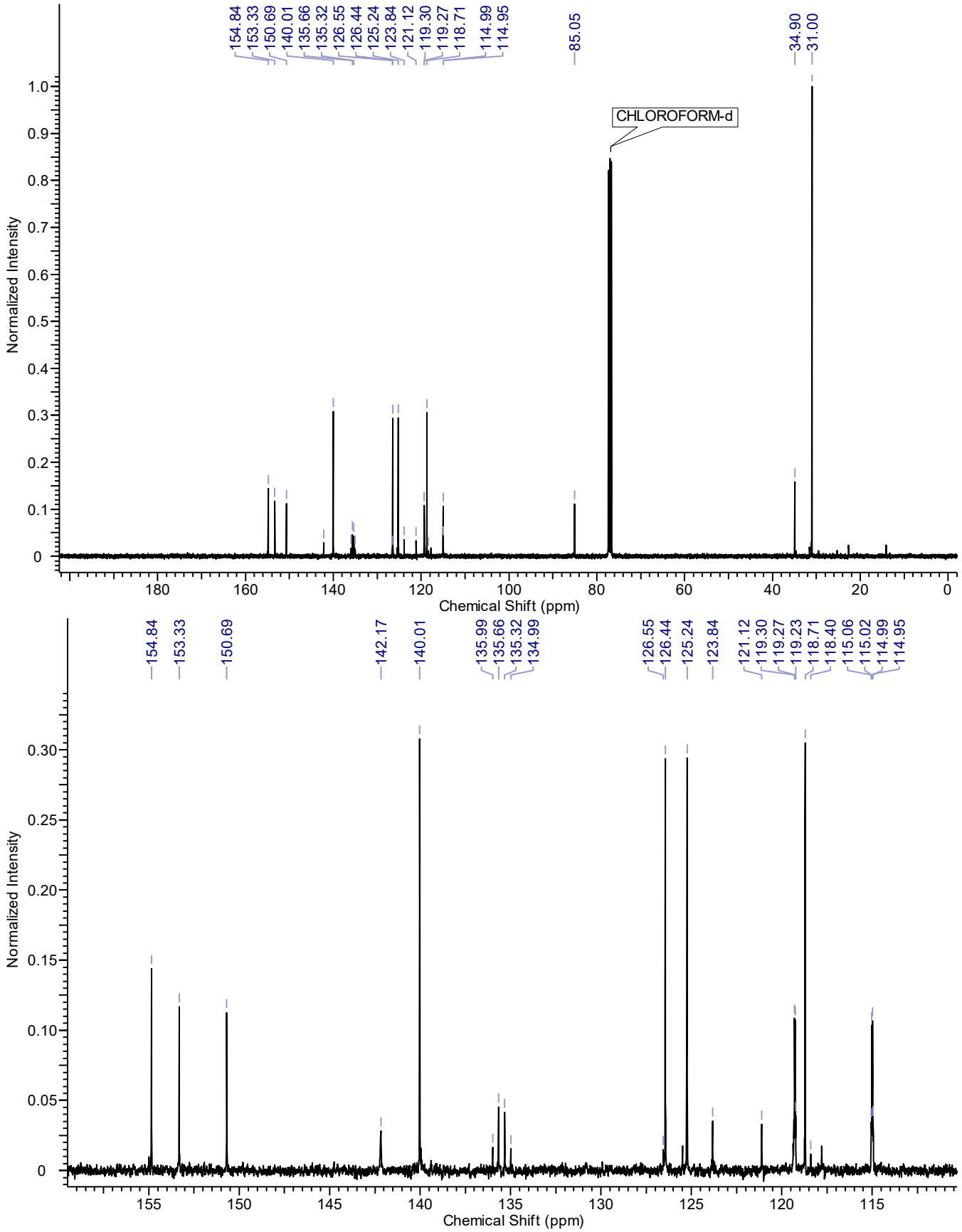


Figure S7.75. Full spectra (*top*) and aromatic region (*bottom*) ^{13}C NMR of 4-(*tert*-butyl)-1-iodo-2-(2-nitro-5-(trifluoromethyl)phenoxy)benzene (**3.10a**) in $CDCl_3$.

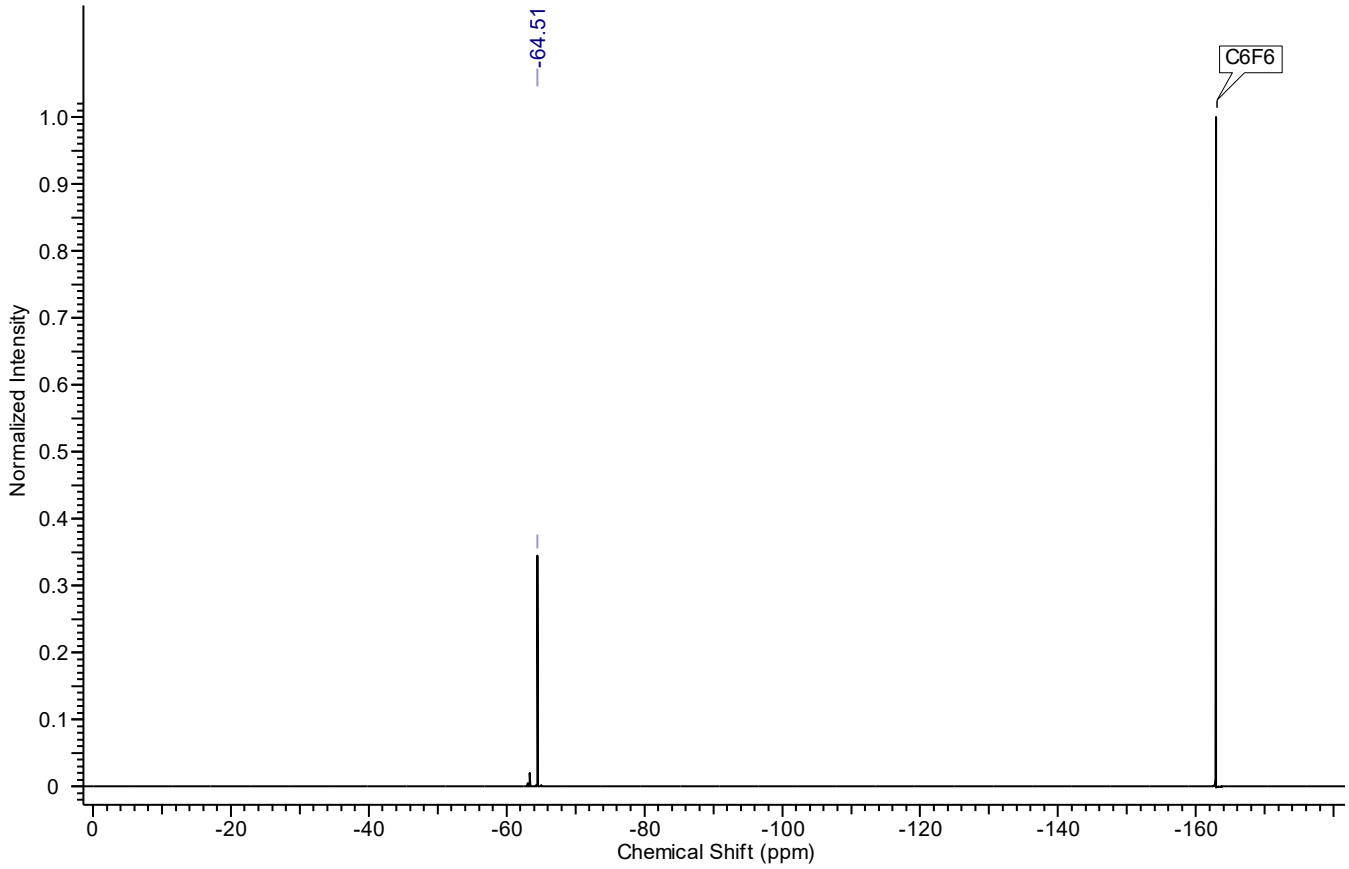


Figure S7.76. ^{19}F NMR spectra of 4-(*tert*-butyl)-1-iodo-2-(2-nitro-5-(trifluoromethyl)phenoxy)benzene (**3.10a**) in $CDCl_3$.

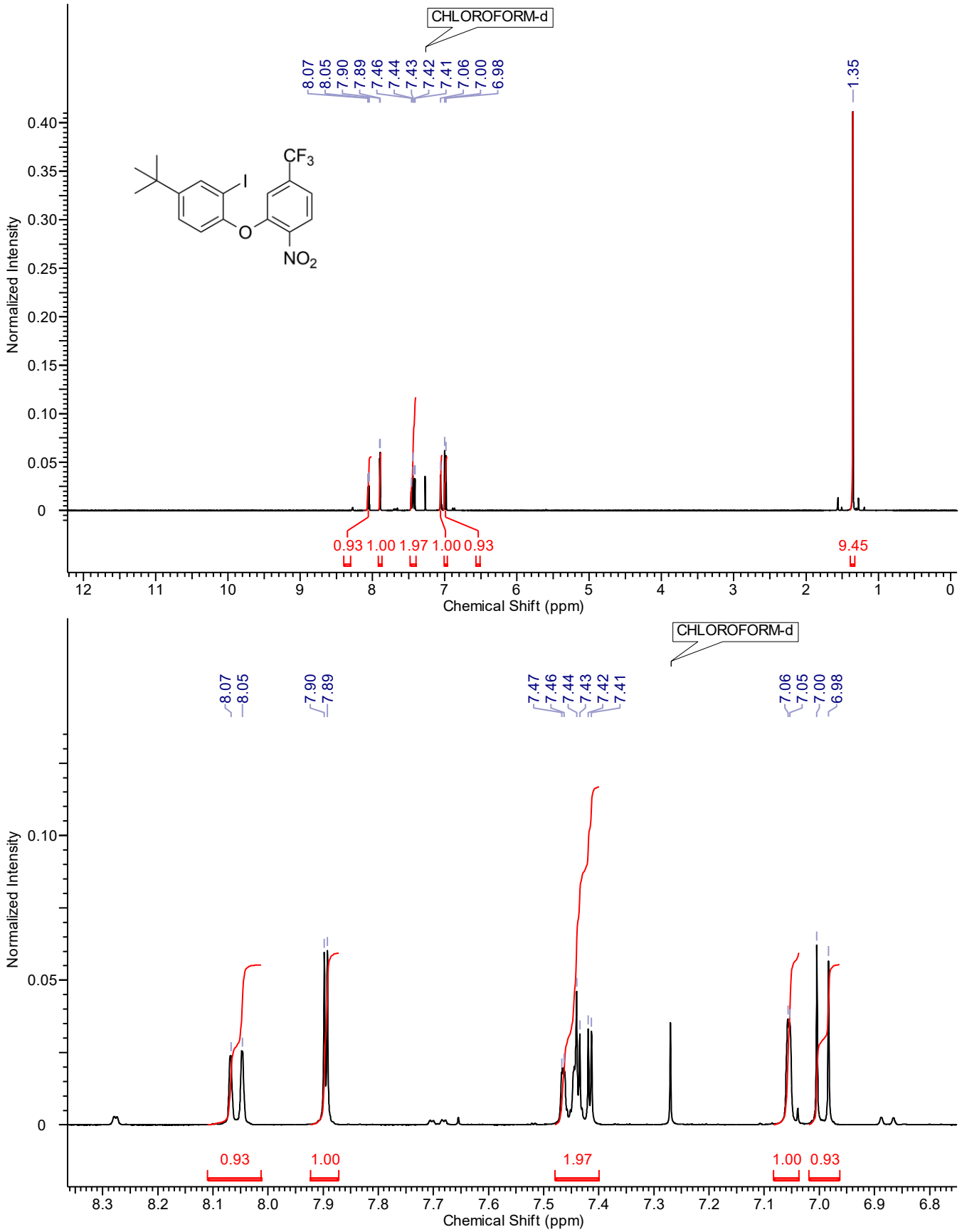


Figure S7.77. Full spectra (*top*) and aromatic region (*bottom*) ^{1}H NMR of 4-(*tert*-butyl)-2-iodo-1-(2-nitro-5-(trifluoromethyl)phenoxy)benzene (**3.11a**) in $CDCl_3$.

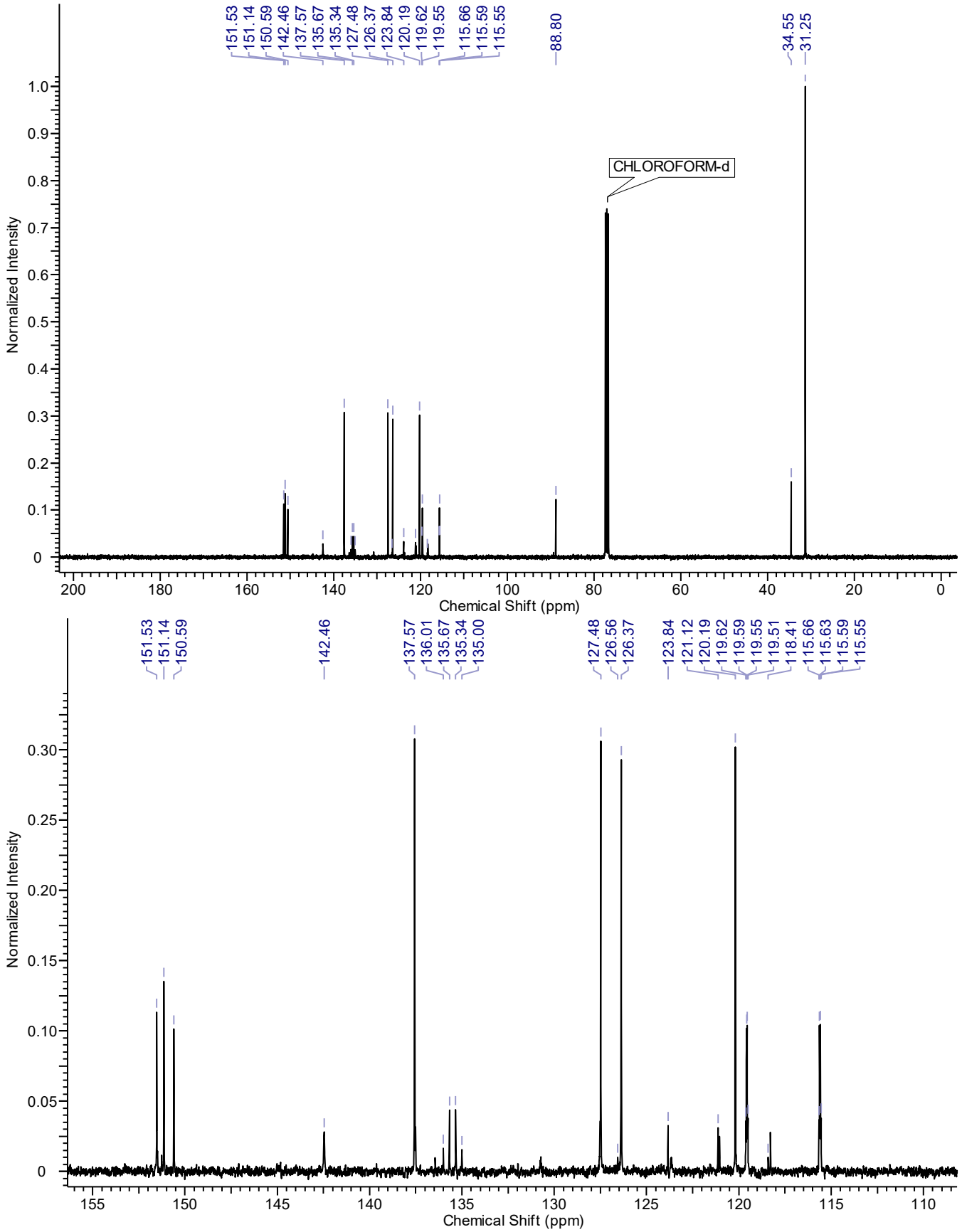


Figure S7.78. Full spectra (*top*) and aromatic region (*bottom*) ^{13}C NMR of 4-(*tert*-butyl)-2-iodo-1-(2-nitro-5-(trifluoromethyl)phenoxy)benzene (**3.11a**) in $CDCl_3$.

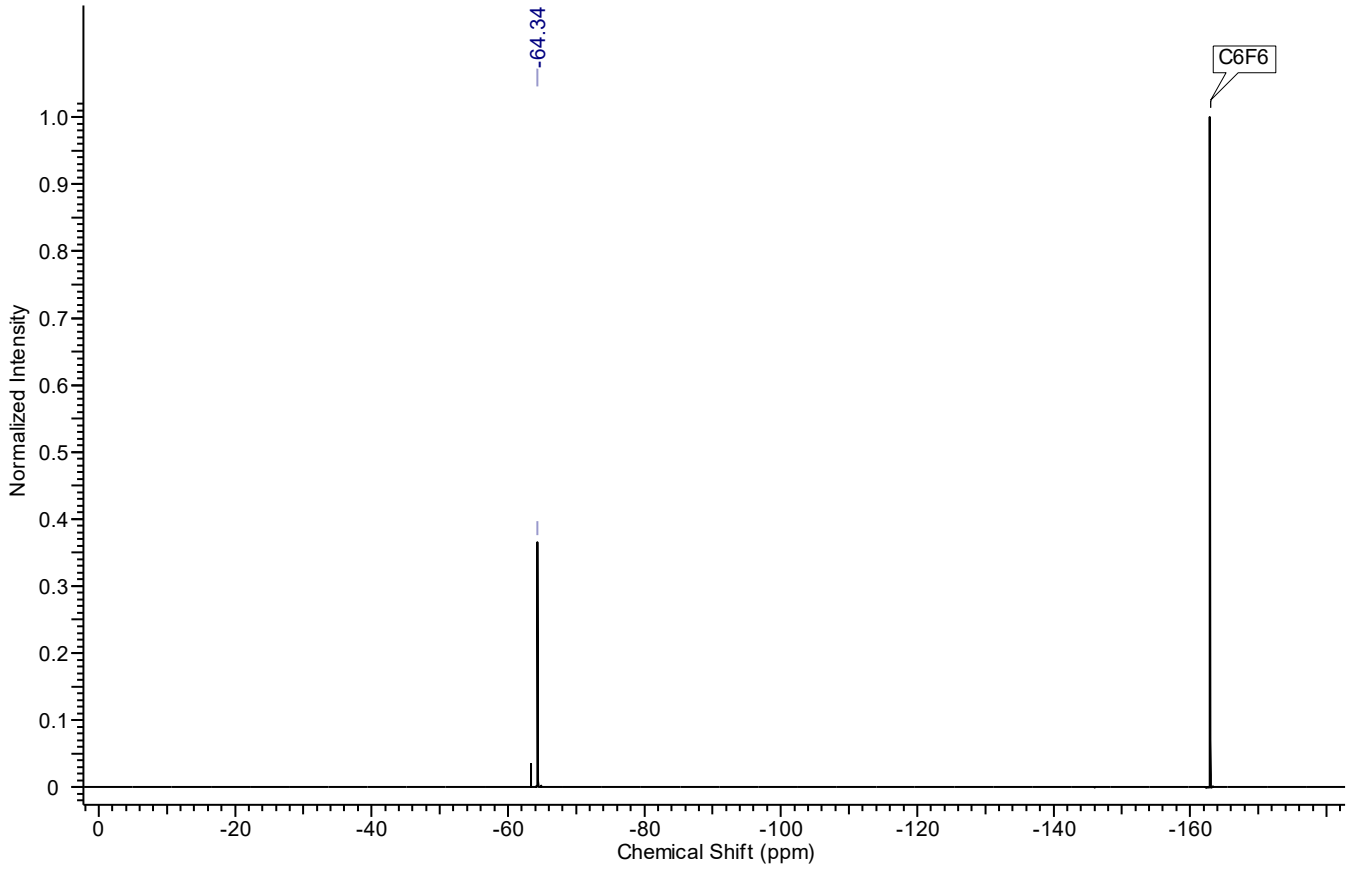


Figure S7.79. ^{19}F NMR spectra of 4-(*tert*-butyl)-2-iodo-1-(2-nitro-5-(trifluoromethyl)phenoxy)benzene (**3.11a**) in $CDCl_3$.

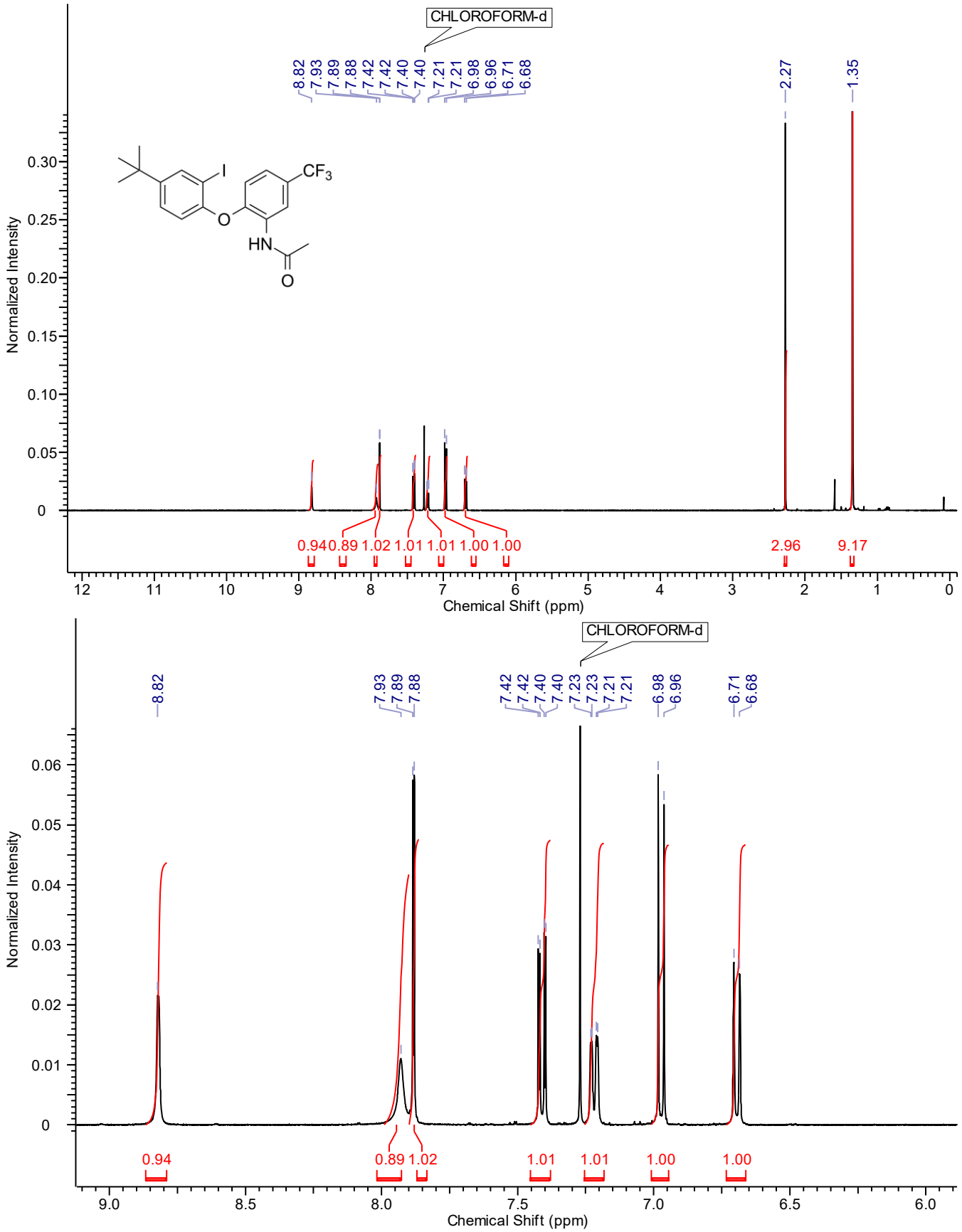


Figure S7.80. Full spectra (*top*) and aromatic region (*bottom*) ^{1}H NMR of N-(2-(4-(*tert*-butyl)-2-iodophenoxy)-5-(trifluoromethyl)phenyl)acetamide (**3.8b**) in $CDCl_3$.

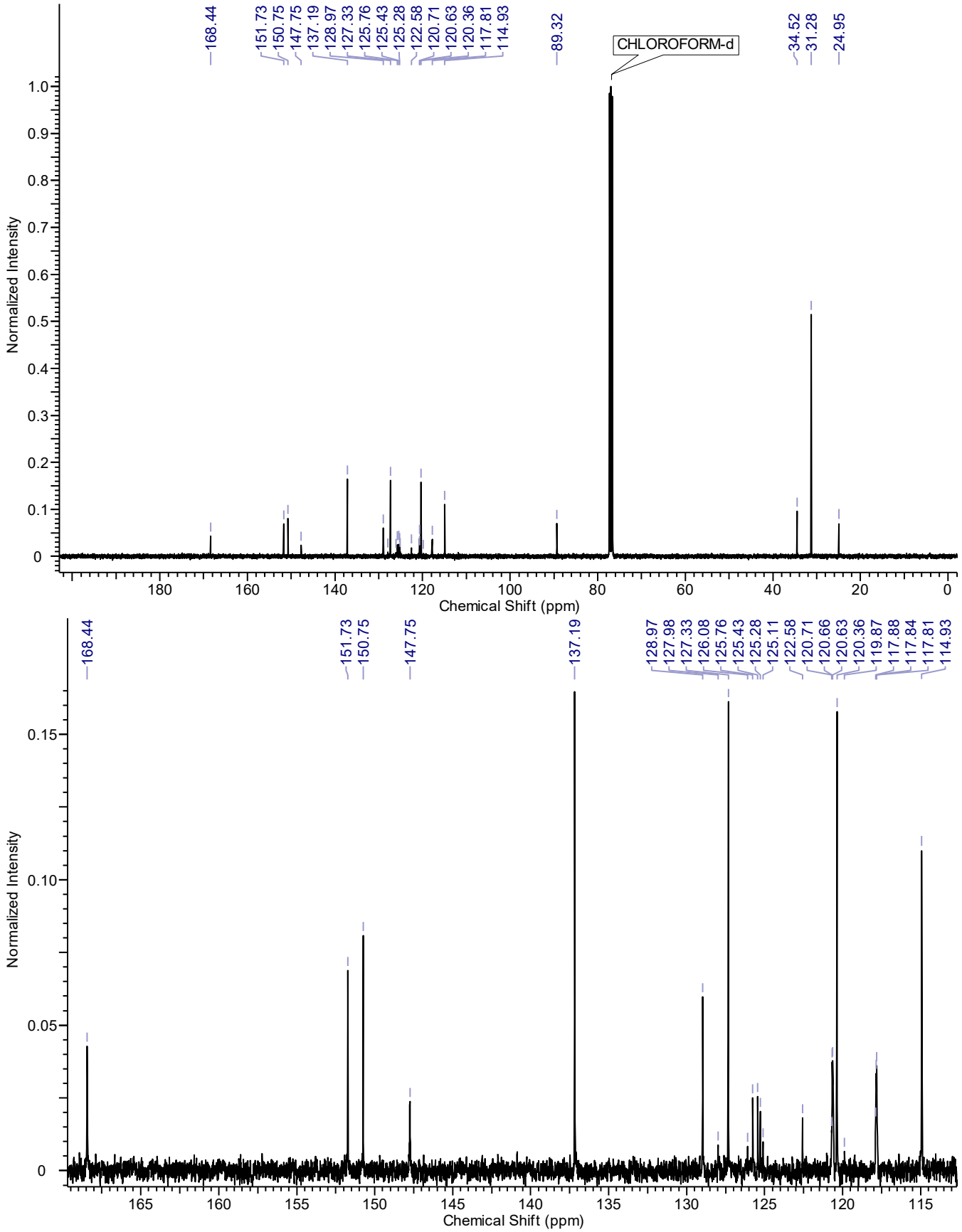


Figure S7.81. Full spectra (*top*) and aromatic region (*bottom*) ^{13}C NMR of N-(2-(4-(*tert*-butyl)-2-iodophenoxy)-5-(trifluoromethyl)phenyl)acetamide (**3.8b**) in $CDCl_3$.

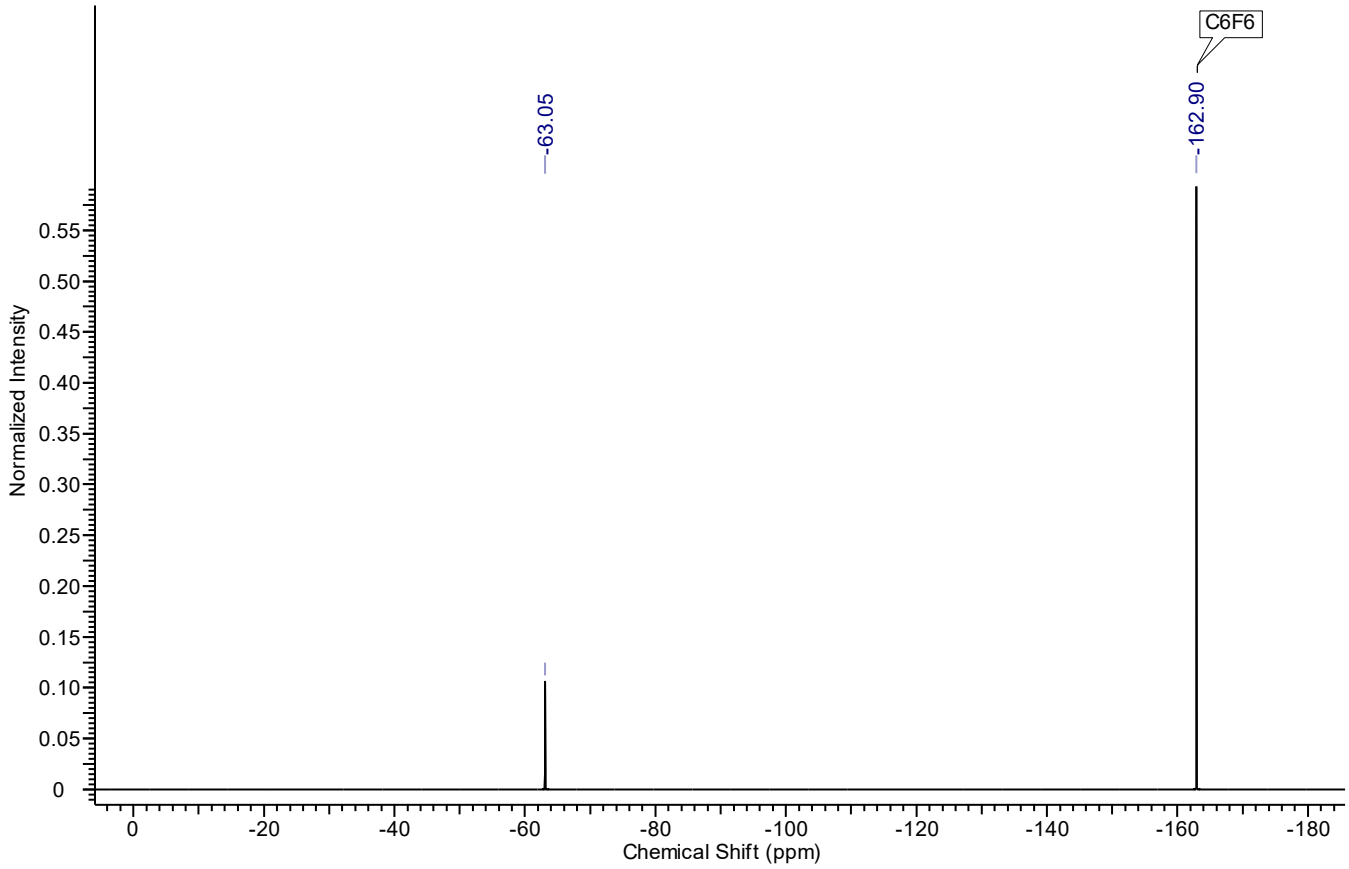


Figure S7.82. ^{19}F NMR spectra of N-(2-(4-(*tert*-butyl)-2-iodophenoxy)-5-(trifluoromethyl)phenyl)acetamide (**3.8b**) in $CDCl_3$.

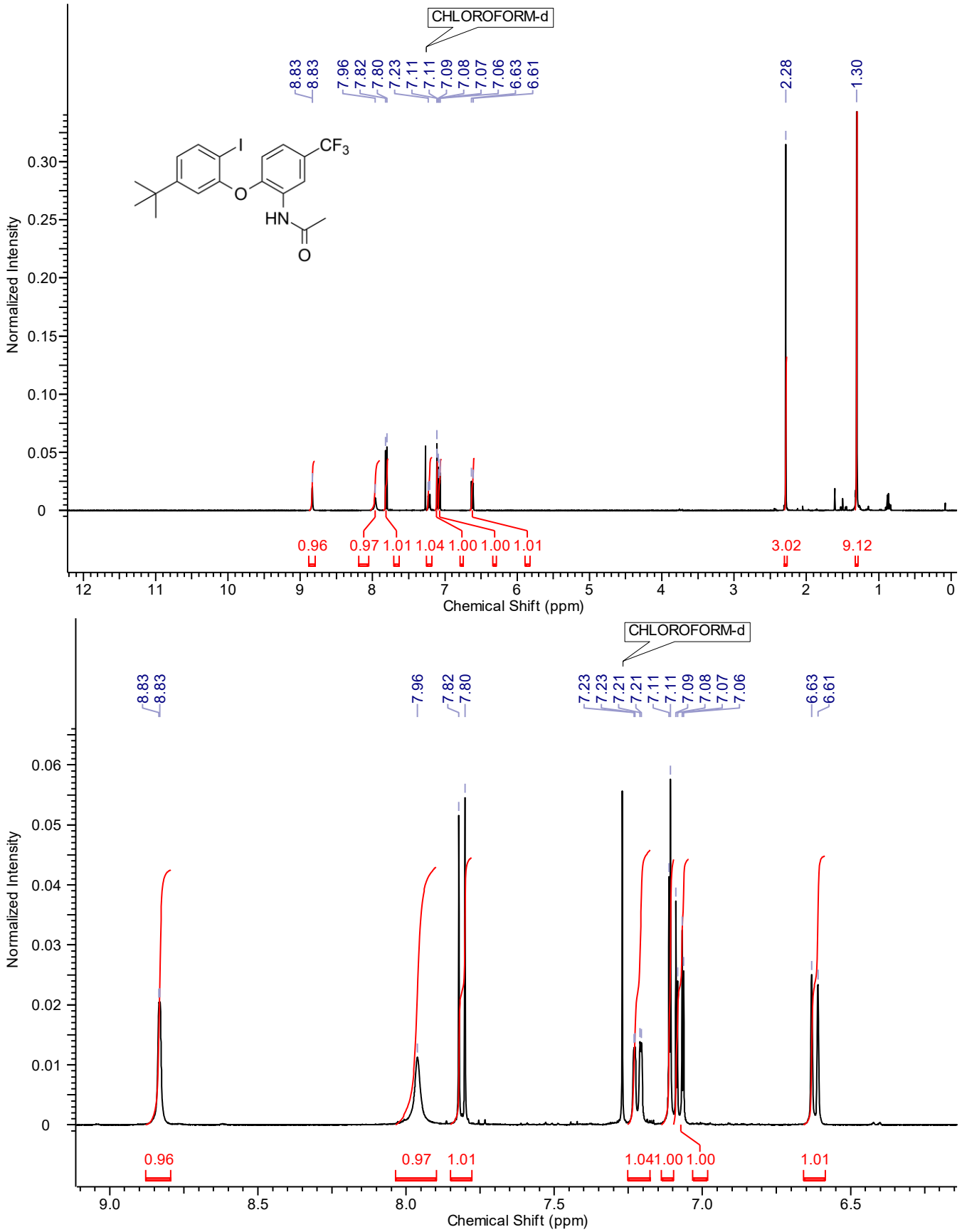


Figure S7.83. Full spectra (*top*) and aromatic region (*bottom*) ^{1}H NMR of N-(2-(5-(*tert*-butyl)-2-iodophenoxy)-5-(trifluoromethyl)phenyl)acetamide (**3.7b**) in $CDCl_3$.

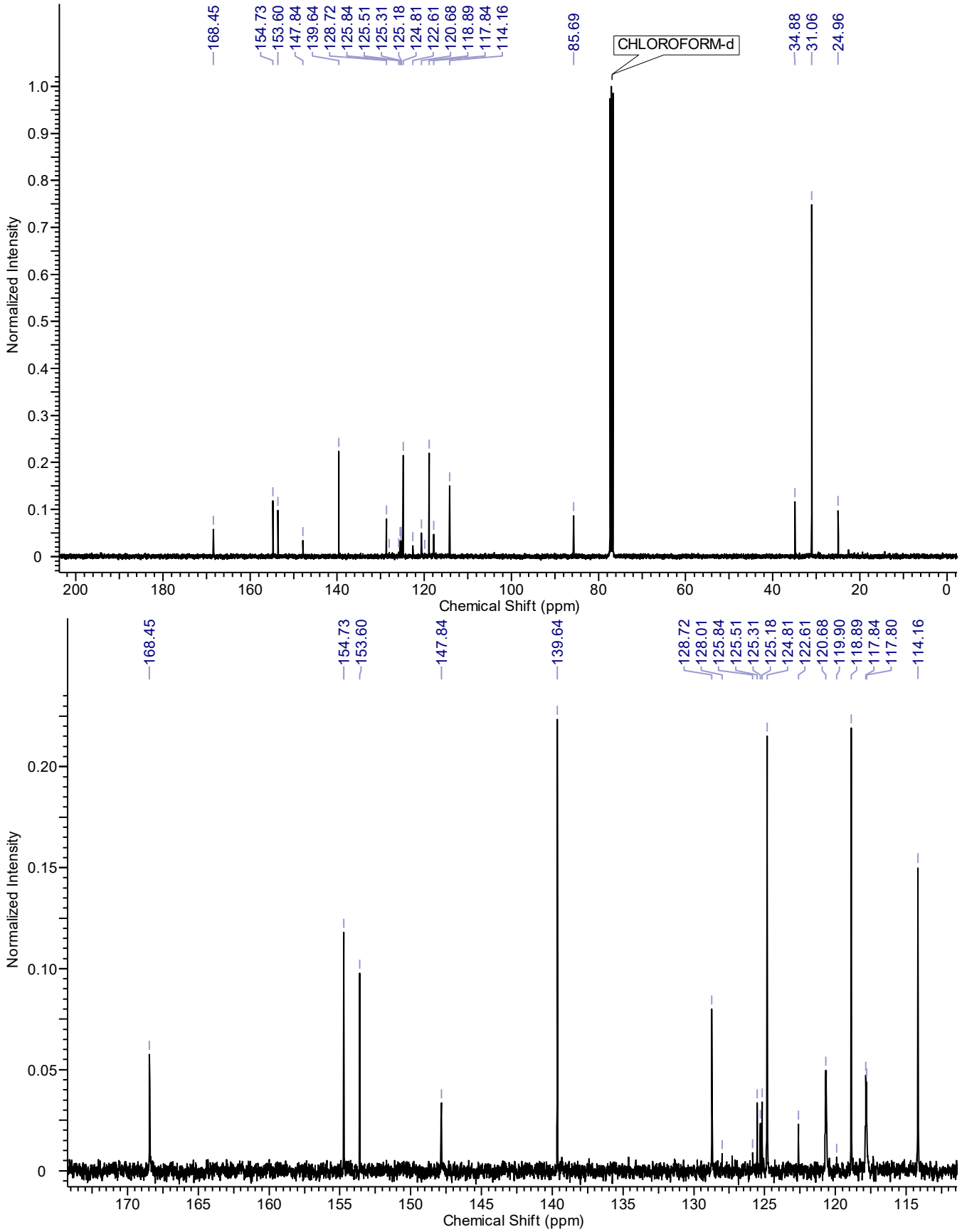


Figure S7.84. Full spectra (*top*) and aromatic region (*bottom*) ^{13}C NMR of N-(2-(5-(*tert*-butyl)-2-iodophenoxy)-5-(trifluoromethyl)phenyl)acetamide (**3.7b**) in $CDCl_3$.

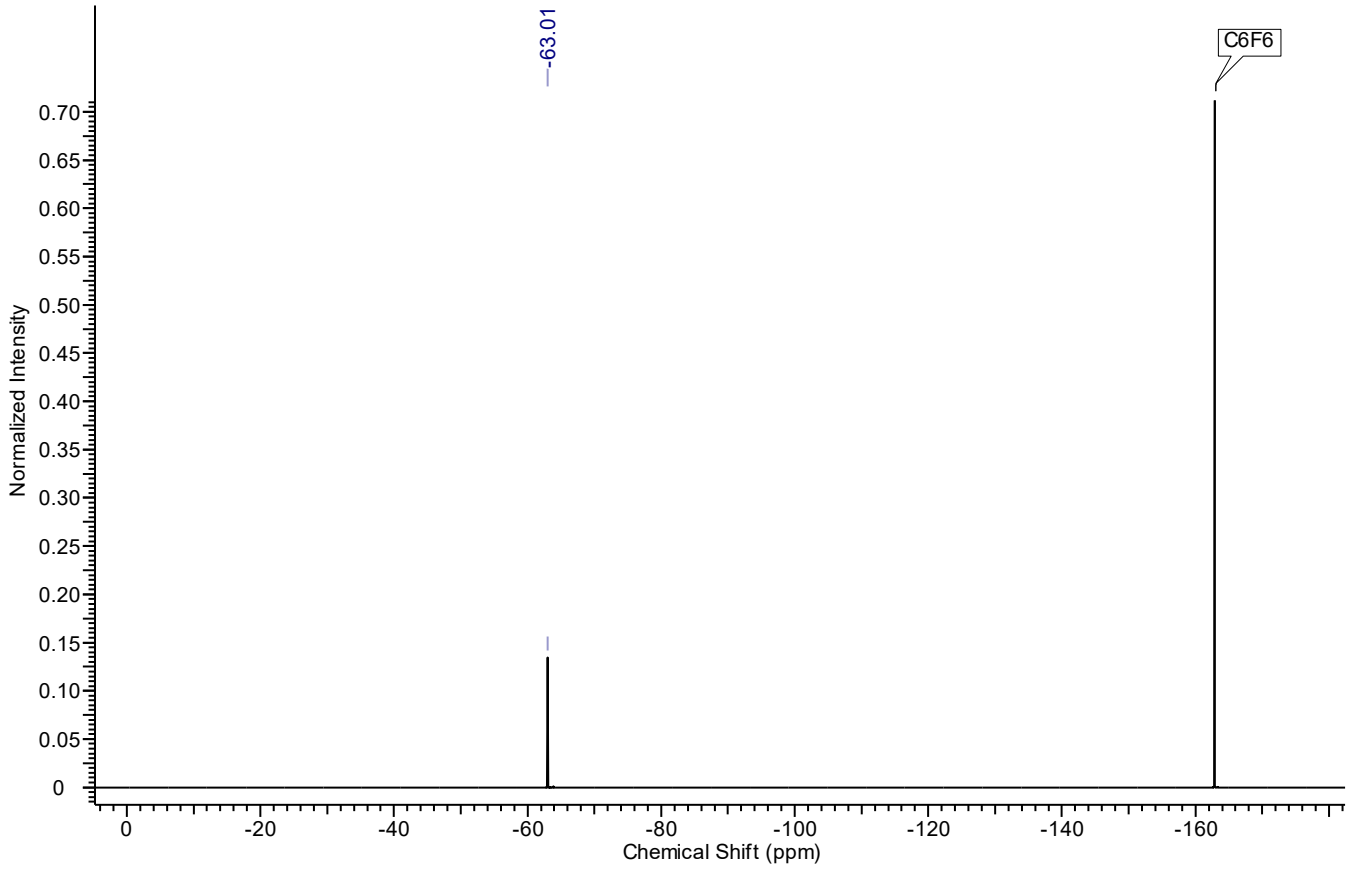


Figure S7.85. ^{19}F NMR spectra of N-(2-(5-(*tert*-butyl)-2-iodophenoxy)-5-(trifluoromethyl)phenyl)acetamide (**3.7b**) in $CDCl_3$.

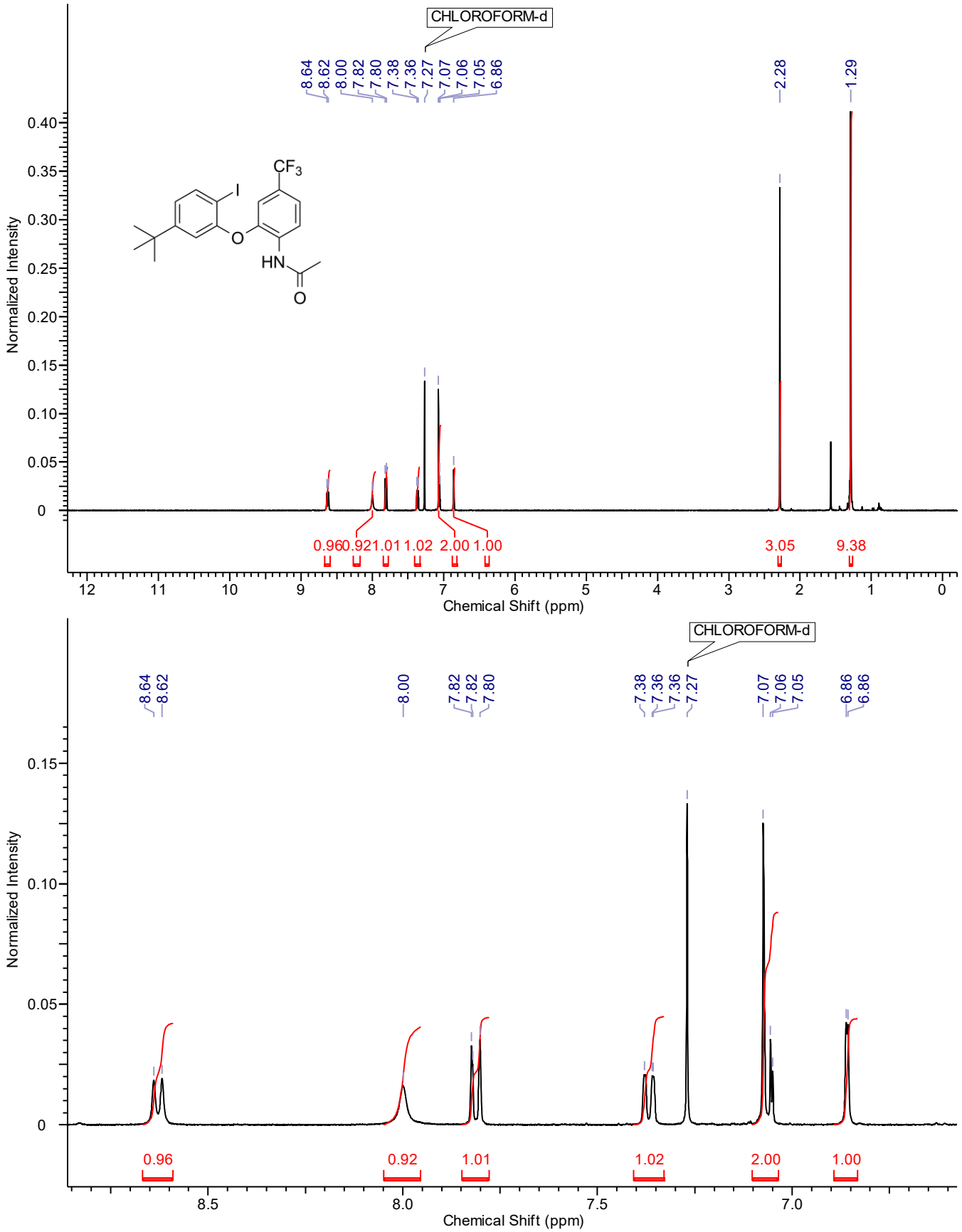


Figure S7.85. Full spectra (*top*) and aromatic region (*bottom*) ^{1}H NMR of N-(2-(5-(*tert*-butyl)-2-iodophenoxy)-4-(trifluoromethyl)phenyl)acetamide (**3.10b**) in $CDCl_3$.

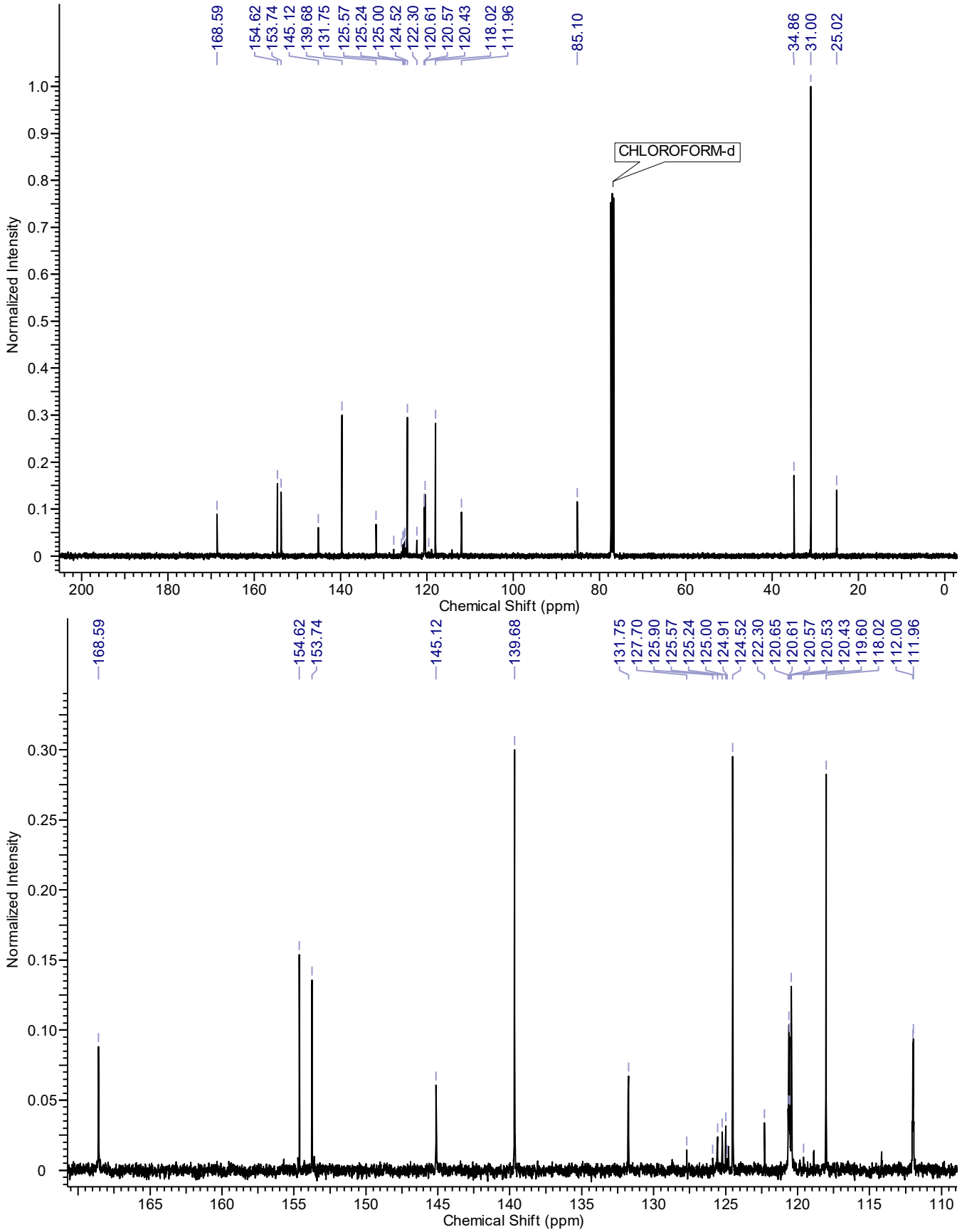


Figure S7.86. Full spectra (*top*) and aromatic region (*bottom*) ^{13}C NMR of N-(2-(5-(*tert*-butyl)-2-iodophenoxy)-4-(trifluoromethyl)phenyl)acetamide (**3.10b**) in $CDCl_3$.

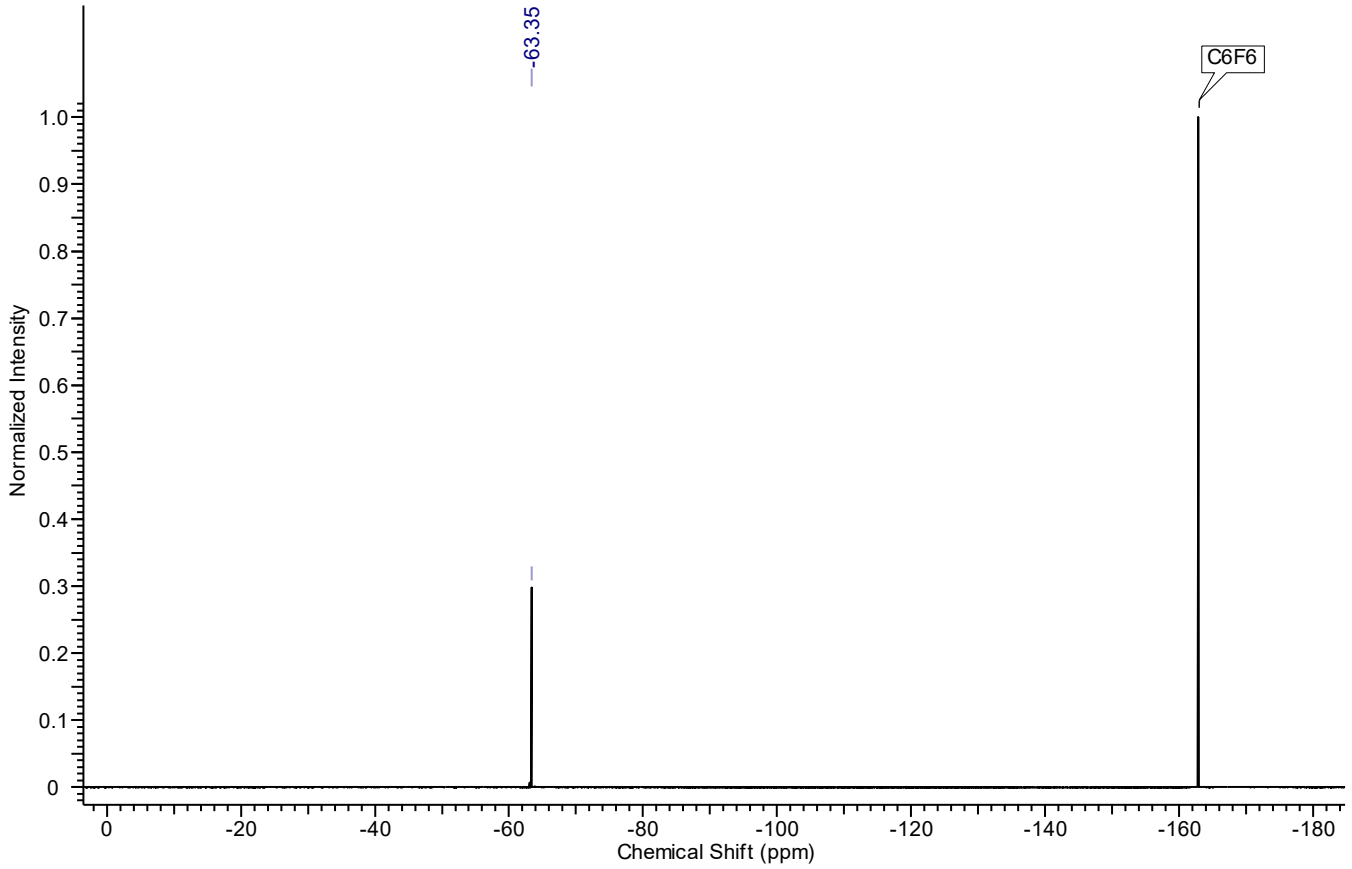


Figure S7.87. ^{19}F NMR spectra of N-(2-(5-(*tert*-butyl)-2-iodophenoxy)-4-(trifluoromethyl)phenyl)acetamide (**3.10b**) in $CDCl_3$.

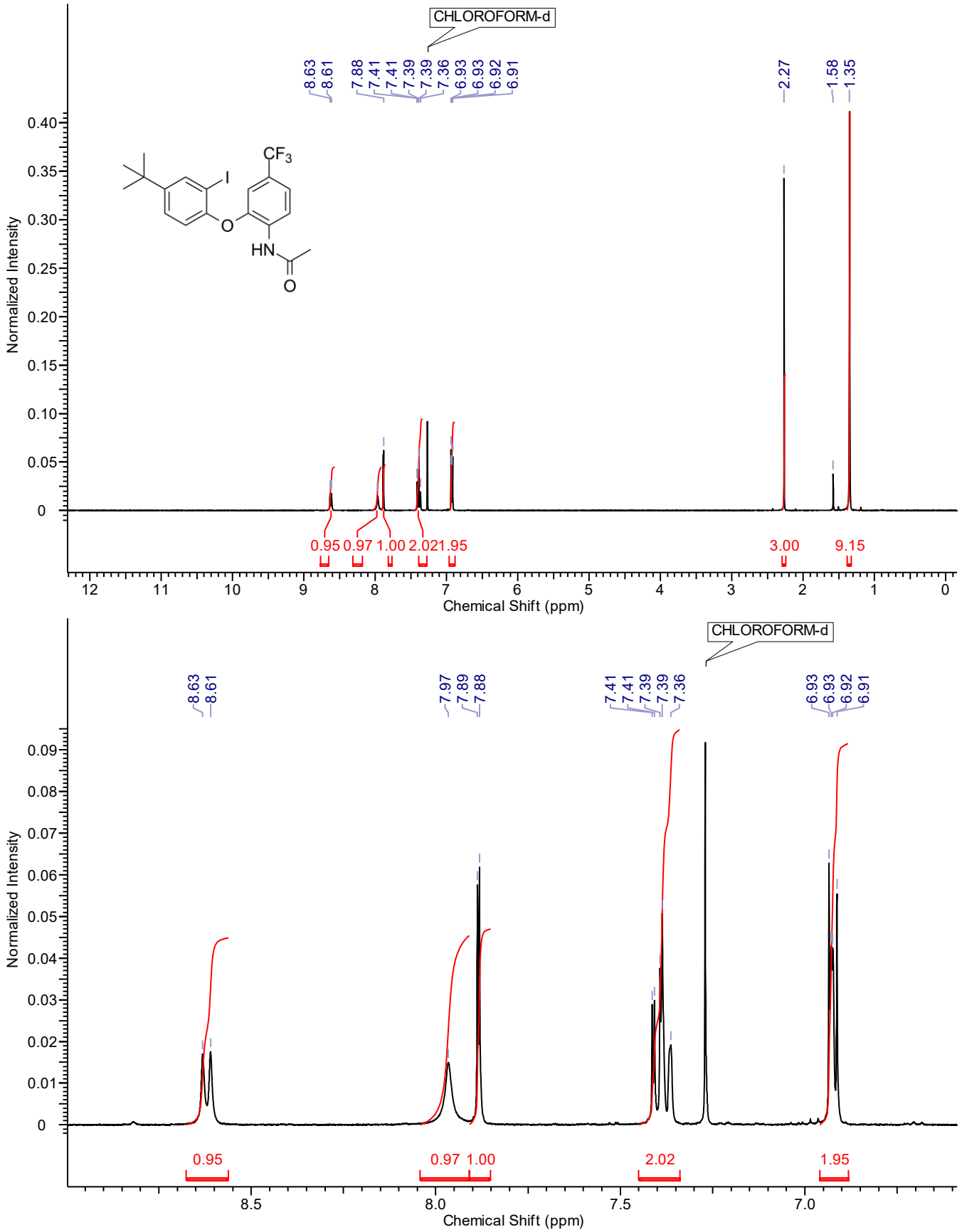


Figure S7.88. Full spectra (*top*) and aromatic region (*bottom*) ^{1}H NMR of N-(2-(4-(*tert*-butyl)-2-iodophenoxy)-4-(trifluoromethyl)phenyl)acetamide (**3.11b**) in $CDCl_3$.

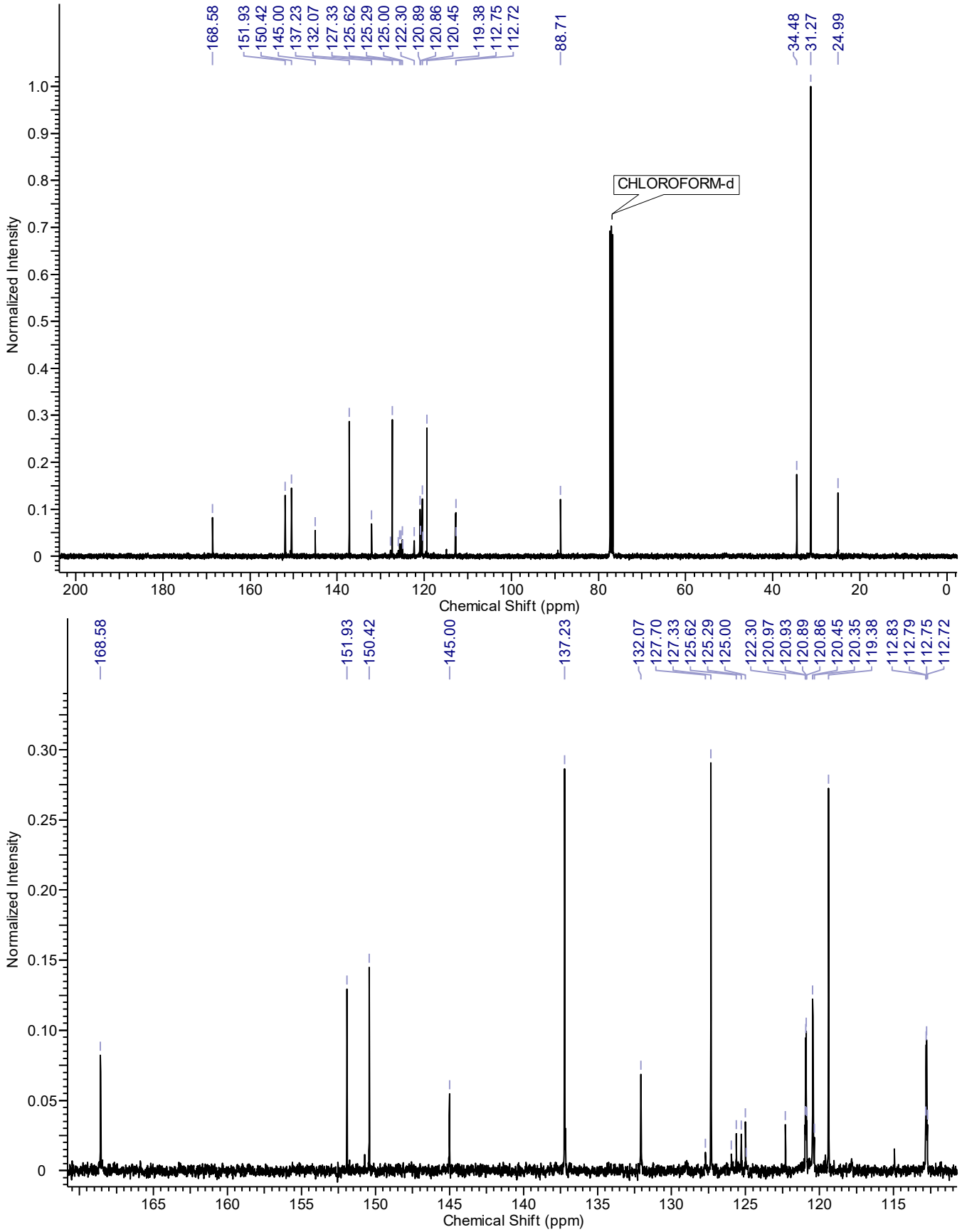


Figure S7.89. Full spectra (*top*) and aromatic region (*bottom*) ^{13}C NMR of N-(2-(4-(*tert*-butyl)-2-iodophenoxy)-4-(trifluoromethyl)phenyl)acetamide (**3.11b**) in $CDCl_3$.

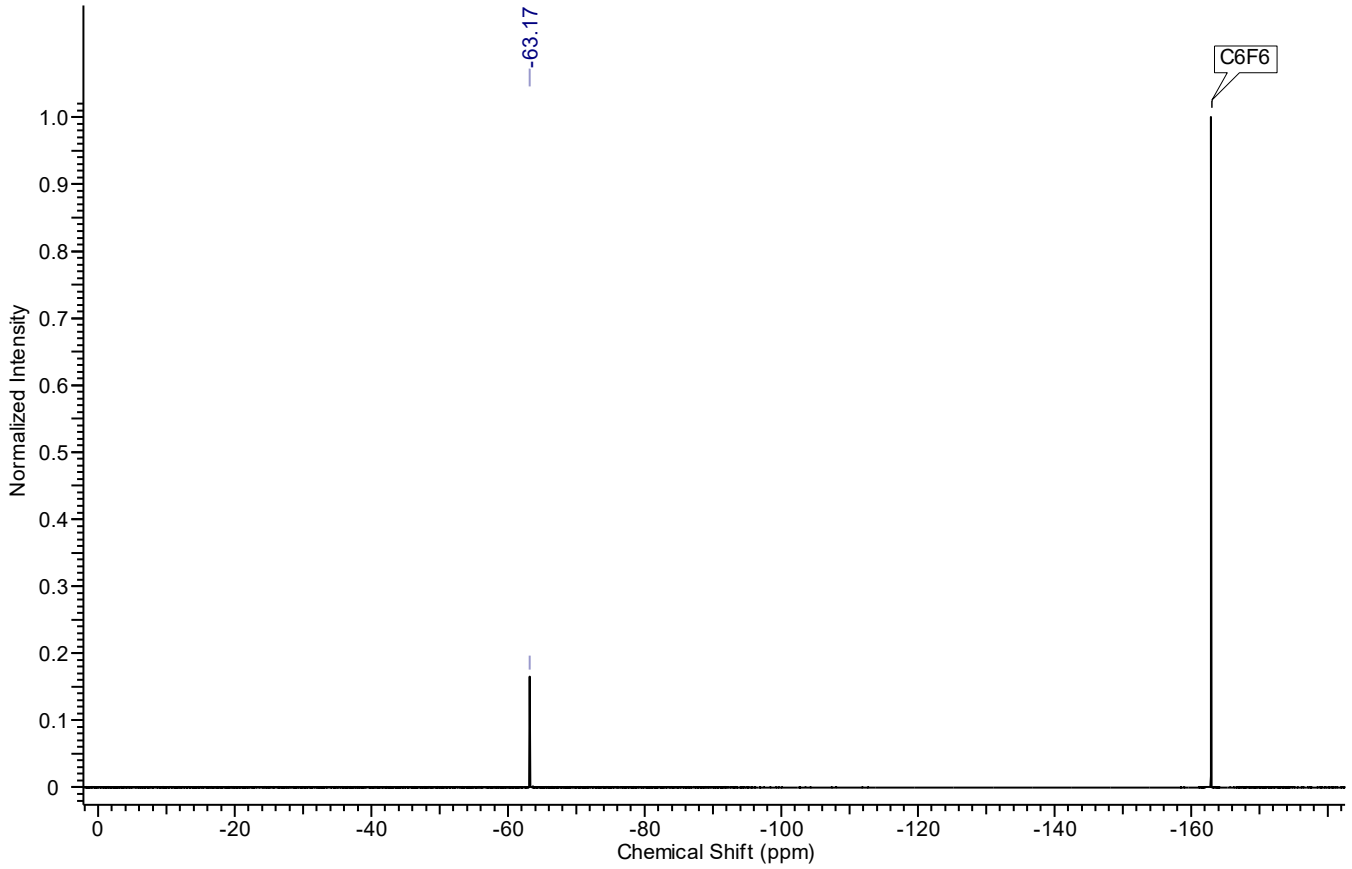
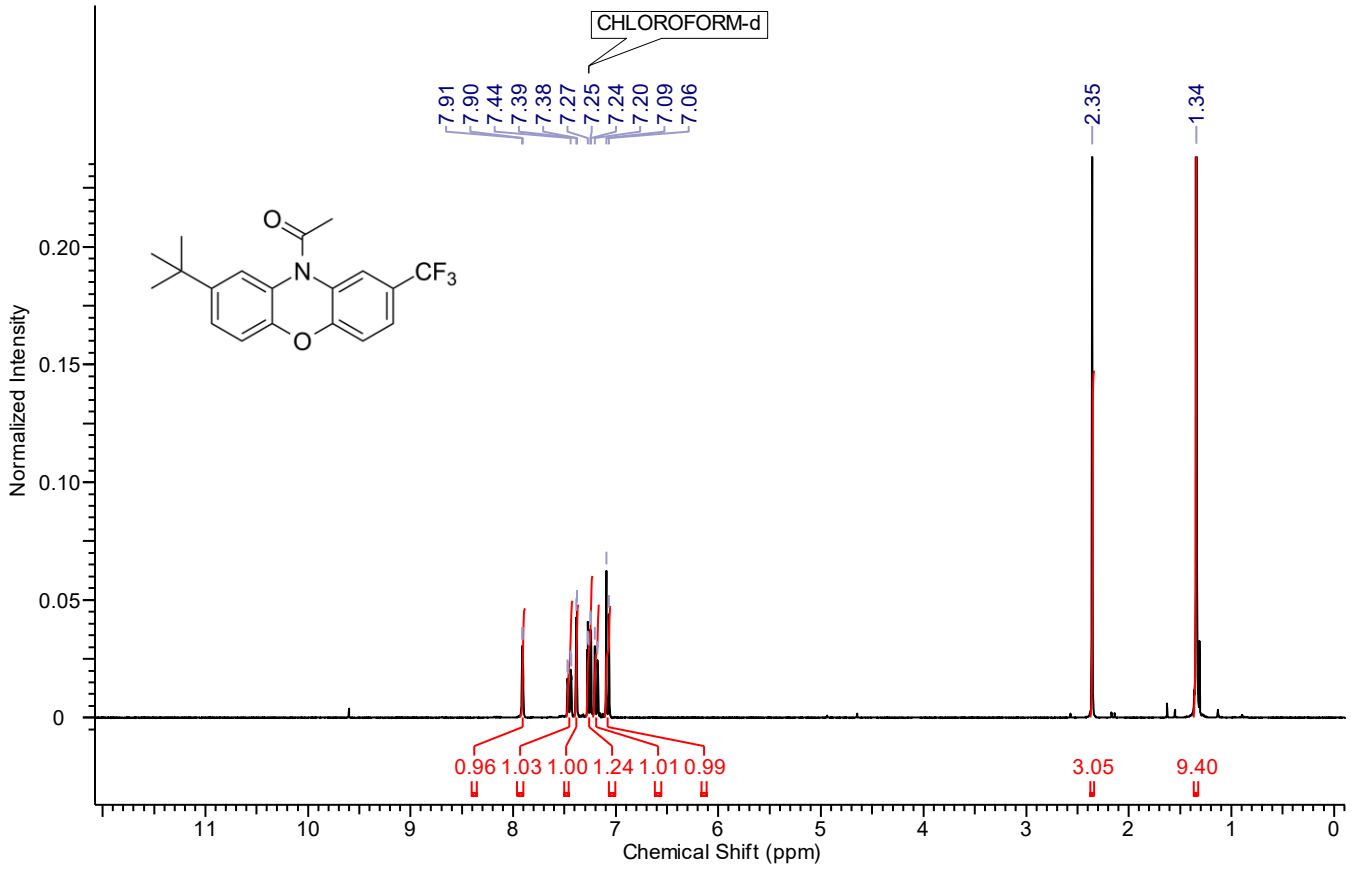


Figure S7.90. ^{19}F NMR spectra of N-(2-(4-(*tert*-butyl)-2-iodophenoxy)-4-(trifluoromethyl)phenyl)acetamide (**3.11b**) in $CDCl_3$.


CHLOROFORM-d
7.91
7.90
7.44
7.39
7.38
7.27
7.25
7.24
7.20
7.09
7.06
2.35
1.34
O
N
O
CF3
Normalized Intensity
0.20
0.15
0.10
0.05
0
0.96 1.03 1.00 1.24 1.01 0.99
3.05
9.40
11
10
9
8
7
6
5
4
3
2
1
0
Chemical Shift (ppm)

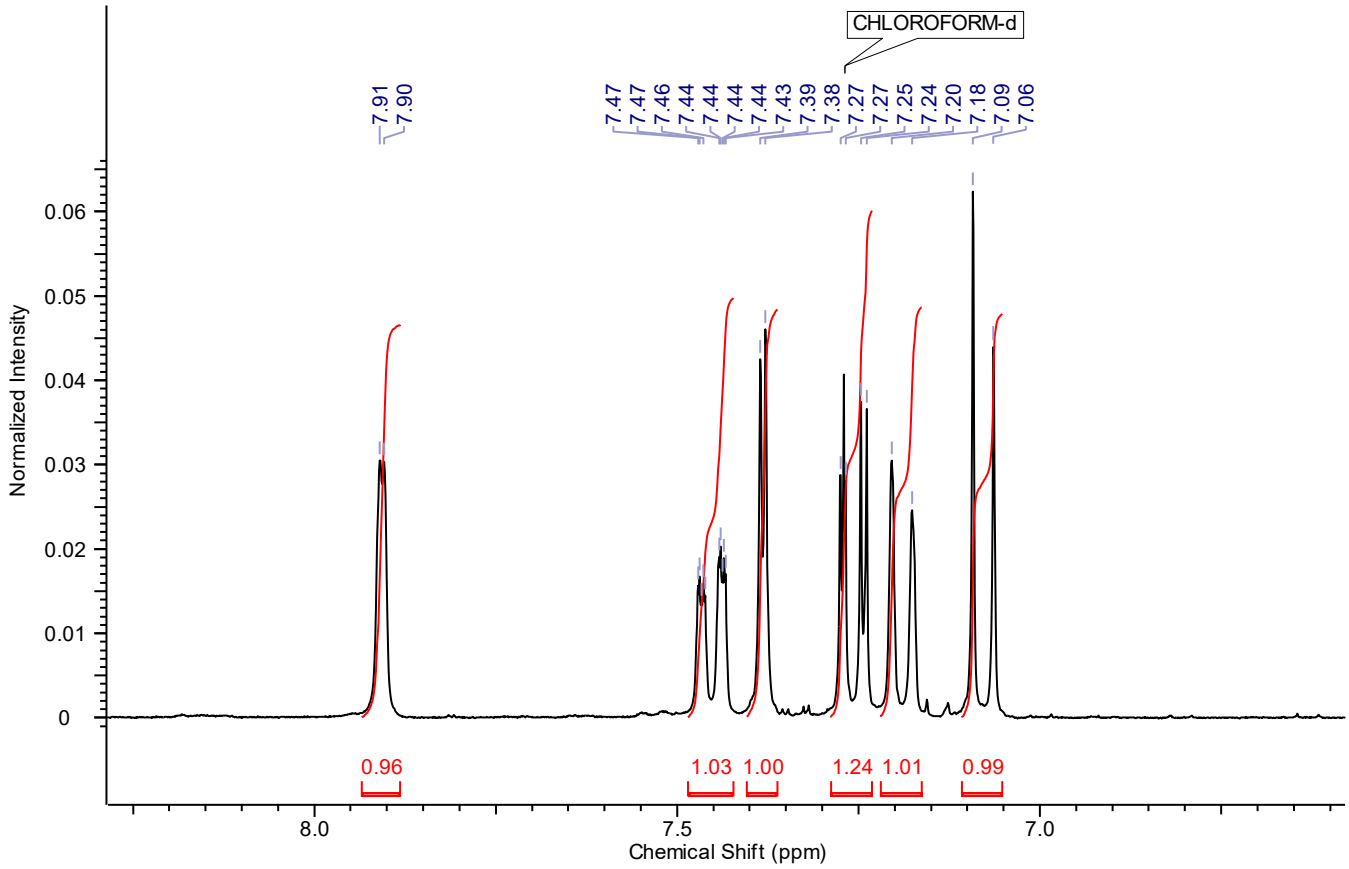
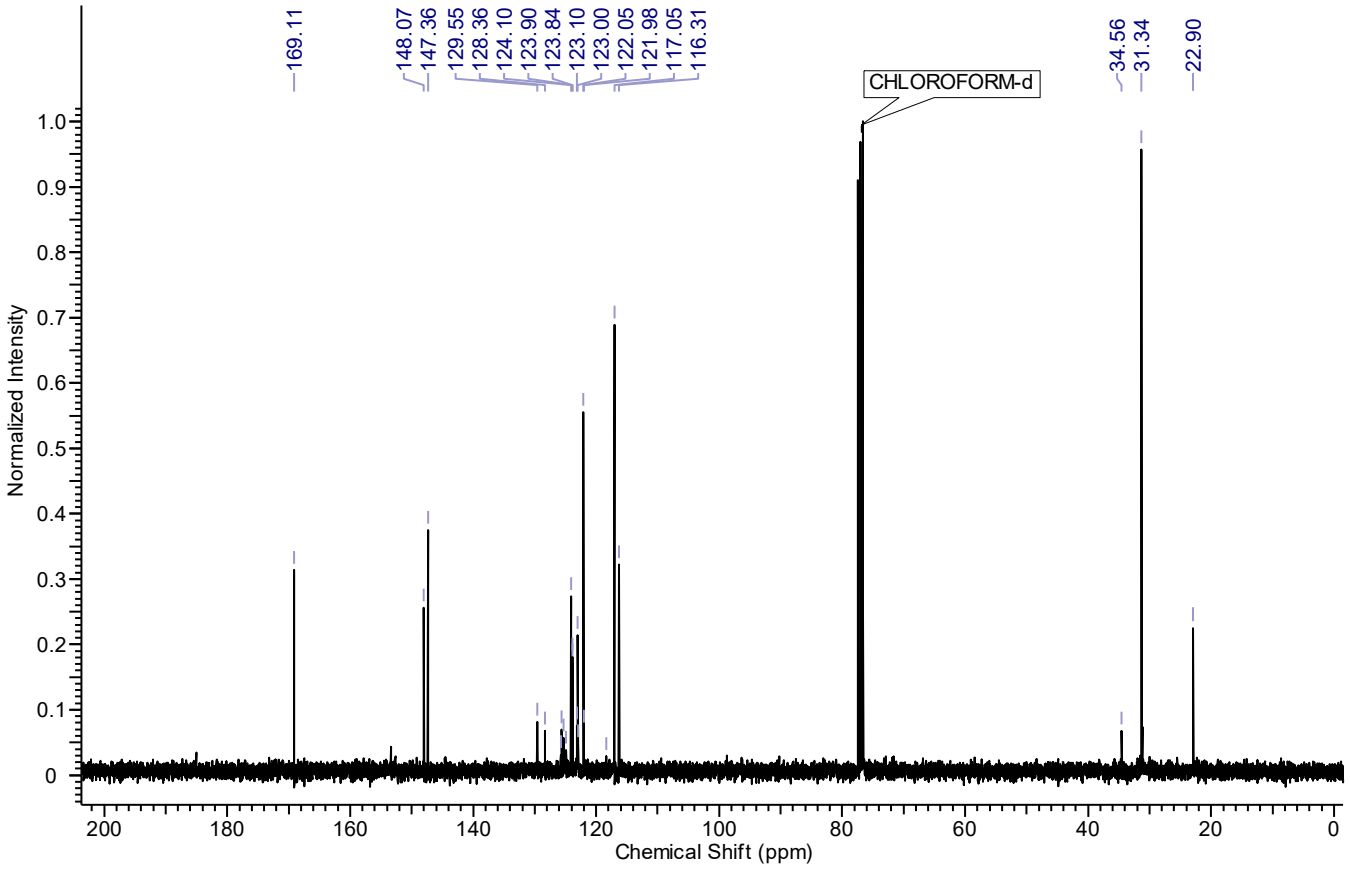


Figure S7.91. Full spectra (*top*) and aromatic region (*bottom*) ^{1}H NMR of 10-acetyl-2-*tert*-butyl-8-trifluoromethylphenoxazine (**3.8c**) in $CDCl_3$.


169.11
148.07
147.36
129.55
128.36
124.10
123.90
123.84
123.10
123.00
122.05
121.98
117.05
116.31
CHLOROFORM-d
34.56
31.34
22.90
Normalized Intensity
1.0
0.9
0.8
0.7
0.6
0.5
0.4
0.3
0.2
0.1
0
200
180
160
140
120
100
80
60
40
20
0
Chemical Shift (ppm)

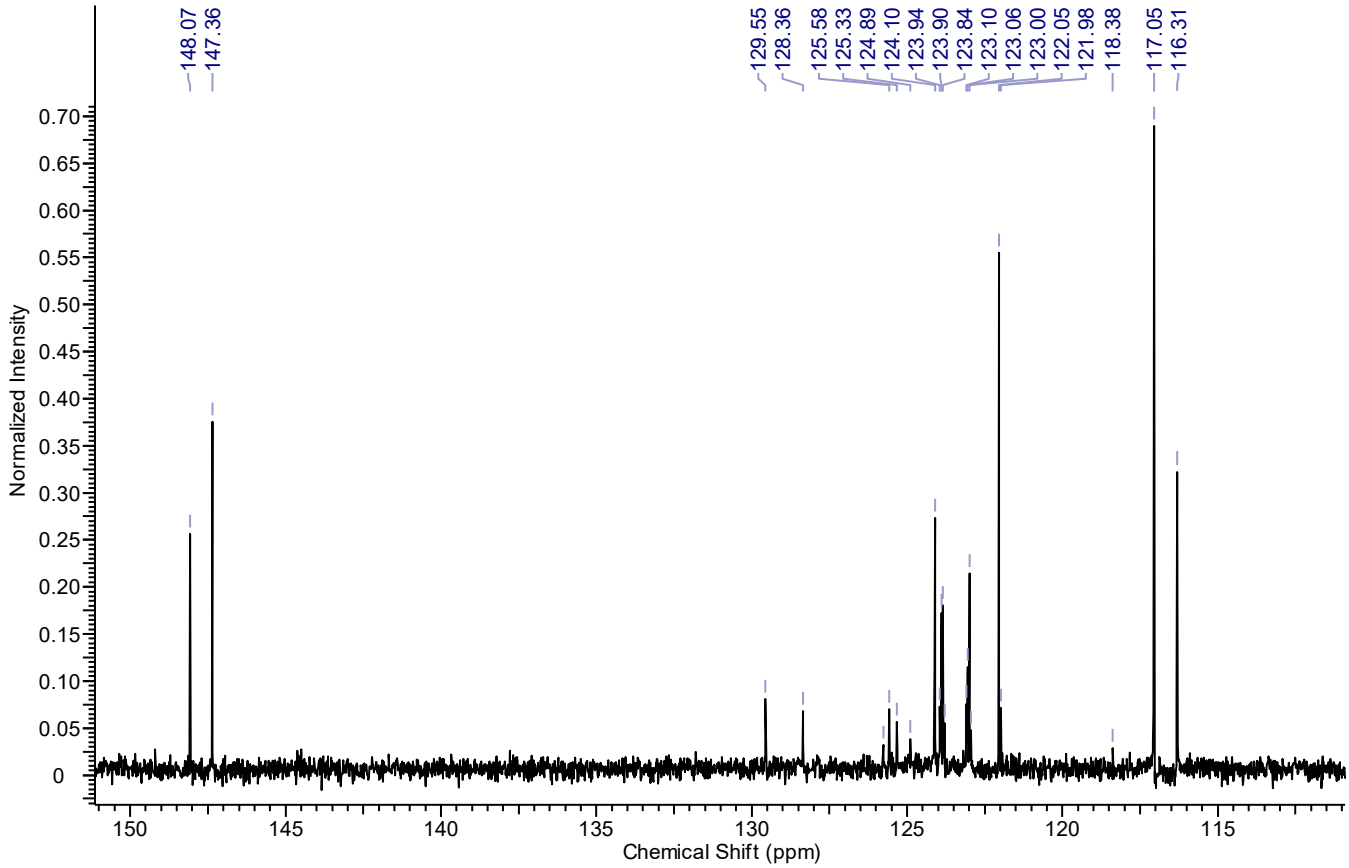


Figure S7.92. Full spectra (*top*) and aromatic region (*bottom*) ^{13}C NMR of 10-acetyl-2-*tert*-butyl-8-trifluoromethylphenoxazine (**3.8c**) in $CDCl_3$.

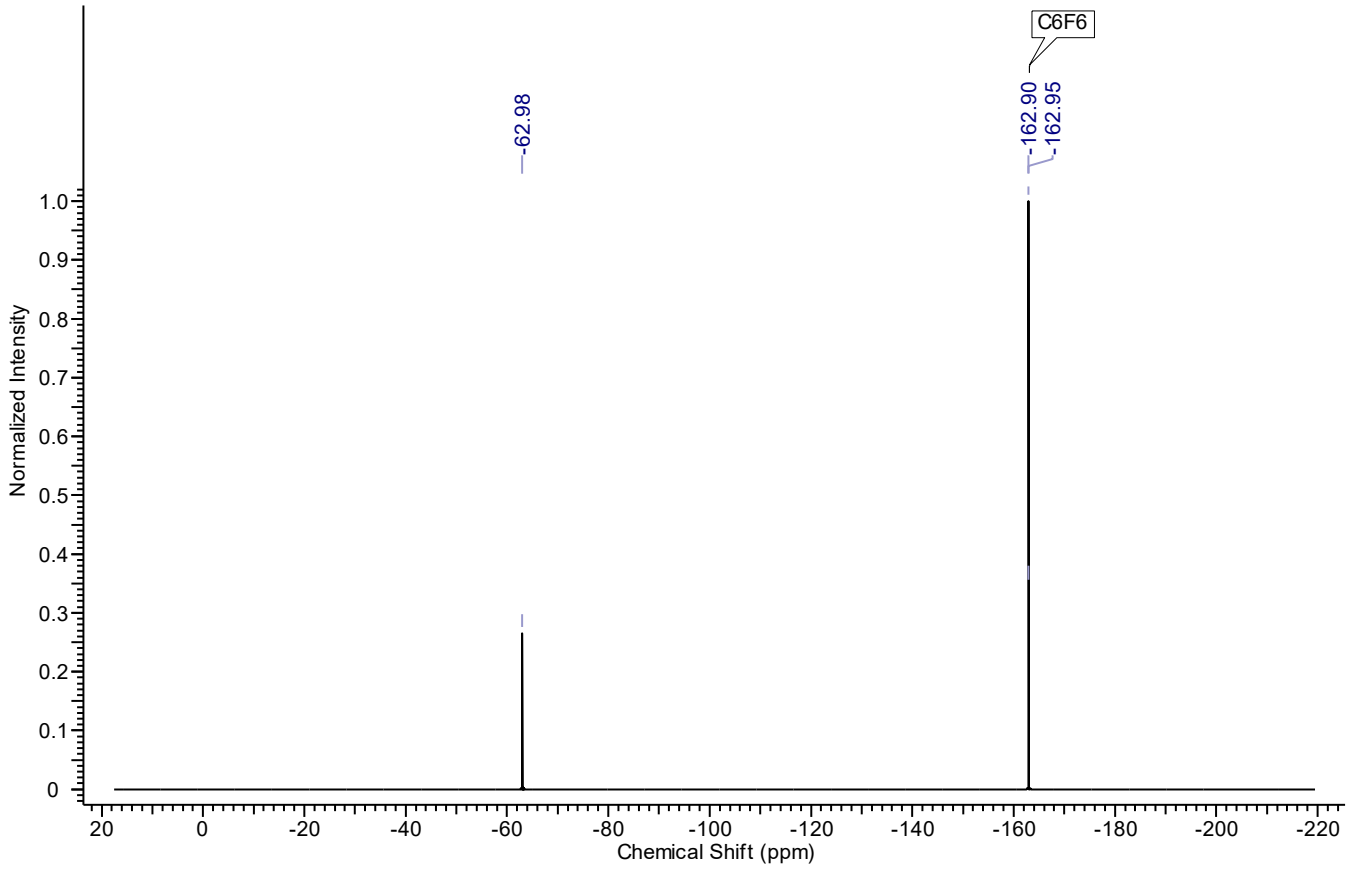
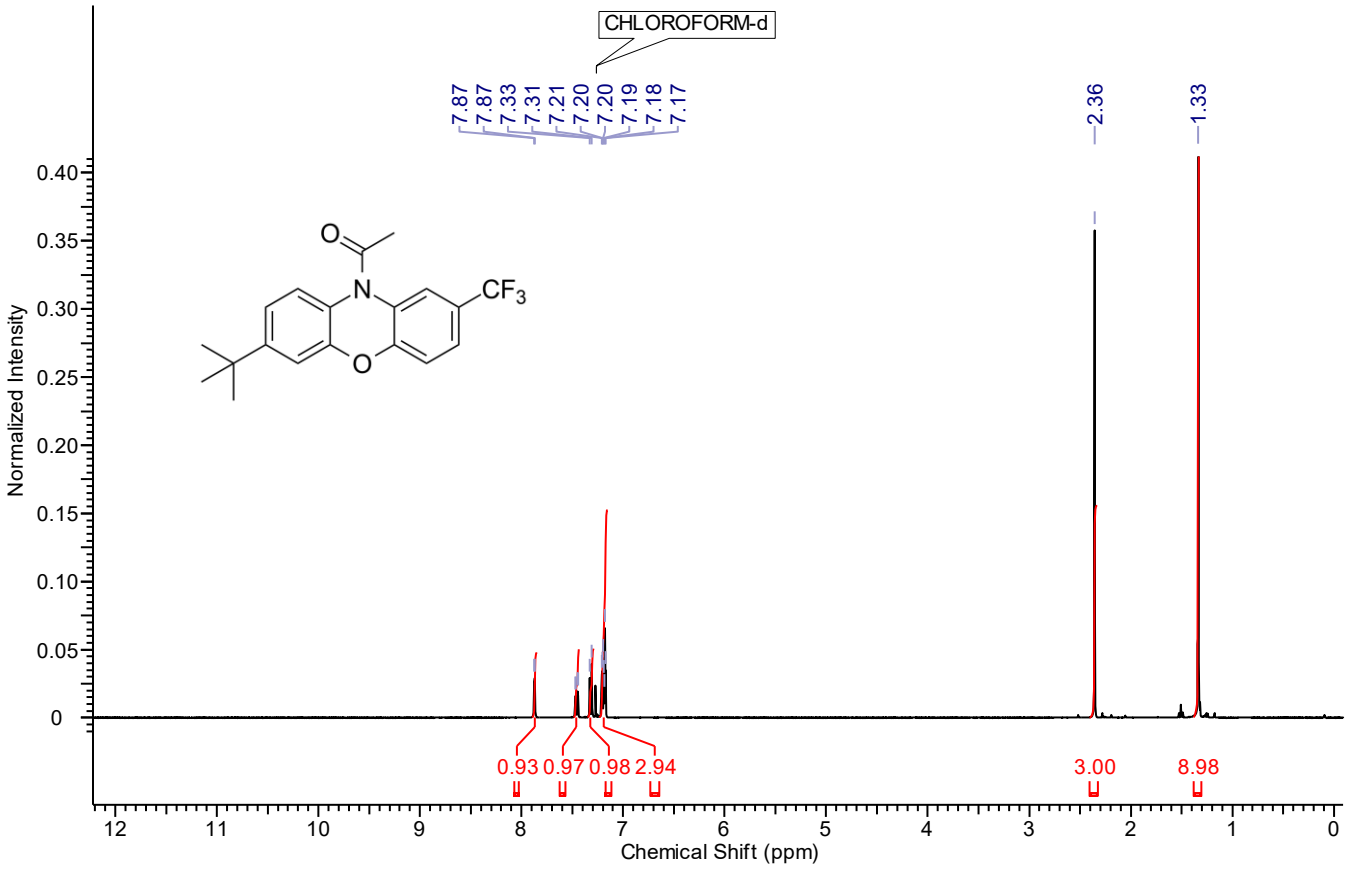


Figure S7.93. ^{19}F NMR spectra of 10-acetyl-2-*tert*-butyl-8-trifluoromethylphenoxazine (**3.8c**) in $CDCl_3$.


CHLOROFORM-d
7.87
7.87
7.33
7.31
7.21
7.20
7.20
7.19
7.18
7.17
2.36
1.33
O
N
CF3
O
Normalized Intensity
0.40
0.35
0.30
0.25
0.20
0.15
0.10
0.05
0
0.93
0.97
0.98
2.94
3.00
8.98
12
11
10
9
8
7
6
5
4
3
2
1
0
Chemical Shift (ppm)

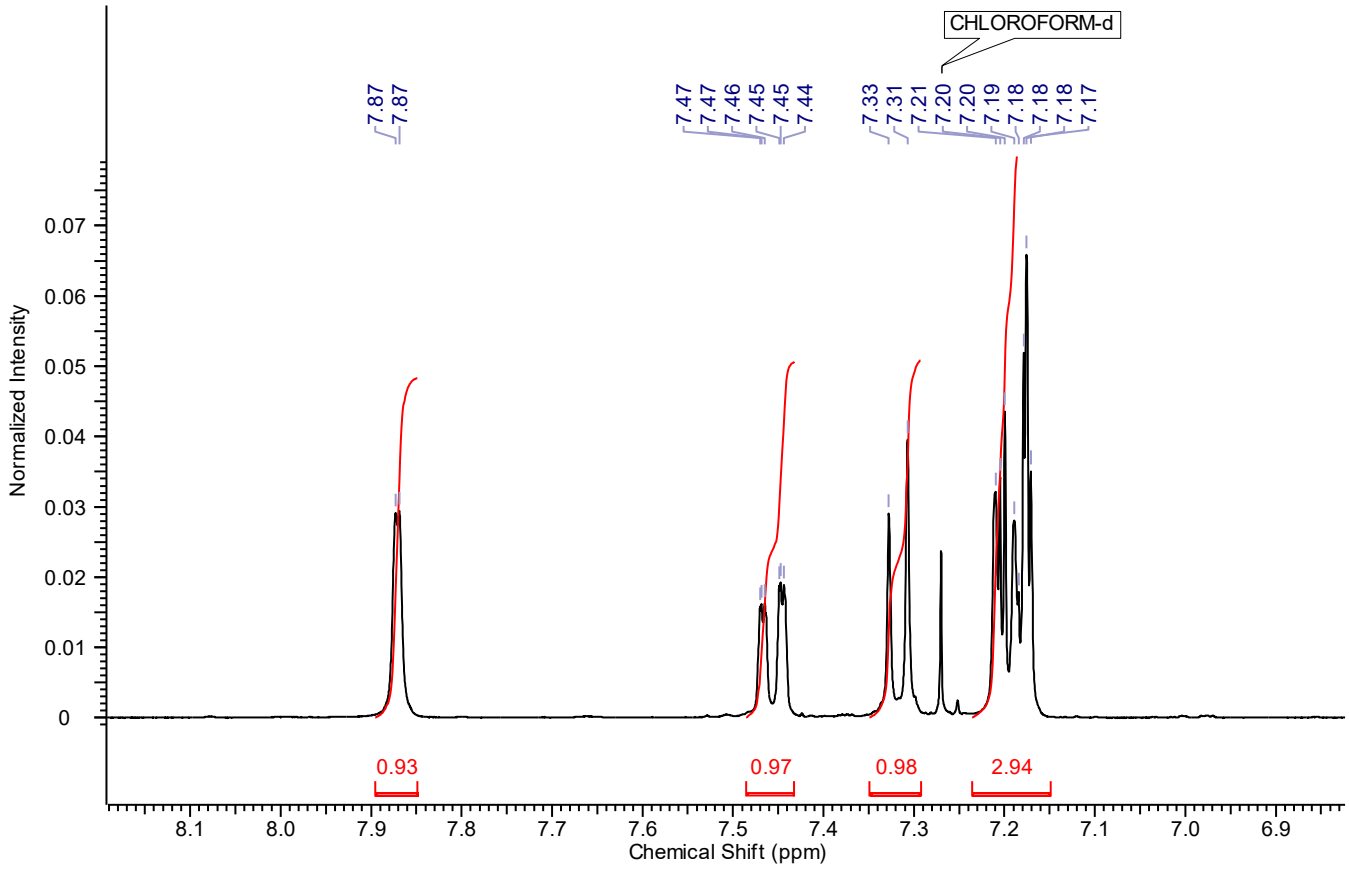


Figure S7.94. Full spectra (*top*) and aromatic region (*bottom*) ^{1}H NMR of 10-acetyl-3-*tert*-butyl-8-trifluoromethylphenoxazine (**3.7c**) in $CDCl_3$.

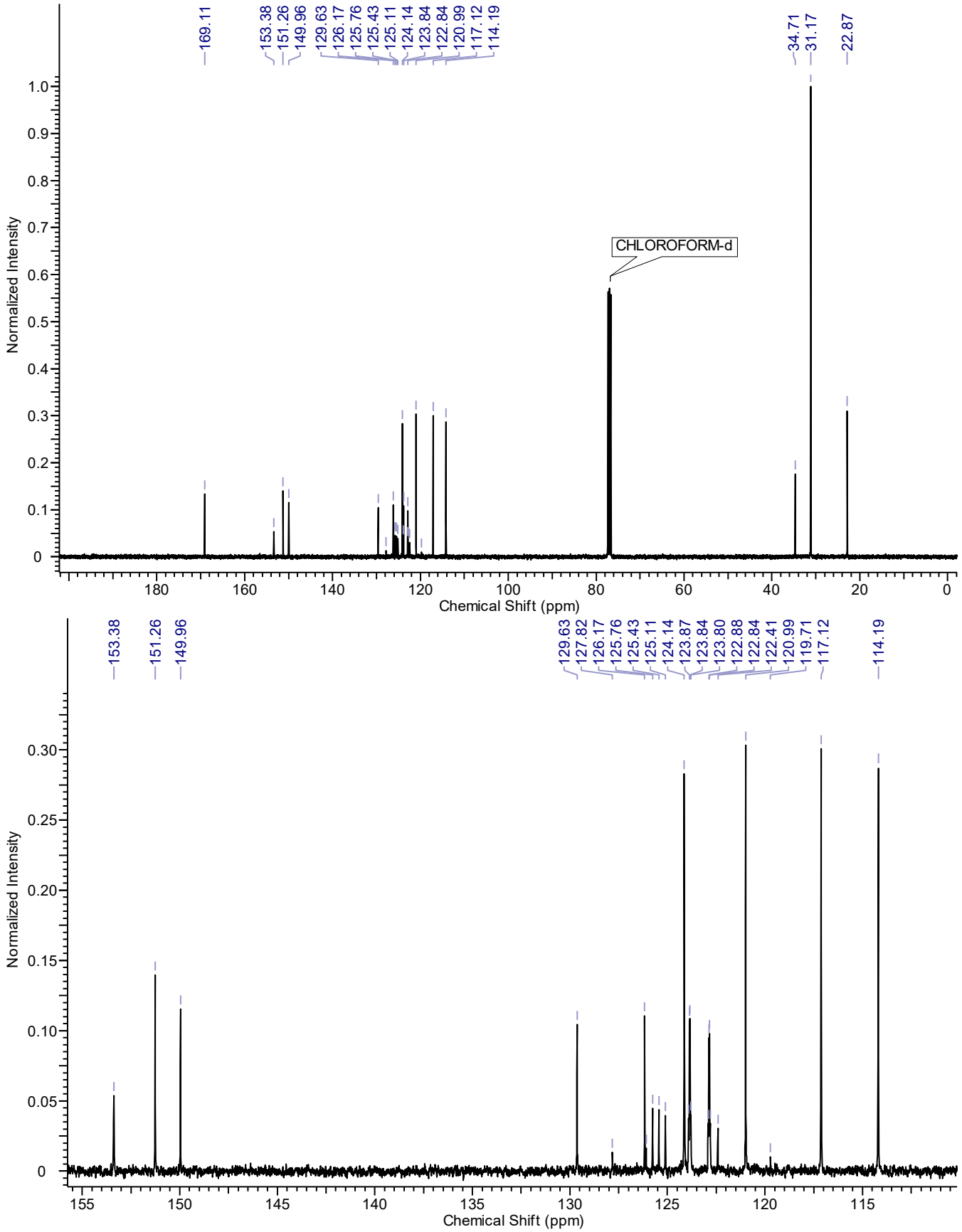


Figure S7.95. Full spectra (*top*) and aromatic region (*bottom*) ^{13}C NMR of 10-acetyl-3-*tert*-butyl-8-trifluoromethylphenoxazine (**3.7c**) in $CDCl_3$.

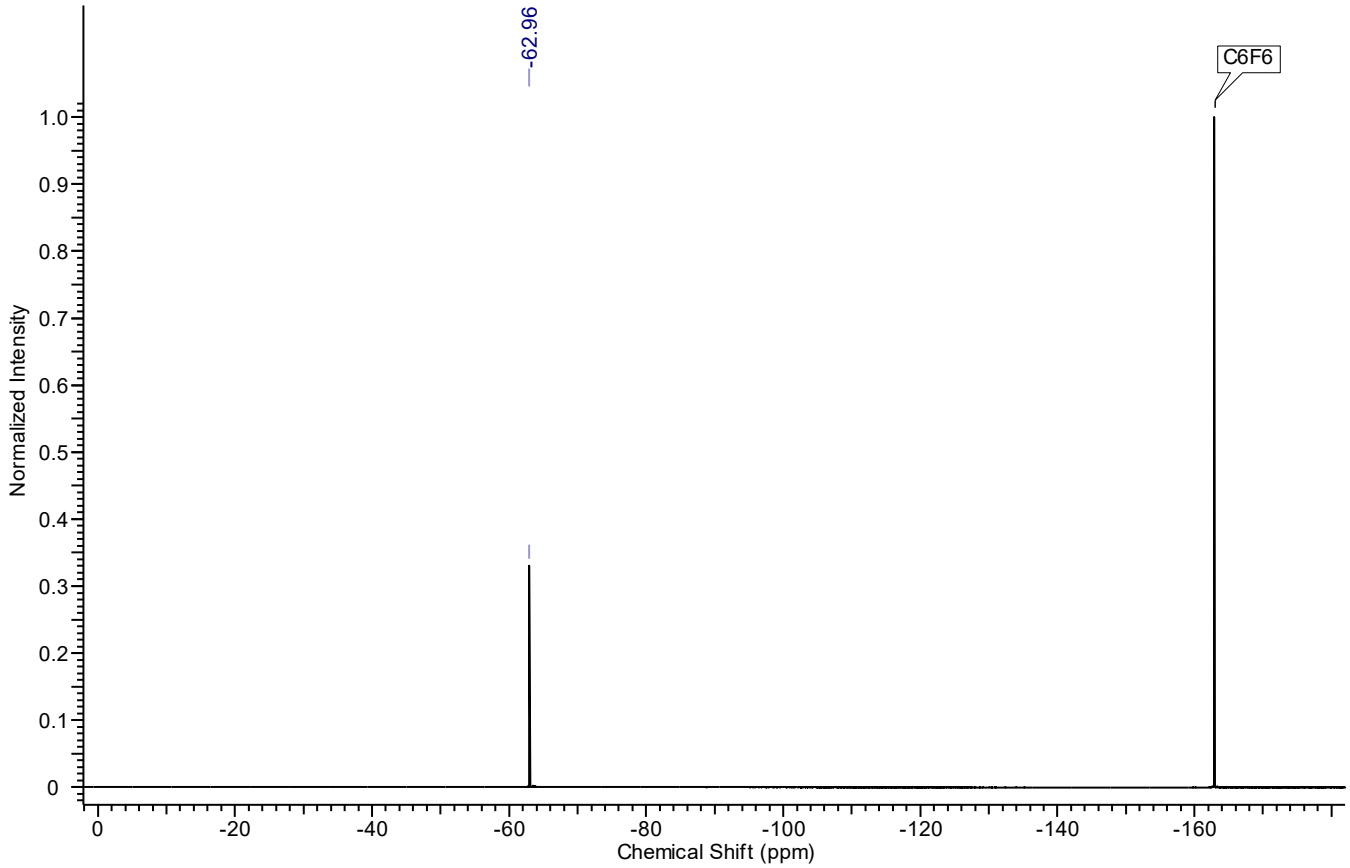


Figure S7.96. ^{19}F NMR spectra of 10-acetyl-3-*tert*-butyl-8-trifluoromethylphenoxazine (**3.7c**) in $CDCl_3$.

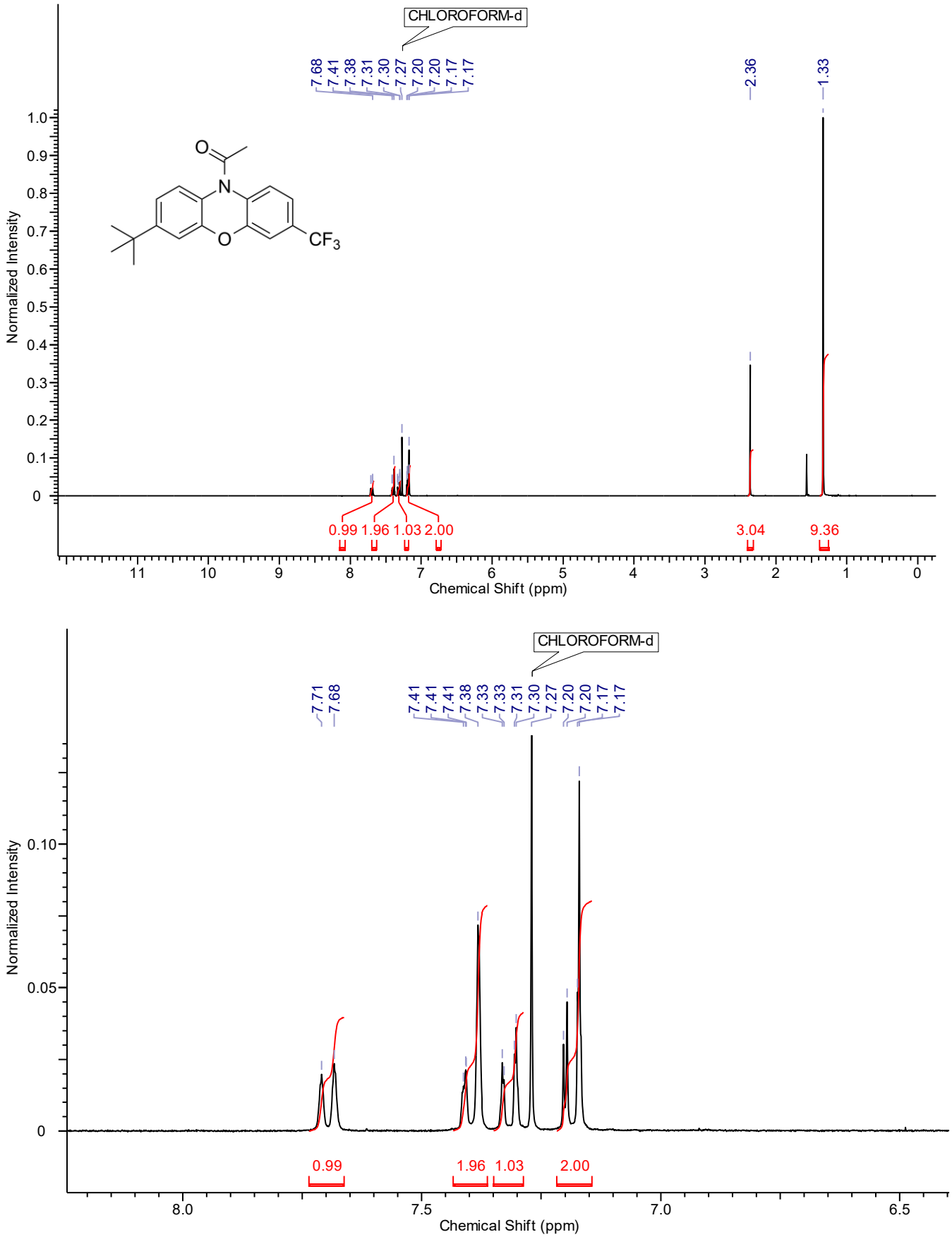


Figure S7.96. Full spectra (*top*) and aromatic region (*bottom*) ^{1}H NMR of 10-acetyl-3-*tert*-butyl-7-trifluoromethylphenoxazine (**3.10c**) in $CDCl_3$.

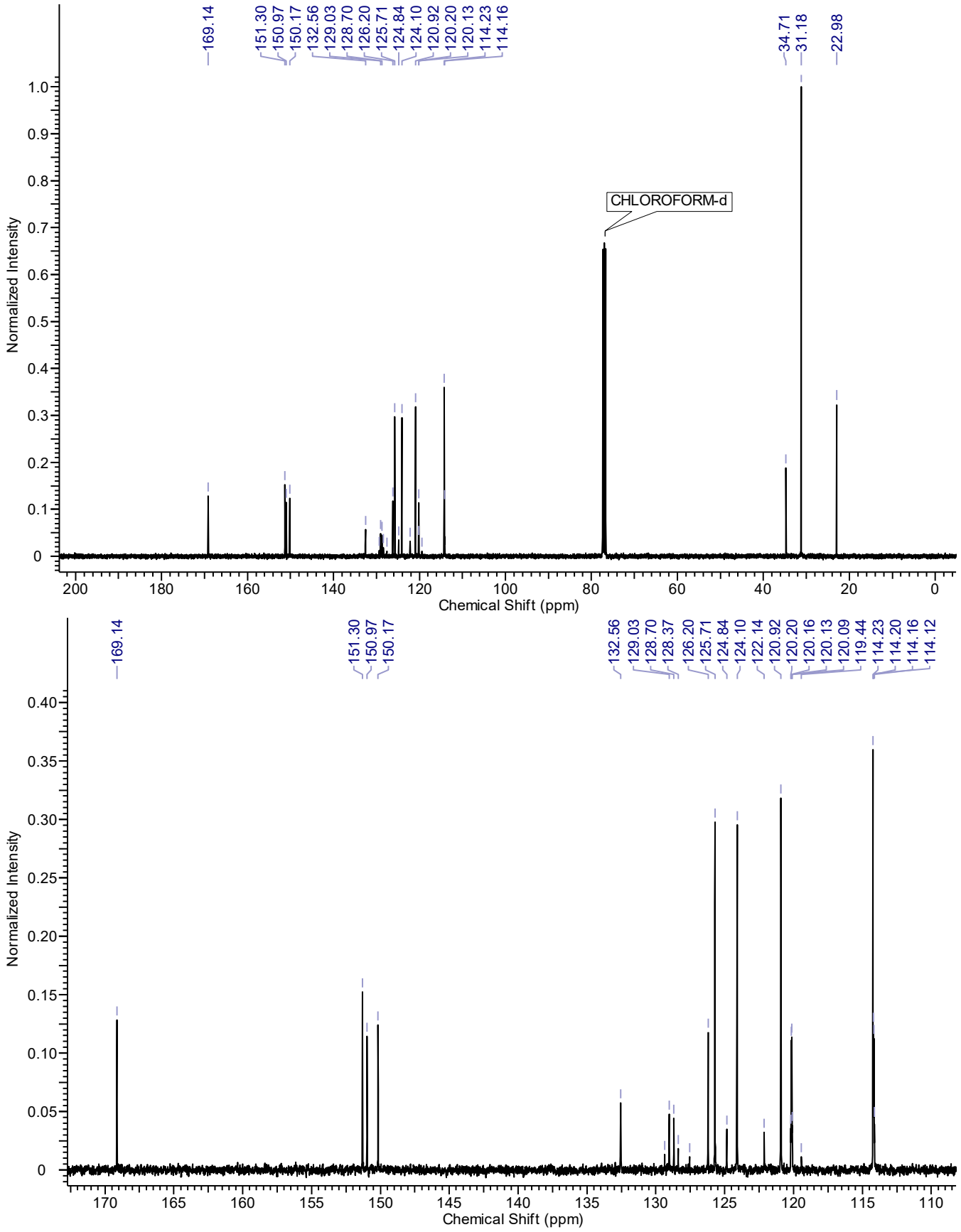


Figure S7.97. Full spectra (*top*) and aromatic region (*bottom*) ^{13}C NMR of 10-acetyl-3-*tert*-butyl-7-trifluoromethylphenoxazine (**3.10c**) in $CDCl_3$.

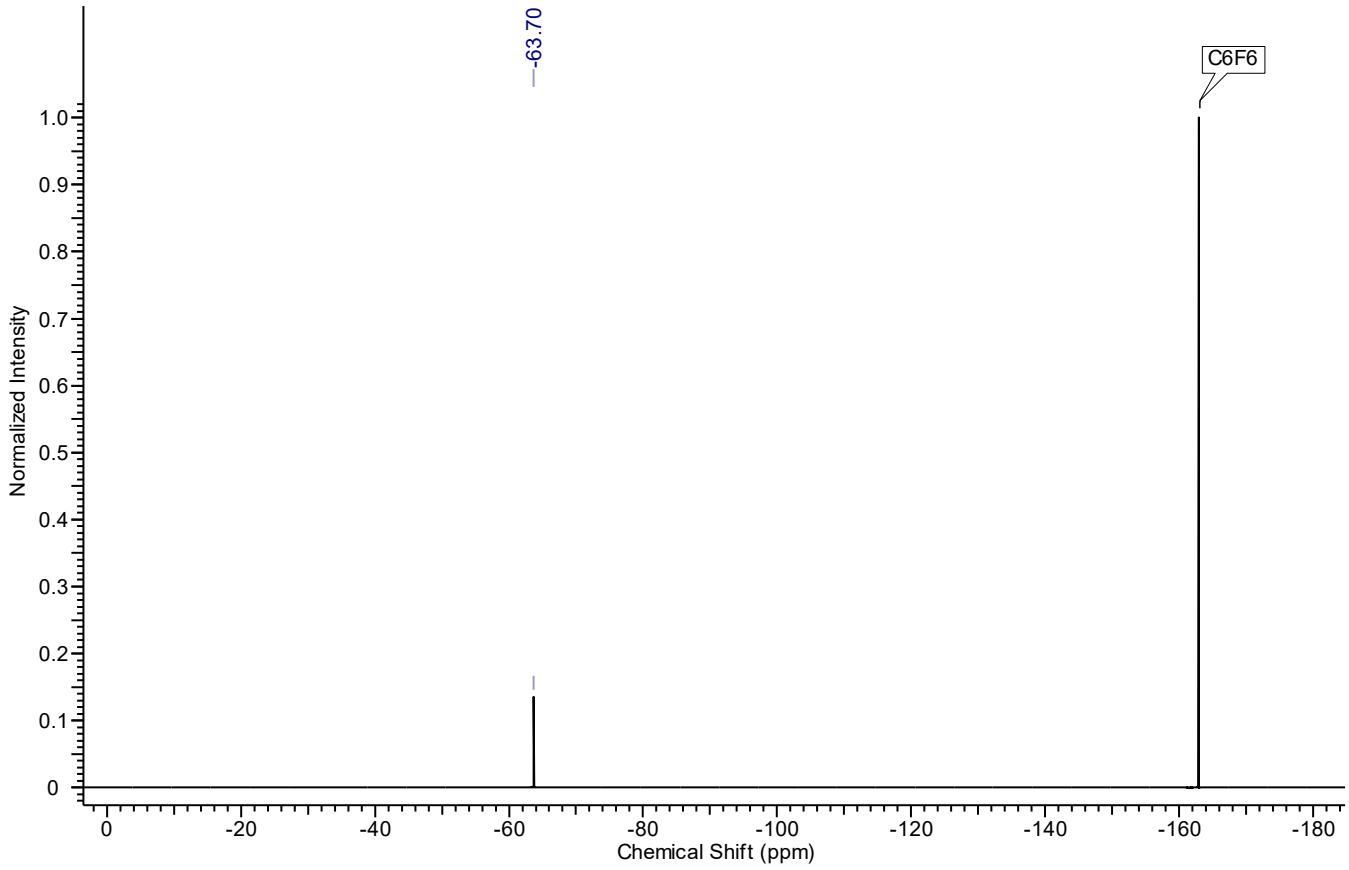


Figure S7.98. ^{19}F NMR spectra of 10-acetyl-3-*tert*-butyl-7-trifluoromethylphenoxazine (**3.10c**) in $CDCl_3$.

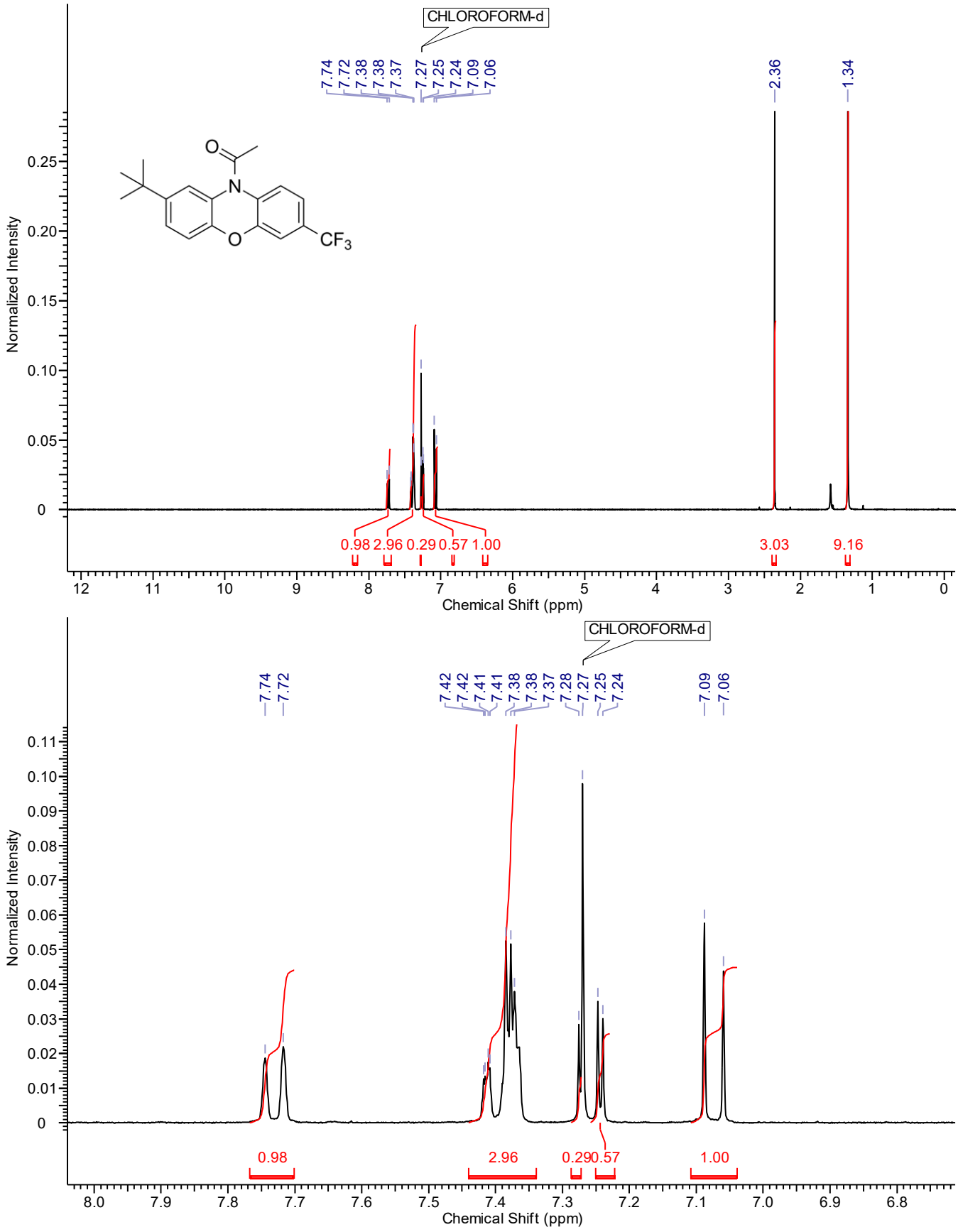


Figure S7.99. Full spectra (*top*) and aromatic region (*bottom*) ^{1}H NMR of 10-acetyl-2-*tert*-butyl-7-trifluoromethylphenoxazine (**3.11c**) in $CDCl_3$.

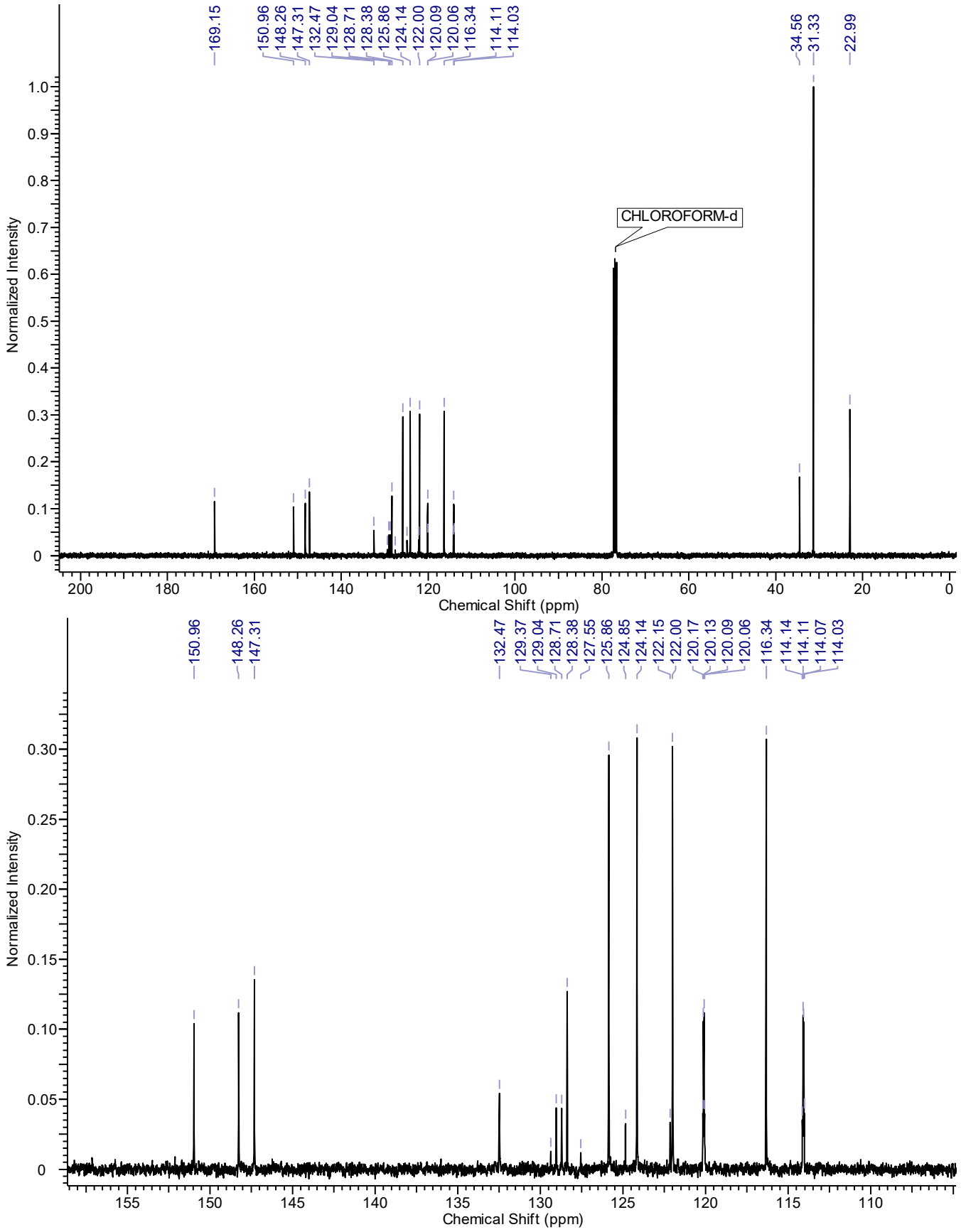


Figure S7.100. Full spectra (*top*) and aromatic region (*bottom*) ^{13}C NMR of 10-acetyl-2-*tert*-butyl-7-trifluoromethylphenoxazine (**3.11c**) in $CDCl_3$.

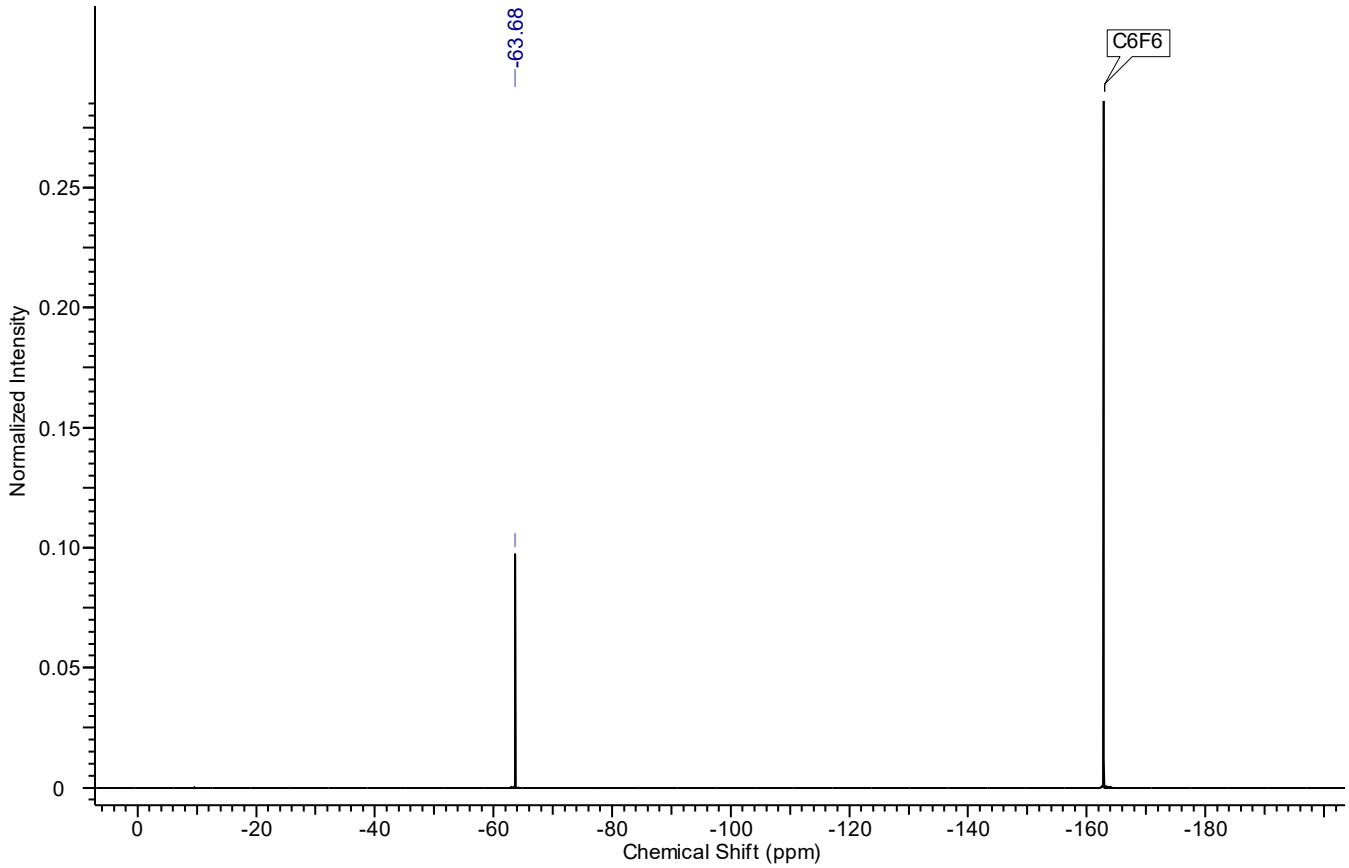


Figure S7.101. ^{19}F NMR spectra of 10-acetyl-2-*tert*-butyl-7-trifluoromethylphenoxazine (**3.11c**) in $CDCl_3$.

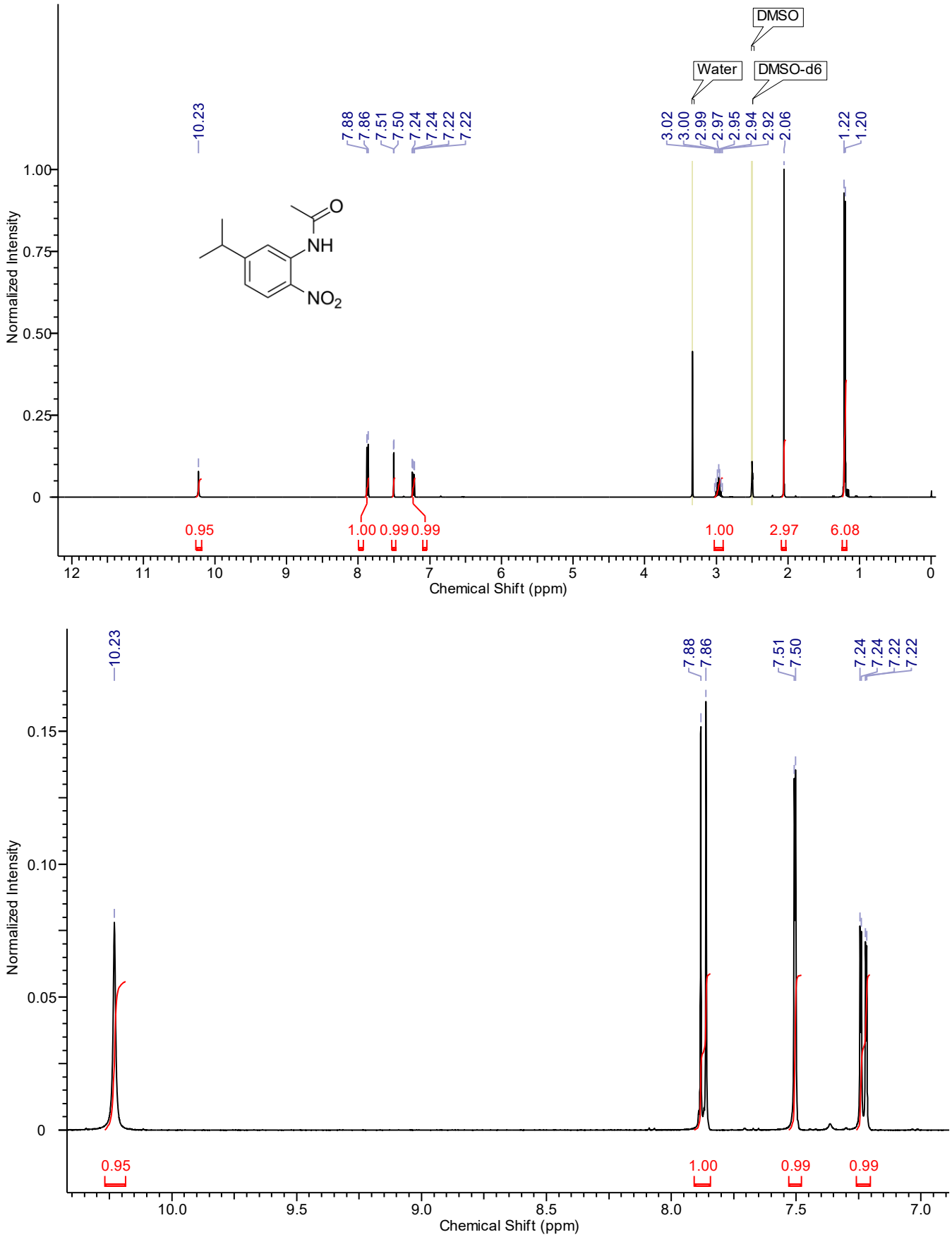


Figure S7.102. Full spectra (*top*) and aromatic region (*bottom*) ^{1}H NMR of *N*-(5-isopropyl-2-nitrophenyl)acetamide (**3.42a**) in DMSO-d6.

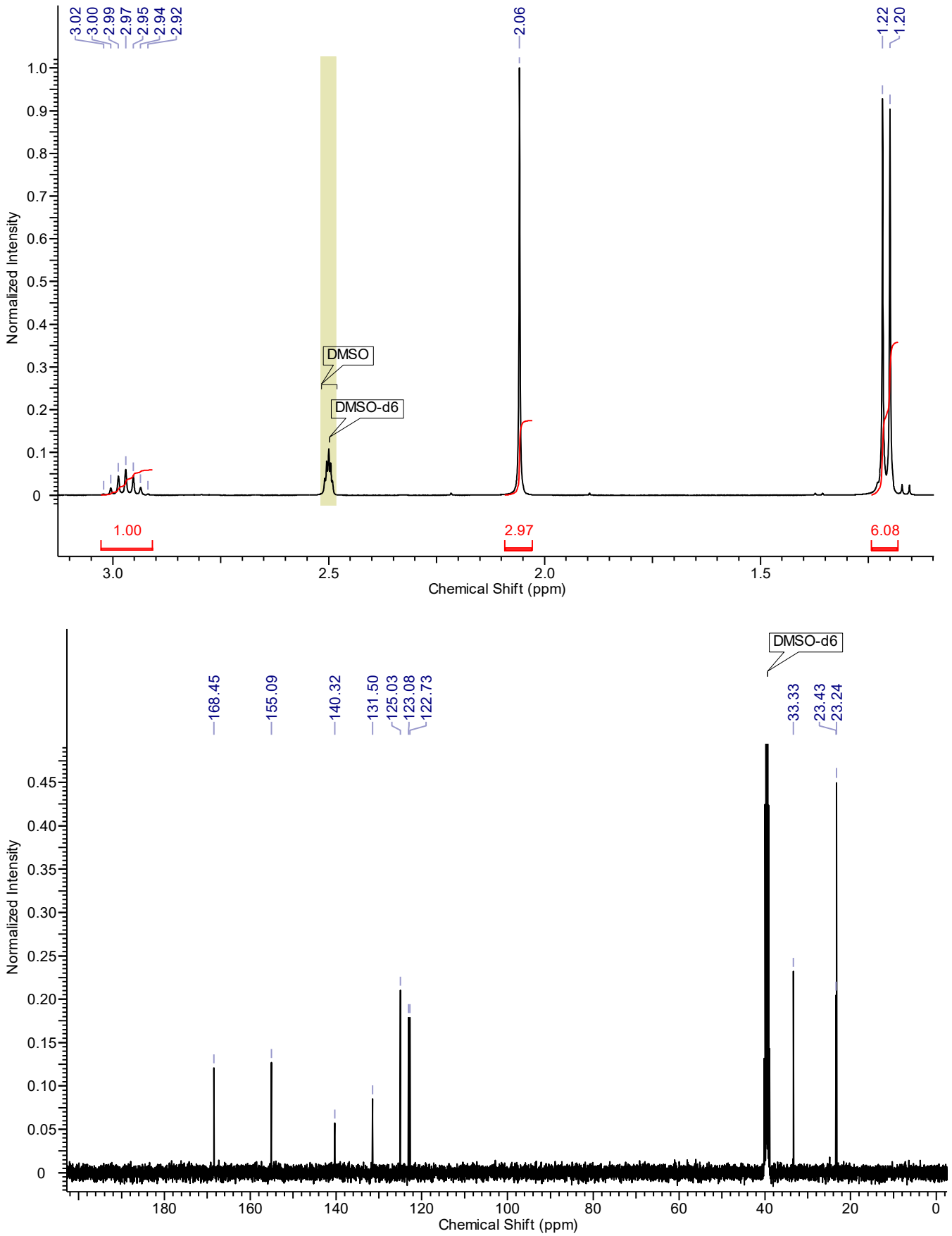


Figure S7.103. Alkyl region ^{1}H NMR (*top*) and full ^{13}C NMR (*bottom*) of *N*-(5-isopropyl-2-nitrophenyl)acetamide (**3.42a**) in DMSO-d6.

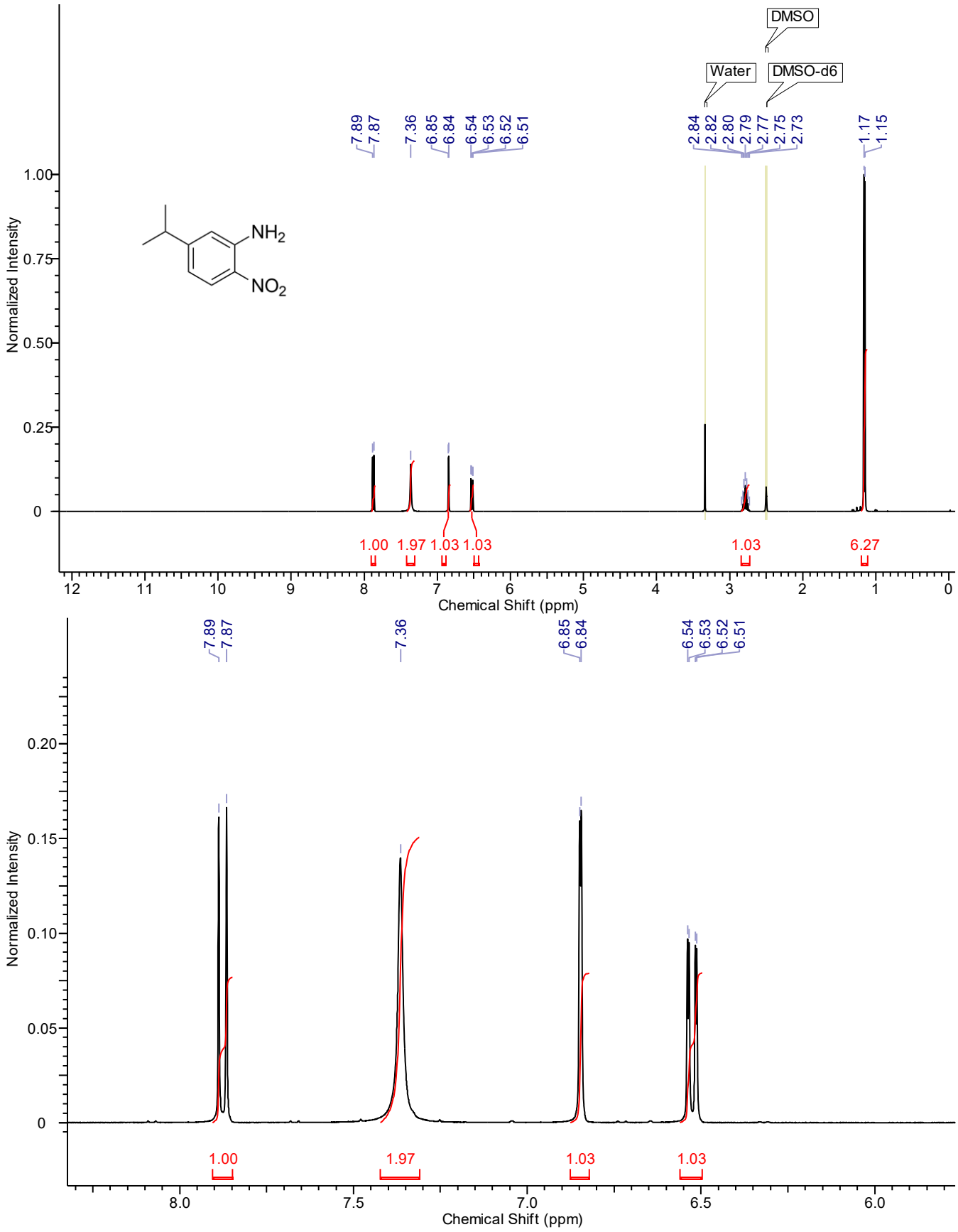


Figure S7.104. Full spectra (*top*) and aromatic region (*bottom*) ^{1}H NMR of 5-isopropyl-2-nitroaniline (**3.42b**) in DMSO-d6.

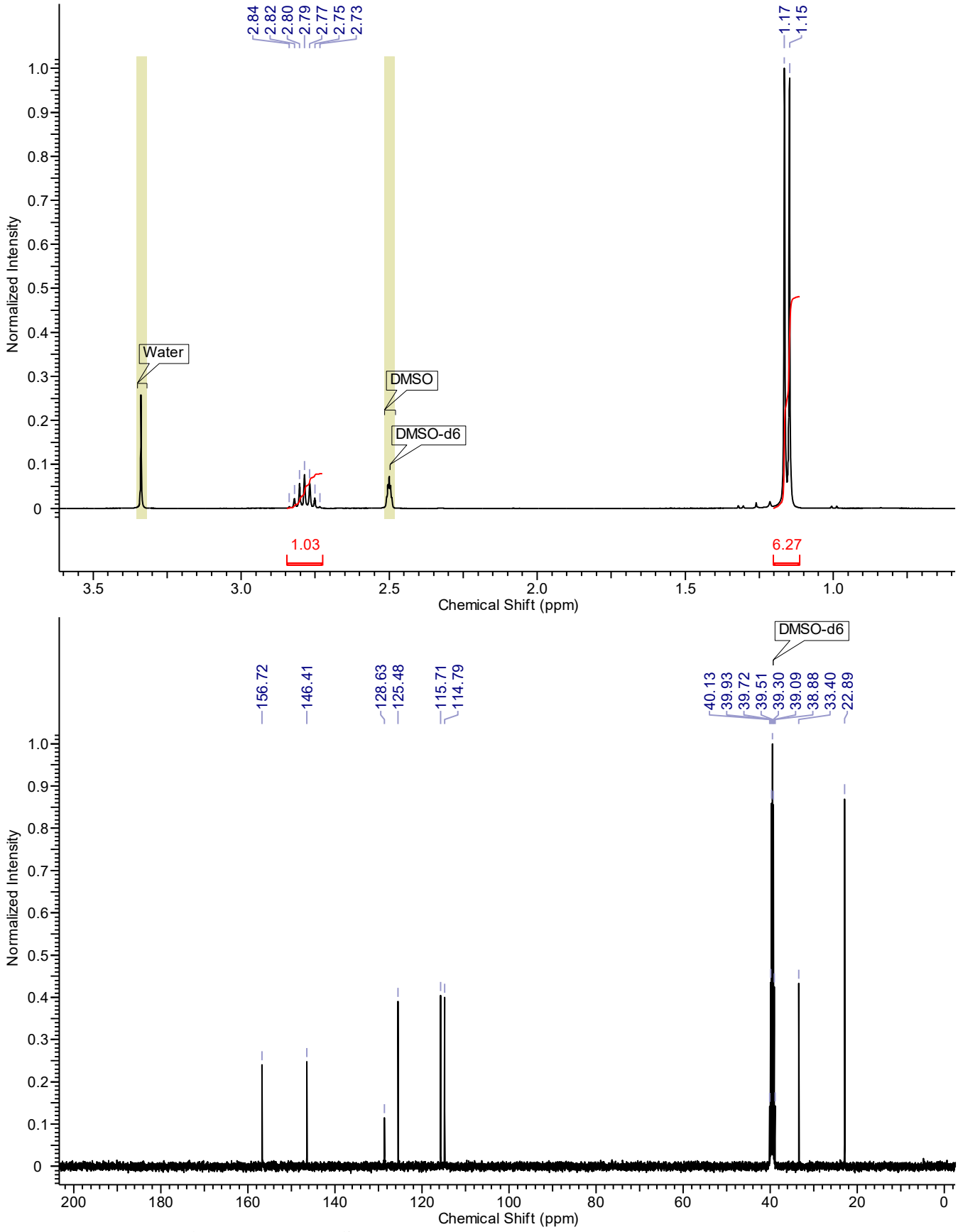


Figure S7.105. Alkyl region ^{1}H NMR (*top*) and full ^{13}C NMR (*bottom*) of 5-isopropyl-2-nitroaniline (**3.42b**) in DMSO-d6.

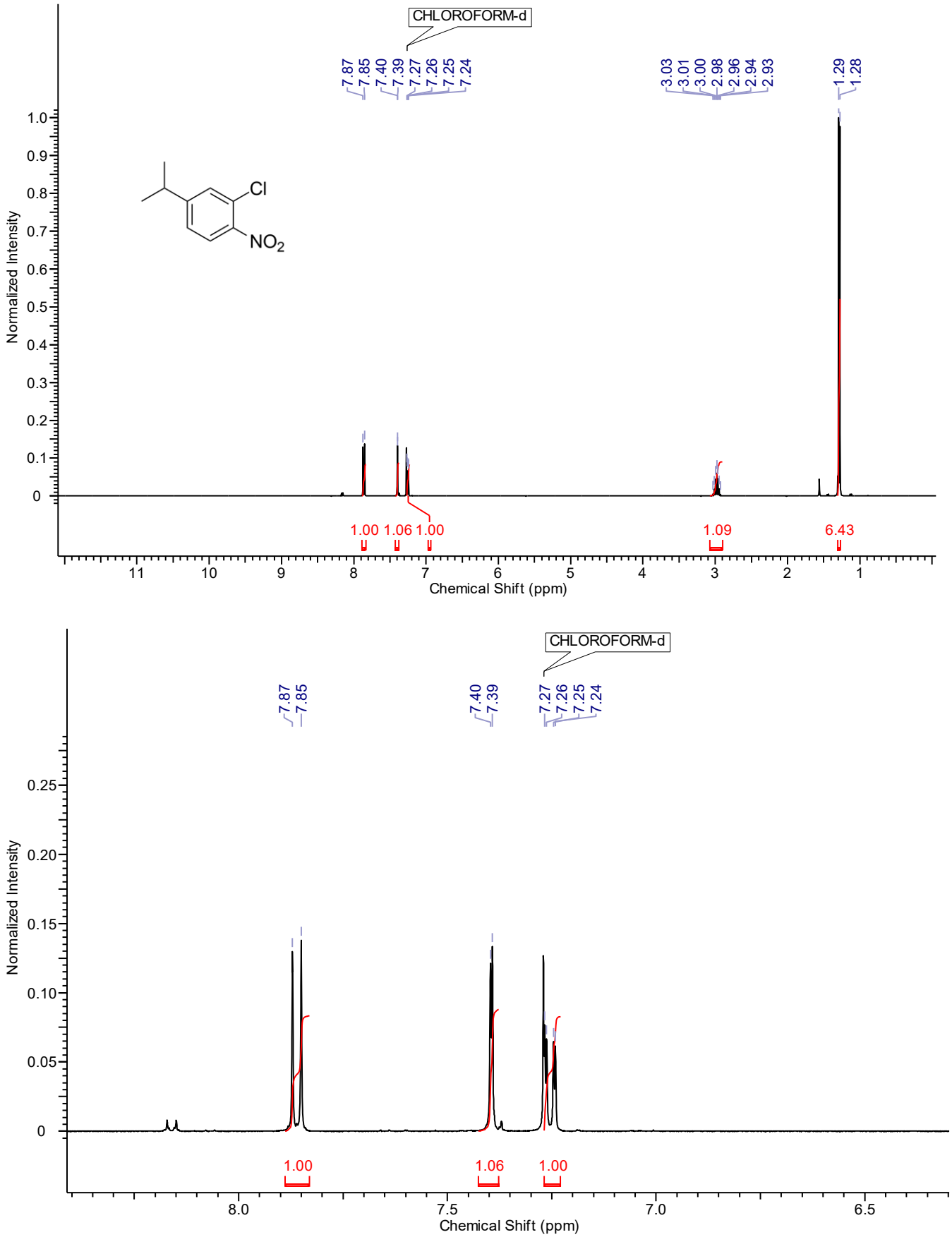


Figure S7.106. Full spectra (*top*) and aromatic region (*bottom*) ^{1}H NMR of 2-chloro-4-isopropyl-1-nitrobenzene (**3.42c**) in $CDCl_3$.

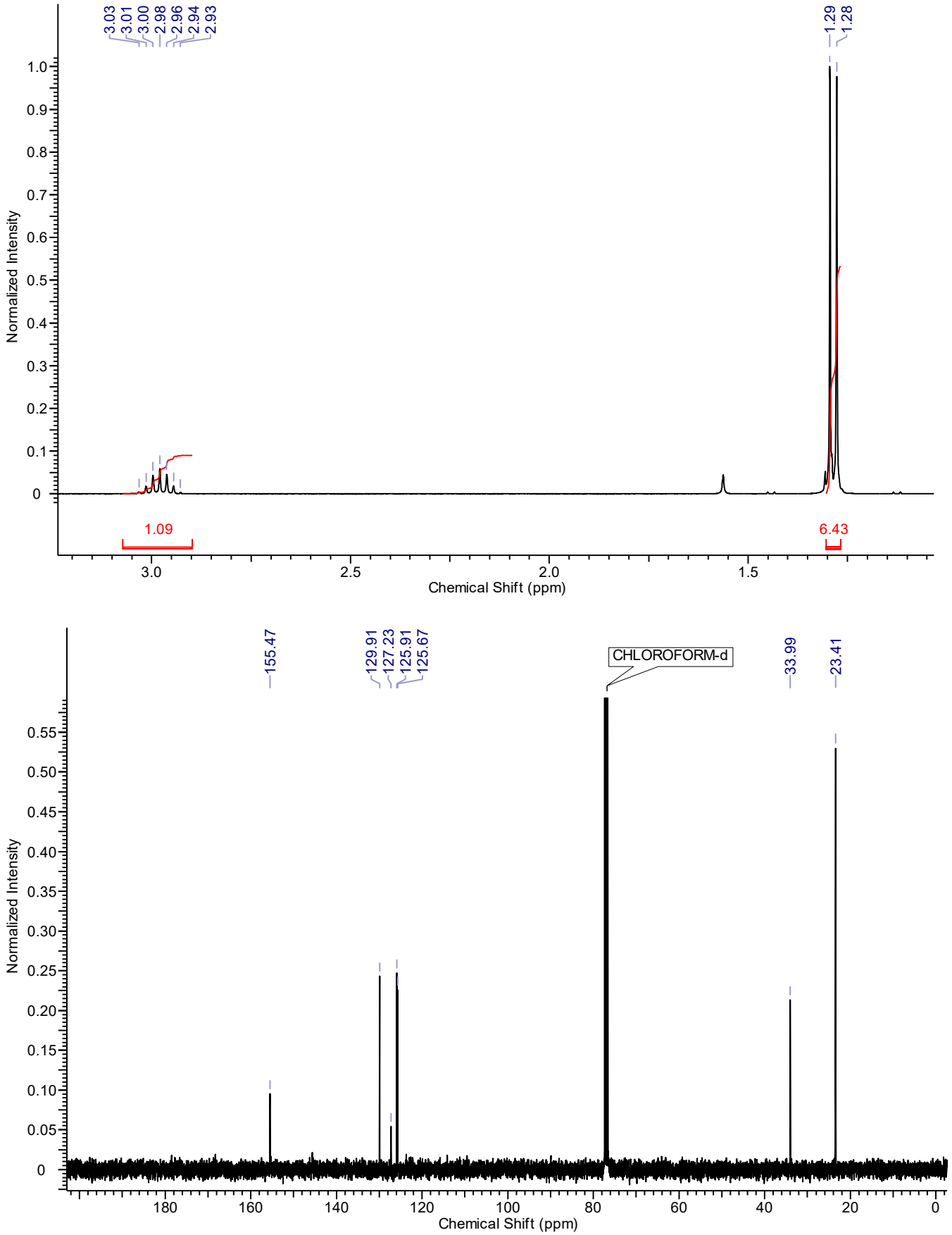


Figure S7.107. Alkyl region ^{1}H NMR (*top*) and full ^{13}C NMR (*bottom*) of 2-chloro-4-isopropyl-1-nitrobenzene (**3.42c**) in $CDCl_3$.

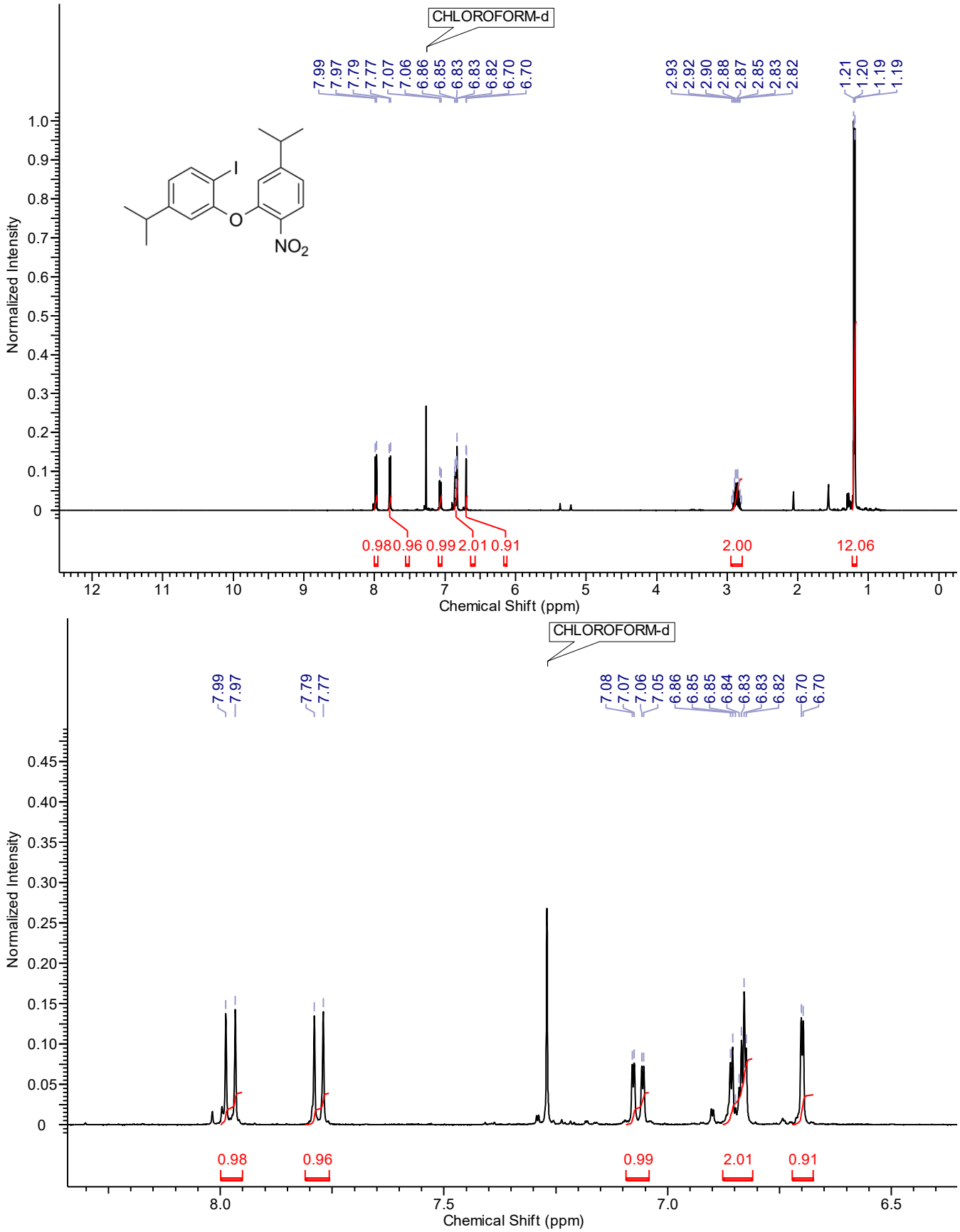


Figure S7.108. Full spectra (*top*) and aromatic region (*bottom*) ^{1}H NMR of 1-iodo-4-isopropyl-2-(5-isopropyl-2-nitrophenoxy)benzene (**3.42e**) in $CDCl_3$.

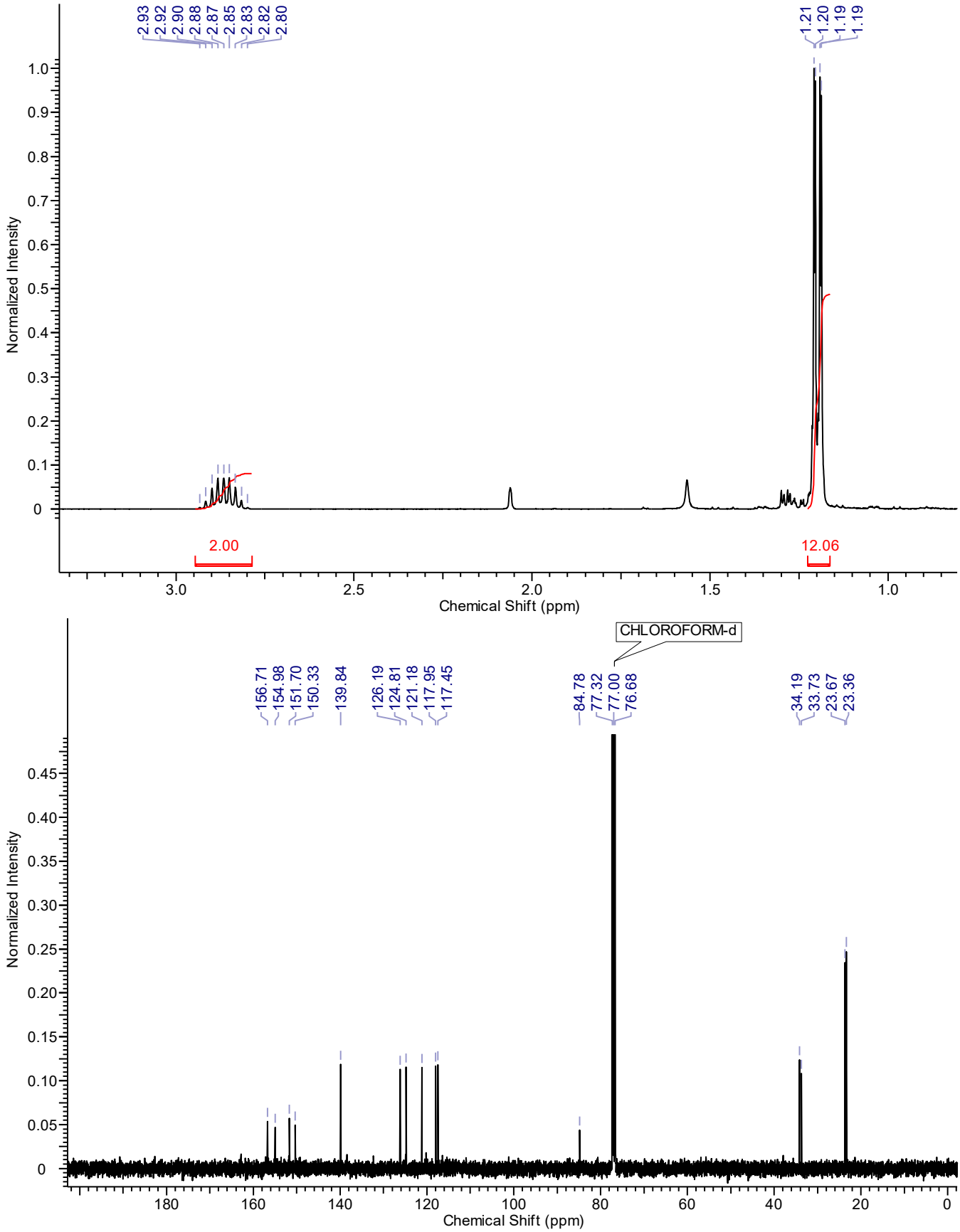


Figure S7.109. Alkyl region ^{1}H NMR (*top*) and full ^{13}C NMR (*bottom*) of 1-iodo-4-isopropyl-2-(5-isopropyl-2-nitrophenoxy)benzene (**3.42e**) in $CDCl_3$.

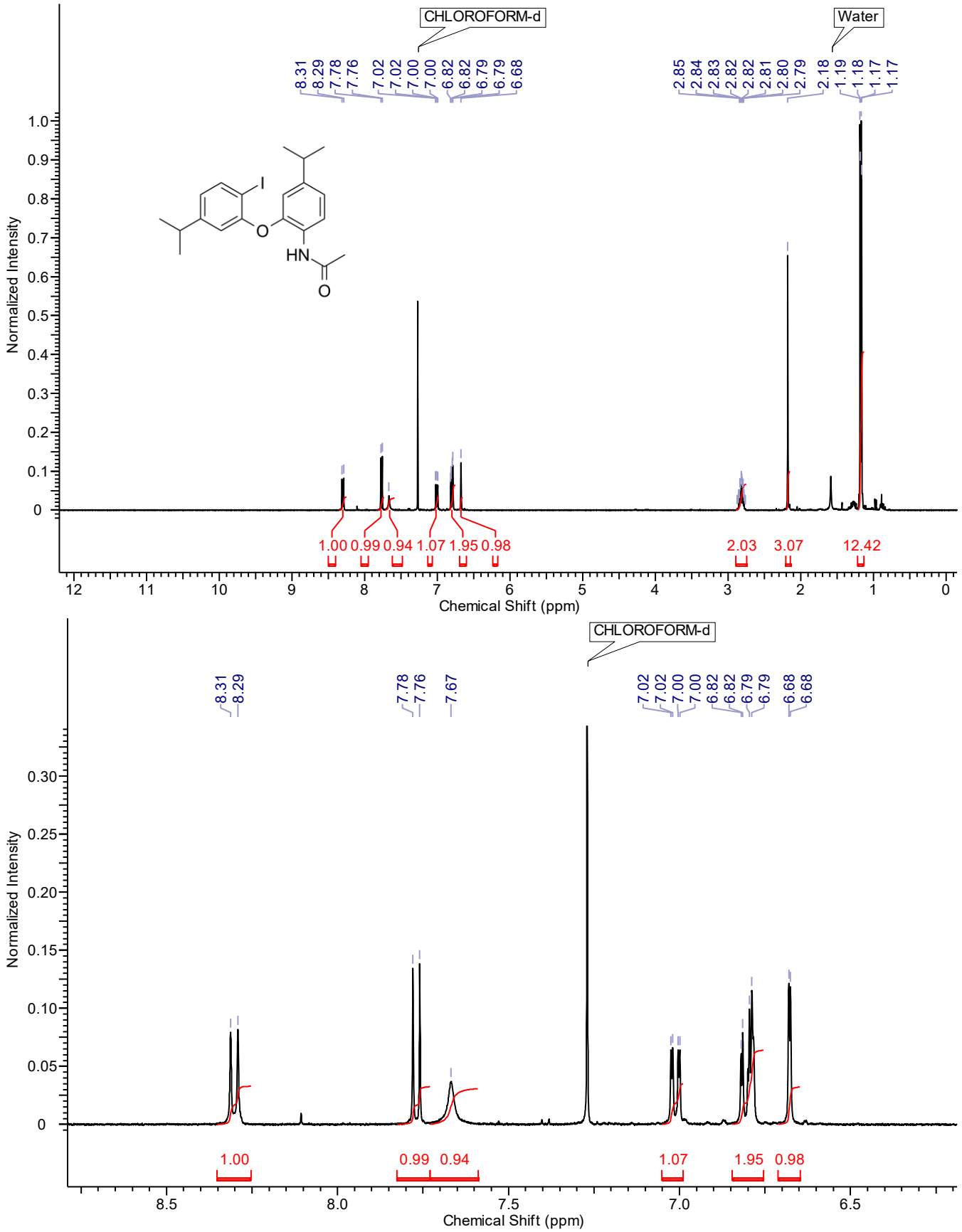


Figure S7.110. Full spectra (*top*) and aromatic region (*bottom*) ^{1}H NMR of *N*-(2-(2-iodo-5-isopropylphenoxy)-4-isopropylphenyl)acetamide (**3.42f**) in $CDCl_3$.

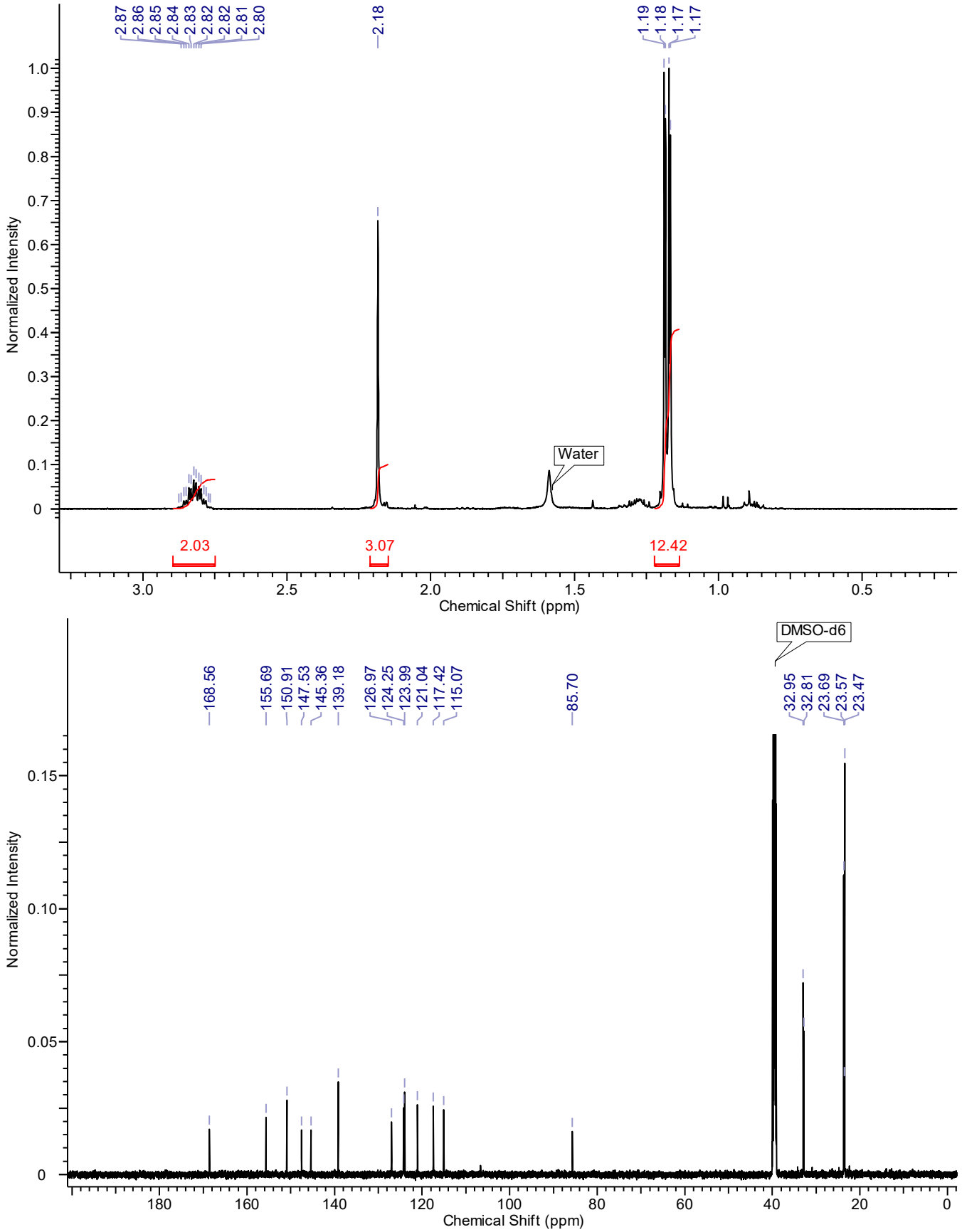


Figure S7.111. Alkyl region ^{1}H NMR (*top*) and full ^{13}C NMR (*bottom*) of *N*-(2-(2-iodo-5-isopropylphenoxy)-4-isopropylphenyl)acetamide (**3.42f**) in $CDCl_3$.

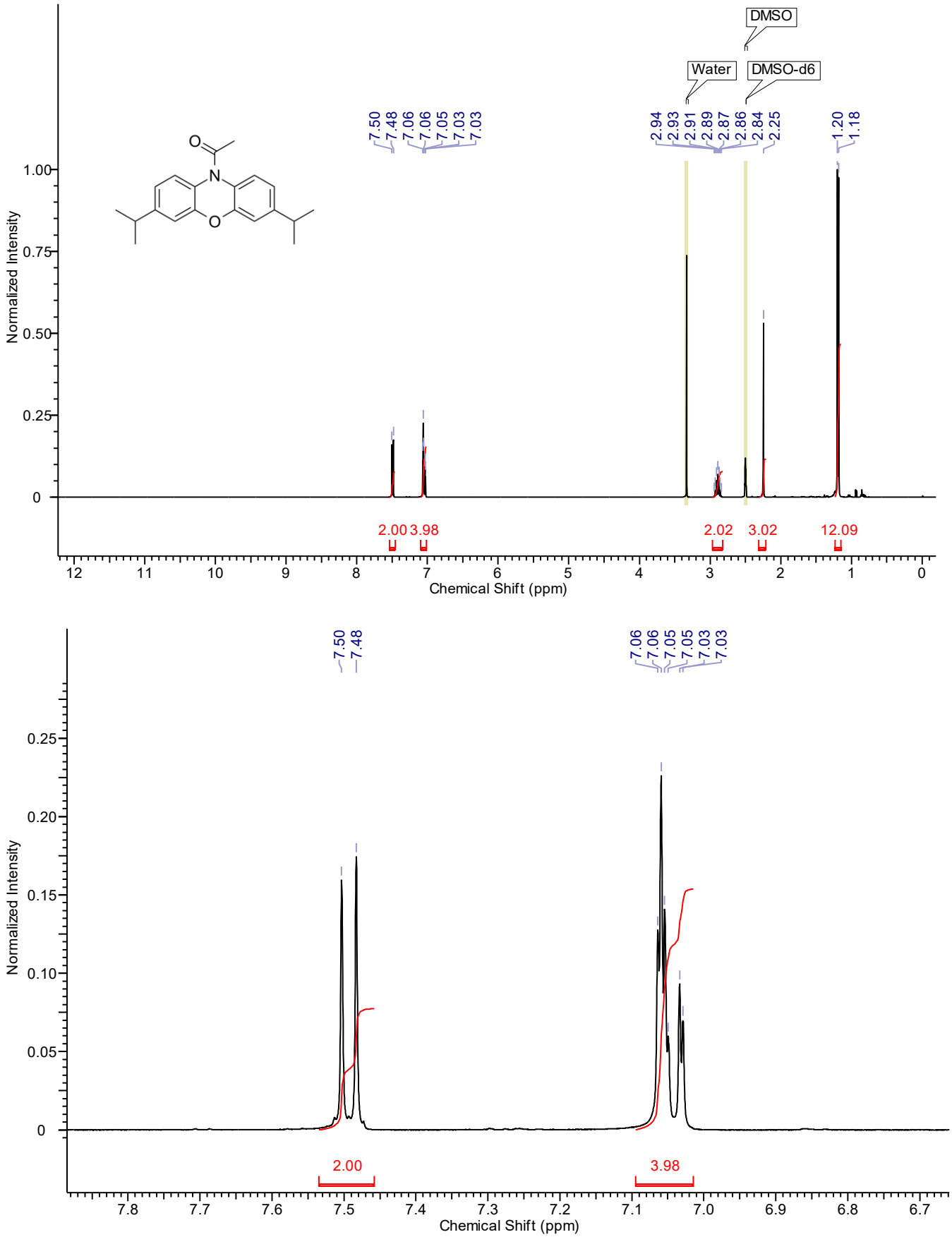


Figure S7.112. Alkyl region ^{1}H NMR (*top*) and full ^{13}C NMR (*bottom*) of 10-acetyl-3,7-diisopropylphenoxazine (**3.42g**) in DMSO-d6.

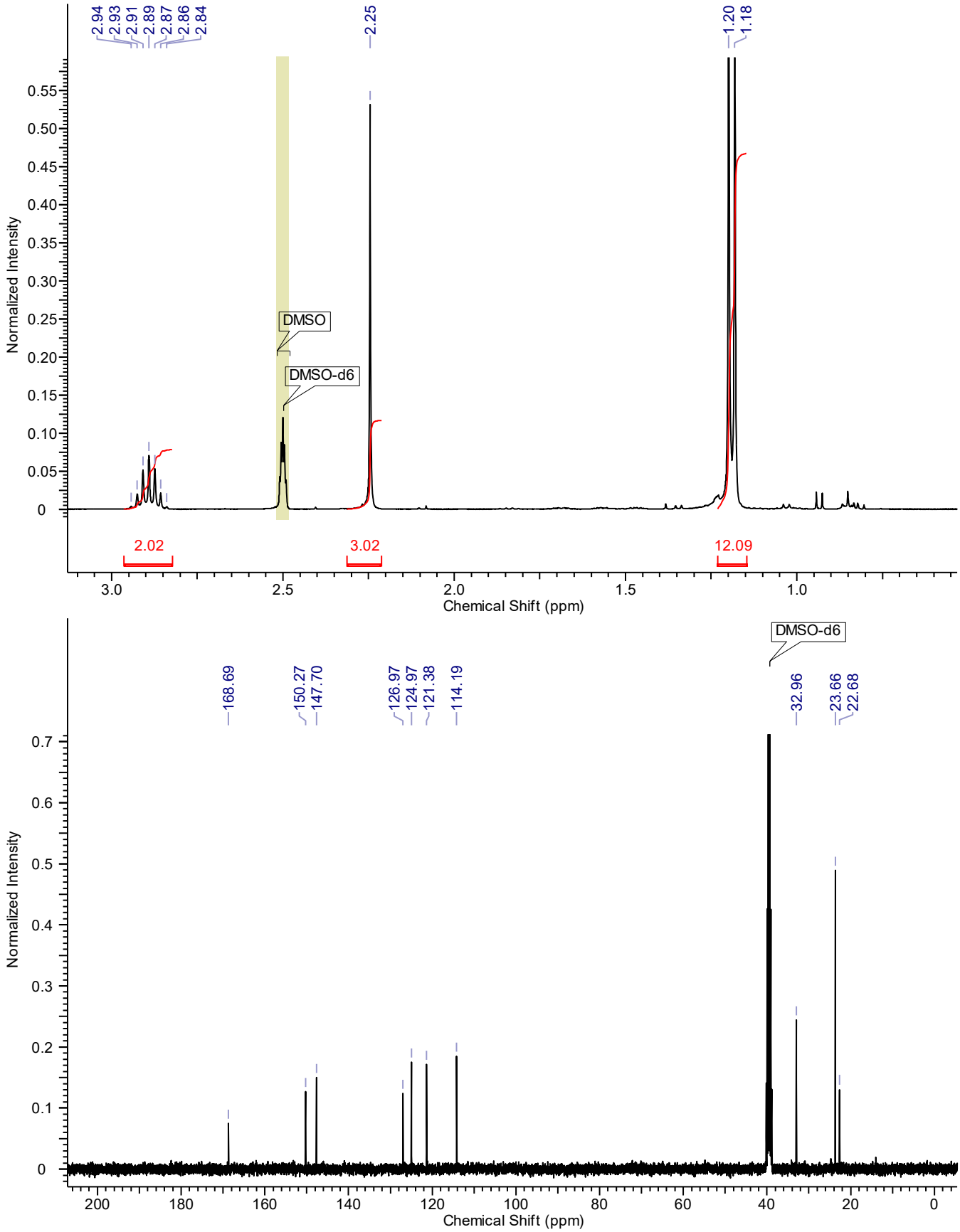


Figure S7.113. Alkyl region ^{1}H NMR (*top*) and full ^{13}C NMR (*bottom*) of 10-acetyl-3,7-diisopropylphenoxazine (**3.42g**) in DMSO-d6.

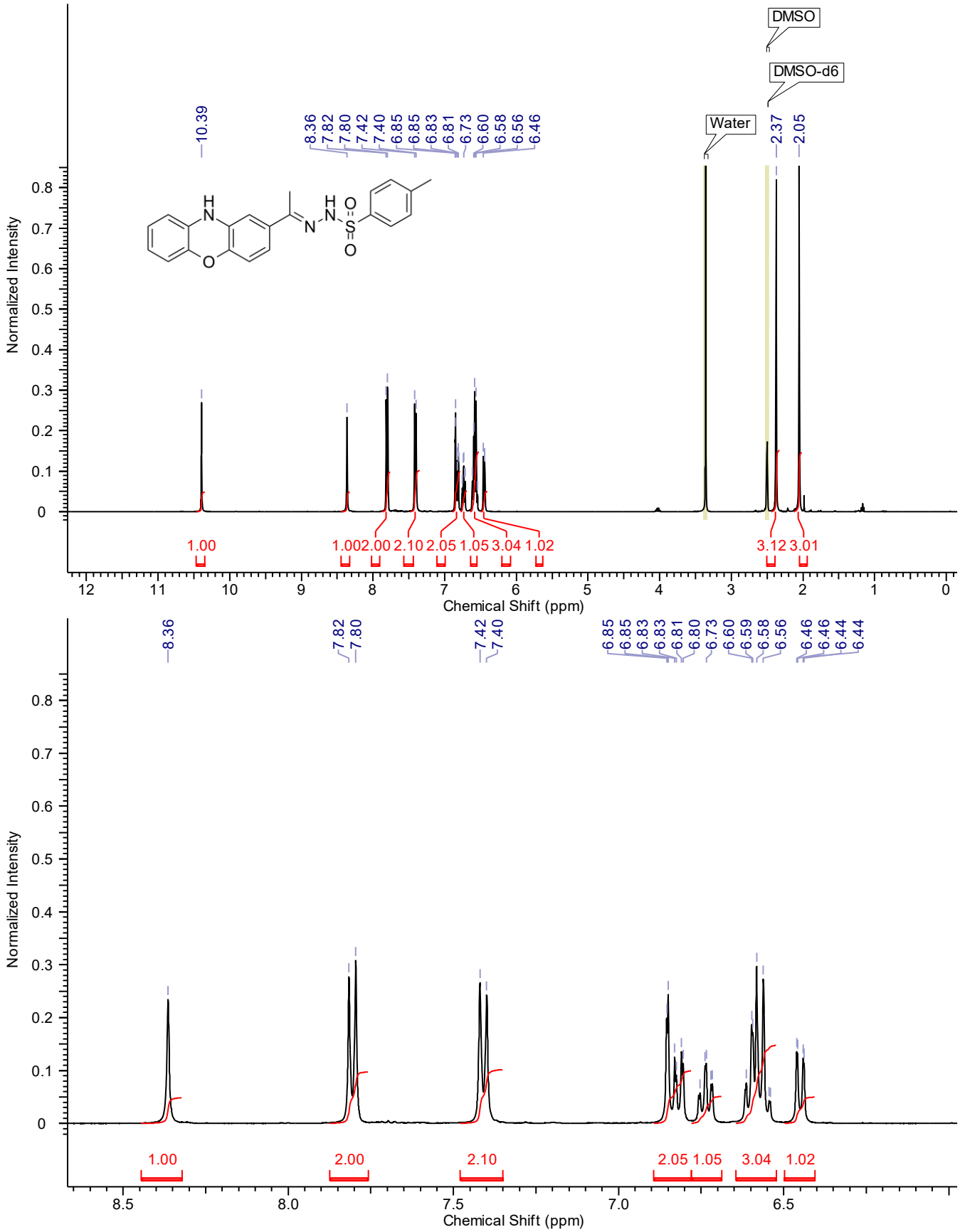


Figure S7.114. Full spectra (*top*) and aromatic region (*bottom*) ^{1}H NMR of (*E*)-*N*'-(1-(10*H*-phenoxazin-2-yl)ethylidene)-4-methylbenzenesulfonohydrazide (**3.44a**) in DMSO-d6.

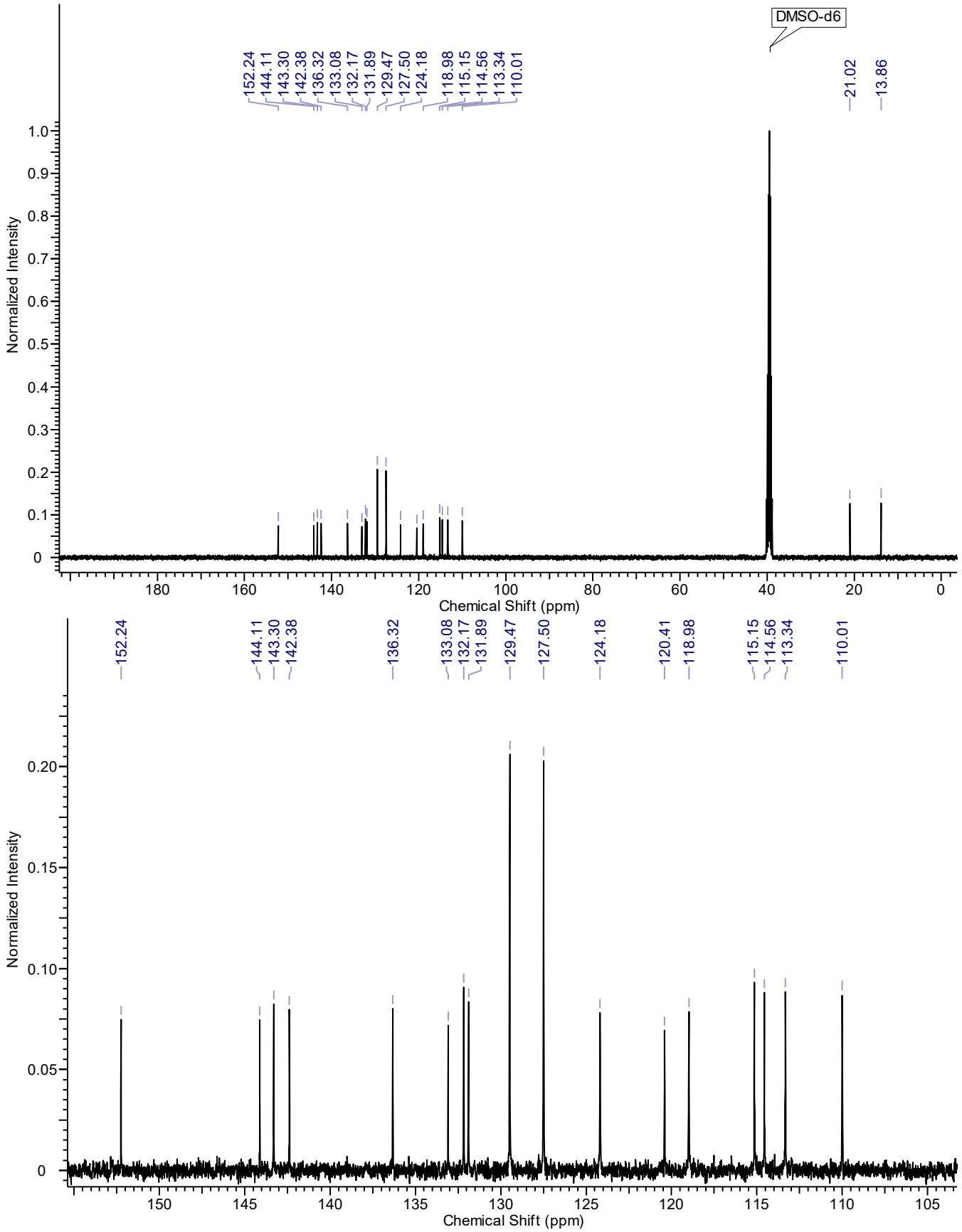


Figure S7.115. Full spectra (*top*) and aromatic region (*bottom*) ^{13}C NMR of (*E*)-*N*'-(1-(10*H*-phenoxazin-2-yl)ethylidene)-4-methylbenzenesulfonohydrazide (**3.44a**) in DMSO-d6.

7.3 Chapter 4 NMR Spectra

(Begins on next page)

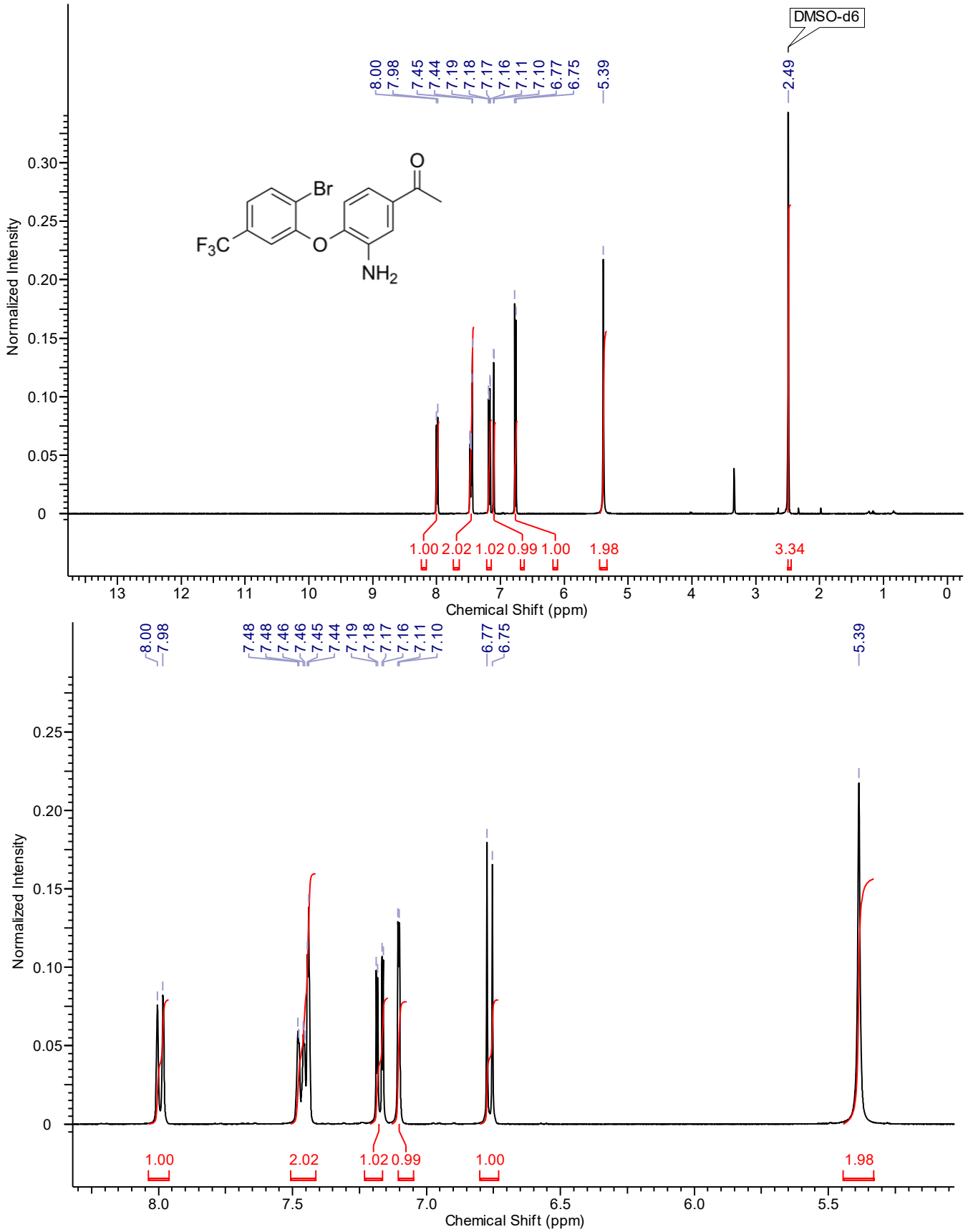


Figure S7.116. Full spectra (*top*) and aromatic region (*bottom*) ^{1}H NMR of 1-(3-amino-4-(2-bromo-5-(trifluoromethyl)phenoxy)phenyl)ethenone in DMSO-d6.

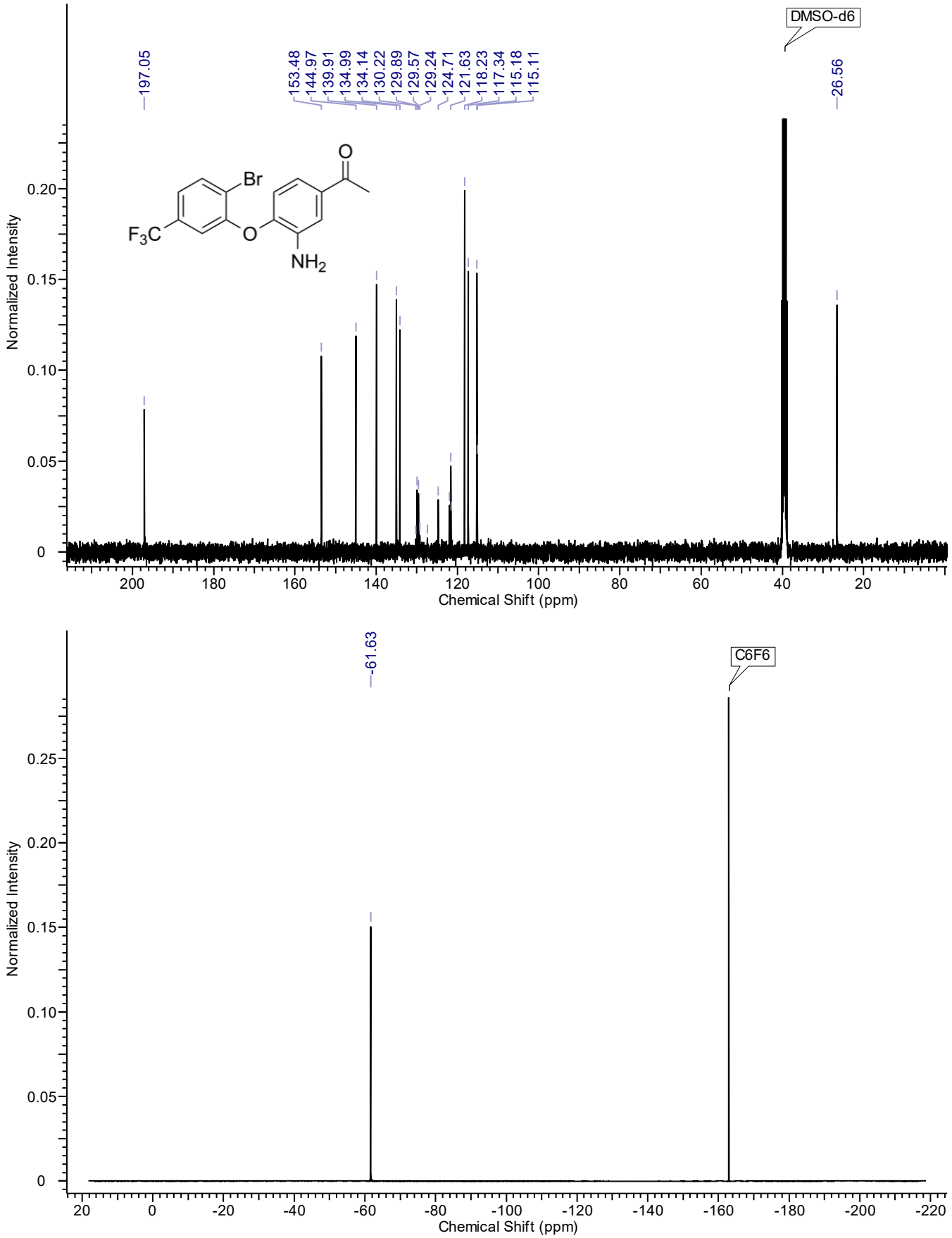


Figure S7.117. ^{13}C NMR (*top*) and ^{19}FNMR (*bottom*) of 1-(3-amino-4-(2-bromo-5-(trifluoromethyl)phenoxy)phenyl)ethenone in DMSO-d6.

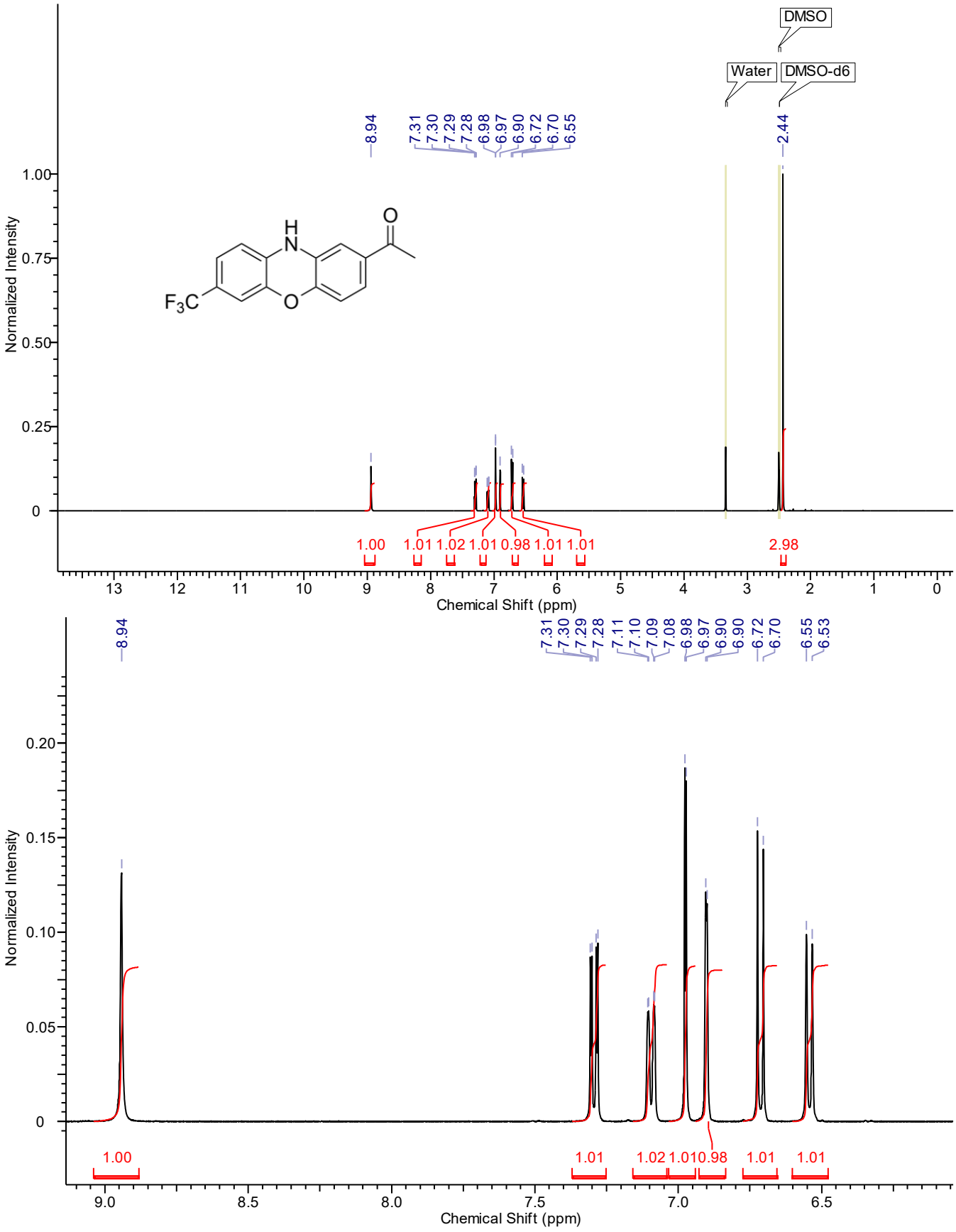


Figure S7.118. Full spectra (*top*) and aromatic region (*bottom*) ^{1}H NMR of 2-acetyl-7-trifluoromethylphenoxazine (**4.2a)** in DMSO-d6.

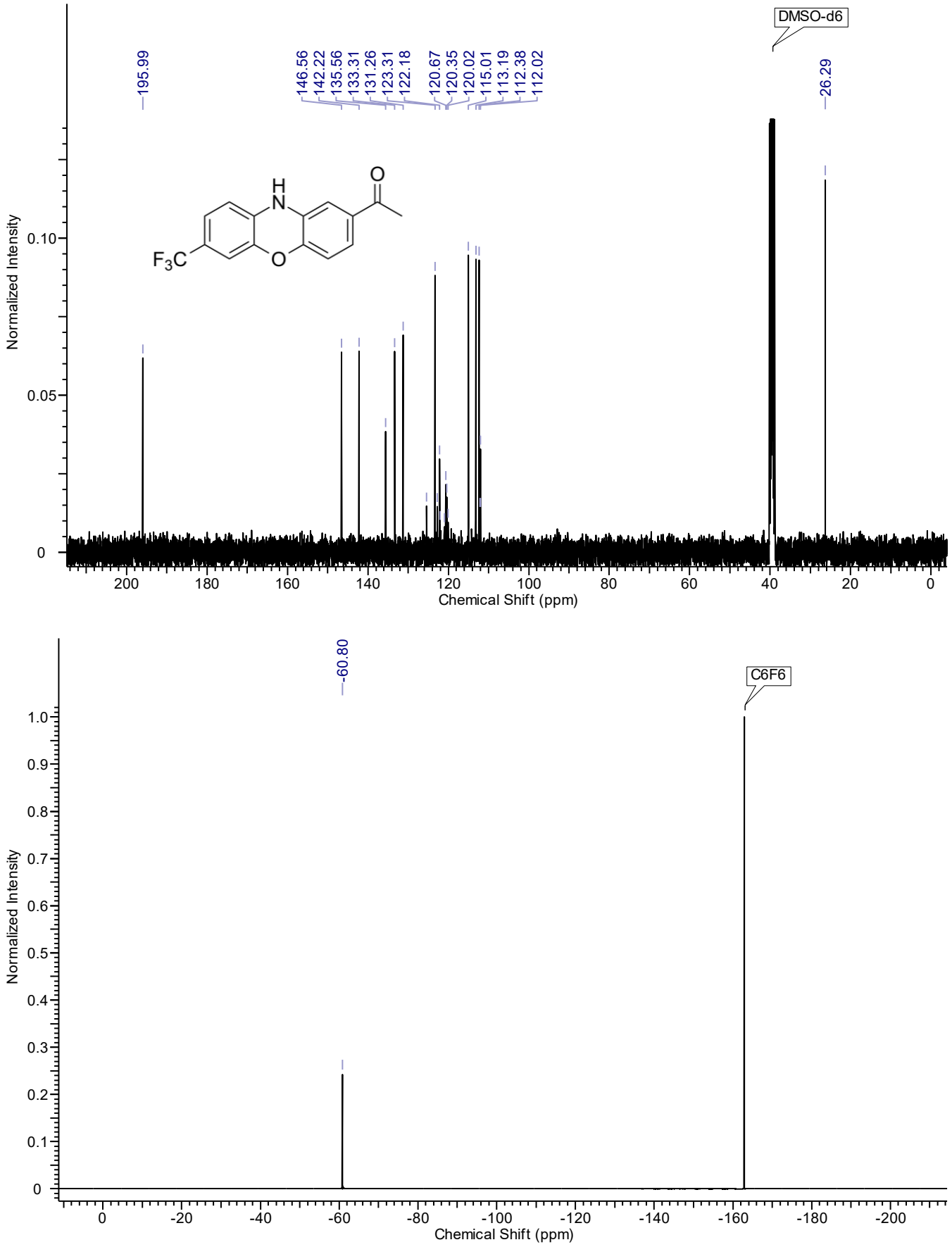


Figure S7.119. ^{13}C NMR (*top*) and ^{19}FNMR (*bottom*) of 2-acetyl-7-trifluoromethylphenoxazine (**4.2a)** in DMSO-d6.

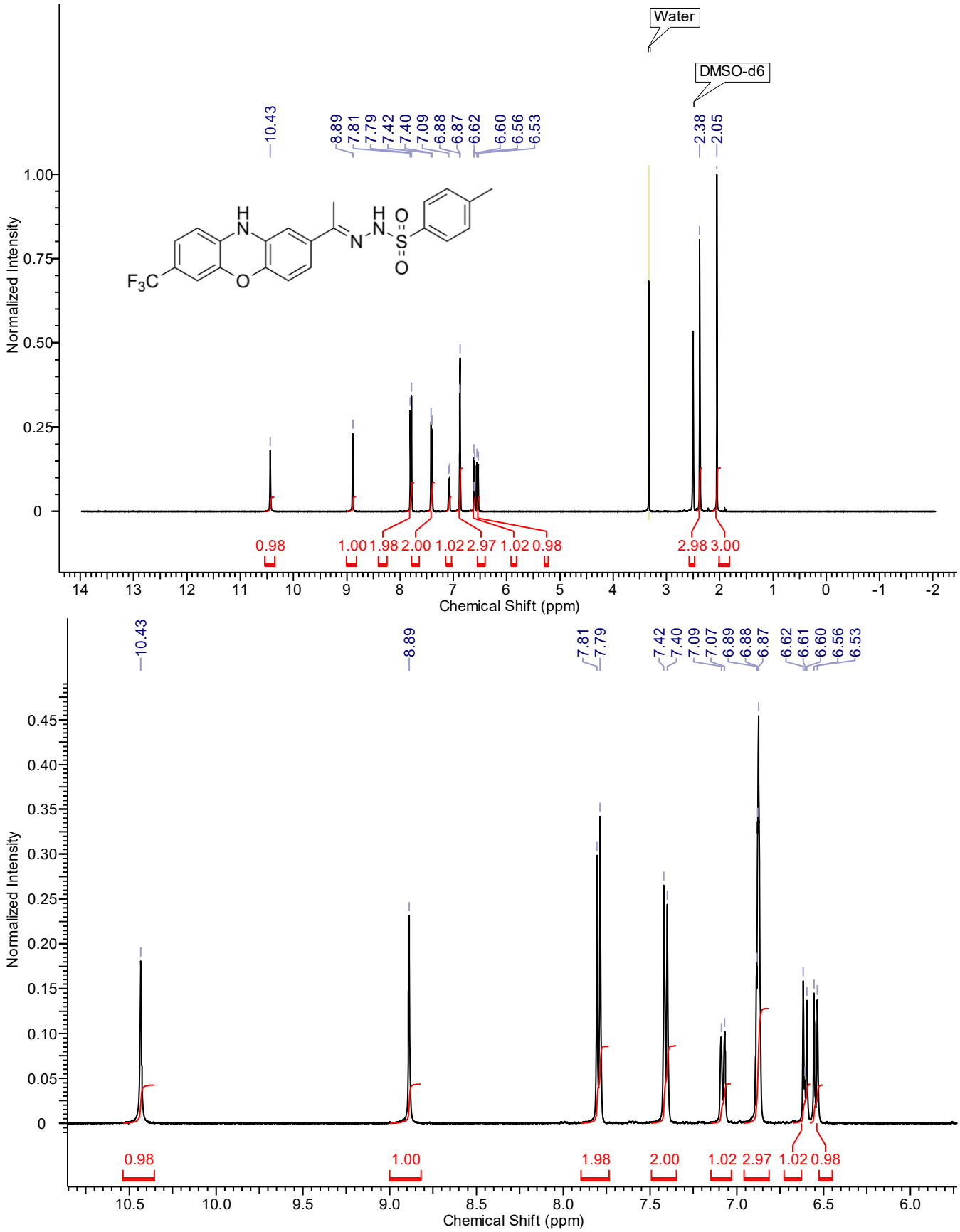


Figure S7.120. Full spectra (*top*) and aromatic region (*bottom*) ^{1}H NMR of (E)-4-methyl-N'-(1-(7-(trifluoromethyl)-10H-phenoxazin-2-yl)ethylidene)benzenesulfonohydrazide (**4.3a**) in DMSO-d6.

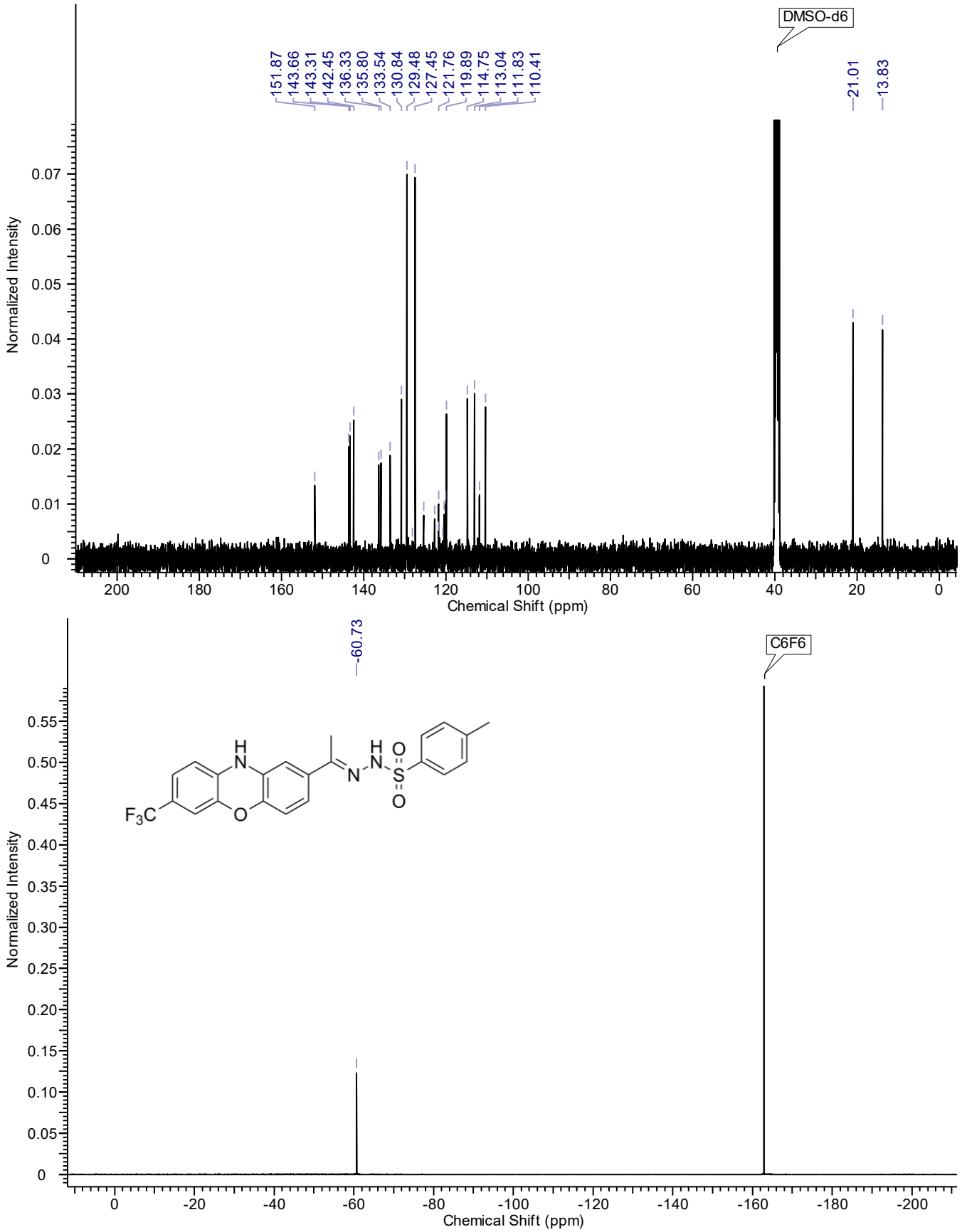


Figure S7.121. ^{13}C NMR (*top*) and $^{19}FNMR$ (*bottom*) of (E)-4-methyl-N'-(1-(7-(trifluoromethyl)-10H-phenoxazin-2-yl)ethylidene)benzenesulfonohydrazide (**4.3a**) in DMSO-d6.

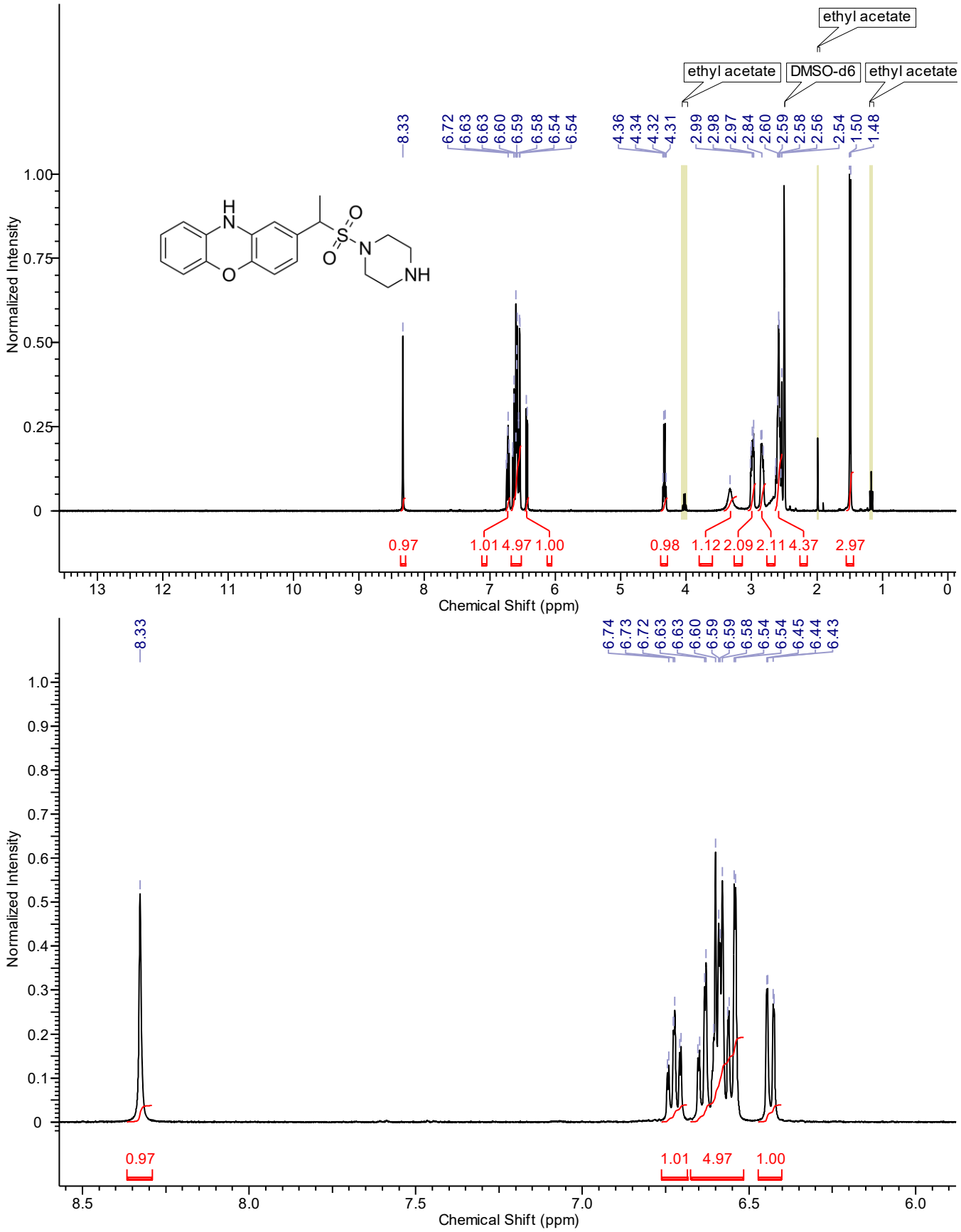


Figure S7.122. Full spectra (*top*) and aromatic region (*bottom*) ^{1}H NMR of 2-(1-(piperazin-1-ylsulfonyl)ethyl)-10H-phenoxazine (**4.5b**) in DMSO-d6.

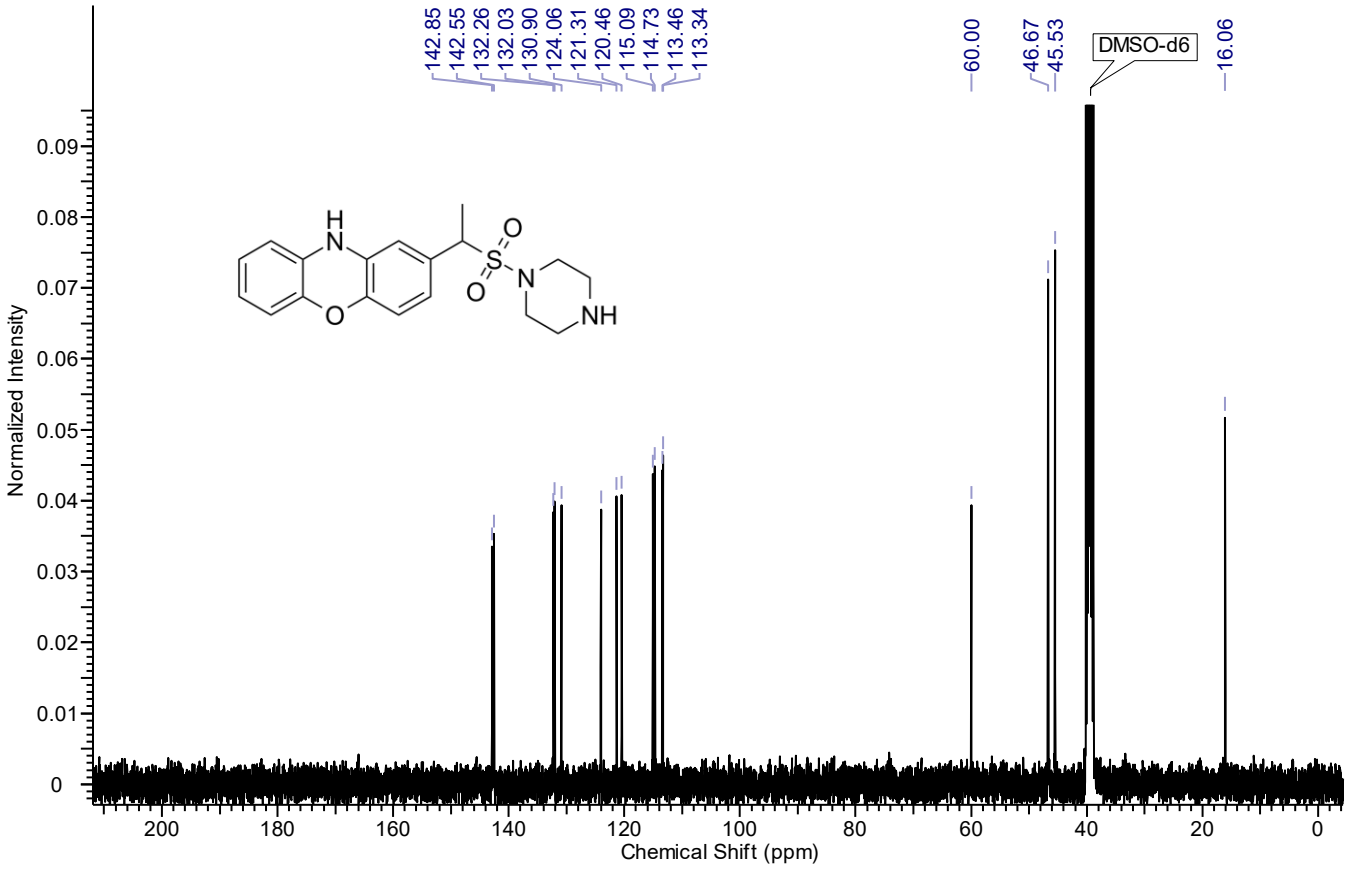


Figure S7.123. Full spectra ^{13}C NMR of 2-(1-(piperazin-1-ylsulfonyl)ethyl)-10H-phenoxazine (**4.5b**) in DMSO-d6

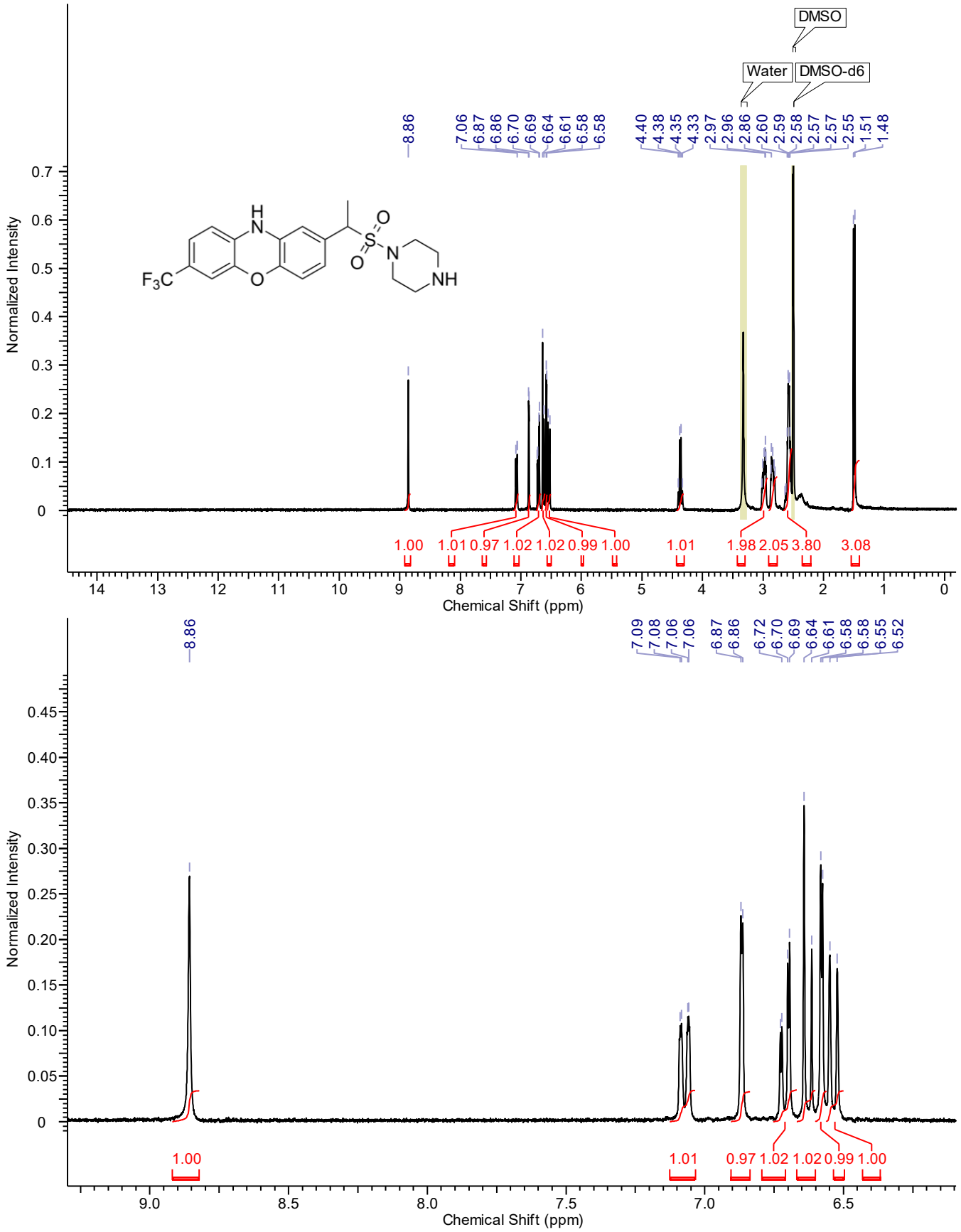


Figure S7.124. Full spectra (*top*) and aromatic region (*bottom*) ^{1}H NMR of 2-(1-(piperazin-1-ylsulfonyl)ethyl)-7-(trifluoromethyl)-10H-phenoxazine (**4.5a**) in DMSO-d6.

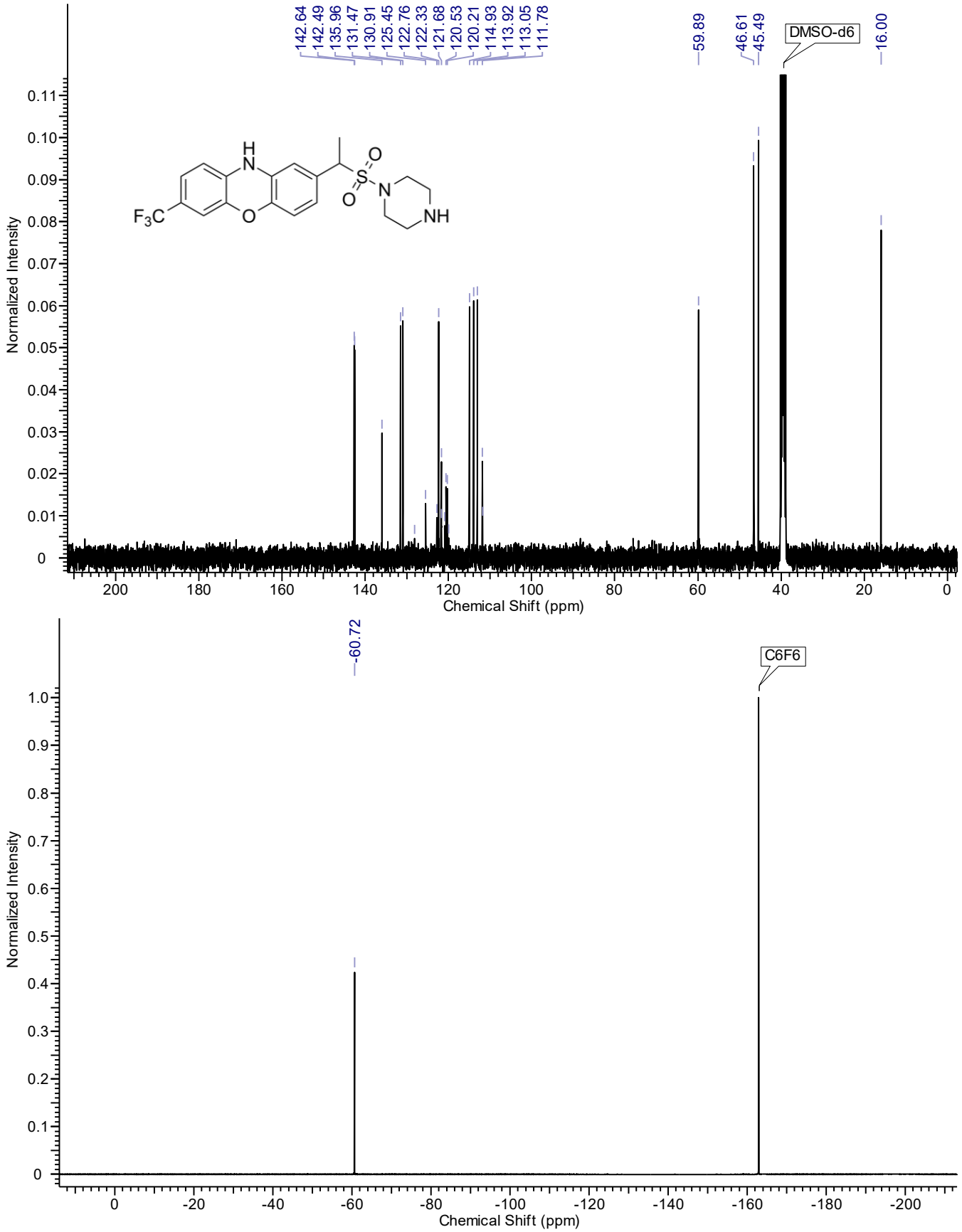


Figure S7.125. ^{13}C NMR (*top*) and ^{19}FNMR (*bottom*) of 2-(1-(piperazin-1-ylsulfonyl)ethyl)-7-(trifluoromethyl)-10H-phenoxazine (**4.5a**) in DMSO-d6.

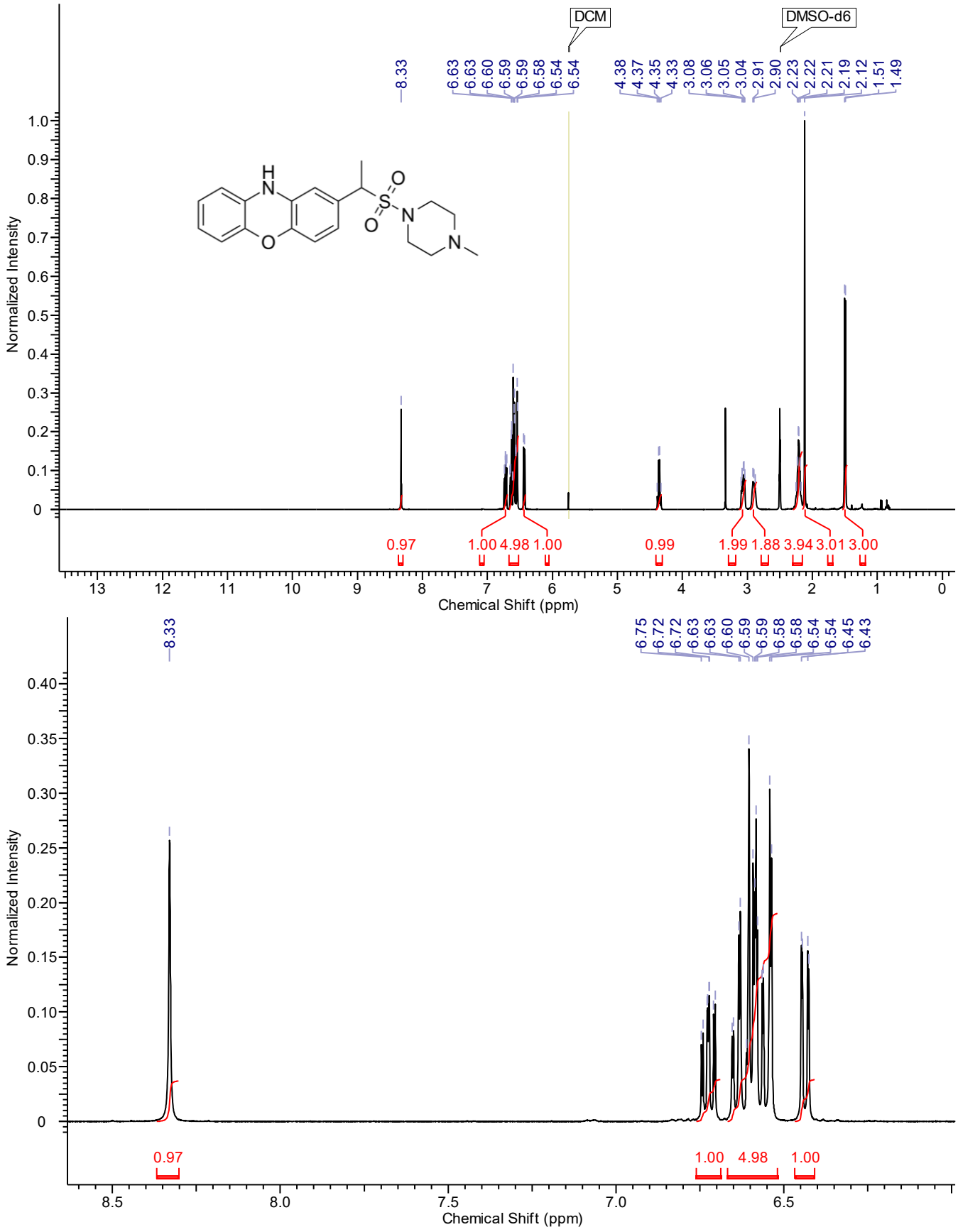


Figure S7.126. Full spectra (*top*) and aromatic region (*bottom*) ^{1}H NMR of 2-(1-(piperazin-1-ylsulfonyl)ethyl)-7-(trifluoromethyl)-10H-phenoxazine (**4.5a**) in DMSO-d6.

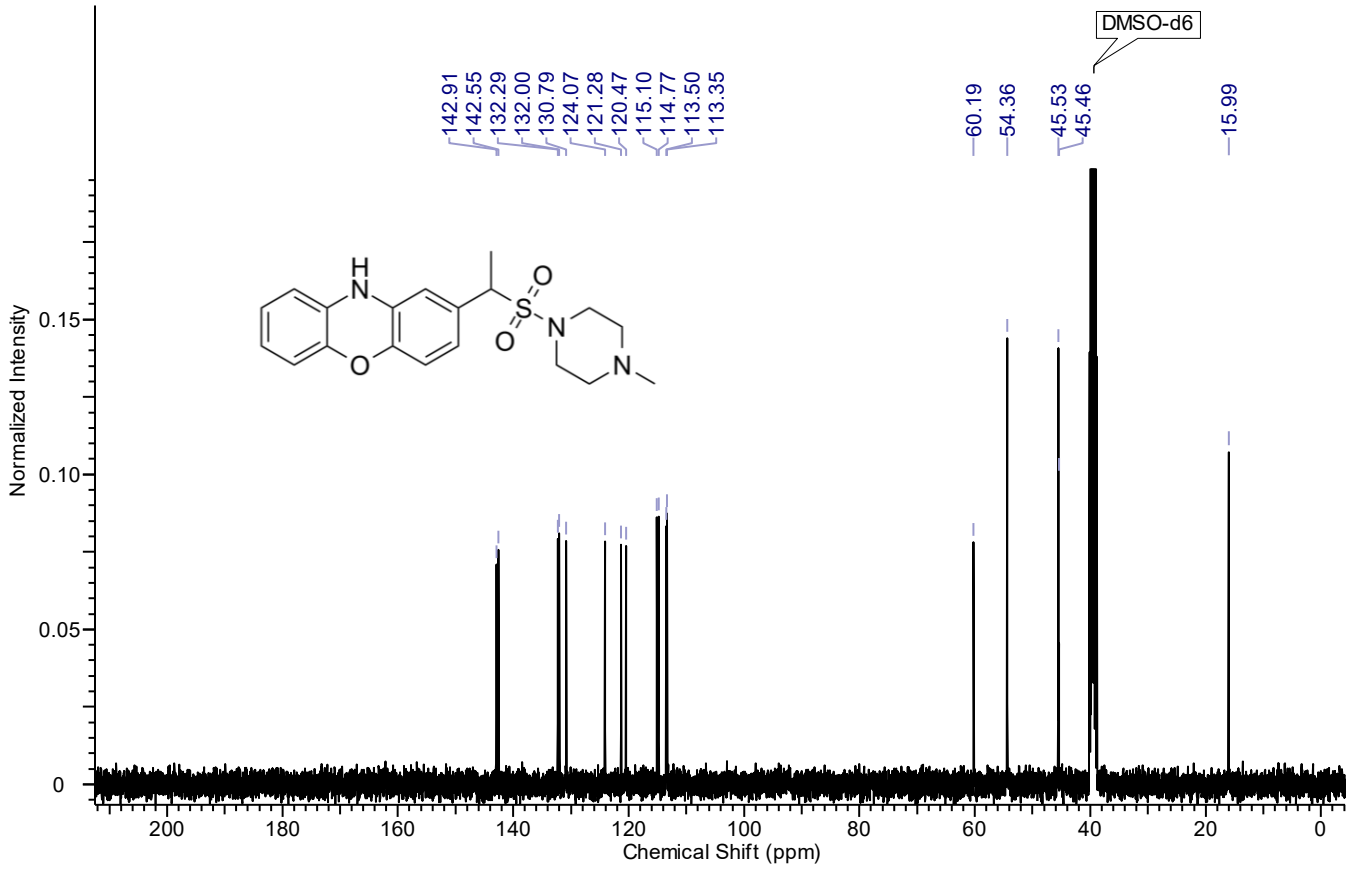


Figure S7.127. Full spectra ^{13}C NMR of 2-(1-((4-methylpiperazin-1-yl)sulfonyl)ethyl)-10H-phenoxazine (**4.6b**) in DMSO-d6

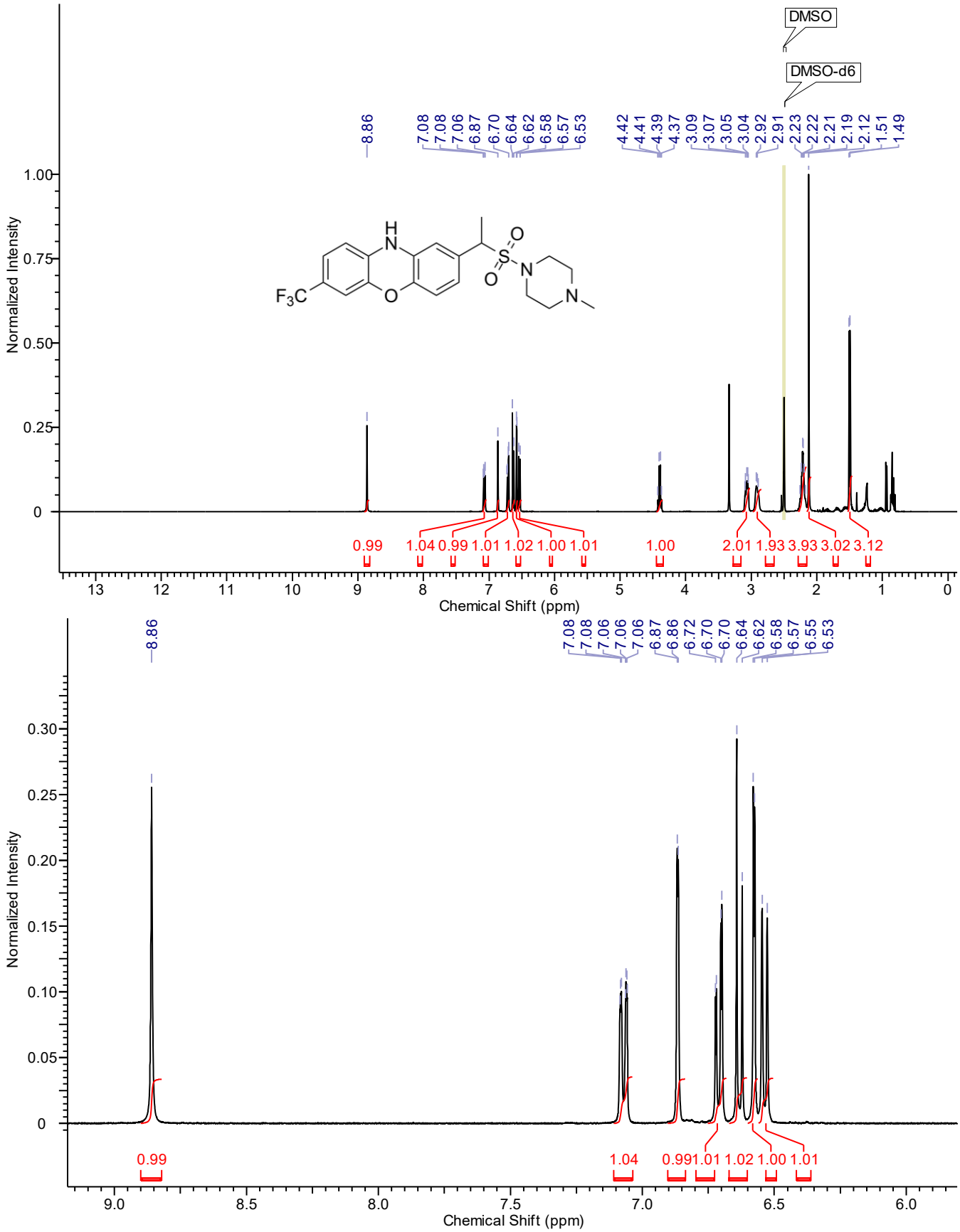


Figure S7.128. Full spectra (*top*) and aromatic region (*bottom*) ^{1}H NMR of 2-(1-((4-methylpiperazin-1-yl)sulfonyl)ethyl)-7-(trifluoromethyl)-10H-phenoxazine (**4.6a**). in DMSO-d6.

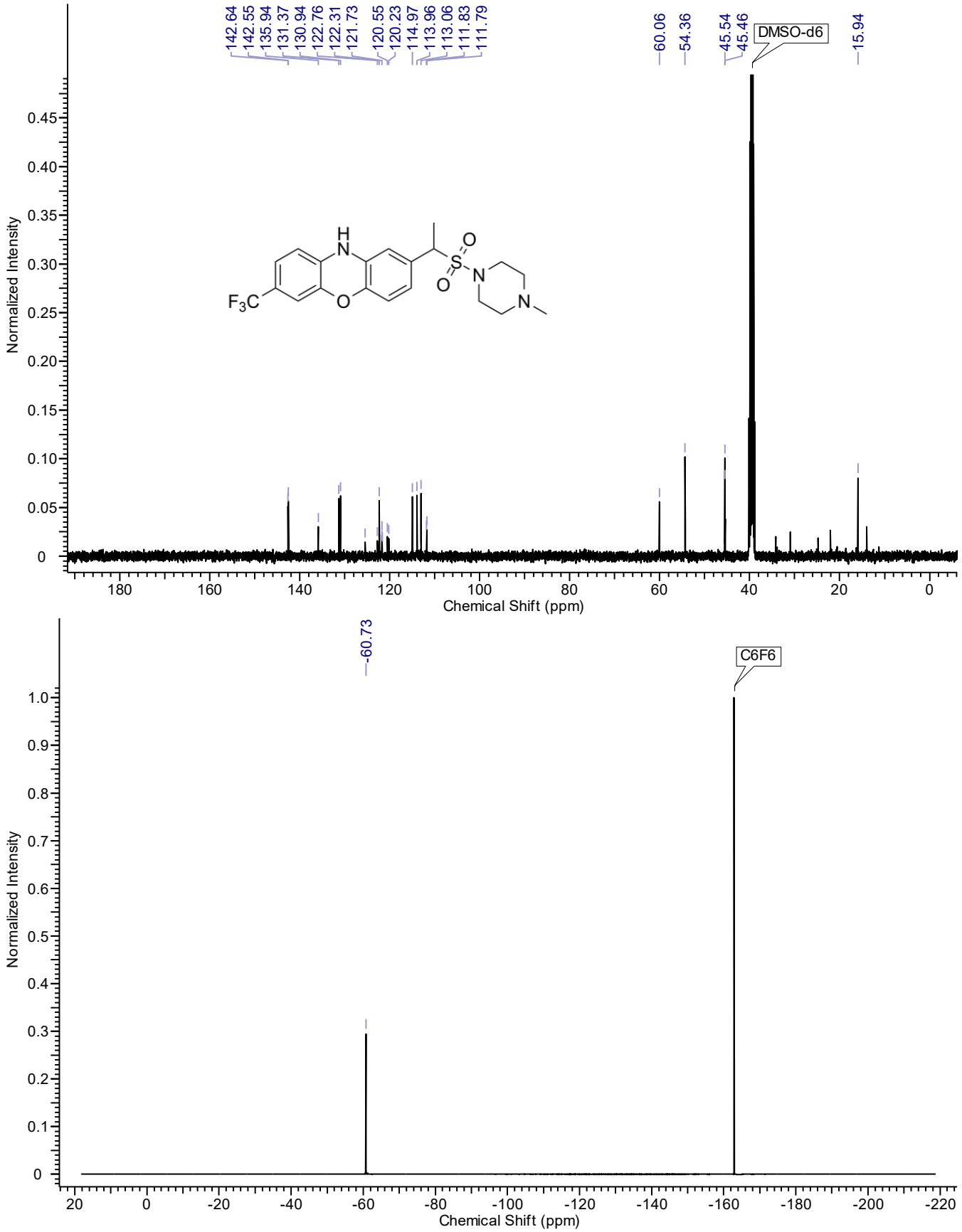


Figure S7.129. ^{13}C NMR (*top*) and ^{19}FNMR (*bottom*) of 2-(1-((4-methylpiperazin-1-yl)sulfonyl)ethyl)-7-(trifluoromethyl)-10H-phenoxazine (**4.6a**). in DMSO-d6.

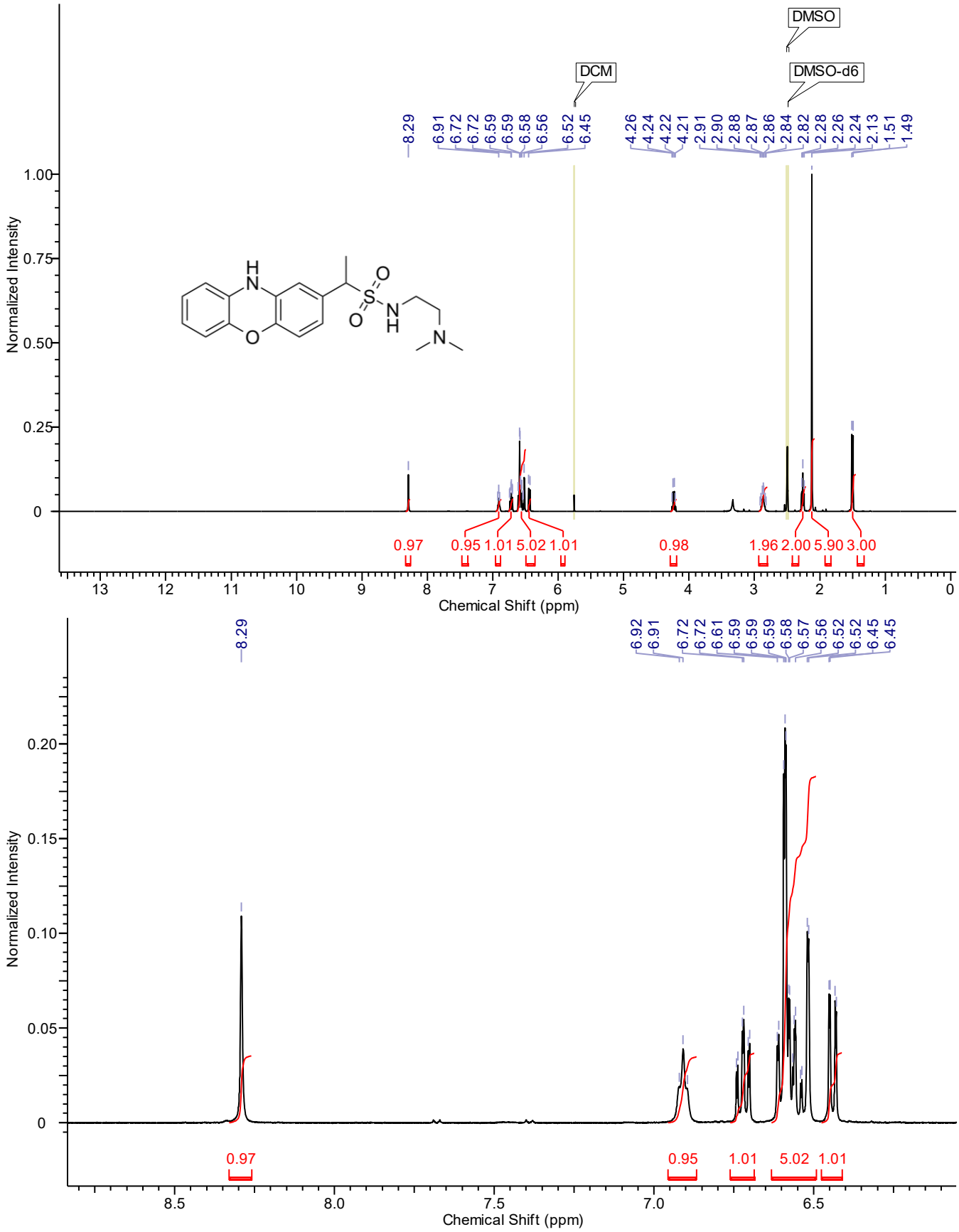


Figure S7.130. Full spectra (*top*) and aromatic region (*bottom*) ^{1}H NMR of. N-(2-(dimethylamino)ethyl)-1-(10H-phenoxazin-2-yl)ethanesulfonamide (**4.4b**) in DMSO-d6.

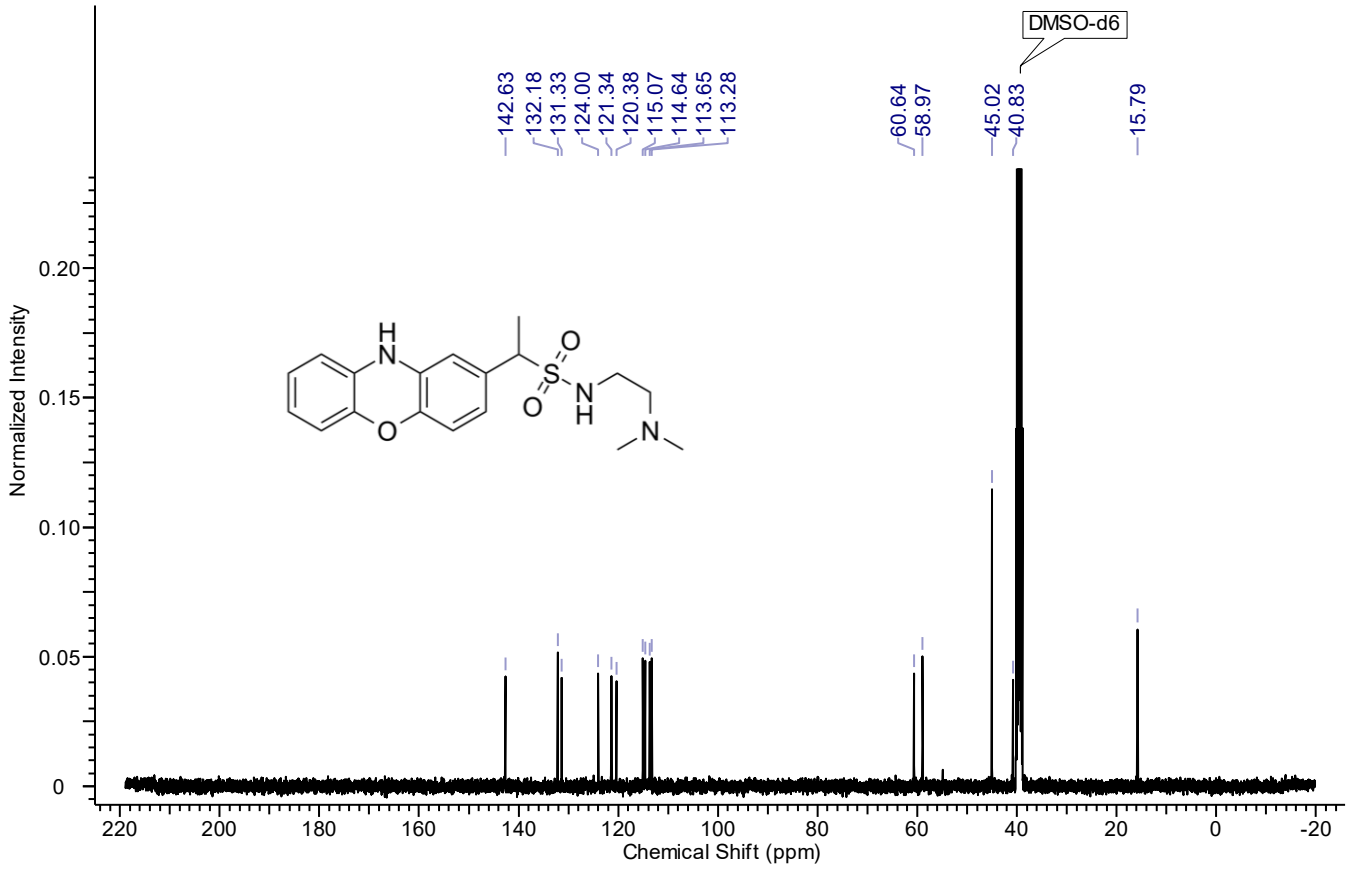


Figure S7.131. Full spectra ^{13}C NMR of N-(2-(dimethylamino)ethyl)-1-(10H-phenoxazin-2-yl)ethanesulfonamide (**4.4b**) in DMSO-d6

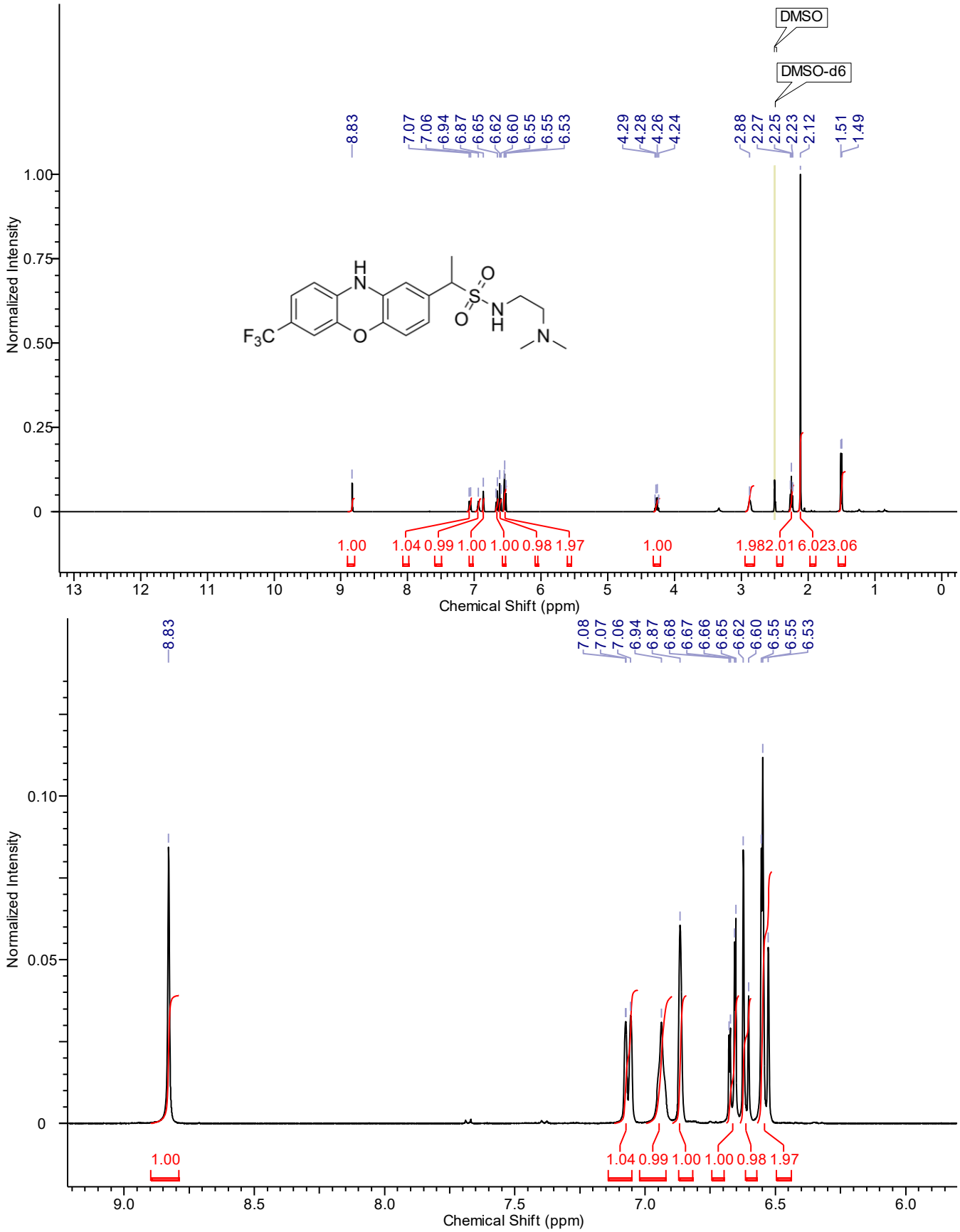


Figure S7.132. Full spectra (*top*) and aromatic region (*bottom*) ^{1}H NMR of N-(2-(dimethylamino)ethyl)-1-(7-(trifluoromethyl)-10H-phenoxazin-2-yl)ethanesulfonamide (**4.4a**).in DMSO-d6.

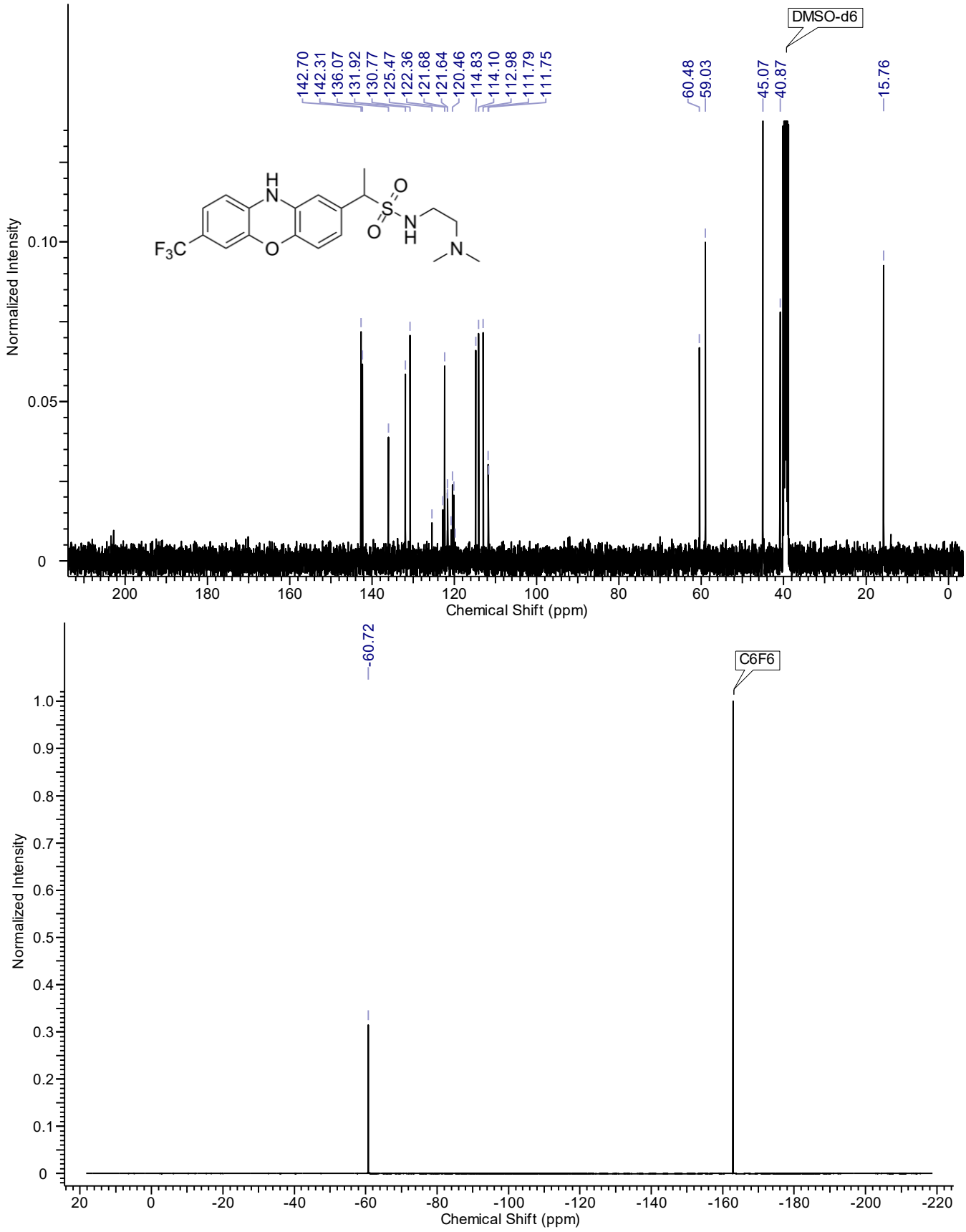


Figure S7.133. ^{13}C NMR (*top*) and $^{19}FNMR$ (*bottom*) of N-(2-(dimethylamino)ethyl)-1-(7-(trifluoromethyl)-10H-phenoxazin-2-yl)ethanesulfonamide (**4.4a**) in DMSO-d6.

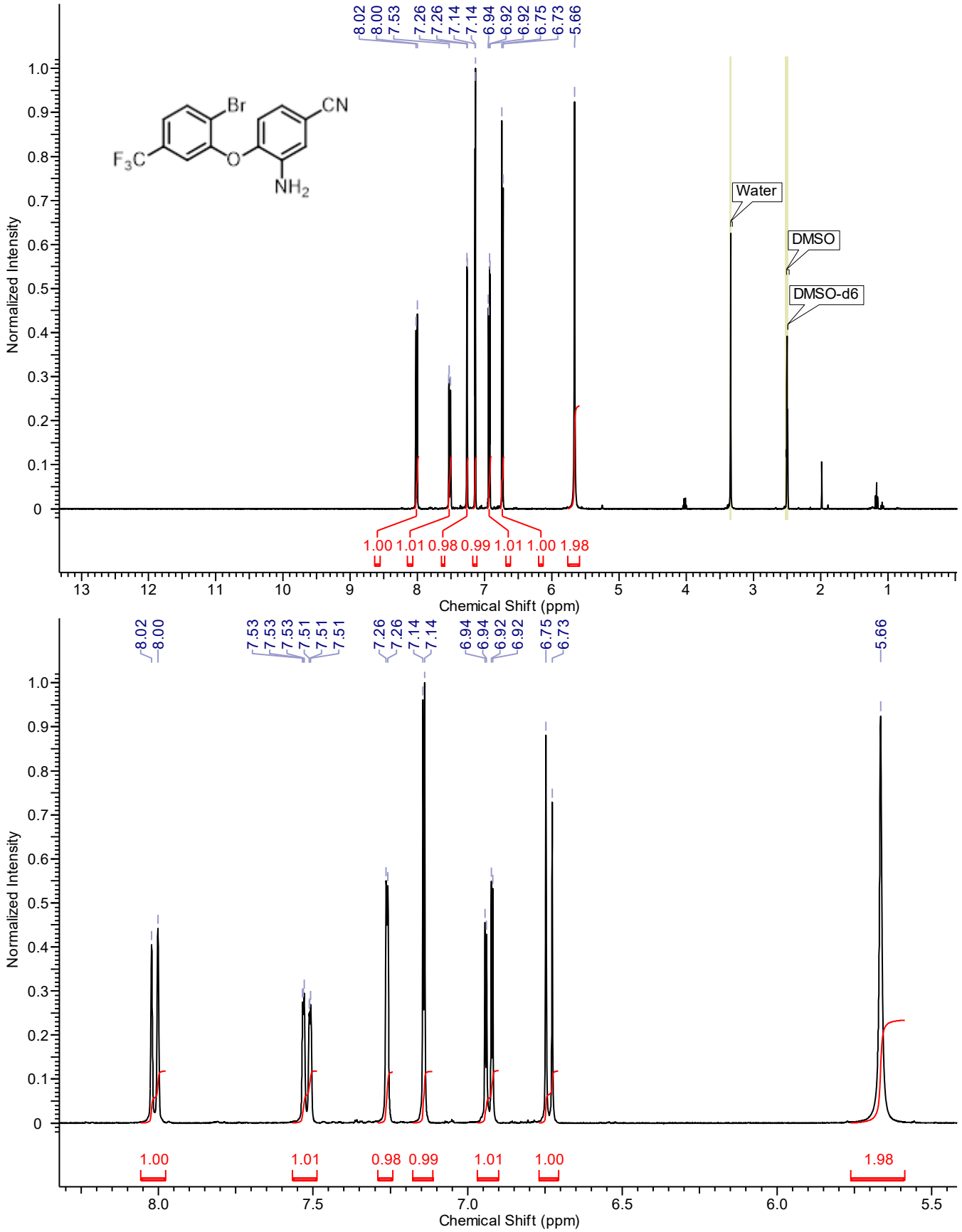


Figure S7.134. Full spectra (*top*) and aromatic region (*bottom*) ^{1}H NMR of 3-Amino-4-(2-bromo-5-(trifluoromethyl)phenoxy)benzonitrile.in DMSO-d6.

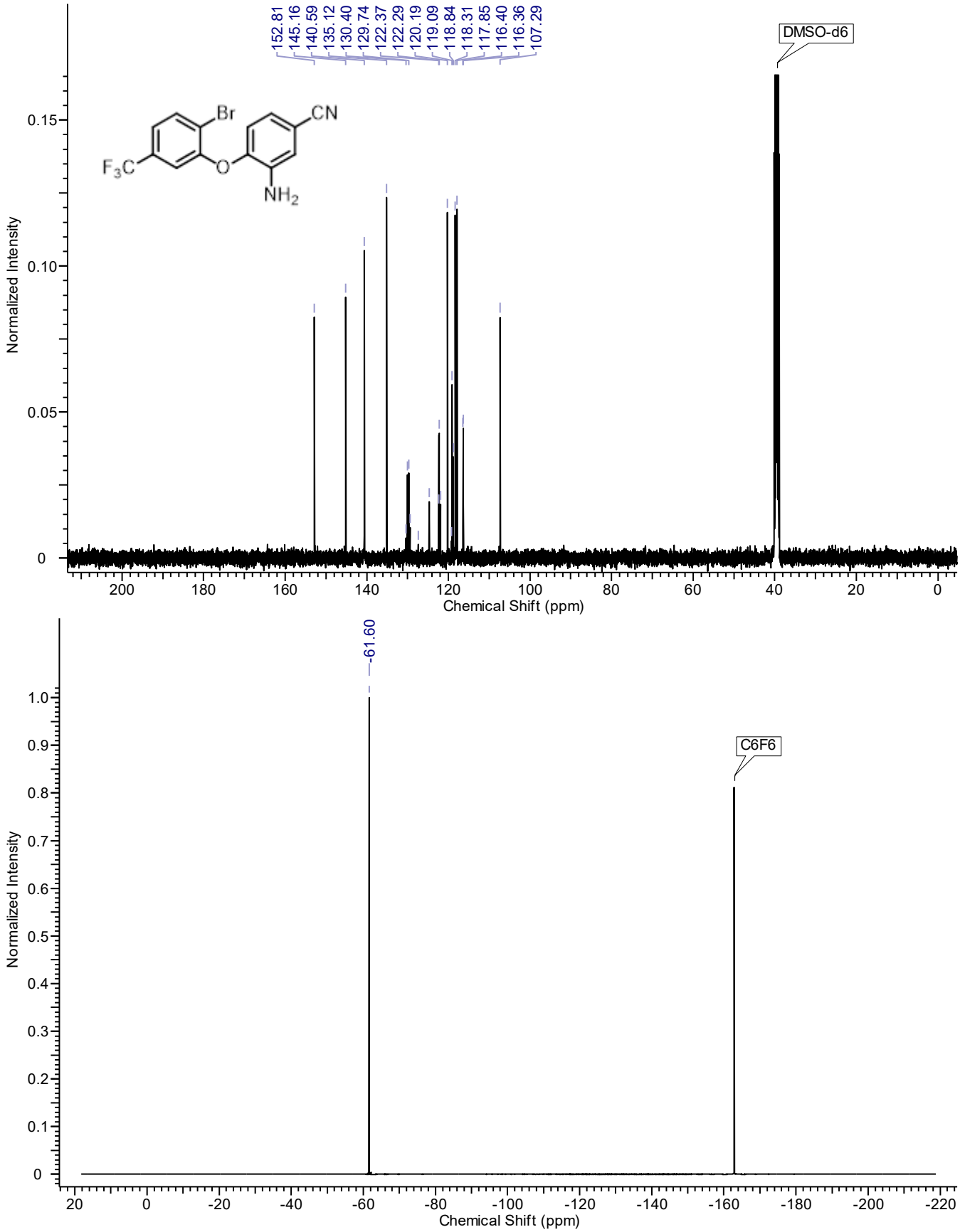


Figure S7.135. ^{13}C NMR (*top*) and ^{19}FNMR (*bottom*) of 3-Amino-4-(2-bromo-5-(trifluoromethyl)phenoxy)benzonitrile in DMSO-d6.

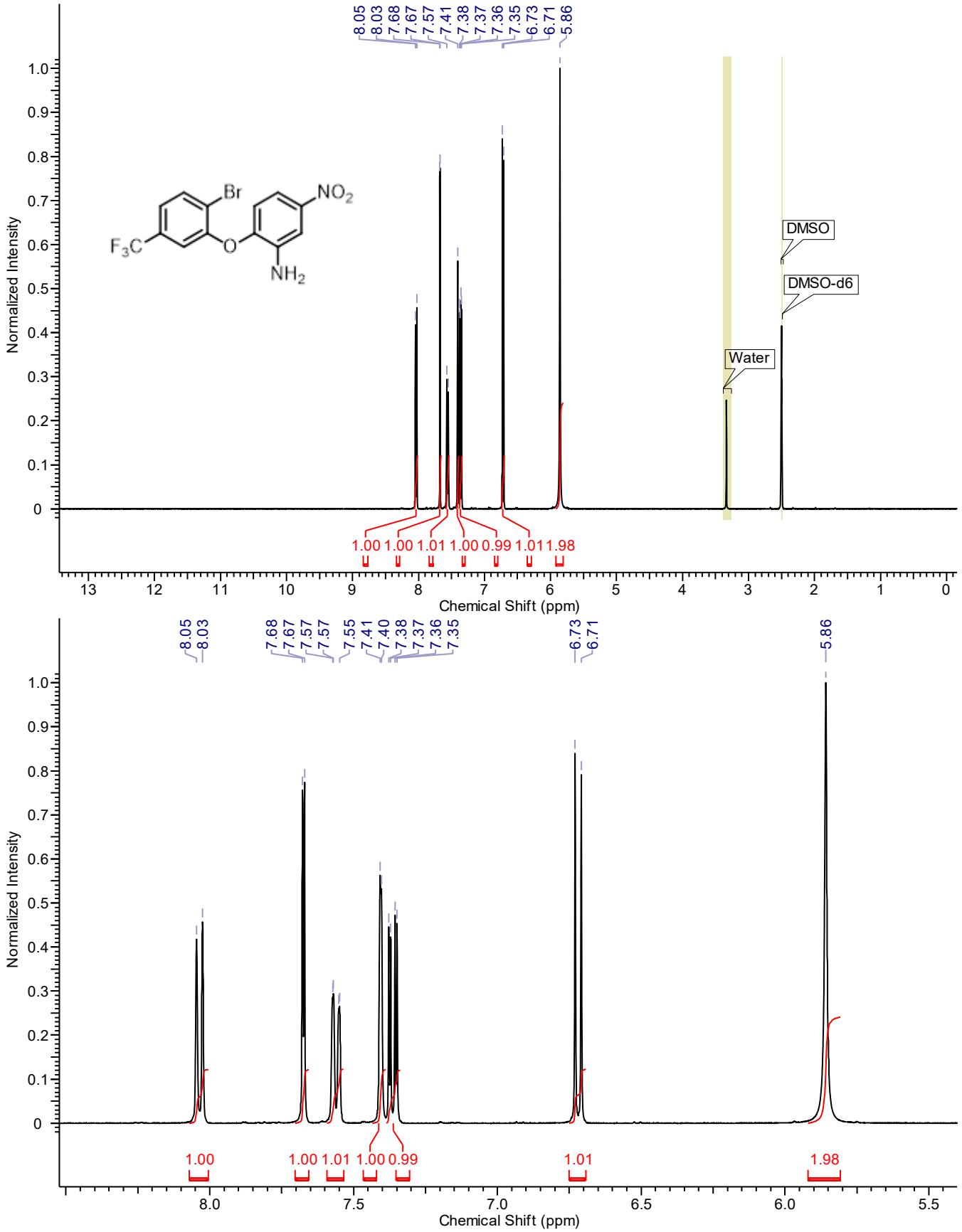


Figure S7.136. Full spectra (*top*) and aromatic region (*bottom*) ^{1}H NMR of 2-(2-Bromo-5-(trifluoromethyl)phenoxy)-5-nitroaniline.in DMSO-d6.

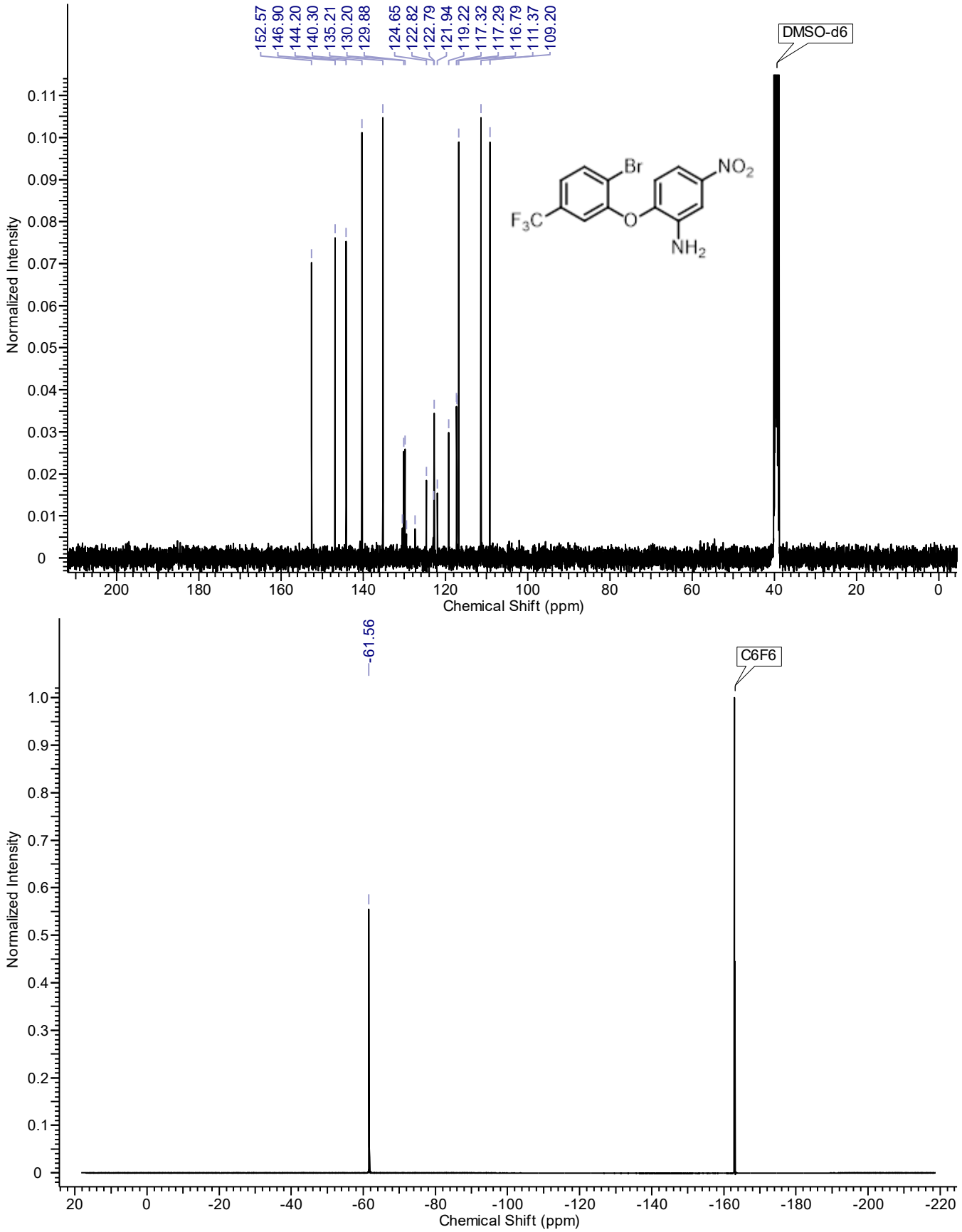


Figure S7.137. ^{13}C NMR (*top*) and ^{19}FNMR (*bottom*) of 2-(2-Bromo-5-(trifluoromethyl)phenoxy)-5-nitroaniline in DMSO-d6.

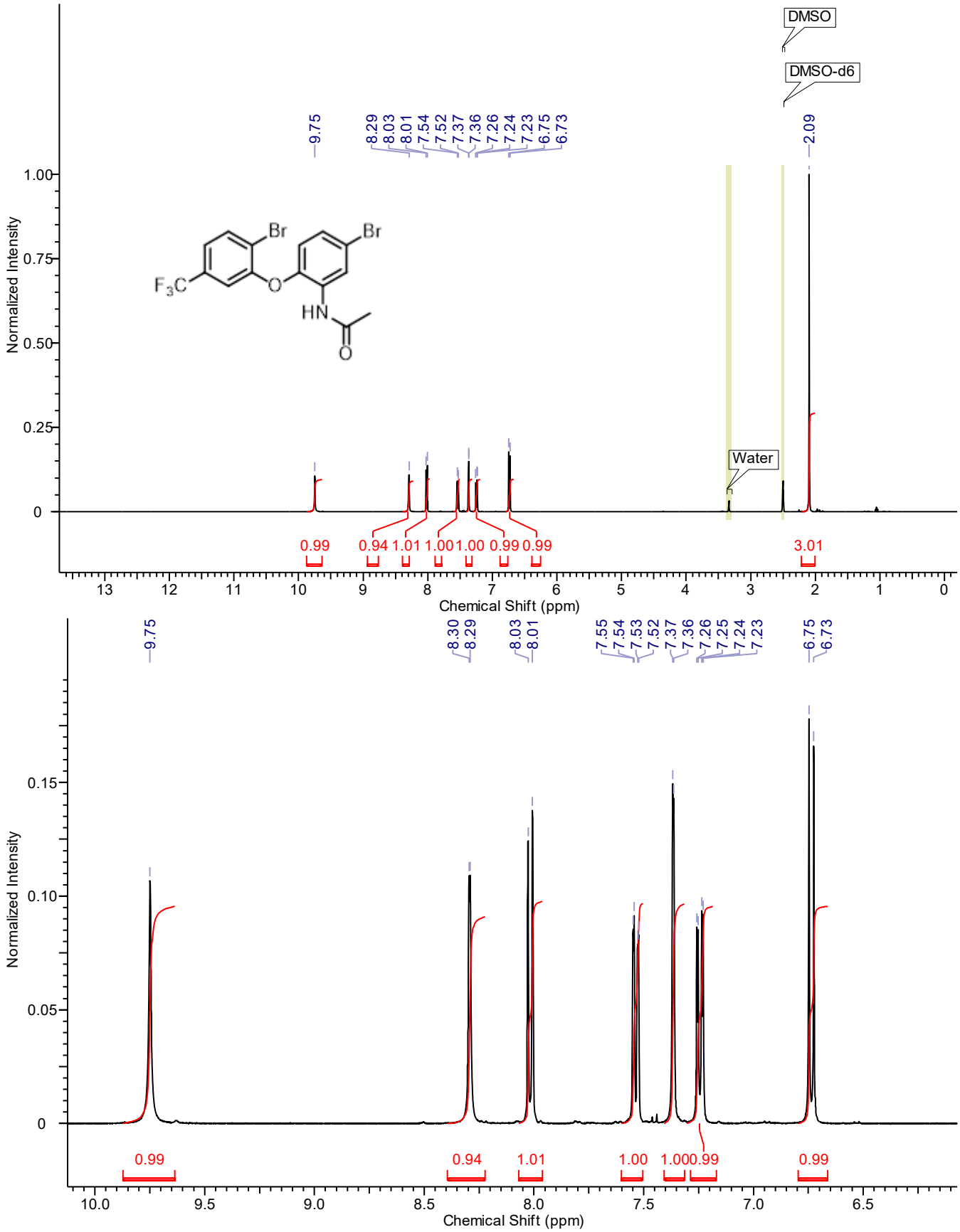


Figure S7.138. Full spectra (*top*) and aromatic region (*bottom*) ^{1}H NMR of N-(5-Bromo-2-(2-bromo-5-(trifluoromethyl)phenoxy)phenyl)acetamide.in DMSO-d6.

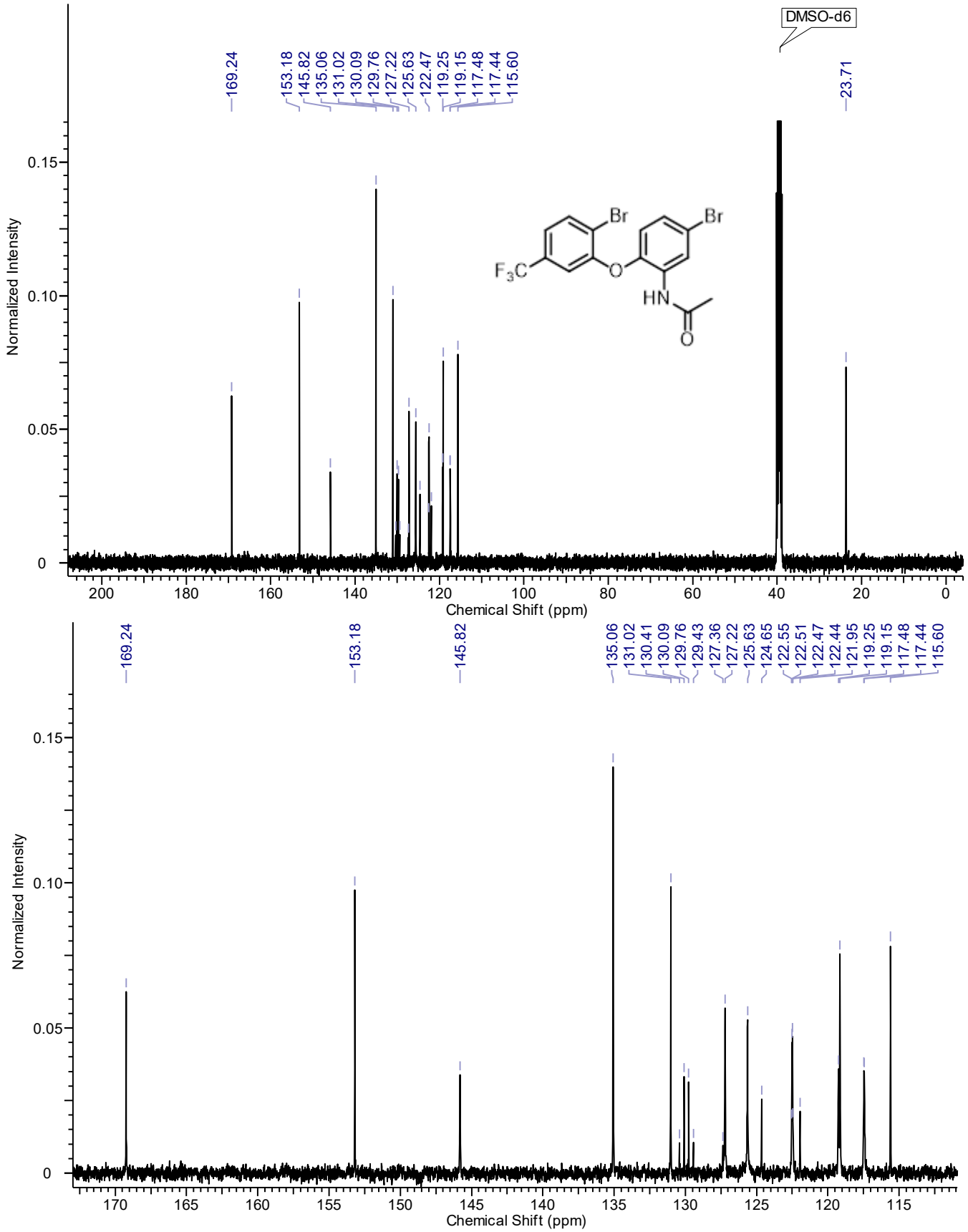


Figure S7.139. Full spectra (*top*) and aromatic region (*bottom*) ^{13}C NMR of N-(5-Bromo-2-(2-bromo-5-(trifluoromethyl)phenoxy)phenyl)acetamide.in DMSO-d6.

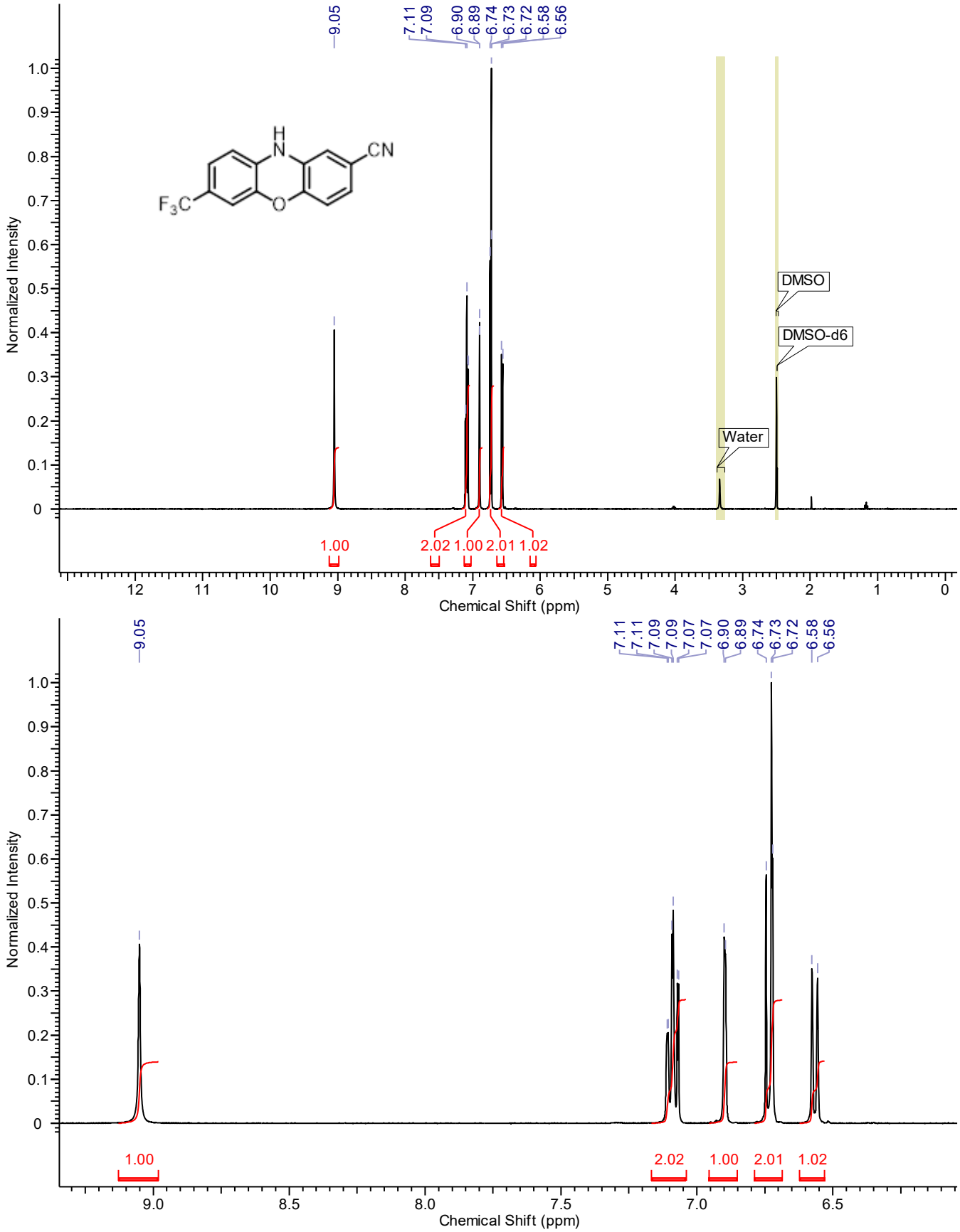


Figure S7.140. Full spectra (*top*) and aromatic region (*bottom*) ^{1}H NMR of 2-Cyano-7-trifluoromethylphenoxazine (**4.7**).in DMSO-d6.

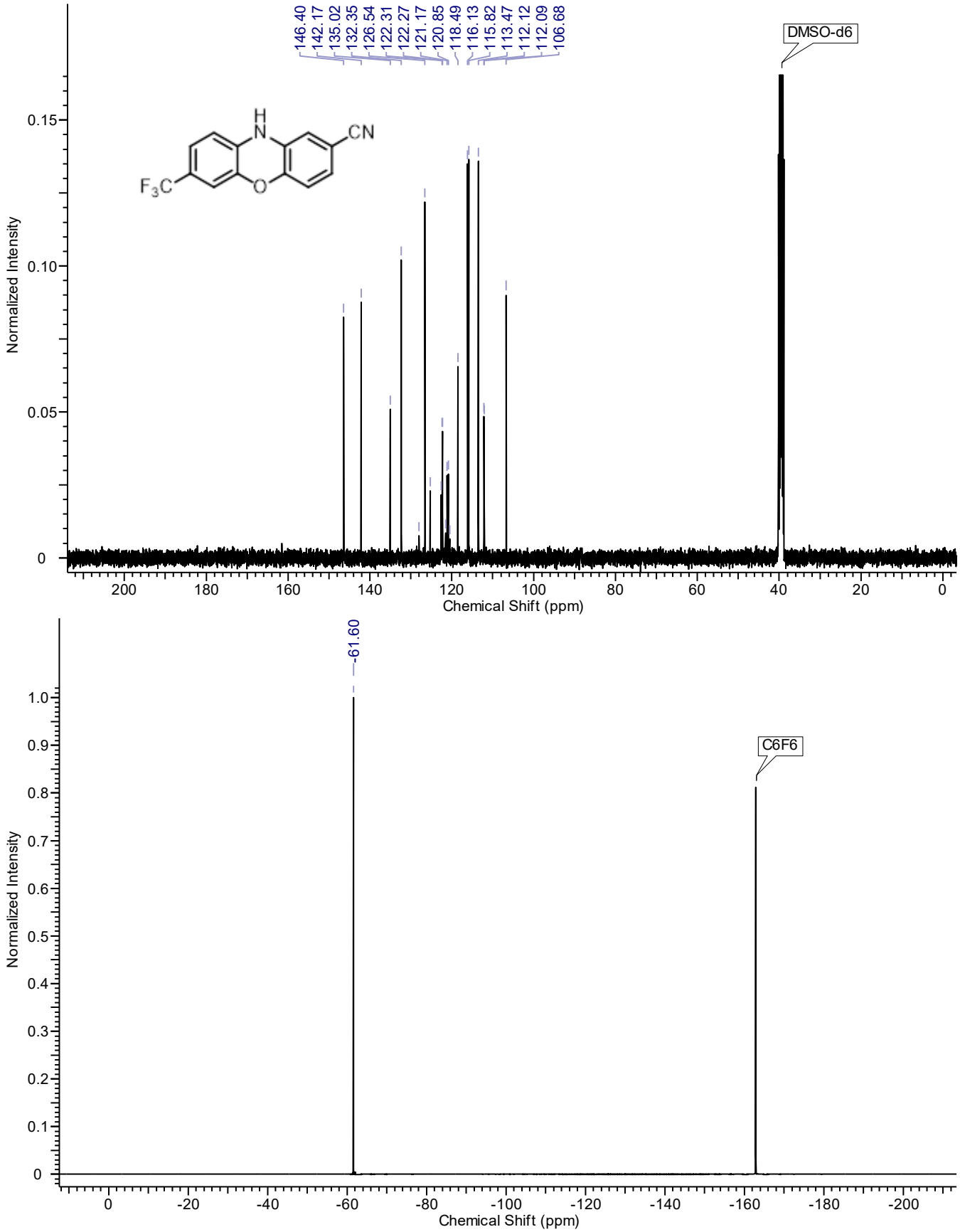


Figure S7.141. ^{13}C NMR (*top*) and ^{19}FNMR (*bottom*) of 2-Cyano-7-trifluoromethylphenoxazine (**4.7**) in DMSO-d6.

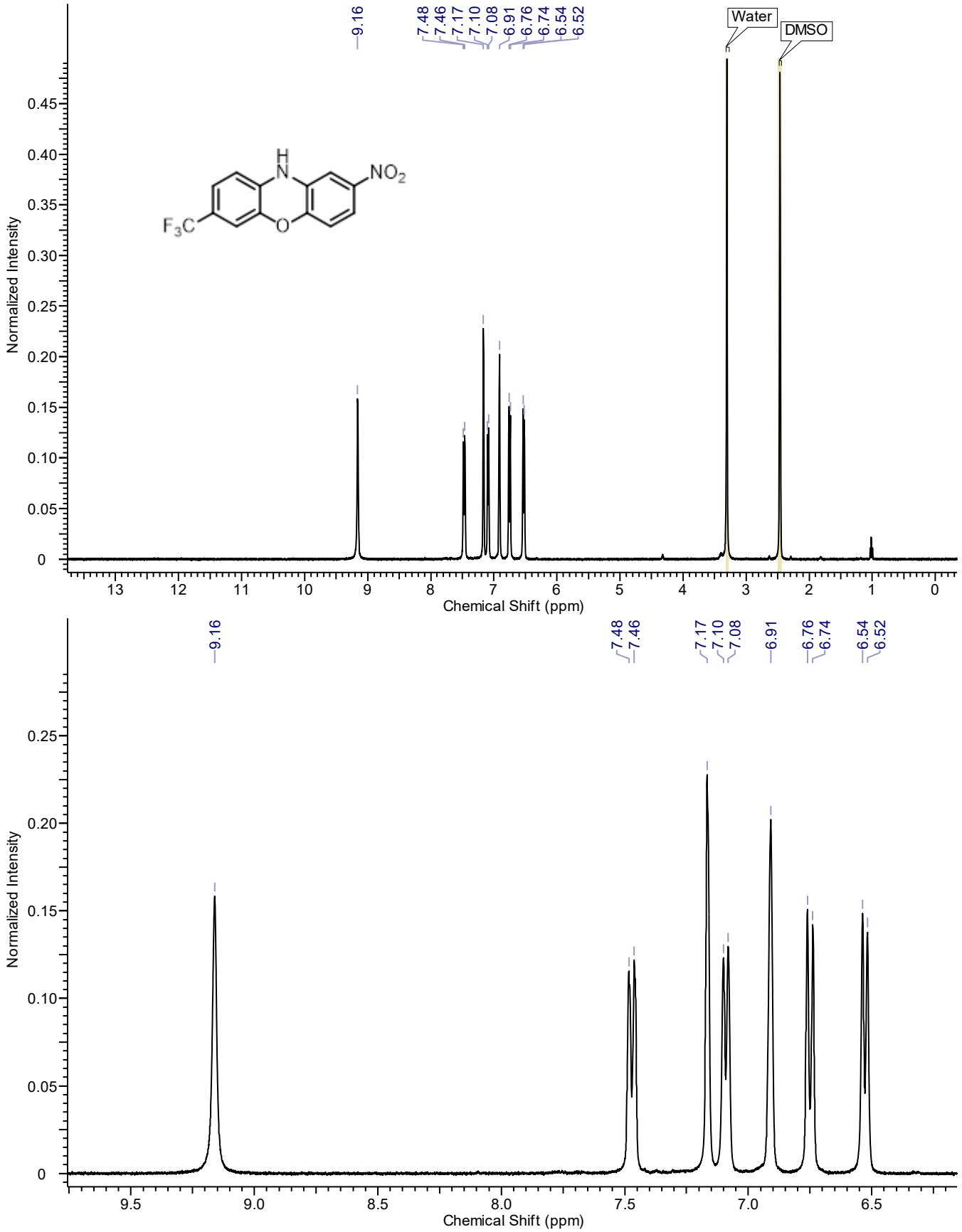


Figure S7.142. Full spectra (*top*) and aromatic region (*bottom*) ^{1}H NMR of 2-nitro-7-trifluoromethylphenoxazine (**4.8**).in DMSO-d6.

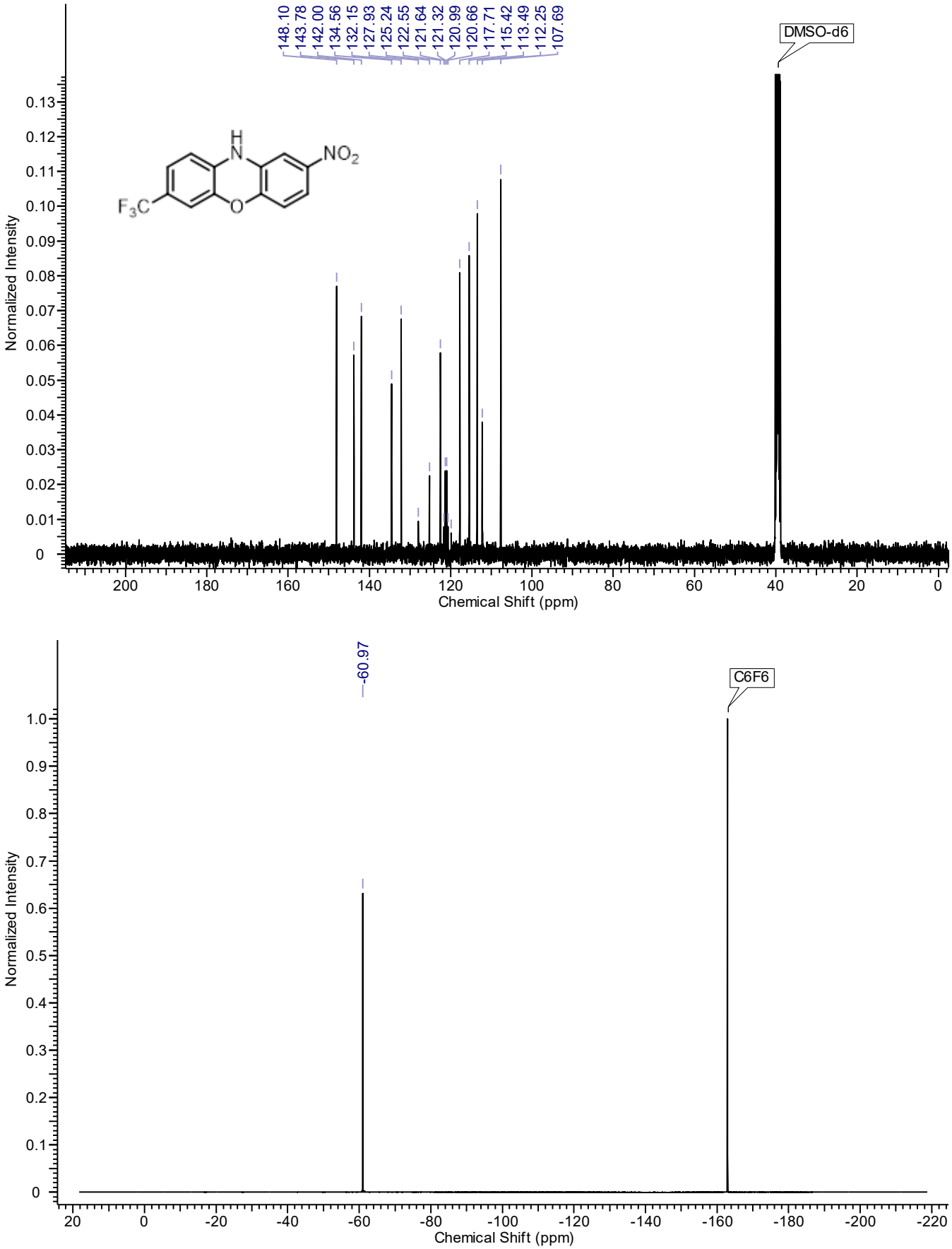


Figure S7.143. ^{13}C NMR (*top*) and ^{19}FNMR (*bottom*) of 2-nitro-7-trifluoromethylphenoxazine (**4.8**) in DMSO-d6.

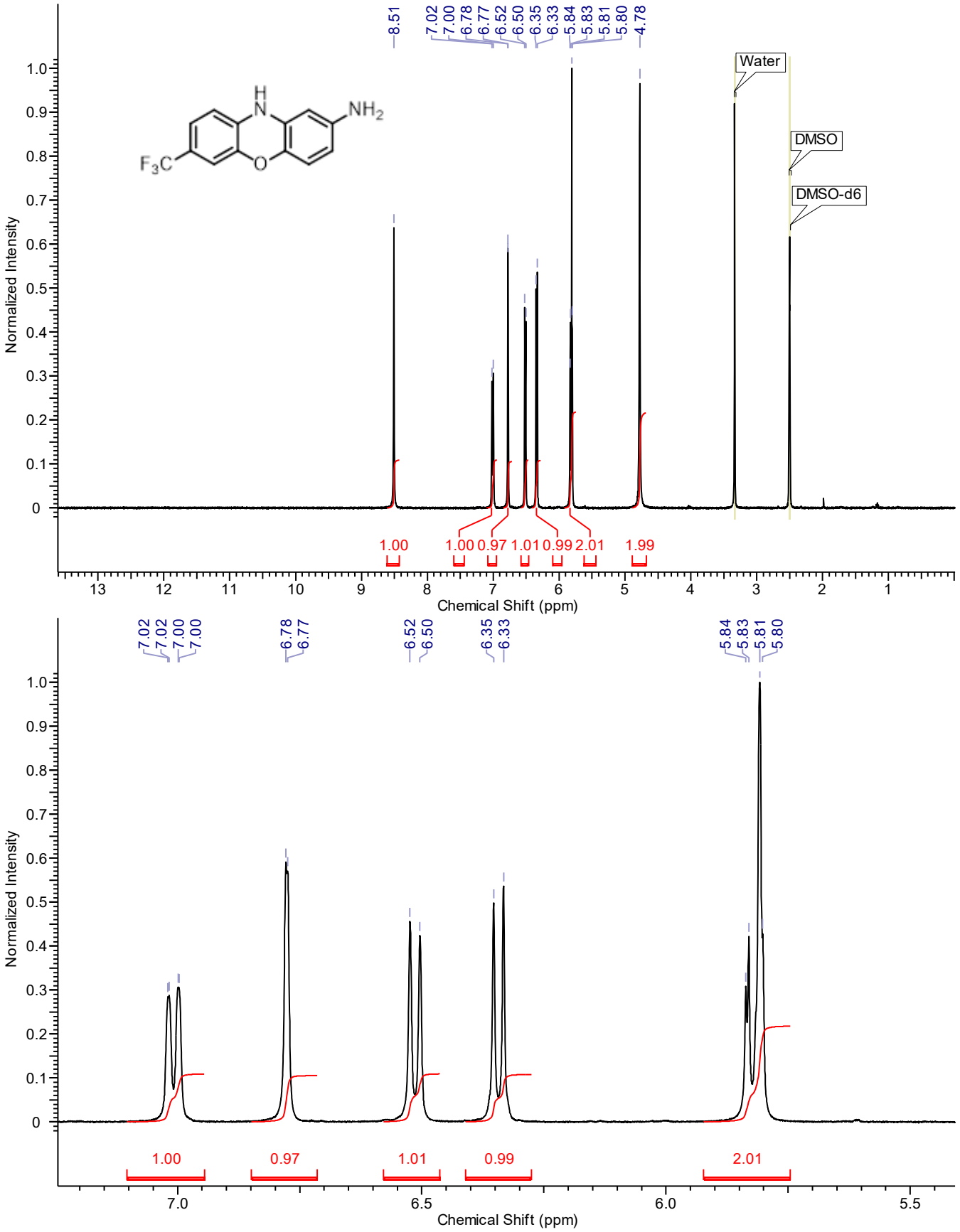


Figure S7.144. Full spectra (*top*) and aromatic region (*bottom*) ^{1}H NMR of 2-amino-7-trifluoromethylphenoxazine (**4.9**).in DMSO-d6.

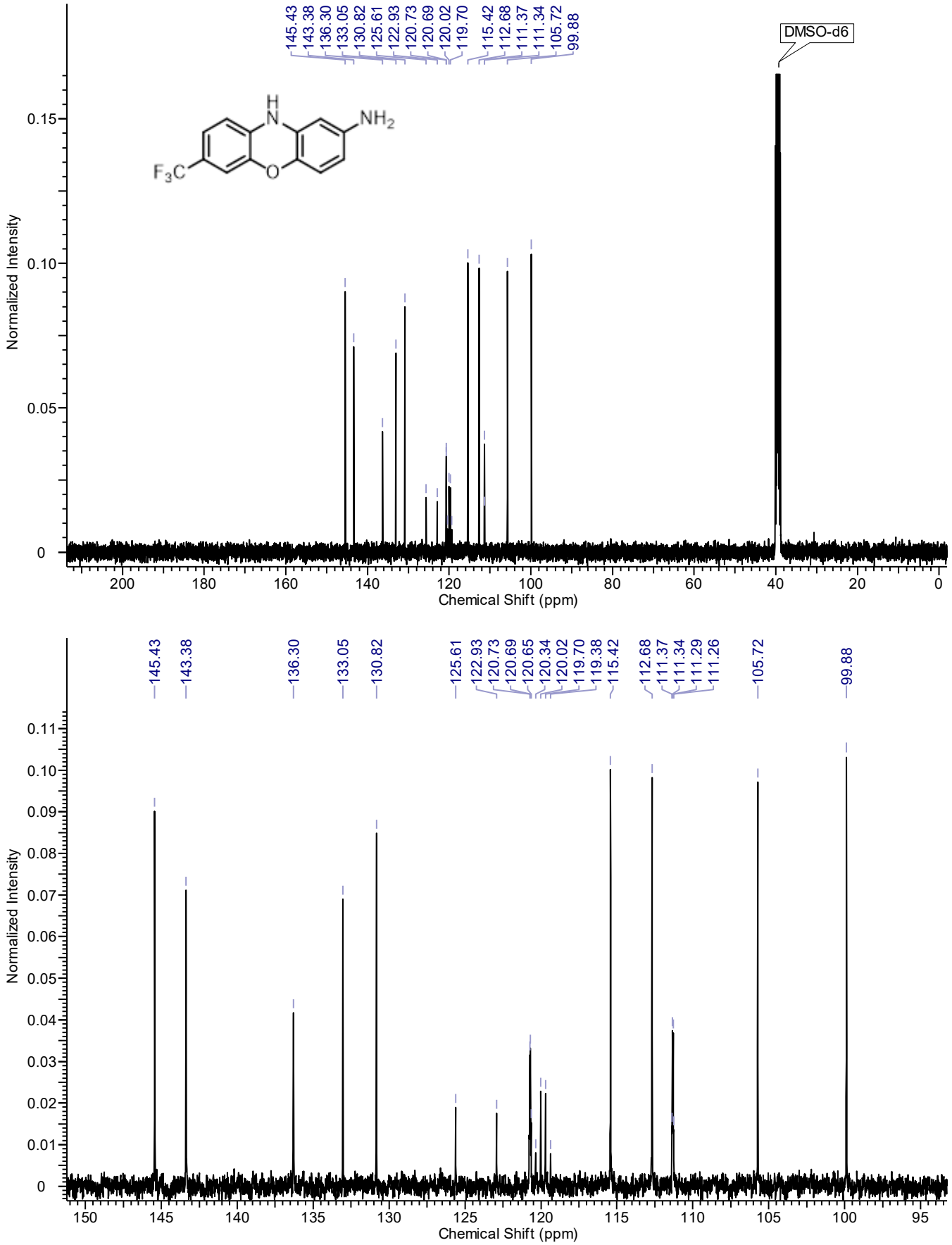


Figure S7.145. Full spectra (*top*) and aromatic region (*bottom*) ^{13}C NMR of 2-amino-7-trifluoromethylphenoxazine (**4.9**).in DMSO-d6.

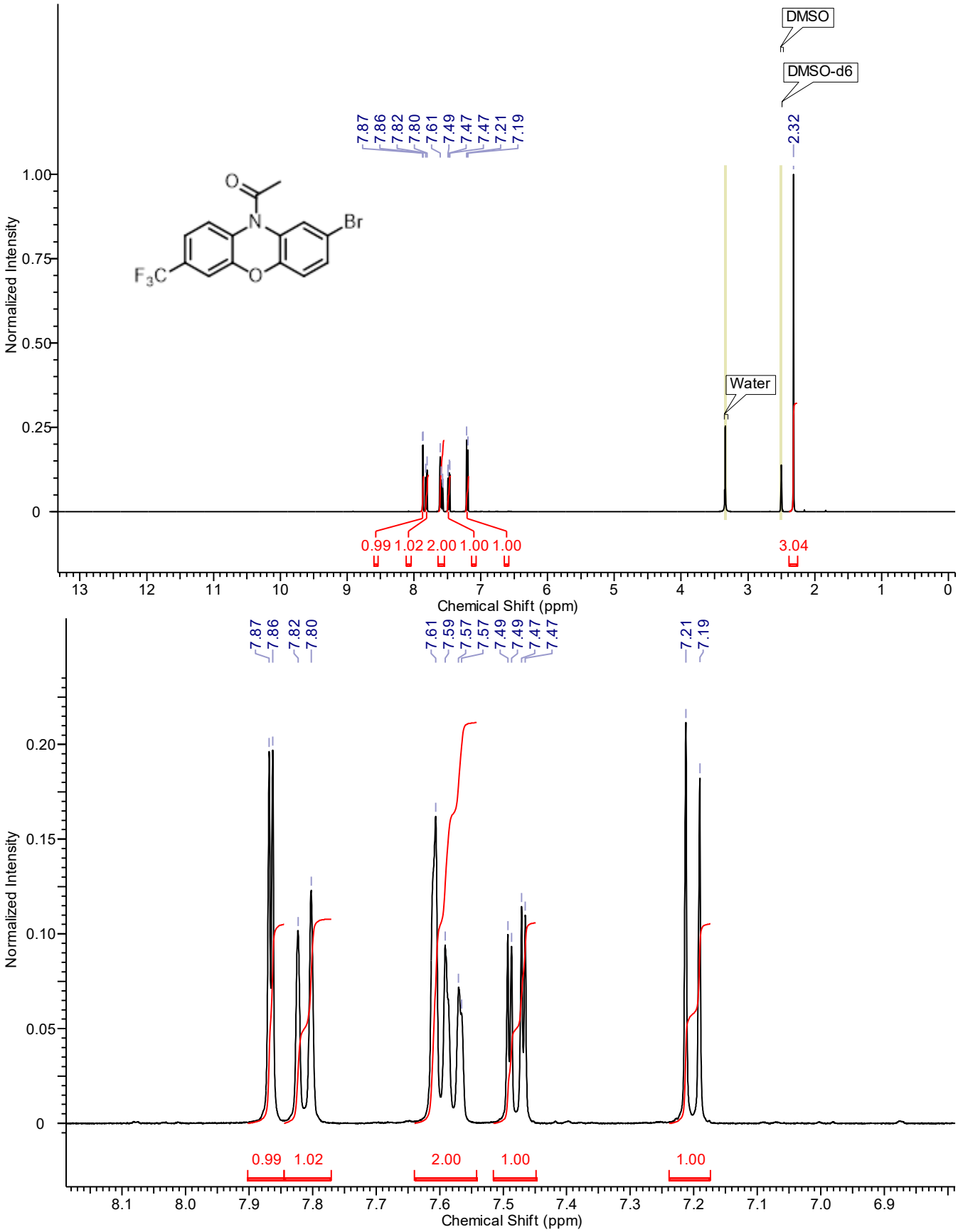


Figure S7.146. Full spectra (*top*) and aromatic region (*bottom*) ^{1}H NMR of 10-Acetyl-2-bromo-7-trifluoromethylphenoxazine.in DMSO-d6.

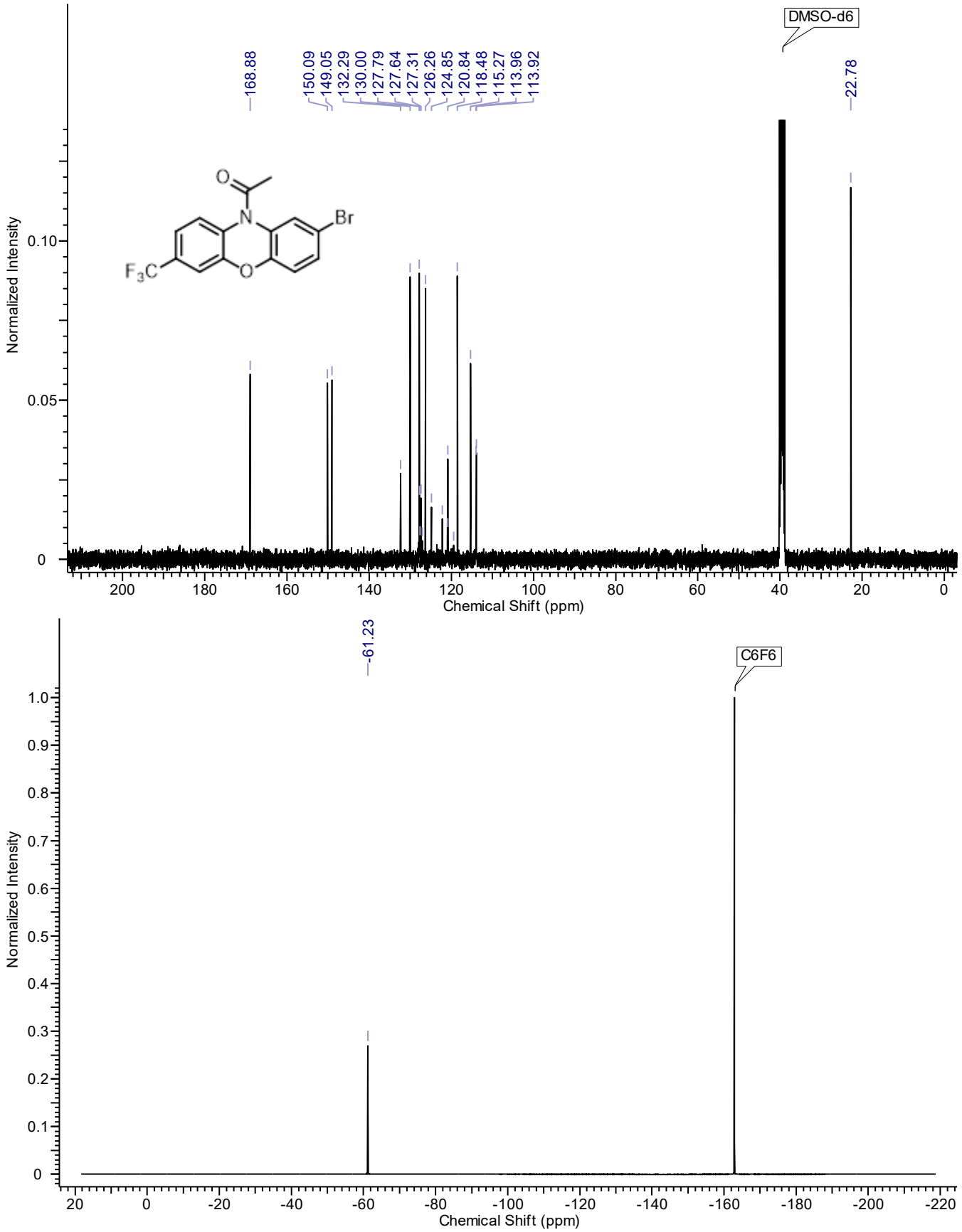


Figure S7.147. ^{13}C NMR (*top*) and ^{19}FNMR (*bottom*) of 10-Acetyl-2-bromo-7-trifluoromethylphenoxazine in DMSO-d6.

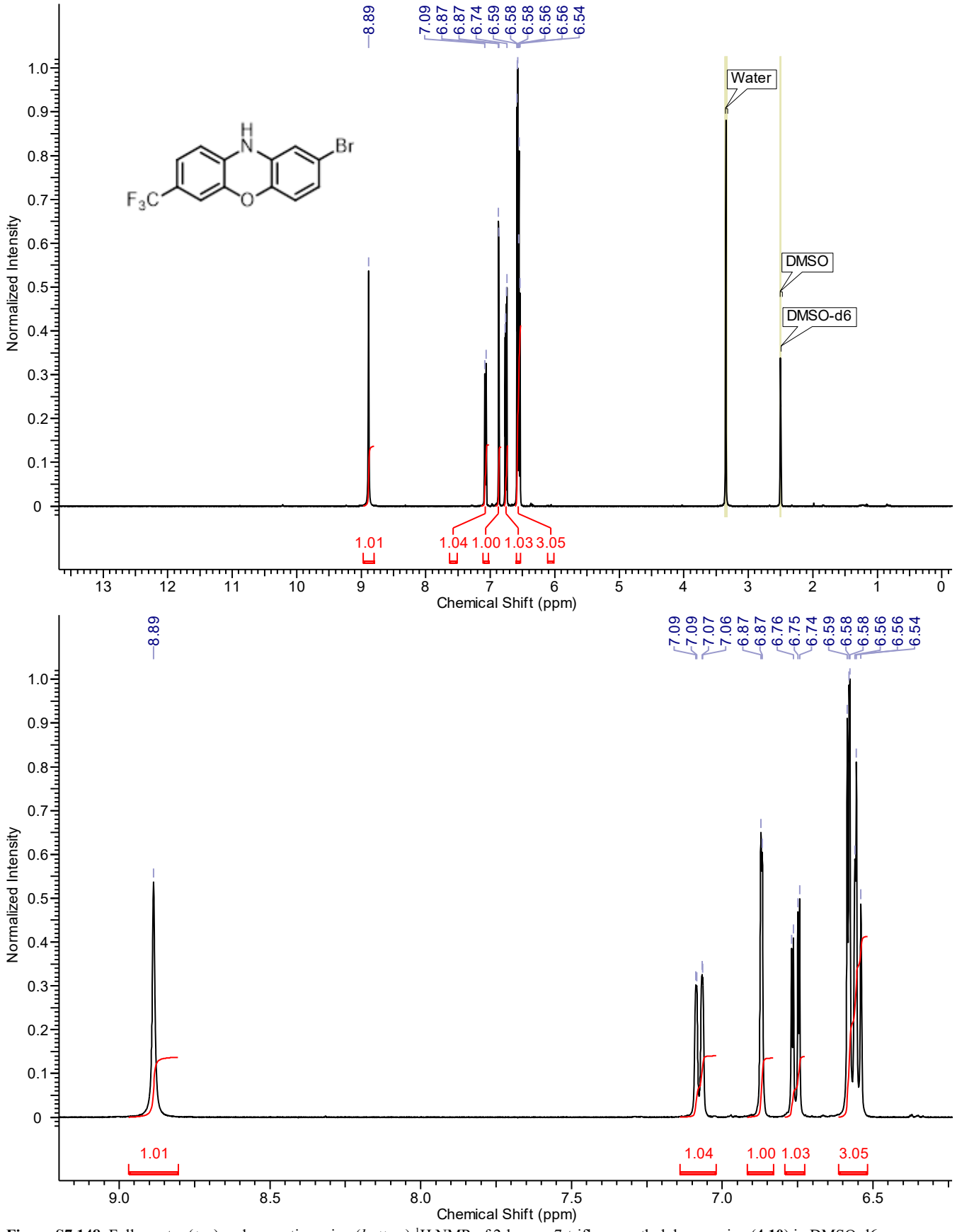


Figure S7.148. Full spectra (*top*) and aromatic region (*bottom*) ^{1}H NMR of 2-bromo-7-trifluoromethylphenoxazine (**4.10**).in DMSO-d6.

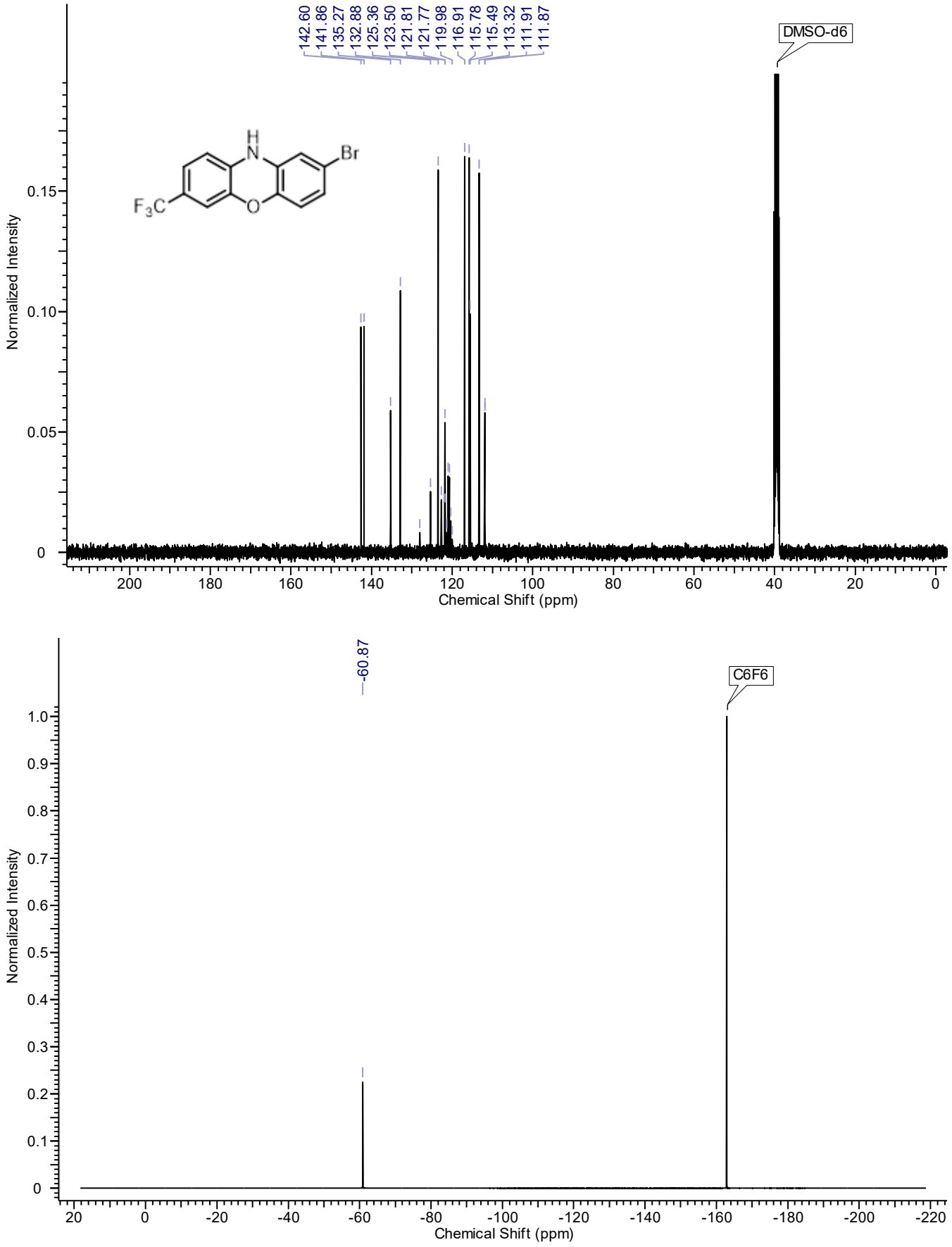


Figure S7.149. ^{13}C NMR (*top*) and ^{19}FNMR (*bottom*) of 2-bromo-7-trifluoromethylphenoxazine (**4.10**) in DMSO-d6.

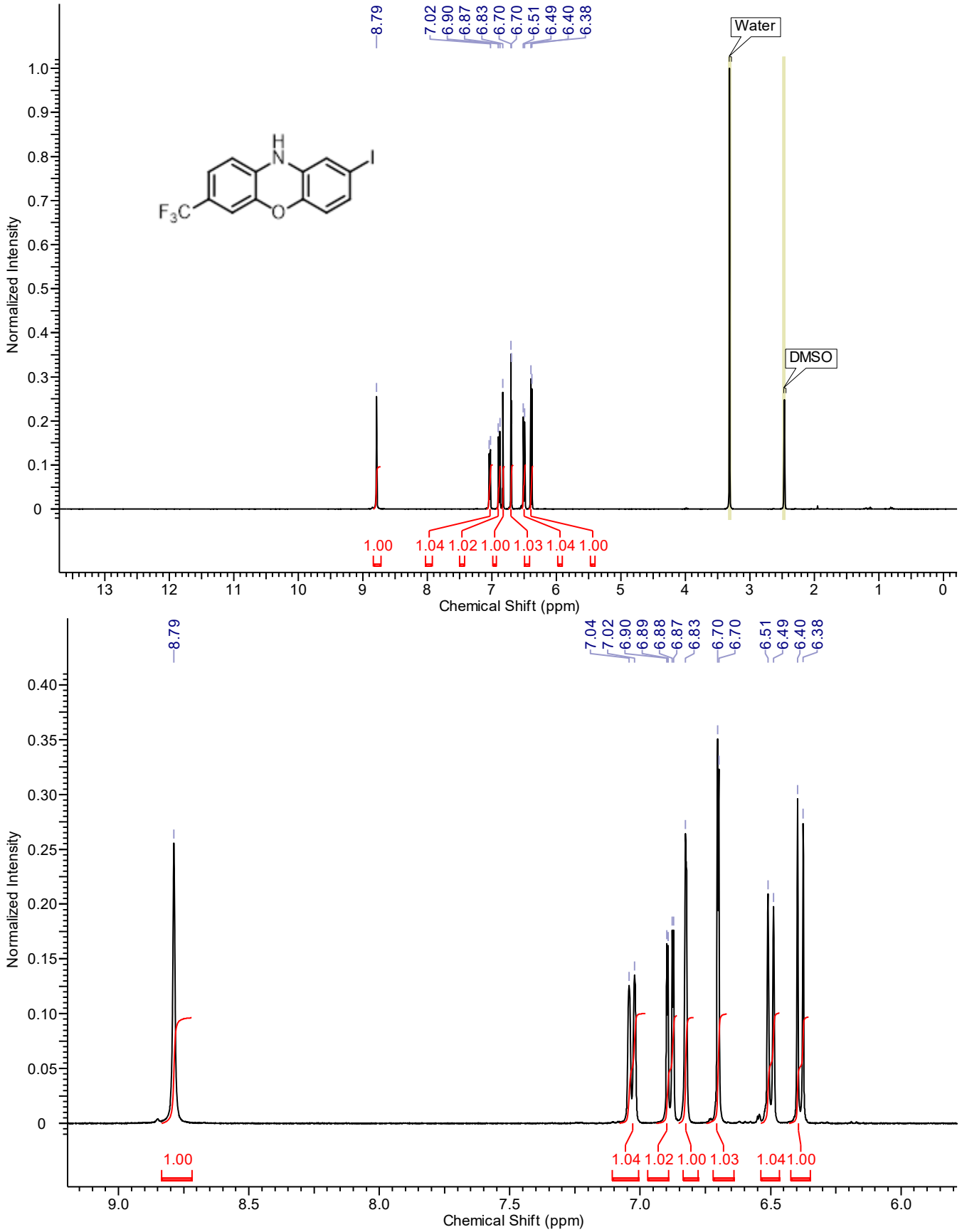


Figure S7.150. Full spectra (*top*) and aromatic region (*bottom*) ^{1}H NMR of 2-iodo-7-trifluoromethylphenoxazine (**4.11**).in DMSO-d6.

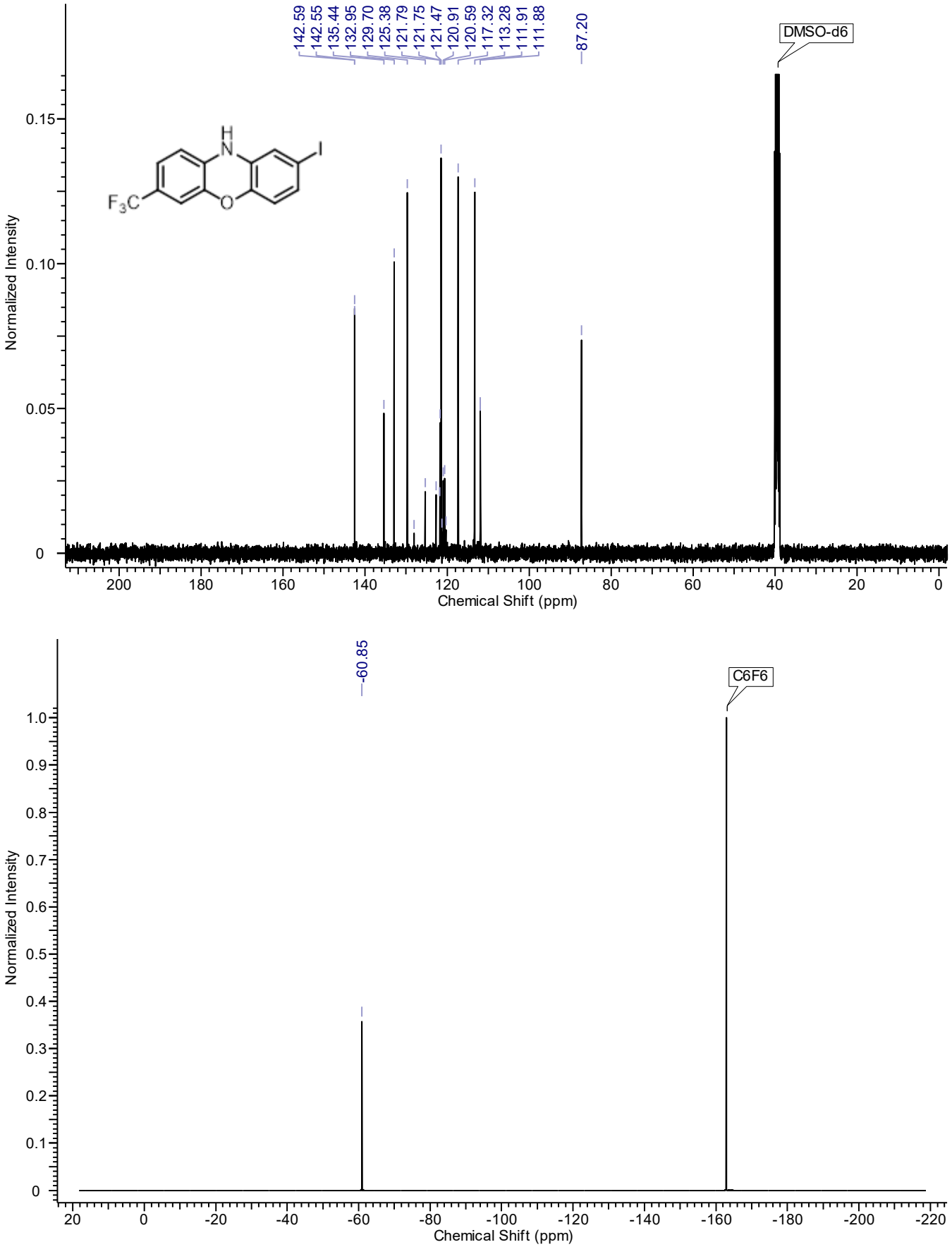


Figure S7.151. ^{13}C NMR (*top*) and ^{19}FNMR (*bottom*) of 2-iodo-7-trifluoromethylphenoxazine (**4.11**) in DMSO-d6.

7.4 Chapter 6 NMR Spectra

Begins on next page

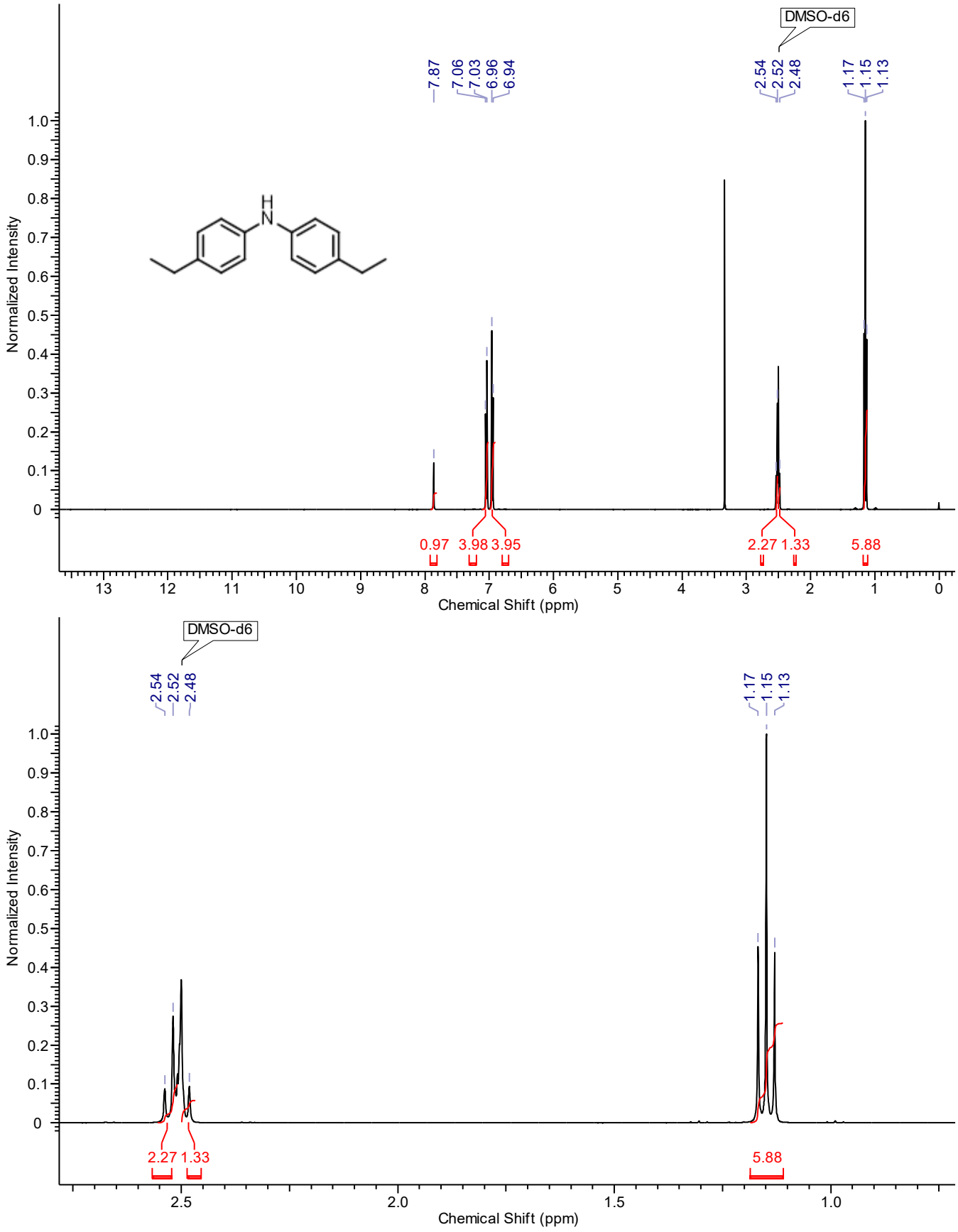


Figure S7.152. Full spectra (*top*) and alkyl region (*bottom*) ^{1}H NMR of 4,4'diethyldiphenylamine in DMSO-d6.

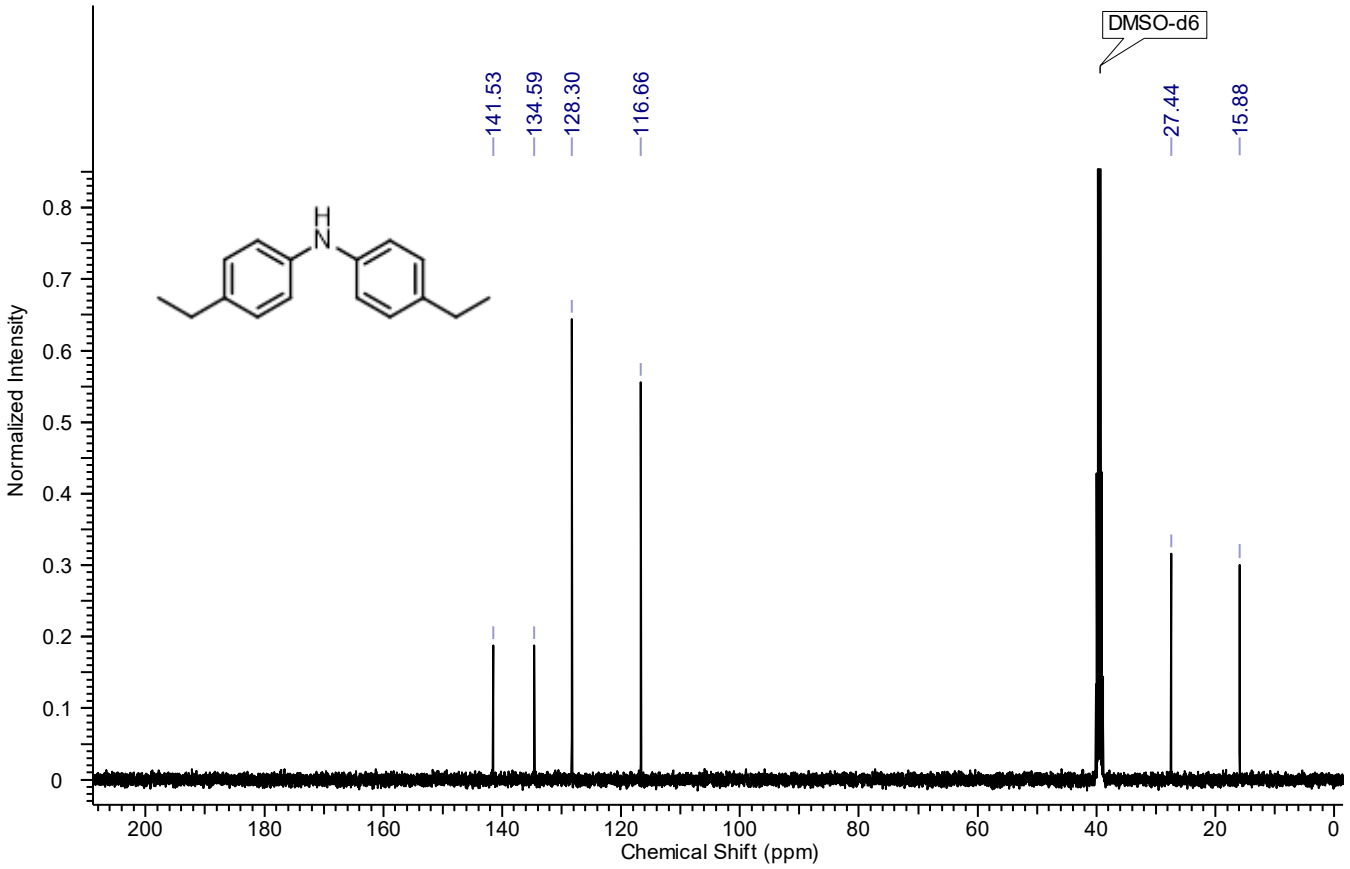


Figure S7.153. Full spectra ^{13}C NMR of 4,4'diethyldiphenylamine in DMSO-d6.

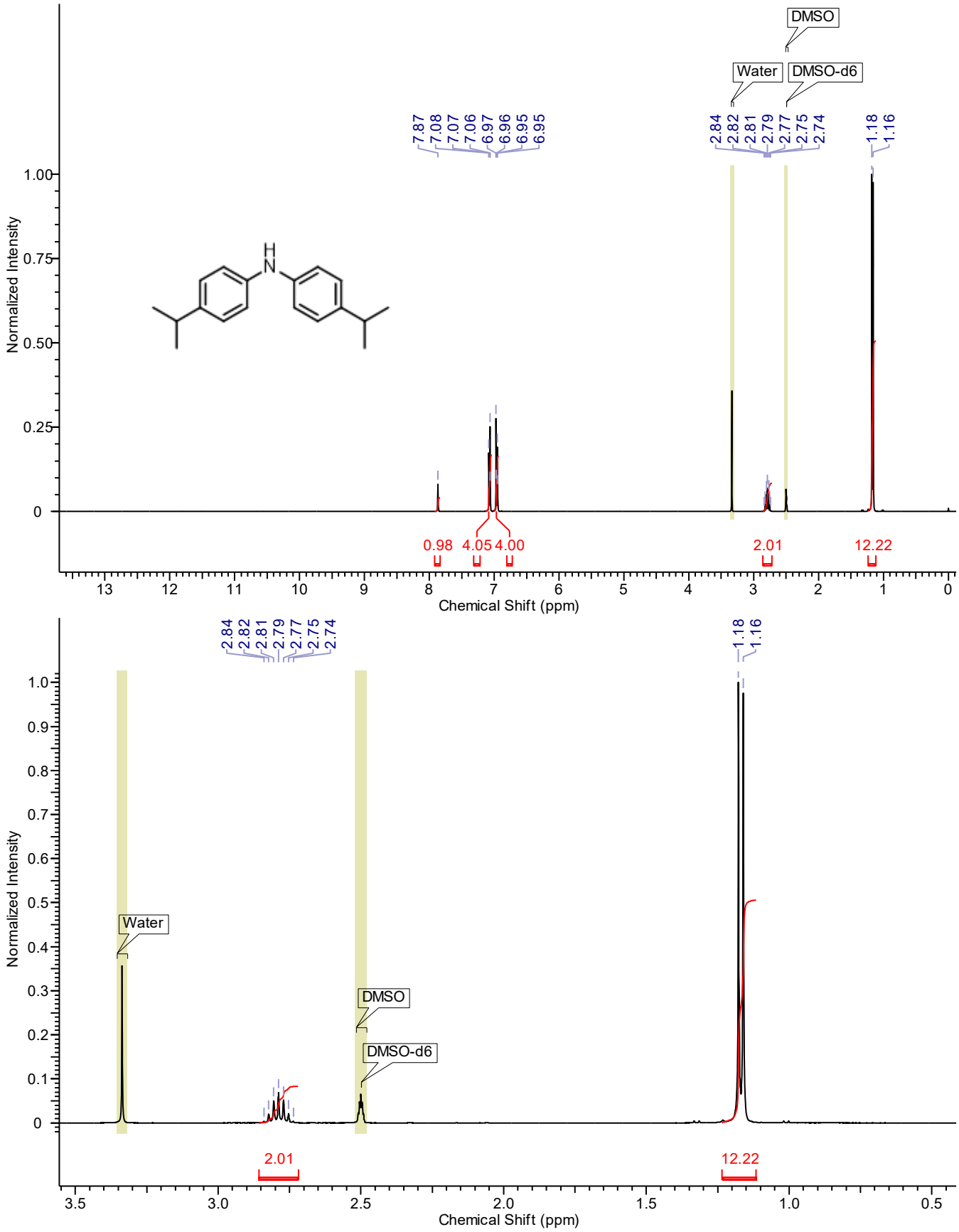


Figure S7.154. Full spectra (*top*) and alkyl region (*bottom*) ^{1}H NMR of 4,4'diisopropyldiphenylamine in DMSO-d6.

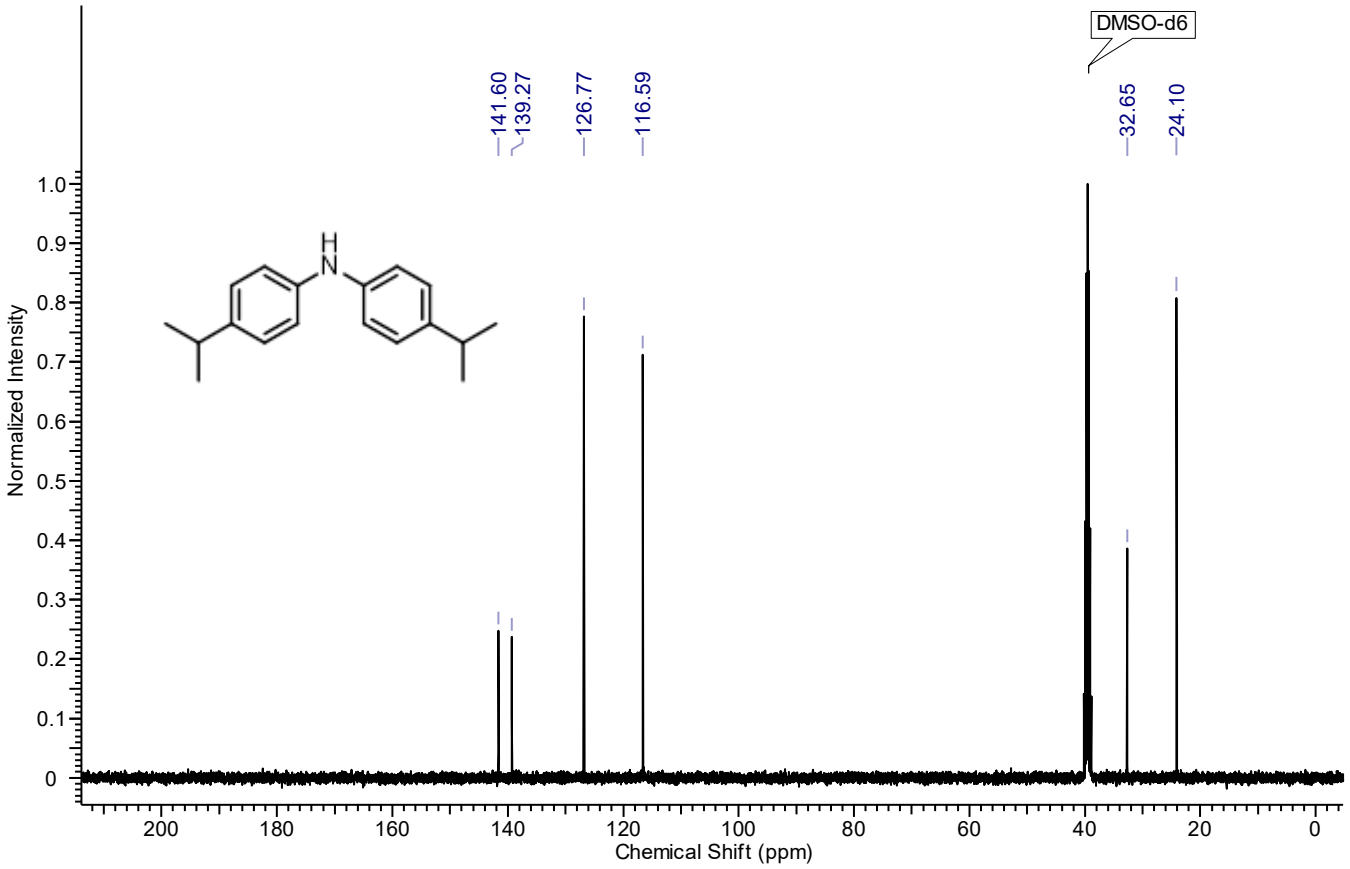


Figure S7.155. Full spectra ^{13}C NMR of 4,4'diisopropyldiphenylamine in DMSO-d6.

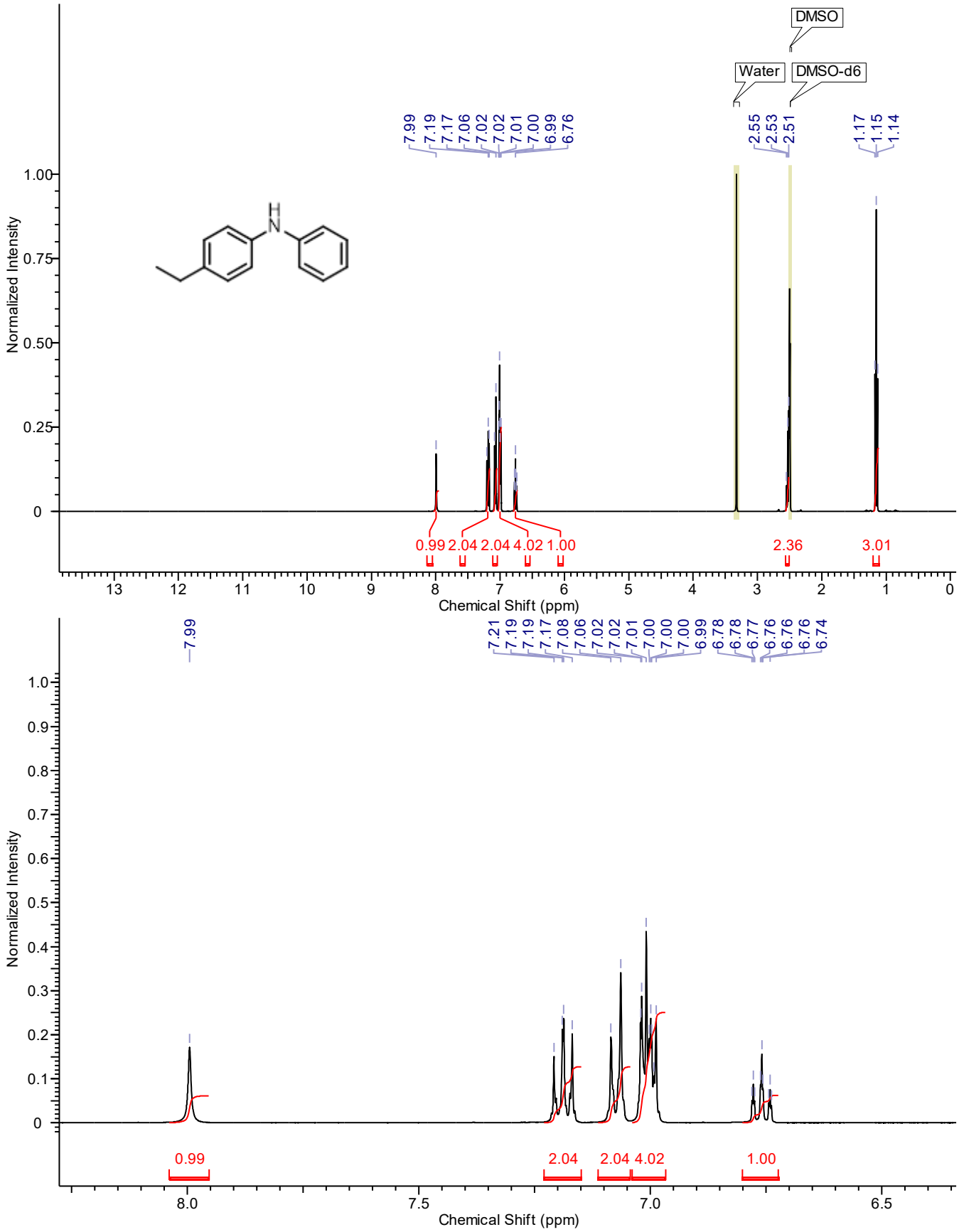


Figure S7.156. Full spectra (*top*) and aromatic region (*bottom*) ^{1}H NMR of 4-ethyldiphenylamine in DMSO-d6.

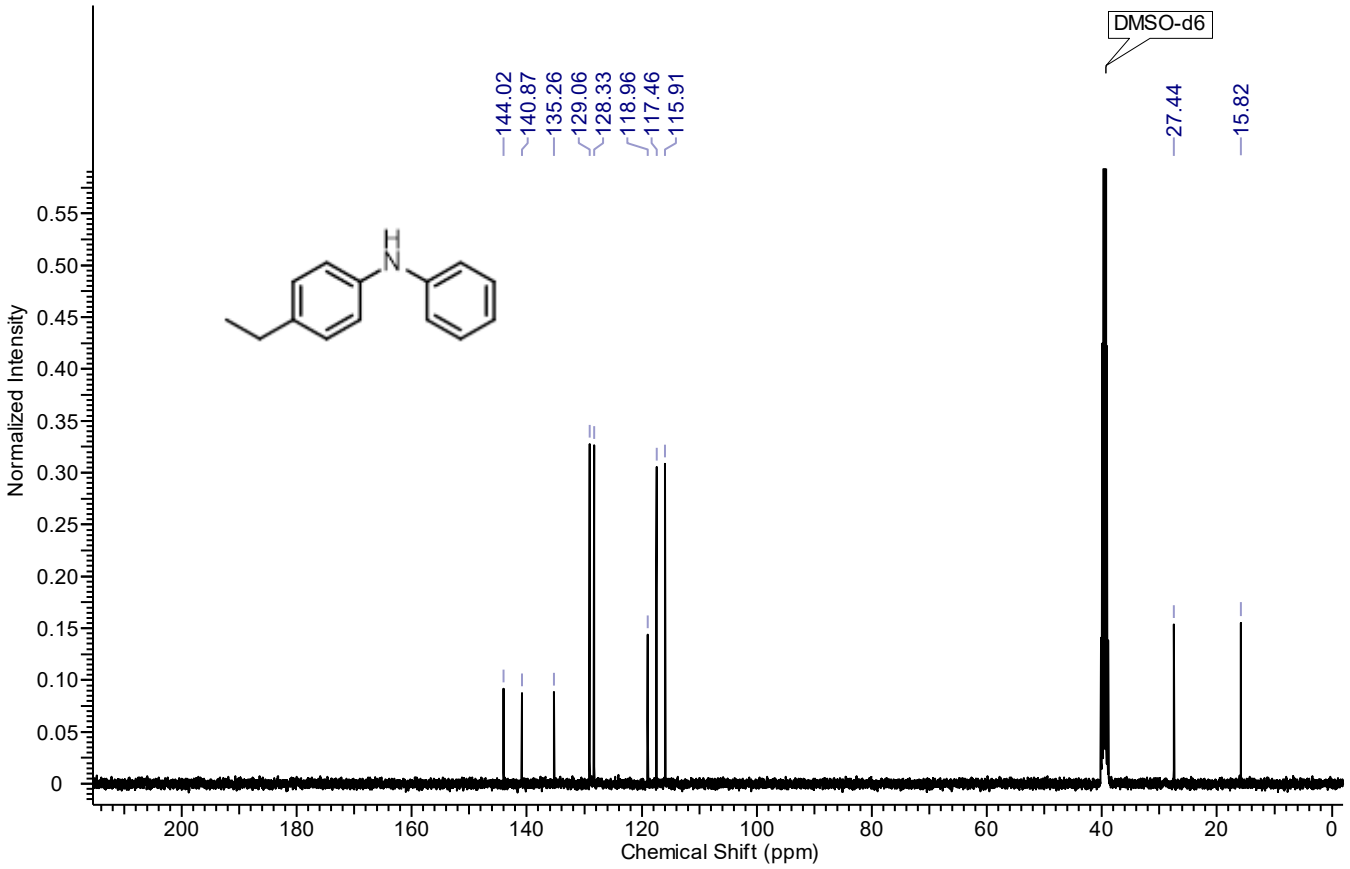


Figure S7.157. Full spectra ^{13}C NMR of 4-ethyldiphenylamine in DMSO-d6.

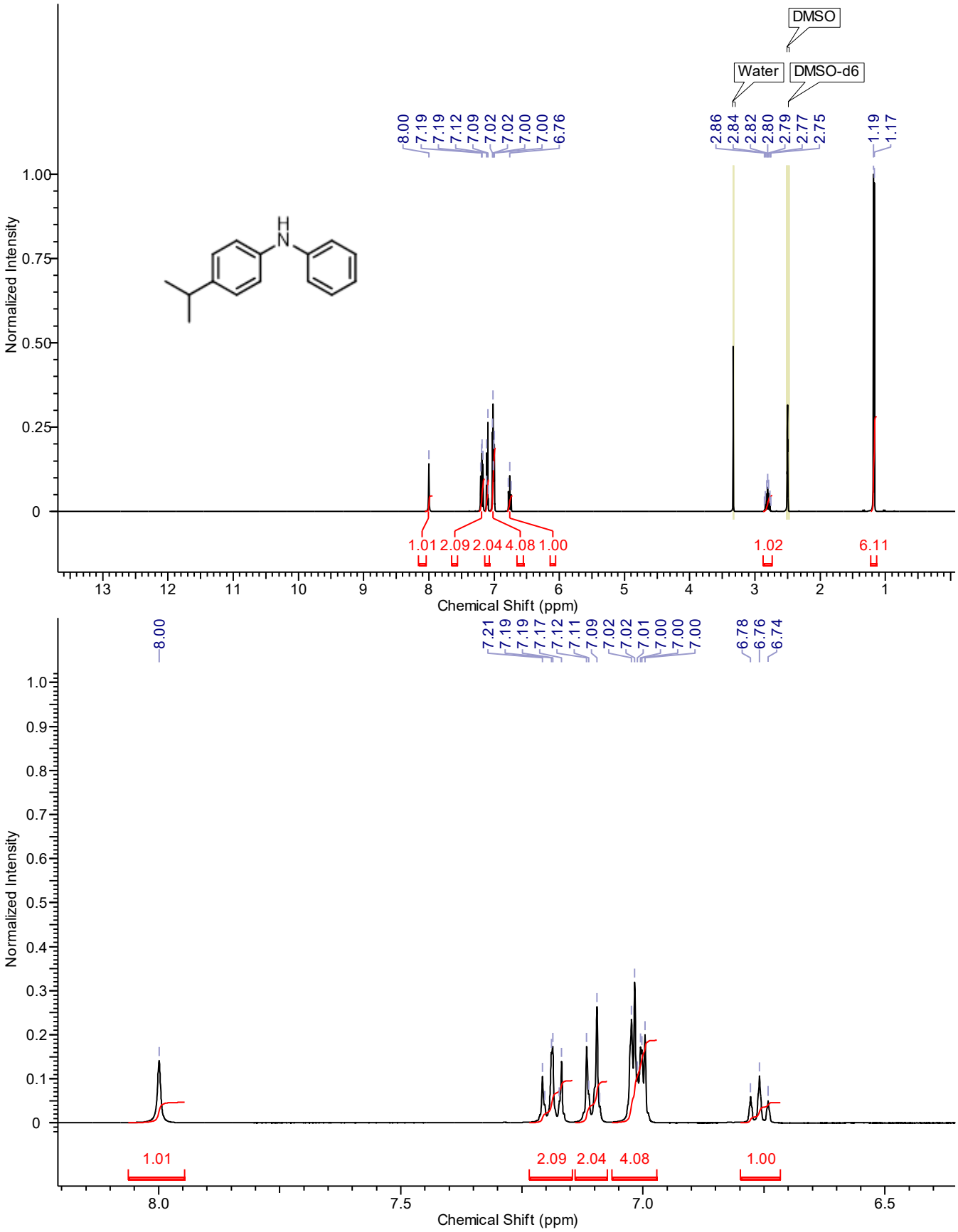


Figure S7.158. Full spectra (*top*) and aromatic region (*bottom*) ^{1}H NMR of 4-isopropyldiphenylamine in DMSO-d6.

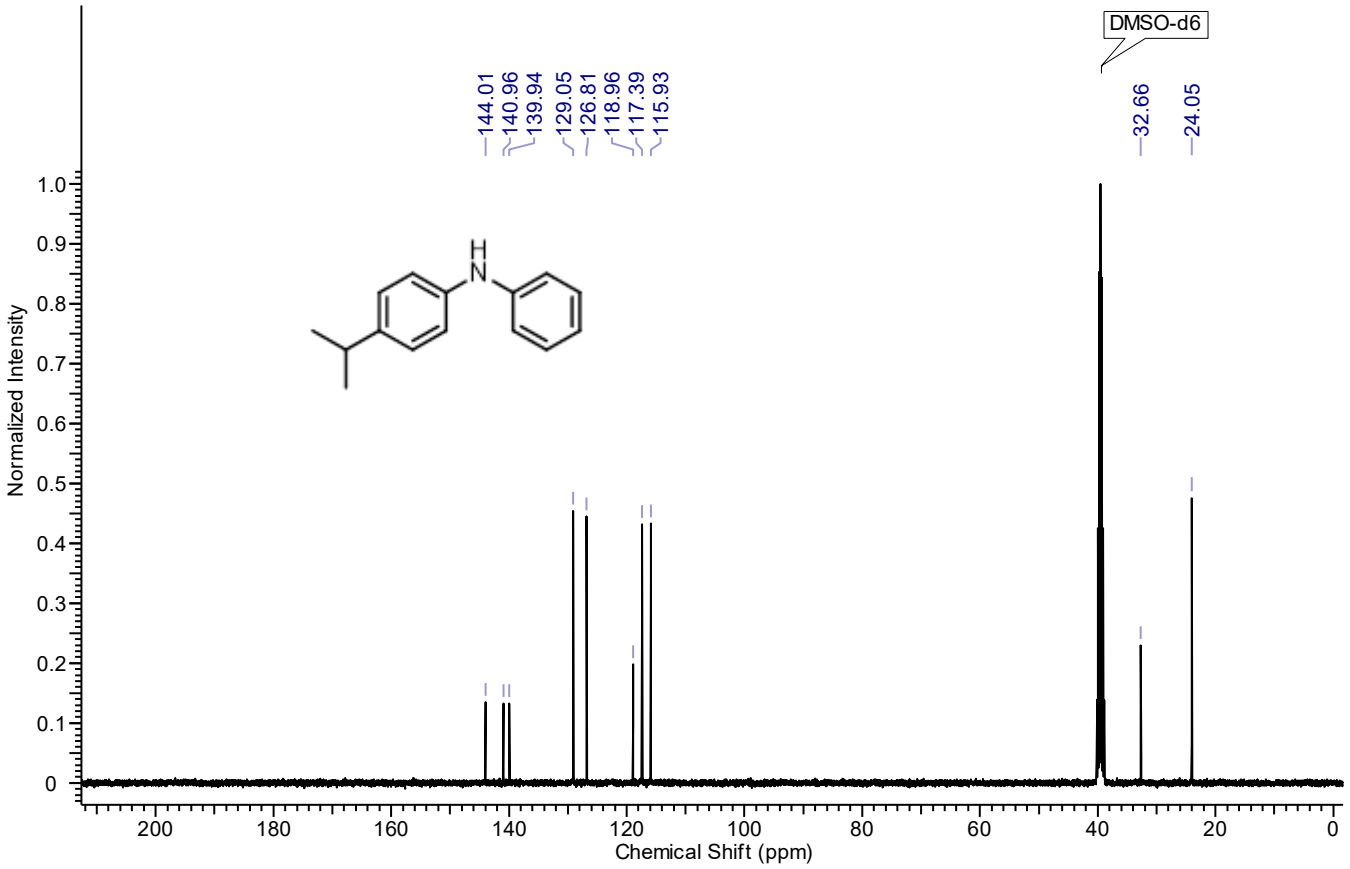


Figure S7.159. Full spectra ^{13}C NMR of 4-isopropyldiphenylamine in DMSO-d6.

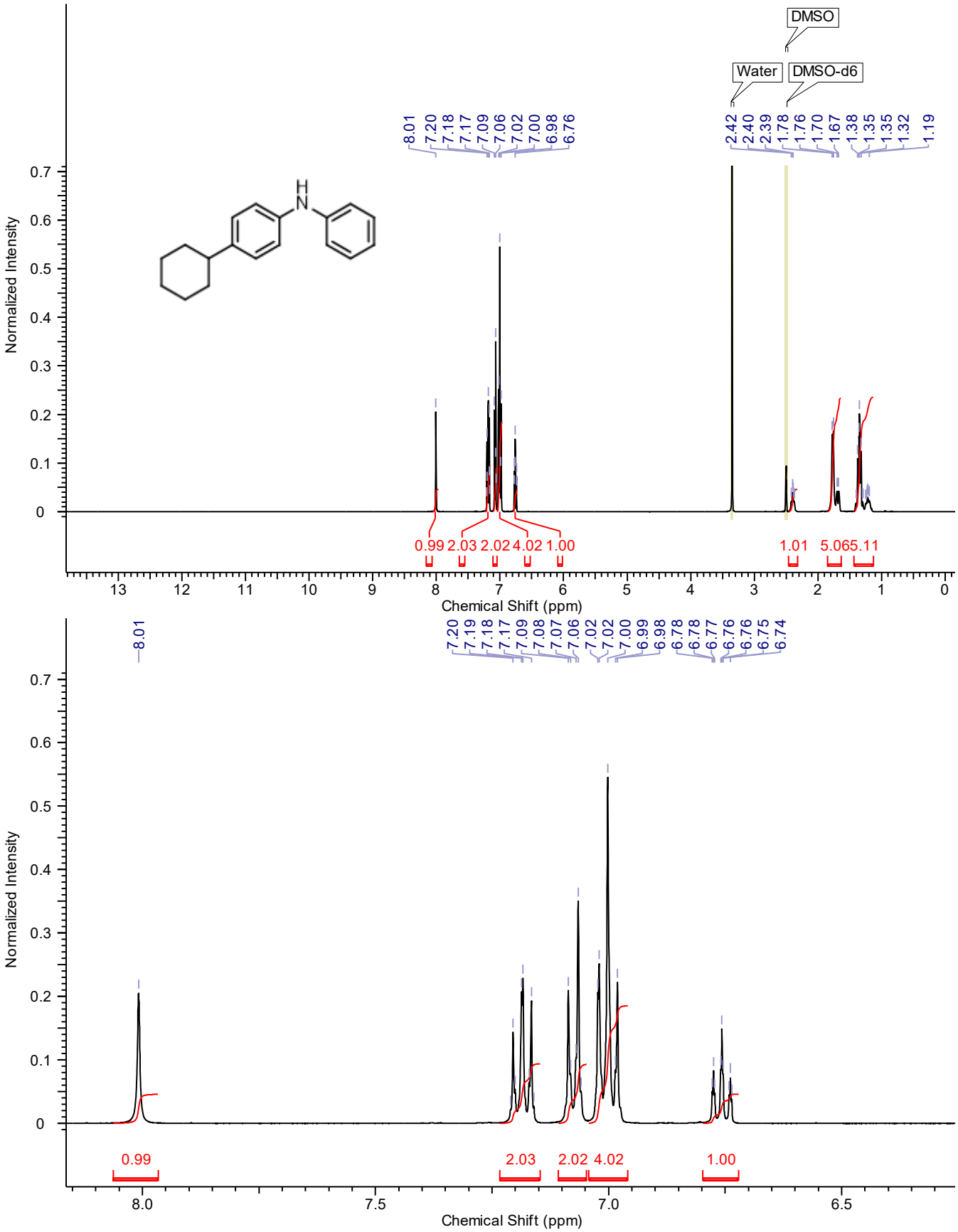


Figure S7.160. Full spectra (*top*) and aromatic region (*bottom*) ^{1}H NMR of 4-cyclohexyldiphenylamine in DMSO-d6.

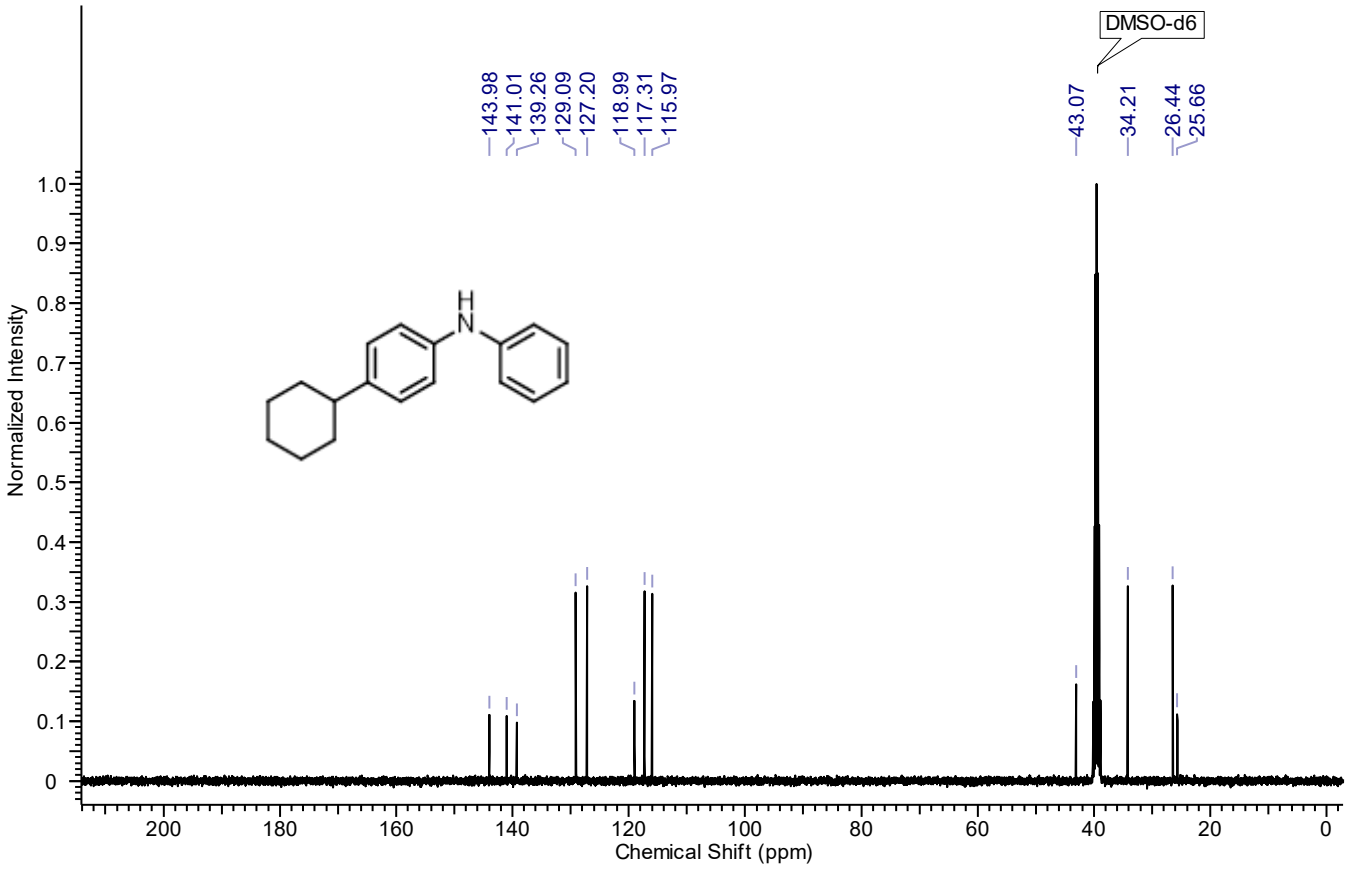


Figure S7.161. Full spectra ^{13}C NMR of 4-cyclohexyldiphenylamine in DMSO-d6.

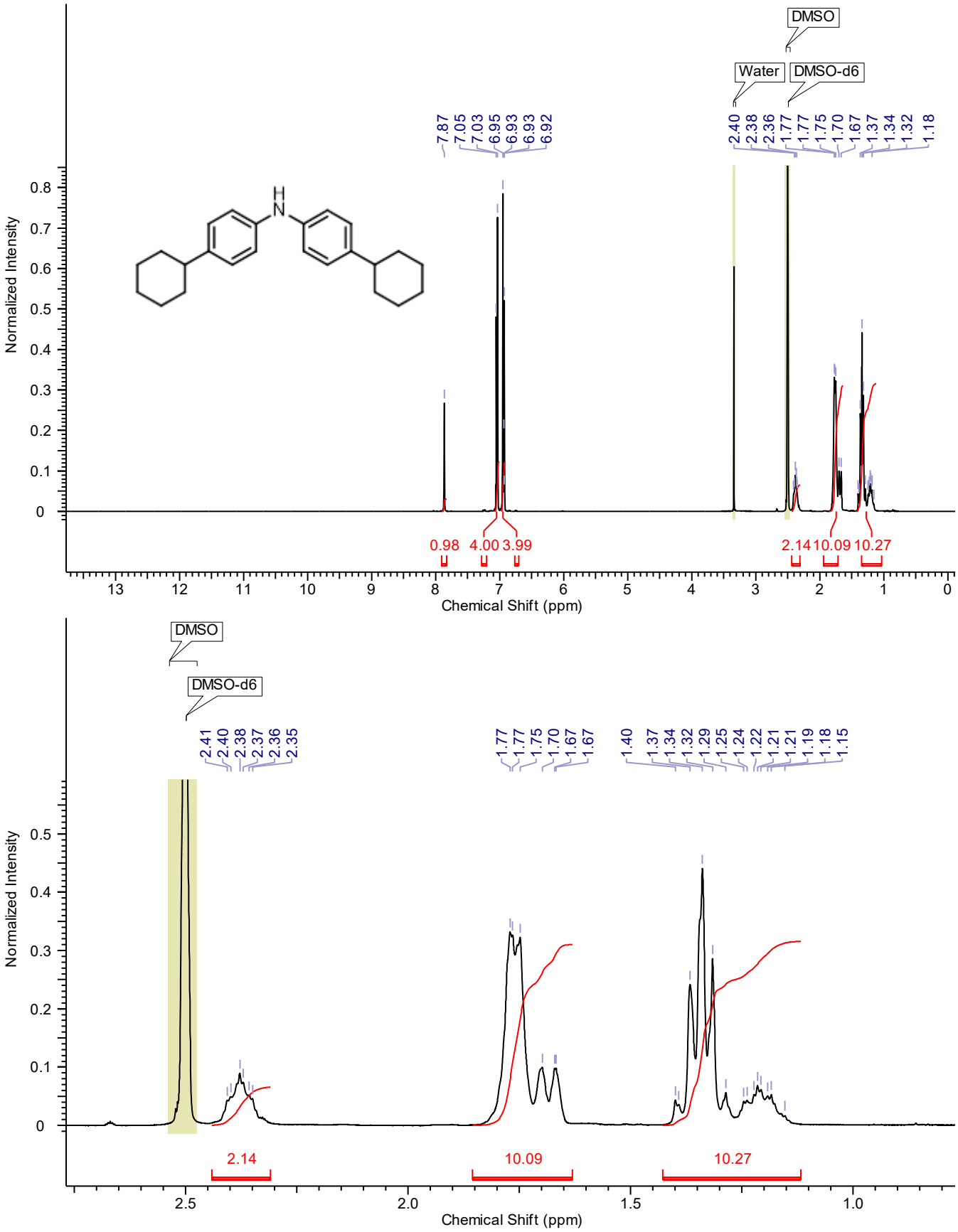


Figure S7.162. Full spectra (*top*) and alkyl region (*bottom*) ^{1}H NMR of 4,4'-dicyclohexyldiphenylamine in DMSO-d6.

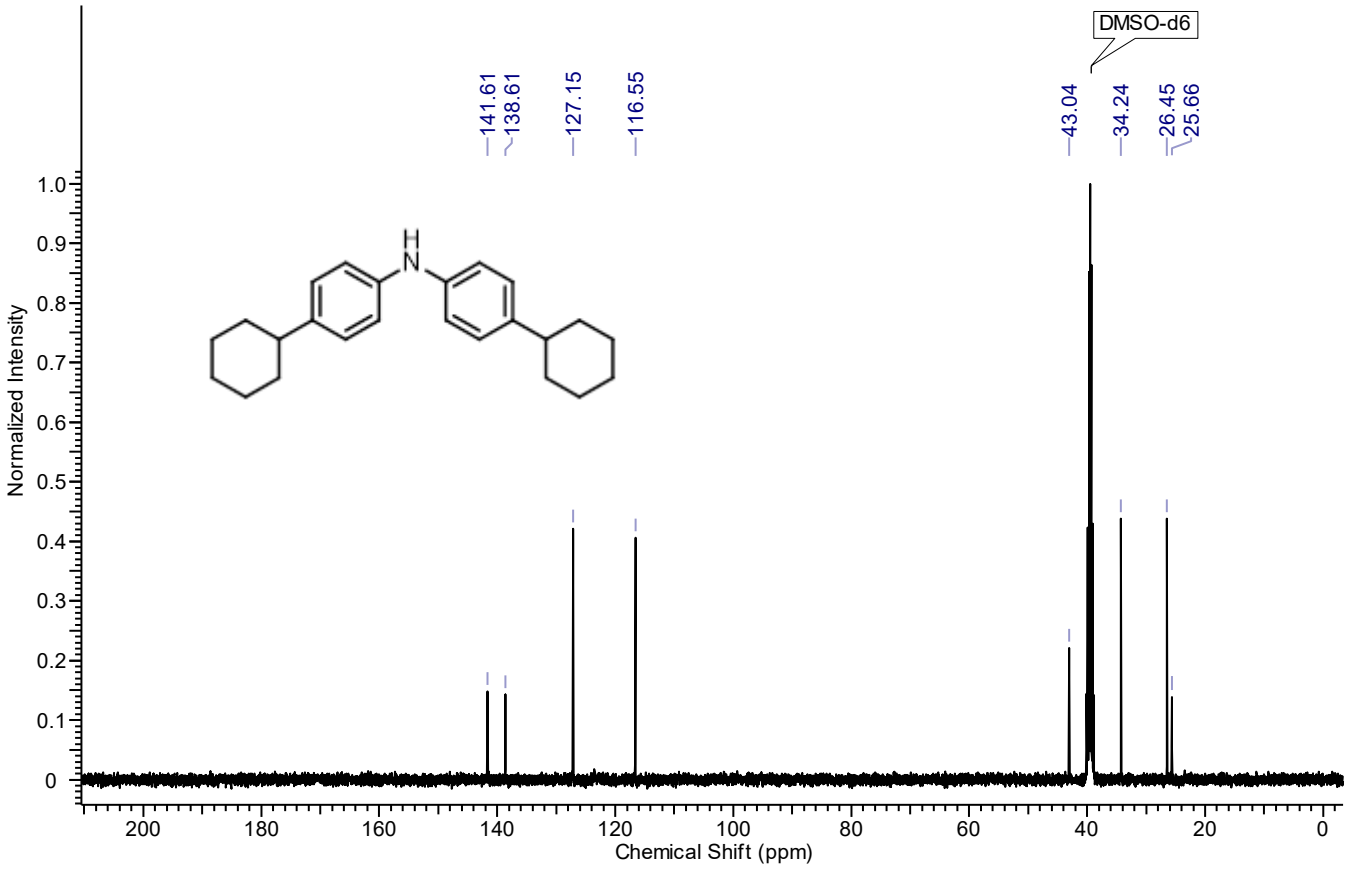


Figure S7.163. Full spectra ^{13}C NMR of 4,4'-dicyclohexyldiphenylamine in DMSO-d6.

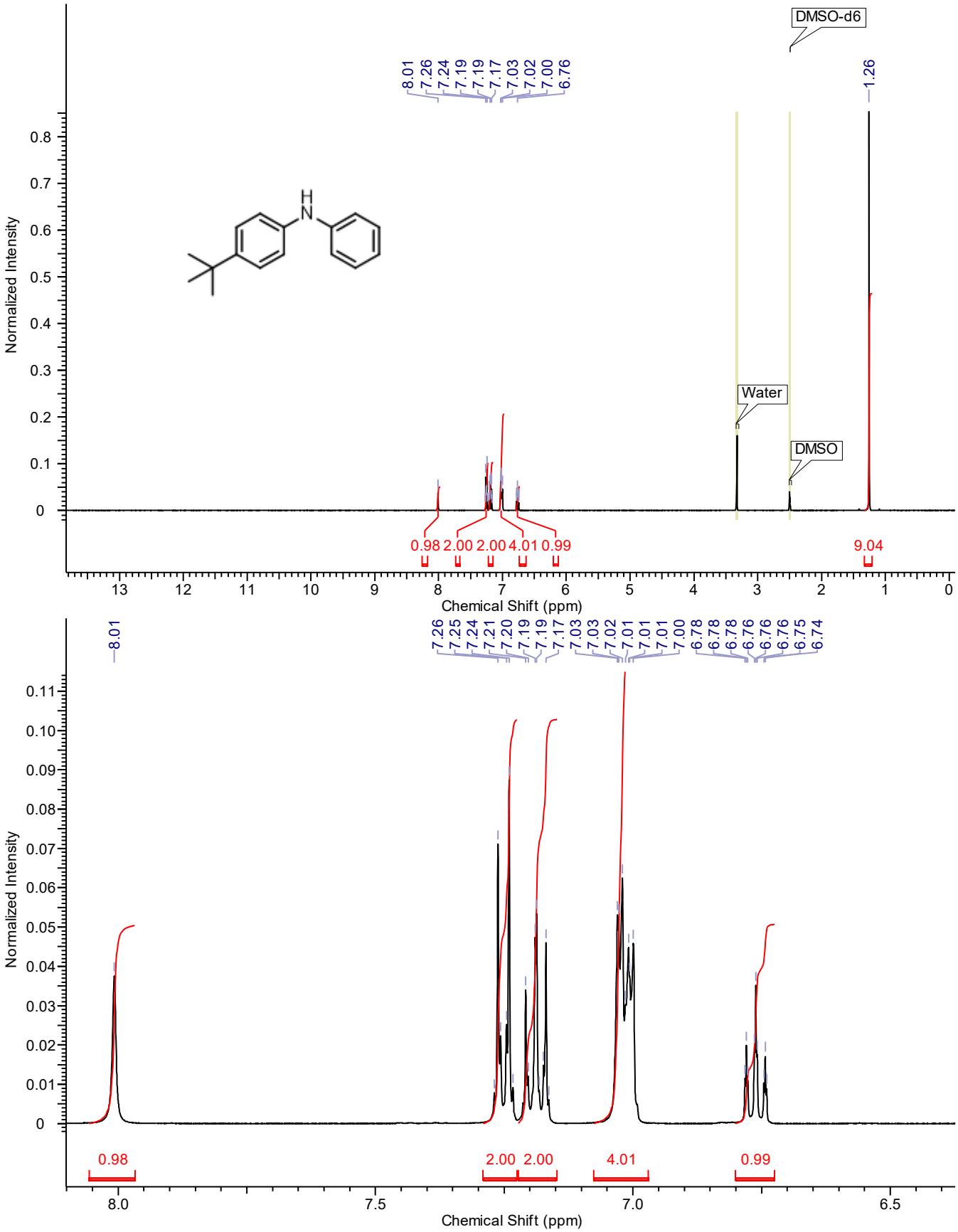


Figure S7.164. Full spectra (*top*) and aromatic region (*bottom*) ^{1}H NMR of 4-*tert*-butyldiphenylamine in DMSO-d6.

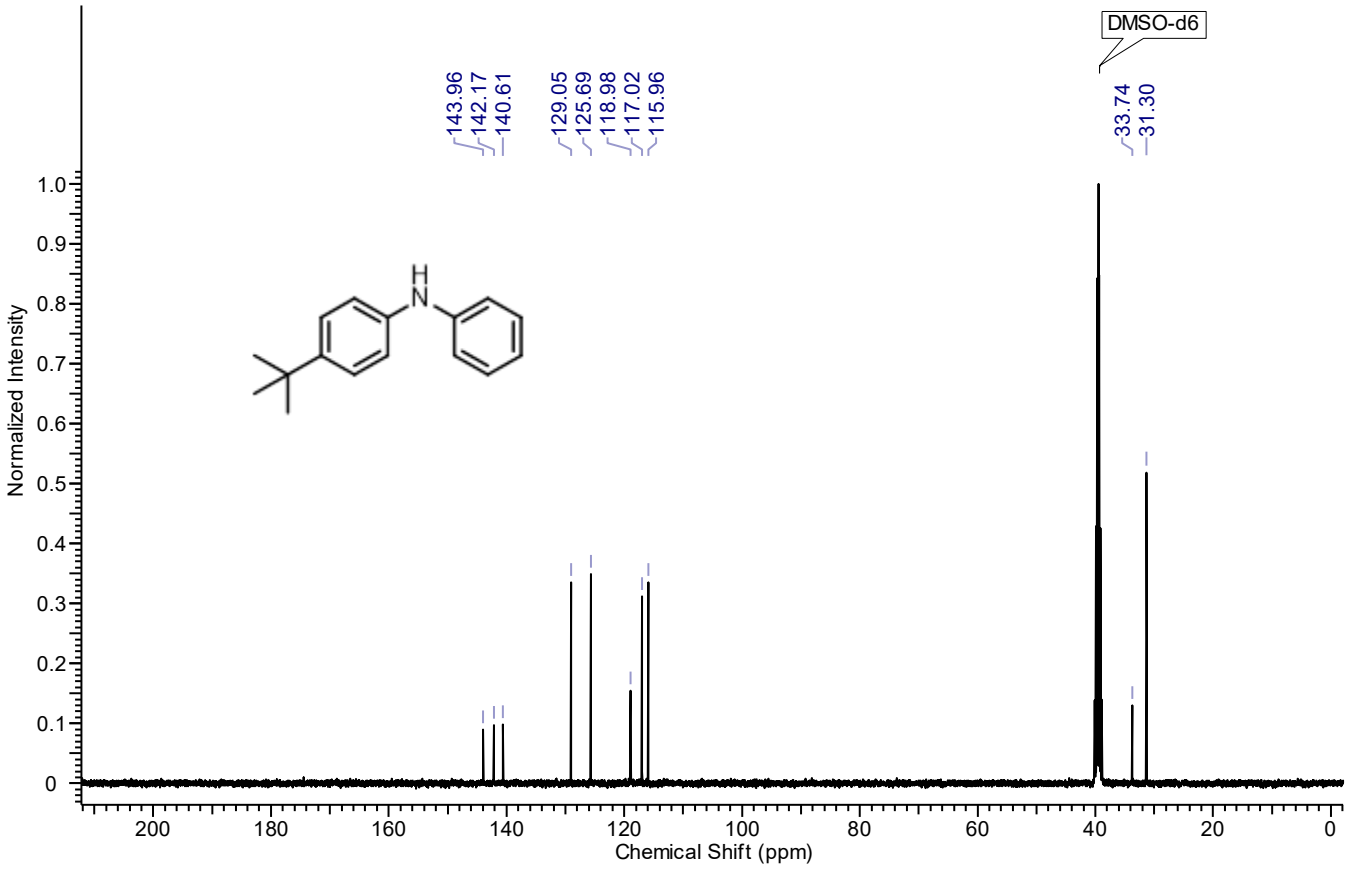


Figure S7.165. Full spectra ^{13}C NMR of 4-*tert*-butyldiphenylamine in DMSO-d6.

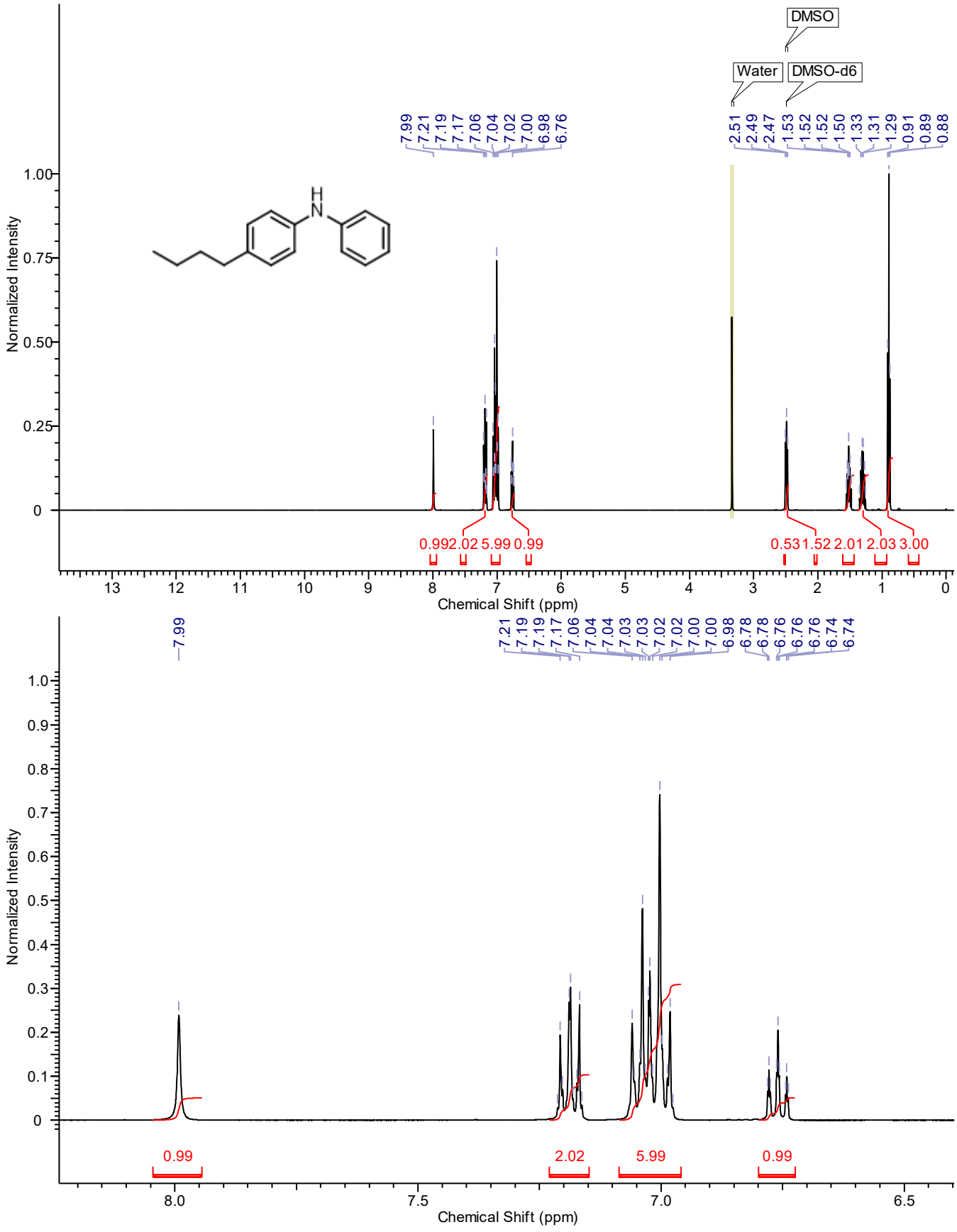


Figure S7.166. Full spectra (*top*) and aromatic region (*bottom*) ^{1}H NMR of 4-*n*-butyldiphenylamine in DMSO-d6.

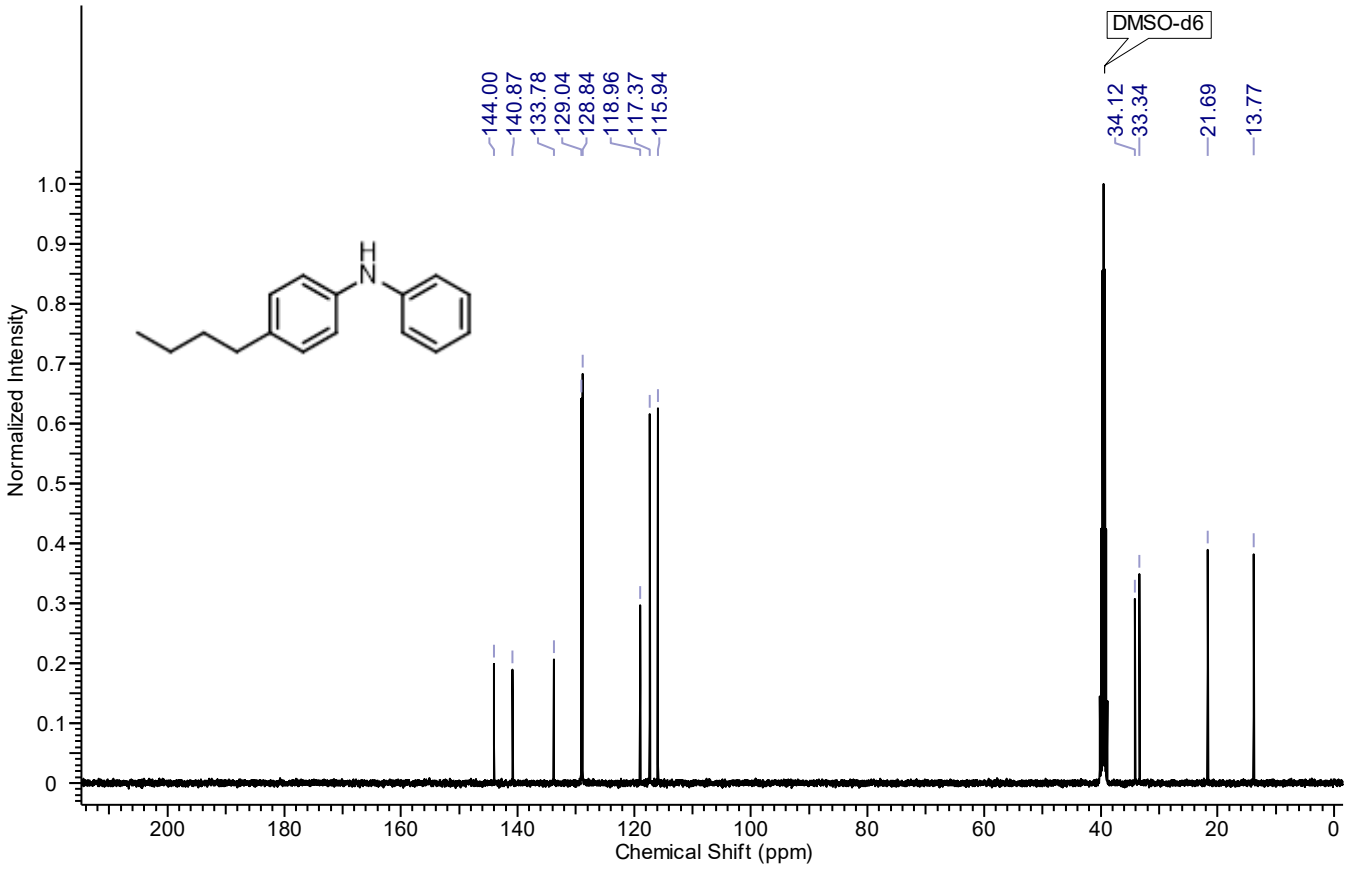


Figure S7.167. Full spectra ^{13}C NMR of 4-*n*-butyldiphenylamine in DMSO-d6.

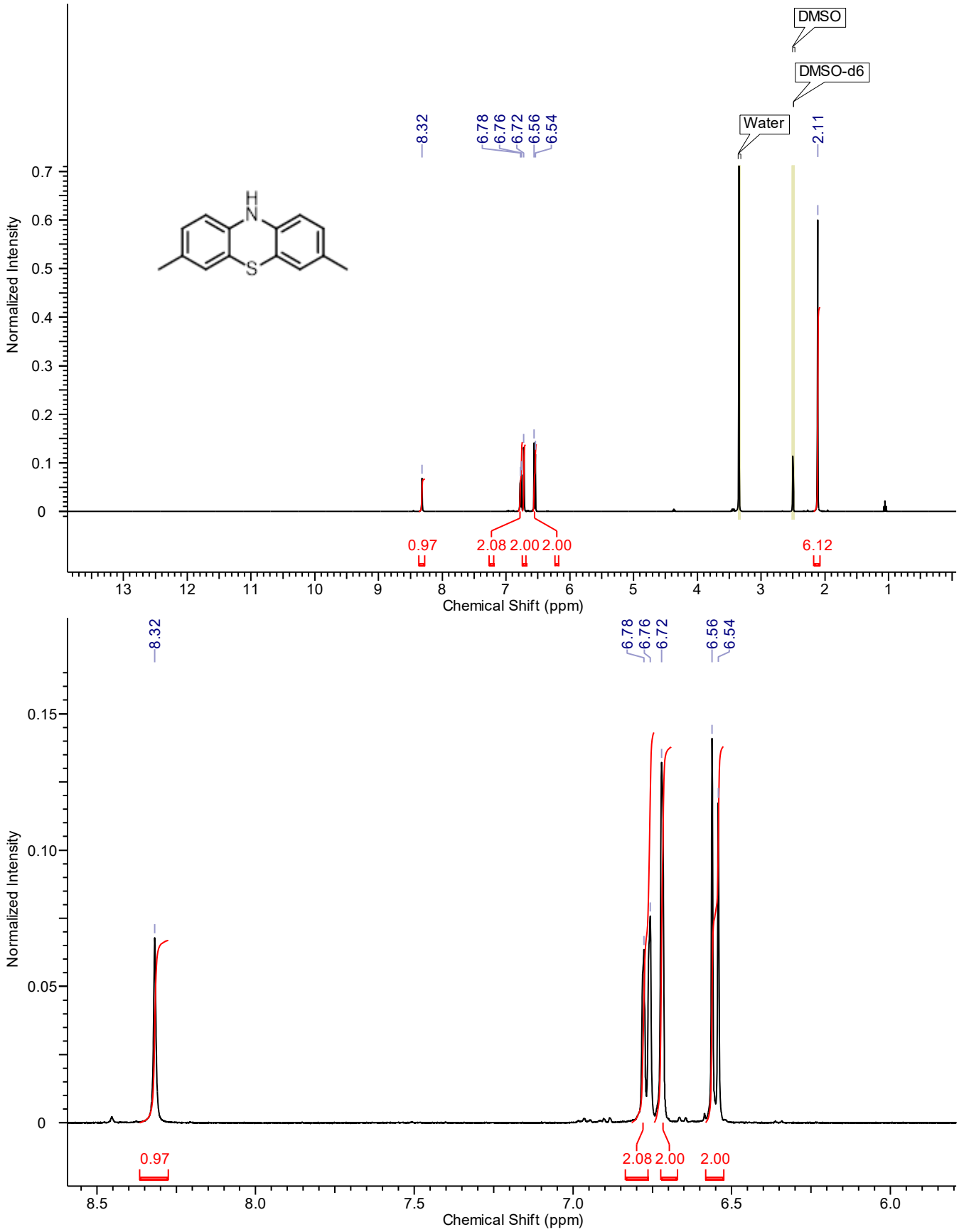


Figure S7.168. Full spectra (*top*) and aromatic region (*bottom*) ^{1}H NMR of 3,7-dimethylphenothiazine in DMSO-d6.

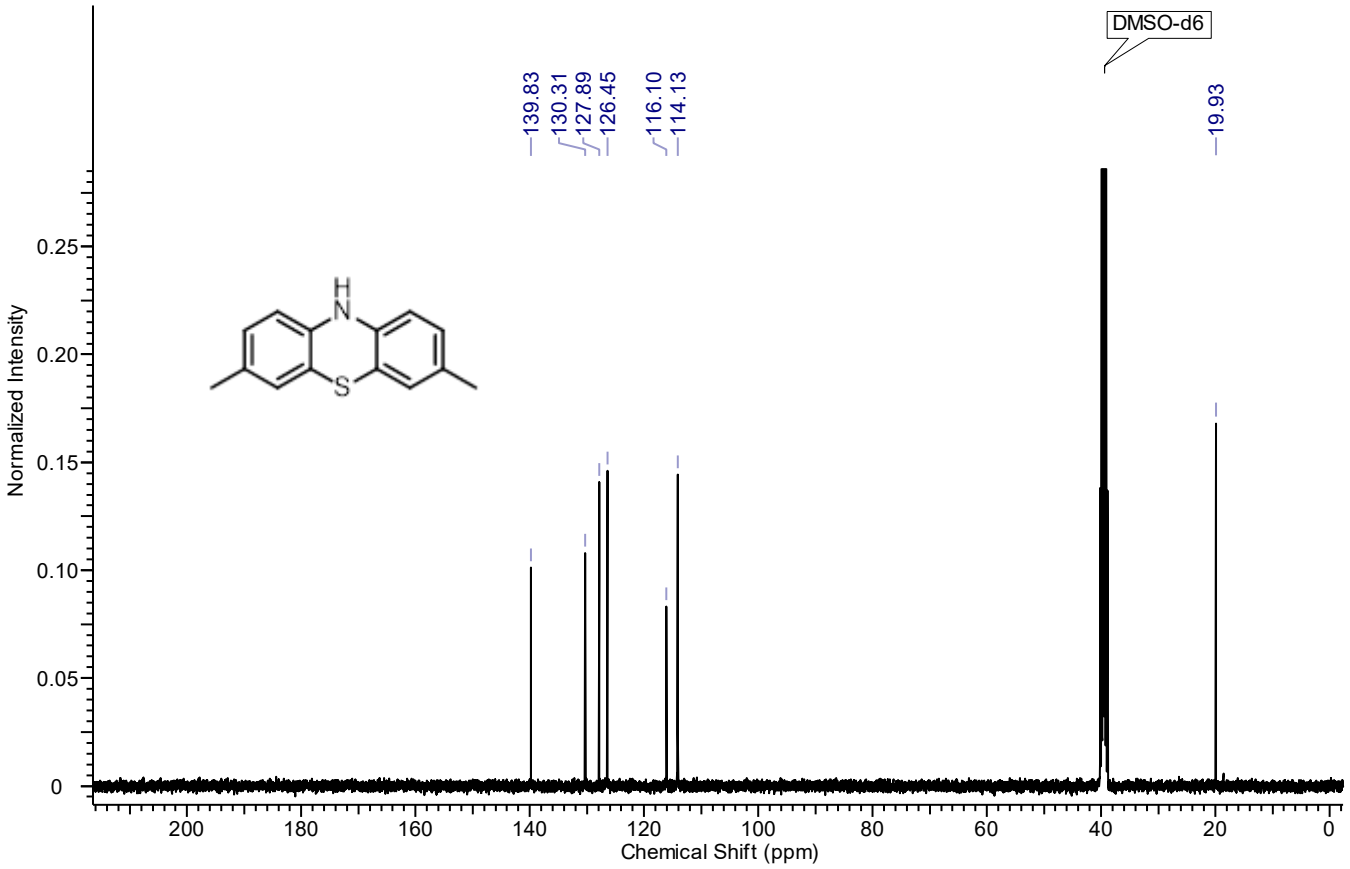


Figure S7.169. Full spectra ^{13}C NMR of 3,7-dimethylphenothiazine in DMSO-d6.

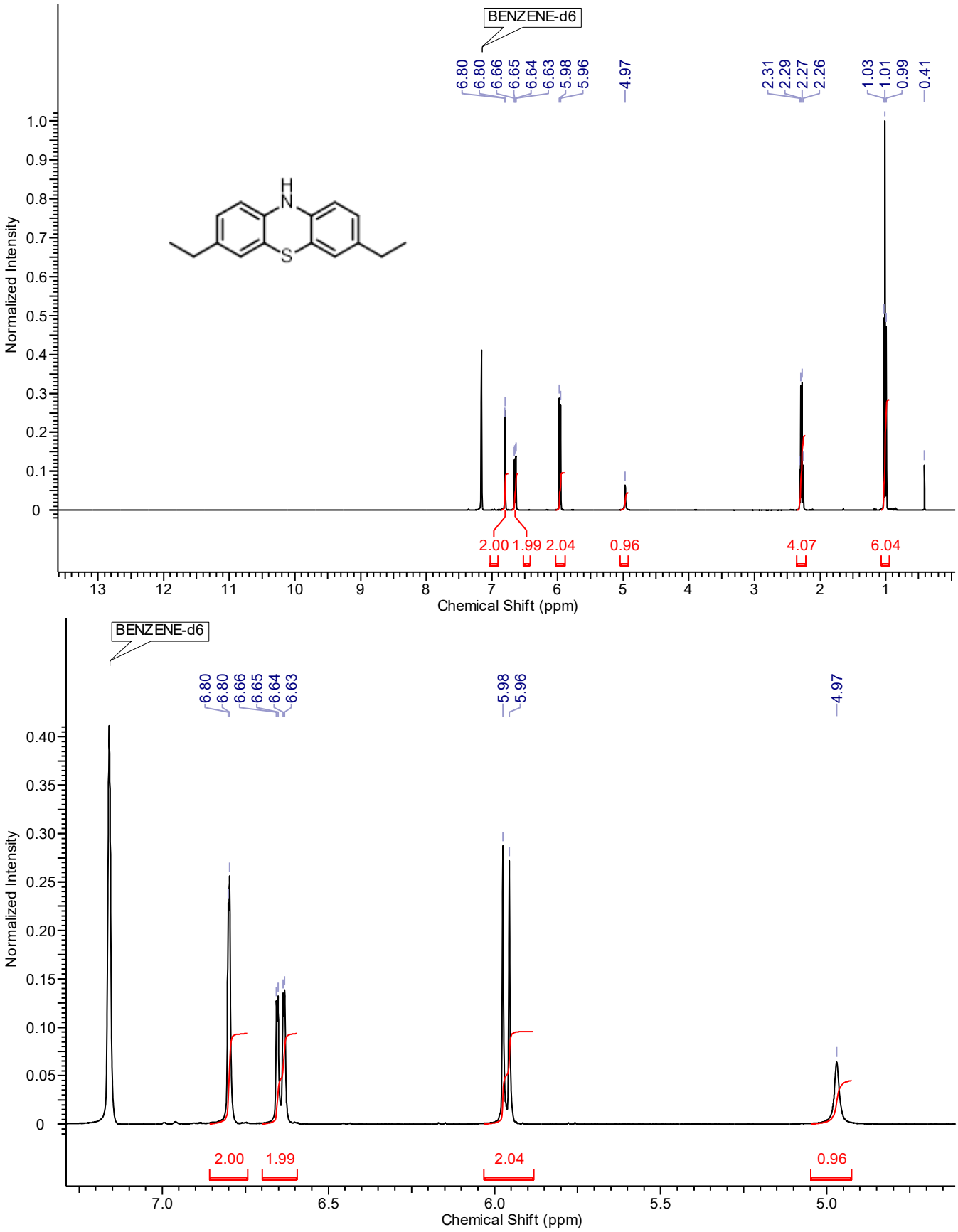


Figure S7.170. Full spectra (*top*) and aromatic region (*bottom*) ^{1}H NMR of 3,7-diethylphenothiazine in C_6D_6.

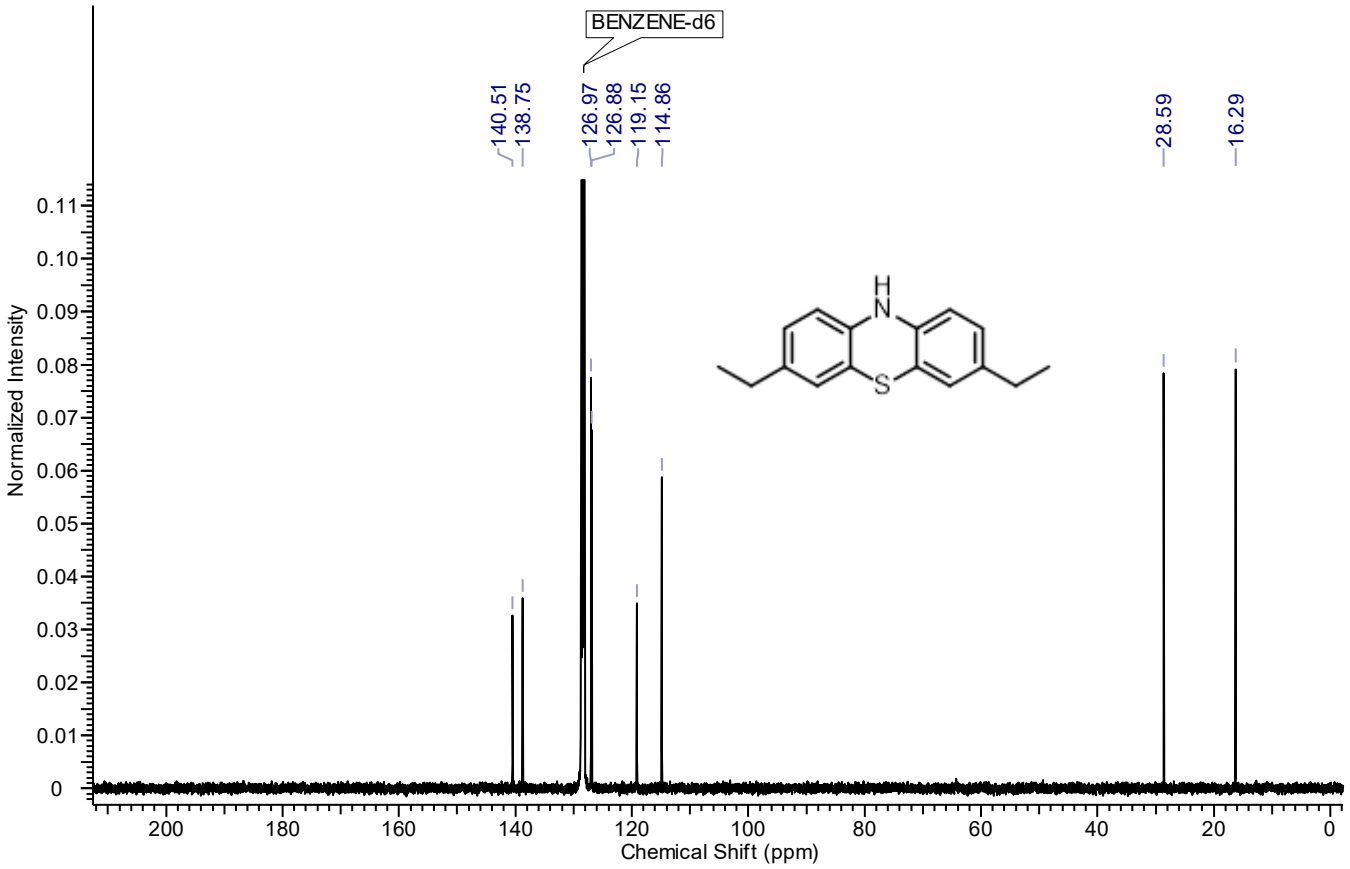


Figure S7.171. Full spectra ^{13}C NMR of 3,7-diethylphenothiazine in C_6D_6.

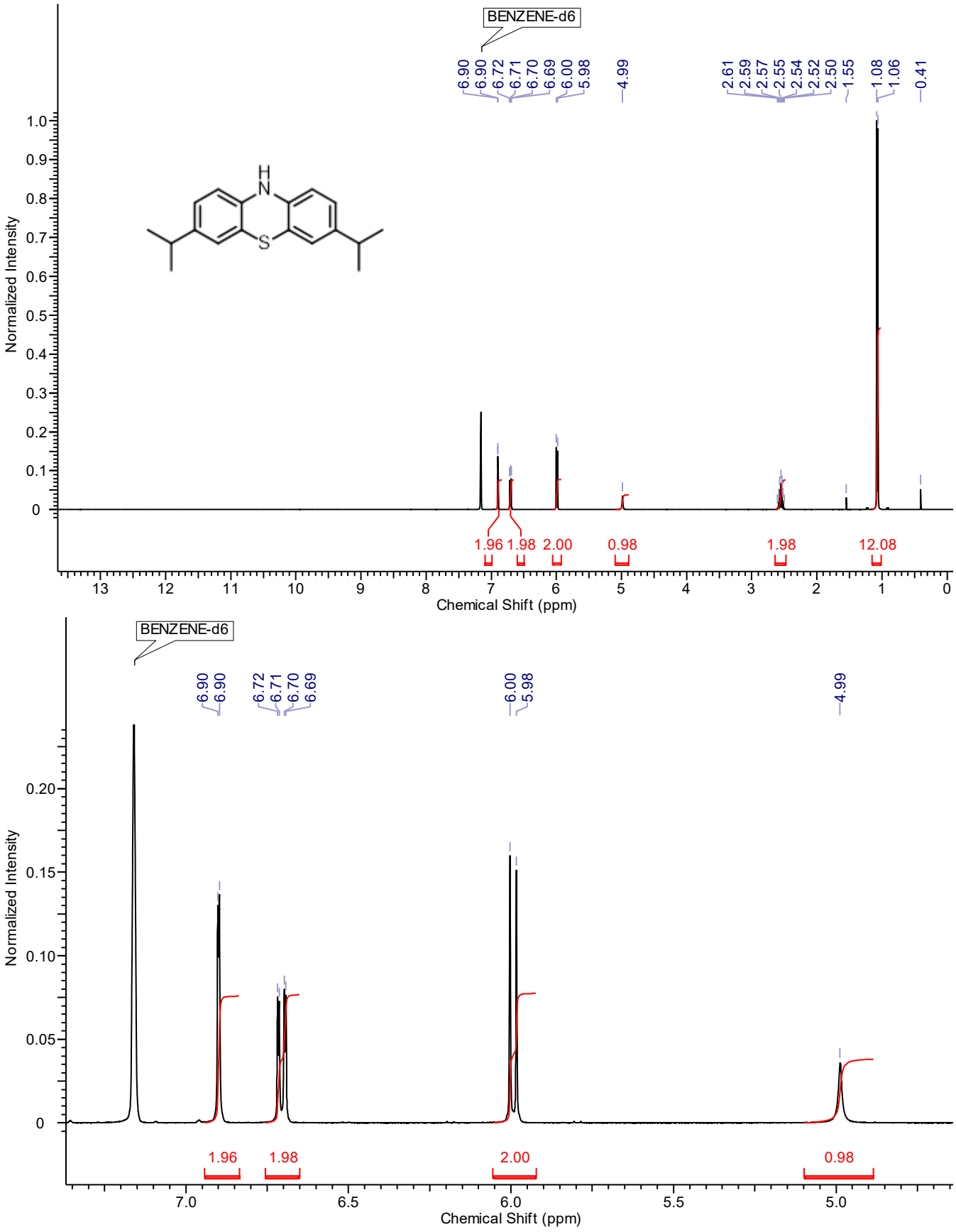


Figure S7.172. Full spectra (*top*) and aromatic region (*bottom*) ^{1}H NMR of 3,7-diisopropylphenothiazine in C_6D_6.

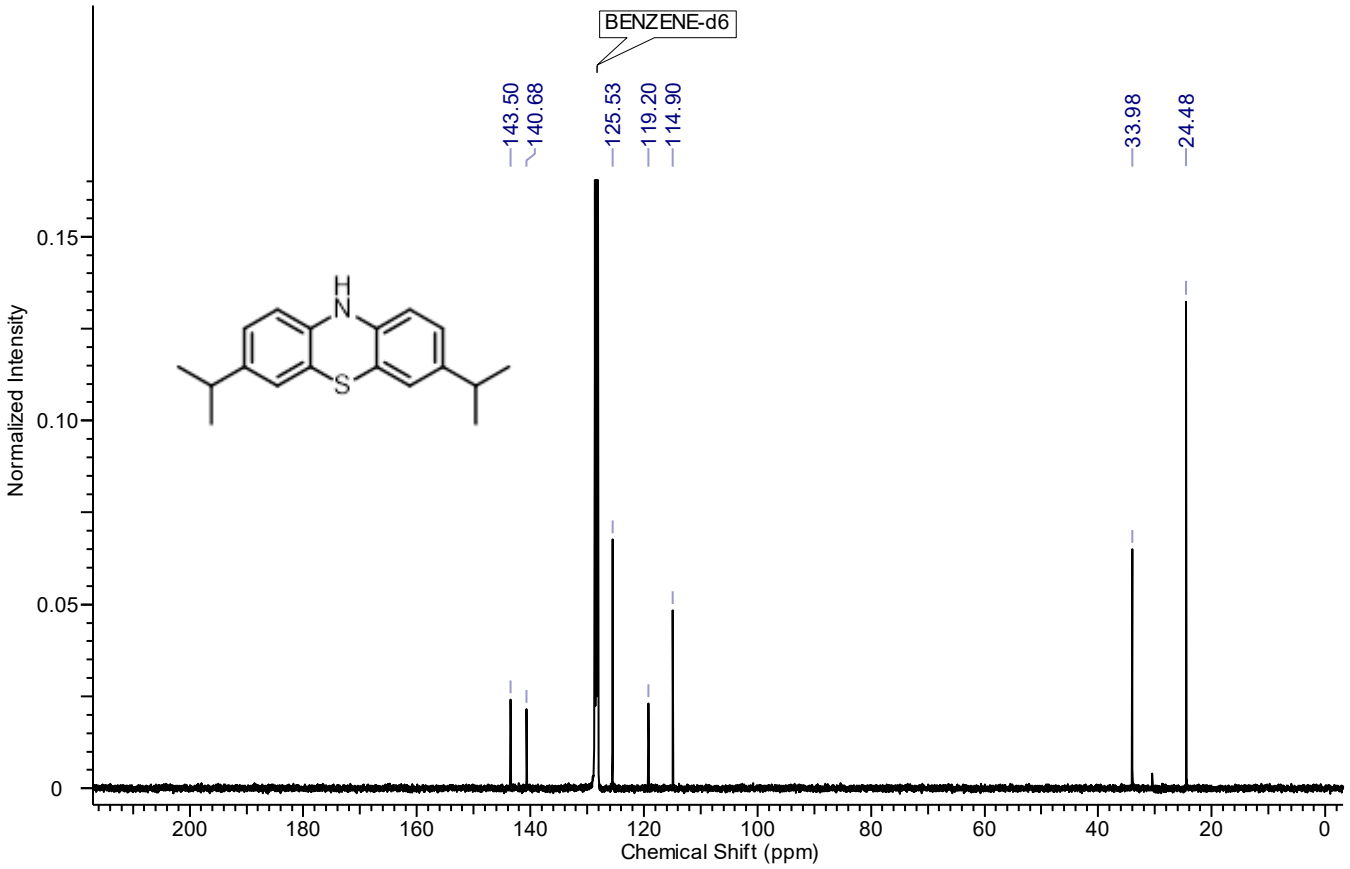


Figure S7.173. Full spectra ^{13}C NMR of 3,7-diisopropylphenothiazine in C_6D_6.

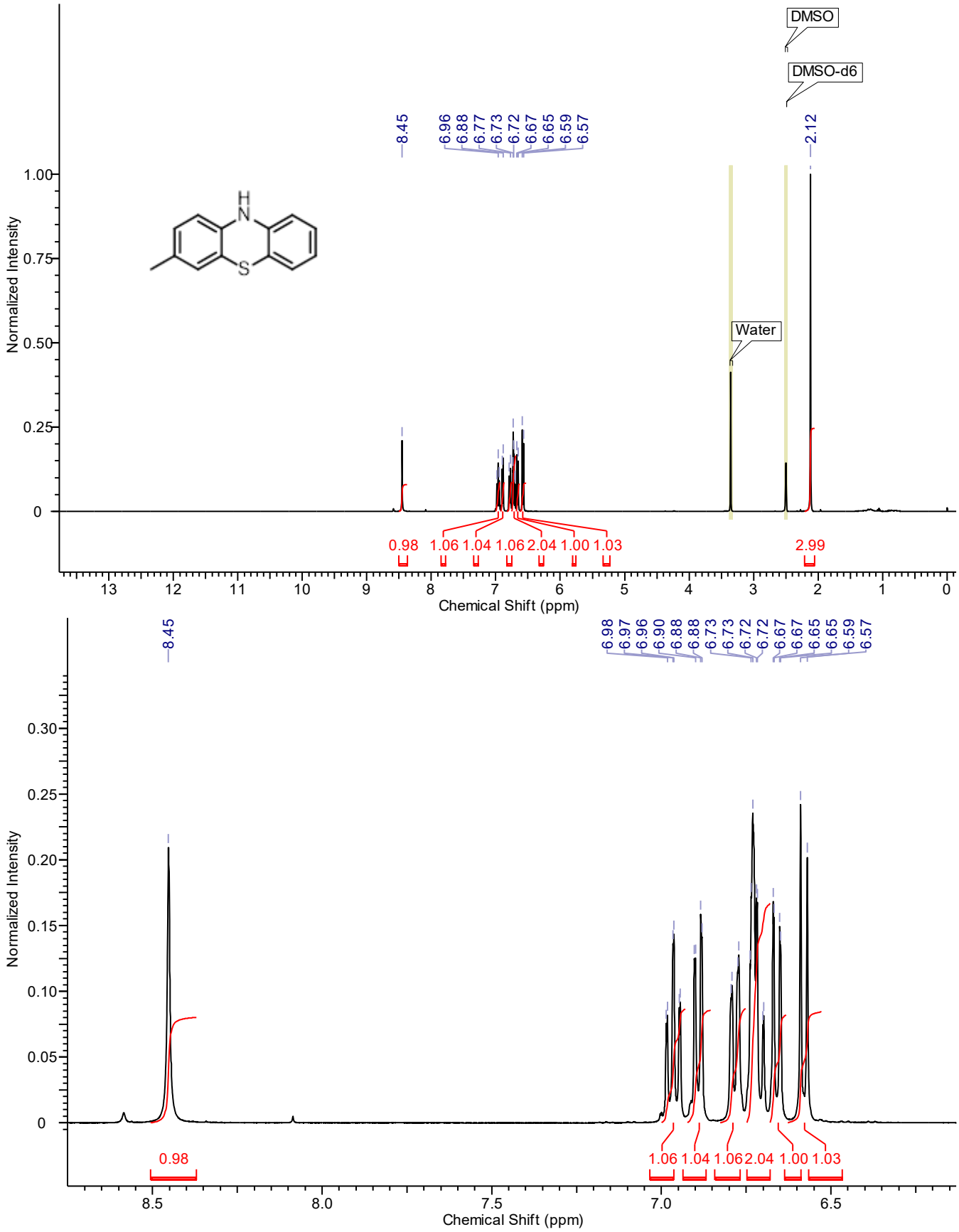


Figure S7.174. Full spectra (*top*) and aromatic region (*bottom*) ^{1}H NMR of 3-methylphenothiazine in DMSO-d6.

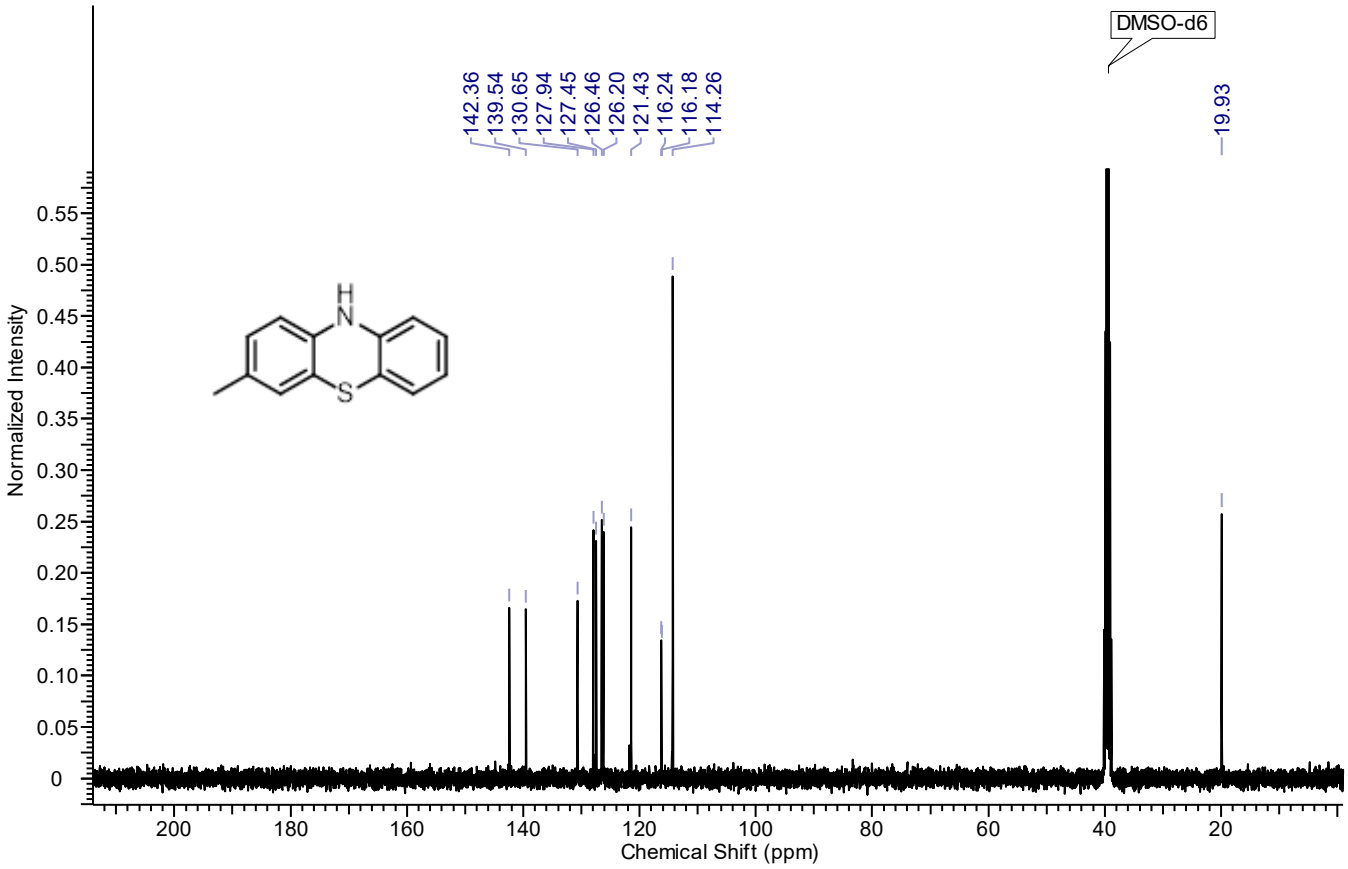


Figure S7.175. Full spectra ^{13}C NMR of 3-methylphenothiazine in DMSO-d6.

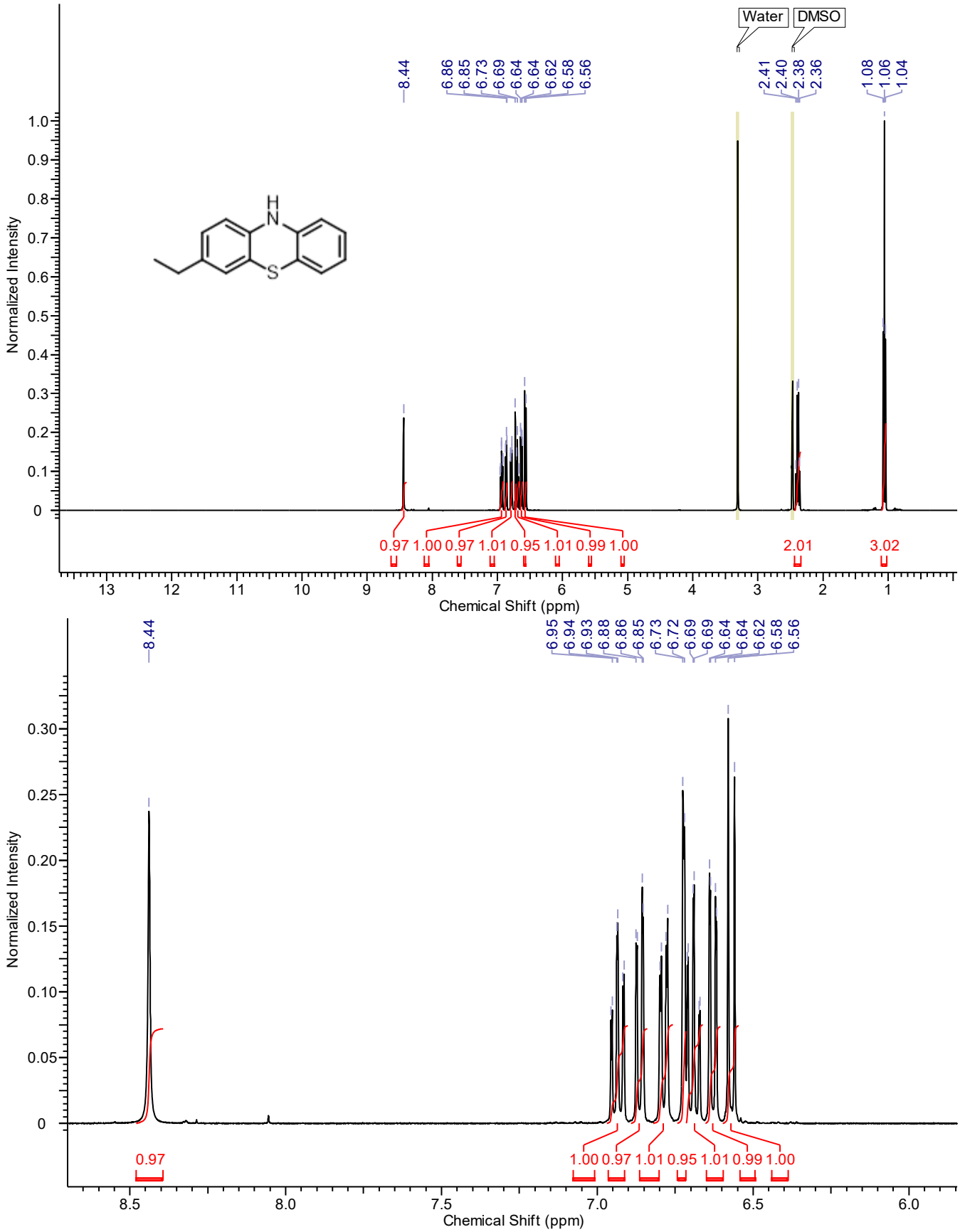


Figure S7.176. Full spectra (*top*) and aromatic region (*bottom*) ^{1}H NMR of 3-ethylphenothiazine in DMSO-d6.

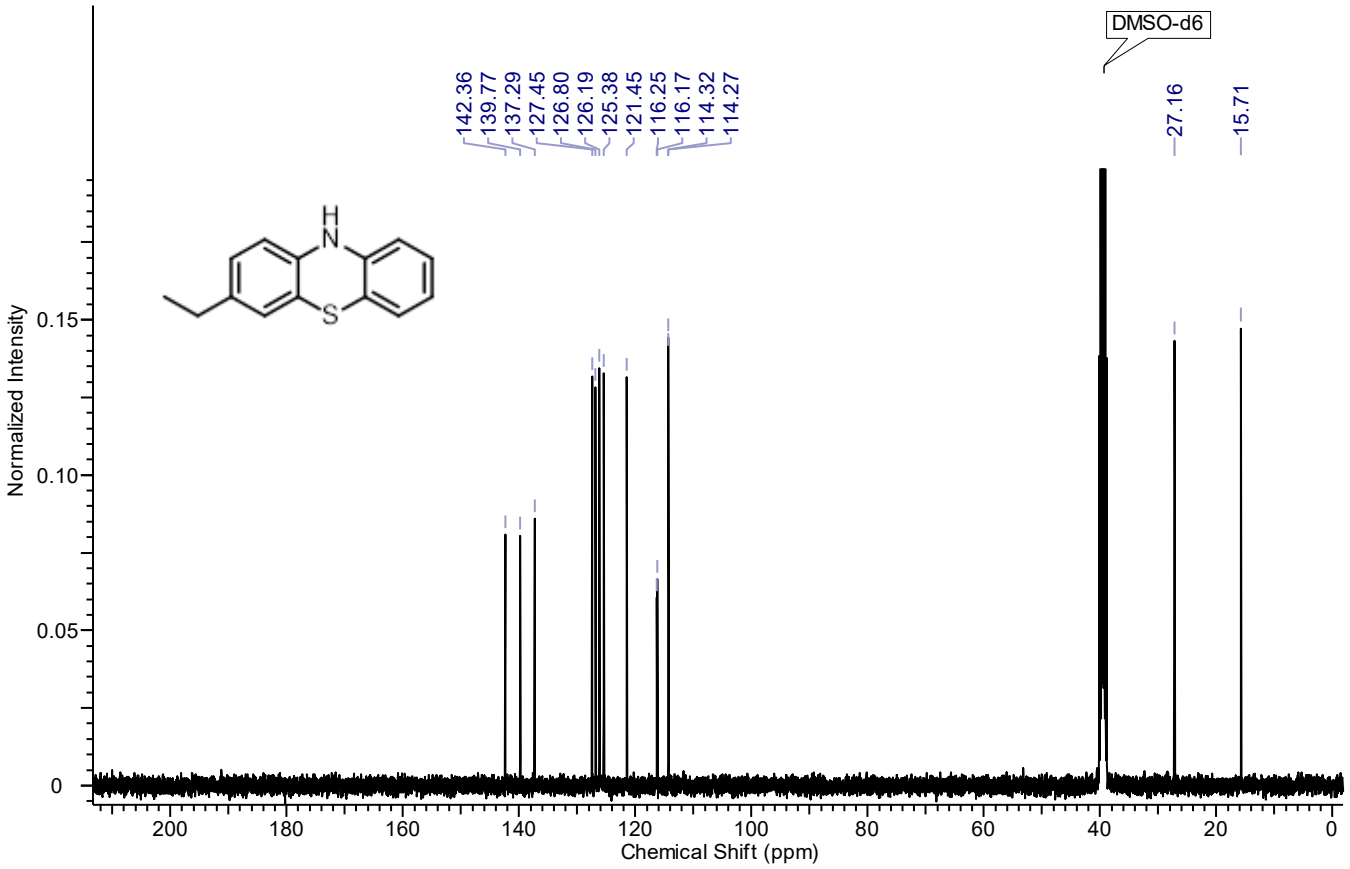


Figure S7.177. Full spectra ^{13}C NMR of 3-ethylphenothiazine in DMSO-d6.

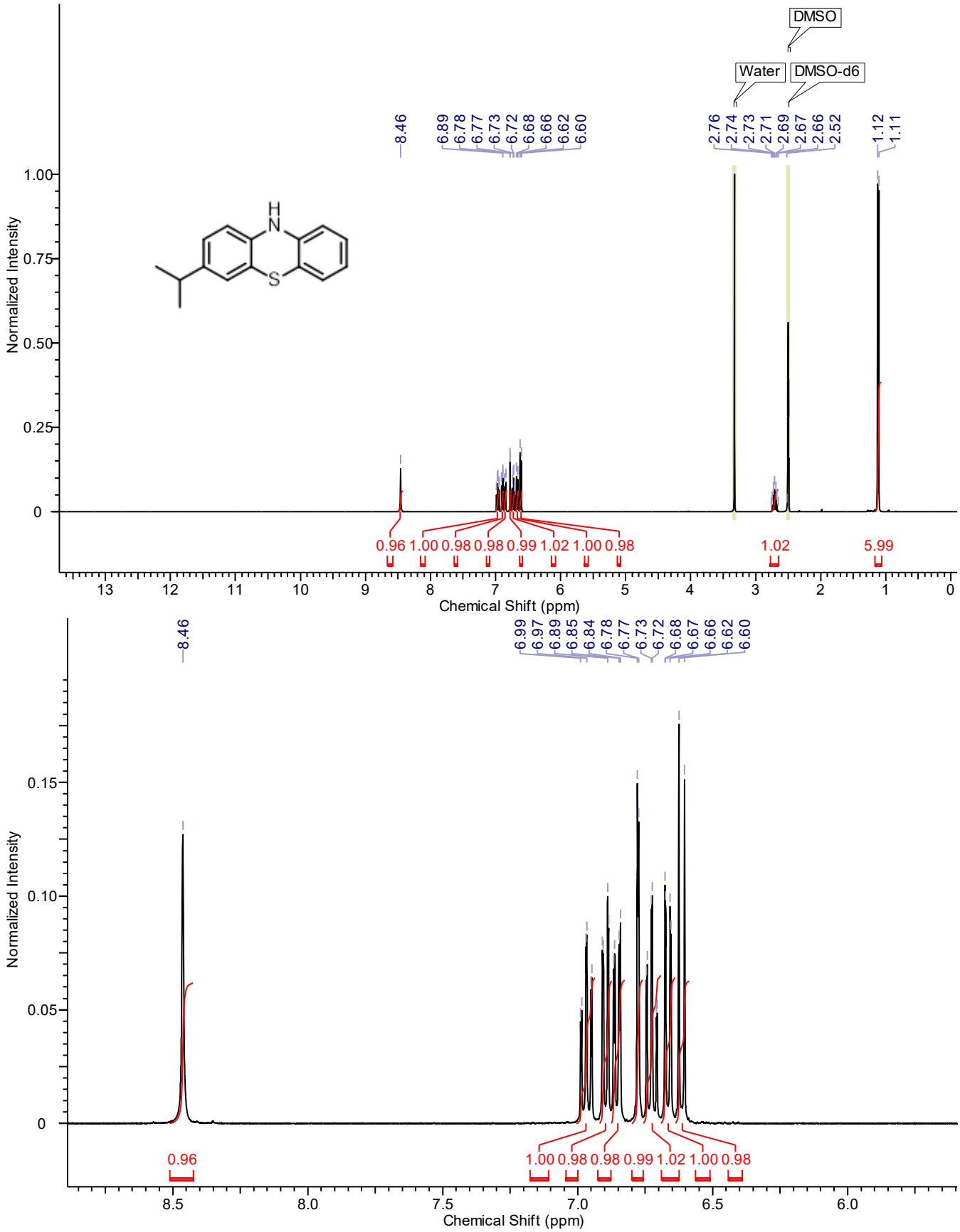


Figure S7.178. Full spectra (*top*) and aromatic region (*bottom*) ^{1}H NMR of 3-isopropylphenothiazine in DMSO-d6.

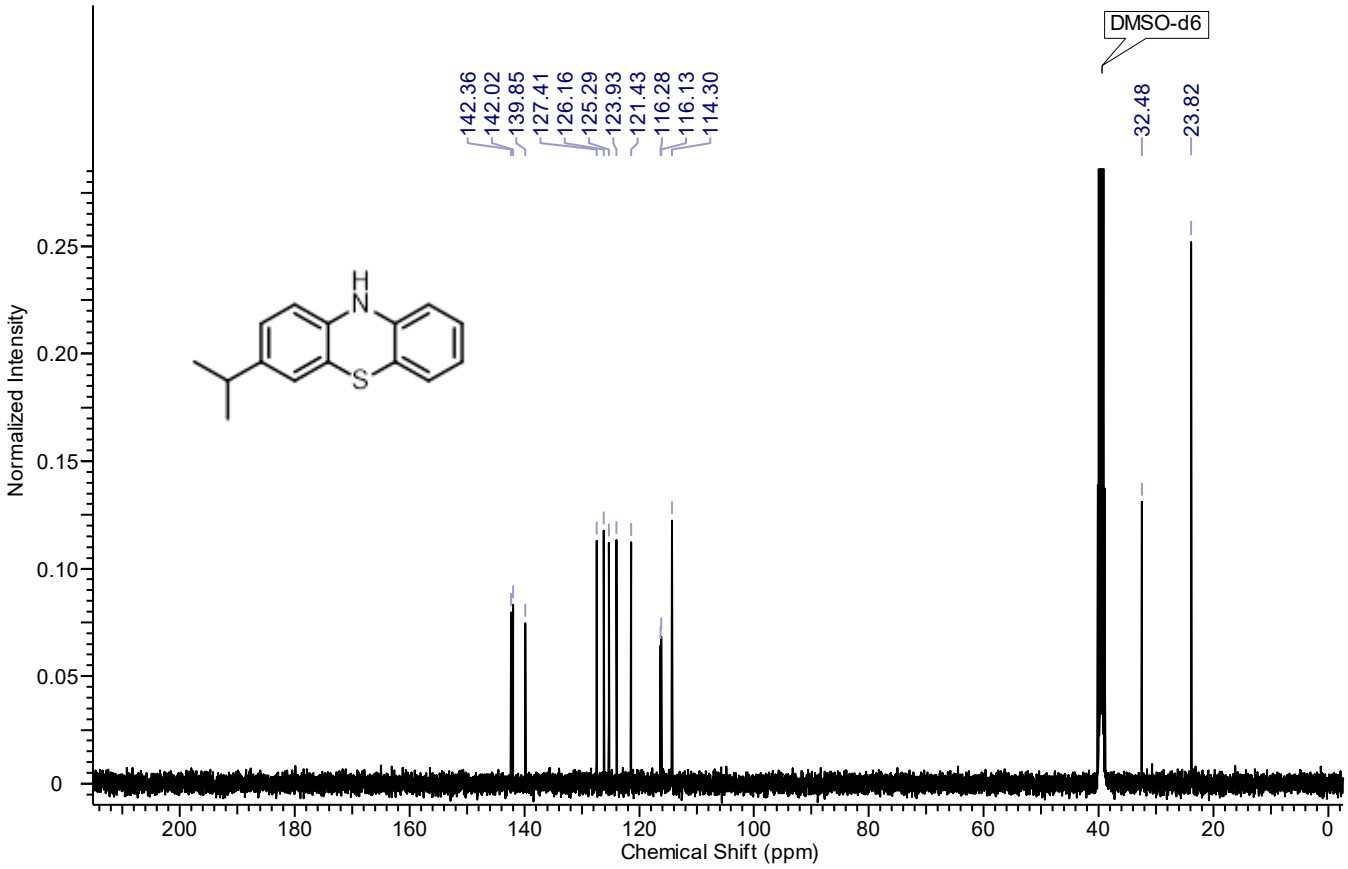


Figure S7.179. Full spectra ^{13}C NMR of 3-isopropylphenothiazine in DMSO-d6.

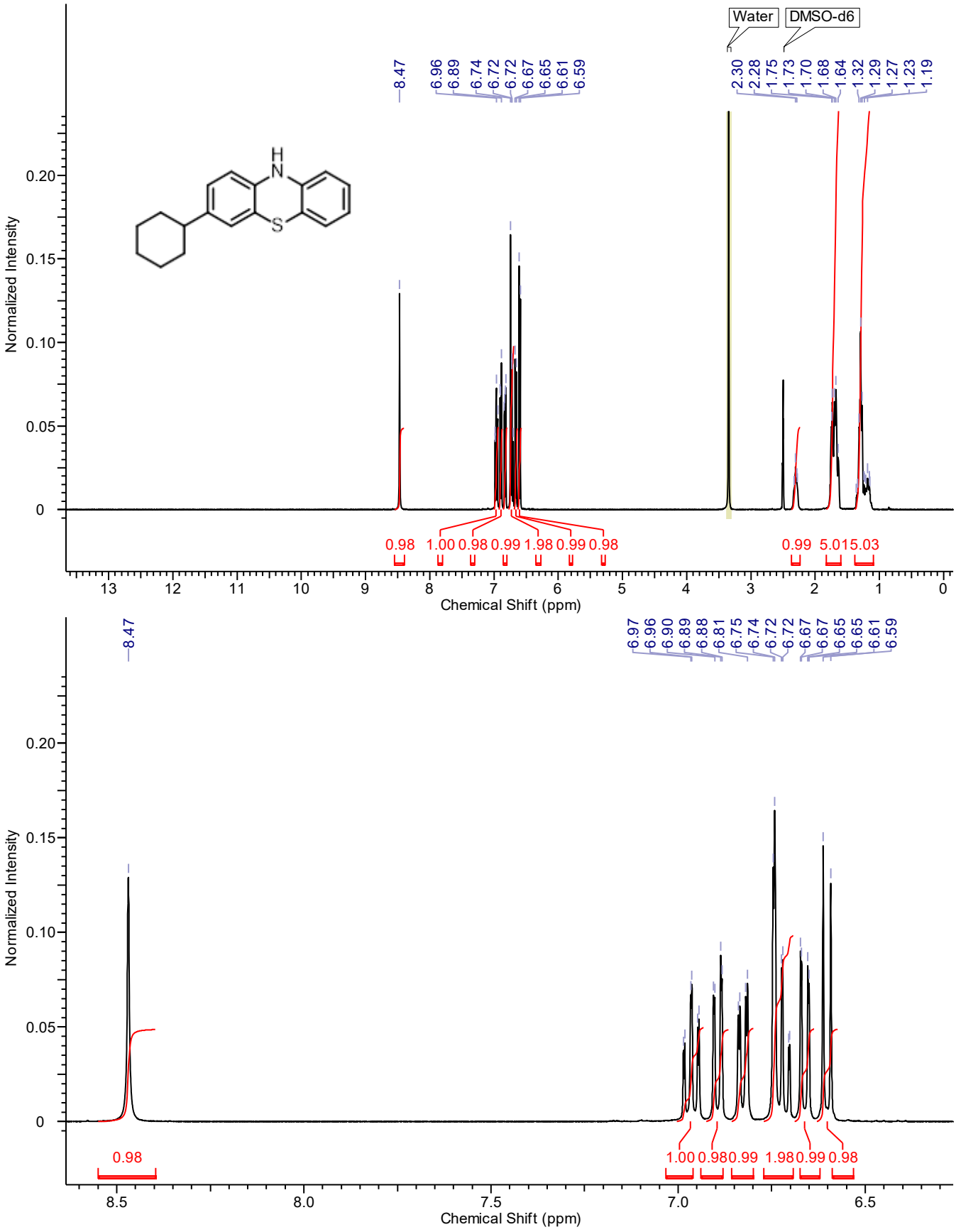


Figure S7.180. Full spectra (*top*) and aromatic region (*bottom*) ^{1}H NMR of 3-cyclohexylphenothiazine in DMSO-d6.

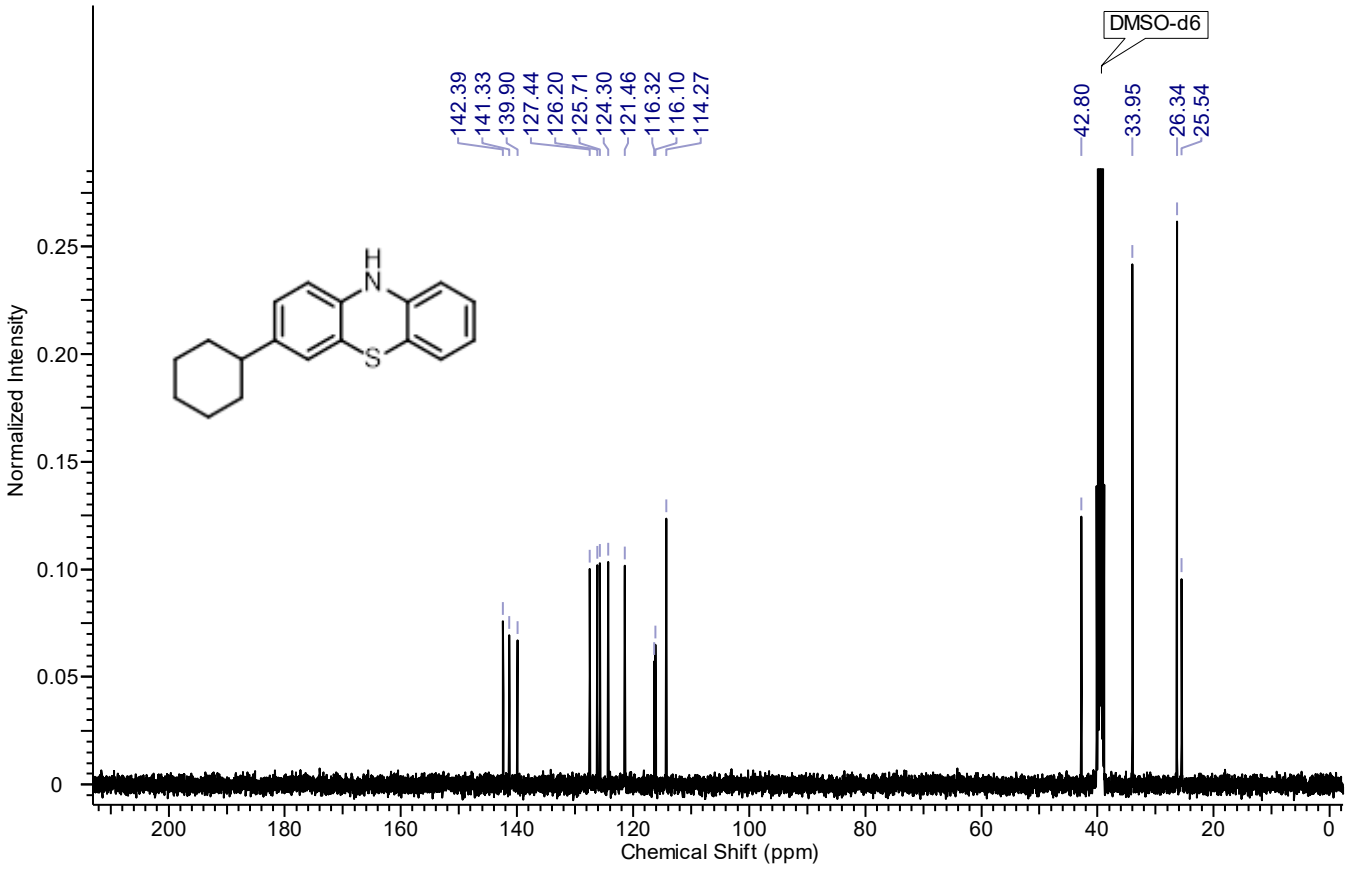


Figure S7.181. Full spectra ^{13}C NMR of 3-cyclohexylphenothiazine in DMSO-d6.

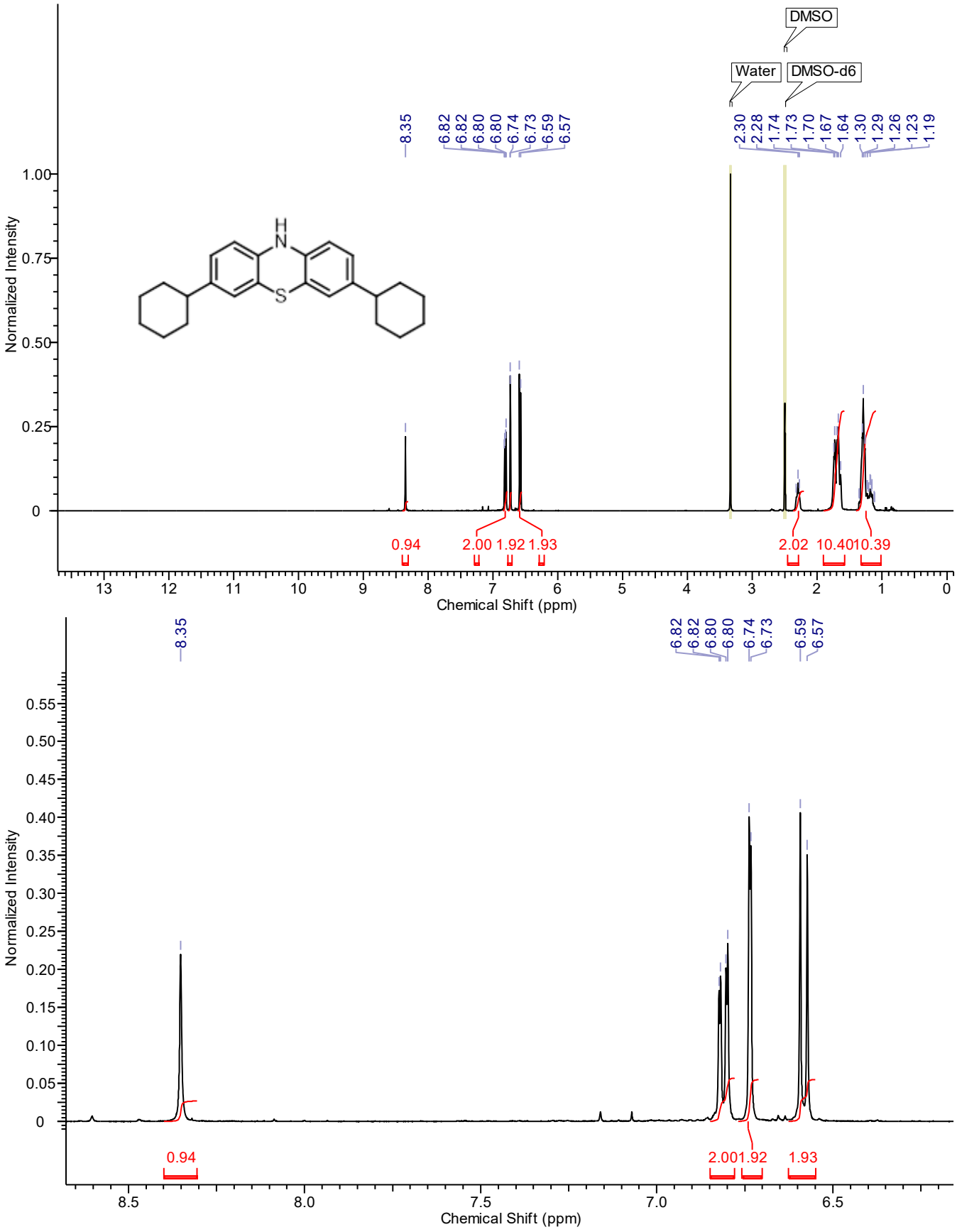


Figure S7.182. Full spectra (*top*) and aromatic region (*bottom*) ^{1}H NMR of 3,7-dicyclohexylphenothiazine in DMSO-d6.

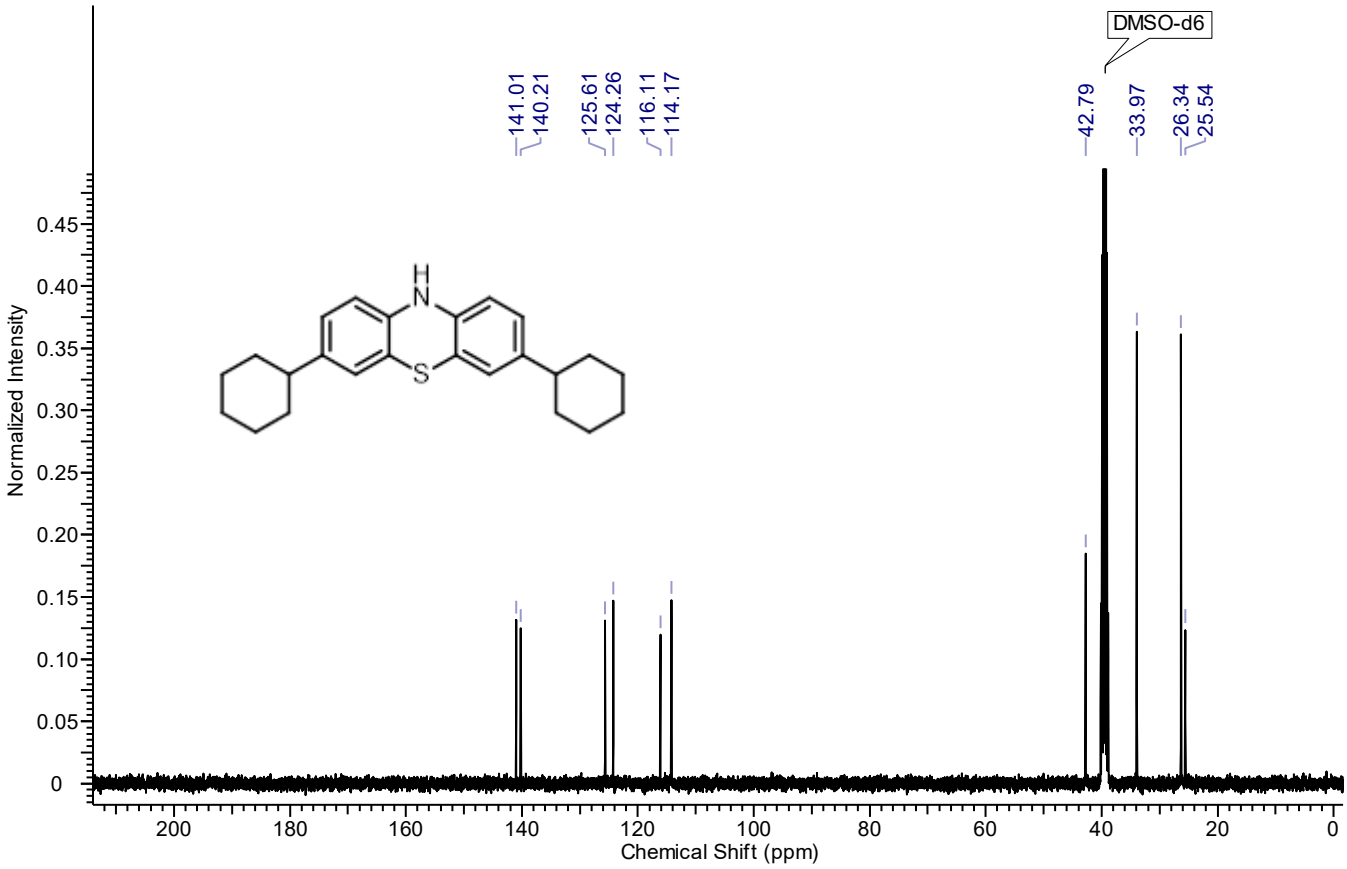


Figure S7.183. Full spectra ^{13}C NMR of 3,7-dicyclohexylphenothiazine in DMSO-d6.

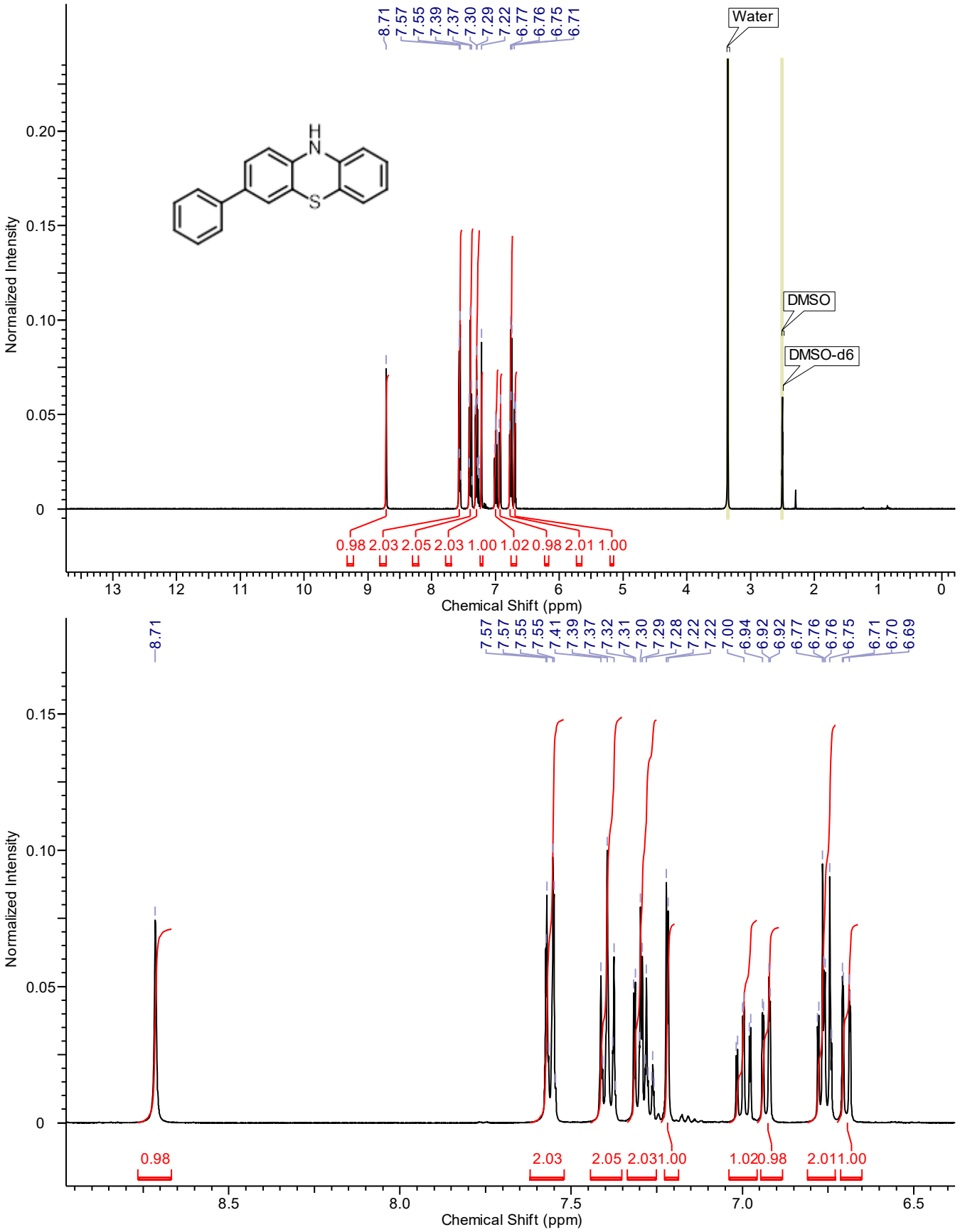


Figure S7.184. Full spectra (*top*) and aromatic region (*bottom*) ^{1}H NMR of 3-phenylphenothiazine in DMSO-d6.

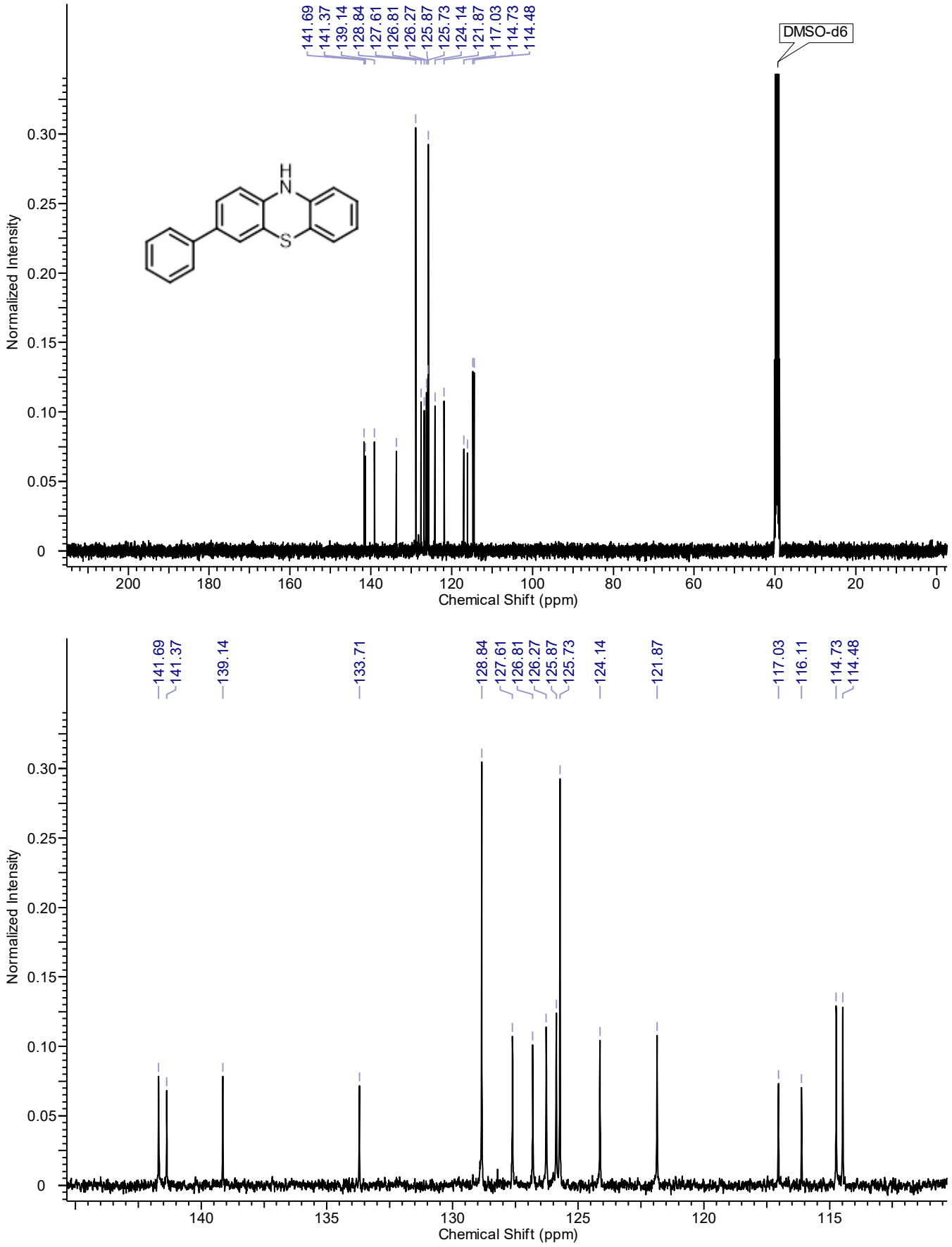


Figure S7.185. Full spectra (*top*) and aromatic region (*bottom*) ^{13}C NMR of 3-phenylphenothiazine in DMSO-d6.

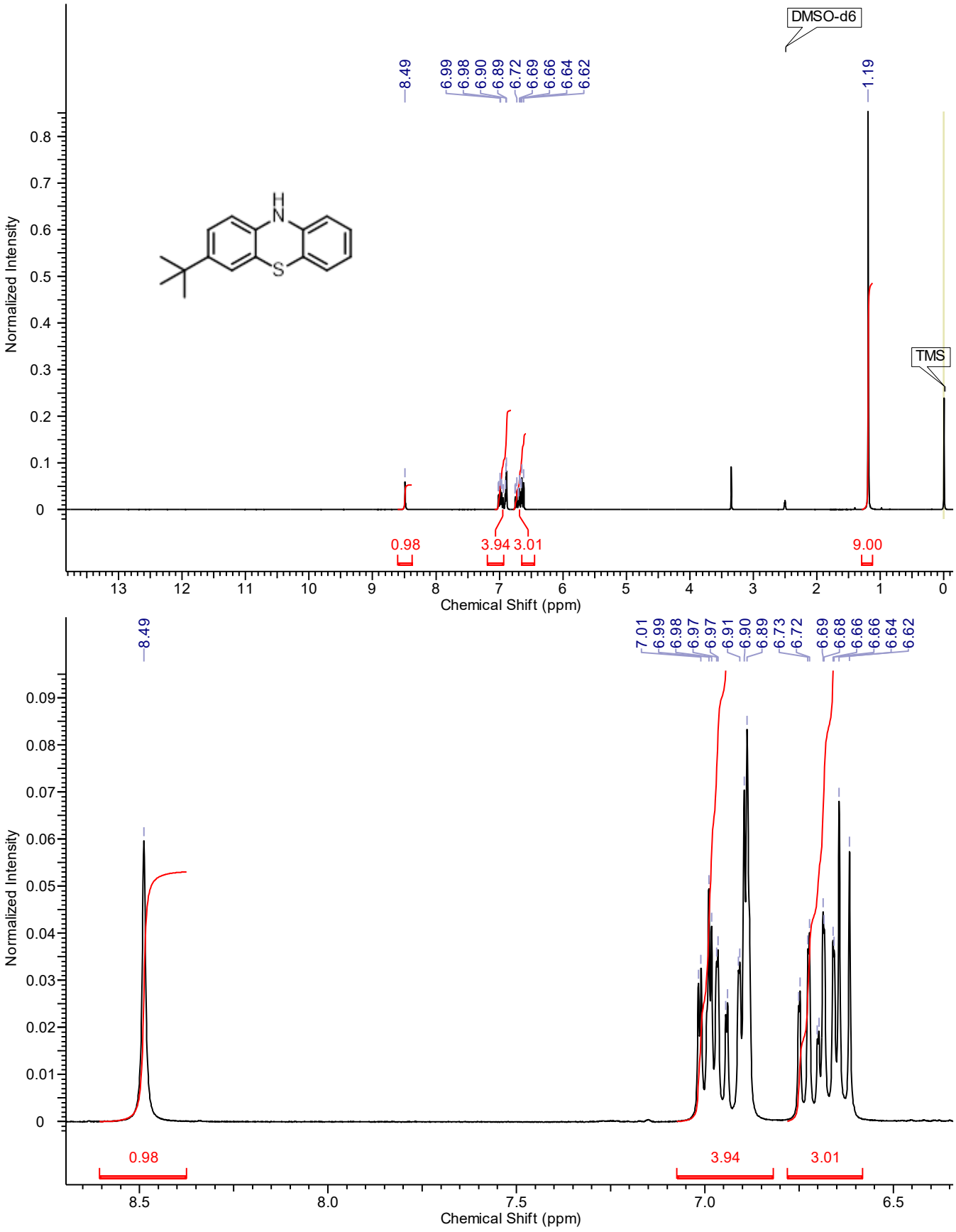


Figure S7.186. Full spectra (*top*) and aromatic region (*bottom*) ^{1}H NMR of 3-*tert*-butylphenothiazine in DMSO-d6.

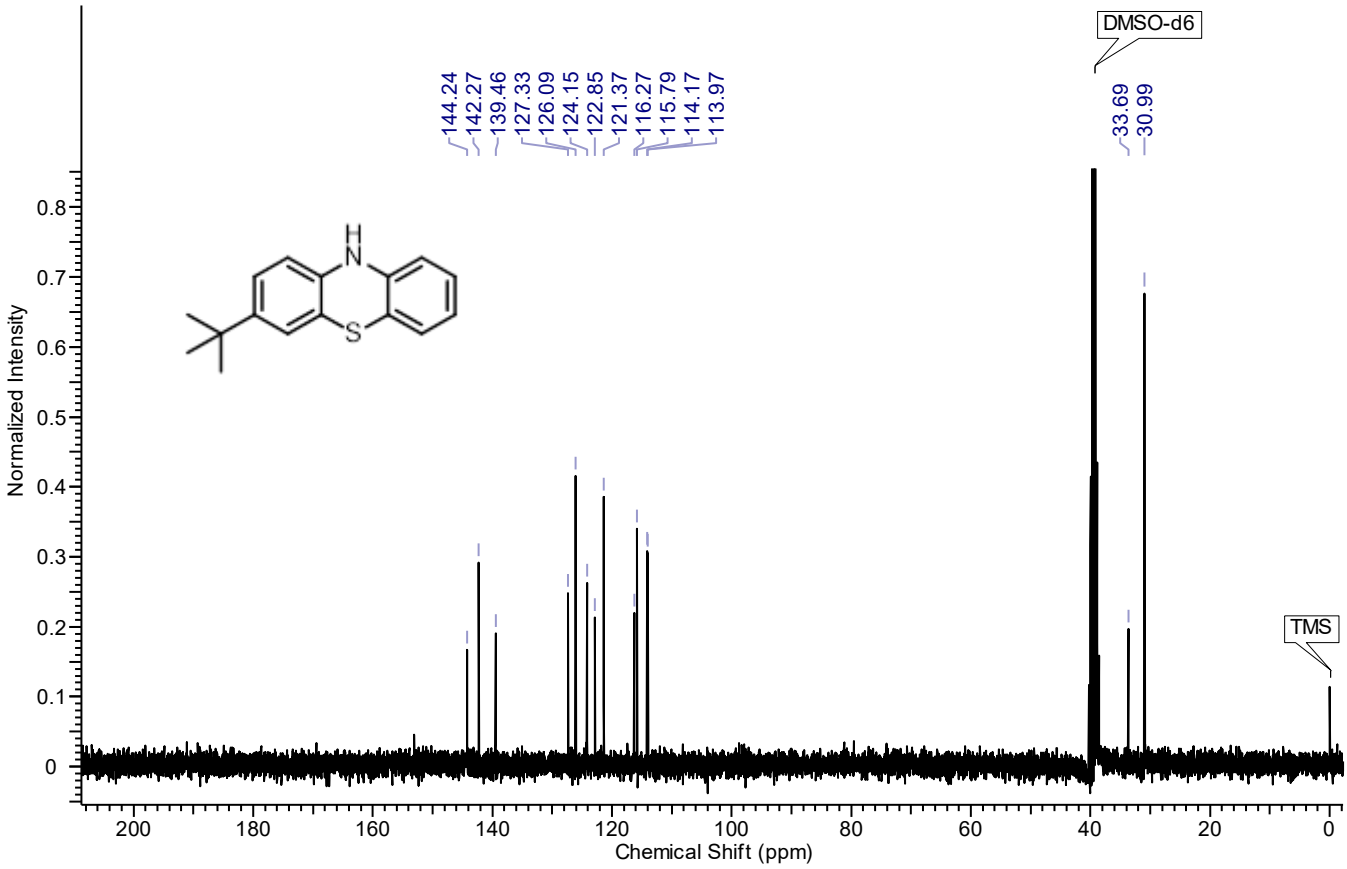


Figure S7.187. Full spectra ^{13}C NMR of 3-*tert*-butylphenothiazine in DMSO-d6.

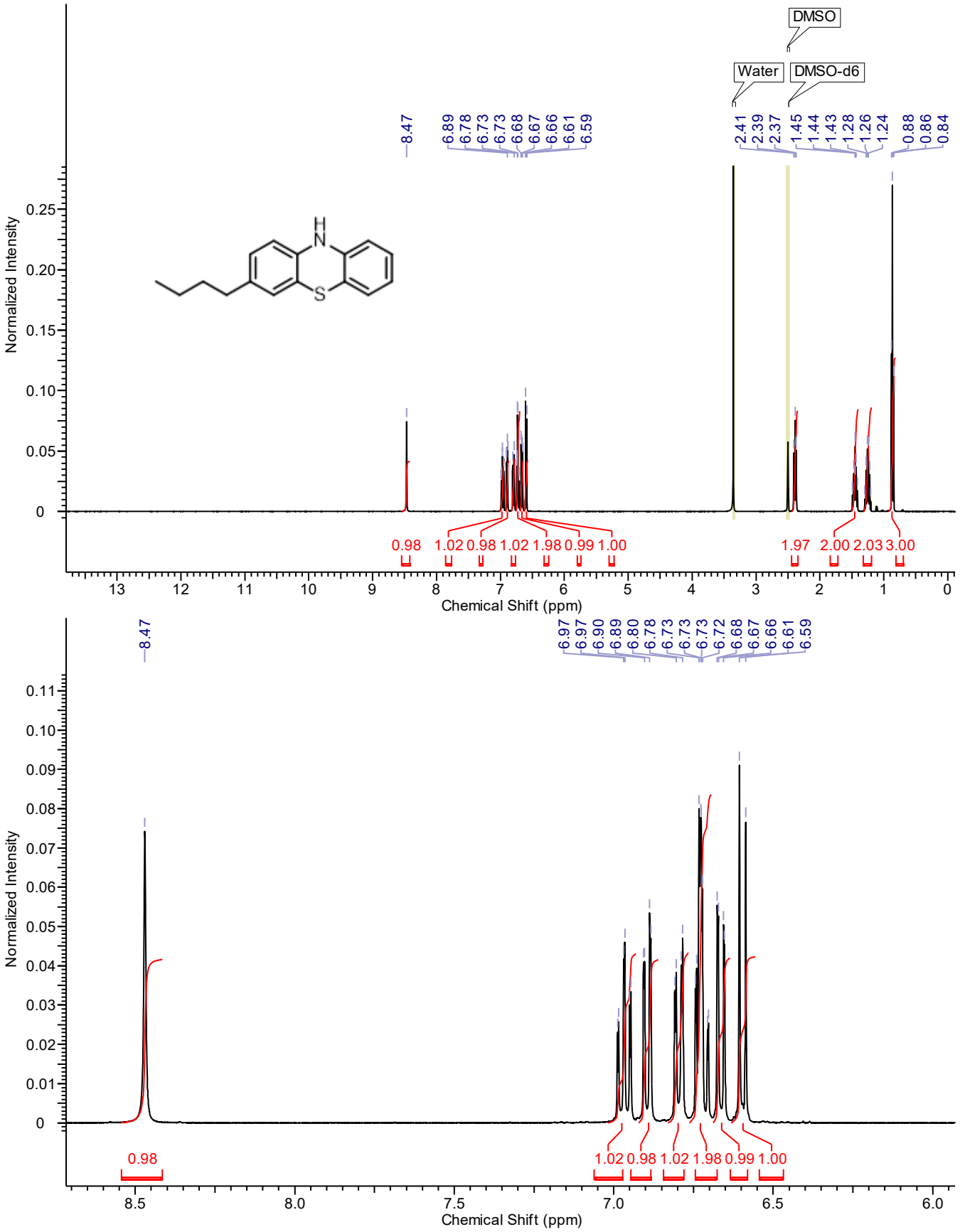


Figure S7.188. Full spectra (*top*) and aromatic region (*bottom*) ^{1}H NMR of 3-*n*-butylphenothiazine in DMSO-d6.

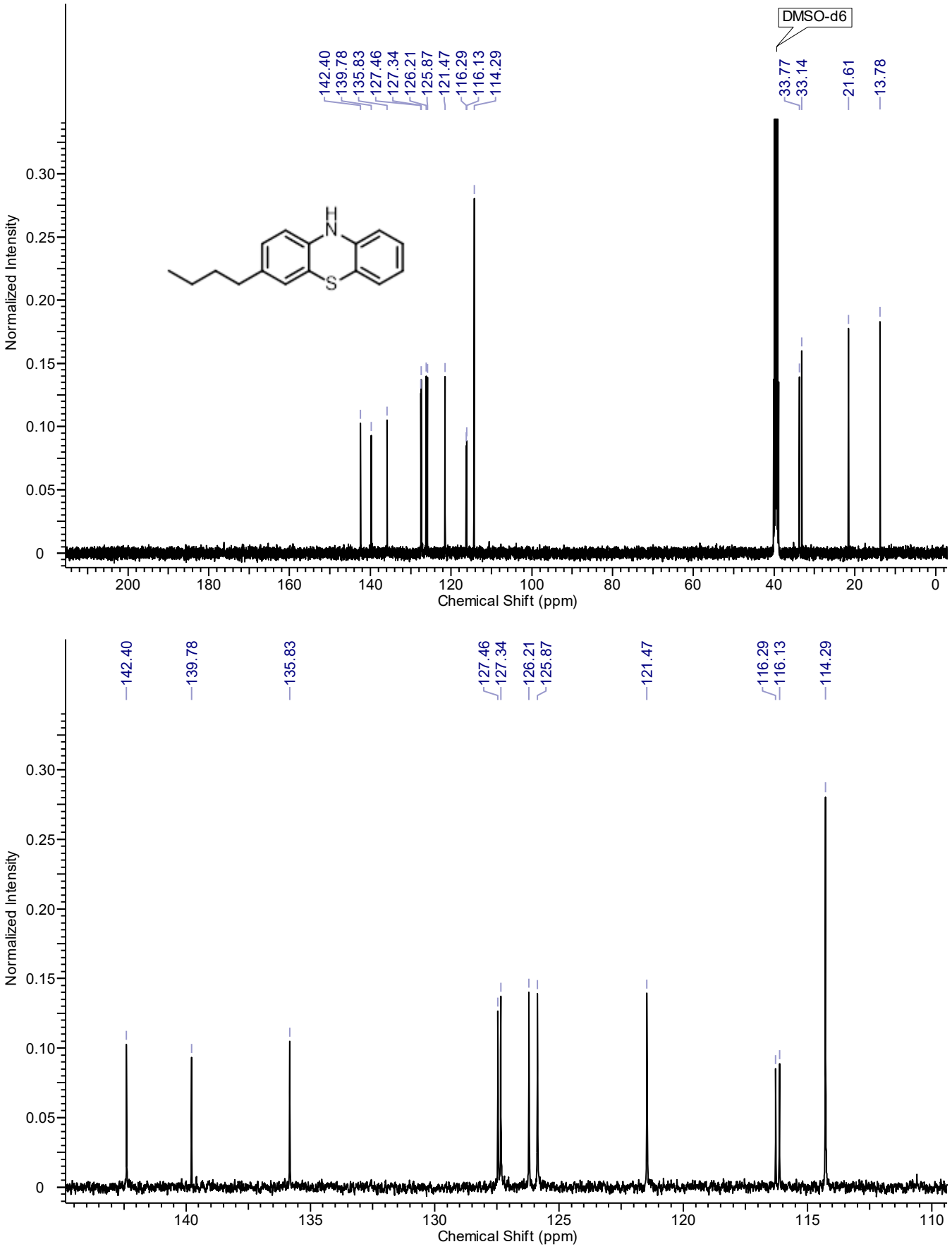


Figure S7.189. Full spectra (*top*) and aromatic region (*bottom*) ^{13}C NMR of 3-*n*-butylphenothiazine in DMSO-d6.

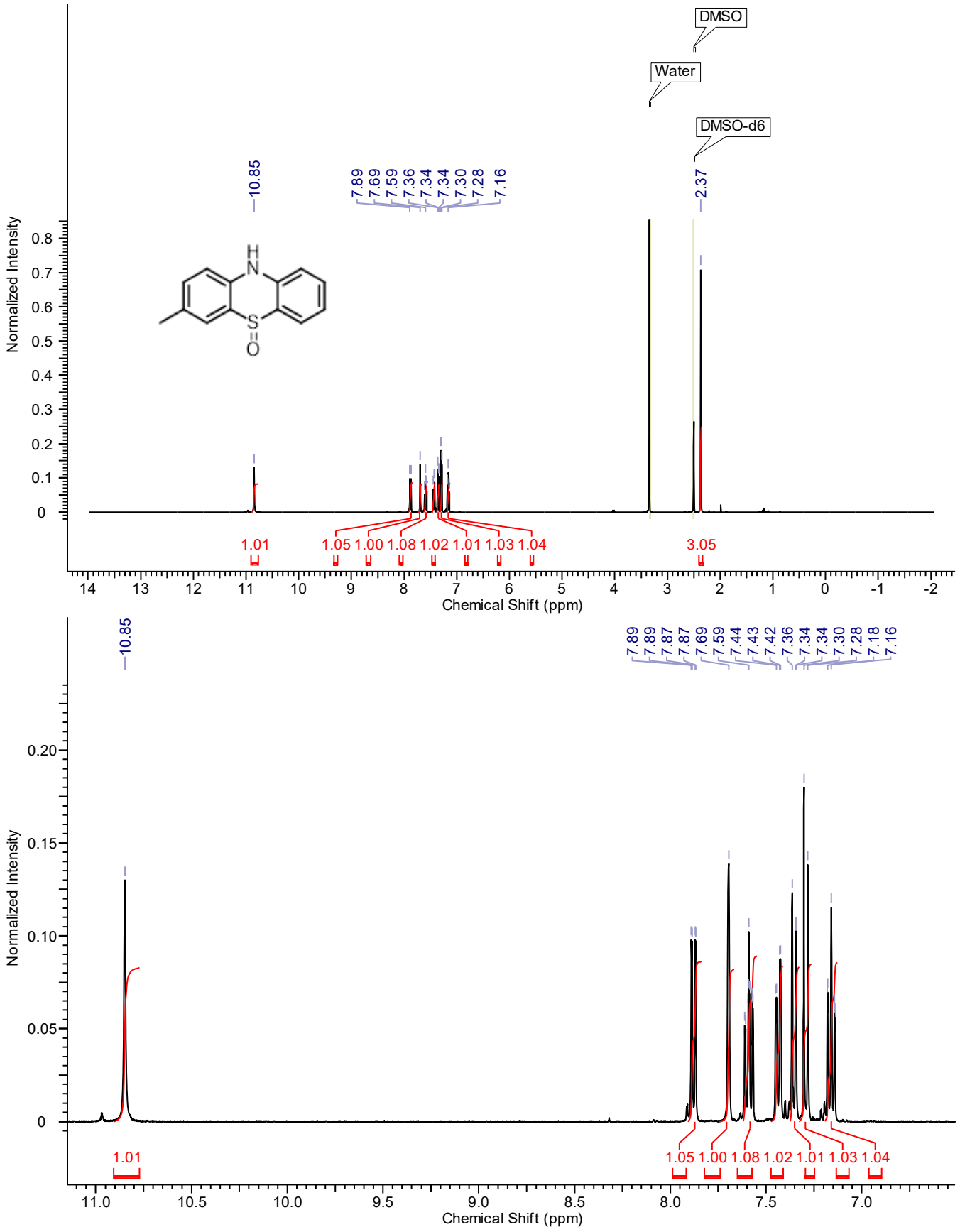


Figure S7.190. Full spectra (*top*) and aromatic region (*bottom*) ^{1}H NMR of 3-methylphenothiazine-S-oxide in DMSO-d6.

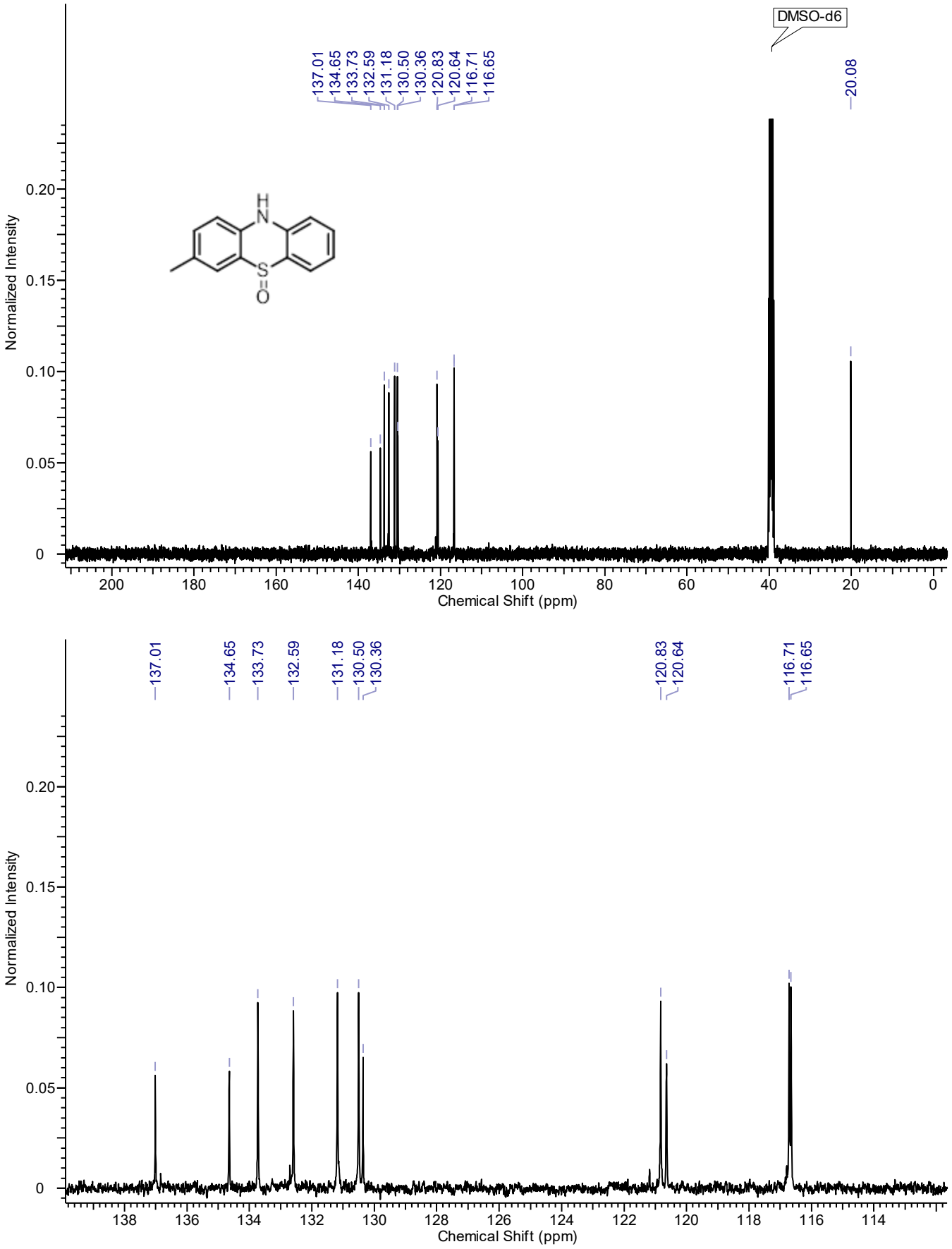


Figure S7.191. Full spectra (*top*) and aromatic region (*bottom*) ^{13}C NMR of 3-methylphenothiazine-S-oxide in DMSO-d6.

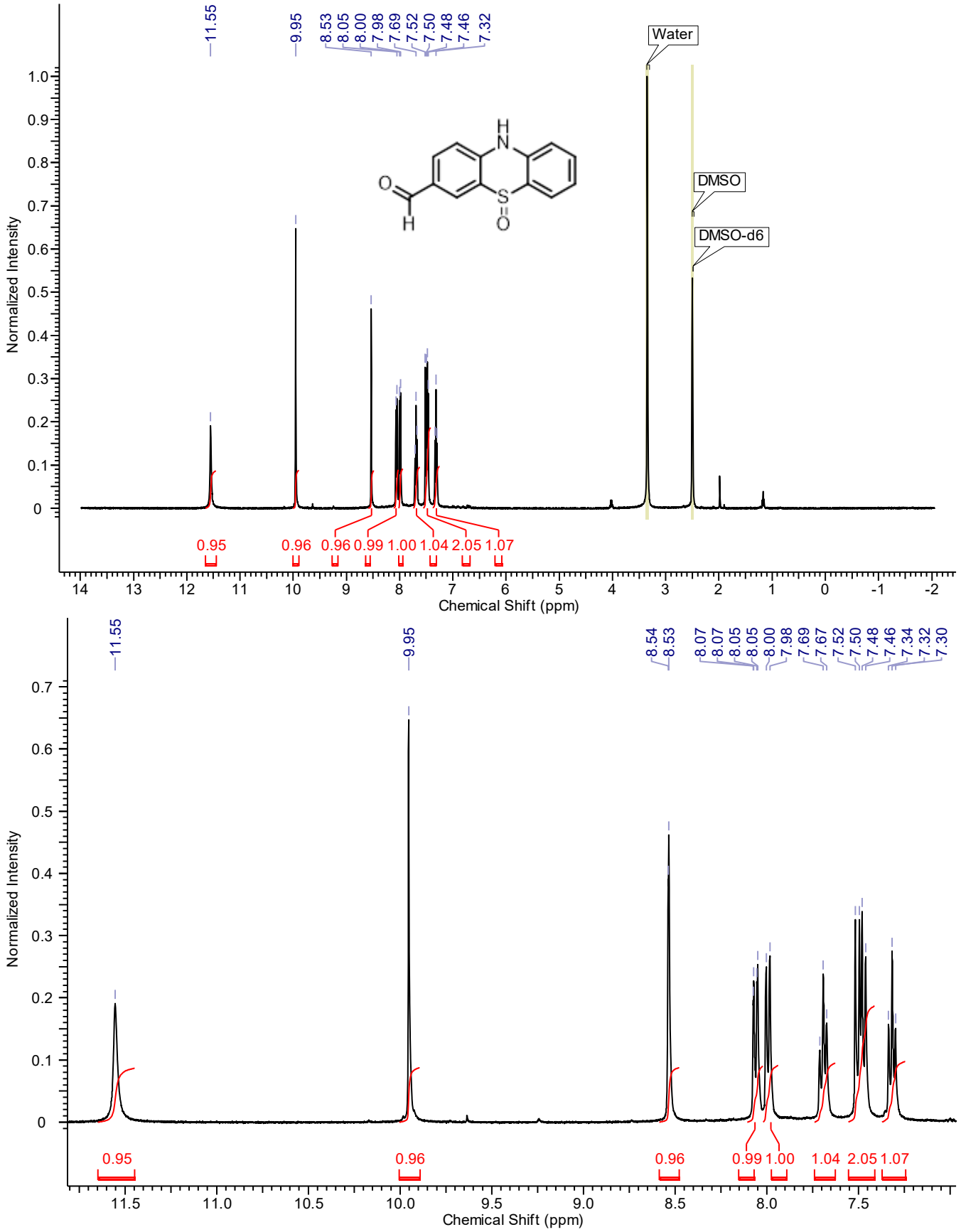


Figure S7.192. Full spectra (*top*) and aromatic region (*bottom*) ^{1}H NMR of 3-formylphenothiazine-S-oxide in DMSO-d6.

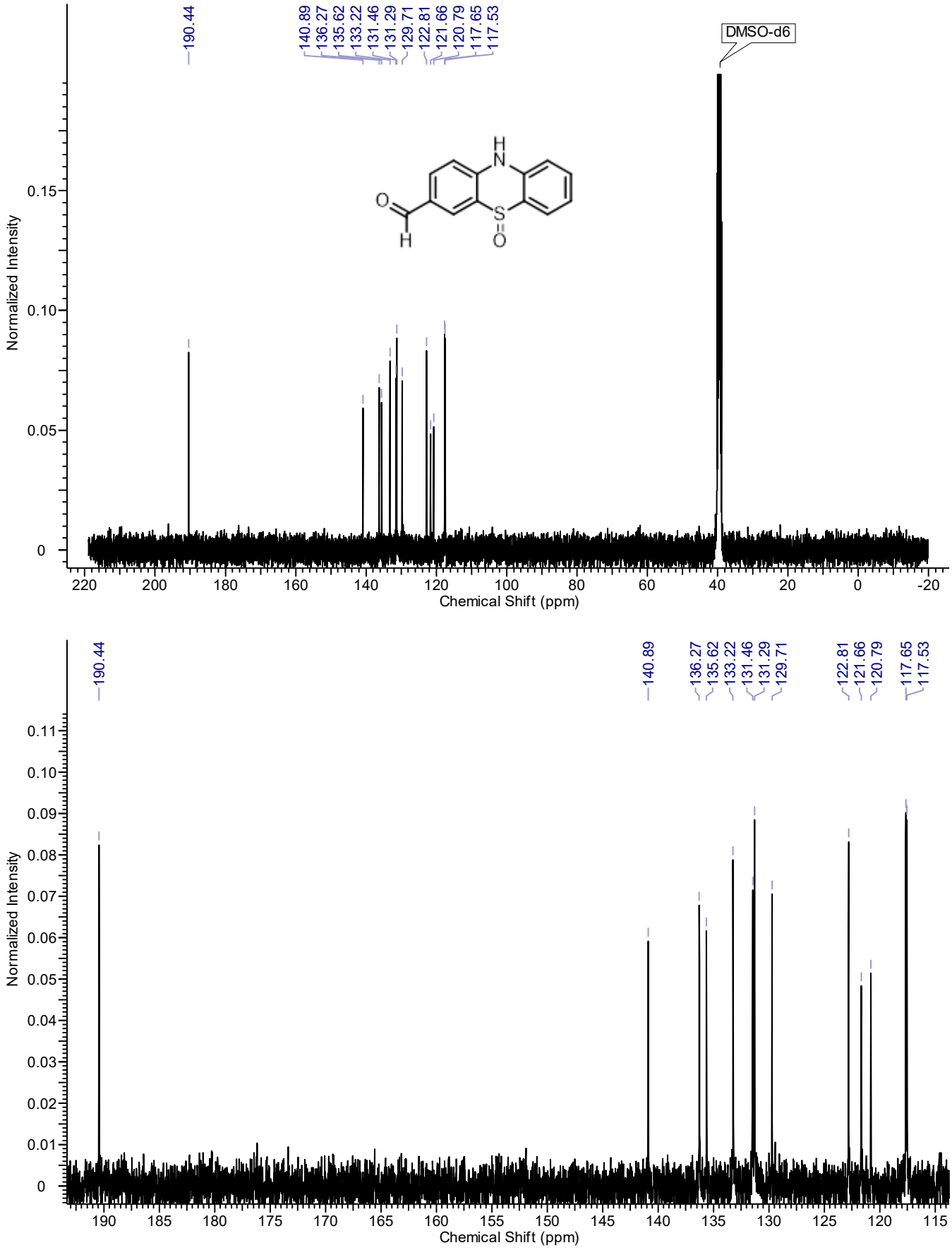


Figure S7.193. Full spectra (*top*) and aromatic region (*bottom*) ^{13}C NMR of 3-formylphenothiazine-S-oxide in DMSO-d6.

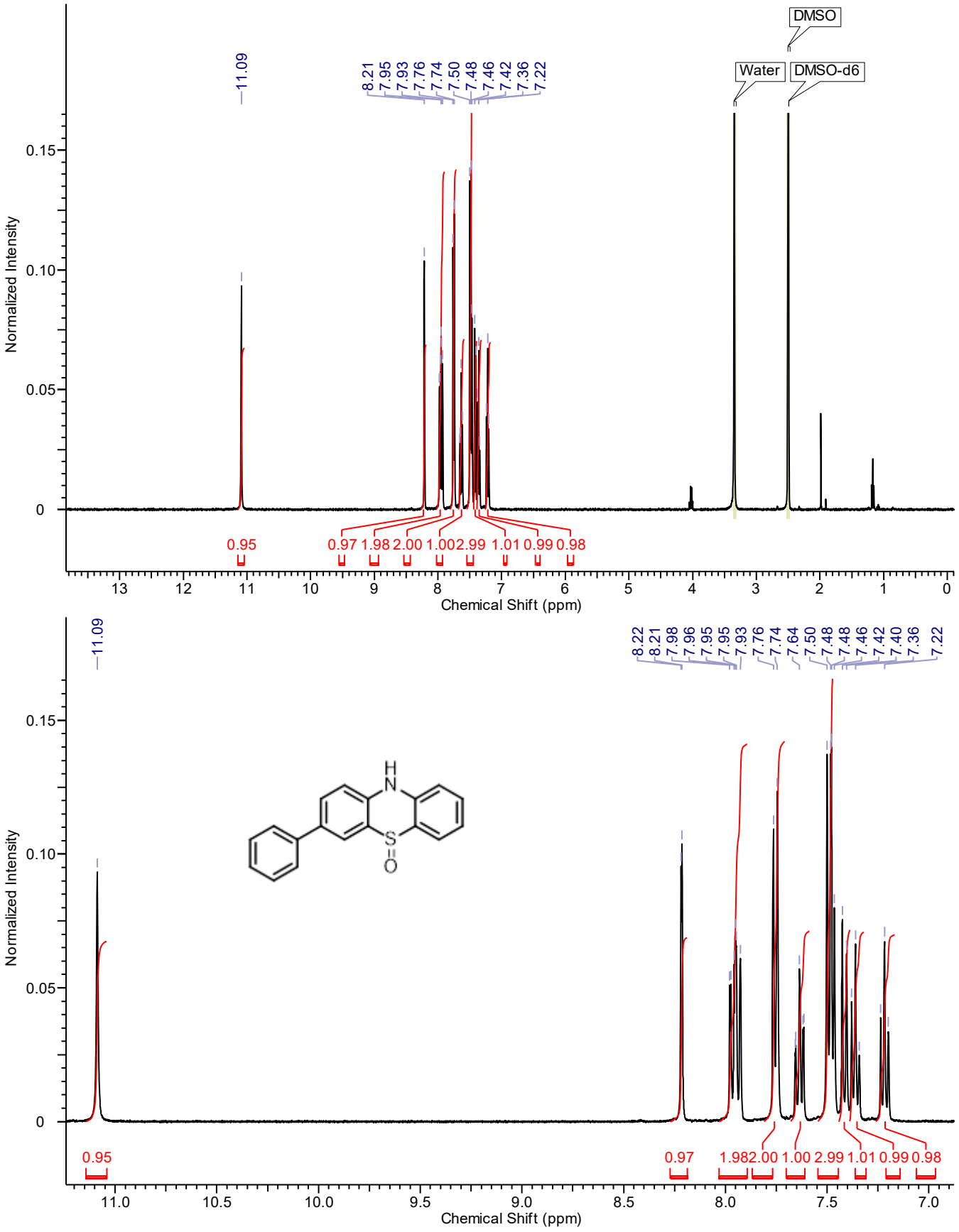


Figure S7.194. Full spectra (*top*) and aromatic region (*bottom*) ^{1}H NMR of 3-phenylphenothiazine-S-oxide in DMSO-d6.

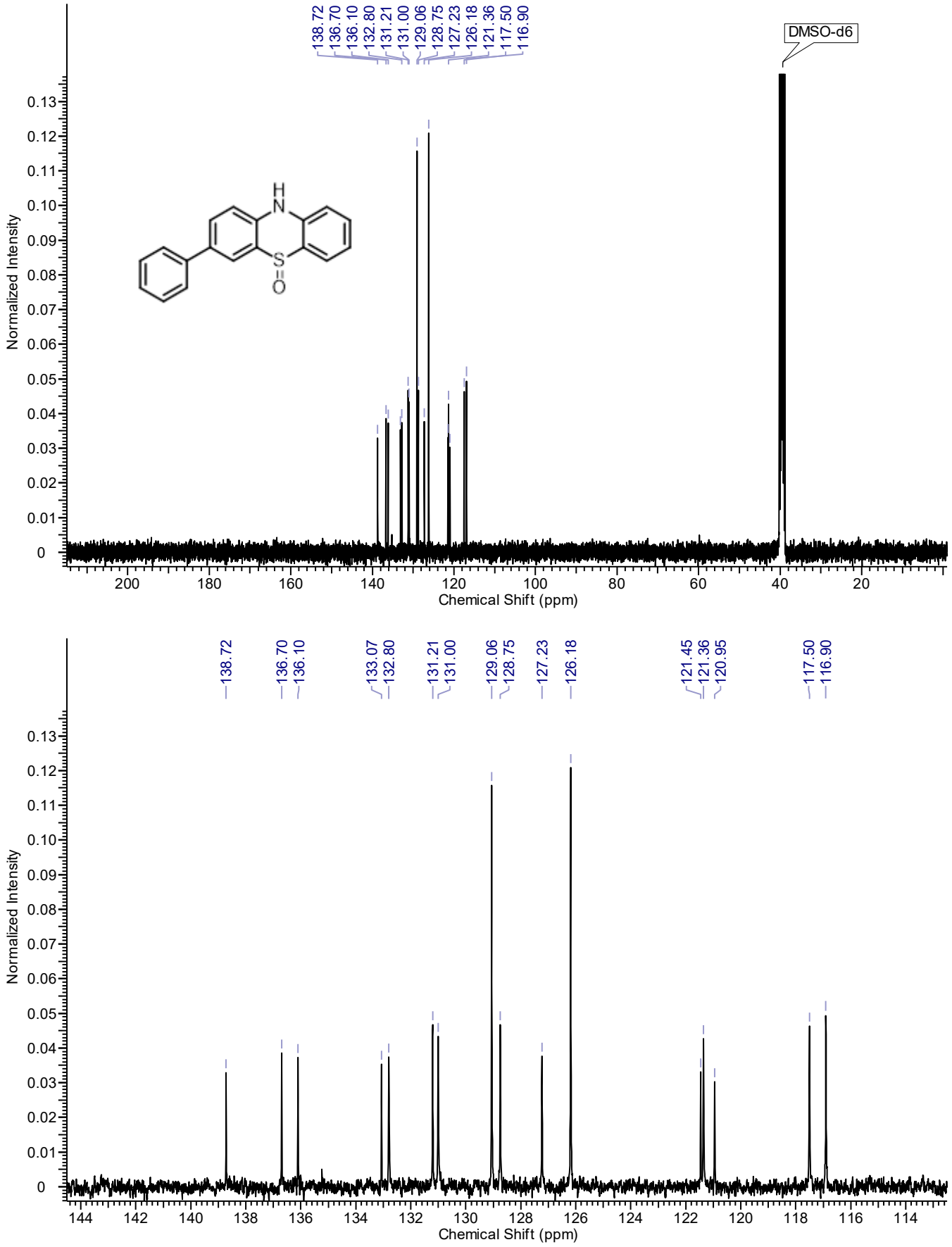


Figure S7.195. Full spectra (*top*) and aromatic region (*bottom*) ^{13}C NMR of 3-phenylphenothiazine-S-oxide in DMSO-d6.

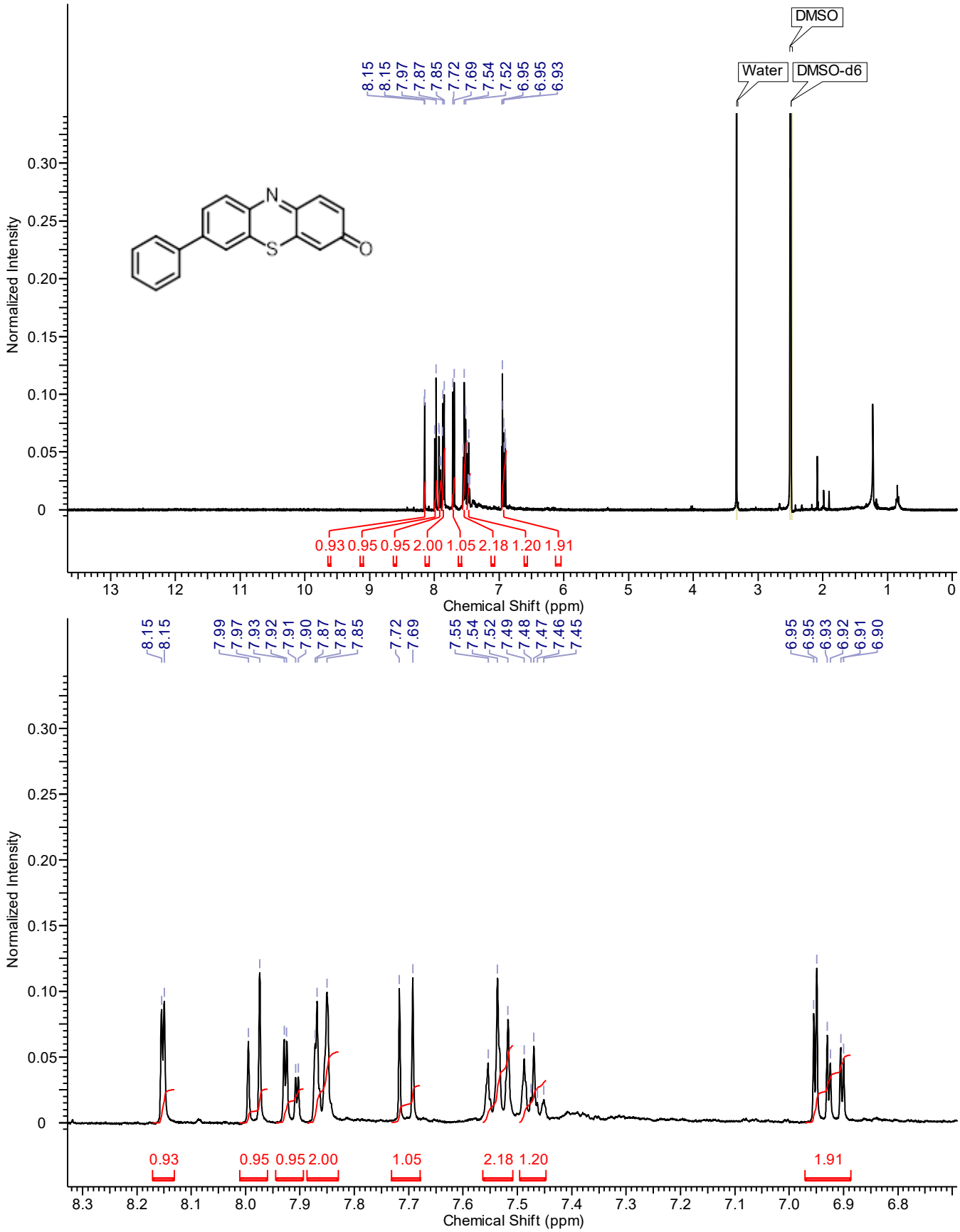


Figure S7.196. Full spectra (*top*) and aromatic region (*bottom*) ^{1}H NMR of 3-phenylphenothiazin-3-one in DMSO-d6.

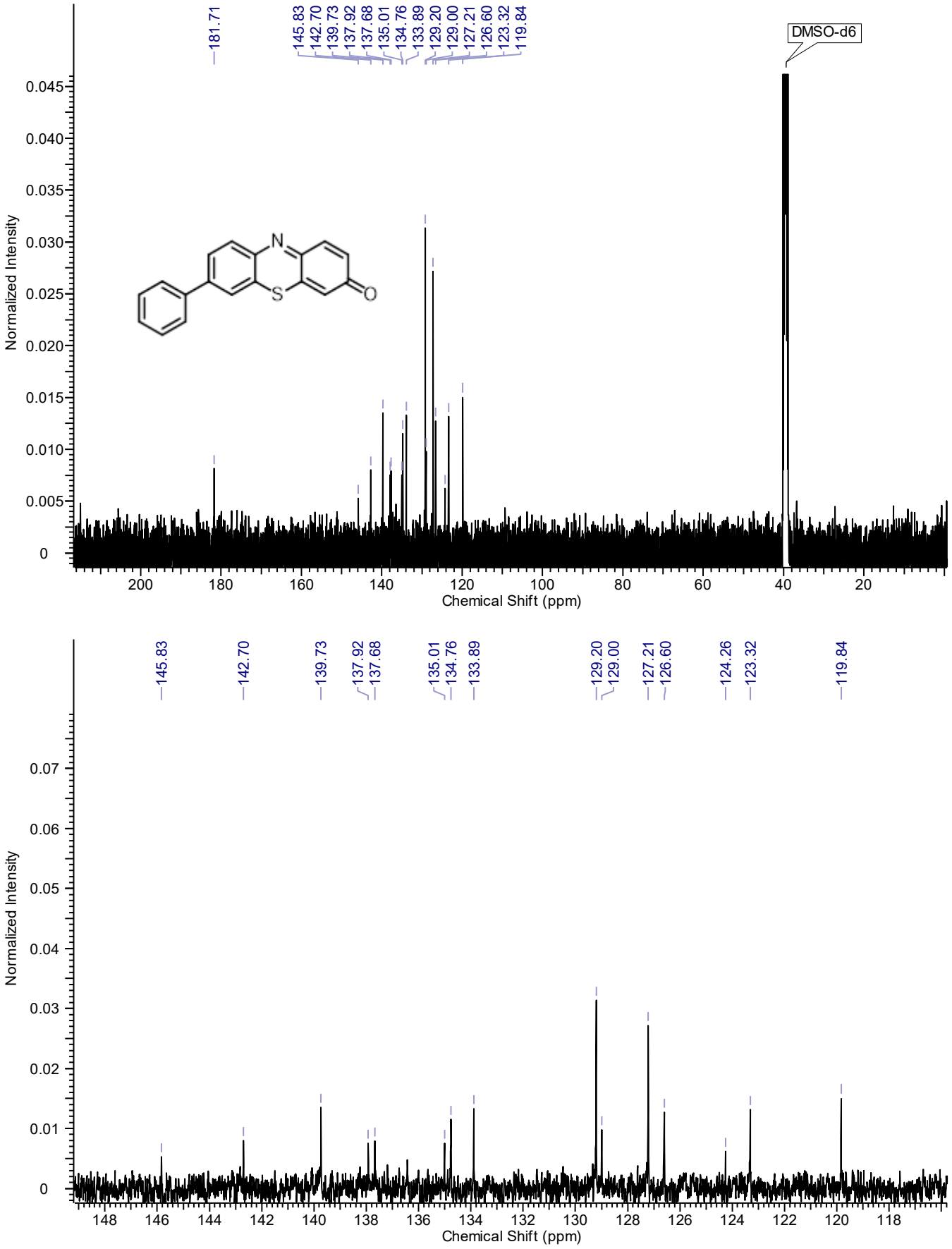


Figure S7.197. Full spectra (*top*) and aromatic region (*bottom*) ^{13}C NMR of 3-phenylphenothiazin-3-one in DMSO-d6.

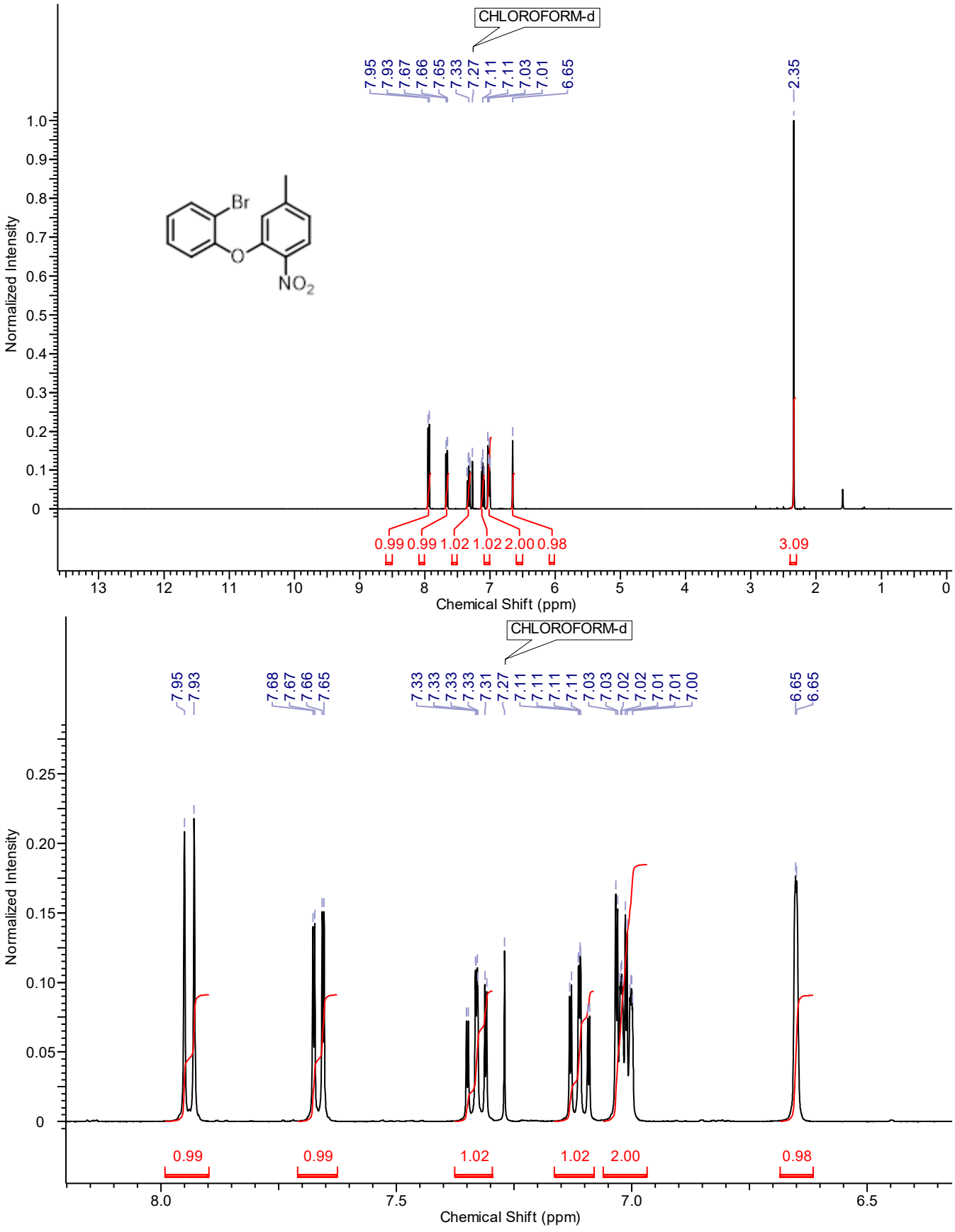


Figure S7.198. Full spectra (*top*) and aromatic region (*bottom*) ^{1}H NMR of 2-(2-bromophenoxy)-4-methyl-1-nitrobenzene in DMSO-d6.

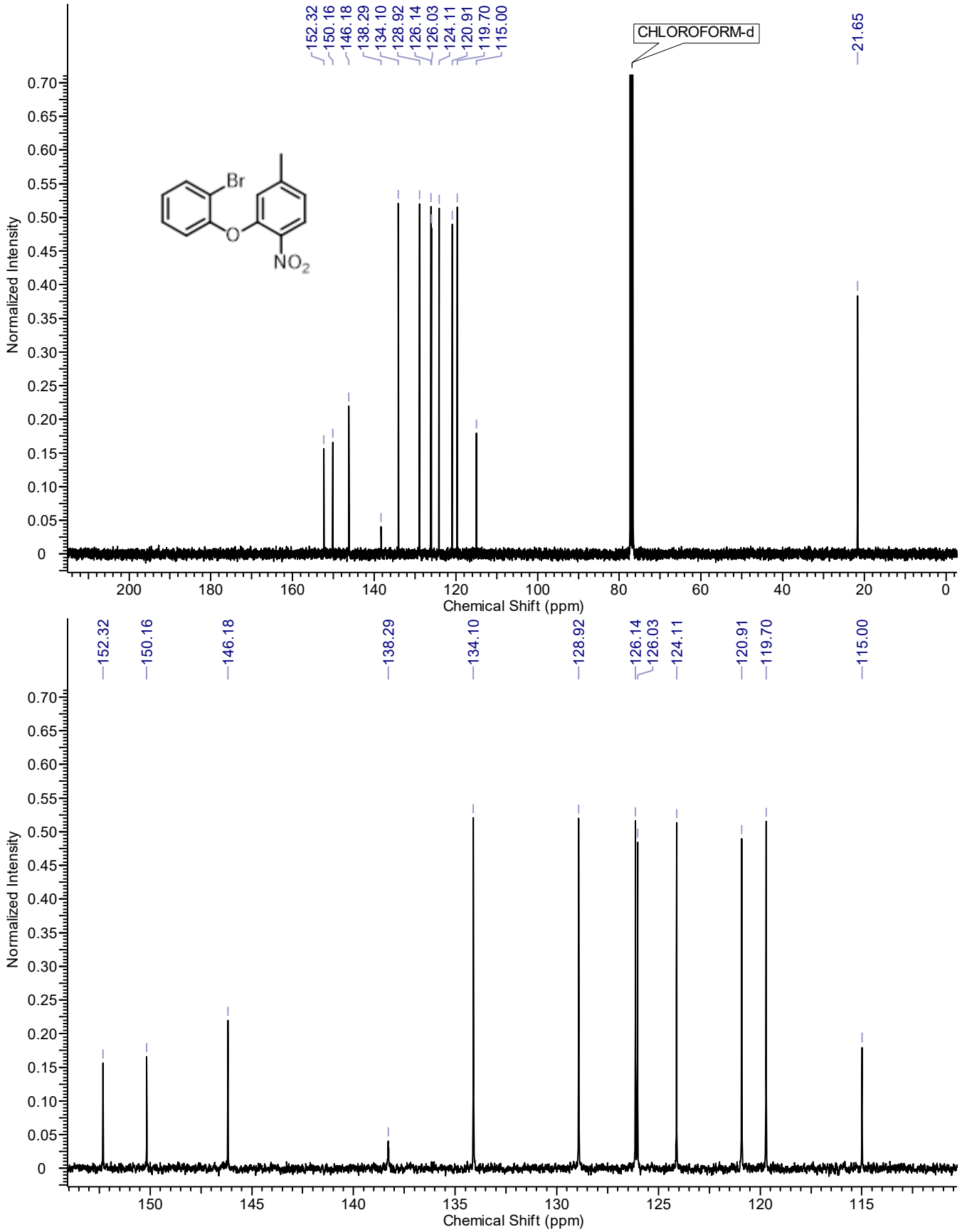


Figure S7.199. Full spectra (*top*) and aromatic region (*bottom*) ^{13}C NMR of 2-(2-bromophenoxy)-4-methyl-1-nitrobenzene in DMSO-d6.

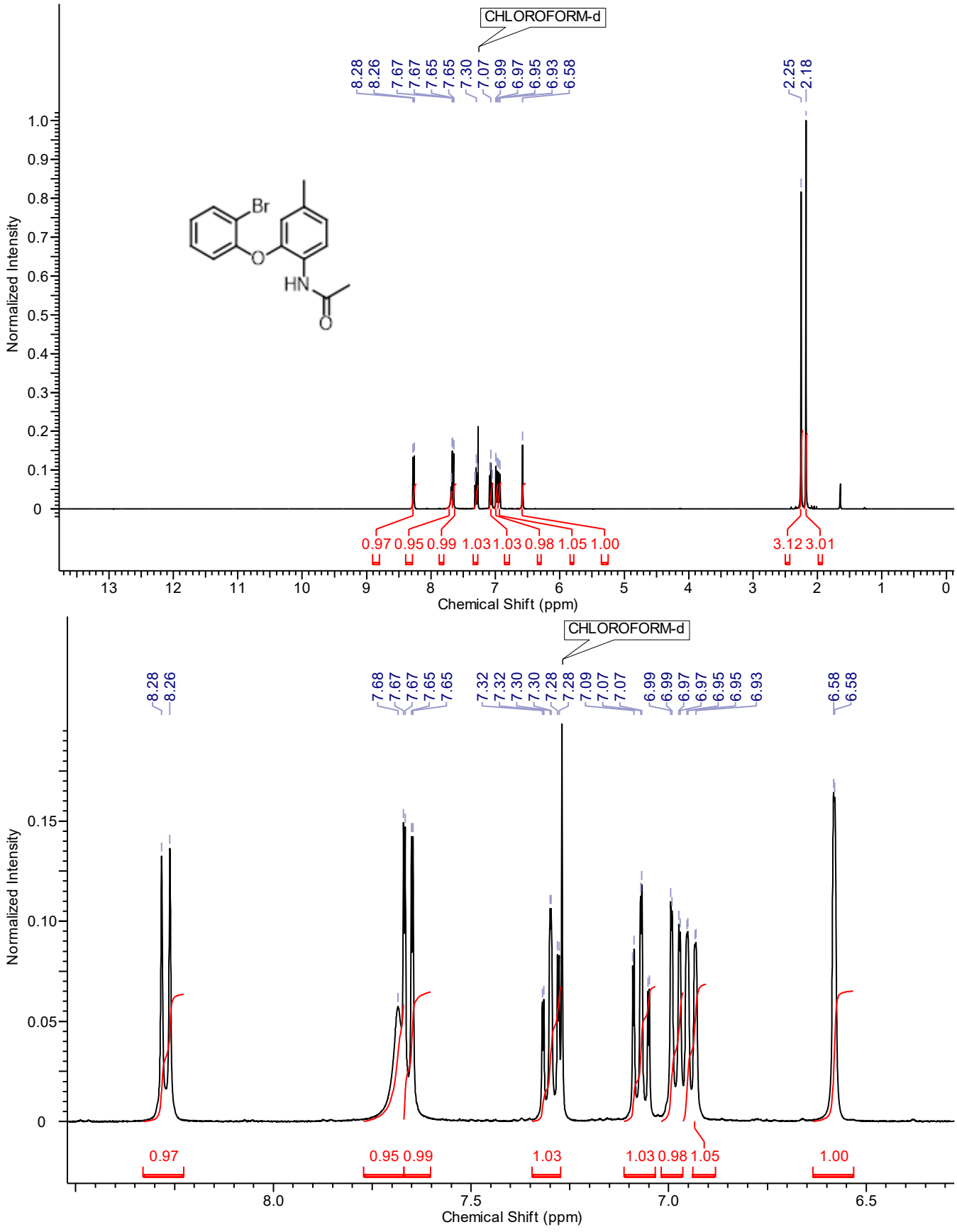


Figure S7.200. Full spectra (*top*) and aromatic region (*bottom*) ^{1}H NMR of *N*-(2-(2-bromophenoxy)-4-methylphenyl)acetamide in DMSO-d6.

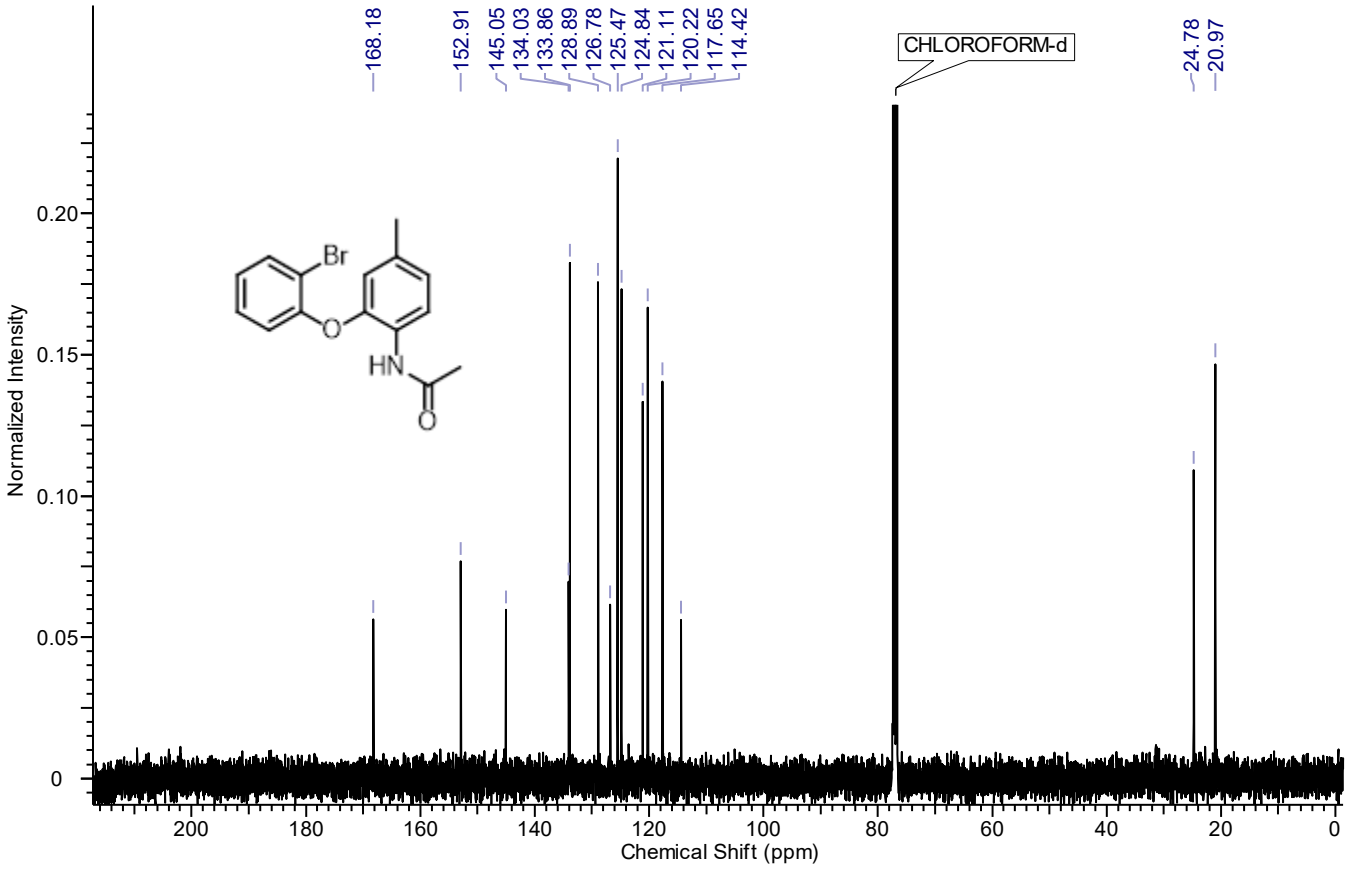


Figure S7.201. Full spectra ^{13}C NMR of *N*-(2-(2-bromophenoxy)-4-methylphenyl)acetamide in DMSO-d6.

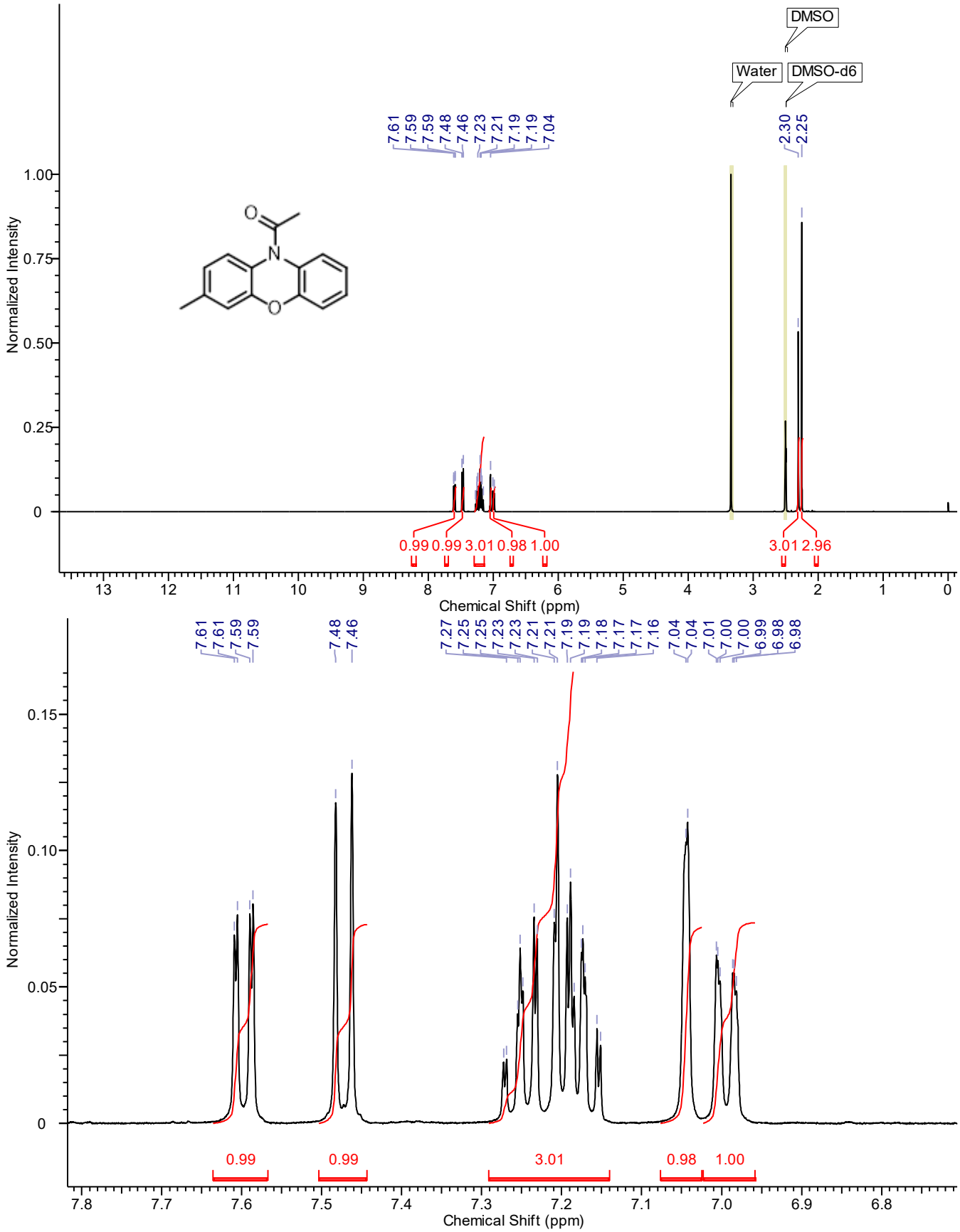


Figure S7.202. Full spectra (*top*) and aromatic region (*bottom*) ^{1}H NMR of 10-acetyl-3-methylphenoxazine in DMSO-d6.

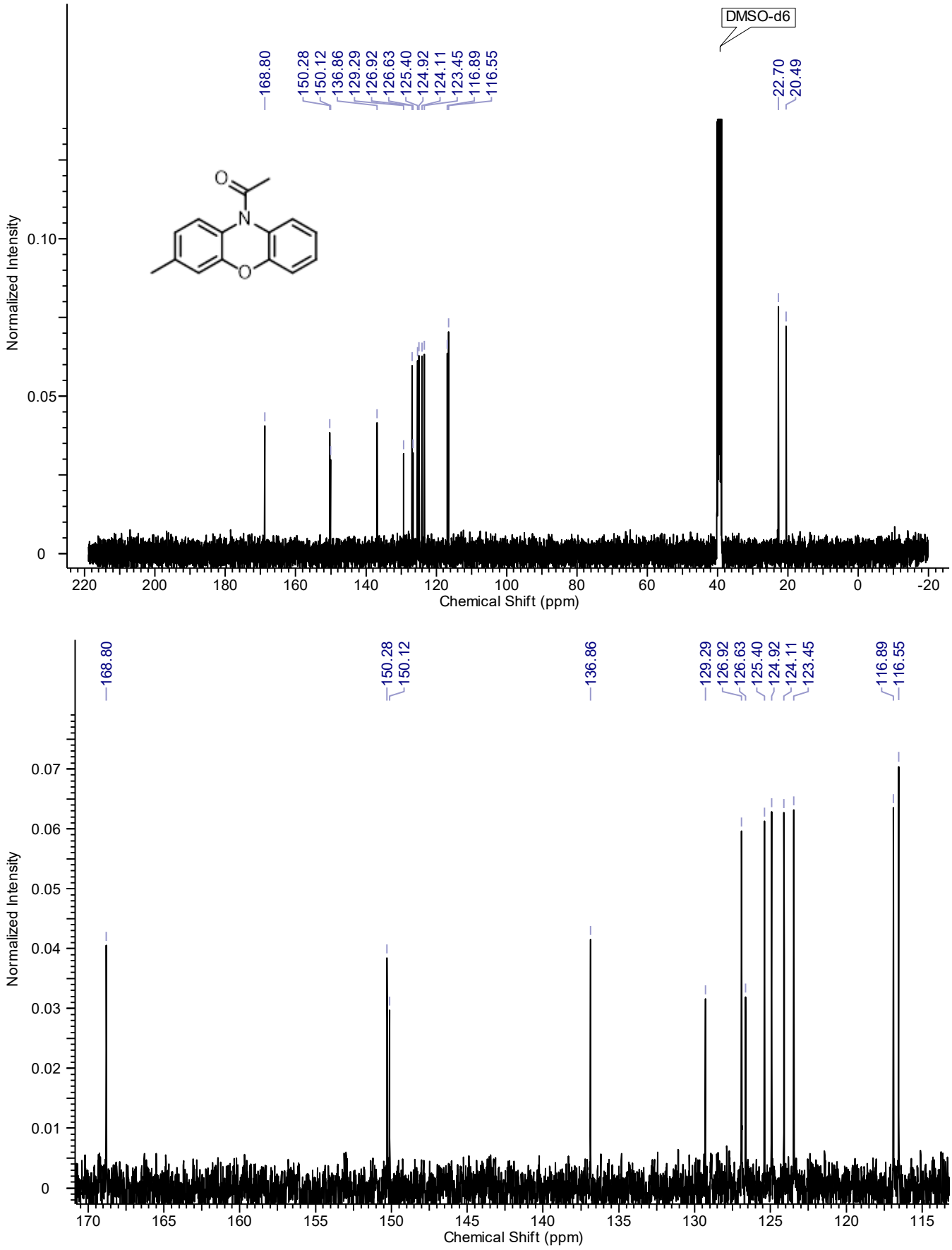


Figure S7.203. Full spectra (*top*) and aromatic region (*bottom*) ^{13}C NMR of 10-acetyl-3-methylphenoxazine in DMSO-d6.

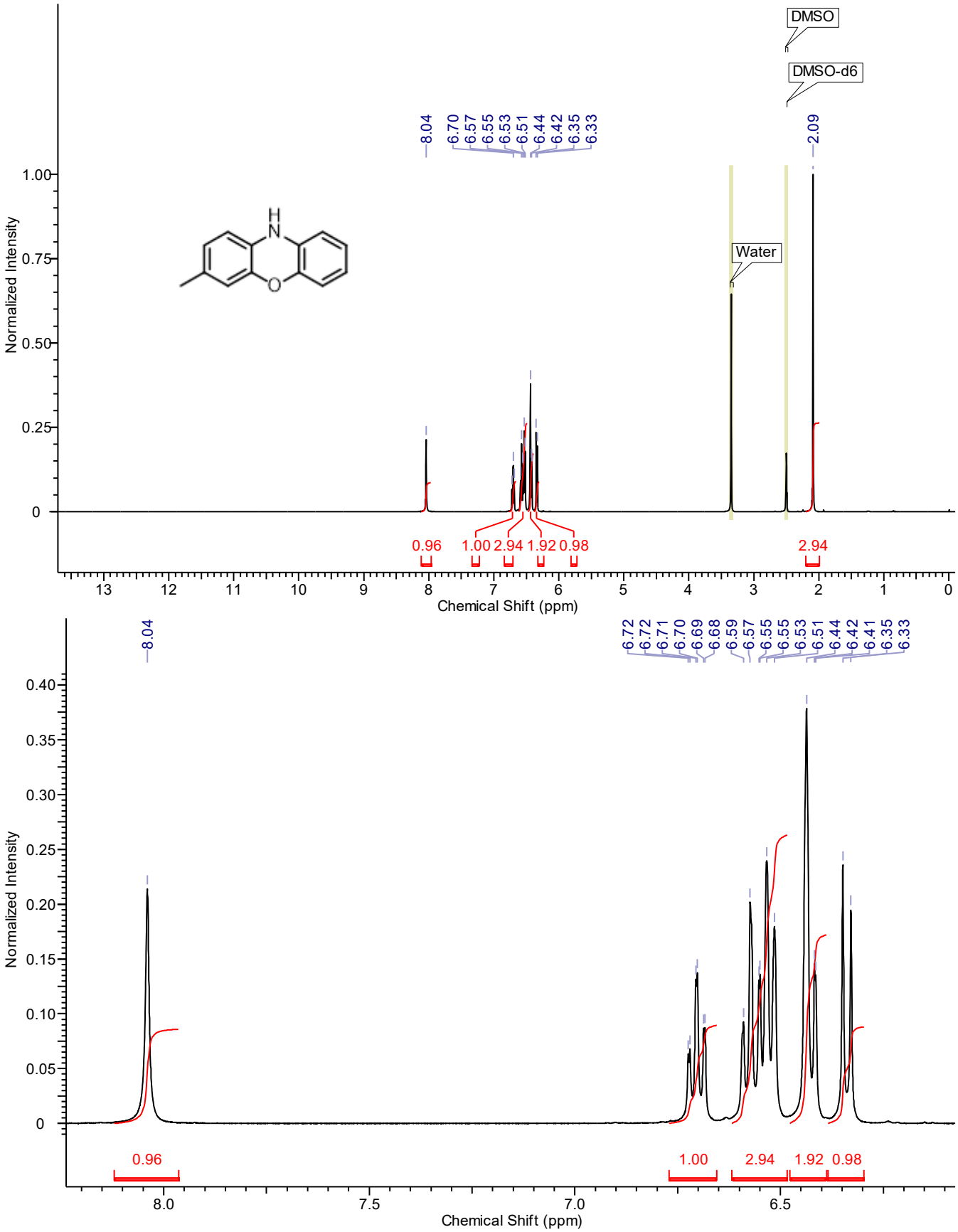


Figure S7.204. Full spectra (*top*) and aromatic region (*bottom*) ^{1}H NMR of 3-methylphenoxazine in DMSO-d6.

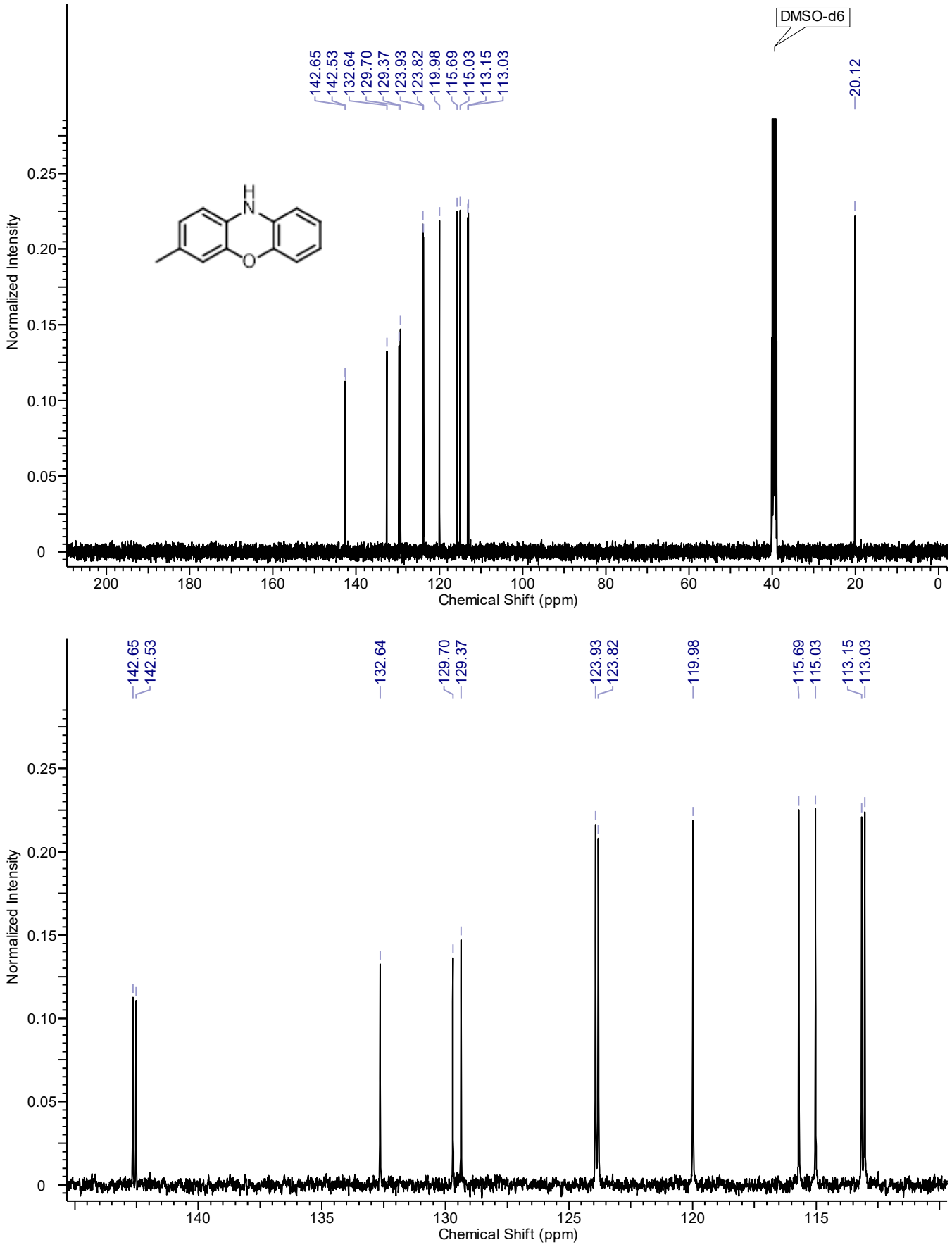


Figure S7.205. Full spectra (*top*) and aromatic region (*bottom*) ^{13}C NMR of 3-methylphenoxazine in DMSO-d6.

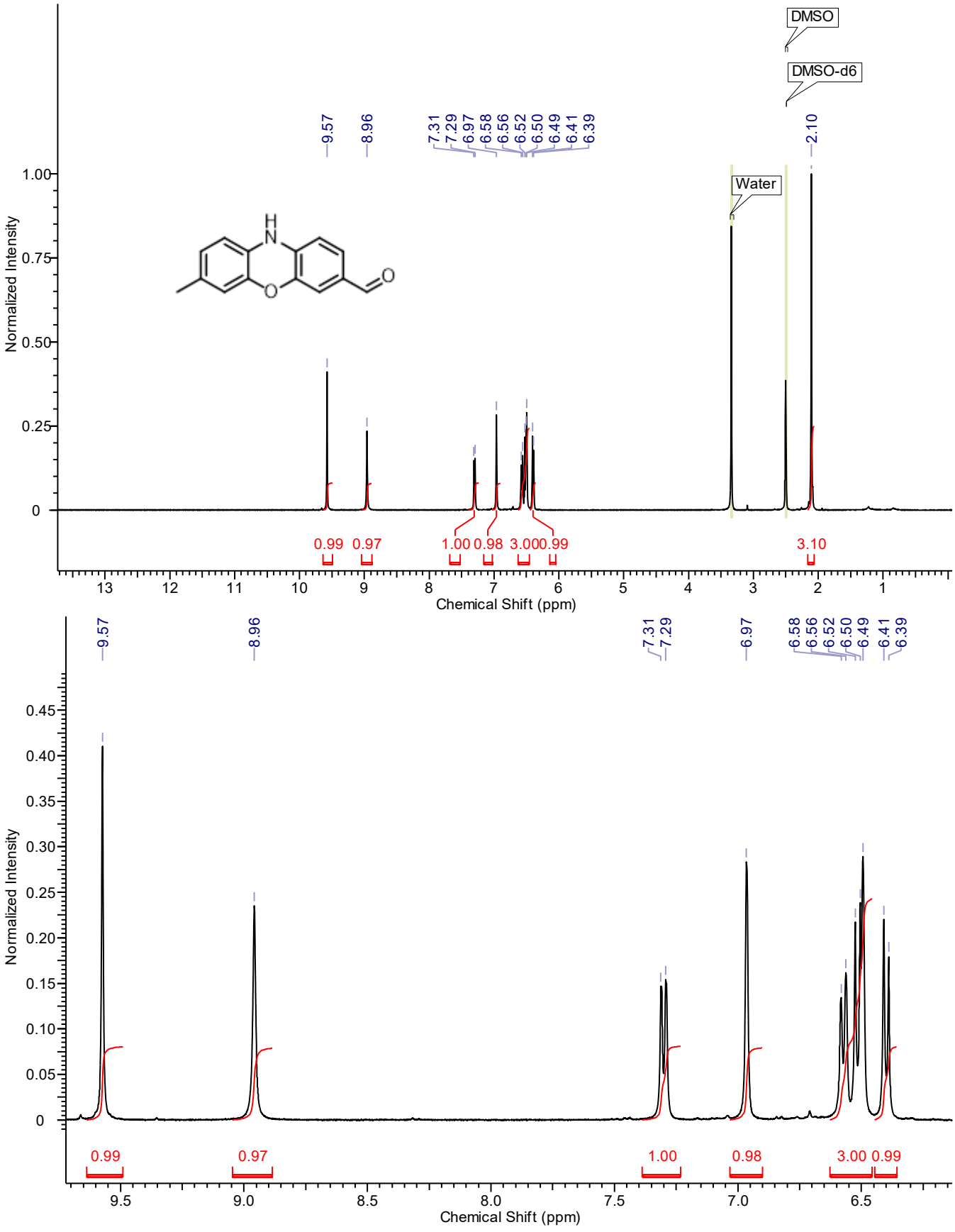


Figure S7.206. Full spectra (*top*) and aromatic region (*bottom*) ^{1}H NMR of 3-formyl-7-methylphenoxazine in DMSO-d6.

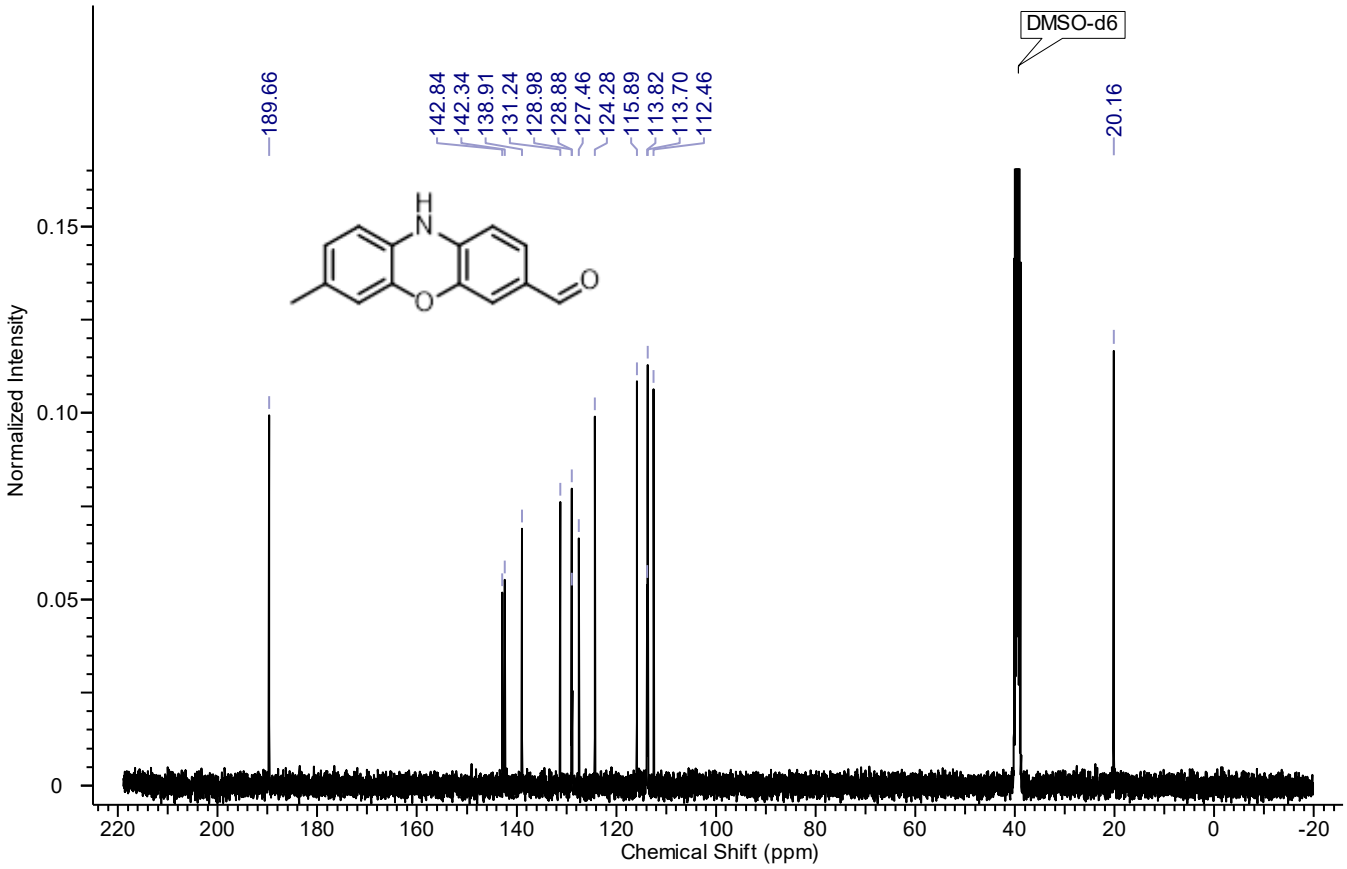


Figure S7.207. Full spectra ^{13}C NMR of 3-formyl-7-methylphenoxazine in DMSO-d6.

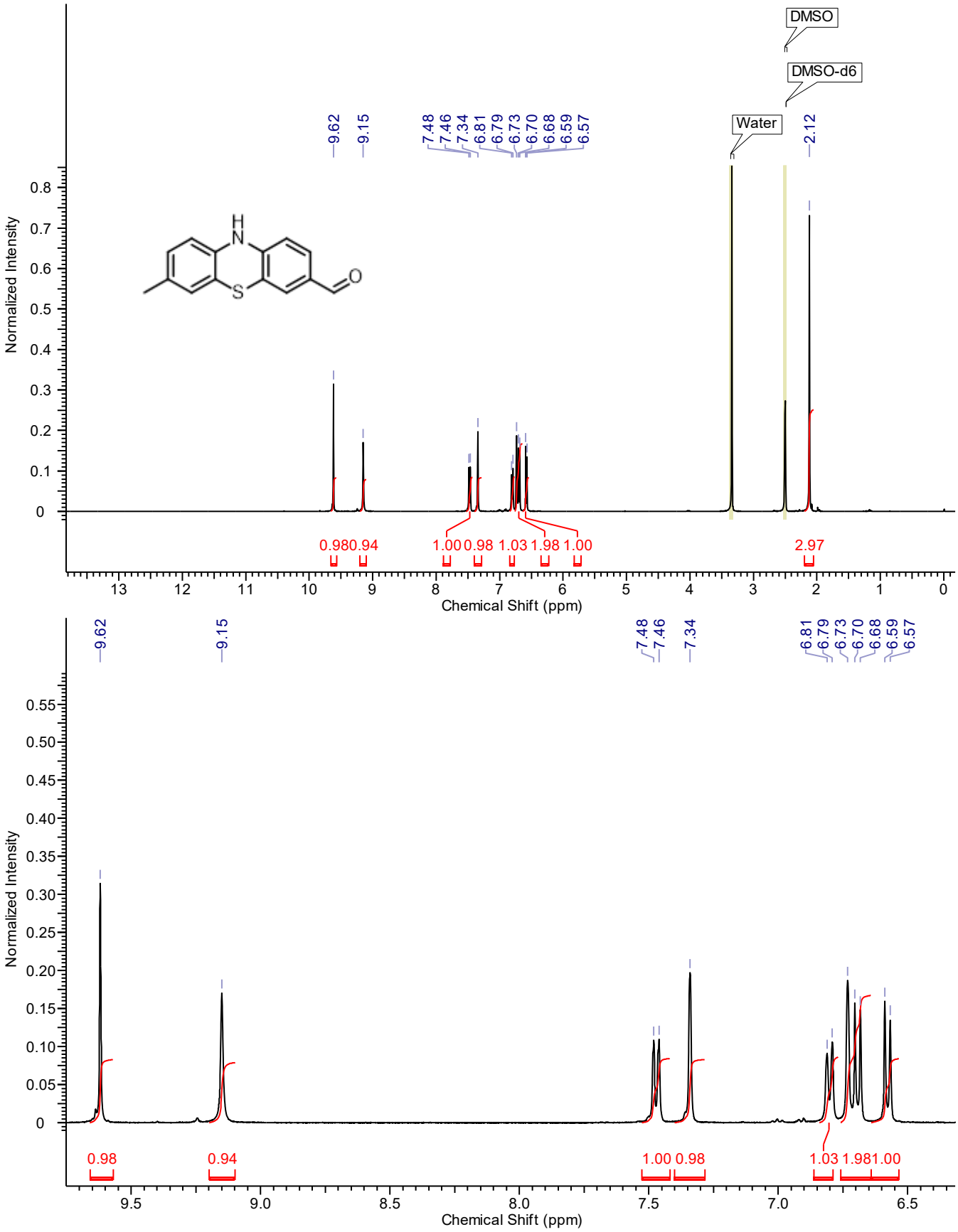


Figure S7.208. Full spectra (*top*) and aromatic region (*bottom*) ^{1}H NMR of 3-formyl-7-methylphenothiazine in DMSO-d6.

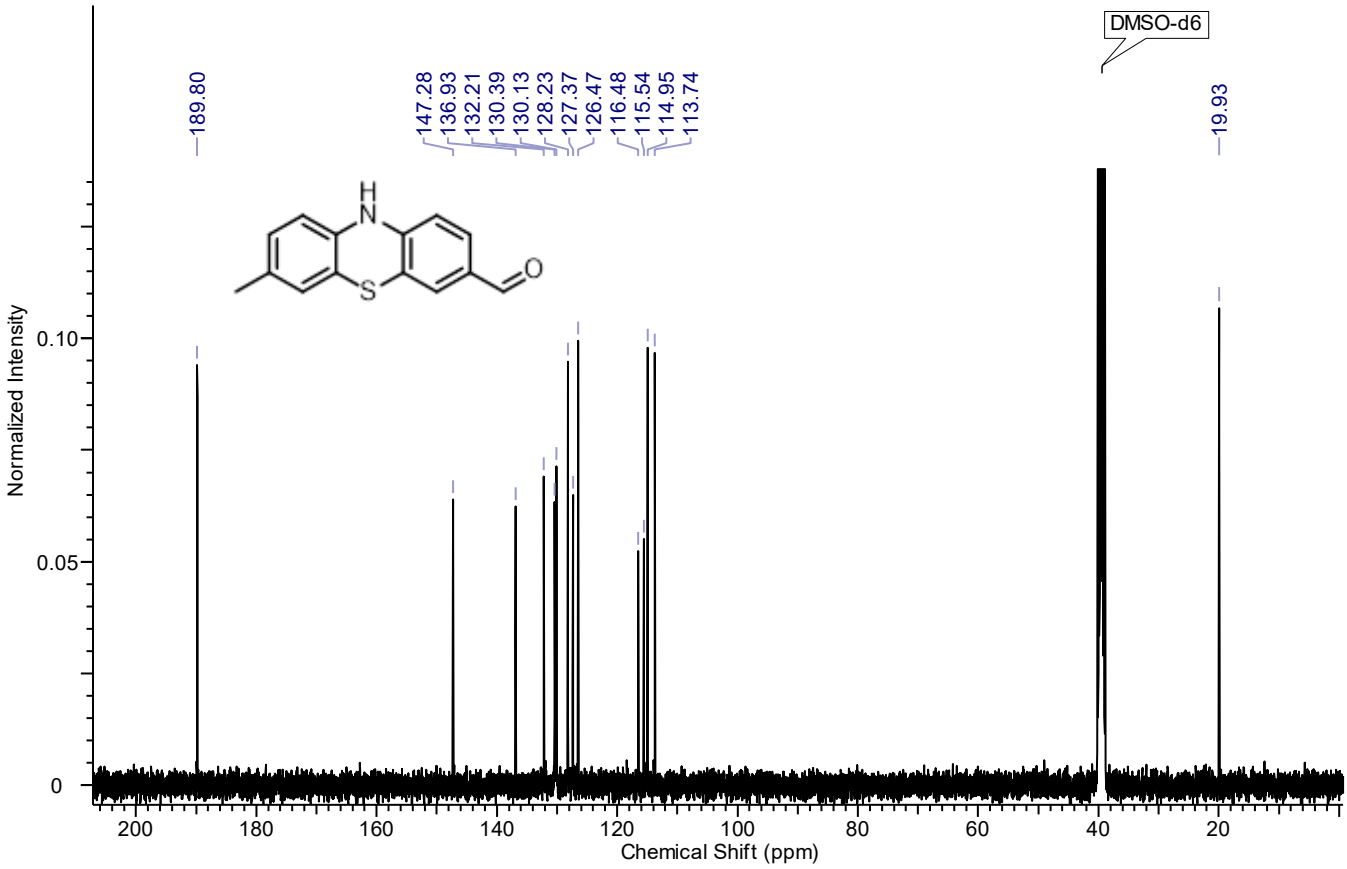


Figure S7.209. Full spectra ^{13}C NMR of 3-formyl-7-methylphenothiazine in DMSO-d6.

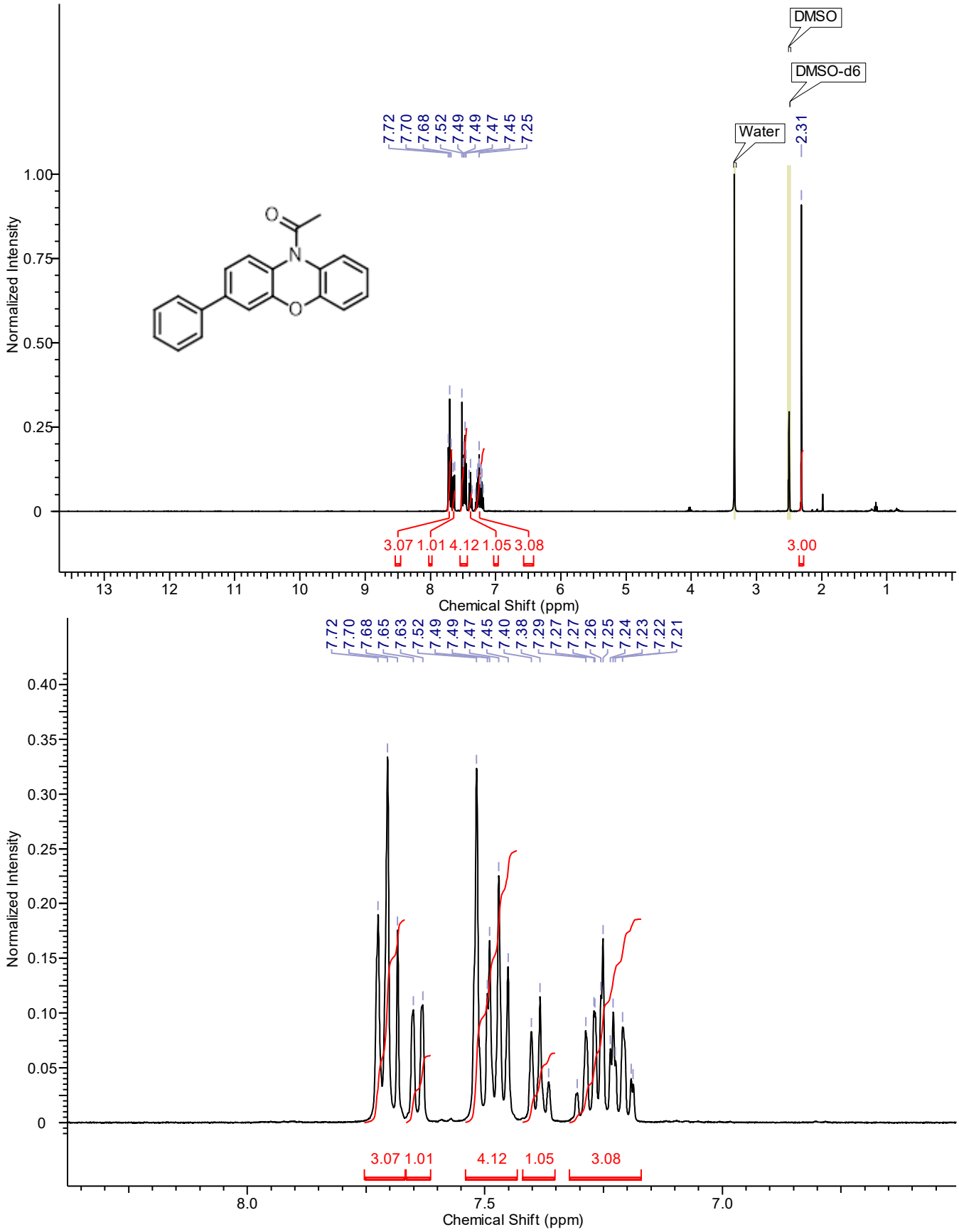


Figure S7.210. Full spectra (*top*) and aromatic region (*bottom*) ^{1}H NMR of 10-acetyl-3-phenylphenoxazine in DMSO-d6.

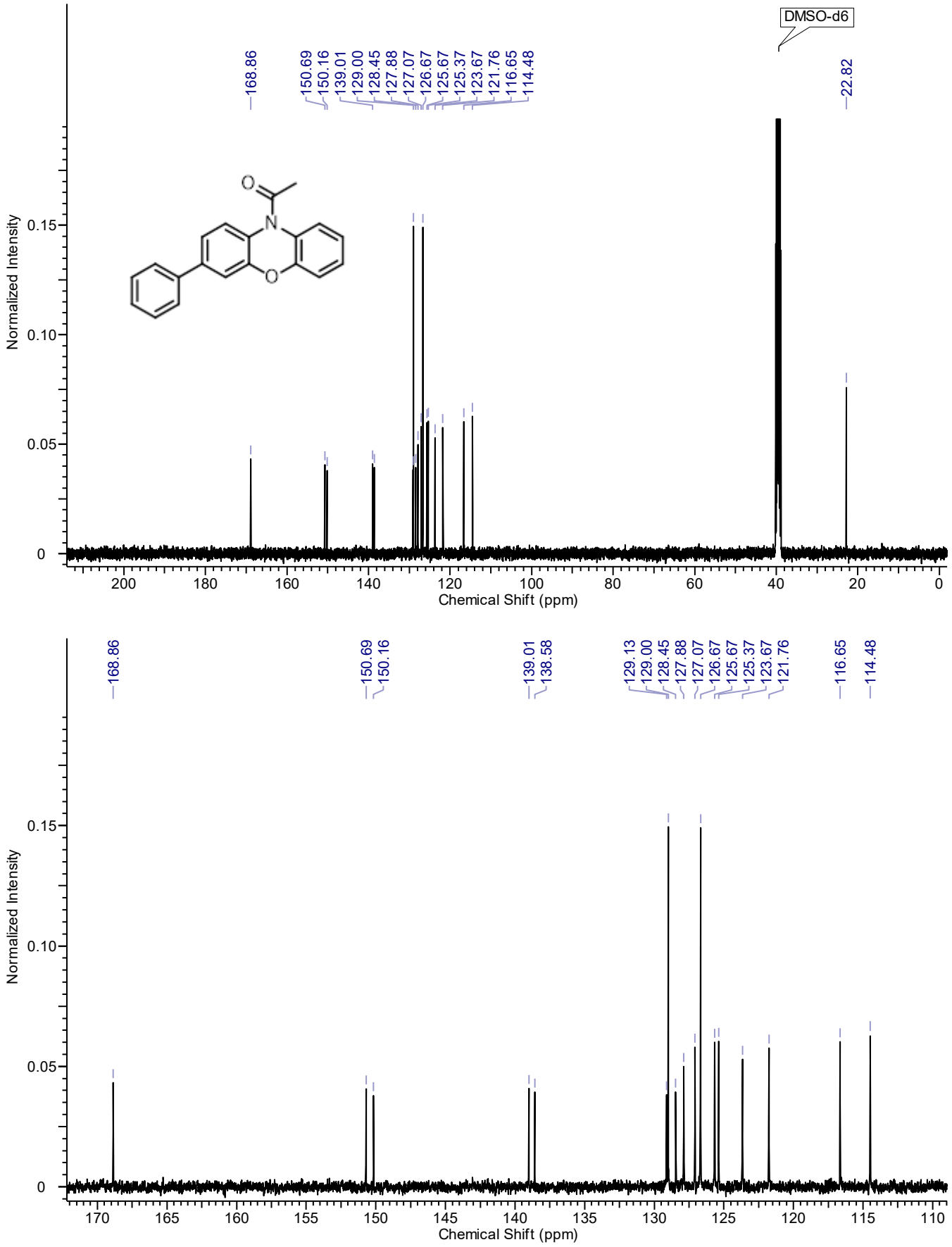


Figure S7.211. Full spectra (*top*) and aromatic region (*bottom*) ^{13}C NMR of 10-acetyl-3-phenylphenoxazine in DMSO-d6.

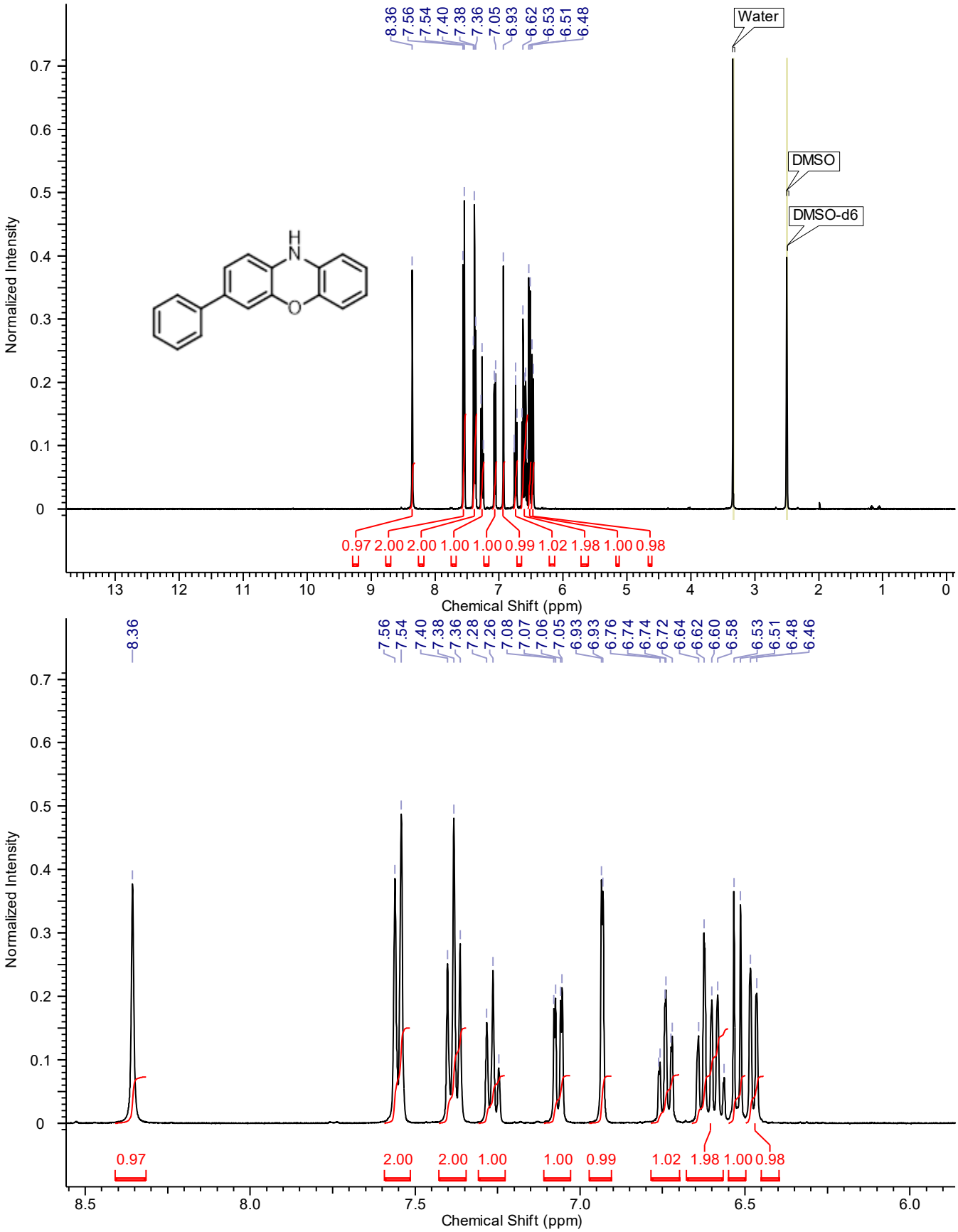


Figure S7.212. Full spectra (*top*) and aromatic region (*bottom*) ^{1}H NMR of 3-phenylphenoxazine in DMSO-d6.

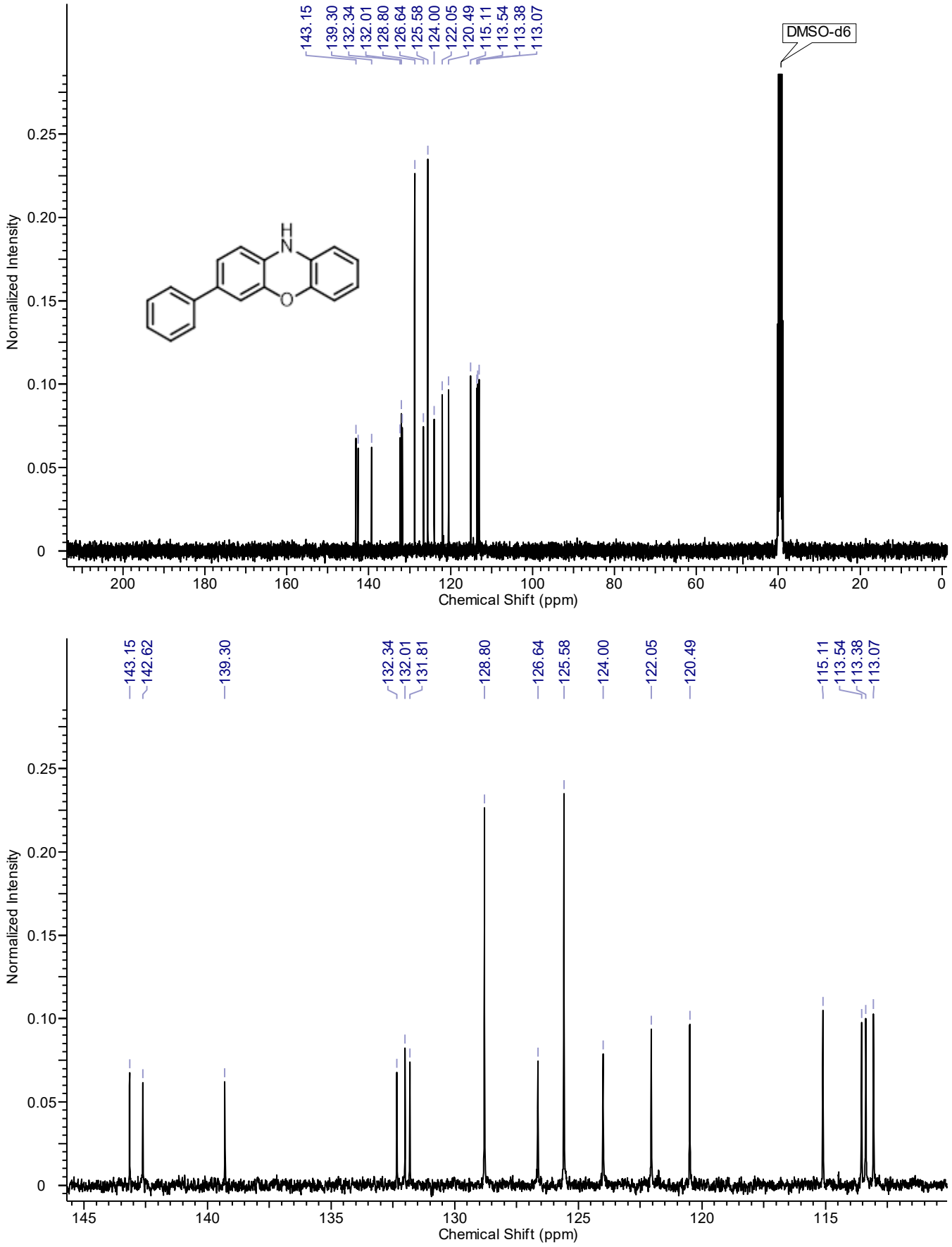


Figure S7.213. Full spectra (*top*) and aromatic region (*bottom*) ^{13}C NMR of 3-phenylphenoxazine in DMSO-d6.

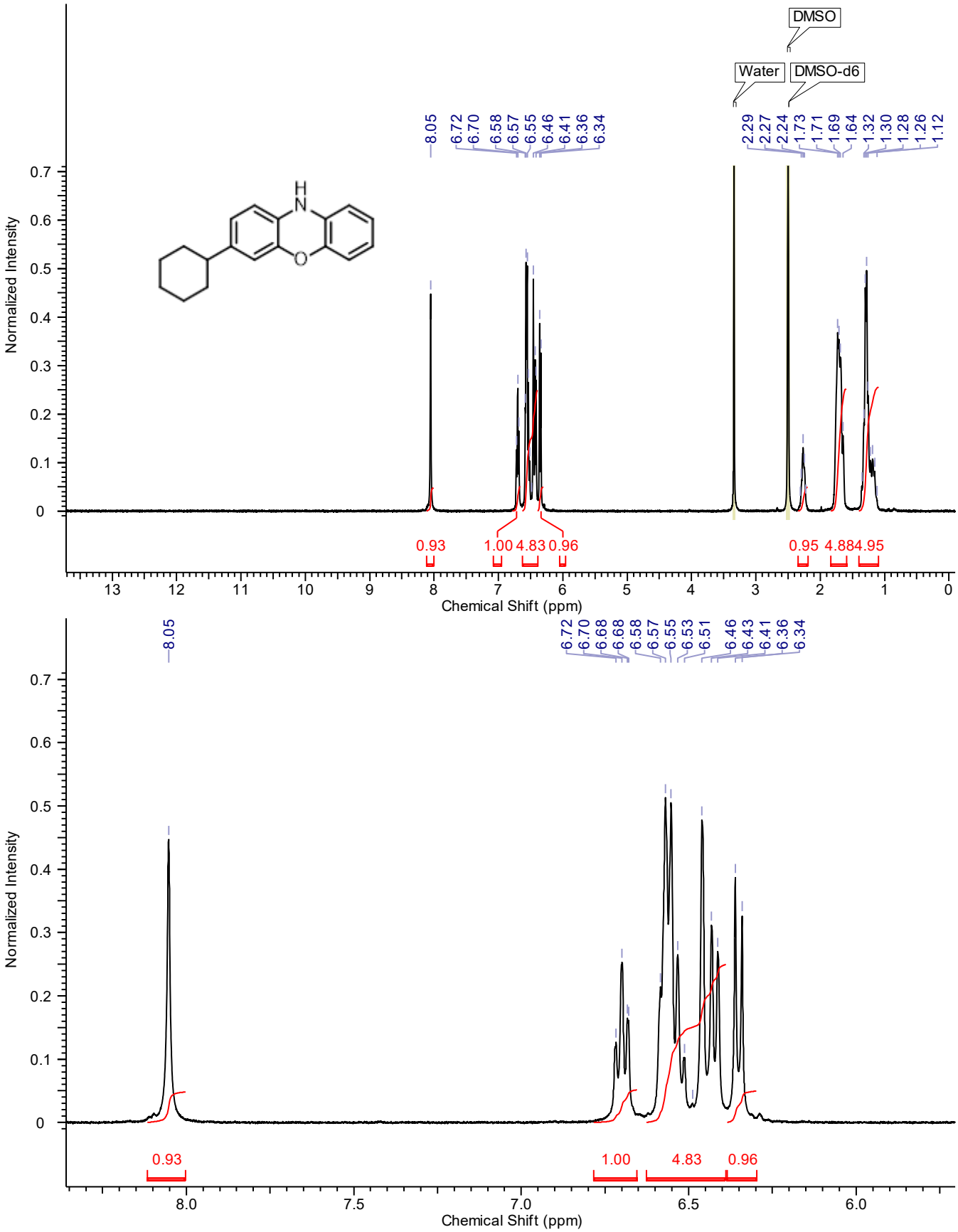


Figure S7.214. Full spectra (*top*) and aromatic region (*bottom*) ^{1}H NMR of 3-cyclohexylphenoxazine in DMSO-d6.

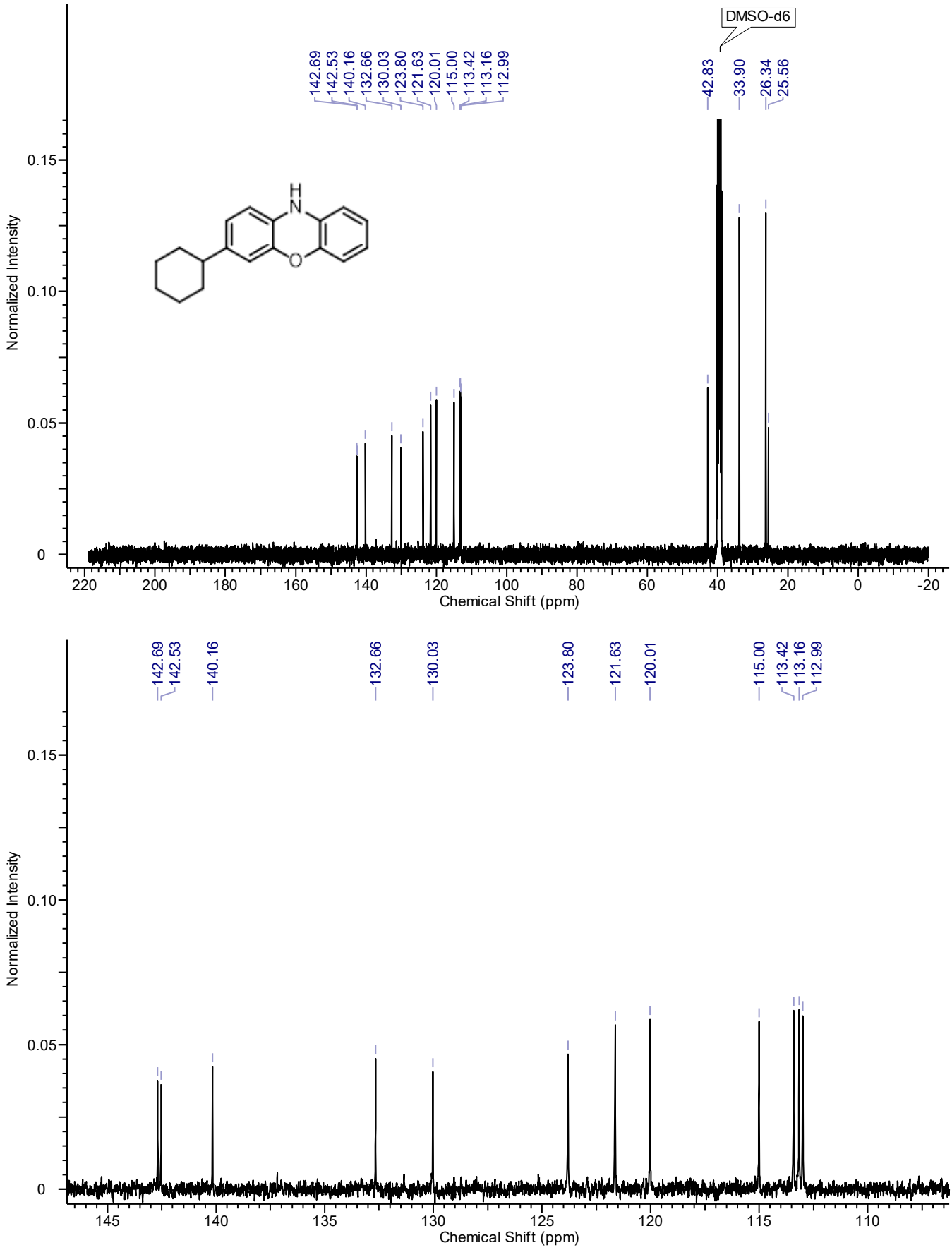


Figure S7.215. Full spectra (*top*) and aromatic region (*bottom*) ^{13}C NMR of 3-cyclohexylphenoxazine in DMSO-d6.

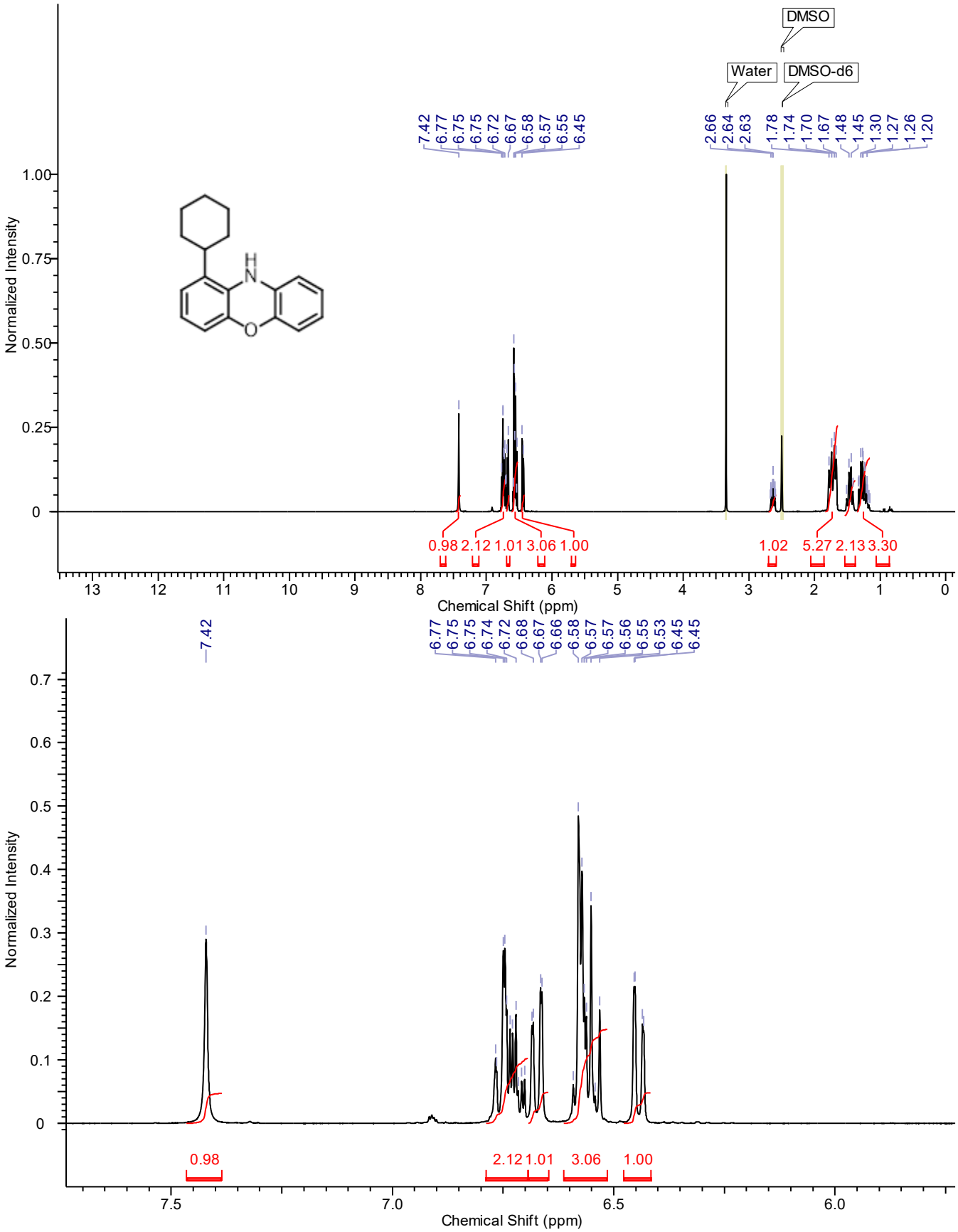


Figure S7.216. Full spectra (*top*) and aromatic region (*bottom*) ^{1}H NMR of 1-cyclohexylphenoxazine in DMSO-d6.

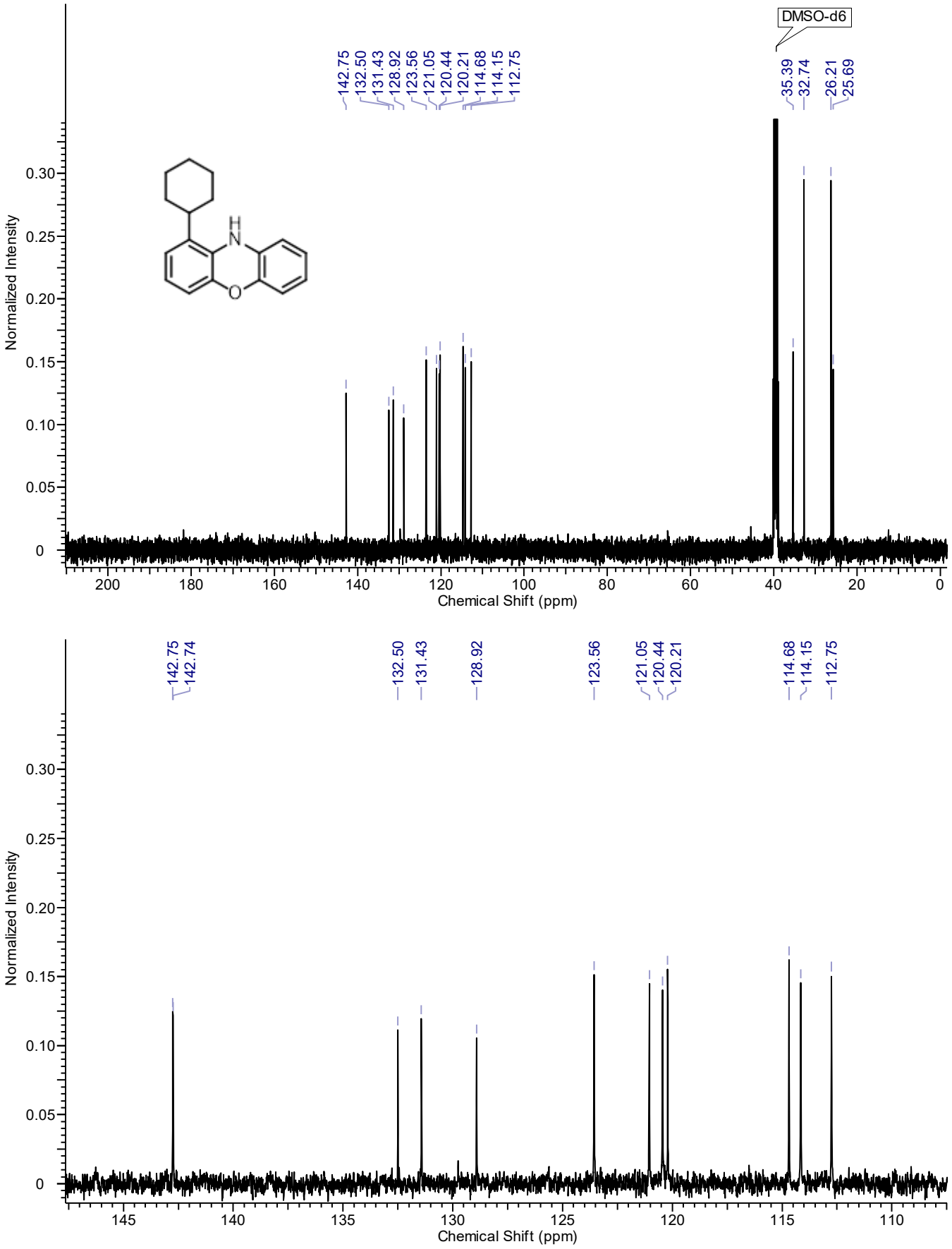
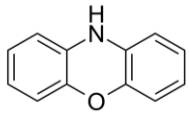


Figure S7.217. Full spectra (*top*) and aromatic region (*bottom*) ^{13}C NMR of 1-cyclohexylphenoxazine in DMSO-d6.

7.5 Chapter 5 Cartesian Coordinates for CBS-QB3

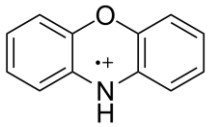
Phenoxazine



CBS-QB3 Enthalpy= -591.634775
CBS-QB3 Free Energy= -591.681608
Electronic energy= -591.823523
EE + Zero-point energy= -591.645815

```
0 1
 C                 -3.58034600   -0.74410900    0.16087500
 C                 -3.61537400    0.64504600    0.16485300
 C                 -2.43345800    1.37704400    0.04249000
 C                 -1.20821900    0.72626400   -0.09293200
 C                 -1.18554300   -0.67718200   -0.09383800
 C                 -2.35559200   -1.40502000    0.03678600
 N                  0.00000000    1.41109700   -0.24980300
 C                  1.20821900    0.72626400   -0.09293200
 C                  1.18554300   -0.67718200   -0.09383800
 O                  0.00000000   -1.37448800   -0.24984400
 C                  2.43345800    1.37704400    0.04249000
 C                  3.61537400    0.64504600    0.16485300
 C                  3.58034600   -0.74410900    0.16087500
 C                  2.35559200   -1.40502000    0.03678600
 H                 -4.49377300   -1.31839200    0.25534500
 H                 -4.55872200    1.16899200    0.26288100
 H                 -2.45861900    2.46207600    0.04341700
 H                 -2.29135500   -2.48631200    0.03290700
 H                  0.00000000    2.40096500   -0.06053500
 H                  2.45861900    2.46207600    0.04341800
 H                  4.55872100    1.16899200    0.26288100
 H                  4.49377300   -1.31839200    0.25534500
 H                  2.29135500   -2.48631200    0.03290700
```

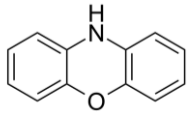
Phenoxazine radical cation



CBS-QB3 Enthalpy= -591.380411
CBS-QB3 Free Energy= -591.426865
Electronic Energy= -591.570463
EE + Zero-point energy= -591.391111

```
1 2
 C                  0.00000000    0.74501500    3.57042600
 C                  0.00000000   -0.66342100    3.60671400
 C                  0.00000000   -1.39773600    2.43843400
 C                  0.00000000   -0.72542100    1.20504300
 C                  0.00000000    0.69010000    1.18125500
 C                  0.00000000    1.42366800    2.36288700
 N                  0.00000000   -1.38605300    0.00000000
 C                  0.00000000   -0.72542100   -1.20504300
 C                  0.00000000    0.69010000   -1.18125500
 O                  0.00000000    1.36629400    0.00000000
 C                  0.00000000   -1.39773600   -2.43843400
 C                  0.00000000   -0.66342100   -3.60671400
 C                  0.00000000    0.74501500   -3.57042600
 C                  0.00000000    1.42366800   -2.36288700
 H                  0.00000000    1.30469100    4.49712600
 H                  0.00000000   -1.17517100    4.56059700
 H                  0.00000000   -2.48148400    2.45973700
 H                  0.00000000    2.50464800    2.30985600
 H                  0.00000000   -2.39981600    0.00000000
 H                  0.00000000   -2.48148400   -2.45973700
 H                  0.00000000   -1.17517100   -4.56059700
 H                  0.00000000    1.30469100   -4.49712600
 H                  0.00000000    2.50464800   -2.30985600
```

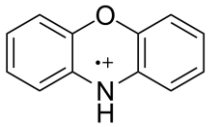
Phenoxazine (Radical Cation Geometry)



CBS-QB3 Enthalpy= -591.631531
CBS-QB3 Free Energy= -591.675354
Electronic energy= -591.819433
EE + Zero-point energy= -591.641798

```
0 1
 C                  0.00000000    0.74501500    3.57042600
 C                  0.00000000   -0.66342100    3.60671400
 C                  0.00000000   -1.39773600    2.43843400
 C                  0.00000000   -0.72542100    1.20504300
 C                  0.00000000    0.69010000    1.18125500
 C                  0.00000000    1.42366800    2.36288700
 N                  0.00000000   -1.38605300    0.00000000
 C                  0.00000000   -0.72542100   -1.20504300
 C                  0.00000000    0.69010000   -1.18125500
 O                  0.00000000    1.36629400    0.00000000
 C                  0.00000000   -1.39773600   -2.43843400
 C                  0.00000000   -0.66342100   -3.60671400
 C                  0.00000000    0.74501500   -3.57042600
 C                  0.00000000    1.42366800   -2.36288700
 H                  0.00000000    1.30469100    4.49712600
 H                  0.00000000   -1.17517100    4.56059700
 H                  0.00000000   -2.48148400    2.45973700
 H                  0.00000000    2.50464800    2.30985600
 H                  0.00000000   -2.39981600    0.00000000
 H                  0.00000000   -2.48148400   -2.45973700
 H                  0.00000000   -1.17517100   -4.56059700
 H                  0.00000000    1.30469100   -4.49712600
 H                  0.00000000    2.50464800   -2.30985600
```

Phenoxazine radical cation (Neutral PNX Geometry)

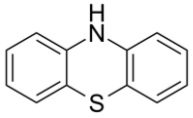


CBS-QB3 Enthalpy= -591.372766
CBS-QB3 Free Energy= -591.419268
Electronic Energy= -591.562425
EE + Zero-point energy= -591.383468

1 2

C	-3.58034600	-0.74410900	0.16087500
C	-3.61537400	0.64504600	0.16485300
C	-2.43345800	1.37704400	0.04249000
C	-1.20821900	0.72626400	-0.09293200
C	-1.18554300	-0.67718200	-0.09383800
C	-2.35559200	-1.40502000	0.03678600
N	0.00000000	1.41109700	-0.24980300
C	1.20821900	0.72626400	-0.09293200
C	1.18554300	-0.67718200	-0.09383800
O	0.00000000	-1.37448800	-0.24984400
C	2.43345800	1.37704400	0.04249000
C	3.61537400	0.64504600	0.16485300
C	3.58034600	-0.74410900	0.16087500
C	2.35559200	-1.40502000	0.03678600
H	-4.49377300	-1.31839200	0.25534500
H	-4.55872200	1.16899200	0.26288100
H	-2.45861900	2.46207600	0.04341700
H	-2.29135500	-2.48631200	0.03290700
H	0.00000000	2.40096500	-0.06053500
H	2.45861900	2.46207600	0.04341800
H	4.55872100	1.16899200	0.26288100
H	4.49377300	-1.31839200	0.25534500
H	2.29135500	-2.48631200	0.03290700

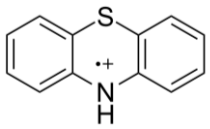
Phenothiazine



CBS-QB3 Enthalpy= -914.252455
CBS-QB3 Free Energy= -914.300126
Electronic Energy= -914.439523
EE + Zero-point Energy= -914.263843

```
0 1
 C                  3.68832700   -0.36566700   -0.51859800
 C                  3.56427500    1.01002500   -0.34743300
 C                  2.33889800    1.56357600    0.01333600
 C                  1.22858700    0.74605800    0.24374000
 C                  1.36229200   -0.64282900    0.08777600
 N                  0.00000000    1.29803700    0.63521500
 C                 -1.22858900    0.74605900    0.24373700
 C                 -1.36228700   -0.64282900    0.08776900
 S                 -0.00000200   -1.71092800    0.51117200
 C                 -2.33890100    1.56357500    0.01334000
 C                 -3.56428000    1.01002300   -0.34742800
 C                 -3.68832300   -0.36566900   -0.51859900
 C                 -2.57982800   -1.18589500   -0.31459500
 H                  4.63588300   -0.80074500   -0.81236800
 H                  4.41677900    1.65994900   -0.50695200
 H                  2.23863300    2.63884000    0.12531800
 H                  0.00000100    2.30563400    0.69581200
 H                 -2.23863700    2.63883900    0.12532800
 H                 -4.41678800    1.65994200   -0.50694200
 H                 -4.63587900   -0.80074800   -0.81237000
 H                 -2.66033000   -2.25815500   -0.45192700
 C                  2.57983300   -1.18589600   -0.31458800
 H                  2.66033700   -2.25815800   -0.45190500
```

Phenothiazine radical cation

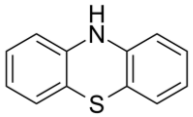


CBS-QB3 Enthalpy= -914.007226
CBS-QB3 Free Energy= -914.055519
Electronic Energy= -914.195271
EE + Zero-point energy= -914.018583

1 2

C	-3.77286800	-0.40794600	0.00000500
C	-2.64985600	-1.21220700	0.00000800
C	-1.37014800	-0.63521100	0.00000100
C	-1.23653600	0.77542600	-0.00000800
C	-2.39356700	1.57808400	-0.00000900
C	-3.64143700	0.99300900	-0.00000600
H	-2.74879500	-2.29131200	0.00001600
H	-2.29118800	2.65774800	-0.00001300
H	-4.52578600	1.61764900	-0.00001000
N	0.00000000	1.37779400	0.00000300
H	0.00000000	2.39089300	0.00000100
C	1.37014900	-0.63521300	-0.00000500
C	2.64985600	-1.21220600	-0.00001200
C	1.23653600	0.77542700	0.00000200
C	3.77286900	-0.40794500	-0.00000500
H	2.74879600	-2.29131100	-0.00002300
C	2.39356700	1.57808300	0.00001100
C	3.64143800	0.99300900	0.00000600
H	2.29118800	2.65774700	0.00001900
H	4.52578500	1.61765000	0.00001300
H	-4.75689500	-0.85910400	0.00001400
H	4.75689500	-0.85910500	-0.00000800
S	-0.00000100	-1.71120400	0.00000300

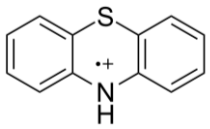
Phenothiazine (Radical Cation Geometry)



CBS-QB3 Enthalpy= -914.247221
CBS-QB3 Free Energy= -914.293231
Electronic Energy= -914.433152
EE + Zero-point Energy= -914.248165

```
0 1
 C                 -3.77286800   -0.40794600    0.00000500
 C                 -2.64985600   -1.21220700    0.00000800
 C                 -1.37014800   -0.63521100    0.00000100
 C                 -1.23653600    0.77542600   -0.00000800
 C                 -2.39356700    1.57808400   -0.00000900
 C                 -3.64143700    0.99300900   -0.00000600
 H                 -2.74879500   -2.29131200    0.00001600
 H                 -2.29118800    2.65774800   -0.00001300
 H                 -4.52578600    1.61764900   -0.00001000
 N                  0.00000000    1.37779400    0.00000300
 H                  0.00000000    2.39089300    0.00000100
 C                  1.37014900   -0.63521300   -0.00000500
 C                  2.64985600   -1.21220600   -0.00001200
 C                  1.23653600    0.77542700    0.00000200
 C                  3.77286900   -0.40794500   -0.00000500
 H                  2.74879600   -2.29131100   -0.00002300
 C                  2.39356700    1.57808300    0.00001100
 C                  3.64143800    0.99300900    0.00000600
 H                  2.29118800    2.65774700    0.00001900
 H                  4.52578500    1.61765000    0.00001300
 H                 -4.75689500   -0.85910400    0.00001400
 H                  4.75689500   -0.85910500   -0.00000800
 S                 -0.00000100   -1.71120400    0.00000300
```

Phenothiazine radical cation (Neutral PTZ Geometry)

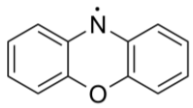


CBS-QB3 Enthalpy= -913.992395
CBS-QB3 Free Energy= -914.040504
Electronic Energy= -914.180087
EE + Zero-point energy= -914.003700

1 2

C	3.68832700	-0.36566700	-0.51859800
C	3.56427500	1.01002500	-0.34743300
C	2.33889800	1.56357600	0.01333600
C	1.22858700	0.74605800	0.24374000
C	1.36229200	-0.64282900	0.08777600
N	0.00000000	1.29803700	0.63521500
C	-1.22858900	0.74605900	0.24373700
C	-1.36228700	-0.64282900	0.08776900
S	-0.00000200	-1.71092800	0.51117200
C	-2.33890100	1.56357500	0.01334000
C	-3.56428000	1.01002300	-0.34742800
C	-3.68832300	-0.36566900	-0.51859900
C	-2.57982800	-1.18589500	-0.31459500
H	4.63588300	-0.80074500	-0.81236800
H	4.41677900	1.65994900	-0.50695200
H	2.23863300	2.63884000	0.12531800
H	0.00000100	2.30563400	0.69581200
H	-2.23863700	2.63883900	0.12532800
H	-4.41678800	1.65994200	-0.50694200
H	-4.63587900	-0.80074800	-0.81237000
H	-2.66033000	-2.25815500	-0.45192700
C	2.57983300	-1.18589600	-0.31458800
H	2.66033700	-2.25815800	-0.45190500

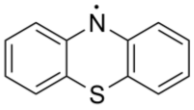
Aminyl radical derived from Phenoxazine



CBS-QB3 Enthalpy= -591.017452
CBS-QB3 Free Energy= -591.063557

```
0 2
 C                  3.57102000   -0.70680000   -0.00000200
 C                  3.58779700    0.69635000    0.00000000
 C                  2.40329400    1.40795100    0.00000200
 C                  1.15420300    0.74334100    0.00000100
 C                  1.17432000   -0.67604900    0.00000000
 C                  2.36198700   -1.39477900   -0.00000200
 N                  0.00000100    1.46544900    0.00000100
 C                 -1.15420400    0.74334000    0.00000000
 C                 -1.17432100   -0.67604900    0.00000100
 O                  0.00000000   -1.38118000    0.00000100
 C                 -2.40329300    1.40795100   -0.00000200
 C                 -3.58779700    0.69635000   -0.00000200
 C                 -3.57102000   -0.70679900    0.00000100
 C                 -2.36198700   -1.39477900    0.00000200
 H                  4.50180300   -1.26128800   -0.00000400
 H                  4.53479600    1.22311500    0.00000100
 H                  2.38489300    2.49090100    0.00000400
 H                  2.32037000   -2.47716700   -0.00000400
 H                 -2.38489200    2.49090100   -0.00000300
 H                 -4.53479600    1.22311600   -0.00000400
 H                 -4.50180300   -1.26128700    0.00000100
 H                 -2.32037100   -2.47716700    0.00000400
```

Phenothiazine radical

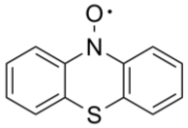


CBS-QB3 Enthalpy= -913.629550
CBS-QB3 Free Energy= -913.677602

0 2

C	3.77014500	0.36440800	0.00002900
C	3.62001500	-1.03130000	0.00001700
C	1.18545600	-0.79066300	-0.00001400
C	1.36699300	0.62382400	-0.00000100
C	2.64899200	1.18139600	0.00001900
N	0.00000000	-1.44978700	-0.00003500
C	-1.18546200	-0.79066300	-0.00001400
C	-1.36699900	0.62382400	-0.00000400
S	0.00000000	1.72450800	-0.00002800
C	-2.36024900	-1.59059300	0.00000000
C	-3.62000900	-1.03129900	0.00002100
C	-3.77014800	0.36440300	0.00002700
C	-2.64899300	1.18139500	0.00001300
H	4.75846400	0.80850000	0.00004000
H	4.49598900	-1.66955300	0.00003800
H	2.76302600	2.26019400	0.00003000
H	-2.21166200	-2.66335600	-0.00001000
H	-4.49597600	-1.66956300	0.00004100
H	-4.75846600	0.80849600	0.00003600
H	-2.76303200	2.26019200	0.00002000
C	2.36025600	-1.59059500	-0.00000800
H	2.21166500	-2.66335900	-0.00001500

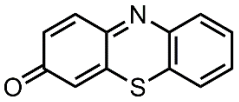
Phenothiazine-*N*-oxyl



CBS-QB3 Enthalpy= -988.731654
CBS-QB3 Free Energy= -988.782591

```
0 2
 C                 -3.77323400   -0.58593900   -0.18991800
 C                 -2.40064000    1.39251200   -0.06866800
 C                 -1.24929400    0.59991400    0.03812400
 C                 -1.37035700   -0.79938400    0.03139500
 C                 -2.63696800   -1.37804900   -0.08893700
 N                  0.00000000    1.26379400    0.15651900
 C                  1.24929400    0.59991400    0.03812400
 C                  1.37035600   -0.79938400    0.03139400
 S                  0.00000000   -1.89469700    0.22586900
 C                  2.40064100    1.39251200   -0.06866600
 C                  3.65073900    0.80433400   -0.17889100
 C                  3.77323400   -0.58593900   -0.18991900
 C                  2.63696700   -1.37804900   -0.08894000
 O                  0.00000000    2.53720900    0.27066100
 H                 -4.74699300   -1.05228100   -0.27969700
 H                 -2.27212400    2.46488600   -0.05633700
 H                 -2.72330400   -2.45880400   -0.10065300
 H                  2.27212400    2.46488600   -0.05633200
 H                  4.53060600    1.43132600   -0.25933900
 H                  4.74699200   -1.05228100   -0.27969900
 H                  2.72330400   -2.45880400   -0.10065800
 C                 -3.65073900    0.80433500   -0.17889300
 H                 -4.53060500    1.43132600   -0.25934000
```

Phenothiazone

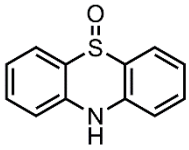


CBS-QB3 Enthalpy= -988.184974
CBS-QB3 Free Energy= -988.234788

0 1

C	-3.97028300	0.93793800	0.00004100
C	-4.07254400	-0.45860200	0.00002500
C	-2.93104800	-1.24699800	0.00000000
C	-1.66599800	-0.64932800	-0.00001100
C	-1.54413800	0.75817400	0.00000000
C	-2.72214200	1.53219100	0.00002800
S	-0.26249200	-1.69856400	-0.00004400
C	1.08356700	-0.56908300	-0.00000500
C	0.81436000	0.87966200	-0.00002600
N	-0.35159000	1.45237400	-0.00002200
C	2.35343800	-1.04536200	0.00002900
C	3.51960100	-0.15970900	0.00002600
C	3.23351400	1.28993800	-0.00002000
C	1.97474900	1.76102700	-0.00004400
O	4.66774500	-0.59066000	0.00006500
H	-4.86469400	1.54895600	0.00006200
H	-5.04703800	-0.93276900	0.00003400
H	-3.01517800	-2.32810200	-0.00000900
H	-2.60153200	2.60843700	0.00003600
H	2.56525700	-2.10877100	0.00005300
H	4.09478400	1.94793500	-0.00003000
H	1.74897800	2.82091100	-0.00007100

S-oxide derived from phenothiazine

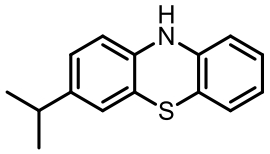


CBS-QB3 Enthalpy= -989.366908
CBS-QB3 Free Energy= -989.416887

0 1

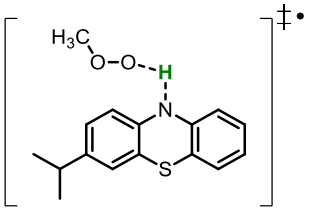
C	1.19868700	-0.42383700	3.51971500
C	-0.17835900	-0.62911600	3.60818700
C	-0.98278200	-0.35102800	2.50683300
C	-0.40901800	0.12578200	1.33437700
C	0.97739000	0.29239100	1.21846100
C	1.77675000	0.01914300	2.33497700
S	-1.49976900	0.69037300	0.00000000
C	-0.40901800	0.12578200	-1.33437700
C	0.97739000	0.29239100	-1.21846100
N	1.54460000	0.69092900	0.00000000
C	-0.98278200	-0.35102800	-2.50683300
C	-0.17835900	-0.62911600	-3.60818700
C	1.19868700	-0.42383700	-3.51971500
C	1.77675000	0.01914300	-2.33497700
O	-2.74760800	-0.13100400	0.00000000
H	1.83352700	-0.62877300	4.37410200
H	-0.62084500	-0.99421800	4.52691000
H	-2.05667300	-0.49549700	2.53685300
H	2.85393800	0.13308300	2.26274300
H	-2.05667300	-0.49549700	-2.53685300
H	-0.62084500	-0.99421800	-4.52691000
H	1.83352700	-0.62877300	-4.37410200
H	2.85393800	0.13308300	-2.26274300
H	2.55304300	0.73635500	0.00000000

7.6 Chapter 6 Cartesian Coordinates for DFT (M062X/cc-pVTZ)



Electronic Energy = -1033.543100 EE + Zero-point Energy = -1033.278608
Enthalpy = -1033.263072 Free Energy = -1033.320657

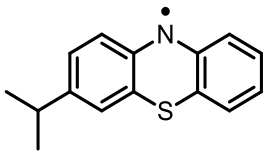
```
0 1
 C                  2.64719400   -0.04585800    0.07203700
 C                  1.57932100   -0.92238800   -0.08148900
 C                  0.29892500   -0.46488300   -0.35984400
 C                  0.04847500    0.90228800   -0.44858300
 C                  1.10722700    1.78717100   -0.27205900
 C                  2.38757800    1.31799600   -0.03295300
 C                 -2.36835900    0.71322600   -0.21235600
 C                 -2.37575700   -0.67821200   -0.09541000
 C                 -3.48848800   -1.32653400    0.41855400
 H                 -3.46746500   -2.40357500    0.51974200
 C                 -4.61956300   -0.60770800    0.77919700
 C                 -4.62077900    0.77254900    0.64893700
 C                 -3.49706300    1.42968000    0.17274400
 H                  1.74434400   -1.99003700    0.00200300
 H                  0.92131600    2.85273200   -0.33270800
 H                  3.19292800    2.03205500    0.08537400
 H                 -5.48861200   -1.12406600    1.16074200
 H                 -5.49341600    1.34562400    0.92988100
 H                 -3.49081200    2.50956500    0.08856300
 N                 -1.24376400    1.36920200   -0.72466000
 H                 -1.32197300    2.37413900   -0.71797700
 S                 -1.00112200   -1.61765400   -0.69675400
 C                  4.04240400   -0.56089400    0.34797600
 C                  5.00899300   -0.18234400   -0.77551600
 C                  4.56394000   -0.06595000    1.69806400
 H                  3.98185600   -1.65080300    0.38840600
 H                  5.11211400    0.90192400   -0.84443200
 H                  4.65503500   -0.54775700   -1.73897100
 H                  4.65603700    1.02147900    1.69951100
 H                  3.89047700   -0.34706800    2.50703800
 H                  5.99865100   -0.60058100   -0.58780100
 H                  5.54953300   -0.48439900    1.90551900
```



Electronic Energy = -1223.741142 EE + Zero-point Energy = -1223.436668
Enthalpy = -1223.416446 Free Energy = -1223.486886
Number of Imaginary Freq = 1 (-2225.68)

0 2

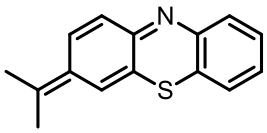
C	2.86442500	-0.42949900	-0.07123400
C	1.83822100	-1.29539400	0.27314300
C	0.50719500	-0.99385300	0.00350700
C	0.17548700	0.21007100	-0.63602100
C	1.21912200	1.08487800	-0.98378000
C	2.52909300	0.77089600	-0.70675000
C	-2.23409400	-0.09453100	-0.52166800
C	-2.19392300	-1.34274600	0.11142700
C	-3.37810600	-1.96955200	0.49117900
H	-3.32882800	-2.93519600	0.97762500
C	-4.59955200	-1.36646300	0.26099900
C	-4.64705400	-0.11698700	-0.35296500
C	-3.48110900	0.50721000	-0.73932100
H	2.07249300	-2.23170400	0.76612500
H	0.95820000	2.01707100	-1.46511000
H	3.30703700	1.47020000	-0.98404300
H	-5.51012900	-1.86353000	0.56359300
H	-5.59724500	0.36767600	-0.52727500
H	-3.49921100	1.48305100	-1.20577200
N	-1.10969500	0.58261900	-0.96400500
S	-0.69421600	-2.19656100	0.42952900
C	4.30360700	-0.77351200	0.23448000
C	5.13229200	-0.88119200	-1.04709300
C	4.92355200	0.24227800	1.19609200
H	4.30747100	-1.75005300	0.72374300
H	5.17090000	0.07937000	-1.56300900
H	4.70647200	-1.61391700	-1.73172100
H	4.95445100	1.23381700	0.74191700
H	4.34902000	0.31306700	2.11908900
H	6.15577500	-1.17694200	-0.81492500
H	5.94594300	-0.04346200	1.44502100
H	-1.23506200	1.69589100	-0.94511200
O	-1.33835000	2.97715700	-0.45832300
O	-0.34973700	3.09904800	0.47724400
C	-0.86405800	2.71024900	1.73360200
H	-1.14418800	1.65346800	1.71416400
H	-0.06592300	2.87308800	2.45513100
H	-1.73774500	3.31399700	1.98119300



Electronic Energy = -1032.909194 EE + Zero-point Energy = -1032.657983
Enthalpy = -1032.642665 Free Energy = -1032.700438

0 2

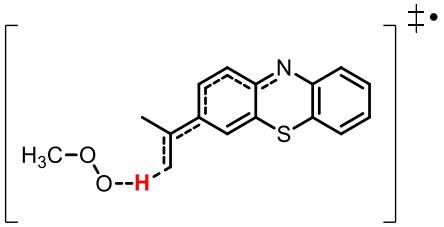
C	-2.68180700	-0.04611500	0.00000800
C	-1.60878600	-0.91690100	-0.00004500
C	-0.29376000	-0.45213100	-0.00002300
C	-0.01286000	0.93472500	0.00005300
C	-1.13011900	1.80671300	0.00010600
C	-2.41502700	1.33579600	0.00008400
C	2.33887700	0.76083200	0.00003200
C	2.40768400	-0.65387900	-0.00004800
C	3.63802900	-1.30950800	-0.00009200
H	3.66090000	-2.39190600	-0.00015400
C	4.81390200	-0.58863500	-0.00005800
C	4.77379500	0.81061500	0.00002200
C	3.56795500	1.46380500	0.00006600
H	-1.78833700	-1.98607900	-0.00010400
H	-0.91397100	2.86606000	0.00016500
H	-3.23865100	2.03860200	0.00012600
H	5.76198000	-1.10757900	-0.00009300
H	5.69497200	1.37658200	0.00004900
H	3.50488200	2.54297600	0.00012700
N	1.21055400	1.50805000	0.00008000
S	0.97462700	-1.64353400	-0.00009500
C	-4.10134200	-0.56076900	-0.00001500
C	-4.85113700	-0.11914300	1.25871300
C	-4.85115700	-0.11898900	-1.25867600
H	-4.05189300	-1.65183300	-0.00008200
H	-4.94011400	0.96772100	1.29343900
H	-4.33315900	-0.44356600	2.16058000
H	-4.94013700	0.96788000	-1.29326700
H	-4.33319200	-0.44329900	-2.16059100
H	-5.85832800	-0.53700600	1.26774400
H	-5.85834600	-0.53685300	-1.26774300



Electronic Energy = -1032.294126 EE + Zero-point Energy = -1032.054327
Enthalpy = -1032.038700 Free Energy = -1032.098068

0 1

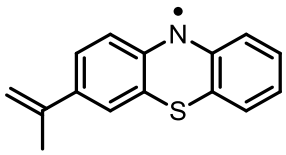
C	2.77029400	0.16955300	0.00779600
C	1.66202200	-0.77073600	0.00285700
C	0.37113200	-0.38777000	-0.01786500
C	-0.00374400	1.02947300	-0.01683700
C	1.10912600	1.96705700	-0.02257100
C	2.38854800	1.57425200	-0.01608800
C	-2.33631300	0.73123300	0.00531400
C	-2.35265900	-0.66857500	-0.01789700
C	-3.55958900	-1.35886900	-0.00522800
H	-3.55297800	-2.44130700	-0.02346000
C	-4.75906300	-0.66859500	0.03141200
C	-4.76012600	0.72152200	0.05648900
C	-3.56015500	1.40558500	0.04311600
H	1.88091900	-1.82916700	-0.01244200
H	0.83465700	3.01268200	-0.02660500
H	3.15984900	2.32925400	-0.00801300
H	-5.69081300	-1.21686400	0.04113100
H	-5.69371300	1.26542900	0.08605900
H	-3.52366300	2.48606900	0.06083300
N	-1.19250100	1.52312000	-0.00804300
S	-0.87980400	-1.61940900	-0.07302900
C	4.06522100	-0.23782800	0.03058500
C	4.47200200	-1.68161000	0.10960100
C	5.24119300	0.68965100	-0.03961600
H	4.67965400	-2.07344200	-0.89060000
H	3.72917700	-2.32112100	0.57612100
H	5.95337200	0.31315200	-0.77790200
H	4.99461800	1.71147000	-0.30475200
H	5.39756200	-1.77268200	0.67951100
H	5.76840000	0.69917200	0.91848500



Electronic Energy = -1222.482479 EE + Zero-point Energy = -1222.203084
Enthalpy = -1222.183293 Free Energy = -1222.253119
Number of Imaginary Freq = 1 (-1890.35)

0 2

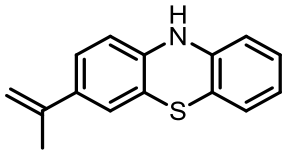
C	-1.89061600	1.43404800	0.14612100
C	-1.11299400	0.23993500	0.23547200
C	0.24395700	0.25290700	0.12649400
C	0.97398900	1.49351200	-0.06564900
C	0.17052900	2.68829700	-0.16963700
C	-1.17404000	2.66003700	-0.08260800
C	3.13684000	0.57180600	-0.07158100
C	2.76570500	-0.77474000	0.07827000
C	3.73634000	-1.77155300	0.14061700
H	3.43031000	-2.80364600	0.25448100
C	5.07683400	-1.44586400	0.05900900
C	5.46383100	-0.11462200	-0.08679700
C	4.50520700	0.87267400	-0.15110400
H	-1.61645500	-0.71220600	0.34099400
H	0.71474900	3.61008700	-0.31927400
H	-1.72651600	3.58597100	-0.15931700
H	5.82107300	-2.22834700	0.10941100
H	6.51178900	0.14242600	-0.15044400
H	4.76958900	1.91462300	-0.26635000
N	2.26612000	1.63798600	-0.15421200
S	1.09442600	-1.27244300	0.18142600
C	-3.27727200	1.41138700	0.26339000
C	-3.97796200	0.20495100	0.63089900
C	-4.09676300	2.63412600	-0.04216400
H	-5.02883100	0.34925300	0.86255800
H	-3.47900600	-0.41946000	1.37166500
H	-4.04697000	3.35010500	0.78280600
H	-3.75682300	3.14494400	-0.94172000
H	-5.14213500	2.36582700	-0.17705500
H	-3.92954100	-0.56215000	-0.31074100
O	-3.60412400	-1.64622100	-1.13510500
O	-2.99559800	-2.52887500	-0.30089600
C	-3.96313000	-3.43342600	0.20119200
H	-3.42095200	-4.13984200	0.82612900
H	-4.70564500	-2.89512700	0.79361000
H	-4.45324300	-3.94934700	-0.62362300



Electronic Energy = -1031.685918 EE + Zero-point Energy = -1031.458029
Enthalpy = -1031.443332 Free Energy = -1031.499747

0 2

C	2.76532200	0.10063100	-0.03207100
C	1.71140900	-0.80326900	0.02984900
C	0.38943800	-0.38032300	0.00851100
C	0.06250700	0.99885900	-0.07040800
C	1.15189700	1.90213800	-0.11400400
C	2.45161400	1.47286100	-0.08704600
C	-2.28174000	0.75106300	-0.04285700
C	-2.30677300	-0.66145500	0.05025200
C	-3.51686100	-1.35171000	0.10456900
H	-3.50754000	-2.43186900	0.17641700
C	-4.71359400	-0.66695700	0.06660400
C	-4.71611000	0.72959000	-0.02725600
C	-3.53021600	1.41652700	-0.08004200
H	1.92011600	-1.86133400	0.12357300
H	0.90494300	2.95318900	-0.16822100
H	3.24778300	2.20281100	-0.12250600
H	-5.64559900	-1.21260100	0.10946900
H	-5.65395100	1.26651700	-0.05783100
H	-3.49919600	2.49469700	-0.15168600
N	-1.17529700	1.53029500	-0.09730700
S	-0.84469500	-1.60589800	0.09915900
C	4.17161000	-0.35789700	-0.02871700
C	4.51949200	-1.55974000	-0.48666600
C	5.20848900	0.60020500	0.49233600
H	5.55051900	-1.88541000	-0.46154500
H	3.80025800	-2.24120700	-0.91933900
H	5.33619100	1.44597800	-0.18556000
H	4.91841000	1.00398400	1.46311300
H	6.17135800	0.10441700	0.59039500



Electronic Energy = -1032.320210 EE + Zero-point Energy = -1032.078931
Enthalpy = -1032.064051 Free Energy = -1032.120005

```
0 1
 C                  2.74350500    0.20469600    0.09001600
 C                  1.71777900   -0.71022500   -0.14879700
 C                  0.41686700   -0.29559800   -0.38623600
 C                  0.08994500    1.05787400   -0.33207600
 C                  1.09831900    1.97512400   -0.04994500
 C                  2.40103800    1.55661100    0.14338400
 C                 -2.31346800    0.70925500   -0.13433100
 C                 -2.24313200   -0.68459900   -0.16796800
 C                 -3.32064600   -1.44460100    0.26110600
 H                 -3.24008900   -2.52344500    0.24631200
 C                 -4.49180800   -0.83195500    0.68427500
 C                 -4.56970000    0.55205800    0.70290100
 C                 -3.48198800    1.31737100    0.31239200
 H                  1.92890100   -1.77057800   -0.17896200
 H                  0.85088500    3.02719200    0.02278300
 H                  3.15867300    2.29080800    0.37873700
 H                 -5.33249700   -1.43344100    0.99871500
 H                 -5.47439500    1.04273600    1.03382900
 H                 -3.53532500    2.39872200    0.34484100
 N                 -1.22384200    1.47922900   -0.55717000
 H                 -1.35885000    2.47210400   -0.44777800
 S                 -0.81629400   -1.47704500   -0.85296800
 C                  4.13827600   -0.25358500    0.29475300
 C                  4.33623800   -1.66217700    0.78430200
 H                  3.72280500   -1.86238300    1.66386900
 H                  4.05020400   -2.38637200    0.01915200
 H                  5.37994400   -1.83809300    1.03405300
 C                  5.18188400    0.53355400    0.04235300
 H                  6.19184700    0.18863800    0.21784600
 H                  5.06685600    1.52941100   -0.36249700
```

H-Atom

Electronic Energy = -0.498135 EE + Zero-point Energy = -0.498135
Enthalpy = -0.495774 Free Energy = -0.508789

```
0 2
 H                  0.00000000    0.00000000    0.00000000
```

Me-OO•

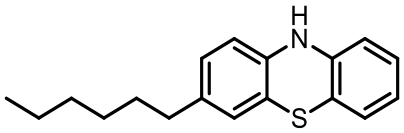
Electronic Energy = -190.205939 EE + Zero-point Energy = -190.162279
Enthalpy = -190.157506 Free Energy = -190.187980

```
0 2
 O                  1.16818900   -0.27664000    0.00000000
 O                  0.15899300    0.53885100    0.00000000
 C                 -1.08154000   -0.17952500    0.00000000
 H                 -1.13174800   -0.79678000    0.89379000
 H                 -1.86472500    0.57302600   -0.00000100
 H                 -1.13174700   -0.79678200   -0.89378900
```

Me-OO-H

Electronic Energy = -190.847177 EE + Zero-point Energy = -190.791830
Enthalpy = -190.787192 Free Energy = -190.816705

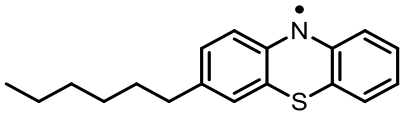
```
0 1
 O                  1.11508500   -0.33449600    0.00000000
 H                  1.85986800    0.27629500   -0.00000200
 O                  0.02912300    0.59861500    0.00000000
 C                 -1.12286400   -0.20377500    0.00000000
 H                 -1.15911400   -0.83016400    0.89322900
 H                 -1.95812100    0.49373100    0.00000000
 H                 -1.15911400   -0.83016400   -0.89322900
```



Electronic Energy = -1151.462403 EE + Zero-point Energy = -1151.111656
Enthalpy = -1151.092026 Free Energy = -1151.160616

0 1

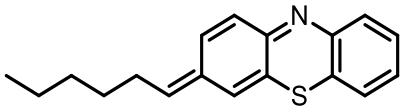
C	1.08310500	-0.23580100	-0.27824300
C	-0.04089300	-1.06188700	-0.29366900
C	-1.31474200	-0.55236500	-0.46773700
C	-1.50750300	0.82581700	-0.58891300
C	-0.39790100	1.65650000	-0.54957200
C	0.88095500	1.13076800	-0.41346300
C	-3.89611000	0.76787500	-0.11407300
C	-3.95827600	-0.61613300	0.06096000
C	-5.04499600	-1.18700700	0.70596600
H	-5.06528500	-2.25924400	0.84940000
C	-6.09959300	-0.39823500	1.14367900
C	-6.04779100	0.97461800	0.95691300
C	-4.94635900	1.55510400	0.34777900
H	0.08207300	-2.13302500	-0.18095200
H	-0.53536700	2.72773900	-0.63421800
H	1.72181600	1.80980000	-0.40077300
H	-6.95049900	-0.85478600	1.62842900
H	-6.86017500	1.60180100	1.29683200
H	-4.89690600	2.62940800	0.21854700
N	-2.79803200	1.34530800	-0.75982100
H	-2.82849500	2.35238400	-0.79110700
S	-2.69635700	-1.64633200	-0.63082900
C	2.44939400	-0.86016800	-0.11428500
H	2.44064700	-1.48074500	0.78667100
H	2.62003500	-1.55041900	-0.94603300
C	3.61896100	0.10993500	-0.03258500
H	3.66442000	0.71266200	-0.94415300
H	3.46157200	0.80807000	0.79469300
C	4.95026800	-0.60539300	0.16037000
H	5.10736600	-1.30808800	-0.66382400
H	4.90834600	-1.20855000	1.07258700
C	6.13499800	0.34823800	0.24162000
H	6.18008700	0.94973500	-0.67180100
H	5.97710100	1.05326700	1.06393200
C	7.46717500	-0.36419700	0.43995800
H	7.62296400	-1.06798000	-0.38177500
H	7.41990900	-0.96412500	1.35246600
C	8.64187100	0.60217800	0.51949800
H	9.58608100	0.07762700	0.66170400
H	8.72077400	1.19227100	-0.39473900
H	8.51608400	1.29729500	1.35091700



Electronic Energy = -1150.827952 EE + Zero-point Energy = -1150.490740
Enthalpy = -1150.471238 Free Energy = -1150.541739

0 2

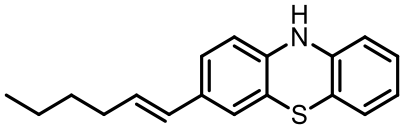
C	-1.09971900	-0.21507100	-0.00107900
C	0.01676900	-1.03851100	-0.00069500
C	1.30562100	-0.52005300	-0.00041100
C	1.52522400	0.88086600	-0.00050200
C	0.37326200	1.69885300	-0.00087800
C	-0.89495700	1.17241100	-0.00115000
C	3.88332100	0.81118200	0.00015200
C	4.01542900	-0.59922200	0.00036100
C	5.27425600	-1.19819900	0.00078900
H	5.34625500	-2.27842400	0.00094300
C	6.41651100	-0.42483600	0.00101400
C	6.31369700	0.97126300	0.00081200
C	5.07962200	1.56909100	0.00039200
H	-0.11785900	-2.11483400	-0.00060200
H	0.54028900	2.76703200	-0.00092700
H	-1.74309000	1.84228500	-0.00140300
H	7.38695500	-0.90070400	0.00134700
H	7.20845500	1.57812200	0.00098700
H	4.96751000	2.64428100	0.00022800
N	2.72333500	1.50702200	-0.00024900
S	2.62869600	-1.65286200	0.00009600
C	-2.47309700	-0.84227200	-0.00146900
H	-2.55213300	-1.49885000	-0.87336500
H	-2.55187800	-1.50043600	0.86924500
C	-3.65053400	0.12194500	-0.00042900
H	-3.59552000	0.77410100	-0.87658800
H	-3.59484700	0.77297800	0.87652700
C	-4.98944900	-0.60509600	-0.00042200
H	-5.04638600	-1.26005900	0.87453600
H	-5.04701700	-1.25891800	-0.87619200
C	-6.18241300	0.34164200	0.00062900
H	-6.12612300	0.99704200	-0.87421100
H	-6.12549200	0.99587600	0.87630000
C	-7.52328400	-0.38195400	0.00062800
H	-7.57739900	-1.03594800	0.87481100
H	-7.57805900	-1.03472800	-0.87442600
C	-8.70601300	0.57777600	0.00174200
H	-8.68288700	1.22234500	-0.87814200
H	-9.65651300	0.04547500	0.00171900
H	-8.68223300	1.22110300	0.88251600



Electronic Energy = -1150.212015 EE + Zero-point Energy = -1149.885988
Enthalpy = -1149.868371 Free Energy = -1149.930862

0 1

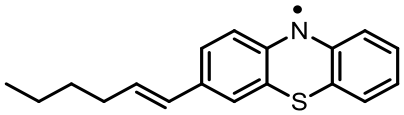
C	-1.16414200	-0.05242500	0.00025000
C	-0.02687900	-0.95185500	0.00016800
C	1.24512300	-0.51453100	0.00007200
C	1.54944900	0.92216000	0.00004000
C	0.39741200	1.81757000	0.00013700
C	-0.86302700	1.37035200	0.00023300
C	3.89447900	0.73589700	-0.00018000
C	3.97814000	-0.66154700	-0.00017100
C	5.21812500	-1.29121500	-0.00029000
H	5.26486200	-2.37276600	-0.00028000
C	6.38208300	-0.54207200	-0.00042000
C	6.31570800	0.84684400	-0.00043300
C	5.08349100	1.47076500	-0.00031300
H	-0.23231800	-2.01636900	0.00018900
H	0.63358900	2.87257000	0.00012300
H	-1.68600900	2.07274500	0.00030600
H	7.33980500	-1.04372900	-0.00051300
H	7.22179600	1.43606500	-0.00053500
H	4.99355900	2.54825600	-0.00031900
N	2.71284800	1.47106700	-0.00006800
S	2.55446800	-1.68485400	-0.00000300
C	-2.42629900	-0.52437700	0.00034300
H	-2.55992300	-1.60265800	0.00036600
C	-3.67798700	0.30232500	0.00041300
H	-3.68887600	0.96339100	-0.87260900
H	-3.68902400	0.96300300	0.87373000
C	-4.94339300	-0.54821600	0.00011800
H	-4.93553800	-1.20404700	0.87565500
H	-4.93538500	-1.20366600	-0.87570300
C	-6.21804900	0.28331800	0.00018900
H	-6.22266900	0.94084300	-0.87496900
H	-6.22282700	0.94045100	0.87564000
C	-7.48503600	-0.56297300	-0.00011600
H	-7.47793800	-1.21867400	0.87436300
H	-7.47778200	-1.21827500	-0.87489300
C	-8.75238900	0.28180000	-0.00003700
H	-8.78950300	0.92512800	-0.88032100
H	-9.64842600	-0.33770200	-0.00026700
H	-8.78966900	0.92471400	0.88054300



Electronic Energy = -1150.241981 EE + Zero-point Energy = -1149.915006
Enthalpy = -1149.895729 Free Energy = -1149.964229

0 1

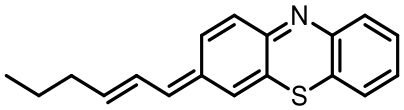
C	1.18616200	-0.02408800	-0.50731400
C	0.10912900	-0.90921900	-0.46738600
C	-1.20060400	-0.46488600	-0.54712500
C	-1.47201000	0.89997600	-0.61948800
C	-0.40370600	1.79353300	-0.62516100
C	0.90069000	1.33978700	-0.58416200
C	-3.82156100	0.70296700	-0.00463200
C	-3.80059100	-0.68614000	0.13425700
C	-4.81791600	-1.33042700	0.82181000
H	-4.77411700	-2.40543300	0.93618700
C	-5.88620200	-0.61072000	1.33844600
C	-5.91719100	0.76705400	1.18774800
C	-4.88350600	1.42094600	0.53564000
H	0.29629000	-1.97362800	-0.39294700
H	-0.60613500	2.85706500	-0.66269500
H	1.70562400	2.06149700	-0.58511400
H	-6.68336900	-1.12466700	1.85595400
H	-6.74100200	1.34096200	1.58868900
H	-4.89752800	2.49926000	0.43412600
N	-2.79202200	1.35727700	-0.69029100
H	-2.87639500	2.36169900	-0.69012300
S	-2.52828900	-1.63064300	-0.65445300
C	2.55266000	-0.55970000	-0.45947100
H	2.62421200	-1.61518800	-0.21062900
C	3.67912000	0.10367900	-0.70466700
H	3.63591100	1.15466300	-0.97739500
C	5.04921400	-0.48919900	-0.61757600
H	5.55311900	-0.39108700	-1.58467800
H	4.97510800	-1.55825900	-0.40567300
C	5.91297500	0.18711400	0.44910500
H	5.95987000	1.26206300	0.24961800
H	5.42965900	0.07597300	1.42346100
C	7.32668500	-0.37734300	0.50987200
H	7.80177300	-0.26050400	-0.46763100
H	7.27533800	-1.45257200	0.69957600
C	8.17712100	0.29430300	1.58021700
H	9.18463300	-0.11905300	1.61119600
H	8.26004800	1.36595900	1.39347500
H	7.73093600	0.16478300	2.56719300



Electronic Energy = -1149.609068 EE + Zero-point Energy = -1149.295398
Enthalpy = -1149.276341 Free Energy = -1149.344821

0 2

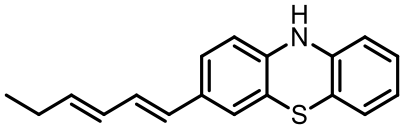
C	-1.19950400	0.07972800	-0.41623900
C	-0.15296400	-0.82747500	-0.31806900
C	1.16472900	-0.41072600	-0.16824900
C	1.48919900	0.96883400	-0.10956300
C	0.40171600	1.87808900	-0.21169600
C	-0.88738400	1.45592100	-0.35876700
C	3.81859000	0.71642000	0.13922300
C	3.84419000	-0.69796400	0.11799700
C	5.04707000	-1.39219800	0.23764800
H	5.03797400	-2.47460100	0.21838700
C	6.23693500	-0.70839700	0.37912300
C	6.23833400	0.69041400	0.40272300
C	5.05827300	1.38087100	0.28561900
H	-0.36835900	-1.88895100	-0.35972100
H	0.65068000	2.92916400	-0.16649900
H	-1.67782200	2.18945600	-0.43149700
H	7.16365400	-1.25698400	0.47114200
H	7.17015900	1.22737700	0.51327200
H	5.02711200	2.46133900	0.30036200
N	2.71607700	1.49970700	0.03242900
S	2.39022700	-1.64201300	-0.05777300
C	-2.56234600	-0.42544100	-0.57278700
H	-2.65196200	-1.50801800	-0.59735200
C	-3.67604800	0.29702200	-0.68884300
H	-3.62183400	1.38143100	-0.66504100
C	-5.04757600	-0.27949500	-0.82790600
H	-4.98649500	-1.36820100	-0.89075700
H	-5.49521200	0.06854600	-1.76467900
C	-5.96930700	0.12022600	0.32657800
H	-6.00556000	1.21130600	0.40014600
H	-5.54135900	-0.23750800	1.26680600
C	-7.38354300	-0.42313100	0.16657200
H	-7.34215000	-1.51238800	0.08594200
H	-7.80208800	-0.06112800	-0.77607500
C	-8.29378400	-0.02638500	1.32150900
H	-8.36734900	1.05906300	1.40185600
H	-9.30078900	-0.42160200	1.19314400
H	-7.90424200	-0.40192000	2.26868600



Electronic Energy = -1148.994872 EE + Zero-point Energy = -1148.692449
Enthalpy = -1148.674306 Free Energy = -1148.740328

0 1

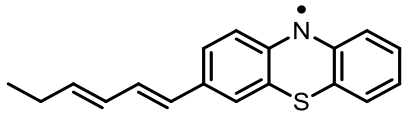
C	-1.23784000	-0.03614400	0.00038700
C	-0.10660800	-0.93510800	0.00017800
C	1.17007700	-0.50378500	0.00006800
C	1.48028700	0.92888800	0.00013500
C	0.33174800	1.82468900	0.00034200
C	-0.93202400	1.38178600	0.00046400
C	3.82383900	0.73210300	-0.00017200
C	3.90029700	-0.66630800	-0.00026600
C	5.13633600	-1.30359000	-0.00046400
H	5.17641800	-2.38542400	-0.00053600
C	6.30477700	-0.56160500	-0.00057000
C	6.24624300	0.82785000	-0.00047900
C	5.01814600	1.45937000	-0.00028200
H	-0.31405900	-1.99921400	0.00012300
H	0.56852300	2.87947200	0.00038500
H	-1.74405700	2.09478000	0.00060500
H	7.25954000	-1.06881400	-0.00072500
H	7.15585600	1.41166600	-0.00056100
H	4.93494700	2.53739100	-0.00020500
N	2.64777200	1.47337000	0.00002800
S	2.47062600	-1.68106500	-0.00014400
C	-2.50248600	-0.53467800	0.00047600
H	-2.60993800	-1.61546200	0.00068100
C	-3.73442600	0.21001900	0.00031900
H	-3.68800100	1.29373100	0.00011400
C	-4.93611000	-0.37762100	0.00040300
H	-4.97827200	-1.46452400	0.00062000
C	-6.24967000	0.34942100	0.00010900
H	-6.30361400	1.00742900	-0.87290500
H	-6.30389400	1.00762600	0.87295700
C	-7.45286500	-0.58680100	0.00002400
H	-7.39714400	-1.23873000	0.87512200
H	-7.39686300	-1.23893100	-0.87490600
C	-8.77428300	0.16831100	-0.00027500
H	-8.85590900	0.80694800	-0.88095500
H	-9.62437900	-0.51244000	-0.00033300
H	-8.85619200	0.80714800	0.88023300



Electronic Energy = -1149.024603 EE + Zero-point Energy = -1148.721191
Enthalpy = -1148.702391 Free Energy = -1148.769396

0 1

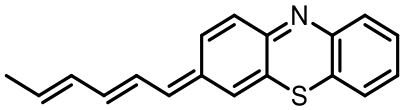
C	1.25245000	0.00361000	-0.32019900
C	0.17738100	-0.88586100	-0.36587200
C	-1.12854800	-0.44378300	-0.49351000
C	-1.40271300	0.92232900	-0.53287200
C	-0.33855000	1.81910400	-0.46397500
C	0.96396700	1.36932500	-0.37574000
C	-3.77932100	0.69602900	-0.04381400
C	-3.75848600	-0.69692500	0.04745100
C	-4.80681800	-1.36814200	0.65834000
H	-4.76384400	-2.44637500	0.73711100
C	-5.90389700	-0.67032600	1.14363600
C	-5.93401900	0.71174300	1.03957800
C	-4.87134100	1.39136600	0.46502300
H	0.36590300	-1.95145300	-0.31710800
H	-0.54353000	2.88253800	-0.48663500
H	1.76374700	2.09519700	-0.33343800
H	-6.72422500	-1.20455500	1.60088000
H	-6.78030900	1.26859800	1.41699500
H	-4.88543200	2.47251300	0.40058200
N	-2.71861600	1.37802900	-0.65065600
H	-2.80830600	2.38153100	-0.62105200
S	-2.44307000	-1.60964500	-0.70702700
C	2.60962500	-0.53004500	-0.21238200
H	2.67528900	-1.61233600	-0.14608700
C	3.75147400	0.16587100	-0.18996000
H	3.73538000	1.24883800	-0.25894800
C	5.06045100	-0.44801300	-0.07772300
H	5.08625800	-1.53261600	-0.01048100
C	6.20711400	0.23204100	-0.05538000
H	6.16968900	1.31760100	-0.11826000
C	7.56605700	-0.37616700	0.07682200
H	8.16376800	-0.12137900	-0.80297500
H	7.47783900	-1.46351700	0.09590400
C	8.29472100	0.11526200	1.32900300
H	9.29502500	-0.31130000	1.39452700
H	8.39186200	1.20145200	1.31840000
H	7.74304100	-0.16113300	2.22705300



Electronic Energy = -1148.389090 EE + Zero-point Energy = -1148.099463
Enthalpy = -1148.081608 Free Energy = -1148.146631

0 2

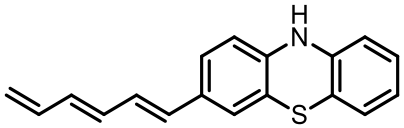
C	-1.25476500	-0.06263500	-0.00018400
C	-0.16653400	-0.92935600	-0.00004400
C	1.14045500	-0.46219100	-0.00004300
C	1.41654300	0.93124900	-0.00019500
C	0.28872300	1.79811000	-0.00034800
C	-0.99052400	1.32663900	-0.00034200
C	3.76676800	0.76878900	-0.00006600
C	3.84518500	-0.64315900	0.00010900
C	5.07997800	-1.28957800	0.00025200
H	5.11124200	-2.37174400	0.00038700
C	6.25046000	-0.55907000	0.00022400
C	6.19949100	0.83865500	0.00004900
C	4.98700600	1.48205400	-0.00009100
H	-0.34438800	-1.99854300	0.00007600
H	0.50054700	2.85822400	-0.00047300
H	-1.81174400	2.02928500	-0.00047100
H	7.20251200	-1.07074500	0.00033600
H	7.11582300	1.41235300	0.00002600
H	4.91501700	2.56068100	-0.00022700
N	2.62764300	1.50832500	-0.00021100
S	2.41860500	-1.64438500	0.00015400
C	-2.59841400	-0.61657300	-0.00015200
H	-2.65446400	-1.70123000	-0.00006000
C	-3.75179000	0.06872700	-0.00006400
H	-3.74482600	1.15362400	0.00000900
C	-5.05451100	-0.55978400	-0.00027900
H	-5.07329400	-1.64691400	-0.00036300
C	-6.20544200	0.11528100	-0.00014800
H	-6.16647300	1.20228400	0.00007900
C	-7.57206100	-0.51259900	-0.00015300
H	-7.67003600	-1.16379700	0.87191500
H	-7.67062400	-1.16249400	-0.87312700
C	-8.69250500	0.52009500	0.00098700
H	-8.62894900	1.16021900	-0.87950700
H	-9.67153900	0.04384200	0.00096600
H	-8.62835200	1.15891900	0.88238100



Electronic Energy = -1147.779076 EE + Zero-point Energy = -1147.500295
Enthalpy = -1147.482506 Free Energy = -1147.547546

0 1

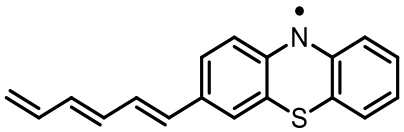
C	-1.33935000	-0.09283800	0.00003500
C	-0.19658000	-0.97338600	0.00011400
C	1.07428200	-0.52187500	0.00001900
C	1.36172800	0.91459700	-0.00017400
C	0.20006100	1.79189400	-0.00025900
C	-1.05693600	1.32840700	-0.00016200
C	3.70788300	0.75485400	-0.00020800
C	3.80599900	-0.64249200	-0.00003300
C	5.05168900	-1.26085400	0.00001900
H	5.10835900	-2.34193100	0.00015500
C	6.20851400	-0.50102600	-0.00010100
C	6.12865900	0.88754700	-0.00027500
C	4.89132000	1.50029400	-0.00032700
H	-0.38696700	-2.04065300	0.00025900
H	0.41975400	2.85034700	-0.00040500
H	-1.88017600	2.02842600	-0.00023400
H	7.17096200	-0.99348900	-0.00005900
H	7.02931500	1.48508800	-0.00036900
H	4.79165600	2.57690600	-0.00046100
N	2.52135400	1.47751900	-0.00027500
S	2.39216200	-1.67863000	0.00012700
C	-2.59962600	-0.61166200	0.00014700
H	-2.68851800	-1.69406100	0.00029300
C	-3.83500100	0.11222700	0.00009800
H	-3.80924900	1.19579500	-0.00001700
C	-5.03767500	-0.49451700	0.00019800
H	-5.07836800	-1.58041800	0.00031100
C	-6.30045500	0.20422900	0.00017500
H	-6.26050500	1.29068500	0.00003600
C	-7.48710400	-0.40838900	0.00028000
H	-7.50117000	-1.49383800	0.00003400
C	-8.80765200	0.30366300	0.00032400
H	-8.90835000	0.94416600	-0.87715500
H	-9.63935200	-0.39653900	-0.00170400
H	-8.90999900	0.94092500	0.87998300



Electronic Energy = -1147.803407 EE + Zero-point Energy = -1147.523202
Enthalpy = -1147.505082 Free Energy = -1147.570076

0 1

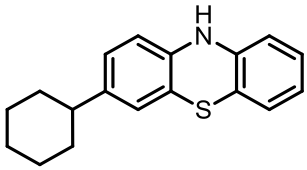
C	1.35239500	-0.01010700	-0.20711800
C	0.27477300	-0.89441700	-0.29081000
C	-1.02415900	-0.44530700	-0.45520500
C	-1.28996300	0.92305500	-0.49435800
C	-0.22364400	1.81438700	-0.38959700
C	1.07308800	1.35776500	-0.26494400
C	-3.68265700	0.70460200	-0.08407300
C	-3.67173600	-0.68890200	-0.00276400
C	-4.74341700	-1.35921400	0.56721300
H	-4.70859200	-2.43820200	0.63926300
C	-5.85273700	-0.65916300	1.02031400
C	-5.87255000	0.72374800	0.92563600
C	-4.78768600	1.40205000	0.39247300
H	0.45681500	-1.96116000	-0.24283100
H	-0.42265500	2.87885200	-0.41397300
H	1.87500700	2.07930100	-0.19746100
H	-6.69073000	-1.19244600	1.44548200
H	-6.72838900	1.28216700	1.27831500
H	-4.79419800	2.48369100	0.33575200
N	-2.59811800	1.38627700	-0.64828900
H	-2.68448100	2.38998400	-0.61620700
S	-2.33620800	-1.60322300	-0.71902400
C	2.70100100	-0.55068200	-0.06071600
H	2.76151800	-1.63435900	-0.01646700
C	3.84534000	0.14067100	0.02249100
H	3.83595900	1.22485700	-0.01914900
C	5.13941600	-0.48316800	0.16843100
H	5.15912800	-1.56887900	0.20940400
C	6.29526400	0.19029300	0.25442000
H	6.28165400	1.27591800	0.21417200
C	7.59016000	-0.44448500	0.40078800
H	7.59392200	-1.52935200	0.43935400
C	8.74062300	0.22017600	0.48761800
H	9.68529200	-0.29299200	0.59612500
H	8.76484100	1.30244400	0.45183200



Electronic Energy = -1147.170772 EE + Zero-point Energy = -1146.903961
Enthalpy = -1146.886086 Free Energy = -1146.951077

0 2

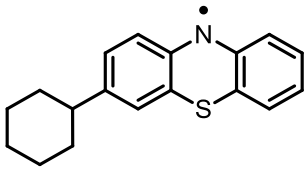
C	-1.37217900	-0.02304800	-0.00002000
C	-0.29365100	-0.90285400	0.00009000
C	1.01803800	-0.45101700	0.00001500
C	1.30984900	0.94013800	-0.00018100
C	0.19155700	1.82042100	-0.00029800
C	-1.09249600	1.36381400	-0.00022200
C	3.65775100	0.75093700	-0.00016900
C	3.72049000	-0.66157100	0.00002700
C	4.94810200	-1.32154600	0.00011300
H	4.96775100	-2.40396300	0.00026300
C	6.12625900	-0.60354400	0.00000800
C	6.09063000	0.79462500	-0.00018700
C	4.88519200	1.45120000	-0.00027200
H	-0.48418000	-1.96984600	0.00024200
H	0.41585400	2.87792900	-0.00045500
H	-1.90582100	2.07555900	-0.00032500
H	7.07272200	-1.12547500	0.00007600
H	7.01318200	1.35821300	-0.00027000
H	4.82489900	2.53052900	-0.00042200
N	2.52618700	1.50284700	-0.00026900
S	2.28306600	-1.64691600	0.00016900
C	-2.71963300	-0.56109100	0.00007500
H	-2.78834300	-1.64502000	0.00018100
C	-3.86802500	0.13690000	0.00005100
H	-3.85066100	1.22139200	-0.00004700
C	-5.16890100	-0.48242200	0.00015900
H	-5.19822500	-1.56848400	0.00025500
C	-6.32488900	0.19933600	0.00014400
H	-6.30030500	1.28544200	0.00003800
C	-7.63095300	-0.42705100	0.00025000
H	-7.64699800	-1.51234400	0.00034700
C	-8.77863300	0.24865000	0.00022900
H	-8.78934500	1.33168500	0.00014400
H	-9.73394500	-0.25614400	0.00029400



Electronic Energy = -1150.270185 EE + Zero-point Energy = -1149.938664
Enthalpy = -1149.921568 Free Energy = -1149.982880

0 1

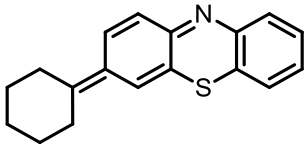
C	1.67334700	0.11124900	-0.12264100
C	0.63230600	-0.79942300	-0.26620900
C	-0.67661500	-0.38196700	-0.46168800
C	-0.98284500	0.97672300	-0.47452000
C	0.04878000	1.89449700	-0.30680300
C	1.35647600	1.46718800	-0.15077800
C	-3.37675800	0.68042800	-0.13547700
C	-3.32566400	-0.71405000	-0.08355800
C	-4.38771600	-1.42872900	0.44951700
H	-4.32098000	-2.50751100	0.49916900
C	-5.52706500	-0.77288700	0.89424500
C	-5.58679600	0.61067100	0.82903800
C	-4.51240700	1.33294300	0.33370400
H	0.84164100	-1.86223100	-0.24072500
H	-0.18055900	2.95331800	-0.30832000
H	2.13866000	2.20704900	-0.03734900
H	-6.35690000	-1.34048600	1.29007000
H	-6.46631600	1.13521300	1.17565400
H	-4.55093900	2.41491600	0.29997300
N	-2.30382900	1.40344800	-0.66761000
H	-2.41959000	2.40310300	-0.60989500
S	-1.94672500	-1.56997400	-0.78981300
C	3.09518800	-0.36053800	0.06088800
C	4.00578300	0.09713800	-1.08582600
C	3.67972400	0.08102900	1.40885500
H	3.08245400	-1.45594100	0.05229100
C	5.43388000	-0.41023500	-0.90238700
H	4.01262300	1.19152400	-1.11731500
H	3.59345300	-0.24239900	-2.03745900
C	5.10777700	-0.42660100	1.59200400
H	3.67674900	1.17489500	1.45509700
H	3.03719500	-0.26997100	2.21808400
C	6.00611900	0.02686700	0.44388200
H	6.06548000	-0.05618800	-1.71831000
H	5.43458300	-1.50365400	-0.95367300
H	5.50792300	-0.08441500	2.54740600
H	5.09691400	-1.52058700	1.62744600
H	7.01561700	-0.36562000	0.57333600
H	6.08530400	1.11862100	0.46133600



Electronic Energy = -1149.636319 EE + Zero-point Energy = -1149.318103
Enthalpy = -1149.301205 Free Energy = -1149.362848

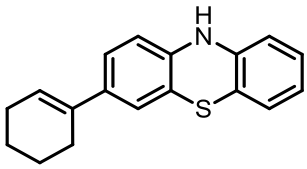
0 2

C	-1.69132400	0.10356800	0.00000300
C	-0.64960300	-0.80602000	-0.00004200
C	0.68100600	-0.39014300	-0.00002000
C	1.01282500	0.98579600	0.00005100
C	-0.07148500	1.89787500	0.00009900
C	-1.37330600	1.47469900	0.00007600
C	3.35684900	0.72605500	0.00003000
C	3.37426300	-0.69036900	-0.00004300
C	4.57987200	-1.39005200	-0.00008600
H	4.56398300	-2.47257500	-0.00014100
C	5.78143400	-0.71216300	-0.00005700
C	5.79214300	0.68742400	0.00001500
C	4.61057400	1.38388400	0.00005700
H	-0.86874300	-1.86774900	-0.00009900
H	0.18316400	2.94864900	0.00015400
H	-2.17003700	2.20762300	0.00011400
H	6.70984600	-1.26555100	-0.00009100
H	6.73316100	1.21976100	0.00003800
H	4.58684700	2.46465200	0.00011300
N	2.25648300	1.51371900	0.00007600
S	1.90571900	-1.62703000	-0.00008200
C	-3.12443000	-0.36088300	-0.00002200
C	-3.87436800	0.09643900	1.25887100
C	-3.87438700	0.09661600	-1.25883800
H	-3.11857700	-1.45617200	-0.00010000
C	-5.31725400	-0.40248000	1.25782900
H	-3.87043300	1.19031300	1.29735300
H	-3.34482200	-0.25219200	2.14700800
C	-5.31727300	-0.40230500	-1.25784400
H	-3.87045800	1.19049600	-1.29716600
H	-3.34485500	-0.25188600	-2.14703300
C	-6.05614000	0.04764400	0.00002900
H	-5.83506500	-0.05083300	2.15109700
H	-5.31789400	-1.49613600	1.30195500
H	-5.83509700	-0.05053400	-2.15105500
H	-5.31791200	-1.49595500	-1.30212200
H	-7.07614300	-0.33874500	0.00001100
H	-6.13021000	1.13974300	0.00010500



Electronic Energy = -1149.019715 EE + Zero-point Energy = -1148.712345
Enthalpy = -1148.695386 Free Energy = -1148.758223

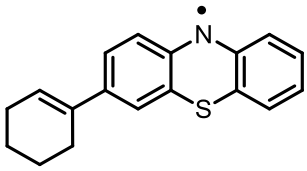
```
0 1
 C                  1.82409400    0.40670200   -0.38192600
 C                  0.76411700   -0.58903100   -0.36329600
 C                 -0.54115600   -0.27737300   -0.25122400
 C                 -0.98642800    1.11215300   -0.11742100
 C                  0.07281800    2.10792600   -0.16216400
 C                  1.36636800    1.78676400   -0.28412700
 C                 -3.28542200    0.67908400    0.11673800
 C                 -3.23300300   -0.71450200   -0.00795200
 C                 -4.39421900   -1.47370000    0.08455200
 H                 -4.33455000   -2.55011600   -0.01431600
 C                 -5.61570700   -0.85915000    0.30143100
 C                 -5.68457000    0.52350700    0.42948200
 C                 -4.52994800    1.27620200    0.33695500
 H                  1.02729400   -1.63276800   -0.45243800
 H                 -0.25249600    3.13590300   -0.08297300
 H                  2.09134600    2.58539800   -0.30518200
 H                 -6.51144900   -1.46056600    0.37086800
 H                 -6.63544700    1.00842900    0.59977500
 H                 -4.54659000    2.35325400    0.43066200
 N                 -2.19186400    1.53583700    0.03907200
 S                 -1.73017600   -1.56988400   -0.30269600
 C                  3.14022000    0.07915900   -0.48224600
 C                  3.66223100   -1.33008200   -0.53665200
 C                  4.26719400    1.07510600   -0.47549900
 C                  4.58051300   -1.60737200    0.66500800
 H                  4.25506200   -1.43984800   -1.45180700
 H                  2.87497500   -2.07499000   -0.58014700
 C                  5.19499100    0.82883700    0.72545600
 H                  4.85147200    0.93384900   -1.39191900
 H                  3.92697600    2.10492200   -0.47576100
 C                  5.72447500   -0.60106200    0.72473800
 H                  4.96787800   -2.62482500    0.60090100
 H                  3.98818000   -1.54362300    1.58157700
 H                  6.01918800    1.54271700    0.70244300
 H                  4.63401500    1.01126500    1.64585400
 H                  6.33949300   -0.77816700    1.60788100
 H                  6.37111000   -0.74255400   -0.14689900
```



Electronic Energy = -1149.048798 EE + Zero-point Energy = -1148.741325
Enthalpy = -1148.724386 Free Energy = -1148.785552

0 1

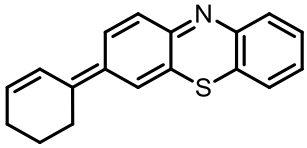
C	1.73504800	0.42142200	-0.13471200
C	0.76187800	-0.57757700	-0.18193000
C	-0.57150200	-0.27947400	-0.41093700
C	-0.98060300	1.04434100	-0.56762500
C	-0.02010400	2.04794000	-0.51188700
C	1.31495900	1.73853600	-0.31888900
C	-3.34739300	0.60519500	-0.19195300
C	-3.19186800	-0.76749100	0.01050400
C	-4.20136500	-1.49861200	0.61808100
H	-4.05432300	-2.55762000	0.78410000
C	-5.39002900	-0.88636700	0.98995500
C	-5.55302900	0.47357700	0.77550100
C	-4.53229600	1.21714700	0.20415900
H	1.03416300	-1.61323300	-0.02957700
H	-0.32427500	3.07944900	-0.64255700
H	2.05002800	2.53177100	-0.31935200
H	-6.17784800	-1.46880700	1.44551600
H	-6.47200600	0.96459800	1.06393600
H	-4.65172900	2.28313400	0.05357000
N	-2.32763500	1.34689700	-0.79833500
H	-2.51909200	2.33523000	-0.84959900
S	-1.74830300	-1.58839200	-0.60098200
C	3.16346900	0.10529800	0.10806700
C	3.74170100	-1.10980300	-0.57920700
C	3.91184700	0.88612600	0.88958600
C	5.11166700	-1.49886300	-0.03259800
H	3.80557900	-0.90302800	-1.65269300
H	3.05440000	-1.95125400	-0.48325900
C	5.38357600	0.69639700	1.12071600
H	3.43830300	1.71654500	1.40242400
C	5.99802500	-0.26783700	0.11197600
H	5.57496200	-2.24007700	-0.68403400
H	4.98865600	-1.96467700	0.94910700
H	5.88291100	1.66677300	1.07553600
H	5.54613700	0.32524900	2.13841100
H	7.00635500	-0.54636500	0.41853900
H	6.08017100	0.22855900	-0.85886200



Electronic Energy = -1148.415065 EE + Zero-point Energy = -1148.120857
Enthalpy = -1148.104102 Free Energy = -1148.165847

0 2

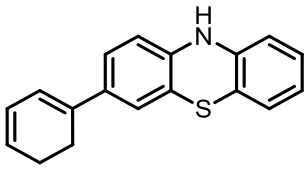
C	1.75766500	0.42850100	-0.01919700
C	0.77635300	-0.55065500	0.06081700
C	-0.57784400	-0.23156300	0.02575400
C	-1.01260800	1.11031600	-0.10719500
C	0.00538900	2.09217100	-0.20783800
C	1.33180000	1.76675100	-0.16888200
C	-3.32965500	0.68026100	-0.06788700
C	-3.24293800	-0.72528200	0.07622200
C	-4.39415300	-1.50718500	0.15884600
H	-4.29862500	-2.57990900	0.26911000
C	-5.64177400	-0.92178200	0.10056900
C	-5.75482600	0.46581300	-0.04224700
C	-4.62704800	1.24243700	-0.12390400
H	1.05182200	-1.59003600	0.17684100
H	-0.32222300	3.11495200	-0.33226300
H	2.07475500	2.54366700	-0.28328600
H	-6.52746600	-1.53784700	0.16542800
H	-6.73227400	0.92555900	-0.08796700
H	-4.68192000	2.31642200	-0.23406300
N	-2.28796600	1.54212200	-0.15650200
S	-1.70993600	-1.54841400	0.15487000
C	3.19809000	0.09619000	0.04021500
C	3.64926200	-1.22860700	-0.53168000
C	4.07315400	0.95411200	0.57404500
C	5.08919300	-1.57418800	-0.16335600
H	3.53140700	-1.19601200	-1.61965200
H	2.99077000	-2.02609900	-0.18697400
C	5.55917700	0.74813100	0.60170800
H	3.70252300	1.86663600	1.02718200
C	5.99666000	-0.36441300	-0.34347800
H	5.43274000	-2.41513200	-0.76580200
H	5.12654400	-1.89155600	0.88242200
H	6.05441000	1.68750800	0.34641500
H	5.87373300	0.51501300	1.62484600
H	7.03898200	-0.62751900	-0.16380800
H	5.92417600	-0.01191600	-1.37589800



Electronic Energy = -1147.803381 EE + Zero-point Energy = -1147.519904
Enthalpy = -1147.503215 Free Energy = -1147.565170

0 1

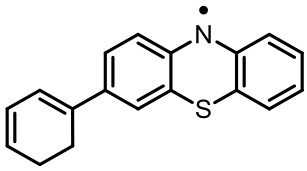
C	1.84217600	0.44251300	-0.03824000
C	0.80291400	-0.56434800	-0.07406900
C	-0.51328200	-0.26799300	-0.04452400
C	-0.98014500	1.11675400	0.03921300
C	0.06758400	2.12295200	0.07527300
C	1.37079000	1.81506300	0.03322000
C	-3.28752800	0.66455900	0.05114800
C	-3.21044700	-0.73103000	-0.03903600
C	-4.36853000	-1.50041600	-0.06850700
H	-4.28913600	-2.57776700	-0.13889500
C	-5.61135000	-0.89430500	-0.00758700
C	-5.70566300	0.49030400	0.08334300
C	-4.55489300	1.25299400	0.11145500
H	1.08719600	-1.60373200	-0.15596400
H	-0.27289100	3.14674500	0.14272500
H	2.08855000	2.61930800	0.07922800
H	-6.50432700	-1.50329700	-0.03089900
H	-6.67387700	0.96837400	0.13134100
H	-4.59094400	2.33139500	0.18054300
N	-2.20058000	1.52937000	0.08336100
S	-1.67768200	-1.57792300	-0.11899000
C	3.17294400	0.11953500	-0.07755400
C	3.65938400	-1.30977700	-0.09054600
C	4.21917300	1.12428200	-0.18415700
C	5.01139100	-1.45728800	0.60610700
H	3.75693500	-1.63756900	-1.13229300
H	2.94098100	-1.97196000	0.38485200
C	5.52460000	0.82769600	-0.21239900
H	3.93604300	2.15954600	-0.30065900
C	6.05774900	-0.55963400	-0.03914900
H	5.32871600	-2.49941000	0.58108700
H	4.89976300	-1.17551700	1.65546500
H	6.23893400	1.62803200	-0.36351200
H	6.96964400	-0.53355200	0.55978000
H	6.35020400	-0.96058900	-1.01642800



Electronic Energy = -1147.827334 EE + Zero-point Energy = -1147.543658
Enthalpy = -1147.527114 Free Energy = -1147.587233

0 1

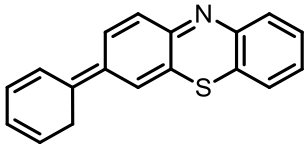
C	-1.81524500	0.45767300	-0.10250400
C	-0.85049700	-0.55029500	-0.15807700
C	0.48399200	-0.26321200	-0.39285900
C	0.90154400	1.05773100	-0.55068300
C	-0.05237700	2.06944400	-0.49184100
C	-1.38728300	1.77303700	-0.28967200
C	3.26829400	0.59939600	-0.19610200
C	3.10389000	-0.77253600	0.00379800
C	4.11356400	-1.51338500	0.59907800
H	3.95987700	-2.57167300	0.76357500
C	5.31071700	-0.91158100	0.96058300
C	5.48242900	0.44760300	0.74826000
C	4.46190500	1.20091100	0.18942900
H	-1.13702400	-1.58379500	-0.01284200
H	0.25955600	3.09789400	-0.62785200
H	-2.11252500	2.57502200	-0.29092400
H	6.09846500	-1.50158400	1.40640800
H	6.40815700	0.93047300	1.02867500
H	4.58820000	2.26636700	0.04076800
S	1.64829800	-1.58111200	-0.59578900
C	-3.22732100	0.13043200	0.15845500
C	-3.74392700	-1.24448500	-0.20559700
C	-4.05635700	0.97080200	0.79634700
C	-5.23217700	-1.22046000	-0.54171500
H	-3.57238800	-1.91404900	0.64664200
H	-3.18281900	-1.65146300	-1.04612500
C	-5.43944200	0.60294700	1.08617000
H	-3.69479200	1.92610800	1.15451000
C	-6.01113700	-0.43479500	0.47520400
H	-5.61173300	-2.23840500	-0.62257200
H	-5.37708700	-0.75406600	-1.52428300
H	-5.99717300	1.20665100	1.78992600
H	-7.04799000	-0.68533500	0.65783700
N	2.24801300	1.35169200	-0.78854100
H	2.44698800	2.33844300	-0.84096700



Electronic Energy = -1147.194257 EE + Zero-point Energy = -1146.923841
Enthalpy = -1146.907507 Free Energy = -1146.968005

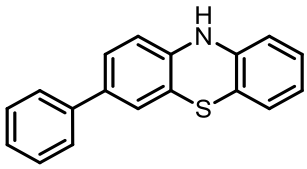
0 2

C	1.83979800	0.46425700	0.02005200
C	0.86667200	-0.52491400	-0.06997900
C	-0.48873600	-0.21912100	-0.03255100
C	-0.93403600	1.11970200	0.11791800
C	0.07769600	2.11064300	0.22787600
C	1.40547400	1.79979100	0.18033300
C	-3.24709500	0.67165600	0.07735500
C	-3.15067900	-0.73033300	-0.08520600
C	-4.29636600	-1.51914400	-0.17604000
H	-4.19366100	-2.58962700	-0.30070600
C	-5.54794900	-0.94297800	-0.10760000
C	-5.67011200	0.44135200	0.05370700
C	-4.54692300	1.22455300	0.14339000
H	1.15944400	-1.55951000	-0.19598300
H	-0.26010000	3.12860800	0.36356300
H	2.13973600	2.58444600	0.29766500
H	-6.42954500	-1.56419300	-0.17890100
H	-6.65045500	0.89398500	0.10736600
H	-4.60887600	2.29660100	0.26774500
S	-1.61159900	-1.54186100	-0.17785400
C	3.26366100	0.12374000	-0.06179000
C	3.70809800	-1.29165700	0.23665700
C	4.18733200	0.99825200	-0.49928400
C	5.13958000	-1.33910400	0.76393000
H	3.63819500	-1.87801600	-0.68798400
H	3.03922400	-1.75715600	0.95934900
C	5.58886300	0.62224500	-0.63930300
H	3.89463800	1.99219300	-0.81049700
C	6.05813300	-0.48393600	-0.06055800
H	5.49018000	-2.36996000	0.79582000
H	5.16034500	-0.97042200	1.79706800
H	6.24435100	1.27545100	-1.19965900
H	7.10663900	-0.74359100	-0.12677200
N	-2.20928600	1.54013500	0.17488100



Electronic Energy = -1146.583203 EE + Zero-point Energy = -1146.323794
Enthalpy = -1146.307500 Free Energy = -1146.368168

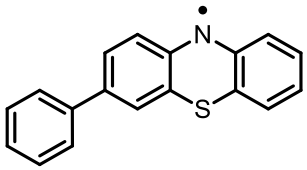
```
0 1
 C                  1.92190500    0.45734200   -0.00000200
 C                  0.89158400   -0.55299400   -0.00000200
 C                 -0.42833800   -0.26033500   -0.00000400
 C                 -0.89775000    1.12542400   -0.00000500
 C                  0.14594000    2.13432200   -0.00000700
 C                  1.45174900    1.82723800   -0.00000600
 C                 -3.20426900    0.66684800    0.00000000
 C                 -3.12248300   -0.73186200   -0.00000100
 C                 -4.27713100   -1.50709000    0.00000400
 H                 -4.19269200   -2.58639100    0.00000300
 C                 -5.52260300   -0.90377700    0.00000800
 C                 -5.62240200    0.48387400    0.00000900
 C                 -4.47534600    1.25205100    0.00000500
 H                  1.18122600   -1.59501800    0.00000000
 H                 -0.19706000    3.15934400   -0.00001000
 H                  2.16712100    2.63526600   -0.00000800
 H                 -6.41319900   -1.51662900    0.00001200
 H                 -6.59288600    0.95979800    0.00001300
 H                 -4.51645000    2.33250300    0.00000600
 S                 -1.58613000   -1.57476300   -0.00000800
 C                  3.25491600    0.11931900    0.00000100
 C                  3.66934500   -1.33793100    0.00000400
 C                  4.30932800    1.10312900    0.00000100
 C                  5.14281800   -1.59992200    0.00000600
 H                  3.22895400   -1.84463600   -0.86672700
 H                  3.22895200   -1.84463200    0.86673700
 C                  5.61308100    0.76674000    0.00000300
 H                  4.05081000    2.15065800    0.00000000
 C                  6.04393900   -0.61992400    0.00000600
 H                  5.45371800   -2.63684200    0.00000700
 H                  6.36428400    1.54483200    0.00000400
 H                  7.10227300   -0.84157800    0.00000700
 N                 -2.12181200    1.53497300   -0.00000400
```



Electronic Energy = -1146.658153 EE + Zero-point Energy = -1146.396788
Enthalpy = -1146.380994 Free Energy = -1146.439615

0 1

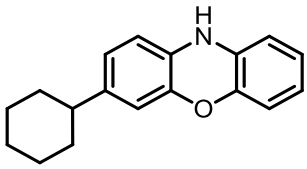
C	-1.88387300	0.41346100	-0.14596300
C	-0.91268700	-0.58673600	-0.18303000
C	0.41982700	-0.28851700	-0.41298000
C	0.82607500	1.03749100	-0.56890200
C	-0.13441300	2.04136800	-0.51043300
C	-1.46980300	1.73225200	-0.31798300
C	3.19345000	0.60110300	-0.18852000
C	3.04011200	-0.77165700	0.01313200
C	4.05040600	-1.50145800	0.62107300
H	3.90504500	-2.56075300	0.78666500
C	5.23768400	-0.88723400	0.99379000
C	5.39852000	0.47310100	0.78001700
C	4.37691000	1.21514200	0.20837000
H	-1.19645600	-1.61883300	-0.02139400
H	0.17074900	3.07318800	-0.63476700
H	-2.20286400	2.52764500	-0.31461500
H	6.02622400	-1.46848400	1.44957000
H	6.31645800	0.96555300	1.06921600
H	4.49450200	2.28140700	0.05837300
S	1.59825700	-1.59544500	-0.59825000
C	-3.30834400	0.07930000	0.07236200
C	-3.87018300	-1.06432100	-0.49578400
C	-4.12272500	0.90127300	0.85198200
C	-5.20480000	-1.37714700	-0.29030900
H	-3.25994700	-1.69980300	-1.12431500
C	-5.45790500	0.59054600	1.05614200
H	-3.69681300	1.77794300	1.32239000
C	-6.00463600	-0.55058500	0.48613600
H	-5.62351300	-2.26453800	-0.74541100
H	-6.07090900	1.23629600	1.67031200
H	-7.04593600	-0.79402000	0.64618200
N	2.17237500	1.34234900	-0.79412000
H	2.36303400	2.33079700	-0.84596600



Electronic Energy = -1146.023962 EE + Zero-point Energy = -1145.775890
Enthalpy = -1145.760299 Free Energy = -1145.819322

0 2

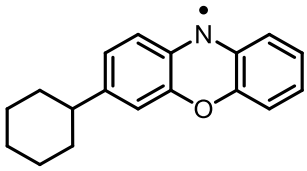
C	-1.90517700	0.41474300	-0.05914500
C	-0.92940900	-0.56469800	0.05460200
C	0.42366400	-0.24495400	0.02078700
C	0.85359800	1.09749900	-0.13294800
C	-0.16301800	2.07819500	-0.24823100
C	-1.49106800	1.75248300	-0.21067700
C	3.17217800	0.67456600	-0.07237700
C	3.08880900	-0.72851400	0.09806100
C	4.24196400	-1.50543400	0.19978200
H	4.14924300	-2.57614000	0.32996300
C	5.48780400	-0.91729900	0.13496400
C	5.59767200	0.46792100	-0.03379900
C	4.46840800	1.23963700	-0.13430800
H	-1.22181600	-1.59725900	0.20088500
H	0.16560500	3.09994000	-0.37713900
H	-2.23712600	2.52696200	-0.32677300
H	6.37511800	-1.52924600	0.21474000
H	6.57409200	0.92924200	-0.08459000
H	4.52062900	2.31147000	-0.26459100
S	1.55842800	-1.55437700	0.18793900
C	-3.33887300	0.06395700	-0.02113700
C	-3.80315200	-1.11995600	-0.59660700
C	-4.26270800	0.91055700	0.59388200
C	-5.14861900	-1.44838800	-0.55627900
H	-3.10646000	-1.77400200	-1.10431000
C	-5.60803800	0.58138900	0.63588000
H	-3.91843100	1.82094100	1.06655100
C	-6.05665500	-0.59940000	0.06096300
H	-5.49031700	-2.36578200	-1.01597700
H	-6.30709300	1.24566500	1.12552900
H	-7.10663200	-0.85564700	0.09261400
N	2.12915400	1.53143900	-0.18062900



Electronic Energy = -827.293926 EE + Zero-point Energy = -826.960162
Enthalpy = -826.943454 Free Energy = -827.004292

0 1

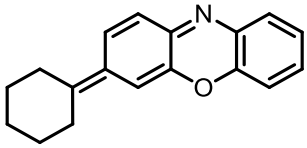
C	1.49630700	0.12564600	-0.05340200
C	0.41748700	-0.73534900	-0.24441900
C	-0.87372500	-0.25344100	-0.30500300
C	-1.13731400	1.10692000	-0.16364900
C	-0.06982400	1.96749300	0.04085100
C	1.22982900	1.48284300	0.08957500
C	-3.47458400	0.60480900	-0.05231300
C	-3.16378400	-0.74909700	-0.19526800
C	-4.13001600	-1.71764900	-0.02661000
H	-3.84394900	-2.75334400	-0.14557400
C	-5.43659900	-1.35010000	0.27732200
C	-5.75588600	-0.01128100	0.42352600
C	-4.77664500	0.96158500	0.26462300
H	0.56916000	-1.80100000	-0.35902900
H	-0.26209600	3.02757600	0.15124500
H	2.04288900	2.18086800	0.24129200
H	-6.19368500	-2.11111200	0.39949100
H	-6.76727300	0.28566800	0.66242000
H	-5.02166400	2.01050400	0.37563600
N	-2.46277300	1.54451700	-0.26198400
H	-2.64738700	2.47512000	0.07597900
O	-1.89275400	-1.14872100	-0.54227700
C	2.90768300	-0.40837600	-0.01220100
C	3.75580300	0.12810100	-1.17278700
C	3.60031200	-0.11885200	1.32552800
H	2.85176300	-1.49675300	-0.12318000
C	5.17161500	-0.44178700	-1.14175300
H	3.80270400	1.21951500	-1.10028400
H	3.26599400	-0.10329000	-2.12014300
C	5.01598000	-0.68980300	1.35658100
H	3.64533500	0.96468200	1.47468500
H	3.00115400	-0.52427900	2.14260000
C	5.85161300	-0.15727500	0.19517700
H	5.75973400	-0.03116900	-1.96370200
H	5.12509900	-1.52443900	-1.29649300
H	5.49398300	-0.45578500	2.30886700
H	4.96357600	-1.78109600	1.28916600
H	6.85099700	-0.59415900	0.21414500
H	5.97560100	0.92432200	0.31031000



Electronic Energy = -826.666282 EE + Zero-point Energy = -826.345000
Enthalpy = -826.328772 Free Energy = -826.388604

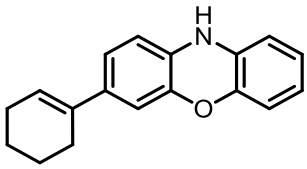
0 2

C	1.47765300	0.09908200	0.00000000
C	0.40764400	-0.78220600	0.00004500
C	-0.89182600	-0.30346800	0.00002000
C	-1.18017200	1.07668300	-0.00005200
C	-0.07736900	1.95595300	-0.00009700
C	1.20969700	1.48030200	-0.00007200
C	-3.43452200	0.63753800	-0.00002800
C	-3.18019500	-0.75041600	0.00004400
C	-4.20358500	-1.68273200	0.00009400
H	-3.95111600	-2.73378500	0.00014800
C	-5.51563900	-1.24482700	0.00007200
C	-5.80289600	0.12397400	0.00000100
C	-4.78292000	1.04626800	-0.00004800
H	0.56418700	-1.85315500	0.00010100
H	-0.29319600	3.01544200	-0.00015300
H	2.03415000	2.18140400	-0.00010900
H	-6.31980900	-1.96693900	0.00011100
H	-6.83140300	0.45649200	-0.00001600
H	-4.97373000	2.11039500	-0.00010300
N	-2.44402800	1.56723800	-0.00007700
O	-1.90094700	-1.21478600	0.00006700
C	2.89481100	-0.41341200	0.00002400
C	3.66007900	0.01752900	-1.25890400
C	3.66009800	0.01768700	1.25888600
H	2.85159200	-1.50770300	0.00009300
C	5.08448800	-0.53171700	-1.25782800
H	3.69445100	1.11077700	-1.29748300
H	3.11864700	-0.31245000	-2.14702900
C	5.08450600	-0.53156200	1.25785700
H	3.69447300	1.11093900	1.29732800
H	3.11867900	-0.31218100	2.14706100
C	5.83860900	-0.10767700	-0.00001700
H	5.61431200	-0.19819600	-2.15102200
H	5.04704900	-1.62472000	-1.30209300
H	5.61434400	-0.19792900	2.15100200
H	5.04706700	-1.62455900	1.30225800
H	6.84451300	-0.52941200	0.00000200
H	5.95079600	0.98119300	-0.00008500



Electronic Energy = -826.050334 EE + Zero-point Energy = -825.739791
Enthalpy = -825.723568 Free Energy = -825.783128

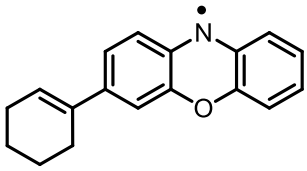
```
0 1
 C                  1.61945900    0.40799500   -0.35867900
 C                  0.53185400   -0.55962300   -0.35600900
 C                 -0.74729100   -0.18883100   -0.20029800
 C                 -1.14739600    1.20285900   -0.02719600
 C                 -0.06767300    2.16839200   -0.03736500
 C                  1.21145200    1.79866700   -0.19063300
 C                 -3.34537000    0.59263900    0.12497300
 C                 -3.02117400   -0.75679000   -0.03736600
 C                 -3.99474700   -1.73789800   -0.03681700
 H                 -3.69783400   -2.76928900   -0.16547300
 C                 -5.32303100   -1.37254900    0.12872300
 C                 -5.66978800   -0.03643300    0.29172500
 C                 -4.68466500    0.93623200    0.28914200
 H                  0.72691000   -1.61362800   -0.47576800
 H                 -0.35276800    3.20394200    0.08536900
 H                  1.96751000    2.56805200   -0.18985500
 H                 -6.08811200   -2.13635300    0.13005600
 H                 -6.70571200    0.24334100    0.42014100
 H                 -4.91908900    1.98454200    0.41332100
 N                 -2.36829400    1.58763300    0.12637100
 O                 -1.72211000   -1.14596800   -0.20244600
 C                  2.92259400    0.04891700   -0.50314500
 C                  3.39212000   -1.37242200   -0.64492500
 C                  4.08498900    1.00255800   -0.45848500
 C                  4.31092500   -1.75156400    0.52754900
 H                  3.97148000   -1.45039500   -1.57189100
 H                  2.57568700   -2.08229100   -0.72311000
 C                  5.01578100    0.65457400    0.71487500
 H                  4.65339700    0.89274100   -1.38899100
 H                  3.78388600    2.04267700   -0.39516200
 C                  5.49164300   -0.79170600    0.62919200
 H                  4.66047800   -2.77697000    0.40196900
 H                  3.73063600   -1.71830800    1.45343300
 H                  5.86620000    1.33745600    0.72125500
 H                  4.47170400    0.80599600    1.65092200
 H                  6.10863600   -1.03927000    1.49384300
 H                  6.12383800   -0.90801800   -0.25665200
```



Electronic Energy = -826.072838 EE + Zero-point Energy = -825.762935
Enthalpy = -825.746458 Free Energy = -825.806470

0 1

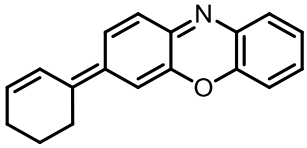
C	1.57003500	0.42938800	-0.07729400
C	0.55362400	-0.52958000	-0.12894300
C	-0.76590500	-0.15637200	-0.25486700
C	-1.13033600	1.18745600	-0.33257300
C	-0.12910300	2.14429200	-0.28252700
C	1.20137200	1.76945700	-0.16522000
C	-3.42597900	0.54028500	-0.13326300
C	-3.01678300	-0.79231100	-0.05379000
C	-3.91289900	-1.78802000	0.27143300
H	-3.55200300	-2.80573400	0.32282500
C	-5.24561800	-1.47150100	0.51256700
C	-5.66205900	-0.15358400	0.43826500
C	-4.75361100	0.84885100	0.12164600
H	0.76681800	-1.58658200	-0.05594400
H	-0.39595900	3.19099300	-0.35978500
H	1.96954400	2.53017800	-0.16355200
H	-5.94734300	-2.25524400	0.75863200
H	-6.69471000	0.10388700	0.62652400
H	-5.07417300	1.88134800	0.06038900
N	-2.48132900	1.50444800	-0.49168800
H	-2.73680500	2.46306400	-0.31872300
O	-1.71690800	-1.14967300	-0.33234900
C	2.99310400	0.03962700	0.06920500
C	3.47698000	-1.16118600	-0.70991900
C	3.81781400	0.74387900	0.84684200
C	4.85390300	-1.63869500	-0.25969700
H	3.49420500	-0.90064200	-1.77343200
H	2.75669900	-1.97516400	-0.61925400
C	5.28977100	0.47932600	0.98404000
H	3.41105400	1.56434900	1.42828300
C	5.80374300	-0.45751800	-0.10372300
H	5.24675600	-2.36501400	-0.97147800
H	4.76117300	-2.14888100	0.70313700
H	5.82985400	1.42840300	0.95775600
H	5.49077700	0.05006800	1.97162000
H	6.81273700	-0.79592800	0.13246700
H	5.85762400	0.08439000	-1.05194500



Electronic Energy = -825.445212 EE + Zero-point Energy = -825.147910
Enthalpy = -825.131837 Free Energy = -825.191712

0 2

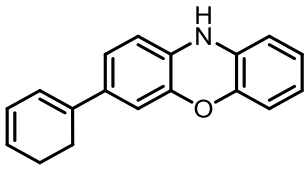
C	1.55347200	0.41967800	-0.02426500
C	0.54222600	-0.53354300	0.06101400
C	-0.78511200	-0.15107900	0.01888100
C	-1.17771100	1.19724500	-0.12375600
C	-0.13997600	2.14773500	-0.22944400
C	1.17612800	1.77023800	-0.18467700
C	-3.39164100	0.59463100	-0.06087800
C	-3.03545200	-0.76206600	0.08702700
C	-3.98764700	-1.76092900	0.19784900
H	-3.65903200	-2.78463200	0.30950200
C	-5.32842900	-1.42205500	0.16271100
C	-5.71547000	-0.08631600	0.01684600
C	-4.76547600	0.90229600	-0.09279700
H	0.75554600	-1.58480800	0.18622300
H	-0.42985600	3.18093800	-0.36152100
H	1.94828300	2.51719100	-0.30276200
H	-6.07727900	-2.19664500	0.24878400
H	-6.76554200	0.16868500	-0.00960600
H	-5.03369900	1.94344600	-0.20617300
N	-2.47070400	1.58924300	-0.17009100
O	-1.72534100	-1.12862100	0.12414100
C	2.98181500	0.03964900	0.04158300
C	3.38896000	-1.30138100	-0.52534400
C	3.88320900	0.86726000	0.57934700
C	4.81242500	-1.69764200	-0.14504300
H	3.28128200	-1.26612700	-1.61431100
H	2.69829500	-2.07305600	-0.18506600
C	5.36088500	0.60917800	0.61565300
H	3.54186900	1.79219800	1.03029800
C	5.76430400	-0.52198000	-0.32263500
H	5.12992100	-2.55265900	-0.74193500
H	4.83040200	-2.01217900	0.90210300
H	5.89018200	1.52959700	0.35951400
H	5.66129700	0.36953300	1.64152900
H	6.79519100	-0.82183200	-0.13478600
H	5.71173100	-0.17089600	-1.35674100



Electronic Energy = -824.833972 EE + Zero-point Energy = -824.547345
Enthalpy = -824.531377 Free Energy = -824.590283

0 1

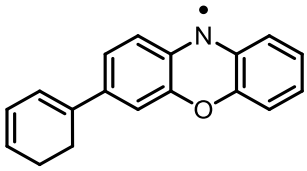
C	1.63749600	0.42390600	-0.02921500
C	0.56786400	-0.55304200	-0.06748700
C	-0.72475200	-0.18874200	-0.03059000
C	-1.14444900	1.20362700	0.05849900
C	-0.07515700	2.17761400	0.10099500
C	1.21526900	1.81356800	0.05397000
C	-3.34415200	0.58013200	0.04574000
C	-2.99930100	-0.77125600	-0.04569800
C	-3.96282200	-1.76092700	-0.09962500
H	-3.64943000	-2.79301400	-0.17037600
C	-5.30231400	-1.40223300	-0.06143700
C	-5.67023600	-0.06438500	0.02970400
C	-4.69553800	0.91657100	0.08253600
H	0.78372200	-1.60663100	-0.15513000
H	-0.37498600	3.21353500	0.17511300
H	1.96527600	2.58734900	0.10326700
H	-6.06006700	-2.17213200	-0.10332900
H	-6.71521400	0.20955400	0.05906800
H	-4.94656600	1.96600500	0.15295400
N	-2.37821100	1.58188300	0.09738000
O	-1.68831000	-1.15281600	-0.08456800
C	2.95714800	0.06133100	-0.07615000
C	3.39139000	-1.38415700	-0.10845700
C	4.03799200	1.03006800	-0.17504600
C	4.74412300	-1.58986200	0.57131600
H	3.46460900	-1.70434400	-1.15462000
H	2.65212400	-2.02281300	0.36732800
C	5.33147400	0.68726300	-0.21828500
H	3.79267800	2.07688400	-0.27224300
C	5.81532800	-0.72144200	-0.07324200
H	5.02344500	-2.64228300	0.52887800
H	4.65389200	-1.31872200	1.62554000
H	6.07311800	1.46396700	-0.36086800
H	6.73474900	-0.73853100	0.51432700
H	6.08043100	-1.11768500	-1.06019600



Electronic Energy = -824.851390 EE + Zero-point Energy = -824.565299
Enthalpy = -824.549211 Free Energy = -824.608210

0 1

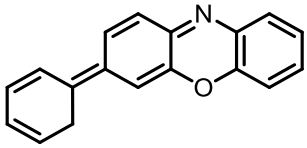
C	-1.65413200	0.45678000	-0.05026100
C	-0.64424900	-0.51028000	-0.10337700
C	0.67696000	-0.14676900	-0.23698900
C	1.04819100	1.19461700	-0.32460800
C	0.05189400	2.15874100	-0.27746300
C	-1.27897100	1.79547300	-0.14908400
C	3.34169700	0.53550600	-0.14058100
C	2.92582500	-0.79430900	-0.05161900
C	3.81930000	-1.79363800	0.26955100
H	3.45330700	-2.80909000	0.32874800
C	5.15590600	-1.48339200	0.49689800
C	5.57900500	-0.16816500	0.41286100
C	4.67329100	0.83796600	0.10034800
H	-0.87080000	-1.56514500	-0.03026400
H	0.32558800	3.20275100	-0.36576500
H	-2.03891200	2.56420200	-0.15256000
H	5.85556000	-2.26992600	0.73988100
H	6.61477300	0.08431000	0.59034800
H	4.99893400	1.86839700	0.03171000
O	1.62109300	-1.14572700	-0.31657300
C	-3.06104900	0.05551700	0.11609500
C	-3.49402400	-1.31830600	-0.34741100
C	-3.96037100	0.82300200	0.75084700
C	-4.96167700	-1.34003100	-0.76460700
H	-3.33823600	-2.02491500	0.47753100
H	-2.87012700	-1.65496100	-1.17468600
C	-5.33883400	0.38125100	0.94228000
H	-3.66156000	1.77085500	1.17954000
C	-5.82916600	-0.64473100	0.24655000
H	-5.28943600	-2.36748500	-0.91893700
H	-5.07502000	-0.82792400	-1.72839700
H	-5.96079700	0.92119300	1.64406500
H	-6.86196200	-0.94865800	0.35697300
N	2.39871100	1.50353100	-0.49300500
H	2.66138200	2.46209200	-0.33115800



Electronic Energy = -824.224351 EE + Zero-point Energy = -823.950864
Enthalpy = -823.935210 Free Energy = -823.993815

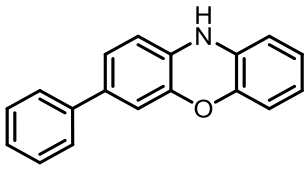
0 2

C	1.63883800	0.45057300	0.02148400
C	0.63444900	-0.51195600	-0.07445400
C	-0.69434700	-0.14130000	-0.02723700
C	-1.09600000	1.20422900	0.13553800
C	-0.06344700	2.16272300	0.25077100
C	1.25414300	1.79856500	0.19542000
C	-3.30532600	0.58714400	0.07057100
C	-2.94163700	-0.76436500	-0.09800300
C	-3.88783600	-1.76716000	-0.22079300
H	-3.55360600	-2.78715700	-0.34848600
C	-5.23067400	-1.43659800	-0.17655500
C	-5.62487200	-0.10590100	-0.00981300
C	-4.67979500	0.88676500	0.11139500
H	0.86511600	-1.55910500	-0.21136200
H	-0.36245000	3.19144500	0.39630100
H	2.01867500	2.55265900	0.31730700
H	-5.97521300	-2.21428000	-0.27170900
H	-6.67626000	0.14268000	0.02371900
H	-4.95368400	1.92455100	0.24088200
O	-1.62877700	-1.12242400	-0.14381700
C	3.04988300	0.06208600	-0.06726200
C	3.44395600	-1.37038600	0.21974100
C	4.00283000	0.90574200	-0.50271100
C	4.87414500	-1.47292500	0.74246000
H	3.35057000	-1.94647100	-0.70925900
H	2.76004300	-1.81713600	0.94013400
C	5.38949400	0.48072200	-0.64907700
H	3.74466200	1.91115800	-0.80756800
C	5.82040300	-0.64549600	-0.07900700
H	5.18752800	-2.51590100	0.76631500
H	4.91108100	-1.11236500	1.77800700
H	6.06651100	1.11370300	-1.20703900
H	6.85876700	-0.94193200	-0.15034200
N	-2.38810700	1.58610900	0.19126100



Electronic Energy = -823.613917 EE + Zero-point Energy = -823.351271
Enthalpy = -823.335711 Free Energy = -823.393567

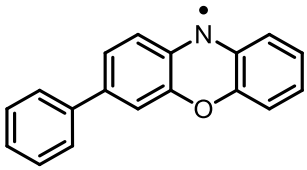
```
0 1
 C                  1.72013600    0.43502200   -0.00000300
 C                  0.65828300   -0.54490900    0.00000000
 C                 -0.63763100   -0.18220900   -0.00000100
 C                 -1.05795900    1.21214500   -0.00000500
 C                  0.00830000    2.18793800   -0.00000900
 C                  1.30126700    1.82279000   -0.00000800
 C                 -3.25723600    0.58437600   -0.00000100
 C                 -2.90983200   -0.76948000    0.00000300
 C                 -3.87009900   -1.76369200    0.00000700
 H                 -3.55328800   -2.79716000    0.00001000
 C                 -5.21043700   -1.40715100    0.00000700
 C                 -5.58183400   -0.06682100    0.00000400
 C                 -4.61049500    0.91833600    0.00000000
 H                  0.87928200   -1.60184600    0.00000400
 H                 -0.29289400    3.22591300   -0.00001400
 H                  2.05008400    2.59962500   -0.00001200
 H                 -5.96639000   -2.17991000    0.00001100
 H                 -6.62777500    0.20509000    0.00000400
 H                 -4.86470200    1.96929100   -0.00000300
 O                 -1.59708900   -1.14866800    0.00000300
 C                  3.04106600    0.05394600   -0.00000100
 C                  3.39956900   -1.41761300    0.00000500
 C                  4.13172900    0.99779400   -0.00000300
 C                  4.86171500   -1.73552900    0.00000500
 H                  2.93825900   -1.90635200   -0.86637600
 H                  2.93826100   -1.90634500    0.86639100
 C                  5.42146200    0.61208900   -0.00000200
 H                  3.91383100    2.05445100   -0.00000600
 C                  5.79907600   -0.79011000    0.00000200
 H                  5.13351000   -2.78338400    0.00000800
 H                  6.20196700    1.36075600   -0.00000300
 H                  6.84831500   -1.05152000    0.00000300
 N                 -2.29489000    1.58845600   -0.00000500
```



Electronic Energy = -823.682234 EE + Zero-point Energy = -823.418469
Enthalpy = -823.403120 Free Energy = -823.460696

0 1

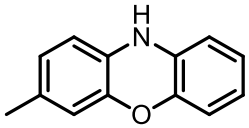
C	-1.72220000	0.41155900	-0.09290500
C	-0.70590700	-0.54690300	-0.13386500
C	0.61208300	-0.17023700	-0.25889500
C	0.97041300	1.17677800	-0.33460900
C	-0.03322800	2.13120900	-0.28243400
C	-1.36326700	1.75315700	-0.16755400
C	3.26861300	0.53829700	-0.12779300
C	2.86531100	-0.79582300	-0.05040400
C	3.76485600	-1.78819500	0.27509200
H	3.40825000	-2.80746100	0.32513800
C	5.09574900	-1.46588300	0.51832400
C	5.50663600	-0.14609200	0.44567900
C	4.59441700	0.85277900	0.12887000
H	-0.92933500	-1.60196000	-0.05225700
H	0.23173800	3.17876000	-0.35209400
H	-2.13149500	2.51411400	-0.16288000
H	5.80056600	-2.24672800	0.76466100
H	6.53792100	0.11558600	0.63546600
H	4.91049800	1.88672600	0.06916500
O	1.56688100	-1.15846200	-0.33125000
C	-3.13892900	0.00250700	0.02376200
C	-3.61077000	-1.13622300	-0.62986000
C	-4.03709700	0.74727100	0.78885600
C	-4.93897400	-1.51792400	-0.52305300
H	-2.93439400	-1.71278300	-1.24737500
C	-5.36589900	0.36762800	0.89457200
H	-3.68241300	1.61742700	1.32560100
C	-5.82278100	-0.76707700	0.23907300
H	-5.28651000	-2.39985900	-1.04397500
H	-6.04444800	0.95448100	1.49888700
H	-6.85910900	-1.06425200	0.32228400
N	2.31972900	1.49907200	-0.48497400
H	2.57142100	2.45916100	-0.31494000



Electronic Energy = -823.054043 EE + Zero-point Energy = -822.802851
Enthalpy = -822.787945 Free Energy = -822.845053

0 2

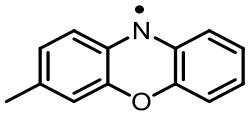
C	-1.70401300	0.39575500	-0.05955100
C	-0.69610800	-0.55597000	0.05631900
C	0.62934000	-0.17003200	0.01194500
C	1.01391700	1.17959100	-0.15081500
C	-0.02446700	2.12649800	-0.26998300
C	-1.34131200	1.74583800	-0.22362200
C	3.23163000	0.59076100	-0.06328400
C	2.88248500	-0.76549000	0.10654800
C	3.83959600	-1.75665700	0.24059100
H	3.51647200	-2.78013000	0.36880000
C	5.17832500	-1.41007800	0.20692300
C	5.55870500	-0.07465300	0.03939400
C	4.60410100	0.90623200	-0.09303800
H	-0.92524800	-1.60126100	0.21187200
H	0.26413800	3.15919800	-0.40766000
H	-2.11791000	2.48875100	-0.34286500
H	5.93122900	-2.17848600	0.31095800
H	6.60745500	0.18571300	0.01425100
H	4.86682100	1.94677500	-0.22337800
O	1.57434900	-1.13872400	0.14270200
C	-3.12478900	-0.00430200	-0.01303500
C	-3.54751800	-1.21127700	-0.57229200
C	-4.07692700	0.81658300	0.59355300
C	-4.88069600	-1.58578600	-0.52669800
H	-2.82825100	-1.84761500	-1.07085700
C	-5.40981400	0.44100800	0.64147400
H	-3.76410400	1.74363700	1.05543200
C	-5.81737300	-0.76141300	0.08104100
H	-5.19046800	-2.52036600	-0.97423600
H	-6.13112300	1.08595900	1.12461800
H	-6.85772800	-1.05376700	0.11724800
N	2.30620500	1.57739100	-0.19409000



Electronic Energy = -631.951878 EE + Zero-point Energy = -631.742121
Enthalpy = -631.729593 Free Energy = -631.780099

0 1

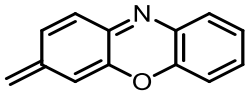
C	3.22256600	-0.30741100	0.12109200
C	2.06266600	-1.06363900	-0.05816600
C	0.83746900	-0.45317600	-0.20204900
C	0.71878300	0.93758500	-0.15951900
C	1.86343900	1.69057900	0.03207100
C	3.10257500	1.07248400	0.16572500
C	-1.66250800	0.69373000	-0.11340800
C	-1.49653000	-0.69186300	-0.15606300
C	-2.56800500	-1.53841500	0.03243600
H	-2.39275700	-2.60436700	-0.00804600
C	-3.83645300	-1.01384100	0.25652500
C	-4.01268800	0.35834900	0.30321900
C	-2.92834600	1.20818100	0.12406400
H	2.10209100	-2.14484500	-0.09631900
H	1.78540000	2.77009900	0.06675500
H	3.98520700	1.68218900	0.30738700
H	-4.67586900	-1.67967300	0.39534500
H	-4.99341200	0.77690800	0.47971000
H	-3.06111800	2.28235300	0.15734400
C	4.55474400	-0.99031100	0.25980000
H	4.55105300	-1.69197400	1.09476800
H	4.80112600	-1.55577800	-0.63990400
H	5.34913800	-0.26618500	0.43052700
O	-0.26507900	-1.24737800	-0.42170600
N	-0.54779800	1.50388600	-0.33978800
H	-0.64191200	2.46958500	-0.06976000



Electronic Energy = -631.323976 EE + Zero-point Energy = -631.126920
Enthalpy = -631.114791 Free Energy = -631.165191

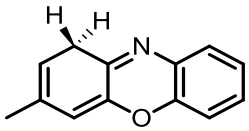
0 2

C	3.21652000	-0.29756900	-0.00004600
C	2.06835900	-1.07265000	-0.00005000
C	0.82187900	-0.46832800	-0.00002600
C	0.66961900	0.93328400	-0.00000200
C	1.85258600	1.70185300	-0.00001400
C	3.08631300	1.10222500	-0.00003900
C	-1.61700200	0.71628200	0.00001200
C	-1.49934500	-0.68984800	-0.00001400
C	-2.60871700	-1.51790700	-0.00001700
H	-2.46047100	-2.58863100	-0.00003900
C	-3.87195900	-0.95389000	0.00000700
C	-4.02423400	0.43630800	0.00003500
C	-2.91899900	1.25472400	0.00003700
H	2.11985200	-2.15342700	-0.00007900
H	1.74113500	2.77729600	-0.00001600
H	3.98088700	1.71216800	-0.00006200
H	-4.74253800	-1.59438500	0.00000500
H	-5.01526700	0.86790900	0.00005400
H	-3.00527400	2.33240000	0.00005700
C	4.57897000	-0.92786600	0.00008600
H	4.51468100	-2.01384400	-0.00124000
H	5.14824700	-0.61825400	-0.87744500
H	5.14705000	-0.62038400	0.87915400
O	-0.27115400	-1.27673200	-0.00003800
N	-0.54042900	1.54475600	0.00001400



Electronic Energy = -630.705053 EE + Zero-point Energy = -630.518144
Enthalpy = -630.506659 Free Energy = -630.554568

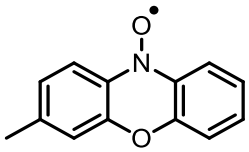
```
0 1
 C                 -3.29553800   -0.36305800    0.00026200
 C                 -2.07381900   -1.14664900    0.00036600
 C                 -0.87336800   -0.55128900   -0.00011300
 C                 -0.72336800    0.90521000   -0.00021200
 C                 -1.95158600    1.68167500    0.00001300
 C                 -3.15020700    1.08873900    0.00032100
 C                  1.55583600    0.70172900   -0.00010400
 C                  1.47084600   -0.69207200   -0.00008800
 C                  2.60403200   -1.48436500    0.00002100
 H                  2.49149200   -2.55935600    0.00003100
 C                  3.85054100   -0.87692200    0.00013700
 C                  3.96012000    0.50972900    0.00014400
 C                  2.81808000    1.29060800    0.00002200
 H                 -2.13350400   -2.22666400    0.00070000
 H                 -1.83443300    2.75625500    0.00002000
 H                 -4.05661400    1.68078800    0.00054400
 H                  4.74025400   -1.49102400    0.00024200
 H                  4.93480600    0.97627600    0.00019400
 H                  2.86556800    2.37087100    0.00003900
 C                 -4.51240300   -0.92947300   -0.00025300
 H                 -4.63329300   -2.00404600   -0.00055900
 H                 -5.40782400   -0.32348100   -0.00040500
 O                  0.25562400   -1.31419600   -0.00026500
 N                  0.41622200    1.50439700   -0.00025500
```



Electronic Energy = -631.912031 EE + Zero-point Energy = -631.703543
Enthalpy = -631.692453 Free Energy = -631.739256

0 1

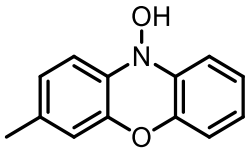
C	3.23684200	-0.30305000	-0.00023700
C	2.00976900	-1.09362400	0.00015000
C	0.79717700	-0.52011200	0.00024400
C	0.62556800	0.93016200	0.00015700
C	3.16848400	1.02966400	-0.00018700
C	-1.65237400	0.68471700	-0.00011500
C	-1.54565900	-0.70568200	0.00011100
C	-2.66517300	-1.51607200	0.00015900
H	-2.53533200	-2.58915300	0.00033800
C	-3.92252700	-0.92859000	-0.00004400
C	-4.05269300	0.45448500	-0.00028400
C	-2.92065200	1.25365700	-0.00031300
H	2.07041700	-2.17396200	0.00017800
H	4.07674300	1.62022900	-0.00060100
H	-4.80240100	-1.55673000	-0.00001800
H	-5.03399900	0.90711800	-0.00044200
H	-2.98565500	2.33305200	-0.00048300
C	4.55580100	-1.03628500	-0.00042400
H	4.40970300	-2.11463700	-0.00525700
H	5.14708100	-0.77608500	-0.87783300
H	5.14314700	-0.78355800	0.88183000
O	-0.31809000	-1.30650600	0.00025600
N	-0.51788900	1.50551700	-0.00010100
C	1.87269200	1.77740100	0.00055400
H	1.81818900	2.44431500	-0.86510800
H	1.81852400	2.44280900	0.86742800



Electronic Energy = -706.510626 EE + Zero-point Energy = -706.308599
Enthalpy = -706.296295 Free Energy = -706.346811

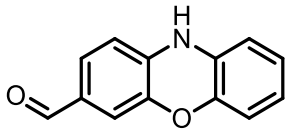
0 2

C	-3.28959500	-0.42158200	0.00005800
C	-2.14747100	-1.21074000	0.00005200
C	-0.89048900	-0.63159000	0.00005200
C	-0.75556900	0.75465700	0.00006900
C	-1.89374100	1.55392900	0.00010600
C	-3.14306600	0.96725400	0.00010300
C	1.63737200	0.46920600	0.00003000
C	1.43750100	-0.91232800	0.00001500
C	2.52140400	-1.77098300	-0.00004200
H	2.33350900	-2.83518400	-0.00006600
C	3.80777200	-1.25400100	-0.00007000
C	4.01013900	0.12122400	-0.00001200
C	2.92877400	0.98368400	0.00004400
H	-2.21109300	-2.29060800	0.00005400
H	-1.75994500	2.62510300	0.00013900
H	-4.02538600	1.59400800	0.00016000
H	4.65227200	-1.92831900	-0.00014000
H	5.01345100	0.52228000	0.00000200
H	3.04481200	2.05678600	0.00006300
C	-4.65801600	-1.04229300	-0.00018700
H	-4.60099100	-2.12870900	0.00163300
H	-5.22464100	-0.72947200	0.87743300
H	-5.22294900	-0.73239000	-0.87995200
O	0.18945400	-1.46807300	0.00014400
N	0.52645300	1.32768400	-0.00008200
O	0.67625900	2.58233600	-0.00015200



Electronic Energy = -707.121962 EE + Zero-point Energy = -706.907831
Enthalpy = -706.894289 Free Energy = -706.947141

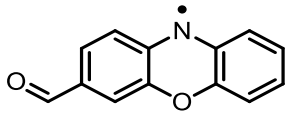
```
0 1
 C                  3.24919300   -0.43234700    0.17095500
 C                  2.12595200   -1.21031000   -0.11220400
 C                  0.89549700   -0.62256800   -0.29975300
 C                  0.74064300    0.76101900   -0.20499000
 C                  1.84260600    1.53831900    0.09672800
 C                  3.08577000    0.94000300    0.27775100
 C                 -1.62218300    0.44371400   -0.14001200
 C                 -1.40868000   -0.93187500   -0.23602600
 C                 -2.43019100   -1.82358400    0.01285400
 H                 -2.22141300   -2.88076500   -0.07120700
 C                 -3.68992100   -1.34906500    0.35875400
 C                 -3.90495300    0.01384800    0.46972400
 C                 -2.87291400    0.91248600    0.22576100
 H                  2.19630300   -2.28748500   -0.19232600
 H                  1.72333900    2.60642100    0.19218800
 H                  3.94044500    1.56251100    0.50785800
 H                 -4.49293100   -2.04733300    0.54631800
 H                 -4.87904300    0.38984400    0.74892600
 H                 -3.02753800    1.97603800    0.31958500
 C                  4.59064000   -1.08495500    0.35764700
 H                  4.55649000   -1.82933100    1.15389600
 H                  4.90731600   -1.59556700   -0.55270600
 H                  5.35073700   -0.34958200    0.61410900
 O                 -0.17932600   -1.42298500   -0.60886200
 N                 -0.54269900    1.28955300   -0.47981000
 O                 -0.70433000    2.59511000   -0.01115400
 H                 -0.79431600    3.12328400   -0.81098400
```



Electronic Energy = -705.970634 EE + Zero-point Energy = -705.778919
Enthalpy = -705.766186 Free Energy = -705.817273

0 1

C	-2.90546200	-0.25702700	-0.04478500
C	-1.76220400	-1.04337400	0.09600000
C	-0.52705100	-0.45033900	0.20851500
C	-0.40304100	0.94277800	0.16684400
C	-1.54750100	1.72202500	0.01471300
C	-2.79078900	1.12759900	-0.08505900
C	1.97901000	0.68194900	0.09333600
C	1.80820900	-0.70183800	0.13797200
C	2.87822900	-1.55079500	-0.04352900
H	2.70191200	-2.61641800	-0.00183100
C	4.14833400	-1.02718200	-0.26180000
C	4.32847700	0.34418400	-0.30844500
C	3.24474900	1.19668200	-0.13615500
H	-1.82762000	-2.12382600	0.12993600
H	-1.44688200	2.79948400	-0.01597200
H	-3.68764500	1.72093700	-0.19690200
H	4.98721400	-1.69462700	-0.39545100
H	5.31097600	0.76025900	-0.47968200
H	3.37880200	2.27051600	-0.17125900
O	0.57327900	-1.25296800	0.39939100
N	0.86019600	1.49428000	0.29984200
H	0.95930600	2.47396900	0.09072200
C	-4.22515700	-0.90324800	-0.15285300
H	-4.20513600	-2.00934200	-0.10771400
O	-5.26666900	-0.31320500	-0.28179800



Electronic Energy = -705.340076 EE + Zero-point Energy = -705.161026
Enthalpy = -705.148747 Free Energy = -705.199358

0 2

C	2.89060800	-0.24766100	-0.00001000
C	1.76159400	-1.05255400	0.00003400
C	0.51179700	-0.46382300	0.00002100
C	0.35313500	0.94222600	-0.00004400
C	1.52813500	1.73281600	-0.00009100
C	2.76668000	1.15280000	-0.00007100
C	-1.93112500	0.70713500	-0.00001600
C	-1.80707200	-0.69812500	0.00005100
C	-2.91315500	-1.53147900	0.00009900
H	-2.76193000	-2.60161600	0.00014900
C	-4.17616800	-0.96980900	0.00008200
C	-4.33466200	0.42100800	0.00001600
C	-3.23392500	1.24356000	-0.00003200
H	1.83965100	-2.13264300	0.00008200
H	1.39628000	2.80563500	-0.00014100
H	3.67025200	1.74652500	-0.00010100
H	-5.04518600	-1.61237300	0.00011900
H	-5.32775500	0.84738900	0.00000200
H	-3.32306300	2.32086600	-0.00008400
O	-0.57689600	-1.27613900	0.00006800
N	-0.85672400	1.53880900	-0.00006400
C	4.22570500	-0.87615600	0.00000400
H	4.22004400	-1.98271800	0.00006000
O	5.26183100	-0.26415500	-0.00005300